NSB2008
Nordic Symposium on Building Physics 2008

Proceedings of the 8th Symposium on Building Physics in the Nordic Countries

Volume 1
Monday, June 16

Copenhagen, June 16-18, 2008

Carsten Rode, editor

The Organizing Committee

Carsten Rode, Technical University of Denmark (chairman)
Svend Svendsen, Technical University of Denmark
Eva B. Møller, The Danish Society of Engineers, IDA, Society for Building Physics
Torben V. Rasmussen, Danish Building Research Institute, Aalborg University (since Dec. 2007)
Morten H. Hansen, Danish Building Research Institute, Aalborg University (until Dec. 2007)
Dan Kallehave, Technical University of Denmark (student help, secretary to the Committee)

Contact Address

Reference to papers

Foreword

The 8th Symposium on Building Physics in the Nordic Countries was held June 16-18, 2008 in Copenhagen, Denmark. The Symposium has been organized jointly by The Technical University of Denmark; The Danish Society of Engineers' Society for Building Physics; and the Danish Building Research Institute, Aalborg University.

The Symposium in Copenhagen invited contributions regarding:
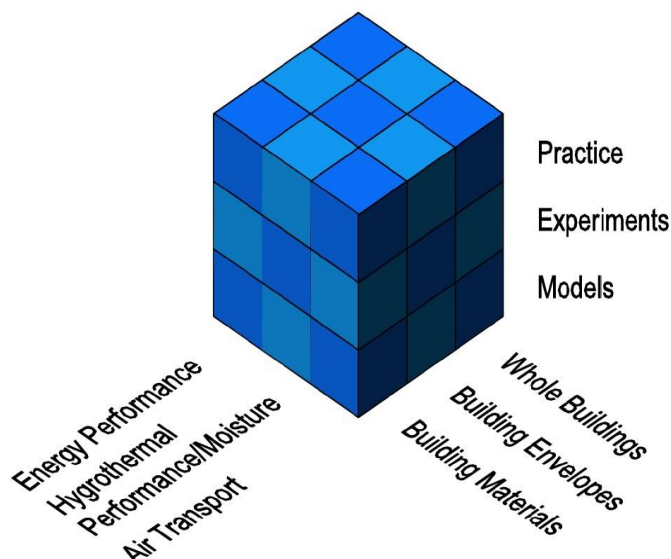
Research results on
- *Energy performance*
- *Hygrothermal performance/moisture*
- *Air transport*

Covering building physical heat, air and moisture transfer in
- *Building materials*
- *Building envelopes*
- *Whole buildings*

With special emphasis on
- *Models*
- *Experiments*
- *Practice*

The Symposium was held in the format of two days as a traditional conference with oral presentations followed by brief discussions. The third day was devoted to the practical use of research results, and the programme on this day was laid such as to allow for more discussion of the presented results, not least with a scope to debate the practical implications.

The Symposium follows previous symposia held in Lund 1987, Trondheim 1990, Copenhagen 1993, Helsinki 1996, Gothenburg 1999, Trondheim 2002 and Reykjavik 2005. While the symposia are always arranged in one of the Nordic countries, they are increasingly attracting participants from other countries. Out of more than 250 abstracts, some 182 papers were eventually prepared for the 2008 Symposium in Copenhagen, half of them by researchers from other than the Nordic countries.

The venue of the Symposium was the meeting centre of the Danish Society of Engineers, IDA, on the harbour front of central Copenhagen. By providing this facility, IDA constituted the main sponsor of the Symposium, and their cooperation is gratefully acknowledged!

The organizers also would like to thank the participants of the scientific committee and people who have assisted in reviewing papers. Their contributions have been very important to ensure the quality of the Symposium.

Personally, I would like to thank my colleagues in the organizing committee for their true dedication to the project.

Copenhagen, June 2008   *Carsten Rode*
                                                     Chairman of the organizing committee

Scientific Committee

Prof. Anker Nielsen, Chalmers University of Technology
Dr. Berit Time, SINTEF Byggforsk
Prof. Carl-Eric Hagentoft, Chalmers University of Technology
Sen.Res.Fel. Chris Sanders, Glasgow Caledonian University
Prof. Georg-Wilhelm Mainka, University of Rostock
Prof. Gerd Hauser, Fraunhofer Institute for Building Physics
Prof. Gudni Johannesson, Royal Institute of Technology in Stockholm
Dr. Gulten Manioglu, Istanbul Technical University
Prof. Hugo Hens, Katholieke Universiteit Leuven
Prof. Ingemar Samuelson, SP Technical Research Institute of Sweden
Prof. Jan Carmeliet, Technische Universiteit Eindhoven
Prof. Jan Vincent Thue, Norwegian University of Science and Technology
Prof. Jesper Arfvidsson, Lund University
Prof. John Grunewald, Technische Universität Dresden
Prof. Kalema Timo, Tampere University of Technology
Prof. Klaus Sedlbauer, Fraunhofer Institute for Building Physics
Prof. Lars-Olof Nilsson,Lund University
Assoc. Prof. Maria Wall, Lund University
Dr. Miimu Airaksinen, Technical Research Centre of Finland
Dr. Monika Woloszyn,University of Science and Technology - INSA Lyon
Prof. Paul Fazio, Concordia University
Prof. Per Heiselberg, Aalborg University
Dr. Phalguni Mukhopadhyaya,National Research Council Canada
Prof. Shuichi Hokoi, Kyoto University
Sen.Res. Targo Kalamees, Tallinn University of Technology
Assoc. Prof. Dr. Thomas Bednar, Vienna University of Technology
Prof. Dr. Holger Wallbaum, Swiss Federal Institute of Technology - ETH Zürich
Prof. Arild Gustavsen, Norwegian University of Science and Technology
Dr. Juha Vinha, Tampere University of Technology
Dr. Morten Hjorslev Hansen, DUKO · Dansk Undertagsklassifikationsordning

Reviewers

The following experts have contributed to the review of papers. Their important contribution is gratefully acknowledged!

Hashem Akbari ; Steve Cornick; Andre Desjarlais; Heiko Fechner; Diana Fisler; Hua Ge; Stig Geving; William Healy; Bengt Hellström; Jonas Holme; Ronald Krpan; Mark Lawton; Qinru Li; Yang Li; Uwe Meinhold; Qian Mao; Wahid Maref; Andreas Nicolai; Mostafa Nofal ; Vildan Ok; Seyhan Onbaşıoğlu; Gul Koclar Oral; Anil Parekh; İsmail Cem Parmaksızoğlu; Hans Petzold; Jiwu Rao; Cynthia Howard Reed; Ian Ridley; Patrick Roppel; Madeleine Rousseau; Uli Ruisinger; Prabal Talukdar; Sergio Vera; Xiangjin Yang; Alpin Yener & Zerrin Yılmaz

Table of Contents

Monday, June 16

Session M1A – Energy Performance of Materials

Session M2A – Energy Performance of Constructions

Session M3A – Energy Performance of Windows

Session M4A – Air Flow in Windows

Session M1B – HVAC System Interaction

Session M2B – Exterior climate interaction

Session M3B – Exterior Climate Interaction / Durability of Surfaces

Session M4B – Thermal Conductivity / HM Salt

Session M1C – Air Flow Assessment

Session M2C – Air in Rooms

Session M3C – Air Flow in The Building Envelope / Air Flow Assessment

Session M4C – Insulation Materials

Tuesday, June 17

Session T4A – Low Exergy Buildings

Session T1B – Mass Exchange 1

Session T2B – Mass Exchange 2 / Tools and Protocols

Session T3B – Building Envelope Issues

Session T4B – Indoor Humidity and Buffering

Session T1C – Silicate Materials and Structures 1

Session T2C – Silicate Materials and Structures 2 / Mould

Session T3C – Measuring Techniques / Wood Materials

Session T4C – Wood Constructions

Wednesday, June 18

Session W1A – Design and Development of Energy Efficient Buildings

Session W2A – Measured Energy Performance of Buildings

Session W3A – Energy Savings in Existing Buildings

Session W4A – Windows and Facades

Session W1B – Moisture Safety

Session W2B – Moisture Sensitive Construction

Session W3B – Building Envelope Issues and Innovation

Session W4B – Innovative Products

Session W1C – Energy Performance in Cold Climate

Session W2C – Heat Capacity and Energy Performance

Session W3C – Air Tightness and Building Envelope

Session W4C – Indoor Humidity in Practice

LIST OF AUTHORS

NAME	VOLUME 1	VOLUME 2	VOLUME 3
ABELÉ, Charlotte		731	
ABUKU, Masaru	245		
ABUKU, Masaru	307		
AFSHARI, Alireza	385		
AHO, Hanna			1405
AIRAKSINEN, Miimu	409		1421
ALLARD, Francis	175		
ALTAMIRANO-MEDINA, Hector			1205
ALTURKISTANI, Arslan		1031	
AMATO, Alex			1151
ANDRESEN, Inger	49		
ANTRETTER, Florian	347		
ARFVIDSSON, Jesper		975	1181
ARNESEN, Heidi	1		
BAKER, Paul	237	793	
BANKVALL, Claes			1389
BARTLETT, Karen		943	
BEDNAR, Thomas	363, 425	573, 581	1103
BENGTSSON, Peter		999	
BERINGER, Jan			1309
BJÖRK, Folke	465, 473		
BLOCKEN, Bert	159, 221, 261, 339, 433	707	
BLOM, Peter		755	
BLUDAU, Christian	213, 441		
BORODIŅECS, Anatolijs		889	
BOSSCHAERTS, Walter	339		
BRAND, Christian		567	
BRAU, Jean		731	
BRAUNS, Janis		1007	
BROSTRÖM, Tor			1143
BURKE, Stephan		975	
BURLINGIS, Arunas			1341
BØHLERENGEN, Trond		761	
CARMELIET, Jan	159, 221, 261, 339	707, 833, 865, 959, 983, 1015, 1023	
CAUBERG, Johannes J. M.	9		
ČERNÝ, Robert	293, 315, 449	895, 903	
CHAUBEY, Yogendra P.		943	
CHIOGNA, Michela			1135

NAME	VOLUME 1	VOLUME 2	VOLUME 3
CHRISTENSEN, Georg			1317
CHRISTENSEN, Jørgen E.		551	
CLAESSON, Johan	17, 25	975, 999	
COPELAND, Curt		1055	
CORNICK, Steve		739	
DAVIES, Mike			1205
de FREITAS, Vasco Peixoto		809, 911	
De MEULENAER, Veerle			1261
De PAEPE, Michel	167	699, 715	
de WIT, Martin	221, 339		
DEFRAEYE, Thijs	159, 261		
DERLUYN, Hannelore		865, 959	
DEROME, Dominique	261, 369	707, 833, 959, 983, 1015, 1023	
DESEYVE, Christoph	425		
DIELS, Stef		559	
DIEPENS, Jan	433		
DREYER, Jürgen		573	1103
DRZIK, Milan	33		
DUFOUR, Marianne Bérubé	369		
EINSTABLAND, Håkon		761	
EL KHANAGRY, Ramez		1055	
ELSEN, Patricia			1261
ENOCHSSON, Tomas	465		
ERIKSEN, Marlene Stenberg Hagen	481		
ERIKSON, Robert		1047	
ESKOLA, Lari			1095
ESSAH, Emmanuel Adu	237	793	
FAUCHOUX, Melanie T			1269
FAZIO, Paul	393	943, 1031	
FIALA, Lukáš	293, 315		
FRATTARI, Antonio			1135
FUJITA, Koji		527	
GALBRAITH, Graham H.	237	793	
GEVING, Stig		801	1213, 1229
GRAU, Karl E.		605	
GRUNEWALD, John	299		
GUDMUNDSSON, Kjartan		967	
GUDUM, Charlotte	41		
GUIMARÃES, Ana Sofia		911	

NAME	VOLUME 1	VOLUME 2	VOLUME 3
GUNNARSEN, Lars B.	385		
GUSTAVSEN, Arild	331, 355, 417	497, 723, 761, 951	
GUYER, Robert		833	
HACHEM, Caroline		943	
HAGENTOFT, Carl-Eric			1237
HANSEN, Klaus		605	
HANSEN, Kurt Kielsgaard	481	661	
HAUPT, Wolfram	347		
HECHT, Clemens			1301
HEISELBERG, Per	143, 151		
HEKKANEN, M.			1119
HELLWIG, Runa Tabea	377		1127
HENS, Hugo			1261
HOKOI, Shuichi	307	543	
HOLM, Andreas	347	825, 841	1127, 1277
HOLME, Jonas		801	1213, 1221
HOLOPAINEN, Riikka			1119, 1325
HOLOPAINEN, Riikka			1119, 1325
HOLØS, Sverre B		755	
HOPPE, Michaela		505	
HOVDE, Per Jostein		951	
HVIID, Christian, Anker	119		
HÖFER, Tanja		573	
HAASE, Matthias	49		1151
IITTI, Hanna		935	
IWAMAE, Atsushi		527, 747	
JANSSEN, Hans	245	653, 669, 677, 865	
JANSSENS, Arnold	167	559, 699, 715, 769	
JANSSON, Anders			1253
JELLE, Bjørn Petter		951	
JENSEN, Eirik Sandberg			1317
JENSEN, Rasmus Lund	143, 151		
JENSSEN, Jon A		801	1213
JERMAN, Miloš	449		
JÓHANNESSON, Gudni	79	613, 967	
JOHANSSON, Dennis	199		
JOHANSSON, Peter S.		857	
JOHANSSON, Sanne		919	
JOHNSEN, Kjeld	111	605	
JUNKER, Elmar	377		

NAME	VOLUME 1	VOLUME 2	VOLUME 3
KALAGASIDIS, Angela Sasic		793	1237, 1365
KALAMEES, Targo		777	1095, 1413
KALEMA, Timo		535	
KALMÁR, F.		637	
KALMÁR, T.		637	
KALYANOVA, Olena	143, 151		
KARAGIOZIS, Achilles		1015	
KARBAUSKAITE, Jurate			1341
KARLSSON, Henrik		519	
KEHRER, Manfred	207		
KILIAN, Ralf		841	
KJELLSTRÖM, Erik			1349
KLOCH, Niels Peter			1317
KNUDSEN, Henrik N.		489	
KONDER, Hannes	363		
KONIORCZYK, Marcin		967	
KORONTHALYOVA, Olga	285	685, 817	
KORPI, Minna			1095, 1397, 1405, 1413
KOSS, Lev	277		
KOVERDYNSKY, Vit	457		
KRAGH, Jesper	95	511	1071, 1173
KRELSINS,Andris		889	
KRUS, Martin	183		
KUMARAN, Kumar		1055	
KUMARAPERUMAL, Ayyapan N	237		
KURNITSKI, Jarek		777	1095, 1397, 1413
KVANDE, Tore			1197, 1221
KWIATKOWSKI, Jerzy		661	
KÜNZEL, Hartwig M.	213, 253, 441		
LARSON. Kennard G.		1047	
LAURSEN, Theresa Back	481		
LAUSTSEN, Jacob B.	95, 103, 111		1173
LAVERGE, Jelle		559	
LAZZAROTTO, Alberto	79		
LEIJONHUFVUD, Gustaf			1143
LEIMER, Hans-Peter			1373
LENGSFELD, Kristin	183		
LESNYCH, Natalia	277		
LYLYKANGAS, Kimmo			1063, 1325

NAME	VOLUME 1	VOLUME 2	VOLUME 3
LÄHDESMÄKI, Kimmo		927, 935	
MADĚRA, Jiří	449		
MAINKA, Georg-Wilhelm		849, 1039, 1047	
MANIOGLU, Gulten			1357
MANNING, Marianne		739	
MARIO, Sofic		581	
MARQUARDT, Helmut		849	
MATIASOVSKY, Peter	33, 285	685	
MATSUSHITA, Takayuki		527	
MELØYSUND, Vivian		761	
MIHALKA, Peter	33	817	
MIJAKOWSKI, Maciej		693	
MINIOTAITE, Ruta	269		
MIXOUDIS,Georgios	127		
MJÖRNELL, Kristina			1181, 1253
MOENS, Jan		769	
MOGA, Ioan	87		
MOGA, Ligia	87		
MOLINARI, Marco		613	
MOONEN, Peter		865	
MORKVENAS, Romaldas			1341
MORTENSEN, Dorthe Kragsig	191		
MORTENSEN, Lone H.	323		
MUKHOPADHYAYA, Phalguni		1055	
MUMOVIC, Dejan			1205
MØLLER, Eva B.			1189
MAALOUF, Chadi	175		
MAAS,Reinier	433		
NEALE, Adam	261	707	
NEUHAUS, Edgar			1293
NEWMAN, Paul J.		1055	
NICOLAI, Andreas	299		
NIELSEN, Anker	57, 229		1365
NIELSEN, Toke Rammer	119, 135, 191	511	
NIEMINEN, Jyri			1063, 1325
NIK, Vahid Moussavi	57		1365
NILSEN, Tom-Nils		951	
NILSSON, Lars-Olof		857	
NILSSON, Stefan F.			1237
NORE, Kristine		991	

NAME	VOLUME 1	VOLUME 2	VOLUME 3
NORENG, Knut			1197, 1221
NOUIDUI, Thierry		825	
NOVIKS, Juris		889	
NYTSCH-GEUSEN, Christoph		825	
NÖSKE, Florian			1277
OJANEN, Tuomo		927, 935	
OLESEN, Bjarne W.	71		
OLSEN, Lars			1349
ORESZCZYN, Tadj			1205
OSTERMEYER, York		567	
PADFIELD, Tim			1429
PASANEN, Pertti	409		
PAVLÍK, Zbyšek	315	903	
PAVLÍKOVÁ, Milena	293, 315	903	
PEDERSEN, Frank		589, 605	
PEGGE, Evelien	339		
PERSOON, Jan	221		
PERSSON, Camilla	17		
PETERSEN, Steffen		597	1159
PEUHKURI, Ruut	323	927, 935	
PHILLIPSON, Mark			1087
PIETRZYK, Krystyna	401		
PIOT, Amandine		731	
PITTARELLO, Emanuele	71		
PLAGGE, Rudolf		881	
PUSKAR, Anton		685	
PYLSY, Petri		535	
PAAJANEN, Leena		935	
RADON, Jan		841	
RAMOS, Nuno		809	
RAO, Jiwu	393	943, 1031	
RASMUSSEN, T. Valdbjørn			1079
REIDHAV, Charlotte	25		
REINTHALER, Petra			1301
RELANDER, Thor-Oskar	417	497	
RIDLEY, Ian			1205
RIESNER, Katrin		1047	
ROCENS, Karlis		1007	
RODE, Carsten	323, 481	653, 661	1333
ROELS, Staf	245	669, 677	

NAME	VOLUME 1	VOLUME 2	VOLUME 3
ROLSTAD, Anna Næss		761	
ROSE, Jørgen			1071
ROSENAU, Britta		1039	
ROUSSEAU, Madeleine		739	
ROUX, Jean-Jacques		661	
RÖSLER, Doris	183		
SAELENS, Dirk			1261
SAGER, Christina		629	
SALMINEN, Kati		927, 935	
SAMUELSON, Ingemar			1253
SANDERS, Chris			
SANDERS, Chris H.	237	793	1087
SANDIN, Kenneth		919	
SANDLAND, Knut Magnar			1229
SANEINEJAD, Saba		1015	
SANTOS, Inês P.	95, 103, 111		
SAUR, Alexandra			1309
SCHEFFLER, Gregor A.		881	
SCHELLEN, Henk			1293
SCHILD, Kai			1165
SCHMIDT, Dietrich		621, 645	
SCHMIDT, Thomas	207		
SCHÖBERL, Helmut			1103
SEDLBAUER, Klaus		825	1127, 1277, 1309
SIKANDER, Eva			1389
SILAROVA, Sarka		785	
SIMONSON, Carey J			1269
SKOGSTAD, Hans Boye			1285
SLANINA, Petr		785	
STANKEVICIUS, Vytautas	65		1341
STEEMAN, Hendrik-Jan		699, 715	
STEEMAN, Marijke	167	699	
STEIGER, Simone	377		
STESKENS, Paul W.M.H.		653	
STRANDER, Tomi		935	
SUZUKI, Hirotaka		747	
SVENDSEN, Svend	95, 103, 111, 119, 135	511, 597	1071, 1173
SZABO, Daniel		685	
TAKADA, Satoru	307		
TALEV, Goce	331	723	

NAME	VOLUME 1	VOLUME 2	VOLUME 3
TARDIF, Michel	369		
TENPIERIK, Martin J.	9		
TESÁREK, Pavel		895	
THIVIERGE, Constance		1023	
THORIN, Marcus			1237
THUE, Jan Vincent	331, 417	497, 723, 991	
TIME, Berit			1229
TOMMERUP, Henrik			1111
TOPP, Claus	191		
TORÍO, Herena		645	
TORVI, David A			1269
TRABERG-BORUP, Steen	111, 385		
UVSLØKK, Sivert	1, 355		1285
VALANCIUS, Kestutis	65		
van BELLEGHEM, Marnix		699	
van den BOSSCHE, Nathan		769	
van den ENGEL, Peter	127		
van der SPOEL, Wim H.	9		
van HOOFF, Twan	221		
van REENEN, David		1055	
van SCHIJNDEL, Jos			1293, 1381
VANLONDERSEELE, Els		559	
VENDELBOE, Morten V.	135		
VENZMER, Helmuth	277		
VERA, Sergio	393		
VESELSKY, Juraj		685	
VIITANEN, Hannu		927, 935	
VILNITIS,Martins		889	
VINHA, Juha		927, 935	1095, 1245, 1397, 1405, 1413
VLADYKOVA, Petra			1333
von WERDER, Julia	277		
VRÁNA, Tomas	473		
WADSÖ, Lars		919	
WALLBAUM, Holger		567	
WARGOCKI, Pawel		489	
WEITZMANN, Peter	71		
WILLEMS, Wolfgang			1165
WITTCHEN, Kim B.		605	
WOLOSZYN, Monika		661, 731	

NAME	VOLUME 1	VOLUME 2	VOLUME 3
WURTZ, Etienne	175		
YILMAZ, Zerrin			1357
ZALOK, Ehab		1055	
ZILLIG, Wolfgang		959, 983	
ZIRKELBACH, Daniel	213, 253, 441		
ZMEUREANU, Radu	369		
ØYEN, Cecilie Flyen			1197
ÅHS, Magnus		873	

Thermal insulation performance of reflective material layers in well insulated timber frame structures

Sivert Uvsløkk, Senior Scientist.
SINTEF Bygforsk;
sivert.uvslokk@sintef.no

Heidi Arnesen, Research Scientist
SINTEF Bygforsk;
heidi.arnesen@sintef.no

KEYWORDS: roof, wall, floor, heat transfer, air cavity, reflective material

SUMMARY:
The paper presents some results from a study of the thermal insulation performance of air cavities bounded by thin reflective material layer integrated in well insulated roofs, ceilings, walls and floors. By use of reflective materials closed air cavities may provide a thermal resistance of approximately 0.6 m²K/W in roofs and ceilings, equivalent to 20 mm mineral wool, and approximately 0.8 m²K/W in walls, equivalent to 30 mm mineral wool. In structures with heat flow direction downwards, like in floors, the potential R-value of a closed air layer is much higher as the natural convection may bee very low due to thermal stabile air layers.

1. Introduction

The interest for single or multi layer reflecting products for use in building structures has increased, even in regions with cold climate and well insulated building envelopes, partly because of a general lack of conventional thermal insulation material due to high activity in the building industry. Another reason may be an overestimated marketing of the thermal performance of these products due to lack of knowledge of building physics in some enthusiastic manufacturing organisations, testing institutes as well as in some certification bodies.
A goal of the study is to show both the possibilities and the limitations of these reflective products used in well insulated building structures.

2. Heat transfer mechanisms in air cavities

A reflecting material layer will improve the thermal resistance of a neighbouring air gap by reducing the long wave radiation heat transfer. For cavities in roofs and walls the improvement is however limited as the natural convection will increase and dominate the heat transfer when the air cavity thickness increase beyond a certain limit. In general there are four main mechanisms of heat transfer through a cavity or a building structure:

- conduction in solid materials or gasses
- long wave radiation in cavities
- natural convection inside closed cavities
- air leakage through the structure

The sum of heat flow of the three first mechanisms is called thermal transmittance, U-value, and is included when estimating the thermal resistance, R-value, of the cavity or the whole building structure. The heat loss by air leakages through the cavity or the structure is not to be included in the terms R-value and U-value, but has to be treated as air infiltration/exfiltration heat loss of a building.

To prevent heat loss by air leakages timber frame structures have to be made airtight by use of special layers, normally a vapour barrier on the hot side and a wind barrier on the cold side. In all calculations made as basis for the figures in this paper the heat loss from air leakage is set to zero.

As shown in figure 1 long wave radiation is the dominating heat transfer mechanism in closed air cavities bounded by ordinary building materials with emissivity $\varepsilon \geq 0.9$.

By use of a reflective foil, with emissivity 0.05, at one face of the cavity the heat flow by radiation is dramatically reduced to approximately 5 % as shown in figure 2. The heat transfer by convection does increase with the thickness of the cavity and will limit the R-values of such cavities in roofs and walls. The heat transfer has been calculated according to ISO 15099:2003, see section 3.
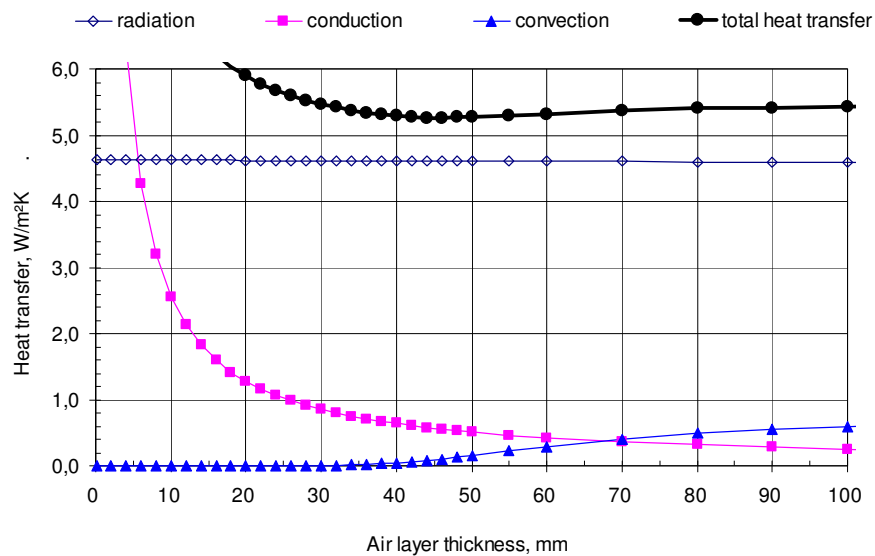
FIG. 1: Estimated heat transfer in a closed air cavity bounded by ordinary materials, $\varepsilon = 0.9$, for various thickness of the air cavity. Total timer frame thickness is 200 mm.
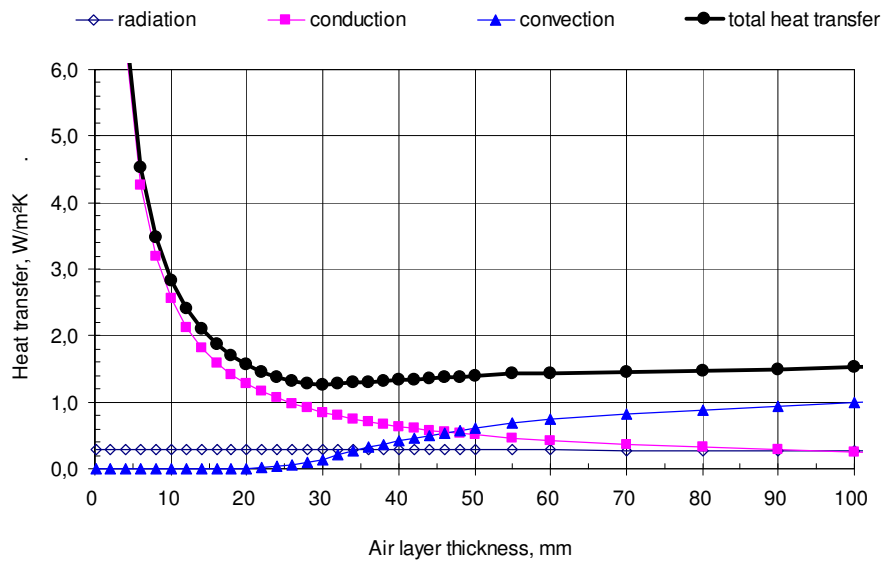
FIG. 2: Estimated heat transfer in a closed air cavity bounded by a reflective material at one face, $\varepsilon = 0.05$, for various thickness of the air cavity. Total timer frame thickness is 200 mm.

3. Estimating R-values of closed air cavities

3.1 Methods

The total heat flow through an air cavity depend on several parameters like

- thickness and height of the air cavity
- emissivity of the air cavity bounding materials
- R-value of the rest of the structure
- indoor- and outdoor temperatures
- direction of the air cavity and the heat flow

These parameters are all influencing the various heat transfer mechanisms. The resulting R-value of the cavity is therefore not a material property of the reflective product, but a property of the complete structure for the given heat flow direction and ambient temperatures. The thermal resistance, R-value, of the cavity and the whole structure can be calculated according to international standards or measured in laboratory by use of hot-box.

The values shown in this paper has been calculated according to *ISO 15099 Thermal performance of windows, doors and shading devices – Detailed calculations*, which is the most updated international standard for heat transfer in closed cavities.

EN ISO 6946:1996, Building components and building elements, Thermal resistance and thermal transmittance, Calculation method, which is the normally used standard for calculating R-values and U-values for building structures may also be used, but the algorithms for natural convection are more simplified and gives some lower cavity R-values compared with *ISO 15099.*

3.2 Accurate measurements require a large hotbox.

The heat flux (W/m²K) through an air cavity with natural convection is not evenly distributed over the cavity area. Due to the convection the temperature gradients will be changed at the top and bottom of the air gap. At the bottom of the cavity the temperature gradient will increase on the warm side giving a locally increased heat flux from the indoor environment into the cavity. On the cold side of the cavity the temperature gradient and heat flux will be somewhat reduced. At the top of the air cavity the situation will be opposite leading to a locally increased heat flux from the air cavity to the outdoor environment. The total heat flux through the entire cavity and the system will increase when natural convection is developed.

To get an accurate measurement of the thermal resistance of a wall with air cavities it is therefore essential that the metering area of the hotbox is large enough to cover the full height of the cavities. To get representative results the measurements need to be carried out on specimen of full height. A metering area covering only the central part of the cavity will give an overestimated R-value. See fig. 6.

3.3 Misinterpreted laboratory tests has led to wrong R-values

In some comparative tests on roof sections which have been carried out at some laboratories the heat loss by air leakages has been included when estimated R-values and U-values of the products. A multi layer reflective product with sealed joints has been compared with pure mineral wool with neither a vapour barrier nor a wind barrier to prevent air leakages. As mineral wool is an air permeable material, most of the heat loss was caused by air leakage. The heat inputs needed to achieve the same temperature difference across the two roofs were approximately similar. This observation has been misinterpreted and led to the false idea that multilayer reflective products with a thickness of approximately 10 mm have the same R-value as 200 mm conventional mineral wool. This is physically impossible for walls and roofs as natural convection will develop and dominate the heat transport when the air cavity thickness exceed approximately 20 mm for roofs and 30 mm for walls. See fig. 4.

3.4 Theoretical calculations

Results from the theoretical calculations are presented in diagrams in the figures 1 to 8. Comparison with hot-box measurements are shown in figures 4 and 5. Main conditions for the calculation shown in fig. 1 to 6 are:

- total thickness of conventional insulation and air cavity is constant 200 mm

- thermal conductivity of the conventional insulation are 0,037 W/mK

- no air leakages through the cavity or the structure

- the emissivity of the reflective layer has been set to 0,05 (except for fig. 6)

- indoor and outdoor temperatures are +20 °C and 0 °C respectively (except for fig. 7)
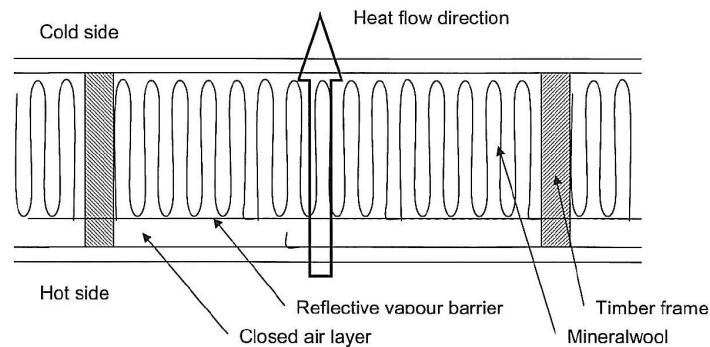
FIG. 3: Estimated heat transfer in a closed air cavity bounded by a reflective material at one face, $\varepsilon = 0.05$, for various thickness of the air cavity. Total timer frame thickness is 200 mm.
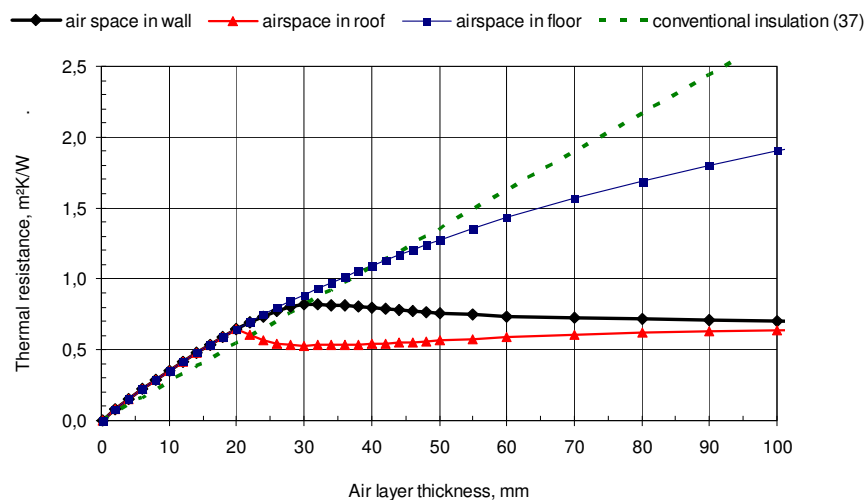
FIG. 4: Estimated thermal resistance of closed air cavities in roofs, walls and floors compared with the thermal resistance of conventional insulation material. The air cavities is bounded by a reflective material at one face, $\varepsilon = 0.05$. Total timer frame thickness 200 mm.

3.5 Direction of heat flow

As shown in figure 3 the R-value of a closed air cavity facing a thin reflective layer is strongly dependent of the heat flow direction. The resistance is equivalent with a conventional thermal insulation layer with a thickness of approximately 30 mm for walls and approximately 20 mm for roofs and ceilings. Increasing the air cavity

thickness beyond these limits will not increase the thermal resistance of the cavity due to the development of natural convection.

In structures with heat flow direction downwards, like in floors, the potential R-value is much higher as the natural convection may bee very low due to thermal stabile air layers.

3.6 Comparison between calculation and measurement

The measured results shown in fig. 5 and 6 are from hot box measurements on a timber frame wall of full height, 2.4 m, with a reflective vapour barrier and a closed air cavity between the vapour barrier and the indoor cladding. The thickness of the conventional mineral wool insulation was 153 mm. Measurements were performed for alternative thicknesses of the air cavity. A comparison of calculated and measured U-values of the wall shows good agreement. The Measured U-values are between 1 % and 6 % lover than the calculated one as shown in fig. 5.
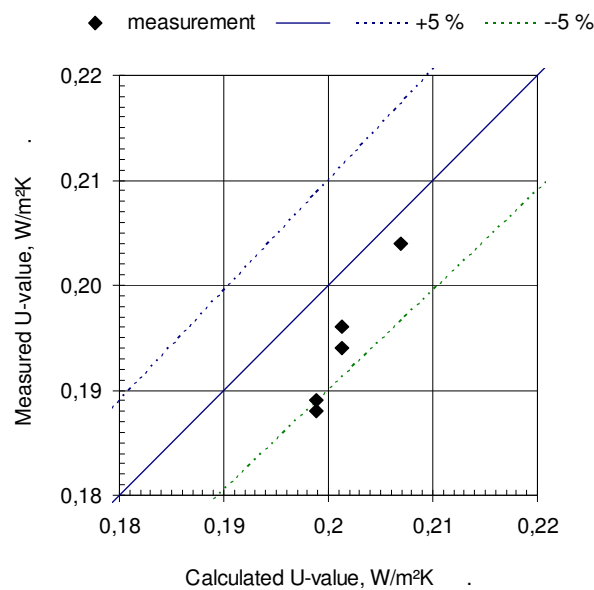
FIG. 5: Comparison of measured and calculated U-values of a timber frame wall with 154 mm conventional insulation, reflective vapour barrier and a closed air cavity of three alternative thicknesses. The emissivity of the reflective vapour barrier was 0.05.

The R-values shown in fig. 6 were measured by use of a heat flow meter located at the middle height of one of the air cavities of the timber frame wall. The heat flow meter was 1 mm thick and had a circular metering area with a diameter of 50 mm. As explained in chapter 3.2 the heat flow meter gives an overestimated R-value of cavities with natural convection. The R-value given for the 32 mm thick air cavity is too high because convection will influence the heat flow primarily at the top and bottom of the air gap where the air flow turns. The resulting heat flow increase will not be "caught" by the heat flow meter located at the middle height where the air flow will be primarily perpendicular to the heat flow direction.
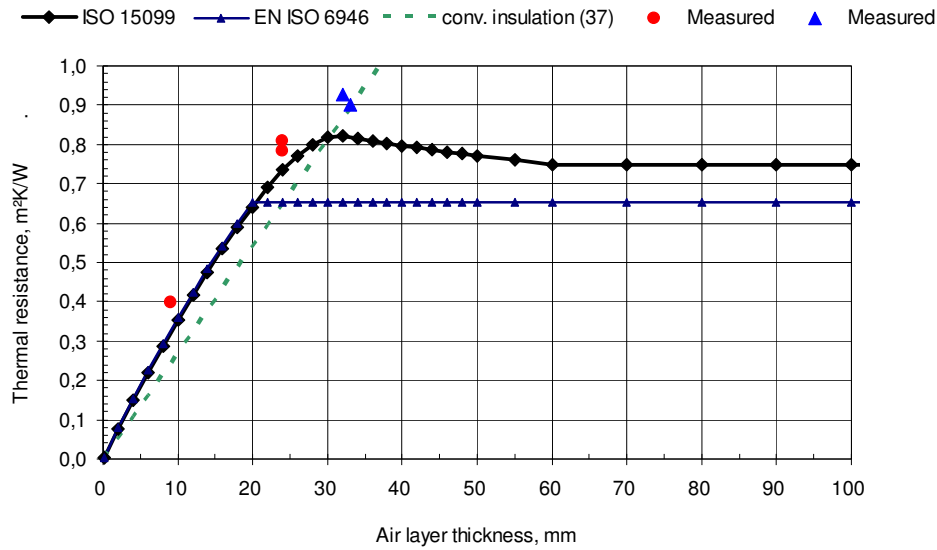
FIG. 6: Measured R-values of a closed air cavity bounded by a reflective material at one face compared with calculated values according to two alternative standards. The air cavities is bounded by a reflective material at one face, $\varepsilon = 0.05$. Thickness of ordinary timber frame/insulation 154 mm

3.7 Emissivity
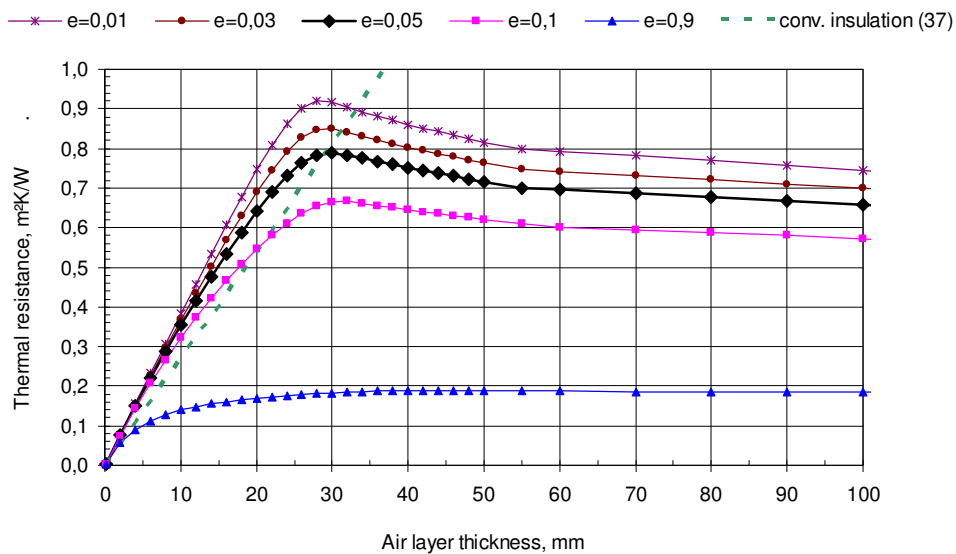
FIG. 7: Thermal resistance of a closed cavity in a timber frame wall calculated for various emissivity of the reflective material. The total thickness of timber frame is 200 mm. The air cavity is bounded by a reflective material at one face.

3.8 Temperature difference
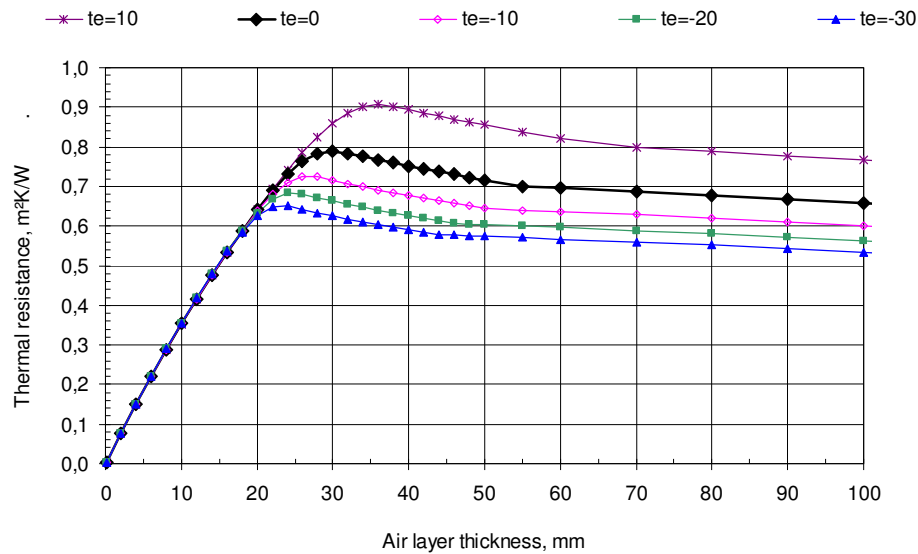
FIG. 8: *Estimated thermal resistance of a closed air cavity, integrated in a timber frame wall, for various outdoor temperatures. The closed cavity is bounded by a reflective material at one face $\varepsilon = 0.05$. The total thickness of the timber frame is 200 mm.*

When the outdoor temperature falls, the temperature difference across the air cavity will increase. The temperature difference across the cavity is the "power" of natural convection which will increase and resulting in a reduced R-value.

4. U values of timber frame walls with air cavities
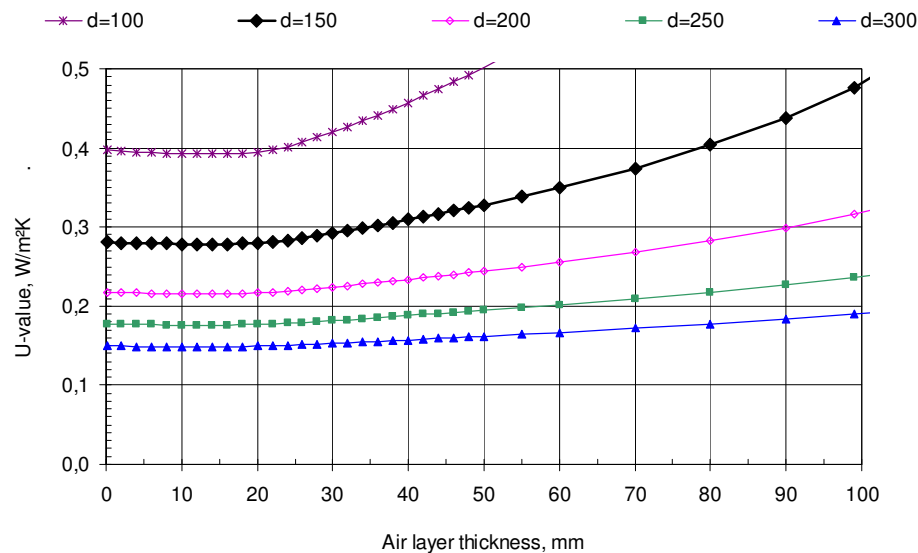
FIG. 9: *Estimated thermal transmittance, U-value of a timber frame wall with conventional insulation combined with one closed air cavity bounded by a reflective material at one face, emissivity 0.05, for various thicknesses of the air cavity and various overall thicknesses of the timber frame wall.*

In timber frame walls it is recommended to put the pipes for water and electricity conductors in a cavity between the vapour barrier and the indoor cladding. This is done to avoid penetration of the vapour barrier in order to achieve good air tightness. Using a reflective vapour barrier the cavity may remain empty, with no conventional insulation, and still have an acceptable R-value.

5. Conclusion

Used in a correct way a reflective vapour barrier will increase the R-value of closed air cavities integrated in timber frame structures. The R-value is strongly dependent on the heat flow direction. The resistance of a closed air cavity can be equivalent with a conventional thermal insulation layer with a thickness of approximately 30 mm for walls and approximately 20 mm for roofs and ceilings. Increasing the air cavity thickness beyond these limits will not increase the thermal resistance of the cavity due to the development of natural convection.

In structures with heat flow direction downwards, like in floors, the potential R-value of a closed air layer is much higher as the natural convection may bee very low due to thermal stable air layers.

To get representative R-values and U-values of structures containing air cavities it is essential that measurements are performed on full height specimen by use of a hot box with a metering area that covers the full height of the cavities. A metering area covering only the central part of the cavity will give an overestimation of the R-value.

6. Acknowledgements

7. References

EN ISO 6946:1996, Building components and building elements, Thermal resistance and thermal transmittance, Calculation method. CEN,

ISO 15099:2003, Thermal performance of windows, doors and shading devices – Detailed calculations

Uvsløkk, S. (1998). Undersøkelse av U-verdi til vegg med uventilert hulrom og "Thermo – brite III radiant barrier" som dampsperre, Oslo, Norway (In Norwegian).

Analytical Model for Computing Thermal Bridge Effects in High Performance Building Panels

Martin J. Tenpierik, MSc, Arch,
Department of Building Technology, Delft University of Technology;
m.j.tenpierik@tudelft.nl

Wim H. van der Spoel, dr.ir.,
Department of Building Technology, Delft University of Technology;
w.h.vanderspoel@tudelft.nl

Johannes J.M. Cauberg, prof.ir.,
Department of Building Technology, Delft University of Technology;
j.j.m.cauberg@tudelft.nl

SUMMARY:
Vacuum insulation panels (VIPs) have recently been discovered by the building sector. Because they are evacuated, their ideal or centre-of-panel thermal conductivity is as low as about 0.004 W·m^{-1}·K^{-1}. As a consequence, vacuum insulation panels combine high thermal performance with limited construction thickness. Integrated into building panels, however, a thermal bridge effect occurs at the panel's edge due to the combined effect of the high barrier laminate around the VIP and the (structural) edge profile along the circumference of the component. Until now, numerical calculation tools are used for estimating the overall thermal performance of building panels. This procedure however is time-consuming and does not give insight into the relations between relevant parameters. This paper therefore presents and numerically validates an analytical model for calculating this thermal edge effect, especially for thermally highly performing building components with vacuum insulation panels as core. The model however is generally valid for thermal shunting effects due to the edge of building panels. Based on a comparison of analytical to numerical data, it is shown that the inaccuracy of the analytical model compared to numerical data is less than about 10% within limitations specified.

1. Introduction

Although vacuum insulation panels (VIPs) have widely been used in refrigerators and transport containers for a long time, they have only recently been discovered by the building sector. A vacuum insulation panel is a thermal insulator consisting of an open-celled core material, which is after evacuation tightly sealed into a high barrier laminate to maintain the state of vacuum. In this state of vacuum, the ideal or centre-of-panel thermal conductivity of a VIP is as low as about 0.004 W·m^{-1}·K^{-1} (Caps et al., 2001; Simmler et al., 2005). As a consequence, vacuum insulation panels combine high thermal performance with limited construction thickness. Integrated into building panels, however, a thermal bridge effect occurs at the panel's edge due to the combined effect of the high barrier laminate around the VIP and the (structural) edge profile along the circumference of the component. Especially the latter effect reduces the overall thermal performance significantly, to the degree depending on the thermal conductivity and thickness of the core, the thermal conductivity and thickness of the face sheets and the width and thermal performance of the edge configuration (Tenpierik and Cauberg, 2007; Tenpierik et al., 2007).

Glicksman (1991) was among the first to mathematically define thermal bridge effects that occur on vacuum and reflective insulations. Other researchers addressed experimental determination of thermal performance of a VIP (Ghazi Wakili et al., 2004) or of a VIP assembly (Brodt and Bart, 1994; Nussbaumer et al., 2006). Different studies aimed at investigating the influence of the high conduction envelope on thermal performance of a VIP (Ghazi Wakili et al., 2004; Nussbaumer et al., 2005; Nussbaumer et al., 2006) or to investigate edges of building panels (Bundi, 2003; Schwab et al., 2005), all applying numerical simulations. Based upon previous numerical studies, Simmler and Brunner (2005) declared design values for VIPs including thermal bridge and ageing

effects. Thorsell (2006) even succeeded in reducing this effect by modifying the shape of the panel edge into a serpentine edge. Although both experimental and numerical studies generated a significant amount of knowledge, they are very time-consuming and labour-intensive. Moreover, these studies did not clearly define relationships between relevant parameters influencing thermal bridging. Because of these issues, Tenpierik and Cauberg (2007) derived and verified an analytical equation that predicts the effect of the thermal bridge induced by thin film VIP barrier laminates. This model however is not valid for building panels having broader edge profiles and larger thermal bridge effects.

Until now, either numerical calculation tools or very inaccurate analytical models (NEN-EN-ISO 6946, 2005) are used for estimating the overall thermal performance of such building panels. These procedures however are either time-consuming or lack accuracy. This paper therefore presents and numerically validates an analytical model for calculating this thermal edge effect, especially for thermally highly performing building components with vacuum insulation panels as core. The model however is generally valid for thermal shunting effects due to the edge of building panels. Based upon this analytical procedure, manufacturers, building scientists and architects can optimise the thermal performance of building constructions, thus contributing to the required energy reduction of buildings in their occupational phase and the desired well-being of the building's occupants.

2. Overall thermal performance

In general, the thermal transmittance, or U-value is used to determine the thermal performance of building enclosures. For non-homogeneous building panels, thermal bridge effects need to be considered when calculating this U-value for the panel as a whole. In contrast to international standard NEN-EN-ISO 10077 (2004), the overall thermal transmittance of a building component here is defined as

$$U_{eff} = \frac{U_{cop}S_{cop} - 4U_{edge}w^2 + \psi_{edge}l_p}{S_{cop} + S_{edge}} \approx \frac{U_{cop}S_{cop} + \psi_{edge}l_p}{S_{cop} + S_{edge}} \tag{1}.$$

In this equation S_{cop} [m^2] is the central area, S_{edge} [m^2] the edge surface area, U_{cop} [W·m^{-2}·K^{-1}] the thermal transmittance of the central area, U_{edge} [W·m^{-2}·K^{-1}] the thermal transmittance of the edge, ψ_{edge} [W·m^{-1}·K^{-1}] the linear thermal transmittance of the edge, w [m] the width of the edge and l_p [m] the length of the panel perimeter. The difference between this definition and the definition given in NEN-EN-ISO 10077 (2004) is that the linear thermal transmittance in the first definition consists of both the heat flow over the edge and the additional heat flow due to centre-of-panel-edge-interactions while in the latter definition it only comprises the additional heat flow due to centre-of-panel-edge-interactions. This new definition is used because it resembles the definition used by Tenpierik and Cauberg (2007) for modelling the linear thermal transmittance of VIP edges and because no immediate knowledge of the thermal performance of the edge is required.

For validation, the 3D steady-state heat transfer simulation tool TRISCO has been employed. For the simulations, the same conditions and accuracy requirements as were used by Tenpierik and Cauberg (2007) have been used here. However, the width of the panels, b_{cop}, was chosen to be 500 mm in stead of 200 mm since 200 mm was not sufficient to obtain adiabatic boundary conditions while 500 mm was.The linear thermal transmittance of the panel's edge can now be derived from

$$2\psi_{edge} = \frac{\phi_{q;total} - 2\phi_{q;cop}}{l^{2D}\Delta T} = \frac{\phi_{q;total}}{l^{2D}\Delta T} - 2U_{cop}b_{cop} \tag{2},$$

with $\phi_{q;total}$ [W] the total heat flow through the building panel numerically calculated, $\phi_{q;cop}$ [W] the heat flow through the central region, l^{2D} the simulated panel length (= 1 m), ΔT [K] the temperature difference across the panel and b_{cop} [m] the width of the central region. In this equation, on both the left side and the right side, the factors 2 result from the geometry defined for numerical simulation, as shown in Figure 1.

Equation (1) already clearly shows that the thermal performance of a building panel including edge effects increases for increasing panel dimensions and decreasing edge width. Moreover, the thermal properties of the edge and the centre-of-panel-edge-interaction, determined by ψ_{edge} can strongly affect the overall thermal performance of a building panel.
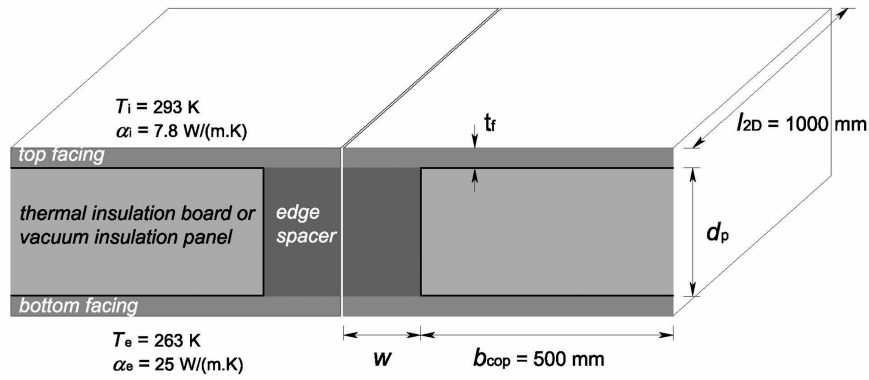
FIG. 1: Schematic representation of the geometry used in numerical simulations for ψ_{edge}-calculations.

3. Analytical model

For deriving the analytical thermal bridge model, the following are assumed:

- The length of the building panel is presumed infinite. At a defined distance L_x and L_y from the corner of the panel, the temperature profile over de thickness of the panel, therefore, equals the undisturbed steady-state one-dimensional temperature profile;

- The boundary heat transmission coefficient α_j is constant across the surface of layer j and the facing temperature $T_{f;j}$ is constant in the cross-section through the facing;

- Additional radiative heat transfer processes that are not covered by the heat transmission boundary coefficients, α_j, are not considered;

- No lateral heat exchange between different VIPs in the panel's edge region occurs.

Using these assumptions, the linear thermal transmittance of the thermal bridge due to the edge of a building component is now computed analytically as

$$\psi_{edge} = \frac{\alpha_1}{(T_1 - T_2)} \cdot \left[w \cdot (T_1 - T_{sx}) - \frac{B_1(T_{sy} - c_{0y})(\lambda_1 - \lambda_2) + B_1 B_2(T_{sx} - c_{0x})\left(\frac{\lambda_2}{(N_2^2 - \lambda_2^2)} - \frac{\lambda_1}{(N_2^2 - \lambda_1^2)} \right)}{\sqrt{CD}} \right] \quad (3).$$

In this equation, (N_1), N_2, B_1, B_2, C and D are calculation parameters, which are defined as

$$N_j = \sqrt{\frac{\alpha_j}{t_{f;j}\lambda_{f;j}} + \frac{\lambda_c}{t_{f;j}\lambda_{f;j}d_p}} \quad (4a),$$

$$B_j = \frac{\lambda_c}{t_{f;j}\lambda_{f;j}d_p} \quad (4b),$$

$$C = N_1^2 N_2^2 - B_1 B_2 \quad (4c),$$

$$D = \left(N_1^2 - N_2^2\right)^2 + 4B_1 B_2 \quad (4d),$$

with $t_{f;j}$ [m], d_c [m], $\lambda_{f;j}$ [W·m^{-1}·K^{-1}] and λ_c [W·m^{-1}·K^{-1}] dimensional or material properties of the building component: $t_{f;j}$ is the thickness of the facing (on side 1 or 2), d_c is the thickness of the panel core, $\lambda_{f;j}$ is the equivalent thermal conductivity of the facing (on side 1 or 2), λ_c is the thermal conductivity of the panel core and T_j [K] is the boundary temperature on side 1 or 2 respectively. c_{0x} [K] and c_{0y} [K] are the temperatures of the face sheets at large distance from the thermal bridge where only 1D effects occur. They are calculated as

$$c_{0x} = \frac{A_1 N_2^2 T_1 + B_1 A_2 T_2}{N_1^2 N_2^2 - B_1 B_2} \tag{5a},$$

$$c_{0y} = \frac{A_2 N_1^2 T_2 + B_2 A_1 T_1}{N_1^2 N_2^2 - B_1 B_2} \tag{5b}.$$

T_{sx} [K] and T_{sy} [K] are fictive temperatures of the face sheet right in front of the thermal bridge, determined from

$$
T_{sx} = \frac{[e_4(K+e_2)+e_1(K-e_3)+e_4\alpha_2 w]c_{0x} - [e_3(K+e_2)+e_2(K-e_3)+e_3\alpha_2 w]c_{0y}}{(K-e_3)(K+e_1)-(K+\alpha_2 w+e_2)(K+\alpha_1 w-e_4)}
$$
$$
- \frac{(K-e_3)\alpha_2 w T_2 + [(K+e_2)\alpha_1 w + \alpha_1 \alpha_2 w^2]T_1}{(K-e_3)(K+e_1)-(K+\alpha_2 w+e_2)(K+\alpha_1 w-e_4)} \tag{6a},
$$

$$
T_{sy} = \frac{[e_4(K+e_1)+e_1(K-e_4)+e_1\alpha_1 w]c_{0x} - [e_3(K+e_1)+e_2(K-e_4)+e_2\alpha_1 w]c_{0y}}{(K-e_3)(K+e_1)-(K+\alpha_2 w+e_2)(K+\alpha_1 w-e_4)}
$$
$$
- \frac{(K+e_1)\alpha_1 w T_1 + [(K-e_4)\alpha_2 w + \alpha_1 \alpha_2 w^2]T_2}{(K-e_3)(K+e_1)-(K+\alpha_2 w+e_2)(K+\alpha_1 w-e_4)} \tag{6b},
$$

In equation (6), the parameters e_1, e_2, e_3, e_4 are defined as

$$e_1 = +\frac{B_1(\lambda_1-\lambda_2)}{\sqrt{D}}\lambda_{f2}t_{f2} \tag{7a},$$

$$e_2 = -\frac{2B_1 B_2}{\sqrt{D}}\left(\frac{\lambda_1}{N_2^2-N_1^2+\sqrt{D}} - \frac{\lambda_2}{N_2^2-N_1^2-\sqrt{D}}\right)\lambda_{f2}t_{f2} \tag{7b},$$

$$e_3 = -\frac{B_1(\lambda_1-\lambda_2)}{\sqrt{D}}\lambda_{f1}t_{f1} \tag{7c},$$

$$e_4 = -\frac{2B_1 B_2}{\sqrt{D}}\left(\frac{\lambda_1}{N_2^2-N_1^2-\sqrt{D}} - \frac{\lambda_2}{N_2^2-N_1^2+\sqrt{D}}\right)\lambda_{f1}t_{f1} \tag{7d},$$

with λ_1 and λ_2 the eigenvalues of the linear system of differential equations derived to represent this thermal phenomenon. They are defined by

$$\lambda_1 = -\sqrt{\frac{(N_1^2+N_2^2)-\sqrt{(N_1^2-N_2^2)^2+4B_1 B_2}}{2}} \tag{8a},$$

$$\lambda_2 = -\sqrt{\frac{(N_1^2+N_2^2)+\sqrt{(N_1^2-N_2^2)^2+4B_1 B_2}}{2}} \tag{8b}.$$

K [W·m^{-1}·K^{-1}] finally is the thermal conductance of the edge defined as

$$K = \frac{w}{R_{edge}+R_{f1}+R_{f2}} \tag{9}.$$

In this equation, R_{edge} [m^2·K·W^{-1}] is the thermal resistance of the edge spacer, which can be estimated using a thermal resistance network of this edge, and R_{f1} and R_{f2} [m^2·K·W^{-1}] are effective thermal resistances of facing 1 and 2 respectively.

TABLE. 1: thermal conductivity of edge construction materials.

Material	λ [W·m^{-1}·K^{-1}]
aluminium	160
silica gel	0.12
polysulfide sealant	0.24
butyl sealant	0.40
non-metallic tape	0.33
air gap (d_c=10/20/30/40 mm)	0.06/0.07/0.07/0.08

TABLE. 2: thermal conductivity and thickness of face sheets and barrier envelopes

Material	t_{facing} [mm]	λ [W·m^{-1}·K^{-1}]
aluminium facing	2	160
polyester facing	3	0.25
stainless steel facing	1.5	16.2
aluminium laminate	0.006	160
metallized film	0.097	0.54

TABLE. 3: equivalent thermal conductivity of facing, λ_f [W·m^{-1}·K^{-1}].

Material	alu. laminate	metallized film
aluminium facing	160.0	152.6
polyester facing	0.569	0.259
stainless steelfacing	16.77	15.25

TABLE. 4: equivalent thermal conductivity of edge spacers, λ_{edge} [W·m^{-1}·K^{-1}].

Edge construction		alu. laminate	metallized film
alu. spacer	10 mm	3.75	3.33
	20 mm	6.21	5.71
	30 mm	8.11	7.55
	40 mm	9.61	9.01
non-metallic tape		2.72	0.317

4. Studied building panels

The analytical model presented in the previous section is validated by studying 24 different symmetrical building panel variants and several asymmetrical building panels. Only the symmetrical variants will be shown here. Furthermore, each variant is simulated for five values of the thermal conductivity of the core material ($\lambda_c = 0.000$ - 0.004 – 0.008 – 0.020 – 0.040 W·m^{-1}·K^{-1}) and for four values of the thickness of this core material ($d_p = 10 – 20 – 30 – 40$ mm), in total thus 480 simulations. The panel variants are made up of four different edge spacers or construction types: 1.) an aluminium spacer typically used for double-glazing systems; 2.) a panel edge construction with an inwards folded facing and a silicone sealant; 3.) an optimized thermoplastic spacer and 4.) an edge consisting of a reinforced non-metallic tape. Due to limited space, solely the results of the first and fourth type are shown in this paper. Their geometry and their thermal properties are presented in Figure 2 and Table 1. Besides these edge construction types, three different facings and two VIP barrier envelopes have been applied, the types and properties of which are shown in Table 2.

First however, we need to explain how the effective thermal conductivity of the facing and the edge spacer are calculated. Since the heat flow in the facings is mainly directed in the in-plane direction, the combination of facing and film can be seen as two parallel thermal resistances. The equivalent thermal conductivity of the facing λ_f, is therefore estimated as a thickness-weighted average thermal conductivity. In the panel edge region, the heat flows are primarily directed from the warm side of the panel towards its cold side. The edge construction type *reinforced non-metallic tape* can thus, similarly to the facings, be considered as parallel resistances and be calculated as a thickness weigthed average. The edge spacer construction *aluminium double-glazing spacer* however is geometrically more complex. The thermal resistance of this edge can be estimated using a resistance network. Table 3 and 4 present the results of the equivalent thermal conductivity calculations for the facings and the edge spacer constructions respectively.
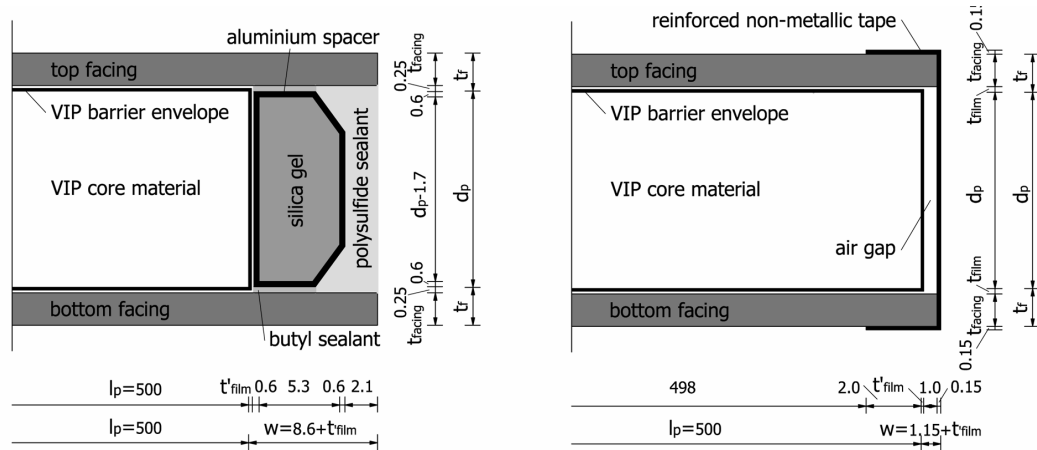
FIG. 2: Schematic representation of the aluminium double-glazing spacer and the non-metallic tape edge type.
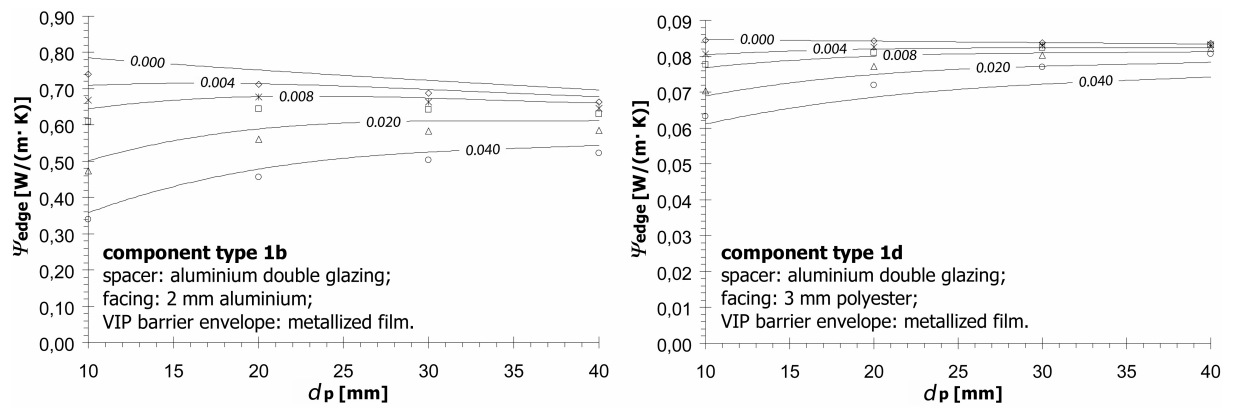
FIG. 3a/b: Comparison of analytical model (lines) to numerical data (markers) for an aluminium double-glazing spacer. The numbers accompanying the lines denote the thermal conductivity of the core in $W \cdot m^{-1} \cdot K^{-1}$.
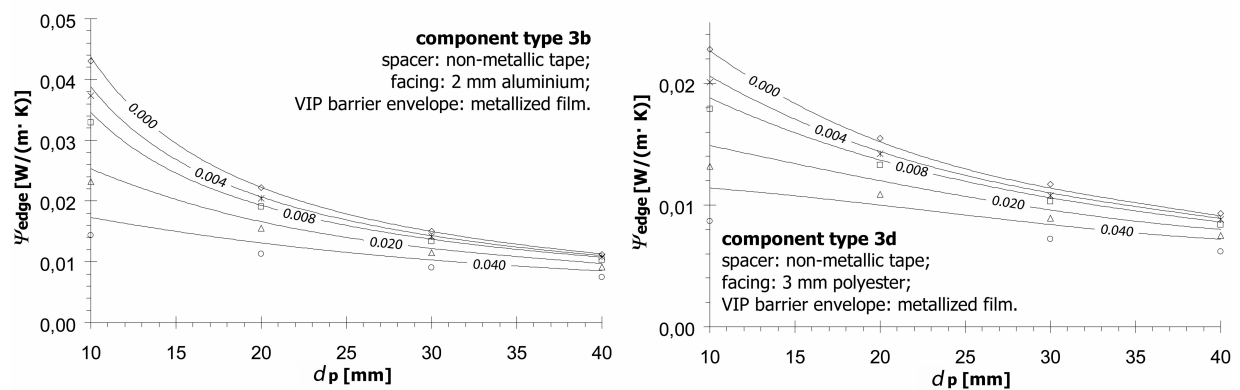
FIG. 4a/b: Comparison of analytical model (lines) to numerical data (markers) for an reinforced non-metallic tape as spacer. The numbers accompanying the lines denote the thermal conductivity of the core in $W \cdot m^{-1} \cdot K^{-1}$.

5. Model validation

The derived model is validated by comparing its results to numerical simulations of the building component types previously discussed. Figures 3 and 4 show a selection of the results. As can generally be seen from these figures, the prediction of equation (3) is quite well for the aluminium (and stainless steel), thus high conductance, facings for both spacers. Not shown in the figures is that this also applies to the optimised thermoplastic spacer. Differences between the analytical model and numerical simulations are however moderately bigger for the inwards folded edge construction. Detailed analysis of these results showed that the differences mainly result from the edge approximation by a thermal resistance network. For building panels with a high conductance facing, differences are thus small. A building component with a 20 mm thick core of a metallised film based VIP, having a central thermal conductance of 0.2 m^2·K·W^{-1} and having a 2 mm thick aluminium facing and an aluminium edge spacer has a ψ_{edge}-value of 0.667 W·m^{-1}·K^{-1} according to numerical simulations, and of 0.714 W·m^{-1}·K^{-1} according to equation (3). This is a difference of only 0.037 W·m^{-1}·K^{-1}, or of $+5.4\%$. As a second example, a building panel with the same VIP core and the same facing, but having an edge consisting of a non-metallic tape has a ψ_{edge}-value of 0.020 W·m^{-1}·K^{-1} according to numerical simulations, while equation (3) predicts a value of 0.021 W·m^{-1}·K^{-1}, which is a deviation of 0.001 W·m^{-1}·K^{-1}, or of $+2.4\%$. For low thermal conductivity facings, like polyester, however, the deviations between modelled and simulated results are moderately bigger, at least if a polyester facing is combined with an aluminium foil based VIP. For an optimized thermoplastic spacer based building component with an aluminium foil based VIP of 20 mm and a 3 mm thick polyester facing, for instance, the deviation between numerical simulation and analytical model amounts to 0.010 W·m^{-1}·K^{-1} ($= 0.080$ W·m^{-1}·K^{-1} - 0.070 W·m^{-1}·K^{-1}), which corresponds to 14.2%. For the same building panel but now with a metallized film based VIP, the deviation is 0.001 W·m^{-1}·K^{-1} ($=0.050$ W·m^{-1}·K^{-1} - 0.049 W·m^{-1}·K^{-1}). Large deviations are thus primarily restricted to panels with a polyester facing and an aluminium foil based VIP.

Based upon a comparison of numerical and analytical data of all calculated variants, Figure 5 plots the difference between both calculation methods. As can be seen from the plot, for relatively high ψ_{edge}-values, the difference between both methods is less than about 5%. Below $\psi_{edge} = 0.1$ W·m^{-1}·K^{-1} however the deviation increases to higher values but almost always stays below 20%. Closer inspection of the panel variants causing these large deviations shows that all of them are constructed with a polyester facing and an aluminium foil laminate as VIP barrier envelope. Since the error is influenced by many parameters, it is not possible to create strict model application boundaries in which all parameters are accounted for. The error analysis, however, indicated that the application range for equation (3) is strongly influenced by two factors: the ratio of the product of film thermal conductivity and thickness to the product of facing thermal conductivity and thickness ($\xi = \lambda_{film}t_{film} / \lambda_{facing}t_{facing}$) and by the equivalent edge thermal conductance, K. Based upon both parameters, an indication of the application range of the analytical equation can now be defined by a limit of the ratio λ_c / d_c, below which value the analytical equation can be applied with certain accuracy. For $\xi \leq 1$, all simulated variants had a deviation of less than 10%. For $\xi > 1$, some had a deviation below 10%, some above. For this category, the following necessary but not sufficient statement can be posed: $(\lambda_c / d_c)_{lim} \approx 0.9 + 0.96K$.
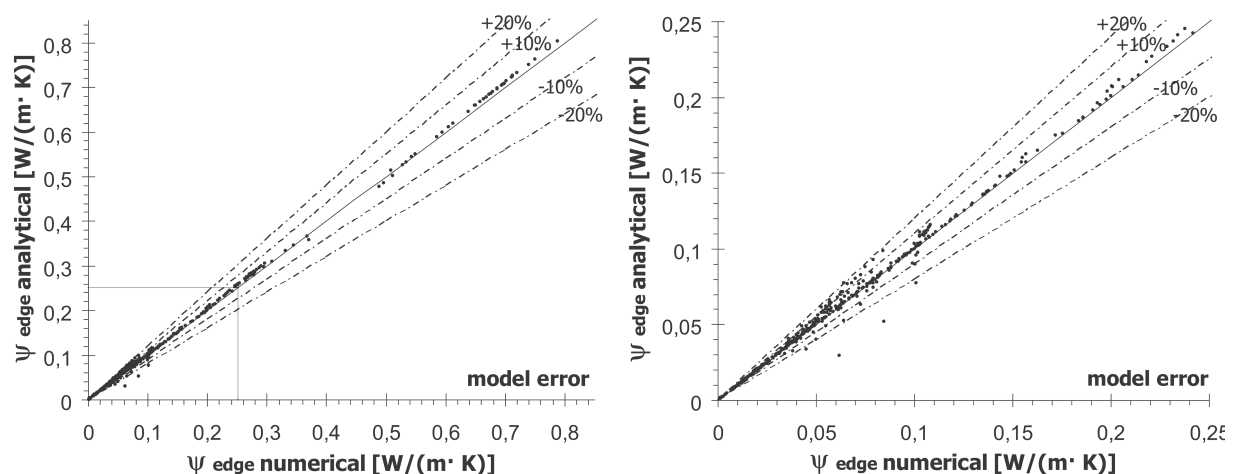
FIG. 5a/b: Plot indicating the (model) error introduced by the analytical model relative to numerical computations. The error due to the edge schematisation is not included in this error.

6. Conclusions

The objective of this paper was to present and validate an analytical model for studying and approximating thermal bridge effects due to component edges in thermally highly performing building panels. Through a comparison of this model with results from numerical simulations for several building components, it was shown that the analytical model can be used with sufficient accuracy, as long as ψ_{edge} is above 0.1 W·m^{-1}·K^{-1}. The analytical model then deviates from numerical results by less than 10%. For most studied building component variants deviations were found to be even less than 5%.

7. References

Brodt, K.H. and Bart, G.C.J. (1994). Performance of sealed evacuated panels as thermal insulation, International Journal of Refrigeration 17(4): 257-262.

Bundi, B. (2003). Vakuumisolierte Paneele. Forschung und Entwicklung im Fassadenbau, Fassade 2003(3): 19-22.

Caps, R., Heinemann, U., Ehrmanntraut, M. and Fricke, J. (2001). Evacuated Insulation Panels Filled with Pyrogenic Silica Powders: Properties and Applications, High Temperatures-High Pressures 33 (2): 151-156.

Ghazi Wakili, K., Bundi, R. and Binder, B. (2004). Effective Thermal Conductivity of Vacuum Insulation panels, Building Research and Information 32(4): 293-299.

Glicksman, L.R. (1991). Two-Dimensional Heat Transfer Effects on Vacuum and Reflective Insulations, Journal of Thermal Insulations 14(4): 281 – 294.

NEN-EN-ISO 10077-1 (2004). Thermal performance of windows, doors and shutters – Calculation of thermal transmittance – Part 1: General, Nederlands Normalisatie Instituut.

Nussbaumer, T., Bundi, R., Tanner, Ch. and Mühlebach, H. (2005) Thermal Analysis of a wooden door system with integrated vacuum insulation panels, Energy and Buildings 37(11): 1107-1113.

Nussbaumer, T., Ghazi Wakili, K. and Tanner, Ch. (2006). Experimental and numerical investigation of the thermal performance of a protected vacuum-insulation system applied to a concrete wall, Applied Energy 83(8): 841-855.

prNEN-EN-ISO 6946 (2005). Building Components and Building Elements – Thermal Resistance and Thermal Transmittance – Calculation Method, Nederlands Normalisatie Instituut.

Schwab, H., Stark, C., Wachtel, J., Ebert, H.-P. and Fricke, J. (2005). Thermal Bridges in Vacuum-insulated Building Facades, J. of Thermal Env. and Bldg. Sci. 28(4): 345-355.

Simmler, H. and Brunner, S. (2005). Vacuum insulation panels for building application. Basic properties, aging mechanisms and service life, Energy and Buildings 37(11): 1122-1131.

Simmler, H., Brunner, S., Heinemann, U., Schwab, H., Kumaran, K., Mukhopadhyaya, Ph., Quénard, D., Sallée, H. , Noller, K., Kücükpinar-Niarchos, E., Stramm, C., Tenpierik, M., Cauberg, H. and Erb, M. (2005), Vacuum Insulation Panels. Study on VIP-components and Panels for Service Life Prediction of VIP in Building Applications. Subtask A, IEA ECBCS Annex 39 HiPTI, 153 pages.

Tenpierik, M.J. and Cauberg, J.J.M. (2007). Analytical Models for Calculating Thermal Bridge Effects Caused by Thin Film High Barrier Envelopes around Vacuum Insulation Panels, Journal of Building Physics 30(3): 185-215.

Tenpierik, M.J., Cauberg, J.J.M. and Thorsell, T.I. (2007), Integrating vacuum insulation panels in building constructions: an integral perspective, Construction Innovation 7(1): 38-53.

Thorsell, T.I. (2006). Edge loss minimization in vacuum insulation panels, In: Fazio, Ge, Rao and Desmarais (eds), Research in Building Physics and Building Engineering, Taylor and Francis Group, London, UK.

Prediction of the long-term insulating capacity of cyclopentane-blown polyurethane foam

Camilla Persson, Licentiate of Engineering   *camilla.persson@chalmers.se*
Johan Claesson, Professor   *johan.claesson@chalmers.se*

Department of Civil and Environmental Engineering, Division of Building Technology, Chalmers University of Technology, SE 412 96 Göteborg, Sweden;
http://www.chalmers.se/cee/EN/divisions/building-technology

SUMMARY:
Polyurethane foam has high insulating capacity and is used in many applications, for example as building, fridge, freezer and pipe insulation. The thermal conductivity of the foam changes over time due to gas diffusion. The insulating gases (cyclopentane and carbon dioxide) diffuse out of and air (nitrogen and oxygen) into the foam over time. The diffusion rates of the gases are temperature dependent. Thus aging is a coupled heat and mass transfer process.

A model that describes the change of the insulating capacity of the foam over time has been derived and applied to determine the long-term insulating performance of district heating pipes. Unlike other models, it takes into account the coupled heat conduction and diffusion, and in particular all cyclopentane phases. Cyclopentane is present as gas in the cells, condensed liquid and dissolved in the polymer matrix. The calculated time-dependent concentrations provide good insight into the aging process.

Calculations reveal that the insulating capacity of a DN100/225 forward pipe decreases by about 10% over its nominal lifetime of 30 years and that the initial cyclopentane content is important. Pipe manufacturers use different amounts of cyclopentane. The insulating capacity of pipes was found to differ by up to 4% between manufacturers, due to differences in the initial gas content.

1. Introduction

Polyurethane foam is a material that is used in many applications, such as building, fridge, freezer and pipe insulation, due to its good insulating capacity. As the insulating capacity of the foam changes over time, it is important to consider the long-term insulating performance and not only the initial performance.

Cyclopentane and carbon dioxide fill and expand cells in the polyurethane matrix at foaming. These two insulating gases diffuse out of the foam while air, mainly consisting of nitrogen and oxygen, diffuses into it until equilibrium is reached with ambient concentrations. The diffusion process and the associated change in cell gas composition are part of the aging of the foam and have a pronounced effect on its insulating capacity (e.g. Isberg 1988, Hilyard and Cunningham 1994). The diffusion rates are temperature dependent. The cell gas composition influences the temperature, which in turn impacts on the diffusion rates. The aging is thus a coupled heat conduction and diffusion process. The importance of temperature feedback has not been investigated.

Another shortcoming when modelling the aging of polyurethane foams has been the treatment of the insulating gas cyclopentane. Cyclopentane is present in the foam as gas in the cells and dissolved in the polyurethane matrix. At a high concentration it may also be present as condensed liquid. Although the importance of all phases of cyclopentane has been pointed out (Holmgren 2004), their influence on the long-term insulating performance of polyurethane foam has not been studied.

The above aspects are addressed in this paper with reference to district heat distribution application. A radial model that takes into account the coupled heat and mass transfer as well as all phases of cyclopentane in the foam has been generated to predict the long-term insulating performance of district heating pipes with cyclopentane-blown polyurethane foam insulation. The importance of the temperature feedback and

cyclopentane content is investigated. The model is also described in (Persson and Claesson 2005). The ability to predict heat losses from district heating networks is important. Heat generation to compensate for heat losses from the networks results in considerable environmental impact and network costs (Persson et al. 1995, Nielsen 2001, Ting Larsen 2004, Frederiksen and Werner 1993).

2. The model

Straight district heating pipes made up of a steel fluid pipe insulated with polyurethane foam inside a polyethylene casing were studied. The foam serves as the main resistance to cyclopentane out-diffusion, while the casing constitutes the main barrier to air in-diffusion and carbon dioxide out-diffusion. The fluid pipe is diffusion-tight.

2.1 Coupled diffusion and heat conduction

The rate of gas diffusion depends on the temperature of the pipe, so that the description of the long-term insulating performance is a coupled heat and mass transfer problem. However, the time scales of the heat- and mass transfer processes differ greatly, as illustrated by the decline times, which are characteristic time scales for equalisation (Claesson 2001).

$$t_{d\_heat} = \frac{L^2}{\pi^2 \cdot \lambda / \rho c} \qquad\qquad t_{d\_diffusion} = \frac{L^2}{\pi^2 \cdot \delta} \tag{1}$$

Here, L [m] is the thickness of the material, λ [J•s^{-1}•m^{-1}•K^{-1}] the thermal conductivity, ρc the volumetric heat capacity [J•m^{-3}•K^{-1}] and δ the diffusion coefficient [m^2•s^{-1}]. The decline time for diffusion is thousands to hundreds of thousand times that of heat conduction, depending on the gas studied. When the aging of the district heating pipes is calculated numerically, it is therefore sufficient to use a stationary temperature profile that is updated at regular time intervals. Different update times have been tested to decide which one is best; see the Modelling results and discussion section. It was found that an annual temperature update is sufficient.

2.2 Diffusion

The transport of each gas through the foam is described by the diffusion equation, which states that the increase in the total molar mass concentration in the foam c_{tot} [mol•m^{-3} foam] is given by the net inflow. Numerically, the diffusion is calculated using explicit finite differences. In discrete form the diffusion equation for each cell n reads:

$$2 \cdot \pi \cdot r_n \cdot \Delta r \cdot \Delta c_{tot,n} = \left(J_{n-1 \to n} - J_{n \to n+1} \right) \cdot \Delta t \qquad n = 1, 2, ..., N \tag{2}$$

Here, r_n [m] is the mid-point of cell n. The width of the cell is Δr [m]. The length of the time step Δt [s] is chosen to meet the requirements of numerical stability for the diffusion. The molar mass flow from cell n to cell n+1 is denoted $J_{n \to n+1}$ [mol•m^{-1}•s^{-1}]

The total molar mass concentration is the sum of all contributions: the concentration dissolved in the matrix c_{pol} [mol•m^{-3} matrix], the concentration in the gas phase c [mol•m^{-3} gas] and the condensed liquid c_{liq} [mol•m^{-3} foam]. The gas fraction of the foam is f_g [-].

$$c_{tot} = c_{pol}(1-f_g) + c \cdot f_g + c_{liq} = \left[S \cdot R \cdot T \cdot (1-f_g) + f_g \right] \cdot c + c_{liq} \tag{3}$$

It should be noted that both here and in equations (6-7) T is in Kelvin.

Henry's law and the ideal gas law (molar gas constant R [J•mol^{-1}•K^{-1}]) are used in equation (3) to rewrite the contribution from the gas dissolved in the matrix into an expression for the gas phase concentration. For carbon dioxide, nitrogen and oxygen, no solubility (*S=0*) or liquid was taken into account. Their solubilities are low and their saturation vapour pressures are high enough to prevent condensation.

The molar mass flow is given by the conductance associated with the diffusion between cell n and cell n+1, $KD_{n \to n+1}$ [m^2•s^{-1}], multiplied by the concentration difference.

$$J_{n \to n+1} = KD_{n \to n+1} \cdot (c_n - c_{n+1}) \qquad n = 0, 1, ..., N \tag{4}$$

The conductance for each gas contains the temperature dependent diffusion coefficient δ (T) [$m^2 \cdot s^{-1}$]. From 15°C to 80°C, the diffusion coefficients increase by factors of 10-40.

$$KD_{n \to n+1} = \frac{1}{\frac{1}{2 \cdot \pi \cdot \delta_n} \cdot \ln\left(\frac{r_n + 0.5 \cdot \Delta r}{r_n}\right) + \frac{1}{2 \cdot \pi \cdot \delta_{n+1}} \cdot \ln\left(\frac{r_{n+1}}{r_n + 0.5 \cdot \Delta r}\right)} \qquad n = 1, 2, ..., N-1 \qquad (5)$$

The flow through the steel pipe at the inner boundary r_s is zero. The casing between r_{ins} and r_c acts as a barrier to diffusion to the surroundings at the outer boundary. The permeability coefficient of the polyethylene is P_{PE} [$mol \cdot m^{-1} \cdot s^{-1} \cdot Pa^{-1}$].

$$KD_{0 \to 1} = 0$$

$$KD_{N \to N+1} = \frac{1}{\frac{1}{2 \cdot \pi \cdot \delta_N} \cdot \ln\left(\frac{r_{ins}}{r_N}\right) + \frac{1}{2 \cdot \pi \cdot P_{PE} \cdot R \cdot T_c} \cdot \ln\left(\frac{r_c}{r_{ins}}\right)} \qquad (6)$$

The above calculations, equations (2-6), are performed for each time step for each of the gases. At each time step, the cyclopentane is partitioned between its phases, according to its saturation vapour pressure and Henry's law. The gas phase concentration is determined by a simple test. Is there enough space for all cyclopentane in the gas phase or does the cyclopentane condense?

$$c_{test,n} = \frac{c_{tot,n}}{S(T_n) \cdot R \cdot T_n \cdot (1 - f_g) + f_g} \qquad (7)$$

If c_{test} is less than the concentration corresponding to the saturation vapour pressure for cyclopentane, the gas phase concentration is c_{test}. Otherwise the gas phase concentration equals the saturation vapour pressure concentration. Once the total cyclopentane concentration, the concentration in the gas phase and the temperature are known, the concentrations in the other phases are easily determined. Henry's law provides the concentration of cyclopentane dissolved in the polymer while the liquid phase concentration is given by the residual amount.

2.3 Temperature update

The temperature update is performed in a loop function that at the same time determines the partitioning of cyclopentane between its phases. The cyclopentane concentration in the gas phase is first calculated for an estimated temperature. The thermal conductivity of the foam and the corresponding temperature profile are calculated on the basis of the determined gas phase concentration. The procedure involving the calculation of gas phase concentration, thermal conductivity and temperature is thereafter repeated until the difference between two consecutive iterations is neglible. Constant temperature boundary conditions are used.

The gas phase concentration and the temperature are connected through the thermal conductivity. The thermal conductivity of the foam is modelled as the sum of contributions from conduction through the gas in the cells, as well as through the polyurethane matrix and radiation. The contribution from conduction through the gas is given by Wassiljeva's equation, which was modified by Mason and Saxena using critical temperatures and pressures for the different gases. The thermal conductivity due to conduction through the polyurethane matrix is modelled by a cubical model valid for both high- and low-density foams. The radiation is modelled by Rossland's equation. These formulas are described in (Nielsen 1998).

3. Modelling results and discussion

As an example, a DN100/225 district heating pipe comprising a steel pipe with an outer diameter of 114.3 mm and about 5 cm of insulation was studied. The outer diameter of the casing was 225 mm. The temperature at the fluid pipe was 80°C and the temperature at the casing 15°C. The effective diffusion coefficients through the foam, permeability coefficients for the casing and solubility coefficient for cyclopentane in the foam were based on data from (Olsson et al. 2002, Mangs S 2005, Brodt 1995, Holmgren 2004). The expressions are presented in (Persson and Claesson 2005).

3.1 Calculation of performance

A calculation of 30 years of aging based on 10 numerical cells in the insulation of the DN100/225 district heating pipe takes about one minute. It can be seen in Table 1 that the equivalent thermal conductivity of the insulation λ_{eq} [J·s^{-1}·m^{-1}·K^{-1}] and the mean heat flow from the pipe Q_{eq} [J·s^{-1}·m^{-1}] over the nominal lifetime were obtained by three significant numbers based on 10 cells in the insulation. The equivalent thermal conductivity of the insulation is the constant thermal conductivity of the whole cross-section over the time period that yields the same heat loss as the actual time and space dependent thermal conductivity. In the same way, the mean heat flow equals the constant heat flow over the time period that yields the same total heat loss as the actual time-dependent heat flow.

TABLE 1: Results from calculations performed with different number of cells N for 30 years of aging of the district heating pipe.

Number of cells N [-]	λ_{eq} [J·s^{-1}·m^{-1}·K^{-1}]	Q_{eq} [J·s^{-1}·m^{-1}]	Calculation time [min]
10	0.02846	17.97	1
20	0.02850	18.00	4
50	0.02851	18.01	-

3.2 Change in heat flow and concentrations

Figure 1 shows how the heat flow from the reference pipe changes over time. The mean heat loss per metre over the aging period is about 160 kWh•m^{-1}•year^{-1}. The heat flow at the end of the nominal lifetime increased by 10% from its initial value of about 17.2 J·s^{-1}•m^{-1}. This increase is due to the change of gas composition in the foam cells. The heat flow decreases during the first few years, due to rapid out-diffusion of carbon dioxide, before starting to increase. Initially, the cells are filled with cyclopentane and carbon dioxide. When carbon dioxide leaves the foam, the mole fraction of cyclopentane increases. As the thermal conductivity of cyclopentane is lower than that of carbon dioxide, the total thermal conductivity of the cell gas decreases. After a few years, the in-diffusion of air becomes noticeable and the thermal conductivity starts to increase.
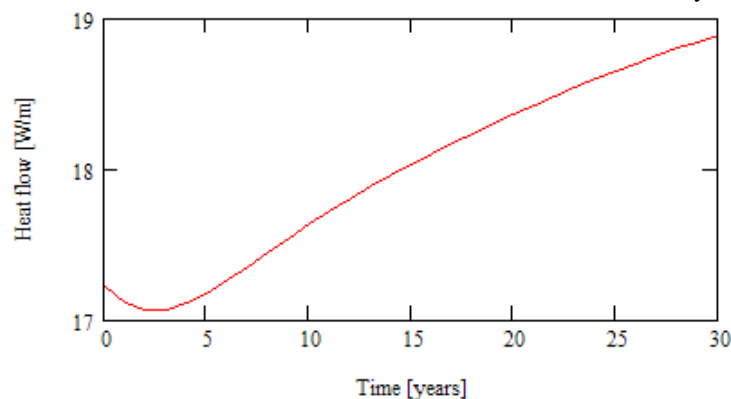
FIG. 1: Change in heat flow from a district heating pipe over time.

Figure 2 illustrates the change of the average gas phase concentrations over time. Studies of the gas phase concentration profiles through the foam over time reveal that the carbon dioxide concentration next to the fluid pipe decreased by 90% from its initial value after about 6-7 years. It takes approximately 30 years for 90% of the oxygen transport into the foam next to the fluid pipe to take place and about 100 years for 90% of the change in nitrogen concentration to occur next to the fluid pipe. For cyclopentane the change is even slower. Gas phase concentration profiles for cyclopentane over time are presented in Figure 3. In Figure 4, the gas phase concentration profiles for the other gases are given.

Figure 3 also illustrates how the concentration of cyclopentane in different phases changes over time. The saturation pressure for cyclopentane is lower in the colder outer part of the insulation than in the hotter inner part. Cyclopentane condenses in the outer parts. A gas concentration profile through the insulation that transports cyclopentane towards the casing is obtained. The relation between cyclopentane in gas and dissolved phases is

provided by the solubility coefficient. The solubility decreases with increased temperature in accordance with an Arrhenius relationship. The coefficient is about 3 times lower at 80°C than at 15°C.
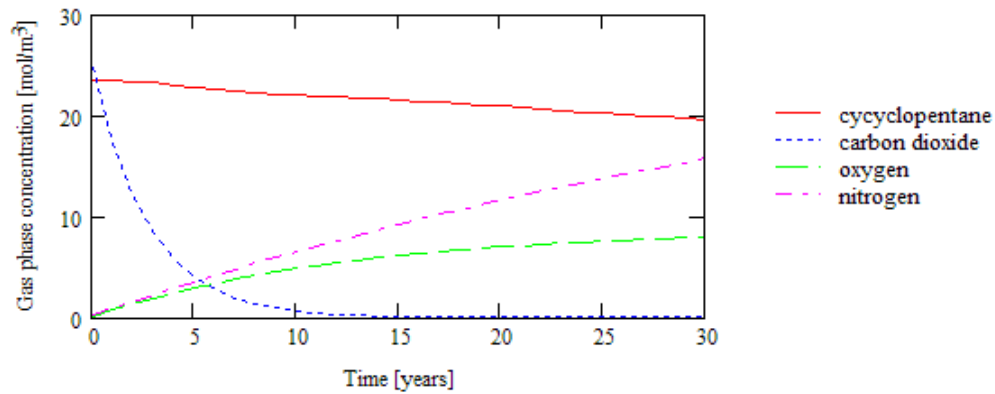
FIG. 2: Average gas phase concentrations in the foam over time.
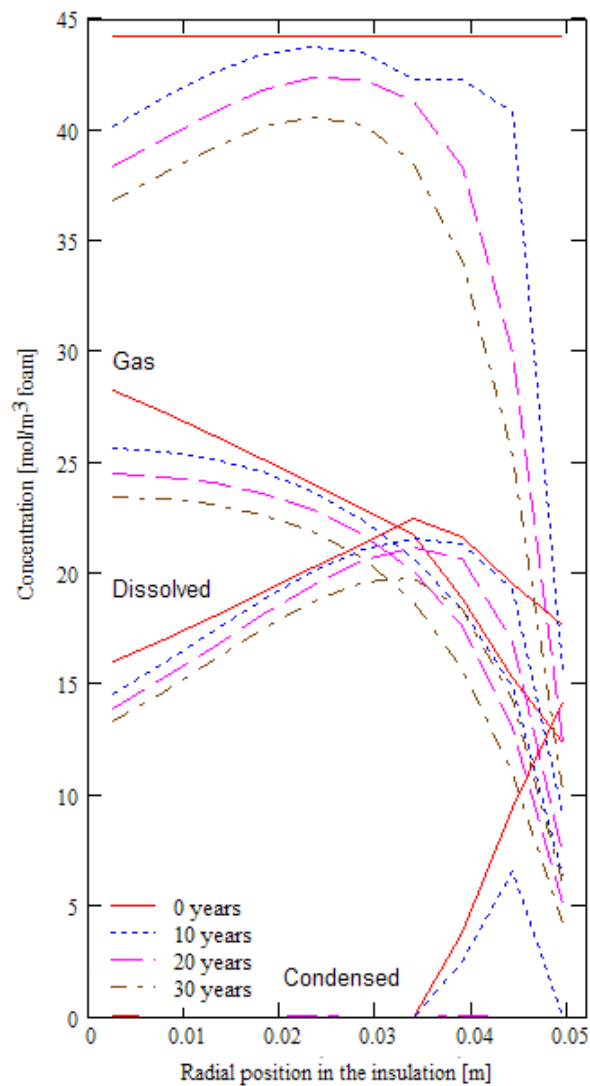
FIG. 3: Division of cyclopentane between phases in the foam over time.
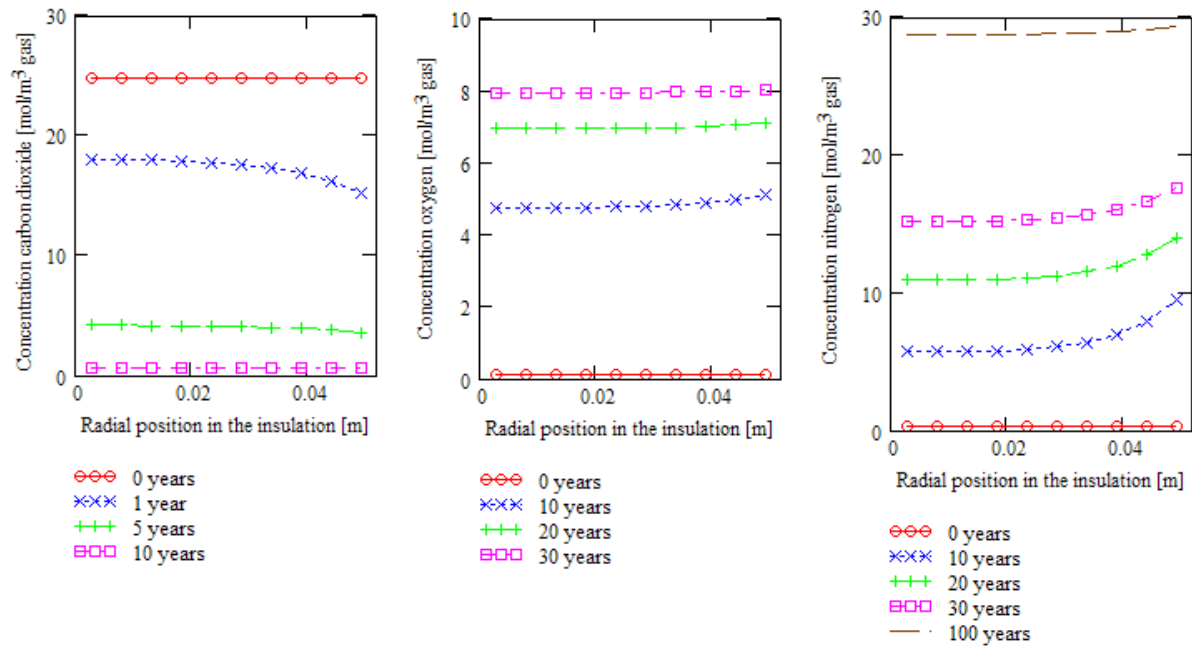
FIG. 4: Gas phase concentration profiles of carbon dioxide (left), oxygen (center) and nitrogen (right) in the foam over time.

For large pipe dimensions with thick insulation and casing, the ageing is slow, while it is fast in small pipe dimensions with thin insulation and casing. According to calculations, the insulation capacity for a larger pipe of DN800/1000 dimension (813.0 mm fluid pipe) with the same initial gas content decrease by only 0.6% over 30 years, while the decrease for a corresponding pipe of DN20/110 dimension (26.9 mm fluid pipe) would be 14.3%.

3.3 Temperature coupling

Calculations were performed with a fixed temperature profile over shorter and longer time periods. The shortest time period tested was a change of temperature at each diffusion time step. Calculations were also performed for changes of temperature each year and for no coupling whatsoever – i.e. with the same temperature profile during the whole calculation period of the 30 year nominal lifetime of the pipes.

Calculations for the reference district heating pipe with the temperature changed at each diffusion time step and for the temperature changed each year resulted in the same equivalent thermal conductivity and mean heat flow. Calculations with the same temperature profile for the 30 years yielded an increase of 0.5% in the determined mean heat flow, which reflects that the change in the temperature profile of the foam due to aging is small (Figure 5).

Calculations with the pipe model coupled to a ground model have been performed (Persson and Claesson 2005), in which the temperature of the casing was allowed to vary due to aging. The ground model indicates the temperature of the casing based on the ground surface temperature and thermal conductivity. The temperature variation of the casings in a DN100/225 district heating network is shown in Figure 6. The network was run with a forward steel pipe temperature of 80°C and a return steel pipe temperature of 40°C in a region with a ground surface temperature of 8°C. The same initial gas concentrations as for the reference pipe were assumed. The pipes were installed with 0.6 m of top filling in a soil with a thermal conductivity of 1.5 $J \cdot s^{-1} \cdot m^{-1} \cdot K^{-1}$. The heat flow from the network increased by about 9% from its initial total value of 24.1 $J \cdot s^{-1} \cdot m^{-1}$ after 30 years of aging. The mean total heat flow over the time period was 25.0 $J \cdot s^{-1} \cdot m^{-1}$. The heat flow from the forward pipe was initially 17.5 $J \cdot s^{-1} \cdot m^{-1}$ and increased to 19.0 $J \cdot s^{-1} \cdot m^{-1}$ after 30 years. Calculations where the temperature changed at each diffusion time step and for each year yielded the same mean heat flow results. The difference was in the third decimal. Calculations with the same temperature profile for the whole period increased the estimation of the mean heat flow by 0.5% out of the forward pipe and 0.9% out of the return pipe.
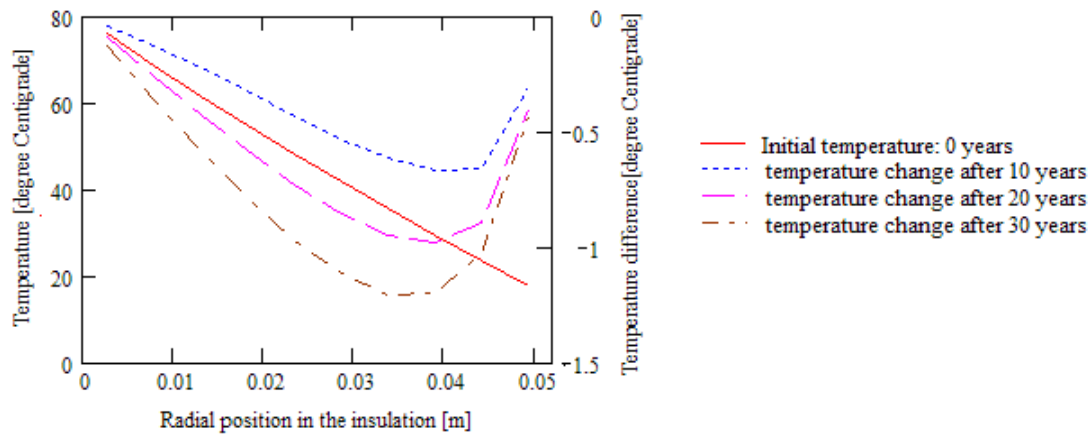
FIG. 5: Initial temperature profile of the foam of the reference district heating pipe (scale to the left) and the change that occurred in the temperature profile after 10, 20 and 30 years due to ageing (scale to the right).
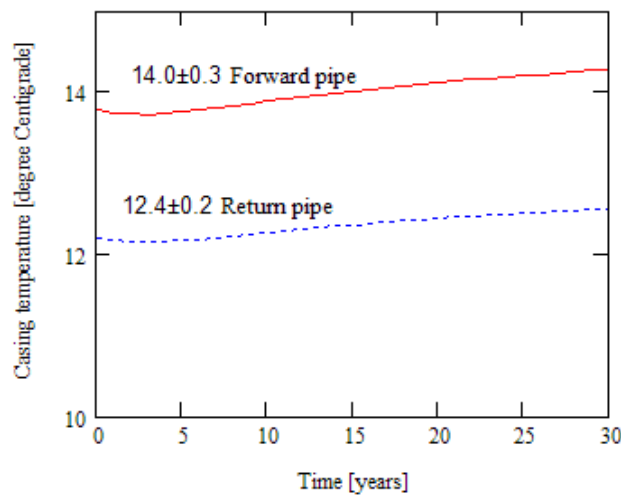
FIG. 6: Variation in the average temperature of the casings in a distribution network due to ageing.

TABLE 2: Results for 30 years of aging of polyurethane insulated pipes from different manufacturers.

	Pipe A DN80/180	Pipe B DN100/225	Pipe C DN80/180	Pipe D DN80/200	Pipe E DN80/180	Pipe F DN80/180
Equivalent thermal conductivity [J·s^{-1}·m^{-1}·K^{-1}]	0.030	0.029	0.030	0.030	0.029	0.030
Mean heat flow [J·$^{-1}$s·m^{-1}]	18.4	18.3	18.1	15.9	17.7	18.0
Time with condensed cyclopentane [years]	1	4	3	0	15	4
Change in the heat flow after 30 years [%]	14.5	9.8	17.1	13.0	12.6	13.3

3.4 Cyclopentane content

Thirty years of aging have been studied in newly produced district heating pipes from different manufacturers (A-F) (Table 2). The predictions were made by calculations, based on measured initial gas compositions in the insulation of each individual pipe. The pipes have steel fluid pipes of DN80 (88.9 mm) and DN100 (114.3 mm) dimensions. The casings are 180-225 mm in diameter. Condensed cyclopentane was initially present in 5 of the 6

pipes. Pipe E had the same initial gas concentrations as the reference pipe. The mean heat flow over 30 years differed by 4% between the best and the worst DN80/180 pipe.

If the cyclopentane content of our reference district heating pipe were decreased so that no condensed cyclopentane was initially present at the casing, the mean heat loss from the pipe over the 30 year aging period would increase by about 5%.

4. Conclusions

A model of the aging of polyurethane foam that considers coupled heat conduction and diffusion has been generated. The model accounts for the diffusion of four gases. Cyclopentane divides into gas, dissolved in the matrix and condensed liquid. The model has been applied to determine the aging of district heating pipes. A calculation of 30 years of aging takes about one minute.

The calculations illustrate how the insulating capacity and gas content of the foam change over time. The heat flow from a studied DN100/225 forward district heating pipe increases by about 10% over a 30 year aging period. The calculations demonstrate that the amount of cyclopentane present in the pipe is very important. Mean heat flows over 30 years were found to differ by up to 4% for the studied pipes from different manufacturers, due to differences in the initial gas content.

It is normally sufficient to perform calculations with the temperature updated each year. Totally neglecting the temperature feedback, i.e. performing the calculations without temperature updates, causes an error for the studied DN100/225 case of less than 1%.

5. References

Brodt K. H. (1995). Thermal insulations: cfc-alternatives and vacuum insulation, Thesis, Delft University of Technology, the Netherlands.

Claesson J. (2001). Partial Differential Equations – Engineering Applications, Mathematical Physics LTH Lund and Building Physics Chalmers Göteborg, Sweden.

Frederiksen S. and Werner S. (1993). Kostnad för distribution, Fjärrvärme – Teori, teknik och funktion (in Swedish), Studentlitteratur, Lund, Sweden.

Holmgren C. (2004). District Heating Pipes – heat losses and environmental impacts, Lic thesis, Department of Building Technology, Chalmers University of Technology, Göteborg, Sweden.

Hilyard N. C. and Cunningham A. (1994). Low Density Cellular Plastics – Physical Basis of Behaviour, Chapman & Hall.

Isberg J. (1988). The thermal conductivity of polyurethane foam. Doctoral thesis, Chalmers University of Technology, Göteborg, Sweden.

Mangs S. (2005). Insulation Materials in District Heating Pipes – Environmental and Thermal Perforance of Polyethylene Terephtalate and polyurethane foam, PhD-thesis, Department of Chemical and Biological Engineering, Chalmers University of Technology, Göteborg, Sweden.

Nielsen L.V. (1998). Materials for District Heating Pipes, PhD Thesis, Department of Chemical Engineering, Technical University of Denmark.

Nielsen L.V. (2001). Life Cycle Assessment of district heating, News from DBDH, Vol. or No. 1, p. 14-17.

Olsson M. et al (2002). Diffusion of Cyclopentane in Polyurethane Foam at Different Temperatures and Implications for District Heating Pipes, Journal of Cellular Plastics, Vol 38, p. 177-188.

Persson C. and Claesson J. (2005). Heat Loss from a District Heating Pipe – Coupled Radial Heat Conduction and Diffusion through the Polyurethane Foam Insulation, Report 2005:14, Department of Civil and Environmental Engineering, Chalmers University of Technology, Göteborg, Sweden.

Persson C. et al (2006). Life Cycle Assessment of the District Heat Distribution System, Part 3: Use Phase and Overall Discussion, International Journal of Life Cycle Assessments, Vol. 11, No. 6, p. 437-446.

Ting Larsen C. (2004). Life time cost of district heating pipes, News from DBDH, Vol. or No. 2, p. 20-21.

A transient method to determine temperature-dependent thermal conductivity of polyurethane foam in district heating pipes

Charlotte Reidhav, PhD-student

Johan Claesson, Professor

Civil and Environmental Engineering, Chalmers University of Technology, Göteborg, Sweden;
charlotte.reidhav@chalmers.se

KEYWORDS:thermal conductivity, temperature, measurement, Kirchhoff transform

SUMMARY:
The thermal conductivity of insulating polyurethane foam in district heating pipes is an important factor when improving the competitiveness of district heating, especially in areas of low heat density, where flexible district heating pipes are widely used. The standardized methods to measure the thermal conductivity of straight pipes are not applicable due to the small pipe dimensions and the fact that they are coiled. The paper presents a new transient method to determine the thermal conductivity, including the temperature dependence, for such district heating pipes. A coil of the flexible pipe is immersed into cold water. The temperature decline of hot water inside the service pipe (starting at $80\,^oC$) is measured. The method is based on the fact that the temperature decline depends on the thermal conductivity of the insulation.

Measured temperatures are compared to corresponding numerically calculated values for different parameter values to characterize λ(T). A Kirchhoff transform is used to simplify and increase the speed of the calculations. The mean square difference between calculated and measured temperatures becomes a function of these parameters. This function is minimized, and the minimum point gives the parameters of λ(T). The minimization gave stable results with a minimal difference of $\pm 0.037\,^oC$. It is shown that a linear form for λ(T) is sufficient.

1. Introduction

Flexible district heating pipes are widely used when areas with detached houses are connected to district heating distribution systems. The flexibility, light weight and few joints of the flexible pipes facilitate the construction of the district heating distribution system. The relative distribution heat losses when distributing district heat to areas with detached houses are considerable. It is important to determine and improve the insulation capacity of flexible district heating pipes. A reliable method for determining the thermal conductivity of flexible district heating pipes and its dependence on temperature is then required.

The standardized available methods for measuring the thermal conductivity of polyurethane foam in district heating pipes are restricted to be used on straight pipes. The steady-state thermal conductivity of straight pre-insulated pipes is determined with the "guarded hot pipe method", either with the "guarded end apparatus" or the "calibrated end apparatus" which are based on Jarfelt (1994) and described in the European standards EN 253:2003 and EN:ISO 8497. These methods use an apparatus where heat is transferred from a heater pipe, placed inside the test specimen's service pipe, through the pipe insulation to the outside. The distance between the heater pipe and the inside of the test pipe shall be constant along the entire test specimen, which is difficult to achieve with a flexible pipe. The radius of the heater pipe is larger than that of most service pipes of flexible district heating pipes. A cross-section of the pipe is shown in Figure 1, right. A similar method is used by the district heating pipe industry for measuring the thermal conductivity of insulation boards in accordance with ISO

8301. This method requires special manufacturing of insulation boards and is not applicable to pipes. These methods are used to determine the steady-state thermal conductivity. A series of tests at different average temperatures are thus required to determine the relation between thermal conductivity and temperature.

This paper presents a new method to determine the temperature-dependent thermal conductivity of semi-flexible polyurethane foam in flexible district heating pipes. It is determined by measuring the declining water temperature in a coil of flexible pipes placed in a pool with cold water, Figure 1. A single experimental test with simple testing equipment gives the thermal conductivity in the relevant temperature interval.

2. Experimental set-up

A pipe coil is placed in a pool with circulating cold tap water (about 9°C) as shown in Figure 1. The length of the pipe is 17 meters and it is coiled with a diameter of 1.8 m. An initial study, where the pipe coil was placed in air at room temperature, showed that air is inappropriate as surrounding medium due to difficulties with unstable temperatures. Water at the temperature of 80°C is circulated in the service pipe until the temperature is equal along the pipe and a steady-state temperature is established through the pipe insulation. Then, at time t=0 s, the pump is turned off and the valves closed leaving stagnant water inside the pipe. The temperatures are measured at several positions during the decline of the coil water temperature.
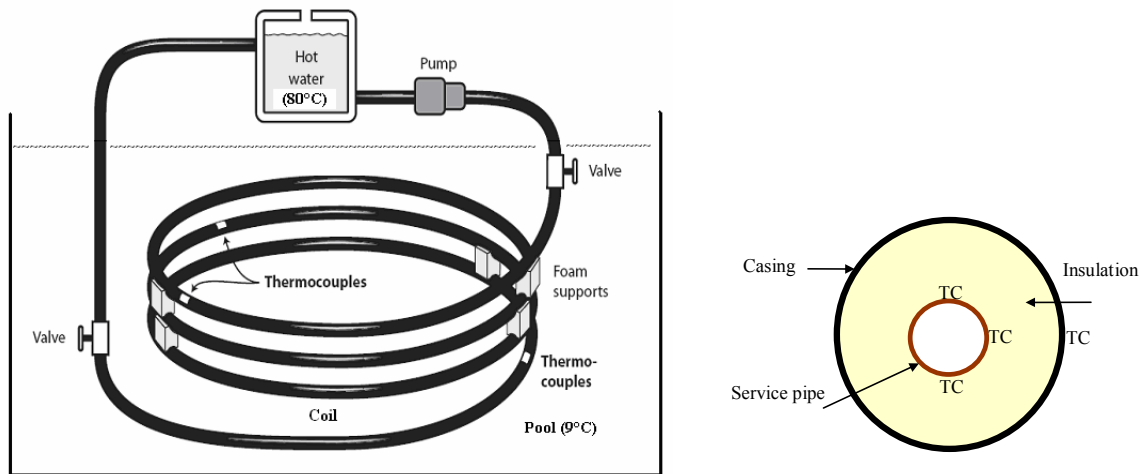
FIG. 1: Left: Experimental set-up. The coil and pool temperatures, $T_w(t)$ and $T_1(t)$, are measured by thermo-couples at three positions along the pipe. Right: Cross-section of the pipe with thermocouple positions TC.

Thermocouples for measuring the water temperature are placed on the outside of the service pipe at one meter from the inlet, at the center of the pipe length and at one meter from the outlet, see Figure 1. Three thermocouples are placed at each position: underneath, on top of and on the side of the pipe as shown in Figure 1. The insulation was peeled off at the positions of the thermocouples, which were attached to the service pipe with plastic stripes. The insulation was put back and the casing was sealed to be water proof.

3. Measurements

An example of measured coil, $T_{w,\text{meas}}(t)$, and pool temperatures, $T_{1,\text{meas}}(t)$, are shown in Figure 2. In this paper, the results of these measurements are evaluated. Other measurements have been conducted on different pipe types.

The flexible pipe analyzed with this method has a service pipe with layers of PEX and aluminum, and insulation of semi-flexible polyurethane foam blown with cyclopentane. The total thermal resistance of insulation and casing is given by insulation foam in the annular region $r_1 \leq r \leq r_0$ (m). The resistance of the casing is represented by a small additional layer of polyurethane foam with a fictitious outer radius r_1 (m) so that the thermal resistance of the casing is accounted for. The radius of the pipes are then given by $r_0 = 0.0102$ m and $r_1 = 0.0465$ m. The initial coil temperature was $T_0 = 81.2$ºC and the initial pool temperature was $T_1 = 9.1$ºC. The pool temperature increases slightly during the 12 hours. The densities and heat capacities of water, service pipe and insulation were assumed to be constant in the temperature interval studied.
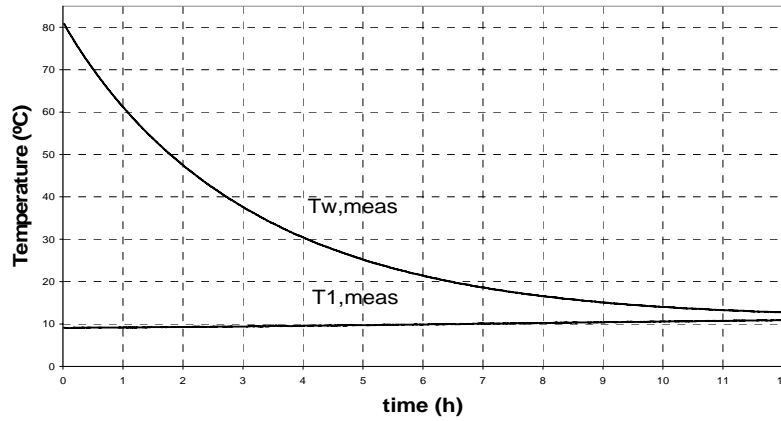
FIG. 2: Measured coil temperature $T_{w,\mathrm{meas}}(t)$ and pool temperature $T_{l,\mathrm{meas}}(t)$.

4. Numerical and mathematical model

The heat balance equation involving the radial temperature $T(r,t)$ (K) and the heat flow $q(r,t)$ (W·m^{-1}) becomes:

$$2\pi r \cdot \rho c \frac{\partial T}{\partial t} = -\frac{\partial q}{\partial r}, \qquad q(r,t) = -2\pi r \cdot \lambda(T)\frac{\partial T}{\partial r}, \qquad r_0 < r < r_1. \tag{1}$$

Here, $\lambda(T)$ (W·m^{-1}·K^{-1}) is the temperature-dependent thermal conductivity and $\rho \cdot c$ (kg·m^{-3}) the volumetric heat capacity of the insulation material.

The numerical calculations of the heat flux are facilitated considerably by the use of a so-called Kirchhoff transform ψ (W·m^{-1}) defined as the integral (Carslaw-Jaeger 1957):

$$\psi(T) = \int_{T_1}^{T} \lambda(T')dT', \qquad \frac{d\psi}{dT} = \lambda(T) \tag{2}$$

The Kirchhoff transform has been used by others to determine temperature-dependent thermal conductivity, whereas Arfvidsson and Claesson (2000) used it for calculation of moisture flow.

The point is that the temperature-dependent factor vanishes, (2) and (1):

$$\frac{\partial \psi}{\partial r} = \frac{\partial}{\partial r}\big[\psi(T(r,t))\big] = \frac{d\psi}{dT} \cdot \frac{\partial T}{\partial r} = \lambda(T)\frac{\partial T}{\partial r} \quad \Rightarrow \quad q(r,t) = -2\pi r \cdot \frac{\partial \psi}{\partial r} \tag{3}$$

From equation (1) and (3), the heat equation becomes:

$$\rho c \cdot \frac{\partial T}{\partial t} = \frac{1}{r} \cdot \frac{\partial}{\partial r}\left(r\frac{\partial \psi}{\partial r}\right), \qquad r_0 < r < r_1, \qquad t > 0. \tag{4}$$

The initial condition at $t=0$ is given by the steady-state heat flux from $T=T_0$ at $r=r_0$ to $T=T_1$ at $r=r_1$. The solution in Ψ is:

$$\psi(r,0) = \psi(T_0) \cdot \frac{\ln(r_1/r)}{\ln(r_1/r_0)}, \qquad r_0 \le r \le r_1. \tag{5}$$

Let us control that this is indeed the steady-state solution. We have from (5) and (3) a constant heat flux:

$$q(r,0) = -2\pi r \frac{\partial \psi}{\partial r} = 2\pi r \cdot \frac{\psi(T_0)}{r} == 2\pi \psi(T_0), \qquad \psi(r_0,0) = \psi(T_0), \qquad \psi(r_1,0) = 0 = \psi(T_1). \qquad (6)$$

The boundary values of ψ correspond to the right boundary temperatures T_0 and T_1. The solution (5) is exact for any temperature-dependent $\lambda(T)$. The Kirchhoff transform gives directly the steady-state solution.

The boundary temperature at $r=r_1$ is given by the measured pool temperature:

$$\psi(r_1,t) = \psi(T(r_1,t)) = \psi(T_{1,\text{meas}}(t)), \qquad t > 0. \qquad (7)$$

The boundary condition at $r=r_0$ is obtained from the heat balance for the declining coil water temperature $T_w(t)$:

$$C_0 \cdot \frac{d}{dt}\left[T_w(t)\right] = 2\pi r_0 \left.\frac{\partial \psi}{\partial r}\right|_{r_0}, \qquad T_w(t) = T(r_0,t), \qquad T_w(0) = T_0. \qquad (8)$$

Here, C_0 (J·m^{-1}·K^{-1}) is the heat capacity of the water and the service pipe.

The thermal problem is defined by Eqs. (4), (5), (7) and (8). The relation $\Psi=\Psi(T)$, (2) and (9)-(10), and the inverse relation $T=T_\psi(\Psi)$ are also needed to perform the calculations. The corresponding numerical model is described in an appendix. The set of numerical equations is quite compact and they are easy to implement in any mathematical computer program such as Matlab. We have used Mathcad. A calculation, using 10 cells and a time step of 10 s, for a decline process during 12 hours requires less than 1 s of computer time. The use of the Kirchhoff transform reduces the calculation time since an interpolation to obtain the thermal conductivity at the current temperature between two adjacent cells is avoided The short time is important since the optimization requires calculations for a large number of cases.

5. Optimization procedure

The thermal conductivity $\lambda(T)$ is in this study represented by a constant term and a linear variation with T ($M=1$), or by terms up to power M in T. In particular we will test quadratic ($M=2$) and cubic ($M=3$) polynomials in T:

$$\lambda(T) = \lambda_1 + \lambda_2 \cdot T' \quad \text{or} \quad \lambda(T) = \sum_{m=0}^{M} \lambda_{m+1} \cdot (T')^m, \qquad T' = \frac{T-T_1}{T_1-T_0}. \qquad (9)$$

Using (2) left, the corresponding Kirchhoff potential becomes:

$$\psi(T) = (T-T_1)\left[\lambda_1 + \frac{\lambda_2}{2} \cdot T'\right] \quad \text{or} \quad \psi(T) = (T-T_1)\cdot \sum_{m=0}^{M} \frac{\lambda_{m+1}}{m+1} \cdot (T')^m. \qquad (10)$$

Consider a case where $\lambda(T)$ is represented by a few parameters. For any chosen values of the parameters, the declining water temperature $T_{w,\text{cal}}(t_n; \text{par})$ is obtained by a numerical calculation as described in Appendix 1. The values are compared with the measured water temperatures. The mean square difference D becomes a function of the parameter values:

$$D(\text{par}) = \sqrt{\frac{1}{N} \cdot \sum_{n=1}^{N} \left[T_{w,\text{cal}}(t_n;\text{par}) - T_{w,\text{meas}}(t_n)\right]^2}. \qquad (11)$$

The optimal parameter values are obtained by minimizing this function.

6. Evaluation of measurements

The optimization is here applied to the measured temperature decline shown in Figure 3. The heat capacity c of the polyurethane thermal insulation was not measured. According to BING (2006) the value lies in the region $1400 < c < 1700$ J·kg^{-1}·K^{-1}. In a first optimization, we consider a linear form for $\lambda(T)$ and include c as parameter.

The unknown parameters are then λ_1, λ_2 and c. The mean square difference $D(\lambda_1,\lambda_2,c)$ is minimized. The result was:

$$\text{Parameters}: \lambda_1, \lambda_2, c; \quad \Delta T_n = T_{w,\text{cal}}(t_n;\lambda_1,\lambda_2,c) - T_{w,\text{meas}}(t_n) \Rightarrow$$

$$\lambda_{1,\text{opt}} = 0.02115, \quad \lambda_2 = 0.0096, \quad c_{\text{opt}} = 1612, \quad D_{\text{opt}} = D_{\text{opt}}(\lambda_{1,\text{opt}}, \lambda_{2,\text{opt}}, c_{\text{opt}}) = 0.0367. \quad (12)$$

Figure 3 shows the difference ΔT_n for the optimum parameter values (lower curve) and for a set of initial guess values (upper curve, λ_1=0.02, λ_2=0.01 and c=1500). There is a noise of ±0.03 ^{o}C in the temperature measurements. The difference in ΔT_n for the optimal, best fit lies in the interval –0.1< ΔT_n<0.08. The mean difference is around D_{opt}=0.037 ^{o}C, (12).
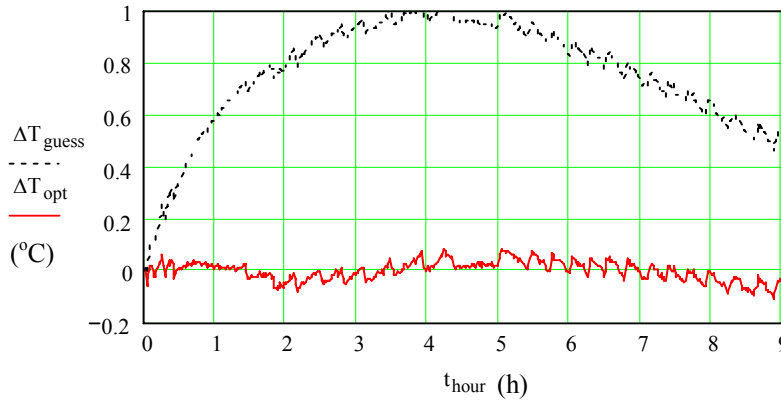
FIG.3: *Difference between calculated and measured temperature for the optimum parameter values (lower curve) and for a set of initial guess values (upper curve).*

The above minimum is obtained after computer calculations during three minutes on a standard PC. The minimization procedure has worked quite well in all cases we have tested. The Mathcad minimization routine is very efficient. A single, very distinct optimum point with the best fit between measured and calculated temperatures is obtained. This distinct optimum is illustrated in Figure 4.
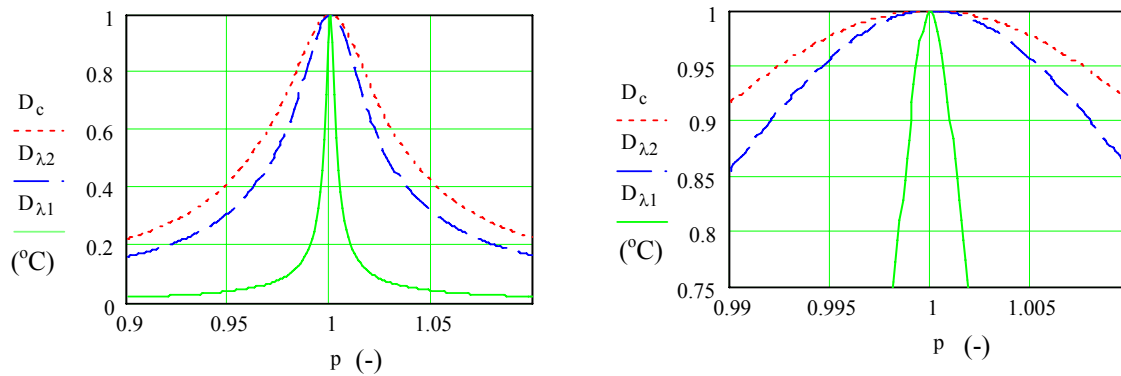
FIG. 4: *Variation of D_{opt}/D around the optimum point in the three parameter directions.*

The three curves show the inverse D_{opt}/D, which means that the optimum corresponds to a maximum +1. The curves show the variation in the three parameter directions through the optimal point. This means that the curve $D_c(p)$ shows the variation in c: $c=p \cdot c_{\text{opt}}$. More precisely, we have:

$$D_c(p) = \frac{D_{\text{opt}}(\lambda_{1,\text{opt}}, \lambda_{2,\text{opt}}, c_{\text{opt}})}{D(\lambda_{1,\text{opt}}, \lambda_{2,\text{opt}}, p \cdot c_{\text{opt}})}, \quad D_{\lambda 2}(p) = \frac{D_{\text{opt}}(\lambda_{1,\text{opt}}, \lambda_{2,\text{opt}}, c_{\text{opt}})}{D(\lambda_{1,\text{opt}}, p \cdot \lambda_{2,\text{opt}}, c_{\text{opt}})}, \quad D_{\lambda 1}(p) = \frac{D_{\text{opt}}(\lambda_{1,\text{opt}}, \lambda_{2,\text{opt}}, c_{\text{opt}})}{D(p \cdot \lambda_{1,\text{opt}}, \lambda_{2,\text{opt}}, c_{\text{opt}})}. \quad (13)$$

The curves show that the three parameters may be determined with an accuracy of three digits.

Figure 5 illustrates the variation around the optimal point for $c = c_{opt}$. Level curves for $D_{opt}/D(\lambda_1,\lambda_2,c_{opt})$ are shown in the figure. The optimum lies at the center of the ellipsoidal level curve 0.9, in accordance with the values given in (12). The optimum difference D_{opt} became 0.037°C, which means that the difference between measured and calculated temperatures is 0.037°C on average during the considered 9 hours of declining water temperature. The value of $D(\lambda_1,\lambda_2,c_{opt})$ is equal to 2·0.037=0.07 °C on the level curve 0.5.
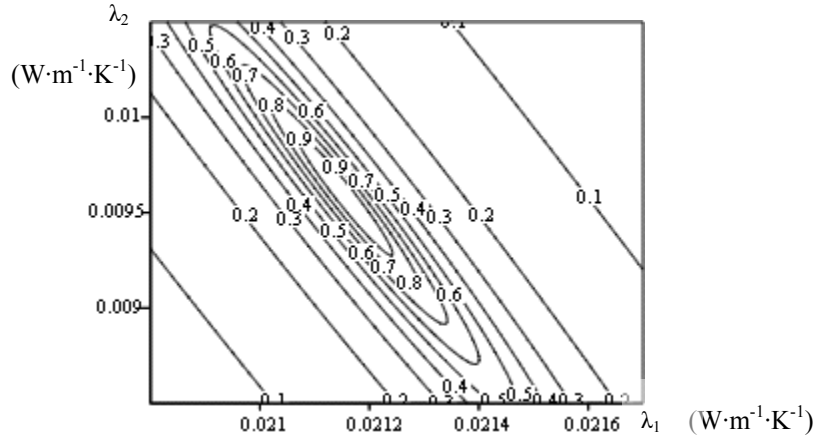
FIG. 5: *Level curves for D*$_{opt}$/*D(λ*$_1$*,λ*$_2$*,c*$_{opt}$*) with the maximum +1*
at the optimal point λ$_{1,opt}$*=0.02115 and λ*$_{2,opt}$*=0.0096.*

An important question is if it is sufficient to use a linear dependence on temperature, or if higher powers in T give a better representation of $\lambda(T)$. Therefore we have performed the optimization for linear, quadratic and cubic polynomials in T:

$$\lambda_l(T) = \lambda_1 + \lambda_2 T', \quad \lambda_q(T) = \lambda_1 + \lambda_2 T' + \lambda_3 (T')^2, \quad \lambda_c(T) = \lambda_1 + \lambda_2 T' + \lambda_3 (T')^2 + \lambda_4 (T')^3. \quad (14)$$

Here, T' is defined in (9). The optimal thermal conductivities are shown in Figure 6. The difference between the curves is less than 2 % for any temperature in the interval $10 \leq T \leq 80$ °C. The conclusion is that the linear expression is quite sufficient for the considered polyurethane.
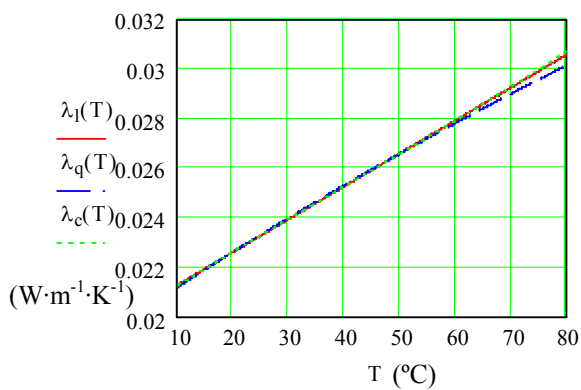
FIG. 6. *Optimal thermal conductivity for linear,*

quadratic and cubic thermal conductivity λ(T), (14).
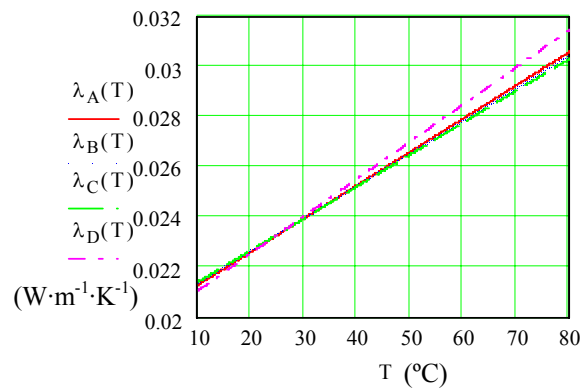
FIG. 7. *Optimal thermal conductivity λ(T) when*

different time intervals are used in the fitting,(15).

Another important question is what happens if we optimize for other time intervals than for first 9 hours. We have in particular considered the intervals:

$$A: 0 \leq t \leq 9, \quad B: 0 \leq t \leq 5, \quad C: 1 \leq t \leq 5, \quad D: 4 \leq t \leq 9 \quad \text{(hours)}. \quad (15)$$

The corresponding linear thermal conductivities are shown in Figure 7. The differences are rather small. The differences for the first three cases are up to 1 % only. The last case D differs with up to 3.4 % from the other ones. It should be noted that the water temperature lies in the interval $25 \geq T \geq 15^{\circ}$C in the time interval from 5 to 9 hours, Figure 2. Even this interval gives a fairly good result. The general conclusion is that, at least in this particular case, the thermal conductivity is quite stable when the evaluation time interval is changed. But it is of course advisable to use the larger interval.

7. Discussion

The presented measurements are from a first set of experiments. Some changes are needed to improve the method. The measurements by the thermocouples placed at the central position along the pipe had to be excluded due to measurement problems. The temperatures shown in Figure 2 are measured by the thermocouples placed closest to the pool bottom. After three hours, the flow of fresh cold water into the pool was closed and, as a consequence, the stirring of the pool water stopped. The pool water close to the surface was warned from room temperature at a somewhat higher rate compared to the water close to the bottom. The pool temperature became uneven. After 9 hours the coil water temperature was 15 ºC and the pool temperature around 10 ºC. The loss of precision in the pool temperature and the small difference between coil and pool temperature made the evaluation more uncertain. The period from 9 to 18 hours was therefore excluded from the evaluation. Efficient stirring of the pool water is required to give high precision.

A large temperature interval between the starting coil temperature and the pool temperature is desirable. A possibility is to fill the pool with cold water and ice to cover the temperature range down to 0 ºC. The measured temperatures show a small noise below ± 0.01ºC, but there is also a sawtooth variation of ±0.03ºC as seen in Figure 3. This should be investigated. But we have seen that the evaluation works quite well with the current accuracy of measured temperatures. It is also important to ensure that steady-state conditions are established at t=0 s, when the declining thermal process starts. The initial warm water should circulate in the coil during at least half an hour (for an insulation thickness of 3 cm) before the circulation is stopped.

The thermal conductivity of polyurethane foam λ (W·m^{-1}·K^{-1}) can be divided into three parts: radiation between cell walls, conduction in cell gases and conduction in the polymer matrix. The contribution from the conduction in the cell gases was estimated by determining the cell gas composition of the polyurethane foam with the experimental method described in Svanström and Ramnäs (1993), and taking literature values for the thermal conductivity of the gases at 50 ºC and for the lumped thermal conductivity due to radiation and conduction in the polymer matrix (Olsson 2001). The calculated λ_{50} is in reasonable agreement that obtained by the method presented in this paper. Furthermore, the cell gas composition and the thermal conductivity of semi-flexible polyurethane foams used for flexible district heating pipes were determined with a heat flow apparatus and cell gas analysis in Jarfelt and Ramnäs (2006). The estimations from this study are in good agreement with the values of the thermal conductivity determined here.

8. Conclusions

The presented transient method to determine the thermal conductivity of semi-flexible polyurethane foam in flexible district heating pipes gives stable results, and the optimization procedure is judged to give an accuracy of at least two significant digits. A linear expression in temperature T is shown to be sufficient to represent $\lambda(T)$.

The measurement procedure may be improved. It is important that the pool water is stirred sufficiently to have constant temperatures around the whole length of the coil. It is also important to ensure that steady-state conditions are attained at the start of the measurements.

9. References

BING, (2006). Federation of European Rigid Polyurethane Foam Associations, Thermal insulation materials made of rigid polyurethane foam (PUR/PIR), Report No 1, October 06, Belgium.

Carslaw and Jaeger (1959). Conduction of heat in solids, Oxford University Press. Page 11.

European committee for standardization (2003). European standard EN 253:2003, Preinsulated bonded systems for directly buried hot water networks – Pipe assembly of steel service pipe, polyurethane thermal insulation and outer casing of polyethylene, Brussels, Belgium.

European committee for standardization (1996). European standard EN ISO 8497:1996, Thermal insulation - Determination of steady-state thermal transmission properties of thermal insulation for circular pipes, Brussels, Belgium.

ISO 8301 Thermal Insulation, Determination of steady-state thermal resistance and related properties-heat flow meter apparatus.

Jarfelt U. (1994). Test apparatus of pipe insulation, Doctoral thesis, Chalmers University of Technology, Sweden, Göteborg.

Jarfelt U. and Ramnäs O. (2006). Thermal conductivity of polyurethane foam-best performance, *Proceedings of the 10th international symposium on district heating and cooling*, Hanover, Germany.

Olsson M. (2001). Long-term thermal performance of polyurethane-insulated district heating pipes, Doctoral thesis, Chalmers University of Technology, Göteborg, Sweden.

Svanström M. and Ramnäs O. (1993). A method for analyzing the gas phase in polyurethane foam, *Journal of Cellular Plastics*, 31, 375-388.

10. Appendix. Numerical solution

The calculation range $r_0 \leq r \leq r_1$ is divided into N cells with the midpoints $r_{c,n}$ and width Δr. The cells are annular rings. The heat capacity of cell n is C_n (J·m^{-1}·K^{-1}), and the thermal conductivity (referring to ψ, in accordance with (19), top left) between cell n and cell $n+1$ is K_n (-):

$$C_n = 2\pi r_{c,n} \Delta r \rho c; \qquad K_n = \frac{2\pi}{\ln\left(r_{c,n+1} / r_{c,n}\right)}, \qquad \left(r_{c,0} = r_0, \quad r_{c,N+1} = r_1\right). \tag{16}$$

The value of C_0 for the left-hand water cell ($n = 0$) is an input. By including the boundary radii, the formula for K_n becomes valid for $n = 0$ and $n = N$ also. The time step must, in order to ensure numerical stability, satisfy:

$$Dt < Dt_{stab} = \min_{1 \leq n \leq N}\left[\frac{C_n}{\lambda_{max} \cdot \left(K_{n-1} + K_n\right)}\right], \qquad \lambda_{max} = \max_{T_1 \leq T \leq T_0}\left[\lambda(T)\right], \qquad Dt \square 0.9 \cdot Dt_{stab}. \tag{17}$$

The initial values for ψ_n and T_n are from:

$$\psi_n = \psi(T_0) \cdot \frac{\ln(r_1 / r_{c,n})}{\ln(r_1 / r_0)}, \qquad T_n = T_\psi(\psi_n), \qquad \left(\psi_n = \psi(T_n)\right), \qquad n = 0, 1, .. \, N+1. \tag{18}$$

The calculations for a time step ν to the next one (new) are now in the discretized form of (3)-(8):

$$q_n = K_n \cdot \left(\psi_n - \psi_{n+1}\right), \quad n = 0, 1, .. \, N; \qquad T_n^{new} = T_n + \frac{Dt}{C_n} \cdot \left(q_{n-1} - q_n\right), \quad n = 1, .. \, N;$$

$$T_0^{new} = T_0 - \frac{Dt}{C_0} \cdot q_0; \qquad T_{N+1}^{new} = T_{1,meas}\left[(\nu+1)Dt\right]; \qquad \psi_n^{new} = \psi\left(T_n^{new}\right), \quad n = 0, 1, .. \, N. \tag{19}$$

These formulas (and nothing else) are used for each time step until the final time step. The first four equations correspond to (3), (4), (8) and (7), respectively.

Determination of thermal conductivity by a combination of monotonic heating and surface heat transfer measuring

Peter Matiasovsky, Dr.Ing.,
Institute of Construction and Architecture, Slovak Academy of Sciences;
usarmat@savba.sk

Peter Mihalka, Ing.,
Institute of Construction and Architecture, Slovak Academy of Sciences;
usarmipe@savba.sk

Milan, Drzik, PhD.,
Institute of Construction and Architecture, Slovak Academy of Sciences;
drzik@ilc.sk

KEYWORDS: *thermal conductivity, monotonic heating regime, convective surface heat transfer coefficient.*

SUMMARY:

The monotonic heating regime method for determination of thermal diffusivity is based on the analysis of an unsteady-state (stabilised) thermal process characterised by an independence of the space-time temperature distribution on initial conditions. At the first kind of the monotonic regime a sample of simple geometry is heated / cooled at constant ambient temperature. The determination of thermal diffusivity requires the determination rate of a temperature change and simultaneous determination of the first eigenvalue. The eigenvalue is found from a relationship between the synchronous temperatures measured at the surface and at the middle of specimen, which is expressed by eigenfunctions in the analytical solution. According to a characteristic equation the first eigenvalue is a function of the Biot number defined by a surface heat transfer coefficient and thermal conductivity of an analysed material. Knowing the surface heat transfer coefficient and the first eigenvalue the thermal conductivity can be determined. The surface heat transport coefficient during the monotonic regime can be determined by the continuous measurement of long-wave radiation heat flow and the photoelectric measurement of the air refractive index gradient in a boundary layer. The obtained eigenvalues and corresponding surface heat transfer coefficient values enable to determine thermal conductivity of the analysed specimen together with its thermal diffusivity during a monotonic heating regime.

1. Introduction

The monotonic heating regime of the first kind method under the boundary conditions of the 3rd kind is advantageous for the determination of thermal difussivity of high-density materials (Klarsfeld 1984). For the determination of thermal conductivity a complementary measurement of the specific heat is necessary. In order to avoid this complication the monotonic heating regime method was combined with a simultaneous measurement of the surface heat tranfer coefficient, especially its convective heat transfer component.

2. Theory

2.1 Monotonic heating regime method

The determination of thermophysical properties by the monotonic heating regime method of the first kind includes the measurements of thermal diffusivity and the measurements of the specific heat of the specimens with a simple geometry. The principle of the measurements is based on the monitoring of a cooling of the specimens with a defined geometry in a constant temperature environment.

There is given an isotropic cube with a side of the length *d*. The initial temperature of the cube is θ_0. At the initial time the cube is suddenly moved from the environment with a constant temperature θ_0 to the environment with a different constant temeperature θ_e ($\theta_0 > \theta_e$). The coefficients of the surface heat transfer are different at various cube surfaces. The temperature course at an arbitrary cube point is given by the solution of the heat transfer differential equation (1) for the case of constant material parameters and zero heat sources:

$$a \cdot \nabla^2 \theta = \frac{\partial(\theta)}{\partial t} \tag{1}$$

where: a is the thermal diffusivity, θ is the temperature, t is the time, under the boundary conditions of 3rd kind.

The analysis of the cube cooling under a constant ambient temperature shows that the whole process can be divided into three states:
- At the first state, random, non-steady state the initial temperature distribution is dominant.
- At the second state, known as a monotonic regime, the temperature change with a time runs according to an exponential law.
- The third state corresponds to a steady state, when the temperature in all points of the cube is equal to the ambient temperature.

The second state, the monotonic regime appears after the time of the cooling, when the Fourier number Fo is higher than 0.4. Then the time course of relative temperatures of the specimen θ_r at all points under constant boundary conditions can be expressed in the form:

$$\theta_r = \frac{\theta(x,y,z,\tau) - \theta_e}{\theta_0 - \theta_e} = A + A_{x1} \cdot \left(\cos\frac{x \cdot \mu_{x1}}{d} + \frac{Bi(d,y,z)}{\mu_{x1}} \cdot \sin\frac{x \cdot \mu_{x1}}{d} \right) \cdot A_{y1} \cdot \left(\cos\frac{y \cdot \mu_{y1}}{d} + \frac{Bi(x,d,z)}{\mu_{y1}} \cdot \right.$$

$$\left. \cdot \sin\frac{y \cdot \mu_{y1}}{d} \right) \cdot A_{z1} \cdot \left(\cos\frac{z \cdot \mu_{z1}}{d} + \frac{Bi(x,y,d)}{\mu_{z1}} \cdot \sin\frac{z \cdot \mu_{z1}}{d} \right) \cdot \exp\left[-\left(\frac{\mu_{x1}^2 + \mu_{y1}^2 + \mu_{z1}^2}{d^2} \right) \cdot a \cdot t \right] \tag{2}$$

where: $Bi(d, y, z)$ is Biot number for the surface heat transfer coefficient at the plane parallel the coordinate axes y, z at the distance d; μ_{x1}, μ_{y1} a μ_{z1} are the first eigenvalues in the directions of the coordinate axes x, y, z.

From equation (2) results that $\ln\theta_r = f(\tau)$ is the line, the tangent of which M equals:

$$M = \frac{\partial[ln(\theta_e - \theta(x,y,z,t))]}{\partial\tau} = \frac{ln\theta_r(x,y,z,t_1) - ln\theta_r(x,y,z,t_2)}{t_1 - t_2} = \frac{a}{d^2} \cdot \left(\mu_{x1}^2 + \mu_{y1}^2 + \mu_{z1}^2 \right) \tag{3}$$

The variable M is usually called the cooling rate and it is constant in the monotonic heating regime. The thermal diffusivity is then given by the following relationship:

$$a = \frac{M \cdot d^2}{\mu_{x1}^2 + \mu_{y1}^2 + \mu_{z1}^2} \tag{4}$$

The essence of the experiment at the determination of thermal diffusivity is the movement of a specimen with the initial temperature θ_0 into the environment with a lower constant temperature θ_e and the registration of cooling courses of selected points of the specimen. It is possible from the measured temperatures courses to determine and put the following parameters into relation (4):
1. The tangent M of the line $\ln\theta(\tau)$
2. The values μ_{x1}, μ_{y1}, μ_{z1}

The value *M* can be obtained by calculating the logarithm of the temperature course at an arbitrary point of the cube during the monotonic regime.

The values $\mu_{x1,}\,\mu_{y1,}\,\mu_{z1}$ for three pairs of opposite surfaces are the functions of the heat transfer coefficient between given surfaces and environment. At their determination it is possible to issue from the following assumptions. During cooling the cube with surfaces oriented parallel with the coordinate axes the heat transfer at 4 vertical surfaces is identical, whilst at the top and bottom horizontal surfaces the heat transfer is different. For the determination of thermal diffusivity then it satisfies to determine only two values: $\mu_{x1} = \mu_{y1}$ for vertical surfaces and μ_{z1} for horizontal surfaces of the cube.

At the determination for example of μ_{x1} – value, given by the heat transfer at two opposite surfaces in *x*-axis direction it is possible to issue from the two-points method, based on the fact that the ratio of the temperatures at an arbitrary point of the cube in each moment of the monotonic regime is constant and it is the function of μ_{x1}. Then for the temperatures of the centres of opposite surfaces and the centre of the cube the following relationships are valid:

$$\frac{\theta(0,\frac{d}{2},\frac{d}{2},t)-\theta_e}{\theta(\frac{d}{2},\frac{d}{2},\frac{d}{2},t)-\theta_e} = \frac{1}{\cos\frac{\mu_{x1}}{2}+\frac{Bi(d,y,z)}{\mu_{x1}}\cdot\sin\frac{\mu_{x1}}{2}} = k_{x0} \qquad (5)$$

$$\frac{\theta(d,\frac{d}{2},\frac{d}{2},t)-\theta_e}{\theta(\frac{d}{2},\frac{d}{2},\frac{d}{2},t)-\theta_e} = \frac{\cos\mu_{x1}+\frac{Bi(d,y,z)}{\mu_{x1}}\cdot\sin\mu_{x1}}{\cos\frac{\mu_{x1}}{2}+\frac{Bi(d,y,z)}{\mu_{x1}}\cdot\sin\frac{\mu_{x1}}{2}} = k_{xd} \qquad (6)$$

And after their arrangement we obtain the equation:

$$\frac{k_{x0}+k_{xd}}{2}=\cos\frac{\mu_{x1}}{2} \qquad (7)$$

enabling the calculation of μ_{x1}, or μ_{z1} from the known values of k_{x0} and k_{xd}, or k_{z0} and k_{zd}.

From the cooling rate and the temperatures ratios with use of relations (6) and (7) it is possible to calculate the first eigenvalues μ_{x1}, μ_{z2} and the thermal conductivity of the sample *a*.

The solution of the following transcendent equation enables to obtain the Biot number expressing the relationship between the thermal conductivity of specimen and the surface heat transfer coefficient:

$$\cot\mu_{x1}=\frac{\mu_{x1}^2 - Bi_{(0,y,z)}\cdot Bi_{(d,y,z)}}{\mu_{x1}\cdot\left(Bi_{(0,y,z)}+Bi_{(d,y,z)}\right)} \qquad (8)$$

2.2 Photoelectric measurement of air refractive index

The wall surface convective heat transfer coefficient can be defined by the expression combining the empirical Newton law and the steady state Fourier law of heat conduction:

$$h_c = \frac{-\lambda \cdot \dfrac{d\theta}{dy}\bigg|_{y=0}}{\theta_{si} - \theta_{\infty}} \qquad (9)$$

where: h_c is the surface heat transfer coefficient, $d\theta/dy$ is the air temperature gradient along the vertical y-axis, λ is the thermal conductivity of air, θ_{si} and θ_{∞} are the temperatures at the surface and outside the boundary layer, respectively.

The experimental determination of the temperature gradient is based on the relationship between the air density dependent on temperature and the air refractive index. This relation is described by the Lorenz-Lorentz law (Fomin 1989):

$$\frac{n^2 - 1}{n^2 + 2} \cdot \frac{1}{\rho} = \frac{N}{M} = const. \qquad (10)$$

where: n is the air refractive index [-], ρ is the air density [kg/m^3], N is the air molar refraction [m^3/mol], M is the air molar mass [g/mol].

In the range of 300 – 400 K and under the atmospheric pressure the air can be regarded as an ideal gas. Under the assumption of isobaric condition, the air density change is proportional inversely to the temperature change. Then the refractive index variation is proportional to the air temperature change. A basic constant can be found for the relationship between air temperature change and refractive index change for the wavelength of 650 nm at the temperature of 300 K:

$$\frac{dn}{d\theta} = 0.961.10^{-6} \qquad (11)$$

Then, the mutual relationship between the refractive index gradients and temperature gradients is as follows:

$$\frac{d\theta}{dy} = \frac{1}{0.961 \cdot 10^{-6}} \cdot \frac{dn}{dy} \qquad (12)$$

Considering the constant distribution of refractive index along the path of optical detection by laser beam and the appropriate geometrical relations, a final equation for the beam deviation in the detector place is:

$$\frac{d\theta}{dy} = \frac{2 \cdot n_0 \cdot \Delta y}{L^2 \cdot 0.961 \cdot 10^{-6}} \qquad (13)$$

where: L is the laser beam path length [m], n_0 is the initial refractive index $\cong 1.0$ for air, Δy is the laser beam deviation.

With use of equation (13) the gradient near the surface and then the near-surface temperature profile can be evaluated. Applying the equation (9) the convective heat transfer coefficient can be calculated.

3. Experiment

The experiment was performed for the PMMA cubic specimen, with the side length of 0.1 m. It consisted of the simultaneous measurement of temperatures at the midpoints of two opposite vertical surfaces and the centre of cube, measurement of the laser beam deviations near one vertical surface (2 mm distance) and measurement of the radiative heat flow between cube vertical surfaces and surrounding isothermal surfaces during the cooling of the specimen. In figures 1 and 2 there are a schematic description and view of the experiment. The initial temperature of the specimen was 40 °C and the controlled ambient temperature was 20 °C. The cooling process continued approximately for 3 hours. The monotonic regime lasted during the second hour of the experiment. In figure 4 there is a time course of the near-surface temperature gradient in the air boundary layer calculated by equation (13) from the laser beam deviation data. The corresponding time courses of vertical convective and radiative surface heat transfer coefficients are in figure 5. An analytical solution of the monotonic cube cooling expressed by equation (2) supposes constant boundary conditions. In reality the total surface heat transfer coefficient is decreasing during the proces of cooling. Therefore its average value from the analysed period must be taken into consideration. The time courses of the temperatures ratio k, the first eigenvalue, the total surface heat transfer coefficient, the Biot number, with the resultant values of thermal conductivity determined from the equations (7) and (8) are in table 1. As the heat transfer at all vertical surfaces of the cube was identical only one k-ratio and Biot number could be considered. The average thermal conductivity obtained during the monotonic regime is in agreement with the known value of the PMMA thermal conductivity – 0.185 W/(m.K) determined by the quarded hot plate method. The measurements were repeated also for other materials. The measurement for concrete (density 2148 kg/m^3) gave the thermal conductivity 1.0 W/(m.K). The measurement for the autoclaved aerated concrete (density 560 kg/m^3) gave the thermal conductivity 0.141 W/(m.K)) in a comparison with the result determined by the guarded hot plate method – 0.138 W/(m.K).
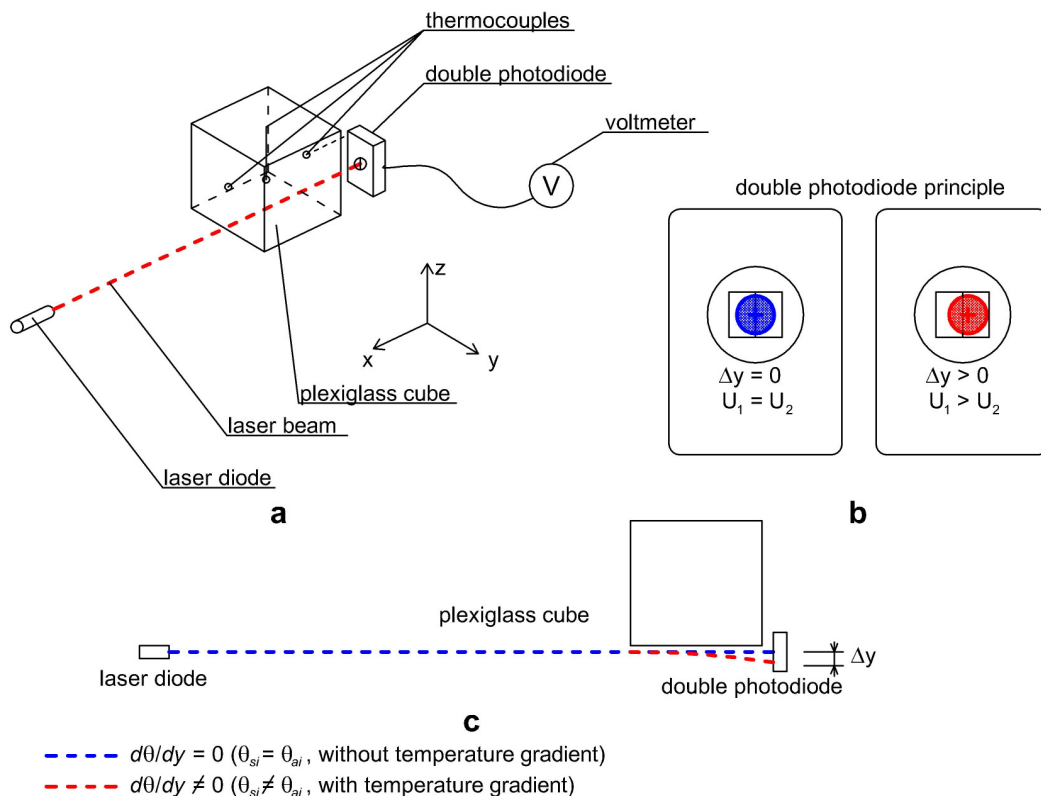
FIG. 1: Scheme of experiment.

FIG. 3: View of experiment.

Equation shown on graph:
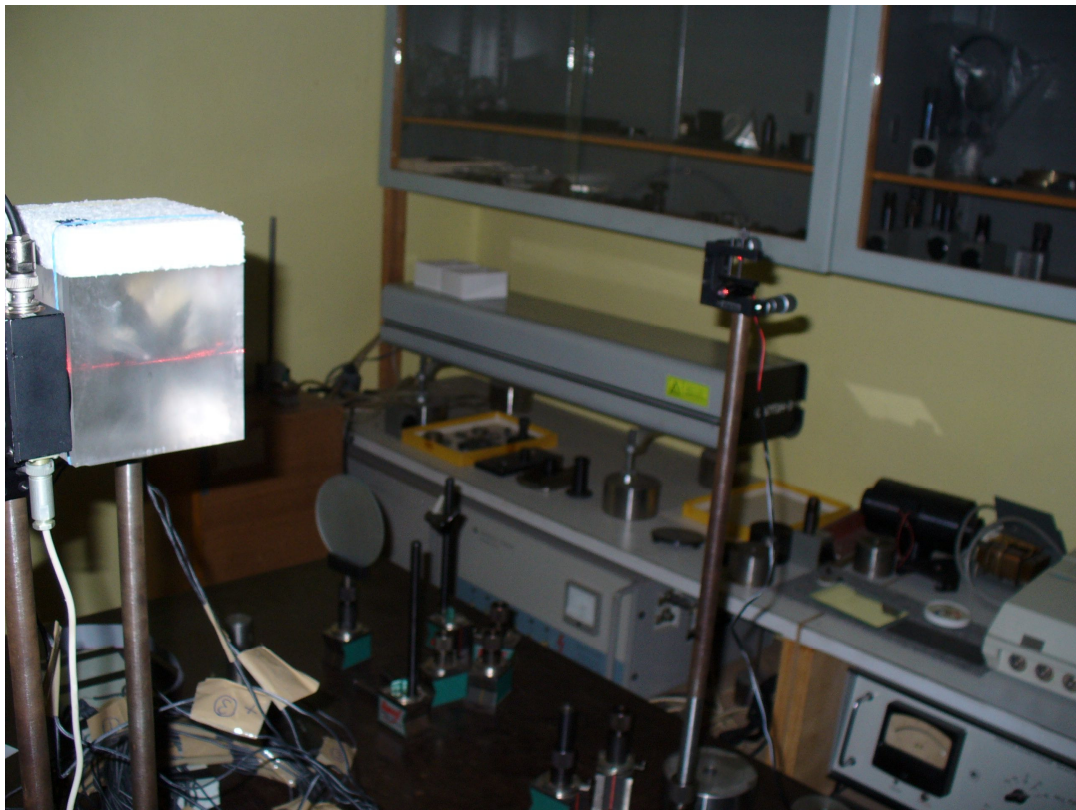
$$dT/dy = 2021.7e^{-0.8926 \cdot t}$$
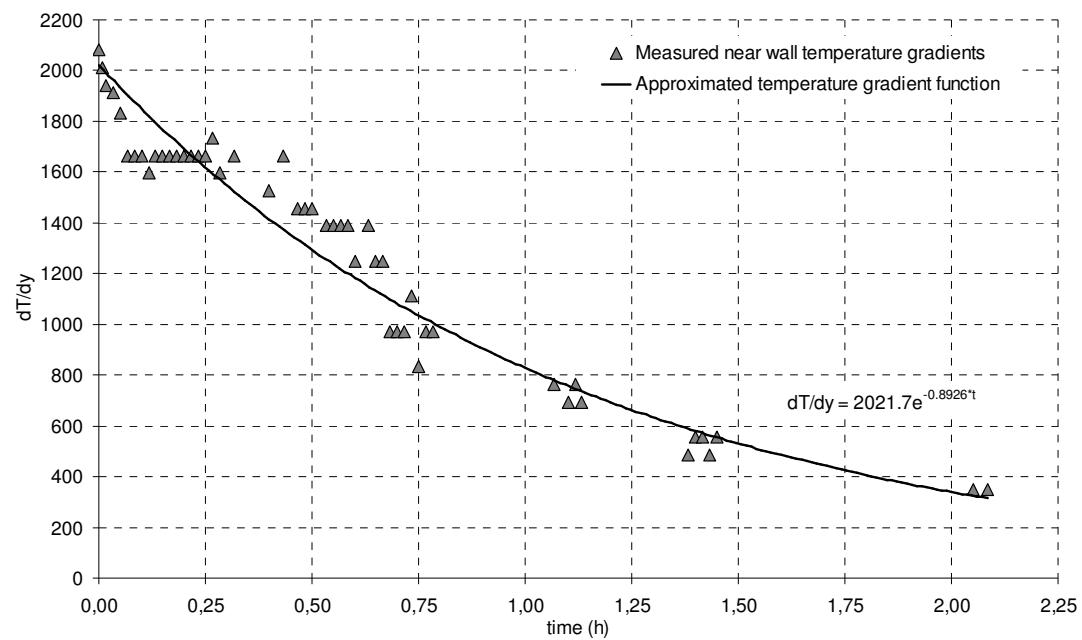
FIG. 4: Time course of near-surface temperature gradient.
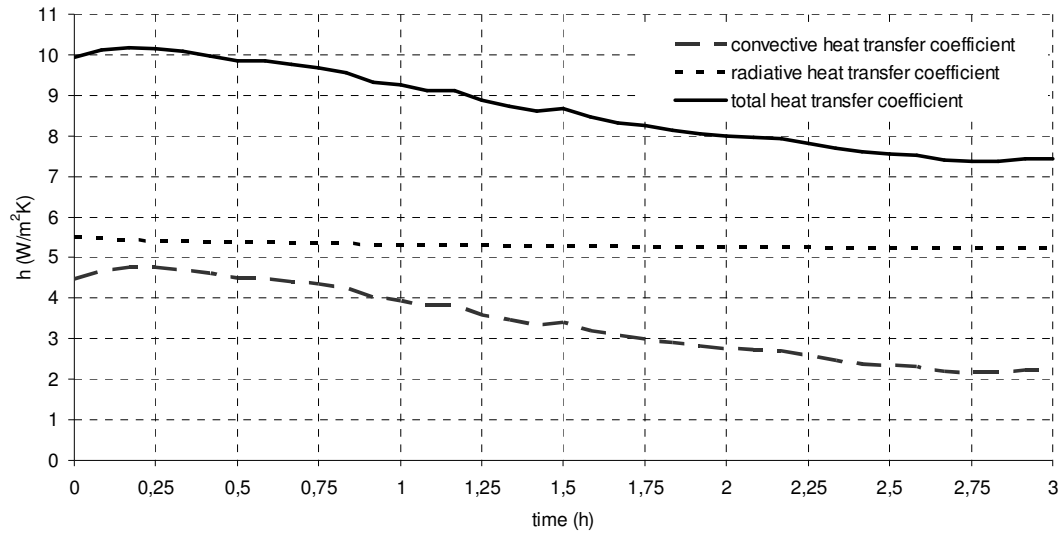
FIG. 5: Time course of convective and radiative surface heat transfer coefficients.

TABLE. 1: Time courses of measured variables and calculated parameters with resultant thermal conductivities.

Time [min]	k [K/K]	μ_1 [1/s$^{1/2}$]	h [W/(m^2.K)]	Bi [-]	λ [W/(m.K)]
60	0.43	2.24	9.25	4.61	0.200
65	0.44	2.24	9.12	4.61	0.198
70	0.44	2.24	9.11	4.66	0.195
75	0.44	2.24	8.87	4.62	0.192
80	0.43	2.25	8.74	4.68	0.187
85	0.43	2.24	8.63	4.67	0.185
90	0.43	2.25	8.66	4.75	0.183
95	0.43	2.24	8.47	4.66	0.182
100	0.44	2.24	8.33	4.63	0.179
105	0.44	2.24	8.24	4.63	0.178
110	0.44	2.24	8.15	4.59	0.177
115	0.44	2.23	8.05	4.57	0.176
120	0.44	2.24	7.99	4.61	0.173
Average	0.44	2.24	8.59	4.64	0.185

4. Conclusions

An applicability of the simultaneous measurement of the near-surface temperature gradient in air boundary layer during the monotonic heating regime test for the determination of thermal conductivity was proved. The

obtained thermal conductivity values were in an agreement with the independent measurements by a guarded heat plate method.

A combination of the monotonic heating regime method with simultaneous the surface heat transfer measuring enables to determine the thermal diffusivity and the thermal conductivity from one measurement.

Acknowledgement

5. References

Fomin N. A. (1989) Speckle interferometrija gazovych potokov. Nauka I technika, Minsk (in Russian).

Chapman A. J. (1960) Heat transfer. The Macmillan Company, New York

Klarsfeld S. (1984) Guarded Hot Plate Method for Thermal Conductivity Measuremenent, in *Compendium of Thermophysical Property Measurement Methods, Vol.1 Survey of Measurement Techniques*, (Maglic K.D, Cezairliyan A., Peletsky V.E., editors), Plenum Press, London p. 169-230.

Matiašovský P., Koronthályová O. (1994) Moisture dependent thermal properties of cellular concrete. *Building Research Journal*, Vol 42, Bratislava, Slovakia, p. 265-273.

Mihálka P., Držík M., Matiašovský P. (2007) Measurement of Local Surface Heat Transfer Coefficient by Photoelectric Method. *Proceedings of Thermophysics 2007*, Vydavateľstvo STU, Bratislava, p. 86-92.

Schlichting H. (1979) Boundary-Layer theory. McGraw-Hill.

Vasiljev L. A. (1968) Tenevije metody. Nauka, Moscow (in Russian).

Evaluation of thermal bridges by means of numerical simulation

Charlotte Gudum, Ph.D.
Bygge- og Miljøteknik A/S
cg@byggeteknik.com

KEYWORDS: *numerical simulation, thermal bridge, condensation, critical surfacetemperature, mould*

SUMMARY:
The paper presents a method to find out where thermal bridging will risk causing damage to a building. The model uses Danish weather conditions. The method is based on the ISO EN 13788:2001. By analysing the outdoor humidity and temperature conditions, and including the contribution of moisture from the indoor climate, the most critical month and the corresponding critical surface temperature is evaluated for different humidity classes. It is found that the most critical month differs with the humidity class. An example of a numerical analysis of thermal bridging is presented in the paper.

1. Introduction

Some thermal bridges will always exist, where parts of the building envelope have reduced insulation thickness. A thermal bridge introduces an area with lower inside surface temperature within the building, where the condensation of indoor moisture risks causing a high relative humidity, and furthermore the risk of mould growth. In practice it is important that all cold bridges are detected in the design phase, before the building is built. This enables the design to be changed and the risk of damage to the building envelope to be avoided. There has not been a standard method in Denmark to evaluated thermal bridges until now.

2. Significant thermal bridge

In the Danish building regulation it is stated that significant thermal bridges may not occure. A significant thermal bridge is here defined as where there is a risk of condensation that may cause mould growth.

Here a method for evalution of significant thermal bridge i.e. cold bridges based on the ISO EN 13788 is presented, based on the Danish weather condition.

3. The conditions for simulation

3.1 Outdoor condition

For the outdoor conditions the monthly mean values of relative humidity and temperatures are calculated for the Danish test reference year (TRY).
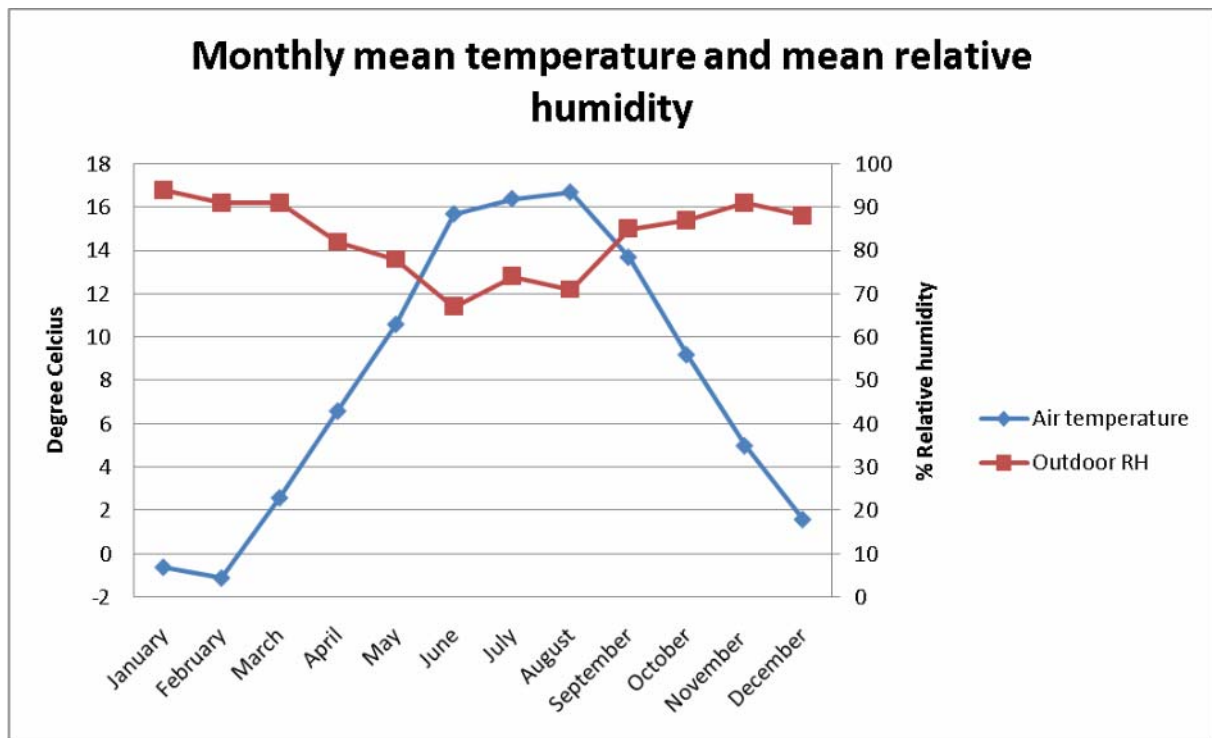
FIG. 1: Monthly temperature and moisture content of outdoor air according to TRY.

3.2 Indoor conditions

The all-year round indoor temperature is defined as 20ºC. The humidity in the indoor climate can be described by using humidity classes corresponding to different internal humidity loads.

Table 1 gives some guidance regarding the selection of humidity class [selected entries EN ISO 13788:2001].

TABLE. 1: Internal humidity classes.

Humidity class	Buildings
1	Storage areas
2	Offices, shops
3	Dwellings with low occupancy
4	Dwellings with high occupancy, sports halls, kitchens, canteens
5	Special buildings, e.g. laundry, brewery, swimming pool
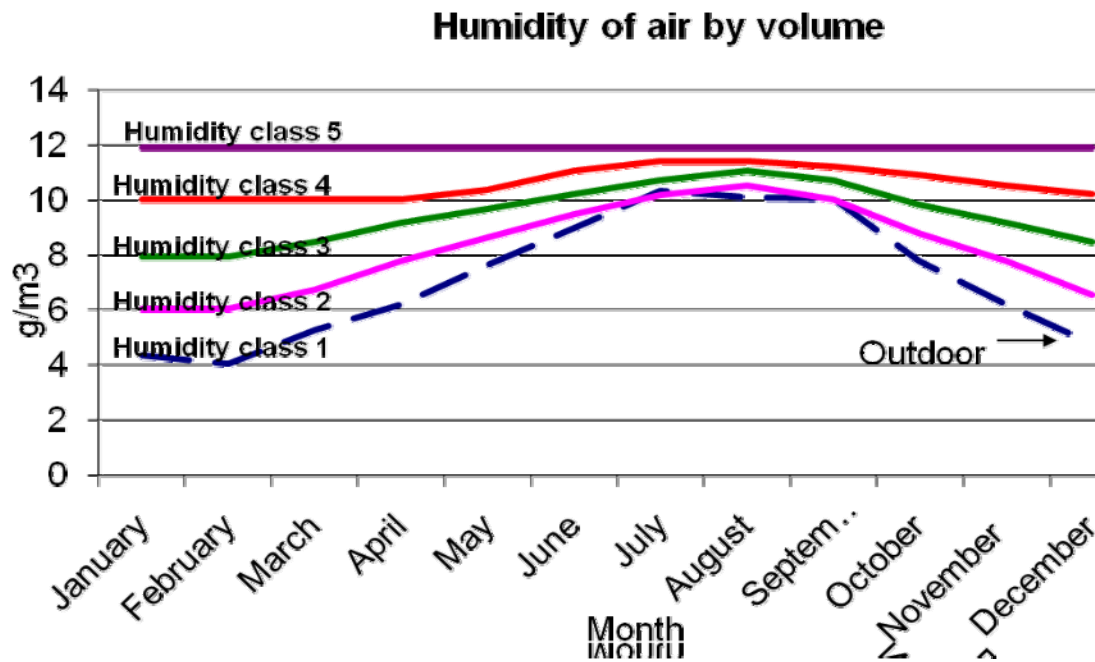
FIG. 2: The lines show the upper and lower limit of humidity of air by volume in different humidity classes, together with the air humidity by volume for outdoor air as a function of the month. Note that the humidity class 5 is above the upper dark blue line, and humidity class 1 is below the pink line.

 In a humid climate (high humidity class) there is more moisture in the air than in a dry climate (low humidity class), as in the drier climate less moisture is added from the activities compared to a humid indoor climate. This is seen in the winter period, where ventilationrates are typically low. In summer periods the ventilation rates are assumed higher. The difference between the humidity classes in summer is less significant. The humidity of air by volume for class1 is equal to the outdoor humidity in July until mid-September.

3.3 Critical temperature

The 80% RH temperature of the indoor air is defined as the critical surface temperature. In summer the dewpoint temperature of the outdoor air is high as is the indoor air temperature corresponding to 80% RH, but the temperature difference between indoor and outdoor air is small. Whereas in winter the dewpoint temperature of the outdoor air is lower and again so is the corresponding indoor air temperature to 80% RH, but the temperturedifference is higher. Therefore the most critical month depends on both the outdoor temperature and the indoor humidity. To evaluate the most critical month, the dimensionless temperature is calculated.

 To evaluate the most critical month the temperature factor at the internal surface is calculated. The temperature factor is defined as the difference between the minimum acceptable temperature of the internal surface and the external air temperature, divided by the difference between the internal air temperature and the external air temperature.

TABLE. 2: The table lists the critical temperatures for the different humidity classes month by month, along with the mean outdoor temperature and outdoor relative humidity definded by TRY.

Month	Outdoor air temperature	Outdoor RH	Humidity classes			
			1	2	3	4
January	-0.6	94	7.1	11.4	14.9	17.7
February	-1.1	91	7.1	11.4	14.9	17.7
March	2.6	91	9.1	12.4	14.9	17.7
April	6.6	82	10.9	13.4	14.9	17.7
May	10.6	78	12.6	14.3	15.4	17.7
June	15.7	67	14.1	15.2	16.5	17.7
July	16.4	74	15.2	15.9	17	17.7
August	16.7	71	15.6	16.3	17	17.7
September	13.7	85	14.8	15.8	16.8	17.7
October	9.2	87	13	14.7	16.3	17.7
November	5	91	10.9	13.5	15.7	17.7
December	1.6	88	8.6	12.2	15.2	17.7

With the conditions assumed in TABLE 3 the critical month is evaluated for each specific humidity class as the month with the highest temperature factor.

TABLE. 3: The table shows the critical dimensionless temperature for the different humidity classes.

Month	Outdoor air temperature	Indoor air temperature	Humidity classes			
			1	2	3	4
January	-0,6	20	0,374	0,583	0,752	0,888
February	-1,1	20	0,389	0,592	0,758	0,891
March	2,6	20	0,374	0,563	0,707	0,868
April	6,6	20	0,321	0,507	0,619	0,828
May	10,6	20	0,213	0,394	0,511	0,755
June	15,7	20	-0,372	-0,116	0,186	0,465
July	16,4	20	-0,333	-0,139	0,167	0,361
August	16,7	20	-0,333	-0,121	0,091	0,303
September	13,7	20	0,175	0,333	0,492	0,635
October	9,2	20	0,352	0,509	0,657	0,787
November	5	20	0,393	0,567	0,713	0,847
December	1,6	20	0,380	0,576	0,739	0,875

For each humidity class the month where the dimensionless temperature is highest is detected. The results of most critical month and the critical temperature for the five different moisture categories are listed in the TABLE 4.

TABLE. 4: The critical month, the mean outdoor temperature, and the critical surfacetemperature for the different indoor climates or humidity classes.

Humidity class	Critical month	Mean Outdoor Temperature [°C]	Critical temperature[°C]
1	November	5.0	10.9
2	February	-1.1	11.4
3	February	-1.1	14.9
4	February	-1,1	17.7

In humidity class 5 the critical temperature must be calculated for the actual situation.

4. Example

The example shows a domestic house with a roofing terrace above the living area. The thickness of insulation is reduced near the drain adjacent to the parapet walling. Thus enabling a rainwater run-off towards the drain. To counteract cold bridging 25 mm insulation and gypsum boarding is placed under the concrete roofing slab. The detail has to be analysed as there could be a condensation risk behind the insulation.
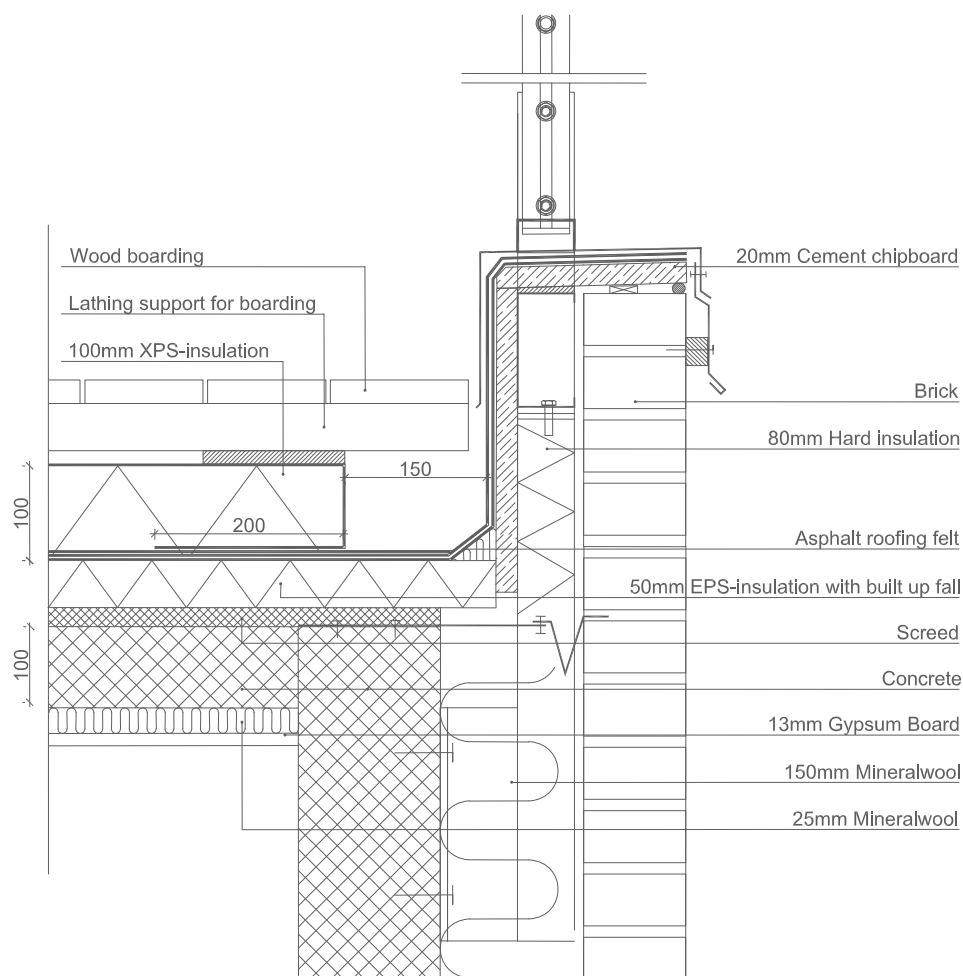
FIG. 3: Cross-sectional detail

A 2-dimensional simulation of the temperature profile is made in order to investigate the miniumum temperature on the surface on the concrete.

A model of the detail is made in the 2-dimensional program Heat 2 from Blocon. The most critical month for domestic buildings is February where the mean outdoor temperature is –1.1ºC, and the indoor temperature is 20ºC. A stationary simulation of the temperature profile is made. The surface conductance is 0.04 m^2K/W between the air and the surface on the outside, and 0.13 m^2K/W between the air and the surface on the inside. The standard thermal resistance for internal surfaces is in Denmark according to DS 418 0.13 m^2K/W for horizontal heat flow, and is used for alle internal surfaces in the simulation. The heat flow is zero through the vertical boundary to the left and through the horizontal boundary in the bottom.
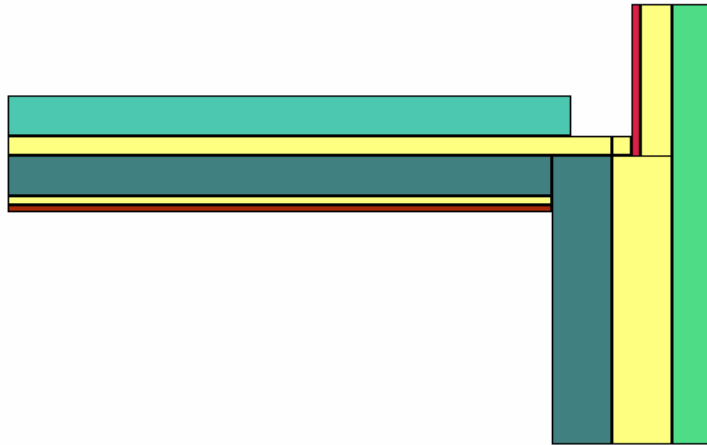
FIG. 4: A model of the cross-section is made in the 2D simulationprogram Heat 2 from Blocon. Only materials which influence the heat flow are considered. Very thin layers and joints are not modelled.

A grid is defined with maxium 25 mm intervals in both the x- and the y-dimension adjacent to the possible cold bridge.

5. Results of simulation

A steady-state simulation is made for the critical month February, and the result is given as a figure with temperature gradients

.
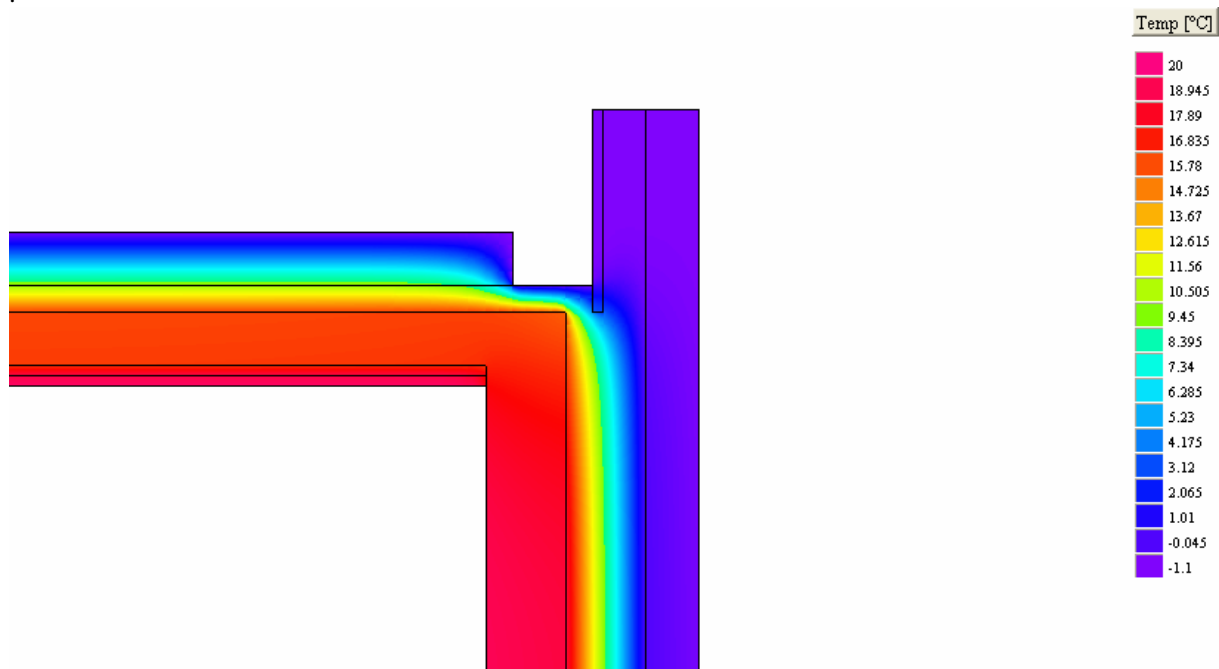
FIG. 5: The temperature profile of the chosen cross-section with the possible cold bridge.

In order to find the minimum surface temperature on the inside of the concrete slab the isothems are evaluated. A closer inspection of the corner under the rain water drain shows a temperatureminimum of 16.4°C behind the insulation.
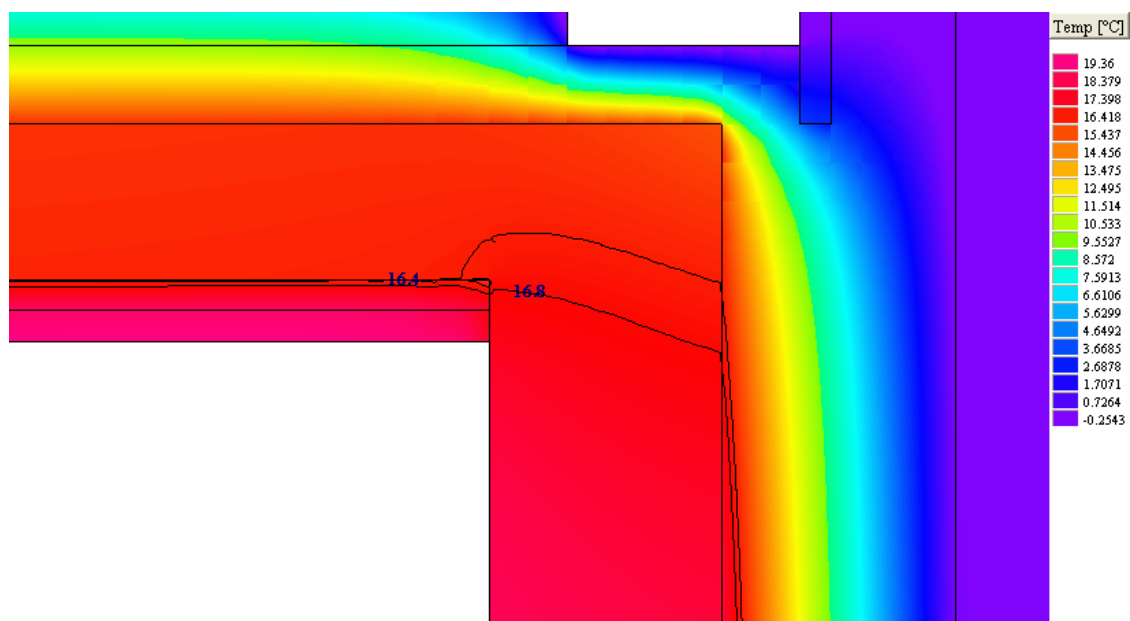
FIG. 6: The minimum surface temperature on the underside of the concrete slab is shown above. Note that the color scale is different from that of FIG. 5.

6. Conclusion and discussion

A table with critical surface temperatures has been produced using Danish weather data and the humidity classes 1 to 4 in accordance with the humidity classes defined in EN ISO 13788:2001 . For humidity class 1 the critical month was November, and for humidity classes 2,3 and 4 the critical month was February.

The results show that the higher humidity the indoor climate has, the higher the minimum surface temperature is required, which seems reasonable.

An example has been given, where the method has been used to evaluate a cold bridge. For humidity classes 2 and 3 the simulation shows that the minimum inside surface of 16.4°C is above the critical temperature. The simulation shows that there is no risk of high relative humidity or condensation during a critically long period, that could cause mould growth.

It should be noted that the critical temperature is evaluated on the interior surfface of the vapour barrier or a material with the same function such as the concrete slab in the example. When the internally concrete slab is covered by mineral wool and gypsum boarding, it is the temperature behind these additional materials which should be evaluated.

The method does not evaluate for condensation risk under extreme conditions such as very low outdoor temperatures. Using the monthly mean temperature seems relevant as the heat capacity of the construction will act as a buffer for temperature changes, and therefore using the mean monthly temperature for steady-state simulation of the temperature profile, as proposed in the standard ISO EN 13788, is found reasonable.

7. References

Dansk Standard (2001).DS/EN ISO 13788 1. udgave 2001-10-09. Byggekomponenter og –elementers hygrotermiske ydeevne – Indvendig overfladetemperatur for at undgå kritisk overflade- og mellemrumskondens – Beregningsmetode, København, Denmark.

Dansk Standard (2002) DS 418 6. udgave 2002-04-03. Beregning af bygningers varmetab, København, Denmark.

Key issues in energy-efficient building envelopes of Norwegian office buildings

Matthias Haase, Research Scientist,
SINTEF Building and Infrastructure, 7465 Trondheim, Norway;
matthias.haase@sintef.no and www.sintef.no/byggforsk

Inger Andresen, Dr.ing, Senior Scientist,
SINTEF Building and Infrastructure, 7465 Trondheim, Norway;
inger.andresen@sintef.no and www.sintef.no/byggforsk

SUMMARY:
This work is part of the project "Climate Adapted Buildings" (CAB) run by SINTEF Building and Infrastructure. The project's principal objectives are to develop more energy-efficient building envelope assemblies and new methods for the design of building envelopes in harsh climates, resulting in more accurate and geographically dependent design guidelines. The project includes analyses of building envelopes applied in different kinds of climates, different uses, and different construction methods.

Nine energy-efficient office buildings in Norway were studied in order to get an overview of the state-of-the-art of low energy office buildings in Norway. This paper includes a description and classification of the energy concepts and the corresponding technologies for reducing energy consumption in the buildings. Then, the implications of these technologies are studied with the help of a simulation model and the key issues that influence the energy performance of these buildings with special emphasis on envelope performance are reported.

The results show that a very airtight envelope is an important step towards low-energy buildings. The supporting effect towards other energy concepts as heat pumps, natural/hybrid ventilation should be fully explored in order to realize sustainable energy-efficient buildings in Norway. A careful design of climate adapted and super-efficient envelope systems can further enhance energy-efficiency.

1. Introduction

More efficient use of energy in the built environment is essential to reach political goals within Norway and the European Union on reliable energy supply and reductions of emissions of greenhouse gases. The built environment affects nature through energy use, emissions and use of raw materials. The total energy use in buildings accounts for about 40% of the total energy use in the country, excluding the energy sectors (Statistics Norway 2006). The construction industry may thus make significant contributions to environmental improvement through energy efficiency and utilization of renewable energy.

In order to realize energy performance requirements of a higher standard in the new Technical Regulations, it is necessary to develop new design strategies to meet these requirements - without sacrifices in other performance codes, standards or guidelines. Prior experience related to the introduction of new energy performance requirements has shown that the design energy performance levels are either not met, or they are fulfilled at the expense of indoor climate, technical quality (e.g. moisture related problems), or architectural quality. Facing the future risks of climate change, Norway also provides a unique "laboratory" for testing of the robustness of new building envelope solutions (Lisø et al. 2005).

Therefore it seems appropriate to determine the parameters of building design that have the biggest influence on energy consumption of buildings. Special focus was put on the building envelope and some parameter that have an influence on the building load (Andresen et al. 2005). The starting point was to focus on office buildings but other building types will be studied in the near future.

2. Objectives

The project's principal objectives are to develop more energy-efficient building envelope assemblies and new methods for the design of building envelopes in harsh climates, resulting in more accurate and geographically dependent design guidelines. The project includes analyses of building envelopes applied in different kinds of climates, different uses, and different construction methods.

Nine energy-efficient office buildings in Norway were studied in order to get an overview of the state-of-the-art of low energy office buildings in Norway. This paper includes a description and classification of the energy concepts and the corresponding technologies for reducing energy consumption in the buildings. Then, the implications of these technologies are studied with the help of a simulation model and the key issues that influence the energy performance of these buildings with special emphasis on envelope performance are reported.

3. Methodology

First, a survey of energy efficient office building projects in Norway has been conducted. Nine projects were identified that meet the following requirements:

- energy consumption data (designed/measured) available

- reduced energy consumption (compared with Norwegian average)

- construction details available

The list of projects is shown in Table 1. The office building projects are located in 4 different climatic zones within Norway according to the classification system given by (Tokle and Tønnesen, 1999), which is coastal climate, inland climate and mountain climate in South Norway and coastal climate in Central Norway.

Then, one building was simulated using SCIAQ (Dokka and Dokka 2004), a dynamic simulation software that calculates annual energy consumption (AEC) for heating, cooling, lighting and equipment. It is based on hourly weather data that were provided by the Norwegian Meterological Institute (met). Although the software has been validated the simulation results have been compared with measured data in order to get confidence in the simulation results (ProgramByggerne ANS 2004).

The building construction details are described in Table 2. The input parameter have been taken and stepwise changed in order to find out the sensitivty of the single input parameter towards the annual energy consumption (AEC) (Lam and Hui 1997; Lomas, K.J. and Eppel, H. 1992).

TABLE. 1: List of projects that have been considered in survey

Name	Location	T(mean)	Client /Developer	Architect	Energy Engineering	Completion year
Bravida	Fredrikstad	6.4 °C	Høienhald Invest AS	Multiconsult AS	Norsk Energi	2003
Hamar Rådhus	Hamar	4.1 °C	Hamar Kommune	Snøhetta AS	-	2001
Miljøsenter Blindern	Oslo-Blindern	5.7 °C	Miljøforsknings senteret ANS	Niels Torp as Arkitekter MNAL	Hambra	2006
MMS Horten	Horten	6.6 °C	Statsbygg	Kristiansen & Bernhard Arkitekter AS	-	1996
Nydalspynten	Oslo	5.7 °C	Avantor	Niels Torp Arkitekter AS	SINTEF	2008
Røstad	Levanger	4.7 °C	Statsbygg	Letnes Arkitektkontor AS	Interconsult Group ASA	2002
Sig. Halvorsen	Sandnes	7.3 °C	Sig. Halvorsen	-	-	2006
Telenor Kokstad	Bergen	7.8 °C	Telenor Eiendom	Pedersen / Ege Arkitekter AS	Vest Consult / OFE AS	2000
Vestveien	Ski	5.4 °C	Knut A. Jacobsen AS	h. arkitektiner AS	SINTEF	2008

TABLE. 2: Building description; Bravida

Location:	Fredrikstad (latitude 59.2"N, longitude 10.5"E)
Building type and storeys:	Office building, 3 storeys above ground
Floor areas:	Total heated floor area = 6,300 m^2
Dimensions and heights:	118 m x 18.1 m; floor-to-floor = 3.5 m ; window height = 1.5 m ; window-to-wall ratio = 0.33

Constructions of building envelope:

(a) External walls (spandrel portion of curtain wall) U-value: 0.2 W/m^{2}K (according to Norwegian building code 1997)
 - Absorption coeff. outside: 0.4; Thermal cap. outside: 5 Wh/m^{2}K; emissivity outside surface: 0.85
(b) Roof U-value: 0.2 W/m^{2}K (according to Norwegian building code 1987)
 - Absorption coeff. outside: 0.5; Thermal cap. outside: 4 Wh/m2K; emissivity outside surface: 0.85

(c) Floor U-value: 0.2 W/m^{2}K (according to Norwegian building code 1987)
(d) Windows Two panes, 4 mm clear glass + 4 mm Optitherm S, 15 mm argon, wood/vinyl frame
 - U-value: 1.4 W/m^{2}K; glazing factor: 0.75; dir. solar transm. factor pane: 0.47; total solar gain factor pane: 0.59
 - Solar shading system: venetian blinds, outside, light color, automatic

Constructions of internal structure :
 - Medium weight furniture; medium weight partition construction; Thermal capacity: 12 Wh/m2K
Operating hours : Mon. to Fri.-0800 to 1600 hr
Sat. and Sun. and Easter and Christmas holidays-closed

HVAC design parameters :

(a) Building load
 - Occupancy density = 0.1 person/m2 (seated working (1.2 Met); normal office clothing (1 clo))
 - Lighting load = 10 W/m^2 ; equipment load = 10 W/m^2
 - Infiltration = 0.15 ach
 - Heating set point temperature 22 °C during operating hours (20 °C outside operating hours)
 - Cooling set point temperature 26 °C (off outside operating hours)

(b) HVAC system
Minimum 3.6 m3/hm^2; maximum 10 m3/hm^2
 - Throttling range = 1 °C
 - operating hours 0600 hr to 1800 hr
 - HVAC system type = VAV Ventilation
(c) Heating
 - capacity: 50 W/m^2; convective share delivered heating: 0.5
 - operating hours 0600 hr to 1800 hr
(d) Cooling
 - capacity: 40 W/m^2; convective share delivered heating: 0.5
 - operating hours 0600 hr to 1800 hr

TABLE. 3: Parameter description (base case values in italic)

Climate	Air tightness	Thermal insulation of the building envelope			Windows/glazing type, size and orientation			Efficiency of heat recovery system
Annual av. temp.	air changes	floor	U-value roof	wall	U-value Window	WWR	orientation	μ
[°C]	[ach]		[W/m^2/K]		[W/m^2/K]	[-]	[degrees]	[-]
-2.5	0.025	0.1	0.15	0.15	0.8	0.22	0	0.55
1	0.05	0.15	*0.2*	*0.2*	1	*0.33*	*26*	*0.6*
1.4	0.075	*0.2*	0.25	0.3	1.2	0.44	45	0.65
3	0.1				*1.4*	0.55	90	0.7
3.8	0.125				1.6	0.66	135	0.75
3.9	*0.15*				1.8	0.77	180	0.8
3.9	0.175				2	0.88		0.85
4.7	0.2					0.99		0.9
5.7	0.225							
6.4	0.25							
6.6	0.3							
7.3	0.35							
7.8	0.4							

TABLE. 4: Parameter description of shading and daylighting system (base case values in italic)

Description	Fs*	Description	Fs**		
			S	E/W	N
No shading	1	Overhang 1 (0.4m)	0.985	0.98	0.98
Curtain. light color. medium transparency	0.72	Overhang 2 (0.8m)	0.91	0.925	0.965
Curtain. dark color. medium transparency	0.92	Overhang 3 (1.2m)	0.65	0.735	0.84
Venetian blinds. inside. light color. manual	0.51	Vertical extension to left and right 1 (0.4m)	0.888	0.854	0.980
Venetian blinds. inside. light color. automatic	0.635	Vertical extension to left and right 2 (0.8m)	0.746	0.742	0.980
Venetian blinds. inside. dark color. manual	0.8	Vertical extension to left and right 3 (1.2m)	0.671	0.686	0.980
Venetian blinds. inside. dark color. automatic	0.8	Overhang. vertical extension to left and right 1 (0.4m)	0.875	0.837	0.960
Venetian blinds. outside. light color. manual	0.4	Overhang. vertical extension to left and right 3 (1.2m)	0.679	0.686	0.946
Venetian blinds. outside. light color. automatic	*0.5*	Overhang. vertical extension to left and right 2 (0.8m)	0.436	0.504	0.823
Venetian blinds. outside. dark color. manual	0.4				
Venetian blinds. outside. dark color. automatic	0.5				

Notes: * Shading factor calculated with simplifying assumption Fs=(Ftot(sunny)+Ftot(cloudy))/2; Ftot from (ProgramByggerne ANS 2004)
            ** Shading factor Fs calculated according to (NS 3031:2007)

Table 3 and 4 show the parameters and the change in input. Special focus was put on eight parameters that are related to the building envelope. First, the air tightness of the building envelope has been chosen. Then, the thermal insulation of the building envelope has been chosen with three different U-values for wall, roof, and floor (to ground). Next, the window specifications, glazing type, size and orientation have been chosen. Windows in the base case building were facing east and west, and north with no windows to the south. A detailed description of the model can be found in Haase and Andresen (2008). Finally, various types of shading system have been studied (details can be found in Table 4).

In order to see the influence of other building related parameter another two parameters were studied (climate and efficiency of heat recovery system). The climate in Norway has been identified as having a major influence. The building was built in Fredrikstad (Rygge climatic data) but it was interesting to simulate the energy consumption if it had been placed in other climatic regions. Next, the efficiency of the heat recovery system has been chosen.

A total of 77 simulation runs have been conducted. With the help of mean value it was possible to analyze the parameters that have the biggest influence on the energy consumption of the building. At the same time it was possible to visualize the amount of change in energy consumption in relation to changing the input parameter. This is a local sensitivity analysis since the results have been compared with a specific base case building (Saltelli et al. 2000).

4. Results

The results can be devided in two sections. First, the results of the survey are shown. The key parameters of the buildings construction are described and performance data is summarized. Secondly, the results of one building that has been simulated together with the results of a sensitivity analysis are given.

4.1 Survey

A classification has been done according to the Kyoto pyramid approach, a procedure proposed by Dokka and Hermstad as detailed in Table 5 (Dokka and Hermstad 2006). The results of the survey with respect to the energy system are shown in Table 6.

TABLE. 5: Classification (Category 1 to 4) for different energy systems

Kyoto pyramid	design strategy
1. reduce energy demand	super insulated and tight building envelopes
1.1 reduce heat loss	efficient heat recovery of ventilation air
1.2 reduce electricity consumption	ee lighting and equipment, low pressure drops in ventilation system
2. Utilize solar energy	optimum window orientation and size, atrium/sun spaces, thermal mass, solar collectors, photovoltaics
3. Display and control energy consumption	demand controlled lighting, cooling and ventilation, user feedback on energy use
4. Selct energy source	solar collector, heat pump, district heating, firewood, gas, electricity

It can be seen from Table 6 that air tightness has not been stated as a specific design goal. In such a case the national standards will be used and tried to be reached. Here, the new Norwegian Standard NS 3031:2007 will help to improve the situation (NS 3031 2007).

TABLE. 6: Classification (Category 1 to 4) for different energy systems

Category	Technology	Bravida	Hamar Rådhus	Miljøsenter Blindern	MMS Horten	Nydalspynten	Røstad	Sig. Halvorsen	Telenor Kokstad	Vestveien
1	double-façade*		X						X	
	superwindow	X		X		X				X
2	double-façade*		X						X	
	earth coupling						X			X
	heat pump	X		X	X			X	X	
	hybrid ventilation						X			X
	passive cooling					X				X
	PV-roof			X						
	biomass	X		X		X				
	thermal collector	X				X				
3	demand control**	X		X		X				
4	district heat			X					X	

Notes: * Category of double-skin facade depends on control strategy of airflow (Category 1 if it reduces energy demand; Category 2 if it utilizes solar energy)
** Demand control can also reduce energy consumption (Category 2) but usually gives feedback on energy use (Category 4)

Figure 1 shows the annual energy consumption for the different projects. Here, it can be seen that the AEC is between 80 kWh/(m^{2}a) (Telenor Kokstad) and 160 kWh/(m^{2}a) (Røstad). It has been divided into energy consumption for heating, Service Hot Water and Electricity Use where data could be found. The amount of energy used for heating varies between 23 kWh/(m^{2}a) (Vestveien) and 111 kWh/(m^{2}a) (Røstad). For most projects the electricity consumption is the largest portion. It ranges between 47 kWh/(m^{2}a) (Nydalspynten) and 85 kWh/(m^{2}a) (MMS Horten).

The electricity consumption is further split into cooling, fan&pumps, lighting, and equipment and the results are shown in Figure 2. In 2 projects no electricity is used for cooling (Nydalspynten and Vestveien). Electricity consumption for equipment varies between 23 kWh/(m^{2}a) (Miljøsenter Blindern) and 34 kWh/(m^{2}a) (Vestveien). The Vestveien project uses electricity consumption for equipment as required in the new NS 3031:2007 while the other projects used older versions to calculate electricity consumption. Electricity consumption for lighting ranges between 17 kWh/(m^{2}a) and 27 kWh/(m^{2}a). Electricity consumption for fan&pump ranges between 6 kWh/(m^{2}a) (Vestveien) and 32 kWh/(m^{2}a) (MMS Horten). No detailed data was available for Bravida, Hamar Rådhus, Røstad, Sig. Halvorsen, and Telenor Kokstad.
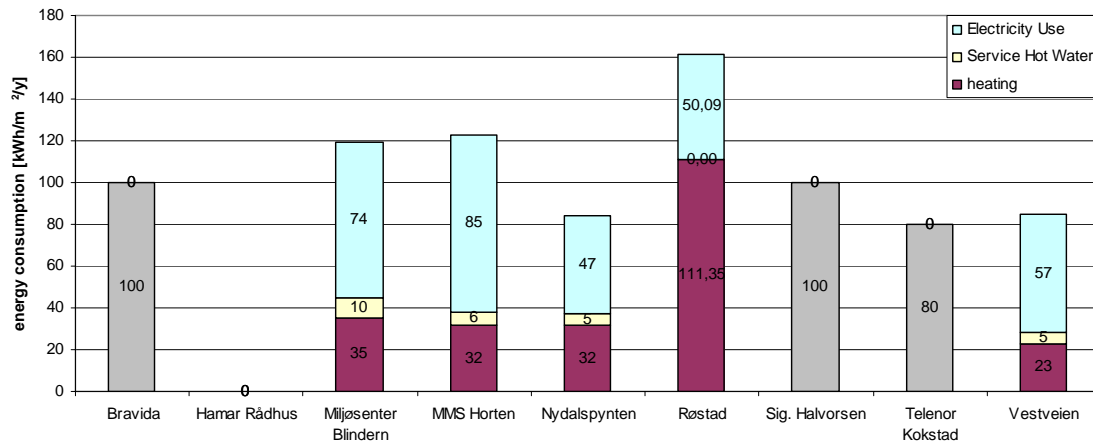
FIG. 1: Annual energy consumption devided into electricity, service hot water, and heating (for projects with grey column no detailed data was available; no data was available for Hamar Rådhus)
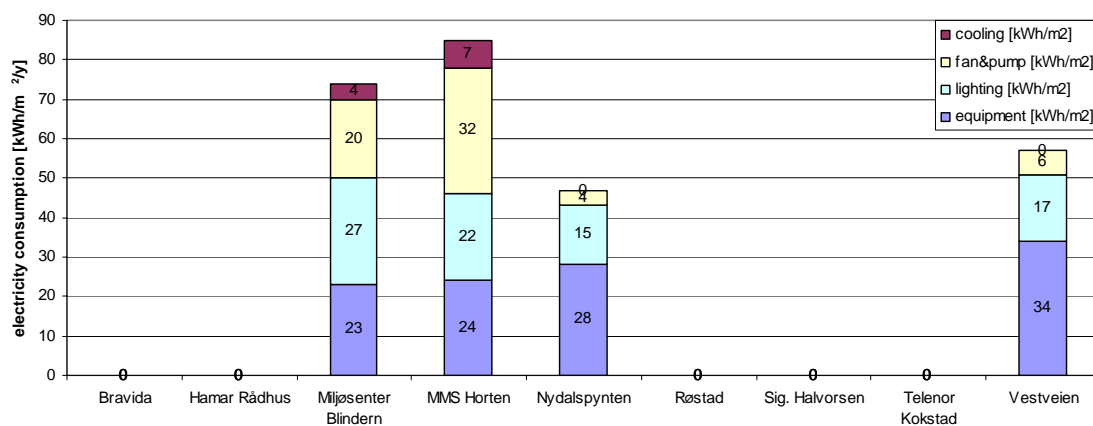
FIG. 2: Annual electricity consumption (no detailed data was available for Bravida, Hamar Rådhus, Røstad, Sig. Halvorsen, and Telenor Kokstad)

4.2 Simulation

The results of the simulation exercise are given in the following section. First, the base case (BC) building was simulated and monthly energy consumption and temperature were compared. Figure 3 shows good agreement between simulation and measurement. Then the base case building was simulated with the parameters from Table 3 and Table 4 (base case values in italic).

Figure 4 gives an overview of the output range of the different parameters that were used in this study. Here, it can be seen that the climatic data used for simulation causes the greatest range in output followed by the air tightness of the building envelope, the efficiency of the heat recovery system, and the windows/glazing type. Thermal insulation of the envelope and the shading system have the smallest output ranges.

The results highly depend on the choice of input data and the range of input data. Since the base case building is already of high standard (compact design, low WWR, very good windows/glazing type) with low AEC some of the parameters provide only little potential for improvements. It turned out that changing the building orientation does not have an influence on AEC.

Figure 5 gives the results in detail. It can be seen that the climate has the biggest influence followed by the efficiency of the heat recovery system, the WWR, and the air tightness. Minor influence has the thermal insulation of the building envelope, the windows/glazing type. The orientation of the building did not result in a change of AEC at all and is not illustrated in Figure 5. The reason for this surprising result is the relatively small window areas together with a very efficient external shading system (as described in Table 4).
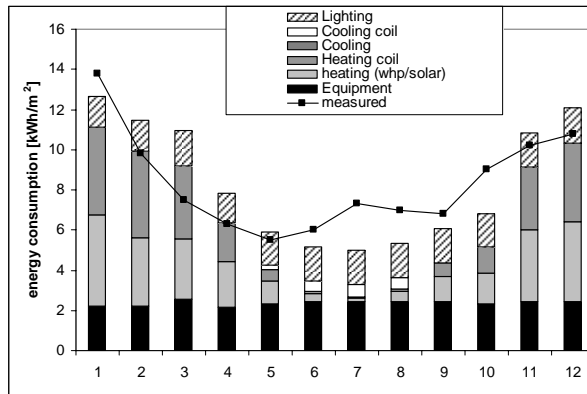
FIG. 3: Comparison of simulated with measured data (annual energy consumption AECsim=100 kWh(/m²a); AECmeas=100 kWh/(m²a))
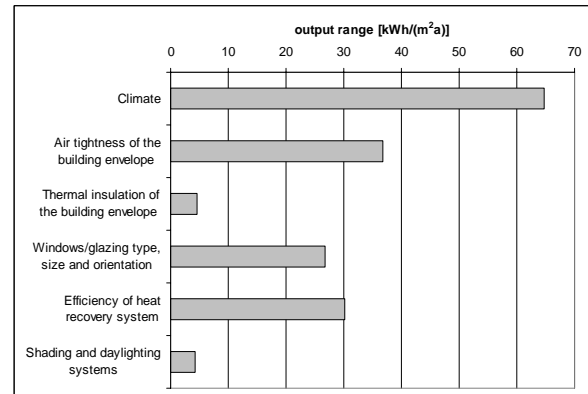
FIG. 4: Output range of different parameter
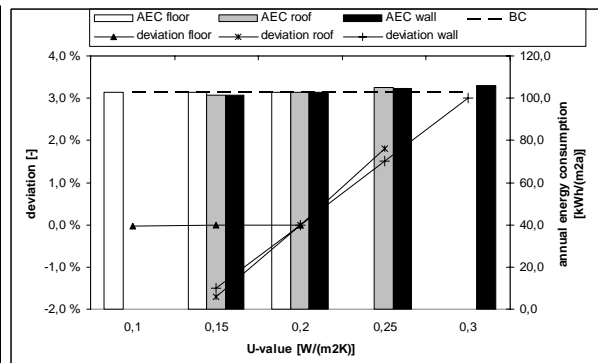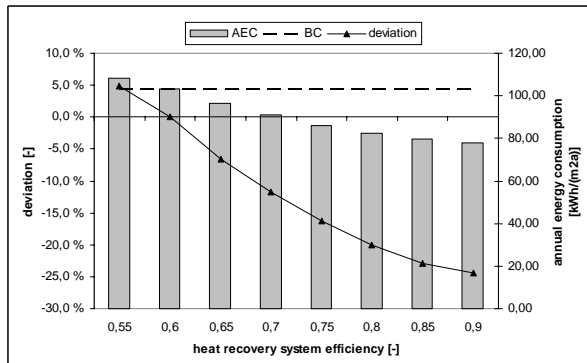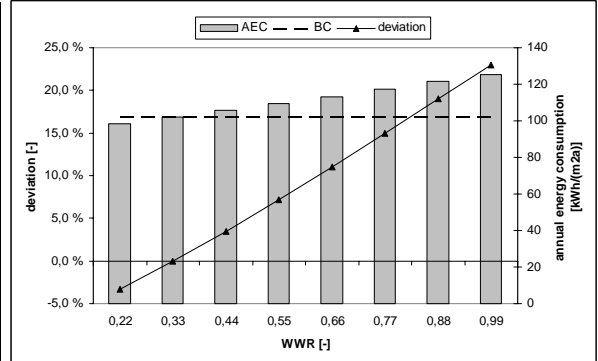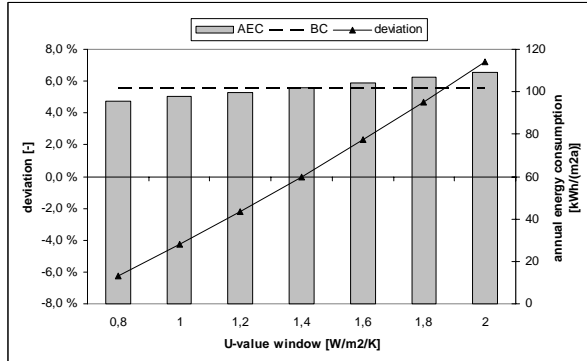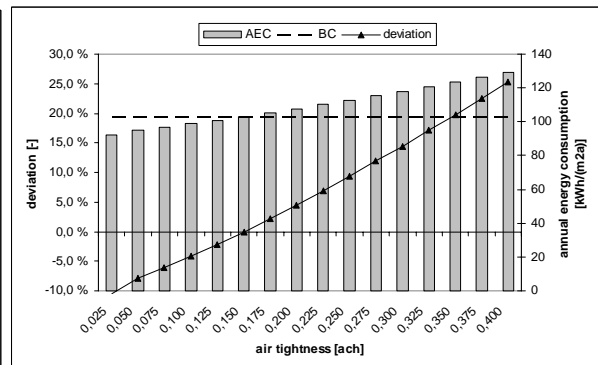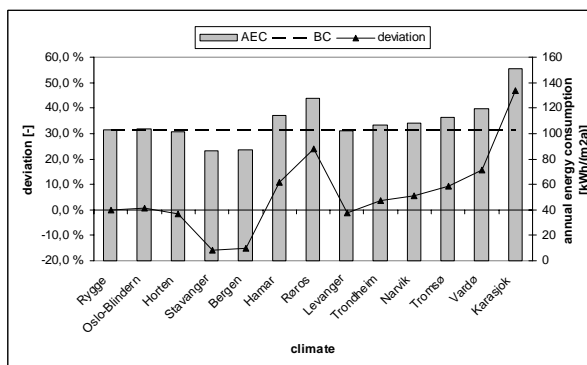
FIG. 3: Results of AEC and deviation compared with base case (BC)

5. Conclusions

The results show that a very airtight envelope is an important step towards low-energy buildings. The supporting effect towards other energy concepts as heat pumps, natural/hybrid ventilation should be fully explored in order to realize sustainable energy-efficient buildings in Norway. The climate has a large influence on the energy performance and should therefore be taken into consideration. Expected climate change over the next 50 years will influence the energy consumption. A sensititvty analysis could be applied in order to evaluate the parameter with the biggest influence on building lifetime energy consumption. A change in annual mean temperature of less than 3 degrees (e.g. from Rygge (6.4°C) to Bergen (7.8°C) changes AEC by more than 20%) can cause great uncertainty in future energy consumption of office buildings. More work is needed in order to accurately quantify the consequences and to develop envelopes that are capable of adapting to the changing climate.

It could be demonstrated that a careful design of climate adapted and super-efficient envelope systems with very good air tightness, moderate WWR as well as ventilation systems with exellent heat recovery system can further enhance energy-efficiency. In a well designed energy efficient office building further increase of thermal insulation does not reduce annual energy consumption significantly. The building orientation does not influence the AEC in this building.

The local sensitivity analysis gives only results for changing one parameter at the time. Synergy or other effects of changing more than one parameter could not be analysed in this work. Future work will focus on this aspect and apply a global sensitivity analysis to the problem. It is hoped that these findings will assist in setting up future analysis work.

6. Acknowledgements

7. References

Andresen, I., Aschehoug, Ø., Bell, D., Thyholt, M. (2005). Energy-Efficient Intelligent Facades. A state-of-the-Art. *Sintef Report* No. STF50 A05021, ISBN 82-14-03559-7.

Dokka, K.A. and Dokka, T.H. (2004). SCIAQ Pro – Simulation of Climate and IndoorAir Quality.

Dokka, T.H. and Hermstad, K. (2006). Energy efficient houses for the future – A handbook for planning of passive houses and low energy houses, SINTEF Buildings and Infrastructure, Trondheim (in Norwegian).

Haase, M. and Andresen, I. (2008). Energy-efficient office buildings in Norway – from low energy standard to passive house standard. Passivhus Norden conference, Trondheim, Norway

Lam, J.C. and Hui, S.C.M. (1996). Sensitivity Analysis of Energy Performance of Office Buildings, *Building and Environment*, Vol. 31, No. 1, pp. 27 – 39.

Lomas, K.J. and Eppel, H. (1992). Sensitivity Analysis Techniques for Building Thermal Simulation Programs, *Energy and Buildings*, Vol. 19, No. 1, pp. 21 – 44.

Lisø, K.R., Kvande, T., Thue, J.V. (2005). Climate 2000—building enclosure performance in a more severe climate. In: Jo` hannesson G, editor. *Proceedings of the seventh symposium on building physics in the Nordic Countries*. Reykjavik: the Icelandic Building Research Institute p. 211–8.

Norsk Standard NS 3031: 2007, Calculation of energy performance of buildings – Method and data, Standard Norge.

ProgramByggerne ANS, User Guide SCIAQ version 2.0.

Saltelli, A., Chan, K., Scott, E. M. (2000). Sensitivity Analysis. *John Wiley & Sons*. ISBN 047 1998 923.

Statistics Norway (2006), Electricity statistics.

Tokle, T. and Tønnesen, J. (1999). Classification of Norway in climatic zones. Technical report A4856, SINTEF Energy Research (in Norwegian).

Using Controlled Active Mass (CAM) to decrease energy demand for cooling

Vahid M. Nik, PhD student,
Division of Building Technology, Department of Civil and Environmental Engineering, Chalmers University of Technology, SE-412 96 Gothenburg, Sweden;
vahid.nik@chalmers.se

Anker Nielsen, Professor,
Division of Building Technology, Department of Civil and Environmental Engineering, Chalmers University of Technology, SE-412 96 Gothenburg, Sweden;
anker.nielsen@chalmers.se

KEYWORDS: CAM, energy simulation, cooling, refilling

SUMMARY:
Effects of using a Controlled Active Mass and refilling it on cooling demand inside a room are studied here. Different models have been simulated in the Simulink toolbox of Matlab using IBPT. The simulations are for the city of Gothenburg in Sweden using the weather data of 1991. The room is made from lightweight constructions. Some of the results are compared with the heavy weight room. Results show that using a CAM and specially refilling it can save considerable amount of energy. The CAM location and refilling time are important parameters to have a good performance of the CAM.

1. Introduction

Lots of energy is consumed in buildings to prepare a suitable indoor climate. Nowadays using advanced insulation methods and improved materials in constructions has decreased energy demand especially in heating. However, the cooling demand increases in warm periods of a year when the building is well insulated. In lightweight constructions, which are common in Scandinavian countries, cooling the building in warm periods can be very energy demanding. Cooling a building costs almost three times more than its heating. In most Scandinavian buildings, cooling in summer period is not applied but in the case of requirement, a traditional cooling system like cooling roof is installed. An alternative is to use heavy mass in the building to reduce the overheating. We describe new method for indoor climate conditioning.

Using *Controlled Active Mass (CAM)* is a method for decreasing energy demand in buildings. CAM is an extra mass that affects the heat transfer and energy storage/consumption inside a room. It can have different shapes, materials and locations and of course, it is possible to remove this thermal mass whenever we want. The flexible performance of a CAM gives us an active mass comparing with the passive mass of the construction. CAM affects both of the heating and cooling demand of a room. In this paper the effects of refilling a CAM on cooling demand of a room in a warm period is studied. The study is based on doing simulation using Simulink toolbox of Matlab and International Building Physics Toolbox (IBPT 2007). The simulation is done for a room, which is described in CEN (prEN ISO 13791 2004), in the city of Gothenburg in Sweden. The weather conditions of the year 1991 are used according to the measured weather data from SMHI (Swedish Meteorological and Hydrological Institute).

As the definition of IEA Annex 44, *responsive building elements* are defined as building construction elements, which are actively used for transfer and storage of heat, light, water and air. Therefor the CAM, which is used for transfer and storage of heat, can be defined as a removable responsive building element. More information is available on the Annex 44 web site.

Some experiments about the CAM including measuring temperatures and thermal comfort have been done at the University of Gävle (Ghahremanian S., Janbakhsh S. 2007). More information on the effect of thermal comfort is found in Törnström T, Nielsen A, Nilsson H, Sandberg M and Wahlström Å 2007 and Törnström T et al 2007a. In addition, numerical simulations of the CAM inside a room have been done at Chalmers University (Nik V.M. 2007). Our case is not the same as those experimental and numerical cases. Here we are more interested in the effects of CAM refilling on cooling demand.

2. Case of study

The indoor temperature and energy consumption in a room is studied. The room is simulated when there is no CAM inside it and when there is a CAM; the refilled CAM or the ordinary one. To study the CAM effects on indoor temperature the heating and cooling system is turned off during the simulation. Simulations are done for different locations of the CAM in room. CAM is placed in 6 different distances from the north wall; 1, 2, 3, 4, 4.5 and 5 m. In this section the characteristics of the model, assumptions, boundary and initial conditions, etc. are described.

2.1 The test room

One of the test rooms of the European Standard, CEN, prEN ISO 13791 2004 has been selected. FIG. 1 shows the room with a CAM inside. Length, width and height of the room are 5.5 m, 3.6 m and 2.8 m. The room is in contact with the outdoor air and is located on the ground. The floor is made of concrete and insulation with the thickness of 0.2 m. The insulation is in contact with the ground, which is assumed as Clay soil. The roof has three layers with different thicknesses. Wood, 20 mm faces the outside. Insulation, 130 mm, in the middle and gypsum with the thickness of 9 mm is the inner layer of the roof. In the case of lightweight construction, the wall construction is the same as the roof. In the heavy weight room, walls have two layers; a layer of mineral wool insulation with 130 mm thickness as the outer layer and 20 mm of lightweight concrete as the inner layer.

There is a window with the area of 3.5 m^2 on the south wall. It is made of two glass layers with the thickness of 3.175 mm. The thickness of the air gap between these two layers is 12 mm. Table 1 shows properties of the materials.

In the Simulink toolbox, the room is modelled as two zones, south and north. These two zones are connected to each other through the CAM and two air exchangers with a high exchanging rate to have the same indoor climate in both zones.
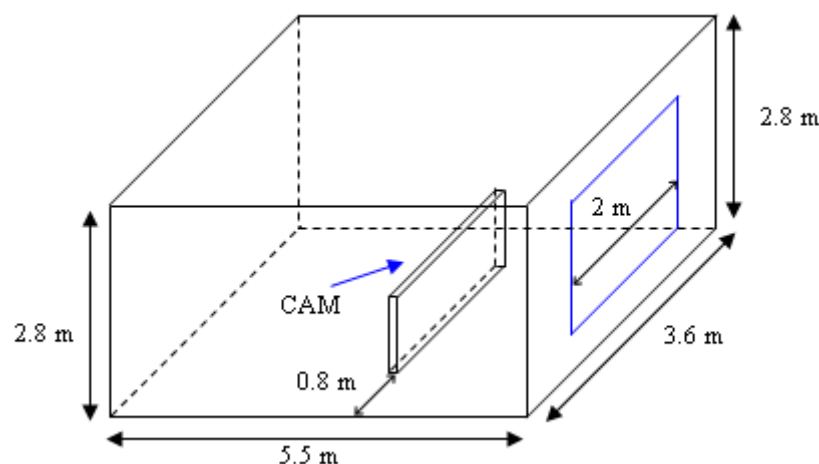
FIG. 1: Schematic drawing of the test room with the CAM inside.

2.2 The CAM

Controlled Active Mass is modelled as a water reservoir. It is a cubic box from aluminium with the width of 2 m, thickness of 0.1 m and height of 1 m. Thickness of the aluminium shell is 10 mm. The CAM is filled with water. In the case of refilling the CAM with fresh water, initial temperature of the CAM is equal to 15°C at 10:00 every morning. CAM is located on the floor and has the same distance from both of the east and west walls. It moves in the length direction of the room. The longitudinal place of a CAM inside the room is measured as the distance between the north face of the CAM and north wall of the room.

CAM is modelled as a wall inside the room. This kind of simulation makes us to neglect heat transfer from side surfaces of the CAM. However, because of the small area of the side surfaces, it does not affect the results.

TABLE 1: Physical properties of the materials.

Material	air	Al	concrete	lw conc.	glass	gypsum	insulation	soil	water	wood
dry Density [kg/m^3]	1.2	2702	2300	1400	2500	900	100	2000	1000	500
Thermal conductivity [W/mK]	0.025	237	1.7	0.65	0.7	0.22	0.04	1.5	0.6	0.14
Specific heat [J/kgK]	1000	900	900	1000	840	800	1000	1500	4181.3	1500
Absorptivity	-	0.6	0.6	0.6	0.1	0.6	0.9	0.9	-	0.6
Emissivity	-	0.09	0.92	0.7	0.8	0.9	0.9	0.9	0.95	0.9
Transmittance	-	0	0	0	0.75	0	0	0	-	0

2.3 Mechanical devices

The room has a ventilation system with the air exchange rate of 0.5 h^{-1}. The volume of the room is 55 m^3. Driving pressure of ventilation system is 1 Pa.

There is a heating and cooling system inside the room. The system starts working when the indoor temperature is not in the comfort limit, which is between 21°C and 24°C. When temperature decreases below 21°C heating system turns on and when it increases above 24°C cooling system starts working. In the selected warm week the energy consumption for heating is very low and is neglected.

2.4 Internal gains and boundary conditions

The heat loads from persons, computers or electricity come to effect from 09:00 to 17:00 each day with the power of 200 W. These loads are named as *Internal Gains.* With internal gains heating demand decreases and cooling demand increases.

The convective heat transfer coefficient for the outside surfaces of the room is 20 W/m^{2}K. It is equal to 3W/m^{2}K inside the room.

The initial temperature of the room and the CAM is 21°C. The simulation starts 14 days before the desired time to eliminate effects of the initial conditions on the results.

When the CAM is refilled, the initial temperature of the CAM is equal to 15°C at 10:00 every morning.

2.5 Weather data

Outside of the room is in contact with the outside weather. The weather data from SMHI is available for each hour of the year 1991. The location is the city of Gothenburg in Sweden with the geographic latitude of 57° 42´ N, geographic longitude of 11° 58´ E and altitude of 31 m. This weather data includes different kinds of information such as ambient temperature, longwave and shortwave radiation, wind speed and direction.

2.6 Period of the study

The indoor temperature and energy demand is studied for a warm week in summer, from 3rd to 9th July.

3. Results

Effects of the CAM on indoor temperature and cooling demand have been considered. The results are divided into two fields; effects of CAM on indoor temperature and cooling demand.

In the case of indoor temperature, there is no heating and cooling system inside the room. Then the indoor temperature varies in its natural way and is not limited in a specific span.

When we talk about effects of the CAM on cooling demand, the cooling system works inside the room and it does not allow the inside temperature to increase more than 24°C.

3.1 Effects of refilling the CAM on indoor temperature

The indoor temperature of the lightweight room without CAM is compared to the room with an ordinary or refilled CAM. Also the inside temperature of the room with heavy weight construction is calculated when there is no CAM inside.

The comfort temperature is between 21°C and 24°C. Studying the indoor temperature of the room in our specific warm period shows that using a CAM increases the number of instances with the comfort temperature. In this paper, this effect is called *in-span effect* of the CAM. In-span effect of a CAM on the indoor temperature is calculated in this way:

$$\text{In-span effect (\%)} \equiv \frac{\sum t1 - \sum t2}{t_{total}} \times 100 \qquad (1)$$

$t1$: the instance that the temperature is in the comfort span with the CAM inside

$t2$: the instance that the temperature is in the comfort span without CAM

t_{total}: simulation time which is equal to one week

The indoor temperature of the room without cooling and heating system for different locations of the CAM is studied in this statistical approach. TABLE 2 shows the in-span effect of the ordinary and refilled CAM inside the light weight room. We achieve to a remarkable improvement by refilling the CAM. The in-span effect when there is no CAM inside the room is 4.17%. In most of the cases, using a CAM increases the in-span effect. The increment occurs at all locations with the refilled CAM. However, in some places it works much better.

The CAM effect on the indoor temperature depends on its location in the room. To find the best location for the CAM in the warm period, we studied the indoor temperature when the ordinary CAM has different locations in the room. The results show that when the CAM is 4 m far from the north wall, the inside temperature is lowest, specially in the sunny hours. At that location, CAM has its maximum shielding effect and prevents some part of solar radiation to come inside the room by reflecting or absorbing it. The absorbed solar radiation heats up the CAM instead of the room air. But the gain of this absorption is limited and depends on the size of the room, CAM and their materials.

TABLE 2: In-span effect of the refilled and ordinary CAM in the lightweight room.

	In-span [%]	
Distance of the CAM from north wall [m]	Refilled CAM	Ordinary CAM
1	4.762	4.167
2	4.76	4.17
3	4.76	4.76
4	5.95	4.76
4.5	6.55	4.76
5	5.95	4.17

FIG. 2 shows the indoor temperature and temperature of the water inside the CAM for the ordinary and refilled CAM. The CAM is located 4 m far from the north wall. It is obvious that refilling the CAM decreases the indoor temperature. The maximum of this decrement, which happens on 8th July, is about 1.8°C. After refilling the CAM, the air temperature difference between two cases starts to increase. A big difference happens at noon, the highest peak in each day. The next big difference happens in the early morning of the next day. Some hours before that, the room temperature in both cases is very close to each other. Both of the room and CAM are

cooling down during night. The lower temperature of the room with the refilled CAM during night occurs because of the lower temperature of the CAM. It is obvious that refilling the CAM at 10:00 in the morning affects the indoor temperature for the next day. This effect is big when the temperature is at its maximum or minimum. In the first three days of the FIG. 2, the temperature difference of the water inside the ordinary and refilled CAM is less the next days. In the first three days, the indoor temperature difference at the peak time is less than the next days.
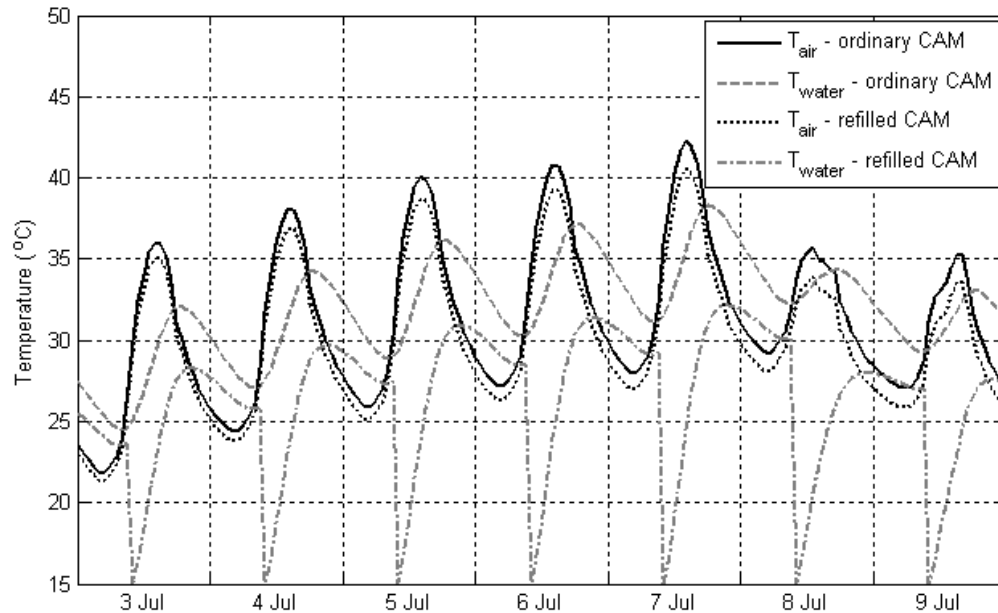
FIG. 2: Temperature of the room air and CAM water for the room with the ordinary and refilled CAM
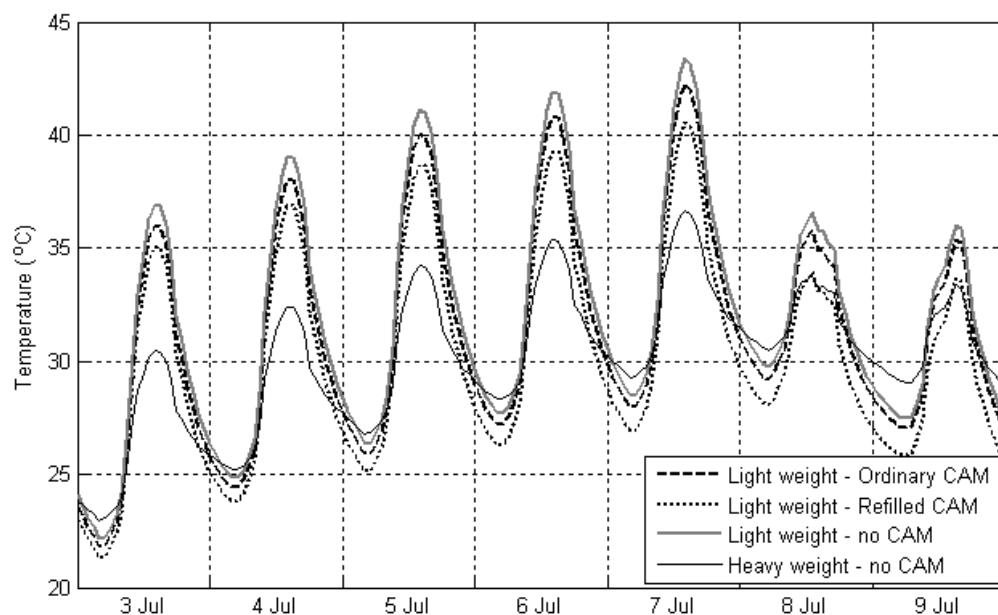
FIG. 3: The indoor temperature of the heavy weight and light weight rooms.

In FIG. 3 the indoor temperature of the light weight room in three different modes, without CAM, with refilled and ordinary CAM, has been compared with the indoor temperature of the heavy weight room. It is obvious that the amplitude of the temperature variations is smaller when the room is made of heavy weight constructions. The

large amount of mass saves energy and releases it when there is a potential. The heavy weight construction does not let the indoor temperature to increase or decrease a lot. However, it does not mean that for a better indoor climate we should use heavy weight constructions.

3.2 Effects of refilling the CAM on cooling demand

In the previous section, which was about the indoor temperature, no heating or cooling system was working in the room and the indoor temperature was not limited. At this stage, both of the cooling and heating systems are working and limiting the indoor temperature between 21°C and 24°C. The amount of heating demand was negligible during the simulation period. The effect of refilling the CAM on cooling demand is considered here. The results are for the ordinary or refilled CAM inside the lightweight or heavy weight room.

In the warm days of July, the angle of incidence of the solar radiation to the window is high. The high angle of incidence causes most part of the solar radiation to hit the area near the window inside the room. When the CAM is close to the window lots of solar radiation hits the CAM instead of the floor. The CAM prevents the indoor temperature increment in two ways; first, it reflects some of the solar radiation to the window, so that part does not warm up the room. Second, CAM has a high heat capacity (ρC_p). Having a high heat capacity means that the amount of energy to increase temperature of the CAM for one degree is more than an equal mass with a lower heat capacity. Therefore, the CAM has the potential to absorb more energy without rapid and high temperature variations.

TABLE 3: Cooling demand in the light weight room using refilled and ordinary CAM.

Distance of the CAM from north wall [m]	Cooling demand [kWh]		Improvement in cooling demand comparing with the empty room [%]	
	Refilled CAM	Ordinary CAM	Refilled CAM	Ordinary CAM
1	59.35	64.3	9.7	2.2
2	60	64.6	8.7	1.7
3	59.42	63.85	9.6	2.8
4	58.9	63.4	10.4	3.5
4.5	59	63.3	10.2	3.7
5	62.2	67.9	5.3	-3.3

TABLE 3 shows the cooling demand for different places of the CAM when it is refilled and it is not. The cooling demand in the same period for the lightweight room is 65.7 kWh and for the heavy weight room is 63.5 kWh. When the CAM is 4 m far from the north wall the maximum amount of energy is saved. When the ordinary CAM is 5 m far from the window and is very close to the window, the cooling demand is more than the room without CAM. At that place, the ordinary CAM absorbs more solar energy and its temperature goes up to higher values. Then the CAM itself works as an extra mass, which heats up the room and consequently cooling demand increases. The table shows that refilling the CAM works well and in most of the cases, it decreases the cooling demand about 10% in comparison with the room without CAM. Comparing with the ordinary CAM, refilling the CAM improves its performance in decreasing cooling demand around 7%.

TABLE 3 shows that the cooling demand in the lightweight room with the refilled CAM is less than the heavy weight room without CAM, which is 63.5 kWh. FIG. 3 shows that the heavy weight room does not allow the temperature to increase or decrease a lot. It is important to remind that the performance of a CAM in making a suitable indoor climate varies depending on the presence or absence of the heating or cooling system. By refilling the CAM in the lightweight room, we can use the fast response of the lightweight construction to the temperature variations.

3.3 Refilling time of the CAM

Assume that you want to use a CAM inside a building to decrease the cooling demand in summer. For a good performance, size, material and location of the CAM should be optimum. These elements depend on the characteristics of the building and weather conditions. After selecting the best choice, you want to refill the CAM to decrease the cooling demand as much as possible. But when the CAM should be refilled with the fresh water?
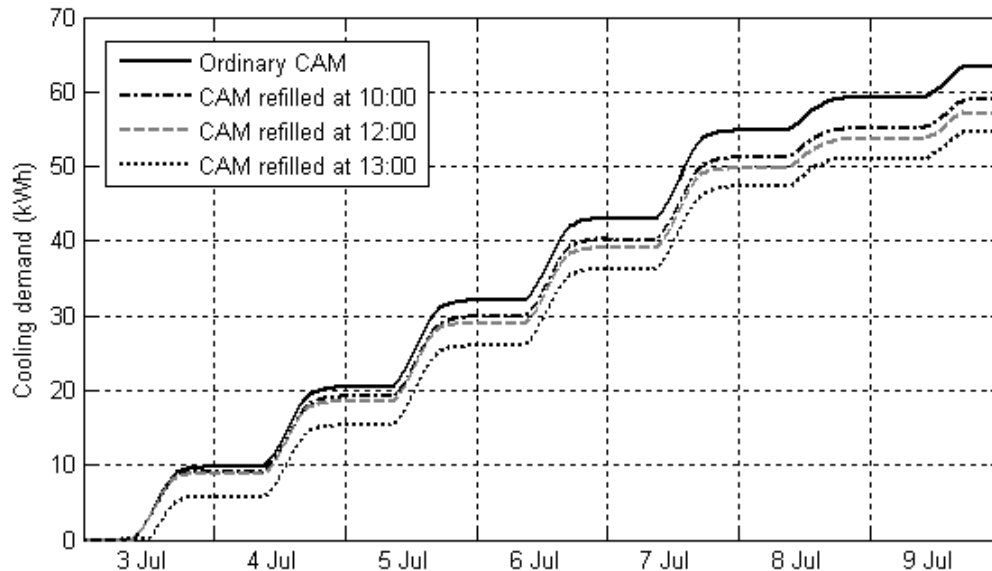
FIG. 4:Integrated cooling demand for different refilling times of the CAM.

FIG. 4 shows the integrated cooling demand during the week when the CAM is located 4 m far from the north wall in the lightweight room. In the previous cases, the CAM was refilled at 10:00. The graphs show that by refilling the CAM at some other hours the cooling demand decreases more than before. The best performance of the refiled CAM is when the refilling time is 13:00. The cooling demand for the week is 54.6 kWh in that case which 17% is less than the cooling demand with the ordinary CAM. For the next refilling hours, which are not shown in the figure, the cooling demand increases. It means that to gain the effects of refilling a CAM as much as possible, it is necessary to find a perfect time of refilling.

3.4 Practical aspects

Using a CAM system gives an alternative to using heavy constructions. It can be installed in existing buildings as an alternative to cooling roof, where the installation is hanging in the roof. At the moment we have not made a comparison between the two systems. A problem with a CAM is the weight of the system – the floor has to be able to cope with the load of the filled system. A discussion that will arise is the risk of leakage from a water based system. There will be a risk for a CAM system that can be eliminated by having a drain in the floor. If we compare the risk with a roof cooling systems, then the risk should be higher for the roof cooling system as there will be more pipes and connexions. We can look at the risk of having an aquarium or a washing machine. The risk should be lower than for a washing machine as the water pressure is lower. Another practical aspect is the risk of condensation on the surface of the CAM – this is similar to the risk of condensation on a cooling roof. This will depend on the climate and in Scandinavia we will normally expect that the lowest acceptable temperature is 15C as we have used in the simulations.

4. Conclusion

Using a CAM and refilling that can decrease the cooling demand in warm periods of a year. The place, material and size of a CAM should be chosen based on its desired performance in each specific time, weather conditions and characteristics of the building. In this paper, there was no obstacle in the way of solar radiation to come into the building. In reality, we use curtains, blinds and different kinds of glasses. In a practical case, we need to take into account all of these parameters.

In studying the CAM effects, it is important to do not mix up the performance of a CAM when there is a cooling or heating system in the room and when there is not. When a cooling or heating system works in the room, the time response of the CAM to the temperature variations becomes more important and the shell material plays an important role.

The performance of the CAM is dependent to its location inside the room. The optimum location varies in each case with the size and materials of the room and CAM. The optimum location also varies during the time. It is possible to calculate the best location for each hour, day, week or month. However, the best result is the more practical one and in that case, other parameters come into effect. In this paper by locating the CAM 4 m far from the north wall the energy consumption decreased optimally. At that location, the shielding effect of the CAM and its thermal behaviour was working optimally.

Refilling a CAM in a light weight room works well. The cooling demand decreases by adding a controlled active mass to the room instead of adding lots of permanent mass like in heavy weight buildings.

It is very important to refill a CAM at a proper time. The suitable time for refilling depends on the size and materials of the CAM and building, weather conditions and performance of the indoor air conditioning system.

5. References

IEA Annex 44 Integrating Environmentally Responsive Elements in Buildings, web site http://annex44.civil.aau.dk

prEN ISO 13791 2004 CEN. Thermal performance of buildings – Calculation of internal temperatures of a room in summer without mechanical cooling – General criteria and validation procedures, prEN ISO 13791:2004: E.

Ghahremanian Sh., Janbakhsh S. 2007. Construction and evaluation of a controlled active mass (CAM) A new cooling system for increased thermal comfort using low exergy sources, *Master's Thesis in building energy system, University of Gävle*, Gävle, Sweden.

IBPT International Building Physics Toolbox, web site http://www.ibpt.org

MATLAB MATLAB and Simulink for Technical Computing, web site http://www.mathworks.com

Nik V.M. 2007. Energy simulation of room with Controlled Active Mass, *Master's Thesis 2007:105, Chalmers University of Technology*, Gothenburg, Sweden.

Sasic Kalagasidis A., H-Tools 2002, *Department of Building Physics, Chalmers University of Technology*, Gothenburg, Sweden, Report R-02:3.

Törnström T, Nielsen A, Nilsson H, Sandberg M and Wahlström Å 2007 Controlled active mass for increased thermal comfort, Proceedings of the International Conference Clima 2007 WellBeings Indoors, Helsinki, Finland

Törnström T, Ghahremanian Sh., Janbakhsh S., Nielsen A, Nilsson H, Sandberg M and Wahlström Å 2007a: Low-energy cooling for improved thermal comfort in offices, Proceedings of the 6th International Conference on Indoor Air Quality & Energy Conservation in buildings, Sendai, Japan

Influence of Active Heat Capacity on Indoor Climate and Energy Demand of a Building

Kestutis Valancius, Assoc. Professor,
Department of Heating and Ventilation, Vilnius Gediminas Technical University;
kestutis.valancius@ap.vgtu.lt

Vytautas Stankevicius, Professor,
Department of Building Materials, Kaunas University of Technology;
v.stankevicius@ktu.lt

KEYWORDS: Active heat capacity, indoor climate, energy demand, building.

SUMMARY:
The paper presents some theoretical aspects of unsteady heat transfer analysis based on the energy conservation law. Additionally, an experimental research made at Solar energy investigation centre in Spain – Plataforma Solar de Almeria - some results are produced. The results of experimental investigation, which was carried out at natural conditions, show the display of violent temperature oscillations thickness and unsteady thermal process period. The influence of active heat capacity and intermittent heating effect on premises indoor climate and thermal energy use was estimated. The results show the heating power increase on behalf of intermittent heating effect according to temperature drop and re-heating time period for particular buildings.

1. Introduction

Heat transfer processes in buildings are always unsteady at real conditions. On the other hand practical calculations of heat exchange processes in buildings are based on steady-state process equations. In spite of modern indoor climate system management, according to practical observations and theoretical investigations, undesirable changes of indoor heat behaviour occur. Such changes have negative influence on indoor heat comfort and misrepresent real energy demands of a building.

Usually, especially during the period of building exploitation, unreasonably installed heat power is noticed. Unevaluated heat inflows cause too big heating power and overheating of a building and, contrarily, intermittent heating arises from too low installed power and is the consequence of too long preheating time. That is why, wrong building maintenance is observed, and that is, indoor climate does not satisfy hygiene requirements. Usually, energy saving is performed at the expense of human health.

The problem is influenced by factors, which have impact on thermal mode of a building. Solving of this problem involves identification and quantitative analysis of these factors. This might be useful in predicting and minimising negative influence of these factors on building indoor climate and energy use.

The main factors, which alteration disturbs steady-state thermal behaviour of a building, can be divided into two general groups:

Outdoor (uncontrolled) – external air temperature, wind speed and solar radiation.

Indoor (controllable) – heating power of a building and internal heat gains.

The first group of factors mainly depends on geographical situation and climate conditions. Exact change and influence prediction of these factors is difficult enough. Investigations can be made only on the basis of previous air temperature records, wind speed and solar radiation intensity data.

It is noticed that namely factors of the first group are considered to be more important to unsteady building thermal behaviour and were investigated by many authors. Nevertheless, results of practical and theoretical investigations show that unsteady heat transfer processes are mainly caused by indoor factors: change of heating power and heat inflows. Influence of outdoor factors – wind and sun – can usually be solved by architectural means. In modern buildings with higher consumption of electricity and intermittent heating, influence of indoor factors influence on thermal behaviour of a building comes out during the comparatively short period of time.

2. Methodology of the research

The method is based on building's temperature evolution calculation when it falls below its normal set-point. This evolution is calculated with the use of the model of a building with three nodes representing internal and external

environment and building structure. The internal thermal inertia of a building is represented by capacitance which temperature is the structure temperature. Heat exchanges between the structure and external environment, between the structure and internal environment and directly between the internal and external environments are taken into account separately.

While extending the thermal scheme and combining it with conservation of energy law for a control volume we can define the scheme of thermal energy balance for a building (Fig. 1).
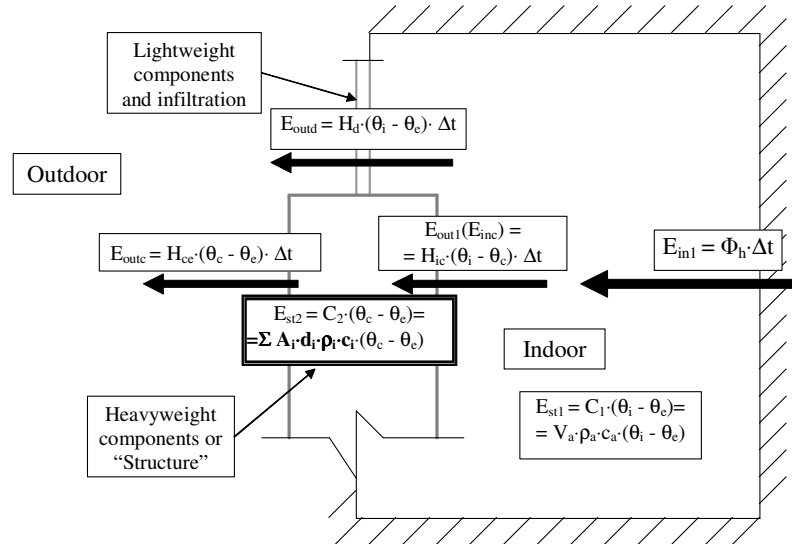
FIG. 1: Thermal energy balance scheme for a building

Known methods of unsteady heat transfer calculations in buildings are mostly inflexible and hardly applicable for engineering analysis. The need of new ways of unsteady thermal processes in buildings still exists.

The solution of unsteady heat transfer problems can be made on the basis of thermodynamic laws, especially conservation of energy law for a control volume.

The subject of thermodynamics and heat transfer is highly complementary. The subject of heat transfer may be viewed as an extension of thermodynamics, because it treats the rate at which heat is transferred. Conversely, for many heat transfer problems, the first law of thermodynamics (the law of conservation of energy) provides a useful, often essential, tool.

Energy balance scheme for a building (Fig 1) consists of two thermodynamic related systems with inflow outflow and stored thermal energies.

3. Active Heat Capacity and Thickness of a Building Components

The term *active heat capacity* (in EN ISO "effective heat capacity") is actually a quantification that corresponds to the part of the total heat capacity of a building component that participates in dynamic heat exchange between the component and the environment:

$$C_2 = \Sigma \, \chi_j A_j = \Sigma_j \Sigma_i \, \rho_{ij} \, c_{ij} \, d_{ij} \, A_j. \tag{1}$$

Where active thickness of a building component:

$$\Sigma_i d_i = d_{active}. \tag{2}$$

And it is the function of:

$$d_{active} = f(T, \, c, \, \rho, \, \lambda), \tag{3}$$

where T is time period of the unsteady thermal process, which is not well-defined or/and arbitrary. Thetheoretical investigation results of the interplay of an active thickness of various building components and time period of the unsteady thermal process is presented in Fig 2.

$$d = -0.0001T^2 + 0.0047T + 0.0087$$
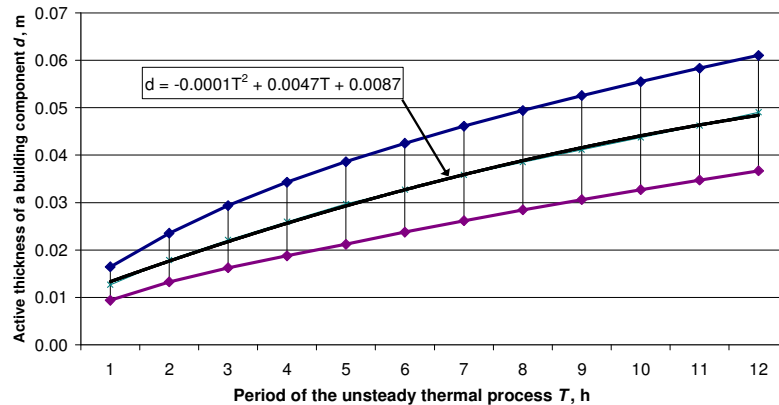
FIG. 2: Interplay (area) of active thickness of a building component and time period of unsteady thermal process

Theoretical analysis shows that active (or violent temperature oscillations) thickness can vary from 0.5 to 12 centimetres according to arbitrary time period of unsteady thermal process, or/and can be estimated by streamlined expression introduced in Fig. 2.

4. Experimental Investigation of Unsteady Heat Transfer Process in a One-cell Building

The experimental investigation was carried out at the Solar energy investigation centre *Platforma Solar De Almeria* (PSA) in Spain. This project was made under the financial support of EU-DGXII "Improving Human Potential" programme.

The aim of the experiment was to investigate unsteady heat transfer process in a one-cell building under natural conditions. Preparation and the main part of the experiment were carried out during the stay in PSA for more than a one-month period of time.

The paper presents methods and results of one-dimensional unsteady heat process experimental investigation in a one-cell building under the impact of solar radiation on one surface and unequal boundary conditions.

The obtained experimental data may be put into practice and can be useful in developing unstable heat transfer theory in multi-layers using various methods of analysis.

4.1 Equipment and methods of the investigation

The LECE (Laboratorio de ensayos Energéticos para Componentes de Edificación), located on the south side of the PSA, forms the part of European PASLINK laboratories' network for energy testing of buildings' components. It consists of four test cells with complete instrumentation for testing thermal performance of building conventional and passive components under real outdoor conditions (Fig. 3).
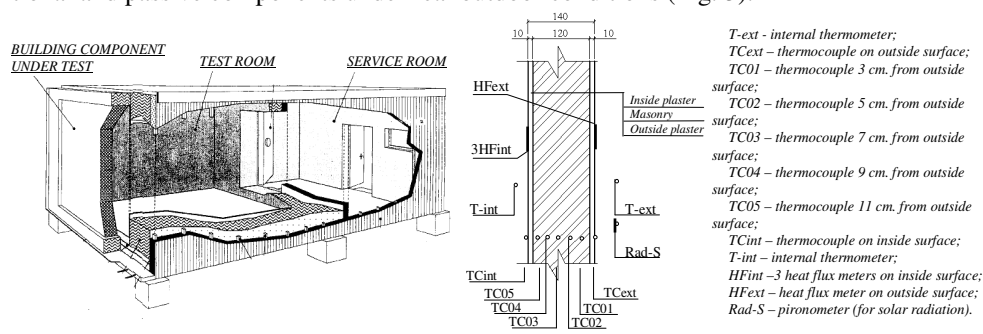
FIG.3: Scheme of a test room and a test component section with installed measuring equipment

A test cell of approximately the same size as a standard room was used in the experiment. The opposite wall to the service room is interchangeable with the test specimen. A test component was a multi-layer wall (Fig. 3) of three different layers, i.e. 2 cm of plaster from the outside, 12 cm of brick wall and 2 cm of plaster from the inside.

Thermocouples were installed in separate layers of the wall. Two thermo- resistant thermometers were installed to meter inside and outside air temperature. A pyronometer was installed on the outside surface to meter the total solar radiation. Heat flux meters were installed to investigate the heat flow – 1 on the outside surface and 3 on the inside surface.

All equipment was connected to a computer. The computer was fixing the test data each 10 minutes.

Orientation of the test's component was to the south, and the experiment was carried out in May of 2003.

4.2 Results of the investigation

Experimental data including the inside and outside air temperatures, temperatures of different layers of the testing wall, solar radiation and heat flow densities through the boundary densities was being collected for a period of longer than a month. The characteristic data of temperature distribution for three days is presented (Fig. 4).
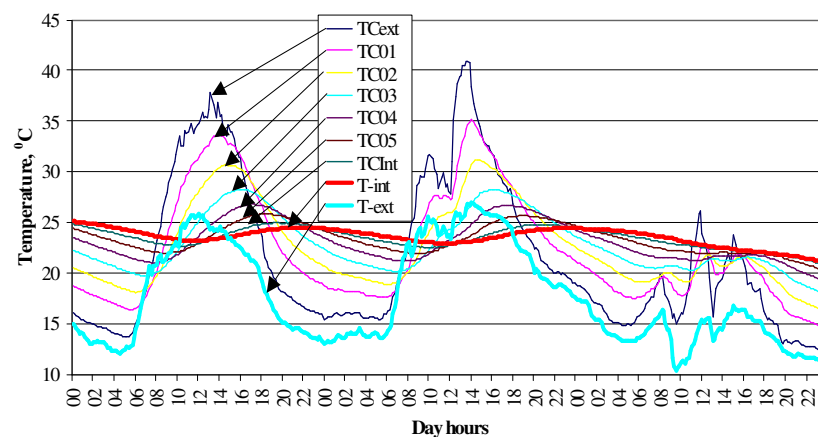
FIG.4: Temperature distribution

The outside air temperature maximum – 27–28 °C appears at about 1 o'clock PM at midday, and minimum – 13–14 °C at 2–4 o'clock AM at night. The third day sticks out because of temperature fluctuation at the bright period of day. The external surface temperature change is parallel to the outside air.

During the sunny days (1st and 2nd day) temperature curves even moves from external surface to internal. "Temperature wave's" – temperature curves' movement – time from external surface to internal is about 7 h, and from outside air to inside air – near 12 h.
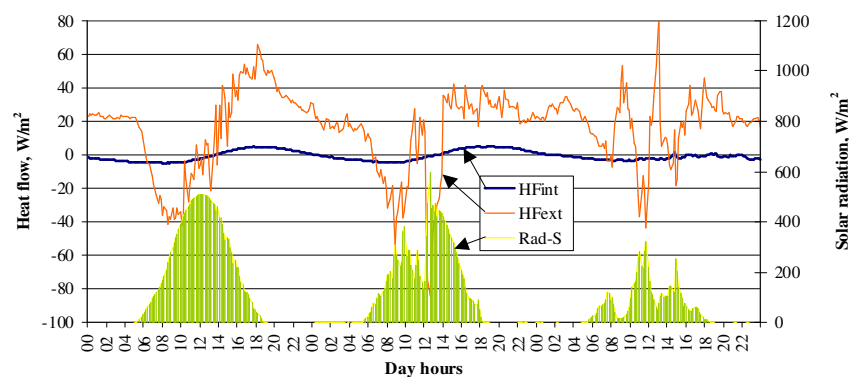
FIG.5: Heat flow densities and solar radiation

Here, "Rad-S" is solar radiation's reading by the pyronometer, "HFext" and "HFint" are the heat flow densities' readings by the flux meters that were installed on the external surface.

The first day sticks out because of no parallel between solar radiation intensity and external surface heat flow density change. High speed of wind at the time of experiment data measurement can be the result of such phenomenon.

5. Investigation of an Unsteady Thermal Regime of the Building

A real building was chosen for practical calculation. Heated area of the building was 9144 m^2, heated volume was 30176 m^3, design indoor temperature was +20 ^{o}C, design average outdoor temperature of heating period was –0.7 ^{o}C lowered heating period was 10 hours, heat loss coefficient of the building was H = 9395 W/K, heat loss per heated area of the building was 44 W/m^2, lowered heating period was 10 hours per day.

Necessary for the investigation data was calculated according to national regulations and energy audit results.

The results of building intermittent heating investigation with 3 ^{o}C lowered heating for 10 hours period are presented in Fig. 6. It is evident, that the same heating power re-creation after lowered heating period is insufficient to reach design indoor temperature. Anytime, after lowered heating period boost heating phase – heightened heating period – it is necessary to re-create design indoor temperature.
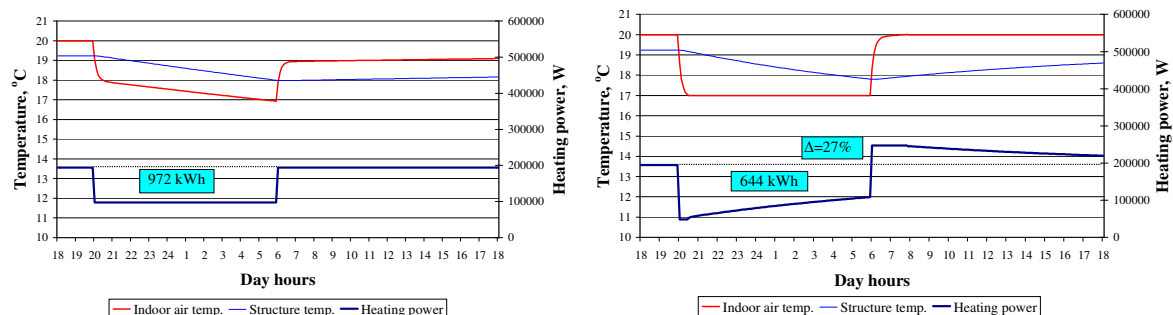
FIG.6: Investigation results of unsteady thermal regime of a building

Boost heating phase is the heating-up capacity of heated space and requires compensation effects of intermittent heating in a heated space. It could be estimated by using the re-heat factor which varies from 2 to 45 W/m^2, depending on the type of building, building construction, re-heat time and assumed drop of internal temperature during setback. Fig. 7 represents additional heating-up capacity (additional heat power) needs for compensation effects of intermittent heating according to comparative heat losses of a building.
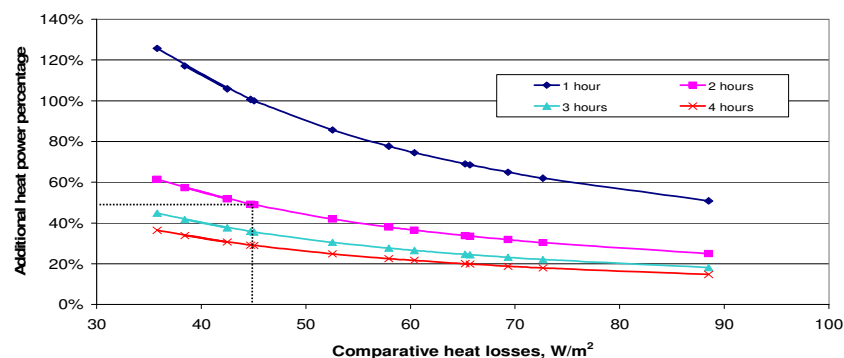
FIG.7: Additional heat power percentage for temperature change 3 ^{o}C

The heating power increase on behalf of intermittent heating effect is ranging from 18 % to 125 % according to temperature drop and re-heating period of time for particular buildings.

6. General Conclusions and Proposals

- The boost heating period is always required for intermittent heating use to achieve the design indoor temperature during the fixed period of time without influence of internal heat gains. The heating power

increase on behalf of intermittent heating effect is ranging from 18 % to 125 % according to temperature drop and re-heating time period for particular buildings. Heating-up capacity on behalf of intermittent heating influence must be optimally chosen according to possible savings and investments.

- The major part of building's thermal energy which is acting in dynamic heat exchange is accumulated in high weight building envelopes. Therefore the master's task is the estimation of stored (accumulated) thermal energy here. The main figure is thickness of massive structure where unsteady thermal processes appear and influence building indoor climate and energy demands. Theoretical analysis shows that – active (or violent temperature oscillations) – thickness can vary from 0.5 to 12 centimetres according to arbitrary time period of unsteady thermal process.

- The results of experimental investigation, which was carried out at natural conditions, show the display of violent temperature oscillations thickness till 7.5 centimetres, and unsteady thermal process of 12 hours on the average. A period of 12 hours for arbitrary unsteady thermal process and 5 centimetres of active thickness are recommended to use as a practical unsteady heat transfer problems' solution. Active thickness of the component can be estimated by a streamlined expression introduced in this work if another period of time for unsteady thermal process is chosen.

7. References

Akander J. (2000). The ORC Method – Effective Modelling of Thermal Performance of Multilayer Building Components, *Doctoral dissertation*, Stockholm, Sweden, p. 24-34

EN 12831:2003. (2003). Heating systems in buildings. Method for calculation of the design heat load, Brussels, Belgium, p. 33-73.

EN 832:2000. (2000). Thermal performance of buildings – Calculation of energy use for space heating, Brussels, Belgium, p. 33-39.

EN ISO 13790:2004. (2004). Thermal performance of buildings – Calculation of energy use for space heating, Sweden, p.10-31.

Incropera F. P., DeWitt D. P. (1996). Introduction to heat transfer, Third Edition, Wiley, New York , p.12-41.

Sommer. K. (2002). The European method for calculation of design heat load, *International HVAC+R technology symposium*, Istambul, p. 10.

Valancius K., Paulauskaite S. (2004). Energy Conservation Law Appliance for Intermittent Heating Analysis, *The 6th international conference "Energy for buildings" proceedings*, Vilnius, Technika, p. 540-547.

Valančius K., Skrinska A. K., Paulauskaitė S. (2006). Investigation of Unsteady Heat Transfer Process in an One-Cell Building, *Journal of Civil Engineering and Management*, Vol 12, No 1, p. 97–101.

The cooling capacity of the Thermo Active Building System combined with acoustic ceiling

Peter Weitzmann, Technical consultant,
BuildDesk A/S;
peter.weitzmann@builddesk.dk

Emanuele Pittarello, MSc,
International Center for Indoor Environment and Energy, Technical University of Denmark
emanuelepittarello@libero.it

Bjarne W. Olesen, Professor,
International Center for Indoor Environment and Energy, Department of Civil Engineering, Technical
University of Denmark;
bwo@mek.dtu.dk

KEYWORDS: TABS, acoustic ceiling, measurements, cooling.

SUMMARY:
This paper describes measurements in a test facility of the cooling capacity of the thermo active building system (TABS) combined with acoustic ceiling. Generally it has been expected that in order to maintain sufficient cooling capacity from the mainly radiant heat transfer, the concrete ceiling must be exposed directly to the room. This in practice would therefore impede the use of TABS in open plan offices where acoustic ceilings are needed to ensure acceptable acoustic conditions. In this work, we have made measurements in a room equipped with TABS combined with an acoustic ceiling covering parts of the ceiling, so that both acoustic and thermal requirements could be met. In the measurements 35%, 47%, 67% (two different patterns), 70% 83% and 100% were covered as well as four different configurations using baffles. Both thermal and acoustic properties were tested. The results showed that even with a covering of 83% of the ceiling surface area, the cooling capacity was still around 70% of the uncovered ceiling for the same temperature difference between mean fluid temperature and room operative temperature, while at the same time the reverberation time in the room was clearly acceptable. This shows that acoustic ceilings and TABS can be combined.

1. Introduction

The use of the Thermo Active Building System (TABS) is currently increasing in use. Since the first mentioning of the concept using air (Andersson and Isfält, 1978) and water (Meierhans, 1993; Meierhans, 1996), a number of projects with different applications have been described (De Carli and Olesen, 2001; Meierhans and Olesen, 2002). The functionality of TABS is to cool or heat the building using pipes integrated in the thermal mass of the building. Due to the large possible surface area between room and building surfaces equipped with TABS, it is possible to use high water temperatures for cooling and low water temperatures for heating. This makes it possible to use a large number of different heating/cooling sources which can very often be combined with renewable energy.

Another property of TABS is the peak-load shaving ability. This means that since the thermal mass can absorb heat from the building and store this in the concrete, it is not needed to dimension the cooling system for the peak-load, but rather for the average load during the whole day (CEN, 2007). This means that since the concrete must absorb the surplus heat, and since this is a slow process compared to airborne cooling systems, the use of TABS means that the temperature in the room is not going to be constant during the day. In stead it will drift. At the same time this physical property also limits the allowed heat loads in the room.

Generally it is stated in the existing work that in order for TABS to work the following must be observed:

> Keep the heat loads as low as possible;
> Make sure to have large surface areas with exposed concrete;
> Accept temperature drifts during the day – lower end of comfort zone in the morning and upper end of the comfort zone in the afternoon;

Low exergy system – low temperature heating and high temperature cooling;
Since there is a need for a large exposed concrete surface, it is not possible to use an acoustic ceiling.

In the previously conducted work, which is based on both theoretical calculations and computer simulations as well as measured and empiric data, TABS is found to be a useful alternative to normal air based cooling, and that at the same time, it can also be used for heating.

However, as it can be seen above, especially the acoustic properties are of concern for the use of TABS. Here the keywords are overall sound intensity and reverberation time. The first tells how "loud" the room is while the second tells how quickly sounds are dampened. In Danish legislation (Arbejdstilsynet, 1995), there are requirements for both, designed as guidelines which will ensure that the requirements are met; for instance in open plan offices, there is a requirement which states that 80% of the ceiling surface should be covered by an acoustic ceiling. This most often translates into a complete covering of the ceiling surface.

It is therefore obvious that there is an obstacle for the use of TABS especially in buildings using open plan offices. On one hand TABS needs to have as much of the concrete surface exposed to the room as possible, while on the other hand there is a need to meet the acoustic demands. In the papers and articles described above, this problem can also be found, as it is normally stated that the acoustic demands were met in "other ways". In this paper, we will show that both thermal and acoustic requirements can in deed be met simultaneously. The method has been to make detailed measurements in a test facility which has been constructed at the Technical University of Denmark (Weitzmann, 2004). The test facility is a room which, as ceiling and floor, is equipped with TABS. In this room we have investigated the thermal properties using a number of different layouts for a suspended ceiling. At the same time the acoustic reverberation time was investigated for some of these layouts.

The investigation showed that even at very high covering percentage of the ceiling surface, the cooling capacity was only decreased by a very small percentage. This shows that it is possible to combine these two properties.

2. Method

2.1 Test facility

The test facility is a room of 6m times 3.6m with a room height of 3.6m which, as ceiling and floor, is equipped with TABS. In these measurements only the upper deck is used. The TABS is integrated in a pre-fabricated hollow core concrete deck as shown in FIG. 1. The pipes are placed 50 mm above the ceiling surface in the 270 mm deck. The reason for this position is that the upper deck should be used mainly for cooling from the ceiling surface. In the pipes, water can be circulated at a predefined temperature and flow rate.

FIG. 1: View of the hollow core concrete deck in which the TABS is integrated

Internally in the room it is possible to add an internal heat load either through wall mounted electrical radiators or through a typical office setup using simulated persons, personal computers and lighting, which is mounted at a height of 3.0m above the floor surface – the same height as the lowered ceiling when this is present.

Measurements include supply temperature, flow rate and temperature difference between supply and return in the deck, internal heat load in the room, surface and air temperatures (to give the operative temperature) in the room as well as surface and air temperatures in the thermal guard.

Two types of lowered ceilings were tested; plywood plates and mineral wool acoustic panels. The reason for using plywood was a greater flexibility in designing the layout. It will later be shown, that this difference does not influence the results. FIG. 2 shows six different layout of the acoustic ceiling with covering percentages between 35% and 80%, called layout 1 to 6. Also used were layouts of 0% (layout 0) and 100% (layout 7).
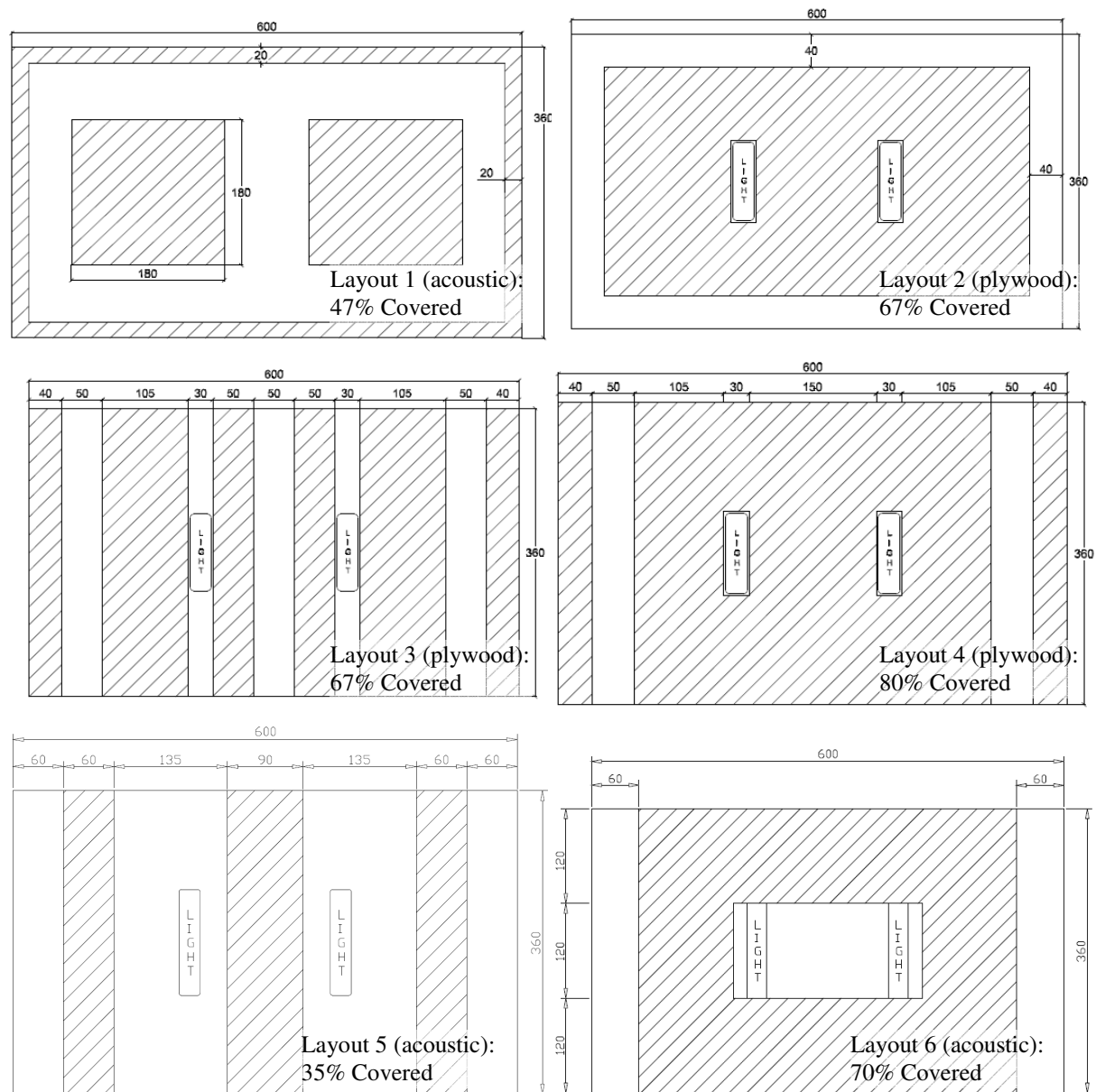
FIG. 2: Different layout of lowered acoustic ceiling.

Secondly, the acoustic panels were mounted in a vertical position as baffles. This is shown in FIG. 3. For this acoustic panels of 600x1200mm were used. This vertical position has the obvious advantage, that they do not block the direct view to the ceiling except for large angles away from the vertical orientation. However, the acoustic material is still present in the room and will lower the sound propagation. The four layouts shown here uses 10, 14, 14 and 27 acoustic panels, which is translated into an equivalent covering percentage of 33%, 47%, 47% and 90% respectively, even if they only cover between 2.8% and 7.5% of the ceiling surface.
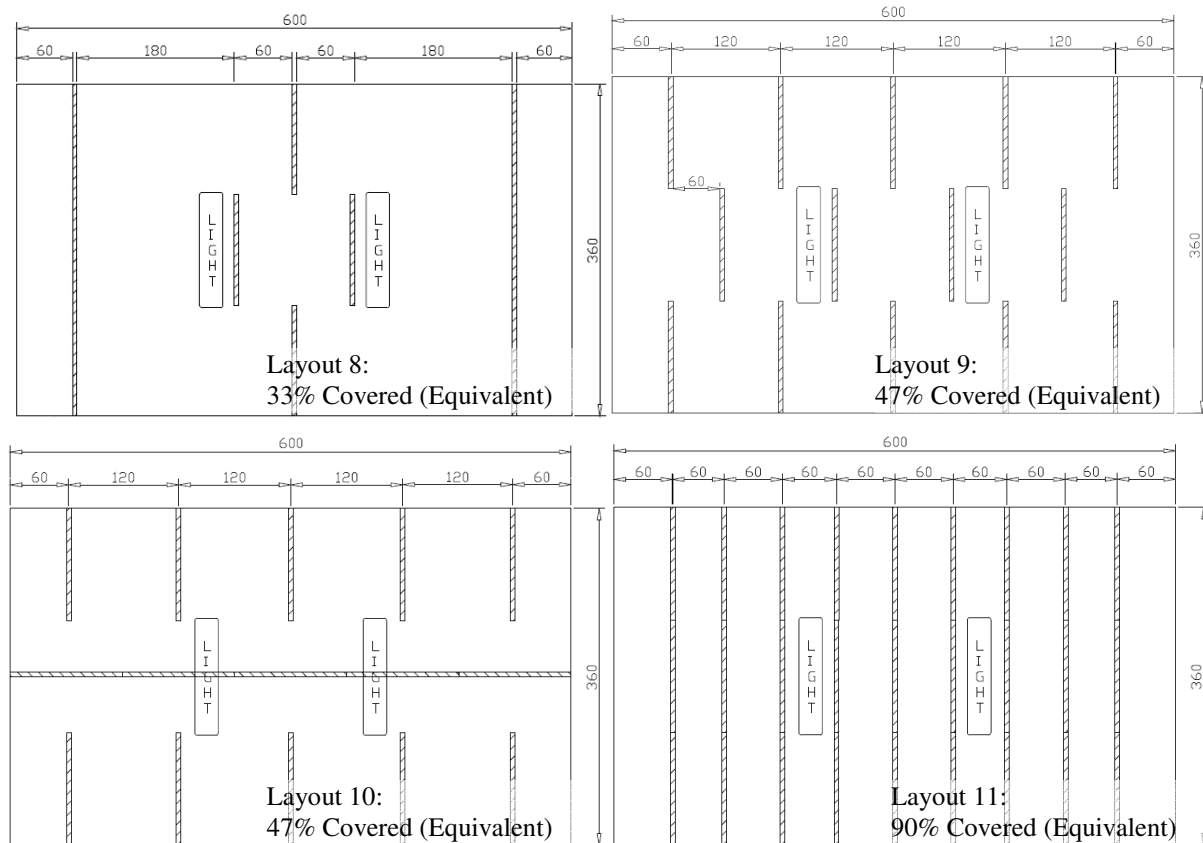
FIG. 3: Different layout of vertical baffles using 10 panels, 14 panels, 14 panels and 27 panels respectively.

FIG. 4: Pictures of acoustic ceilings – left a plywood lowered ceiling and right acoustic panels as baffles

The different layouts will be used the following investigations:

> Correlation between covering percentage and cooling capacity;
> Difference between covering material;
> Decrease of cooling capacity for different cover percentage and baffles;
> Reverberation time for different layout

2.2 Thermal properties

For the upper deck with integrated active TABS, the overall energy balance, assuming steady state conditions is:

$$q_{pipe} = q_{up} + q_{down} + q_{guard} \ [\text{W/m}^2]$$ *(1)*

The term on the left expresses the energy flow in the pipe, where the terms on the right expresses the heat flow through the ceiling surface, floor surface and sides and ends of the deck respectively. In this work, we want to express the heat flux through the ceiling as the function of the temperature difference between operative temperature in the room and the mean fluid temperature. Therefore Eq. *(1)* is rewritten as,

$$q_{up} = q_{pipe} - q_{down} - q_{guard} \ [\text{W/m}^2]$$ *(2)*

The heat flux in the pipe can be found from:

$$q_{pipe} = \frac{1}{A_{deck}} \dot{m}_{fluid} \cdot c_{p,fluid} \cdot (T_{return} - T_{supply}) \ [\text{W/m}^2]$$ *(3)*

The heat flow through the floor surface, q_{down}, can be calculated based on the temperature difference across the floor covering material, which therefore functions as a heat flow meter. The final heat flow, q_{guard}, which is the unwanted but inevtible heat flow through the ends and sides of the deck, has been found to be small compared to the two other heat flows, giving an error in most cases around 2% to 3%, with a maximum of 7% in a few measurements where there is a small temperature difference between deck and room.

From this, the cooling capacity coefficient, U_{cc}, is defined as shown in Eq. *(4)*.

$$q_{up} = U_{cc} \cdot \left(T_{room} - T_{fluid} \right) \ [\text{W/m}^2]$$ *(4)*

Here T_{room} is the operative temperature in the room and T_{fluid} is the average value of the fluid temperature.

Finally solving the equations for the cooling capacity coefficient, U_{cc}, the following is found.

$$U_{cc} = \frac{\dot{m}_{fluid} \cdot c_{p,fluid} \cdot (T_{return} - T_{supply})}{A_{deck} \cdot (T_{room} - T_{fluid})} \ [\text{W/m}^2 \ \text{K}]$$ *(5)*

It is assumed that the temperature difference in the fluid between supply and return is small, so that the surface temperature of the deck is almost uniform and the heating of the fluid in the pipe can be neglected.

2.3 Acoustic properties

Since the Danish building regulation sets requirements for the reverberation time, this value will be assessed in this work. Also, since the room is not a standard size laboratory, the sound level is not directly useful for other applications than this one. In the standard DS EN ISO3282, (CEN, 1998), the measurement of the reverberation time is described and the requirements are stated. Here the reverberation time is evaluated based on the averaged slope of the measured decay curve for six different frequency bands.

Based on the reverberation time, the sound absorption area index (SAA) is calculated as a single value expressing the performance for each of the layouts using the acoustic ceiling.

2.4 Measurement series

The measurements in the test facility were carried out using different combinations of fluid temperature and internal heat load, which was supplied either through wall-mounted radiators or through simulated persons, computers and lighting. The supply temperature was 15°C or 17°C with a heating of the fluid of less than 2K from inlet to outlet. The operative temperature was in the range of 23°C to 30°C, which was measured in the middle of the room. In total these temperatures corresponds to an internal heat load in the room between 20 W/m² and 70W/m², which is then also the range of the cooling capacity from the ceiling surface.

Steady state measurements were used. Depending on the actual setup, temperatures and the previous experiment, it would normally take up to three days to reach steady-state followed by approximately 12 hours from which data were used. All different layouts were investigated using different supply temperature and internal heat load. However, since each measurement series could last up to four to five days, this obviously limited the number of series.

3. Results

Initially, FIG. 5 shows the heat flow through the ceiling surface as a function of the temperature difference between operative temperature in the room and the mean fluid temperature in the deck. In other words this shows the cooling capacity of the ceiling surface. The operative temperature is in all cases measured in the middle of the room. The mean fluid temperature is found from the supply temperature and the heating through the pipe. In all cases the heating is less than 2K, giving uniform surface temperatures. On the graph, each point represents one measurement series. It can be seen that the highest heat flows occurs for the ceiling without acoustic measures for Layout 0. The legend notes if the measurements are using radiators, otherwise the setup of simulated persons and PC's is used. Without acoustic ceiling (Layout 0), there are little or no differences in the heat flows in these two cases. This conclusion is, however, not valid for acoustic ceilings. Comparing Layout 2 and 3 for radiators and people and PC's, it can be seen that there is a difference in the cooling from the ceiling, which is smaller for the more realistic setup. One very possible explanation is that the air flow pattern in the room when the air is heated at the perimeter of the room is more favourable than heating in the middle of the room. Also notice that there is a near linear correlation between the temperature difference and the heat flow through the ceiling surface, which is the easiest visible for the uncovered ceiling.

Looking at the other data points, it can be seen that the introduction of a lowered ceiling decreases the cooling capacity of the ceiling surface. Generally, it can be seen that the larger the covering percentage, the lower the heat flow.
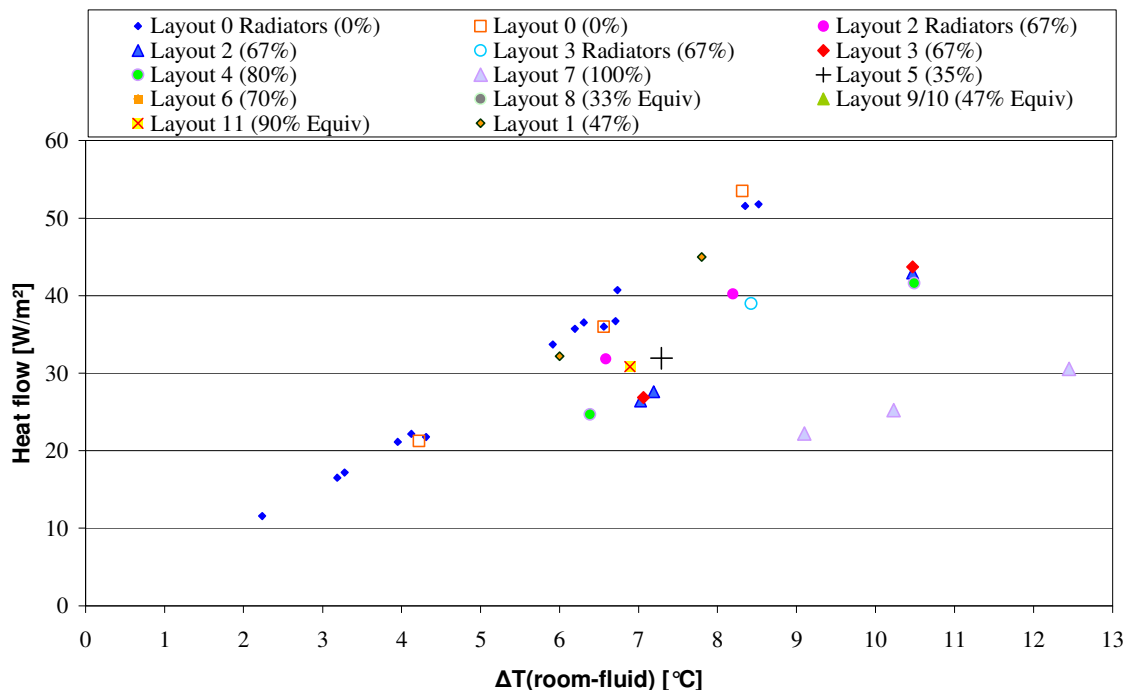
FIG. 5. Heat flow through the ceiling surface as function of the temperature difference between the operative temperature in the room, and the mean fluid temperature in the deck

FIG. 6 shows the cooling capacity coefficient calculated based on Eq. *(5)* as a function of the covering percentage. Again one data point is shown for each measurement series. Here it is obvious that even at 80% covered area, the cooling capacity coefficient is still only around 30% smaller than for the uncovered ceiling.

Looking at the data points for the case of 67% covered using two different layout schemes of the acoustic ceiling, it can be seen that there are no differences in the cooling capacity coefficient. In fact, the type of heat load in the room is more important than the layout.

The measurements showing the baffles can also be seen in the figure, where the percentage of covered area is recalculated as an equivalent covering area. Here it can be seen, that using baffles only results in a minor lowering of the cooling capacity compared to the uncovered conditions.
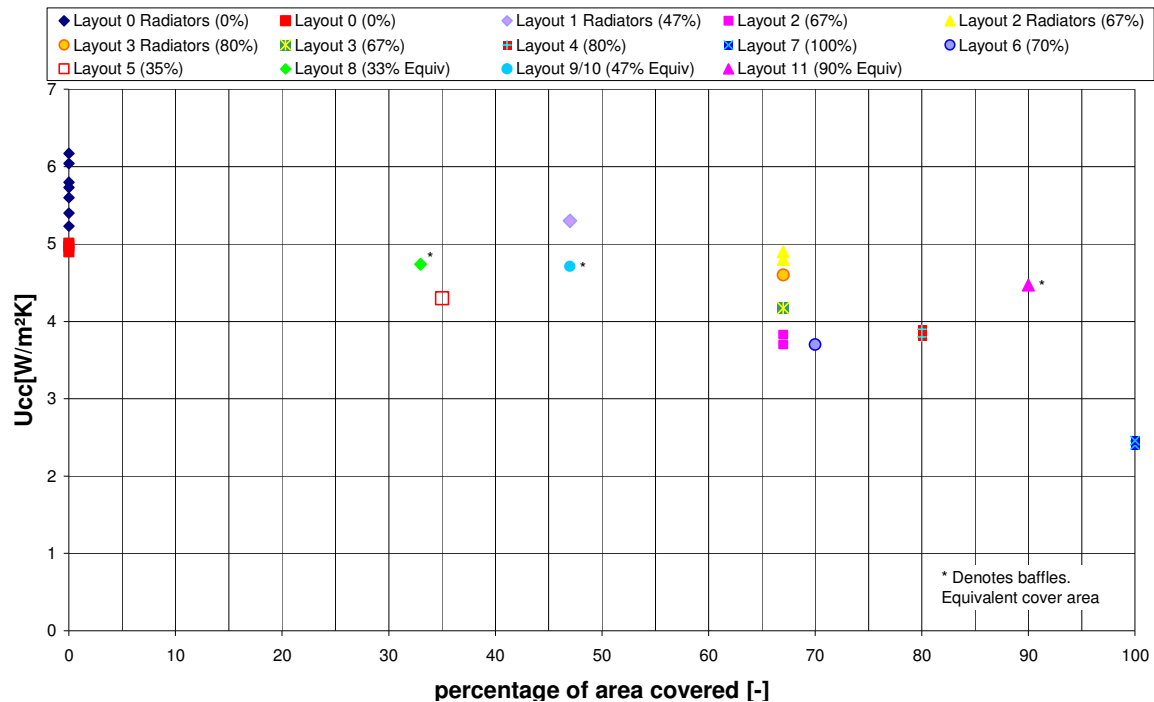
FIG. 6. The cooling capacity coefficient as function of the covered percentage of the ceiling surface

The results from the acoustic measurements are shown in TABLE. 1, were only performed for the empty room and for the layouts using acoustic panels. As it can be seen, the reverberation time is much larger for the case without the panels than all other cases. This can also be seen from the SAA index, which tells about the ability to absorp noise; the higher the value, the better. Briefly described, it can be seen, that there has been a significant reduction in the reverberation time compared to the uncovered ceiling – and consequently a large increase in the SAA index. Comparing the horizontal acoustic ceilings, the values for 100%, 70% and 35% shows a poorer performance for the smaller covering. For the baffles it is actually possible to have a larger SAA-value than for the 100% covering, even using fewer acoustic panels.

TABLE. 1: Measurements of the reverberation time in seconds for six different sound frequency bands.

Layout	Number	125	250	500	1000	2000	4000	SAA
Without panels	0	0,77	1,33	1,5	1,41	1,34	1,05	0,015
100% covered	7	0,54	0,66	0,56	0,6	0,64	0,57	0,52
70% covered	6	0,66	0,69	0,61	0,62	0,66	0,58	0,46
35% covered	5	0,63	0,84	0,73	0,67	0,66	0,58	0,38
10 baffles	8	0,5	0,77	0,7	0,65	0,66	0,6	0,43
14 baffles	10	0,48	0,69	0,63	0,58	0,59	0,52	0,53
27 baffles	11	0,47	0,64	0,58	0,54	0,57	0,52	0,57

4. Discussion

The work presented in this paper has a large number of interesting implications for the use of TABS. In general it has been believed that it was not possible to combine TABS and acoustic ceilings. However, the measurements in this paper show that even a fairly large covering percentage only lowers the cooling capacity from the ceiling to a much smaller extent than expected. In fact, covering up to 50% of the ceiling area has no significant influence on the cooling capacity coefficient. The measurements also show that using vertical baffles does not lower the cooling capacity from the ceiling at all.

The actual layout does not influence the results, since two different patterns with the same covering percentage gave almost identical results. Also the cover material does not influence the results. For practical reasons

measurements were made using plywood panels in stead of acoustic panels, which by comparing identical covering percentages gave the same result.

One issue which has not been investigated is the mode of heat transfer between ceiling surface and room. Since the normally dominant direct radiation heat exchange with the occupants and other room surfaces is impeded by the acoustic ceiling which also changes the air flow patterns.

In the measurements, the fluid temperature difference between inlet and outlet is always less than 2K, which means that there is no need to investigate differences the cooling along the length of the pipe. This is also how the system is expected to be operated in an actual building where water is used as the cooling medium. The conclusions would probably not be applicable for airborne systems, where the temperature difference is normally larger in the flow direction, requiring a subdivision of the deck in the calculations. Also, the acoustic ceiling influences the operative temperature in the room as it covers the direct view from the room in certain positions. However, the measured values only changed slightly when measuring either under or between an acoustic plate.

For the uncovered ceiling, the measurements indicate that a linear relation between the temperature difference between operative and fluid can be assumed as a first estimate. A closer analysis shows that an exponential correlation is more adequate. This is also in line with EN1264 (CEN, 1998), which has an exponent of 1.1 in the correlation. For the covered ceiling, the fairly limited number of measurements could not be used to correlatie covering percentage and cooling capacity coefficient. This requires further measurements using different covers.

The acoustic properties have not been investigated in great detail in this work as the main point has been to establish a dependency of the covering percentage on the depreciation of the cooling capacity. Therefore the acoustic investigation is made in order to determine the probability that these requirements can also be met.

However, in spite of these shortcomings, the results show that it is possible to combine TABS and acoustic ceilings and get both the cooling from the ceiling and at the same time be able to meet the acoustic requirements.

5. Acknowledgements

6. References

Andersson L O and Isfält E (1978): Hus med betongstomme spar 80 procent värme. (In Swedish) In: Byggnadstidningen nr. 18.

Arbejdstilsynet (1995): AT-anvisning 1.1.0.1. Akustik i arbejsrum. http://www.at.dk/sw5110.asp, AT

CEN (1998): DS ISO 3382:1998. Acoustics - Measurement of the reverberation time of rooms with reference to other acoustical parameters. Euopean Committee for Standardization, CEN

CEN (1997): DS EN ISO 1264: Floor Heating – Systems and Components. Euopean Committee for Standardization, CEN

CEN (2007): DS EN 15377-3: Heating systems in buildings - Design of embedded water based surface heating and cooling systems - Part 3: Optimizing for use of renewable energy sources. CEN

De Carli M and Olesen B W (2001): Field Measurements of Thermal Comfort Conditions in Buildings with Radiant Surface Cooling Systems. In Proceedings from Clima 2000/Napoli 2001 World Congress

Meierhans R A (1993): Slab cooling and Earth Coupling. In: ASHRAE Transactions. Vol 99, pp. 511-518.

Meierhans R A (1996): Room Air Conditioning by Means of Overnight Cooling of the Concrete Ceiling. In: ASHRAE Transactions. Vol 102(1), pp. 693-697

Meierhans R A and Olesen B W (2002): Art Museum in Bregenz – Soft HVAC for a Strong Architecture. In: ASHRAE Transactions. Vol. 108(2), pp. 708-713

Weitzmann P (2004): Modelling Building Integrated Heating and Cooling Systems. BYG.DTU R-091. Technical University of Denmark

Ground Storage Heat Transfer with Non-linear Features Modeled in the Frequency Domain

Gudni. Jóhannesson, Professor, Dir. General.
KTH - The Royal Institute of Technology, Div. of Building Technology
Orkustofnun – The Icelandic National Energy Authority
gudni.a.johannesson@os.is*, www.os.is*

Alberto Lazzarotto, MSc student,
KTH - The Royal Institute of Technology, Div. of Building Technology
alaz@kth.se*, www.byv.kth.se*

KEYWORDS: *Buildings, ground heat storage, finite element, modelling, frequency domain, variable mass flow*

SUMMARY:
The strategy chosen in the present work is to use standard finite element software which gives the possibility to use triangular elements and to run different physical models in parallel and with interaction between the models. This creates possibilities of rational solution of large thermal field problems. The modern finite element software gives the user the possibility to create macros or scripts for administration of calculations giving the possibility within the software environment to convert real time data into Fourier series, run the solution for a large set of frequencies and to carry out the inverse transformation of the results to time series. By separation of the ground heat flow and the duct heat balance a technique for the introduction of variable air flow is developed. The use of the technique is demonstrated for annual ground heat storage in a duct under a building. As shown by the examples in the paper the new tools for finite element modeling of different processes opens up a new field of opportunities in the treatment of problems within building physics. An advantage is that the solution for various processes can be interlinked and the high level script formalism gives the possibility to implement the field problems in the treatment of whole systems in a rational way. In the paper it is shown how the frequency domain solution for heat transfer can be implemented into existing finite element software and how the solution can be combined with constant mass flow in pipes and ducts. It is furthermore outlined and demonstrated how the treatment of variable mass flow can be carried out in reasonable time utilizing advanced iterative solutions.

1. Introduction

The calculation of heat transfer in systems with large thermal inertia in the time domain is a process that needs high computer capacity and CPU time. This is the case for problems as two or three dimensional heat transfer to the ground when calculating ground heat loss from buildings and different configurations for ground heat storage. The strategy chosen in the present work is to use standard finite element software which gives the possibility to use triangular elements and to run different physical models in parallel and with interaction between the models. From earlier work the formulation of the solution for the heat transfer equation in the frequency domain gives the possibility to formulate the problem as two steady state temperature fields, one for the real and one for the imaginary parts of the solution. The different temperature fields are interlinked via the heat source term. In this way the solution time for each frequency will be of the same order of magnitude as for the steady state solution. The modern finite element software, *COMSOL (2007),* gives the user the possibility to create macros or scripts for administration of calculations giving the possibility within the software environment to convert real time data into Fourier series, run the solution for a large set of frequencies and to carry out the inverse transformation of the results to time series. In this way a rational and highly effective calculation technique for this problem area can be reached. By separation of the ground heat flow and the duct heat balance a technique for the introduction of variable air flow is developed. The use of the technique is demonstrated for annual ground heat storage in a duct under a building.

2. Ground heat exchange

In many design problems we are depending on modeling the heat exchange with the ground. Simulations of such

problems in the time domain are however very tedious since we have to include large ground volumes in our simulations and the time for convergence may be of the order of magnitude 10 to 100 years in real time. It is therefore tempting to move the calculation work to the frequency domain and use the Fourier transform for the representation of the actual boundary conditions in time. Furthermore the system is assumed to be linear and the boundary conditions are expressed as Fourier series. The solution can the be limited to the frequency domain where each entity can be expressed as a complex numbers representing amplitude and phase shift from a basic oscillation. The solution for each frequency can be found in similar way and with similar calculation effort as for the steady state solution and the results for the different frequencies are then transformed back to time series showing for instance different temperatures in the crawl space as a function of time.

The heat conduction evaluation in two dimensions can be expressed

$$\frac{\partial^2 \vartheta}{\partial x^2} + \frac{\partial^2 \vartheta}{\partial y^2} = -\frac{1}{a}\frac{\partial \vartheta}{\partial t} \qquad (1)$$

If the temperature variation over time now is limited to a harmonic variation that can be expressed as a sinus function or expressed in exponential form,

$$\vartheta = (u + i \cdot v) \cdot e^{i\omega t} \qquad (2)$$

where the exponential part is the basic unit oscillation with angular frequency ω and (u+i·v) is a complex quantity giving the amplitude and phases shift. In this way the equation to be solved is

$$\frac{\partial^2 \vartheta}{\partial x^2} + \frac{\partial^2 \vartheta}{\partial y^2} = -\frac{i\omega}{a}\vartheta \qquad (3)$$

The finite element formulation for direct solution of this equation, where the temperatures are represented by complex numbers, has been implemented a computer code in and utilized to investigate the dynamic properties of water coils embedded in an intermediate floor construction, Weber (2004)

Inserting equation 2 into equation 3 we get one equation for the real part and one equation for the imaginary part

$$\frac{\partial^2 u}{\partial x^2} + \frac{\partial^2 u}{\partial y^2} = \frac{\omega}{a} \cdot v \qquad \frac{\partial^2 v}{\partial x^2} + \frac{\partial^2 v}{\partial y^2} = -\frac{\omega}{a} \cdot u \qquad (4)$$

The solution for the real term is the steady state solution with the complex part of the temperature as a source term. The solution for the imaginary part is in the same way depending on the real part. The solution for each frequency can be set up as two steady state temperature fields, the real and the imaginary, that are solved simultaneously. This is nicely solved by the multi-physics approach where the two temperature fields are given in separate models and where the source term for the real temperature models is calculated from the complex model and vice versa. The calculation work for each frequency will be of the same order of magnitude as that of solving a steady state two dimensional temperature field. The periodic boundary conditions such as the outdoor temperature can be expressed in Fourier series and the Fourier coefficients also represent the real and imaginary inputs for corresponding frequencies.

When computer codes are used for other purposes than intended it is important to have access to analytical solutions for various problems where the methodology can be tested. Such solutions for heat conduction in the frequency domain are for instance provided in basic course material semi infinite solids and for problems with axial symmetry solutions based on modified Bessel functions can be found in *Schmidt (2004)*.

As a demonstration of this solution technology we can take the case of a ventilation duct in the ground. It is well known that we can use a duct to reduce the temperature swing of the outdoor air and thereby reduce peak power for heating in winter and cooling in summer. We can characterize the dynamics of the ground by calculation a two-dimensional section perpendicular to the duct direction. For each frequency, ω, we calculate the real and imaginary temperature fields for two cases. One is when we have a unit oscillation of temperature for the duct air T_{da}. The other is when we have a unit oscillation of the outdoor air temperature T_{out}.

Case 1: $\qquad \tilde{T}_{da} = (1 + i) \cdot e^{i\omega t} \qquad \tilde{T}_{out} = 0 \qquad (5)$

$$\text{Case2}: \qquad \tilde{T}_{da} = 0, \qquad\qquad \tilde{T}_{out} = (1+i) \cdot e^{i\omega t} \qquad\qquad (6)$$

Now we define for each frequency the admittance, E, for the duct as the heat flow from the duct air to the duct wall for boundary temperatures according to case 1 and, F, the transmittance from the outdoor temperature to the duct temperature as the heat flow towards the duct air for a unit temperature oscillation according to case 2. Note that F and E are complex numbers that represent the amplitude and phase shift of the heat flow relative to the unit temperature oscillation. If we assume that the cross section is constant along the duct, and if we assume that the heat conduction along the duct in the ground can be neglected, we can use the exponential solution for the temperatures along the duct in the frequency domain.

$$\tilde{T}_{da}(x,\omega) = (\tilde{T}_{inl} - \frac{F \cdot \tilde{T}_{out}}{A \cdot \rho \cdot c_p \cdot i \cdot \omega + E}) \cdot e^{-\frac{A \cdot \rho \cdot c_p \cdot i \cdot \omega + E}{u \cdot A \cdot \rho \cdot c_p} \cdot x} + \frac{F \cdot \tilde{T}_{out}}{A \cdot \rho \cdot c_p \cdot i \cdot \omega + E} \qquad (7)$$

and at the outlet of a duct with the length L

$$\tilde{T}_{da}(L,\omega) = (\tilde{T}_{inl} - \frac{F \cdot \tilde{T}_{out}}{A \cdot \rho \cdot c_p \cdot i \cdot \omega + E}) \cdot e^{-\frac{A \cdot \rho \cdot c_p \cdot i \cdot \omega + E}{u \cdot A \cdot \rho \cdot c_p} \cdot L} + \frac{F \cdot \tilde{T}_{out}}{A \cdot \rho \cdot c_p \cdot i \cdot \omega + E} \qquad (8)$$

Which is a complex number times the basic oscillation

$$\tilde{T}_{outl} = (c + i \cdot d) \cdot e^{i\omega t} \qquad\qquad (9)$$

Since we are dealing with linear systems in the frequency domain all time dependent variables and results are a product of the complex number and the basic oscillation. A convention is therefore to simply write the quantities as the complex number

$$\tilde{T}_{outl} = (c + i \cdot d) \qquad\qquad (10)$$

In the frequency domain we choose to use apart from $\omega_0 = 0$ for the steady state solution based on average values six frequencies starting with the annual oscillation.

The inverse Fourier transform will give the solution for the outlet temperature in the time domain.

$$T_{outl} = \frac{c(\omega_0)}{2} + \sum_{n=1}^{6} (c(\omega_n) \cdot \cos(\omega_n \cdot i) + d(\omega_n) \cdot \sin(\omega_n \cdot i)) \qquad (11)$$

We now test a more active solution where we use an air borne solar collector to heat the air before it enters the ground coil. In the first approximation we assume that we have a solar collector upstream that gives an average monthly temperature of the inlet air for the duct.

$$\tilde{T}_{inl} = \tilde{T}_{out} + 0.07 \cdot \tilde{I}_m = (a + i \cdot b) \qquad\qquad (12)$$

where a and b are the real and imaginary part of $\tilde{T}_{inl}$ respectively.

The input data for the calculated case are as follows:

Duct diameter: 400 mm

Duct center to ground surface: 1000 mm

Duct length 60 meters

Air in duct with velocity 3 m/s, density 1.2 kg/m^3 and the specific thermal capacity 1000 J/(kg·K)

Convective surface heat transfer coefficient in duct is 10 W/m^{2}K. The surface heat transfer coefficient on the top surface is 25 W/m^{2}K. For the steady state solution the temperature at 6 m depth is assumed to be constant equal to the average annual temperature outdoors.

Insulation layer on the ground above duct has thickness 200 mm, width 2000 mm, thermal conductivity 0.036 W/(mK), density 30 kg/m^3 and specific thermal capacity 1000 J/(kg·K)

The ground body in the calculation is 2000x6000 mm with a surface heat transfer coefficient of 25 W/m^{2}K on top and an assumed adiabatic boundary at the sides and at the bottom, thermal conductivity 1.6 W/(mK), density 1800 kg/m^3 and specific thermal capacity 1000 J/(kg·K). FEM model for the cross section is shown in FIGURE 1. The calculated unit temperature responses in the frequency domain are shown in FIGUR 2-4.
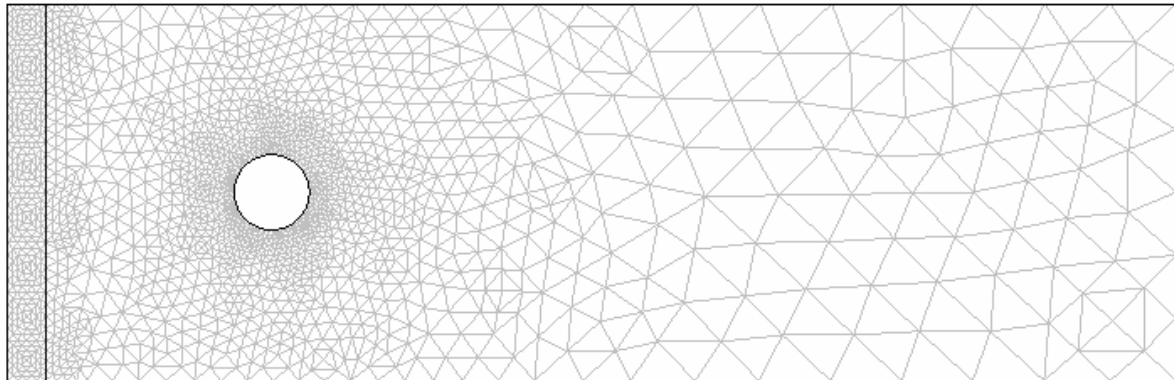
FIGURE 1 Finite element mesh for the calculated ground body. The geometry is rotated 90 Deg to the left
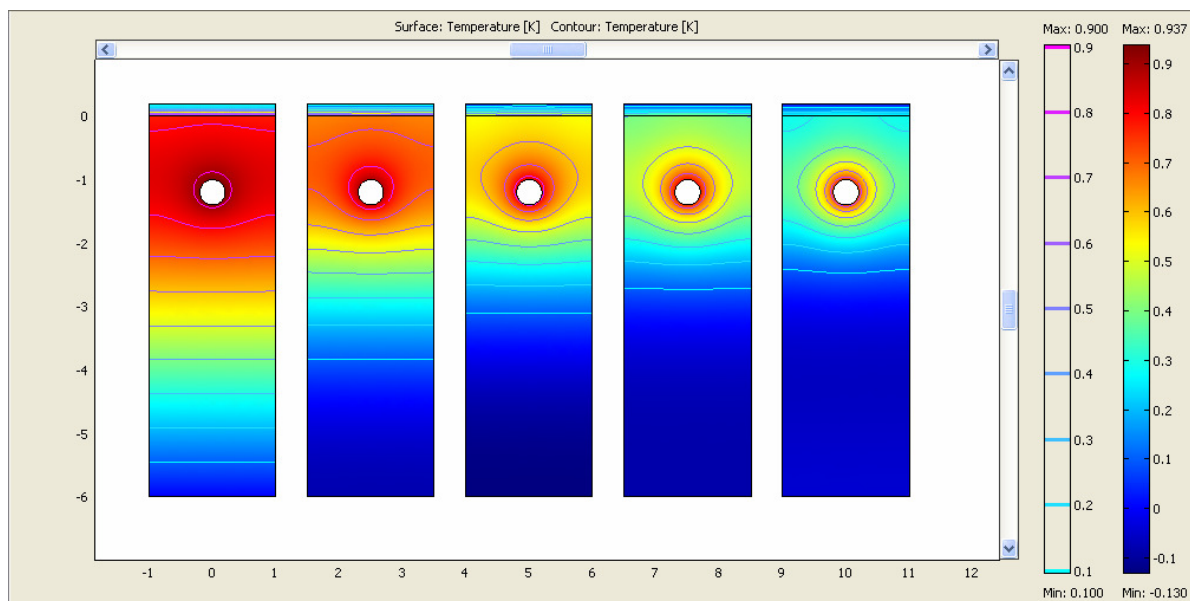
FIGURE 2 The real part of the calculated emittances for the steady state solution and the for first frequencies corresponding to periods of 1, ½, 1/3 and ¼ years
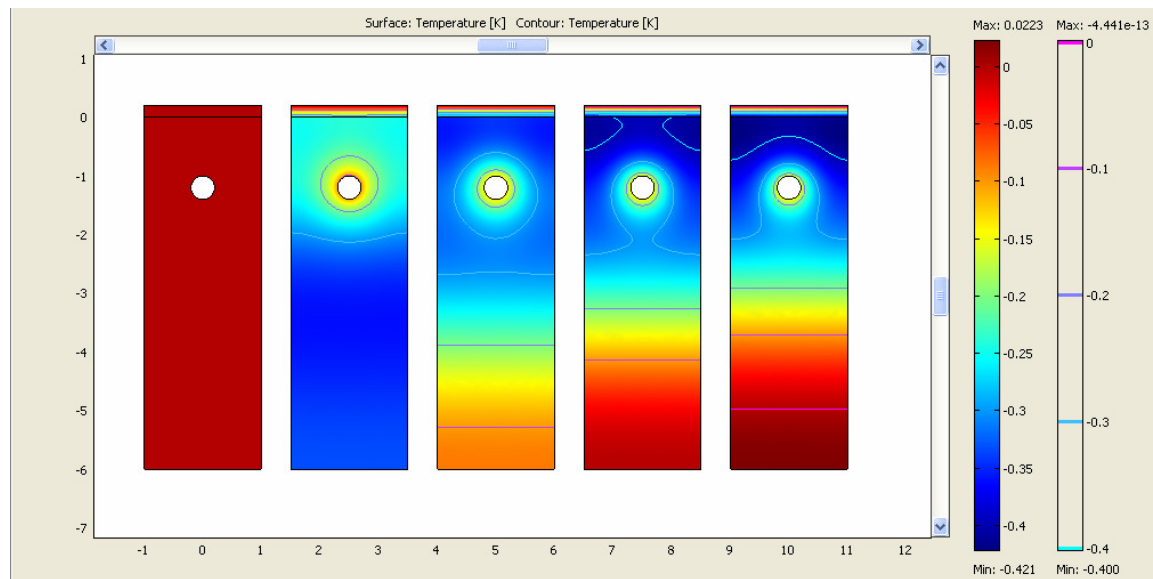
FIGURE 3 The imaginary part of the calculated emittances for the steady state and the for first frequencies corresponding to periods of 1, ½, 1/3, and ¼ years
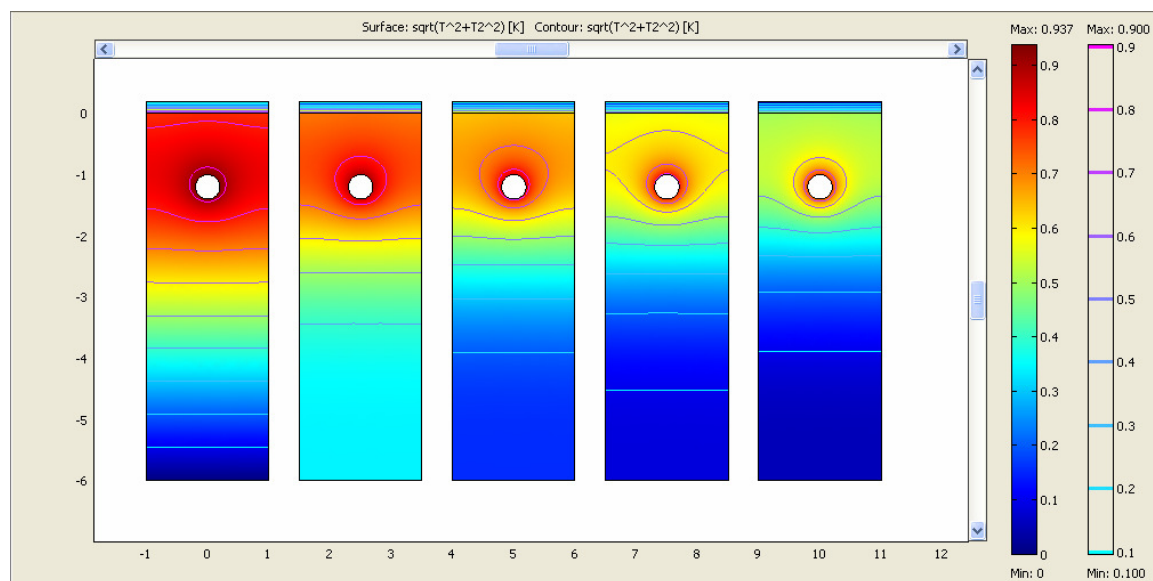
FIGURE 4 The magnitude of the calculated emittances for the steady state solution and the for first frequencies corresponding to periods of 1, ½, 1/3, and ¼ years
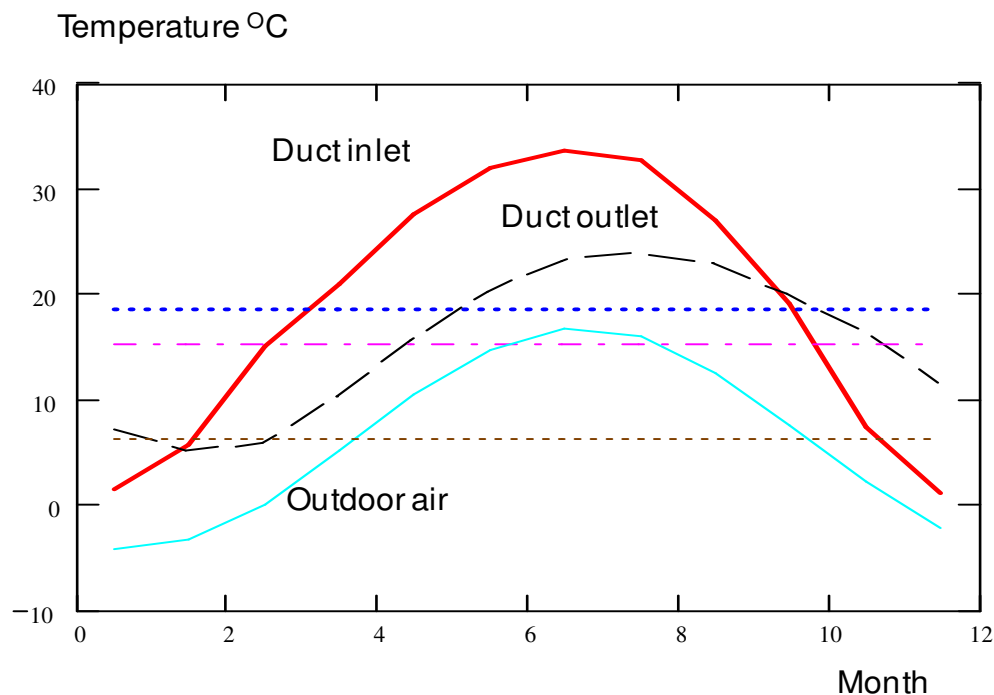
Temperature ^{O}C

FIGURE 5 The annual variations in temperatures for a 60 m long duct coil with a diameter of 400 mm calculated from the inverse Fourier transform. The adiabadic conditions are assumed to be reached if the duct is laid in a spiral at a depth 1000 mm with center - center distance of 2000 mm with 200 mm EPS insulation on the top.

The resulting temperature variations given in FIGURE 5 show that the winter temperatures for the ventilation air can be on average raised for more than 10 degrees during the coldest winter month. We also have to bear in mind that this solution has so far only be analyzed as a linear system with constant air flows and temperatures based on monthly mean temperatures and solar radiation. With a non linear operation of the duct coil, such as reversing the flow and varying flow rates based on available solar radiation, the solution can be developed towards a better performance. If the duct is placed under the ground plate of a building heated to 20 ^{O}C the average temperature of the duct outlet air will rise somewhat.

3. An approach to modelling of non-linear problems

In the previous ections the analysis is done based on constant velocity in the pipe and that gives us the idea of the dynamic characteristics of the system. A more effective utilisation of the system demands that we can vary the mass flow through the storage in time and thereby introducing elements of non-linearity into the calculations. For example during the summer the temperature from a solar collector during the day is higher than the ground temperature but during the night it can be lower and running air or water through the system would actually cool the storage. The approach here is to try to use the same technique as used for the previous work for the linear transfer functions for the linear cross section problem and then introduce the analysis to get the system parameter to get the transfer function from a finite element analysis and interactively link this solution to the resulting temperature distribution of the mass flow along the duct. The main issue is, as explained below, introducing variable velocity results in the solution of a large system of nonlinear equations. The solution here is based on the GMRES (General Minimal Residual) method that gives a substantial reduction in calculation time compared with the Newton-Raphson method, Peter et al (1990), Knoll et al (2004).

3.1 New formulation

In the first formulation in the FEM (Finite Element Method) analysis, the potentials chosen for the formulation of the transfer functions along the ducts were the outside temperature T_{out} and the temperature for the flowing mass inside the duct T_x, with a constant heat transfer coeffficient between the flowing mass and the duct wall h depending on the velocity. In the present approach this is no longer possible since varying heat surface heat transfer coefficients will introduce a non-linear component in the modelling of the cross section. To overcome this problem we assume the temperature around the duct or pipe to be more or less constant. Then the new transfer functions for the cross sections will express the heat flows in terms of the outdoor temperature and the temperature of the duct surface T_s. The expression for the temperature of the flowing mass along the duct can now be formulated numerically based on the inlet temperatures and the surface temperature along the duct. Basically the calculation is carried out in the following steps

1. The transfer functions $E*$ and $F*$ for the cross section are calculated with a finite element method.

2. The system along the duct is divided into a finite number of cross sectional elements in which the temperatures of the surfaces $T_s(t)$ is supposed to be a function of the time but not of the space. In each of these elements the temperature of the surface $T_s(t)$ are assumed to be known

3. For each of the cross sectional elements we express the heat flow at the duct surface based on the and temperatures on the duct surface and outside

$$Q(\omega) = E^*(\omega) \cdot T_s(\omega) + F^*(\omega) \cdot T_{out}(\omega) \tag{13}$$

and get the time domain function, $q_2(t)$, from the inverse Fourier transform.
The heat flow based on the conditions inside the duct surface is

$$q_2(t) = h(t)\big(T_x(t) - T_s(t)\big) \tag{14}$$

4. Given the inlet temperature and mass flow as a function of time the temperature change of the flowing mass along the duct can be expressed in time for the sequence of cross sectional elements based of the heat flow to the surface.

$$h(t) \cdot \big(T_x(t) - T_s(t)\big) + \frac{\partial T_x(t)}{\partial x} \cdot \rho \cdot c_p \cdot u(t) \cdot A = 0 \tag{15}$$

$$\frac{\partial T_x(t)}{\partial x} = -\frac{h(t) \cdot \big(T_x(t) - T_s(t)\big)}{\rho \cdot c_p \cdot u(t) \cdot A} \tag{16}$$

$$T_{x+1}(t) = T_x(t) + \frac{\partial T_x(t)}{\partial x} \cdot dx$$
(17)

5. The solution of the problem is to find for all the cross sectional elements of the ducts a temperature for the flowing mass varying in time $T_x(t)$ that, fullfilling the conditions in 3 and 4.

In FIGURE 6 results from a calculation for the Helsinki climate are given. Before entering the duct the air is preheated by a horizontal solar panel with a surface $A = 15m^2$ and efficiency of 0.25. The velocity is constant in winter and is variable between 0.0 and 1.0 m/s in summer depending on the available solar radiation.

4. Conclusion

As shown by the examples above the new tool for finite element modeling of different processes opens up a new field of opportunities in the treatment of problems within building physics. An advantage is that the solution for

various processes can be interlinked and the high level script formalism gives the possibility to implement the field problems in the treatment of whole systems in a rational way. In the paper it has been shown how the frequency domain solution for heat transfer can be implemented into existing finite element software and how the solution can be combined with constant mass flow in pipes and ducts. It is furthermore outlined and demonstrated how the treatment of variable mass flow can be carried out in reasonable time utilizing advanced iterative solutions.
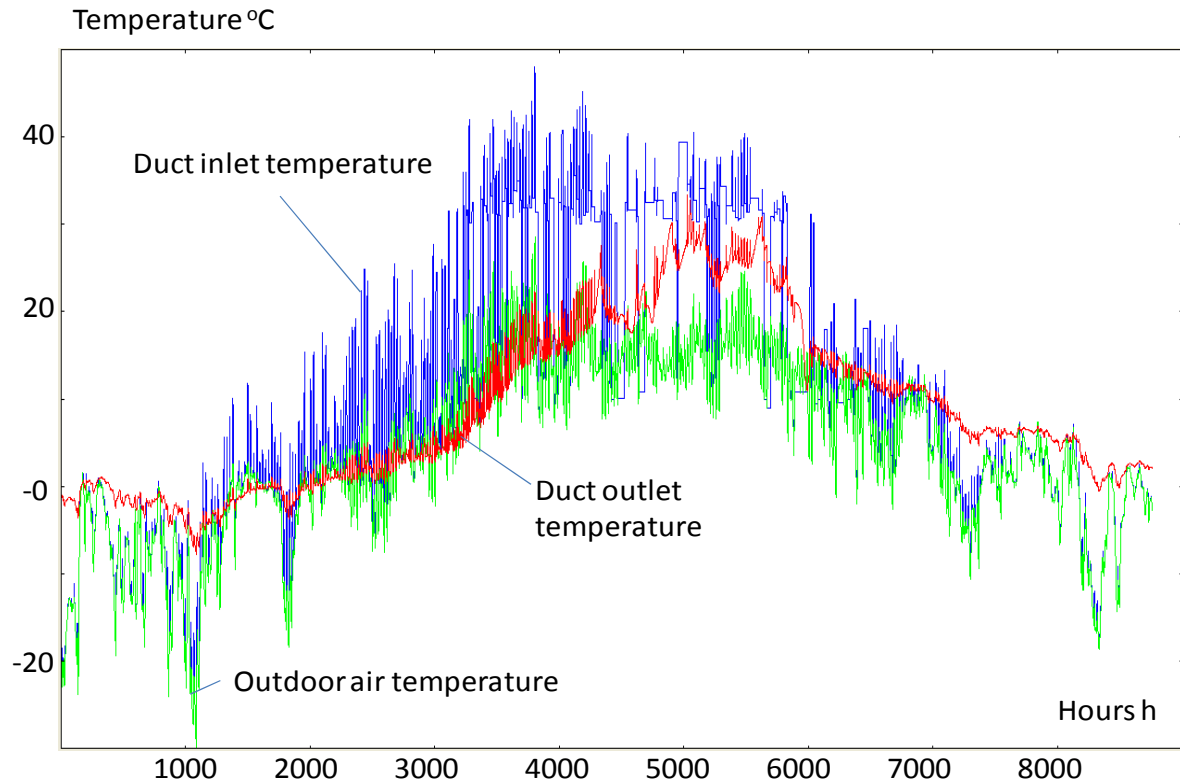
FIGURE 6 The results from a non linear simulation of solar preheated air through a 80 m long ground duct in Helsinki climate.

5. References

Schmidt D, Johannesson G (2001). Approach for the Modelling of Thermally Activated Building Constructions with an Optimized RC Network   Nordic Journal of Building Physics Volume 2, 1999-2001

Schmidt D, Johannesson G (2001). Model for the Thermal Performance of Double Air Gap Wall Constructions. Nordic Journal of Building Physics Volume 2, 1999-2001

Weber T (2004). Energy Performance of Building / Methodologies for Experimental Verification. PhD Thesis, KTH, The Royal Institute of Technology.

Schmidt D (2004). Methodology for the Modelling of Thermally Activated Building Components in Low Exergy Design. PhD Thesis. KTH, The Royal Institute of Technology

COMSOL (2007), www.comsol.com

Peter N Brown Youcef S Siam (1990) Hybrid Krylov Methods for Nonlinear Systems of Equations J. ScI. Stat. Comput. Vol. 11, No. 3, pp. 450-481, May 1990

D.A. Knoll, D.E. Keyes (2004). Jacobian-free Newton–Krylov methods: A Survey of Approaches and Applications. Journal of Computational Physics 193 (2004) 357–397

Adam Fic, Magorzata Hanuszkiewicz-Drapaa, Robert Pitek, Jan Skadzieñ (2000) HEAT Transfer Analysis in Ground Heat Exchanger Systems OF Heat Pumps, European Congress on Computational Methods in Applied Sciences and Engineering, ECCOMAS, Barcelona, 11-14 September 2000

Applications of the Calculus Program "Spatial Glazing" for Windows

Ligia Moga, Teaching Assistant,
Department of Physics of Constructions, Technical University of Cluj-Napoca;
ligia.moga@cif.utcluj.ro

Ioan Moga. University Professor,
Department of Physics of Constructions, Technical University of Cluj-Napoca;
ligia.moga@cif.utcluj.ro

SUMMARY:
The paper presents the calculus program expert kind "SPATIAL GLAZING" for the modelling and simulation of the physical spatial phenomena of thermal transfer through structures with complex formation, for the estimation of the heat flow and thermal resistance, for determination of the energetic performance of windows in divers placing modes in the walls belonging to the building envelope. The findings and the measurements made upon the same window type with the same energetic performances taken from the catalogue, for different conditions in exploitation, led us to the conclusion that the energetic performance of a type of window is very much influenced by the contour conditions in which is placed and is in exploitation. The necessity and the suitability of the automaton calculus program was imposed upon the need of explaining the differences in behavior of the same window type which has been placed in divers constructive solutions for walls and for divers placing positions of the same window type in the wall thickness. The calculus program expert kind "SPATIAL GLAZING" uses and develops other automaton calculus programs made by our research collective from the department of Physics of Constructions in the last 30 years of activity in the physics building field.

1. Introduction

The calculus program "SPATIAL GLAZING", was used for designing new window profiles, at designing new buildings, for determining the energetic performance of envelope elements of new buildings and for energetic rehabilitation of the existing ones.

The program represents a valuable implement for establishing the energetic performance of windows in actual conditions for exploitation, for the four standardized climatic zones in Romania: I zone -12°C, II zone -15 ^{o}C, III zone -18 ^{o}C and IV zone -21°C. The use of the calculus program gives offers structural solutions for the ensemble window- wall which have a direct and favorable effect upon energy economics in building exploitation and for reducing the pollution emissions in the atmosphere.

Graphical and numerical results for plane sections for various windows types are presented in the current bibliography. Results for the spatial calculus that takes into consideration the heat transfer, in the way we approached it in the paper, are not available in the current bibliography.

In the 2nd catalogue-*Isothermen* are presented the climatic conditions where the calculus were made. In Romania the climatic conditions are harsher, having four climatic zones with the following annual medium temperatures during winter time: -12 ^{o}C for the 1st zone, -15 ^{o}C for the 2nd zone, -18 ^{o}C for the 3rd zone, -21 ^{o}C for the 4th zone, with a relative humidity of the exterior air of 80% for each zone.

Specific for Romania for the interior environment the temperature of the air is 20°C while the relative humidities for the interior air range between 60% and 75%, values mainly due to current activities in the dwelling houses (cooking, washing clothes etc.).

While in the *Praxishandbuch (Isothermen)* the value for the given condense temperature is 9.3^{o}C, in our country in the conditions of the current humidity of 60% existing in our dwelling houses, the condense temperature is 12°C. For kitchens where food is usually cooked, the condense temperature is over 13°C.

The analysis of the interior microclimate conditions existing in the dwelling houses from our country, leads to the necessity of a better knowing of the heat transfer phenomena closer to the real phenomenon that takes place in the case of the termopane glass windows placed in different situations of exploitation. The practical finding of different behavior of termopane glass windows, the condense phenomenon met on the interior surface of the window framework and the contour in which the window is placed, calls for the necessity of the calculus presented in the paper. Most of the existing buildings in Romania were designed in the energy abundance conditions and therefore they have a value for the thermal resistance under 0.7 m^2K/W which means the value of the thermal transmittance U is higher than 1.4 W/m^2K.

An example for the apearance of the condense phenomenon on the interior glass surface is a five room PVC framework window. The declared energetic performances by the beneficiary: U_f=2.0W/m^2K, U_g=1.2W/m^2K and ψ= 0.08 $W/m \cdot K$ for the aluminium distance piece with a width of 16 mm placed between 2 glass leaves each of 4 mm.

FIG. 1: Window having a PVC framework placed in a wall made of big prefabricated panel of 27 cm thickness with condense on the interior surface of the glass

With the rehabilitation of the existing buildings the improvement of those phenomena is observed. The value of the thermal resistance will increase over 1.4 m^2K/W and the value of the thermal transmittance U will decrease under 0.7 W/m^2K.

2. The geometrical model

The calculus program "SPATIAL GLAZING" uses the profiles geometry and the calorific characteristics identified from a data library and post them in the structure of the analysed ensemble.
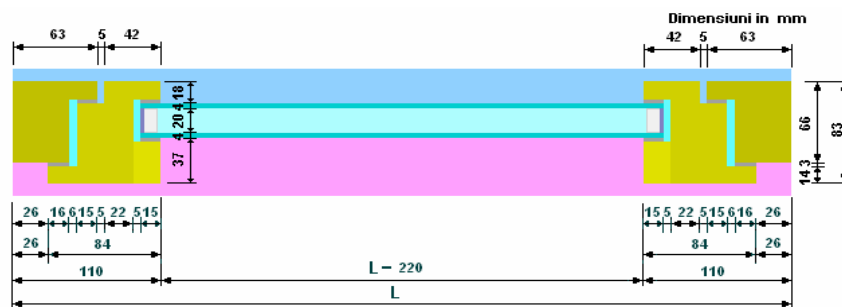
FIG. 2: The geometry and the calculus dimensions of the window.

From the many studied cases we present the results obtained for the types of windows placed in window hollows having the next dimensions: 0,60x0,60; 0,60x1,20; 1,20x0,60; 1,20x1,20; 1,80x1,20; 2,40x1,20; with one up to

four sashes and with one up to 3 movable frames 30 cm high (H_1=30cm).

The program is based upon the mathematical modeling for the heat transfer in spatial thermal stationary regime such as:

$$\frac{\partial}{\partial x}\left[\lambda(x,y,z)\cdot\frac{dT(x,y,z)}{dx} + \lambda(x,y,z)\cdot\frac{dT(x,y,z)}{dy} + \lambda(x,y,z)\cdot\frac{dT(x,y,z)}{dz}\right] = 0 \qquad (1)$$

The programming language used for the calculus program has developed from Fortran to Pascal and up to Delphi 7, having inserted the calculus modules in C++ language. The number of the material types that can be used in the program for describing the geometrical model and the contour conditions is unlimited.

The number of the digitization calculus network nodes is conditioned by the computer memory. For example, when a single window is analyzed, the nodes of the network can range between 30000 thousands and 50000 thousands equations. When windows placed on the whole façade of a building are simultaneously analyzed the program works with 500-600 thousands nodes. For the digitization of the entire building the digitization networks having minimum 2 million nodes (that depend on the computer memory) are used.

The time calculus for a window having a wood framework is about 90 seconds. For a window having a PVC framework the calculus time is about 120 seconds and for windows having aluminium framework the time calculus is about 200 seconds.

In time the calculus program has been optimized and after compilation sizes of 619 kb.

3. Subdivisions of the geometrical model

The geometrical model contained between the horizontal and vertical cutting planes was divided with the help of some sectional planes to form the orthogonal temperature field design network.

The program places the calculus network automatically with steps covering between 1 and maximum 10 mm in all directions.

The numerical method used is the one for the energetic equilibrium in each node of the plane or spatial digitization network for the ensemble window- wall. The calculus program takes into consideration the stipulations in accordance to EN ISO 10211/1-95 regarding the realization mode of the digitization network and the estimation mode for the flows equilibrium in the calculus network nodes of the ensemble frame- window.

FIG. 3: Digitization network.

Type 1,6,   *Type 2*   *Type 3*

Type 4   Type 5   Type 7   Type 8
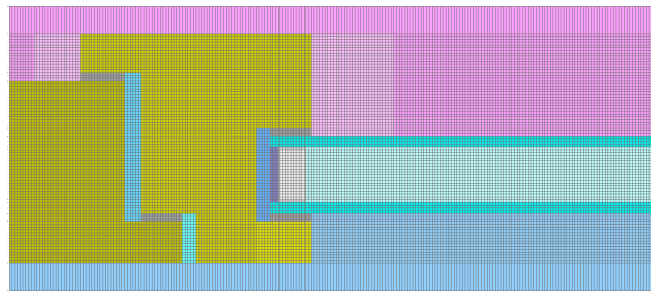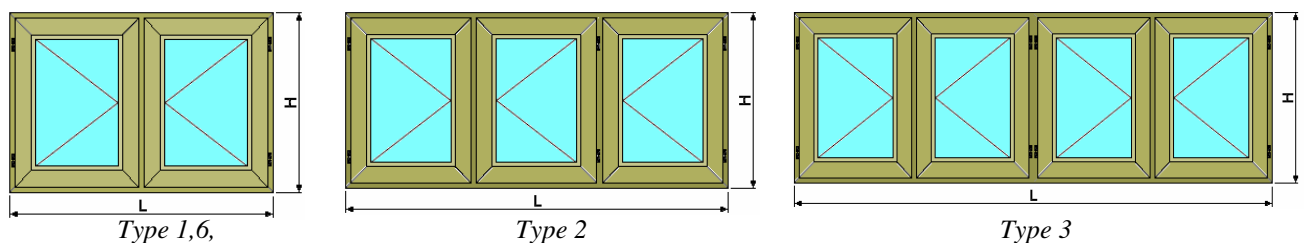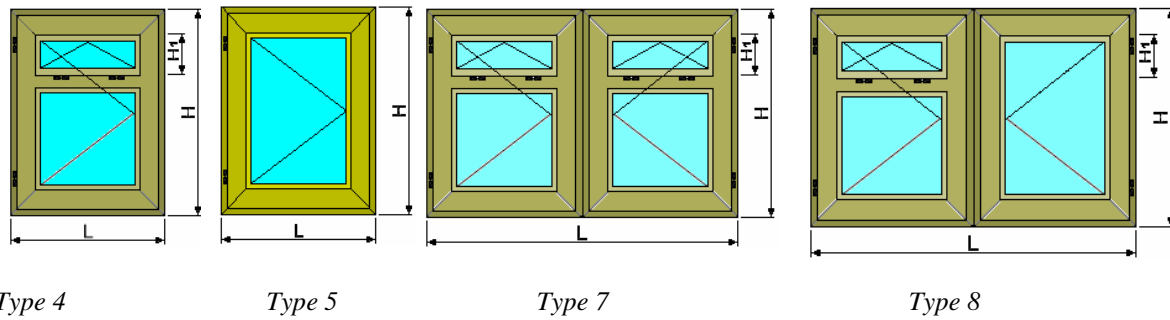
FIG. 4: The studied types of windows.

4. Contour conditions

The contour conditions regarding the superficial resistances and the temperatures of the exterior and interior medium, were taken the ones in accordance with the stipulations from the norm EN ISO 10077-2:2003.

The following conventional temperatures were used for the purpose of this study: +20 ^{0}C inside, and -18 ^{0}C outside.

5. Thermo-technical design features of the utilized building materials

The design heat characteristics of the building materials used for our study were those taken from the European standards regarding the energy performance of buildings.

6. Analysis and presentation of the obtained numerical results on real cases studied by our research collective

The results obtained with the calculus program "SPATIAL GLAZING", are presented numerical and graphics form under curved shapes and isothermal surfaces.

The example presented in the paper refers to the window having the frame profile of wood – figure D4 from the Norm EN ISO 10077-2:2003 and the detail for the aluminium element of spacing between the glass leaves- figure D10. The next values were taken into consideration U_g=1.3 W/m$^{2.}$K, U_f=1.36 W/m$^{2.}$K, the bi-dimensional thermal coupling coefficient L^{2D}=0.481 W/m$^.$K and the linear thermal transfer coefficient of the aluminium element of spacing ψ=0.084 W/m$^.$K.
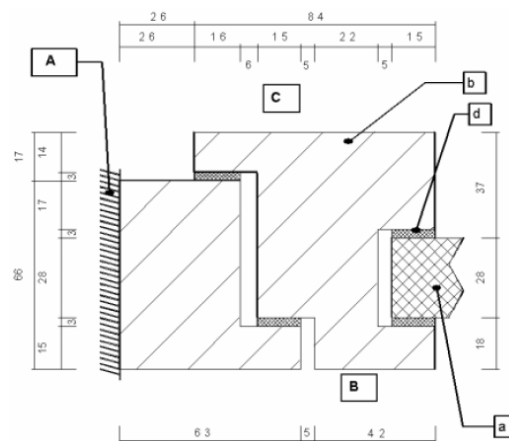
FIG. 5: Figure D4 from Norm EN ISO 10077-2:2003 showing a wood profile frame of a window with an insulating panel (b_f=110 mm)
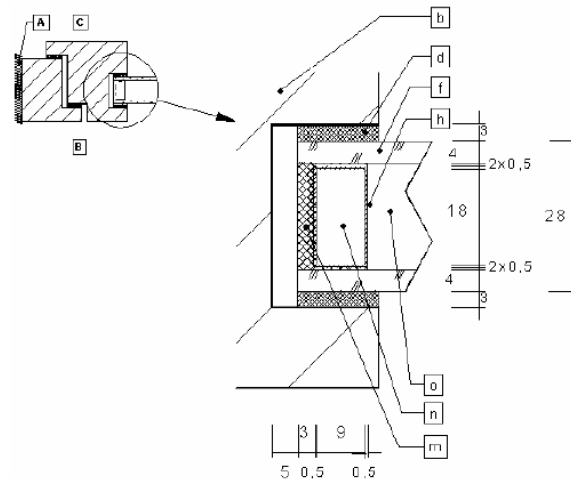
FIG. 6: Figure D10 from Norm EN ISO 10077-2:2003 showing a aluminium element of spacing between the glass leaves of the window having a wood profile frame

In the figure 5 and 6 the notations stand for:

A, B and C limit conditions for A-adiabatic, B-exterior and C-interior

a- for insulating panel

b- light wood

d- ethylene propylene diene monomer rubber

f- glass

h- aluminium

m- polysulfure

n- silica gel (dessicatif)

o- filling air

In order to compare the results obtained with the calculus program for the spatial phenomena and the ones obtained by a manual calculus, the Norm EN ISO 10077-1:2000 was used were the formula for the calculus of the thermal glazing transmittance of the window is given:

$$U_W = \frac{A_g \cdot U_g + A_f \cdot U_f + I_g \cdot \psi_g}{A_g + A_f} \quad (2)$$

where: U_g is the glazing thermal transmittance

U_f is the frame thermal transmittance

ψ_g is the linear thermal transmittance for the combined effects of the glazing, spacing element and the frame.

A_g is the area of the glass

A_f is the area of the frame

l_g is the perimeter of the glass

In the brakedown table are presented the results obtained with the calculus program "SPATIAL GLAZING" and the ones obtained by the manual method in accordance with the Norm EN ISO 10077-1:2000.

By a comparative analyse between the results obtained by the manual calculus from the norm and the ones obtained with the spatial calculus, significant differences are observed between the two types of results.

The thermal performance and the thermal transmittance of a window obtained with the two methods are different for the presented types of windows with percentages varying between 9.25 and 15.49 %. The results obtained for the spatial calculus are more averse than the ones obtained with the manual calculus, because the last one does not take into account the heat spatial transfer.

The different results are natural considering the general idea of the differences between a manual unidirectional calculus and a spatial automaton calculus closer to the real phenomenon of the heat transfer through those complex non homogenous systems.

The energetic performance of a building is directly influenced by the contour conditions, by the wall type in which is placed, by the position of the window in the wall thickness. The position will either accentuate or diminish the convective heat transfer on the surface of the interior glass, because of the natural movement of the air in the room (vertical gradients of temperature).

TABLE. 1: Tabel with results

Window type	Dimensions							U_W		Differences	
	Length		Area					Norm	Spatial	U_W^{3D} - U_{WN}	Percent
	L	H	Total	Framework		Glass		U_{WN}	U_W^{3D}	W/(kN·m²)	%
	m	m	m²	m²	%	m²	%	W/(kN·m²)	W/(kN·m²)		
1	1.2	1.2	1.44	0.678	47.05	0.762	52.95	1.648	1.803	0.155	9.43
2	1.8	1.2	2.16	1.008	46.64	1.152	53.36	1.648	1.814	0.166	10.07
3	2.4	1.2	2.88	1.337	46.44	1.543	53.56	1.648	1.816	0.168	10.17
4	0.6	1.2	0.72	0.424	58.94	0.296	41.06	1.694	1.956	0.262	15.45
5	0.6	0.6	0.36	0.216	59.89	0.144	40.11	1.691	1.864	0.173	10.26
6	1.2	0.6	0.72	0.424	58.94	0.296	41.06	1.694	1.851	0.157	9.25
7	1.2	1.2	1.44	0.835	57.97	0.605	42.03	1.698	1.961	0.263	15.49
8	1.2	1.2	1.44	0.756	52.51	0.684	47.49	1.673	1.931	0.258	15.44

Analysing the disposition of the isothermal curves in a vertical section through the window frame, at the interior surface of the glass the deviation of the flow lines and the concentration of the heat flows at the spatial intersections of the window frame are observed.

This phenomenon explains the increased value of the thermal transmittance of windows, calculated in a spatial manner compared to the ones calculated manual, because of the increased flow in those zones.
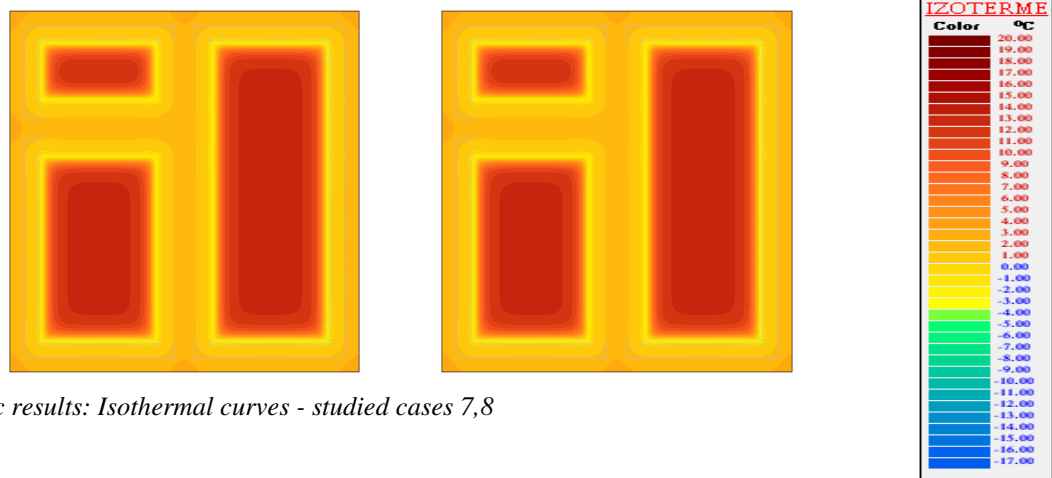
FIG. 7: Graphic results: Isothermal curves - studied cases 7,8
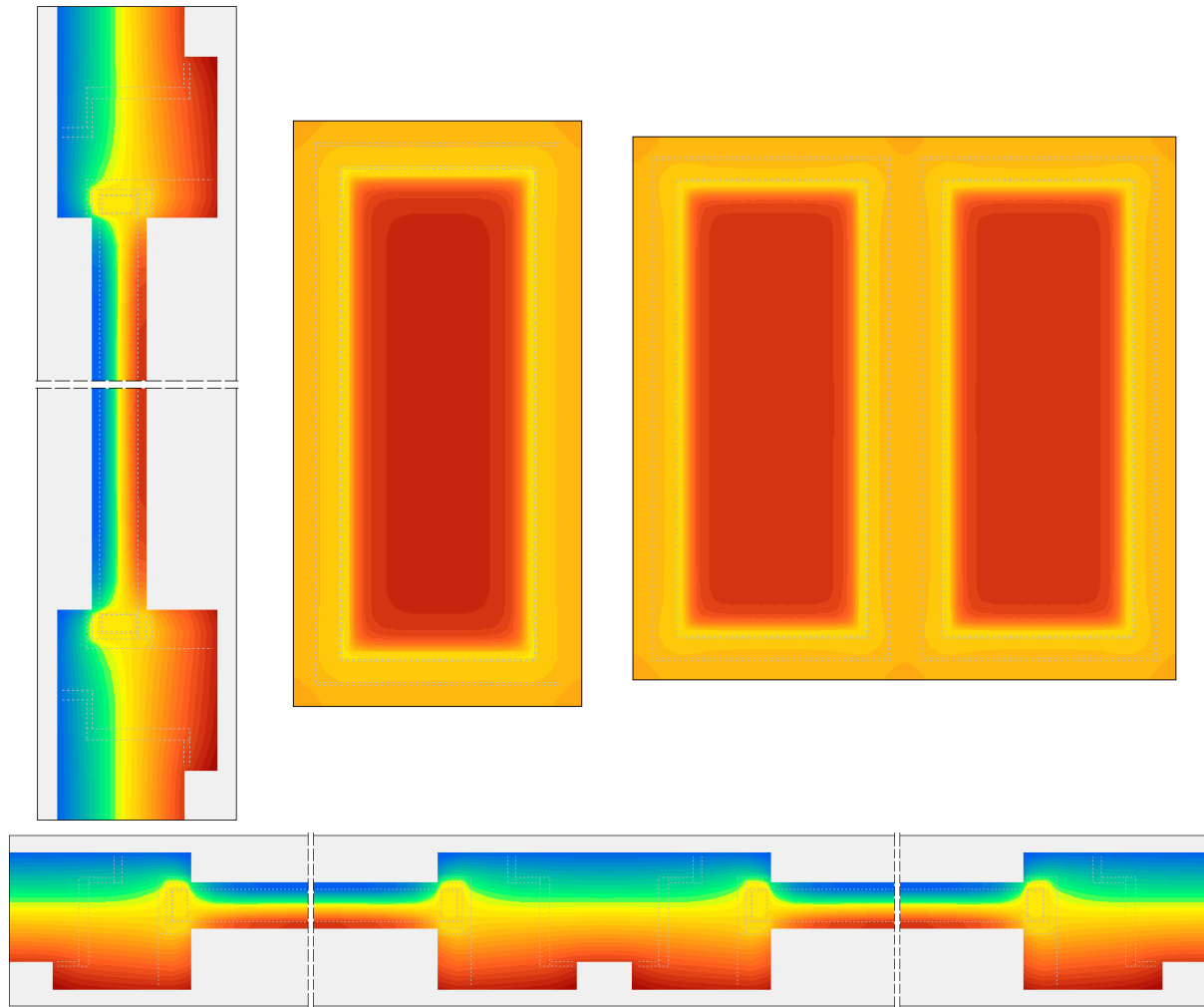
FIG. 8:Graphic results:Isothermal curves- studied cases 4,1

7. Conclusions

Because of it's "easy and friendly" nature, staff with medium knowledge in the computer usage can use the calculus program.

The negative phenomena mentioned in the paper were met in the exploitation of the existing buildings and at some of the buildings where termopane glass windows were placed. In the thermal technical designing of windows buildings the energetic performances utilized were the ones declared by the producers in the firm catalogues. The values had not been adapted to the real exploitation conditions of the buildings and windows in Romania. This fact is also explained by the absence of a handy working instrument for the designers, like the calculus program "SPATIAL GLAZING" can be.

The making of the calculus program "SPATIAL GLAZING" appeared because of the persistent demand from the designers.

In comparison with the stipulations from the Norm 10077/2:2003 which determines the energetic performance for the window frameworks for standard conditions that do not take into consideration the contour conditions, the calculus program presented in the paper represents a step forward regarding the analysis of the glazing surfaces in real working.

The conclusion is obvious and is a characteristic feature for each technical calculus that goes from the phenomena study in plane coordinates to the phenomena study in spatial coordinates.

The calculus program was utilized in the energy audit process for the thermal rehabilitation of 97 buildings from Cluj-Napoca city, in designing of 3 buildings having a low energy consumption and for the energy expertise and redesigning of a passive house placed in Cluj-Napoca town.

The calculus program "SPATIAL GLAZING" has a prompt practicability in the designing phase of new buildings and also in the phase for energetic rehabilitation of the existing ones.

8. References

*** Thermal bridges in building construction – Heat flows and surface temperatures – Part 1: General calculation methods, *EN ISO 10211/1-98*

*** Thermal performance of buildings – Specific transmission heat loss – Calculation method, *EN ISO 13789-99*

*** Directive 2002/91/EC of the European Parliament and of the Council of 16 December 2002 on the energy performance of the buildings.

*** Thermal performance of windows, doors and shutters- Calculation of thermal transmittance- Part 2: Numerical method for frames, *EN ISO 10077-2:2003*

*** Glass for constructions. Determination of the solar and luminous characteristics of glazing, *EN 410:2003*

*** Glass for constructions. Determination of the thermal transmittance U. Calculus method, *EN 673:2000*

*** Glass for constructions. Determination of the thermal transmittance U. Calculus method, *EN 673:2000/A1:2002*

Herausgeber GEALAN, Raumluftung, Luftungsfenster auf dem Prufstand, *Praxishandbuch Nr.1 -* Anwendugstechnik,

Herausgeber GEALAN, Isothermen, Luftungsfenster auf dem Prufstand, *Praxishandbuch Nr.2 -* Anwendugstechnik,

Herausgeber GEALAN, Montage, Luftungsfenster auf dem Prufstand, *Praxishandbuch Nr.3 -* Anwendugstechnik,

Herausgeber GEALAN, Konstruktionen, Luftungsfenster auf dem Prufstand, *Praxishandbuch Nr.4 -* Anwendugstechnik,

Herausgeber GEALAN, Konstruktionen, Luftungsfenster auf dem Prufstand, *Praxishandbuch Nr.5 -* Anwendugstechnik,

Herausgeber GEALAN, Statik, Luftungsfenster auf dem Prufstand, *Praxishandbuch Nr.6 -* Anwendugstechnik,

Herausgeber GEALAN, Warmeschutz, Luftungsfenster auf dem Prufstand, *Praxishandbuch Nr.7 -* Anwendugstechnik,

Herausgeber GEALAN, Schallschutz, Luftungsfenster auf dem Prufstand, *Praxishandbuch Nr. 8 -* Anwendugstechnik,

Herausgeber GEALAN, Einbruchschutz, Luftungsfenster auf dem Prufstand, *Praxishandbuch Nr.9 -* Anwendugstechnik,

Tool for Selection of Windows in Dwellings

Svend Svendsen, Professor,
Department of Civil Engineering, Technical University of Denmark;
ss@byg.dtu.dk, www.byg.dtu.dk

Inês P. Santos, Research Assistant,
Department of Civil Engineering, Technical University of Denmark;
isa@byg.dtu.dk, www.byg.dtu.dk

Jacob B. Laustsen, Assistant Professor,
Department of Civil Engineering, Technical University of Denmark;
jbl@byg.dtu.dk, www.byg.dtu.dk

Jesper Kragh, Assistant Professor,
Department of Civil Engineering, Technical University of Denmark;
jek@byg.dtu.dk, www.byg.dtu.dk

KEYWORDS: windows, dwellings, energy performance, indoor climate, economic evaluation

SUMMARY:
The paper presents a new tool to be used by architects and engineers for an optimized selection of windows in dwellings. The tool has been developed using Microsoft Office Excel 2007 and VBA and aims to be user-friendly and flexible, so it can be suitable for different levels of user expertise.
The tool organizes the process of selecting windows in four different stages.
A first stage, in which the user is able to compare the energy performance of different individual windows (varying in configuration, size and component performances) using the concept of net energy gain.
In a second stage, the user may define a combination of windows to be used in a dwelling and calculate their energy use on a seasonal basis, taking into account the utilization factors of the solar gains and heat losses for the heating and cooling seasons respectively, according to (CEN, 2007, prEN ISO 13790).
The main purpose of the third stage is to evaluate the indoor environment of critical rooms of the dwelling in order to verify whether or not the windows solutions selected as having a good energy performance also allow fulfilling the indoor comfort requirements defined in(CEN, 2007, EN 15251). The method used is the simple hourly method defined in (CEN, 2007, prEN ISO 13790). In this stage the indoor temperature and the heating/cooling energy demand are calculated for every hour of the year for each critical room of the dwelling.
The fourth step consists of a simple economic evaluation for the combinations of windows previously selected, based on cost of conserved energy during the dwelling lifetime.
Based on the overview of the stages previously mentioned, the optimum windows solution can be selected for each specific dwelling. In this way, the full potential of optimizing the energy performance of dwellings by optimizing the selection of windows can be used in an easy way.

1. Introduction

The increasing concern about energy related issues, i.e. lack of energy supply security and climate problems, is resulting in a requirement for more and more energy efficient buildings. In Denmark, Be06 is the program used to document that the building design fulfills the energy frame required by the building code. However, with this software, it is not easy to evaluate and compare the performance of different solutions of windows in buildings. Furthermore, with Be06, it is not possible to analyze the quality of the indoor climate and how the windows influence on it. There was, therefore, a need to develop a calculation tool to be used by architects and engineers in the early phase of residential buildings design, in order to select the most appropriate solutions of windows for each particular case, with regard to area, configuration, orientation, solar shading devices and energy performance of the window components. This tool is to be used either when designing new dwellings/flats or when renovating existing ones.

A similar tool, Resfen (Mitchell R. et. al., 2005), had already been developed in the Lawrence Berkeley National Laboratory, also with the purpose of helping designers and constructors during the selection procedure of windows in residential buildings. Based on some input data, such as U-value, g-value and air-leakage rate of the windows and some other information about the building, Resfen is able to calculate, on an hourly basis, the relative energy and economic performances of the windows in comparison to an insulated wall without windows. If the user wants to compare two different solutions of windows, he must perform two independent simulations and compare the final results.

However, Resfen, is not able to perform indoor climate evaluations, which is one of the main differences when compared to the new tool in this paper. The new tool also allows the user to create windows by selecting the desired configuration and components (glazing, frame/sash, transoms, mullions and glazing bars) from pre-defined lists. As a consequence the U-value, g-value and net energy gain of each individual window are automatically calculated. The results are presented in tables, which makes it very easy to compare the performance of different individual windows and of different solutions of windows applied to a house.

2. The method and the calculation program

2.1 Overview

The tool presented in this paper has been developed with the purpose of helping architects and engineers in the process of selecting the optimal windows solution for residential buildings. It can be used during the design phase of new buildings or for the renovation of existing ones.

Built in Microsoft Office Excel 2007 and Visual Basic for Applications (VBA), the tool aims to be user-friendly and based on simple input data. At the same time, it is adapted to different expertise levels: for example the inexperienced user has the option of using pre-defined solutions and default suggestions, while the experienced user can have a very high level of flexibility.

The method/tool organizes the process of selecting windows in four different stages named as *Step1*, *Step 2*, *Step 3* and *Step 4*.

In *Step 1*, the user can evaluate and compare the energy performance of different individual windows based on the knowledge of their configurations, sizes and components (glazings and frames). This first evaluation is based on the concept of the net energy gain defined in (Nielsen T. R. et. al., 2001).

In the second step, picking from the windows previously characterized, different combinations of windows (orientations, windows types, number of windows, tilt angles, shadings from horizon, overhangs, fins and movable solar shading devices) can be defined for a specific dwelling/flat. These combinations of windows may differ regarding the windows components as well as the windows configurations, sizes and orientations depending on the flexibility of each particular design case. The final result of this stage is the energy use of different combinations of windows integrated in the house. The calculation is made on a seasonal basis (winter/summer) taking into account the gain and loss utilization factors for heating and cooling, respectively, according to (CEN, 2007, prEN ISO 13790).

The basis *Step 3* is the simple hourly method defined in (CEN, 2007, prEN ISO 13790). In this stage the indoor temperature and the heating/cooling energy demand are calculated on an hourly basis for each critical room of the dwelling. The main goal of this stage is to verify whether or not the windows solutions selected as having a good energy performance also allow fulfilling the indoor comfort requirements defined in (CEN, 2007, EN 15251).

The *Step 4* consists of an economic evaluation for the combinations of windows previously selected. In this stage, it is possible to calculate the cost of conserved energy when using the selected windows solutions, in comparison to a reference solution.

Based on the overview of the analyses made during the four steps, the user is, at this stage, able to select the windows solutions with the optimal performance in the actual dwelling/flat.

Furthermore, the user is not obligated to follow the four steps. The user may only use *Step 1* to have a very quick idea of the energy performance of different individual windows with regard to configuration, size and components. Or the user may use only *Step 2* in order to perform a seasonal calculation knowing previously the

U-value and g-value of the windows that he wants to use. *Step 3* and *Step 4* are independent from each other but require *Step 2* to be previously performed.

In *Fig.1* a sketch with the overview of the method and calculation program is presented.

Step 1:
Net energy gain of each individual window

Step 2:
Energy use of the windows in the dwelling (seasonal calculation)

Step 3:
Indoor comfort and energy use of the windows in critical rooms (hourly calculation)

Step 4:
Economical evaluation (cost of conserved energy for the windows lifetime)
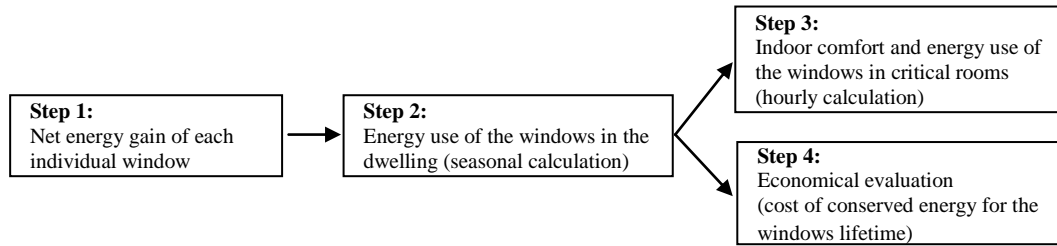
FIG. 2 - Sketch with the overview of the method and calculation program.

2.2 Step 1: Net energy gain of windows

2.2.1 The method

In this first step, the goal is to express, in an easy and simple way, the energy performance of different individual windows varying in configuration, dimension and components (glazing, frame, transoms, mullions and glazing bars). The concept used for this purpose is the net energy gain defined in (Nielsen T. R. et. al., 2001).

According to (Nielsen T. R. et. al., 2001), the net energy gain of a window is the difference between the solar gains and the heat losses that occur through that window during the heating season and it can be calculated for a reference house located in Denmark according to the following equation:

$$E_{ref} = I \cdot g_w - D \cdot U_w = 196.42 \cdot g_w - 90.36 \cdot U_w \ [kWh/m^2] \qquad (1)$$

in which $I = 194.42 kWh/m^2$ is the solar radiation calculated for the reference house during the heating season and $D = 90.36 kKh$ is the degree hour number during the heating season in Denmark. Both I and D are calculated using the Danish Reference Year (Jensen J.M. and Lund H., 1995)). g_w and U_w are, respectively, the total solar energy transmittance and the thermal transmittance of the window.

The net energy gain for the reference house indicates the energy performance of a window for an averaged orientation defined by the distribution of windows in the reference house (North 26%; South: 41% and East/West: 33%).

g_w and U_w are calculated according to equations *(2)* and *(3)*:

$$U_w = \frac{A_g \cdot U_g + A_f \cdot U_f + A_t \cdot U_t + A_m \cdot U_m + A_{gb} \cdot U_{gb} + l_{gf} \cdot \psi_{gf} + l_{gt} \cdot \psi_{gt} + l_{gm} \cdot \psi_{gm} + l_{ggb} \cdot \psi_{ggb}}{A_w} \ [W/m^2 K] \qquad (2)$$

$$g_w = \frac{A_g \cdot g_g}{A_w} \ [-] \qquad (3)$$

where A_w is the area of the window (in m^2), A_g is the area of the glazing (in m^2), A_f is the area of the frame/sash (in m^2), A_t is the area of the transoms (in m^2), A_m is the area of mullions in (m^2), A_{gb} is the area of glazing bars (in m^2), l_{gf} is the perimeter of the glazing along the frame (in m), l_{gt} is the perimeter of the glazing along the transoms (in m), l_{gm} is the perimeter of the glazing along the mullions (in m), l_{ggb} is the perimeter of the glazing along the glazing bars, U_g is the thermal transmittance of the glazing (in $W/m^2 K$), U_f is the thermal transmittance of the frame (in $W/m^2 K$), U_t is the thermal transmittance of the transoms (in $W/m^2 K$), U_m is the thermal transmittance of the mullions (in $W/m^2 K$), U_{gb} is the thermal transmittance of the glazing bars (in $W/m^2 K$), ψ_{gf} is the linear thermal transmittance due to the combined thermal effects of the glazing, spacer and frame/sash (W/mK), ψ_{gt} is the linear thermal transmittance due to the combined thermal effects of the glazing, spacer and transoms (W/mK), ψ_{gm} is the linear thermal transmittance due to the combined thermal effects of the glazing, spacer and mullions (W/mK), ψ_{ggb} is the linear thermal transmittance due to the combined thermal effects of the glazing, spacer and glazing bars (W/mK) and g_g is the total solar energy transmittance. In *Fig. 1* the different components of a window are presented.
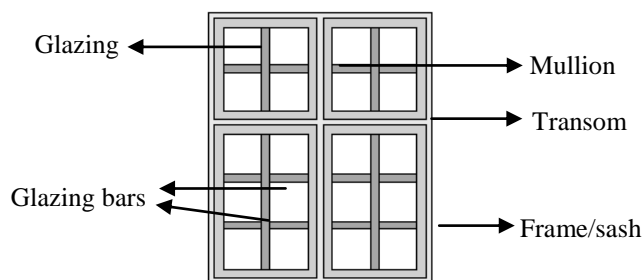
FIG. 2 - Sketch in which the different possible components of a window are represented.

2.2.2 The user interface of the program

In this first step, the user has the opportunity to set up different types of windows varying the configuration, size and components. For each type of window (which consists of a combination of configuration, size and components), the net energy gain for the reference house is calculated as described previously. The result is presented in a table, similar to the one shown in *FIG.2*, which makes it easier to compare the energy performance of different window types in an early design phase.

There are some default defined configurations that the user can pick in order to optimize the process of selecting windows. On the other hand, if the desired configuration is not available the user may create it by inserting its geometric characteristics. This option makes the procedure fast and flexible.

Regarding the windows components (glazing, frame/sash, transoms, mullions and glazing bars), there are pre-defined lists of possible solutions from which the user can create his window. For each type of component the possible solutions are organized in energy classes and a correlation is made between these classes and real products available in the market. Furthermore, the user can add new components to the existing lists by inserting their thermal properties.

Window configuration and size	Window 1	Window 2	Window 3	(…)

Window components			
Glazing	Frame/sash	Mullion	Glazing bar
Class 1	Class 1	Class 1	Class 1
Class 1	Class 2	Class 2	Class 2
Class 2	Class 1	Class 1	Class 1
Class 2	Class 2	Class 2	Class 2
(…)			

Eref	Eref	Eref	(…)
Eref	Eref	Eref	(…)
Eref	Eref	Eref	(…)
Eref	Eref	Eref	(…)
(…)	(…)	(…)	(…)

FIG. 2 - Sketch of the user interface in Step 1.

2.3 Step 2: Energy use due to windows - Seasonal Calculation

2.3.1 The method

Picking from the window types characterized during the previous step, in this stage the user is able to create different combinations of windows that can be integrated in the dwelling. For each combination the energy performance is calculated on a seasonal basis (heating and cooling seasons).

First, the energy use is calculated for each window, *k*, for the heating and cooling seasons. The difference from the previous step is that this energy use is calculated for the window being part of the actual house and not for a reference house. For the heating season, the energy use of each window *k*, is the difference between the heat losses and the solar gains that occur through the window during the heating season, taking into account the

dimensionless utilization factor of the solar gains (equation *(4)*). In the same way, for the cooling season, for each window *k*, the energy use is the difference between the solar gains and the heat losses that occur through the window during the cooling season, taking into account the dimensionless utilization factor of the heat losses (equation *(5)*). The heat losses, solar gains and utilization factors are calculated according to CEN (2007, prEN ISO 13790).

$$E_{HS,k} = \underbrace{U_{w,k} \cdot A_{w,k} \cdot G_{HS}}_{\text{Heat losses}} - \eta_{HS} \cdot \underbrace{F_{sh,k} \cdot A_{sol,k} \cdot I_{sol,HS,k}}_{\text{Solar Gains}} [kWh/m^2] \tag{4}$$

$$E_{CS,k} = \underbrace{F_{sh,k} \cdot A_{sol,k} \cdot I_{sol,CS,k}}_{\text{Solar Gains}} - \eta_{CS} \cdot \underbrace{U_{w,k} \cdot A_{w,k} \cdot G_{CS}}_{\text{Heat losses}} [kWh/m^2] \tag{5}$$

where $U_{w,k}$ is the thermal transmittance of the window *k* (in W/m^2K), $A_{w,k}$ is the area of the window *k* (in m^2), G_{HS} is the number of degree-hours during the heating season in Denmark (in kKh) - calculated for a reference indoor temperature of 20ºC using the Danish Reference Year (Jensen J.M. and Lund H., 1995), G_{CS} is the number of degree-hours during the cooling season in Denmark (in $kK.h$) - calculated for a reference indoor temperature of 26ºC using the Danish Reference Year (Jensen J.M. and Lund H., 1995), $F_{sh,k}$ is the shading reduction factor, for the window *k*, due to external obstacles - calculated according to (CEN, 2007, prEN ISO 13790), it takes into account the shadings from horizon, overhangs, fins and movable solar shading devices, $A_{sol,k}$ is the effective collecting area of the window *k* with a given orientation and tilt angle (in m^2) - calculated according to (CEN, 2007, prEN ISO 13790), $I_{sol,HS,k}$ is the mean energy of the solar irradiation over the heating period per square metre of the window *k*, with a given orientation and tilt angle (in W/m^2) - calculated using the Danish Reference Year (Jensen J.M. and Lund H., 1995), $I_{sol,CS,k}$ is the mean energy of the solar irradiation over the cooling period per square metre of the window *k*, with a given orientation and tilt angle (in W/m^2) - calculated using the Danish Reference Year (Jensen J.M. and Lund H., 1995), η_{HS} is the dimensionless utilization factor for the solar gains during the heating season - determined according to (CEN, 2007, prEN ISO 13790) and η_{CS} is the dimensionless utilization factor for the heat losses during the cooling season - determined according to (CEN, 2007, prEN ISO 13790).

In order to obtain the energy use of each window *k* integrated in the dwelling during the heating and cooling seasons (equations *(4)* and *(5)*), some new information must be provided by the user in this step. In order to calculate the solar gains, information is required regarding shadings from horizon, overhangs, fins and movable solar shading devices, as well as the orientation and tilt angle of the windows. For the calculation of the utilization factors for the solar gains and heat losses, information is required regarding the thermal performance and thermal capacity of the construction, as well as the type of ventilation system.

The overall energy use of the windows of the dwelling, during the heating season, is given by equation *(6)*. A similar calculation is performed for the cooling season in equation *(7)*.

$$E_{HS} = \sum_{k, if E_{HS,k} > 0} \frac{E_{HS,k}}{A_f} [kWh/m^2] \tag{6}$$

$$E_{CS} = \sum_{k, if E_{CS,k} > 0} \frac{E_{CS,k}}{A_f} [kWh/m^2] \tag{7}$$

where E_{HS} is the overall energy use of the windows of the dwelling during the heating season (in kWh/m^2), E_{CS} is the overall energy use of the windows of the dwelling during the cooling season (in kWh/m^2), $E_{HS,k}$ is the energy use of each window *k* during the heating season (in kWh), $E_{CS,k}$ is the energy use of each window *k* during the cooling season (in kWh) and A_f is the heated floor area of the dwelling (in m^2).

Summing E$_{HS}$ and E$_{CS}$, the overall energy use of the windows of the dwelling is obtained for a whole year.

2.3.2 The user interface of the program

In this step, the user can create different combinations of windows for the dwelling and compare their energy performance on a seasonal basis (heating and cooling seasons). For each combination, the user must specify the windows according to the room in which they are placed, their orientation, type, tilt angle and shadings (from horizon, overhangs, fins or movable solar shading devices). The windows types can be selected from the ones previously characterized in *Step 1*, or they can be inserted in terms of thermal transmittance, total solar energy transmittance and area of the window.

The user must also provide some general information about the dwelling, such as floor area, thermal capacity and thermal transmittance of the construction, as well as type of ventilation system. As an alternative some default values are available for typical buildings.

The definition of the rooms would not be required for the calculation procedure in this step. However, this information is asked in order to facilitate the use of *Step 3*, in which the calculation is performed for each room. If *Step 3* is not desired, in *Step 2*, the windows may all be defined in one single room.

The result is the energy use of each combination of windows applied to the dwelling for the heating and cooling seasons. The result for the whole year is also presented. In this way, the user can select from different combinations of windows the ones with optimal energy performance.

A scheme of the user interface for this step is presented in *FIG. 3*.

Combination 1	Combination 2	Combination 3	(…)
Room 1	Room 1	Room 1	(…)
(orientations,windows types, number of windows, tilt angles, shadings from horizon, overhangs, fins and movable solar shading devices)	(orientations,windows types, number of windows, tilt angles, shadings from horizon, overhangs, fins and movable solar shading devices)	(orientations,windows types, number of windows, tilt angles, shadings from horizon, overhangs, fins and movable solar shading devices)	(…)
Room 2	Room 2	Room 2	(…)
(…)	(…)	(…)	(…)
Room 3	Room 3	Room 3	(…)
(…)	(…)	(…)	(…)
(…)	(…)	(…)	(…)

windows energy consumption	heating season	$E_{HS,1}$	$E_{HS,2}$	$E_{HS,3}$	(…)
	cooling season	$E_{CS,1}$	$E_{CS,2}$	$E_{CS,3}$	(…)
	total	$E_{Tot,1}$	$E_{Tot,2}$	$E_{Tot,3}$	(…)

FIG. 3 - Sketch of the user interface in Step 2.

2.4 Step 3: Indoor environment and energy use due to windows - Hourly calculation

2.4.1 The method

From the previous step, the user obtains the energy use of different combinations of windows applied to the dwelling on a seasonal calculation basis. However, a low energy use obtained with a seasonal calculation does not mean that the indoor climate level required by (CEN, 2007, EN 15251) is fulfilled for every hour of the year. In this way, it is important to perform an hourly calculation to check if the combination of windows previously selected, as having a low seasonal energy use, also guarantee a good level of indoor climate. To perform the hourly calculation, the method used is the *simple hourly method* described in (CEN, 2007, prEN ISO 13790).

Using this method, an hourly calculation may be performed for critical rooms of the dwelling in order to evaluate the indoor climate. For each of the critical rooms, the air temperature, θ_{air}, is calculated for every hour and, if the temperature obtained is not inside the range defined by the heating and cooling setpoints, the energy needed for heating or cooling in order to set back the temperature inside the comfort range is calculated. The room annual energy needs for heating and cooling are obtained by summing the energy needs for heating and cooling, respectively, for every hour.

2.4.2 The user interface of the program

In this step, the user may select, from *Step 2*, the critical rooms for which he wants the hourly calculation to be performed. For every hour, the air temperature, θ_{air}, and the energy needs for heating and cooling are calculated. In this way, it is possible to ensure that the windows solutions previously selected, as having a good energy performance, also provide a good level of indoor comfort.

This step can be performed for different rooms and the different combinations of windows previously defined may be compared. If the indoor comfort is not accomplished, the windows solutions may be improved including the definition of better use of the solar shading devices.

If *Step 3* is applied to all the rooms of the dwelling, the annual heating and cooling demands of the whole dwelling may be determined, on an hourly basis, by summing the annual energy demand of each room.

2.5 Step 4: Cost of conserved energy due to windows

2.5.1 The method

After evaluating the energy performance of different combinations of windows and their influence on the indoor environment, in this step, it is possible to perform a simple economic evaluation for the lifetime of windows.

For each combination of windows defined in *Step 2*, the cost of conserved energy, CCE, for the lifetime of the windows, can be calculated according to equation *(8)*:

$$CCE = \frac{I - I_{ref}}{E_{ref} - E} \cdot \frac{d}{1 - (1+d)^{-n}} \ [DKK/kWh] \tag{8}$$

where $(I - I_{ref})$ represents the investment cost, defined as the difference between the cost of the combination of windows and the cost of a reference combination (in Danish kroner), $(E_{ref} - E)$ represents the annual savings, expressed as the difference between the energy use of the reference combination of windows and the energy use of the actual combination, calculated on a seasonal basis (in kWh), n is the economic evaluation period taking into account the lifetime of the windows (usually 30 years) and d is the net discount rate.

The investment cost only includes the initial cost of the windows. No costs for maintenance are included since significant variations may occur depending on each particular situation. The costs are defined for the entire windows.

The reference combination of windows may vary according to the purpose. If the purpose is to replace the windows solution of the house, the reference should be the existing windows solution. If the purpose is the design of a new house, then the reference solution may be the poorer solution available in the market that still fulfils the building code requirements.

The lifetime of the windows is simply assumed to be 30 years, based on the individual lifetime of the glazing units and frames, which are around 20 and 40 years, respectively.

Finally, the cost of conserved energy, in DKK/kWh, may be compared between different possible combinations of windows and with the cost of the energy type used to provide heating and cooling. This should be the procedure to ensure that the investment is profitable.

2.5.2 The user interface of the program

As stated before, in this step, the user is able to evaluate the economic performance of different combinations of windows, previously defined in *Step 2*, in comparison to a reference combination. The economic evaluation is made in terms of cost of conserved energy for the life time of the windows.

The user must specify the reference combination of windows that will be used, costs, lifetime and net discount rate. However some values are suggested as default.

3. Conclusion

Based on the results of all the steps, an overall performance of different combinations of windows regarding energy, indoor climate and economics is provided, for the user to select the optimal solution of windows for the dwelling.

In this way, it is our hope that once the tool is completed, tested and validated, the full potential of optimizing the energy performance of dwellings by optimizing the selection of windows can be used in an easy way.

4. Acknowledgments

5. References

CEN (2007, EN 15251). EN 15251, Indoor environment input for design and assessment of energy performance of buildings addressing indoor air quality, thermal environment, lightning and acoustics.

CEN (2007, prEN ISO 13790). prEN ISO 13790, Energy performance of buildings - Calculation of energy use for space heating and cooling.

Jensen J.M. and Lund H. (1995). Design Reference Year, DRY - a new Danish Reference Year (in Danish: et nyt dansk reference år), Department of Buildings and Energy, Technical University of Denmark, in Danish.

Mitchell R., Huang J., Arasteh D., Huizenga C. and Glendenning S. (2005). RESFEN 5: A PC program for calculating the heating and cooling energy use of windows in residential buildings - Program Description, Lawrence Berkeley National Laboratory, Berkeley, USA.

Nielsen T. R., Duer K. and Svendsen S. (2001). Energy performance of glazings and windows, Solar Energy, Vol. 69 (Suppl.) Nos. 1-6, 137-143.

Svendsen S., Kragh J. and Laustsen J. B. (2005). Energy performance of windows based on net energy gain, 7th Symposium on building physics in the Nordic countries, Reykjavik.

Characterization and performance evaluation of solar shading devices

Inês P. Santos, Research Assistant,
Department of Civil Engineering, Technical University of Denmark;
isa@byg.dtu.dk, www.byg.dtu.dk

Jacob B. Laustsen, Assistant Professor,
Department of Civil Engineering, Technical University of Denmark;
jbl@byg.dtu.dk, www.byg.dtu.dk

Svend Svendsen, Professor,
Department of Civil Engineering, Technical University of Denmark;
ss@byg.dtu.dk, www.byg.dtu.dk

KEYWORDS: *solar shading devices, energy performance, office buildings, WIS, BuildingCalc/LightCalc*

SUMMARY:
In the decision process of office building design, it is important to take the effect of solar shading devices into account as they have a large influence on the indoor climate and energy consumption.
This paper describes a user-friendly method, based on the use of the programs WIS and BuildingCalc/LightCalc, of how to evaluate the performance of different solar shading devices during an early design phase of a building. The window systems combining glazing and shading devices are characterized in WIS giving the transmittance and reflectance as functions of the solar profile angle. BuildingCalc/LightCalc allows defining a simple model of the building in which the windows systems characterized in WIS may be integrated. Heating, cooling, ventilation, lighting and solar shading may be dynamically controlled and the energy and daylight performances of the building, as well as the indoor thermal climate, may be evaluated.
A case study of a landscaped office building in which different solar shading devices are tested for two different cities (Copenhagen and Lisbon) is presented. Examples and suggestions of how to overcome the lack of information available about thermal and optical properties of solar shading devices are included in the paper.

1. Introduction

Energy savings are essential for the general long term solution of the problems with use of energy from fossil fuels. In buildings, to maintain a good indoor environment, energy is used for heating, cooling, ventilation and electrical lighting. If correctly selected and used, solar shading devices may decrease the overheating and cooling demand of buildings significantly without largely increasing the electrical lighting demand. As solar shading devices influence the appearance of the building façade and they have a large impact on the energy demand, it is important that they are included in the early design phase of buildings. In this way, methods to characterize the properties of shading devices and simple calculation tools to determine the effect on indoor climate and energy demand are required.

However, there is often neither sufficient optical data available nor calculation tools that can determine the optimal use of solar shadings and their effect on indoor climate in a satisfactory way. Therefore, there was a need for developing a new calculation program that can simulate the performance of solar shading devices, used in a building, in a realistic way, taking the variation of the optical properties over the day and year into account.

In this paper a simple and user-friendly method of how to evaluate the energy and daylight performance of solar shading devices in buildings in an early design phase is illustrated. The method is based on the use of two simulation tools: WIS and the recently developed program, LightCalc, which is an extension of BuildingCalc. A case study of a landscaped office building in which different solar shading devices are applied is presented and two different locations are studied: Copenhagen and Lisbon. Also some suggestions of how to overcome the lack of information characterizing the solar shading devices available on the market are included in the paper.

2. Solar shading devices

There are many different types of solar shading devices available on the market. When designing a building, besides the aesthetical component also the energy performance and indoor comfort including temperature and daylight must be taken into account.

The solar shading devices should be as flexible as possible so they can adapt to the outdoor conditions. According to their position on the window, they may be categorized in internal, interpane and external (Wall M. and Bülow-Hübe H., 2001 and 2003). The external solar shading devices are the most efficient in reducing the cooling loads. As they are placed outside they reflect the solar rays before they enter the room. Furthermore, the heat they absorb is dissipated to the outside air by radiation and convection. The solar control glasses are not included in the groups referred before but also constitute a type of solar shading device. They are integrated in the window, replacing the panes.

Different types of internal, interpane and external roller blinds and venetian blinds were studied. Also external glass lamellas devices and solar control glasses were investigated. Some of the results are presented in this paper.

3. Method to evaluate the performance of different solar shading devices: WIS and BuildingCalc/LightCalc

To evaluate the performance of different solar shading devices two softwares were used: WIS (TNO, 2004) and BuildingCalc/LightCalc (BYG.DTU, 2007).

Traditionally, the performance of solar shading devices has been described by a simple fixed shading factor defined as the fraction of transmitted solar energy through a standard glazing including the shading device compared to the transmitted solar energy through a standard glazing alone. This measure can be useful for comparison of different solar shading devices, but it is not sufficient when evaluating their performance in a specific building, since the performance depends on the actual glazing and on the position of the sun.

In order to take the varying performance of solar shading devices into consideration, the optical properties, transmittance and reflectance of the window system, consisting of the solar shading device and the actual glazing, must be given for specific positions of the sun. This can be done in the program WIS (TNO, 2004), in which is possible to calculate the thermal and optical properties of window systems combining solar shading devices with glazings available on the market. The properties of the window systems are calculated as a function of the solar profile angle which is defined as the incidence angle projected into the vertical plane normal to the window.

In most existing building simulation tools, the dynamic impact of solar shading devices on indoor climate and the energy demand are not taken into account in a satisfactory way. Therefore, with the purpose of increasing the accuracy of simulations, the calculation tool LightCalc was developed and integrated in the existing program BuildingCalc. With BuildingCalc/LightCalc, it is possible to evaluate the energy and daylight performance of buildings in which the window systems defined in WIS are applied. BuildingCalc/LightCalc simulates the performance of solar shading devices used in a building in a realistic way taking the variation of the optical properties over the day and year into account. It is possible to set different systems: heating, cooling, ventilation, venting and variable solar shading. The systems are controlled by different settings which can be specified for different periods.

The solar shading devices may be automatically controlled according to the indoor temperature. If at the same time the indoor daylight is not enough to accomplish the standard requirements, electrical lighting is switched on and its energy demand is calculated. BuildingCalc/LightCalc is described in detail in (Hviid C. A. et. al., 2008).

4. Case study - Landscaped office building

The test room is a storey of a landscaped office building located first in Copenhagen (North Europe) and then in Lisbon (South Europe).

The inner dimensions of the room are 20m width, 10m depth and 3.3m height (*Fig. 1*).
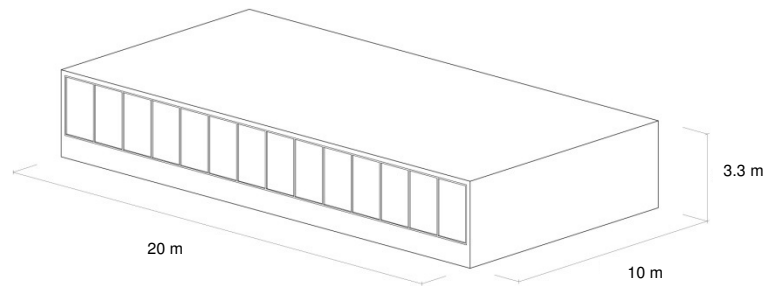
FIG. 1 - Model of the landscaped office building used in the calculations in BuildingCalc/LightCalc.

The window area is 44.7m^2 and it is facing south. The reference glazing is a triple pane with a U-value of 0.68W/m^{2}K, g-value of 0.49 and visual transmittance of 0.68. The frame profiles have a U-value of 0.73W/m^{2}K. The overall UA-value of the building envelope is 15.46W/K for Copenhagen (this value takes into account the sum of transmission losses through the elements facing outside excluding the window). For the building in Lisbon less restrictive thermal solutions were selected because of the warmer climate and the UA-value is 61.85W/K. The heat capacity of the building was assumed to be middle light and also the heat capacity of the furniture was taken into account.

The systems in the building were defined by specifying the settings for heating, cooling, ventilation, lighting and solar shading for different periods (winter / summer / working hours / non-working hours). Two different scenarios were studied: no mechanical cooling available (when there is need for cooling, the cooling systems are activated in the following order: shading and venting); mechanical cooling available (when the previous solutions are not sufficient to set the required level of indoor comfort, the mechanical cooling is activated). The first scenario is the more environmental friendly, however, in most cases this solution is not enough to achieve the indoor comfort level required, especially regarding South European countries like Portugal.

The office is equipped with district heating and cooling. There is a heat exchanger (with an efficiency of 0.85) incorporated with the heating system. The heating system and the mechanical cooling (when available) are only active during working hours. The heating setpoint is 20ºC while the cooling setpoint is 22ºC (in this way the cooling process will start before the indoor temperature reaches 26ºC which is a measure of discomfort (CEN, 2007, EN 15251).

Only during working hours mechanical ventilation is active with a constant air change rate of 0.9h^{-1} (minimum required in (CEN, 2007, EN 15251)). Venting is set only during non-working hours (in Lisbon during all the year and in Copenhagen only outside the coldest months).

The internal loads due to people and equipment were also taken into account (2250W considering 15 working places).

The artificial lighting level is automatically controlled during the working hours in order to keep a general indoor lighting level of 200lux and a level of 500lux at working areas.

5. Energy Performance and indoor comfort evaluation

5.1 Requirements and expected results

To be in accordance with the (Danish building regulations, 2005) the office room should have a total energy demand for heating, cooling, and lighting lower than 78kW/m^2. However, a much lower energy demand should be expected due the nowadays need to save energy. (The hot water and the ventilation (assumed to be constant during the working hours) are excluded from this calculation since they are not influenced by the shading devices).

In Portugal, as a complement to the requirement for total energy demand for heating, cooling and lighting (estimated as 104kWh/m^2, according to the Portuguese building code (RCCTE, 2006), there are also limits for the different types of energy needed in a building: for this office room, the limit for heating is 52kWh/m^2, while for cooling it is 32kWh/m^2.

Regarding indoor comfort, it was assumed that the landscaped office building should fulfil category II of the indoor environment standard (CEN, 2007, EN 15251): this means less than 108 working hours per year above 26° and a PPD index (predicted percentage of dissatisfied) lower than 10%.

5.2 Results and discussion

In *Table. 1* and *Table. 2*, the performance of the office building is presented for the different solutions of solar shading devices in combination with the reference glazing for both locations: Copenhagen and Lisbon. The results painted as grey are the ones that do not fulfil the standards (For the solar control glazing, the outer pane of the reference glazing is replaced by a solar control glass).

Table 1 and *Table 2* are organized in three distinct groups of columns:

> *System properties* - where the performance of the different solar shading devices in combination with the reference glazing is presented (U-value: thermal transmittance, g-value: total solar energy transmittance and τ_V: visual transmittance of the reference glazing. These values were obtained in WIS and refer to the solar shading devices completely activated: venetian blinds slats and glass lamellas tilted 90 degrees from the horizontal position and roller blinds pulled down).

> *Without mechanical cooling* - the values presented in these columns were calculated in BuildingCalc/LightCalc. They represent the performance of the landscaped office room (previously described) when different solutions for solar shading devices are applied on its façade. No mechanical cooling was set. The performance of the office room with the different solar shading devices is presented in terms of energy demand for heating and total energy demand, hours of overheating and PPD index. To calculate the total energy demand, the demand is multiplied by the factor 2.5 because it is provided by electricity. The same does not happen with the cooling demand since it is assumed to be provided by district heating (Danish building regulations, 2005).

> *With mechanical cooling* - these columns also refer to the performance of the office building with the different solutions for the solar shading devices. In this case mechanical cooling was applied to eliminate completely the hours of overheating (as 22°C is the setpoint defined for cooling, no hours above this temperature will be registered).

The results for the reference glazing for the office room in Copenhagen show that the total number of working hours with overheating is 260 per year which is higher than the requirement, 108. However, using mechanical cooling (air-conditioning system), the indoor comfort may be achieved with a total energy demand of 31kWh/m^2.year. With most types of solar shading devices the indoor comfort may be achieved even without the use of mechanical cooling. However, if better indoor comfort level is desired, mechanical cooling may be used and the total energy demand may be reduced by 50% (for the case of the external venetian blind) when compared to the reference glazing.

For Lisbon the scenario is different. For the reference glazing, the total number of working hours with overheating is 1009 per year, which is extremely high. On the other hand, when using mechanical cooling, the cooling demand is 61kWh/m^2 year which is twice the requirement, 32kWh/m^2 year. In this way, this solution is not possible for Lisbon. Results for the different solutions of solar shading devices show that most of them are not able to allow the required indoor comfort without the use of mechanical cooling. And even with mechanical cooling some of them are not viable solutions since the cooling demand is higher than the limit (32kWh/m^2 year). With the use of mechanical cooling the optimal analyzed solution regarding energy consumption is the external venetian blind, which reduces in more than 50% the total energy demand of the office room, when compared to the reference glazing.

6. Some tips on how to overcome the lack of data available for solar shading devices

As it was stated before there is a lack of information about the properties of the solar shading devices available on the market. Often the shadings properties that are required in WIS, to characterize a shading device are not given by the manufacturers. For instance, some of the WIS inputs are the thermal conductivity (λ), outdoor and indoor

TABLE. 1 - Energy and indoor comfort performance of the landscaped office room in Copenhagen for the reference glazing and for the combination of the reference glazing with the different solar shading devices.

ID	Position/Type (Product name)	system properties			without mechanical cooling					with mechanical cooling				
		U-value [W/m²K]	g-value [-]	τv [-]	heating [kWh/m²]	lighting [kWh/m²]	total [kWh/m²]	T>26°C [h]	PPD [%]	heating [kWh/m²]	cooling [kWh/m²]	lighting [kWh/m²]	total [kWh/m²]	PPD [%]
REF	Reference Glazing	0.68	0.49	0.68	0.6	3.2	8.6	260	12	0.6	22.6	3.2	31.2	7
A	Internal Roller Blinds *Verosol SilverScreen white ED01 HT*	0.51	0.25	0.05	0.4	7.2	18.3	101	9	0.4	12.5	6.7	29.6	8
B	Interpane Roller Blinds *Verosol SilverScreen white ED01 HT*	0.70	0.10	0.05	0.8	6.6	17.4	2	8	0.8	5.4	6.4	22.2	8
C	External Roller Blinds *Verosol SilverScreen white ED01 HT*	0.62	0.04	0.01	0.8	6.3	16.6	0	8	0.8	3.2	6.2	19.5	8
D	Internal Venetian Blinds *Luxaflex venetian blind High Mirror*	0.58	0.23	0.00	0.5	4.5	11.7	214	12	0.5	19.8	4.3	31.0	7
E	Interpane Venetian Blinds *Luxaflex venetian blind High Mirror*	0.57	0.07	0.00	0.5	4.3	11.3	89	9	0.5	11.4	4.2	22.3	8
F	External Venetian Blinds *Aluminium lamellas_60mm*	0.62	0.01	0.00	0.7	4.1	11.0	0	8	0.7	4.0	4.1	14.9	8
G	External Glass Lamellas *SGG_Antelio Silver_500mm*	0.63	0.28	0.20	0.8	4.1	11.1	74	9	0.9	9.1	4.0	20.1	8
H	Solar Control Glazings *SSG Reflectasol Green*	0.96	0.17	0.21	3.8	5.7	17.9	0	9	3.8	4.0	5.6	21.9	9

TABLE. 2 - Energy and indoor comfort performance of the landscaped office room in Lisbon for the reference glazing and for the combination of the reference glazing with the different solar shading devices.

ID	Position/Type (Product name)	system properties			without mechanical cooling					with mechanical cooling				
		U-value [W/m²K]	g-value [-]	τv [-]	heating [kWh/m²]	lighting [kWh/m²]	total [kWh/m²]	T>26°C [h]	PPD [%]	heating [kWh/m²]	cooling [kWh/m²]	lighting [kWh/m²]	total [kWh/m²]	PPD [%]
REF	Reference Glazing	0.68	0.49	0.68	0.0	1.5	3.8	1009	28	0.0	61.3	1.5	65.1	5
A	Internal Roller Blinds *Verosol SilverScreen white ED01 HT*	0.51	0.25	0.05	0.0	9.5	23.8	451	14	0.0	36.5	8.4	57.6	6
B	Interpane Roller Blinds *Verosol SilverScreen white ED01 HT*	0.70	0.10	0.05	0.0	8.8	22.1	168	9	0.0	20.5	8.0	40.6	6
C	External Roller Blinds *Verosol SilverScreen white ED01 HT*	0.62	0.04	0.01	0.1	8.2	20.5	108	8	0.1	14.6	7.6	33.8	6
D	Internal Venetian Blinds *Luxaflex venetian blind High Mirror*	0.58	0.23	0.00	0.0	4.4	11.1	763	22	0.0	51.6	3.9	61.3	5
E	Interpane Venetian Blinds *Luxaflex venetian blind High Mirror*	0.57	0.07	0.00	0.0	4.2	10.6	431	14	0.0	35.1	3.7	44.4	6
F	External Venetian Blinds *Aluminium lamellas_60mm*	0.62	0.01	0.00	0.0	3.9	9.7	136	9	0.0	17.4	3.6	26.4	6
G	External Glass Lamellas *SGG_Antelio Silver_500mm*	0.63	0.28	0.20	0.0	3.6	8.9	392	13	0.0	31.2	3.2	39.3	6
H	Solar Control Glazings *SSG Reflectasol Green*	0.96	0.27	0.21	0.3	3.8	9.8	159	10	0.3	17.3	3.8	27.1	7

IR emissivities ($IR\varepsilon_{out}$ and $IR\varepsilon_{ind}$) and IR transmissivity (IR transm.) of the material that composes the shading device and usually manufacturers do not have this information available. Regarding optical properties, the preferred input for WIS is spectral data but most manufacturers only give simplified information such as the solar transmittance (τ_S), solar reflectance (ρ_S), light transmittance (τ_V) and light reflectance (ρ_V). These values are also accepted in WIS, though they represent integrated data and include direct and diffuse components (which should be set separately in WIS).

In *Table. 3* some tips are suggested on how to input new solar shadings systems in WIS when the complete technical information is not available (the tips are organized according to the different WIS input fields: geometry, thermal properties and optical properties).

TABLE. 3 - Tips on how to use simplified data from manufacturers.

WIS input field	Properties to be defined	Tips
Geometry	*Roller blinds* (thickness) *Slat shading device* (thickness, slat chord width, crown height, slat pitch)	The shading system geometry must be given by the manufacturer.
Thermal properties	Material conductivity	*Roller blinds* (assume 0.2W/mK for ordinary fabrics) *Venetian blinds* (assume 150W/mK for aluminium slats)
	Material IR emissivity (outdoor/indoor)	Assume 0.5 for metallic surfaces and 0.8 for non-metallic surfaces*.
	Material IR transmissivity	Assume that it is zero.
Optical properties	*Roller blinds* Integrated data (solar, visual and UV) for outdoor and indoor transmittance and reflectance for different angles of incidence - the values must be separated into direct and diffuse components	*Roller Blinds* Assume that the optical properties are equal for the different angles of incidence. However, assume that for 90º or -90º angles of incidence there is only reflectance and no transmittance. Assume that all of the transmittance is direct and that all of the reflectance is diffuse (Assuming that the transmittance is direct is valid for the normal angle of incidence. For different angles of incidence the shape of holes has an influence on the direct and diffuse components of the transmittance through the fabrics. Through thick and long holes (tunnel shape) the diffuse component is higher while through wide and short holes the direct component is higher. More studies should be done regarding this subject). Assume that the optical properties are equal for the outside and inside surfaces. If no information about the UV transmittance (τ_{UV}) and UV reflectance (ρ_{UV}) is given by the manufacturer assume that they are equal to the solar transmittance (τ_S) and solar reflectance (ρ_S)*.
	Venetian blinds Integrated data (solar, visual and UV) for transmittance and for outdoor and indoor reflectance for normal angle of incidence - the values must be separated into direct and diffuse components	*Venetian Blinds* Assume that all of the transmittance is direct and that all of the reflectance is diffuse. (see comments above for the same assumption for the roller blinds). Assume that the optical properties are equal for the outside and inside surfaces. If no information about the UV transmittance (τ_{UV}) and UV reflectance (ρ_{UV}) is given by the manufacturer assume that they are equal to the solar transmittance (τ_S) and solar reflectance (ρ_S)*.

* These suggestions are in accordance with typical solar shading devices available in the *WIS* database (TNO (2004)).

TABLE. 4 - Comparison of the complete and simplified data of the solar shading devices.

ID	Position/Type (Product name)	thermal properties					optical properties			
		thickness [mm]	λ [W/mK]	IRε$_{out}$ [-]	IRε$_{ind}$ [-]	IRtransm* [-]	τ$_S$ [-]	ρ$_S$ [-]	τ$_V$ [-]	ρ$_V$ [-]
A	**Internal Roller Blinds**									
	Verosol SilverScreen black EB01 HT	0.50	0.15	0.160	0.810	0.000	0.05	0.75	0.05	0.74
	SIMPLIFIED_Verosol SilverScreen black EB01 HT	0.50	0.20	0.500	0.800	0.000	0.05	0.75	0.05	0.74
C	**External Roller Blinds**									
	Verosol SilverScreen black EB01 HT	0.50	0.15	0.160	0.810	0.000	0.05	0.75	0.05	0.74
	SIMPLIFIED_Verosol SilverScreen black EB01 HT	0.50	0.20	0.500	0.800	0.000	0.05	0.75	0.05	0.74
D	**Internal Venetian Blinds**									
	Luxaflex venetian blind High Mirror 4078	0.22	100.00	0.710	0.680	0.000	0.00	0.83	0.00	0.83
	SIMPLIFIED_Luxaflex venetian blind High Mirror	0.22	150.00	0.800	0.800	0.000	0.00	0.83	0.00	0.83

*IR transm= IR transmissivity

TABLE. 5 - Comparison of results obtained with complete and simplified data. Landscaped office building in Copenhagen.

ID	Position/Type (Product name)	system properties			without mechanical cooling					with mechanical cooling				
		U-value [W/m²K]	g-value [-]	τ$_V$ [-]	heating [kWh/m²]	lighting [kWh/m²]	total [kWh/m²]	T>26°C [h]	PPD [%]	heating [kWh/m²]	cooling [kWh/m²]	lighting [kWh/m²]	total [kWh/m²]	PPD [%]
REF	Reference Glazing	0.68	0.49	0.68	0.6	3.2	8.6	260	12	0.6	22.6	3.2	31.2	7
A	**Internal Roller Blinds**													
	Verosol SilverScreen black EB01 HT	0.51	0.25	0.04	0.4	7.3	18.6	101	9	0.4	12.4	6.8	29.8	8
	SIMPLIFIED_Verosol SilverScreen black EB01 HT	0.57	0.27	0.04	0.5	6.8	17.5	112	9	0.5	13.2	6.4	29.7	8
C	**External Roller Blinds**													
	Verosol SilverScreen black EB01 HT	0.62	0.03	0.03	0.8	6.3	16.6	0	8	0.8	3.0	6.2	19.2	8
	SIMPLIFIED_Verosol SilverScreen black EB01 HT	0.62	0.03	0.04	0.8	6.0	15.8	0	8	0.8	3.0	5.9	18.4	8
D	**Internal Venetian Blinds**													
	Luxaflex venetian blind High Mirror 4078	0.58	0.23	0.00	0.5	4.5	11.7	214	12	0.5	19.8	4.3	31.0	7
	SIMPLIFIED_Luxaflex venetian blind High Mirror 4078	0.59	0.25	0.00	0.5	4.4	11.6	173	11	0.5	17.6	4.2	28.7	7

For a better understanding of *Table.5* see the explanation of *Table.1* and *Table.2* in section 5.2.

Simulations for some solar shading devices studied before were performed but using the data usually given by the manufacturers and doing the assumptions proposed. (For the simulations, the solar shading devices were integrated in the landscaped office building in Copenhagen)

The purpose was to compare the results between the use of complete and simplified data and analyze the influence of the proposed simplifications and assumptions on the final performance of the office room. The goal was also to demonstrate whether or not results closer to reality can be obtained when using simplified data.

For a better understanding of the different results when using simplified and complete data, the complete data (from WIS) and simplified data (from manufacturer and assumptions) for the analyzed solar shading devices are presented in *Table. 4*. The spectral optical properties are not presented but they can be consulted in the WIS database (TNO, 2004).

In *Table. 5*, the results of the performance of the landscaped office room in Copenhagen obtained when using complete and simplified data are presented. When simplified data is used the name of the solar shading system is preceded by the word "SIMPLIFIED". The similarity obtained between results for complete and simplified data shows that the used simplified data is valid. However, only few cases were studied and more research should be done in this field.

7. Conclusions

The combination of WIS and BuildingCalc/LightCalc is a very promising tool when evaluating and comparing the performance of buildings with different types of solar shading devices in an early design phase. From the simple model of the room and the thermal/optical properties of shadings devices, it is possible to calculate on an hourly basis the yearly energy demand for heating and cooling as well as some indoor comfort parameters. The program takes the dynamic influence of solar shading devices on the energy demand and indoor climate into account, which makes the performance evaluation of the shading device much more realistic when compared to the use of fixed values.

Nowadays there is still a lack of data about the thermal and optical properties of the solar shading devices. Some particular cases studied show that the use of simplified data gives raise to results close to the ones obtained with the complete data. However, only few cases were studied and more research should be done in this field.

8. References

BYG.DTU (2007). BuildingCalc/LightCalc, Building simulation tool, Computer program, Department of Civil Engineering, Technical University of Denmark.

CEN (2007, EN 15251). EN 15251, Indoor environment input for design and assessment of energy performance of buildings addressing indoor air quality, thermal environment, lighting and acoustics.

Danish building regulations (2005). Danish Ministry for Housing and Urban Affairs.

Hviid C. A., Nielsen T. R. and Svendsen S. (2008). Simple tool to evaluate the impact of daylight on building energy consumption, Submitted to Nordic Symposium on Building Physics 2008, Copenhagen, Denmark.

RCCTE (2006). RCCTE - Regulation for the Thermal Performance Characteristics of Buildings, Collection Regulamentos, Vol. 1, Porto Editora, Porto, Portugal (only Portuguese version available).

TNO (2004). Advanced Window Information System, WIS - Window simulation program, TNO Building and Construction Research, Delft, The Netherlands.

Wall M. and Bülow-Hübe H. (2001). Solar Protection in Buildings, Lund University, Sweden.

Wall M. and Bülow-Hübe H. (2003). Solar Protection in Buildings - Part2:2000-2002, Lund University, Sweden.

Solar Shading System Based on Daylight Directing Glass Lamellas

Jacob B. Laustsen, Assistant Research Professor,
Department of Civil Engineering, Technical University of Denmark;
jbl@byg.dtu.dk

Inês D. P. Santos, Assistant Research Professor,
Department of Civil Engineering, Technical University of Denmark;
isa@byg.dtu.dk

Svend Svendsen, Professor,
Department of Civil Engineering, Technical University of Denmark;
ss@byg.dtu.dk

Steen Traberg-Borup, Senior Researcher,
Danish Building Research Institute;
stb@sbi.dk

Kjeld Johnsen, Senior Researcher,
Danish Building Research Institute;
kjj@sbi.dk

SUMMARY:
The overheating problems in office buildings must be solved with efficient solar shadings in order to reduce the energy demand for cooling and ventilation. At the same time the solar shading should not reduce the daylight level in the building on overcast days because it would result in a lower visual comfort level and increased energy consumption for lighting.

The paper describes a new type of solar shading system based on dynamic lamellas made of solar control glass with high reflectance coating which reduces the solar gain on sunny days and at the same time is able to redirect some of the daylight further into the back of the room where it is needed on overcast days. Measurements of the daylight performance were carried out on a full scale model of the solar shading system in SBi's Daylight Laboratory. The results show that the shading system under overcast conditions reduces the daylight factor close to the façade while it is unchanged or even higher in the back of the room. Under sunny sky conditions the daylight level is reduced in the office. Compared to traditional solar shading systems with less transparent or opaque lamellas the proposed solar shading system yields a higher daylight factor improving the distribution and exploitation of daylight in the office and furthermore it gives a less obstructed view out. Calculations show that the new system reduces the energy demand for cooling and ventilation when it is used as a traditional solar shading device and furthermore the energy demand for lighting is reduced when the glass lamellas are rotated for redirecting the daylight further into the room.

1. Introduction

The increasing need for energy savings and good daylight conditions in buildings brings about large challenges when designing facades for future buildings since the façade has significant impact on the energy consumption and the utilization of daylight.

A large part of the energy consumption in buildings with glass facades is used for cooling and ventilation to avoid overheating which occurs as a result of the solar gains through the façade. The most efficient way to reduce the cooling demand is by using efficient solar shading devices. The energy demand for electrical lighting represents another large part of the total energy consumption in typical commercial buildings. This can be reduced by optimizing the utilization of the daylight which is also needed in order comply with the requirements of

a daylight factor of 2 % on the working place. In buildings with large room depth compared to the window area, the daylight level is normally sufficient or even too high close to the façade but in the back of the room there is often not enough daylight to fulfil the requirements for a satisfactory visual indoor climate.

In many office buildings with glass facades, the solar shading used consists of horizontal fixed lamellas made of opaque materials. These shading systems can reduce the solar gains efficiently but they deteriorate the view out and reduce the daylight level in the building. Thus, there is a need for developing combined systems of flexible solar shading and light directing devices that in addition to reducing the solar gain will ensure a more gradual distribution of the daylight in buildings which will improve the visual indoor climate.

This paper describes a solar shading system based on dynamic glass lamellas with high reflectance. Besides acting as typical solar shading systems reducing the solar gains and consequently the cooling demand, they may at the same time allow better indoor daylight levels than the common shading systems thanks to the transparent properties of glass. During overcast days if they are correctly tilted they may slightly increase the indoor daylight by redirecting the light form the sky up into the ceiling and further into the back of the room.

2. Description of the system

In order to meet the combined needs for reducing the energy demand for cooling by controlling the solar gain and also obtain a better distribution of the daylight in buildings a new solar shading system was developed and a full scale prototype built up.

The solar shading system consists of horizontal glass lamellas with high reflective coating. The lamellas are 50 cm wide and the distance between the lamellas is 50 cm. The large dimensions are chosen to optimize the view out. The lamellas are supported by metal profiles. The lamellas can be rotated in different positions depending on the weather and the requirements for solar shading and improved daylight conditions. On sunny days when the solar gain must be reduced the lamellas are rotated into vertical position acting as an extra layer of solar control glass that reduces the solar energy gain but still allows a good view out. The design of the glass lamella system fitted on a typical glass façade is shown in *FIG. 1* and FIG. 2

Preliminary daylight simulations performed in IESve/Radiance (*IESve(2003)*) show that the maximum effect of redirecting the daylight on overcast days is obtained with a slat angle of 30° with the reflective surface upwards. In this position the light from the sky is reflected into the room, up in the ceiling and further back in the room where the light is most needed (Skotte, T. (2007)). See *FIG. 3*. The glass lamellas are positioned 40 – 70 cm from the façade to provide space for maintenance and window cleaning.
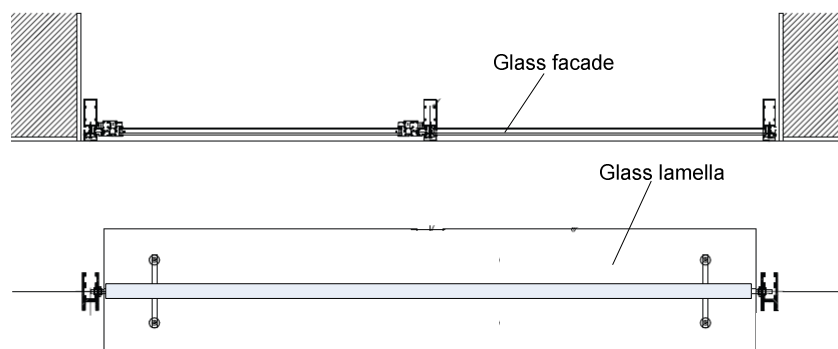
FIG. 2 Vertical cross section of the shading system
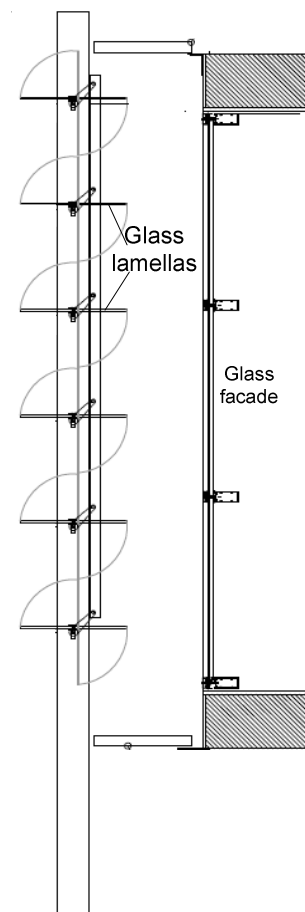
FIG. 1: Horizontal cross section of the shading system.
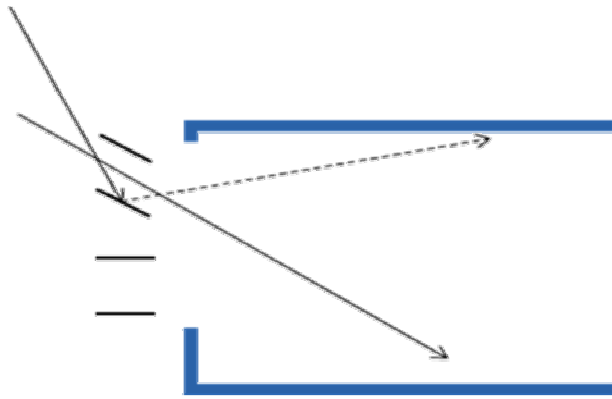
FIG. 3: Principle of the light directing lamellas.

The properties of the solar control glass lamellas are shown in ***Fejl! Et bogmærke kan ikke henvise til sig selv.***.

TABLE. 1: Properties of the glass lamellas.

thickness	Solar energy transmitance	Light transmittance	Solar energy reflectance	Light reflectance
8 mm	0.63	0.65	0.25	0.31

3. Measurements

3.1 Description test facilities

Daylight measurements on the glass lamella system were performed in SBi's Daylight Laboratory situated in Hørsholm (latitude 55.86°N, degree of longitude 12.49°Ø). The daylight lab has two experimental rooms positioned approximately 13 meters above terrain with the façade facing 7.5 degree east of south.

FIG. 4. The Daylight Laboratory at SBi

The interior dimensions of the two experimental rooms are 3.5m wide × 6.0m deep × 3.0m high. The two rooms which are identical are named the test room and the reference room. The space in front of the experimental rooms is a field of grass which is essentially empty from obstructions, apart from the distant row of trees towards south and the group of trees towards the south-west direction.

Both rooms have a glass façade divided in 9 sections. During the measurement some of the sections were blocked so the effective window size was reduced to the middle and upper section corresponding to the size of the glass lamellas. The glass lamellas were mounted outside the facade of the test room, see FIG. 6. The length of the lamellas was 2.95 m. The glazings in the façade of the experimental rooms are sealed low-e double glazing units with low emittance coating and argon filling and U-value of 1.1 1 W/m^{2}K, g-value of 0.56 and a light transmittance of 0.72. The two rooms are designed like traditional cell office rooms but furnished with only two tables. The reflectances of the inner surfaces in the rooms are given in TABLE. 2.

TABLE. 2. Reflectance of the inner surfaces in the experimental rooms in the daylight lab.

Surface	Reflectance
Walls	62%
Ceiling	88%
Floor	11%
Tables	80%

The illuminance values were measured in the experimental rooms with lux meters located in different points of the working plane 0.85 m above the floor and in the ceiling as shown in FIG. 5
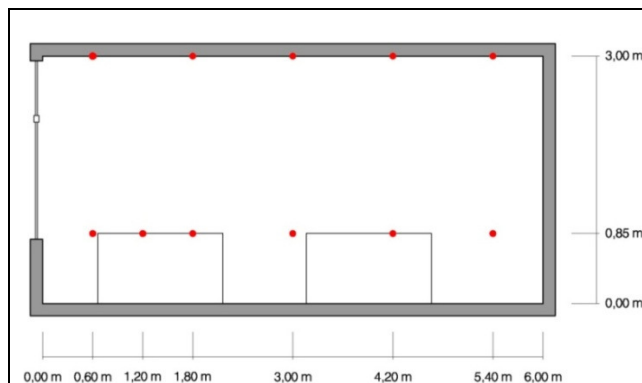
FIG. 5: Cross section of the test room/reference room with location of the measuring points

FIG. 6: Picture of the glass lamella system mounted on the test room façade.

The measurements were performed for four different cases which correspond to different sky conditions and different positions of the glass lamellas as shown in FIG. 7. Case one and two are measured during overcast sky and case three and four are on sunny days with clear sky and direct sun on the façade. For each case measurements of the Test room and Reference room were performed simultaneously so the influence of the lamellas could be assessed.
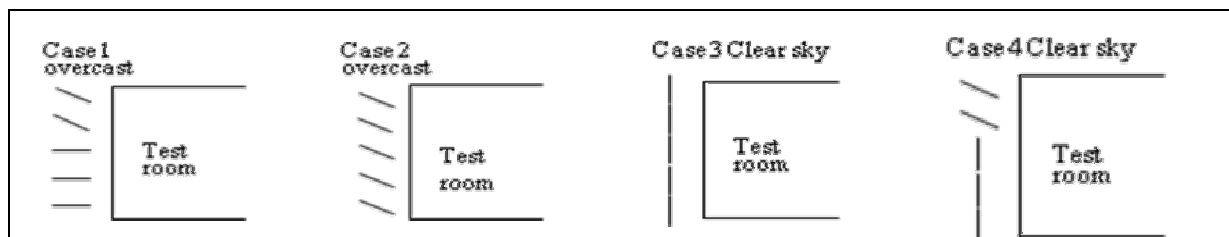
FIG. 7: Sky conditions and position of the glass lamellas in the four cases.

4. Results of daylight measurements

The results of the measurements are presented in the following for cases 1 to 4. Case 1 and 2 are evaluated on basis of the daylight factor which describes the ratio of outside horizontal illuminance under an overcast sky and inside illuminance measured in a specific point. For case 3 and 4 the measurements were performed under sunny sky and therefore the measured illuminances are evaluated directly.

4.1 Case 1, overcast sky

The results of the measurements in case 1 are shown in FIG. 8. It appears that the daylight factor is reduced in the test room with the lamellas compared to the reference room. The reduction is largest close to the facade where the daylight level anyway is abundant and it decreases with the room depth. In the rear most point in the room (5.5m from the facade) where the need for light is highest the daylight factor is equal for both rooms. Thus, the tilted position of the uppermost two lamellas and the horizontal position of the rest of the lamellas result in a small reduction of the total amount of daylight but an improved distribution of the daylight in the room.

The measurements for the ceiling show that the daylight factor increases significant near the façade indicating that the lamellas reflect the daylight up into the ceiling, but the difference decreases gradually in through the room. In the rear most point in the room the daylight factor is highest in the test room (0.9) compared to the reference room (0.8).
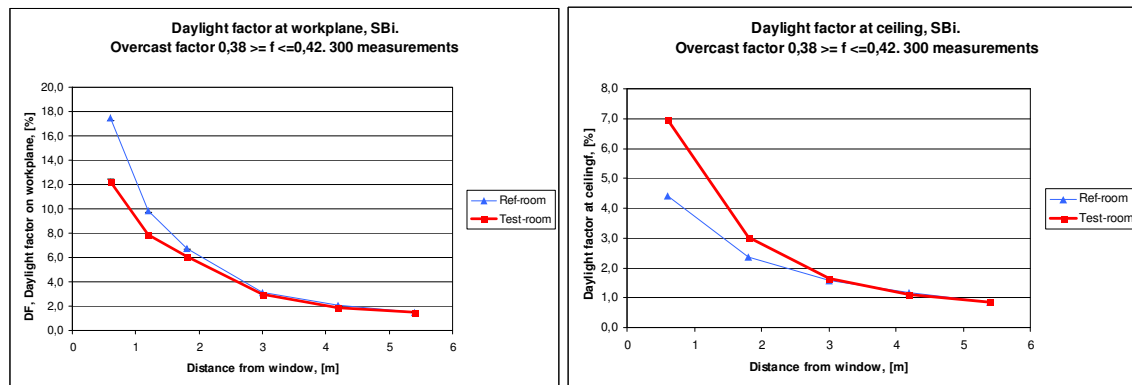
FIG. 8: Case 1. Measured daylight factors for overcast sky. Left : Working plane. Right: Ceiling

4.2 Case 2, overcast sky

The tilted position of all the lamellas in case 2 influences the daylight conditions in the same way as in case 1 as shown in *FIG. 9* but the tendency is less significant. Again the reduction of the daylight factor on the working plane is largest close to the façade and it declines rearwards in the room. This shows that rotating all the glass lamellas 30 degrees towards the façade slightly reduces the daylight factor close to the façade but in the back of the room it is unchanged or actually increased a bit. Hence, the glass lamellas redirect the daylight for the sky resulting in improved daylight distribution and exploitation. The measurements for the ceiling show again that the daylight factor increases significantly near the façade and it is almost unchanged in the back of the room.
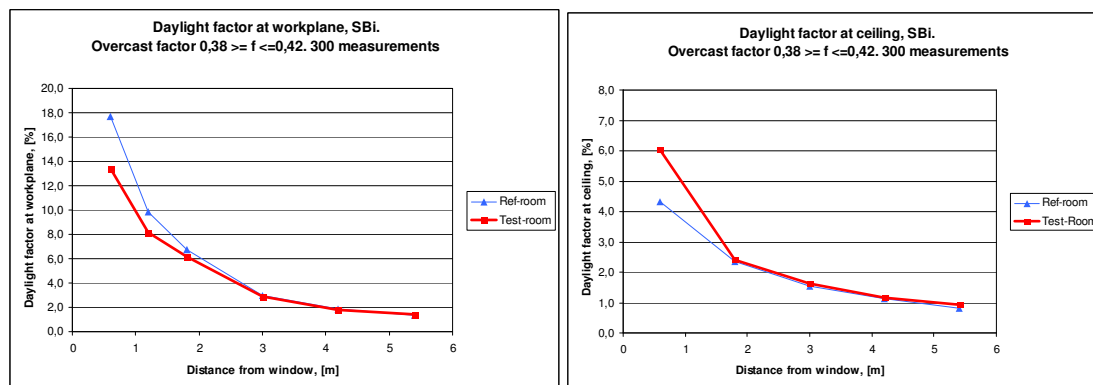
FIG. 9. Case 2. Measured daylight factors for overcast sky. Left: Working plane. Right: Ceiling

4.3 Case 3, Clear sky

In case 3 all the lamellas are in vertical position and because the width of the lamellas and the distance between them are the same they cover the whole façade like an extra layer of solar control glass. The measurements in this case show that the glass lamellas decrease the illuminance levels throughout the room. See

FIG. 10
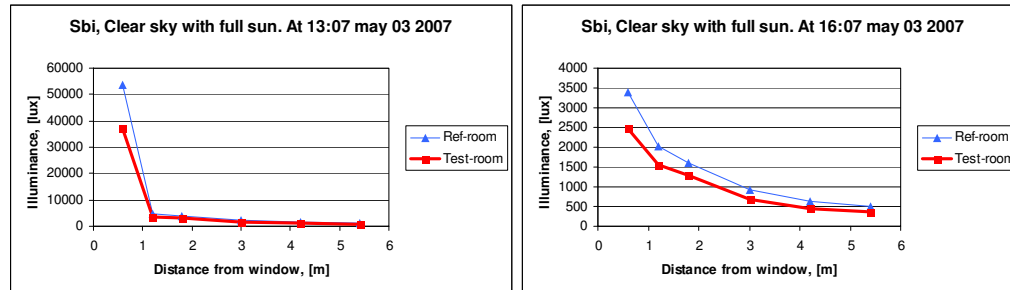
FIG. 10: Case 3. Illuminaces measured on working plane at noon and afternoon.

 The reduction is largest close to the window and it decreases gradually with the distance to the window. This position will be used on sunny days when there is a need for solar shading in the traditional way.

4.4 Case 4, clear sky

In case 4 the two upper most lamellas are rotated in light redirecting position and the rest are vertical. The measurements show that the effect of the lamellas in this case depends on the time of day. In the morning the daylight factor is slightly reduced throughout the room but in the afternoon it is only reduced close to the façade. In longer distance from façade the daylight factor is a bit higher in the test room with the lamellas than in the in reference room because of the two rotated lamellas reflecting some extra light into to room.
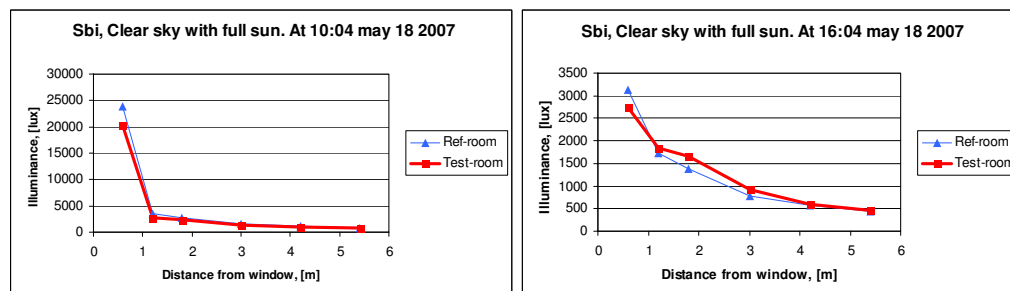
FIG. 11 Case 3. Illuminances measured on working plane at noon and afternoon.

In general the measurements show that the glass lamella system has the expected daylight performance. Compared with the reference room without glass lamellas the daylight factor is under overcast sky reduced close to the façade where the daylight level already is more than sufficient and the reduction is gradually reduced towards the back of the room where the daylight factor is unchanged or even higher with the lamellas. Consequently the light directing glass lamellas provide a better distribution of the daylight in the room resulting in improved visual indoor climate and reduced energy demand for electric lighting compared with traditional non transparent lamella systems. Under sunshine conditions the illuminance level is reduced in the entire room which indicates that the solar gain also will be reduced resulting in energy saving for cooling and ventilation.

4.5 Glare and the effect on the view out

During the measurement period some inconvenient visual effects of the glass lamellas were observed. The high reflectance of the lamellas can cause glare problems when they are rotated upwards in the light directing position. This problem is most significant in direct sun but also in overcast weather the reflected sky luminance can cause vision discomfort. The reflections in the lamellas furthermore reduce the transparency of the lamellas resulting in an obstructed view out as illustrated on

FIG. 12. Therese problems are mainly connected to the lamellas positioned below eye level i.e. 1.8 m above the floor. Therefore the light directing glass lamellas should in some cases only be used in the uppermost part of the façade to avoid glare and obstructed view out. A comprehensive subjective visual evaluation involving the users is needed in the further work of optimizing the design.
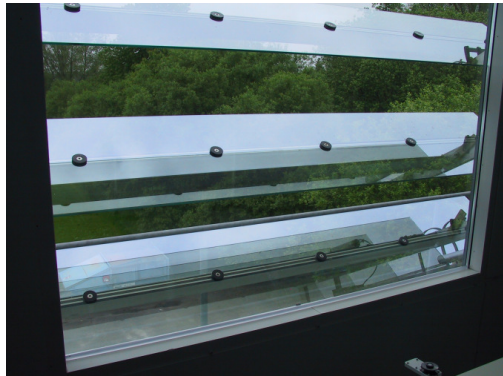
FIG. 12: Reflections in the glass lamellas which can reduce the view out.

5. Calculations

5.1 Energy performance, BuildingCalc

In order to evaluate the impact of the solar shading device on the energy consumption in a building, integrated thermal and lighting simulations were carried out using BuildingCalc/LightCalc (DTU, 2005). The calculations were made on a simple model of a traditional cell office with the dimensions 5m wide × 6.0m deep × 3.0m high with mechanical ventilation and cooling.

The thermal and optical properties of the transparent system consisting of the glazing in the façade in combination with the glass lamellas were determined in WIS (Van Dijk, D., Goulding, J. (1996)). In WIS all the radiation reflected by the shading device is treated as diffuse radiation which is a simplification of reality but it was assessed that the results are reliable. For the same reason WIS cannot handle light redirecting devices correctly which has an impact on the lighting demand. This was compensated for by entering assessed values in LightCalc for the fraction of transmitted light that is redirected (Hviid C. A. et al. (2008)).

The results are given in TABLE. 3

TABLE. 3. Calculated energy consumption for cooling, lighting, mechanical ventilation and heating in an office building for different solar shading devices.

kWh/m^2 year	Total	Cooling	Lighting	Ventilation	Heating
No shading	76	23	23	26	4
Fixed dark opaque lamellas	72	3	41	21	7
Fixed white opaque lamellas	64	4	31	22	7
Dynamic reflective solar control glass lamellas	60	9	24	23	4

The calculations show that traditional fixed non-transparent lamellas reduce the solar gain more efficiently resulting in a lower cooling and ventilation demand than the proposed light directing glass lamellas. On the other hand the glass lamellas reduce the energy demand for lighting resulting in a lower total energy demand. These calculations are only preliminary and must be followed up by more detailed calculations and measurements of the effect of the glass lamella system on the energy demand in a building. Anyway the results indicate that further investigations on the impact of the optical properties of the glass lamellas are needed in order to select a glass type with reflectance and transmittance which will improve the solar shading properties without reducing the daylight properties.

6. Conclusion

A new solar shading system based on flexible glass lamellas with reflective solar control coating was developed and a prototype built up. Daylight measurements in the daylight laboratory at SBi on overcast days showed that the shading device improves the daylight distribution in the building when the glass lamellas are rotated 30° outwards with the reflective surface upwards. The daylight factor is decreased close to the façade and thanks to the daylight redirecting properties of the glass lamellas the daylight factor is unchanged or even higher in the back of the room where daylight is most wanted. Compared to traditional non retractable opaque slat shading devices the new glass lamella system yields a better utilisation of the daylight.

On sunny days, with the lamellas rotated into vertical position, the measurements showed that the illuminance level is reduced throughout the room indicating that also the solar gain is reduced. The impact of the shading system on energy consumption and indoor visual and thermal climate was evaluated in preliminary calculations showing energy savings for both cooling and lighting. Thus, the presented solar shading system is able to reduce the energy demand for cooling and ventilation by controlling the solar gains and still maintaining good daylight conditions and a satisfactory view out. However it is important to take into account the possible glare problems caused by the high reflectance of the glass lamellas. When they are tilted outwards for light redirection the reflections from the sky or sun can be severe resulting in visual discomfort for the users. In some cases the glass lamellas should only be used above 1.8 m from floor level to avoid glare and ensure unobstructed view out.

7. References

Santos, I. D. P. (2007). Performance evaluation of solar shading devices. Master thesis project, BYG-DTU, Technical University of Denmark, Department of Civil Engineering. Kgs Lyngby Denmark.

CEN (2007, EN 15251). EN 15251, Indoor environment input for design and assessment of energy performance of buildings addressing indoor air quality, thermal environment, lightning and acoustics.

Lee, E.S., DiBartolomeo, D.L., Selkowitz, S.E.. Thermal and daylighting performance of an automated Venetian blind and lighting system in a full-scale private office. Energy and Buildings 29 (1998) 47-63

IESve(2003). *IES<virtual environment>, version 5.5*. Integrated Environmental Solutions Ltd., Glasgow, UK, 2003.

Van Dijk, D. and Goulding, J. (1996). WIS reference manual, TNO Building and Conbstruction Research.

TNO (2004). Advanced Window Information System, WIS - Window simulation program, TNO Building and Construction Research, Delft, The Netherlands.

BYG.DTU (2007). BuildingCalc/LightCalc, Building simulation tool, Computer program, Department of Civil Engineering, Technical University of Denmark.

Skotte, T. (2007). Dagslysdirigerende solafskærmende glaslameller. Master thesis project, BYG-DTU, Technical University of Denmark, Department of Civil Engineering. Kgs Lyngby Denmark.

Tzempelikos, A., Athienitis, A. K. The impact of shading design and control on building cooling and lighting demand. Solar Energy 81 (2007) 369–382

Hviid C. A., Nielsen T. R. and Svendsen S. (2008). Simple tool to evaluate the impact of daylight on building energy consumption, Submitted to Nordic Symposium on Building Physics 2008, Copenhagen, Denmark.

Danish building regulations (2008). Danish Enterprise and Construction. Authority. Copenhagen, Denmmark. http://www.ebst.dk/br08.dk

Simple tool to evaluate the impact of daylight on building energy consumption

Christian Anker Hviid, Indutrial Ph.D. student,
Alectia A/S;
crh@alectia.com

Toke Rammer Nielsen, Assoc. prof.,
Depatment of Civil Engineering, Technical University of Denmark;
trn@byg.dtu.dk

Svend Svendsen, Professor,
Department of Civil Engineering, Technical University of Denmark;
ss@byg.dtu.dk

KEYWORDS: Simulation, daylight, validation, radiosity, integration, building design

SUMMARY:
This paper presents a simple building simulation tool for integrated daylight and thermal analysis. The tool is capable of importing the thermal and visual properties for different glazings and shading positions from the Window Information System (WIS) program. Radiosity methodology is used to derive the daylight levels for different sky conditions on an hourly basis. The daylight levels are fed into an existing simple thermal simulation program capable of calculating energy demand and the indoor environment. Straightforward control systems for general and task lighting systems have been implemented together with a shading control strategy that adjusts the shading according to the indoor operative temperature and the profile angle of the sun. The implemented daylight calculation method allows for shades from the window recess and overhang. Comparisons with the ray-tracing program Radiance show that the accuracy of this approach is adequate for predicting the energy implications of photoresponsive lighting control.

1. Introduction

For integrated daylight and thermal simulations several approaches and programs have been developed. One approach which is implemented in the program Adeline (Fraunhofer-Institut für Bauphysik 2006) generates an annual output file for lighting which may be used as an internal load file in a thermal simulation program. However, this method lacks interactivity between daylight, lighting, solar shading and the thermal performance of the building. Another approach is to use Radiance (Ward, G.L. and Shakespeare, R.A. 1998) in combination with a thermal simulation program. This approach has been implemented in ESP-r (Clarke, J. and Janak, M. 1998). Generally lighting simulation packages involve a lengthy learning effort, which restricts their use to expert designers, and they are computationally costly for general architectural and engineering purposes, especially during the initial design stage. In order to reduce the computational burden the daylight coefficient method has been suggested as a third approach (Tregenza,P.R. and Waters, I.M. 1983; Reinhart, C.F. and Herkel, S. 2000).

The tool described in this article encompasses an integrated thermal and lighting simulation approach for evaluating the impact of daylight and dynamic shading device design on energy demand. The amount of input is small yet it provides detailed hourly output of the daylight level, the electrical energy consumption for lighting, heating load, cooling load and indoor operative temperature. An existing simplified thermal simulation tool BuildingCalc (Nielsen, T.R. 2005) and a daylight simulation tool LightCalc (Nielsen, T. 2005) formed the starting point for the work.

2. Calculation procedures

There are several different methods and tools for determining daylight distribution in rooms. Methods vary from simple factor calculations through radiosity methods to complex computer algorithms, such as ray-tracing. In this tool, the radiosity method is employed for internal daylight reflections, while the incident initial light is calculated using a ray-tracing approach. This gives a reasonable balance between accuracy and calculation time.

2.1 External light distribution

External daylight may be divided into direct light from the solar disc, diffuse light due to the scattering properties of the atmosphere, and diffuse light reflected from the ground and surroundings. The diffuse light is modelled using the approach in Robinson and Stone (2006) and summarized here. An upper sky dome for atmospheric light and a lower (inverted) sky dome for ground reflections (one above and one below the horizontal plane) are used to model diffuse light. Each sky vault is divided into 145 patches using a discretization scheme proposed by Tregenza (1987). Each patch subtends a similar solid angle Φ (Sr), which enables every patch to be treated as a point source with insignificant error. The sky vault is divided into seven azimuthal bands of equal angular height ($\sin \gamma_{i,max}$ -$\sin \gamma_{i,min}$), in which the azimuthal range $\Delta\alpha$ increases towards zenith (12°, 12°, 15°, 15°, 20°, 30°, 60°).

$$\Phi_i = \Delta\alpha_i \left(\sin \gamma_{i,max} - \sin \gamma_{i,min} \right) \tag{1}$$

Let L denote the luminance (Lm m^{-2} Sr^{-1}) of the i'th patch, ξ the mean angle of incidence (rad), and σ ($0 \leq \sigma \leq 1$) the visible proportion of the patch, then the illuminance E_{sky} on an external plane due to diffuse light from the sky vault is expressed as:

$$E_{sky} = \sum_{i=1}^{145} \left(L\Phi\sigma\cos\xi \right)_i \tag{2}$$

Let E_n denote the direct normal illuminance and ξ the incidence angle (solar zenith angle), then the illuminance on an external inclined plane due to direct light E_{sun} is expressed (Scharmer, K. and Greif, J. (2000):

$$E_{sun} = E_n \cos\xi \tag{3}$$

Having determined the light sources, the reflecting ground can be represented as a luminous up-side down sky with constant brightness. Given the ground patch luminance L^*, the illuminance due to reflected light E_{ground} is written as:

$$E_{ground} = \sum_{j=i}^{145} \left(L^*\Phi\sigma\cos\xi \right)_j \tag{4}$$

where L^* is expressed as a function of the total horizontal diffuse illuminance E_{sky}, the direct illuminance E_{sun} on a horizontal plane and the mean ground reflectance ρ (albedo):

$$L^* = \frac{\rho}{\pi} \left(E_{sun} + E_{sky} \right) \tag{5}$$

The Perez anisotropic sky model (Perez et al. 1993) is amenable to implementation in a computer program while maintaining good overall performance. The luminance of a sky point L_i is given here:

$$L_i = \frac{lv_i dh}{\sum_{j=1}^{145} \left(lv\Phi\cos\xi \right)_j} \tag{6}$$

where the relative luminance lv is normalized to diffuse horizontal illuminance dh as recommended by Perez et al. (1993). Diffuse horizontal and direct normal illuminances are obtained from measured horizontal and direct normal irradiances respectively by a luminous efficacy η given in Perez et al. (1990).

The visible proportion σ is calculated by establishing a 10x10 grid of each patch and evaluating the visibility of each grid point for all internal surfaces. Thus σ is a function of both distant objects (other buildings, the landscape) and near shades like the window recess and overhang. Reflected light from opposing building façades is not yet treated.

2.2 Internal daylight distribution

The calculation of the internal distribution of light is based on the luminous exitance method. This method is analogous to the radiosity method, in that all the restrictions and assumptions are the same. Internal subsurfaces hit by transmitted direct and diffuse light act as light sources, with the initial exitance *Mo,* if we assume these

surfaces have Lambertian optical characteristics and reflect incident light perfectly diffusively and ignore any specular properties. The methodology and implementation of the daylight distribution algorithms are described in detail by Park (2003).

2.3 Coupling of external and internal light distribution

To establish the initial light exitance *Mo* of a subsurface the amount and the direction of the light and the reflectance of the surface has to be known. Therefore the external and internal light distributions is coupled in a simple ray-tracing approach that assumes the luminance of the sky hemisphere and ground hemisphere patches can be considered as point sources.

2.3.1 Diffuse light

For diffuse sky and ground light penetrating into the room, the exitance for each internal subsurface is calculated using eq. (2) and eq. (4) multiplied by the profile-angle dependent light transmittance τ_θ and the surface reflectance ρ:

$$Mo_i = \rho \left(\sum_{i=1}^{145} \left(L \Phi \sigma \cos \xi \tau_\theta \right)_i + \sum_{j=1}^{145} \left(L^* \Phi \sigma \cos \xi \tau_\theta \right)_j \right) \tag{7}$$

The profile angle θ is defined as the line of elevation projected unto the vertical normal plane of a surface. We may also name it the perpendicular incidence angle on a vertical surface. The profile-angle dependent light transmittance is used because it is calculated directly by the WIS program (van Dijk, D. and Oversloot, H. 2003), see section 2.4. However for clear glazings with isotropic optical properties we use the profile-angle dependent data directly as dependent on incidence angle.

2.3.2 Direct light

For direct light a different approach is applied. It is evident that all direct light transmitted through the glazing hits a subsurface. Subdividing the internal surfaces, however, may result in false prediction of the amount of incoming direct light. Let E_{dir} denote the incident sun light on the window plane obtained by eq. (3), A_g the glazing area, A_j the area of the *j*'th internal subsurface and *m* the total number of internal subsurfaces. If we define a normalization factor $\chi = E_{dir} A_g \tau_\theta \Big/ \sum_{j=1}^{m} E_n A_j \tau_\theta \cos \xi_j$ then the initial exitance *Mo* of the *i*'th subsurface is written:

$$Mo_i = E_n \rho_i \tau_\theta \cos \xi_i \, \chi = E_{dir} A_g \rho_i \tau_\theta \frac{\cos \xi_i}{\displaystyle\sum_{j=i}^{m} A_j \cos \xi_j} \tag{8}$$

When the direct light is transmitted through the glazing, some of the direct light may be transformed into diffuse light in a diffusing device, e.g. blinds placed in conjunction with the glazing. This effect is taken into consideration by calculating the light contribution from sun, sky, and ground on the window plane by using eq. (2), (3), and (4). The exitance of the inner glazing surface Mo_g is determined by multiplying the total light contribution with the light transmittance for direct light that is diffused when it passes the glazing/shading system: $\tau_{dir \rightarrow dif}$. This light transmittance is calculated by WIS, see section 2.4.

$$Mo_g = \left(E_{sun} + E_{sky} + E_{ground} \right) \tau_{dir \rightarrow dif} \tag{9}$$

Devices that redirect the incoming light, e.g. a specular light shelve are modelled using a simple implementation. It is achieved by setting a special redirecting light transmittance τ_{redir} to a value between 0 and 1 where 0 means that no light is redirected and 1 that all incoming light is redirected. This means that for an incoming ray of light with a given profile angle θ the following applies: $\tau_\theta + \tau_{dir \rightarrow dif, \theta} + \tau_{redir, \theta} = 1$ (FIG. 1). The inclination angle β of the slat or light shelve determines the reflection angle. Only fully specular devices are considered and any specular interreflections between slats and between slats and glazing are ignored.
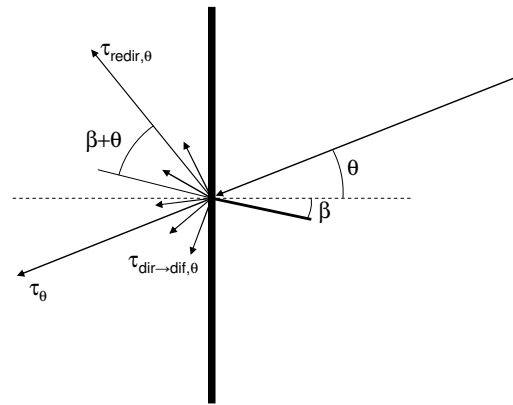
FIG. 1. Illustration of how an incoming ray of light from the sky, sun or ground is transmitted directly, diffused in the combined glazing and shading, or redirected specularly with equal inbound and outbound angle.

2.4 Light transmittances

A critical element in the daylight calculation routine is the light transmittance of the combined glazing/shading system. For this purpose the European software tool called WIS (van Dijk, D. and Oversloot, H. 2003) is used. This tool implements algorithms from the ISO standard 15099 (ISO 15099 2003) capable of calculating the light transmittance of a transparent system for both direct and diffuse light.

WIS calculates the thermal and solar performance of multilayered window systems, allowing the user unlimited combinations of glazing and solar shading devices. This makes WIS a very powerful tool for evaluating various integrated daylight designs. Currently the improvement and verification of WIS, and its database format and database population are the responsibility of the EU Thematic Network WinDat, which consists of major European research institutions and manufacturers of window components.

The output from a WIS calculation may be in the format of a text file. The file includes the light transmittances and solar energy transmittances for different solar profile angles (-90° to 90° at 10° increments), and may be loaded seamlessly into the tool described in this article. If the shading device has multiple shading positions, e.g. Venetian blinds, the user may generate and load files for every position required. The tool will linearly interpolate between the transmittance data loaded, thus making the number of loaded positions a question of desired accuracy.

Because the employed method of calculating incident light on internal subsurfaces is equivalent to a ray-tracing technique, the WIS transmittance for direct light is employed for both diffuse and direct light. WIS cannot yet handle specular shading devices, e.g. light shelves or light redirecting devices.

3. CONTROL STRATEGIES

3.1 Thermal simulation

The simplified thermal model is described in detail in Nielsen (2005). It is capable of evaluating the thermal indoor environment and heating and cooling loads in a building with very few input parameters while providing the option of sophisticated controls.

3.2 Electrical lighting

The electrical lighting system can be divided into general and task lighting. Both systems are defined by the power consumption of the lighting fixtures in W/m^2 when providing an illuminance of 100 lux, and the minimum (standby) power consumption. The linear relationship is shown on FIG. 2. The values for power density and corresponding illuminance are often supplied by the producers of lighting fixtures, and the maximum illuminance is calculated using the maximum power density.
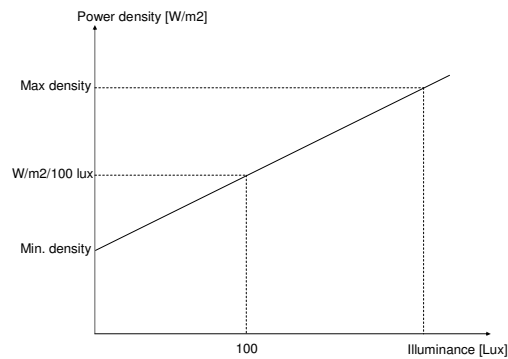
FIG. 2. Definition of illuminance and power density relationship for lighting systems in the tool.

Both systems can be defined and controlled separately with respect to daylight in two arbitrary points within the simulated enclosure. The possible control strategies are 'always max', 'always min', 'on-off', and 'continuous'. The hourly incoming daylight in the point is evaluated and the electrical lighting is switched on/off or dimmed according to the chosen control strategy. The 'on-off' control switches between the maximum and minimum power consumption when the daylight level is below or above the illuminance setpoint. The 'continuous' control interpolates linearly between the maximum and minimum power consumption in order to meet the specified setpoint. Electrical losses in the ballasts must be included in the power density.

3.3 Shading

The indoor air temperature controls the systems including the shading. This means that shading is activated only when excess heat gains occur, thus ignoring the risk of glare for the time being. In the case of screens or similar, the controls are limited to screen up or screen down.
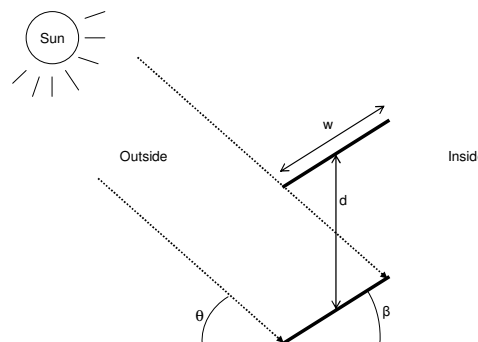
FIG. 3. Illustration of the cut-off shading control strategy for adjustable slats.

In the case of adjustable slats or similar the shading is lowered and adjusted to 'cut-off' angle when the indoor air temperature exceeds the specified cooling setpoint. Let d denote the distance between two slats (m), θ the profile angle of the sun (degrees), and w the width of the slats (m), then the cut-off angle is calculated:

$$\beta_{cut\,off} = \arcsin\left(\frac{d\cos\theta}{w}\right) - \theta \tag{10}$$

3.4 Thermal simulation coupling

It requires a sophisticated coupling to calculate the incoming daylight, the effect of shading on daylight levels, and thus electrical lighting consumption and indoor air temperature. This is achieved by pre-calculating the hourly daylight levels in the room *without* shading, initiate the thermal simulation, evaluate the hourly indoor operative temperature with respect to the cooling setpoint, possibly lower the shading and adjust the slat angle (for blinds) to cut off direct sunlight, and calculate the daylight levels again. If the operative temperature still exceeds the cooling setpoint, venting, increased ventilation, and mechanical cooling are employed in that order. The daylight levels are evaluated at two arbitrary points specified by the user.

4. Validation

Of the numerous lighting simulation programs available, Radiance has been extensively validated and repeatedly surpassed competing programs in terms of both functionality and accuracy. For these reasons, we chose Radiance as our reference model. The validation of the daylight calculation algorithm is carried out for a single office room as depicted on FIG. 4. Three different setups are carried out for a clear glazing, external blinds adjusted to cut-off angle and an external screen. The property data is listed in TABLE. 1

TABLE. 1: Input data for validation.

Properties	WIS Code	Property	Value [-]	Remarks
Glazing	4-15Ar-SN4	Light transmittance	0.782	Double glazing w/ lowE coating
Blinds	Windat #01	Diffuse reflectance	0.096	Slat width: 0.08m, slat distance: 0.072m
Screen	Verosol Silverscreen	Light transmittance	0.035	Total transmittance for screen+glazing
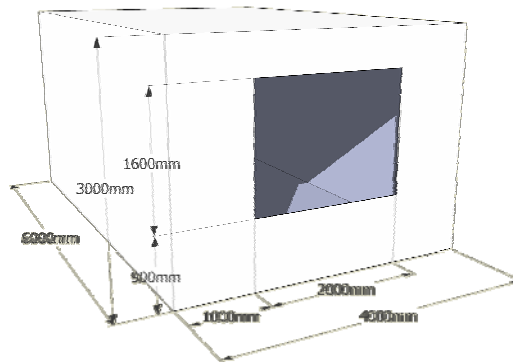
FIG. 4. Room dimensions for validation.

The chosen validation date is the 21st of September at 3 p.m. because it involves complex calculation of solar position, incidence angles and cut-off angle. The radiation data is from the Danish Design Reference Year and the measurements are performed at desktop height 0.85m in interval points along the centre line of room.

FIG. 5 to FIG. 7 compares the illuminance levels computed by Radiance and by the simple tool. The relative error is within ±20% for the clear glazing and for the blinds which is considered satisfactory in daylight research. However the largest discrepancy is for the screen, but this is due to two facts: the light transmittances from WIS are unidirectional but screens have bidirectional properties and the screen is defined in Radiance as a glazing with reduced transmittance ignoring the diffusing properties of the real screen.
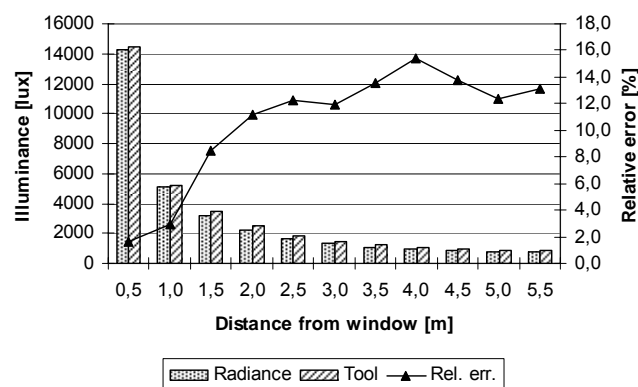
FIG. 5. Clear glazing. Absolute illuminance levels and relative error.
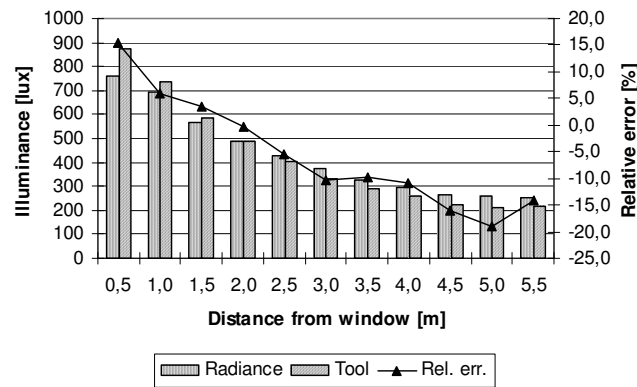
FIG. 6. External blinds at cut-off angle. Absolute illuminance levels and relative error.
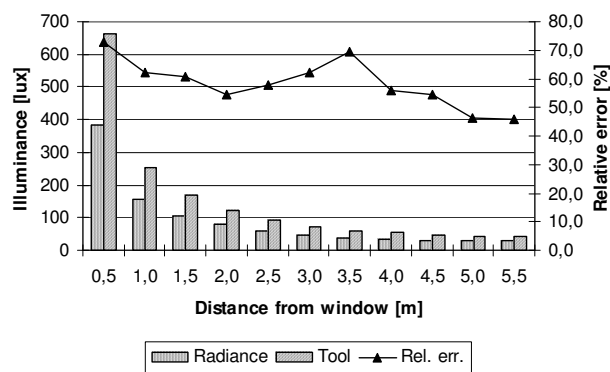
FIG. 7. External screen. Absolute illuminance levels and relative error.

5. Combined simulation

FIG. 8 depicts the implications of daylight responsive lighting systems. The artificial lighting system adjusts continuously with respect to the incoming daylight complementing the illuminance deficit. If overheating occurs the shading device is activated and the effect on daylight, casual gain and the thermal balance is quantified. Consequently the tool aids in producing daylight friendly design and quantifies the effect of 'smart' solar shadings that allows the maximum amount of direct sunlight to be tranferred diffusively in order to save electrical energy.
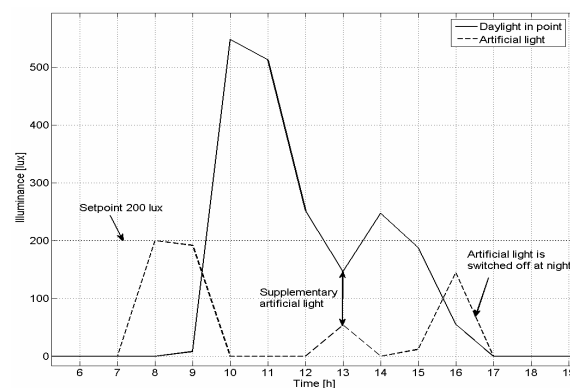
FIG. 8. Daylight and artificial light in a point. Continuous dimming control of the lighting system.

6. Conclusion

The tool described here is developed to evaluate the impact of incoming daylight on the energy consumption for lighting. The tool calculates the daylight distribution on the basis of a ray-tracing approach and the radiosity

method to enhance accuracy while maintaining calculation speed. The sky is divided into patches with individual luminances in order to imitate the energy distribution of the real sky. Rays are traced from each individual sky patch to the surfaces of the room through glazing and shading giving the initial input to the radiosity algorithm which is employed for internal light distribution. Window overhang and recess as well as distant objects like other buildings reduce the visible proportion of the sky.

The daylight distribution is calculated every hour, thus providing the information necessary for the thermal program to control the photoresponsive lighting and to calculate the heat load of the electrical lighting system. The daylight and thermal simulations are integrated meaning that the indoor temperature is recalculated if overheating has caused the shading to be activated.

The daylight algorithms were validated by comparison with the state-of-the-art ray-tracing program, Radiance, using the Perez anisotropic sky. The results show agreement within 20 % relative error, thus the simplified tool is adequate for predicting the electrical energy consumption of photoresponsive lighting systems, including the impact of complex shading systems such as external Venetian blinds.

7. References

Clarke, J. and Janak, M. (1998). Simulating the thermal effects of daylight-controlled lighting. *Proceedings of Building Performance (BEPAC UK)*, Issue 1.

Fraunhofer-Institut für Bauphysik, 2006. ADELINE 3.0, Abteilung Wärmetechnik, Stuttgart, Germany. Available from: http://www.ibp.fhg.de/wt/adeline/

ISO 15099 (2003). ISO 15099:2003 Thermal performance of windows, doors and shading devices – Detailed calculations, International Organization for Standardization, Geneva, Switzerland.

Nielsen T.R. (2005a). Simple tool to evaluate energy demand and indoor environment in the early stages of building design, *Solar Energy*, Vol. 78, No. 1, 73-83.

Nielsen, T., Nielsen, T. R. and Svendsen, S. (2005b). Calculation of daylight distribution and utilization in rooms with solar shadings and light redirecting devices. *Proceedings of 7th Symposium on Building Physics in the Nordic Countries*, 1011-1018.

Park K.-W. and Athienitis A.K. (2003). Workplane illuminance prediction method for daylighting control systems, *Solar Energy*, Vol. 75, No. 4, 277-284.

Perez R., Ineichen P., Seals R., Michalsky J. and Stewart R. (1990). Modeling daylight availability and irradiance components from direct and global irradiance, *Solar Energy*, Vol. 44, No. 5, 271-289.

Perez R., Seals R. and Michalsky J. (1993). All-weather model for sky luminance distribution - preliminary configuration and validation, *Solar Energy*, Vol. 50, No. 3, 235-245.

Reinhart C.F. and Herkel S. (2000). The simulation of annual daylight illuminance distributions - a state-of-the-art comparison of six RADIANCE-based methods, *Energy and Buildings*, Vol. 32, No. 2, 167-187.

Robinson D. and Stone A. (2006). Internal illumination prediction based on a simplified radiosity algorithm, *Solar Energy*, Vol. 80, No. 3, 260-267.

Scharmer, K. and Greif, J. (2000). The European Solar Radiation Atlas. École des Mines de Paris, France.

Tregenza P.R. (1987). Subdivision of the sky hemisphere for luminance measurements, *Lighting Research & Technology*, Vol. 19, No. 1, 13-14.

Tregenza P.R. and Waters I.M. (1983). Daylight coefficients, *Lighting Research & Technology*, Vol. 15, No. 2, 65-71.

van Dijk, D. and Oversloot, H. (2003). WIS, the European tool to calculate thermal and solar properties of windows and window components. *Proceedings of IBPSA, Building Simulation*, Vol. 1, 259-266.

Ward, G. L. and Shakespeare, R. A. (1998). Rendering with Radiance - The art and science of lighting visualization. Morgan Kaufmann, San Francisco.

The Development of a Climate Façade for a Hot Humid Climate

Peter van den Engel, Dr. Ir.,
Deerns Consulting Engineers and Delft University of Technology, subdepartment Climate Design;
p.vd.engel@deerns.nl

Georgios Mixoudis, Ir.,
Deerns Consulting Engineers;
g.mixoudis@deerns.nl

KEYWORDS: climate façade, mock-up, hot climate

SUMMARY:
After simulating the thermal performance of a climate façade for Abu Dhabi, a climate façade was tested in a mock-up room. This façade is compared with combinations of other façade and building services.

1. Introduction

The "green building concept" is the starting point of design for many new buildings in the United Arabic Emirates, in cities like Dubai and Abu Dhabi. These buildings should have a modern and open character, integrated with Arabic cultural elements. One of the goals of the green building concept is a low energy consumption. Some principles of energy reduction are:

◻ Cool as much as possible with water instead of air.

◻ Reduce solar heat entering the façade.

◻ Make use of daylight as much as possible.

At the moment several buildings with almost 70% glass façades - related tot the total façade surface - are developed in the U.A.E.. This normally creates both problems of overheating and a high energy consumption. However, with the use of a climate façade, it is possible to compensate these negative influences.

The g-value of the glass is a very important factor to evaluate the external heat load. The g-value of conventional glass in the U.A.E. is 0.26. In order to limit the external heat load the maximum glass percentage of the façade is normally 40%. Combining lower g-values with enough visible light transmittance, a higher percentage of glass is possible, up to even 70%. The g-value is defined as the amount of solar energy that enters the office room via radiation and convection.

2. Methods

Design and physical principles of conventional climate façades were analysed. Based on these analyses the climate façade concept was adapted to hot and humid climates. For instance, double glass on the outside should have a low g-value of at least approx. 0.3. By means of simulations in TRNSYS and CFD (Phoenics), predictions of temperatures were made. A mock-up room with a climate façade was built. The mock-up room has the following dimensions: L x w x h = 6.2 x 6.2 x 2.8 m. The climate façade has a height of 2.6 m. The roof has an U-value of 0.4 W/m^2K. The walls are double and are cooled mechanically.

Measurements of airflow, temperature, solar radiation and humidity gave a lot of information. Moreover, indicative measurements showed the effect of this type of façade equipped with reflecting blinds on visual comfort.

One of the most important evaluation parameters is the technical performance of the façade; damage to the façade due to local high temperatures or quick changes in temperatures should be prevented.

In order to predict the energy qualities, the climate façade is compared with other façades like a conventional façade with solar protected (reflecting) glass, a natural ventilated second skin façade and a façade with solar shading elements on the outside.

3. Results

3.1 Simulations

3.1.1 TRNSYS-simulations

With TRNSYS simulations an overview of the thermal behaviour of the façade of a whole year can be given.

The solar energy at a south facade in Dubai is ca 850 W/m^2 in winter and ca 450 W/m^2 in summer due to the altitude of the sun, which leads to a higher external heat load in winter than in summer.

The parameters used in the simulation include:

- airflow   = 35 m^3/h per 1.20 m façade
- g-value of the double glass   = 0.29
- U-value of the glass   = 1.04 W/m^{2}K
- visible light transmittance of the double glass = 56%
- indoor temperature   = 24°C
- height of the climate façade   = 2.6 m
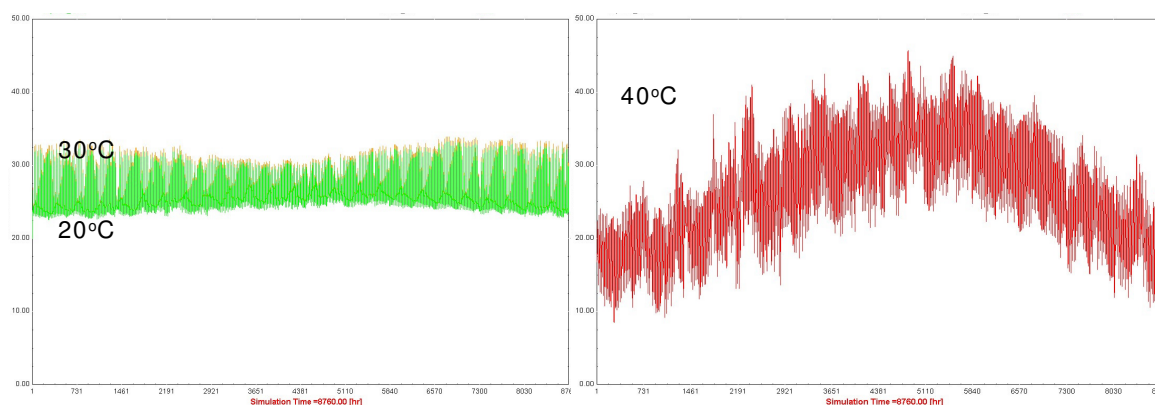
FIG.1: Cavity and surface temperature of the glass at the office-side (left) and ambient air temperature in ^{o}C (right).

TRNSYS-simulations of a whole year show a maximum surface temperature of the glass at the office-side of 29 (summer) - 33°C (winter). A simulation of one day – the 6th of September – (fig. 2) can be compared with measurements on that day (figure 7 - 9). The TRNSYS-year is an average of climatical data of the past (1961-1990). At the moment the temperature and humidity has become higher than the TRNSYS-simulations suggest.
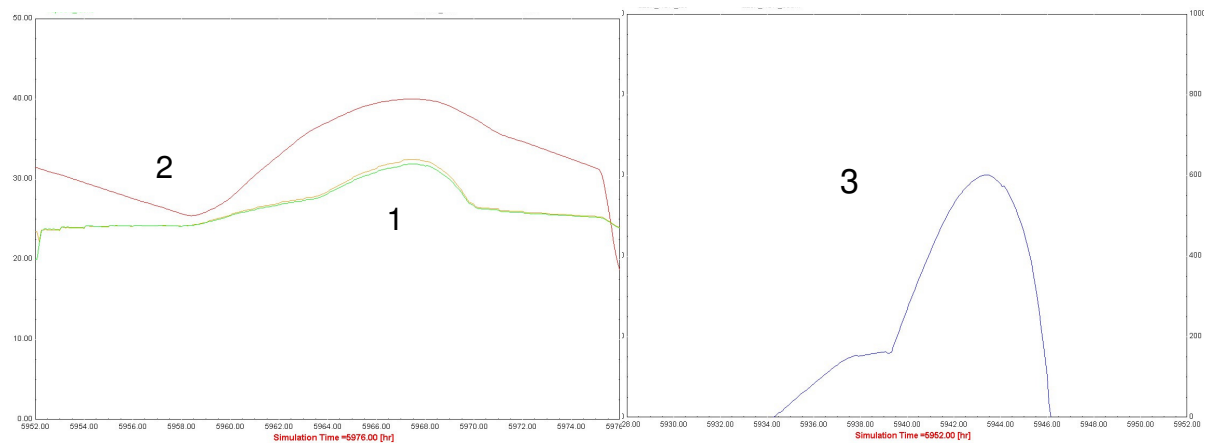
FIG.2: Simulated temperatures of the air in the cavity and glass (1) at the office-side and the ambient temperature of the 6th of September (2, max. ca 40°C). The amount of solar energy is presented at the right side (3, max. ca 600 W/m²).

TRNSYS-simulations show that the g-value is not a fixed value. When the blinds are open the effective g-value in summer will be 0.29 and in winter 0.26. With blinds closed the g-value will be lower than 0.18 in summer and 0.10 in winter (table 1):

TABLE 1: Overview of temperatures, energy transport, external heat load and g-values (south façade)

	Solar energy	Outdoor temperature	Heat transport to office	Heat load office	Effective g-value
Blinds closed winter	850 W/m² glass surface	20°C	88 W/m² glass surface	40 W/m² floor surface	0.10
Blinds closed summer	450 W/m²	45°C	80	36 W/m²	0.18
Blinds open winter	850 W/m²	20°C	220	100 W/m²	0.26
Blinds open summer	450 W/m²	45°C	130	59 W/m²	0.29

3.1.2 CFD-calculations

CFD-calculations were made with blinds fully closed and fully opened.

Fully closed blinds

The parameters used in the simulation with closed blinds include:

- ☐ Outdoor temperature   = 48°C
- ☐ Outdoor heat transfer coefficient   = 25 W/m²K
- ☐ Indoor temperature   = 22°C
- ☐ Indoor heat transfer coefficient   = 8 W/m²K
- ☐ Gap ventilation supply temperature   = 22°C
- ☐ Solar radiation on the façade   = 800 W/m²

- ☐ A gap between the top of the blinds and the top of the cavity and the lowest blinds and the bottom of the cavity.
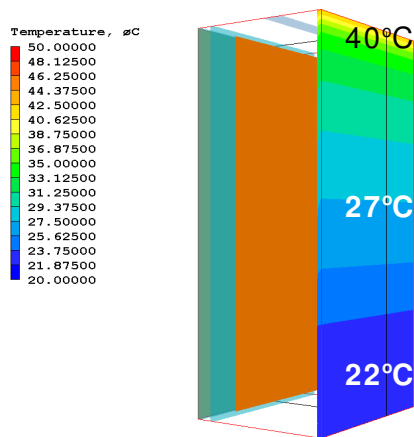
FIG.3: CFD simulations of the façade with closed blinds

At the inside the average temperature of the glass is 27°C, with 22°C near the floor and 40°C near the top

Fully open blinds

☐   20% of the solar radiation via the double window (240 W/m^2, g = 0.3) is absorbed by the blinds.

☐   80% = 192 W/m^2 solar radiation passes the single glass at the office-side and enters the office.
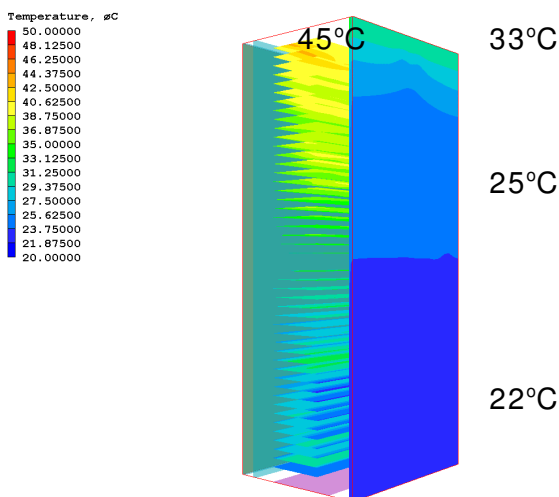
FIG.4: CFD simulations of the façade with open blinds

At the inside the average temperature of the glass is ca. 25°C, with 22°C near the floor and 33°C near the top. The maximum temperature of the blinds is 45°C. The CFD-simulations show lower average glass temperatures than the TRNSYS-simulations.

Points of attention that are checked by the CFD-simulations are:

☐   When the ventilation system of the façade fails, it is necessary to pull up the blinds to prevent overheating. This requires an automatic control system.

☐   The air should be extracted at the top fo the cavity to prevent heat accumulation at the top of the façade.

☐   Equal distribution of air at the bottom of the cavity is necessary, the air inlet velocity schould be ca. 0.3 - 0.5 m/s in order to produce effective heat removal at both sides of the blinds.

3.2 Measurements

3.2.1   Thermal comfort

In a mock-up room (6 x 6 m) measurements of the thermal comfort and the performance of the climate façade have been carried out. The mock-up room is cooled by water, by cooled beams in the ceiling (induction unit) and by a cooled floor and by (fresh) air via the cooled beams.

FIG.5: Surface temperature of the glass at the inside and ceiling temperature

Measurements of a façade in a mock-up room in Abu Dhabi on the 6th September 2007 (2 pm) show an inside glass temperature of 27-28°C at a height of 1,4 m, 24-25°C near the floor and 25°C near the top. The lower surface temperature near the top is created by cooled beams (induction unit) in the ceiling near the façade (fig. 5, to the right at the top). The air inlet temperature near the floor is 23°C. The influence of the high outside glass temperatures (fig. 6) is low.
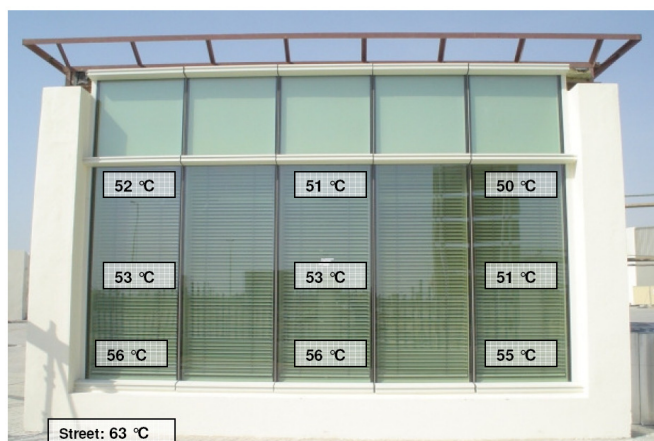
FIG.6: Surface temperature of the glass at the outside

Due to high street temperatures the outside glass temperature is 56°C near the street and 51°C near the top.

The 6th September 2007 shows the following climate:
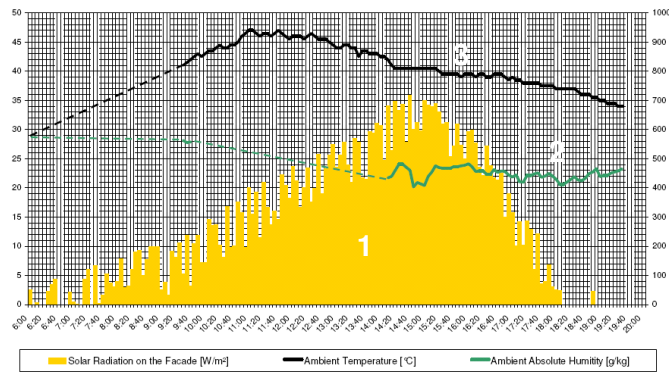
FIG.7: Ambient temperature (3, ^{o}C), absolute humidity (2, g/m^3) and solar radiation (W/m^2) on the façade on the 6th September 2007 (1, max. 600 W/m^2, with peaks of 100 W/m^2 above this maximum).
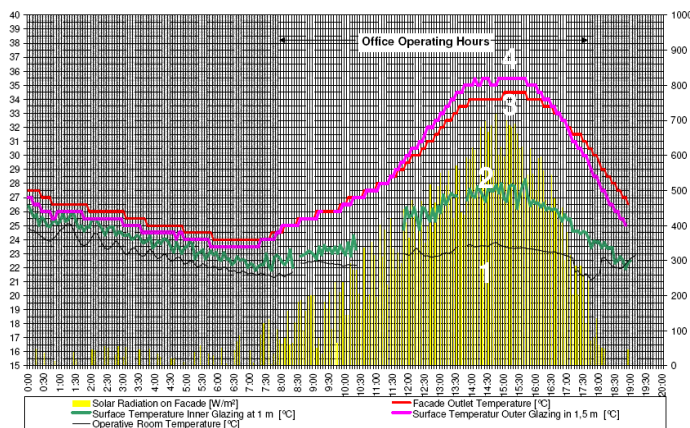
FIG.8: Inner glass surface temperature (2) and operative room temperature (1). The other temperatures are the surface temperature of the outer glazing at the cavity side (4) and the façade outlet temperature (3).

Surface temperatures of the inner glazing show a maximum of 28°C. In the cavity the glass temperature of the outer glazing is maximal 35.5^{o}C. The inside glass temperatures are ca. 2°C lower than predicted with TRNSYS.
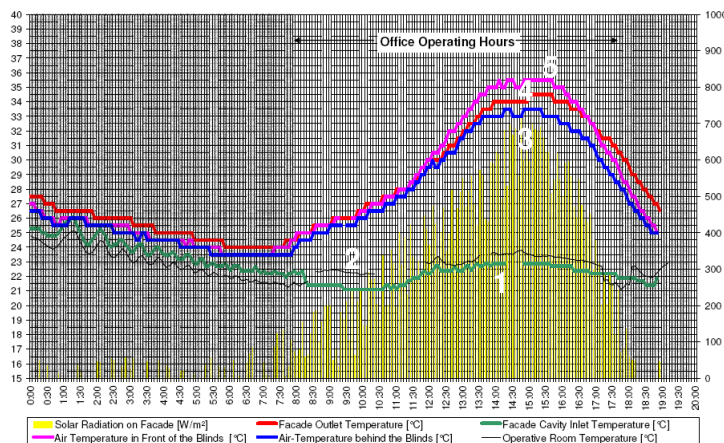
FIG.9: Façade inlet and outlet temperature and air temperature of the cavity behind and in front of the blinds. The following parameters are represented: Façade cavity inlet temperature (1), operative room temperature (2), cavity temperature at the room side (3), façade outlet temperature (4) and cavity temperature in front of the blinds (5).

The maximum air temperatures in the cavity are ca 33°C. TRNSYS simulations show lower maximum temperatures of 30°C. However, the measured average outdoor temperature and the amount of solar radiation is more than in the TRNSYS model.

The results show an acceptable relation between simulations and measurements of the thermal performance of the façade. The tools proved to be reliable enough for engineering purposes. Measurements of the thermal comfort in the office showed a comfort level equivalent to class A of the NEN-ISO 7730.

3.2.2 Energy

The measurements give some information about the energetic performance as well. The amount of heat absorbed by the cavity (open blinds) is 58 W per m^2 façade. This a little more than the presumed 48 W per m^2 facade for the CFD simulations (fig. 4). It is calculated after measurements of the airflow and air inlet and outlet temperature of the cavity. It was not possible to measure the external heat load in more detail. This is only possible when a mock-up room is highly insulated and is shielded very well from the outdoor climate.

3.2.3 Visual comfort

Reflecting blinds (61% reflection) are applied in order both to promote the use of daylight and to reflect solar energy effectively. The position of the blinds is mechanically controlled via a control algorithm (Warema, Germany) which has to be adapted to the circumstances in Abu Dhabi. The measurements indicate that glare can occur in the office, when the blinds are open in summer. Consequently the control of the blinds should take into account the risk of glare. Brightness ratios of 1:60 between an average computer screen and the blinds can occur. Winter requires another kind of attention, since there will be more sunlight at the south facing facade with a low sun altitude, compared to the the summer when the sun approaches the zenith at midday. A possible alternative to the current design of the facade could be the use of 2 segments. A lower part of the facade with manual blind control, to make it easy to close the blinds in case of glare, and an upper part with automatic blind control to maximize the use of daylight.

3.3 Exploitation analysis

The climate façade is compared with a room with a traditional façade with glass with a g-value of 0.26:
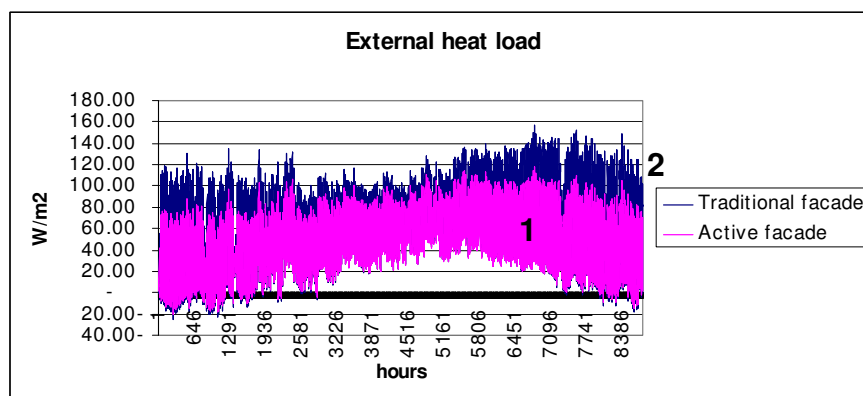
Fig. 10: Comparison external heat load of an office with a façade with a façade (70% glass) with an average g-value of 0.14 (climate façade, 1) with a traditional façade with a g-value of 0.26 (2).

Four different combinations of façade design and installation-types are compared. The operation and maintenance costs of the climate façade-options proved to be lowest (price level 2008). The combination with cooled beams (induction) with a cooled floor is the most favorable:

Operation & Maintenance Costs
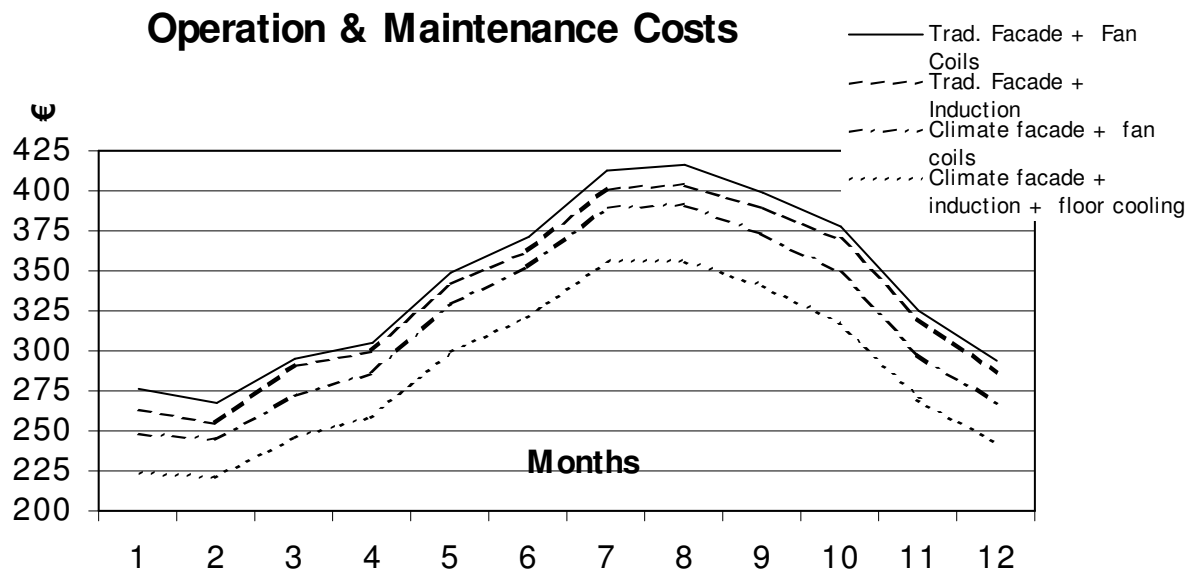
Fig. 11: Operation and maintenance costs of traditional climate design options with a high glass percentage of ca 70% (average g-value = 0.26) versus design options with a climate façade (average g-value = 0.14). The costs per month are related to the seize of the mock-up room.

3.4 Alternative types of façades

☐ It might be possible as well to design a second skin façade (Hamza et al, 2007). However, Abu Dhabi has a very dusty environment, which prevents this option.

☐ Making use of external sunshade might be another possiblity. In order to have advantage of daylight and a maximum of outdoor view, external sunshades should be movable. Maintenance problems and limitations in case of high rise buildings make this option less attractive.

4. Conclusion

This research of the climate façade fo Abu Dhabi shows the usefulness of design tools and shows that it is possible to design open transparent buildings with a high glass percentage in hot humid climates as well . Only small adaptations of the original climate façade concept are necessary. With this information the performance of other types of climate façade's can be predicted more accurately in the future.

5. References

Hamza N., Gomaa A., Underwood C. (2007). Daylighting and thermal analysis of an obstructed double skin façade in hot areas, Proceedings of Clima 2007 Well Being Indoors, Helsinki, Finland.

Bekker J., Renes S. (1987). Laboratoriumonderzoek naar ontwerpcriteria voor klimaatramen (research report climate façade's), Bronswerk Airconditioning Research Centre, The Netherlands.

6. Acknowledgements

CFD modelling of 2-D heat transfer in a window construction including glazing and frame

Morten V. Vendelboe, Ph.D student
Technical University of Denmark – Department of Civil Engineering
mvv@byg.dtu.dk

Svend Svendsen, Professor
Technical University of Denmark – Department of Civil Engineering
ss@byg.dtu.dk

Toke R.. Nielsen, Associate Professor
Technical University of Denmark – Department of Civil Engineering
trn@byg.dtu.dk

KEYWORDS: *fenestration, window, numerical simulation, thermal transmittance, glazing temperature, CFD*

SUMMARY:
A numerical model for the simultaneous calculation of 2-D heat transfer and indoor surface temperatures for a three layer glazing unit and a frame construction based on a commercial CFD code is presented. The calculated heat flow and the surface temperatures of the inner glazing layer are compared to results obtained using the finite element code Therm 5.2 by calculations according to EN ISO 10077-2 and ISO 15099. The models compared produce almost identical results with respect to the overall thermal transmittance of the glazing and frame, whereas differences in the range 3-7% are found for the thermal transmittance of the frame part only. The calculated distributions of surface temperatures for the inner pane also agree quite well when convection in the glazing cavities is accounted for in the finite element calculation.

1. Introduction

Window design affects energy consumption in buildings significantly with respect to both cooling and heating demand. Sensible design solutions to improve the thermal properties of windows are therefore crucial in the effort to reduce the overall energy consumption in buildings.

One of the most widely used tools (Gustavsen 2005, Song 2007) for detailed analysis of the thermal properties of the connection between glazing and window frames is the 2-D finite element code Therm5.2 (Finlayson 1998). The code can be used for calculation of the thermal transmittance of glazing and frame connections according to the EN ISO 10077-2 (CEN 2003) and the ISO 15099 (ISO 2003) standards. The EN ISO 10077-2 procedure for calculation of thermal transmittance is however not suited for determination of condensation risk due to low inside surface temperatures but a suitable alternative is not prescribed in the European standards (CEN 2001).

A condensation resistance model has however been implemented in Therm for more precise calculation of indoor surface temperatures (Zhao 1996, Mitchell 2003, Kohler 2003) in compliance with North American standards (NFRC 2004).

In the following the preliminary investigations regarding the possibility to apply a commercial CFD code for detailed 2-D analysis of heat transfer and simultaneous calculation of indoor surface temperatures is presented. Calculated thermal transmittances as well as indoor surface temperature distribution are compared to Therm models to observe the difference due to more comprehensive modelling of the cavities of the glazing and frame.

2. Method

2.1 Geometry and materials

The modelled window cross section consists of three 4 mm glass layers and two 12 mm air cavities. The panes have an emissivity of 0.84 on all surfaces except the outer surface of the inner pane which has a low emissivity coating with an emissivity of 0.037. Since the focus is on model comparison, and not on calculating the properties of an actual window, all other emissivities are set to 0.9. For the same reason the detailed geometry and thermal properties of the spacer are represented by a box of an equivalent fixed thermal conductivity. The applied thermal properties of the materials used in the calculations are listed in TABLE. 1. The model geometry is displayed in FIG. 1.
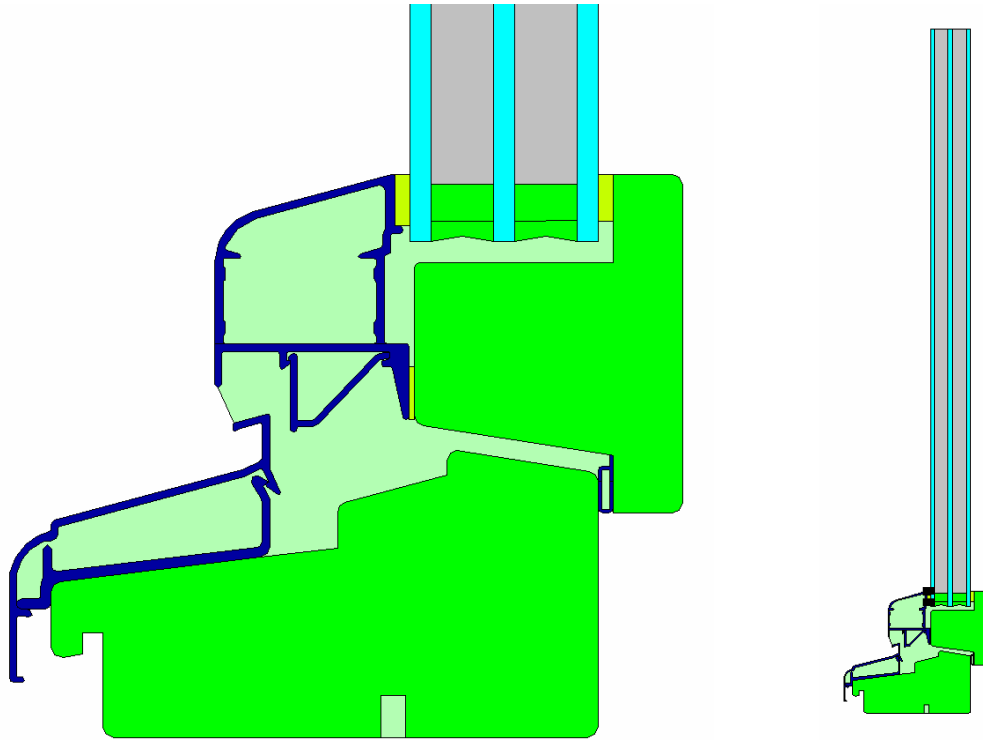
FIG. 1: Figure showing the cross section of the window. Left: The sill and the lower part of the glazing unit. Right: The entire model.

TABLE. 1: Material properties used for the calculations.

Material	Conductivity [W/mK]	Emissivities [-]
Aluminium	160	0.9
Wood	0.13	0.9
EPDM	0.25	0.9
Sealing	0.4	0.9
Spacer	0.246	0.9
Glass	1	0.84
Glass with low emissivity coating	1	0.037

2.2 Boundary conditions

For all models boundary conditions are chosen according to EN ISO 13788. Constant heat transfer coefficients of 7.69 W/m²K and 25 W/m²K are assigned to the internal and external boundaries respectively. The indoor temperature is set to 20 °C and the outdoor temperature to 0 °C.

2.3 Glazing

For the finite element calculations thermal properties of the glazing unit are calculated in Window5.2 (Mitchell 2001) and imported to Therm.

To ensure that the glazing unit, modelled using the CFD code, has the same thermal properties as the glazing unit imported for the finite element calculations, a comparison is made for the two models of the glazing unit alone. In both cases boundary conditions according to section 2.2 are applied for the internal and external boundaries while the top and bottom of the glazing is adiabatic. The height of the glazing is 0.5 m. The calculated thermal transmittance of the glazing using Window is 1.25 W/m²K.

The calculated thermal transmittance for the CFD model is 1.27 W/m²K. The calculated thermal transmittances of the two models are in very good agreement with a difference of 1.6 % and are thus used in the integrated calculations for glazing and frame. The settings for the separate CFD model for the glazing are presented in section 2.5.

For the finite element calculations two calculations are performed for each model. For calculations of thermal transmittance (U-value) the air in the glazing cavities is replaces by a solid material with a thermal conductivity that is calculated based on the heat transfer due to convection and radiation across the cavity. For calculation of indoor surface temperatures a convection model for the local temperature distribution inside the glazing cavities developed for Condensation Resistance rating according to NFRC 500 is applied.

2.4 Frame cavities

While the thermal properties for the solid domains are identical for the finite element models and the CFD model, the cavity modelling is different. In the first two finite element models the frame cavities are modelled according to EN ISO 10077-2 where a simplified radiation model is prescribed. These models are referred to as 'CEN CR' and 'CEN U-value'. In the other two models the frame cavities are modelled according to ISO 15099 including a detailed view factor based radiation model. These models are referred to as 'ISO CR' and 'ISO U-value'.

In all cases the cavities are defined as non ventilated to match the assumptions made in the CFD model.

The settings for the CFD model for the convective and radiative heat transfer in the frame cavities is presented in section 2.5

2.5 CFD settings and mesh

2.5.1 CFD settings

A list of settings for the CFD model is presented in TABLE 2. The settings are used for both the separate model for the glazing and the model including both the frame and the glazing.

TABLE. 2: Settings for CFD model.

Solver	Stationary	
Viscous model	Laminar	
Fluid thermal properties	Density modelled according to the Boussinesq approximation. All other properties are constant.	
Discretization schemes	Pressure	Standard
	Momentum	2nd order
	Energy	2nd order
Radiation model	Discrete Transfer Radiation Model (DTRM)	

Though the PRESTO! discretization scheme for pressure is recommended for modelling of natural convection (Fluent Inc. 2005) convergence is only achieved when the standard scheme is applied for the model including both the frame and the glazing. A comparison for the separate glazing model does not however show any effect of enabling the PRESTO! discretization scheme for pressure.

2.5.2 Mesh

The calculation of heat transfer across the window construction including glazing and frame is performed with a triangular mesh of ~120,000 cells. The solution is grid independent with respect to the total thermal transmittance of the glazing and frame to less than 1 %. Grid independence could probably be achieved with a lower number of cells, but due to the complex nature of the geometry a fine mesh is needed to reduce the number of poor quality cells. Thus critical mass imbalances due to poor mesh quality within key areas of the frame cavities occurs at both ~30,000 and ~60,000 cells. While calculation time is not comparable to that of Therm (order of seconds) the model does however converge in less than 1 hour (Intel Centrino Duo, 2 GHz, 4 GB).

3. Results and discussion

3.1 Comparison of total thermal transmittance of glazing and frame

The calculated total thermal transmittance of glazing and frame is presented in

TABLE. *3*. Since the modelled thermal transmittance of the glazing in the CFD model is 1.6 % higher than for the glazing imported in the finite element calculations and the thermal transmittance of the glazing make up the majority of the total thermal transmittance the results for the CFD model have been corrected for appropriate comparison. As TABLE. 3 shows the calculated results are essentially identical whether or not the CFD results are corrected.

TABLE. 3: Comparison of calculated total thermal transmittance of window cross section including glazing and frame

Model	Thermal transmittance (corrected with regard to U_{gl}) [W/m^{2}K]	Relative difference to CFD model [%]
CFD	1.38	-
CEN U-value	1.40	1.7
ISO U-value	1.39	0.8

3.2 Comparison of thermal transmittance of the frame

By subtracting the '1-D' thermal transmittance from the separate glazing models calculated in section 2.3 from the total thermal transmittances presented in section 3.1 the following results are obtained for the thermal transmittance of the frame including the spacer.

TABLE. 4: Comparison of calculated thermal transmittance of frame

Model	Thermal transmittance $[W/m^2K]$	Relative difference to CFD model [%]
CFD	1.95	-
CEN U-value	2.08	6.7
ISO U-value	2.01	3.0

Though larger discrepancies are found compared to the total thermal transmittance of glazing and frame the results shown in TABLE. 4 still agree very well. The reason why the results agree so well despite the different treatment of the heat transfer in the frame cavities is probably that the size and temperature difference across the cavities result in only very limited convection as illustrated in FIG. 2.
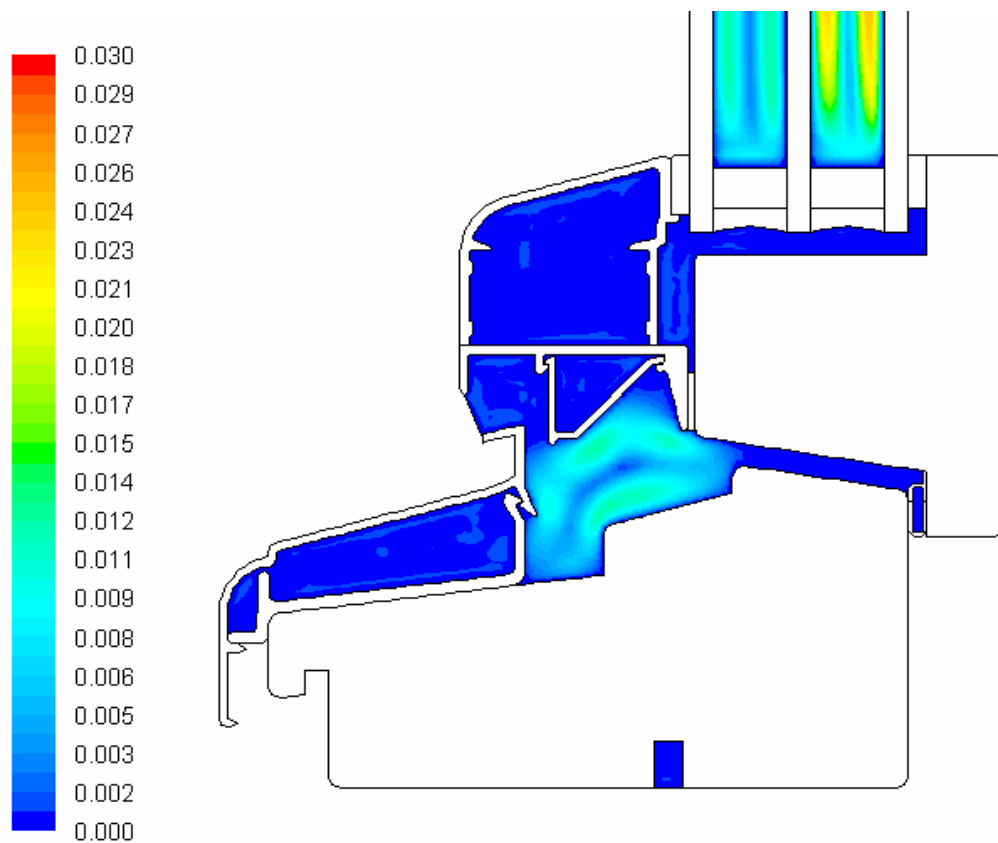
FIG. 2: Calculated velocity distribution for the CFD model for the frame cavities and the lower part of the glazing cavities.

3.3 Calculated indoor surface temperature distribution of the glazing

The calculated surface distribution for the inside of the innermost glazing for the 5 models is shown in FIG. 3. The x-axis shows the vertical distance from the top of the glazing (x=500 mm denotes the lower edge of the daylight opening). Since the results from the CEN and ISO U-value models as well as the CEN and ISO CR models are practically identical, only one plot is included for each model category.
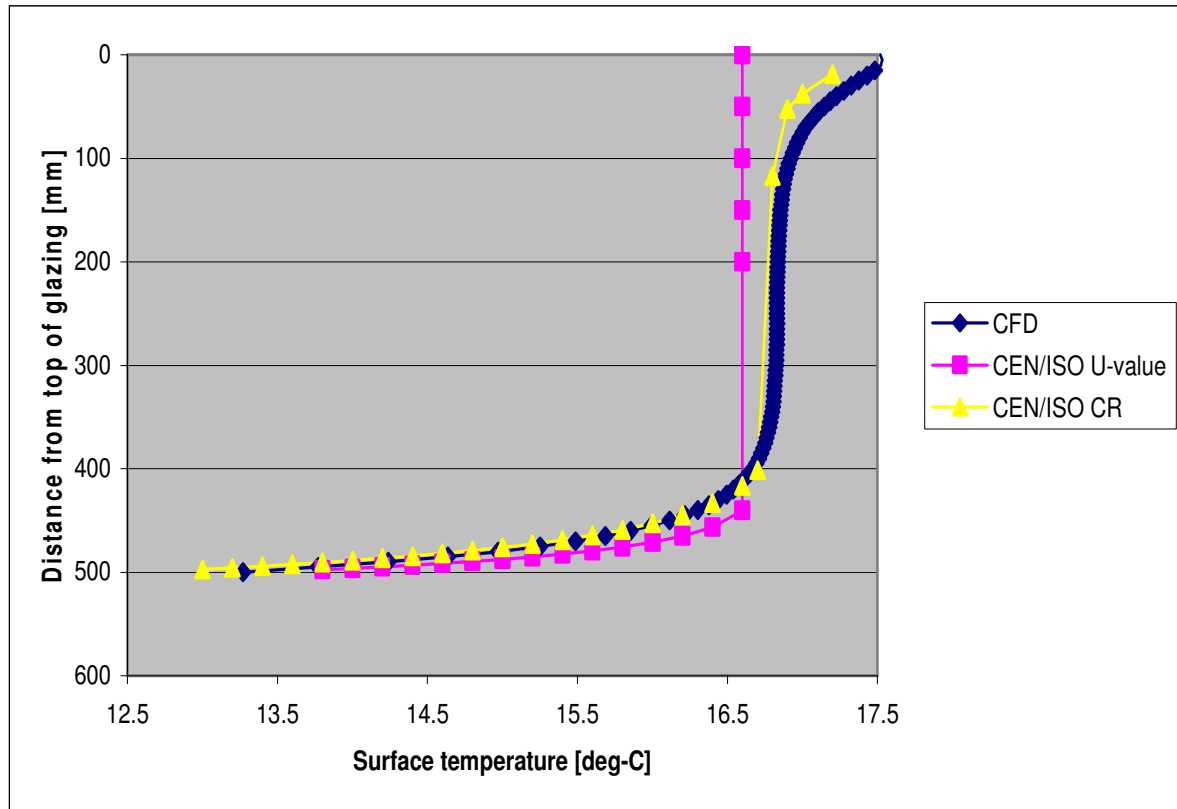
FIG. 3 : Calculated surface distribution on the inside of the innermost glazing for the 5 models as a function of the vertical distance from the top of the glazing.

As FIG. 3 shows, the results for the CFD model and the CR models are very similar regarding the overall tendency as well as local values with a predicted minimum temperature of 13.3 °C and 12.9 °C respectively. The U-value models on the other hand display similar surface temperatures on average but poor agreement concerning both overall tendency and local values in certain points. Due to the omission of the convective effects in the glazing cavities the predicted minimum temperature at the lower daylight opening is higher than predicted by the CFD and CR models with 13.8 °C.

4. Conclusions and further work

The conclusions are as follows:
- There is excellent agreement between the calculated values for the total thermal transmission whether calculated using the CFD model, the CEN U-value model or the ISO U-value model.
- There is good agreement between the three model types for the thermal transmittance of the frame with differences of less than 7 % in all cases.

- There is good agreement between the calculated indoor surface temperatures of the glazing for the CFD model and the CR models whereas the U-value models perform poorly with respect to both overall tendency and local values.

Given the overall agreement with the results based on the simplified finite element modeling of the glazing and frame cavities the application of the more comprehensive and time consuming CFD modelling is not justifiable for the given case. This is however believed to be attributed to the limited convection occurring in the glazing and frame cavities. Further work will therefore include similar comparisons for window constructions where convection is more significant for the overall heat flow as for window solutions with larger glazing distances and cases where non laminar flow conditions may occur.

In addition the comprehensive modelling capabilities of the CFD software facilitate further investigation of the impact of detailed modelling with respect to variable radiative and convective indoor boundary conditions for more precise indoor surface prediction in particular.

5. References

European Committee for Standardization (2003). EN ISO 10077-2: Windows, doors and shutters – Calculation of thermal transmittance – Part 2: Numerical method for frames.

European Committee for Standardization (2001). EN ISO 13788: Hygrothermal performance of building components and building elements - Internal surface temperature to avoid critical surface humidity and interstitial condensation - Calculation methods.

Finlayson, E., Mitchell R., Arasteh D., Huizenga C. and Curcija D. (1998). THERM 2.0: Program description. A PC program for analyzing the two-dimensional heat transfer through building products. University of California, Berkeley, CA, USA.

Fluent Inc. (2005). Fluent 6.2 Users Guide.

Gustavsen A., Uvsløkk S. and Jelle P. (2005). Numerical and experimental studies of the effects of various glazing spacer on the windows and the glazing temperature, *Proceedings of the 6th Symposium on Building Physics in the Nordic Countries,* Reykjavik, Iceland, June 13-15 2005.

International Organization for Standardization (2003). ISO 15099:2003(E) - Thermal performance of windows, doors and shading devices – Detailed alculations.

Kohler C., Arasteh D. and Mitchell R. (2003). THERM simulations of window indoor surface temperatures for predicting condensation, *ASHRAE 2003 Winter meetings CD, Technical and SymposiumPapers,* Vol.109, Issue 1, p. 587-593.

Mitchell R., Kohler C., Arasteh D., Carmody J., Huizenga C. and Curcija D. (2003). Therm5/Window5 NFRC Simulation manual, Lawrence Berkeley National Laboratory, Berkeley, CA, USA.

Mitchell R., Kohler C., Arasteh D., Huizenga C., Yu T., and Curcija D. (2001). WINDOW 5.0 User Manual. Lawrence Berkeley National Laboratory, Berkeley, CA, USA.

National Fenestration Rating Counsel (2004). NFRC 500: Procedure for determining fenestration product condensation resistance values.

Song S., Ho J.,Yeo M., Kim Y. and Song K. (2007). Evaluation of inside surface condensation in double glazing window system with insulating spacer: A case study of residential complex, *Building and Environment,* Vol. 42, p. 940-950.

Zhao Y., Curcija D. and Goss P. (1996). Condensation Resistance Validation Project – Detailed Computer Simulations Using Finite-Element Methods. *ASHRAE Transactions*, Vol.102 Issue 2, p. 508-515.

Modeling a Naturally Ventilated Double Skin Façade with a Building Thermal Simulation Program

Rasmus Lund Jensen, Research Assistant,,
Aalborg University;
rlj@civil.aau.dk

Olena Kalyanova, Ph.D-student,
Aalborg University;
ok@civil.aau.dk

Per Heiselberg, Professor,
Aalborg University;
ph@civil.aau.dk

KEYWORDS: Double Skin Façade, natural ventilation, building simulation, validation.

SUMMARY:
The use of Double Skin Façade (DSF) has increased during the last decade. There are many reasons for this including e.g. aesthetics, sound insulation, improved indoor environment and energy savings. However, the influence on the indoor environment and energy consumption are very difficult to predict. This is manly due to the very transient and complex air flow in the naturally ventilated double skin façade cavity.

In this paper the modeling of the DSF using a thermal simulation program, BSim, is discussed. The simulations are based on measured weather boundary conditions, and the simulation results are compared to e.g. the measured energy use for cooling, air temperature, temperature gradient and mass flow rate in the DSF cavity, etc.

The thermal simulation program does not at the moment include a special model to simulate the DSF. However, the results show that it was possible to predict the energy flow, temperature distribution and airflow in the DSF. Some agreement between the measured and simulated results was unfortunately very sensitive to the model. This implies that without the possibility to calibrate the simulation model with measured data the risk of generating poor results is imminent. Therefore further work including both measurements and more detailed and robust simulation programs are necessary.

1. Introduction

Double Skin Façade (DSF) is a relatively young concept, which is distinct from the conventional buildings by its ability to react to and to take advantages from various weather conditions. The use of double-skin façade has increased during the last decade. There are many reasons for this including e.g. aesthetics, sound insulation, improved indoor environment and energy savings. Due to the numerous functioning modes, every double-skin façade building is unique in its physics and performance. Compared to a conventional glazed building and depending on the functioning mode, DSF can function as a barrier for solar radiation or it can preheat the ventilation air; DSF can reduce the penetration of noise (i.e. traffic) from the outside; it can improve perception of comfort (increased surface temperature of the glazing); it allows for application of night cooling and at the same time it is burglary safe; in some cases, it gives better possibility for fire escape and fire protection; it provides better protection of shading devices and allows to open windows on the top floors in a multistory building.

Energy efficiency of the DSF, however, is difficult to achieve due to the lack of a suitable simulation tool, able to deal with the very transient and complex air flow in a ventilated double skin façade cavity. As pointed out by H. Manz and Th.Frank:*"…the thermal design of buildings with the DSF type of envelope remains a challenging task. As, yet, no single software tool can accommodate all of the following three modeling levels: optics of layer sequence, thermodynamics and fluid dynamics of DSF and building energy system"* (Manz and Frank, 2005).

The DSF-buildings are extremely dynamic, especially, if the cavity is naturally ventilated. DSF continuously adjusts its performance not only to the solar irradiation, but also to the highly fluctuating natural driving forces. Due to the extreme dynamics of the system, the changes happen very rapidly and they can rarely be smoothed in time. Consequently, any shortcomings in the design will result in increased energy use and increased temperature fluctuations in the occupied zone.

In the DSF-building the great part of the energy flow happens through the DSF construction and, for that reason, it is extremely important to be able to predict its performance. The main difference between the DSF and a conventional window is that in case of DSF it is difficult to estimate what part of the solar heat gains that will penetrate through the DSF into the adjacent zone and what part of solar gains will be captured by the DSF and then removed with the cavity air. At the same time: "*global heat transfer coefficients, such as overall heat transfer coefficient (U-value) and the solar heat gain coefficient (g-value) cannot be directly applied to ventilated facades*"(Faggembauu, et al., 2003) as these are standard coefficients, which *assume steady state and one directional heat flow.* These coefficients are only wise to apply as characteristics of DSF constructions, yet not as an overall attribute of DSF.

However, U-value and g-value are inevitable inputs in the majority of thermal building simulation tools, so it is important to be aware that: g-value expresses the amount of solar radiation, which is transmitted to the room through the fenestration plus amount of solar radiation absorbed by glass and then re-transmitted towards the interior mainly by means of convection and radiation.

In this case the convective and radiative surface heat transfer coefficients are considered to be characteristic for a building. However, these differ a lot for DSF, since the surface temperature of the glazing and shading in DSF increase significantly with the height of the cavity. Thus the local g-value of the glazing may differ a lot, as well as the actual area averaged g-value of the glazing, compared to its characteristic g-value, normally provided by a producer.

The convective heat transfer contribution to the g-value is also important, since the air velocities in the DSF cavity are normally higher than the ones in a conventional room and the surface temperatures of the glazing/shading can also become relatively high. Finally, the convective and radiative heat transfer contribution in the actual g-value are not straight forward and the g-value is actually varying in time, and depends not only on angle of incidence, but also on surface temperatures and mass flow rates.

Surface heat transfer is also included into the U-value characteristic and therefore the same limitations are valid if it is necessary to estimate an actual U-value of the DSF constructions.

On the whole, the complexity of the DSF concept has already been realized and, in the literature (Gertis, 1999, Saelens, 2002, Zöllner, 2002 and the others) one can frequently meet a request for validation of the building simulation tools for DSF modeling in order to evaluate the limitations of the software.

This paper describes an empirical validation process of the Danish building simulation tool, BSim, where a model of a DSF-building is built up to simulate the outdoor DSF test facility, 'the Cube'. An attempt is also made to demonstrate that the modeling of the DSF requires not only a reliable tool and experience in its application, but also special attention to the input of the DSF constructions properties.

2. Empirical data

In the fall of 2006, a set of experiments was conducted in the outdoor DSF test facility 'the Cube', see Figure 1. An empirical dataset is now available for two double-skin façade functioning modes: thermal buffer mode and external air curtain mode, however only the results for the external air curtain mode are reported in this paper. In this mode, the external operable windows at the top and bottom of the cavity are open to the outside, the air enters the DSF at the bottom of the cavity, heats up when passing through the DSF cavity and then released through the top openings to the external environment, carrying away some amount of the solar heat gains. The flow motion in the cavity is naturally driven.

The empirical data set is available for a 2 weeks period, starting from 1st of October until 15th of October and includes all necessary weather data, such as wind speed, wind direction, outdoor air temperature and humidity, total and diffuse solar irradiation on a horizontal surface, ground temperature under the foundation and atmospheric pressure.

The air temperature in the DSF cavity, vertical temperature gradient in the cavity, surface temperatures of the glazing, mass flow rate in the DSF are available in the empirical data set. During the experiments, the air

temperature in the room adjacent to the DSF cavity was kept constant at 22°C. The cooling/heating power load to the room was measured and included into the empirical data set as a parameter that reflects the performance of the DSF.
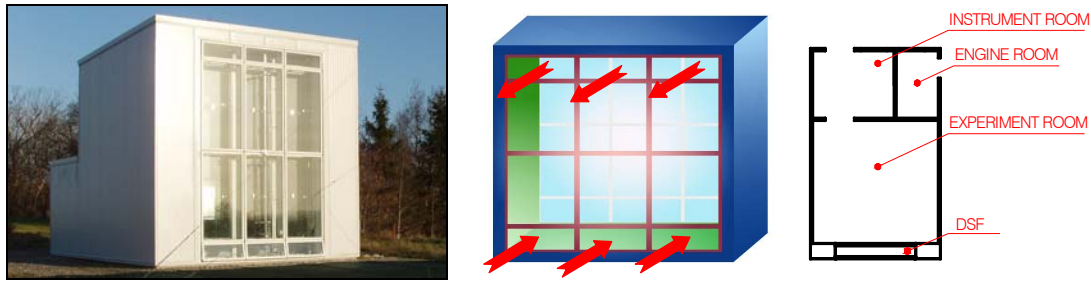
Figure 1. 'The Cube' (left). Illustration of principle of the external air curtain mode (centre). Plan of 'the Cube' (right).

Thermal properties of all constructions in the test facility, its detailed geometry and dimensions were documented during the construction and were updated later during the preliminary measurement phase (see more in Kalyanova, et al. 2008). The spectral properties of the window glazing were tested at the EMPA Materials Science & Technology Laboratory. The information about the optical properties of the surfaces is available as a function of the wave length, in the wave length interval 250-2500nm for the following surfaces: Glazing, Ceiling and wall surface finishing in the DSF; Ceiling and wall surface finishing in the experiment room; Carpet in front of 'the Cube'.

No shading devices were used during the experiments.

3. BSim

BSim is an ISO STEP based, integrated building design tool, BSim (Wittchen et al. 2005). The core of the design tool is a common building data model shared by the different design tools, and a common database with typical building materials, constructions, windows and doors. Figure 2 illustrates the user interface of BSim.

In BSim the direct solar radiation is calculated every ½ hour based on the actual position of the sun. The surfaces where the ray of sunshine hits is also the surfaces that receive the energy and it is possible to have light passing through a room without affecting the heat balance. The diffuse radiation from the sky entering a zone is distributed according to a chosen weight factor.

Calculation of heat flow from a surface is based on dynamic calculations of both the convective heat transfer coefficient and long wave heat exchange. The convective heat transfer coefficients are calculated based on empirical correlations, mainly using dimensionless numbers. This means that the limitations discussed previously are not applicably to the calculation of U-value for BSim, but are for the calculation of the g-value.
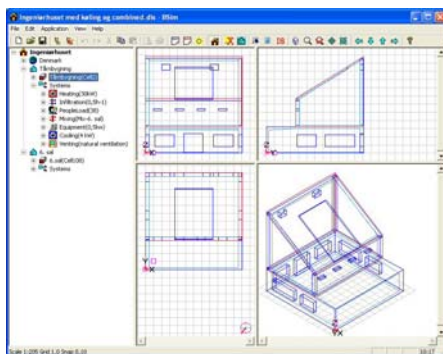
Figure 2. SimView, the user interface of BSim for editing and viewing the layout of the building.

4. BSim model

The model where constructed according to the documented geometry and thermal properties of the constructions in 'the Cube'. It consists of four thermal zones (Figure 1):

- double-skin façade (DSF)
- experiment room
- instrument room
- engine room

Since the thermal simulation program does not, at the moment, include a special model to simulate a DSF unit, the double-skin façade was modelled identically to any other thermal zone. .The external dimension of the experiment room together with the DSF is 6x6x6m. Internal dimensions of the DSF cavity is 0.56m depth, 5.5m height and 3.2m width. The main thermal characteristics of the building and model are available in Table 1.

Table 1. Thermal characteristics of 'the Cube'.

Terrain type	Scattered windbreaks
Longitude	9°59'44.44"E
Latitude	57°0'41.30"N
Total area of windows (visible glazing)	6·3.229(2.693) m^2
Total area of top openings open	0.32 m^2
Total area of bottom openings open	0.39 m^2
External windows of DSF	Clear glass
Internal windows of DSF	4-Ar16-4
U-value of external windows	5.33 W/m^{2}K
U-value of internal window	1.39 W/m^{2}K
U-value of external walls	0.08 W/m^{2}K
U-value of the floor construction	0.15 W/m^{2}K
g-value of external window	0.8
g-value of internal window	0.63
Net volume of DSF	11.24 m^2
Net volume of exp.room	143.11 m^2

Table 2. Weather conditions during the experiments.

Mean outdoor air temperature	Mean wind speed	Mean diffuse solar irradiation	Mean total solar irradiation on horizontal
^{o}C	m/s	W/m^2	W/m^2
12.5	3.6	91*	175*

* Mean for solar irradiation is given only for the periods with sun.

Simulation period was set according to the length of the weather file for the external air curtain mode (01.10.2006 – 15.10.2006), using the weather data file to define the outdoor thermal conditions.

Available weather data includes a wide spectrum of various thermal conditions: periods with high direct solar radiation, with high diffuse solar radiation, cool and warm outdoor air temperature, various wind directions and wind speeds. This allows to scrutinize the model for different circumstances. In the model, the air temperature in the experiment room was set to 22°C.

No shading devices were included in the model. Natural ventilation mass flow rate in the DSF cavity is defined via the area of the openings, height of the openings, discharge coefficients and pressure coefficients. The discharge coefficient of the top and bottom opening was measured prior to the experiments in a wind tunnel. In BSim, surface average pressure coefficients are used. Therefore the calculated airflow in the DSF is mainly dependent on the calculated thermal driving force.

5. Comparative and Empirical Validation

Prior to the empirical model a set of the comparative test cases were completed with BSim software in the framework of IEA Annex 34/43, subtask E. The subtask was focused on validation of building simulation

software for modeling of DSF. Comparative exercises were completed by five different organizations, using different building simulation tools to simulate 'the Cube'.

Completed set of the comparative exercises has demonstrated the magnitude of differences between different building simulation tools and have confirmed the complexity of the task to simulate building with a double skin façade. The most important achievement in the comparative exercise was the experience gained by the modelers regarding DSF modeling, the justification of their models against each other and, finally, the demonstration of how important it is to conduct further empirical validation for modeling of buildings with the DSF, and thus to provide the reference against which modeling predictions could be compared. The empirical model which simulations are presented in this paper was prepared based on the comparative validation results, hence it has been justified against the other models, and the errors have been eliminated.

The empirical validation was completed in the 'blind'-form, which means that the modeler received the experimental results only after submitting the results of simulations.

The building simulation tools can also be validated on their performance *together with their limitations,* yet the best possible software performance must be achieved. Considering limitations of various software tools the quantitative measure for the empirical validation should be chosen between the global parameters, as the accuracy in predictions of minor parameters can be limited.

Only simulation results for the global parameters are reported here. These are the power loads to the experiment room, the air temperature and the mass flow rate in the DSF cavity. Although the experimental data is available for many other parameters such as surface temperatures of the glazing, walls, etc. these are not included into the list of global parameters. The reason for this, is that the resulting surface temperatures, for example, depend on computations and assumptions in a model, such as distribution of solar radiation and shadow to the surfaces, level of detail in longwave radiation exchange calculation, flow regime at the surface and assumptions made towards the calculation of the convective heat exchange at the surface etc. These computations and assumptions vary from one tool to another, but in a larger perspective, the ability of a building simulation tool to model DSF is expressed by its ability to accurately predict the power loads in the building.

The air flow rate in a double skin facade cavity is rather high compared to the temperature difference between the air in the cavity and outdoor therefore it is essential to perform the empirical validation of the air temperature predictions in the models via *'the temperature raise in the DSF '* to track the amount of energy transported by the air flow. Due to the magnitude of mass flow rate, an error in prediction of the air temperature in the range of 1°C can mean hundreds of watts of error in energy balance.

Figure 3 illustrates the temperature raise in the DSF cavity above the outdoor air temperature and power loads to the experiment room for two days with the principally different boundary conditions:
- 10th of October – a day with high direct solar radiation
- 11th of October – a day with mainly diffuse solar radiation
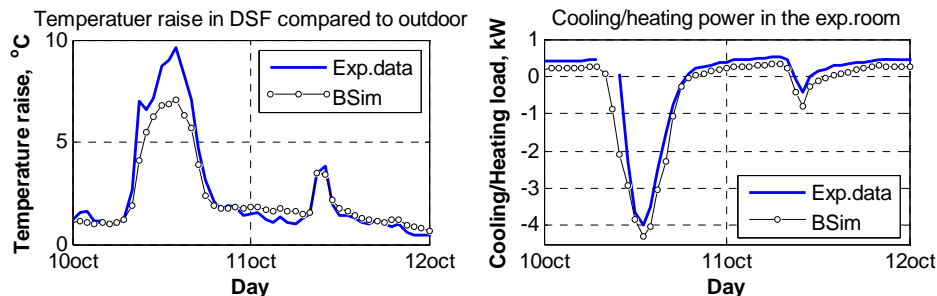
Figure 3.Measured and simulated temperature raise in the DSF cavity compared to outdoor air temperature (left). Measured and simulated power loads to in the experiment room (right).

The power loads in the experiment room vary between day and night time period. Normally the experiment room was cooled during day- and heated during night-time.

The BSim model underestimates the heating loads during night time since the thermal bridges were not included into the model, while days with strong direct solar radiation, cooling loads are overestimated. This, however, depends not only on predicted air temperature in the DSF cavity and mass flow rate, but also on the amount of

solar radiation that has been transferred into the experiment room in the first order of solar transmission, as this part does not influence the calculation of the air temperature and mass flow rate in the DSF cavity.

Cooling load in the experiment room is, still, the result of interplay of many parameters, such as mass flow rate in the cavity, convection and radiation heat transfer, transmission of solar radiation etc. At the same time, it is not possible to validate all of these parameters separately, as many of those are the challenge for the whole field of building simulations. Calculation of natural ventilation is particular interesting: as the natural mass flow rate is exceptionally difficult to simulate, yet, it is one of the key actors in DSF performance. So, the mass flow rate was chosen as one of the main targets in evaluation and validation of BSim model.

In Figure 4 it is shown that prediction of the mass flow rate in the DSF cavity is not good enough and, as a consequence, predictions of the air temperature in the cavity and power loads in the experiment room can not be regarded as reliable. The reason for flawed performance of the BSim model towards the mass flow rate calculations is the simplified model for calculation of the naturally driven flow. BSim uses an empirical expression for single sided natural ventilation at different levels. Accordingly, the impact of wind pressure in the model is almost negligible, as in BSim, the average surface pressure coefficients are used. This is in large contrast to the experimental data, as the mass flow rate in the DSF cavity was driven by both buoyancy *and wind*, see Figure 7. In the figure, it is seen that the major part of experimental data is available for the wind dominated or assisted driving forces, although it is common to assume that the mass flow rate in a double-skin façade cavity is buoyancy driven. In the Figure 7 (left) it is also illustrated what was the expected mass flow rate in the cavity if the wind force is neglected.
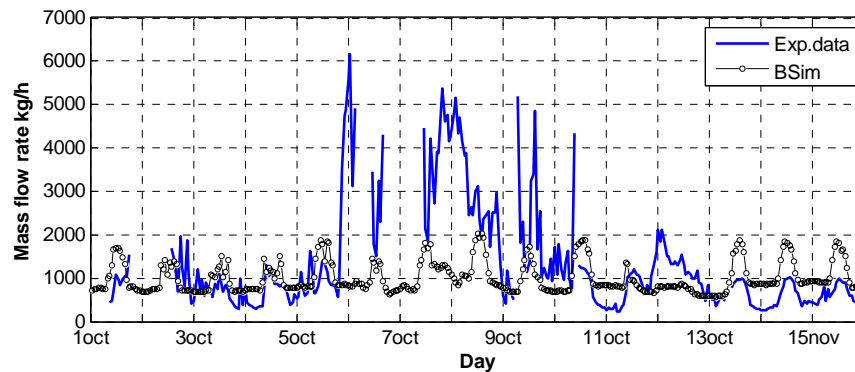
Figure 4. Mass flow rate in the DSF cavity measured with the tracer gas method and simulated in BSim.
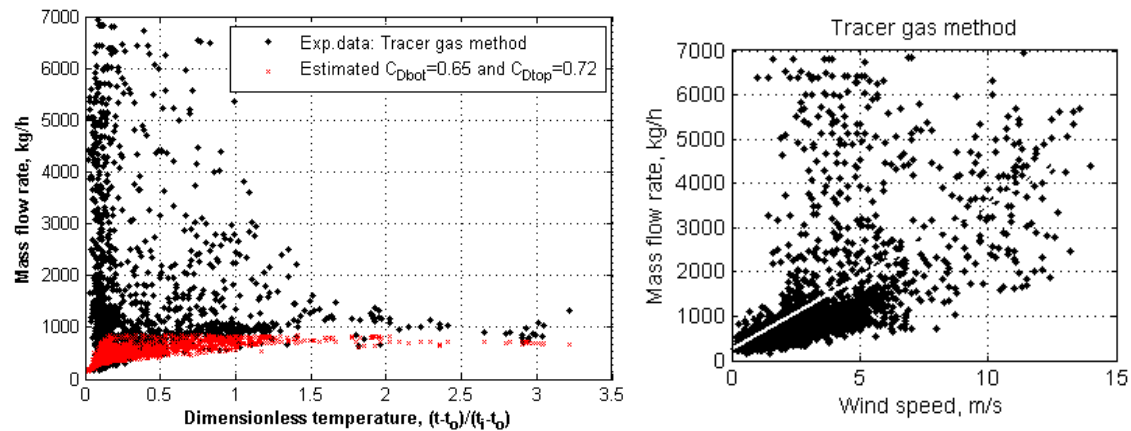
Figure 5. Illustration of the estimated mass flow rate in the DSF cavity for pure buoyancy natural ventilation (left). Mass flow rate as a function of the wind speed- experimental data (right).

When the results from the simulations where compared against the experimental data, then the information about the measurement procedure and experimental set-up can be critical for evaluation of measurement accuracy and the possibility of error. Overall, the main details of measurement procedure were explained in Kalyanova et al.

(2007) and possible errors in the measurements of the mass flow rate measurements were also discussed in the paper.

6. Example

It is important to remember that the performance of the DSF and comfort conditions in the occupied zone in the experiment room, on the preliminary design stage, are defined via the internal window and external window thermal and optical properties. Optical properties mainly determine what fraction of solar radiation is to be kept in DSF and what fraction is to be transferred further. In a detailed model this is done via the transmission, reflection and absorption properties of the glazing, in a simplified model this is done via the g-value. The thermal properties of windows, besides the magnitude of heat transfer, determine also the relationship between the outdoor-DSF and DSF-adjacent room and how fast one thermal zone reacts to the changes in another one.

BSim, as many others building simulation tools uses the g-value for calculation of solar gains into a thermal zone and therefore the software's ability in accurate estimation of secondary solar gains is limited, also, there are no studies available able to asses the impact of this limitation. Whereas the model of a DSF building can be very sensitive to the g-value input in the model.

Table 3. Test cases with modified g-value

Model	g-value	
	External window	Internal window
Low (**L**)	0.75 (-6%)	0.53 (-16%)
Normal (**N**)	0.8 (100%)	0.63 (100%)
High (**H**)	0.85 (+6%)	0.73 (+16%)
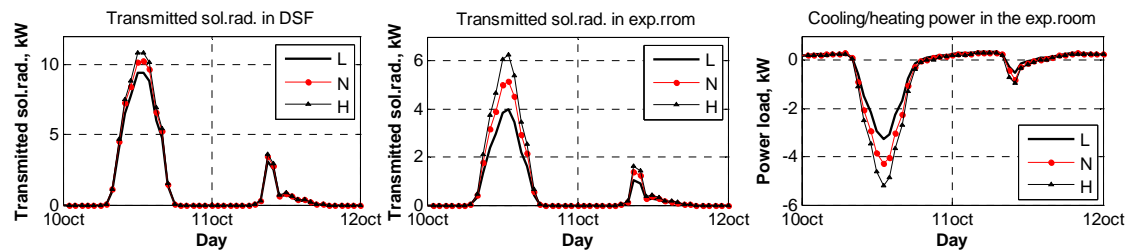
Figure 6. Simulation results for the test cases with different g-value of the glazing.

In this section, a simple sensitivity study was made to investigate how the small variation of g-value in a model will affect the output. Additional simulations have been made, all of them were based on the BSim model described earlier in the paper and only the changes of the g-value took place in the model. Considered cases are explained in Table 3.

In the Figure 6 the results of the simulations from three cases are illustrated. The figure includes results for two days: a day with clear sky and a day with the heavy cloud cover. It must be mentioned, that the changes, given in Table 3, were applied simultaneously to the external and internal window, i.e. the test case Low (L) represents a model, when the g-value of both the internal and external window was reduced as in the Table 3. From the figure, it can be seen that 6% reduction of the g-value of external window, results in 1.5 kW deviation in solar gains to DSF, if compare between test case Normal and test case Low. Comparing the impact of the g-value modification on the solar gains to the experiment room, one can see that the cooling load has changed ±1 kW, depending on the test case. This example, of course is very plain, but the point was to demonstrate the sensitivity of the model to the input parameters associated with heat transfer through the windows in a DSF envelope. Also, this example is limited to the g-value only, which combines together the optical and the thermal properties of the glazing, while repeating of the same study, varying the reflectance/absorbance/transmittance properties of the glazing and convective/radiative surface film coefficients in the model would lead to better technical insight to DSF envelope.

In the Figure 7 it is shown the difference between the test cases when considering the whole set of experimental data. Total cooling load for the whole period, when the normal solar radiation (I_{ns}) is higher than its mean value, represents the differences between the test cases of apx. 40 kWh during two weeks. These are the differences in cost to have a cooling unit running in order to maintain comfort conditions in the experiment room. However, this requires an ideal AC-system that can react immediately to the conditions in the zone. Mean cooling loads in

the experiment room are also given in the Figure 7, which demonstrates the difference in the dimensioning of the cooling system if the results of one or another test case is used.

$I_{ns} >$ mean I_{ns} - for the periods when normal solar radiation is higher than mean normal solar radiation
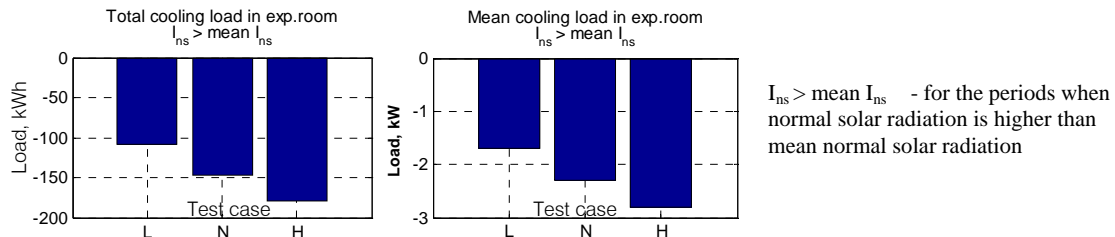
Figure 7. Mean and total cooling load to experiment room for the whole set of experimental data.

The U-value of a window construction, generally, is higher than the U-value of wall construction, also the area of windows in the DSF buildings is high, for example for 'the Cube' (when the outer skin of the DSF is neglected):

$$\sum A_w U_w = 26.06 \; \frac{W}{K} \qquad \sum A_c U_c = 14.329 \; \frac{W}{K}$$

A_w, U_w -area and U-value of a window in 'the Cube'
A_c, U_c -area and U-value of a constructions in 'the Cube'

Accordingly, the heat transfer through the DSF envelope is a significant part of the overall heat transfer in the experiment room and therefore minor inaccuracy of the input parameters can lead to wrong estimation of the energy use.

In this example, the authors have demonstrated the consequence of small errors present in a model when a building with the DSF is simulated. It was shown that even small uncertainties in the thermal properties of windows can be particularly significant for the simulation of energy performance in a DSF building. Hence, a modeler must be certain to use the exact properties of the window construction in his model. In conclusion, it is necessary to say that such a sensitivity of a small and simple model to the input data is exceptionally difficult to work with in practice, as there is a high risk of generating poor results if the simulation model has not been calibrated against experimental data. Also, one must bear in mind, that erroneous results in simulations of DSF buildings are not caused by the wrong input data only, but also the assumptions made towards the convective/radiative heat transfer, mass transfer etc. are very significant. Since these assumptions are very difficult to decide on and there are no guidelines exist, then the assumptions must be empirically validated, as a part of complete model. Empirical validation of each and every DSF model is time consuming and unrealistic in practice. Therefore further work including both measurements and more detailed and robust simulation programs are necessary.

7. References

Gertis K. (1999). Sind neuere Fassadenentwickelungen bauphysikalisch sinnvoll? Teil 2: Glas-Doppelfassaden (GDF) (English translation), Bauphysik, vol. 21, pp. 54-66.

Kalyanova O., Jensen R.L. and Heiselberg P. (2007). Measurement of air flow rate in a naturally ventilated double skin facade. Proceedings of Roomvent 2007: Helsinki 13-15 *June 2007* . Finland: FINVAC ry.

Kalyanova O., Jensen R.L. and Heiselberg P. (2008). Data Set for Empirical Validation of Double Skin Facade Model. Nordic Building Physics Symposium 2008.

Kalyanova O., Poirazis H. and Heiselberg P. (2005). Literature Review of Double Skin Facades Modeling Approaches: Report for IEA ECBCS Annex 43/SHC Task 34 Validation of Building Energy Simulation Tools, Instituttet for Bygningsteknik, Aalborg Universitet.

Manz H. and Frank T. (2005). Thermal Simulation of Buildings with Double-Skin Facades. Energy and Buildings, 37 (2005) 1114-1121.Saelens D. (2002). Energy performance assessments of single storey Multiple-Skin Facades. PhD thesis, Catholic University of Leuven, Belgium.

Wittchen, K.B., Johnsen, K. and Grau, K. (2005). BSim - User's Guide, Danish Building Research Institute, Hørsholm, Denmark.

Zöllner A., Winter, E.R.F., and Viskanta, R.(2002). Experimental Studies of Combined Heat Transfer in Turbulent Mixed Convection fluid Flows in Double-Skin-Facades. International Journal of Heat and Mass Transfer 45 (2002) 4401-4408.

Data Set for Empirical Validation of Double Skin Facade Model

Olena Kalyanova, Ph.D-student,
Aalborg University;
ok@civil.aau.dk

Rasmus Lund Jensen, Research Assistant,
Aalborg University;
rlj@civil.aau.dk

Per Heiselberg, Professor,
Aalborg University;
ph@civil.aau.dk

KEYWORDS: Full-scale experiments, natural ventilation, air flow, temperature gradient, tracer gas, velocity profile, hot-sphere anemometer

SUMMARY:
During recent years, attention to the double skin facade (DSF) concept has greatly increased. Nevertheless, the application of the concept depends on whether a reliable model for simulation of the DSF performance will be developed or pointed out. This is, however, not possible to do, until the model is empirically validated and its' limitations for the DSF modeling are identified. Correspondingly, the existence and availability of the experimental data is very essential.

Two sets of accurate empirical data for validation of DSF modeling with building simulation software were produced within the International Energy Agency (IEA) Task 34 Annex 43. This paper describes the full-scale outdoor experimental test facility 'the Cube', where the experiments were conducted, the experimental set-up and the measurements procedure for the data sets. The empirical data is composed for the key-functioning modes of a double skin facade: 1. External air curtain mode, it is the naturally ventilated DSF cavity with the top and bottom openings open to the outdoor; 2. Thermal insulation mode, when all of the DSF openings are closed.

Available data sets consist of two groups of parameters, which were measured simultaneously. These are the parameters of boundary conditions and the parameters that reflect the DSF performance. The boundary conditions include the climate data, e.g. wind profile, outdoor temperature etc. Parameters of the DSF performance discussed in the paper are: temperature gradients in the DSF cavity, mass flow rate in the naturally ventilated cavity, surface temperatures, etc.

1. Introduction

The DSF concept is relatively young and belongs to the dynamic building systems, which act in unison with weather variation, taking the benefits from the outdoor climatic conditions. The DSF concept carries the notion of transparency, openness and intelligence, which are highly appreciated together with the concept's advantages, if well designed, in improving the acoustics, providing daylight and being energy efficient.

The design, dimensioning and application of DSF must be carried out meticulous, as insufficiencies will lead to an increased energy use (mainly for cooling) and inferior indoor climate. However, standard tools for designing conventional buildings are not sufficient enough when designing a DSF, as it requires results from detailed dynamic simulations.

In the literature one of the main problems reported regarding DSF modeling and simulations are the absence of experimental data (Gertis 1999, Saelens 2002). Most of the mathematical models have not been validated against empirical data and require an expert knowledge in the physics of DSF to perform the simulations. Consequently, the degree of confidence in the simulated results is rather low. There is a lack of systematic literature or

guidelines on how to model DSF and what are the most suitable tools to use, most of this is caused by the lack of empirical validations.

Still, DSF solutions are being proposed in the building design and erected, resulting in poor indoor climate and unnecessary energy use. It is therefore critical to expand knowledge about dimensioning of DSF buildings, to obtain some tools, which can help to optimize the performance of DSF systems.

To address the problem of lacking experimental data a wide range of measurements has been carried out in an outdoor, double-skin façade full-scale test facility 'the Cube'. This work has been conducted in the framework of IEA SHC Task 34 /ECBCS Annex 43 "Testing and Validation of Building Energy Simulation Tools".

2. Ventilation modes

According to the literature, there are many classification schemas exist for describing the DSF performance (Poirazis 2004, Loncour et al., 2004). However, focusing on the energy performance and flow path in the double skin façade, the DSF classification according to the ventilation principle is being used, as in Loncour et al., (2004):
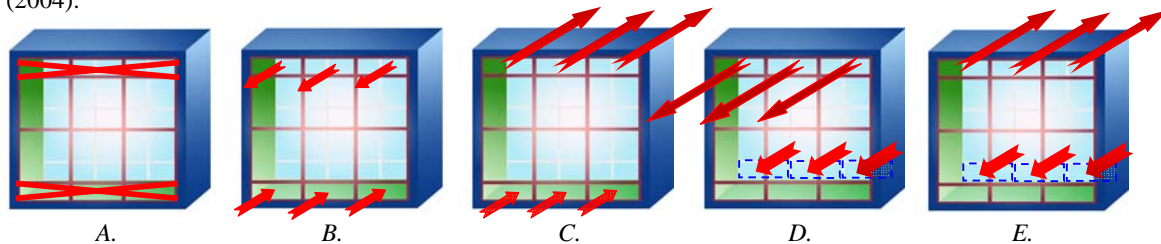
Figure 1. Classification of DSF according to ventilation principle. A- thermal insulation, B-external air curtain, C- preheating mode, D- exhaust mode, E-internal air curtain.

Due to the extremely time consuming and complex procedure involved in operating and data processing, only two ventilation modes were tested:

- External air curtain; (01.10.2006 – 15.10.2006)

- Transparent insulation mode/thermal buffer. (19.10.2006 - 06.11.2006)

MODE 1: External air curtain mode. The external operable windows at the top and bottom of the cavity were open, the air entered the DSF at the bottom of the cavity, it was heated while passing through the DSF cavity and then, released to the external environment, carrying away some amount of the solar heat gains. The flow motion in the cavity was naturally driven.

MODE 2: Transparent insulation mode. All the openings were closed. The principle of this mode is the same as of the conventional window. Air in the DSF cavity is heated to the temperature higher than the outside temperature, this decreases the radiant heat exchange between the internal window surface and the adjacent room.

3. Experimental test facility

'The Cube' is an outdoor test facility located at the main campus of Aalborg University. It has been built in the fall of 2005 with the purpose of detailed investigations of the DSF performance, development of the empirical test cases for validation and further improvements of various building simulation software for the modeling of buildings with double skin facades in the frame of IEA ECBCS ANNEX 43/SHC Task 34, Subtask E- Double Skin Facade.

The test facility is designed to be flexible for a choice of the DSF operational modes, natural or mechanical flow conditions, different types of shading devices etc. Moreover, the superior control of the thermal conditions in the room adjacent to the DSF and the opening control allow to investigate the DSF both as a part of a complete ventilation system and as a separate element of building construction.

The accuracy of these measurements is justified by the quality of the facility construction: 'the Cube' is very well insulated and tight.
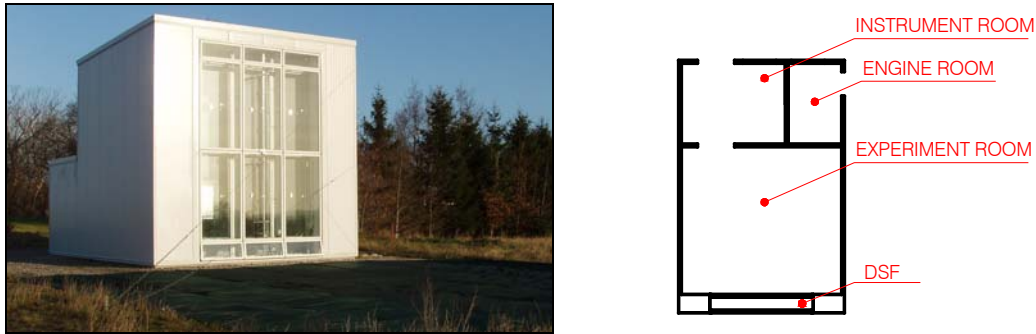
Figure 2. 'The Cube' (left). Plan of 'the Cube' (right).

'The Cube' consists of four domains, which are named as: Double Skin Façade, Experiment room, Instrument room and Engine room.

All openings of the double skin façade are controlled and can be operated separately. The combination of open openings defines the operative strategy of the DSF, see Figure 1. Depending on the mode of DSF performance, it can function as a barrier for the solar heat gains, as an additional insulation, can preheat the air coming into the occupied zone, etc. In any of the above cases, the DSF affects the thermal conditions in the experiment room.

The temperature in the experiment room can be kept constant, as there is a cooling unit installed in the engine room and a ventilation system with the heating and cooling unit installed in the experiment room, Figure 3. In order to avoid temperature gradients in the experiment room, a recirculating piston flow with an air speed of approximately 0.2 m/s is used. This resulted in typical temperature gradient of approximately 0.02°C/m and maximum of 0.1°C/m. The air intake for recirculation is at the top of the room, after the intake the air passes through the preconditioning units of the ventilation system and then it is exhausted at the bottom of the room through the fabric ke-low impulse ducts. Maximum power on cooling and heating unit is 10 kW and 2 kW respectively.

Figure 3. KE-low impulse fabric ducts in the experiment room (left, centre), Ventilation system in the experiment room (right).

Knowledge of solar radiation is crucial for the task of these experiments. However, in non-laboratory conditions the ground reflected solar radiation depends on the surrounding of the test facility and therefore it can vary a lot. For this reason, a large carpet was fixed on the ground from the side of the southern façade of 'the Cube' to achieve uniform reflection from the ground. The size of the carpet ensures a view factor between the DSF and the ground of approximately 0.5. Achieving of a reasonably higher view factor would require to double-up the carpet size.

The fabric of the carpet was chosen so that it does not change reflectance property when it is wet due to its permeability and have reflectance property of apx. 0.1, close to the generally assumed reflectance property of the ground. The carpet is also seen in the Figure 2.

Absorption, reflection and transmission properties of all the surfaces in the DSF, experiment room and windows were tested at the EMPA Materials Science & Technology Laboratory. This was also the case for the ground

carpet. The information about the optical properties of the surfaces is available as a function of the wavelength, in the wave length interval 250-2500nm.

4. Preliminary tests

A number of preliminary experiments were completed before the final experimental set-up. Preliminary experiments were focused on improvements and "calibration" of the test facility, improvements of measurement techniques and on best suitable positioning of equipment.

The air tightness of 'the Cube' was measured during construction, insulation and air tightening of the test facility, before and after installation of the experimental setup to ensure the tightness. The final infiltration rate was 0.3 h^{-1} at 100 Pa. Transmission heat losses were estimated for two set points, when the difference between the air temperature in the test room and outdoors was $16^{o}C$ and $21^{o}C$ resulting in a heatloss of 0.26 $W/(m^{2o}C)$. These tests have confirmed that 'the Cube' is extremely tight and well insulated.

5. Experimental data sets

5.1 Measurement conditions

Duration of each experiment was approximately 2 weeks and started in fall 2006. Since the autumn/spring season represents the most complete spectrum of the DSF performance, the experiments were carried out in autumn. Contrary to summer, climatic conditions in early autumn (or late spring) are more inconsistent, there are many periods with large cloud cover of the sky, while the solar radiation intensity with the clear sky can still be relatively strong, the temperature variation between day and night time is more considerable and, consequently the day time periods may lead to significant solar heat gains, while the night time periods may lead to significant heat losses if the DSF performance has not been optimized.

The air temperature, air flow rate in the cavity and, correspondingly, the amount of surplus heat gains removed with the cavity air are the main measures of the double skin façade performance, and also it can be used as a measure for validation of a building simulation tool for modeling of a DSF performance. The air temperature in the experiment room of 'the Cube' was kept uniform and constant at approximately $22^{o}C$ to minimize the influence of the interior environment on DSF performance.

Both, the interior and exterior environment define the boundary conditions for the DSF, and the detailed knowledge of those was essential for further application of the experimental results and evaluation of the DSF performance.

The surplus solar gains into the experiment room were measured indirectly, by assessment of the total cooling power delivered to the experiment room in order to keep the air temperature constant. All of the equipment in the experiment room, which function as a heat source, was connected to the wattmeter to keep track of all loads and losses in the room.

5.2 Boundary conditions

5.2.1 Wind speed, wind direction and mean wind speed profile

The natural wind speed varies in time and space, the character of its variation is highly random and the wind flow is highly turbulent. At the same time, the wind speed is one of the main contributors to the natural ventilation flow.

The change of the mean wind velocity depending on height and intervening terrain is expressed through the mean wind speed profile. Once the mean wind speed profile is identified based on a wide spectrum of wind velocities and wind directions with a substantial number of measurement points, then the wind profile turns to be one of the characteristics of the test facility.

Experimental data for the vertical wind speed profile covers a measurement period from 1st of June 2006 until 1st of January 2007. This period includes various wind directions and wind speeds. Wind velocity and wind direction was measured in six points above the ground in order to build a vertical wind profile. Both 2D and 3D ultrasonic anemometers were placed on the mast in the centre line of the building, 12m away from its South façade (Figure 4). The sampling rate was 5 Hz.
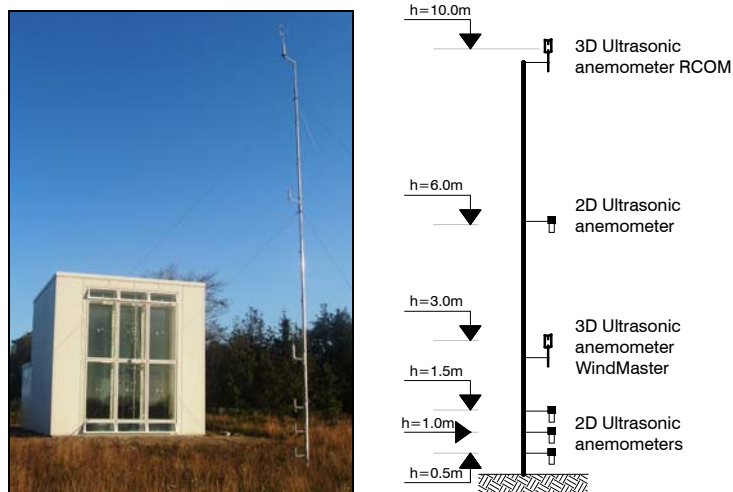
Figure 4. Wind mast in front of 'the Cube' (left). Positioning of equipment on the mast (right).

5.2.2 Outdoor air temperature, air humidity and solar radiation

Outdoor air temperature was measured using two thermocouples type K at the height of 2 m above ground. Air humidity of the outside air was measured continuously for completing the list of required climate data parameters for building simulation tools. Outside air humidity was measured every 10 minutes.

For purpose of weather data assembling two pyranometers were placed horizontally on the roof of 'the Cube'. BF3 pyranometer measures Global and Diffuse solar irradiation on the horizontal surface. Another pyranometer, Wilhelm Lambrecht, measures only Global solar irradiation on the horizontal surface and was placed on the roof for control of BF3-readings. In the Table 1, the weather boundary conditions are divided into two groups, corresponding to each test mode.

Table 1. Weather conditions during the experiments.

MODE	Mean outdoor air temperature	Mean wind speed	Mean diffuse solar irradiation on horizontal	Mean total solar irradiation on horizontal
	^{o}C	m/s	W/m^2	W/m^2
1	12.5	3.6	91*	175*
2	9.6	5.2	58*	89*

* Mean for solar irradiation is given only for the periods with sun.

5.2.3 Air temperature and vertical temperature gradient in the DSF cavity

Direct solar radiation is an essential element for the façade operation, but it can heavily affect measurements of air temperature and may lead to errors of high magnitude using bare thermocouples. A number of tests were carried out preliminary to the experiments, where various techniques were investigated on their ability to shield thermocouples from direct irradiance, in order to achieve an accurate and reliable way to measure the air temperature reducing the error caused by radiation (Kalyanova et al., 2007). As an outcome of these tests, all of the thermocouples placed free in the DSF cavity were protected: thermocouples were coated with silver, shielded from direct solar radiation by a silver-coated tube, which was continuously ventilated by a minifan, see Figure 5. The air temperature in the DSF cavity was measured at six different heights in the centre line of the cavity. The measurements were carried out with the sampling frequency 5Hz and averaged for every 10 minutes.

The dimensionless air temperature was used to investigate the vertical temperature gradients in the DSF cavity, the definition of it is given in equation 1.
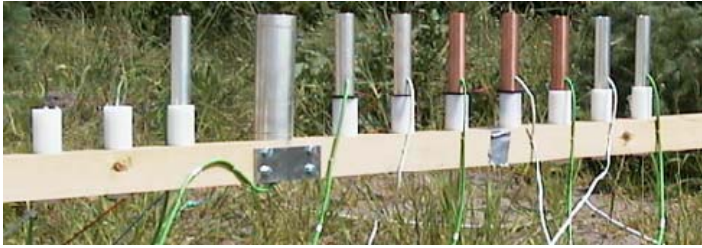
Figure 5. Experimental setup: testing of shielding techniques for air temperature measurements under direct solar access.

$$t_{\mathrm{dim}} = \frac{t_h - t_o}{t_i - t_o} \tag{1}$$

t_h - temperature in the DSF cavity at the height h, $^{\circ}$C

t_o - outdoor air temperature, $^{\circ}$C

t_i - indoor air temperature (in the experiment room), $^{\circ}$C
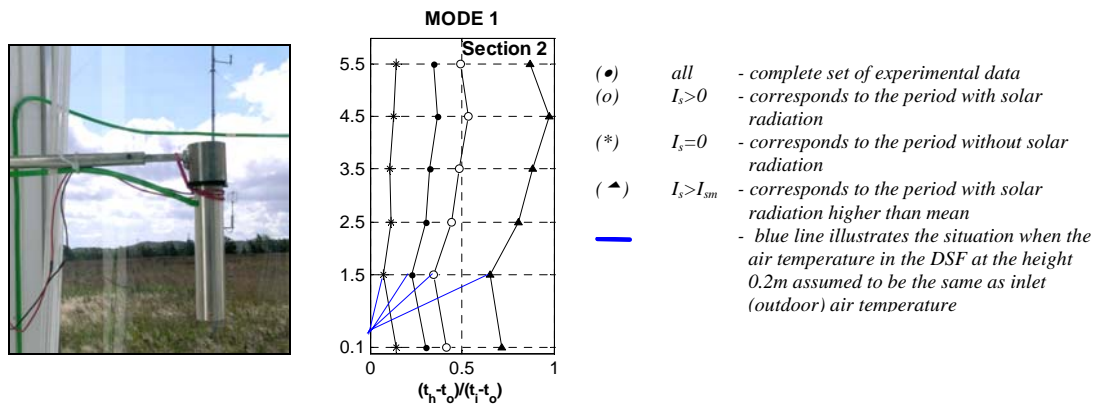
Figure 6. Silver coated ventilated tube for shielding a thermocouple from solar radiation (left). Dimensionless temperature gradient in the DSF cavity in the MODE1 (right).

For all sections the measurements at the bottom of the cavity were at the height of 0.1m above the floor. Looking upon the dimensionless profiles (Figure 6) it is possible to observe that the air temperature measured at the bottom of the DSF is relatively high. This is likely to be an experimental error. If the inlet air temperature is assumed to be the same as the outdoor air temperature, then it is reasonable to approximate the dimensionless air temperature in the centre of the inlet opening to zero (at the height 0.2m), which is illustrated with a *blue line*.

5.2.4 Surface temperature of the glazing

Measurement of glazing surface temperature was performed in the centre of a glazing pane for each large window section. The temperature was measured at: the internal surface of the inner window (ii), the external surface of the inner window (ei), the internal surface of the outer windowpane (ie).

This measurement was conducted with sensors shaded from direct solar access. Continuous shading of the thermocouple sensor at the inner pane (ie) was ensured by a thin aluminium foil fixed around the sensor at the external surface. As a result, the foil shaded both a sensor at the external (ie) and internal (ii) surfaces. The thermocouple at the internal surface of the outer pane (ei) was shaded in a similar way by a piece of aluminium sticky tape on the external surface of the outer pain.

5.2.5 Mass flow rate in the DSF cavity

Assessment of the air change rate is crucial for the evaluation of indoor climate and the performance of a double skin façade. As a result, the air change rate repeatedly becomes a target for measurement, prediction and simulation. In the meantime, the air flow occurred in the naturally ventilated spaces is very intricate and

extremely difficult to measure. The stochastic nature of wind and as a consequence non-uniform and dynamic flow conditions in combination with the assisting or opposing buoyancy force cause the main difficulties. There were three techniques used for the air flow measurements, but only two of them were successful:

Velocity profile method. This method requires a set of anemometers to measure a velocity profile in the opening, and then the shape of the determined velocity profile depends on amount of anemometers installed. Instead of placing equipment directly in the opening in the case of the double skin façade, it can be placed in the DSF cavity, where the velocity profile can be measured in a few levels instead for one.

Tracer gas method. This method requires the minimum amount of measurements and equipment, but it is characterized with frequent difficulties to obtain uniform concentration of the tracer gas, disturbances from the wind washout effects and finally with the time delay of signal caused by the time constant of gas analyzer. The constant injection method (Etheridge, 1996) was used in the experiments.
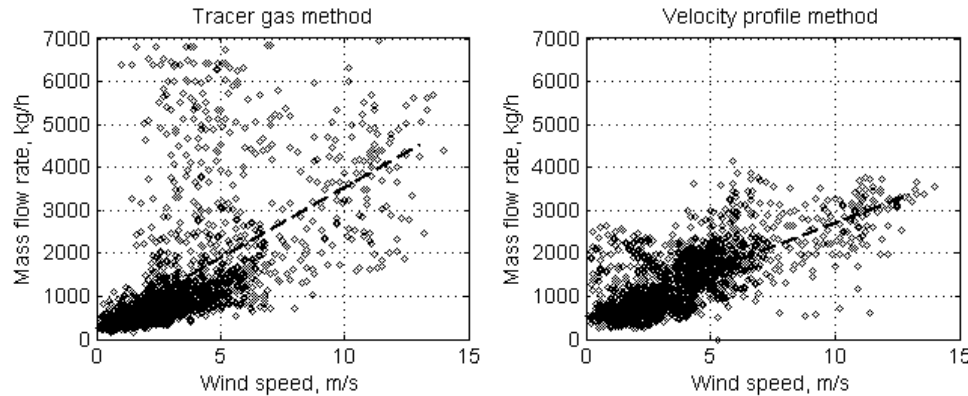
Figure 7. Mass flow rate measured in the DSF cavity with the tracer gas method (left), velocity profile method (right) and illustrated as a function of the wind speed. MODE 1.
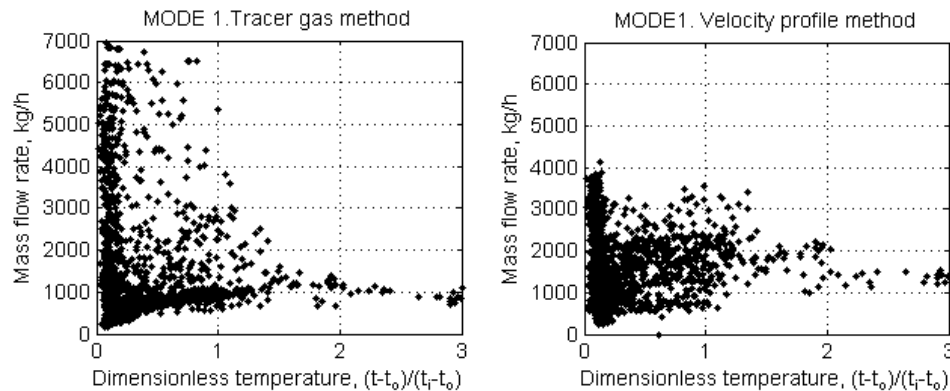
Figure 8. Mass flow rate measured in the DSF cavity with the tracer gas method (left), velocity profile method (right) and illustrated as a function of dimensionless temperature in the cavity. MODE 1.

In the Figure 7 and Figure 8, it is illustrated that the major part of experimental data is available for the wind dominated driving forces, although it is common to assume that the mass flow rate in a double-skin façade cavity is buoyancy driven. The wind impact is present even for the periods with relatively strong solar radiation.

Both of the measurement methods have sources of errors and comparing their outputs have some level of disagreement. However, the natural air flow phenomena is very complex and this results is the best approximation to the long time monitoring of natural air flow phenomena and can be used for experimental validation of numerical models of natural ventilation air flow, for more information see Kalyanova (2007).

5.2.6 Power loads in the experiment room

One of the main targets of this experimental work was to accurately estimate solar gains and heat losses by the room adjacent to the double skin façade, as these parameters independently reflect the performance of the DSF cavity. Their independence is assured by the minimized influence of the experiment room on the DSF performance, as the thermal conditions in the room were kept constant, no regulation of the window openings used and no shading devices installed, building is very well insulated and air tight, the air tightness of the building, the transmission heat losses are known and all influencing climate parameters were measured.

Water was used in the cooling unit of the ventilation system. With the purpose to avoid the condensation on the surface of the surface of the cooling unit, the minimum water temperature was set to 12^oC. The difference between the supply and return water temperature from the cooling unit in the experiment room was measured using one thermocouple type K with a maximum uncertainty of 0.1^oC. The mass flow of the water supplied to the cooling unit was measured with a water flow meter MULTICAL from Kamstrup, which measures in a range from 0 to 1 kg/s and calibrated to an uncertainty of $\pm0.1\%$ of the reading. Both the temperature difference and the water mass flow were collected by Helios data logger at a frequency 0.1 Hz.

The heating unit in the ventilation system was rarely activated, as in most cases, the additional heating load from the fan of the ventilation system in the experiment room ensured a sufficient cooling load. To keep a track on all loads to the experiment room, including the heating unit, all equipment in the room was connected to a wattmeter. The accuracy of the device was 0.1% of the reading (2.6 kW).

6. Summary

The details about the experimental test facility and experimental set-up, described in this paper, provide a good foundation for empirical validation of thermal building simulation tools for modeling double-skin façade buildings. In this work, extensive studies of the mass flow rate and air temperatures in the cavity and adjacent zone are supported with detailed information on the input parameters for a building thermal simulation tool. The generally rare experimental data for the DSF-buildings, containing results of the mass flow rate measured in a naturally ventilated are especially unique.

The experimental methods used for measurements do have sources of errors; the experimental results are limited in time and available only for certain boundary conditions. Nevertheless, the availability of these results are very important for further research within the DSF concept. Also, the results are usefull for further improvement of building simulation tools and models when predict the performance if the double-skin façade.

7. Anknowledgement

8. References

Gertis K. (1999). Sind neuere Fassadenentwickelungen bauphysikalisch sinnvoll? Teil 2: Glas-Doppelfassaden (GDF) (English translation), Bauphysik, vol. 21, pp. 54-66.

Kalyanova, O., Jensen, R. L. and Heiselberg, P. (2007). Measurement of air flow rate in a naturally ventilated double skin facade. Proceedings of Roomvent 2007: Helsinki 13-15 *June 2007*.

Kalyanova O., Zanghirella F., Heiselberg P, Perino M. and Jensen R. L. (2007). Measuring air temperature in glazed ventilated façades in the presence of direct solar radiation. Proceedings of Roomvent 2007.

Loncour X., Deneyer A., Blasco M., Flamant G. and Wouters P. (2004). Ventilated Double Facades. Classification & Illustration of façade concepts. Belgian Building Research Institute.

Poirazis H. (2004). Double Skin Facades for office buildings—Literature review, Report EBD-R-04/3, Division of Energy and Building Design, Lund University (2004).

Saelens D. (2002). Energy performance assessments of single storey Multiple-Skin Facades. PhD thesis, Department of Civil Engineering, Catholic University of Leuven, Belgium.

Analysis of the exterior convective heat transfer coefficients of a cubic building with CFD

Thijs Defraeye, Ph.D. Student,
Laboratory of Building Physics, Department of Civil Engineering, Katholieke Universiteit Leuven, Belgium,
thijs.defraeye@bwk.kuleuven.be

Bert Blocken, Assistant Professor,
Technische Universiteit Eindhoven, The Netherlands

Jan Carmeliet, Professor,
Chair of Building Physics, Swiss Federal Institute of Technology ETHZ, Empa, Swiss Federal Laboratories for Materials Testing and Research, Laboratory for Building Technologies, Zürich, Switzerland

KEYWORDS: exterior convective heat transfer coefficient, CFD, RANS, unsteady, wind flow.

SUMMARY:
Wind-induced convection at the exterior surface of specific building components or constructions has a noticeable effect on the heat transfer in the building envelope. Hence a proper knowledge of the convective heat transfer coefficients (CHTC) can improve the accuracy of numerical heat transfer modeling. In this paper, the forced CHTC on the surfaces of a cubic building is studied with CFD. Steady RANS (Reynolds-Averaged Navier-Stokes) simulations provide, for each facade, correlations of the surface-averaged transfer coefficient with the wind speed at a height of 10 m. These are compared with existing correlations. Results show a distinct variation of the values of the coefficient over the facade and significant differences are found between the surface-averaged transfer coefficients of the facades. RANS simulations are also compared with unsteady simulations with the Detached-Eddy Simulation (DES) model. The predicted transfer coefficients for DES and RANS are found to differ both in magnitude and distribution over the facades. Significant differences are found for the value of the CHTC on the windward facade which is partially attributed to the rather simplified inlet conditions that are used for DES. Nevertheless, a good similarity is found in the distribution over the windward facade for all models. In contrast to RANS, DES does incorporate the unsteady nature of the separated flow in the distribution of the heat transfer coefficient. This is clearly manifested in a more uniform and relative high CHTC on the leeward facade.

1. Introduction

The air flow along a building facade, due to wind and buoyancy effects, can have a significant effect on the heat transfer in the building envelope. This convective heat transfer is usually modeled by CHTCs which are readily used in hygrothermal analysis of building components or building energy calculations. They represent the major part of the overall exterior heat transfer coefficient, which also includes the radiative heat transfer coefficient, and consequently the CHTC will also affect the equivalent outside temperature. The CHTC is particularly relevant, under strong winds, for structures or building components that have a low thermal resistance such as glazed facades, greenhouses and solar collectors. For forced convection, these transfer coefficients are dependent on factors such as the wind speed, wind direction, surface roughness and the facade location. Nevertheless, CHTCs are generally reported as empirical correlations that are only a function of the wind speed measured at some distance from the surface, at a meteorological station or at a certain distance above the roof top. Usually, linear or power-law relationships are reported. These coefficients are generally taken to be uniformly distributed over the entire facade. The effect of wind direction is mostly taken into account by classifying it as windward or leeward, which is a rather crude approximation.

A lot of research on CHTCs was done by laboratory experiments on flat plates and some correlations were derived (Jürges 1924). For building applications, these correlations somehow lack physical similarity regarding the flow pattern. Moreover, these studies correlate the CHTC with the free-stream velocity along the plate which makes it difficult to relate the obtained correlations unambiguously to a velocity near the building surface. In most cases, the velocity near the building surface with which the CHTC is correlated is arbitrarily chosen.

Wind-tunnel experiments on cubes placed in a turbulent boundary layer have proven that a distinct variation of the CHTC can be noticed over each facade (Chyu and Natarajan 1991, Meinders et al. 1999, Nakamura et al. 2001, Nakamura et al. 2003), together with a dependency on wind direction. Although these experiments provide valuable information regarding the CHTC distribution, they were mostly carried out for rather thin turbulent boundary layers and at relatively low Reynolds numbers, compared to those encountered for real buildings.

Correlations were also obtained by full-scale experiments on buildings (Ito et al. 1972, Sharples 1984, Loveday and Taki 1996, Liu and Harris 2007). These however only provide data at a limited number of facade locations and inherently incorporate the effect of building geometry and the surroundings in the resulting correlations. Despite their limitations, the resulting correlations have been used for years in many design guides and building energy simulation programs. More detailed information on the CHTC distribution on building facades could contribute to the accuracy of the numerical models that use it.

Apart from experimental work, Computational Fluid Dynamics (CFD) work was also done to assess the effect of wind on the heat transfer at building facades (Emmel et al. 2007). In building aerodynamics, steady Reynolds-averaged Navier-Stokes simulations are commonly used to model air flow, combined with wall functions to take care of the boundary-layer region because of the low computational cost. The use of steady RANS however implies the complete modeling of turbulence by which none of it is actually resolved. Moreover the unsteady character of the flow is not taken into account which has proven to lead to unsatisfactory predictions of the flow field (Murakami 1993, Murakami et al. 1996, Iaccarino et al. 2003), and consequently of the CHTC. The flow unsteadiness is manifested by a periodic vortex shedding phenomenon in the wake of the building which affects the heat removal from the building facades. The unsteady behaviour can be modeled by using unsteady RANS (URANS) or more advanced turbulence modeling techniques, such as the Detached-Eddy Simulation (DES) model (Spalart et al. 1997), which is a hybrid RANS/LES (Large-Eddy Simulation) turbulence modeling technique. It uses RANS to take care of the near-wall region and switches to LES in the core region of the flow. LES implies resolving the large-scale, energy-containing eddies while the small-scale eddies are modeled by a subgrid-scale model. For more detailed information on the DES model, the reader is referred to Spalart et al. (1997) and Spalart (2001). Unsteady simulations could provide more realistic information regarding the transfer coefficients. Another important issue is the use of wall functions, with which the lower part of the boundary layer is modeled instead of resolved. Since the major part of the boundary layer's thermal resistance is found in this region, wall functions should be avoided when considering heat transfer (Murakami 1993). Instead of wall functions, low-Reynolds number modeling can be used.

In this paper, CFD is used to assess the CHTC distribution on the facades of a cubic building, placed in an atmospheric boundary layer. Steady RANS simulations are performed and correlations of the surface-averaged CHTC with the wind speed are provided for each facade. They are compared with existing empirical correlations. Moreover, the variation of the local transfer coefficients over the facade is presented. Afterwards, the steady simulations are compared with unsteady simulations with DES. The inlet conditions for DES are however specified in a rather simplified way. The influence of the latter on the results is discussed.

2. Numerical model

2.1 Geometry and boundary conditions

The building is a cube with a height of 10 m. The size of the three-dimensional computational domain is determined according to the guidelines by Franke et al. (2007) and is presented in **Figure 1**. A blockage ratio of 1.5 % is obtained, which is sufficiently low (Baetke et al. 1990). At the inlet of the domain, an atmospheric boundary layer is imposed. This boundary layer can be described by a vertical profile of the mean horizontal wind speed which is represented by a logarithmic law together with profiles for turbulent kinetic energy and turbulent dissipation rate (Richards and Hoxey 1993):

$$U(z) = \frac{u^*_{ABL}}{\kappa} \ln(\frac{z+z_0}{z_0})$$

$$k = 3.3 u^{*}_{ABL}{}^2 \tag{1}$$

$$\varepsilon = \frac{u^{*}_{ABL}{}^3}{\kappa(z+z_0)}$$

where u_{ABL}^* is the friction velocity, κ is the von Karman constant, z is the height above the ground and z_0 is the aerodynamic roughness length. The friction velocity is linked to a reference wind speed U_{10}, taken at building height (H = 10 m). The roughness of the Earth's surface is taken into account by the parameter z_0, for which a value of 0.03 m is chosen. This value corresponds to a land surface with low vegetation and isolated obstacles (Wieringa 1992). Wind is blowing perpendicular to the windward facade. Since the Spalart-Allmaras model and the DES model only solve for turbulent viscosity, appropriate values for this parameter at the inlet of the domain are derived out of the turbulence parameters defined in **Eq. 1**. It has to be noted that these inlet boundary conditions for DES are rather simplified since the inlet profile somehow lacks "LES content" (random eddies) associated with the atmospheric boundary layer. Only the turbulent viscosity profile is provided to the subgrid-scale Spalart-Allmaras model in the LES regions and a steady wind speed profile (**Eq. 1**) is imposed at the inlet. This simplification can have an influence on the results, as will be discussed later in the paper. There are more accurate but complex ways to provide better inlet conditions (Kondo et al. 1997, Bechmann 2006). Furthermore a zero static pressure is imposed at the outlet.
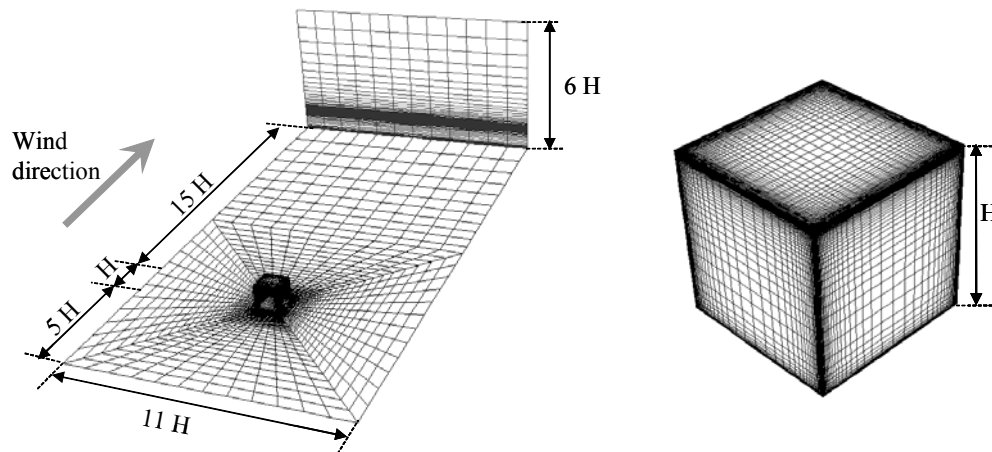
FIG.1: Computational domain and grid (H = building height).

For the lateral boundaries, symmetry boundary conditions are generally used (Franke et al. 2007), which assume that the normal velocity component and the normal gradients at the boundary are zero, resulting in flow parallel to the boundary. Since this type of boundary does not allow any flow through the boundary, periodic boundaries seem more appropriate if the unsteady character of the wake is to be taken into account. These boundary conditions are used when the expected flow pattern has a periodically repeating nature and boundaries are treated as if the two opposing planes are direct neighbours of one another.

For the top boundary, symmetry boundary conditions are used. We note that other ways to model the top boundary in a more optimised way have been reported by Blocken et al. (2007). This is however considered less important in the present case, since a relatively short upstream fetch is considered.

The ground boundary and the surfaces of the building are modeled as no-slip boundaries. The surface roughness values cannot be specified for these boundaries due to the near-wall modeling technique that is used to resolve the boundary-layer region. This will inevitably introduce streamwise gradients in the vertical profiles of mean wind speed and turbulence quantities (Blocken et al. 2007).

The surfaces of the building are heated with a constant temperature of 20°C whereas the temperature of the approach flow is set at 10°C and the ground is taken adiabatic. This boundary condition is a rather crude simplification of the reality since the specific wall composition of the building is not modeled. Taking into account the wall itself would invoke dynamic heat transfer by conduction in the wall which would markedly increase the time frame that should be dealt with in the unsteady simulations. Moreover, the influence of geometric effects (thermal bridges) would be included in the CHTC. The CHTC itself is defined as:

$$q_w = h_c(T_w - T_{ref}) \qquad\qquad (2)$$

where q_w is the heat flux at the wall, T_w is the surface temperature and for T_{ref}, the temperature of the approach flow (10°C) is chosen.

2.2 Spatial and temporal discretisation

The required spatial resolution of the control volumes is dependent on the turbulence modeling technique that is used, namely steady RANS or (unsteady) DES and on the treatment of the boundary-layer region for which low-Reynolds number modeling is used in this study. Low-Reynolds number modeling implies a sufficiently high cell density in the wall-normal direction of the boundary layer in order to resolve it appropriately, in contrast to wall-function modeling, in which the lower part of the boundary-layer region is modeled, i.e. approximated. Low-Reynolds number modeling however results in a high cell density in the near-wall region and consequently increases the computational cost. These grids typically require a non-dimensional wall distance (y^+) of about 1 (Franke et al. 2007). Moreover, an expansion ratio between two consecutive cells of 1.3 or less should be respected in the wall-normal direction (Franke et al. 2007) to provide sufficient resolution in the near-wall region. The computational grids that are used all have a y^+ value below 3 and in most regions not exceeding 1. An expansion ratio of 1.25 is used in the near-wall region.

Apart from the near-wall region, the required grid resolution in the remainder of the computational domain has to be determined. For the RANS simulations, an appropriate grid is built up according to general RANS practice, based on a grid sensitivity analysis. It is a hybrid grid (hexahedral and prismatic cells) consisting of about 1.6 million cells. For DES, other grid requirements have to be fulfilled (Spalart 2001). The most important feature is the choice of a grid spacing Δ, defined as the largest dimension of a grid cell. It determines the spatial resolution and thus the length scale of DES and should prevail over a specific region close to the building which is called the focus region. It is the region from which particles can still propagate to the flow region of interest. In this case, this region is near the building surfaces. Hence the region will surely contain all of the recirculation regions. It has to be stressed that there is no stringent guideline for choosing Δ and therefore simulations are performed with the original RANS grid and also with a grid which has an increased grid resolution in the wake of the building resulting in a grid of about 1.9 million cells. It has to be noted however that grid refinement will extend the range of scales that is resolved. Although discrepancies are found between the results of these grids on the leeward facade, the overall similarity is satisfactory. Results are reported for the finer grid. This grid has a Δ value of about 0.8 m in the wake of the building. Closely related to the spatial discretisation is the temporal discretisation for unsteady simulations. Both are related by the CFL (Courant-Friedrichs-Levy) number:

$$CFL = \frac{u\Delta t}{d} \qquad\qquad (3)$$

where u is a characteristic velocity in the cell, Δt is the time step and d is a characteristic cell dimension. Time steps resulting in CFL numbers of 1 are suggested (Spalart 2001), based on Δ and the maximal velocity in the focus region, which is however only a guideline.

2.3 Numerical simulation

The simulations are performed with the CFD package Fluent 6.3, which uses a control volume method. In the RANS simulations, a modified version of the two-equation k-ε model is used, namely the realizable k-ε model (Shih et al. 1995), to model turbulence in the core flow together with low-Reynolds number modeling for the near-wall region. For this, the one-equation model of Wolfshtein (1969) is used. Moreover, the one-equation Spalart-Allmaras RANS model is also evaluated which is used to model both core flow and near-wall region. This is done for comparison with DES, in which the Spalart-Allmaras model is used as a RANS model in the near-wall regions and as a subgrid-scale model for LES in the core flow. Second-order discretisation schemes are used throughout except for the momentum equation in DES where a bounded central-differencing scheme (Fluent 2006) is used. The SIMPLE algorithm is used for the pressure-velocity coupling. For the unsteady simulations, second-order implicit time stepping is used. It has to be noted that only forced convection is taken into account and buoyancy effects or radiation are not considered in the simulations.

3. Results and discussion

3.1 Steady simulations

First, the results of the steady simulations, which are only performed with the realizable k-ε model, are discussed. Several wind speeds are evaluated in order to obtain correlations of the CHTC with the wind speed at a height of 10 m, which is in general available from measurements at a meteorological station. The chosen

reference wind speeds, at a height of 10 m, are respectively 0.05, 0.5, 2.5 and 5 m/s. This results in Reynolds numbers, based on the building height and the reference wind speed, of about 3.5 x 10^4 to 3.5 x 10^6. The use of rather low wind speeds originates from the required grid resolution in the boundary-layer region which is necessary for low-Reynolds number modeling. Using a lower wind speed to determine the correlations gives a noticeable reduction of the grid resolution in the near-wall region. Since only forced convection is accounted for, the air flow field will not be affected by buoyancy effects at such low speeds.

The correlations for the surface-averaged CHTCs, obtained by numerical simulations, are presented in **Figure 2a** for the different facades of the building. In **Figure 2b**, the surface-averaged coefficient of the windward facade is compared with correlations at several distinct locations on that facade. It should be noted that the numerical simulations only provide data for wind speeds up to 5 m/s. Correlations are obtained by fitting the data for which a power-law relationship gives the best fit and are presented in **Table 1**. These correlations are then extrapolated to higher wind speeds which are commonly encountered at that height. It is clear that there is not only a distinct variation of the transfer coefficient over the different facades but even a large variation can be noticed over a specific facade. The highest heat transfer coefficients are found at the windward facade.
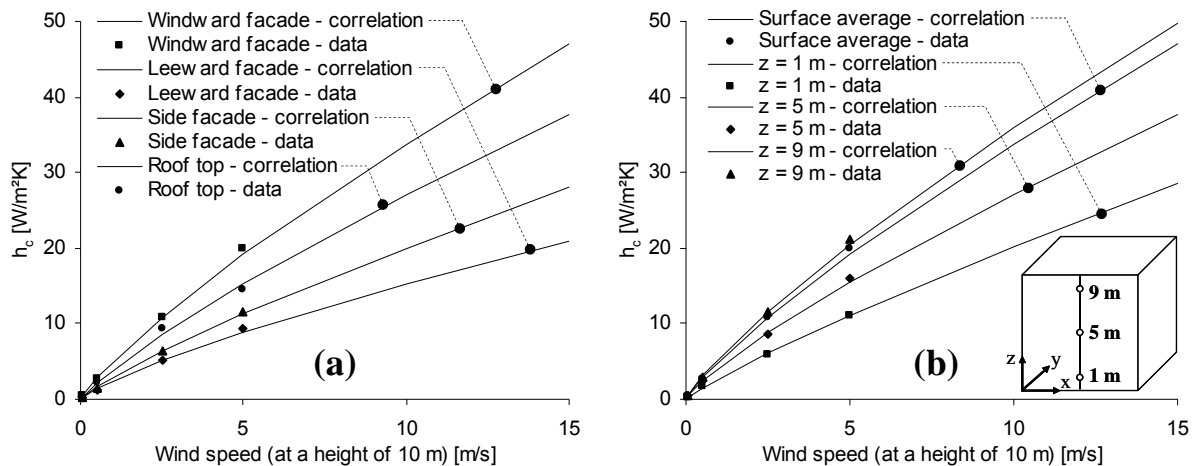
FIG.2: (a) CHTC correlations for different facades, (b) CHTC correlations on various locations on the windward facade.

The correlations are compared with the existing correlations for windward and leeward facades in **Figure 3**. For the windward facade, a large spread can be found on the correlations but the results give a very good agreement with the correlation of Sharples (1984) for the edge site and with that of Emmel et al. (2007). This is believed to be rather coincidental since considerable differences exist between geometry and boundary conditions for these cases. For the leeward facade, the results give somewhat lower values. It has to be noted that most existing linear correlations use an intercept to account for buoyancy effects at low wind speeds.

Table 1: Surface-averaged CHTC correlations ([W/m²K]) for various facades

	Windward facade	Leeward facade	Side facade	Roof top
Sharples (1984)	$h_{c,centre} = 1.4U_{10} + 6.5$	$h_{c,centre} = 1.4U_{10} + 4.4$		
	$h_{c,edge} = 2.9U_{10} + 5.3$	$h_{c,edge} = 1.5U_{10} + 4.1$		
Liu and Harris (2007)	$h_c = 1.53U_{10} + 1.43$	$h_c = 0.90U_{10} + 3.28$		
Emmel et al. (2007)	$h_c = 5.15U_{10}^{0.81}$	$h_c = 3.54U_{10}^{0.76}$		
Present study	$h_c = 5.16U_{10}^{0.82}$	$h_c = 2.52U_{10}^{0.78}$	$h_c = 2.99U_{10}^{0.83}$	$h_c = 4.05U_{10}^{0.82}$
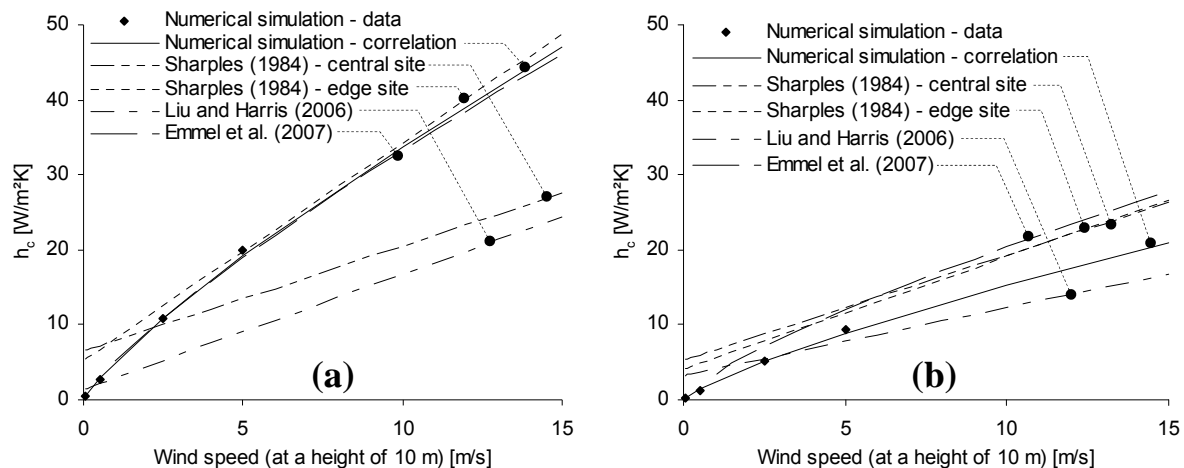
FIG.3: (a) CHTC correlations on windward facade, (b) CHTC correlations on leeward facade.

3.2 Unsteady simulations

In this section, the results of unsteady simulations with the DES model are compared to those of steady RANS simulations, for which the Spalart-Allmaras model is also evaluated. For these simulations, only a reference speed of 0.5 m/s is used. A time step of 5 seconds is chosen, resulting in CFL numbers below 5 in most parts of the focus region, which includes the recirculation zones at the side walls and roof top and a part of the wake of the building. Here, the CFL number is based on the wind speed in the cell and the third root of the cell volume. The typical periodic vortex shedding phenomenon is noticed for the unsteady simulations with a Strouhal number of about 0.3, based on the reference wind speed and the building height. The flow quantities are averaged over 50 vortex shedding cycles.

In **Figure 4 and 5**, the distribution of the CHTC along the different facades is given. In general, significant differences are found for the transfer coefficients, both in magnitude and in distribution. Since heat transfer is taken care of in the same way for the Spalart-Allmaras model and the realizable k-ε model, the main reason for the differences are attributed to the way the flow field is solved. Although it is obvious that the different turbulence modeling techniques will give different results in regions of flow separation and recirculation, it is remarkable that large differences are even found for the windward facade. Validation (Blocken 2004) of the flow field around a cube placed in a turbulent boundary layer showed that the realizable k-ε model performed well in predicting the flow field in front of the cube. This is an argument to believe that this model will also provide an accurate prediction of heat transfer for the windward facade. The upstream flow for this model noticeably differs from that of the Spalart-Allmaras model and the DES model. The difference between the two RANS models could be attributed to the degree of complexity of the used turbulence model, the Spalart-Allmaras being only a one-equation turbulence model. However, a remarkable similarity of the upstream flow and of the CHTC distribution is found for Spalart-Allmaras and DES. This similarity seems to be a result of the lack of "LES content" in the approach flow of DES by which DES tends to react more like its subgrid-scale model. A rapid decay of the turbulence imposed at the inlet is also noticed, which seems to support this assumption. Consequently, lower heat transfer coefficients are found for DES although the overall distribution over the windward facade is quite similar to that of the two RANS models that are evaluated. There are other ways to provide inlet conditions for the LES regions of the DES model, as was mentioned above. The use of these methods could provide more realistic predictions of the CHTC but will require an additional computational effort.

Despite the disparity between the different models, some interesting features stand out with respect to the unsteady simulations. Regarding the leeward facade, the DES model shows a more uniform distribution of the heat transfer coefficient and relative high values are found for this facade compared to the other facades, in contrast to simulations with steady RANS. This is probably due to the unsteady character of the flow in the wake, namely the periodic vortex shedding, which enhances heat transfer on the leeward facade. The latter can also be noticed in **Table 2**, where the contribution of each facade to the total heat loss of the building is presented for all simulations. Moreover, a relatively lower heat loss is found for the roof top for the DES model.

This is attributed to the absence of flow reattachment on this surface. It has to be noted however that, apart from the windward facade, the use of simplified inlet conditions for DES can also have an influence on the CHTC predictions of the other facades.
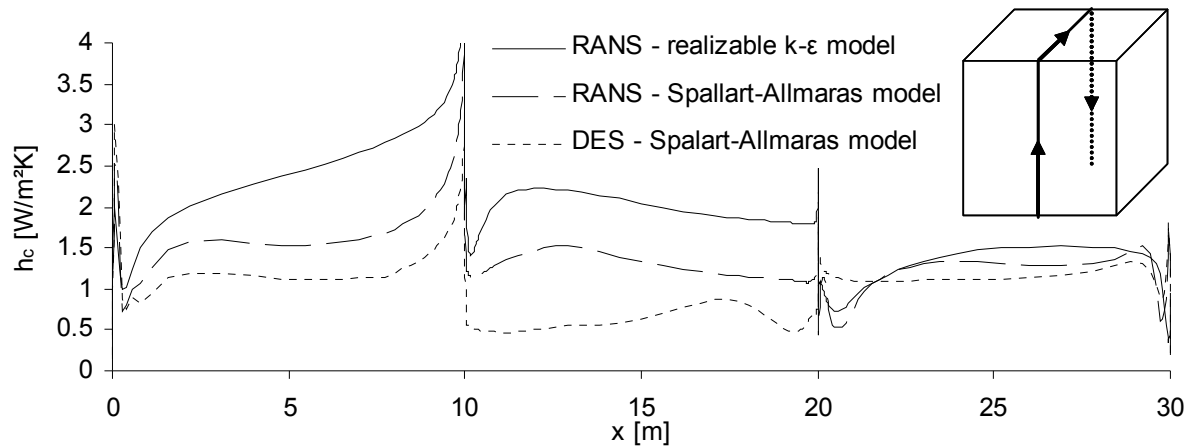
FIG.4: CHTC distribution along vertical plane
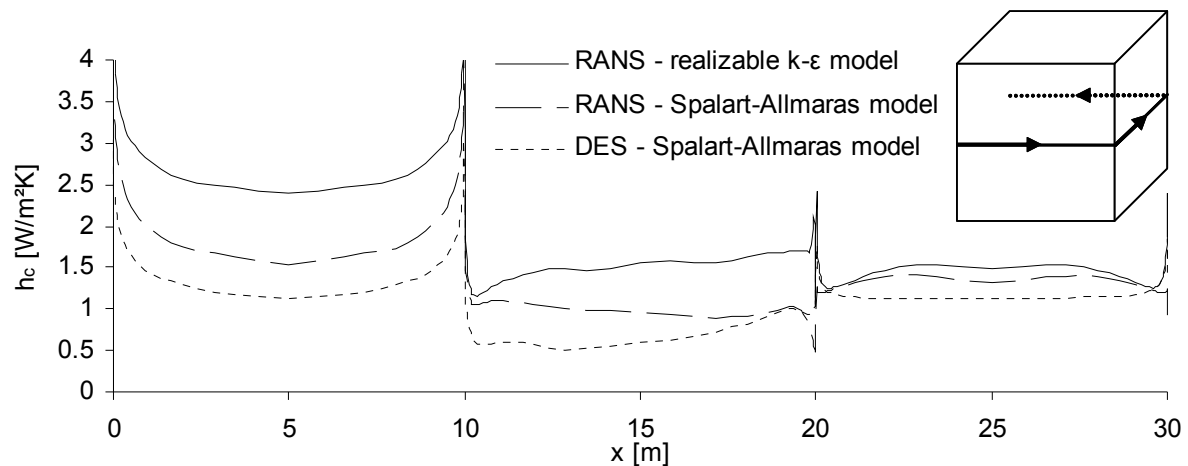
FIG.5: CHTC distribution along horizontal plane

Table 2: Percentage of amount of facade heat loss to total heat loss for different facades of the building

	Windward facade	Leeward facade	Side facade	Roof top
RANS – realizable k-ε model	29	14	17	23
RANS – Spalart-Allmaras model	27	17	17	22
DES – Spalart-Allmaras model	28	25	16	16

4. Conclusion

In this study, the effect of wind-induced convection at the exterior surfaces of a cubic building is investigated with CFD. Regarding the steady RANS simulations, the results show a distinct variation of the transfer coefficient over the facade and also a significant difference is noticed between the surface-averaged transfer coefficients of each facade. The correlations agree well with existing correlations despite the considerable differences in geometry and boundary conditions with the latter. Power-law relationships provide the best fits with the simulations. Unsteady simulations with the DES model show large discrepancies with the RANS models but discrepancies also exist between the two evaluated RANS models themselves. These differences are

related to the prediction of the flow field around the building and, for DES, some of them might be attributed to the simplified inlet conditions that are used. Nevertheless, unsteady simulations can provide valuable information regarding the influence of unsteady flow features on the heat transfer. The unsteady nature of the wake leads to relative high CHTCs and a uniform distribution on the leeward facade, compared to RANS simulations. No reattachment is found at the roof top for the DES model, which results in lower heat transfer coefficients. It is shown that if CFD is to be used for the prediction of the CHTC, it is important to acknowledge the limitations of the numerical modeling techniques that are used since significant differences can be found for these different techniques.

5. References

Baetke F., Werner H. and Wengle H. (1990). Numerical simulation of turbulent flow over surface mounted obstacles with sharp edges and corners, *Journal of Wind Engineering and Industrial Aerodynamics*, Vol. 35, 129-147.

Bechmann A. (2006). Large-Eddy Simulation of atmospheric flow over complex terrain, PhD thesis, Riso National Laboratory, Technical University of Denmark, Roskilde, Denmark.

Blocken B. (2004). Wind-driven rain on buildings: measurements, numerical modeling and applications, PhD thesis, Laboratory of Building Physics, Katholieke Universiteit Leuven, Belgium.

Blocken B., Stathoupoulos T. and Carmeliet J. (2007). CFD simulation of the atmospheric boundary layer: wall function problems, *Atmospheric Environment*, Vol. 41, 238-252.

Chyu M.K. and Natarajan V. (1991). Local heat/mass transfer distributions on the surface of a wall-mounted cube, *Transactions of the ASME: Journal of Heat Transfer*, Vol. 113, 851-857.

Emmel M.G., Abadie M.O. and Mendes N. (2007). New external convective heat transfer coefficient correlations for isolated low-rise buildings, *Energy and Buildings*, Vol. 39, 335-342.

Fluent 6.3 (2006). Fluent 6.3 User's Guide, Lebanon, New Hampshire.

Franke J., Hellsten A., Schlünzen H. and Carissimo B. (2007). Best Practice guideline for the CFD simulation of flows in the urban environment, *COST Action 732: Quality assurance and improvement of microscale meteorological models*.

Iaccarino G., Ooi A., Durbin P.A. and Behnia M. (2003). Reynolds averaged simulation of unsteady separated flow, *International Journal of Heat and Fluid Flow*, Vol. 24, 147-156.

Ito N., Kimura K. and Oka J. (1972). A field experiment study on the convective heat transfer coefficient on exterior surface of a building, *ASHRAE Transactions*, Vol. 78, 184-191.

Jürges, W. (1924). Der Wärmeübergang an einer ebenen Wand, *Beihefte zum Gesundheits-Ingenieur*, Vol. 1 (19).

Kondo K., Murakami S. and Mochida A. (1997). Generation of velocity fluctuations for inflow boundary condition for LES, *Journal of Wind Engineering and Industrial Aerodynamics*, Vol. 67-68, 51-64.

Liu Y. and Harris D.J. (2007). Full-scale measurements of convective coefficient on external surface of a low-rise building in sheltered conditions, *Building and Environment*, Vol. 42, No. 7, 2718-2736.

Loveday D.L. and Taki A.H. (1996). Convective heat transfer coefficients at a plane surface on a full-scale building facade, *International Journal of Heat and Mass Transfer*, Vol. 39, No. 8, 1729-1742.

Meinders E.R., Hanjalic K. and Martinuzzi R.J. (1999). Experimental study of the local convection heat transfer from a wall-mounted cube in turbulent channel flow, *Transactions of the ASME: Journal of Heat Transfer*, Vol. 121, 564-573.

Murakami S. (1993). Comparison of various turbulence models applied to a bluff body, *Journal of Wind Engineering and Industrial Aerodynamics*, Vol. 46-47, 21-36.

Murakami S., Mochida A., Ooka R., Kato S. and Iizuka S. (1996). Numerical prediction of flow around a building with various turbulence models: Comparison of k-ε EVM, ASM, DSM and LES with wind tunnel tests, *ASHRAE Transactions*, Vol. 102, No. 1, 741- 753.

Nakamura H., Igarashi T. and Tsutsui T. (2001). Local heat transfer around a wall-mounted cube in the turbulent boundary layer, *International Journal of Heat and Mass Transfer*, Vol. 44, 3385-3395.

Nakamura H., Igarashi T. and Tsutsui T. (2003). Local heat transfer around a wall-mounted cube at 45° to flow in a turbulent boundary layer, *International Journal of Heat and Mass Transfer*, Vol. 24, 807-815.

Richards P.J. and Hoxey R.P. (1993). Appropriate boundary conditions for computational wind engineering models using the k-ε turbulence model, *Journal of Wind Engineering and Industrial Aerodynamics*, Vol. 46-47, 145-153.

Sharples S. (1984). Full-scale measurements of convective energy losses from exterior building surfaces, *Building and Environment*, Vol. 19, No. 1, 31-39.

Shih T.H., Liou W.W., Shabbir A., Yang Z. and Zhu J. (1995). A new k-ε eddy viscosity model for high Reynolds number turbulent flows, Computers & Fluids, Vol. 24, No. 3, 227-238.

Spalart P.R., Jou W.H., Strelets M. and Allmaras S.R. (1997). Comments on the feasibility of LES for wings, and on a hybrid RANS/LES approach, 1st AFOSR International Conference on DNS/LES Ruston, LA. In: Advances in DNS/LES (Liu C. and Liu Z., editors), Greyden Press, Columbus, OH.

Spalart P.R. (2001). Young person's guide to Detached-Eddy Simulation grids, NASA CR-2001-211032.

Wieringa J. (1992), Updating the Davenport roughness classification, *Journal of Wind Engineering and Industrial Aerodynamics*, Vol. 41-44, 357-368, 1992.

Wolfshtein M. (1969), The velocity and temperature distribution in one-dimensional flow with turbulence augmentation and pressure gradient, *International Journal of Heat and Mass Transfer*, Vol. 12, 301-318.

A 1D stationary model for assessing the performance of indirect evaporative cooling

Marijke Steeman, PhD-student
Ghent University, Department of Architecture and Urban Planning
Marijke.Steeman@UGent   http://www.architectuur.ugent.be/bouwfysica

Arnold Janssens, Professor
Ghent University, Department of Architecture and Urban Planning
Arnold.Janssens@UGent.be   http://www.architectuur.ugent.be/bouwfysica

Michel De Paepe, Professor
Ghent University, Department of Flow, Heat and Combustion Mechanics
Michel.Depaepe@UGent.be   http://www.floheacom.ugent.be

KEYWORDS: numerical modelling, evaporative cooling, heat exchangers, validation

SUMMARY:
Indirect evaporative cooling (IEC) is an interesting passive cooling technique in which water is sprayed over the return air in the secondary channel of a heat exchanger. By combined heat and moisture transport this air cools down. At the same time fresh outdoor air is cooled indirectly by passing over the other path of the heat exchanger. To assess the performance of this technique a 1D stationary model of a wet surface heat exchanger was developed in order to calculate the outlet conditions of the system. First validation experiments in an installation in operation showed that modelling results agree well with measured data. The recirculated water in the second part of the heat exchanger was heated up and showed to have a non-negligible influence on the temperature of the exhaust air. Using the developed model the influence of different parameters on the effectiveness is studied and it was found that the air flow rate and ratio, together with the heat transferring surface are the most important.

1. Introduction

As the internal loads are increasing due to e.g. computer equipment and lighting, the use of mechanical refrigeration units is growing (JRAIA, 2007) and passive cooling techniques are becoming more and more important in the last years. The main drawback of active cooling systems is their large energy consumption and their significant contribution to the emission of greenhouse gases. Contrary to air conditioning, passive cooling techniques may provide cooling with more limited environmental impact.
Two types of evaporative cooling systems can be distinguished. In a direct evaporative cooling installation (DEC) the supply air to the building is directly humidified. In an indirect evaporative cooling system (IEC) a secondary air flow is cooled by adiabatic humidification using sprayed water. In an air to air heat exchanger this air cools down the supply air to the building. Fresh outdoor air or return air from the building can be used as secondary air. The system generally uses a plate heat exchanger although also tube heat exchangers have been reported (Chen et al., 1991). The advantage of doing so is that in contrast to direct evaporative cooling the moisture content of the primary air is not increased. This leads to a more comfortable indoor climate and fewer problems, e.g. mould and condensation, are expected. As the return air is humidified in an indirect evaporative cooling installation, a clear interaction can be observed between the indoor humidity and the thermal performance of the technique. Advantages of indirect evaporative cooling are its low energy consumption and easy maintenance. The technique performs best in dry hot areas although the potential in most locations in Europe is also good because of the moderate humidity during summer. It is most appropriate in buildings with relatively small cooling loads. The technique has a good peak performance, during moderate periods the achieved cooling amount is limited (Steeman et al. 2007)
In this paper first a literature survey of existing models is presented. A 1D stationary model of a wet surface heat exchanger was developed to calculate the outlet conditions of an indirect evaporative cooling installation. By use of the model in TRNSYS (2004) a validation against experiments in an installation in operation is performed and an explanation for the deviations between the results is given. Furthermore the different parameters which have an influence on the effectiveness of indirect evaporative cooling are evaluated.

2. State of the art

As the return air is wetted in the secondary channel of a heat exchanger (HX), the air is cooled by combined heat and mass transport. By flowing over the other side of the heat exchanger, the primary air is cooled sensibly by heat transport (conduction and convection) over the plates. This modified type of heat exchanger is also known as a wet surface heat exchanger (Fig.1).
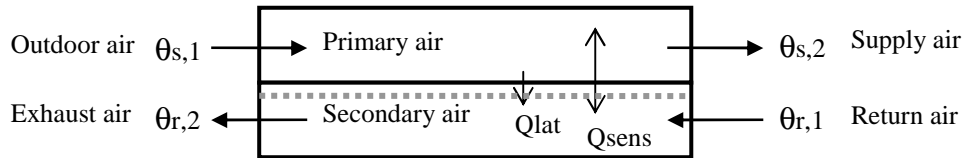
FIG. 1: Schematic principle of indirect evaporative cooling

The effectiveness of a wet surface heat exchanger can be written as the ratio between the depression of the supply temperature and the maximum possible temperature change in the supply air (Eq.1). The supply air can cool down at most to the wet bulb temperature of the return air θ'_r. Measurements in two installations in operation showed that an indirect evaporative cooling installation has a constant effectiveness (Steeman et al. 2007). This means the effectiveness is independent of the conditions of the outdoor air and the return air.

$$\varepsilon = \frac{\theta_{s,1} - \theta_{s,2}}{\theta_{s,1} - \theta'_{r,1}} \tag{1}$$

In literature several analytical models are found to predict the outlet temperatures of a wet surface heat exchanger. Pecod (1968) was the first to propose a simple design method for an indirect evaporative cooler using a parallel plastic plate heat exchanger with small protrusions. Maclaine Cross and Banks (1981) developed a linear approximate model to describe a counterflow wet surface heat exchanger. They assumed complete wetting and a water film which is stationary and continuously replenished with water at the same temperature. This enabled using the same equations as for dry heat exchangers. Kettleborough and Hsieh (1983) proposed a 1D differential model for a counterflow heat exchanger to study the effect of different factors on the effectiveness: air flow rate and ratio, surface treatment and path length are found to influence most the performance. A wettability factor is used to estimate the effect of incomplete wetting. Stoitchkov and Dimitrov (1998) developed a short method for calculating the effectiveness of crossflow heat exchangers with a correction to the overestimated effectiveness by Maclaine-Cross and Banks. In the model the water flow is more accurately modelled and the influence of the barometric pressure is added. Peterson (1992, 1993) emphasizes that the analytical models of e.g. Maclaine-Cross and Banks, and Kettleborough and Hshieh tend to overpredict the cooling effectiveness. Furthermore he states that analytical models are inappropriate in case return air is used as secondary air as the impact of incomplete wetting and miscellaneous loads is larger. More recently Yang and Ren (2006) took the possible condensation in the primary air flow into account in their mode. They introduced the fraction of the condensation area to the total heat transfer area which is an important parameter in the energy performance of the system. Wang (1996) studied the effect of surface wettability on the effectiveness: coatings may enlarge the contact area between water and air and therefore the water evaporation rate at the surface.

3. Modelling

3.1   1D numerical model for a stationary wet surface heat exchanger

Using a control volume method a 1D stationary model was developed for a counterflow heat exchanger in order to calculate the temperatures in the primary and secondary air channel by solving five partial differential equations. The model does not use the same approximations as the analytical models. For symmetry reasons only half of the path is modelled in a control volume (Fig.2). The airflow paths are discretized exponentially using a grid concentration factor, resulting in smaller control volumes at both path endings (Nelis, 2003). Following assumptions were used:
-    1D stationary heat transfer. Negligible heat transfer to the surroundings is negligible.
-    Specific heat, mass flow rates and heat and mass transfer coefficients are constant.

- The heat resistance of the water film and the plate is neglected because the values are small compared to the heat transfer coefficients at the surfaces.
- The water film is stationary. An equilibrium temperature between both airstreams is calculated from the initial water temperature. The model does not take into account the heating of the water by recirculation in the heat exchanger. The plate surface is completely wetted.
- Condensation may occur in the primary air flow.
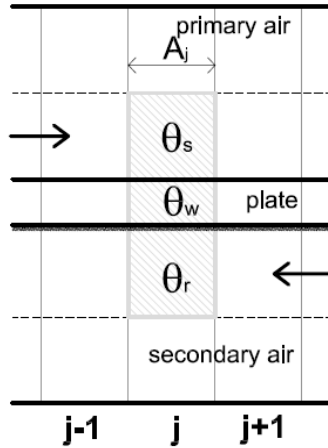
FIG. 2: 1D numerical model for a wet surface heat exchanger

Heat balance secondary air
$$m_r c_r \left(\theta_{j-1,r} - \theta_{j,r} \right) = A_j \alpha_r \left(\theta_{j,r} - \theta_{j,w} \right) \tag{2}$$

Heat balance primary air
$$m_s c_s \left(\theta_{j+1,s} - \theta_{j,s} \right) = A_j \alpha_s \left(\theta_{j,s} - \theta_{j,w} \right) \tag{3}$$

Heat balance water film
$$A_j \alpha_r \left(\theta_{j,r} - \theta_{j,w} \right) + A_j \alpha_s \left(\theta_{j,s} - \theta_{j,w} \right) + \beta A_j h_{ev} \left(p_{j,r} - p_{j,w} \right) + h_{ev} g_{j,s} = 0 \tag{4}$$

Mass balance secondary air
$$m_r \xi_a \left(p_{j-1,r} - p_{j,r} \right) = \beta A_j \left(p_{j,r} - p_{j,w} \right)$$
$$\text{Max} \left(p_{j,r} \right) = p_{sat} \left(\theta_{j,r} \right) \tag{5}$$

Mass balance primary air
$$m_s \xi_a \left(p_{j+1,s} - p_{j,s} \right) = g_{j,s}$$
$$\text{if } p_{j,s} > p_{j,w}: \quad g_{j,s} = \beta A_j \left(p_{j,s} - p_{j,w} \right) \tag{6}$$

TABLE1: Correlations for calculating the heat transfer coefficients in the heat exchanger

Re < 2300	Re > 8000 (ASHRAE, 2005)	2300 < Re < 8000 (Shah, 2003)
	$f = \dfrac{1}{\left(1.58 \log(\text{Re}) - 3.28 \right)^2}$	$\phi = 1.33 - \dfrac{\text{Re}}{6000}$
$Nu_{lam} = 3.66$ (flow in channel) $Nu_{lam} = 8$ (flow between plates) (Bejan, 1999)	$Nu_{turb} = \dfrac{\frac{f}{2}(\text{Re}-1000)\text{Pr}}{1 + 12.7 \left(\frac{f}{2} \right)^{0.5} \left(\text{Pr}^{2/3} - 1 \right)} \left(1 + \left(\dfrac{D_h}{L} \right)^{2/3} \right)$	$Nu = \phi \cdot Nu_{lam} + \left(1 - \phi \right) Nu_{turb}$

$$\alpha = \frac{Nu \cdot k}{D_h} \tag{7} \qquad\qquad \beta = \frac{\alpha}{c \cdot P_{air}} \tag{8}$$

Table 1 was used to determine the heat transfer coefficients in both air channels. For Reynolds numbers between 2300 and 8000 the correlation of Taborek is used in which Nu_{lam} and Nu_{turb} are calculated through their respective correlations (Shah, 2003). The mass transfer coefficient was calculated using a Lewis number of one.

3.2   Model validation

To validate the model, experiments were carried out in an air handling unit with indirect evaporative cooling which is installed to provide cool air in the library of a new university building in Ghent, Belgium. The installation for the library was in operation since October 2006 and was dimensioned to a maximum air flow rate of 10,000m³/h. Indirect evaporative cooling is working during the occupancy hours if the outdoor air is warmer than 18°C and if the wet bulb temperature of the return air exceeds 16°C. The air handling unit consists of a polypropylene double cross flow heat exchanger with dimensions 1950mm x 1215mm x 997mm (Fig. 3a). The total heat exchange surface was approximately 500m² which results in an air flow rate of about 20m³/h per m² heat exchange surface. At the return air side the air is ventilated between parallel plates while at the supply side

distance holders are introduced in order ensure stability of the parallel plates. The distance between the plates is approximately 5.2mm. Both the supply and return fans are frequency controlled and their air flow rates are balanced. Water sprayers are placed at the top of the first part of the heat exchanger (Fig. 3b). The water is collected in a sump below and recirculated. Approximately every hour the system is replenished with fresh water to avoid problems e.g. with bacteria.
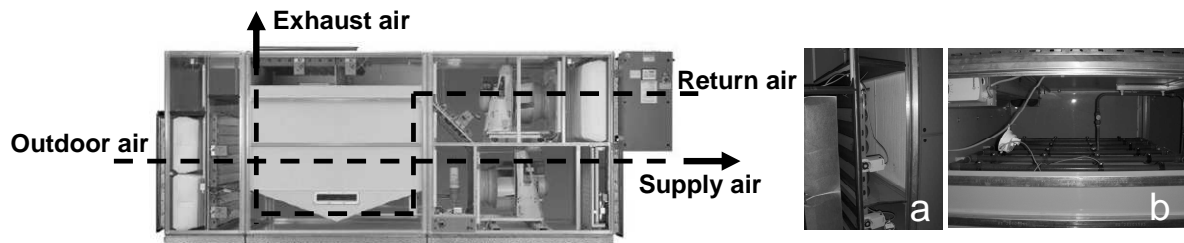
FIG. 3: Operation of the air handling unit with indirect evaporative cooling. (a) Spraying installation in secondary channel and (b) filter, valve and heat exchanger in primary air channel (Menerga, 2007)

The air flow rate in the installation was measured using a tracer gas method with CO_2 gas in the supply air channel. During the measurements the position of the fans and valves was manually set and all bypasses were closed in order to make sure the installation works at 100% fresh outdoor air. Also the evaporative cooling was working continuously. Temperature and relative humidity of supply and return air before and behind the heat exchanger were measured. The measurement interval was five minutes.

To understand what is happening in the heat exchanger the state of the airstreams during two measured periods is schematically given shown on a psychometric diagram. The return air is wetted following lines of constant wet bulb temperature in the first part of the heat exchanger (**1**-**2**). At the exit of the first part, the return air is saturated and reaches its wet bulb temperature (**2**). During the experiments a mist came out of the exhaust air flow which means that the collected water from the sump is carried along the second part of the heat exchanger together with the ventilation air. The sprayed water is heated up by recirculation in the first part of the heat exchanger. To have an indication of the water temperature the water exiting the sprayers was measured and was about 17-18 °C. Due to evaporation effects the water itself will be slightly warmer.
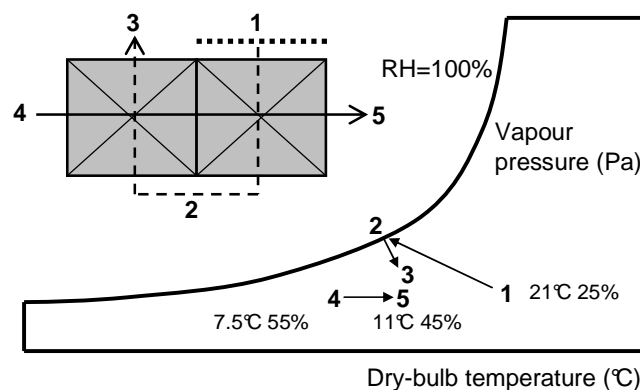
*FIG. 4: State of the air flows in the heat exchanger during the first measured period
(Dashed line: return air – Solid line: supply air)*

During the first measurements the outdoor air temperature was about 7.5°C and 55% RH and the return air was 21°C and 25% RH. The air flow rate was 2000m³/h (Fig. 4). It must be noted that the humidification of the return air was manually activated in this case. The measured data showed that the exhaust air is not saturated (**3**): condensation may have occurred in the second part of the heat exchanger due to contact with the cold outdoor air in the supply air channel. The outdoor air in the primary air channel was heated to 11°C and 45% RH in the installation because its temperature was lower than the wet bulb temperature of the return air (**4**-**5**).
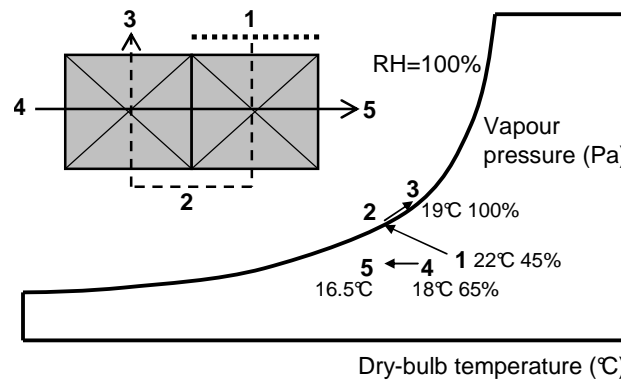
FIG. 5: State of the air flows in the heat exchanger during the second measured period
(Dashed line: return air – Solid line: supply air)

During the second measured period (Fig. 5) the outdoor air was about 18°C and 65% RH and the return air was 22°C and 45% RH. The air flow rate was approximately 4300m³/h. The outdoor air was now cooled in the heat exchanger to about 16.5°C (**4-5**). After passing the first part the return air was heated up slightly by flowing over the second part of the heat exchanger due to the warmer outside air in the primary air channel and the water carried along (**2-3**). The air was further heated in the second part of the heat exchanger and thus it was able to take up more water vapour. As a result the exhaust air stayed saturated (19°C/100% RH).

In order to model the double cross flow heat exchanger the first part of the heat exchanger was assumed completely wetted. The second part of the heat exchanger was modelled as a dry heat exchanger. This is an appropriate approximation because the return air is already saturated when exiting the first part of the heat exchanger. The dry heat exchanger will slightly precool the primary air before entering the wet part of the heat exchanger. At the same time the secondary air is heated up a bit when flowing through the dry part of the heat exchanger. The outlet temperatures of the dry heat exchanger are calculated using a ε – NTU correlation for a cross flow heat exchanger with one side mixed and one side unmixed (Eq. 9) (Shah, 2003). The combination of both heat exchangers was modelled by using the developed wet surface heat exchanger model and the ε – NTU relation for the dry heat exchanger in TRNSYS (2004).

$$\varepsilon = 1 - \exp(-1 + \exp(-NTU)) \qquad NTU = \frac{A.k}{m.c} \qquad \qquad (9)$$

To validate the model the same measured data as shown in Fig.4 and 5 are used. The first part of the heat exchanger can be well described by the wet surface heat exchanger model. In Fig.6a the measured return temperature just above the water sump is also given. The model shows good agreement with the measured return temperature after the first part of the heat exchanger and with the measured supply temperature. Average deviations were respectively 0.15°C and 0.8°C. Because the model does not take into account the heating of the water due to recirculation, the calculated exhaust temperature is approximately 2.2°C underestimated. The same trend can be seen in Fig.6b.

The developed model gives a good insight in what happens in an indirect evaporative cooling system. There are still some deviations mainly due to:
-   The influence of the water temperature is not taken into account in the model. Furthermore it is not sure to which amount the plates of the second part are really wetted.
-   In reality the heat exchanger is a cross flow type which means that not all the air paths will be cooled or heated equally. In dry heat exchanger theory a correction factor may be applied to account for the lower performance of a cross flow heat exchanger compared to a counterflow heat exchanger. To determine if a similar correction can be applied to wet surface heat exchangers more research should be performed.
-   The measurements showed that the return air flow rate was slightly higher than the supply air flow rate. In the model it was assumed that the air flow rates were balanced and equal to the measured values at the supply side.

171
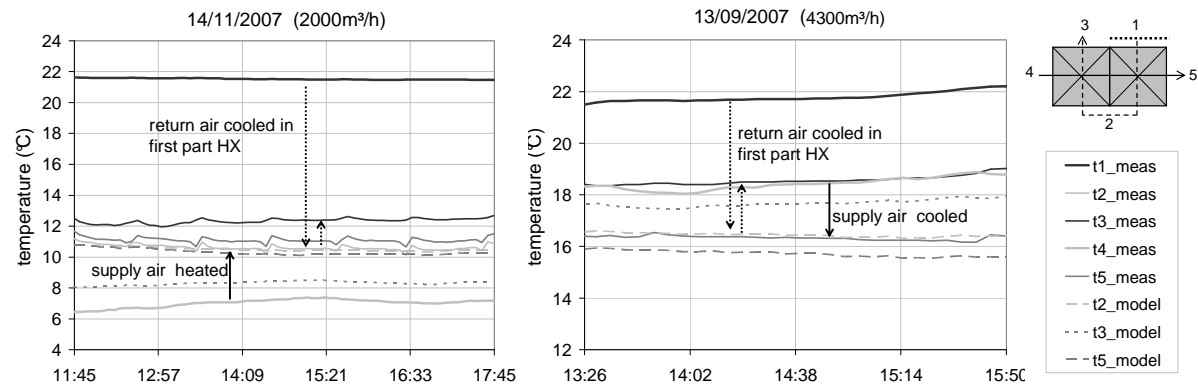
FIG. 6: Validation of the model for a wet surface heat exchanger. The double cross flow heat exchanger is modelled using a wet surface heat exchanger followed by a dry heat exchanger in TRNSYS.

4. Model analysis

In this part the different parameters which influence the performance of a wet surface heat exchanger were evaluated. Several runs were performed varying one parameter in the model while the others were kept constant. For the parametric runs 50 control volumes and grid concentration factor of 2 was used which gave good results. The simulations started from a wet surface heat exchanger with following conditions: flow paths with 1m length, 5.2mm width between the plates and 4000m³/h supply and return air flow rate. The effectiveness of the base case wet surface heat exchanger was on average 96%. Measured inlet conditions of one day in September 2007 were used.

As a first parameter the length of the air flow paths of the heat exchanger was varied. Fig. 7a shows that increasing the length of the paths and thus the available surface for heat transfer exponentially increases the effectiveness. The air has a longer mass and heat exchange with the water film surface. Doubling the path from 0.5m to 1.0m changes the effectiveness from 77% to 96%, doubling it again to 2.0m increases the effectiveness up to 106%. Increasing the length from 1m on only has a small influence on the performance because the return air has already reached saturation and cannot be cooled further. An effectiveness above 100% is theoretically possible because in the model the evaporation takes place on the plate. This means the plate is able to cool down under the wet bulb temperature of the return air.

The air flow rate through the heat exchanger has a large influence on its performance as it determines the heat and mass transfer (Fig.7b). Increasing the air flow rate, the system's performance will drop especially in the laminar flow region because the heat transfer coefficient (HTC) is constant. In this case the flow is laminar up to air flow rates of approximately 8000m³/h. After this point the flow starts to behave partly turbulent: the heat transfer coefficients increase which results in a more stable effectiveness. Measurements in the installation showed the same trend (Table2). For different positions of the supply and return air fan the supply and return temperature before and behind the heat exchanger were measured and the effectiveness of the indirect evaporative cooling installation was deduced using Eq (1).

TABLE 2: Measured effectiveness dependent on air flow rate (Library, Ghent)

Air flow rate (m³/h)	2000	4300	6900
Effectiveness (%)	95	80	77

Apart from the air flow rate through the heat exchanger also the ratio between supply and return air flow is of importance (Fig.7c). If the supply air flow rate was doubled compared to the base case (ratio 2), the effectiveness dropped to 65%. The capacity of the return air to cool the supply air is reduced and as a result the effectiveness of the indirect evaporative cooling installation drops. If the return air flow rate is doubled compared to the base case the effectiveness raises up to more than 100% (ratio 0.5).
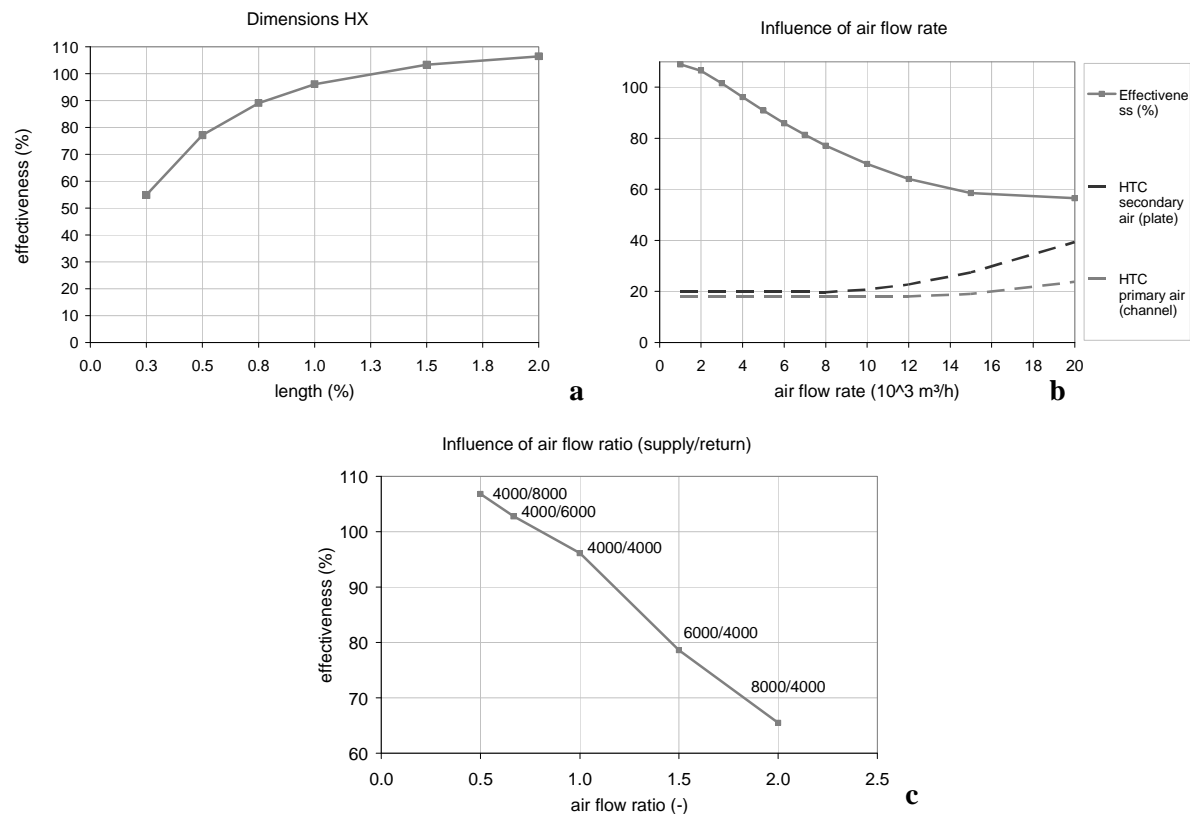
FIG. 7: Parameters influencing the performance of indirect evaporative cooling: length of flow paths (a), air flow rate (b) and air flow ratio (c)

5. Conclusions

A 1D numerical model describing a counterflow wet surface heat exchanger was developed based on the heat and mass balance of the supply and return air. Using a control volume method the outlet conditions of both supply and exhaust air can be calculated. The model assumes that the heat transfer resistance of both water film and plate are negligible and that the water film is stationary and continuously replenished with water. The model has been validated using measured data in a double crossflow heat exchanger. The installation has been modelled assuming evaporation only takes place in the first part of the heat exchanger. The second and dry part of the heat exchanger was modelled using ε – NTU correlation and linked behind the wet surface heat exchanger model in TRNSYS. The supply air temperature and the return air temperature just behind the first part of the heat exchanger were in good agreement with the measured data. The model underestimated the temperature of the exhaust air because it does not take into account the fact that the return air is heated by the recirculated water in the second part of the heat exchanger.

In addition different parameters influencing the effectiveness of an indirect evaporative cooling installation were evaluated using the developed model for a wet surface exchanger. The ventilation air flow rate has an important effect on the performance: increasing the air flow rate results in a lower effectiveness of the heat exchanger. Small air flow rates result in a laminar flow regime. In this case the effectiveness drops with increasing air flow rate. In a non – developed turbulent flow regime the effectiveness is more constant. Apart from the air flow rate, the ratio between supply and return air flow rate is of importance. If the return air flow rate is higher than the supply air flow rate the capacity for cooling the supply air is higher and the performance increases. Furthermore the length of the paths determines the area available for heat transfer and influences the amount of water that can evaporate along the paths. Extending the flow paths increases the effectiveness of the indirect evaporative cooling system exponentially.

This summer more temperature and humidity measurements will be performed in the installation in order to have better validation results. The supply and return air flow rate will be measured continuously to have a better insight on the influence of the ventilation flow rate on the effectiveness of the installation.

6. Acknowledgements

7. Nomenclature

A	Heat transfer surface (m²)	$Qlat$	Latent heat transfer
c	Specific heat of air (J/kg K)	α	Heat transfer coefficient (W/m²K)
D_h	Hydraulic diameter (m) (Dh = 2b for plates; Dh=b for channels; b distance between plates)	P_{air}	Air pressure (101325 Pa)
		β	Mass transfer coefficient (kg/Pa/s/m²)
		ε	Effectiveness (%)
g	Condensation flow rate (kg/s)	θ	Dry bulb temperature (°C)
h_{ev}	Latent heat (J/kg)	θ'	Wet bulb temperature (°C)
k	Conductivity of air (0.025 W/m²K)	ξ_a	Specific vapour capacity air (kg/kg/Pa)
m	Mass flow rate (kg/s)	s	Supply air
Nu	Nusselt number (-)	r	Return air
NTU	Number of transfer units (-)	w	Water film interface
p	Vapour pressure (Pa)	1	Inlet
$Qsens$	Sensible heat transfer	2	Outlet

8. References

ASHRAE (2005). Handbook Fundamentals (SI). Atlanta, USA, American Society of Heating, Refrigeration and Air Conditioning Engineers.

Bejan A. (1999). Heat Transfer, Wiley, ISBN 0-471-50290-1.

Chen PL, Qin, HM, et al. (1991). A heat and mass transfer model for thermal and hydraulic calculations of indirect evaporative cooler performance, ASHRAE Transactions, Research, IN 91-11-2, p. 852-865.

JRAIA (2007). The Japan refrigeration and air conditioning industry association. Estimate of world demand for air conditioners (2000-2008). http://www.jraia.or.jp/frameset_english.html.

Kettleborough CF, Hsieh CS. (1983).The thermal performance of the wet surface plastic heat exchanger used as an indirect evaporative cooler, Transactions of ASME105,p. 366-373.

Maclaine – Cross IL, Banks PJ. (1981). A general theory of wet surface heat exchangers and its application to regenerative evaporative cooling, Transactions of ASME 103, p. 579-585.

Menerga Klimatechnologie. (2007). www.menerga.de

Nelis GF. (2003). A heat exchanger model that includes axial conduction, parasitic heat loads and property variations, Cryogenics 43, p. 523-538.

Pescod D. (1968). Unit air cooler using plastic plate heat exchanger with evaporatively cooled plates. Australian Refrigeration Air Conditioning and Heating, Vol.22, p. 22-26.

Peterson JL, Hunn BD (1992). Experimental performance of an indirect evaporative cooler, ASHRAE Transactions Research, 3598, p. 15-23.

Peterson JL. (1993). An effectiveness model for indirect evaporative coolers, ASHRAE Transactions Research, 3731, p. 392-399.

SEL, TRANSSOLAR, CSTB, TESS. (2004). Trnsys 16: A TRanSient SYstem Simulation program. University of Wisconsin, Madison, USA.

Shah RK, Sekulic DP. (2003). Fundamentals of Heat Exchanger Design, p. 482.

Steeman M, Janssens A, De Paepe M. (2007). Performance evaluation of indirect evaporative cooling by means of measurements and dynamic simulations, Proceedings of 6th International Conference on Indoor Air Quality, Ventilation & Energy Conservation in Buildings, Oct. 28-31, Sendai, Japan.

Stoitchkov NJ, Dimitrov GI. (1998). Effectiveness of a crossflow plate heat exchanger for indirect evaporative cooling, Int. J. Refrigeration 21(6), p. 463-471.

Yang H, Ren C, Cui P. (2006). Study on the performance correlations of an indirect evaporative cooler with condensation from primary flow, HVAC&Research 12(3), p. 519-532.

Wang TA, Reid RL. (1996). Surface wettability effect on an indirect evaporative cooling system, ASHRAE Transactions Research 3975, p. 427-433.

Evaluation of the cooling potential of a dessicant evaporative cooling system using the SimSPARK environment

Chadi Maalouf, Assistant Professor
UTAP, University of Reims, Campus du Moulin de la Housse, Reims, France
chadi.maalouf@univ-reims.fr

Etienne Wurtz, Research Director
INES-CNRS,LOCIE, University of Savoie, Campus Scientifique, Le Bourget du Lac, France
etienne.wurtz@univ-savoie.fr

Francis Allard, Professor
LEPTAB, University of La Rochelle, avenue Michel Crépeau, La Rochelle, France.
francis.allard@univ-lr.fr

KEYWORDS: *Simulation, experimental set up, desiccant cooling, air dehumidification, SPARK.*

SUMMARY:

Being heat driven, the desiccant cooling cycle can be coupled to solar collectors to produce a cooling system with low environmental impact. In this paper, we present the first solar desiccant cooling system in France. A dessicant wheel model is presented and validated experimentally. Then, using computer simulation, a graphical aided concept is used to evaluate system feasibility and its limitation. It is shown that the system is suited to tempered regions with moderate humidity ratios.

1.   Introduction

In order to maintain comfortable indoor conditions an air conditioner must evacuate both building latent and sensible loads. Usually latent load is evacuated by mechanical dehumidification which consists on cooling air below its dew point temperature to condense water vapour. Then air is heated to the required supply temperature. When building latent load is high these two processes become more important and thus electrical energy consumption increases and also CO_2 emission.

Desiccant evaporative cooling system is a friendly environmentally technology which can replace traditional air conditioning systems or be added to them to attenuate their effects. Being thermally driven, it can be used with solar energy which is a clean and free energy.

In literature, we find several studies related to desiccant systems as detailed in Daou et al. (2004). Jurinak (1982) studied seasonal performance of two open desiccant cooling cycles with a silica gel dehumidifier: ventilation cycle(known as Pennington cycle and it is the most used) and recirculation cycle. Jain et al. (1995) compared 4 desiccant cycles for several Indian cities : ventilation cycle, recirculation cycle, Dunkle cycle and a cycle with a wet return surface heat exchanger. They found that the cycle with wet surface heat exchanger has the highest efficiency for all the cities (however the cost of this exchanger is high). Mavroudaki et al. (2002) and Halliday et al. (2002) have separately presented two different feasibility studies for the Pennington cycle used with solar energy in Southern Europe and in UK. They showed that important energy reduction can be obtained and for all the climatic conditions. However for humid regions this reduction is limited because high regeneration temperatures are required.

The main focus of this paper is to study the cooling potential of desiccant evaporative cooling cycle in France. For this purpose a simulation model was developed and an experimental set up was built to validate components modelling. Simulations were carried with the simulation platform SimSPARK developed at LEPTAB (La Rochelle, France) (Mora et al., 2003). This tool generates building models automatically and uses SPARK (Sowell and Haves, 2001) as the solver. It is suitable for adding new components such as our system, since it facilitates models coupling through a simple connection language. A general algebraic and differential equation solver handles the whole problem solution process. Simulations were used to evaluate system cooling potential in France through the boundary line methodology (a graphic aided methodology developed by Lindholm (2000)).

The system was installed in a building in Chambery in Eastern France. It is used to meet cooling load for a training room containing 40 persons. Some preliminary experimental investigations have been made to validate component modelling.

2.   System configuration and working principle

Figure 1 shows the desiccant cooling air-handling unit. It comprises a desiccant wheel in tandem with a thermal wheel with evaporative coolers in both supply and return air streams before the thermal wheel. This system allows cooling and dehumidifying air without using conventional refrigerants. The desiccant wheel contains a desiccant material (Lithium Chloride) which needs to be regenerated with an external heat source (Klingenburg). This heat is taken from a solar installation consisting of a solar storage tank and solar collectors. Since the required regeneration temperatures are low (40°C to 70°C) liquid flat plate collectors are used. Depending on outside air conditions and on building loads, air installation has five operating modes:

- Ventilation mode in which only the supply fan (D-E) is running.

- Direct humidification mode in which supply air is directly humidified (C-D).

- Indirect humidification mode where supply air is sensibly cooled through a rotating heat exchanger (B-C). On the other side of the exchanger, return air is cooled by humidification (G-H).

- Combined direct-indirect humidification mode where both humidifiers and rotating heat exchanger are running on.

- Desiccant mode in which outdoor air is dehumidified through the desiccant wheel. During vapour absorption in the wheel, air is dehumidified almost adiabatically (A-B). Its temperature increases and humidity ratio decreases. Then its temperature is lowered in the rotating heat exchanger (B-C), and in the direct humidifier (C-D). Return air is cooled in an evaporative cooler (F-G) and is used to cool down the process air in the heat exchanger (G-H). Then it is heated to regenerate the desiccant wheel (J-I). The states of the process and exhaust air are represented on the psychometric chart (figure 1).
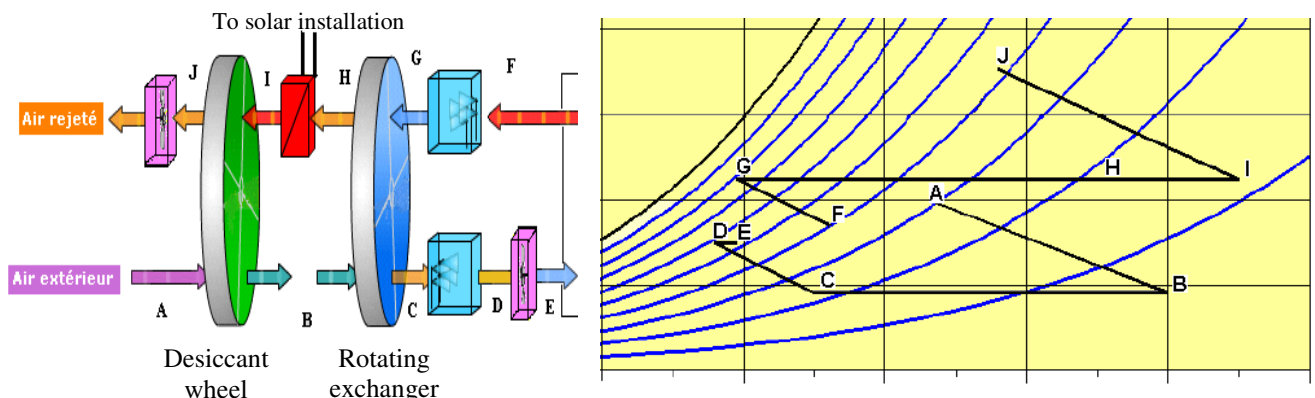
FIG 1: Schematic representation of the desiccant cooling system and the corresponding air evolution in the air diagram.

3.   System modeling

To study system operation and evaluate its performance, it should be coupled with a building for different climatic conditions. This evaluation requires a powerful modeling environment that allows user to test new models and run complex simulations with a short running time. That is why models are developed within the Simulation Problem Analysis and Research Kernel (SPARK), an equation based modeling environment developed by the Simulation Research Group at Lawrence Berkeley National Laboratory (Sowell and Haves, 2001). Description of a problem for SPARK solution begins by breaking it down in an object-oriented way. This means thinking about the problem in terms of its components, where each component is represented by a SPARK object. A model is then developed for each component. Since there may be several components of the same kind, SPARK object models, equations or group of equations, are defined in a generic manner called classes. Classes serve as templates to create any number of objects required to formulate the whole problem. The

problem model is then completed by linking objects together. Using graph-theoretic techniques, SPARK reduces the size of the equation system and uses a Newton-Raphson iterative method to solve the reduced system and, after convergence, solves for the remaining unknowns.

For large and complex problems, building a SPARK simulation can be long and error prone. Therefore a tool called SimSPARK was developed at LEPTAB (La Rochelle, France), to automatically generate simulations for building applications (Mora et al., 2003) and visualize results.

In our simulation, building model was generated by SimSPARK. It is based on a heat balance model and assumes a well-mixed zone with uniform temperature (Mora et al., 2003). Room area is 70 m^2. It has a vegetalized roof and a double glazing southern facade.

Internal radiation exchange was modeled using the fictitious enclosure method developed by Walton (1980). The envelope submodel being expressed as partial differential equations is discretized using a finite difference method within building materials.

Modeling of desiccant wheel is based on analogy theory (Close, 1971; Banks, 1972, Maclaine-cross, 1974). Equations for coupled heat and mass transfer are reduced in two uncoupled differential equations of two independent variables called characteristic potentials which replace humidity ratio and enthalpy. In the psychometric chart and for the lithium chloride in the dilute form, these potentials are approximated by a constant relative humidity curve (from regeneration air inlet conditions) and a line which is close to an isenthalpic curve (from process air inlet conditions) (Rau et al., 1991). Their intersection gives the outlet conditions of process air in the ideal case (Id) (for a wheel with infinite thermal and mass conductances). Then actual outlet conditions are estimated using two efficiencies defined on temperature and humidity ratio (Stabat, 2003):

$$\varepsilon_{dw,1} = \frac{T_{p,o} - T_{p,i}}{T_{Id} - T_{p,i}} \qquad\qquad (1)$$

$$\varepsilon_{dw,2} = \frac{w_{p,o} - w_{p,i}}{w_{Id} - w_{p,i}} \qquad\qquad (2)$$

Where p refers to process air, o outlet conditions of the wheel, I inlet conditions and Id ideal conditions.
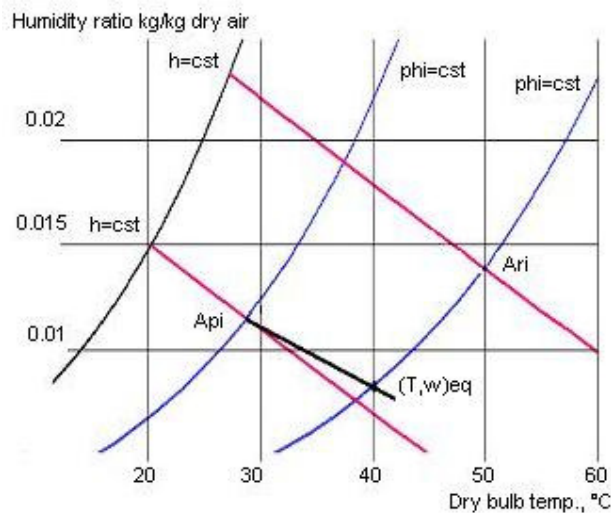
FIG 2: Representation of the characteristic potentials in the air diagram: the first potential is a constant relative humidity curve drawn from regeneration inlet conditions (Ari) and the second is a straight line close to an isenthalpic line (from process inlet conditions Api). Their intersection gives the process outlet at equilibrium conditions.

4. Experimental set-up

The system is installed in a building in Chambery in Eastern France and it uses solar energy to regenerate desiccant wheel. An additional electric heater was added to allow controlling regeneration temperature. Air system has been followed up experimentally and primary results allowed to validate component modeling and mainly the desiccant wheel which is made of fibrous material impregnated in a viscous solution of Lithium Chloride (Klingenburg). Regeneration temperature for this material should not exceed 70°C. Electronic sensors were placed around each component in order to measure temperature and relative humidity. Air flow rate was measured by measuring fan pressure gain.
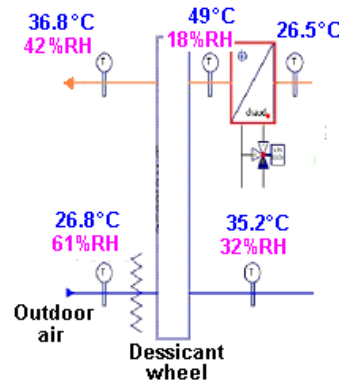
FIG 3 : Operation of the desiccant wheel with a regeneration temperature of 49°C.

Figure 3 shows operation of the desiccant wheel. Return air from the outlet of the rotary heat exchanger has a temperature of 26.5°C. Then it is heated to a temperature of 49°C through regeneration exchanger. On the process side, air inlet temperature is 26.8°C and its relative humidity is 61% and it gets out at 35.2°C and 32% of relative humidity. These results are compared with model results (table 1). We can notice that simulation results are nearly close to experimental values. Differences can be explained by model simplifying hypothesis and also to sensor accuracy which is 2% for the relative humidity.

Table 1 : Air properties on the process side.

	Process inlet	Process outlet	Model outlet
Temperature (°C)	26.8	35.2	35.5
Hum. ratio (kg/kg dry)	0.0135	0.0114	0.01081
Relative hum. (%)	61	32	30
Enthalpy (kJ/kg dry air)	61.4	64.8	63.5
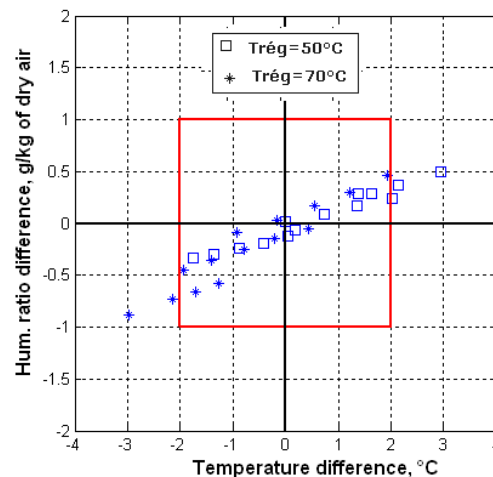
FIG 4 : Comparison between model outlet (for process conditions) and experimental values for the desiccant wheel and for regeneration temperatures of 50 and 70°C.

Figure 4 shows process air temperature and humidity ratio differences for different air conditions and for regeneration temperatures of 50°C and 70°C. The values of ±2°C and ±1g/kg on temperature and humidity ratio differences are limit values for which the maximal error on supply air in a desiccant system is ±1.1°C and ±0.7g/kg (Stabat, 2003). We can notice that model results are acceptable. In general, humidity ratio differences are in the range of ±0.5g/kg. Few points are out of these limits. These points correspond to dry air conditions for which desiccant wheel will not run.

5.   System cooling potential

5.1.   Boundary lines methodology

To study system interaction with outdoor conditions, boundary lines methodology was used. It is a graphic way to display the cooling capacity (how much the air can be cooled in a psychometric chart). A boundary line is "the locus of ambient air states in a psychometric chart, from which the ventilation air can be cooled to a particular required supply air temperature" (Lindholm, 2000)
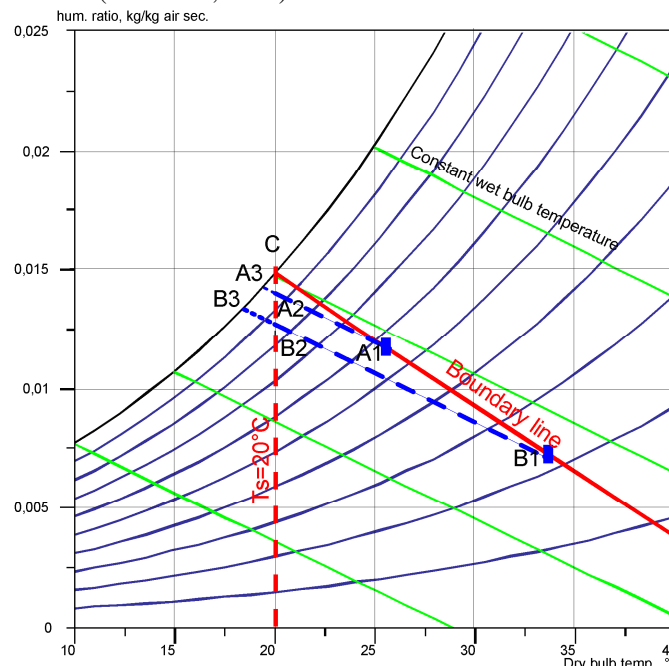
FIG 5 : Boundary line of the direct humidification mode for a supply temperature of 20°C and a humidifier effectiveness of 0.9.

Figure 5 shows the boundary line for the direct humidification mode for a supply temperature of 20°C and a humidifier effectiveness of 90%. This line was drawn using simulations. Each state laying on this line (points A1 and B1 for example) can be cooled by direct humidification to a supply temperature of 20°C (points A2 and B2). If humidifier effectiveness was 100% humidifier outlet would be on the saturation curve (points A3 and B3). Each outdoor state laying to the right of this boundary line cannot be cooled to the required supply temperature. If it is to the left it can be cooled to a lower temperature.

5.2.   System boundary lines

Table 1 : Outdoor conditions for which a supply temperature of 20°C is obtained for different operating modes.

	Outdoor temperature	Outdoor humidity ratio	Outdoor relative humidity
HI	30	0.0087	32,8%
HD	30	0.0092	34,9%
HI-HD	30	0.01305	48,9%
DC	30	0.01527	57%

Table 2 shows outdoor humidity ratio and relative humidity for which a supply temperature of 20°C can be obtained for different modes and for an outdoor temperature of 30°C. As humidity ratio increases, we pass respectively from indirect mode to direct mode, combined mode and to the desiccant mode (Maalouf, 2006).
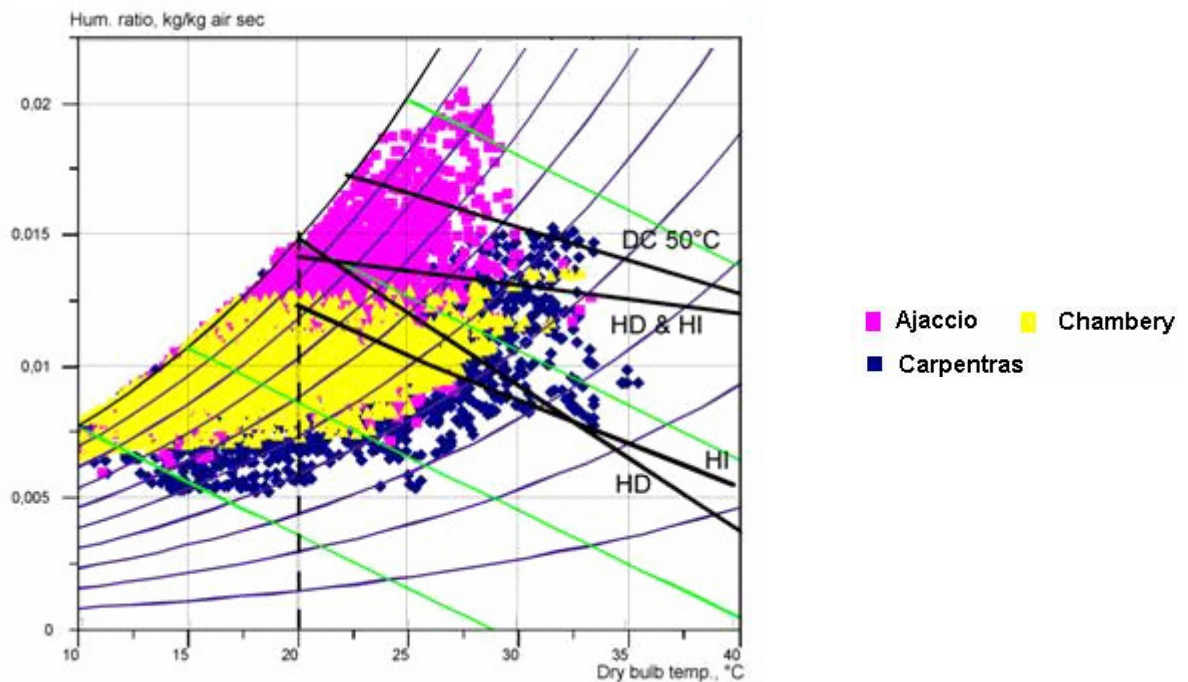
FIG 6 : Boundary lines for system modes and for a supply temperature of 20°C.

Figure 6 shows boundary lines for system different operating modes and for a supply temperature of 20°C (HD refers to direct humidification, HI indirect humidification, HD&HI combined humidification, DC 50°C desiccant cooling with regeneration temperature of 50°C). We notice that for low humidity ratios, direct and indirect humidifications are sufficient to obtain supply temperatures below 20°C. As humidity ratio increases, combined humidification and desiccant mode are better suited. For regions with humidity ratio higher than 14 g/kg of dry air only the desiccant mode supplies temperatures below 20°C. Besides it can be noticed that as outdoor conditions become hotter desiccant boundary line decreases and tends to the combined humidification line which suggests that combined humidification is suited to hot and dry region and desiccant dehumidification is suited to more humid regions. However as humidity ratio increases and becomes higher than 16 g/kg of dry air, regeneration temperature should be increased to allow cooling to temperatures below 20°C.

On the same figure, summer outdoor conditions are also plot for three French cities: Chambery, Carpentras which is more tempered and Ajaccio which has a mediterranean climate (more humid, with outdoor humidity ratio exceeding 20 g/kg of dry air). We can notice that all Chambery states are to the left of the combined mode boundary line which suggests that for this city evaporative systems are enough and there is no need for desiccation (for indoor relative humidity, we tolerate values exceeding 70% for few days). For Carpentras the desiccant mode is satisfying. For Ajaccio conditions, there are some states higher than the desiccant boundary line which means that for this city regeneration temperature should be increased and system primary energy requirement will increase. However using the highest allowed regeneration temperature of 70°C (to avoid harming wheel material), simulations show that there still will be some points upper to the boundary line and indoor relative humidity for this city will exceed 80% for several days during summer. These results suggest that for this city desiccant wheel is not enough (with viscous Lithium Chloride). An additional dehumidification system should be added. These results have also been checked quantitatively using seasonal simulations with a convenient regulation strategy as shown in the following section.

6.   Seasonal simulations

We run simulations for several outdoor conditions and for a period of three months in summer from June to August. The system is coupled to a training room containing 40 persons from 9 A.M. till noon and from 1 P.M. till 6 P.M. Lighting load is 15W/m^2. Humidifiers have an efficiency of 0.85 and rotating heat exchanger efficiency is 0.8. Fans have a multiple speed motor and an efficiency of 0.8. We chose outdoor conditions for the cities shown in figure 6. System regulation is based on occupation time. When room is occupied, system can run in ventilation mode, in indirect humidification mode or in desiccant mode. Air flow rate is 9 Ach. During inoccupation period, system runs either in ventilation or in direct humdification mode. Air flow rate is 3 Ach. Details of regulation strategy are given in Maalouf (2006). To evaluate room comfort conditions, we calculated two parameters:

Temperature index:

$$TI = \sum (T_i - T_{ref}) * \delta(T_i) \qquad (3)$$

$\delta(T_i)$ is equal to 1 if $T_i > T_{ref}$ else it is null. This parameter indicates the values of indoor temperature that exceed reference temperature (its value depends on outdoor temperature).

Relative humidity index:

$$HI = \sum (HR - 70) * \delta(T_i, HR) \qquad (4)$$

$\delta(T_i, HR)$ is equal to 1 if $T_i > 25°C$ and $HR > 70\%$. This parameter adds values of indoor relative humidity that exceed 70% when room temperature is higher than 25°C.

Table 2 : Simulation results

	TI (° hrs)	HI (%hrs)	Regeneration energy (KWh)
Carpentras	6	10	3100
Chambery	2	0	2150
Ajaccio	210	480	5200

Table 2 shows simulation results for the three cities. As expected from figure 6, room conditions for Carpentras and Chambery are satisfactory (TI and HI values are low). For Ajaccio, both TI and HI values are high. Regeneration energy for Ajaccio is also high because of the humid weather.
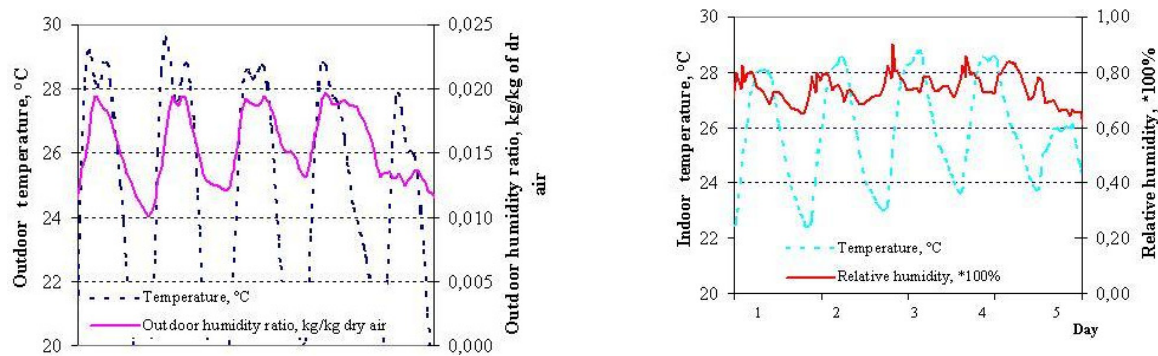
FIG 7 : Outdoor and indoor air conditions for Ajaccio during a week of August.

Figure 7 shows Ajaccio outdoor and indoor air conditions during a week of August. It can be seen that indoor temperature is higher than 28°C and indoor relative humidity higher than 70% almost for the whole week. So in this case (40 persons in the room) the lithium chloride desiccant cooling system should be coupled also to an additional air dehumidifier to insure acceptable indoor conditions (for ex. an electrical cooling and dehumidifying coil).

7.   Conclusion

Provided that it is used appropriately, desiccant cooling technology is a feasible technique. In this paper a model of a desiccant wheel was presented and validated experimentally. It was used to evaluate cooling potential of a desiccant cooling system in France. For this, seasonal simulations were used and also a graphical aided methodology called the boundary lines method. It is shown that outdoor humidity ratio influences system performance. The system is suited to regions where humidity ratio varies between 12 and 16 g/kg of dry air, evaporative cooling being enough for lower values. For Mediterranean coastal regions where humidity ratio exceeds 20 g/kg of dry air, system is less efficient, it requires high regeneration temperatures and it cannot provide comfortable indoor conditions.

8.   Bibliography

Banks P.J. (1972). Coupled equilibrium heat and single adsorbate transfer in fluid through a porous medium – I Characteristic potentials and specific capacity ratios. *Chemical Engineering Science*, Vol. 27.

Close, D.J. (1971). Combined Heat and Mass Transfer in Porous Media: The Further development of an analogy with Heat Transfer, Ph.D. Thesis, Dept. Mech. Eng., Monash University, Clayton, Vic., Australia.

Daou K., Wang R.Z. and Xia Z.Z. (2004). Desiccant cooling air conditioning : a review*, Renewable & Sustainable Energy Reviews*, 1-23.

Halliday S.P., Beggs C.B and Sleigh P.A. (2002). The use of solar desiccant cooling in the UK : a feasibility study, *Applied Thermal Engineering*, 22, p.1327-1338.

Jain S, Dhar PL. (1995). Evaluation of solid desiccant- based evaporative cooling cycles for typical hot and humid climates. *Int J Refrig*, 18 (5):287-96.

Jurinak J.J. (1982). Open Cycle Desiccant Cooling Component Models and System Simulations, Ph. D. thesis, Dept. Mech. Eng.,University of Wisconsin-Madison.

Klingenburg, SECO Dessiccant rotor, installation, operation maintenance, http://www.klingenburg.de/ENGLISH/F_engl.htm.

Lindholm T. (2000). Evaporative and Dessicant Cooling Techniques : Feasibility when applied to air conditioning, Ph. D. thesis, Chalmers University of Technology, Göteborg, Sweden.

Maalouf C. (2006). Etude du potentiel de rafraîchissement d'un système évaporatif à désorption avec régénération solaire, PhD thesis, Université de La Rochelle, France.

Maclaine-cross, I.L., (1974). A Theory of Combined Heat and Mass Transfer in Regenerators, Ph.D. Thesis, Dept. Mech. Eng., Monash University, Clayton, Vic., Australia

Mavroudaki P., Beggs C.B., Sleigh P.A. and Halliday S.P. (2002). The potential for solar powered single-stage desiccant cooling in southern Europe*, Applied Thermal Engineering* 22, pp. 1129-1140.

Mora L., Mendonça K.C., Wurtz E., Inard C.(2003). Simspark: an object-orientedenvironment to predict coupled heat and mass transfers in buildings, Building Simulation'03 Conference, Eindhoven, The Netherlands, 903-910.

Rau J.J., Klein S.A.and Mitchell J.W. (1991). Characteristics of lithium chloride in rotary heat and mass exchangers*, Int. J. heat Mass Transfer*, Vol. 34, No 11, pp. 2703-2713

Sowell E.F. and Haves P. (2001). Efficient solution strategies for building energy system simulation, *Energy and Buildings*, 33, p. 309-317.

Stabat P. (2003). Modélisation de composants de systèmes de climatisation mettant en œuvre l'adsorption et l'évaporation d'eau, Ph. D. thesis, Ecole des Mines de Paris, France.

Walton, G. 1980. A new algorithm for radiant exchange in room loads calculations. *ASHRAE Transactions* 86(2):190–208.

Comparison of a novel ventilation system with a system controlled by relative humidity – influence on comfort, hygiene and energy demand -

Martin Krus, Dr.-Ing.,
Fraunhofer Institute for Building Physics;
krus@hoki.ibp.fhg.de

Doris Rösler, Dipl.-Phys.
Fraunhofer Institute for Building Physics;
doris.roesler@hoki.ibp.fhg.de

Kristin Lengsfeld, Dipl.-Ing.
Fraunhofer Institute for Building Physics;
lengsfeld@hoki.ibp.fhg.de

KEYWORDS: *Novel ventilation system, comfort, hygiene, energy demand, mould growth.*

SUMMARY:
After the energetic renovation of old buildings (installation of air-tight windows) mould growth frequently occurs due to traditional ventilation habits. Mould on internal surfaces of external building elements can be a health risk for the residents. Adequate ventilation, intended to avoid mould growth, must avoid surface boundary conditions suited for mould growth. From the energetic point of view, forced permanent ventilation does not solve the problem. In this paper we will present a novel ventilation system - the dew point switch - in comparison to a ventilation system controlled by indoor relative humidity. This novel ventilation system is based on the idea to install an "artificial thermal bridge" at a selected point of the external wall with a switching dewing sensor on the internal surface. The investigations are executed in a test house with a bad insulation standard, located at the outdoor testing site of the IBP. Measuring sensors were installed at different places to determine temperature and humidity conditions as well as the energy consumption of the heating and the effectiveness of the ventilation system on the indoor climate. The test house is heated and, to comply with the requirement of a realistic moisture load, humidity is supplied to the room according to a humidity profile,which simulates a normal housing. The measurements show the influence of the different ventilation strategies on comfort, hygiene and energy demand.

1. Introduction

After the energetic renovation of old buildings (installation of air-tight windows) mould growth frequently occurs due to traditional ventilation habits. Mould on internal surfaces of external building elements can be a health risk for the residents. Biocides or similar products avoid mould growth in rooms over a certain period of time, but it cannot be completely excluded that the application of these products is a health risk either. Temperature and humidity are the decisive influencing factors for mould growth. Yet, indoor air temperature and humidity are not significant for the risk of mould growth, but the hygrothermal boundary conditions on indoor surfaces. Adequate ventilation, intended to avoid mould growth, must avoid surface boundary conditions as well suited for mould growth, at least in the long run. From the energetic point of view, forced permanent ventilation does not solve the problem. The solution must be found in dependence of boundary conditions occurring on surfaces and caused primarily by non-stationary humidification processes (cooking, showers etc.). Continuous experimental recording of the surface humidity and temperatures is not applicable due to the sensors and costs. Thus, ventilation systems, which are operated at present, are mostly regulated by air quality (CO_2 concentration). Moisture load and the risk of mould growth remain unconsidered.

2. Novel ventilation system

The idea of the development, described in the following and derived from new knowledge about mould growth, is to install artificial thermal bridges at selected points of the external wall. By means of novel programmes e.g. WUFI (Künzel, 1995, Krus, 1996), the hygrothermal room model (Holm et al, 2002), the bio-hygrothermal method to assess the risk of mould growth (Sedlbauer, 2001, Sedlbauer et al, 2002), which were developed by

the IBP this "thermal bridge" may be thermally designed in a way that condensation is developed, if the surface humidity has reached a value in the problematic areas of the internal surfaces of external walls (e.g. corners) to expect mould growth. Fig. 1 (left) shows the draft of a simple structure of such an artificial "thermal bridge".
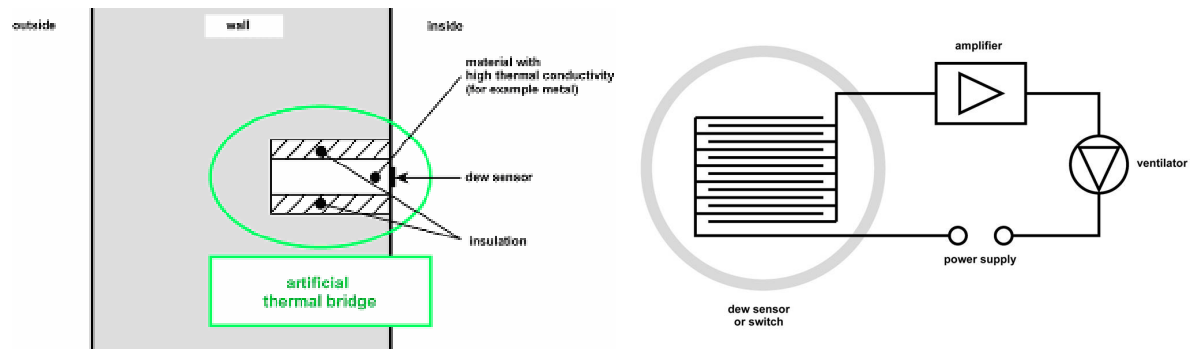
FIG. 1: Schematic design of an artificial "thermal bridge" with dewing sensor (left) and of a dewing sensor itself for the regulation of ventilation (right).

If there are simple, switching dewing sensors on the internal surface of such an artificial "thermal bridge" (structure e.g. as in FIG. 1 (right), but also simple resistive sensors or others), ventilation systems can be operated, as long as there is condensation. Without condensation, the ventilation system will be automatically switched off according to requirements. The advantage is that with the application of such a dew point switch the ventilation is only operated, if the external air temperature is lower than the internal air temperature, what is correct from the building physical point of view. Thus, ventilation is only working, if the indoor air humidity is high and the internal wall temperature is so far below the indoor air temperature that the indoor surface humidity is too high. Unnecessary and partly false ventilation is thus prevented. The special advantage of the application of such a dew point switch is that it is working without any measurement equipment. The dew point switch is cost-efficient and almost maintenance-free, regular calibration measures are unnecessary.

3. Test Procedures

3.1 Facility and Measurement Installation

The investigations are executed in a test house (FIG. 2), located at the outdoor testing site of the IBP. The test house is an old building with two small rooms and bad insulation. The ground plan of the building is shown in FIG. 3. The wall structure is made of 27 cm pumice concrete blocks with internal and external plaster. A window is at the south side, which is covered by a wool blanket on the outside during the investigations to guarantee that there is no influence of solar radiation during the measurements. The infiltration air exchange of the building was determined by Blower-Door measurement, before the ventilation system was installed to obtain values on the natural air exchange. The measurement provided a value for the infiltration air exchange of $n = 0.26$ h^{-1}.

FIG. 2: Aerial view of the IBP outdoor testing site marking the test house (left) and north side of the test house.

Measuring sensors were installed at different places to determine temperature and humidity conditions as well as the energy consumption of the heating and the effectiveness of the ventilation system on the indoor climate. Heating energy consumption and ventilator performance is determined by an energy performance transmitter. All measurement data are recorded per minute by means of the measurement data acquisition system IMEDAS®.
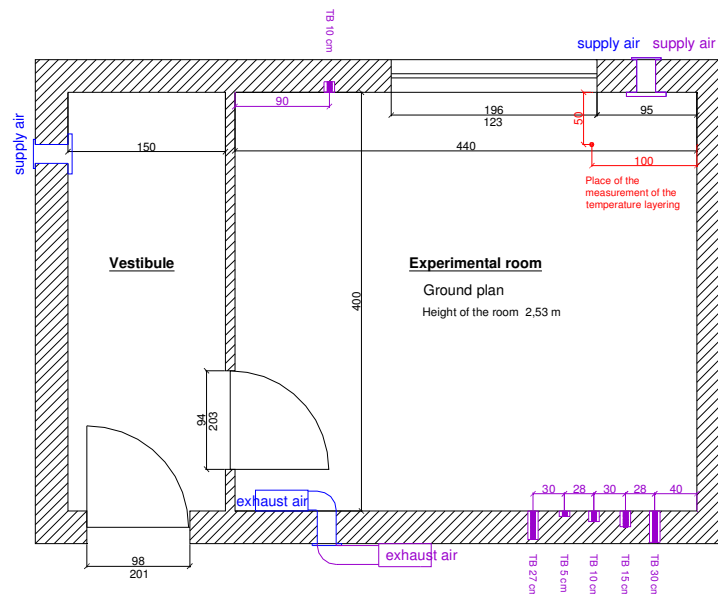
FIG. 3: Ground plan of the test house including the location of the ventilation system and of the different artificial thermal bridges.

Artificial thermal bridges of metal cylinders (see FIG. 4 left) of different length were installed in the wall (FIG. 4 right). Location and length of the thermal bridges are enlisted in the ground plan of FIG. 3. Each dew point sensor on the thermal bridges can be used to regulate ventilation.
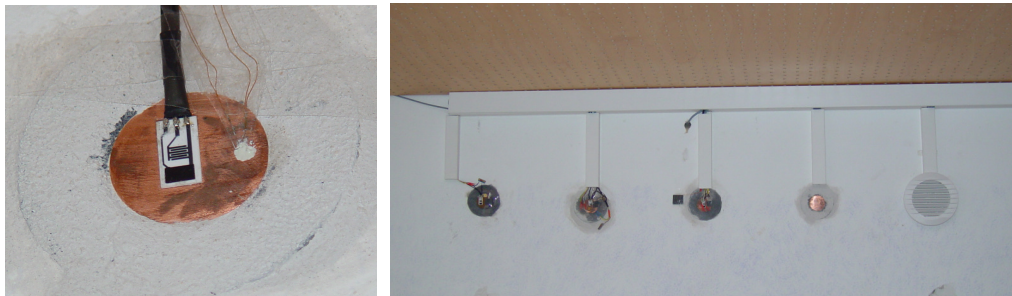
FIG. 4: Photo of an artificial thermal bridge with dewing sensor (left) and installation in the south wall (right).

Besides the newly developed ventilation system with dew point switch another commercial and retrofit ventilation system was investigated for comparison. This system has an air supply element with opening dampers, which are regulated by an installed humidity sensor. The ventilator in the air outlet element is regulated to a constant pressure difference. With increasing opening of the dampers in the air supply element, the pressure difference is falling and the ventilator must work under higher performance to regain the desired pressure difference.

The test building is heated in the test room. A temperature sensor is installed in the centre of the room beneath the ceiling to control the room temperature, and by means of the temperature at this point the heating is controlled. In addition, the humidity sensor measuring the relative air humidity in the room is installed at the same point. The adjacent room is heated by a heating radiator, but the temperature in this room is not connected to the control device in the test room. The air temperature of the adjacent room is approx. 17 °C. Further measuring sensors are installed at the north wall on the internal and external surfaces, and in the corner areas of

the north-west corner at the top and at the bottom, as well as in the south-west corner at the top and in the south-east corner at the bottom. A further temperature sensor is installed at the air supply element measuring the temperature directly at or in the range of the humidity sensor. During the measurements, this sensor was mounted to the element at different positions for test measurements. As air exchange in the room is controlled by the positions of the dampers at the air supply and air outlet elements, a sensor (potentiometer) is installed at the air supply element demonstrating the opening position of the damper. These measurement values only serve for the qualitative presentation allowing the demonstration of the time of reaction as well as the effectiveness.

3.2 Indoor Climate Conditions

To give a clear demonstration and assessment of the effectiveness of a ventilation system, a few boundary conditions must be defined. The window was covered by a wool blanket during the investigations to prevent solar radiation. Moreover, indoor room temperature was kept constant at 20 °C by means of temperature control.

To allow the determination of the influence of a ventilation system in case of humidity being generated in a room, the test room was supplied with a defined amount of humidity. The humidity supplied is equivalent to the normal household of three persons on the basis of the moisture load of 7.8 l/d in a 65 m² apartment. Referred to the size of the test room, humidity amounts to 2.1 kg/d. To comply with the requirement of a realistic moisture load, humidity is supplied to the room daily according to FIG. 5. The humidity profile simulates a normal day including showers in the morning between 6 a.m. and 8 a.m. as well as cooking, washing and general humidity production of human beings in the evening between 4 p.m. and 10 p.m. In the periods between the peaks, humidity is reduced to a lower value simulating the moisture load caused by plants and pets. The slightly lower humidity amounts in comparison to chapter 4.4 result from the smaller size of the rooms.
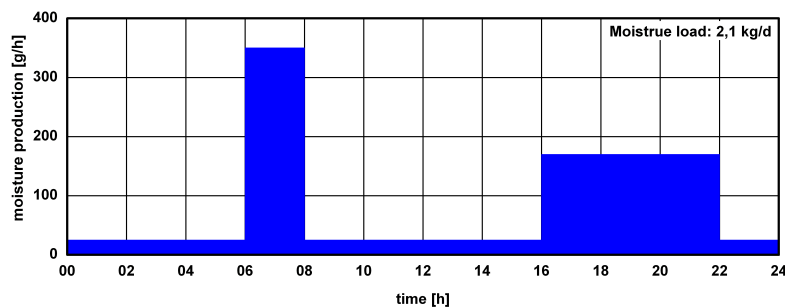
FIG. 5: Daily humidity generation in the test room.

Humidity is supplied to the room by means of ultrasound evaporators regulated by clock timer. These are commercial air humidifiers generating cold mist and have only a low energy input (50 W).

4. Results

The results of the individual investigation periods are presented below. The significant aspect of the investigations is the assessment of the risk of mould fungus growth, the problem of compliance with the criteria of a comfortable indoor climate and the necessary energy demand.

4.1 Indoor climate in the test house without ventilation system

For an appropriate assessment of the influence of the ventilation system it is important to know the indoor climate conditions in the test house in case that the ventilation system is not operating. In this case, the supplied humidity can only be absorbed or ventilated by the sorption behaviour of the room-enclosing materials and by natural air exchange. The courses of the temperature and humidity in the test room are shown in FIG. 6. Indoor air temperature shows constancy at 20 °C and humidity behaviour reflects the reaction to the supplied humidity profile. The humidity input between 6 a.m. and 8 a.m. amounts to 350 g/h and between 4 p.m. and 10 p.m. to approx. 170 g/h. The rise in humidity during humidity peaks is clearly discernible. In the morning, relative humidity increases by 16 % and in the evening by 11 %.
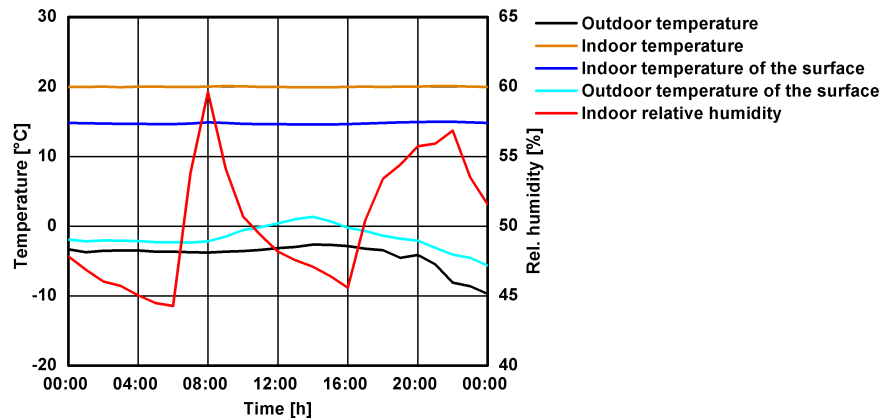
FIG. 6: Courses of temperature and humidity conditions in the test room for one day, if air exchange is only effected by natural infiltration.

4.2 Effect of the ventilator regulation on climate boundary conditions

In the following, exemplary results are presented for periods, in which the ventilator regulation was effected by the dew point switch of the 15 cm thick thermal bridge. FIG. 7 (left) shows the course of the temperatures for two subsequent selected days with temperatures at night of down to – 13 °C and temperatures during the day of approx. – 3 °C. It can be clearly seen that the indoor air temperature (red curve) remains almost constant at 20 C; only during humidification there is a slight decrease in temperature. The internal surface temperature (blue curve) is clearly lower with a value of 13 °C due to the bad insulation of the building. As expected, the temperature of the thermal bridge (green curve) is still lower with a value of 10°C. Compared to the daily course of the external air (black curve) it is considerably higher, but with a phase shift of approx. 6 hours.
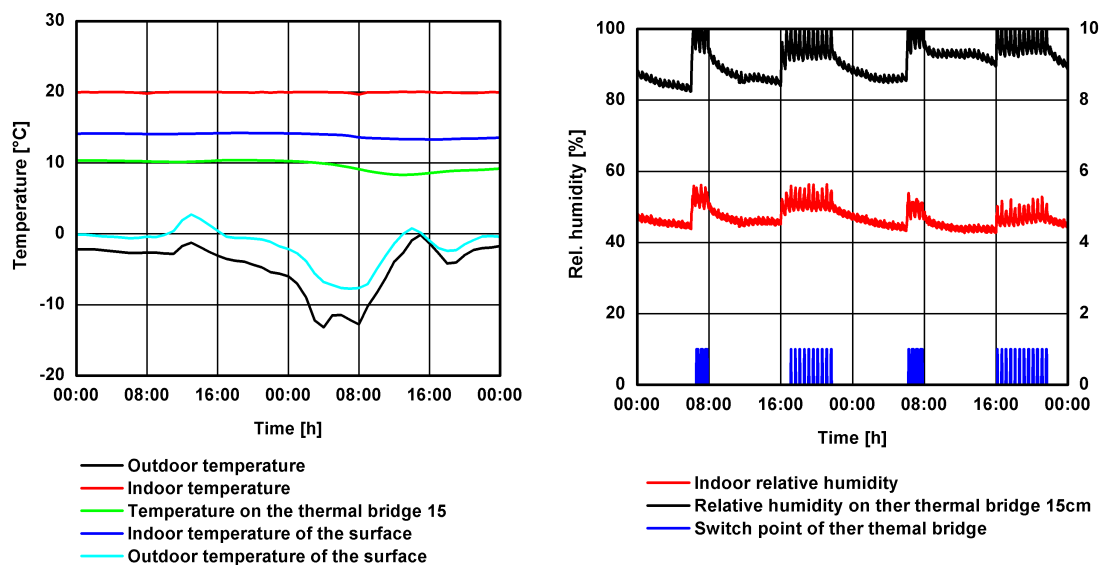
FIG. 7: Temperature courses (left), coursess of humidity values and of the switch point with ventilator regulation by the dew point switch of the 15 cm thick thermal bridge for two subsequent selected days.

FIG. 7 (right) presents the courses of the relative humidity in the room (red curve) for the same period and the relative humidity on the thermal bridge surface (black curve) as well as the switch points of the dew point switch (blue curve). It is discernible that the dew point switch correctly switches on the ventilation, if 100 % humidity is reached at the surface and condensation occurs. The indoor humidity (red line) increases during humidification by approx. 10 % to a maximum of approx. 55 % of relative humidity. In the process, the striking effect is that the

dew point switch again and again switches on and off the ventilation during the periods of humidification. One reason is probably the fact that the performance of the installed ventilator is too high. It can be expected that the restriction of the ventilator results in a clear reduction of the switching operations. This remains to be rechecked in future test series.

Comparable temperatures occur with similar external air conditions (see FIG. 8, left) in case of ventilator regulation by the relative humidity of indoor air within the air supply element. In this case, the green curve indicates the temperature at the point of the air supply element, where the humidity sensor is installed.
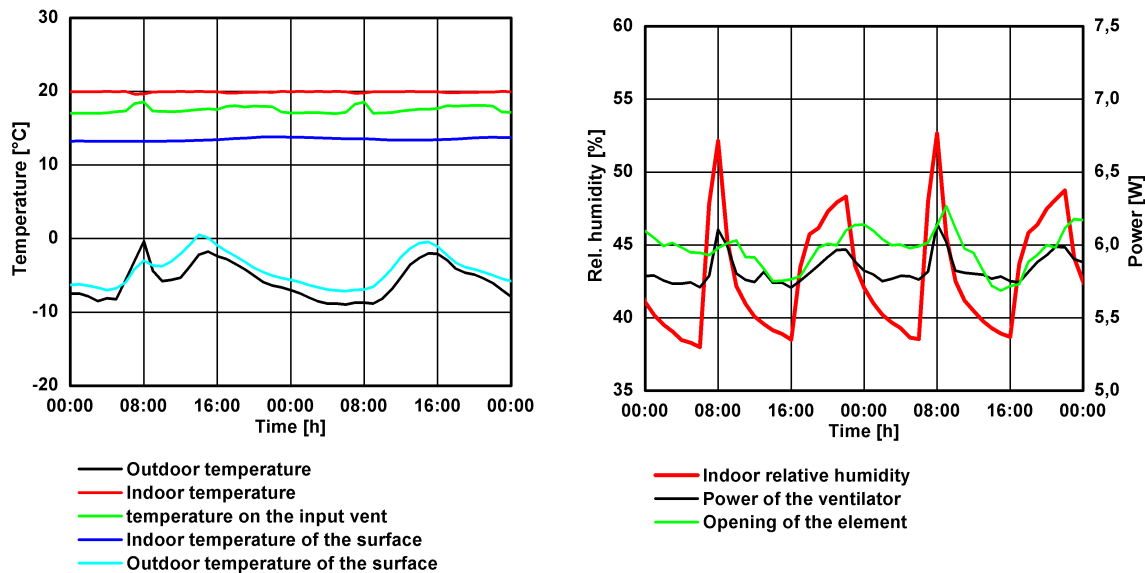
FIG. 8: Temperature courses (left), courses of relative indoor air humidity in the test room and of the damper position at the air supply element as well as of the ventilator performance(right) of two subsequent selected days with ventilator regulation by the relative humidity of indoor air.

The course of indoor air humidity, presented in FIG. 8 (right), shows a similar range of fluctuations as the course with the application of a dew point switch, presented in FIG: 7 (right). Besides the measured ventilator performance (black curve) the damper position (green curve) is also presented where the value at the low end of the diagram indicates completely closed and at the upper end completely open. It is discernible that the ventilation system is constantly working in this case, thus providing a permanent air exchange, which is higher than the infiltration air exchange.

4.3 Effect of ventilation regulations on comfort and mould growth risk

Hourly values of the indoor climate are listed as points of different colour in the comfort diagram in FIG. 9 (left) for the investigation periods in dependence of the kind of ventilation regulation. Climate conditions for both ventilation regulations are always within the range of comfort during the measurement periods. Only when using the dew point switch on the 27 cm thick thermal bridge, the indoor climate is rated as "still comfortable" for a few hours. The reason is primarily a decrease in temperature. Heating output was not sufficient in this case to completely compensate the thermal loss during augmented ventilation. FIG. 9 (right) presents surface conditions and mould growth isopleths of the substrate classes I and II. Boundary conditions are below the LIMs for all kinds of ventilator regulation, meaning that mould growth can be excluded. But the risk of mould growth in the north-west corner still exists, even if applying a 27 cm thick thermal bridge for ventilator regulation. It must be stated that a building with bad insulation was deliberately selected for the investigations. However, after the investigations were started, an infrared photo (see FIG. 10) showed that there was an extreme drop in temperature in the corners of this building. The photo also demonstrates that the temperature in the corners is lower than the temperature at the 30 cm thick metal thermal bridge (the temperature of the 27 cm thick thermal bridge cannot be seen, as it is covered by a plastic grid, as is shown in FIG. 4 on the right). Under these extreme conditions, condensation at the thermal bridge 27 can only be expected, if mould growth conditions are already attained in the corners long ago.
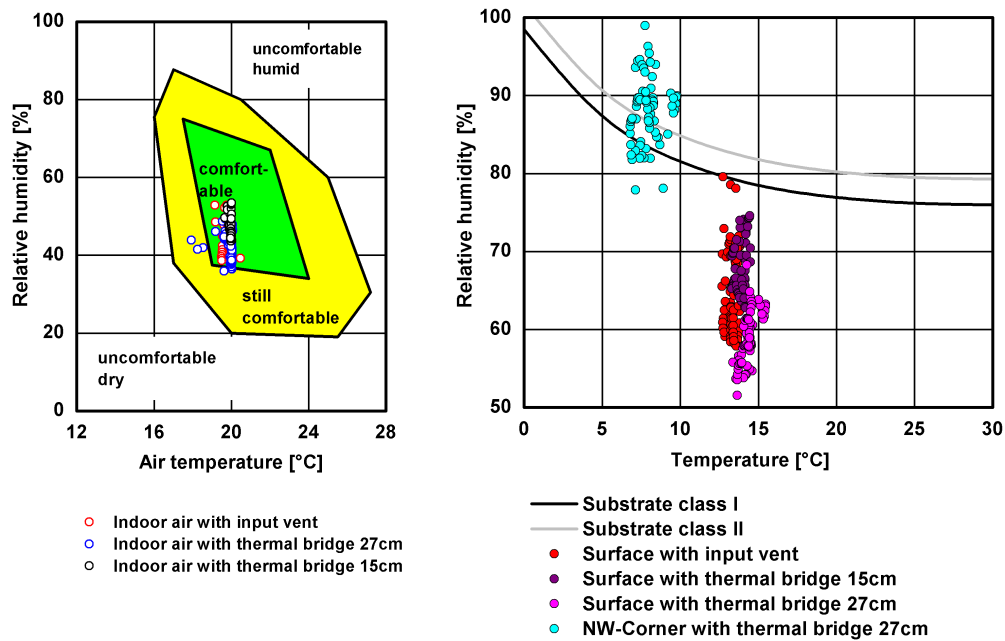
FIG. 9:Comfort diagram (left), representing the humidity-related range of comfort in dependence of indoor air temperature. Hourly values of the indoor climate of the measurement periods are marked as point for the different kinds of ventilator regulation. Growth isopleths(right) for substrate classes I and II. The enlisted points indicate hourly values of the surface conditions of the wall for the different kinds of ventilator regulation and for the north-west corner by applying the dew point switch of the thermal bridge of 27 cm thickness.
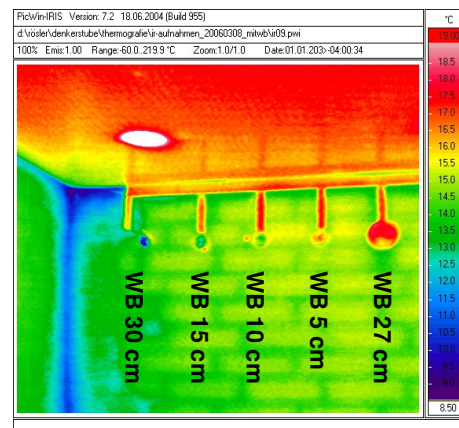
FIG. 10: Infrared photo of the north wall in the test building.

4.4 Impact of ventilator regulation on heating energy consumption

The effect of the electrical room heating was also recorded during the measurement periods. FIG. 11 shows indoor and outdoor temperatures for both regulation systems as well as the course of the heating output. As is obvious, the heating output clearly increases during the humidification phases in case of the regulation with dew point switch (left) as well as in case of the regulation with humidity-regulated air supply element. Yet this fact is not only due to an increase in air exchange at that point of time. In this case, the evaporation heat of the humidity supplied by the ultrasound evaporator must also be added. If comparing both figures, it is easily discernible that there is a lower heating output between the humidification phases in case of ventilation regulation by means of the dew point switch, but that heating output increases in a similar way during the humidification phases. During these measurement periods with similar medium outdoor temperatures of approx. – 5 °C the result for the medium heating output was 1320 W in case of heating with the regulated air supply element. In case of applying

the dew point switch, the result was only 1160 W, although the adjacent room was not heated. But long-term measurements would be necessary to give a secure assessment of the energetic savings by using the dew point switch.
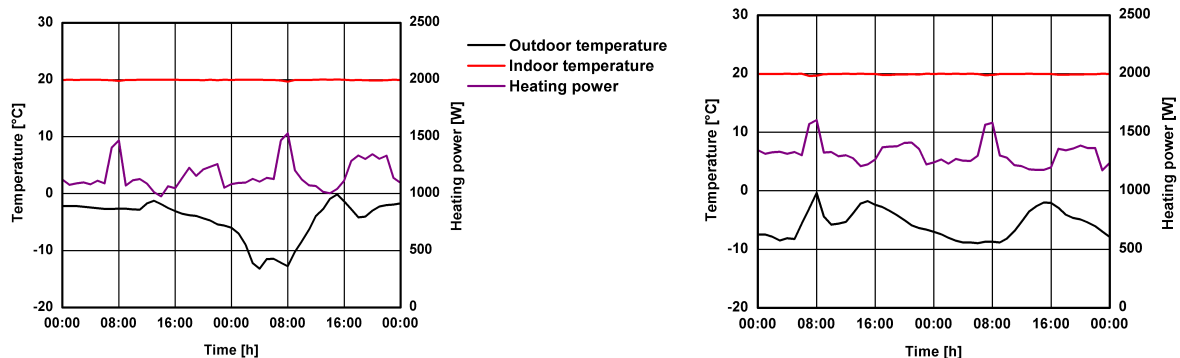
FIG. 11:Gradients of temperatures and heating output for two subsequent selected days with ventilator regulation by means of the dew point switch (left) and of the humidity-regulated air supply element (right).

5. Summary

The submitted measurement results demonstrate the efficiency of the dew point switch on an artificial thermal bridge. Due to the operating mode of the dew point switch, the ventilator is only switched on if necessary, thus avoiding unnecessary ventilation losses. The comparison with another ventilation system, based on humidity-dependent regulation, seems to confirm the energetic advantages of this system. But more profound long-term investigations are necessary for a secure statement in this context. The advantages of this novel ventilation system are first of all that it can be easily retrofitted (of significant importance for old buildings), the low investment costs to be expected, and the fact that it is maintenance-free (humidity and temperature sensors) due to the renunciation of all measurement equipment. The essential difference in comparison to other ventilation systems is that the purpose of this device is not to care for ventilation in favour of the resident and to patronize him or her. The system is only operated, if the ventilation behaviour of the users is insufficient, or so to speak a kind of automatic emergency ventilation. In case of sufficient ventilation, the resident will not take any notice of the device. These are the reasons, why such a ventilator regulation is promising for the area of social housing, as especially in this field conscious handling of living space and ventilation cannot be taken for granted.

6. References

Holm A., Sedlbauer K., Künzel H.M. and Radon J. (2002). Berechnung des hygrothermischen Verhaltens von Räumen – Einfluss des Lüftungsverhaltens auf die Raumluftfeuchte (Calculation of the hygrothermal behavior of rooms – influence of the ventilation habits an the course of the relative humidity in the room), *Tagungsbeitrag für das 11. Bauklimatische Symposium der TU Dresden,* Technical University Dresden, 562 – 575.

Krus M. (1996). Moisture Transport and Storage Coeffizients of Porous Mineral Builduing Materials. Theoretical Principles and New Test Methods, *Dissertation,* IRB-Verlag Stuttgart, p. 1 - 172.

Künzel H.M. (1995). Simultaneous Heat and Moisture Transport in Building Components. – One- and two-dimensional calculation using simple parameters, *Dissertation*, IRB Verlag Stuttgart, p. 1 - 154.

Sedlbauer K. (2001). Vorhersage von Schimmelpilzbildung auf und in Bauteilen (Prediction of mould growth on and in builduing constructions), *Dissertation*, Universität Stuttgart.

Sedlbauer K., Krus M. and Zillig, W. (2002). Vorhersagemodell zur Schimmelpilzbildung bei Wechselklima – Praktische Beispiele (Model for the prediction of mould growth with transient climatic conditions – Application of practice), *Tagungsbeitrag zum Architekten- und Ingenieurtag zum Thema Bauphysik im Holzbau*, Nürnberg, 43 – 55.

Comparison of a Constant Air Volume (CAV) and a Demand Controlled Ventilation (DCV) System in a Residential Building

Dorthe Kragsig Mortensen, Ph.D. student,
DTU BYG;
dkm@byg.dtu.dk

Toke Rammer Nielsen, associate professor,
DTU BYG;
trn@byg.dtu.dk

Claus Topp, Ph.D. Skills Network Manager,
ALECTIA A/S;
clt@alectia.com

SUMMARY:
The aim of this paper was to compare the indoor climate and the energy performance of a Constant Air Volume (CAV) system of $0.5h^{-1}$ with a Demand Controlled Ventilation (DCV) system controlled by occupancy and relative humidity for a studio apartment. Furthermore the impact of building materials hygroscopic properties on indoor climate and energy consumption was investigated for the two systems. Dynamic simulations of the studio apartment were carried out in the program WUFI+ with weather data from Copenhagen including outside temperature end relative humidity. For the non-hygroscopic case it was found that the energy consumption for heating and operating the ventilation system could be reduced by respectively 8.0% and 10.6 % in the case of DCV without negative impact on the indoor climate. Including the hygroscopic properties of the materials resulted in a reduction of the energy consumption for heating and operating the ventilation system by respectively 9.5% and 17.1 % in favour of the DCV system.

1. Introduction

Improved energy performance of building envelopes have during the past decades made buildings more air tight and active ventilation strategies are necessary to provide a good indoor climate. More energy is therefore needed to provide a good indoor climate, at least if the energy performance of the ventilation system is not improved. Five means of how to improve the energy performance of the ventilation system are: 1)Minimize the air change rate; 2)Minimize the energy used to condition the air; 3)Minimize the fan power; 4)Use efficient controls; 5)Behavioural incitement to save energy (Santamouris M. and Wouters P. (2006)). Demand Controlled Ventilation (DCV) and utilization of building materials' ability to exchange moisture with the surroundings represent two possible actions of how to realize the two first means and thereby achieve a good indoor climate and reduce the energy consumption simultaneously.

The main function of the ventilation system in residential buildings is to remove moisture. Thermal sensation and perceived air quality are only effected little by the level of humidity, however relative humidity (RH) levels above 70% during longer periods provide optimal conditions for microbial growth and can over time result in deterioration of building materials. Poor ventilation and the consequences of this can cause adverse health effects such as allergy and asthma etc. (EN15251 (2007), CEN1752 (1998)). The Danish building code requires a constant ventilation rate of $0.5h^{-1}$ in residential buildings (EBST (2008)). This ventilation rate has empirically proven to keep the relative humidity at a level where moisture related problems are kept at a minimum. Maintaining the ventilation rate at a constant level will induce unnecessary energy consumption during periods where the demand for ventilation is low and poor indoor climate during periods where the demand for ventilation is high. In a DCV system the ventilation rate flow is governed by a sensor detecting pollutants, in order to keep the concentration level of the detected substance below a preset value. In a study where the ventilation rate was adjusted according to the production of moisture in a typical apartment it was found that the ventilation rate could be reduced by 20-30% without negative influence on the indoor climate (Bergsøe N.C. (2000)).

Conditioning of air by utilization of building materials' ability to exchange moisture with the surroundings is used in e.g. unventilated museum archives to passively bring the climate close to the strict limits given for such places (Padfield T. (2007)). Opposed to museum archives a substantial amount of moisture is produced in residential buildings and ventilation is a must. The effect of moisture storage in a bedroom was in a study investigated for different ventilation rates and it was found that the indoor humidity conditions fluctuated less in the hygroscopic case compared to the non-hygroscopic case independent of the ventilation rate. The difference in relative humidity between the hygroscopic and the non-hygroscopic case was notably higher at low ventilation rates $(1.0h^{-1})$ compared to high ventilation rates $(1.0h^{-1})$ (Simonson C. J. (2004)). As the ventilation rate of a DCV system varies between high and low values the influence of materials' hygroscopic properties on indoor climate and energy consumption is of interest.

In the present study dynamic simulations of a studio apartment with a CAV system of $0.5h^{-1}$ and a DCV system controlled by occupancy and relative humidity are carried out. Subsequently simulations of the same two systems including the hygroscopic properties of the building materials are carried out.

This paper presents the indoor climate and the energy performance of a DCV system compared to a CAV system. Furthermore the impact of building materials hygroscopic properties on indoor climate and energy consumption is presented for the two ventilation system and finally results of the non-hygroscopic and hygroscopic DCV cases are compared.

2. Method

The simulations are performed in the program WUFI+ (Wärme und Feuchtetransport Instationär) which calculates transient heat and mass transfer. The program considers interactions between the indoor air and the building envelope which enables the possibility to evaluate the effect of interior materials hygroscopic properties on comfort and energy consumption (WUFI+ (2008)).

2.1 Test Model

A studio apartment with an area of $30.0m^2$ and a volume of $75.0m^3$ is used for the investigation, see Figure 1. One wall face outdoors and the rest face zones with the same conditions as in the apartment.
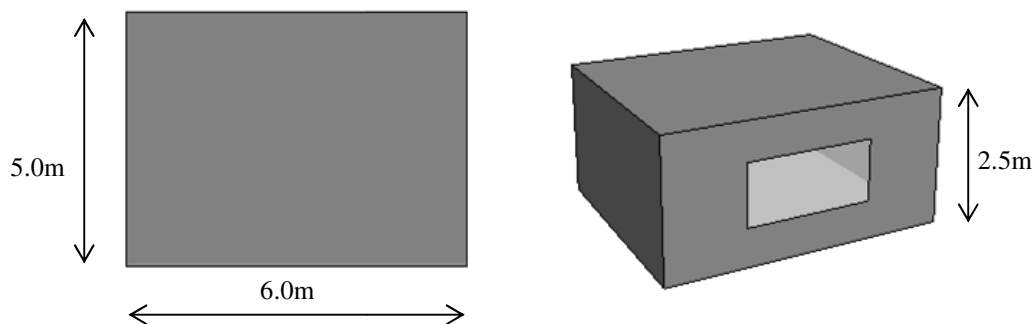
Figure 1: Inner dimensions of the studio apartment

The set point of the heating system is 20°C. The outer wall faces north and has a double glazed window of $6.6m^2$. From the outside the outer wall consists of brick (110mm), mineral wool (200mm) and aerated concrete (100mm). Inner walls and intermediate floors consist of aerated concrete (100mm), mineral wool (80mm) and aerated concrete (100mm). In the non-hygroscopic case (nonH) the surface vapour transfer coefficient is zero and in the hygroscopic case (H) it is $2.2 \cdot 10^{-8}$ kg/m²sPa. Weather data including outside temperature and relative humidity from Copenhagen is used in the simulation. Solar radiation is not included and the simulations therefore represent a worst case situation with regard to relative humidity inside the apartment.

2.1.1 Daily Behavioural Profile

The apartment is occupied by one person who eats breakfast and dinner in the apartment. Table 1 shows the daily profile for moisture production from people and activities in the apartment (WUFI+ (2008)).

Table 1: Daily profile for moisture production from people and activities in the apartment

Time	Human activity level and moisture production		Activity and moisture production	
00:00-07:00	Asleep	0.7g/min	None	0.0g/min
07:00-07:15	Awake	1.0g/min	Showering	44.0g/min
07:15-07:50	Awake	1.0g/min	Cooking	22.9g/min
07:50-08:00	Awake	1.0g/min	None	0.0g/min
08:00-18:00	Away	0.0g/min	None	0.0g/min
18:00-19:00	Awake	1.0g/min	Cooking	15.8g/min
20:00-22:00	Awake	1.0g/min	None	0.0g/min
22:00-24:00	Asleep	0.7g/min	None	0.0g/min

2.1.2 Ventilation System

The ventilation system has a heat exchanger with an efficiency of 87%. The ventilation rate of the CAV system corresponds to $0.5h^{-1}$ ($0.35l/s$ pr. m^2) and the ventilation rate of the DCV system is varied according to the presence of the occupant and the relative humidity in the apartment.

The occupancy of the apartment determines the basic ventilation rate of the system. During unoccupied periods ventilation is needed to dilute pollutants emitted by the building materials and standard EN15251 (2007) states a ventilation rate of $0.1l/s$ pr. m^2 ($0.14h^{-1}$) to do so. For occupied periods the basic ventilation rate must ensure an acceptable indoor air quality and the concentration of CO_2, which is a surrogate for human presence/odour, is used for this purpose. By allowing the concentration of CO_2 to reach 1000ppm at the maximum, the basic ventilation rate of the DCV system must be $0.27l/s$ pr. m^2 ($0.38h^{-1}$) during occupied periods.

A relative humidity above 70% increases the ventilation rate to a maximum value which is reached at 71% RH. The maximum ventilation rate is determined by the air handling unit. An air handling unit which can supply 150-$1350m^3$ per hour supplies 16 studio apartments and the maximum possible ventilation rate is therefore 0.80 l/s pr. m^2 ($1.15h^{-1}$). In Figure 2 the ventilation rates of the CAV and DCV systems are given as a function of relative humidity for occupied and unoccupied hours.
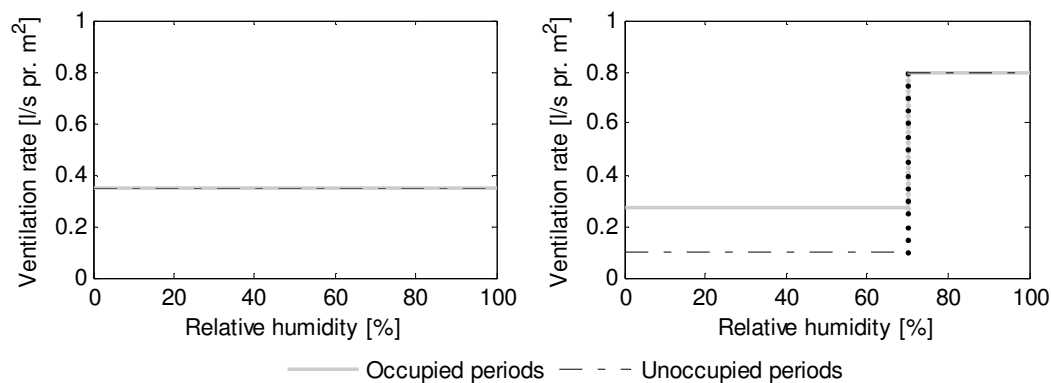
Figure 2: Left figure: Ventilation rate of the CAV systems as a function of the relative humidity in the apartment for occupied and unoccupied periods. Right figure: Ventilation rate of the DCV systems as a function of the relative humidity in the apartment for occupied and unoccupied periods.

2.1.3 Energy Consumption

The energy consumed by the fan, E_{fan}, is a product of time the fan is operated multiplied with the power consumption during that time. The power consumed by the fan, P_{fan}, depends on the pressure drop in the system, Δp_t, and on the efficiency of the air handling unit, η, at a given ventilation rate, q_v.

$$P_{fan} = \frac{q_v \cdot \Delta p_t}{\eta}$$

A static pressure of 100Pa is maintained at reference point in the system to ensure even distribution of the air. At a ventilation rate corresponding to $0.5h^{-1}$ in all 16 apartments the pressure drop in the system is assumed to be 150Pa. A fan performance curve is created based on these assumptions and the following equation (Hansen H. E. (-)):

$$\Delta p_t = p_{ref} + r \cdot q_v^{1.4}$$

Where, p_{ref}, is the pressure maintained in the reference point and, r, is the specific resistance of the system. The efficiency of the complete air handling unit assumed to be 10%. In Figure 3 the power consumption of the fan is plotted as a function of the ventilation rate given in l/s pr. m^2.
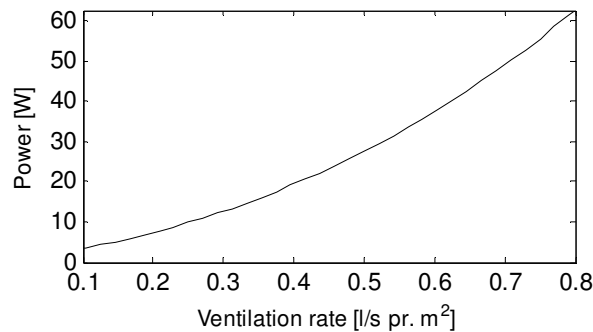
Figure 3: The power consumption of the fan as a function of the ventilation rate given for one apartment.

2.1.4 Indoor Climate

The indoor climate in the apartment is evaluated based on the mean value of the relative humidity and the CO_2 concentration and on the number of hours above 70% RH and above 1000ppm respectively. The CO_2 concentration is used as a measure of the indoor air quality and a concentration below 1000ppm indicates an acceptable indoor air quality.

3. Results

3.1 Overall Performance

In Table 2 the yearly results of the indoor climate and the energy consumption of the CAV and DCV systems are given for the non-hygroscopic and the hygroscopic case.

Table 2: Yearly results of the indoor climate and energy consumption of the CAV and DCV systems.

		Non-hygroscopic case		Hygroscopic case	
		CAV_{nonH}	DCV_{nonH}	CAV_H	DCV_H
Ventilation rate	[l/s]	10.4	3.0 to 24.0	10.4	3.0 to 24.0
	[h^{-1}]	0.5	0.14 to 1.15	0.5	0.14 to 1.15
q_{mean}	[l/s]	10.4	8.0	10.4	7.7
$q_{mean, spring}$	[l/s]	10.4	7.5	10.4	6.5
$q_{mean, summer}$	[l/s]	10.4	9.4	10.4	10.4
$q_{mean, fall}$	[l/s]	10.4	8.0	10.4	7.9
$q_{mean, winter}$	[l/s]	10.4	7.1	10.4	6.1
RH_{mean}	[%]	54.0	56.6	56.3	62.8
>70%	[h]	1900	1075	1304	1352
$CO_{2, mean}$*	[ppm]	792	855	792	873
$CO_{2, max}$*	[ppm]	865	983	865	1010
>1000ppm*	[h]	0	0	0	8
T_{mean}	[°C]	20.5	20.5	20.5	20.5
T_{max}	[°C]	22.0	22.5	22.0	22.5
$E_{heating}$	[kWh/m^2]	24.18	22.25	24.21	21.9
E_{fan}	[kWh/m^2]	4.63	4.14	4.63	3.84

*Results are given for the period where the apartment is occupied; 18:00 - 8:00.

In Figure 4 the number of hours above a given relative humidity and number of the hours above a given CO_2 concentration are seen for respectively a year and the occupied periods in a year.
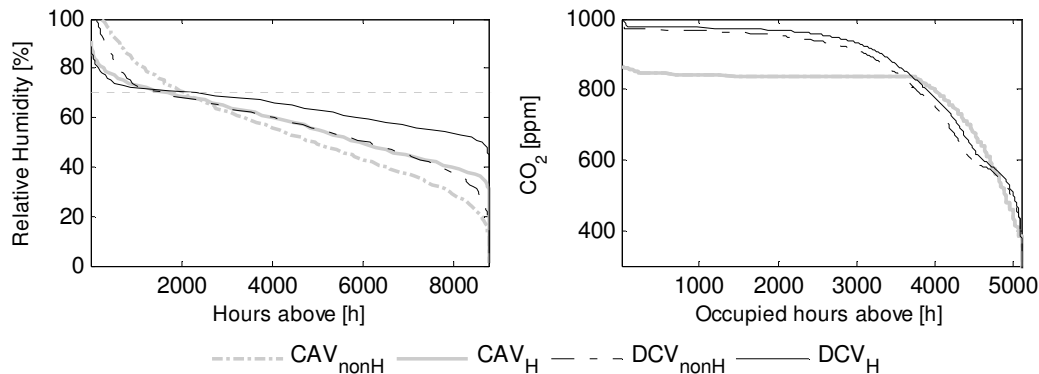
Figure 4: Left graph: Hours above a given relative humidity during a year. Right graph: Hours above a given CO_2 concentration during the occupied periods in a year

3.1.1 Comparison of the CAV and DCV System in the Non-Hygroscopic Case

In the non-hygroscopic case the yearly mean ventilation rate of the DCV system is reduced by 2.4l/s (23.1%) compared to the CAV system. Divided over seasons the highest mean ventilation rate of the DCV_{nonH} case occurs during summer, but is lower than the constant ventilation rate of the CAV system. The mean ventilation rate increases in the summer season due to higher water content of the outside air which results in a high relative humidity indoor, hence a higher ventilation rate. The mean relative humidity of the DCV_{nonH} case is slightly higher compared to the CAV_{nonH} case; however the number of hours with a relative humidity above 70% is considerably lower (43.3%) and the risk of indoor climate problems is therefore reduced. This signifies that moisture is removed faster by DCV_{nonH} system compared to the CAV_{nonH} system due to the higher ventilation rate during periods with high moisture load. The mean CO_2 concentration is also slightly higher for the DCV_{nonH} case but fairly below 1000ppm. The mean relative humidity and CO_2 concentration are increased due to the lower mean ventilation rate of the DCV system. The energy consumption for heating and operating the ventilation system in the case of DCV_{nonH} is reduced by 8.0% and 10.6% respectively compared to the case of CAV_{nonH}.

3.1.2 Comparison of the CAV and DCV System in the Hygroscopic Case

In the hygroscopic case the yearly mean ventilation rate of the DCV systems is 2.7l/s (26.0%) lower compared to the CAV system. As for the non-hygroscopic case the highest mean ventilation rate occurs during summer and in this case it equals the ventilation rate of the CAV system. The number of hours above a relative humidity of 70% is similar for the two cases; however the mean relative humidity is higher in the DCV_H case compared to the CAV_H case. As for the non-hygroscopic case the mean and maximum CO_2 concentrations are higher for the DCV_H case compared to the CAV_H case. The energy consumption for heating and operating the ventilation system in the case of DCV_H is reduced by 9.5% and 17.1% respectively compared to the case of CAV_H.

3.1.3 Comparison of the Non-Hygroscopic and the Hygroscopic Case

The yearly mean ventilation rate of the DCV system is lowest for the hygroscopic case; however the difference in seasonal ventilation rates varies more. The reductions of the mean ventilation rates (23.1% in the non-hygroscopic case; 26.0% in the hygroscopic case) accord well with the Danish study (Bergsøe N.C. (2000)). The mean relative humidity of the CAV and the DCV system is highest for the hygroscopic case but the number of hours above 70% RH is increased for the DCV system and reduced for the CAV system compared to the non-hygroscopic case.

3.2 Diurnal Performance

In Figure 5 the relative humidity (top figures) and the ventilation rate (bottom figures) are given as a function of time during day 2 (Jan 2nd) and day 206 (June 24th).
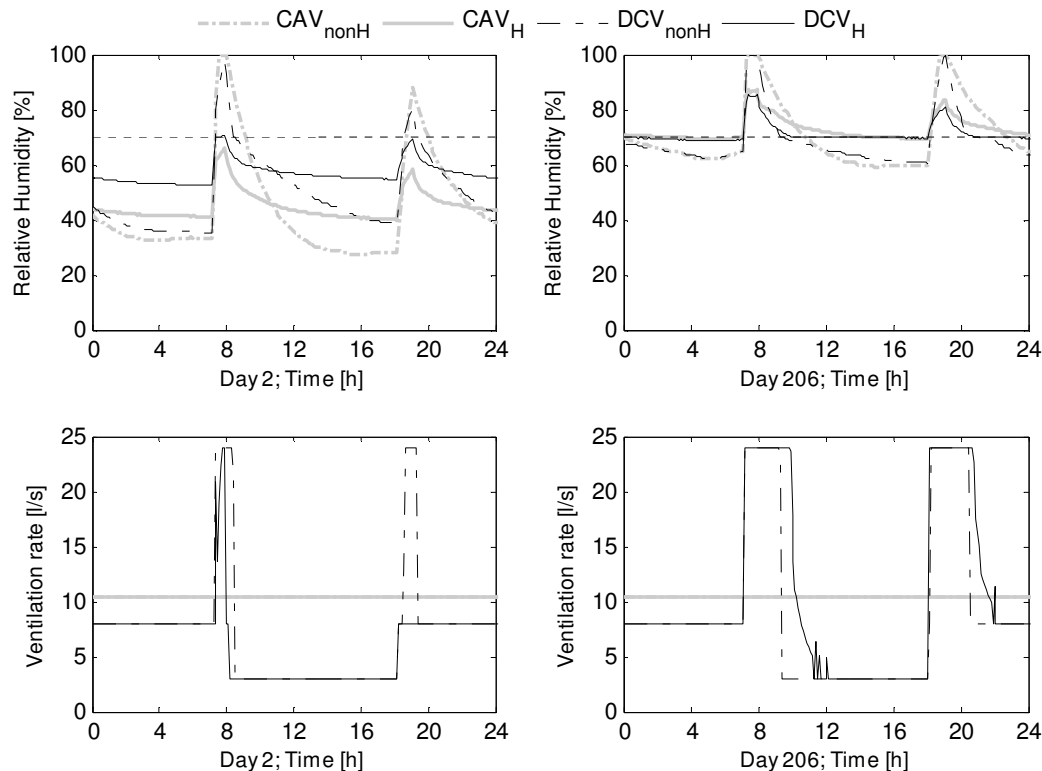
Figure 5:Left figures: RH(top figure) and ventilation rate (bottom figure)as a function of time during day 2(Jan 2nd). Right figures: RH(top figure) and ventilation rate (bottom figure)as a function of time during day 206 (June 24th)

On the top figures it is seen that the building materials are able to reduce the fluctuations of the relative humidity during the periods with high moisture load (7:00-7:50 and 18:00-19:00).The difference in relative humidity between DCV_{nonH} and DCV_H at the basic ventilation rate (3.0l/s during unoccupied periods; 7.9l/s during occupied periods) is higher compared to the difference in relative humidity between CAV_{nonH} and CAV_H (see top left figure). The opposite applies when the ventilation rate of the DCV system increases due to a relative humidity above 70%. The building materials effect on the indoor relative humidity is most pronounced at low ventilation rates which accords with the findings of Simonson et al. (2004).Looking at the diurnal variation of the relative humidity of the DCV system on day 2 (winter season) it is seen that the building materials reduce the relative humidity in the hygroscopic case so that it only exceeds 70% in the morning, hence the ventilation rate of DCV_H is maintained at the maximum level for a shorter period compared to DCV_{nonH}. On day 206 (summer season) the relative humidity exceeds 70% in the morning and in the evening for both DCV_{nonH} and DCV_H; however the relative humidity decrease faster in the non-hygroscopic case compared to the hygroscopic case. The slower decrease is a result of moisture being released from the building materials, which means that the relative humidity is maintained at a higher level for a longer period. Hence the ventilation rate is maintained at the maximum level for a longer period. The diurnal behaviour of the relative humidity and the ventilation rate for a winter and summer day is in agreement with the fact that the difference in seasonal ventilation rates is higher for the hygroscopic case compared to the non-hygroscopic case.

4. Discussion

The reduced energy consumption of the DCV system compared to the CAV system verify the fact that controlling the ventilation rate by demand improves the energy performance of the ventilation system due to a reduced mean ventilation rate. However the size of the reduction of the mean ventilation rate depends very much on the set point of the pollutant which the ventilation rate is controlled by, but also on the preset daily behavioural pattern. For optimization of the DCV system with regard to improving the energy performance and

maintaining an acceptable indoor climate substantial focus should be put on these two topics. Moreover selection of a suitable pollutant to control the ventilation rate and thereby the indoor climate is important.

The hygroscopic materials reduced the fluctuations of the indoor relative humidity due to high moisture load and thereby reduced the mean ventilation rate. This shows that building materials are able to minimize the energy used to condition the air. However in the hygroscopic case the building materials also caused the moisture to stay within the building for a longer period and thereby increase the mean relative humidity. For the DCV system this resulted in more hours with a relative humidity above 70% compared to the non-hygroscopic case but for the CAV system it resulted in fewer hours above 70% RH. The building materials influenced the indoor climate and the energy consumption to some extent and it is therefore reasonable to include moisture transport between the indoor air and the building envelope in future simulation of demand controlled ventilation systems.

The indoor climate of the CAV and the DCV systems in both the non-hygroscopic and hygroscopic cases are after all within similar ranges and a comparison of the energy consumptions of the systems is therefore acceptable. The DCV system controlled by occupancy and relative humidity maintained an indoor climate similar to that of the CAV system but at a lower energy cost in this worst case situation where solar radiation was not included. The Danish building code's requirement of a constant ventilation rate of $0.5h^{-1}$ in residential buildings therefore induces an unnecessary consumption of energy when considering the indoor climate, but with regard to deterioration of the building materials further and more detailed investigations should be performed. This could include analysis of the duration of the periods with a relative humidity above 70% to determine how critical the situation is. Simulations with weather data including solar radiation should be performed.

5. Conclusion

Dynamic simulations of a studio apartment with a CAV system of $0.5h^{-1}$ and a DCV system controlled by occupancy and relative humidity were carried out in the program WUFI+ with weather data from Copenhagen including outside temperature and relative humidity. It was found that the DCV system can maintain an indoor climate similar to that of the CAV system; however at a lower energy cost. The energy consumption for heating and operating the ventilation systems was reduced by respectively 8.0% and 10.6%.

The simulation including the hygroscopic properties of the building materials showed that the materials influenced both the indoor climate and the energy consumption. The energy consumption for heating and operating the ventilation systems was reduced by respectively 9.5% and 17.1% in favour of the DCV system.

Acknowledgement

References

Bergsøe N.C. (2000). Vurdering af ventilationsbehov - Meddelelse 130, SBi. (In Danish)

CEN1752 (1998). Ventilation for buildings – Design criteria for the indoor environment, European Committee for Standardization

EBST (2008). Homepage: http://www.ebst.dk (In Danish)

EN15251 (2007). Indoor environmental input parameters for design and assessment of energy performance of buildings addressing indoor air quality, thermal environment, lighting and acoustics, *CEN*

Hansen H.E. (-). Danvak Grundbog – Varme og Klimateknik, 2. edition. (In Danish)

Padfield T. Larsen P. K., Jensen L. A. And Ryhl-Svendsen M (2007). The potential and limits for passive air conditioning of museums, stores and archives, *http://www.padfield.org/tim/cfys/musmic/musmicbuf.pdf*

Santamouris M. and Wouters P. (2006). Building Ventilation - The state of the art, *Earthscan*.

Simonson C. J., Salovaara M. and Ojanen T. (2004). Moderating Indoor Conditions with Hygroscopic Building Materials and Outdoor Ventilation, *ASHRAE Transactions*, Vol. 110 part II, p. 804-819.

WUFI+ (2008). Homepage: http://www.wufi.de/index_e.html

Under-balancing mechanical supply and exhaust ventilation systems with heat recovery – effects on energy use

Dennis Johansson, PhD
Swegon AB, Tomelilla, Sweden, Building Physics/Building Services, Lund University, Sweden
dennis.johansson@swegon.se

KEYWORDS: leakage, energy use, heat recovery, under balance, under pressure.

SUMMARY:
Mechanical supply and exhaust ventilation with heat recovery is usually slightly under-balanced. That means that the supply air flow rate is lower than the exhaust air flow rate. That is made in cold climates to prevent moist air from infiltrating the building construction parts. If the ratio between supply and exhaust airflow rate is zero, the ventilation system can be understood as an exhaust only system. The under-balanced supply air flow affects the pressure difference between the inside and the outside of the house. This pressure difference in turn affects the sensitivity for infiltration due to buoyancy and wind. A higher under-pressure inside due to under-balance prevents air that comes in with the wind to pass through the building which means that the unintentional air leakage decreases. On the other hand, if the supply air flow is under-balanced, the available air flow for heat exchange in the heat recovery unit is decreased which means that the recovered heat decreases. This effect is dampened by the fact that the temperature efficiency related to the supply air of the heat recovery unit increases if the supply air flow is lowered. Still, the decreasing amount of recovered heat increases the need for heating the ventilation air. This study analyzed the effect of under-balanced supply air on the energy use. Theories were compared to simulations with actual wind data for Swedish climate. It was found that there is a minimum energy use for an optimal under balance ratio in some cases depending on the air tightness and nominal ventilation air flow rate..

1. Introduction

Since buildings are not completely air tight, wind and buoyancy will create unintentional air infiltration, further on denoted leakage. Natural ventilation systems rely on these principles but they are not discussed in this paper. The leakage influences the energy use of the building. The heat recovery unit can not recover heat to air that enters the building through the construction. If the mechanical ventilation system has lower supply airflow rate than exhaust airflow rate, further on denoted under-balanced, the rest of the supply air must be supplied through leaks in the construction. If the wind or buoyancy drives air into the building, this will not be a waste before air is exfiltrating the building due to wind or buoyancy. An under-balanced ventilation system means that there need to be a certain amount of natural forces before the infiltration is unintentional.

That means that an under-balanced system decreases the energy use for leakage but increases the energy use for heating the supply air. On the other hand, the temperature efficiency of the heat recovery system increases based on the supply flow, when the supply airflow rate decreases. This paper compares these two effects due to under-balanced ventilation systems. If the supply airflow rate is zero, the system can be understood as a mechanical exhaust system only.

In cold climates, such as in Sweden, buildings should not have higher air pressure indoors than outdoors to avoid the indoor air, which has higher water content than the outdoor air, to be driven through the construction. If so, there is a risk for condensation since the wall, in a cold climate, gets colder and colder from inside to outside (Hagentoft, 2001). The problem with moist air in the construction can be and is preferably reduced by a vapour barrier on the inside of the wall, which also reduces the energy loss through unintentional infiltration even though complete air tightness is not realistic. To further reduce the problem, the supply airflow rate of the ventilation system is usually designed to be slightly lower than the exhaust airflow rate, which means an under-balanced system. Since the exhaust filter gets polluted more rapidly than the supply filter, the under-balance also gives a margin against a decreasing exhaust airflow rate over time due to increasing filter pressure drop.

The mechanical ventilation is normally designed to handle requirements all the year round. Even if it would be possible to measure the air exchange rate inside the building and adjust the mechanical system to give the correct total airflow rate, including both ventilation airflow rate and leakage, this is not applicable in practice since it is

difficult to measure air exchange rates constantly. Therefore, leakage is here seen as a waste that is not of use, even though it can be argued that, for example, research shows that people would work better with higher airflow rates, which occurs during windy days (Wargocki et al., 2000).

*TABLE 1: The nomenclature used in this paper. * The unit varies with b.*

Quant.	Description	Unit	Def.	Quant.	Description	Unit	Def.
A_1	Area, front wall	m²	50	q_{ex}	Exhaust airflow rate	l/s	70
A_2	Area, the other walls	m²	150	q_{exf}	Exfiltration	l/s	
A_3	Area, roof	m²	100	q_i	Airflow rate into surface i	l/s	
A_4	Area, bottom floor	m²	100	q_{inf}	Infiltration	l/s	
A_m	Envelope area	m²	400	q_{sa}	Supply airflow rate	l/s	56
b	Flow exponent	-	0.7	Δt	Temperature difference	°C	12
C_i	Flow factor, surface i	*		t_{ex}	Exhaust temperature	°C	22
c_p	Air heat capacity	kJ/(kg·K)	1.0	t_{hr}	Heat recovery temperature	°C	
f_i	Form factor	-		t_{out}	Outdoor temperature	°C	8
h	Height of building	m	5.0	t_{room}	Room temperature	°C	22
l_f	Specific leakage	l/(s·m²)	0.8	v	Wind speed	m/s	3.9
P_{inf}	Power for heating infiltration	W		W_{heat}	Total air heating energy	Wh	
P_{sa}	Supply air heating power	W		y	Height level in building	m	
P_{heat}	Total air heating power	W		α	Temperature efficiency increase coefficient	-	1.0
p_0	Pressure inside	Pa		η	Temperature efficiency	-	
p_i	Pressure on surface i	Pa		η_0	Reference temperature efficiency	-	0.70
p_w	Wind pressure	Pa		ρ	Air density	kg/m³	1.2
p_b	Buoyancy pressure variation	Pa					

Thorsell (2005) showed by the use of the computer program VIP+ (Strusoft, 2003), that a ratio between supply and exhaust airflow rate around 80% was an optimal under-balance ratio regarding heating energy use. VIP+ is a building energy use calculation program that takes into account pressure drops over single walls, wind and buoyancy. This study was made on a typical Swedish single family house. The typical under-balance ratio used by designers of air handling units is around 90%. The aim with this figure is to prevent from over-pressure indoors.

1.1 Objectives and limitations

The energy use for heating the air entering the building either by the mechanical supply system with heat recovery or through the building envelope was analyzed due to the under-balance of the supply airflow rate. Annually comparisons were performed with the intention to optimize the under-balance regarding the energy use and present the annual average leakage.

A number of simplifications were made. Only the energy for air heating was taken into account. The energy use for fan electricity was not studied. Cooling was not studied. Only theoretical examples were calculated.

2. Methods

To make the necessary calculations, there is a need for describing the leakage depending on the wind and buoyancy. The heat recovery unit must be described regarding the temperature efficiency as function of the supply airflow rate. The heating power for all entering air must be calculated and applied with outdoor climate data to give examples of actual figures.

2.1 Unintentinal air inflitration

A house was used in this study as shown in Figure 1. This house is a one zone house that could contain two stories with a total floor area of 200 m². Based on Sandin (1990), the pressure obtained by the wind outside each surface of the house can be described by Equation 1. The form factors, f_i, were simplified to 0.7 for the front surface, with the wind direction as normal and -0.7 for the other sides. The bottom floor was supposed to have no influence from the wind. The nomenclature is given by Table 1.
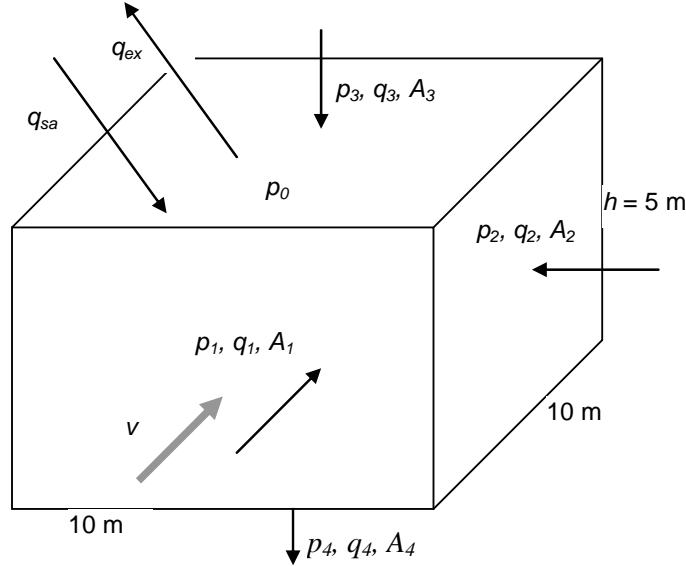
FIG. 1: The example house used in the study. The air entering through surface 2 refers also to the counter surface and the back surface since these three surfaces were assumed to have the same wind pressure coefficient, f_2.

$$p_w = f_i \cdot \frac{\rho}{2} \cdot v^2 \qquad\qquad (1)$$

Equation 2 gives a simplification of the pressure variation obtained due to the buoyancy. This pressure variation is constant for the floor and the roof but varies with the height for the other walls where y can be referred to any height but p_0 must be referred to the same height.

$$p_b = 0.04 \cdot \Delta t \cdot y \qquad\qquad (2)$$

To be able to describe each possible combination of buoyancy and wind influence, the building envelope was split into four parts. The indoor pressure is supposed to be p_0. The pressure that drives air through the wall is the sum of the wind pressure and the buoyancy pressure minus the indoor pressure. The front wall is one part. The rest of the walls is one, the roof is one and the floor is one.

The airflow through an entire surface is given by Equation 3, but for the roof and the floor, no integration is needed over the height. The constant b describes if the flow is laminar, b = 1 or turbulent, b = 0.5, or somewhere between. Nevander and Elmarsson (1994) recommend 0.7 if there is no measurements, which was also used in this study as default. That means that the airflow rate is somewhere between laminar and turbulent, which is reasonable due to the size of leaks. If b were 0.5 and the wind speed were doubled, that would result in a doubled airflow rate due to the wind. If b>0.5, an increasing wind speed will increase the airflow rate through the wall more than linear.

$$q_i = \frac{C_i}{h} \cdot \int_0^h \left(f_i \cdot \frac{\rho}{2} \cdot v^2 + 0.04 \cdot \Delta t \cdot y - p_0 \right)^b \cdot dy \qquad\qquad (3)$$

The walls can have incoming air below and outgoing air above a certain height level at the same surface, which must be taken care of in Equation 3. The constant C_i is given by Equation 4. Leakage in a house is measured as an airflow rate, l_f at 50 Pa pressure difference per m² envelope surface (Boverket, 2002). The Swedish regulation gives the maximum value 0.8 l/(s•m²) for dwellings. All air going in through a wall, denoted infiltration, must be heated with the power P_{inf}. If air was going out from a wall, denoted exfiltration, it was assumed that it was unintentional leakage. The exfiltration is denoted q_{exf}. The infiltration is called q_{inf}.

$$C_i = A_i \cdot \frac{l_f}{50^b} \tag{4}$$

Equation 5 gives flow continuity where constant density is assumed to simplify the expressions. The difference between all incoming and all outgoing air is the air extracted by the exhaust fan minus the air supplied by the supply fan. The difference between the mechanical exhaust airflow rate and the mechanical supply airflow rate must be equal to the sum of the airflow rates entering the envelope by wind and buoyancy. Equation 5 can be solved algebraically if $b = 1$ or if $b = 1/2$ and buoyancy is neglected but in realistic cases, a numerical solution for p_0 is needed and thereafter a calculation of the airflow rates through each surface.

$$q_1 + q_2 + q_3 + q_4 = q_{ex} - q_{sa} = q_{inf} - q_{exf} \tag{5}$$

2.2 Heat recovery unit

The heat recovery unit recovers heat from the exhaust air to the supply air. The temperature that the outdoor air can be heated to is described by Equation 6. Freezing in the heat recovery unit was neglected. The temperature efficiency of the heat recovery unit depends on the supply airflow rate. If the supply airflow rate decreases while the exhaust airflow rate is constant, η increases, which is reasonable to believe due to the longer time in the heat exchanger. It is not realistic that the temperature efficiency exceeds 1 but it is reasonable that it will be close to 1 at zero supply airflow rate. In this study, it was assumed that the temperature efficiency followed Equation 7, with η_0 taken from measurements of the heat recovery unit with equal airflow rates.

$$\eta = \frac{t_{hr} - t_{out}}{t_{ex} - t_{out}} \tag{6}$$

$$\eta = \eta_0 + \alpha \cdot (1 - \eta_0) \cdot \left(1 - \frac{q_{sa}}{q_{ex}}\right) \qquad 0 \leq \alpha \leq 1 \tag{7}$$

2.3 Power balance

Equation 8 gives the power needed to heat the infiltrating air to the room temperature. The power needed to heat the air coming from the supply side of the heat exchanger to the room temperature is described by Equation 9. In this study, it was assumed that $t_{ex} = 22°C$ and $t_{room} = 20°C$. That means that it was assumed to be slightly warmer at roof level where the exhaust devices are located than in the centre of the room. The infiltrating air as well as the supply air is assumed to be heated to the room temperature. That means that the possible internal heat gains were neglected.

$$P_{inf} = \rho \cdot c_p \cdot q_{inf} \cdot (t_{room} - t_{out}) \tag{8}$$

$$P_{sa} = \rho \cdot c_p \cdot q_{sa} \cdot (t_{room} - t_{hr}) \tag{9}$$

The two powers P_{inf} and P_{sa} were summed to give the power needed to heat the total airflow rate, P_{heat}, for both ventilation and leakage. It was not analyzed how the air infiltration eventually influences for example the heat transmission. It was not analyzed how the electricity use for the fans changed even though it should benefit the under-balanced system since the pressure drop through the building is much lower than through the supply system.

To obtain the annual energy use, the wind speed and the outdoor temperature were inserted for each annual hour and the resulting powers were summed.

2.4 Outdoor climate

Outdoor climate data was used regarding wind speeds and outdoor temperatures for the annual energy use comparisons. These data were taken from Meteonorm (Meteotest, 2003) for average years for Malmö, southern Sweden, N55.6°, and Kiruna, northern Sweden, N67.8°. The annual average wind speed in Malmö is 5.5 m/s and the annual average outdoor temperature is 8.0°C. In Kiruna, the annual average wind speed is 3.7 m/s and the annual average outdoor temperature is -1.2°C.

The wind measurements are usually made 10 m above the ground in free areas. This measured wind speed was scaled to 71% of the measured wind speed before it was used according to Sandin (1990). This was made since a typical house is located in a more crowded area with shading effects that lowers the air speed of the wind.

3. Results

Results from the calculations are presented based on the typical house described. To determine the ratio between the supply and exhaust airflow rate from the difference between them, the actual exhaust airflow rate is needed. The influence from leakage will be larger if the envelope area of the house is larger compared to the mechanical exhaust airflow rate. Standard values for the different parameters were set according to Table 1. If nothing else is mentioned, these values were used for the non-varied parameters.

3.1 Unintentional air leakage
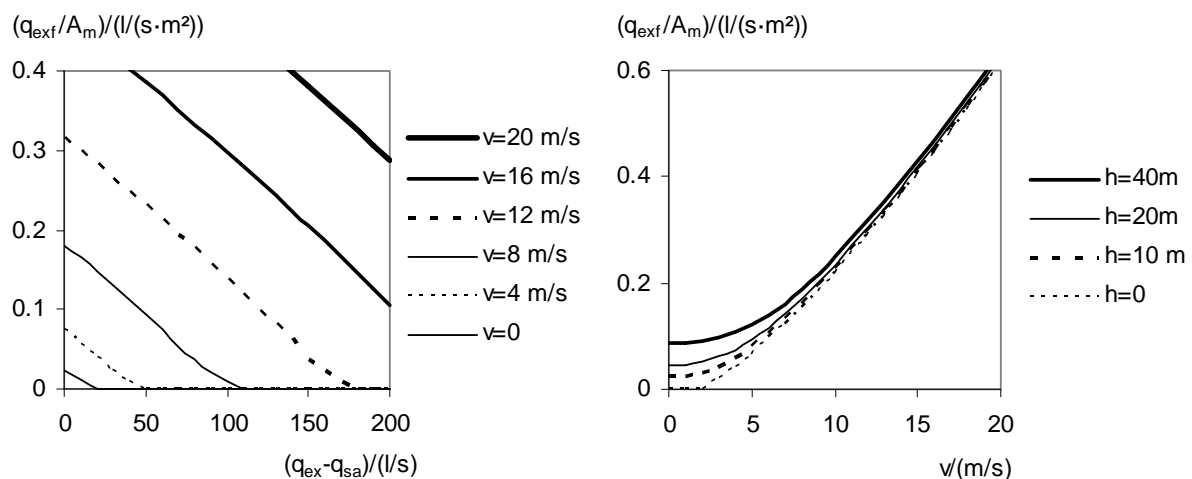
FIG. 2: Left: The leakage divided by the envelope area at different wind speeds. At a certain under-balance, the leakage is zero. Right: The leakage as a function of the wind speed and the building height. Zero height is a way to describe what happens without buoyancy.

The air leakage, q_{exf}, depends on all mentioned parameters. The wind speed, v, and the outdoor temperature, t_{out}, varies over time. The specific leakage, l_f, is a building design parameter. The areas and the height are probably determined by other aspects than the leakage and are constant. The form factors are determined by physics. Figure 2 shows the leakage for the typical house at different differences between the exhaust and supply airflow rate of the ventilation system. The influence from different building heights is also given by Figure 2. The default $q_{ex}-q_{sa}$ makes the leakage zero at low building heights. At high wind speeds, the height influence is negligible.

The annual average leakage divided by A_m and l_f is given by Figures 3 for the Malmö and Kiruna outdoor climate respectively. This means that if the l_f = 0.8 l/(s•m²), the location is Malmö and $q_{ex}-q_{sa}$ = 20 l/s, the annual average leakage is 4.4% of the measured value at 50 Pa.
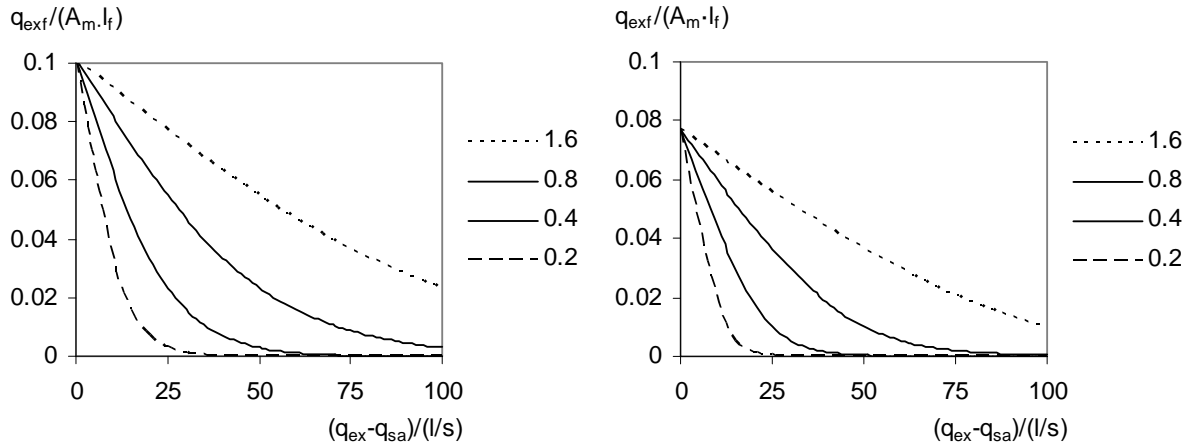
FIG. 3: Left: The annual average leakage as a ratio of the leakage factor, l_f, for Malmö. Right: The annual average leakage as a ratio of the leakage factor, l_f, for Kiruna. L_f is given the legend.

3.2 Power need

The power need at a certain time with the parameters according to the default in Table 1 is shown in Figure 4. The $q_{ex}-q_{sa}$ is rewritten to the ratio q_{sa}/q_{ex} with q_{ex} at default value. There is a minimum that varies with l_f. The linear behavior at low airflow rate ratios means that there is no leakage at all when $q_{ex}-q_{sa}$ increases.

In Figure 4, to the right, the performance of the heat recovery unit is varied regarding η_0 and α. At those conditions, there is no optimum if the increase of the performance of the heat recovery unit is too small when q_{sa} decreases.
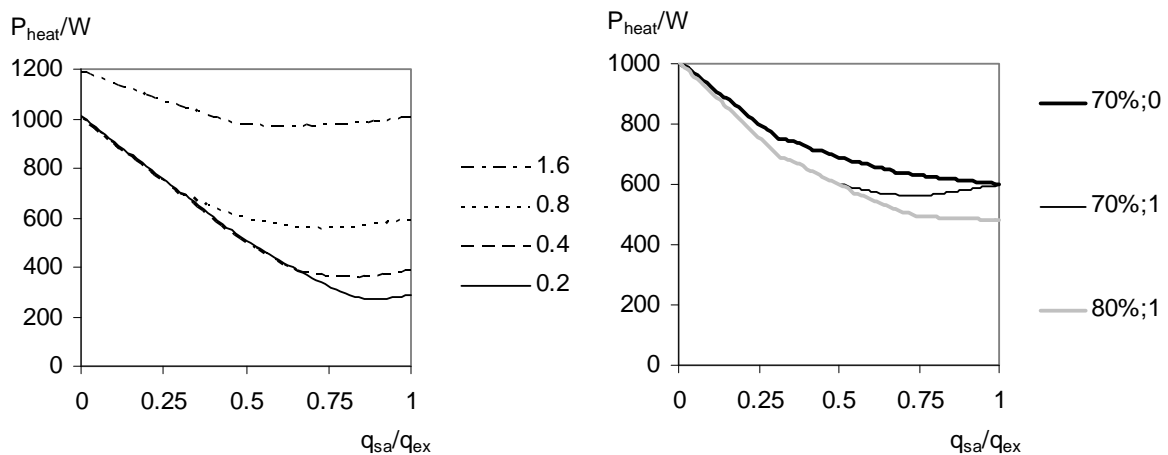
FIG. 4: Left: The total power for heating the air at default conditions. The legend gives l_f in $l/(s•m^2)$. Right: The total power for heating the air at default conditions. The legend gives η_0 and α respectively.

3.3 Energy use

If the power at a certain condition is calculated for each annual hour, the annual energy use will be obtained. Figure 5 gives the annual energy use for heating all air for the Malmö case and the Kiruna case respectively. The optimal ratio between the supply and exhaust airflow rate regarding the energy use for heating air depends slightly on the exhaust airflow rate, which is shown in Figure 6 for Malmö. Figure 6, to the right, gives q_{sa}/q_{ex} at the lowest annual energy use for different η_0 for Malmö. At a certain level around $\eta_0 = 80$ %, the optimal ratio becomes one. For Kiruna, it was around the same value.
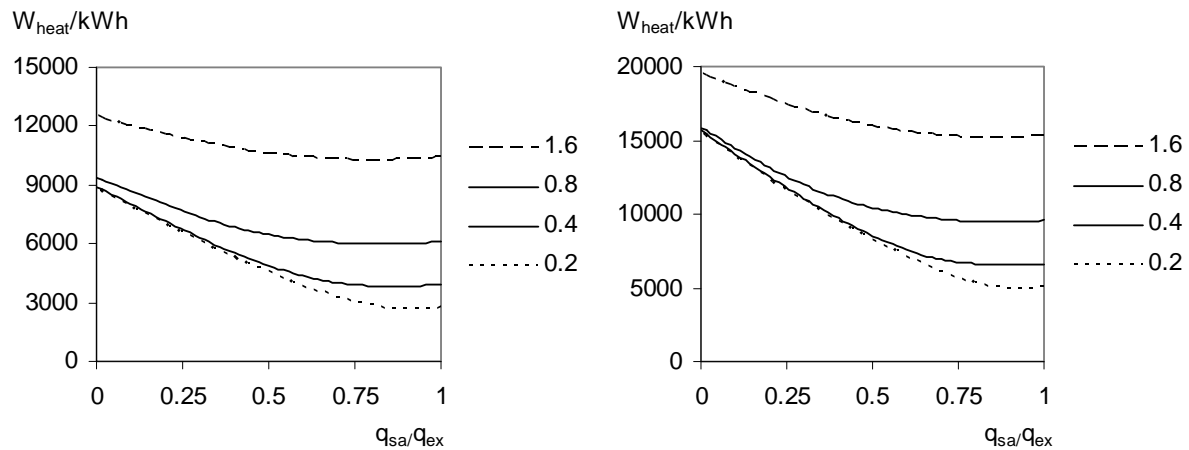
FIG. 5: The annual energy use for heating air for Malmö (left) and Kiruna (right) depending on the ratio between supply and exhaust airflow rate. The legend shows lf in l/(s•m²) in falling order.
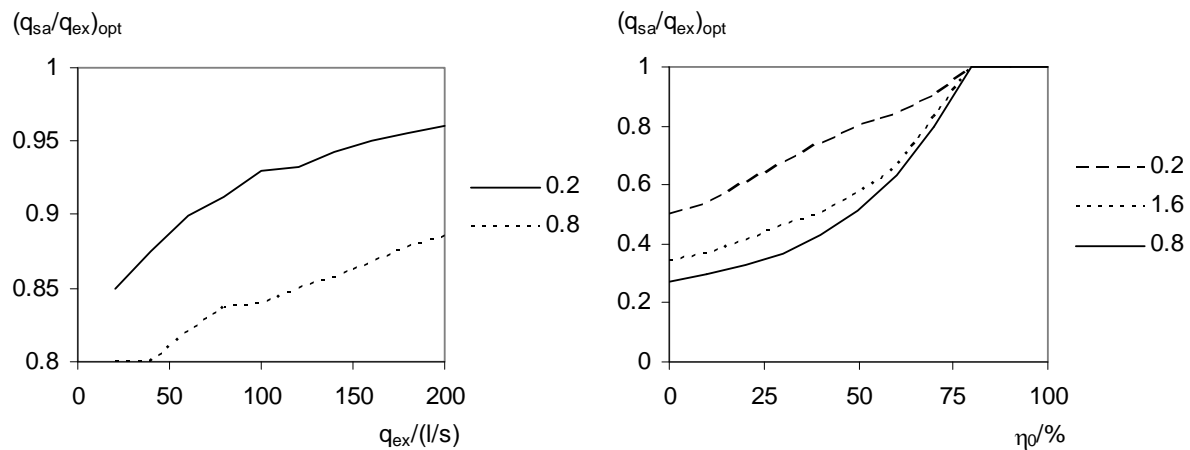
FIG. 6: Left: The optimal ratio between supply and exhaust airflow rate due to an energy use perspective for Malmö. The figures in the legend is lf in l/(s•m²). Right: The optimal ratio between supply and exhaust airflow rate due to an energy use perspective for Malmö. The figures in the legend is lf in l/(s•m²).

4. Discussion and conclusion

The leakage and the use of heating for the air depends on a number of parameters that has been numerically tested in this study. Generally, a low leakage results in a low energy use for air heating. It is also shown that there is a minimum energy use at a certain under-balance in some cases, though there is no large influence on the energy use due to the under-balance that is needed for moisture safety in cold climates. At certain cases, an optimal under-balance was shown to be lower than one. In a leaky house with a moderate heat recovery unit, the ratio between supply and exhaust airflow rates can be typically 80% which is lower than the common design. For more air tight houses, the optimal ratio is higher.

On the other hand, the actual benefit from an optimal design is lower with a more airtight house. In Malmö, an optimal design in the default case, with $l_f = 0.8$ l/(s•m²), can save 2.0% of the air heating energy or 120 kWh for the house compared to the balanced ventilation, which yields 6109 kWh annually. If it is assumed that the house has a floor area of 200 m², the energy use for air heating in the balanced case is 30.5 kWh/m² of floor which is reasonable. If $l_f = 0.4$ l/(s•m²) for Malmö with other parameters according to the default case, the energy use for balanced ventilation becomes 3923 kWh, or 19.6 kWh/m², and the saving from optimal under-balance would be 99 kWh which is 2.5%. That comparison clearly states that the air tightness itself is of much more importance for

the energy use than the under-balance. If η_0 is lowered to 60% and the rest of the parameters are default, the saving due to optimal under-balance becomes 599 kWh or 8.4%.

The temperature efficiency of the heat recovery unit seems to highly influence the possible saving from under-balance. Here, it was assumed a linear increase when q_{sa} decreased, but in further studies it should be measured how the heat recovery works with under-balance.

The computer program Enorm (Svensk Byggtjänst, 2000), a Swedish building energy calculation program that simplifies the leakage to an assumeption that there is a constant annual leakage of 5% of the measured value at 50 Pa pressure difference, l_f, for supply and exhaust systems. For exhaust systems, 4% is assumed. The annual average leakage seems to be able to reach 10% of the leakage at testing pressure, 50 Pa. If an under-balance of 10%, or 7 l/s, and the Kiruna outdoor climate is used according to Figure 3, the figure becomes around 6%. An under-estimation of the annual average leakage result in an even higher under-estimation of the energy use since the leakage is higher at cold outdoor temperatures when the buoyancy is higher. This is shown in the data by comparison between the summed P_{inf} and a multiplication of the density, heat capacity, average flow and the number of degree hours. A b close to 1 would decrease the annual leakage to around 5% of the testing value.

If actual houses are protected locally by other buildings, fences or vegetation, the leakage should be lower than indicated in this study. On the other hand, the simplifications of the wind form factors, f_i, to two average values for the whole building should increase the leakage since there are spots with higher negative form factors that can increase the leakage.

The ratio between the leakage for balanced ventilation and for exhaust ventilation was 8 for the Malmö case, where the leakage is 8.8% for a system with 10% under-balance and 1.1% for a system with 100% under-balance. It can be argued that a house with an exhaust system has fresh air valves that increase the leakage. On the other hand, the resulting under-pressure for the default case with 100% under-balance and $l_f = 0.8$ l/(s•m²) is around 5 Pa which is reasonable both from the fact that most buildings seems to be less air tight than the requirements say and from the fact that 5 Pa is needed to, at least partly, control the air movements in the house.

In the future, this study could be added with a more comprehensive power balance for the entire house. The influence on fan electricity use and the airflow rate from the under-pressure was neglected sinze these around 10 Pa is small compared to other pressure drops in the ventilation system. This could be anlayzed further.

This study shows that a supply and exhaust system with heat recovery uses less energy than an exhaust system even though the leakage is decreased several times due to the under pressure from an exhaust system. The optimal under-balance for a supply and exhaust system should not be large enough to undermine the benefit with a controlled air path and heated supply air.

5. References

Boverket (2002). *Boverkets byggregler – BFS 1993:57 med ändringar till och med 2002:19*, Karlskrona, Sweden, in Swedish

Hagentoft, C.E. (2001). *Introduction to Building Physics*, Studentlitteratur, Lund, Sweden

Meteotest (2003). *Meteonorm handbook, manual and theoreti-cal background*, Switzerland, http://www.meteonorm.com/, 2008-01-15

Nevander, L.E., Elmarsson (1994). *Fukthandbok – Praktik och teori*, Svensk Byggtjänst, Stockholm, Sweden, in Swedish

Sandin, K. (1990). *Luftströmning*, Building Physics, Lund Univerity, Lund, Sweden, in Swedish

Strusoft (2003). *VIP+, software manual*, Limhamn, Sweden, http://www.strusoft.com, in Swedish

Svensk Byggtjänst (2000). *Enorm 1000*, Manual, http://www.byggtjanst.se/, in Swedish

Torsell, R. (2005). *Energianvändning och livscykelkostnad för ventilations- och uppvärmningssystem i småhus*, Building Services, TVIT—05/5004, Lund University, Lund, Sweden, in Swedish

Wargocki, P., Wyon D.P., Sundell, J., Clausein, G. and Fanger O. (2000). The effects of outdoor air supply rate in an office on perceived air quality, sick building syndrome (SBS) symptoms and productivity, *Indoor Air*, 10, pp.222-236

Radiation Effects On Exterior Surfaces

Kehrer Manfred, Dipl.-Ing.,
Hygrothermics Department, Fraunhofer IBP;
Manfred.Kehrer@ibp.fraunhofer.de

Schmidt Thomas, Dipl.-Phys.,
Hygrothermics Department, Fraunhofer IBP;
Thomas.Schmidt@ibp.fraunhofer.de

SUMMARY:
In hygrothermal simulations usually the long-wave radiation effects are ignored or treated in a simplified way. Temperatures at exterior surfaces can not be calculated accurately in that way. A detailed radiation model has been developed to simulate the hygrothermal behaviour at the exterior surface of building components. Multiple experimental validation calculations show the capability of that model. Furthermore it is shown that neglecting the long-wave radiation effects on exterior surfaces can lead to simulation results which are not "on the safe side".

1. Introduction

Temperatures at exterior surfaces of building components are affected by heat fluxes in various ways. Beside heat fluxes due to heat conduction within the component and convective heat exchange with the surrounding air radiation effects play a decisive role. Usually only the short wave solar radiation heating up the surface during the day is taken into account explicitly. The long wave, thermal radiation exchange between the exterior surface and the surroundings is often neglected or only modelled with a constant overall increase of the heat transfer coefficient as for instance in a German standard (EN ISO 6946, 1996). Most hygrothermal simulation tools use this simplified model. The real temperatures at surfaces can only be reproduced with limited accuracy in this way. Especially overcooling in the night-time of sky-oriented exterior surfaces below the temperature of the surrounding air can not be calculated. To estimate the risk of algae growth due to temperatures below dew point and water condensation, the effect of thermal emission must be taken into account. An investigation reported in (Energy Design Update, 2006) speculates that in specific climatic zones flat roofs begin to accumulate water if these effects are ignored in their design.

2. Radiation Model

In order to accurately calculate the temperatures of exterior surfaces a detailed radiation model was developed at Fraunhofer IBP based on physical fundamentals. This model was integrated into well established hygrothermal software (Künzel, H.M., 1995) for the calculation of the coupled heat and moisture transport in building components.

To quantify all relevant radiation terms affecting an exterior surface a complete balance of all these terms is set up:

$$I = a \cdot I_s + \varepsilon \cdot I_l - I_e \qquad (1)$$

I	[W/m²]	balanced net radiation at the component's surface
a	[-]	short wave absorption coefficient of the component's surface
I_s	[W/m²]	short wave solar radiation incident onto the component's surface
ε	[-]	long wave emission coefficient (=absorption coefficient) of the component's surface
I_l	[W/m²]	long wave radiation incident onto the component's surface
I_e	[W/m²]	long wave radiation emitted by the component's surface

A positive value of the balanced net radiation I will then lead to a heating up of the component's surface and a negative value will lead to a cooling off. The solar radiation I_s and the long wave radiation I_l can be splitted as follows:

$$I_s = I_{s,dir.} + g_{atm.} \cdot I_{s,diff.} + g_{terr.} \cdot I_{s,refl.}$$ *(2)*

$I_{s,dir.}$	[W/m²]	direct solar radiation
$g_{atm.}$	[-]	atmospheric field-of-view fraction (atm. FoV)
$I_{s,diff.}$	[W/m²]	diffuse solar radiation
$g_{terr.}$	[-]	terrestrial field-of-view fraction (terr. FoV)
$I_{s,refl.}$	[W/m²]	solar radiation reflected by the ground

$$I_l = g_{atm.} \cdot I_{l,atm.} + g_{terr.} \cdot (I_{l,terr.} + I_{l,refl.})$$ *(3)*

$I_{l,atm.}$	[W/m²]	atmospheric long-wave counterradiation
$I_{l,terr.}$	[W/m²]	terrestrial long-wave counterradiation
$I_{l,refl.}$	[W/m²]	atmospheric long-wave counterradiation reflected by the ground

The two field-of-view fractions are calculated (see DIN EN ISO 6946, 1996) as follows:

$$g_{atm.} = \cos^2(\frac{\beta}{2})$$ *(4)*

β [°]   inclination of the component (90° for a vertical wall)

and

$$g_{terr.} = 1 - g_{atm.}$$ *(5)*

Figure 1 shows the radiative situation of an exterior wall where all radiation terms can be seen.
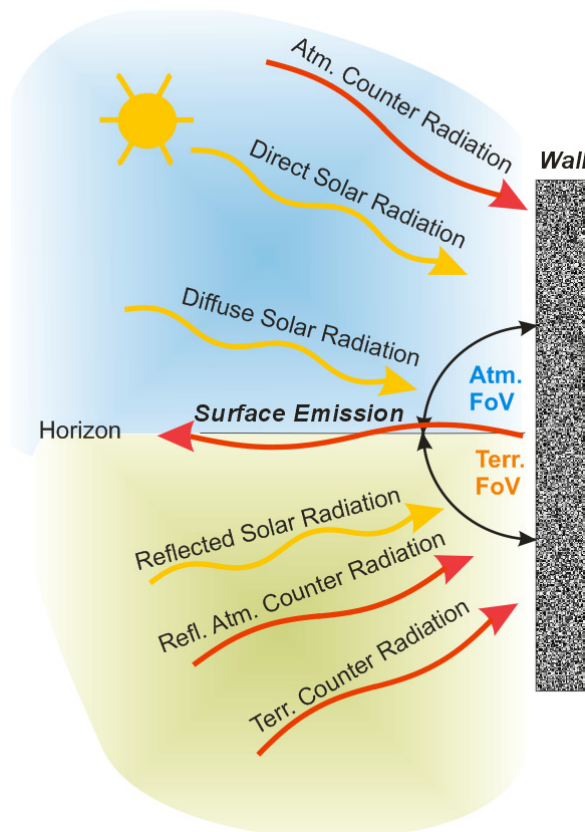
FIG. 1: Radiative situation of an exterior wall.

The equations (2) and (3) contain 3 radiation terms each that we need to know (in hourly values if possible). On the other hand most climatic data sets available typically contain only:

$I_{s,diff.}$ [W/m²]   (see above)
$I_{s,dir.,h.}$ [W/m²]   direct solar radiation on a horizontal surface
$I_{l,atm.}$ [W/m²]   (see above)

To be able to use those generally available climatic data, the other needed radiation terms can be derived as follows:

$$I_{s,refl.} = \rho_{s,terr.} \cdot (I_{s,dir.,h} + I_{s,diff.}) \qquad (6)$$

$\rho_{s,terr.}$ [-]   short wave reflection coefficient of the ground

$$I_{l,terr.} = \varepsilon_{l,terr.} \cdot \sigma \cdot T_{terr.}^4 \qquad (7)$$

σ [W/m²K^4]   Stefan-Boltzmann constant ($5,67 \cdot 10^{-8}$)
$\varepsilon_{l,terr.}$ [-]   long wave emission coefficient of the ground
$T_{terr.}$ [K]   temperature of the ground

$$I_{l,refl.} = \rho_{l,terr.} \cdot I_{l,atm.} \qquad (8)$$

$\rho_{l,terr.}$ [-]   long wave reflection coefficient of the ground

The temperature of the ground is set to the air temperature as an approximation, because the ground temperature itself is usually not available. $I_{s,dir.}$ can be calculated from $I_{s,dir.,h.}$ as described in (VDI-Guideline 3789, 1994) if the position of the sun is known.

So far, all mentioned radiation terms are explicitly known before the calculation and do not depend on unknown calculation results. In contrast the last radiation term, the long-wave emission from the component's surface, depends on the temperature of the component's surface as follows:

$$I_e = \varepsilon \cdot \sigma \cdot T_{Sur}^4 \qquad (9)$$

T_{Sur} [K]   temperature of the component's surface

To solve this nonlinear dependency in a linear equation system, as used in our hygrothermal software, equation (9) must be linearized by using a Taylor series. This leads to the following linearized term which can be added to the linear equation system.

$$I_{e,lin} = \varepsilon \sigma T_0^4 + 4\varepsilon \sigma T_0^3 \cdot (T - T_0) \qquad (10)$$

$I_{e,lin}$ [W/m²]   linearized emitted radiation
T_0 [K]   temperature of the component's surface before an iteration step
T [K]   implicit temperature of the component's surface after the iteration step

3. Validation

The validation of the model above is split into two parts. Part No.1 will validate the calculation of the surface temperature if the short-wave and long-wave radiation onto the surface are well known because they have been measured. Part No. 2 will validate the calculation of the long-wave radiation incident onto the surface from the climatic data typically available.

3.1 Calculation of the surface temperature

For this validation documented field test at the IBP is used. The considered wall assembly has the following composition starting from the exterior:

light-gray wall colour;

2 mm finishing plaster;

3 mm reinforcement plaster;

10 cm polystyrene insulation;

36,5 cm masonry wall;

1 cm gypsum plaster.

Because of the thermal decoupling of the exterior plaster and the small heat capacity of the exterior plaster the temperature at the component's surface is mainly depending on the exterior boundary conditions (temperature and radiation). In addition, the wall is north oriented, therefore night-time overcooling below ambient air temperature is expected. Surface temperature, air temperature, short-wave and long-wave radiation onto the surface (I_s and I_l) have been measured. Also the RH of the air was measured at the IBP weather station nearby. The long-wave and short-wave absorptivity (a=0.39; ε=0.96) were measured at the IBP laboratory. A convective heat transfer coefficient of 8 W/m²K was used which corresponds roughly to a mean air speed of 1 m/s during the investigated time period (see EN ISO 6946, 1996).
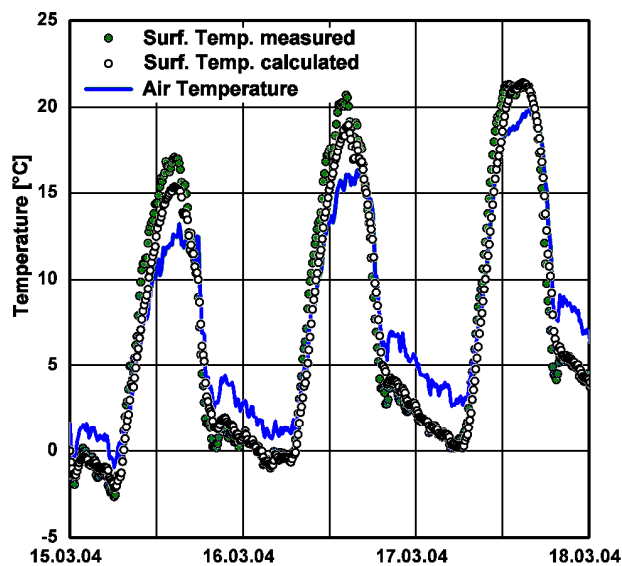
FIG. 2: Measured and calculated surface temperatures at IBP test site.

Figure 2 shows the comparison of measured and calculated temperatures at the surface of the EIFS wall at the IBP test site during a period of three days. We can see a maximum deviation of about 2 °C between measured and calculated temperatures by day. In particular, we notice good agreement of both temperatures by night. The overcooling effect is represented very well and one should notice that the calculated surface temperatures would not fall at all below the ambient air temperature if these long-wave radiation effects were just modelled with an overall increase of the heat transfer coefficient.

3.2 Calculation of the long-wave radiation incident onto the surface

To validate equation (3) we use the measured values of two pyrgeometers at the IBP test site which have a wavelength range from 5 µm to 25 µm (see Figure 3). We use the measured long-wave radiation data $I_{l,atm}$ of the horizontal pyrgeometer and calculate the long-wave radiation I_l expected on a vertical wall. For this we need the air temperature taken from the IBP weather station as an approximation for ground temperature. Afterwards we can compare the calculated and the measured long-wave radiation onto a vertical wall (see Figure 4). Hourly values of a three year period are shown in this diagram and every dot represents a one hour value which ideally should be on the bisecting line. We can see generally good agreement, but we also have to notice a systematic difference between measurement and calculation (about 9 W/m²). The reason for this systematic difference is probably the fact that we assume all parts of the sky to contribute equally to the long-wave radiation measured on the horizontal surface which is only an approximation of the reality. Further investigations will follow.

FIG. 3: Horizontal (left) and vertical (right) pyrgeometers at the IBP test site.
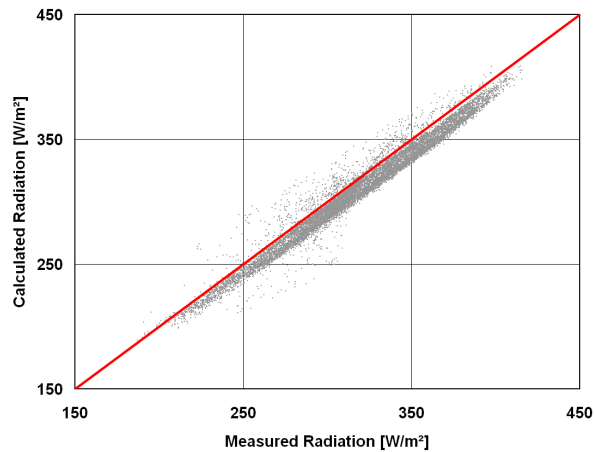
FIG. 4: Comparison of calculated and measured long-wave radiation onto a vertical wall.

4. Application and Conclusion

The following application will show the hygrothermal consequences if the complete radiation model described above is used. Figure 5 shows the assembly and the hygrothermal model of a typical wooden flat roof construction. The exterior bitumen felt is white colored (short-wave absorptivity 0.2; long-wave emissivity 0.9) to protect the roof from solar heat gain in summer. The roof is located in Holzkichen, Germany and the climate file of 2003 is used where hourly values of $I_{s,diff}$, $I_{s,dir.,h.}$ and $I_{l,atm.}$ were measured hourly at the IBP weather station.
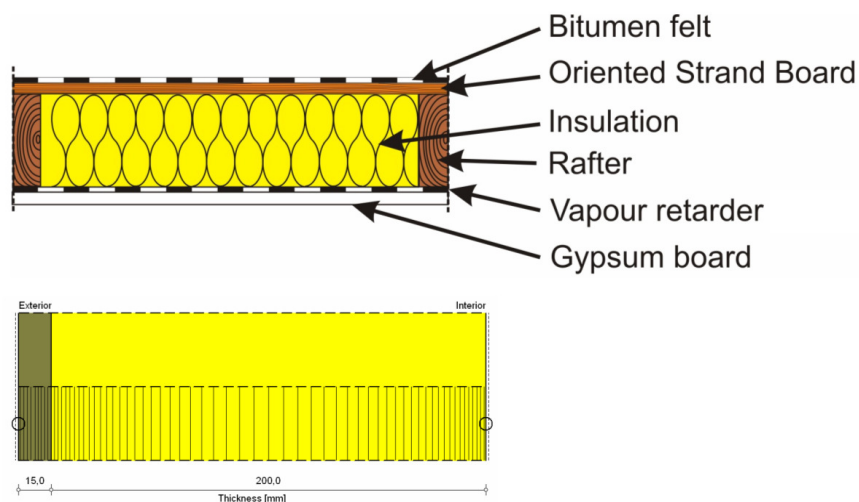
FIG. 5: Assembly (top) and hygrothermal model (bottom) of a typical wooden flat roof construction.

The following three variants were considered:

simplified long-wave exchange (traditional approach);

complete radiation balance;

no solar radiation.

The variant "simplified long-wave exchange" models the long-wave exchange by adding a constant contribution to the heat transfer coefficient. A standard value is used for this constant.

The variant "no solar radiation" uses the simplified long-wave exchange, too, but tries to compensate for the lack of night time overcooling by omitting the drying potential furnished by solar heating. If validated, this approach could be used by simulation tools with simplified radiation models to obtain nevertheless results "on the safe side".

The water content of the OSB board in all three variants can be seen in Figure 6. The variant "simplified long-wave exchange" shows a decreasing water content of the OSB board. This could lead to the mistaken conclusion that the construction performs well. In contrast the variant "complete radiation balance" shows that moisture damage will most likely occur, because of the accumulation of water within the OSB board. Also, the variant "no solar radiation" has an increasing water content and will lead to the conclusion that this is a problematic construction. But the moisture accumulation is not as large as in the variant "complete radiation balance". Therefore we should notice that neglecting solar radiation effects on the exterior surface need not to produce results which are "on the safe side", if white paint on the exterior surface is used.
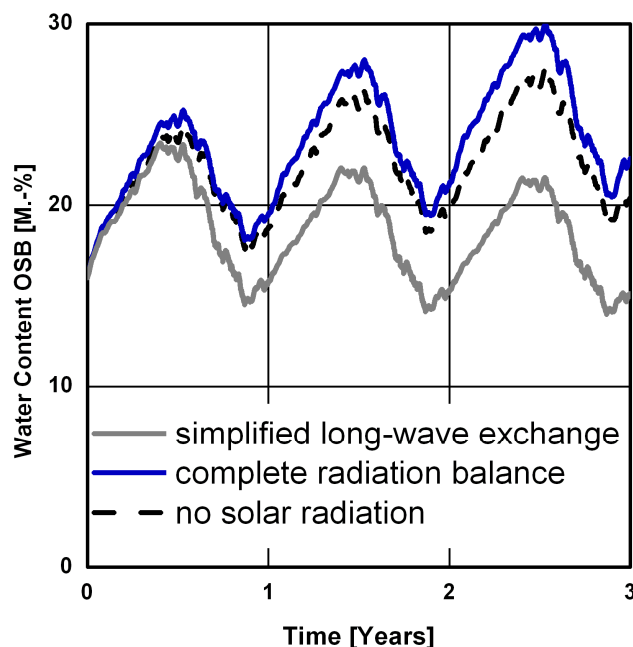
FIG. 6: Water content within the OSB board of all three variants.

5. References

Energy Design Update® (2006). In Arizona, White Roofing Causes Wet Insulation, Vol. 26, No. 6, S. 4-6, Aspen Publishers.

EN ISO 6946 (Nov. 1996). Bauteile – Wärmedurchlasswiderstand und Wärmedurchgangskoeffizient – Berechnungsverfahren.

Künzel H.M. (1995). Simultaneous Heat and Moisture Transport in Building Components. - One- and two-dimensional calculation using simple parameters, University Stuttgart, IRB Verlag.

VDI-Guideline 3789 (1994). Umweltmeteorologie –Wechselwirkungen zwischen Atmosphäre und Oberflächen. Berechnung der kurz- und langwelligen Strahlung.

Surface Temperatures on Flat Roofs and Hygrothermal Consequences

Christian Bludau, Dipl.-Ing.,
Department of Hygrothermics, Fraunhofer Institute for Building Physics;
christian.bludau@ibp.fraunhofer.de

Daniel Zirkelbach, Dipl.-Ing.,
Department of Hygrothermics, Fraunhofer Institute for Building Physics;
daniel.zirkelbach@ibp.fraunhofer.de

Hartwig M. Künzel, Dr.-Ing.,
Head of Department of Hygrothermics, Fraunhofer Institute for Building Physics;
hartwig.kuenzel@ibp.fraunhofer.de

KEYWORDS: temperature, long wave radiation, cold pond, flat roof.

SUMMARY:
In this paper the temperature conditions on flat roofs are discussed considering the influence of long-wave radiation to the sky and the effect of a parapet as an important factor for the nighttime roof temperature. The parapet leads to retention of cold air on the roof. Results of measurements on flat roofs and special meteorological data collected at the field test site in Holzkirchen are presented.

For realistic assumptions of the boundary conditions a heat transfer coefficient depending on the ambient conditions including the temporary insulation effects of a cold surface air pond forming between the parapet walls is determined for flat roofs. The surface measurements on flat roofs with a parapet show a significant decrease of the temperature below the ambient air conditions during night time. These surface temperature recordings and meteorological data are used to validate hygrothermal simulations.

Furthermore the possibility of interstitial condensation is investigated using an adapted hygrothermal simulation tool. The results show that the use of reflecting surfaces on flat roofs can lead to severe moisture accumulation in colder regions of Europe. Thus the color of the roofing membrane appears to be an important factor for the hygrothermal performance and moisture tolerance of certain constructions.

1. Introduction

For the results of hygrothermal simulations the boundary conditions play a significant role. A drop in surface temperatures of flat roofs may result in moisture accumulation in the construction. For this reason it is important to research the prevailing conditions. In this paper the thermal behavior of flat roofs is discussed with special consideration of the effect of an existing parapet wall as an important factor for the nighttime roof temperature. The parapet leads to retention of cold air on the roof. Some approaches are given to include the formation of a cold pond of stagnant air in an existing hygrothermal simulation tool. Further calculations are performed to show the influence of different colors of the roofing membrane on the behavior of a typical flat roof construction.

2. Fundamentals

2.1 Nighttime Cooling below ambient air temperatures

Long wave radiation is permanently emitted by all terrestrial objects and by some gases in the atmosphere. This thermal radiation can reach several hundred W/m^2 depending on the temperature of the emitting surface. The

intensity of the atmospheric counter radiation strongly depends on the current amount of cloud cover. Typical values at temperate latitudes for the counter radiation emitted by a cloudless sky range between about 180 W/m² (cold, dry air) and about 400 W/m² (warm, humid air). With a closed opaque cloud cover, the sky behaves like a Planckian emitter whose temperature is equal to the dew point temperature of the air. Building components absorb long-wave radiation emitted from other objects, but they also emit this radiation themselves and are thus in continuous radiation exchange with their surroundings. By day, this heat loss is not noticeable because of the heat gained by incident solar radiation. By night, however, the loss is not compensated and usually causes cooling of the surface below ambient air temperature ("overcooling"). This overcooling can lead to temperature differences from the ambient air temperature of about 5 to 10 °C and more. Dew deposition and the risk of algae and mold growth may result from overcooling.

2.2 Development of a cold pond on a flat roof

A typical construction for flat roofs is to surround the roof top by parapet walls. Such a wall forms a closed dam around the roof where the cold and thus heavier air can not flow out. The accumulated cold air is cooling below the ambient air temperature due to the long wave radiation of the roof surface and the interaction of the trapped air with higher air layers. Further the effects of wind in the area protected by the parapet walls can be lower reducing natural convection. Measurements show that the cold within the parapet walls lead to temperatures clearly beneath the temperatures that can develop on an unobstructed flat roof surface. The data presented here are recorded on a flat roof with a size of about 19 m by 6 m. The influence of the pond of cold air development should appear on a bigger roof as well depending on the air flow conditions caused by wind. Ignoring this effect during the design of a roof can lead to hygrothermal problems in the construction.

3. Measurements

On the field test site in Holzkirchen many different roofing types have been build up and the hygrothermal behaviors have been investigated over many years. An important source for data is the weather station where in addition to the usual recordings like temperature, relative humidity and wind speed special radiation values like the diffuse solar radiation, the radiation in west direction, atmospheric counter radiation, the vertical counter radiation and surface temperatures of black and white surfaces in horizontal and vertical direction are measured. Further a new measuring device was installed at one of the flat roofs in the area. This allows measuring the thermal behavior of the surface. In Fig. 1 in the left picture the test setup is shown; in the right picture a detail of the sensor ladder to measure the temperature in different heights in the surrounded roof is shown. Each of the both test areas contains of four measuring fields with different colors. A black one, a white one, a gray one (this is the typically one used for flat roof constructions in Germany) and a reflecting one. The test areas are insulated below the surface and separated from the roof by a ventilated air gap to assure that there is no influence to the construction below. The one in the front is free-standing to eliminate influences from the parapet walls. The short wave absorptivity for the different surfaces is given in Table 1. The long wave emissivity is assumed to be around 0.9. It will be determined after the final tests. The silver surface is covered with a thin plastic layer so the emissivity should be close to the one of the other layers. It will be replaced by a uncoated metal foil in the next test period.

TABLE. 1: Short wave absorptivity of the different surfaces..

Surface color	Absorptivity [-]
black	0.949
grey	0.849
silver	0.130
white	0.234

The test setup in the back is surrounded by parapet walls with a height of about 40 cm. The sensor ladder in the right picture allows measuring the temperatures at 11.5 cm below the surface top of the test setup in the back (on the roof surface) and further in heights of 0, 10, 20, 30 and 40 cm beginning on the surface top of the test setup.
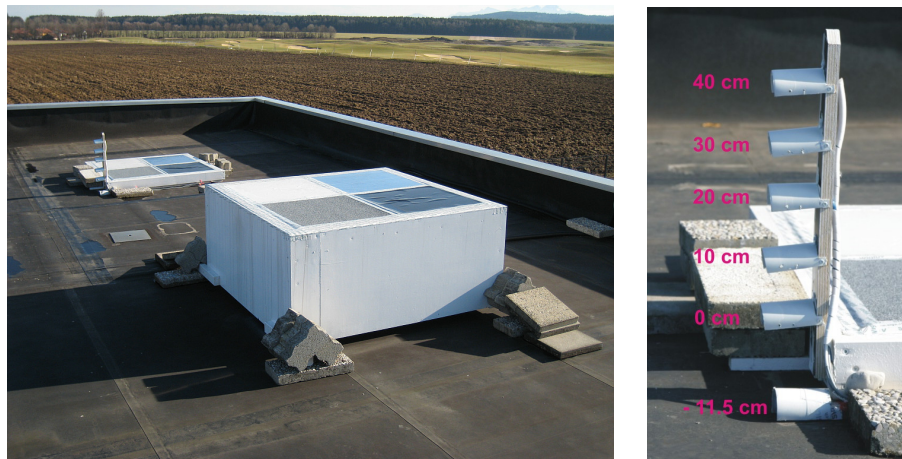
FIG. 1: Test setup for temperature recordings. The left picture shows test patches to measure the surface temperatures; the right picture shows the sensor ladder for measuring the stratification between the parapet walls.

The nighttime overcooling of surfaces is shown in Fig. 2. The thicker black line is the ambient air temperature measured two meters over the ground at our weather station close to the test setup. The other lines show the temperatures of the different colored surfaces. In the left diagram the temperature of the free-standing surfaces are shown (Fig. 1 right picture – test setup in the front).
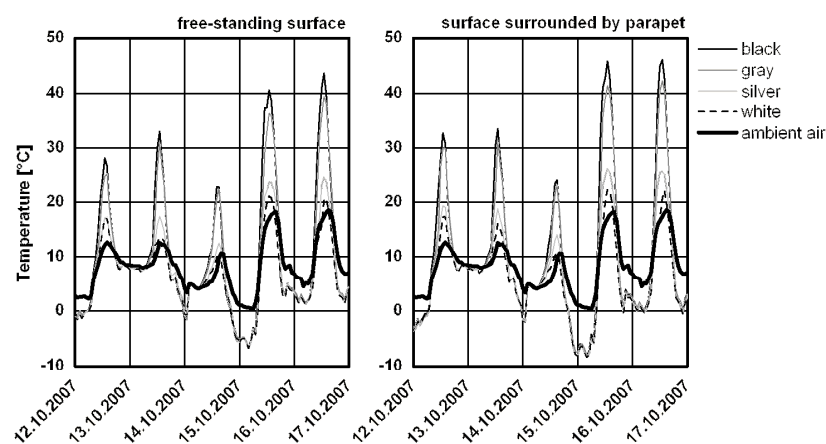
FIG. 2: Surface temperatures for the black, gray, silver and white surface, free-standing an d surrounded by parapet walls.

Examining the temperatures for the displayed five days in Fig. 2 during the night one can see the cooling below the ambient air temperatures. There is no recognizable overcooling in the morning of the 13th of Oct. due a cloudy night. Analysis of the climatic data for the displayed days have shown that the sky most time was cloudy during the nights from 12th to 14th Oct. and then clear for the 15th and 16th of October. In the morning of the 15th of Oct. a overcooling of the surfaces of about 7.3 °C down to -6.7 °C was measured. The lowest temperatures were measured at 4 a.m.. The color of the surface is not important for the overcooling only the long wave emissivity has an influence. During the day time a high temperature develops on the surface depending on the color (more precisely the short-wave radiation absorptivity). In the right diagram the temperatures of the test surfaces which are surrounded by parapet walls are shown (Fig. 1 right picture – test setup in the back). Comparing the two diagrams the test setup surrounded by the parapet walls nearly shows the same behavior like the free standing one except for the maximum and minimum temperatures forming. For example at the 15th of Oct. the temperature at 4 a.m. shows a difference to the ambient air temperature of 9.0 °C down to a surface temperature of -8.4 °C. This confirms earlier measurements where temperatures down to 10 °C beneath the ambient air temperatures where measured on the same roof but without the test setup

In Fig. 3 the measured temperatures of the sensor ladder (Fig. 1 right picture) in the same time period are shown. Again concerning the morning of the 15th of Oct. one can recognize a temperature gradient between the free moving air and the surface in the surrounded area. The sensor at 0 cm in the diagram is not the surface level of the roof but the surface level of the lower test setup. The sensor is situated 11.5 cm over the top of the roof surface.
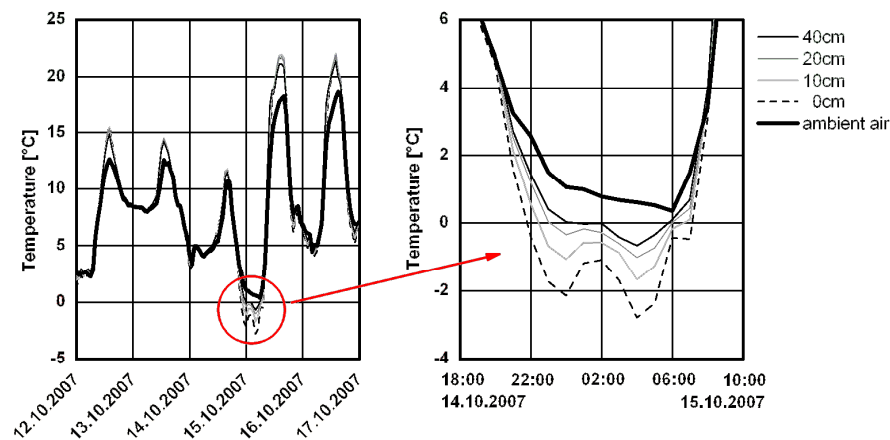
FIG. 3: Measured temperature in different heights above the roof surface in the area protected by parapet walls.

4. Calculations

All calculations were performed with the at the Fraunhofer Institute for Building Physics developed and validated method for simultaneous calculation of heat and moisture transport in building components WUFI[®] [Künzel 1994]. The simulation program allows calculating nearly any construction using measured climatic values as boundary conditions for example. Further it includes an explicit consideration of the different appearing radiations. Aim of the investigations is to develop more detailed models to simulate the short term surface conditions on flat roofs and include them into simulation tools. The models are validated using the performed measurements.

4.1 Heat Transfer Coefficient

4.1.1 Flat roofs

For the use of the hygrothermal simulation tool WUFI a heat transfer coefficient was determined by comparing calculated profiles with measured profiles of certain flat roofs at Holzkirchen. Only the convective part was determined because WUFI can calculate an explicit part for radiation [Kehrer and Schmidt 2006]. The convective part for flat roofs was determined to $\alpha = 12.8$ W/m^{2}K. This value is close to the coefficient used in WUFI to calculate roofs $\alpha = 12.5$ W/m^{2}K which was determined for measured values below the roof tiles for an inclined roof [Kaufmann 1995]. Fig. 4 shows the comparison of the measurement and the calculation using the determined heat transfer coefficient for flat roofs. The determination of the coefficient for flat roofs is not completely exact at the moment. The influence of the wind is not included yet.
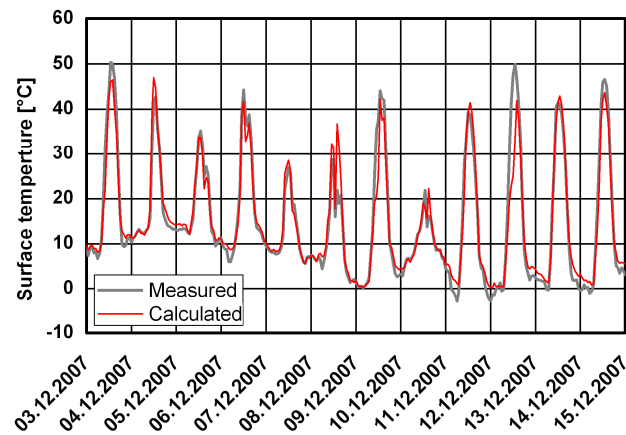
FIG. 4: Comparison of measurement and calculation using the determined heat transfer coefficient for flat roofs.

4.1.2 Simulation of the cold pond influence

The behavior of cold air which can not flow out though the surrounded walls is not totally investigated yet. There are a few possibilities on how to include the factor of the insulating air layers into the used calculation model. One possibility is to simulate it by adapting the heat transfer coefficient as well as the radiation absorptivity and emissivity of the surface. Another possibility is to simulate the pond of cold air as one or more air layers which insulate the surface of the roof from the ambient air. The investigations are running and are not finished at the moment.

4.1.3 Snow and wind

Free-standing surfaces like the here discussed flat roofs offer a large contact surface for the wind. The model for the wind dependent heat transfer coefficient used in the current version of the software was developed for vertical construction parts. This model only uses fixed parameters and seems not to be accurate enough for the explicit calculation of the short term variation of surface temperatures.
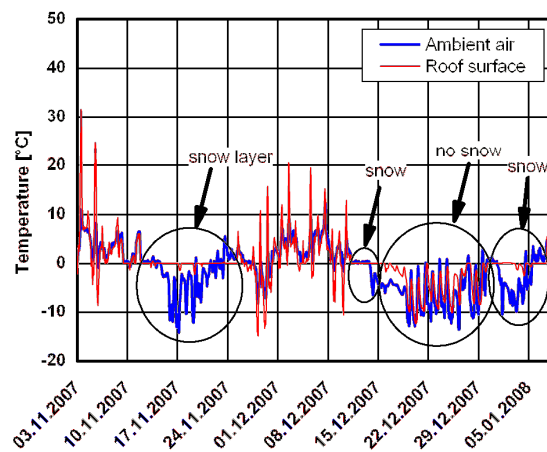
FIG. 5: Insulation effect of a snow layer on a flat roof. .

Snow is hard to include in simulation tools, because the appearance like the layer thickness strongly depends on the exhibition of the researched surface like angle, wind, construction (e.g. parapet walls). A snow layer leads to an insulation layer which keeps the temperature of the surface constant at about 0 °C. Fig. 5 shows the insulating effect of a snow layer. The thickness of the layer is not very important. This effect can be observed at very thin

layer thicknesses. Considering thin layers of snow there is a translucency so there may be a small energy increase by absorption of solar radiation of the roof surface leading to a faster melting of the layer.

Including the snow in a hygrothermal simulation tool would not be very complicated. It is enough just to set the temperature and the heat transfer coefficient to zero during the snow is laying on the surface. The problem is getting the data of the snow periods. Most stations do not measure this value and it is not included in the available climatic data files.

Not including snow layers leads to an underestimation of the prevailing temperature. This leads to a calculation on the unfavorable side most of the time. If the mean temperatures are higher than the snow temperature during the covered time the temperatures is more moderate than the ambient air temperature. This can lead to a lower accumulation of condensation water than calculated.

4.2 Investigation of interstitional condensation

For determining the interstitional condensation in a typical flat roof the construction displayed in Fig. 6 was chosen and simulated with a dark (short wave radiation absorption factor 0,9) and a bright (absorption factor 0,2) surface at for different climatic locations.
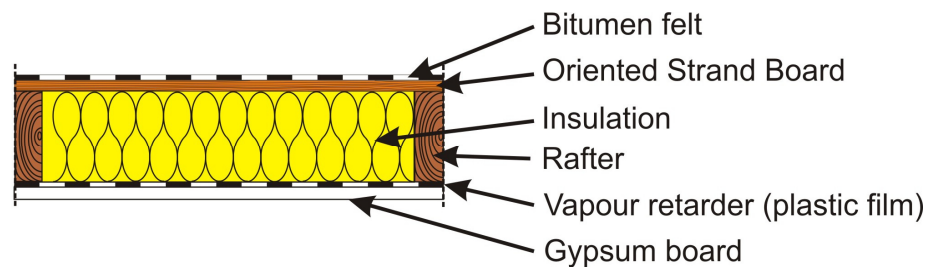
FIG. 6: Flat roof construction.

From inside to outside the construction consists of a gypsum board, a vapor retarder with a s_d-value of 20 m, a mineral wool insulation layer with a thickness of 20 cm. On the top there is an oriented strand board and the construction is sealed with a bituminous felt. Helsinki (Finland) is used as cold location, Holzkirchen (Germany) and Copenhagen (Denmark) are used as moderate location and Dubai (United Arab Emirates) is used as warm location. From this locations hourly given climatic data were used as boundary conditions for the simulation. Table 1 shows the minimum, mean and maximum temperatures for the used climatic data.

For the investigations the indoor conditions according to the [WTA-Guideline 2004] are used. The temperature moves in the yearly course between 20 and 22 degree Celsius while the relative humidity show values between 40 and 60 % RH. The calculations were performed for three years, starting in October.

TABLE. 2: Minimum, mean and maximum temperatures at the climatic locations.

Location	Min. Temperature [°C]	Mean Temperature [°C]	Max. Temperature [°C]
Helsinki	-30.0	4.3	28.5
Holzkirchen	-20.1	6.6	31.1
Copenhagen	-9.6	8.3	26.8
Dubai	10.9	27.0	43.1

Fig. 7 shows in the left diagram the water content in mass percent in the OSB layer and in the right diagram the total water content of the construction. Many standards do not accept moisture contents in wooden materials above 20 M.-% to avoid damage by rot or mould growth. The value of the total water content is not significant but the tendency shows if there is water accumulating in the construction or if the construction has enough potential to dry out.

In Helsinki the winters are quite cold and the summers only show moderate high temperatures. In this climate using the discussed construction the water content in the OSB layer as well as the total water content is increasing over the years (black lines). At this location the color only show a low influence on the hygrothermal behavior of the construction. This construction will fail after some years and is not useable at this location.

For Holzkirchen the graph for the roof with the dark roofing membrane (red solid line) shows a moisture content in the OSB layer between 12 and 19 M.-% which is not increasing over the calculated years. The course of the total water content is decreasing. This shows that the roof has enough potential to dry out. Concerning the courses of the roof with the bright surface the results change. The water accumulates in the OSB layer (red broken line). The temperatures in the construction during summer and day time are too low. The total water content is increasing during the calculated three years. The construction has no potential to dry out. Already in the first winter the OSB board reaches critical moisture values.

The construction in Copenhagen shows the same behavior (blue lines). Analogical to the courses of the calculations with the climate in Holzkirchen the dark surface color leads to high enough temperatures to dry out the construction during the summer periods. The water content in the OSB layer oscillates between about 13 M.-% in summer and about 19 M.-% in winter. The course of the total water content again decreases. This construction can be build at locations with similar climatic behavior without restrictions. On the other hand the bright construction again shows moisture problems. The water content in the OSB layer exceed the limit of 20 M.-% during the first winter. The total water content is steady increasing. This construction can fail after a view years only by using a bright surface color instead of a dark one.

In Dubai the construction is unproblematic. The water contents (green graphs) stay very low at this location. During the year there is nearly no change of water content in the OSB layer (swinging between about 10 and 13 M.-%). The total water content is decreasing very fast which points to a drying of the build up water content. In Dubai this construction can be engineered with any color of the surface. There are no restrictions due to the hygrothermal behavior. For saving cooling energy a bright roof can be useful.
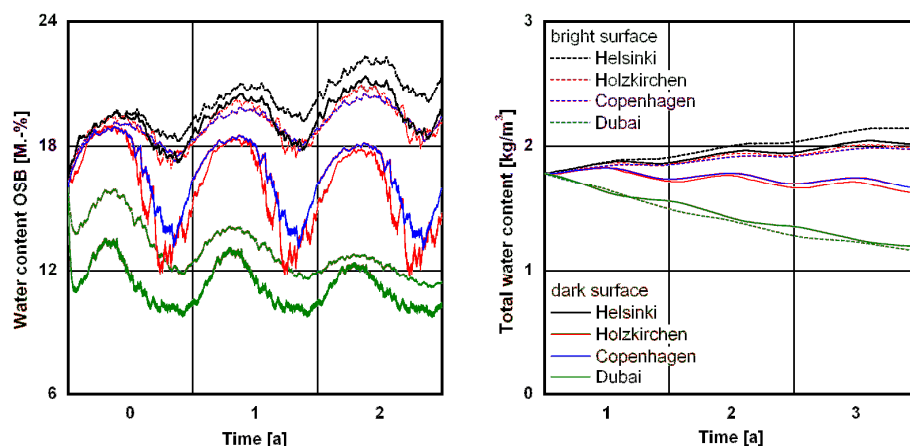
FIG. 7: Water content in the OSB layer and in the complete construction calculated with two surface colors for four different climatic locations.

5. Summary and conclusions

In this paper measurements and a test setup are presented dealing with temperature conditions of flat roofs. The measurements clarify the overcooling effect due to long wave radiation and due to this the building of a cold pond on surfaces that are surrounded by parapet walls. The temperatures of the surfaces within the parapet walls are even lower than of the unobstructed. Surface temperatures about 10 °C lower than the ambient air temperature were measured. For unobstructed flat roofs a heat transfer coefficient is determined, not yet including the factor wind.

Possibilities are suggested to include the formation of a pond of cold air into simulation models as well as the influence of wind or snow. Further investigations are needed on flat roofs surrounded with parapet walls. Here especially the air flow pattern due to wind have to be determined.

The effect of the surface color by simulating a dark and a bright roof are discussed on the interstitial condensation of a typical flat roof construction at four different locations. The calculations show that accumulation of water occurs in the construction using a bright surface in moderate climate zones. In these locations the bright surface reaches not very high temperatures during the day and low temperatures below the ambient temperature during the night. The construction can not dry out. In warm regions the color does not show a high influence on the hygrothermal behavior of the used construction. In very cold regions the roof considered here will fail.

6. References

Kaufmann, A. (1995). Untersuchungen zur Auswahl geeigneter Materialien für den Einsatz als feuchteabhängige Dampfbremse bei vollgedämmten Dachkonstruktionen und rechnerische Abschätzung ihrer praktischen Feuchtewirkung. Diplomarbeit Technische Physik, Fachhochschule München, Germany

Kehrer M., Schmidt Th. (2006).Temperaturverhältnisse an Aussenoberflächen unter Strahlungseinflüssen, Proceedings BauSIM2006, 9.-11. Okt., TU München, Germany

Künzel, H.M. (1994). Simultaneous Heat and Moisture Transport in Building Components. One- and two-dimensional calculation using simple parameters. Dissertation Universität Stuttgart

WTA-Guideline (2004). WTA Merkblatt 6-2-01/ E: Simulation of heat and moisture transfer. Fraunhofer IRB Verlag, ISBN 978-3-8167-6827-2

Spectator comfort in sports stadiums: on the impact of roof geometry on wind-driven rain shelter

Twan van Hooff, M.Sc. Student,
Building Physics and Systems, Technische Universiteit Eindhoven, The Netherlands
email: t.a.j.v.hooff@student.tue.nl

Jan Persoon, M.Sc. Student,
Building Physics and Systems, Technische Universiteit Eindhoven, The Netherlands
email: j.w.p.persoon@student.tue.nl

Bert Blocken, Dr. Ir.,
Building Physics and Systems, Technische Universiteit Eindhoven, The Netherlands
email: b.j.e.blocken@tue.nl

Jan Carmeliet, Prof, Dr. Ir.,
Chair of Building Physics, Swiss Federal Institute of Technology ETHZ, Zürich, Switzerland
Empa, Swiss Federal Laboratories for Materials Testing and Research, Laboratory for Building
Technologies, Switzerland

Martin de Wit, Prof. Dr. Ir.,
Building Physics and Systems, Technische Universiteit Eindhoven, The Netherlands
email: m.h.d.wit@tue.nl

KEYWORDS: *wind-driven rain, wind flow, rain shelter, sports stadium, numerical simulation, CFD.*

SUMMARY:
The main aspect for spectator comfort in outdoor stadiums is protection from wind and rain. This paper presents an investigation of the impact of roof geometry on rain shelter for stadiums that consist of two separate roof-covered stands facing each other. 2D CFD simulations and Lagrangian particle tracking are performed to analyse the wind flow pattern and rainfall distribution in seven generic stadium configurations and to assess the performance of each roof type. Although most existing stadium roofs are built with a light to medium upward slope towards the field, the analysis indicates that roofs with a downward slope of 13° provide significantly better rain shelter. The reason is not only the well-known trigonometric shielding effect. In addition, this roof type – as opposed to its counterparts – restricts the extent of the primary vortex in the stadium and generates a sufficiently strong counter-rotating secondary vortex below the roof that sweeps the rain away from the stands.

1. Introduction

Apart from sports purposes, stadiums are also increasingly being used for other activities such as concerts, outdoor movie festivals and other events with large spectator attendance. Spectator comfort is very important and it includes protection of the spectators at the stands from wind and rain. In the design of many existing stadiums however, rain shelter has insufficiently been taken into account because most roofs have been designed with vertical rainfall in mind, while often no consideration has been given to rain that is blown onto the stands and spectators by wind (wind-driven rain or WDR). This is reflected by the fact that the roofs often extend not much further than just above the separation between the stands and the field, which is the case in most stadiums worldwide.

Insufficient shelter from rain is one of the main reasons why the bottom rows of many stadiums are unpopular and are often left untenanted. In some stadiums, this problem has been tackled by providing an excessively large roof overhang or by completely closing the stadium roof. However, several disadvantages are associated with these options, such as a reduced lifetime of natural and semi-artificial grass covers due to insufficient daylight and CO_2 depletion of stagnant near-surface air layers, insufficient smoke removal from the field and stands, excessive reverberation times, etc. For these reasons, "outdoor" or "open" stadiums are preferred and a

compromise has to be found between a roof that performs well concerning the above-mentioned issues but that also provides sufficient shelter from WDR.

WDR has received quite some attention in the past in other applications. Most recently, numerical simulation of WDR with Computational Fluid Dynamics (CFD) has been applied to investigate wetting patterns on building facades (Choi 1991, 1993, van Mook 2002, Blocken and Carmeliet 2002, 2004, 2007, Tang and Davidson 2004) and to determine WDR distributions over small-scale topographic features such as hills and valleys (Arazi et al. 1997, Choi 2002, Blocken et al. 2005, 2006). Recent validation efforts for CFD WDR studies for these applications (Blocken and Carmeliet 2002, 2004, Tang and Davidson 2004, Blocken et al. 2006) have provided confidence to extend the use of CFD WDR simulation to other applications.

In this paper, 2D CFD WDR simulations are performed to investigate the impact of roof geometry on rain shelter in football stadiums. The study focuses on stadiums that consist of two separate roof-covered stands facing each other. Many existing stadiums over the world have this type of geometry. Examples include the "Estádio Municipal de Braga" (Braga, Portugal), the "Saitama Stadium 2002" (Saitama, Japan) and the Atatürk Olympic Stadium (Istanbul, Turkey). In Section 2, the seven generic stadium configurations that will be studied are presented. Section 3 briefly describes the numerical models. In Section 4, model validation is briefly reported. The simulation results of wind flow and rain impact are presented and discussed in Section 5. Finally, Sections 6 (discussion) and 7 (conclusions) conclude the paper.

2. Generic stadium configurations

To reduce the extent of the study and to enhance its general character, a classification of existing stadiums based on roof geometry has been made. From this classification, seven generic stadium configurations have been derived. The basic shape (without roof) of all configurations is taken from the DSB stadium of football club AZ in Alkmaar, the Netherlands. This stadium is characterised by a roof with a downward slope towards the field (Fig. 1a). The designers of the stadium chose this roof type because they expected that it would provide some more rain shelter than traditional roofs with a light, medium or large upward slope towards the field.
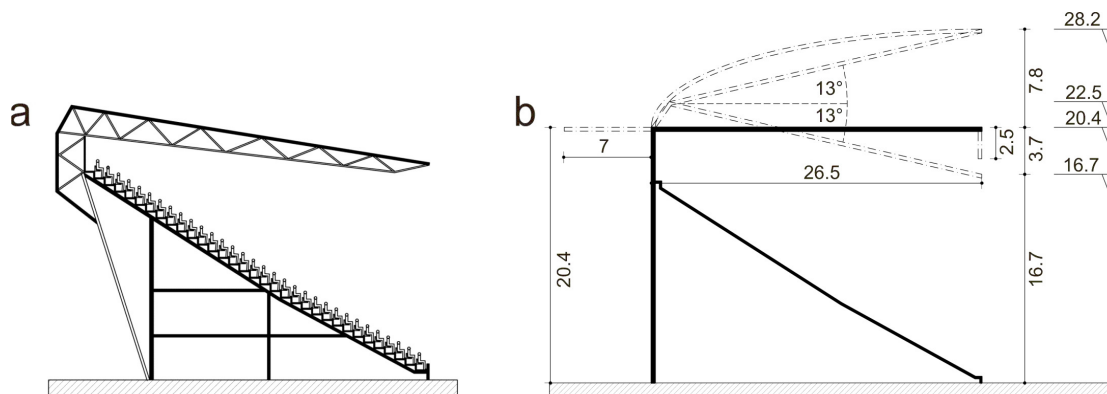
FIG.1: (a) Stand cross-section of the DSB stadium (AZ, Alkmaar, the Netherlands) with downward sloping roof. (b) Cross-sections of the seven generic stadium configurations with the different roof geometries (dimensions in meters).

The seven roof type configurations are (Fig. 1b): (1) a flat roof; (2) a flat roof with a signboard; (3) a flat roof with a backward extension; (4) an elevated roof with a backward extension; (5) a curved roof with an upward slope; (6) a straight roof with an upward slope; and (7) a straight roof with a downward slope. Fig. 1b shows the dimensions of the different generic cross-sections. The 13° roof slope is based on the DSB stadium roof. Note that in all generic configurations, the roof overhang extends just beyond the first row of seats, such that vertical rainfall (rain without wind) does not wet the stands.

3. Numerical models

The steady-state wind-flow pattern over and in the stadiums is obtained by solving the 2D Reynolds-averaged Navier-Stokes (RANS) equations in combination with a turbulence model and an appropriate near-wall treatment, using the commercial CFD code Fluent 6.1.22 (Fluent Inc. 2003). As turbulence modelling inherently

imposes the need for model validation, the performance of several turbulence models for two geometries, the flow in which shows some resemblance to the flow in the stadium geometry, is assessed in the next section. From this study the most suitable turbulence model is selected and used for predicting 2D stadium flow. In order to avoid the very large amount of cells needed for near-wall modelling, wall functions are used in this study. The standard wall functions by Launder and Spalding (1974) are employed with a sand-grain based roughness modification which requires additional care to limit the occurrence of unintended streamwise gradients of flow variables in the upstream part of the computational domain (Blocken et al. 2007).

Lagrangian particle tracking is performed. The motion of a raindrop moving in a wind-flow field characterised by a mean velocity vector $\vec{V}$ is given by:

$$\left(\frac{\rho_w - \rho}{\rho_w}\right)\vec{g} + \frac{3\mu}{\rho_w d^2} \cdot \frac{C_d Re_R}{4} \cdot \left(\vec{V} - \frac{d\vec{r}}{dt}\right) \quad = \quad \frac{d^2\vec{r}}{dt^2} \qquad (1)$$

where Re_R is the relative Reynolds number (referring to the airflow around the raindrop):

$$Re_R \quad = \quad \frac{\rho d}{\mu} \left\| \vec{V} - \frac{d\vec{r}}{dt} \right\| \qquad (2)$$

and ρ_w is the density of the raindrop, ρ the density of the air, g the gravitational acceleration, μ the dynamic air viscosity, d the raindrop diameter, C_d the raindrop drag coefficient, $\vec{r}$ the position vector of the raindrop in the xyz-space and t the time co-ordinate. More information on the implementation and parameters for Lagrangian particle tracking for raindrops can be found in (Blocken and Carmeliet 2004).

4. Model validation

In this study, the experiments by Kovar-Panskus et al. (2002) in an idealised street canyon (cavity) are used, because the flow in the cavities exhibits similar vortex structures as will be present inside the stadiums. Note however that there are also significant differences between the two configurations, as will be explained later in section 6. The experiments in the street canyon were conducted in a wind tunnel at a scale of 1:500 for nominally 2D cavities with a height (H) equal to 106 mm and a variable depth (W) in order to create cavities with several aspect ratios including W/H= 1 and 2. The neutrally-stratified approach conditions in the experiments were a turbulent boundary layer with height δ = 737 mm (δ/H = 6.95) characterised by a logarithmic vertical velocity profile with free-stream velocity U_{ref} = 8 m/s, aerodynamic roughness length y_0 = 0.3 mm, displacement height d = 1 mm and a friction velocity u^*_{ABL} = 0.4 m/s. In addition, the flow turbulence characteristics were provided. Measurements of mean wind speed in the canyons were made along 5 vertical lines (Fig. 2).
The CFD simulations are performed at model scale, in a 2D computational domain with the same height as the wind tunnel (H_{WT} = 964 mm). The domain is discretised with a structured grid consisting of about 25,000 control volumes. The grid resolution is based on grid-sensitivity analysis. Different turbulence models are tested. In all cases, pressure-velocity coupling is taken care of by the SIMPLE algorithm, pressure interpolation is second order and second order discretisation schemes are used for both the convection terms and the viscous terms of the governing equations. The inlet mean wind speed profile is taken equal to the measured "incident" wind tunnel profile (Blocken et al. 2007).
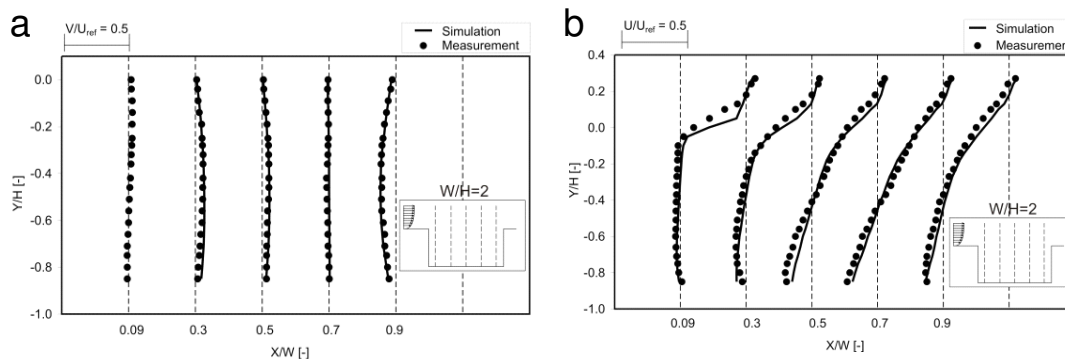
FIG. 2: Comparison between wind tunnel measurements and CFD simulation results for W/H = 2: (a) horizontal and (b) vertical velocity component.

From all turbulence models, the best results were obtained with the Reynolds Stress model (RSM). The results of this model and their comparison with the experiments are presented as profiles of the horizontal and vertical wind speed components along the 5 vertical lines along which the measurements were made (Fig. 2). Based on the quite good general outcome of the validation study with the RSM, this model is selected for the simulations of wind flow in the generic football stadiums in the next section.

Note that validation of the Lagrangian particle tracking model was not performed for two reasons: (1) Particle tracking involves numerically solving the raindrop's equation of motion, which is more straightforward and to a lesser extent based on important assumptions, as is the case for turbulence modelling; (2). The results of particle tracking for raindrops have been validated on several occasions in the past (Blocken and Carmeliet 2002, 2004, Tang and Davidson 2004, Blocken et al. 2006).

5. Results

5.1 Wind-flow pattern

For the calculations of the wind-flow pattern four sets of inlet boundary conditions are used. The first two sets correspond to wind-flow over a uniformly rough, grass-covered terrain (power-law exponent $\alpha_p = 0.15$) with a reference wind speed at 10 m height of $U_{10} = 5$ m/s for the first set and $U_{10} = 10$ m/s for the second set. The third and fourth set represent wind-flow over suburban terrain ($\alpha_p = 0.20$), with $U_{10} = 5$ m/s and 10 m/s respectively. A terrain with $\alpha_p = 0.15$ corresponds approximately to $y_0 = 0.03$ m and $\alpha_p = 0.20$ corresponds to about $y_0 = 0.1$ m. All configurations show a large primary vortex with a centre that is located near the downstream stand, similar to the vortex in the cavity with W/H = 2 that was used for model validation. This provides some confirmation of the suitability of the cavity configuration for model validation and turbulence model selection. The extent to which the primary vortex penetrates below the roof is dependent on the roof geometry. This effect is significant for configuration 6, with the upward sloping roof (Fig. 3a). It is less pronounced for the configurations with the flat roofs (Fig. 3d) and appears to be absent for configuration 7 with the downward-sloping roof (Fig. 3g). In most cases, a secondary (counterclock-wise rotating) vortex is present below both the upstream and downstream roof, which is driven by the primary vortex (see Fig. 3a,d,g). No significant qualitative differences were found between the wind-flow patterns for $U_{10} = 5$ and $U_{10} = 10$ m/s and between the patterns for $\alpha_p = 0.15$ and $\alpha_p = 0.20$.

5.2 Raindrop trajectories and rain shelter

For all seven configurations the raindrop trajectories are calculated using Lagrangian particle tracking. Figure 4 displays trajectories for raindrops of 0.5 mm diameter, for configurations 6, 1 and 7 and for the wind-flow field characterised by $\alpha_P = 0.20$ and $U_{10} = 10$ m/s. While the downstream stand is for a large part wetted in case of roof type 6, almost no wetting occurs for roof types 1 and 7. For raindrops of 5 mm diameter the downward-sloped roof performs much better than the other two roof types (Fig. 3c,f,i). The behaviour of the raindrops near the downstream stand is significantly influenced by the roof type. Figure 4 shows that 0.5 mm raindrops that impact on or near the stand have convex trajectories below the upward-sloped roof, almost rectilinear and vertical trajectories below the flat roof and concave trajectories below the downward-sloped roof.

To some extent, the superior performance of the downward-sloping roof and the poor performance of the upward-sloping roof could be expected. Indeed, if raindrop trajectories were straight lines, it is clear that a down-sloping roof would provide more shelter from rain than a flat roof, and even more than an upward-sloping roof. This is indicated in Fig. 5. Trigonometry yields the following expression for the percentage of the stand that is wetted:

$$\frac{L_{WET}}{L_{TOT}} = \frac{H_R}{H_S + \dfrac{D_S}{tg\gamma}} \tag{3}$$

where H_R is the height of the roof edge, H_S the height of the uncovered stand (without roof), D_S the depth of the stand and γ the rain trajectory inclination angle, i.e. the angle between the raindrop trajectory and the vertical. With $H_R = 28.2$ m, 20.4 m and 16.7 m for roof type 6, 1 and 7 respectively (see Fig. 1b), $H_S = 16$ m and $D_S = 26$ m, L_{WET}/L_{TOT} is shown in Table 1 for $\gamma = 10°$ and $20°$.
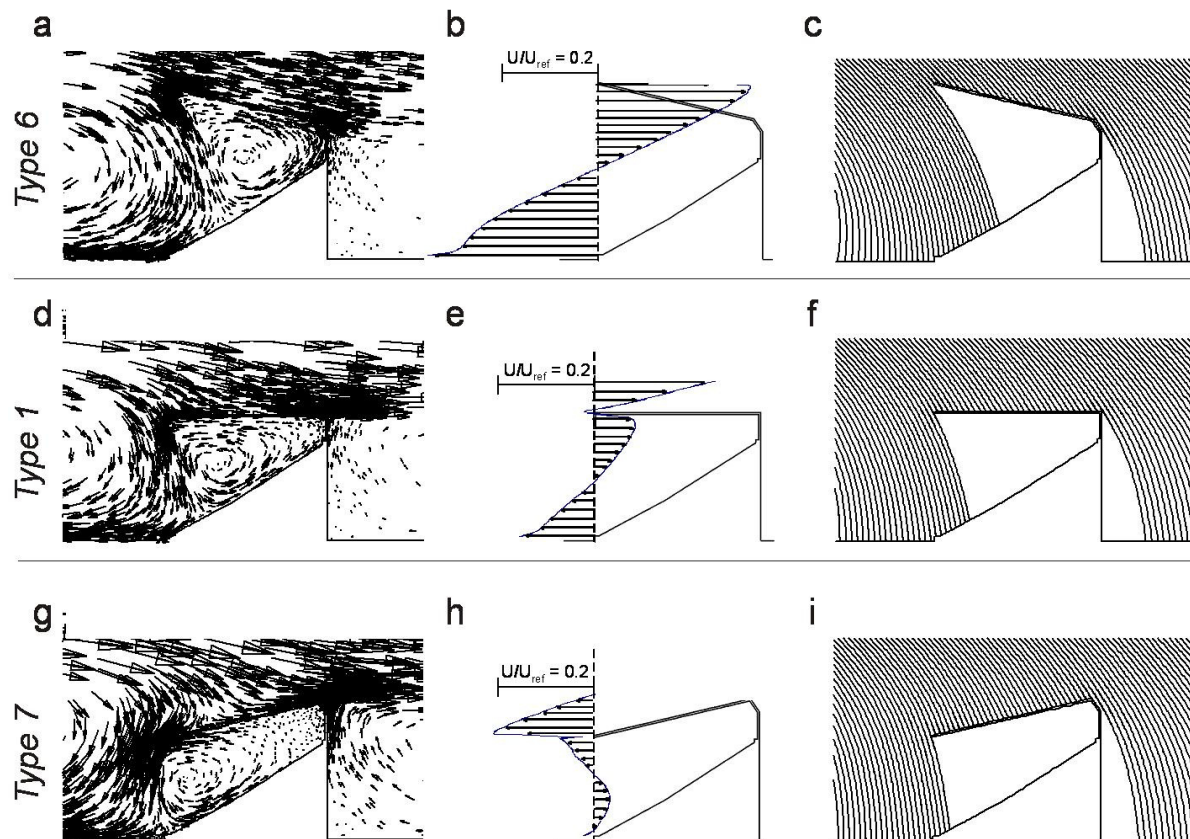
FIG. 3: (a, d, g) Detail of interaction between primary and secondary vortex near the stand; (b, e, h) Horizontal mean velocity component along a vertical line below the roof edge; (c, f, i) Trajectories of 5 mm raindrops as influenced by the local wind-flow pattern (note: $U_{ref} = U_{10}$).
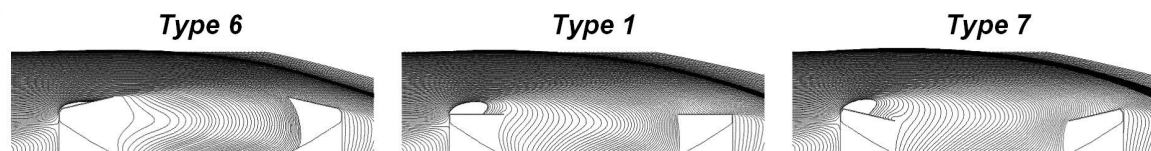
FIG. 4: Trajectories of raindrops; d = 0.5 mm, U_{10} = 10 m/s and α_P = 0.20 wind-flow pattern, for three roof types.

The angles 10° and 20° are chosen because they are to some extent representative for the inclination of the drop trajectories near the roof edge, in the U_{10} = 10 m/s flow pattern. Table 1 indicates that roof type 7 performs best according to Eq. (3). In this paper, the rain shelter effect that is predicted by this simple equation will be called the trigonometric shielding effect. This term is adopted from earth sciences in which a trigonometric model (assuming rectilinear raindrop trajectories) is often used to determine the WDR intensity on sloping soil surfaces (Fourcade 1942, Blocken et al. 2006).

Trigonometric reasoning is probably why the designers of the DSB stadium (Fig. 1a) chose a roof with a downward slope. However, the particular inclination of the roof in combination with the wind-flow pattern in the stadium appears to give rise to an important additional effect. Fig. 3 shows the details of the extension of the primary vortex into the region below the downstream roof and the interaction of this vortex with the secondary vortex below the roof.
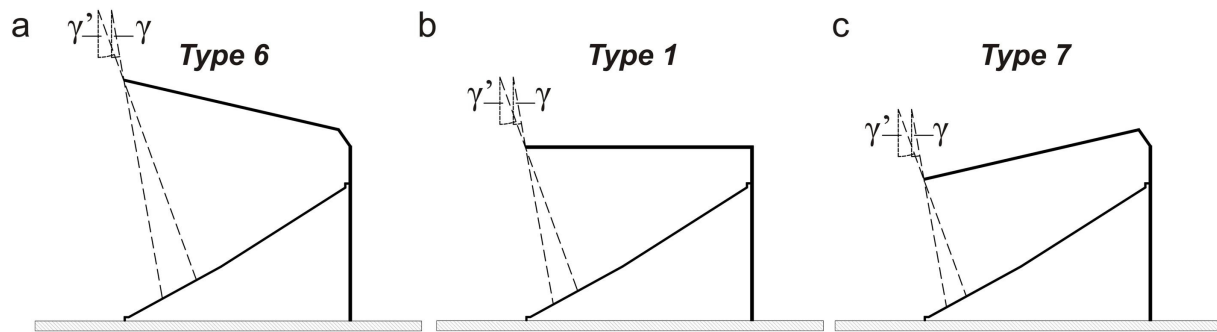
FIG. 5: Illustration of the trigonometric shielding effect, for different rain trajectory inclinations ($\gamma = 10°$ and $\gamma' = 20°$) and for stadiums with (a) roof type 6, (b) roof type 1 and (c) roof type 7.

TABLE 1: Comparison between the predicted percentage of wetted stand (L_{WET}/L_{TOT}) by the trigonometric model and the CFD model.

	Trigonometric model		CFD model ($U_{10} = 10$ m/s $\alpha_p = 0.15$)			
	$\gamma = 10°$	$\gamma = 20°$	0.5 mm	1 mm	2 mm	5 mm
Type 6	17.0	31.8	6.9	14.1	25.0	36.5
Type 1	12.3	23.0	0.0	0.0	1.3	15.1
Type 7	10.0	18.8	0.0	0.0	0.0	5.9

Fig. 3a illustrates that the primary vortex is not significantly restricted by the upward-sloping roof and extends a considerable distance below this roof. This is more clearly indicated in Fig. 3b that shows the horizontal velocity component along a vertical line below the edge of the roof. The extent of the primary vortex provides an extra driving force to the rain and sweeps it towards the stands (Fig. 3c). In Fig. 3d the primary vortex experiences a larger obstruction by the roof type and its strength below the roof is weakened, as indicated in Fig. 3e. Less rain is therefore swept towards the stands (Fig. 3f). Finally, the downward-sloping roof prevents the primary vortex from entering the region below the roof (Fig. 3g). As a result, the secondary vortex, which rotates in opposite direction, governs the flow below the roof edge. Fig. 3h and 3i show that this vortex sweeps the raindrops that are falling passed the roof away from the stand.

To indicate the importance of this effect compared to the trigonometric shielding effect, Table 1 compares the ratio L_{WET}/L_{TOT} obtained by the two models, the trigonometric model (with trajectory inclinations 10° and 20°) and the CFD model (for $\alpha_p = 0.15$ and $U_{10} = 10$ m/s). Comparing the values in the different columns in Table 1 shows that the trigonometric model significantly underestimates the rain shelter for roof type 1 and 7 compared to roof type 6.

Finally, Fig. 6 summarises the performance of all seven roof types in terms of rain shelter by plotting the percentage of the stand that is wetted for the wind-flow pattern with $U_{10} = 10$ m/s and $\alpha_P = 0.15$. The order on the horizontal axis indicates decreasing performance in terms of rain shelter. The roof with the downward slope is clearly superior in all circumstances investigated, followed by the different flat roof types. Roofs with upward slopes can experience considerable wetting, going up to even 50% for rain spells in moderately strong winds.
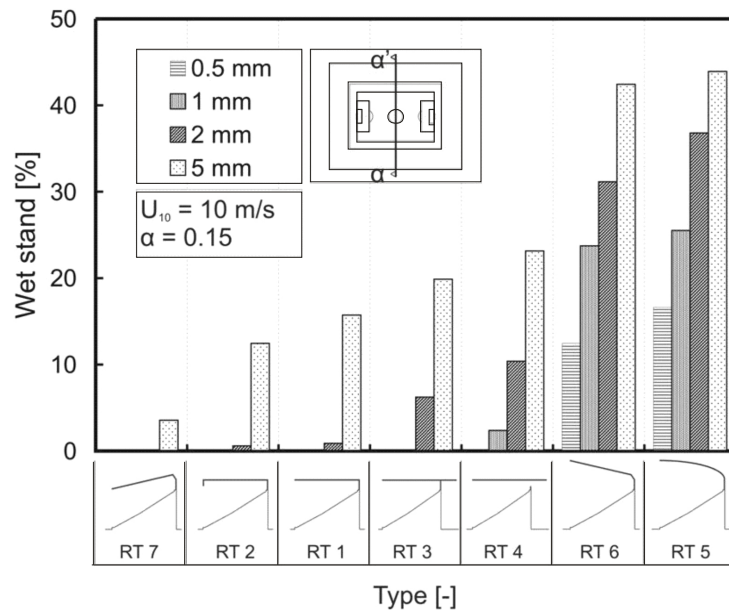
FIG. 6: Comparison of roof type performance in terms of the percentage of wetted stand length for $\alpha_P = 0.15$, $U_{10} = 10$ m/s.

6. Discussion

It is important to note the limitations of this study. The validation was conducted for idealised canyons (cavities), while the geometry of the 2D stadium model is quite different from a cavity because it is a semi-enclosed space that is separated from the exterior by walls. Furthermore, the cavity aspect ratios were limited to W/H = 1 and 2, while the stadium aspect ratios are W/H = 4 and 6, depending on the cross-section. In spite of these differences and although the aspect ratio of the structure influences the aspect ratio of the primary vortex, the essential features of the vortices in the cavities and the stadiums are quite similar. The validation is considered suitable to select the turbulence model in this study, but future research should focus on more detailed validation studies. These studies will include wind tunnel experiments performed in 3D generic stadium models.

Only 2D simulations were performed in a vertical cross-section of the stadium. These simulations only provide an indication of roof performance for stadiums that consist of two roof-covered stands facing each other. Further research will include 3D simulations in other stadium geometries and for different wind directions.

7. Conclusions

The impact of roof geometry on rain shelter in football stadiums consisting of two separate roof-covered stands facing each other has been investigated with 2D Computational Fluid Dynamics simulations and Lagrangian particle tracking. The following conclusions are made:

•   The horizontal extent of the primary vortex in the stadium is limited by the roof construction. This limiting effect is least pronounced for an upward-sloping roof, more pronounced for a flat roof and most pronounced for a downward-sloping roof, where the primary vortex does not enter the region below the roof.
•   The downward-sloping roof prevents the primary vortex from entering the region below the roof. Instead, a counter-rotating secondary vortex occupies this space and sweeps the raindrops away from the stand. The upward-sloping roofs allow the primary vortex to significantly extend below the roof and to sweep the raindrops to the stands.
•   Although the better performance of the downward-sloping roof compared to the flat roofs and upward-sloping roofs could be expected based on trigonometric reasoning, the CFD study has revealed an important additional effect, being the action of the primary and secondary vortices on the raindrops entering the region below the roof.
•   This study was performed with simplified 2D modelling. Further research includes 3D CFD simulations for other stadium geometries and different wind directions.

8. References

Arazi, A., Sharon, D., Khain, A., Huss, A., Mahrer, Y., 1997. The windfield and rainfall distribution induced within a small valley: field observations and 2-D numerical modeling, Boundary-Layer Meteorology 83, 349-374.

Blocken, B., Carmeliet, J., 2002. Spatial and temporal distribution of driving rain on a low-rise building. Wind and Structures 5(5), 441-462.

Blocken, B., Carmeliet, J., 2004. A review of wind-driven rain research in building science. Journal of Wind Engineering and Industrial Aerodynamics 92, 13, 1079-1130.

Blocken, B., Carmeliet, J., Poesen, J., 2005. Numerical simulation of the wind-driven rainfall distribution over small-scale topography in space and time, Journal of Hydrology 315, 1-4, 252-273.

Blocken, B., Poesen, J., Carmeliet, J., 2006. Impact of wind on the spatial distribution of rain over micro-scale topography – numerical modelling and experimental verification, Hydrological Processes 20, 2, 345-368.

Blocken, B., Carmeliet, J., 2007. On the errors associated with the use of hourly data in wind-driven rain calculations on building facades, Atmospheric Environment 41, 11, 2335-2343.

Blocken, B., Stathopoulos, T., Carmeliet, J., 2007. CFD simulation of the Atmospheric Boundary Layer – wall function problems, Atmospheric Environment 41, 2, 238-252.

Choi, E.C.C., 1993. Simulation of wind-driven rain around a building. Journal of Wind Engineering and Industrial Aerodynamics 46&47, 721-729.

Choi, E.C.C., 2002. Modelling of wind-driven rain and its soil detachment effect on hill slopes, Journal of Wind Engineering and Industrial Aerodynamics 90, 9, 1081-1097.

Fluent Inc., 2003. Fluent 6.1 User's Guide, Fluent Inc., Lebanon.

Fourcade, H.G., 1942. Some notes on the effects of the incidence of rain on the distribution of rainfall over the surface of unlevel ground. Transactions of the Royal Society of South Africa 29, 3, 235-254.

Franke, J., Hirsch, C., Jensen, A.G., Krüs, H.W., Schatzmann, M., Westbury, P.S., Miles, S.D., Wisse, J.A., Wright, N.G., 2004. Recommendations on the use of CFD in wind engineering, in: proceedings of the International Conference on Urban Wind Engineering and Building Aerodynamics, (Ed. van Beeck JPAJ), COST Action C14, Impact of Wind and Storm on City Life Built Environment, von Karman Institute, Sint-Genesius-Rode, Belgium, 5 - 7 May 2004.

Kovar-Panskus, A., Louka, P., Sini J-F., Savory, E., Czech, M., Abdelqari, A., Mestayer, P.G., Toy, N., 2002. Influence of geometry on the mean flow within urban street canyons – A comparison of wind tunnel experiments and numerical simulations, Water, Air, and Soil Pollution: Focus 2, 365–380.

Launder, B.E., Spalding, D.B., 1974. The numerical computation of turbulent flows, Computer Methods in Applied Mechanics and Engineering 3, pp. 269-289.

Tang, W., Davidson, C.I., 2004. Erosion of limestone building surfaces caused by wind-driven rain. 2. Numerical modelling. Atmospheric Environment 38(33), 5601-5609.

van Mook, F.J.R., 2002. Driving rain on building envelopes, Ph.D. thesis, Building Physics and Systems, Technische Universiteit Eindhoven, Eindhoven University Press, Eindhoven, The Netherlands, 198 p.

Snow and ice on roofs – icicles and climate change

Anker Nielsen, Professor,
Division of Building Technology, Department of Civil and Environmental Engineering, Chalmers University of Technology, Gothenburg, Sweden;
Anker.Nielsen@chalmers.se

KEYWORDS: ice, icicles, snow, roofs, risk and climate.

SUMMARY:
Snow and ice is a typical winter problem. Snow accumulates on roofs and icicles can hang at the eaves. The downfall of icicles can kill people. To prevent that we need to look at architecture, meteorology, glaciology and building physics. The physical theory for growth of icicles and their geometry is described. The spacing between icicles is explained. To get icicles to grow we need melting water comes either from solar radiation or heat loss from buildings. Two cases with icing on roofs are shown. Rules for reducing the risk for snow and ice problems on roofs are described. The effect of climate change on icicles is discussed.

1. Introduction

Snow and ice on roofs is occurring during the winter. This gives a many problems related to building physics. An example is icing and generation of icicles on the roof edges. Icicles hanging from the eaves look nice but are a serious problem as they can fall down and hit people. Icicles have killed people. That had happen in Sweden. According to the law is the owner of the building responsible for prevention of sliding of snow and ice from the building. The Swedish Association of Buildings Owners (Fastighetbranchens Utviklingsforum) has made a report (Snö och is på tak 2004) about the problems of snow and ice on roofs. It describes some legal cases and examples of contracts with firms for snow and ice removal. A short evaluation of risk is mentioned.

The problem with icing and icicles on roof is a complex problem involving architecture, meteorology, glaciology and building physics (Nielsen A 2005). The architect decides the layout of the building and the type of roof and its geometry. The architectural solution can reduce or increase the risk of icicle generation. The meteorology comes in, as we must know the weather that will permit the icicles formation. The glaciology describes the physics behind ice and snow. The building physic is involved as heat air and moisture transfer is involved.

2. Model and results

Icicles are all different in details depending on the local conditions, as snow crystals are also unique. The source of the icicles is liquid water, so we need to have water temperatures above the freezing point to develop icicles. A water source at the root of the icicle will make a liquid film on the surface of the icicles that will cover the entire icicle if the flux of water is not very small. The thickness of the liquid film is 40-100 µm. To get the icicle to grow the air temperature must be below 0 C. When the icicle grows the latent heat from freezing must be taken from the ice-water interface. The heat loss rate from the surface to the surrounding will control the growth rate of the icicle. In cold temperatures, the freezing will go faster but also the humidity, wind speed and solar radiation is important. The heat loss from the surface to the air is mainly by thermal convection and by evaporation. Radiation to the surrounding is of minor importance and heat conduction in the interior of the icicle is negligible. When the water flow down the surface of the icicle parts of it will freeze. However, if the water supply is large enough a water drop will be formed at the end of the icicles. This drop grows until it reached a certain size around 5 mm in diameter and then falls and a new drop will be formed.

Numerical models for icicle growth have been made by Makkonen (1988) and Maeno et al (1994).The model shows that the growth rate of an icicle under constant conditions is strongly time dependent. The elongation rate increases with time under fixed atmospheric conditions and water supply rate. This is mainly do to the increasing freezing area of the icicle as it get bigger and the decreasing drip rate. The grow rate in the width will decrease in time as the heat transfer coefficient decreases with increasing icicles diameter. Under fixed conditions will the growth rate increases until there is no drip and length growth stops. At that time is all the supply water collected by the icicle. The model suggests no upper limit for the size of an icicle if conditions for growth exist. In practice several factors limit the icicle size. If the water supply is high, the icicle will grow slowly and is unlikely to grow

big. If the water supply is low, the icicle will soon stop to elongate as no flow reach the icicle tip. Very big icicles can therefore form under conditions in which the water supply rate is first small and then increases. This explains the formation at roofs where the flow rate is low in the morning and increases during the day from heat loss from the building and/or solar radiation on the snow covered roof surface to increase the snow melting water rate as the icicle grow.
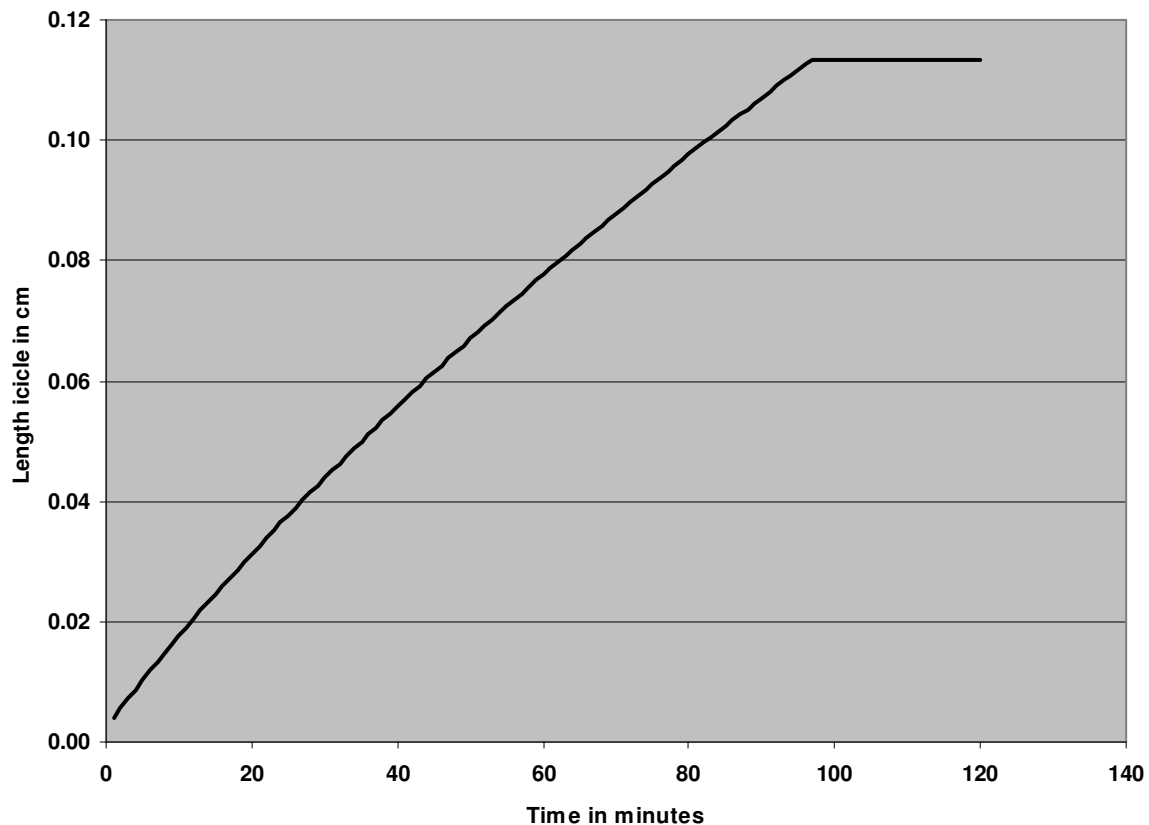
FIG. 1: Example of calculation of icicle growth with an outdoor temperature of −10 C.

Figure 1 is a calculation of the length of the icicles under constant water flow rate and constant outdoor temperature of −10 C. The length-growing rate will decrease with time as surface area increases. The icicle stop to grow in length after 97 minutes as the water flow is all freezing on the surface of the icicles – no water reach the tip. The icicle will still increase in weight and in diameter. The figure will look the same, if the water flow just stopped after 97 minutes but a figure showing the diameter or weight would have shown the difference.

3. Icicle geometry

In most literature and in the previous simulation we have assumed, that the icicles are cone shaped. This is found not to be correct. A paper by Short M, Baygents J and Goldstein R from 2006 has described the growing of an icicle and the expected geometry based on a free-boundary problem. The energy balance between the icicles is defined by the thin layer of water flowing on the surface of the icicle and a thermal boundary layer of warmer air rising around the icicle. Setting up the energy balance and rewriting the equations will describe the geometry of the icicles as a formula (1) with the dimensionless variables A and B.

$$A = 4/3*(B^{0.5}+2)*SQRT(B^{0.5}-1) \tag{1}$$

A is a dimensionless radius and B is a dimensionless length.

The theoretical formula will described the form of icicles as seen in figure 2. It has a convex carrot like form. This can be compared with the conical form with the same total volume. The carrot like form gives a larger radius in the lower part of the icicle and a smaller radius in the upper part. An effect of this is that the strength is less for real form, as the area is smaller at the top of the icicle. This expression for the icicle form has been compared with natural icicles and is found to fit very well with their geometry.

Stalactites in limestone caves – has a striking resemblance with icicles with a convex carrot like form. They are generated by another physical process from precipitation of calcium carbonate. The mathematical description of this process gives the same formula (1) as for icicles. This explains why icicles and stalactites are so similar in form.
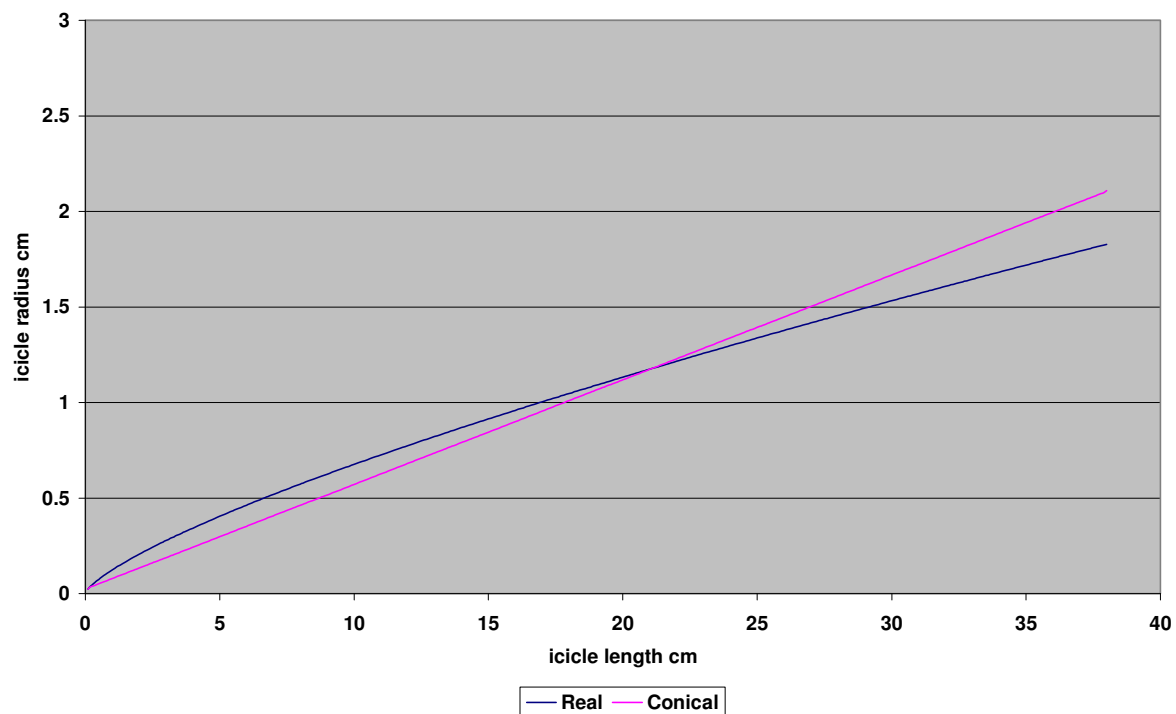
FIG. 2: Comparing simplified icicle form – conical – with the real curve (formula 1).

4. Icicle distance

If we look at icicles at for instance a gutter we will in many cases see that there is a number of icicles with a regular spacing. This spacing is actually determined by the spacing of the water droplets from which they form. The assumption is that first is formed a water film under the solid material and then the water will generate water droplets hanging down from the water film. The distance between the droplets will mostly depend on a balance between surface tension and gravity. Makkonen and Fujii (1993) assume that the weight of the water at a point on the profile is equal to the vertical component of the surface tension force. Using a differential equation for this condition can be solved with zero-order Bessel function of the first kind, covering the domain from zero to the next point where the function has zero slope. This gives a drop radius of 1.06 cm. The spacing between adjacent droplets will be twice this value or 2.13 cm. Using another theory from de Bruyn (1997) gives a value 2.47 cm. This has been compared with measurements of icicles in actual freezing condition and the value is mostly between 1.6 and 3 cm, which include the two theoretical values.

The distance between icicles is interesting for calculation of melting water flow from a roof. The area for each icicle will be 2-3 cm wide and with a length as the roof. The catch area will be larger or smaller depending on the roof type. If we look at hip roof as seen in figure 3 we can see that the catch area is lower near the roof corner at a hip. Larger catch areas for corners with a valley is seen in picture 3. The result is that an icicle in a corner with a valley will typical be larger than others as the water flow will continue for a longer time. Based on the geometry of the roof is it possible to note areas with a higher risk for generation of large icicles. This will typical

be at the end of valleys if we do not have a downpipe in the corner. But inside the downpipe is also a risk as the water can freeze in the pipe, so that melting water cannot drain away.

The theory expects that the droplets are generated on a horizontal surface. If the surface is sloping, then the water will run to the lower end of the slope or a point with a scratch. A scratch will probably be able to stop the water so much that it can generate an icicle at this point. Gutters will typical have a slope to drain the roof water to the downpipes. The icicle will most likely by at the lower end. The problem is that the water will freeze in the gutter. Then the water flow stops and we can get icicles hanging from the ice at the top of the gutter.
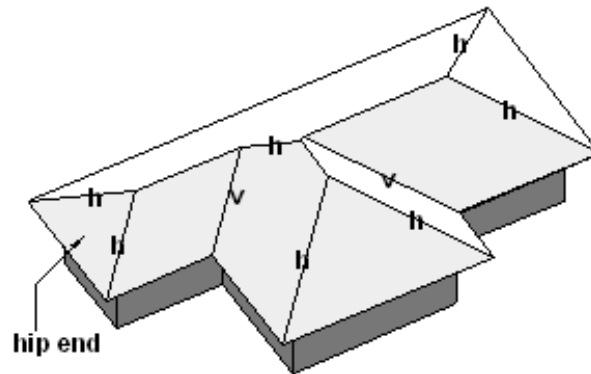
FIG. 3: Hip roof, where "h" is a hip a and "v" is a valley (Wikipedia picture by Bill Bradley)

5. Practical cases

The previous chapter explains that icicles can be generated with a spacing of 2-3 cm. Figure 4 shows an case with many similar spaced icicles. It is from a freezing rain period where raindrops freeze on surfaces, as seen on the very steep roof and the tree in the background. These icicles are very similar with a length of 20 cm and will not give serious risks of damages when they fall down.

FIG. 4: Icicles at the eaves after a freezing rain period (Wikipedia photo by Jonathan Zander)

Figure 5 is a case with an old house with much icing on the roof. The house has a low thermal insulation level and a high heat loss trough the roof. In this case there are heavy icing in the gutter along the façade and in some

places icicles are hanging from the ice in the gutter. The icing in the gutter is less in front of the dormers as the catch area is less here. The dormers will increase the water flow and the icing on both sides of the dormers. This building has two types of risk scenarios. The first is that icicles can fall down, when the temperature rises. The second is that ice above or in the gutter on the lower part of the roof can break loose for instance from snow sliding of the upper part of the roof. This can give a more serious risk that larger ice trunks can fall down. For this building is it necessary to keep people and cars away from the façade of the building. It is recommended to insulate the roof to reduce the risk of icing. The insulation does not totally prevent snow sliding, so using snow guard is a good solution.

FIG. 5: An old house with icicles at the gutter filled with ice (photo Anker Nielsen)

6. Reducing the risk for snow and ice problems on roofs

The previous article Nielsen A, 2005 discussed when icicles will be grow and when they will fall down and not so much the design of the roof. Design methods has previous been discussed in Buska J and Tobiasson W, 2001. This is special important in areas with much snow in the winter. In most cases will the snow load on roofs be lower than on the ground, as some of the snow will be blown away or slide from the roof.

A possible solution is to use a flat roof with internal downpipes and a parapet along the perimeter. The problem with a flat roof will always be the waterproofing. A minimum slope must be used. There is a risk for icing around downpipes. This can give water dams that are not drained. If the flat roof is watertight then it will avoid many of the snow and icing problems on a sloped roof.

Another possibility is to have so steep a roof that the snow would fall of. To get that the slope has to be more than 60-75 degrees and then it is more like a wall. In most practical cases we have to have sloped roofs with a slope of 20-45 degrees. The melting water from a snow layer will run from the ridge to the eaves. A long distance from the ridge to the eaves will increase the risk for icicles. At valleys we will get more melting water and a higher risk for icicles. The melting water will typically run down in the gutter and could freeze here. If the freezing continues the ice-layer will reach over the top of the gutter and onto the lower part of the roof as seen in figure 5. Snow guards as described in Byggforsk A525.931 in the lower part of the roof will stop snow slides. In case of icing as in figure 5 can the snow guard also hold back part of the icing as ice can be expected both in

front and behind the guard. This will reduce the possible size of ice falling down. It is very important that the mechanical strength is high for the fastening of both the gutters and the snow guard. They must not fall down in case of a snow slide on the roof. They must be able to withstand the full load of the snow and ice on the roof.

The surface of the roofing material will influence the risk for snow slides from the roof. A roof with a low sliding resistance as a metal roof will have a high risk for sliding snow. A rougher surface as for instance an unglazed tile roof will have a lower risk.

The length of overhang with the eaves is important for the function of the roof. A narrow overhang can cause icing on the walls. A wide overhang may generate larger icicles. Practical recommendation is an overhang with minimum 30 cm and maximum 60 cm.

Different obstacles on the roof can change the snow sliding and water flow pattern. This can be from dormers, ventilation boxes and chimneys. They can work as snow guards in some places but most likely will they direct the water and snow to adjacent areas. These areas will have a higher risk for icicles. Chimneys, ventilation ducts and other obstacles should be placed near the ridge of the roof as this reduces the risk for being damaged. A plumbing ventilation duct can in worst case be bend by sliding snow.

Roof windows are not a good thing in areas with much snow, as the snow will melt on the window. The result is a higher risk of icicles at the eaves below the window. It is also a risk for snow slides from the roof surface above the window. The best solution is to use dormers with a vertical window.

Electric heating cables can be used in gutters to prevent the freezing of melting water. They can also be used to drain ice dams behind ice blocks in the gutter for instance in valleys. Using electric heating cables is not a good method as the energy cost will be high specially if the effect is not controlled by temperature. Only heat in freezing weather.

It is very important to have a well-insulated and ventilated roof to reduce the heat loss from the building to the roof. The ventilation with outdoor air will keep the attic temperature low, so the snow melting is reduced until it melts from non-freezing outdoor temperatures.

7. Climate Change

Climate projections from climate models point to a warmer climate with an intensified hydrological cycle in the future (Nielsen A., Kjellstrom E and Sasic Kalagasidis A., 2007) But, such changes are already observed both globally and regionally. In Sweden, for instance, the last 10-15 years have been mild and wet compared to previous periods. The trend in the recent Swedish warming is in line with climate change scenarios. The climate projections include changes in both average conditions and in the frequency and magnitude of extreme events. Climate model experiments can be done with coupled atmosphere-ocean general circulation models (AOGCMs). These models are applied with different external climate forcing factors as changing greenhouse gas concentrations or changes in solar intensity etc. The response of the climate system to changes in forcing factors depends on the climate sensitivity of the AOGCM. According to the climate change scenarios described in the previous mentioned paper, the future climate in northern Europe can be summarized as warmer with an increase in the mean average yearly temperature of 1.8C to 4.0C to year 2100. This is particularly true for wintertime conditions when retreating snow cover amplifies the warming at high latitudes. Also, precipitation is expected to increase in all of northern Europe in these scenarios for the winter. Summer temperatures are also projected to increase, but precipitation will increase only in northernmost Scandinavia while decreases in precipitation are projected for most of Europe.

As the formation of icicles is a complex process, it is not trivial to judge what impact climate change may have on their occurrence. In a warmer climate, the snow season and the amount of snow will decrease in most areas, which will favour diminishing the problems. The number of days when the temperature is critical, i.e. going from below to above 0C, will be lower in the southern part of Scandinavia but higher in the north, as seen in figure 6. More information in: Nielsen A., Kjellstrom E and Sasic Kalagasidis A., 2007. This indicates that the problems with icicles will not disappear and may even be worse in some areas, but the risk can be higher or lower depending on the climate scenarios. More simulations with different climate scenarios will be made to evaluate the risks.
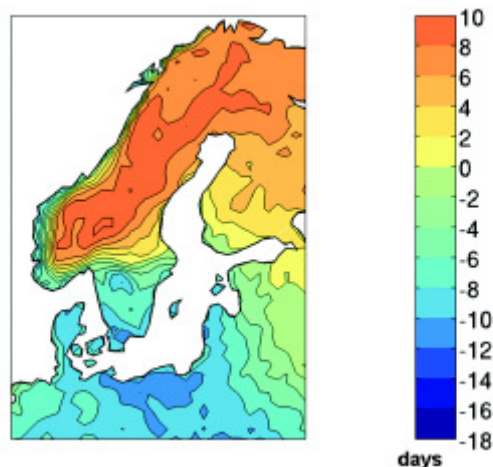
FIG. 6: Change in the number of days when the temperature crosses $0^{o}C$ in Scandinavia during winter (December, January and February). Shown is the average change for 2041-2070 compared to 1961-1990.

8. Conclusions

A well-insulated and ventilated roof will reduce the heat loss from the building and reduce the risk for icicles on the roof. Designing the roof for snow and ice is important in areas much snow in winters. Keep the roof geometry simple and take away as much as possible of obstacles on the roof.

The geometric form of icicles (carrot-like) has been described in Short M, Baygents J and Goldstein R 2006. Theoretical evaluation on spacing of icicles on a horizontal surface is presented. The distance is 2-3cm. This is important for calculation of water flows to each icicle on a roof.

Two practical cases are discussed.

A preliminary evaluation of scenarios for climate projections in Sweden to year 2100 shows a warmer climate and more precipitation. This will influence the risk for problems with snow and ice on roofs. The indication is that problems with icicles will not disappear and may even be worse in some areas. Future simulations with different scenarios will give a better risk evaluation.

9. Acknowledgements

10. References

De Bruyn, J 1997: On the formation of periodic arrays of icicles, Cold Regions Science and Technology vol 25 (1997) page 225-229

Buska J and Tobiasson W, 2001 Minimizing the adverse effects of snow and ice on roofs, International Conference on Building Envelope Systems and Technologies (ICBEST-2001), Ottawa, Canada, page 339-346

Byggforsk A525.931 1996, Building Detail Sheet A525.931, Tak, Snøfangere (Roof – Snow guards), Norwegian Building Research Institute, Oslo, Norway (in Norwegian)

Makkonen L 1988 A model of icicle growth, Journal of Glaciology vol. 34, page 64-70

Makkonen L and Fujii Y 1993: Spacing of icicles, Cold Regions Science and Technology vol 21, 317-322

Nielsen A 2005: Snow, Ice and Icicles on Roofs – Physics and Risks, Sixth Nordic Conference on Building Physics in the Nordic Countries, Reykjavik, page 562-569

Nielsen A., Kjellstrom E and Sasic Kalagasidis A., 2007: Sustainability of the Swedish built environment towards climate change. Hygro-thermal effects and design criteria for buildings with respect to future climate scenario. Thermal Performance for the Exterior Envelopes of Whole Buildings X, December 2-7, Clearwater beach, Florida, USA. s. 10. ISBN/ISSN: 978-1-933742-28-1

Maeno N, Makkonen L, Nishimura K, Kosugi K and Takahashi T 1994: Growth rate of icicles, Journal of Glaciology vol.40, page 319-326

Short M, Baygents J and Goldstein R 2006: A free-boundary theory for the shape of the ideal dripping icicle, Physics of Fluids vol 18, 083101, 5 pages

Snö och is på tak – risker och riktlinjer 2004 (Snow and ice on roofs – risks and guidelines) Fastighetsbranchens Utviklingsforum, Stockholm, Sweden ISBN 91-975422-0-2 (In Swedish)

Wind-Driven Rain Distribution and its Hygrothermal Effect on Two Different Types of Building Geometry

Ayyapan N. Kumaraperumal, PhD. Student,
RICH Centre, School of BNE, Glasgow Caledonian University, Glasgow;
aku1@gcal.ac.uk

Chris H. Sanders, Mr,
RICH Centre, School of BNE, Glasgow Caledonian University, Glasgow;
chs@gcal.ac.uk

Paul H. Baker, Dr,
RICH Centre, School of BNE, Glasgow Caledonian University, Glasgow;
pba3@gcal.ac.uk

Graham H. Galbraith, Professor,
Glasgow Caledonian University, Glasgow;
ghga@gcal.ac.uk

Emmanuel Adu Essah, PhD Student,
RICH Centre, School of BNE, Glasgow Caledonian University, Glasgow;
ees1@gcal.ac.uk

KEYWORDS: Wind-driven rain, Indoor air quality, numerical simulation, experimental database, HAM-Tools; validation

SUMMARY:
The lifetime of buildings in UK is between 40 to 75 years and historic buildings stand for many centuries. Protecting these buildings from the external environment is a difficult and expensive task. This study is focused on the effects of wind-driven rain, which is the main cause of water penetration and moisture load on building components. Two different buildings, one a historical castle and another a low rise modern commercial building which are of different geometry, material and surrounding topography are investigated. Numerical simulation is carried out to calculate wind-driven rain for various raindrop sizes, rainfall intensities, wind speed and directions. The influence of wind-driven rain loading is examined by modifying existing hygrothermal modelling tools. The moisture effect within the indoor environment due to the effects of the exterior weather conditions was measured and compared to computer predictions.

1. Introduction

Buildings in the west of Scotland are highly exposed to wind-driven rain (WDR) which causes excess moisture that penetrates into the building components. Presence of moisture on the building structures are to be considered as one of the important agent of building deterioration, durability and the indoor air humidity. Research on WDR was originally mainly experimental and semi-empirical (Lacy & Shellard 1962; Sanders 2004). It was in the late 1990's, when many researchers adopted numerical simulation techniques to predict the driving rain impacts and patterns on building exterior surfaces (Choi 1993; Sankaran & Paterson 1997). From these studies it is well understood that, out of all exterior environmental loads, the effect of WDR causes more than 90% of critical damage to the buildings (Karagiozis et al. 2003). Apart from wind and rain, temperature and humidity are another two important parameters which influences moisture movement and sorption characteristics of building materials. The combination of wind-driven rain, temperature and relative humidity leads to interstitial condensation in the façade is on roof structures which can cause the wood frames to decay and lead to structural failure (Sanders 1998). Moreover the important consequences of climate change for buildings in UK are associated with increased moisture stress.

This investigation is part of ongoing research on wind-driven rain which has established the importance of moisture stresses, wind flow and impacts due to rain on commercial and historical buildings. For both the

buildings, the south-west facing facades are highly exposed to driving rain and have suffered some damage due to moisture penetration. Figure 1 shows the interior section of the west façade of the historic building in which much damage is caused due to water incursion. Based on semi-empirical equations and numerical solutions, wind-driven rain is calculated and compared with the hourly data of measured driving rain. Based on numerically calculated wind-driven and considering other environmental parameters, the hygrothermal performance of both buildings are predicted.

FIG. 1: Moisture damage to interior of the castle

2. Methodology

Over the past two decades, many researchers have concentrated on weather data based on hourly events. The British Standard Code of practice BSI (BS8104 1992) for assessing the exposure of a wall to wind-driven rain is the only available standard method to estimate driving rain quantities in the UK. On the basis of BS8104, a draft CEN standard (CEN 2005) has been completed based on the work done by Sanders (1996) which requires hourly values of rainfall, wind speed and wind direction. Recent investigation on WDR impact on a historic building (Brodick castle) in Scotland (Kumaraperumal et al. 2006) and calculation of moisture contents play a vital role to formulate further research on different Scottish buildings. The outcome from that investigation showed higher values of the wall factor on the west façade of castle, when the wind deviates even slightly from the normal. Recently, there is an increased demand for calculation methods to evaluate the moisture behavior of building components. In general, most of the computer simulation software source codes are closed to the user which makes it difficult to implement changes in the original code. The present methodology is useful to calculate the moisture behavior in the zone and the building structures. This paper is focused on the west facing facades of the structures.

2.1 Derivation of wind speed

The wind velocity across the building is calculated according to the logarithmic law and the expression is as follows (Hoxey & Richards 1993).

$$U(z) = \frac{U^{*}_{ABL}}{\kappa} \ln(\frac{z + y_0}{y_0}) \qquad (1)$$

The kinetic energy profile

$$k = \frac{U^{*2}_{ABL}}{\sqrt{C_u}} \qquad (2)$$

and the dissipation of kinetic energy

$$\varepsilon = \frac{U_{ABL}^{*3}}{\kappa(y_0)} \qquad\qquad\qquad (3)$$

In Equation 1, $U(z)$ is the mean wind speed at the height z, κ the Von Karman constant and y_0 the aerodynamic roughness length. The WDR for urban and open flat country is derived based on the above wind velocity.

2.2 WDR for the west facades of the buildings

Using the vector concept, the ratio between the wind speed, U, and the raindrop terminal velocity, when falling vertically, V_t (Best 1950) equals the ratio between the wind driven rain intensity and horizontal rainfall intensity.

$$R_v = R_h \cdot \frac{U}{V_t} \qquad\qquad\qquad (4)$$

where R_v is the rate of driving rain or wind driven rain intensity on a vertical surface and R_h is the rainfall intensity on the horizontal surface.

Prior (Prior 1985) developed a directional driving rain map for the UK by analyzing hourly measured rainfall, wind speed and wind directions for an average annual driving rain index. The total amount of driving rain over a year on a wall in open 'airfield' site is given by

$$I_A = 0.22 \times \sum U \cdot R_h^{0.88} \cdot \cos(D - \theta) \qquad\qquad\qquad (5)$$

where D is the hourly mean wind direction from north and θ is angle between north and the line normal to the wall. The summation is taken over all the hours when $cos(D-\theta)$ is positive. Equation (5) was used to develop the detailed maps in the British Standard Code of Practice BSI for assessing the exposure of wall to wind-driven rain (BSI 1992). On the basis of BS8104, a draft CEN standard (CEN 2005) has been completed and will be published in 2008, which requires hourly values of rainfall, wind speed and wind direction. Both standards provide methods to calculate the total amount of driving rain over a period in open 'airfield' site I_A. The amount of rain impacting on a real building, the wall index I_{WA}, is calculated from the airfield index I_A, by applying four empirically derived correction factors, the terrain roughness factor, R, the topography factor, T, the obstruction factor, O, and the wall factor, W.

$$I_{WA} = I_A \cdot R \cdot T \cdot O \cdot W \qquad\qquad\qquad (6)$$

Three of these factors, R, T and O, are well understood and are, in any case, close to 1 in most situations. The wall factor, W, which determines the distribution of driving rain over the façade of a building, is much more significant, varying from 0.2 to 0.6 in most buildings. The only available information is a very simple table of values in BS8104, which covers all types of buildings, and takes no account of façade details such as overhangs, parapets and other features which have large effects on the distribution of driving rain. In the present work, to estimate wall factor based on CEN standard, 0.4 and 0.5 wall factor are adopted for commercial and historic building respectively.

Based on the above equations, Choi (1993) proposed a steady state numerical simulation technique to evaluate wind-driven rain called local intensity factor (LIF).

$$LIF = \frac{\text{WDR intensity on building face}}{\text{u.r.i}} \qquad\qquad\qquad (7)$$

$$= \int LEF(d) f(d) dd \qquad\qquad\qquad (8)$$

where *u.r.i* is unobstructed rainfall intensity, the *LEF* (local effect factor) is related to the raindrop diameter d and *LIF* is related to the entire spectrum of raindrop diameter (d).

2.3 Heat and moisture transfer through the building structure

External weather conditions, mainly wind-driven rain, play an important role to raise the moisture level in structures. The capillary suction of rainwater impacting in amounts depending on wind speed and direction, geographical location, building orientation is the parameter which affects the durability and performance of building enclosures (Kus et al. 2004). Out of the whole building structure, external walls come under the most

extreme weather conditions from wind speed, incident solar radiation, long-wave radiation and rain/ driving rain. In the present work, the transport coefficients are estimated by assuming linear variation (Sasic 2004). The model is further modified and additional set of blocks is implemented in the computational domain which can calculate hourly driving rain based on the rain falling on the unobstructed horizontal surface, roughness factors, topography, wind speeds and directions.

The basic transport equations to predict temperature and moisture distribution are as follows;

Heat transfer

$$\rho c_s \frac{\partial T}{\partial t} = \frac{\partial}{\partial x}\left(\lambda \frac{\partial T}{\partial x}\right) + h_v \frac{\partial}{\partial x}\left(\delta_p \frac{\partial p_v}{\partial x}\right) \qquad (9)$$

Moisture transfer

$$\frac{\partial w}{\partial t} = \frac{\partial}{\partial x}\left(\delta_p \frac{\partial p_v}{\partial x}\right) + \frac{\partial}{\partial x}\left(D_l \frac{\partial P_h}{\partial x}\right) \qquad (10)$$

where t is time (sec), ρ is material density (kg/m^3), c_s is specific heat capacity (J/kg·K), λ is thermal conductivity (W/m·K), T is temperature (K), h_v the latent heat of phase change (J/kg), δ_p is water vapour permeability (kg/m·s·Pa), p_v is water vapour pressure (Pa), w is moisture content (kg/m^3), D_l is liquid conductivity (kg·m/s) and P_h is capillary water pressure (Pa). Further details can be refer to Sasic (2004).

3. Experimental investigation

Full-scale experiments were conducted at two different types of buildings (figure 2). Both the buildings are situated in west part of Scotland where the prevailing direction of wind and rain is between south and west. The first building is the 19th century historic monument called Brodick Castle situated on the Isle of Arran. The second is the modern commercial building called BRE Scotland which is situated in East Kilbride. The building material of Brodick castle it is sandstone while for BRE is concrete block. The BRE is surrounded by an open area near to the centre of the city and the Brodick castle is surrounded by rural, hilly region and open sea on S-W direction.
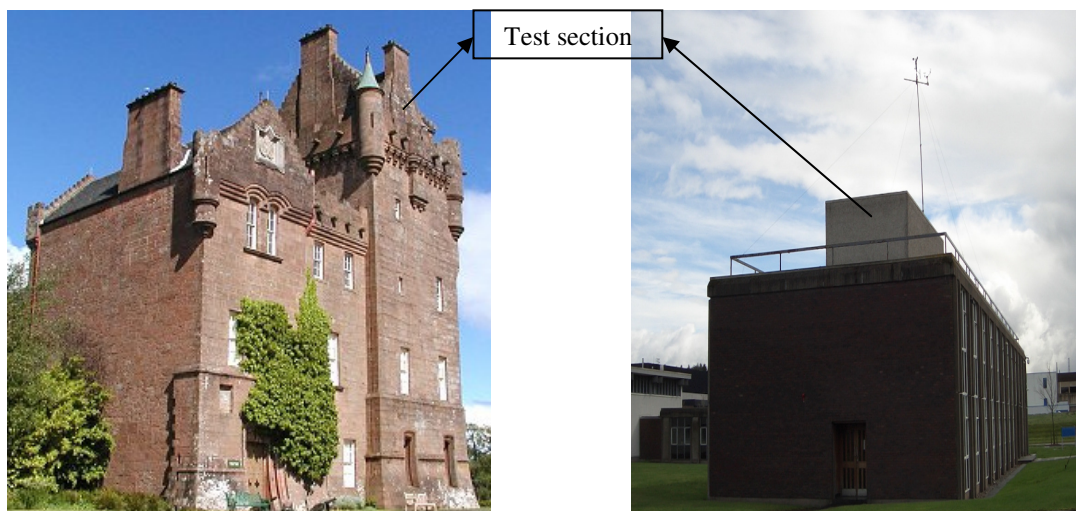
FIG. 2: West facing façade, Brodick Castle (L) and BRE building (R)

The reference wind speed and wind direction is measured at 10m and 20m from the ground for BRE and Brodick Castle respectively. For both the buildings, driving rain gauges with the catchment area of 0.1m^2 are mounted on the top section of the facades. These driving rain gauges do not follow any standards and are not made industrially. For these reasons testing and calibration of the gauges were performed before mounting on the experimental site. The reference horizontal rain intensity is measured by normal rain gauge (tipping bucket) which is placed on the roof of the building free from any nearby obstacles. For both the locations hourly weather

data are available. To improve the measurements, a disdrometer was mounted on the BRE building to determine the drop size distribution of the rain (Kumaraperumal et al. 2007). The basic hourly elements are, wind speed and direction, driving rain, horizontal rainfall intensity, solar radiation, indoor and outdoor temperature and relative humidity.

4. Results

4.1 Computational Fluid Dynamics

For both the buildings, the air flow field is modelled in three dimensions using FLUENT (Fluent 2006), solving the Reynolds-averaged Navier-Stokes and continuity equations numerically to obtain the steady-state velocity field (equation 1). Closure is achieved with the aid of the realizable k-ε turbulence model, where k is the turbulent kinetic energy and ε is the turbulent kinetic energy dissipation (equation 2 & 3). A no-slip wall function on the ground (wall roughness is 0.01m) and zero static pressure boundary condition at the outlet are imposed. The top and sides of the domain are symmetrical boundary conditions, which set the normal velocity to zero at the symmetry plane. The mesh used in both the models is of unstructured nodes and the grid contains about 2.6 and 2.2 million tetrahedral elements for Brodick castle and BRE building respectively. The densities of the nodes are higher near to the building and the ground.

Once the solution has converged, the u, v, w component velocity field is exported for calculating trajectories of individual rain drops. Approximately 1000 trajectories were calculated for each wind flow (1, 2, 3, 5 & 10m/s) condition and drop diameter (0.04, 0.06, 0.08, 1, 1.4, 2, 3, 4, 5, 6 mm). Based on equation 8, the wind-driven rain distributions for both the buildings are calculated (Blocken & Carmeliet 2002).
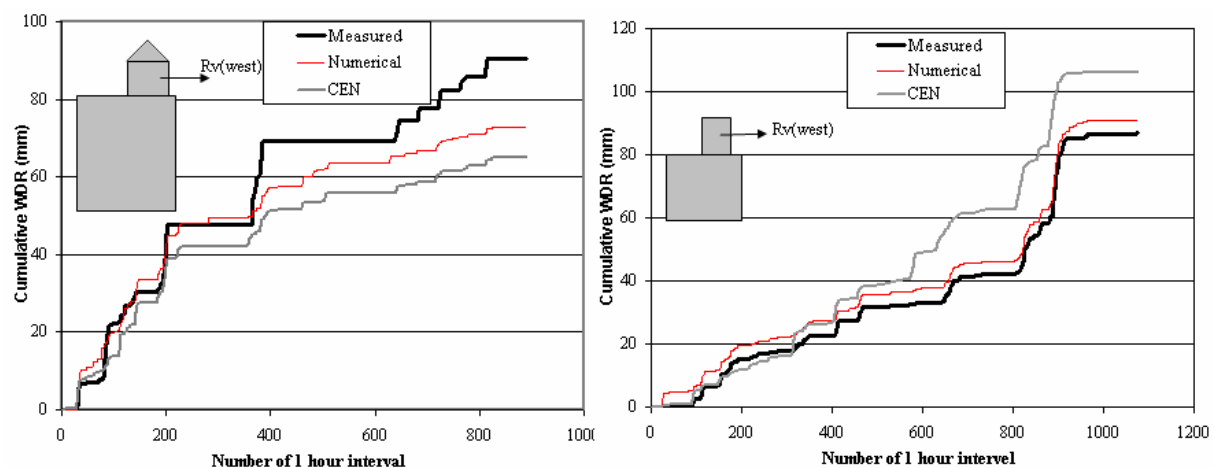
FIG. 3: Cumulative WDR for a rain event on Brodick castle (L) and BRE building (R)

The result presented in Figure 3 shows the cumulative WDR on a driving rain gauge on the west façade (Rv) for an intense rain event during November and December 2006. Comparison of measured WDR data is made with numerical and CEN standards for Brodick Castle and the BRE building (equation 5 & 6). For Brodick Castle, good agreement between the numerical and CEN has been seen for the first quarter of the period but for the rest of the period the CEN is lower compared to the measurements. The reason may be due to inappropriate consideration of three important correction factors i.e. a terrain roughness factor, a topography factor and an obstruction factor. The BRE building shows reasonably good agreement between the measured, CEN and numerical simulation for the complete set of rain events.

4.2 Hygrothermal Model and Problem Description

Recently sophisticated heat air and moisture (HAM) transfer models have been developed at various research institutes and universities across the globe. The development of these codes has been aided by the tremendous computer power which has let to opportunities to develop more advance moisture transfer models. Few of these models incorporate driving rain, because there is little data available. HAM-Tool is a building simulation

software package, in which the hygrothermal performance of a building indoor environment and envelope is analysed. The toolbox is constructed using Simulink which is integrated with Matlab. The program is well designed by using a graphical programming environment which consists of a library of blocks representing the building parts, weather database and zone of interest (Sasic 2004). HAM-Tools provide an open source code to work and expand the program for further investigation. Figure 4 depicts the modelling process of the package. The model uses real-time meteorological data to account for the exterior environmental conditions that affects the performance of indoor environment. Hourly weather data, including external temperature, relative humidity, wind speed and direction, driving rain and global solar radiation, are employed in the hygrothermal calculations. The incidence radiation on vertical surfaces (west facing wall) is calculated from the measured global solar radiation intensity data.

The availability of material properties to evaluate hygrothermal performance is limited, particularly for the sandstone material of the castle. Material properties for concrete blocks are available in the material property database of HAM-Tools, while preliminary experiments were carried out to acquire accurate properties for the sandstone material for modelling. The standard material properties for the natural sandstone and concreted block are listed in Table 1.
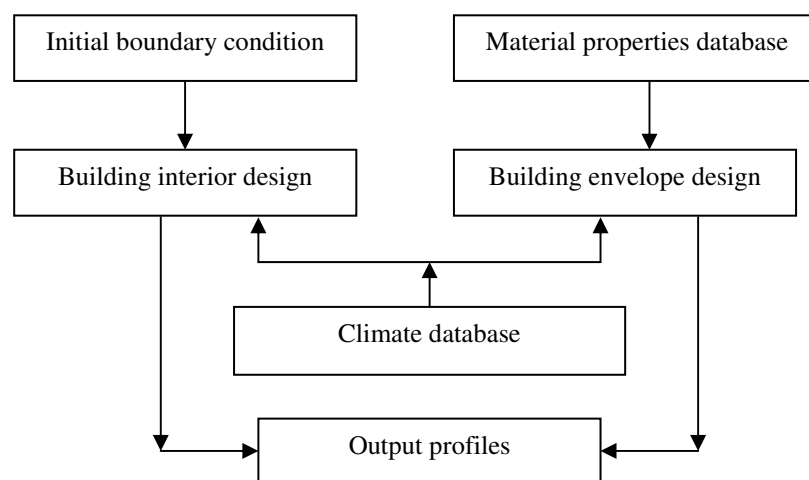
FIG. 4: HAM-Tool modelling process

TABLE. 1: Standard Material Properties of Sandstone and Concrete block

Parameters	Sandstone	Concrete block
Bulk Density [kg m^{-3}]	2200	2300
Porosity [m^3 m^{-3}]	0.26	0.16
Heat Capacity [kJ kg^{-1} K^{-1}]	0.85	0.84
Heat Conductivity Dry [W m^{-1} K^{-1}]	0.6	0.6

The effects of wind-driven rain on the building facades and hygrothermal performance on the internal environment have been determined. Measurements of temperature and relative humidity at different locations on both buildings have been carried out. Considering the west façade of both buildings, numerically calculated WDR from section 4.1 is linked to the model. Simulations from HAM-tool are carried out to predict the temperature and relative humidity for a period of one year for the interior environment of both buildings. The initial conditions for the simulation are set as 20^0C and 70%RH. For Brodick Castle, the modelled temperature profiles are in good agreement with measured ones- they show the same trend and response. For the first quarter of the year, the relative humidity results agree well with the measured. From the middle of the year, simulation results shows difference of 10-15% rise in RH (figure 5). This is because the RH is very sensitive to the ventilation rate which is being terminated from the model. The intense WDR during the winter period i.e. October till January, increase the rate of moisture level across the castle component which affects the interior

conditions of castle, particularly where RH values peak up to saturation, temperature remains low. This may lead to high presence of condensation on the interior facades which will affect the indoor air quality of the castle.

For the BRE building, the numerically calculated relative humidity profiles were fluctuating considerably throughout the year. Though there is some disagreement between the simulation model and the measured (i.e. starting from March till June), simulation results agrees well the measurement for the rest of the period. However, the temperature increases to 3 to 5 °C for the first quarter of year and the rest of year the profile follows the measured one (figure 6).
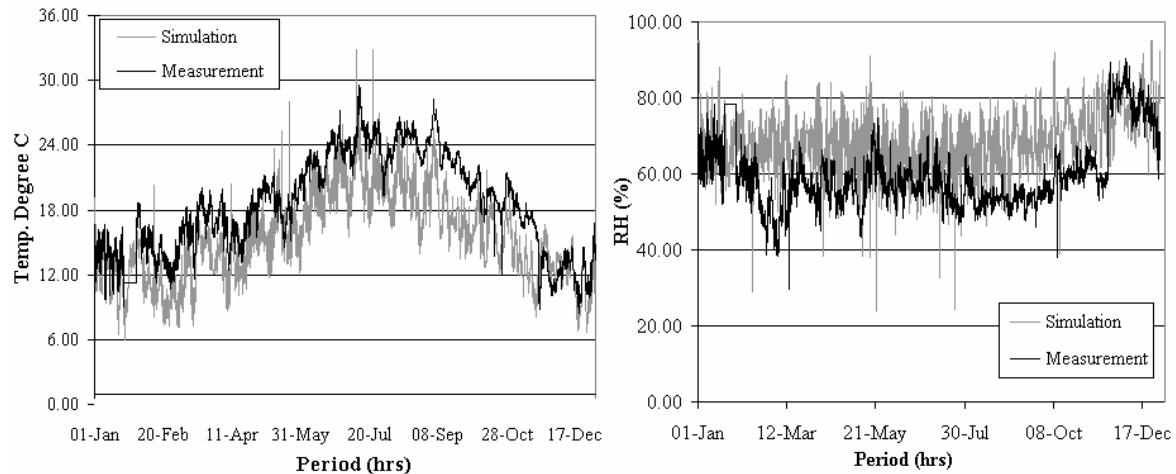
FIG. 5: Calculated and measured room air Temperature and RH indoor environment of Brodick Castle
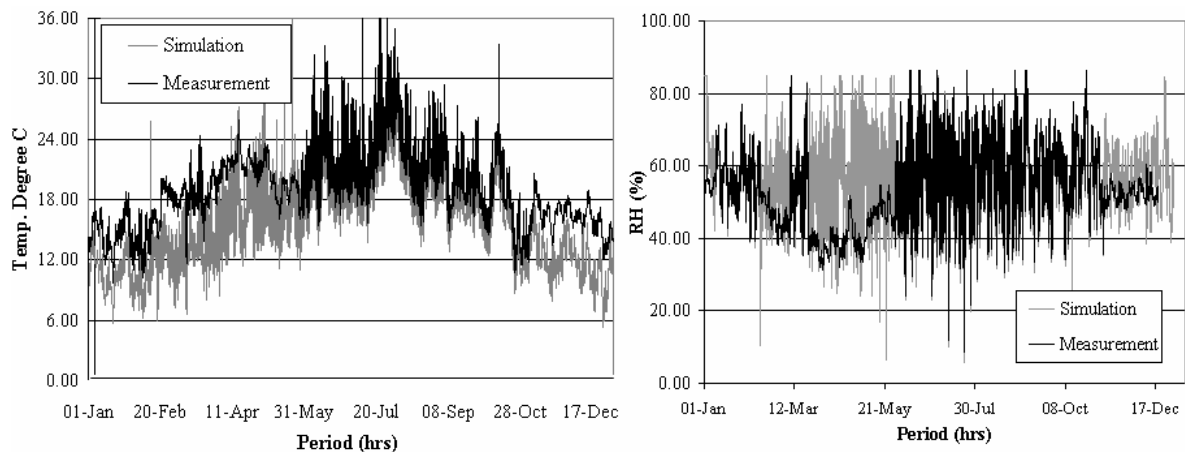
FIG. 6: Calculated and measured room air Temperature and RH for indoor environment of BRE building

5. Conclusions

The preliminary assessment of the effect of wind-driven rain loads on the hygrothermal performance on two different types of building system is investigated. The analysis in this paper has demonstrated the importance of semi-empirical, numerical modelling and measurement to estimate wind-driven rain for the commercial and historic building. On the basis of the simulation results, it is suggested that wind-driven rain plays an important role in the hygrothermal performance of the interior environment. For the castle, the sandstone material which is highly hygroscopic, it is expected to have high rise in dampness during winter period due to increase in driving rain and relative humidity. On the other hand, the BRE building of concrete material which is less porous than the sandstone shows that the RH values fluctuates around 60% throughout the year. Hence uses of measurements and simulations have proven to be useful in investigating the hygrothermal performance on both buildings.

6. Acknowledgements

7. References

Best A. (1950). The size distribution of raindrops. *Quarterly Journal of the Royal Meteorological Society*, Vol 76, p 16-36.

Blocken B. and Carmeliet J. (2002). Spatial and temporal distribution of driving rain on low-rise building. *Wind and Structures*, Vol 5, p 441-462.

British Standard Institution. (1992). BS8104: Code of practice for assessing exposure of walls to wind-driven rain. Milton Keynes, London, United Kingdom.

CEN. (2005). Hygrothermal performance of buildings- Climatic data- part 3: Calculation of a driving rain index for vertical surfaces from hourly wind and rain data. Draft prEN 13013-3.

Choi E.C.C. (1993). Simulation of wind-driven-rain around a building. *Journal of Wind Engineering and Industrial Aerodynamics*. Vol 46 & 47, p 721-729.

Fluent Inc. (2006). Fluent User's Guide.

Hoxey R.P., and Richards P.J. (1993). Flow patterns and pressure fields around a full-scale building. *Journal of Wind Engineering and Industrial Aerodynamics,* Vol 50, p 203-212.

Lacy R.E. and Shellard H.C. (1962). An index of driving rain. *Meteorological magazine* 91: 177-184

Sanders C. H. (1996). IEA Annex 24, Final Report, Volume 2, Task2: Environmental Condition, *International Energy Agency*, ISBN 90-75741-03-0.

Sanders C. H. (1998). Condensation Effect of Structure Durability, *Journal of CIBSE*, November.

Sanders C. H. (2004). Comparison of the 'British Standard' and 'French' methods for estimating driving rain impacts on walls, *IEA Annex 41 meeting Glasgow*, Report A41-T3-UK-04-2.

Sankaran R. and Paterson D.A. (1997). Computation of rain falling on a tall rectangular building. *Journal of Wind Engineering and Industrial Aerodynamics*, Vol 72, p 127-136.

Sasic Kalagasidis A. (2004) HAM-Tools: An Integrated Simulation Tool for Heat, Air and Moisture Transfer Analyses in Building Physics. PhD Thesis.

Karagiozis A. N., Salonvaara M., Holm A. and Kuenzel H. (2003). Influence of Wind-driven rain on hygrothermal performance. *Eight international IBPSA Conference.* Eindhoven.

Kumaraperumal A., Baker P.H., Sanders C.H., Galbraith G.H. and McLean R.C. (2006). Comparison of measured and modelled driving rain data on a historic building with standard assessment methods. *Proceedings of the Third international Building Physics Conference, Research in Building Physics and Building Engineering*, Concordia University, Montreal, Canada., p. 897-904.

Kumaraperumal A., Sanders C.H., Baker P.H., Galbraith G.H. and McGlinchey D. (2007). Analyzing wind-driven rain on a building façade using the laser precipitation monitor (LPM). *Proceedings of sixth international Conference on Indoor Air Quality, Ventilation & Energy Conservation in Building,* Sendai, Vol 3, p.365-375.

Kus H., Nygren K. and Norberg P. (2004). In-use performance assessment of rendered autoclaved aerated concrete walls by long-term moisture monitoring. *Building and Environment*, Vol 39, p. 677-687.

Prior M.J. (1985). Directional driving rain indices for the United Kingdom – computational and mapping. Building Research Establishment Report. Garston.

Wind-Driven Rain Impact on Historical Brick Wall Buildings

Masaru Abuku, PhD student,
Laboratory of Building Physics, Department of Civil Engineering, Katholieke Universiteit Leuven;
masaru.abuku@bwk.kuleuven.be

Hans Janssen, Assistant professor,
Department of Civil Engineering, Technical University of Denmark;
haj@byg.dtu.dk

Staf Roels, Professor,
Laboratory of Building Physics, Department of Civil Engineering, Katholieke Universiteit Leuven;
staf.roels@bwk.kuleuven.be

SUMMARY:
This paper gives an onset to whole building modelling in which the interaction between interior and exterior climates via building enclosures is simulated. The focus is particularly on the impact of wind-driven rain (WDR) on the hygrothermal response, indoor climate, energy consumption, and mould growth at interior wall surfaces. First the WDR load on the facades of a tower is numerically determined. Then the hygrothermal behaviour of the brick walls is numerically analysed on a horizontal slice through the tower. The simulations demonstrate that for the case analysed, the WDR load causes a significant increase of indoor relative humidity and energy consumption for heating. Finally, the obtained relative humidity and temperature at the interior wall surfaces are combined with isopleths of generalised spore germination time of fungus mould. The results show that WDR loads can have a significant impact on mould growth especially at the edges of the walls.

1. Introduction

Since the 1970s Building Energy Simulation (BES) models have been developed for the numerical prediction of the thermal condition and energy performance of a building. Though most BES models nowadays also (partially) solve the hygric balance, moisture analysis is mainly limited to water vapour transport and its influence through latent heat effects and moisture buffering. The comprehensive hygrothermal interaction between the exterior and interior climates, as dealt with in building envelope models (e.g. Pedersen, 1990; Künzel, 1994; Grunewald, 1997), is only incorporated to a limited extent. Recently, Nakhi (1995), Holm et al. (2003), Rode et al. (2003) and Mendes et al. (2003) have combined a model of heat, vapour and liquid transport in walls with a BES model, to come to whole building hygrothermal modelling. This paper addresses such simulation with special emphasis on Wind-Driven Rain (WDR) impacts and liquid water transport.

Concerning WDR as boundary condition for the hygrothermal analysis of building envelopes, a lot of progress has been made in the last decades. Advanced numerical techniques based on Computational Fluid Dynamics (CFD) enabled the accurate numerical prediction of WDR loads on building facades (Choi, 1993; Blocken and Carmeliet, 2002). However, several topics related to the response of a wall to the driving rain load still need further investigation. Examples are durability issues of building facades, algae formation at exterior surfaces, the possible impact on mould growth at inside wall surfaces, and the impact on indoor climate and energy consumption. The answers to these questions do not only depend on the composition of the wall and the outside climate, but also on the building configuration, moisture buffering capacity of the interior, heat and moisture sources in the building, ventilation rate, etc. Such multicausal problems cannot be adequately dealt with via a component hygrothermal model, but do require whole building hygrothermal simulation.

Some of these interactions/dependencies are not of great concern for recent wall configurations, such as well-insulated walls with air cavity, walls with impermeable siding or sheathing, etc. On the other hand, in historic buildings in Europe, solid masonry systems have often been used for outer walls, without the installation of an adequate air space, insulation and/or vapour retarder, resulting in a direct capillary transmission between exterior and interior. For such walls, absorption of WDR loads may result in a moisture flow towards the interior surface

and/or environment, potentially yielding mould growth at inside wall surfaces and/or increased indoor humidity. Hall and Lalimeris (1982) is perhaps the first case in which the impact of WDR loads on the moisture content in walls is investigated numerically. Janssen et al. (2007a, 2007b) and Blocken et al. (2007) first formulated the implementation of numerically determined WDR loads as boundary condition in the heat and moisture transfer analysis in building enclosures. Also Häupl et al. (2005) numerically investigated the impact of the rain on the hygrothermal performance of the facade of the 'Rijksmuseum' in Amsterdam, the Netherlands. Kumaraperumal et al. (2006) recently showed an experimental and numerical analysis of WDR loads on and the hygric response of the walls for a Scottish castle. Although the distribution of the WDR load, with an intensity often highest near the upper edges and the sides of building facades, is considered to have an important role in the hygrothermal performance of buildings, so far no quantitative investigation of the impact of such distributed WDR load has been performed on the whole building scale. Neither has WDR been studied in relation to the durability, indoor environment and energy performance of the building. This paper presents an onset of such a study: the impact of the distributed WDR loads on the hygrothermal behaviour of the walls and the indoor environment of a tower building has been investigated. In the first part of this paper, the methodology of the whole building simulation and WDR simulation and the implementation of WDR loads in hygrothermal simulation of building components are briefly presented. In the second part, the WDR load on the facade of a $4 \times 4 \times 10$ m^3 tower is numerically determined. Then the heat and moisture transfer in the brick walls and the hygrothermal conditions in the room are numerically analysed on a horizontal slice through the walls at half the tower height. Finally the impact of WDR on the indoor climate, energy consumption and mould growth potential is discussed.

2. Methodology

In this paper a whole building simulation is defined as the numerical simulation of coupled heat, air and moisture transfer in building components and interior environment in rooms, with the aim of investigating the durability of building facades, together with an analysis of indoor climate and energy consumption of the building. When "perfect mixing" of indoor air is assumed, the whole building modelling of the interactions between exterior and interior climates via building components usually comprises: (1) the heat, air and moisture balance of the indoor environment; (2) the heat, air and moisture transfer in building components; and (3) the boundary conditions for (1) and (2) and the coupling of (1) and (2). Because essential parts of the whole building simulation are widely known and used in this field and only simple case studies are presented in this paper, the reader is referred to e.g. Nakhi (1995), Holm et al. (2003), Rode et al. (2003) and Mendes et al. (2003) for a mathematical formulation of the whole building simulation. Note that the air transfer in building components has neither been considered in these whole building simulation models nor will be dealt with in the current study.

The heat and moisture transfer equations in building components is coupled with the heat, air and moisture balance in the indoor environment by boundary conditions for heat and moisture at inside wall surfaces of the room, usually using heat and moisture surface transfer coefficients. At the same time the heat, air and moisture balance in the room is also directly linked to the outside environment through ventilation and solar and diffuse radiation. Similarly, the heat and moisture transfer equations in building components require boundary conditions at the exterior side: outdoor air temperature and humidity, cloudiness, solar and diffuse radiation, convective heat and moisture transfer coefficient, and wind-driven rain rainfall intensity. Because until now WDR load has hardly been taken into account in current examples of whole building modelling, influences of WDR on the whole building simulation are particularly focused on in this paper.

The WDR load I_{WDR} (kg/m^{2}s) at building facades can be obtained by multiplying the horizontal rainfall intensity I_h (kg/m^{2}s) by the global catch ratio η (-) (Blocken and Carmeliet, 2002):

$$I_{WDR} = I_h \times \eta \left(\theta, U_{ref}, I_h \right) \tag{1}$$

where, η is a function of the angle θ (°) between reference wind direction and orientation of the wall, reference wind speed U_{ref} (m/s) and I_h, all obtained from meteorological data. η can be obtained from measurements (e.g. Sanders, 1996), empirical relations (Sanders, 1996) or numerical simulations (Choi, 1993; Blocken and Carmeliet, 2002). Note that detailed values of η can only be obtained by numerical simulation in a practical sense. For the methodology and a detailed discussion of the accuracy of such numerically determined catch ratio's the reader is referred to Blocken and Carmeliet (2002). The difference between determined WDR load and the actual moisture load on the surface, due to the splashing and bouncing of raindrops, is discussed in Abuku et al. (2008), based on numerical and experimental investigations.

The numerical simulation of WDR as a source of moisture and enthalpy for a vertical wall is typically conducted assuming the WDR load spatially continuous and temporally averaged over a certain period. For the mathematical basis, the reader is refered to Janssen et al. (2007a).

3. Different calculation steps and building configuration under study

The current study focuses on the hygrothermal response of a $4\times4\times10$ m^3 tower with brick walls of 29 cm thickness taking into account the WDR load on the facades. Fig. 1 (a) shows the configuration of the tower. Although the dimension of $4\times4\times10$ m^3 is rather small as building scale, this was adopted due to limits in computer capacity. WDR loads on the facades of this tower are first numerically determined by Computational Fluid Dynamics (CFD) and particle tracking simulations (Choi, 1993; Blocken and Carmeliet, 2002). As a second step, the hygrothermal response of the first floor (3.5 to 6.5 m above the ground) is analysed. Because of limits in computer capacity, the analysis is performed on a 2-dimensional horizontal slice of the walls and the room (4×4 m^2). Thus it is assumed that the rain load on this part is vertically uniform and hence that the vertical distribution of heat and moisture in the walls of this part is also uniform. WDR loads are vertically averaged to obtain representative WDR loads for vertical segments from 3.5 to 6.5 m above the ground. Fig. 1 (b) and (c) show the mesh of the walls and the intersection of the walls, which will be used in section 5. In the current study the masonry is treated as homogeneous, while in reality masonry consist of brick and mortar, which may change the penetration rate of rain into the wall and thus have some influence on results in section 5.
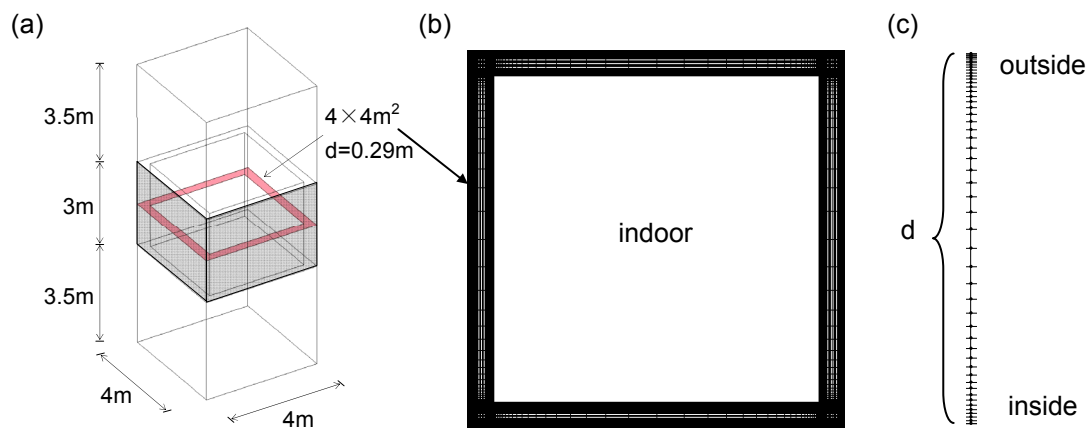
FIG. 1: (a) Configuration of the building and section under study, (b) mesh of the walls and (c) intersection of the wall. d: thickness of the walls(m) (=0.29 m).

4. Numerical quantification of WDR loads

The WDR for the facades of the $4\times4\times10$ m^3 tower was calculated with the method of Blocken and Carmeliet (2002). As a first step, the simulation of the airflow field was performed by CFD. The detailed condition of this CFD simulation is described in Abuku et al. (2007). Secondly, the trajectories of raindrops with a diameter of 0.3, 0.4, 0.5, 0.6, 0.7, 0.8, 0.9, 1.0, 1.2, 1.4, 1.6, 1.8, 2.0, 3.0, 4.0, 5.0 and 6.0 mm were simulated for 5 reference wind speeds (2, 4, 6, 8 and 10 m/s). Then the specific catch ratio was calculated based on the trajectory of raindrops, and the specific catch ratio data were integrated into the global catch ratio. The catch ratio η for a wind perpendicular to the facade was vertically averaged from 3.5 to 6.5 m above the ground. When the wind is oblique to the facade, the cosine projection method was adopted for the calculation of the catch ratio based on Janssen et al., 2007b.

Finally, WDR intensities at the exterior wall surfaces with an interval of 0.2 m were calculated for the climate conditions of Essen of Germany, using the catch ratio data determined above, depending on wind speed, wind direction, horizontal rainfall intensity, and orientation of the building facades. The time course of their cumulative amounts over the year at the edges and the centres of the walls is shown in Fig. 2. Due to the prevailing SW wind direction in Essen, the WDR load is concentrated at the west-facing facade and some WDR is loaded onto the north- and south-facing facades, while almost no WDR reaches the east-facing facade. For each facade, the WDR load is the highest at the edges of the wall and the lowest at the centre of the wall.
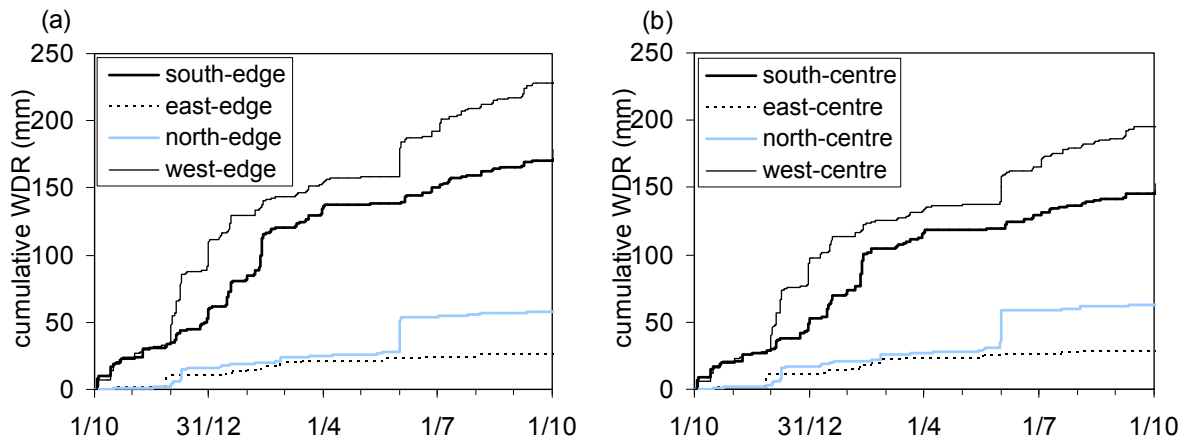
FIG. 2: Cumulative wind-driven rain (WDR) vertically averaged from 3.5 to 6.5 m above the ground at (a) the edges and (b) the centres on the facades.

5. Numerical assessment of the WDR impact on mould growth, indoor climate, and energy consumption

5.1 Condition of numerical analyses

In this section, three simulations are conducted: (1) the interior relative humidity over the year was calculated taking into account a constant ventilation rate of 0.5 ACH and a constant indoor temperature of 20 °C, but not linked to heat and moisture transfer through the walls; (2) in addition to the conditions of (1), the evaporation and absorption at the outside and inside wall surfaces were taken into account but WDR loads at the outside wall surfaces were neglected; (3), in addition to the conditions of (2) the WDR were loaded onto the outside wall surfaces. Case (1) purely shows the ventilation effects on the heat and moisture balance in the room. The comparison of case (1) and (2) shows the importance of the hygric inertia. The comparison of case (2) and (3) shows the WDR impact.

Numerical simulations were carried out with the 2-dimensional horizontal slice of the brick walls (4×4 m^2) and the room. The room temperature and humidity was assumed spatially uniform in the room, employing the "perfect mixing" assumption, and was calculated in all three cases. The heat and moisture transfer in the horizontal slice of the brick walls was analysed in case (2) and (3) with the FEM method (Janssen, 2007a) under the following conditions. The horizontal slice of the walls was discretised with 18000 linear triangular elements (18360 nodes) (see Fig. 1 (b)). 51 nodes were assigned for an intersection of the walls (see Fig. 1 (c)). The material properties of brick were taken from the benchmark 'Response analysis' of the European project HAMSTAD (Hagentoft et al., 2004). Note that short wave absorptivity and long-wave emissivity of brick were taken as 0.5 and 0.9 respectively. In the current study, a yearly climate data record of Essen of Germany was used. The cloudiness was kept constant at 0.6. The WDR loads calculated in the previous chapter (the data at the edges and centres of the facades are given in Fig. 2) were used in the current simulation. Note that the catch ratios for the positions of the nodes at the exterior wall surfaces were calculated by a linear interpolation of the given values for the two neighbouring positions which are given with an interval of 0.2 m.

Outside surface film coefficients were kept constant at 20 W/m^{2}K for heat transfer and 1.54×10^{-7} s^{-1} for moisture transfer. In reality, these values depend on wind speed, wind direction and position on the facade, and they may have a significant influence on the moisture response (Janssen et al., 2007b). However, because the exact spatial and temporal variation of the values is unknown, constant values (independent of space and time) were adopted in the current simulations. Inside surface film coefficients are based on the measurement results of IEA Annex 14 (1991). The total inside surface film coefficient for heat transfer at a position x m away from the edge of the inside wall surface $\alpha_{ti}(x_i)$ (W/m^{2}K) is expressed by:

$$\alpha_{ti}\left(x\right) = \alpha_{ti,centre}\left\{1 - \left(1 - \frac{\alpha_{ti,edge}}{\alpha_{ti,centre}}\right)\exp\left(-3\frac{x_i}{d}\right)\right\} \qquad (2)$$

with $\alpha_{ti, centre}$ the total surface film coefficient at the centre of the inside wall surface (W/m²K); $\alpha_{ti, edge}$ the total surface film coefficient at the edge of the inside wall surface (W/m²K); d the wall thickness (m) (=0.29 m). In the current simulations $\alpha_{ti, centre}$ and $\alpha_{ti, edge}$ were kept constant at 8 W/m²K and 6 W/m²K respectively. The inside surface film coefficient β_i for moisture transfer was determined by use of the Lewis relation from the convective surface film coefficient α_{ci} for heat transfer (assumed equal to α_{ti} /2 to exclude the radiation effects).

5.2 Result and discussion

5.2.1 Impact on indoor climate and energy consumption

In this part, the three simulations are compared to show influences of ventilation, moisture buffering effects of the walls and impacts of the WDR loads.

The evolution with time of the indoor RH of the 3 cases over the year and an excerpt of March are shown in Fig. 3. Comparing the simulation results without WDR load and those with only ventilation shows that the absorption and evaporation at the wall surfaces have a very small effect on indoor RH change (see Fig. 3 (b)), which is attributable to the low buffering potential of the ceramic brick in the hygroscopic region. On the other hand, the comparison of the results with WDR load to those without WDR load shows that WDR load causes a significant increase of indoor relative humidity of up to 55 % under the conditions considered, which is seen at 7th of March. The differences between the results with WDR load and those without WDR load are significant in winter and summer due to increases of the moisture content at the inside wall surfaces; it is less significant in spring and autumn.

Seasonal energy consumptions are given in Table 1, comparing the results of the 3 cases. Comparing the results without WDR (case (2)) to those with only ventilation (case (1)) shows that the energy consumption is mainly influenced by the heat flow through the (uninsulated) walls and that ventilation is less important for energy consumption in the current conditions. When the results with WDR load (case (3)) are compared to those
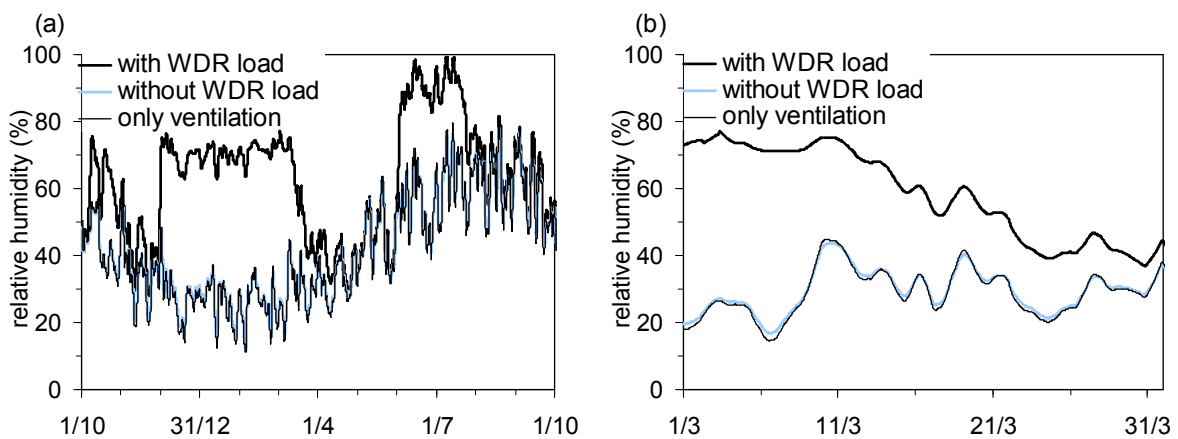
FIG. 3: (a) Time evolution of indoor relative humidity of the 3 cases over the year and (b) an excerpt of March.

TABLE. 1: Seasonal and annual energy consumption.

	(1) only ventilation	(2) ventilation + evaporation/absorption without WDR load	(3) ventilation + evaporation/absorption with WDR loads	((3)-(2))/(2)×100 (impact of WDR)
winter	77.8 kWh	852.9 kWh	1012.7 kWh	18.7 %
spring	50.0 kWh	516.4 kWh	535.9 kWh	3.8 %
summer	20.3 kWh	165.0 kWh	200.5 kWh	21.5 %
autumn	43.6 kWh	464.7 kWh	485.2 kWh	4.4 %
annual	191.7 kWh	1999.0 kWh	2234.3 kWh	11.8 %

without WDR load (case (2)), the seasonal impact of WDR on energy consumption under such conditions is estimated as 18.7 % in winter (December, January and February); 3.8 % in spring (March, April and May); 21.5 % in summer (June, July and August); and 4.4 % in autumn (September, October and November). The energy consumption for heating in summer is very low, though. Note that the current building configuration has no window, so that the impact on energy consumption in summer can be much smaller in reality due to the solar and diffuse radiations. The annual impact is estimated as 11.8 %. The impact of WDR is considered to be smaller when the ventilation rate is more important for energy consumption. Note that for hot climates the results may be different, since the energy consumption for cooling in summer periods may decrease through increased transmission losses to the outside due to rain loads (Hokoi, 1986), while the increased RH due to rain loads may still increase the latent cooling loads and a rain load may also increase the energy consumption for heating in winter.

5.2.2 Impact on mould growth

One of the advantages of whole building simulations is the possibility of assessing the risk of mould growth at building wall surfaces. In this part, the simulation results without WDR load are compared with the one with the WDR load and the impact of the WDR load on mould growth at inside wall surfaces is discussed.

The growth condition for mould can be described in isopleth diagrams, which express germination time or growth rate (Sedlbauer, 2001). So the daily averaged temperature and relative humidity at the edge (facing
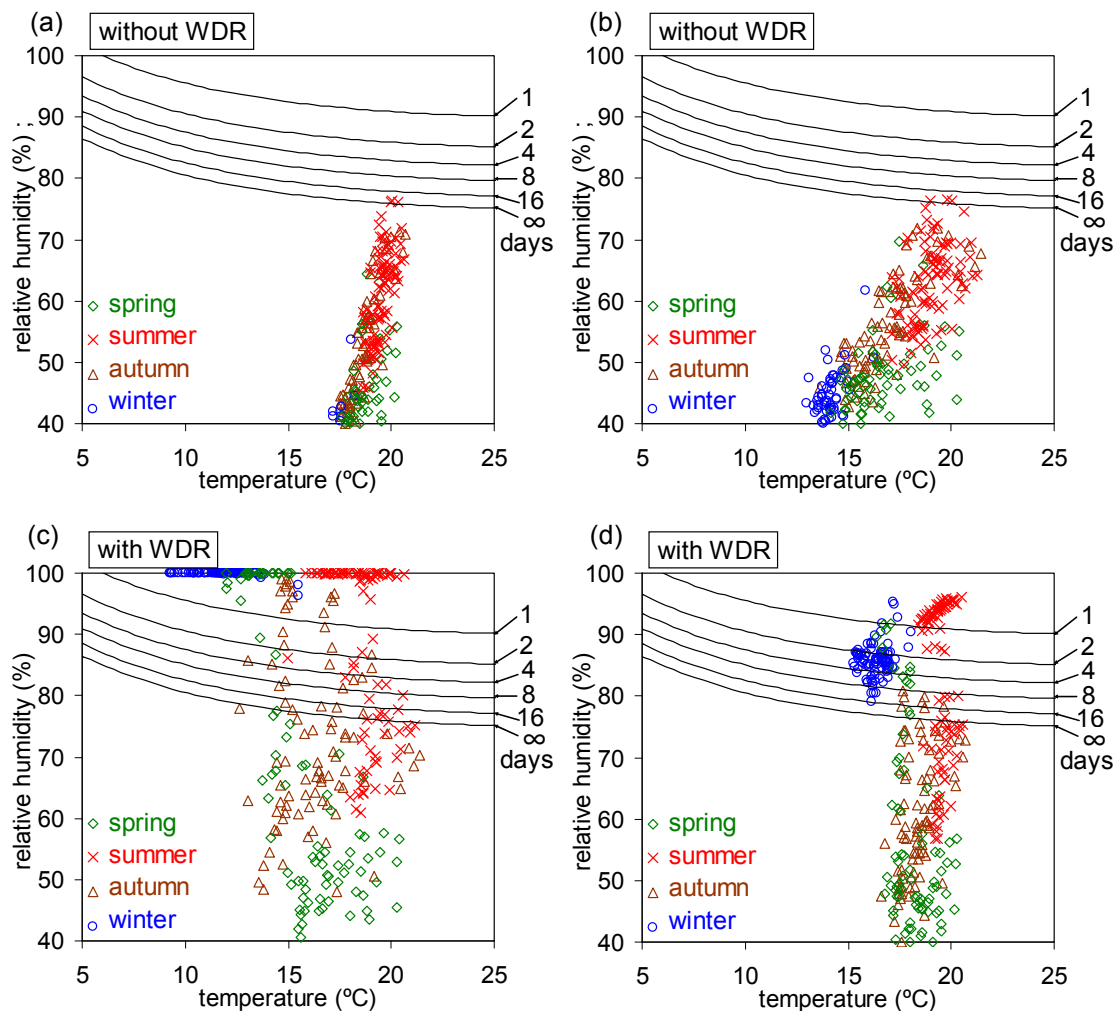
FIG. 4: Daily averaged temperature and humidity at the inside wall surfaces on the graph of generalised isopleths of the spore germination time (black solid lines) of the fungus mould for the substrate category I. (a) and (c) At the south-west facing edge of the wall; (b) and (d) at the south facing centre of the wall. In (a) and (b), no wind-driven rain load (WDR) is loaded; in (c) and (d) wind-driven rain loads are loaded.

south-west) and centre (facing south) of the inside wall surfaces are plotted on the graphs of generalised isopleths of the spore germination time of the fungus mould for substrate category I (Sedlbauer, 2001) and are shown in Fig. 4. Fig. 4 (a) and (b) show the results of the simulation without WDR load and Fig. 4 (c) and (d) show those with the WDR load. The same plots can be applied to the mycelium growth rate and similar conclusions can be drawn as shown below. Though brick is considered to be in the substrate category II, the isopleths for the substrate category I are adopted here as worst case scenario. If the relative humidity for a given temperature is below the line of ∞ days, no biological activity is expected. Note that, when the RH is too high (e.g. RH > at least 96 % (Sedlbauer, 2001)), the mould may not grow but can still exist.

Each figure compares seasonal risks. Analysing the risk without taking into account WDR (see Fig. 4 (a) and (b)), no mould growth is expected; but, when the WDR is taken into account, looking at Fig. 4 (c) and (d), a serious risk on mould growth can be expected, mainly in summer and winter, with a more serious risk in summer than in winter. The comparison of the results of the simulation with WDR and those without WDR shows that the impact of WDR on the mould growth at the inside wall surfaces is significant.

Comparing Fig. 4 (c) and Fig. 4 (d), a wider variation of surface temperatures is seen at the edge than at the centre and the surface temperatures are averagely lower at the edge than at the centre. The reason of this difference is that the surface temperature at the edge is more influenced by the outdoor temperature, which can even result in a lower risk at the edge than at the centre. When the variations and criteria of temperature and relative humidity are considered together, it is concluded that, for the current case, the criterion of relative humidity for mould growth is more severe than that of temperature.

6. Conclusion

An onset was given to whole building modelling and simulations of the interaction between interior and exterior climates via building enclosures with emphasis on wind-driven rain (WDR). The impacts of WDR loads on the hygrothermal response of the walls, indoor climate, energy consumption and mould growth risk at the inside wall surfaces were investigated. The hygrothermal response of the solid brick walls and indoor climates of a cubic building with distributed WDR loads was numerically analysed. For the case analysed, the simulations showed that WDR causes a significant increase of indoor relative humidity and energy consumptions for heating. Furthermore the obtained relative humidity and temperature at the interior wall surfaces were combined with isopleths of generalised spore germination time of fungus mould. The results showed that WDR loads can have a significant impact on mould growth especially at the edge of the wall.

The results obtained here are considered to strongly depend on the material properties, climate, etc. Yet the climate and some of the historical buildings in Europe and some other countries are indeed not far from the conditions used for the current study. The results also adequately indicated that similar investigation of WDR load impact even for different climates and other building wall materials, such as natural stone, can be worth the effort.

7. References

Abuku M., Janssen H., Poesen J. and Roels S. (2007). Impact, absorption and evaporation of raindrops on building facades, Building and Environment, In press (doi:10.1016/j.buildenv.2008.02.001).

Blocken B. and Carmeliet J. (2002). Spatial and temporal distribution of wind-driven rain on low-rise building, Wind and Structure, Vol.5, No.5, 441-462.

Blocken B., Roels S. and Carmeliet J. (2007). A combined CFD-HAM approach for wind-driven rain on building facades, Journal of Wind Engineering and Industrial Aerodynamics, Vol.95, No.7, 585-607.

Choi E.C.C. (1993). Simulation of wind-driven-rain around a building, Journal of Wind Engineering and Industrial Aerodynamics, Vol. 46&47, 721-729.

Glacer H. (1958). Wärmeleitung und Feuchtigkeitsdurchgang durch Kühlraum-isolierungen, Kältetechnik, nº 3.

Grunewald J. (1997). Diffusiver und konvektiver stoff- und energietransport in kapillarporösen baustoffen, PhD thesis, Dresden University of Technology.

Hagentoft C.-E., Kalagasidis A.S., Adl-Zarrabi B., Roels S., Carmeliet J., Hens H., Grune-wald J., Funk M., Becker R., Shamir D., Adan O., Brocken H., Kumaran K. and Djebbar R. (2004). Assessment method of

numerical prediction models for combined heat, air and moisture transfer in building components: benchmarks for one-dimensional cases, Journal of thermal envelope and building science, Vol.27, No.4, 327-352.

Hall C. and Lalimeris A.N. (1982). Water movement in porous building materials–V. Absorption and shedding of rain by building surfaces, Building and Environment, Vol.19, 13-20.

Häupl P., Grunewald J. and Ruisinger U. (2005). Hygrothermal 2-dimensional analysis of critical constructive details of the Rijksmuseum Amsterdam, Report, Institute for Building Climatology, Dresden University of Technology, Germany.

Hokoi S. (1986). Fundamental study of thermal characteristics of wet building walls, PhD thesis, Kyoto University.

Holm A., Kunzel H., and Seldbauer K. (2003). The hygrothermal behaviour of rooms: combining thermal building simulation and hygrothermal envelope calculation, in: Proceedings of the Eighth International IBPSA Conference, Eindhoven, The Netherlands, August 11-14, 2003, 499-505.

IEA Annex 14. (1991). Condensation and Energy, Final Report, Volume1, Source Book, Leuven: Acco Uitgeverij, 3.50-3.53.

Janssen H., Blocken B. and Carmeliet J. (2007a). Conservative modelling of the moisture and heat transfer in building components under atmospheric excitation, International Journal of Heat and Mass Transfer, Vol.50, 1128-1140.

Janssen H., Blocken B., Roels S. and Carmeliet J. (2007b). Wind-driven rain as a boundary condition for HAM simulations: Analysis of simplified modelling approaches, Building and Environment, Vol.42, 1555-1567.

Kumaraperumal A., Sanders C. and Baker P. (2006). CFD and hygrothermal modeling are compared with full-scale measurements to predict the fabric moisture contents due to wind-driven rain on a Scottish castle, International Report, IEA Annex 41, Task 3 - Boundary condition, A41-T3-UK-06-2.

Künzel H.M. (1994). Verfahren zur ein- und zweidimensionalen Berechnung des gekoppelten Wärme- und Feuchtetransports in Bauteilen mit einfachen Kennwerten, PhD thesis, University of Stuttgart.

Mendes N., Oliveira R. and Henrique dos Santos G. (2003). Domus 2.0: a whole-building simulation program, in: Proceedings of the Eighth International IBPSA Conference, Eindhoven, The Netherlands, August 11-14, 2003, 863-870.

Nakhi A.E. (1995). Adaptive construction modelling within whole building dynamic simulation. PhD thesis, University of Strathclyde.

Pedersen C.R. (1990). Combined heat and moisture transfer in building constructions, PhD thesis, Technical University of Denmark.

Rode C., Salonvaara M., Ojanen T., Simonson C. and Grau K. (2003). Integrated hygrothermal analysis of ecological buildings. in: Proceedings of the 2nd International Conference on Building Physics, Leuven, Belgium, September 14-18, 2003, 859-868.

Sanders C. (1996). Heat, air and moisture transfer in insulated envelope parts. IEA Annex 24, Final report – Vol. 2, Task 2: Environmental conditions, Acco Leuven, 75-85.

Sedlbauer K. (2001). Vorhersage von Schimmelpilzbildung auf und in Bauteilen (Predictuion of mould manifestation on and in building parts), PhD thesis, University of Stuttgart.

Acknowledgements

Influence of rain water leakage on the hygrothermal performance of exterior insulation systems

Hartwig M. Künzel, Dr.-Ing.
Department of Hygrothermics, Fraunhofer Institute for Building Physics;
hartwig.kuenzel@ibp.fraunhofer.de

Daniel Zirkelbach, Dipl.-Ing.,
Department of Hygrothermics, Fraunhofer Institute for Building Physics;
daniel.zirkelbach@ibp.fraunhofer.de

SUMMARY:
This investigation shows that ETICS on light weight structures pose no moisture problem in cold and moderate climates when the detailing of joints and openings is well done, i.e. there is no rain water leakage. This holds for all locations investigated. However, if water leakage cannot be excluded completely and therefore the North-American Standard assumptions - penetration of 1% of the driving rain load - are applied this picture changes, making the drying potential an essential feature. The normal ETICS composed of vapour retarding EPS insulation slabs cannot provide much drying towards the exterior and may therefore bear a moisture damage risk for the underlying substrate. The application of a humidity controlled vapour retarder (PA-film) instead of a conventional polyethylene film at the interior side of the building assembly enhances the overall drying potential of the construction by allowing some vapour diffusion towards the interior spaces. But only in warmer locations, like Wilmington in North Carolina or Lisbon, employing such a vapour retarder may be a compensation for small rain water leaks. The best but also most expensive solution would be to replace the expanded polystyrene (EPS) by high density mineral wool insulation slabs in the ETICS.

Alternative ways of solving the rain penetration problem are currently being developed and tested in North-America. Many systems now provide a drainage plane between the substrate and the ETICS and flashing to force the water out at the bottom of the wall. Other systems keep the face seal approach and rely on more sophisticated detailing and flashing. In both cases the long-term performance is still unknown. In order to avoid a repetition of the North-American problems with ETICS on wooden structures, it is important to communicate this issue and possible solutions to the European construction trades. Hygrothermal simulations may help to raise the awareness to the damage risks and the importance of qualified workmanship involved in the application of ETICS especially in cases of high wind driven rain loads.

1. Introduction

External Thermal Insulation Composite Systems (ETICS) also called Exterior Insulation Finish Systems (EIFS) in North America have been installed on buildings for about 50 years. Despite being exposed to higher hygrothermal loads than most façade systems, ETICS on concrete or masonry have done very well in Europe. They seem to be at least as durable as conventional façades with render or stucco [Künzel et al. 2006]. However, there is only little long-term experience concerning the application of ETICS on wood frame structures in Europe where these systems are increasingly installed to alleviate thermal bridging caused by the framework or to retrofit existing buildings. Therefore, it makes sense to analyze the situation in North America where ETICS on wooden structures have a mixed track record due to numerous failures related to elevated moisture in the construction. Since it is unlikely that the reported damage cases will remain confined to North America, this paper will investigate the hygrothermal behaviour of ETICS on wooden structures under selected climate conditions in North America and Europe.

2. Composition of External Thermal Insulation Composite Systems

ETICS in North America usually closely resemble those in Europe. The standard composition of an ETICS is shown in Fig. 1. The ETICS is usually fastened to the exterior sheathing of a wood stud wall or on a masonry wall. In most ETICS expanded Polystyrene (EPS) is used as insulation material. The use of high-density mineral fiber insulation which is also quite common in Europe is practically unknown in North America. On top of the insulation slabs a polymer modified base coat including a reinforcing glass fiber mesh are applied, followed by a finish coat. The reinforced base coat together with the finish or top coat is usually 5 to 10 mm thick.
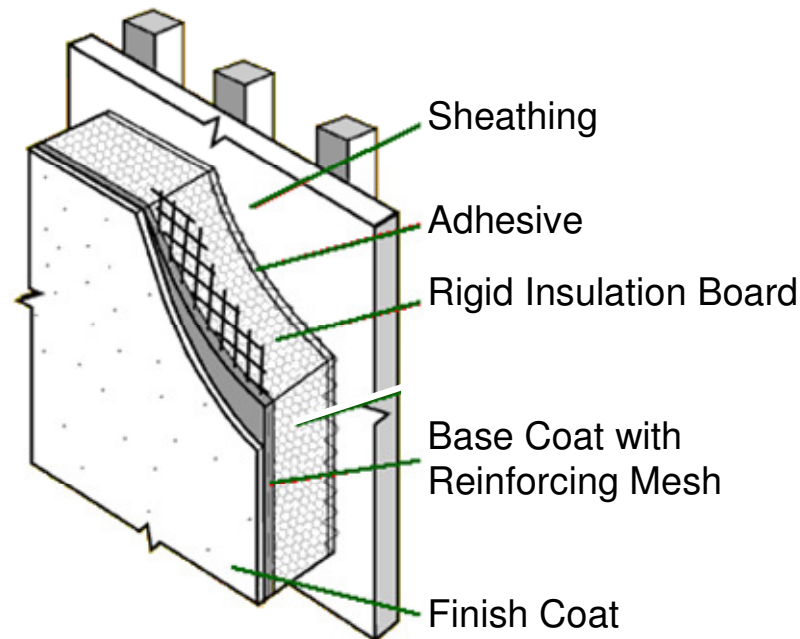
Fig. 1: Composition of a typical External Thermal Insulation Composite System

3. Track record of ETICS

In the middle of the 90s the first substantial damage cases associated with ETICS were reported from North Carolina. Similar reports from other regions with high precipitation intensities (e.g. Seattle, Vancouver) followed. The moisture problems occurred mostly at the exterior sheathing boards that served as substrate for the ETICS. Pictures of rotten OSB or disintegrated gypsum board quickly spread among the building community and forced manufactures to react [Nisson & Best 1999]. A comprehensive literature review analysing more than 10 investigations carried out on several objects each, comes to the following conclusions [Cheple & Huelman 2000]. The main reasons for moisture damage are leaks around windows and joints where rainwater penetrates beneath the insulation layer. However, problems due to air convection or diffusion of indoor air may also have caused elevated moisture in some cases. An aggravating factor is the low drying potential of the construction. Moisture can neither dry-out quickly to the exterior because of the vapour retarding foam insulation nor to the interior due to the usual presence of a polyethylene vapour barrier. The solutions proposed in [Cheple & Huelman 2000] are limited to managing rain water penetration by proper sloping and flashing of joints and wall openings and by applying drainable insulation systems. Sheathing materials that are sensitive to moisture such as untreated gypsum board are considered inappropriate as ETICS substrates. Other work has shown that enhancing the drying potential towards the interior spaces by an innovative vapour control strategy may also alleviate the problem [Karagiozis & Kumaran 1997].

The moisture problems that occurred in North American in the 90s were not limited to walls having ETICS. Buildings with normal stucco façades (render applied on building paper over OSB or plywood) were also affected [Lawton 1999]. This resulted in a new design approach that aimed at better detailing to reduce rainwater penetration and at increasing the drying potential of the whole assembly. It has been realized that it is difficult to set-up a perfect building that will never leak. Therefore the building envelope should be designed in such a way that small leaks can be handled. Consequently the ASHARE Standard 160 on criteria for moisture design [BSR/ASHRAE 2006] states that in the absence of performance proofs it should be assumed that 1% of the wind driven rain hitting the façade is deposited on the weather resistive barrier (WRB) behind the cladding. If there is

no WRB another layer should be selected where the penetrating rainwater is likely to go (e.g. sheathing beneath the ETICS in Fig. 1). The selected leakage rate in this standard is not meant to be a worst case scenario. It is not based on field test results but on hygrothermal simulations (e.g. Desjarlais et al. 2001) that showed that more than 1% of rainwater penetration may be detrimental for a large portion of existing wall structures.

In Europe ETICS are applied for about 50 years. More than 40 million square meters of ETICS are installed on new and existing buildings every year in Germany and severe problems or damage cases have been rare [Künzel et al. 2006]. In contrast to North America where ETICS are mainly considered as a finish system, the purpose of ETICS in Europe is to provide adequate thermal performance of external walls that usually consist of masonry or cast-in-place concrete. Therefore the average insulation thickness is higher in Europe (approx. 100 mm in 2006) than in the U.S. (25- 50 mm). ETICS in Europe require a Technical Approval as a system ensuring harmonized system components and trained installers. However, it is doubtful that better quality control and workmanship alone can explain the huge difference in past performance of ETICS between Europe and North America. An important reason is probably the sensitivity of the substrate. While concrete and masonry readily absorb and redistribute small quantities of leakage water without any signs of degradation, the same amount of water may severely damage typical sheathing materials of North American stud walls such as OSB, plywood or gypsum board. Since ETICS have more recently been applied to wooden wall structures in Europe too, there may also be an increase in moisture problems as the ones described in [Schulze & Radovic 1992] and [Schumacher 2006]. Therefore it makes sense to investigate the moisture tolerance of wooden structures with ETICS for European construction types and climate conditions in order to prevent moisture-related problems.

4. Hygrothermal simulations

The transient temperature and moisture distributions in external wall assemblies with ETICS are calculated using version 4.1 of the hygrothermal simulation model WUFI® [Künzel 1995] which has been validated many times by comparison with experimental building envelope investigations including measurements on wall structures with ETICS (e.g. [Künzel 1998a]). In order to cover North American and European building traditions the following wall assembly has been selected.

- ETICS: 10 mm lamina (exterior rendering) on 60 mm EPS

- Sheathing: 15 mm OSB

- Cavity insulation: 160 mm glass fiber

- Vapour retarder: polyethylene film ($s_d = 20$ m) or polyamide film (0.1 m $< s_d < 5$ m)

- Interior panelling: 12 mm gypsum board (installation gap 40 mm)

The material properties are taken from the WUFI® database. The polyethylene (PE) film represents a standard vapour retarder with a diffusion resistance (s_d) of 20 m. The polyamide (PA) film is a humidity controlled vapour retarder whose diffusion resistance varies with ambient humidity conditions [Künzel 1998b]. It has been developed to enhance the drying potential of building assemblies [Künzel & Leimer 2001]. The colour of the exterior stucco is assumed to be bright (solar absorptivity 0.4).

4.1 Selected locations and loads

The first location considered is North Carolina where the ETICS problems started. As representative weather conditions the meteorological data for a cold year in Wilmington are selected from the WUFI® climate database. For Europe a sample of four locations is chosen: Hannover in the middle of Germany's Northern plain, Lisbon at the Atlantic South-West Coast of Europe, Locarno in the Southern part of the Swiss Alps and Vienna at the edge of the East-European plain. The average temperatures and humidities as well as the annual sum of wind driven rain hitting the middle of a low-rise building at the most exposed orientation are displayed for all selected locations in Table 1. While the average relative humidity does not differ much from one location to the other, the average temperature ranges from approximately 17°C to 25°C in summer and from 0°C to 10°C in winter. Hannover is the coldest place and Wilmington and Lisbon which are the warmest locations experience the highest wind driven rain loads.

The hygrothermal simulations which begin in October of the representative year are continued over a period of three years by repeatedly running through the same meteorological data-set. The initial conditions in all material layers of the building assembly are set to EMC_{80} (equilibrium moisture content at 80% RH). If rainwater penetration through imperfections cannot be ruled out, 1% of the wind-driven rain load from Table 1 is deposited on the exterior surface of the OSB sheathing [BSR/ASHRAE 2006].

Table 1:   Driving rain load at the surface of the most exposed façade orientation and average hygrothermal conditions at the selected locations in North America and Europe.

Location	Driving rain load (façade orientation)	Rel. Humidity (annual mean)	Temperature (annual/monthly mean)		
			Year	January	July
Wilmington	186 l/m²a (S)	73%	16.1 °C	5.7 °C	24.9 °C
Hannover	160 l/m²a (W)	80%	8.6 °C	-0.1 °C	17.1 °C
Lisbon	193 l/m²a (W)	75%	15.6 °C	9.8 °C	20.7 °C
Locarno	133 l/m²a (E)	72%	11.5 °C	2.1 °C	22.2 °C
Vienna	112 l/m²a (W)	73%	10.4 °C	0.1 °C	20.6 °C

4.2 Simulation results

The North American damage cases have shown that the substrate layer to which the ETICS is applied, experiences the most critical moisture conditions in the assembly. Therefore the moisture content of the OSB sheathing is monitored in the present study. Fig. 2 displays the temporal variations in OSB moisture under three different scenarios. Assuming perfect workmanship (no leaks) results in permanently dry conditions (MC < 13 M-%) no matter what vapour retarder is applied to the interior side of the stud wall. If rainwater leaks are present the OSB moisture content will rise in wintertime with extended drying spells in summer. However, when there is only very little vapour diffusion towards the interior because of the rather impermeable vapour retarder (PE-film), the drying potential is limited and long-term moisture accumulation may occur (MC > 25 M-% after 3 years). By replacing the PE-film with the humidity controlled PA-film the drying potential is enhanced enough to assure long-term OSB moisture conditions below 18 M-%.
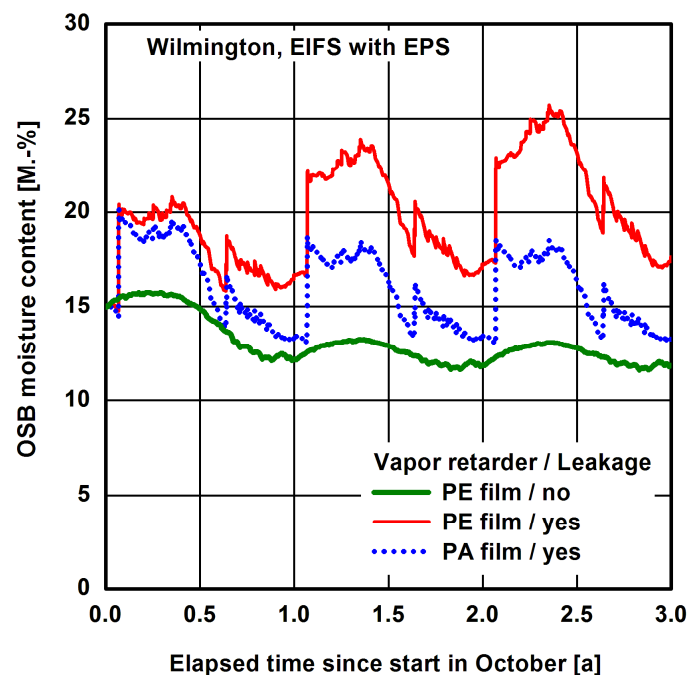
Fig. 2: Temporal variations of OSB sheathing moisture content beneath the ETICS in Wilmington for the standard case with and without rainwater leakage and with a PA-film replacing the PE-film as vapour retarder of the stud wall.

When the simulations are repeated for the coldest location considered (Hannover) there is a different picture (Fig. 3). Again, when there is no leak there is no problem. However, when there is a leak the OSB moisture content will repeatedly exceed 20 M.-% even if the dying potential to the interior is enhanced by the PA-film. An explanation for the different behaviours of the investigated building assemblies investigated under different climate conditions lies in the divergence in vapour gradients. The high summer time temperatures in Wilmington result in a considerable inward vapour drive making efficient use of the drying potential provided by the

humidity controlled vapour retarder. Without such a strong inverse vapour pressure gradient the drying rate towards the interior cannot compensate the rainwater leakage and damage may occur.
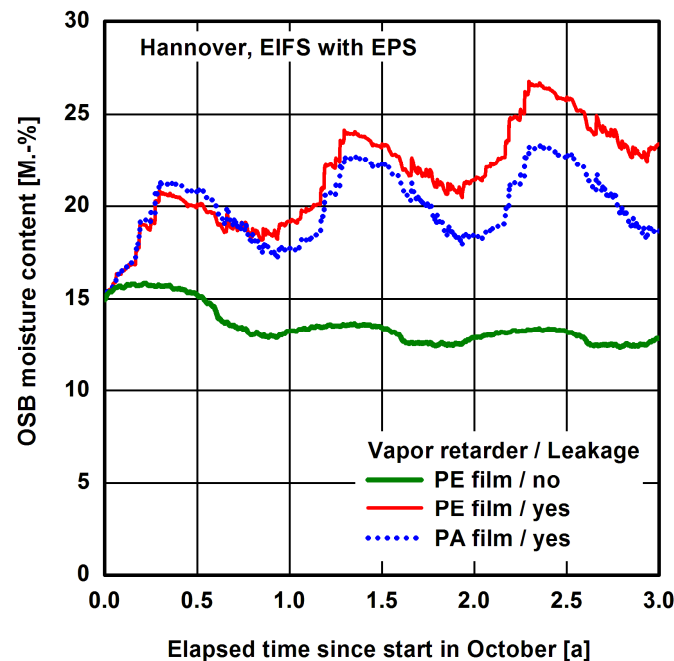
Fig. 3: Temporal variations of OSB sheathing moisture content beneath the ETICS in Hannover for the standard case with and without rainwater leakage and with a PA-film replacing the PE-film as vapour retarder of the stud wall.

A good indicator of potential problems is the maximum OSB moisture content attained during the 3rd year of the simulation period. In order to be on the safe side it should not exceed 20 M.-%. That means if rainwater penetration through imperfections is assumed, enhancing the drying potential towards the interior is no solution for Hannover. However it may help to enhance the drying potential towards the exterior by replacing the EPS insulation of the ETICS with high-density mineral wool slabs (MW). This kind of insulation material which is largely unknown in North America is widely used for ETICS in Europe. Its thermal conductivity is very similar to that of EPS but its vapour permeability is very high. When such a system is applied to a stud wall in Hannover, the OSB moisture content remains well below 20 M.-%, even if the defined rain water penetration occurs.

The simulation results of all European locations are summarized in Fig. 4 by comparing the maximum moisture content in the OSB sheathing during the third year. The best solution with the lowest OSB moisture content at all locations is the choice of mineral wool (MW) as ETICS insulation material. However, all variants seem to work in Locarno and Vienna where the annual wind driven rain load is less than 140 l/m²a. In Lisbon the situation is comparable to Wilmington, i.e. enhancing the drying potential towards the interior by employing a special vapour retarder appears to be sufficient.
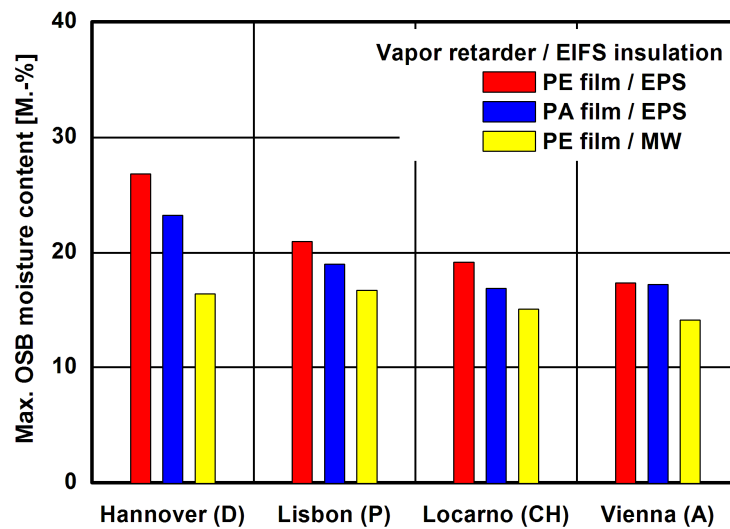
Fig. 4: Maximum moisture content of the OSB sheathing during the simulated 3-year period at different European locations depending on the vapour retarder of the stud wall and the insulation material of the ETICS.

It has been already mentioned that the rainwater leakage rate of 1% of the total amount if wind-driven rain hitting the wall in the ASHRAE draft standard 160 [BSR/ASHRAE 2006] is not a worst case scenario. Therefore, the simulations are repeated for the best performing walls with mineral wool insulation, this time with higher rainwater leakage rates. Fig. 5 shows the OSB moisture content of the stud wall when 1%, 2%, 3% or 4% of the wind-driven rain load is deposited evenly over the thickness of the OSB sheathing. While the wall can still handle an increase in rain water penetration rate by the factor of 2 compared to the specifications in the ASHRAE draft standard 160, a further increase (3% or 4% of wind-driven rain load) will lead to OSB moisture content peaks in excess of 20 M.-%.
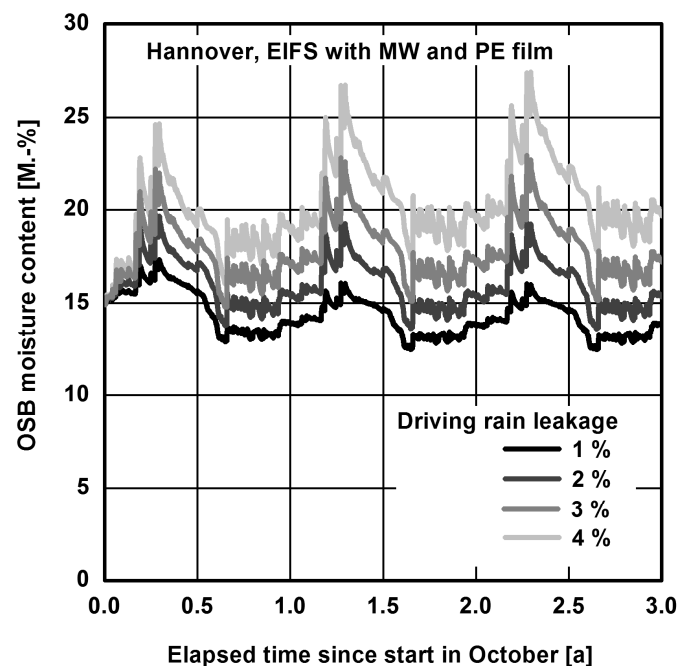
Fig.5: Temporal variations of OSB sheathing moisture content beneath the ETICS with mineral wool insulation in Hannover with different rainwater leakage rates.

5. Summary and Conclusions

This investigation shows that ETICS on lightweight structures pose no moisture problem in cold and moderate climates when the detailing of joints and openings is well done, i.e. there is no rainwater leakage. This holds for all locations investigated. However, if water leakage cannot be completely excluded and therefore the North American Standard assumptions - penetration of 1% of the driving rain load - are applied this picture changes, making the drying potential of this type of wall assemblies an essential feature. The normal ETICS composed of vapour retarding EPS insulation slabs cannot provide much drying towards the exterior and may therefore be responsible in part for increasing the risk of moisture damage for the underlying substrate. The application of a humidity controlled vapour retarder (PA-film) instead of a conventional polyethylene film at the interior side of the building assembly enhances the overall drying potential of the construction by allowing some vapour diffusion towards the interior spaces. But only in warmer locations, like Wilmington in North Carolina or Lisbon, the effect of employing such a vapour retarder is great enough to compensate for small rainwater leaks. The best but also most expensive solution to reduce the risk of moisture related problems in EITCS wall assemblies would be to replace the expanded polystyrene (EPS) by a high-density mineral wool insulation. However, even this solution will not work if the rainwater penetration exceeds the amount specified in the ASHRAE draft standard. Therefore, proper detailing and good workmanship are essential prerequisites when classical ETICS systems are installed.

Alternative ways of solving the rain penetration problem are currently being developed and tested in North America [Onysko & Thivierge 2007]. Many systems now provide a drainage plane between the substrate and the ETICS and flashing to force the water out at the bottom of the wall. Other systems keep the face seal approach and rely on more sophisticated detailing and flashing. In both cases the long-term performance is still unknown. In order to avoid a repetition of the problems with ETICS applied to wood frame structures in North America, it is important to communicate this issue and possible solutions to the European construction trades. Hygrothermal simulations may help to raise the awareness to the risks of damage and the importance of qualified stuff involved in the application of ETICS especially for locations having high wind driven rain loads.

6. References

BSR/ASHRAE Standard 160P (Sept. 2006). Design Criteria for Moisture Control in Buildings, Public review draft.

Cheple, M. & Huelman, P. (2000). Literature Review of Exterior Insulation Finish Systems and Stucco Finishes, Report MNDC/RP B80-0130, University of Minnesota.

Desjarlais, A.O., Karagiozis, A.N. & Aoki-Kramer, M. (2001): Wall Moisture Problems in Seattle. Buildings VIII proceedings, ASHRAE, 8p.

Karagiozis, A. & Kumaran, K. (1997). Drying Potential of EIFS Walls: Innovative Vapor Control Strategies. STP 1339, American Society for Testing and Materials (ASTM), West Conshohocken.

Künzel H.M. (1995). Simultaneous Heat and Moisture Transport in Building Components, - One- and two-dimensional calculation using simple parameters, Fraunhofer IRB Stuttgart.

Künzel, H.M. (1998a). Drying of Masonry with Exterior Insulation. Proceedings of the Fifth International Masonry Conference, British Masonry Society, No. 8, Stoke-on-Trent, p. 245-250.

Künzel, H.M. (1998b). The Smart Vapor Retarder: An Innovation Inspired by Computer Simulations, ASHRAE Transactions, Vol 104, Pt. 2, pp 903-907.

Künzel, H.M. and Leimer, H.-P. (2001). Performance of Innovative Vapor Retarders Under Summer Conditions. ASHRAE Transactions, Part. 1, p. 417-420.

Künzel, H, Künzel, H.M. & Sedlbauer, K. (2006). Long-term Performance of External Thermal Insulation Systems (ETICS), ACTA Architectura 5,Vol 1, p. 11-24.

Lawton, M. (1999). Vancouver's Rotting Condominium Problem – How Did We Get into This Mess? Journal of Thermal Envelope & Building Science, Vol 22, p. 356-363.

Nisson, N. & Best, D.(1999). Exterior Insulation and Finish Systems. Compilation of articles from EDU-Newsletter, Cutter Information Corp., Arlington.

Onysko, D. and Thivierge, C. (2007): Drainage and Retention of Water by Cladding Systems – Part 3: Drainage Testing of EIFS Wall Systems. CMHC Research Report, Canada.

Schulze, H. & Radovic, B. (1992). Zweigeschossiges Holzhaus mit Wäremedämm-Verbundsystem; Putzschäden im Bereich der Geschossdecke, Deutsches Archiktektenblatt 1, p. 123.

Schumacher, R. (2006). Außenwand aus Holztafeln mit Wärmedämmverbundsystem – Feuchte¬schaden wegen fehlerhaftem Sohlbankeinbau, Der Bausachverständige 6, p. 14-16.

High-resolution CFD simulations of forced convective heat transfer coefficients at exterior building surfaces

Bert Blocken, PhD, MASc
Eindhoven University of Technology, The Netherlands
b.j.e.blocken@tue.nl

Thijs Defraeye, MASc
Katholieke Universiteit Leuven, Belgium

Adam Neale, MASc
Concordia University, Montreal, Canada

Dominique Derome, Prof, PhD, MASc
Empa, Swiss Federal Laboratories for Materials Testing and Research, Switzerland

Jan Carmeliet, Prof, PhD, MASc
Chair of Building Physics, Swiss Federal Institute of Technology ETHZ, Zürich, Switzerland;
Empa, Swiss Federal Laboratories for Materials Testing and Research, Switzerland

KEYWORDS: *wind flow; Computational Fluid Dynamics; boundary layer; heat and mass transfer*

SUMMARY:
High-resolution CFD simulations of forced convective heat transfer at the facades of a low-rise cubic building (10x10x10m³) are conducted to determine convective heat transfer coefficients (CHTC). CFD model validation is performed based on wind tunnel measurements of the upstream near-field velocity pattern. A particular feature of the CFD simulations is the use of a high-resolution grid with control volumes of only 160 μm near the building surfaces to resolve the entire boundary layer, including the laminar sublayer that dominates the convective surface resistance. The study shows that: (1) wind flow around the building introduces a very distinct CHTC distribution across the facade; (2) no significant correlation exists between the CHTC and the local wind speed across the facade; (3) for a reference wind speed of 3 m/s, the laminar sublayer has a thickness of about 1 mm; (4) standard and non-equilibrium wall functions are not able to capture the complexity of wind-induced heat transfer, therefore low-Reynolds number modelling on high-resolution grids is imperative; (5) the CHTC distribution across the windward facade shows some similarity to the distribution of wind-driven rain (WDR), with both parameters reaching high levels near the top edge of the facade. This suggests that also the convective vapour transfer coefficient will be higher at this location and that the facade parts that receive most WDR also experience most intensive drying.

1. Introduction

Hygrothermal (HAM) analysis of building components requires the knowledge of the convective heat (h_c) and vapour (β) transfer coefficients at exterior and interior building surfaces:

$$q_c = h_c(T_{ref} - T_s); \qquad g_v = \beta(p_{v,ref} - p_{v,s}) \tag{1-2}$$

where q_c is the convective heat flux density (W/m²), h_c the CHTC (W/m²K), T_e the reference temperature (K) and T_S the surface temperature (K). g_v is the vapour flux density (kg/m²s), β the convective vapour transfer coefficient (CVTC) (s/m), $p_{v,ref}$ the reference vapour pressure (Pa) and $p_{v,s}$ the vapour pressure at the surface (Pa). Most research on CHTC and CVTC in the past has focused on interior conditions. Exterior transfer coefficients have received relatively little attention. Exterior transfer coefficients are a complex function of building geometry, local wind speed, turbulence intensity, surface roughness, texture and geometry, temperature, moisture content, etc. Little however is known about the actual values and the variability of these coefficients across building facades as a function of the different parameters.

This paper focuses on exterior CHTC only. In the past, three methods have been employed to investigate and determine exterior CHTC: wind tunnel measurements, full-scale measurements and numerical simulations based

on Computational Fluid Dynamics (CFD). By far most research has been experimental. Only more recently, CFD has been introduced in this field.

Jürges (1924) performed a wind tunnel study of the convective heat transfer from small, flat, heated plates attached to the wall of the wind tunnel. He provided the following relationship of h_c with the free-stream wind speed in the tunnel V_∞:

$$h_c = 4.0V_\infty + 5.6 \quad ; \quad V_\infty < 5 \, m/s \, ; \qquad h_c = 7.1V_\infty^{0.78} + 5.6 \quad ; \quad V_\infty > 5 \, m/s \qquad (3\text{-}4)$$

These results were the basis of the design values of h_c given in the CIBS Guide (1979). Although the influence of wind speed is very important, as indicated by Eqs. (3,4), this Guide does not provide sufficient information on local wind speed. Actually, V_∞ in Eqs. (3,4) has been replaced by the local wind speed $V_{3D,loc}$, although both parameters can be considerably different. Furthermore, the Guide assumes a constant value of $V_{3D,loc}$ across the facade and does not specify at what distance from the facade this value has to be taken. Note that the subscript 3D refers to the magnitude of the 3D velocity vector.

From the mid 1960's, several attempts were made to measure h_c with heated plates or strips on full-scale buildings. Detailed work was done by Ito et al. (1972) who measured h_c, $V_{3D,loc}$ (at 0.3 m distance from the heated surface) and $V_{3D,R}$ (roof-top wind speed) at the facade of a 6-storey building in Tokyo. Two important conclusions from this work were: (1) The h_c-$V_{3D,loc}$ relationship is relatively independent of surface location and wind direction; and (2) $V_{3D,loc}$ is about 0.20-0.33 times $V_{3D,R}$. These conclusions however can be questioned, since the results were obtained from only a few measurement positions on the facade and for a narrow range of wind directions. The work by Ito et al. (1972) was the basis for the empirical relationships between $V_{3D,S}$, U_{10} and h_c set forth by ASHRAE (1975). Surprisingly and unfortunately, $V_{3D,R}$ in the equations of Ito et al. (1972) appears to have been substituted by U_{10}, while it has been often shown in wind engineering studies that the difference between U_{10} and $V_{3D,R}$ can be very large. Sharples (1984) measured h_c, $V_{3D,loc}$ (at 1 m from the surface) and $V_{3D,R}$ for a high-rise building, as well as U_{10} at a nearby meteorological station. As opposed to the findings by Ito et al. (1972), the h_c-$V_{3D,loc}$ relationship did not appear to be independent of surface location and wind direction. Sharples attributed this to the limited number of measurement points in the study by Ito et al. (1972) and to the specific features of the boundary layer near the building edges. The disadvantage however of the work by Sharples (1984) is the rough classification of wind direction (only two classes: windward and leeward): "data was classified as windward if the angle of incidence between the normal to the monitored facade and the wind direction was less than +/-90° and leeward for all other directions". Since the wind-flow pattern around a building changes markedly with wind direction, this is considered to be one of the main reasons for the low correlation coefficients found by Sharples (1984). For a "worst-case" situation, i.e. a location at the top edge of a 18-storey high-rise building, Sharples (1984) presents the following relationship:

$$h_c = 1.7V_{3D,loc} + 5.1 \qquad (5)$$

where $V_{3D,loc}$ is the local wind speed (m/s) measured at 1 m distance from the surface. It is expressed as a simple function of the reference wind speed U_{10}:

$$V_{3D,loc} = 1.8U_{10} + 0.2 \quad (windward) \, ; \qquad V_{3D,loc} = 0.4U_{10} + 1.7 \quad (leeward) \qquad (6\text{-}7)$$

CFD simulations of the forced exterior CHTC on the surfaces of a rectangular building model were performed by Emmel et al. (2007). However, the low resolution of the grid near the building surfaces and the use of wall functions have compromised the accuracy of the calculated CHTC, as will be shown later in the present paper.

It is known that exterior CHTC are to a large extent influenced by the local wind speed near the surface ($V_{3D,loc}$) and that the relationship CHTC-$V_{3D,loc}$ is dependent on the building geometry and the position on the building facade. Many HAM models use the equations by Sharples (1984) for CHTC, and the convective vapour transfer coefficients are generally determined from the CHTC using the Chilton-Colburn analogy that assumes conformity between the thermal and hygric boundary layer near the surface (Eq. 8).

$$\beta = 7.7 \; 10^{-9} h_c \qquad (8)$$

However, since the existing empirical formulae for the CHTC as a function of wind speed are based on only a limited number of measurements at a few facade positions and for a few building configurations, and more detailed information is not available, HAM models use Eq. (5) at all facade positions. Therefore, more research is needed. Wind tunnel and especially full-scale measurements are expensive and time-consuming. CFD can provide a suitable alternative, but the accuracy of CFD is an issue of concern and careful application and model validation are imperative.

This paper presents high-resolution CFD simulations of forced convective heat transfer at the facades of a low-rise cubic building (10x10x10m³). The objectives are: (1) to analyse the distribution of CHTC across the facades; (2) to investigate the correlation between CHTC and local wind speed across the windward facade; (3) to analyse the thickness of the laminar sublayer dominating boundary layer heat transfer; (4) to assess the impact of high-resolution versus low-resolution grids on the accuracy of CTHC simulations; and (5) to briefly address the relationship between CHTC and wind-driven rain (WDR) distributions across the facade. In section 2, two near-wall modelling approaches are briefly outlined. In section 3, CFD model validation is performed. Section 4 describes the application of the model for forced exterior convective heat transfer. The results are reported in section 5. Sections 6 present discussion and conclusions.

2. Wall functions versus low-Reynolds number modelling

In CFD simulations, generally, two options exist for modelling near-wall turbulence: wall functions or low-Reynolds number modelling. They differ in the way in which the boundary layer at wall surfaces is taken into account. This boundary layer consists of an inner layer, including the thin laminar sublayer, the buffer layer and the logarithmic layer, and a fully turbulent outer layer. Low-Re number modelling refers to resolving the whole boundary layer by placing control volumes in each part of the boundary layer. Because the thickness of the laminar sublayer is inversely proportional to the flow Re number and Re numbers for wind flow around buildings are quite large, the laminar sublayer is often very thin and a high to very high grid resolution is required close to the walls. Because of the computational cost associated with low-Re number modelling, wall functions are often used instead. They are semi-empirical formulae that bridge the region between the wall and the logarithmic layer, and provide an approximation of the effect of the wall on the mean wind speed and turbulence quantities in the logarithmic layer. Much coarser grids can be used here. This is schematically depicted in Fig. 1. The grid resolution at a wall boundary is characterised by the dimensionless wall distance $y^+ = u^* y_P / \nu$, where u^* is the friction velocity, y_P the distance from the centre point P of the wall-adjacent cell to the wall and ν the kinematic viscosity. Appropriate grids for low-Re number modelling have a y^+ below 5 (and about equal to 1) to ensure that the centre point P of the wall-adjacent cell is situated in the laminar sublayer. Wall functions grid should have a y^+ above 30 and below 500 to ensure that P is situated in the logarithmic layer.

3. Model validation

CFD simulations based on the steady-state Reynolds-averaged Navier-Stokes (RANS) equations in combination with a turbulence model require model validation, i.e. the comparison of simulation resuls with accurate experimental data that is relevant for the situation under study. Due to lack of available experimental data of CHTC at realistic Reynolds numbers for building applications (Re ~ 10^5-10^6), validation is performed based on wind tunnel measurements of the velocity field very close to the windward surface of a cubic building with dimensions 0.2x0.2x0.2 m³ (Minson et al. 1995). The CFD simulations are performed at wind tunnel scale. The building model is placed in a computational domain of length x width x height = 4.2 x 4.2 x 2 m³. The domain is discretised by a hybrid grid with about 1.5x10⁶ cells, with the centre of the smallest cell being at a distance y_P = 160 μm from the building surface. While this very high resolution is strictly not necessary for the velocity simulations, it is very important for the heat transfer simulations that will be performed with low-Re number modelling in the next section.

.
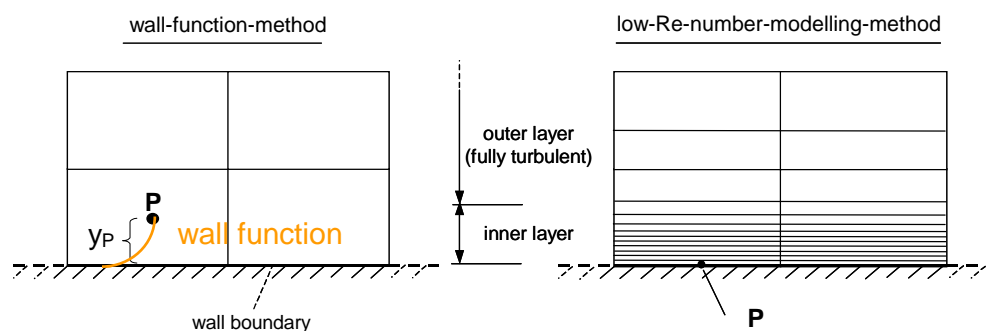
FIG. 1: Schematic representation of part of a grid with control volumes near a wall boundary. Left: wall function grid. Right: low-Re number modelling grid. P denotes the centre point of the wall-adjacent cell.

The inlet mean wind speed and turbulence profiles are taken equal to the measured wind tunnel profiles. Because low-Re number modelling in Fluent 6.3 is employed, no roughness can be assigned to the bottom of the computational domain and it is treated as a zero-roughness no-slip boundary. This will inevitably give rise to unintended streamwise gradients (horizontal inhomogeneity; Blocken et al. 2007). To limit these gradients, the distance between the inlet plane and the windward facade of the building model is limited to 5H (H = 10 m). At the outlet of the domain, zero static pressure is specified. The sides and the top of the domain are modelled as slip walls (zero normal velocity and zero normal gradients of all variables).

Steady-state, isothermal, 3D RANS simulations are made using the high-Reynolds number realizable k-ε model (Shih et al. 1995) in combination with the low-Reynolds number Wolfhstein model (Wolfhstein 1969). Except for a very thin region at the top edge of the building, y^+ values are below 1 across all facades with the present grid and with the reference wind speed U_{10} = 3 m/s. Pressure-velocity coupling is taken care of by the SIMPLE algorithm. Pressure interpolation is second order. Second order discretization schemes are used for both convection terms and viscous terms of the governing equations.

The results are presented as ratios of the streamwise (U) and vertical (V) wind speed to the reference wind speed U_{10} at building height, along a set of vertical lines in the cube centreplane (Figs. 2 and 3). A fair to good agreement is obtained. The agreement is less good for the frontal vortex region upstream of the cube (shown in Fig. 4), but very good for the upper part (y/H > 0.4) close to the cube. The discrepancies are attributed to the well-known stagnation point anomaly of the k-ε models (Franke et al. 2007). A better agreement would have been obtained with Reynolds stress models, however convergence with such models could not be obtained with steady-state simulations on the high-resolution and high-gradient grid used in this study. Regardless, the performance of steady-state RANS with the realizable k-ε is considered sufficient for the purposes of this paper. Note however that larger discrepancies than shown in Fig. 3 will occur for wind speed downstream of the windward facade and for other wind directions because of the limitations of the realizable k-ε model.
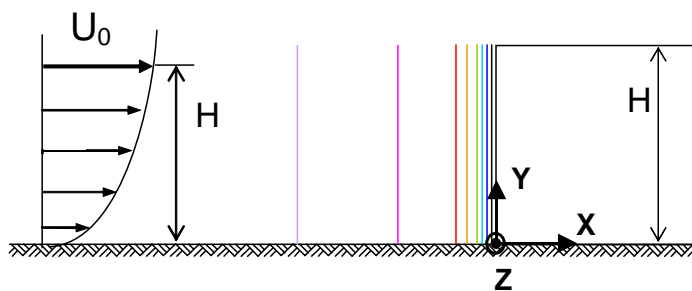
FIG. 2: Vertical lines in the cube centreplane along which wind speed ratios are presented in Fig. 3.
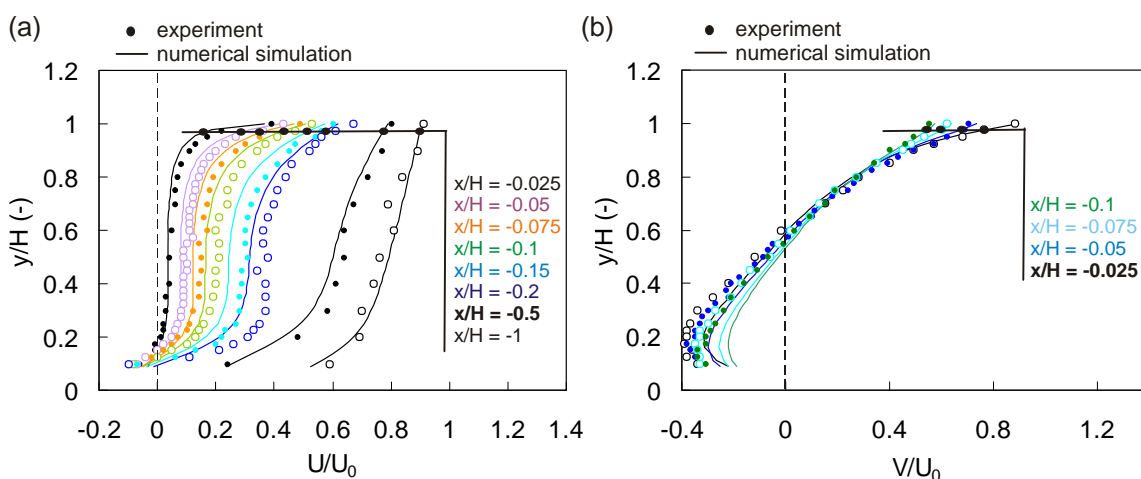
FIG. 3: Numerical and experimental results for the wind speed ratios U/U_0 and V/U_0 along the vertical lines shown in Fig. 2.
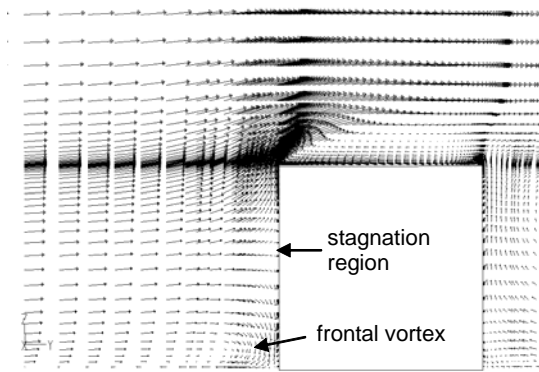
FIG. 4: Velocity vectors in the vertical cube centreplane with indication of stagnation region and frontal vortex.

4. Model application for forced convective heat transfer

The geometrical model, the computational domain and the computational grid are scaled up to full scale (10 m cubic building). Steady-state simulations with the RANS approach and the realizable k-ε model are conducted. The low-Re number Wolfhstein model, as well as standard and non-equilibrium wall functions will be used. These thermal simulations are performed with a fixed building surface temperature of 303 K and an inlet air temperature of 283 K. The bottom wall of the computational domain is adiabatic. The reference temperature to determine the CHTC is the inlet temperature (283 K). Only forced convection is taken into account. This situation is physically only valid for high wind speed. The threshold reference wind speed value for which forced convection eliminates buoyancy effects is not known and is the subject of future research.

The simulations are performed with typical atmospheric boundary layer wind speed profiles over a grass-covered terrain with aerodynamic roughness length $y_0 = 0.03$ m. The reference wind speed at building height $U_{10} = 3$ m/s. The turbulence intensity ranges from 20% at ground level to 5% at gradient height. Turbulent kinetic energy is calculated based on turbulence intensity ($k = \frac{1}{2}(\sigma_u^2 + \sigma_v^2 + \sigma_w^2) \approx (I_u U)^2$) and turbulence dissipation rate $\varepsilon = u^{*3}/\kappa(y+y_0)$ where u^* is the friction velocity, κ the von Karman constant (~ 0.42) and y the height co-ordinate. CFD simulations are performed for wind directions perpendicular to the windward facade ($\theta = 0°$) and for oblique wind ($\theta = 22.5°$, $45°$ and $67.5°$). The results are presented in the next section.

5. Results

5.1 CHTC distribution across the facade

The ratio of CHTC to reference wind speed (h_c/U_{10}) is shown along the perimeter of a vertical and a horizontal cross-section of a plane midway through the building (Fig. 5). Results are given for $\theta = 0°$ and $\theta = 45°$. High gradients exist across the facade, with maximum values at the windward top and vertical edges.

5.2 Correlation between CHTC and local wind speed

Fig. 5 has shown that the CHTC reaches its highest values at positions where also the local wind speed is high, i.e. near the top edge and the vertical side edges of the windward building facade(s). This might suggest that there is a strong correlation between CHTC and the local wind speed $V_{3D,loc}$ or $V_{2D,loc}$ taken at a certain distance from the facade. $V_{2D,loc}$ refers to the magnitude of the wind velocity vector parallel to the facade. For each separate point at the building facade, the correlation between CHTC and $V_{2D,loc}$ is indeed present, as demonstrated by the full-scale measurements by Sharples (1984) and as confirmed by the present simulations. Note that changing $V_{2D,loc}$ for $V_{3D,loc}$ has no significant influence on the correlations. However, it might also be suggested that the relationship between both parameters is similar across the facade. In other words, that CHTC and $V_{2D,loc}$ are spatially correlated, and that this correlation will be stronger when $V_{2D,loc}$ is taken closer to the facade. Figs. 6a-c show the correlation for the windward facade, for $\theta = 0°$ and for $V_{2D,loc}$ taken in the laminar sublayer/buffer layer (d = 0.001 m) and at a distance of 0.1 and 0.3 m from the facade. The correlation is not significant, which is not surprising given the presence of heat fluxes across the facade in the boundary layer. Fig. 6d shows that a stronger correlation exists between CHTC and the turbulent kinetic energy for d = 0.001 m, indicating the importance of turbulent fluctuations in the wind velocity pattern on surface heat transfer.
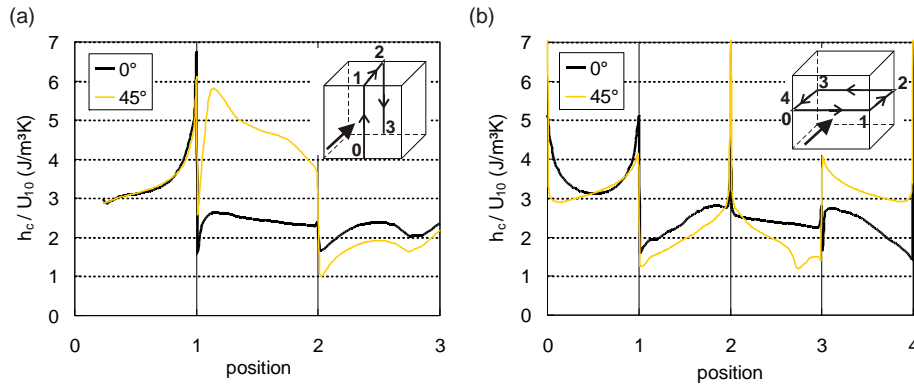
FIG. 5: Ratio of CHTC to reference wind speed U_{10} along lines on the cubic building surfaces, for wind direction $\theta = 0°$ and $\theta = 45°$.
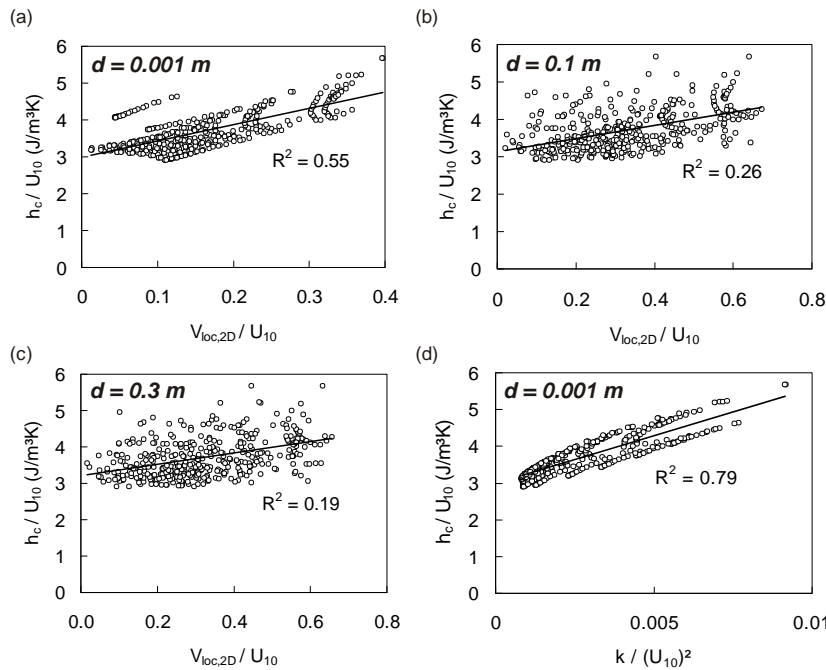
FIG. 6: (a-c) Correlation between the ratios h_c/U_{10} and $V_{loc,2D}/U_{10}$ for positions at different distances from the windward facade ($\theta = 0°$). (d) Correlation between h_c/U_{10} and $k/(U_{10})^2$.

5.3 Thickness of the laminar sublayer

As mentioned earlier in section 2, low-Reynolds number modelling requires grids where the first cell is situated in the laminar sublayer ($y_P < d_{lam}$). This requirement is similar to the requirement $y^+ < 5$. However, to the knowledge of the authors, there is no information in literature on the thickness of the laminar sublayer (d_{lam}) at building surfaces. In addition, y^+ values for a certain grid and simulation can only be obtained after a simulation has been performed, because the value of u^* that is required to calculate y^+ is not known a priori. Therefore, an iterative procedure is required. First, the required y_P value is estimated, then the simulation is performed, and after the y^+ values are checked. Based on these values, the grid is refined or coarsened, after which the simulation is repeated on the adapted grid. For future simulations, information on d_{lam} can be useful to provide a better initial guess for y_P and/or to avoid this iterative procedure. In this study, d_{lam} for the windward facade, for $U_{10} = 3$ m/s and for $\theta = 0°$ was calculated based on the obtained y^+ values, using the knowledge that the laminar sublayer ends to about $y^+ = 5$. Fig. 7 shows the distribution of d_{lam} along the two cross-section perimeters. Note that U_{10} and d_{lam} are inversely proportional. Fig. 7 indicates that the present grid (with $y_P = 160$ μm) includes several cells in the laminar sublayer.

5.4 Wall functions versus low-Re number modelling

Previous CFD simulations of exterior forced CHTC for buildings were made using wall functions (Emmel et al. 2007). Wall functions allow avoiding high-resolution computational grids and performing faster and computationally less expensive simulations. However, wall functions are based on certain assumptions. The standard wall functions by Launder and Spalding (1974) assume local boundary layer equilibrium, which is certainly not a valid assumption for the complex flow around buildings. The non-equilibrium wall functions by Kim and Choudhury (1995) take into account effects of pressure gradients and strong non-equilibrium. However, both types of wall functions do not take into account the specifics of flow in the laminar sublayer. Because heat transfer in this layer occurs mainly by conduction, it determines to a large extent the CHTC. Therefore, accurate simulations of CHTC in complex flow patterns can generally not be obtained with wall functions. Instead, low-Reynolds number modelling on high-resolution grids is required. To demonstrate this, simulations have also been made with a low-resolution wall function grid ($y^+ > 30$). Both standard wall functions and non-equilibrium wall functions have been used. Fig. 8 indicates that the use of wall functions significantly overestimates the CHTC at almost all positions along the two perimeters. As expected, standard wall functions perform worse than non-equilibrium wall functions.

5.5 CHTC and wind-driven rain

Fig. 9 compares the spatial distribution of the ratio CHTC to U_{10} and the catch ratio (WDR rain intensity divided by reference horizontal rainfall intensity R_h), both for the same building and for wind direction $\theta = 0°$. Note that the data below the dashed line in Fig. 9a is unreliable due to grid resolution issues near the bottom of the computational domain (Blocken et al. 2007). Fig. 9 shows a strong similarity between both spatial distributions. This implies that also the CVTC will be higher at this location and that the facade parts that receive most WDR also experience most intensive drying.
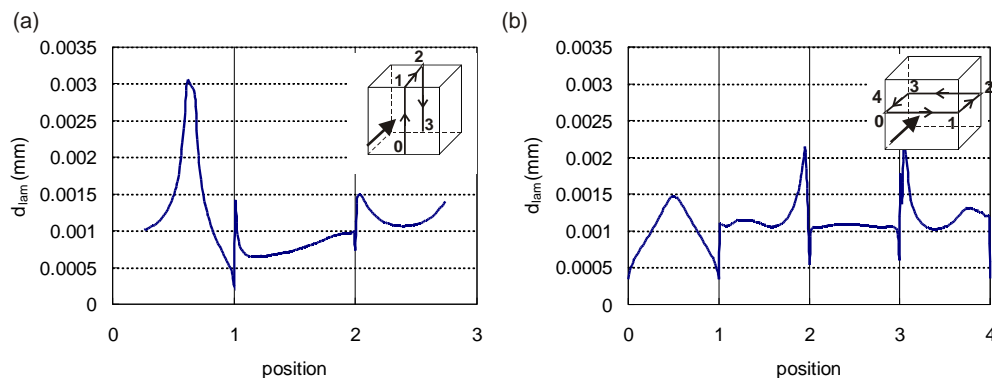
FIG. 7: *Thickness of the laminar sublayer d_{lam} along the perimeter of a vertical and horizontal cross-section.*
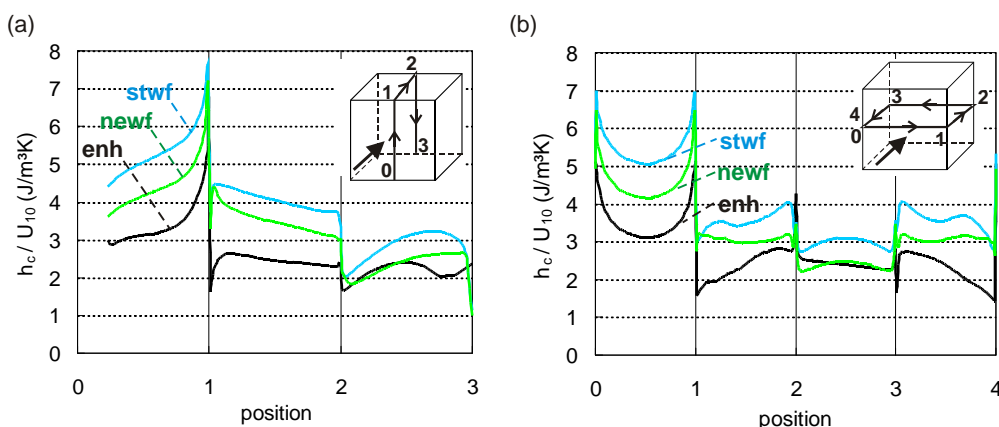
FIG. 8: *CFD simulation results for the ratio of h_c/U_{10} as obtained with low-Reynolds number modelling ("enh") and with standard ("stwf") and non-equilibrium wall functions ("newf").*

(a) h_c/U_{10} (J/m³K)   (b) cath ratio
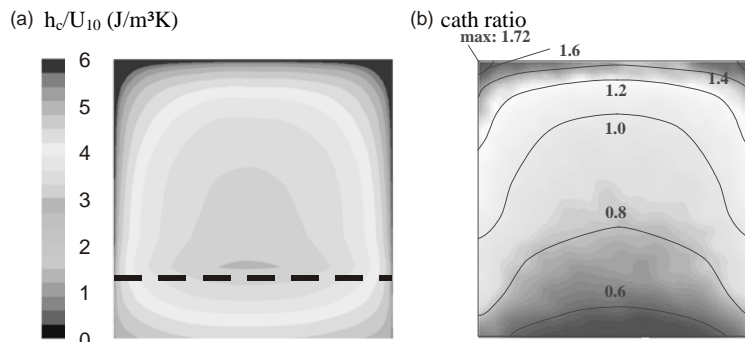
FIG. 9: (a)Distribution of h_c/U_{10} across the windward facade (for U_{10} = 3 m/s, θ = 0°); (b) Distribution of the WDR catch ratio across the same windward facade (for U_{10} = 10 m/s, R_h = 1 mm/h, θ = 0°).

6. Discussion and conclusions

This study was based on the steady-state RANS approach in combination with the realizable k-ε model and the Wolfhstein model. These models are less appropriate for solving wind flow around buildings downstream of the plane in which the windward facade is situated, because in this downstream region transient features, separation and recirculation dominate the flow. Therefore, this paper has mainly focused on the windward facade. Future and ongoing research includes transient simulations on high-resolution grids (Defraeye et al. 2008).

The conclusions of this study are: (1) wind flow around the building introduces a very distinct CHTC distribution across the facade; (2) no significant correlation exists between the CHTC and the local wind speed *across* the facade; (3) the laminar sublayer for the building and conditions in this paper has a thickness of about 1 mm; (4) standard and non-equilibrium wall functions are not able to capture the complexity of wind-induced heat transfer, therefore low-Re number modelling on high-resolution grids is imperative; (5) the CHTC distribution across the windward facade shows some similarity to the distribution of wind-driven rain (WDR), with both parameters reaching high levels near the top edge of the facade. This implies that also the convective vapour transfer coefficient will be higher at this location and that the facade parts that receive most WDR also experience most intensive drying.

7. References

ASHRAE (1975). ASHRAE Task Group. Procedure for determining heating and cooling loads for computerising energy calculations. Algorithms for building heat transfer subroutines. New York.

Blocken B, Stathopoulos T, Carmeliet J. (2007). CFD simulation of the atmospheric boundary layer: wall function problems. Atmospheric Environment 41(2): 238-252.

CIBS. 1979. Chartered Institute of Building Services Guide Book A, Section A3. London.

Defraeye T, Blocken B, Carmeliet J. (2008). Analysis of the the exterior convective heat transfer coefficients of a cubic building with CFD. This symposium.

Franke J, Hellsten A, Schlünzen H, Carissimo B. (2007). Best practice guideline for the CFD simulation of flows in the urban environment. COST Action 732: Quality Assurance and Improvement of Microscale Meteorological Models.

Ito N, Kimura K, Oka J. (1972). A field experiment study on the convective heat transfer coefficient on exterior surface of a building. ASHRAE Trans. 78: 184-191.

Jürges W. (1924). Der Wärmeübergang an einer ebenen Wand. Beizh. z. Gesundh. Ing. 1(19)

Kim SE, Choudhury D. (1995). A near-wall treatment using wall functions sensitized to pressure gradient", ASME FED Vol. 217, Separated and Complex Flows.

Launder BE, Spalding DB. (1974). The numerical computation of turbulent flows. Comput. Method. Appl. M. 3: 269-289

Minson AJ, Wood CJ, Belcher RE. (1995). Experimental velocity measurements for CFD validation. Journal of Wind Engineering and Industrial Aerodynamics 58: 205-215

Sharples S. (1984). Full scale measurements of convective energy losses from exterior building surfaces. Building and Environment 19: 31-39.

Shih TH, Liou WW, Shabbir A, Zhu J. (1995). A new k-ε eddy-viscosity model for high Reynolds number turbulent flows – model development and validation. Computers and Fluids 24 (3): 227-238

Wolfstein M. (1969). The velocity and temperature distribution of one-dimensional flow with turbulence augmentation and pressure gradient. International Journal of Heat and Mass Transfer 12: 301-318.

Destructive Factors Causing Deterioration of Paints on Buildings Walls

Ruta Miniotaite, Associate Professor, Doctor,
Department of Civil Engineering Technologies, Faculty of Civil Engineering and Architecture, Kaunas
University of Technology, Studentu Str. 48, 51367 Kaunas, Lithuania;
ruta.miniotaite@ktu.lt

SUMMARY:
The durability of surface layers of enclosures (outside walls of buildings) is highly influenced by stresses occurring in the plane of contact between finishing materials and that of the enclosure. Damage of external walls depends on a high moisture content, which in turn depends on high water absorption during driving rain. One example of such damage is damage due to direct water penetration in homogeneous walls. The other negative effects of a high moisture content are impaired heat insulation and accelerated degradation. The investigation of the external layer of walls and durability of different paints is carried out in the present article. In case of bi-laminar system "paint film - the wall being painted" two opposite processes take place: water flow rate from outside towards the wall, and water vapour flow rate of the wall to outside. For the wall to be painted, optimum selection of paint is necessary. Investigation on the durability of the building walls external surfaces paints by modelled complex effects in a climatic chamber is purposive only after intermediate investigations and measurements of the substrate physical and mechanical properties that aid in predetermining durability. Influence of moisture deformations upon degradation of coatings depends on the porosity of materials of the surface being coated and on the origin and macrostructure of the coating.

1. Introduction

Durability of the surfaces depends on prevailing climate effects and on a complex of physical and mechanical values of the materials used (Lentinen, 1996; Freitas et al., 1996; Bednar and Dreyer, 1999). Physical and mechanical properties of constructions substrate and finishing layer can supplement one another or, quite contrary, stimulate destruction. A task is raised to investigate the complex derivative of finishing layer forming materials with surface layer of walls as well as the reaction of the above materials to external effects, their force and intensivity.

Much information is given on paint and coatings, physical and chemical nature of paints structure formation, the results of investigations of physical and mechanical values, however, the data on complex investigations of the surfaces already finished are insufficient. Usually, physical and mechanical values of individual components – the coating and the wall being painted are known. However, little is known about the resulting, not the arithmetic quality of the whole complex of properties of a new derivative, – the surface layer.

For the wall to be painted, optimum selection of paint is necessary. The investigation of the external layer of walls and durability of different paints is carried out in the present article. In case of bi-laminar system "paint film - the wall being painted" two opposite processes take place: water flow rate from outside towards the wall, and water vapour flow rate of the wall to outside. Water vapour accumulated in the wall, when disturbed from escaping through a very dense film might cause blebs, or tear off the whole film or its parts.

It was foreseen before investigations of paints on durability that theoretical attitude: low vapour resistance - low rain penetration - "good"; high vapour resistance - high rain penetration - "bad" - can be insufficient evaluating paints durability (Miniotaite, 1996, 1999, 2001; Hansen et al., 1995). During investigation the changes of surface layer, showing decrease in adhesion between paint and surface were fixed. After the investigations in climate chamber were finished and the results were calculated, the reliability of theoretical statement was verified. The value of resistance to complex effects was compared with resistance of non-painted surface in modelled cycles (Miniotaite, 1998, 1999).

A laboratory research work was done, looking for paints suitable for applying on different materials of external surfaces of walls. The investigations in climate chamber indicated that the provided physical-mechanical properties of the paints and adhesion may change in the new combination of "paint - substrate".

Different building materials (concrete, plasters, sand-lime brick) were investigated as a substrate in this experimental studies.

2. Investigations on the durability of paints considering water sorption and vapour permeability

The comparative results of durability were obtained by the classification of coatings in three groups according to their structural nature: 1) paints formed out of aqueous polymeric dispersions; 2) silicate paints; 3) paints formed out of polyacrylates and silicone solutions in organic solvents, or silicone dispersions.

Several hundreds of combinations of coating and substrate are possible considering the many different surfaces to be coated with a selection of various paints. In this study, cement plaster was the substrate chosen for investigation. The plaster was coated using paints of different origin (total 26 compositions). Analyses of compositions of the paints indicate that vapour permeability depends on the paint used, polarity of film-makers, and bonding agents used.

It was found while analysing the results of investigations of paints that specific nature of vapour permeability and water sorption, their contrary effect for destruction and for difference of its symptoms are characteristic of these groups.

Vapour permeability of individual materials and water sorption process have been sufficiently well analysed, however, physical values were obtained irrespective of paint – substrate interaction. The influence of opposition of water vapour escape and water sorption processes upon paint adhesion and destruction has not been evaluated either (Miniotaite, 2001; Hedenblad, 1995; Brocken et al., 1998; Hulden and Hansen, 1985).

The methods of generalized complex investigations was made up on the basis of the results of investigations carried out according to the stage-by-stage methods.

Water vapour permeability coefficient was determined at 20 ^{o}C environment according to requirements of the EN ISO 12572:2001 (EN ISO 12572 2001). Measurements were performed using 3 specimens of 100 mm diameter and 25 mm thickness of the uncoated mortar and others materials (concretes, sand-lime brick) and 3 specimens with surfaces painted for each of the 26 coatings in the study. The painted specimens were fixed on a cup, paint facing down (cup method).

The specimens used for determination of vapour permeability were also used for determination of the surface water sorption coefficient by DIN 52 617 (DIN 52 617 1987).

The specimens oriented with the paint facing downward were soaked in a water bath maintained at 20 ^{o}C temperature. Measurement results are given in Figures 1-3.

Water sorption coefficient w, [kg/(m^2·h$^{0.5}$)] is calculated:

$$w = \frac{m}{\sqrt{t}}$$
(1)

where m is a mass of absorbed water related to 1 square meter of sample, in kg/m^2; t is duration of soaking, in hours.

After vapour permeability coefficient and surface water sorption were determined the new stage of methodical investigation in climate chamber took place where the value of resistance to complex effects was detected in the modelled cycles (Miniotaite, 2001).

The basic conditions and means used for climatic tests were as follows:

a) in the warm part of the chamber room temperature is automatically maintained at $\theta_i = (18 \pm 2)$ ^{o}C and RH $\phi = (50 - 70)\%$;

b) an automatic climatic regime was maintained in the cold part of the chamber:

room temperature during 15 hours freezing down to θ_e = -(15 ± 5) $^{\circ}$C;

the temperature of a protective finished layer of the wall θ_{se} = (15 - 20) $^{\circ}$C during 8 hours reheating;

UV light lamp was used during the last hour of heating; irradiation intensivity 600 W/m^2;

in the cold part of the chamber, water-spray equipment was installed. During a one hour water-spary operation, the finish of the wall had to be covered by a uniform water film (with a spray intensity = 1 L/m^2 min, temperature θ = (7 - 12) $^{\circ}$C, and water pressure = 0.15 MPa);

air circulation at the velocity of v = (2 - 4) m/s was maintained by a ventilating device installed in the cold part of the chamber.

Figure 1 shows that positive influence of vapour permeability upon paints durability is negligible.

Negative influence of water sorption (paints *C1* and *C2*) excels positive influence of vapour permeability upon paints durability (as can be seen in Fig. 1).

3. Summarized results of complex research dealing with painted surfaces of walls

As was foreseen before beginning these investigations the theoretical characterization of the paints (low vapour resistance - low rain penetration – "good"; high vapour resistance – high rain penetration – "bad") can be insufficient to evaluate a paint's durability.

During the investigations changes in the surface layer resulting in decreases in adhesion between a paint and the cement plaster were fixed. After the exposures in the climate chamber were finished and the results were analyzed, the reliability of the theoretical statement was verified. The value of vapour resistance due to complex effects created by application of the coating on the cement plaster was compared with the resistance of non-painted cement plaster surface for the selected cycles.

The tests carried out in the chamber indicated that the paints of identical vapour resistance could be compared even though the nature of deterioration and ageing as well as protective significance of such paints for the painted surface were different. The mechanism of such differences is explained taking into account additionally the complex effects of the moisture-caused deformations of the substrate and physical and mechanical values of the paints (Miniotaite, 2001).

Paint - substrate adhesion is explained by interaction between polar and ionic groups of the bonding agent of paint and functional groups of substrate surface.

Investigation on durability results of paints formed out of silicates and pigments are given in Figure 1 made up on the basis of the results of experiments.

As can be seen in Figure 1 negative influence of water sorption and positive influence of vapour permeability upon silicate paints durability prevail. This influence especially distinct for durability of paint (*C8*): water sorption coefficient distinctly decreased and vapour permeability distinctly increased.

High water sorption coefficient [w = 0.63 kg/(m^2·h$^{0.5}$) and w = 0.32 kg/(m^2·h$^{0.5}$)] has negative influence for indurable paints (*C1* and *C2*).

These paints are formed of derivatives of salts of silicic acid and fillings inside the film. Adhesion with substrate is assured by forces of electrostatic interaction between surface groups. Van der Waals forces and polar interaction exist also.

The paints of this group get polarized on the scale of increased cement plaster's water sorption moisture u_{24} = (4 - 6)%. A stiff framework is typical of surface macrostructure. Therefore the durability of paints of this group is negligibly influenced by moisture-caused deformations of substrate.

Parameters of surface water sorption and vapour resistance have approximately identical influence upon durability of paints. Vapour resistance should be Z_p ≤ 1.3 m^2·h·Pa/mg and water sorption coefficient – w < 0.88 kg/(m^2·h$^{0.5}$). Reducing water sorption coefficient to w = 0.4 kg/(m^2·h$^{0.5}$) and vapour resistance to Z_p = 0.7 m^2·h·Pa/mg might increase durability (15–20)%.
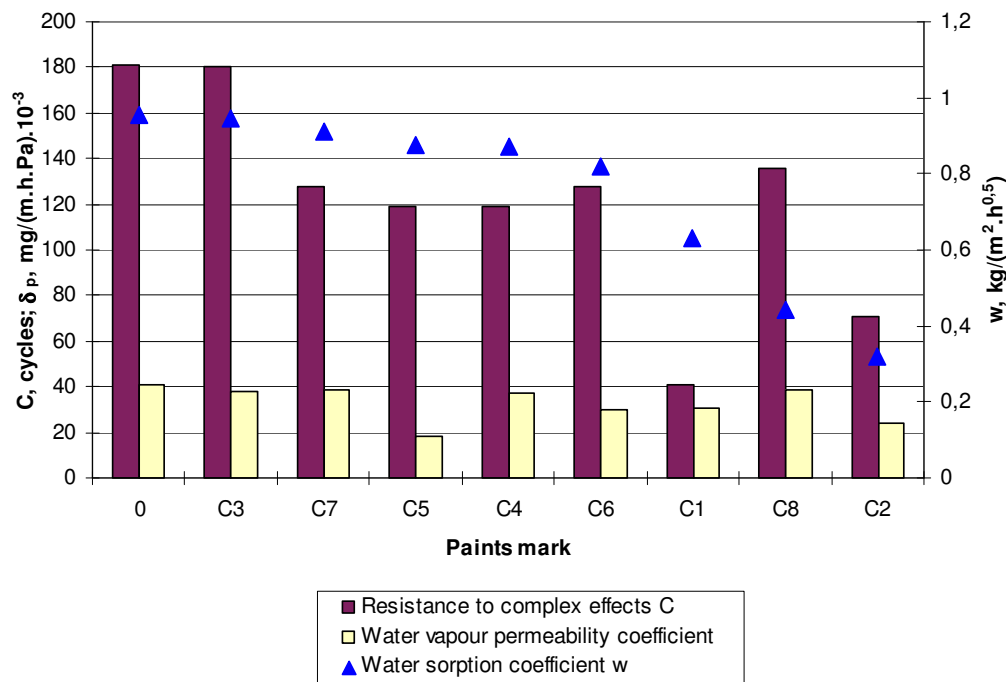
FIG. 1: The comparison of physical values of cement plaster and durability of silicate paints.
Note: paints mark 0 – non-painted plaster.

Durability of properly hardened paints should be attributed to the category of acceptable durability ($C = 120 – 180$ cycles).

Physical properties (i.e., vapour resistance and water sorption coefficient) of the surface layer (0.025 m) of cement plaster coated with aqueous polymeric dispersion paints are compared in Figure 2 (Miniotaite, 2001).

The aqueous polymeric dispersion paints are distributed according to the water sorption coefficient in two subgroups: a) *D1, D2, D3, D4* [$w > 0.55$ kg/(m$^2 \cdot$h$^{0.5}$)]; b) *D5, D6, D7, D8, D9* [$w \leq 0.30$ kg/(m$^2 \cdot$h$^{0.5}$)] (Fig. 2). As can be seen at the increase of vapour resistance of less than a factor of two decreases the water sorption coefficient more than a factor of 30. The water sorption coefficients of paints *D1* and *D5* in separate subgroups vary by a factor of 5.

Figure 2 shows that surface water absorption in the case of the paints of subgroup "a" is high – these are relatively "rain permeable" paints: $w = (0.56 - 0.66)$ kg/(m$^2 \cdot$h$^{0.5}$). Their vapour resistance $Z_p = (0.63 - 0.64)$ m$^2 \cdot$h$\cdot$Pa/mg [$\delta_p = (0.039 - 0.040)$ mg/(m$\cdot$h$\cdot$Pa)].

Surface water absorption in the case of paints of subgroup "b" is low – these are rather "tight" paints $w = (0.024 - 0.10)$ kg/(m$^2 \cdot$h$^{0.5}$) (Fig. 2). Their vapour resistance $Z_p = (0.87 - 1.49)$ m$^2 \cdot$h$\cdot$Pa/mg [$\delta_p = (0.029 - 0.017)$ mg/(m$\cdot$h$\cdot$Pa)] is on the average 35% higher than those of subgroup "a".

Durability of the aqueous polymeric disperse paints is described (considering two basic physical properties) in Figure 2.

In the all cases the vapour resistance increase was influenced by using the acrylic bonding agent in appropriate proportions. However, the increase of vapour resistance is permissible and does not reduce durability of a properly selected composition of the paint. In the case of subgroup "a" permissible water sorption coefficient $w < 0.66$ kg/(m$^2 \cdot$h$^{0.5}$) and the highest value of vapour resistance $Z_p < 1.38$ m$^2 \cdot$h$\cdot$Pa/mg [$\delta_p > 0.018$ mg/(m$\cdot$h$\cdot$Pa)] are suitable with respect to durability. In the case of subgroup "b" all physical parameters are high enough. The reason for classifying two paints *D8* and *D9* as non-durable considers the bonding agent: specifically, the amount of bonding agent was insufficient.
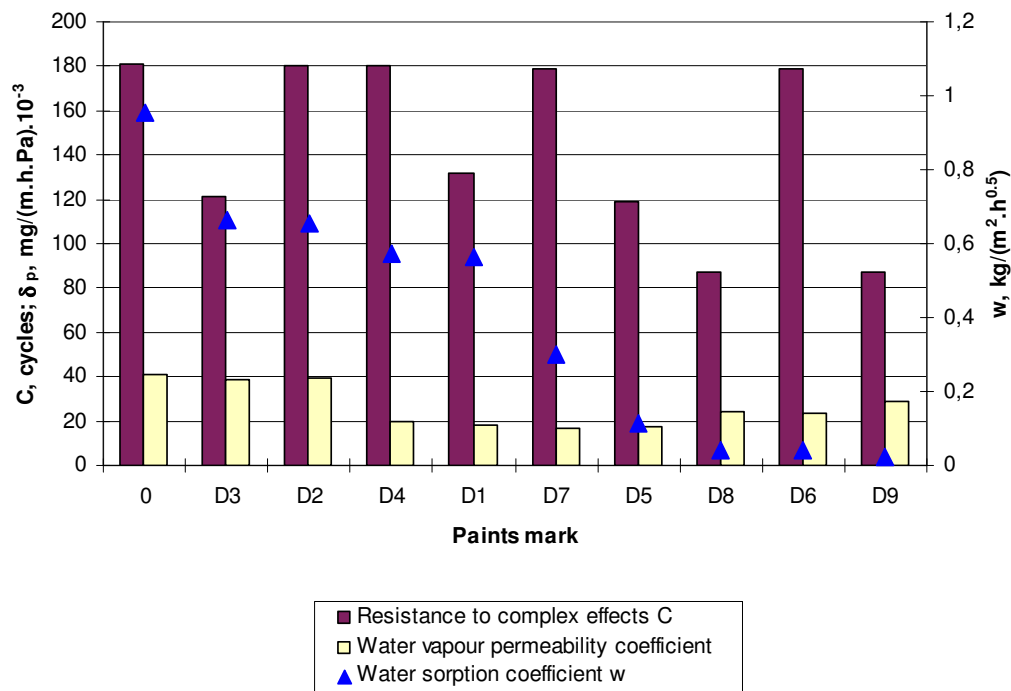
FIG. 2: The comparison of physical values of cement plaster and durability of aqueous polymeric disperse paints.

Durability of paints in the case of insufficiently stabilized compositions of the aqueous polymeric dispersions is defined as C < 80 cycles irrespective of the values of the water sorption and vapour permeability coefficients. Destruction of the paint specimens in the study is manifest through fast wrinkling of the film, mould formation, loss in the adhesion and washing off after 50-80 cycles.

Paints formed out of polyacrylates and silicones solutions in organic solvents, or silicone dispersions. Hardened films of polyacrylates' or silicones constitute uniformity of the paints. They have no emulsifiers. Adhesion of paint - substrate is ensured by intermolecular interaction between bonding agent of paint and substrate. Because of the organic polymers of silicons are highly resistant, their films are stronger, more elastic and more resistant to temperature.

In respect of a cement plaster, the paints of the group concentrate on the scale of low and average water sorption moisture (Fig. 3). Macrostructure of the surface is uniform, not textured.

The durability of the paints containing pigment of the above group is extremely sensitive to vapour resistance. With increase of $Z_p > 0,64$ m^2·h·Pa/mg, negative influence of vapour resistance grows fast. Appearance of blebs indicate reduced adhesion.

The nature of destruction is close to lamination: occurrence of tiny blebs - their merging and bursting; lamination or "scale" type cracking of a paint. Chemically instable paints are spotty. In some cases the spots are already observed following 90-140 testing cycles. Appearance of spots preceding mechanical desintegration of pants is not analysed in the article, even though the spots have aesthetic depreciation sense. Aesthetic destruction is also typical of some compositions with acceptable mechanical durability.

150 accelerated cycles in the climatic chamber correspond to 12 years at an average natural ageing.

By analysing the results of grouped paints it was found that peculiar nature of vapour permeability and water sorption was typical of each group; distibution of the paint destruction is different. The nature of paint destruction depends on the moisture-caused deformation of the substrate on the different level.
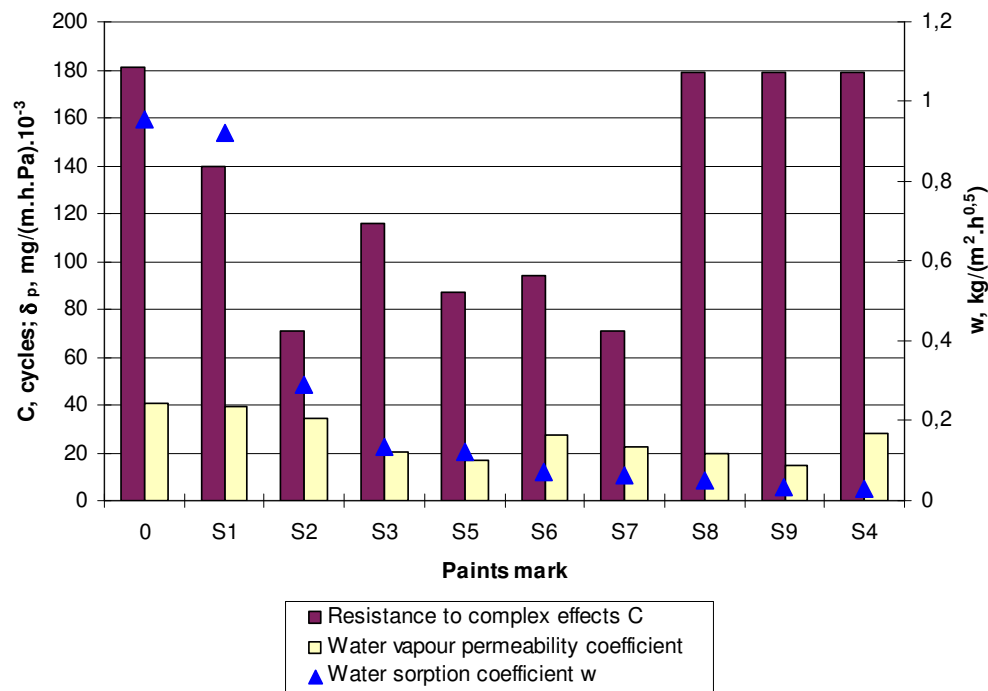
FIG. 3: The comparison of physical values of cement plaster and durability of paints made out of polyacrylates and silicone solutions in organic solvents or silicone dispersions.

4. Conclusions

Investigation on the durability of the building walls external surfaces paints by modelled complex effects in a climatic chamber is purposive only after intermediate investigations and measurements of the substrate physical and mechanical properties that aid in predetermining durability, that is, adsorption-desorption and moisture-caused deformations. The effect of the above mentioned properties upon durability should be evaluated.

Influence of moisture deformations upon degradation of coatings depends on the porosity of materials of the surface being coated and on the origin and macrostructure of the coating.

Silicate paints resistance to climate effects is more dependent on surface water absorption and less dependent upon vapour permeability. Water absorption of non-durable paints is high; vapour resistance has no significant influence.

Durability of the paints formed out of aqueous polymeric dispersions as well as the subgroups of paints is distributed in the direction of fast decrease of water sorption coefficient.

Resistance of paints made out of polyacrylates and silicone solutions in organic solvents or silicone dispersions to climate effects depends mined by investigations. There are no lamination and no cracks in case of nonpigment silicone paints. Hydrophobic properties of such paints decrease with time.

Durable coatings should be considered to be those which have withstood from 150 to 180 modelled complex cycles of climate effects. The coatings of acceptable (permissible) durability are those withstanding 110-150 cycles. Non-durable coatings are those withstanding less than 100-110 cycles - their aesthetic depreciation usually starts following 30-50 testing cycles. The coatings which begin to deteriorate after 80-100 cycles are not recommended either.

5. References

Bednar T. and Dreyer J. (1999). Moisture transport in masonry. Influence of different historic and modern renders on the moisture performance of walls under rain load, *Proceedings of 5th symposium on building physics in the Nordic Countries*, Gothenburg, Sweden, Vol. 2, 529-536.

Brocken H. J. P., Spiekman M. E., Pel L., Kopinga K. and Larbi J. A. (1998). Water extraction out of mortar during brick laying: A NMR study, *Materials and structures*, Vol. 31, No. 5*,* 49-57.

DIN 52 617:1987. Determination of the water absorption coefficient of building materials.

EN ISO 12572:2001 - Building materials. Hydrothermal performance of building materials and products – Determination of water vapour transmission properties.

Freitas V. P., Abrantes V. and Crausse P. (1996). Moisture migration in building walls – analysis of the interface phenomena, *Journal of building and environment,* Vol 31, No. 2, 99-108.

Hansen K. K., Baroghel V. B., Quenard D. and Künzel H. (1995). Water vapour absorption isotherms for porous building materials, *Proceedings international symposium on moisture problems in building walls*, Portugal, (Abrantes V., editor), 248-257.

Hedenblad G. (1995). Moisture permeability and sorption isotherms of some porous materials, *Proceedings International Symposium on moisture problems in building walls* (Abrantes V., editor), Portugal, 238 – 247.

Hulden M. and Hansen C. (1985). Water permeation in coatings. *Progress in organic coatings*, 13, 171-194.

Lentinen T. (1996). Capillary moisture transfer in combined porous building materials, *Proceedings symposium building physics in the Nordic Countries*, Finland, 483-490.

Miniotaite R. (1996). Determination method for weather durability of finish layers in external walls of buildings, *Proceedings conference on the subject of construction and architecture*, Kaunas University of Technology, Kaunas, Lithuania, 140-145 (in Lithuanian).

Miniotaite R. (1998). The durability of finish layers and coatings of external walls of buildings, *Conference on the subject of construction and architecture*, Kaunas University of Technology, Institute of Architecture and Construction. Kaunas, Lithuania, 248-253 (in Lithuanian).

Miniotaite R. (1999). *Compatibility of finishing layer and external surface of buildings' walls from the standpoint of durability.* Summary of the Thesis for a doctor's degree, Kaunas, Lithuania, 47 p. (in Lithuanian).

Miniotaite R. (2001). The durability of finishing layer external surface of buildings' walls, *Monograph*, Lithuania, 175 p.

Algal defacement of facade materials –results of long term natural weathering tests obtained by new diagnostic tools

Helmuth Venzmer, Professor
Faculty of Engineering, University of Technology, Business and Design, Wismar, Germany
helmuth.venzmer@hs-wismar.de

Julia von Werder, Natalia Lesnych and Lev Koss, research assistants
Faculty of Engineering, University of Technology, Business and Design, Wismar, Germany
julia.von_werder@hs-wismar.de, natalia.lesnych@hs-wismar.de, lev.koss@hs-wismar.de

SUMMARY:
The main reason for the primarily esthetical problem of algae growth on facades is a raised humidity level on the building envelopes. Due to the high thermal insulation levels the surface temperature of renovated or new buildings dropped significantly so that it takes very long before moisture films dry.
To avoid guarantee claims manufacturers of building materials are researching new strategies to prevent the green discolorations. Because until today there is no representative laboratory method to test the sensitivity of materials to algal growth, long-term natural weathering experiments are the only means to test the effectiveness of innovations.
A field study over four years showed that algal growth became visible earlier on the synthetic resin and silicon plasters than on the mineralic systems. It is assumed that the higher sensitivity to algal defacement is caused by the lower absorptive capacity of the affected systems. More humidity can accumulate on the surface and is available to the microorganisms. The regular examinations demonstrated that PAM-Fluorometry is an effective and non-destructive diagnostic tool to evaluate algal growth on naturally weathered samples a long time before it gets visible with the bare eye.

1. Problem of building physics

The repeatedly raised requirements for the thermal insulation of building envelopes have led to a significant decline of the surface temperatures. Moisture films due to driving rain and condensate dry only very slowly on the cold surfaces and are the most important pre-condition for algal growth (FIG. 1). Due to their specific set-up (decoupled system) and small heat storage capacity ETICS (External Thermal Insulation Composite Systems) are especially affected by cooling due to long wave radiation. Consequently ETICS are affected to a greater extent by condensation than solid systems [1, 2, 9, 10].

FIG. 1: Compact algal growth on the northern facade of a thermally upgraded building

The primarily esthetical problems of the green-grey discolorations are to an increasing degree the reason for guarantee claims [4]. Manufactures of paints and plasters are researching new strategies to prevent the algal growth by efficient mixtures of biocides, by manipulation of the thermal and hygric properties of the building materials and by creating self-cleaning surfaces. In order to advance product development reliable laboratory tests and objective diagnostic methods for evaluation and quantification of algal growth in the very early stages are urgently needed.

2. Long term natural weathering tests

Until today there is no reliable laboratory test for evaluating the sensitivity of building materials to algal growth. All results gained from the inoculation of samples with an algal solution or from pollination of samples with dry algae did not correspond to the results obtained by natural weathering. The factors facilitating natural growth are obviously to complex to be simulated in the laboratory.

For the evaluation of products with new properties long term natural weathering tests are the only means to get reliable and reproducible results. For each system tested there have to be at least three test specimen of an adequate size (minimum: 20 x 20 cm). In order to get representative humidity loads products for facades should be attached vertically to the weathering stand, which should be preferably situated on ground level (FIG 2).

For a better interpretation of the results it is recommended to record the meteorological data (air temperature, relative humidity, precipitation, total radiation and wind velocity) of the natural weathering period. Additional, valuable information can be gained if the dew point temperature of the air and the surface temperatures of the samples are monitored.

FIG. 2: One of several free weathering stands at the university of Wismar

3. Diagnostic Tools

The results of several natural weathering tests carried out by different institutes show that it takes minimum 18 month before algae get visible on the samples with the bare eye [5,8]. Obviously specific weathering processes must have taken place before biological growth can establish on the surfaces - regardless if the systems do or do not contain biocides.

Diagnostic tools, which allow the detection and quantification of algae on the microscopic level could be an important means to early screen the resistance of products against algal growth and therefore to enhance product development. At the university of Wismar the applicability of two diagnostic tools is presently researched: Pulse Amplitude Modulation (PAM) fluorometry and DNA-diagnostics.

Aerophytic algae are ubiquitous in the aeroplankton and are carried to the facades by wind and driving rain. However only if specific conditions are given over an adequate period of time the microscopic organisms attach to the surface and start growing. To distinguish between algae, which adhere only superficially to the surface and algae already grown to the surface, it is essential for both diagnostic methods to quantify the detection limit regarding to the background level.

3.1 Pulse Amplitude Modulation (PAM) fluorometry

The Pulse Amplitude Modulation (PAM) fluorometry is based on the fact that chlorophyll is emitting fluorescence light after irradiation with light of appropriate wavelength. The relation between the photons emitted during fluorescence and the preliminary absorbed photons is called the fluorescence yield (equation 1).

$$\Phi_F = N_F / N_A \qquad\qquad\qquad (1)$$

Φ_F *fluorescence yield*
N_F *number of emitted photons*
N_A *number of absorbed photons*

In photosynthetic organisms the emission of fluorescence light competes with photochemical energy conversion at the reaction centres (light reaction of the photosynthesis) and energy dissipation into heat. Therefore the measurement of chlorophyll fluorescence yield under different light conditions can provide detailed information about the physiological state of an organism.

Assuming energy dissipation into heat is constant there are two extreme situations possible for the competition of fluorescence light with photochemical energy conversion. Either all reaction centres of photo system II are open (dark- adapted state) and the fluorescence yield is minimal (F_0 = initial fluorescence yield) or all reactions centres are closed (in saturating light) and the fluorescence yield is maximal (F_m = maximum fluorescence yield).

Research at the university Rostock showed that for chlorophyll-a concentrations between 3,5 mg/m² and 20 mg/m² there is a linear relationship between the chlorophyll-a concentrations as a measure for the biomass and the initial fluorescence yield of dark-adapted samples (algal suspensions filtered onto glass micro fibre filters) [3]. Because biofilms, which are visible with the bare eye contain chlorophyll-a concentrations between 50-100 mg/m² [3], PAM fluorometry is especially appropriate to detect, monitor and roughly quantify initial algae growth on building materials at the microscopic level.

For the examination of weathered samples we are using a portable PAM-Fluorometer with image analysis (*IMAGING-PAM*) especially developed by the company Waltz for the study of plants in the field. The basic parts of the measuring system are a control unit with rechargeable battery and processor, a triple-row LED-ring-array consisting of a total of 112 LEDs and a CCD-camera, which digitises the data and transfers them via a Firewire interface to the PC.

The universal sample holder was replaced by a custom-built x-y-scanner allowing to assign x and y coordinates to a representative number of irradiated areas (25mm x 18 mm) of the sample (FIG 3). This way the initial fluorescence yield F_o after dark adaptation can repeatedly be measured on the very same areas and the growth dynamics can be monitored (TABLE 1).

legend:

1 control unit**, 2** LED Ring -Array**, 3**   CCD camera
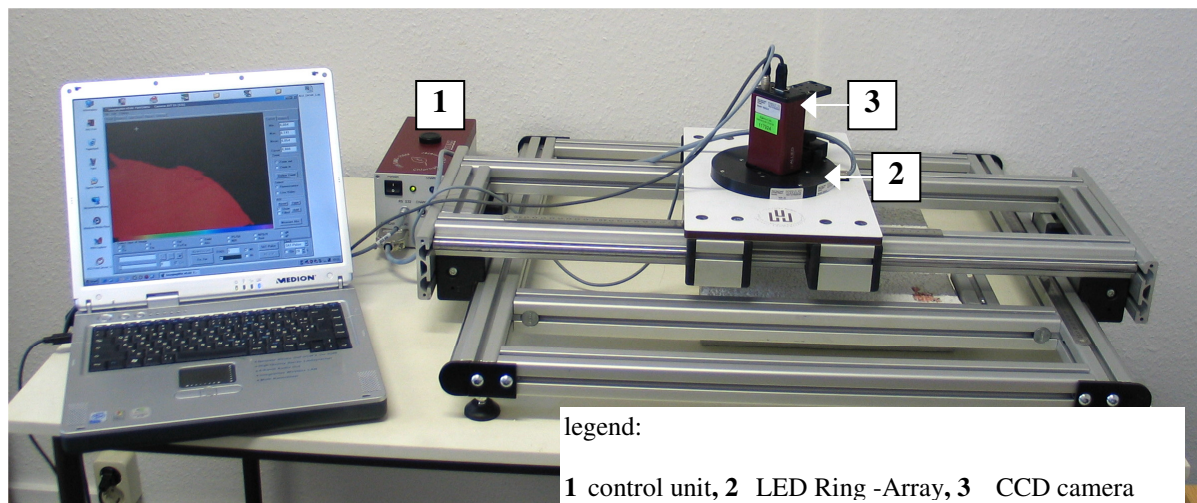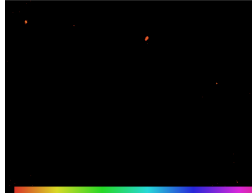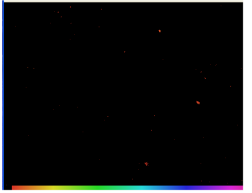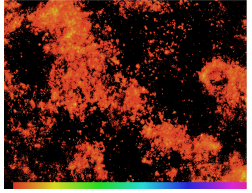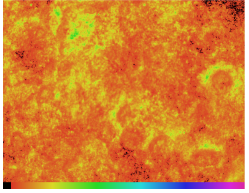
FIG 3: Measuring set-up in the laboratory

TABLE 1: Growth dynamics of test specimen SRP_1, field no. 5

time	April 2006	October 2006	April 2007	October 2007
Fluorescence image 25 x 18 mm				
MFA	0,010	0,010	0,036	0,114

The result is represented graphically as fluorescence image and in numbers as minimum, maximum and mean fluorescence yield (dimensionless number) in the examined area. The mean value of the initial fluorescence yield after dark adaptation in a specific area we termed *MFA* for purposes of clarity.

In order to roughly quantify the biomass present on the surface the MFA is measured in an appropriate number of areas n dependent on the specimen size ($MFA_1 - MFA_n$). Because the instrument settings and the hydration state of the sample have great influence on the measured data it is very important to follow an appropriate measuring algorithm [7,11]. The arithmetic mean of the single mean values in the different measuring areas we defined as mean fluorescence of the sample *MFS* (equation 2) and serves as criterion for the intensity of the algal growth.

$$MFS = (MFA1_1 + MFA_2 + MFA_3 + \quad MFA_n) / n \qquad\qquad (2)$$

MFS   mean fluorescence yield of the sample (dimensionless)
MFA   mean fluorescence yield of specific measuring area (dimensionless)
n   number of measuring areas dependent on specimen size

According to our experience MFS values below 0,015 correspond to the ubiquitous presence of algae on surfaces exposed to air and have to be classified as *background level*. Only if the MFS exceeds the value of 0,015 it can be assumed that the growth develops to a size visible with the bare eye in the foreseeable future. There is no distinct correlation between the MFA or MFS and the visual perceptible discoloration of the measuring area / specimen surface. Our experience shows that in the majority of cases colorations can be only discerned when the MFS rose to a level above 0,03 before.

4. Results of Field studies

From October 2003 until October 2007 20 different ETICS were exposed to natural weathering and examined every six months. 10 systems belonged to the group of synthetic resin / silicon / silicate plasters and the other 10 systems were assigned to the group of mineral plasters. In both groups the systems were partially coated and contained biocides (TABLE 2).

Three parallel test specimen (30 x 35 cm) of every type of the 20 systems were attached to free weathering stands facing northeast. In addition to the test specimen 20 sample areas were built up on the northeast facade of a one-storied lecture building. To prevent vandalism the free weathering stands are situated on top of a four-storied building.

After four years of free weathering 6 out of 20 test areas showed green discolorations visible with the bare eye. Affected were the uncoated and coated synthetic resin plasters not containing biocides (SRP_1 and SRP_3) and three out of the four silicon plasters (SICO_1, SICO_3 and SICO_4). From the mineral systems only the plaster with silicate paint exhibited algal growth (MP_7).

The survey of the test specimens however resulted in only one explicitly discoloured system: silicon plaster SICO_1. Obviously the specific microclimate on the rooftop, in particular the high wind speeds prevailing there, are leading to a significant delay of the algal growth.

The PAM measurements of the test specimens (8 measuring areas per specimen) and the samples areas (one measuring area on every retained plaster sample) reveal a time-delayed but very similar growth dynamic. The majority of test specimens corresponding to the systems, which are already exhibiting green discolorations on

the test facade, show raised levels of MFS (FIG 4). It can be assumed that the algal growth on these systems will become discernible with the bare eye in the foreseeable future. Noticeable is the high MFS of the test specimen SICA_1 compared to the corresponding sample area. The reason could be unintentional differences in the composition of the two systems.

TABLE 2: List of products examined

Sample ID	Description
SRP_1	Synthetic resin plaster
SRP_2	Synthetic resin plaster containing biocides
SRP_3	Synthetic resin plaster with coating
SRP_4	Synthetic resin plaster containing biocides with coating containing biocides
SICO_1	Silicon plaster
SICO_2	Silicon plaster containing biocide
SICO_3	Silicon plaster with coating
SICO_4	Silicon resin plaster containing biocides with coating containing biocides
SICA_1	Silicate plaster containing biocides
SICA_2	Silicate plaster containing biocides with coating containing biocides
MP_1	Standard mineral plaster
MP_2	Standard mineral plaster containing biocide A
MP_3	Standard mineral plaster containing biocide B
MP_4	Standard mineral plaster coated with emulsion paint
MP_5	Standard mineral plaster coated with silicon paint (2 layers)
MP_6	Standard mineral plaster coated with silicon paint (1 layer)
MP_7	Standard mineral plaster coated with silicate paint
MP_8	Pebble dash plaster containing biocide 1
MP_9	Pebble dash plaster
MP_10	Thick-film plaster
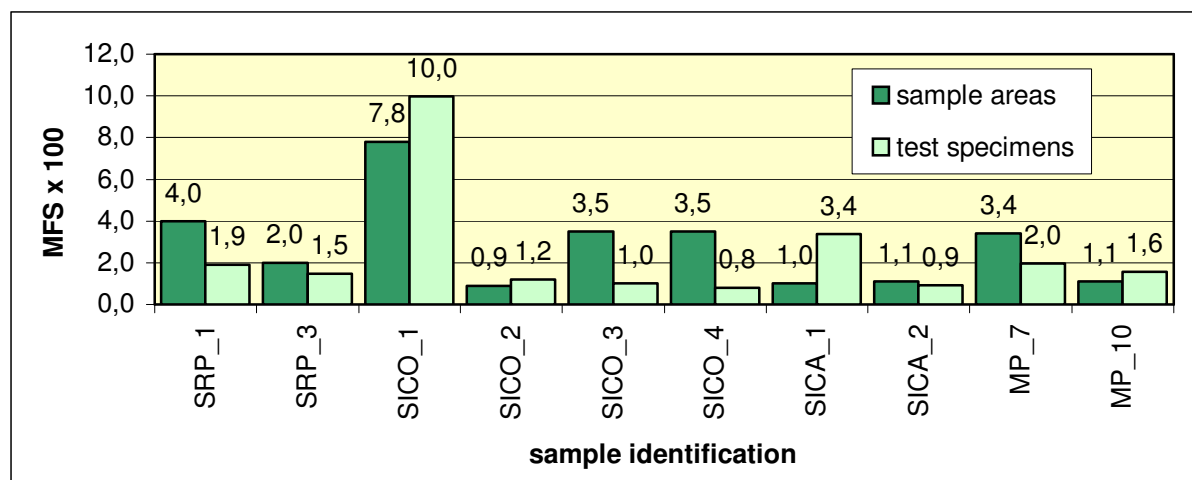
FIG 4: MFS values of selected sample areas and corresponding test specimens

The major results after four years of free weathering can be summarized as follows:
- The synthetic resin and silicone plasters exhibit a stronger sensitivity to algal growth than the mineralic systems.
- The biocide-free synthetic resin and silicone plasters are the first systems affected by algal growth.
- Whereas the coating of the biocide free silicone plaster with biocide free paint delays algal growth for approximately 1- 2 years, the coating of the biocide containing silicone plaster with biocide containing paint increases the sensitivity to algal growth.
- PAM diagnostics allows evaluation and quantification of algal growth on the microscopic level 0,5 – 1 year before the systems exhibit green discolorations.

5. Hygrothermal Parameters

The reason for the higher sensitivity of the synthetic resin and silicone plasters compared to the mineralic surfaces is presumably the longer availability of liquid water on these surfaces. Because of their higher hydrophobicity less water is absorbed by the plaster system following driving rain and condensation and remains on the surface where it is easier available to the algae. To quantify the hydrophobic properties of the plaster systems the water uptake coefficient was determined according to DIN 52617 (equation 3).

$$w_{24} = \frac{\Delta W_{24}}{\sqrt{24}} \tag{3}$$

To assess also the drying process subject to capillary action a drying coefficient was determined analogical the water uptake coefficient (FIG 5). The increase of mass after 24 hours of water immersion ΔW_{24} in equation 3 was for this reason substituted by the decrease of mass after 24 hours of drying under indoor conditions.

The results of the assessment of the water uptake show that after immersion in water for 24 hours the mineralic systems can store in average (MP_1 – MP_9) 1 kg /m^2 in the plaster system. The storage capacity of the synthetic resin and silicone plasters however averages only about 0,3 kg resulting in a factor between the corresponding average water uptake coefficients of 3,5. The drying coefficients demonstrate that the synthetic resin and silicone plasters have regained or almost regained their initial mass before wetting after 24 hours of drying. In contrast the mineralic systems still contain part of the water absorbed during immersion. However the immersion of the samples in water for 24 hours simulates an extreme exposure. Under practical conditions there is no risk that the water remaining in the system builds up and substantially reduces the storage capacity. Condensation takes place primarily in clear nights which are often followed by sunny mornings offering good drying conditions.
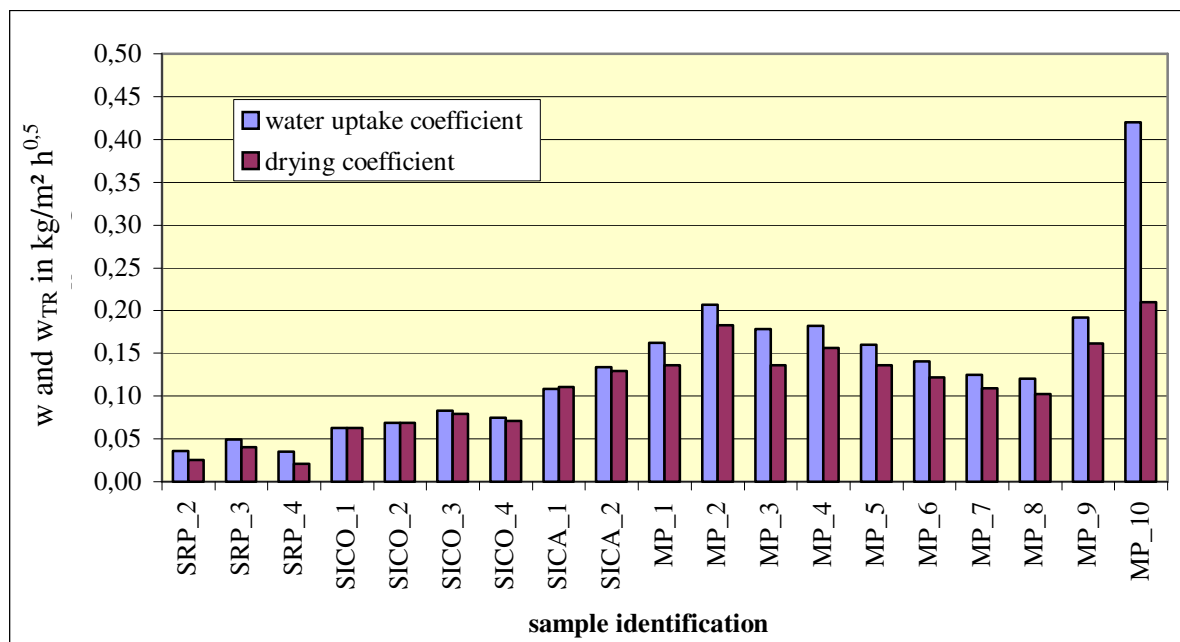
FIG 5: Water uptake and drying coefficients of the examined systems

6. Meaurement of humidity films on site

By measuring the surface temperature and the corresponding dew point temperature the duration of time when a test specimen is passing below the dew point can be calculated. The effective retention period of the humidity film on the specimen surface differs however from this time span and depends on the hygric properties of the plaster system. On hydrophobic surfaces the water remains on the surface whereas on absorptive surfaces it is transported to the background.

At the university of Wismar we are therefore trying to measure directly the humidity film on the specimen surface. For this purpose a water detector probe of the company *Ahlborn*, originally designed for the rapid detection of unbound water within control surveys, was modified for continuous operation. In short intervals the electrical conductivity is measured between two electrodes attached to the surface at short distance. If water is collecting between the electrodes the measuring signal rises steeply.

The measuring set-up does not allow a quantification of the humidity (yes/no answer) but a roughly estimation of the retention period of humidity films caused by driving rain and condensation.

The measuring results show that on plaster systems with smaller water uptake the humidity stays longer than on more absorptive systems (figure 7). This is especially true for the humidity caused by condensation, which is characterized by very small drop sizes (figure 6 and 7).
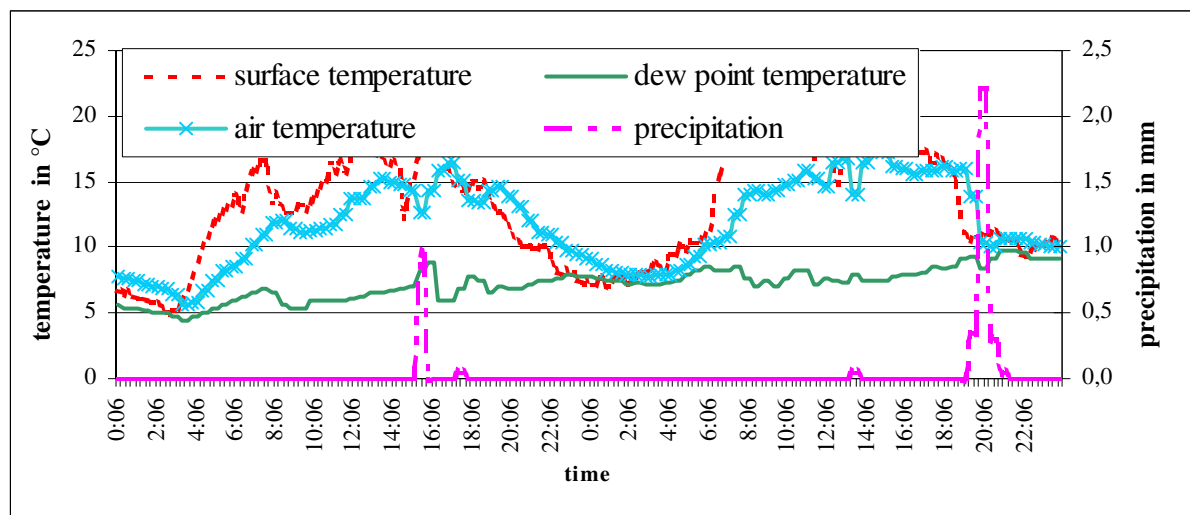
FIG 6: Measured temperature profiles and precipitation, 20th-21st June 2004, ETIC-test specimen facing NE
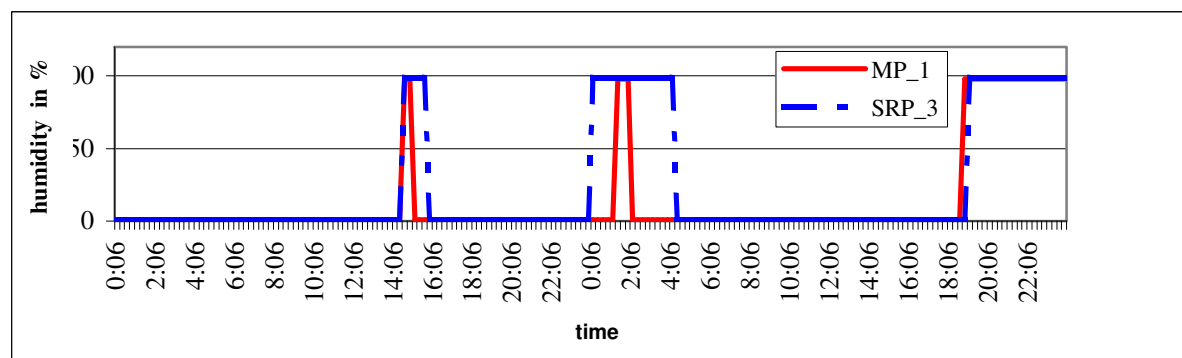
FIG 7: Humidity film on the specimen surfaces of hydrophobic (SRP_3) and hydrophilic (MP_1) plaster system

Gravimetric measurements and numeric simulations of the surface humidity of facades coated with different paints confirm that on hydrophobic surfaces humidity accumulates on the surface. [5, 6]
To minimize the sensitivity to algal growth strongly hydrophobic surfaces seem therefore not an appropriate mean.

6. Conclusion

By combining free weathering tests with modern diagnostic tools the evaluation of the sensitivity of products to algal growth can be significantly enhanced. PAM fluorometry allows non-destructive detecting of algal growth on the microscopic level by measuring the fluorescence yield after irradiation. If the fluorescence yield is measured repeatedly on predefined areas of the sample growth dynamics can be monitored and visualized. If the mean fluorescence yield of a certain sample clearly exceeds the value of the background level it can be assumed that that the growth develops to a size visible with the bare eye in the near future.

Long term natural weathering tests of 20 different ETICS showed that the synthetic resin and silicone plasters are earlier affected by algal growth than the mineralic systems.

It is assumed that the sensitivity of plaster systems to algal growth correlates with the hygric properties of the building materials. On plaster systems exhibiting hydrophobic properties liquid water remains longer on the surface whereas on more hydrophilic systems it is transported to the background. The hygric properties can be estimated measuring the water uptake coefficient or by directly measuring the humidity film on the specimen surface.

7. References

[1]   Büchli R. and Raschle P. (2004). Algen und Pilze an Fassaden – Ursachen und Vermeidung, *Fraunhofer IRB Verlag*, Stuttgart, Germany

[2]   Doldt P. (2004). Algen-Pilze-Fassaden: Mängel vermeiden, rechtlich absichern – Fachwissen und Tipps für den Handwerker, *C. Maurer Druck und Verlag*, Geislingen/Steige, Germany

[3]   Eggert A. et al. (2006). Quantification of algal biofilms colonising building materials: chlorophyll a measured by PAM-fluorometry as a biomass parameter, *Biofouling* 2006, 22(1/2), London, UK, 79-90

[4]   District Court jurisdiction from 01.12.1999, Frankfurt am Main, file reference 3-13 O 104/96

[5]   Fits C., et al. (2006). Mikrobielles Wachstum auf Fassaden – Ergebnisse einer mehrjährig kontrollierten Freilandexposition, *Altbauinstandsetzung 8: Fassadenbiofilme* (Venzmer H., editor), HUSS-Medien GmbH - Verlag Bauwesen, Berlin, Germany

[6]   Krus M., Rösler D., Sedlbauer K. (2006). Mikrobielles Wachstum auf Fassaden – Hygrothermische Modellierung, *Altbauinstandsetzung 8: Fassadenbiofilme* (Venzmer H., editor), HUSS-Medien GmbH - Verlag Bauwesen, Berlin, Germany

[7]   Lange O. L., Bilger W., Rimke S., Schreiber U. (1989). Chlorophyll Fluorescence of Lichens Containing Green and Blue-Green Algae During Hydration by Water Vapor Uptake and by Addition of Liquid Water, *Botanica Acta*, 102, Deutsche Botanische Gesellschaft e. V., Berlin, Germany, 306-313

[8]   Nay M. (2003). Algen und Pilze an Fassaden – Forschung an der EMPA St. Gallen, *Altbauinstandsetzung 5/6: Algen an Fassadenbaustoffen II* (Venzmer H., editor), HUSS-Medien GmbH - Verlag Bauwesen, Berlin, Germany

[9]   Sedlbauer K. et al. (2006). Algenbildung an Außenfassaden – Eine Übersicht über Forschung und Entwicklung, *Altbauinstandsetzung 8: Fassadenbiofilme* (Venzmer H., editor), HUSS-Medien GmbH - Verlag Bauwesen, Berlin, Germany

[10]   Venzmer H. et. al. (2004). Bautechnische Grundlagen zur Algenbesiedlung nachträglich wärmegedämmter Fassaden, *Bauphysikkalender 2004* (Cziesielski E., editor), Ernst und Sohn Verlag, Geislingen/Steige, Germany

[11]   von Werder J. and Venzmer H. (2007). New diagnostic strategies to quantify algal growth on facade materials – an important step in advancing product development, *Proceedings of the 12th Symposium for Building Physics*, Vol. 2, March 2007, Technical University of Dresden, Germany, 963-971

Analysis and modelling of effective thermal conductivity of dry porous building materials

Peter Matiasovsky, Dr.Ing.,
Institute of Construction and Architecture, Slovak Academy of Sciences;
usarmat@savba.sk

Olga Koronthalyova, PhD.,
Institute of Construction and Architecture, Slovak Academy of Sciences;
usarkoro@savba.sk

KEYWORDS: *effective thermal conductivity, models, fractal dimension.*

SUMMARY:
Thermal conductivity of dry porous building materials is determined by configuration of their solid and gaseous phases. Particular solid components and pore volume fractions can have different configurations in a material volume. For materials with the ideally continuous high conductivity components and the discrete low conductivity components the macroscopic transport coefficient can be obtained by summation the thermal conductivities of all particular components fractions proportionally to their relative volume portions. In case of the materials with discrete high conductivity components in the ideally continuous low conductivity volume fractions a serial configuration of the components can be applied. These two models represent the simplest - Wiener bounds of thermal conductivity. In practice the models for evaluation of the effective thermal conductivity of porous composite materials are based on the combination of parallel and serial configuration of particular phases and components. The problem of empiric factor of each model is to determine the adequate portion of the serial and parallel components depending on their microstructure. The thermal conductivity of dry porous building materials can be expressed by Wiener models of the configuration of high and low conductivity components, in which the degree of the regularity of continuous phases is expressed by the power functions of their volume fractions. The exponents express the degree of deviations of real component volumes from an ideal continuity supposed in Wiener models. The exponents include a fractal dimension of particular components. Relationships between the exponents and the fractal dimensions of various materials were analysed. The fractal dimensions were determined from microscopy pictures of the considered materials by a box counting method.

1. Introduction

Most of the building materials are composites, and their thermal pproperties result from the properties of their particular phases and components. The components can be differentiated according to their function in a material. Usually the composite consists of the bonding matrix, aggregate and the pore space. Thermal properties of dry porous materials are predominantly given by the properties of the solid phase as a whole and the pore volume. The known relationships among the solid phase composition and properties, the pore structure parameters and the composite material thermal properties enable to model, predict and develop the thermal properties of the porous materials only from the knowledge of properties of the solid phase and the pore space. In practice the thermal parameters of the porous composite material always represent the complex and mutual interaction of the solid and fluid phases in the heat transport process. Therefore it is difficult to produce the pure dense single solid phase component material for testing which would have the properties identical with the properties of the solid in a real porous composite. The simplest way to determine the solid phase properties for modelling is still to measure the thermal parameters of real porous materials and to analyse them using standard information on the composition and pore structure. In order to analyse the microstructure – thermal conductivity relationships the thermal conductivities and composition of the 26 various dry materials as fired clay bricks, mortars, plasters and insulation boards and the autoclaved aerated concrete, foamglass, expanded polystyrene and aluminium foam were compared. From the analysis of these data two basic models of thermal conductivity were proposed.

2. Theory

Considering the links between microscopic and macroscopic material parameters the basic material properties for modelling are the parameters of the solid or its components and the pore space parameters. Generally, the relationships between micro- and macro- structural porous material parameters can be expressed by a model in which the transport parameter k of the *ith* percolated material component fraction can be approximated according to the power law expression (Sahimi 1996, Berkowitz&Balberg 1993, Bunde&Dieterich 2000):

$$k = k_i \left(\Phi_i - \Phi_{i,crit} \right)^{n_i} \tag{1}$$

where: $n_i = 1+FD$ is the crical exponent, k_i is the thermal conductivity, Φ_i is the volume fraction, $\Phi_{i,crit}$ is a critical volume needed for a connected network to be formed through the material, the term Φ_i - $\Phi_{i,crit}$ is a relevant volume portion considered.

- The *critical volume* is also known as the critical threshold volume for transport parameter percolation. The critical volume value is specific for particular transport processes. The volume participates in the transport only if some critical minimum part of the volume is present. If $\Phi_i < \Phi_{i,crit}$, the component volume fraction is not percolated in the material volume. In such a case it is necessary to take into consideration the dispersion of the component fraction in/with other components fractions.

- FD is *the fractal* dimension of the component. For example in case of the pore volume the pore size distribution curve in a double logarithmic representation can be divided into the pore space fractions characterized by a constant slope and indicating the ranges of self-similarity. The slope of each fraction gives the fractal dimension of the pores in the fraction. The exponent n_i expresses the deviations of the real component from a continuous model: variable cross-sectional shape, variable cross-sectional size, tortuosity, connectivity of the component network, existence of the insulated components, abrupt changes of cross-sectional shape.

Particular components of a material can have a different dominant configuration in material volume. For the materials containing continuous high conductivity components fractions, together with the discrete low conductivity components, the macroscopic (effective) thermal conductivity can be obtained by the summation of the contribution of all particular components fractions:

$$\lambda = \sum_i \lambda_i \left(\Phi_i - \Phi_{i,crit} \right)^{n_i} \tag{2}$$

where $n_i = 1$ in case of the ideal parallel configuration of the components.

In case of the discrete high conductivity components dispersed in the continuous low conductivity components the following relation can be applied:

$$\lambda = \frac{1}{\sum_i \dfrac{\left(\Phi_i - \Phi_{i,crit} \right)^{n_i}}{\lambda_i}} \tag{3}$$

where $n_i = 1$ in case of the ideal serial configuration of the components.

In next parts the materials, the thermal conductivities of the materials, which can be modelled by equations (2) and (3) will be analysed.

3. Results

3.1 Materials with continuous low conductivity components

Some dry building materials (fired clay bricks, mortars, plasters, calcium-silicate boards) can be supposed as typical two-phase composites, consisting of the bonding matrix, reinforcement, aggregate or lightweight filler. Generally, they consist of the discretly dispersed high conductivity aggregate and dense binder matrix and the continuous low conductivity zone created by a pore space in a combination with some part of the binder matrix.

The thermal conductivity of the analysed materials was measured by the guarded hot plate method and the monotonic heating regime method (Klarsfeld 1984). The dry bulk density of the considered materials was in the range of $\rho = 200 - 2000$ kg/m^3. The best correlation between the thermal conductivity and the total porosity of the analysed bricks, plasters (Matiasovsky&Koronthalyova 2003) can be expressed by the following empirical formula:

$$\lambda_{dry} = \frac{1}{\dfrac{\Phi^2}{0.064}} \qquad\qquad (4)$$

where Φ is the total porosity [m^3/m^3].

In figure 1 the measured dry thermal conductivity values for materials with different total porosities are shown.
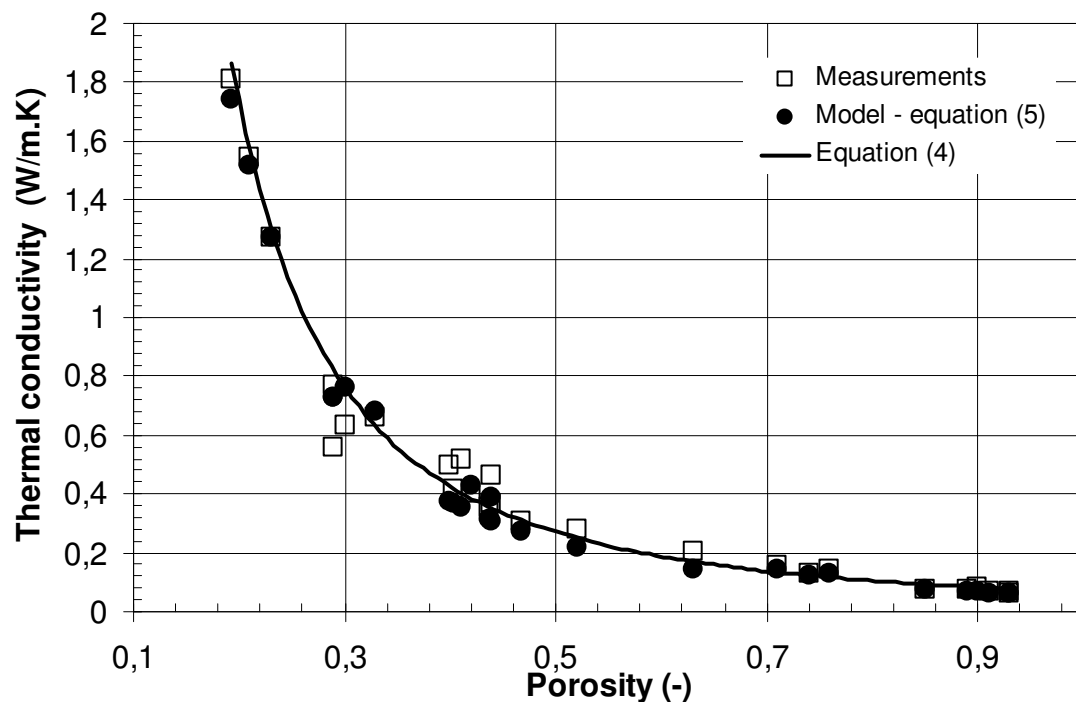
FIG. 1: Effective thermal conductivity of clay bricks, mortars, plasters and insulation boards vs. total porosity [m^3/m^3], comparison of calculated and measured values.

3.2   Materials with continuous high conductivity components

The other types of building materials (the foam glass, the aluminium foam, the expanded polystyrene, the polystyrene plaster, the autoclaved aerated concrete, etc.) are characterised by two components: the continuous zone created by the high conductivity matrix, possibly with micropores, and the dispersed low conductivity components (lightweight fillers), or macropores. The widely available data on parameters of these materials are in table 1.

TABLE. 1: Compositions, components and effective thermal conductivities of materials with continuous high conductivity components, their critical exponents.

Material	High conductivity component		Low conductivity component		Effective thermal conductivity	Critical exponent
	Volume portion	Thermal conductivity	Volume portion	Thermal conductivity		
AAC	0.5	0.26	0.5	0.025	0.43	1.0
Foamglass	0.1	0.76	0.9	0.025	0.058	1.34
Expanded polystyrene	0.02	0.154	0.98	0.025	0.033	1.0
Aluminium foam	0.1	204.0	0.9	0.025	9.60	1.33
Perlite plaster	0.18	0.77	0.82	0.1	0.13	1.6
Perlite plaster	0.2	0.77	0.8	0.1	0.155	1.45
Polystyrene plaster	0.149	0.77	0.57	0.043	0.075	1.43
Polystyrene plaster	0.11	0.77	0.73	0.043	0.076	1.29

4. Analysis

4.1   Materials with continuous low conductivity components

Dry bricks, plasters and mortars are typically viewed as two-phase composite materials consisting of discrete aggregate dispersed in a continuous porous matrix. Considering that in the dry matrix the region of the discontinuous material and the region of the bulk material can be distinguished the model of the thermal conductivity of these materials should issue from the following assumptions:
- in general the materials consist of two different zones: the aggregate and bulk matrix zone and the porosity including discontinuous matrix.
- the most conductive zone – aggregate is discontinuously dispersed in the matrix. The bulk matrix and aggregate are practically disconnected by the low conductivity continuous porous zone.

For the thermal conductivity of the mixture of two components: the continuous and porous matrix and the bulk matrix and ggregate for example the model of coated spheres assemblage is typical. For creating this model it is necessary to define the volume portion of the continuous zone.

It is interesting that the critical volume for pore space percolation of these materials in average equals 12 % (Matiasovsky, Koronthalyova 2006). This practically means that the low conductivity zone of the pore volume and discontinuous matrix fraction zone is percolated always. From the analysis of the results of measurements by fitting equation (3) it was found that the discontinuous matrix volume fraction represents in average ca 10 % of the total porosity. The resulting effective thermal conductivity of the bricks, mortars, plasters and insulation boards can be then expressed as a serial configuration of the high and low conductivity regions by the relation:

$$\lambda = \frac{1}{\dfrac{(1-1.1\cdot\Phi)^{n_1}}{\lambda_1} + \dfrac{(1.1\cdot\Phi)^{n_2}}{\lambda_2}}$$

<div align="right">(5)</div>

where: λ_1 and λ_2 are the thermal conductivities of high and low conductivity components respectively, Φ is the porosity.

The influence of a bulk paste to the material conductivity is relatively negligible. The whole pore space and discontinuous matrix zone volume portion is not ideally continuous, which is expressed by its critical exponents higher than 1.0. The exponents in relation (5) express mainly the fractal character of a pore structure – Eq. (1). From the fractal analysis of the considered materials the fractal dimensions of low conductivity zone from 1.0 to 1.8 were obtained, which gives the values of the exponent n_2 equal 2.0 for high porosity calcium-silicates and equal 2.8 for low porosity clay bricks. The values of critical exponent n_1 for high conductivity inclusions were considered equal to 1.0. The fractal dimensions were determined from SEM pictures of the considered materials by a box counting method (Zmeškal et al, 2001). Figure 2 describes the relationship between the fractal dimensions and the continuous component volume fractions of the imaginary two-component materials, characterized by the difference between fractal dimensions of ideally continouous volumes, close to 0.0 and the fractal dimensions of highly irregular volumes, diverging to the values higher than 2.0. The trends in the figure correspond well with the fractal dimensions of real materials.
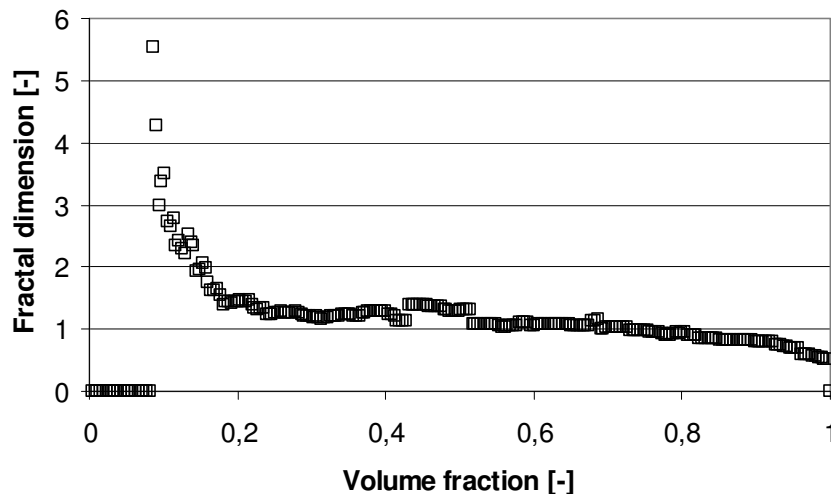
FIG. 2: Dependence of fractal dimension on continuous component geometry and volume fraction.

As the thermal conductivities of the bulk paste and mainly the aggregate in the relation (5) are significantly higher than thermal conductivity of the low conductivity zone, including porosity, the relation has practically a form of the approximation (4) obtained from the measurements. Considering the thermal conductivity of aggregate in the interval 3.0 – 6.0 W/(m.K) and the thermal conductivity of CSH 1.0 W/(m.K) the model expressed by relation (5) gives the values of thermal conductivity for different total porosity values close to the measured values, considering the thermal conductivity of quartz aggregate equal to 6.0 W/(m.K) (Matiasovsky&Koronthalyova 2003). The thermal conductivity of the low conductivity zone 0.064 W/(m.K) in relation (4) corresponds to the values measured for the pure CSH – xonotlite (Koronthalyova& Matiasovsky, 2003) representing the limit case material with 93 % porosity.

There are a lot of models for evaluation of the thermal conductivity of porous composite materials. Most of them are based on the combination of parallel and serial configuration of particular phases and components. The problem of empiric factor of each model is to determine the adequate portion of the parallel and serial

components. Simultaneously the thermal conductivities of components are significantly variable which increases the uncertainty of the model used. The models formulated by relation (3) try to minimize these uncertainties for a selected group of materials. They estimate the effective composite thermal conductivity from two relatively easily measurable parameters – the total porosity and the pore size distribution. From figure 1 it can be seen that the relationship (5) satisfactorily fits the thermal conductivities in a wide porosity range.

4.2 Materials with continuous high conductivity components

The materials with continuous high conductivity components can be divided into two characteristic groups: the materials with the dispersed low conductivity spheres of the same size (AAC and expanded polystyrene) and other materials. For the first group of materials it is typical that the fractal dimension of the high conductivity zone is 0.0. The fractal dimension of the second group varies in the range 0.0 – 0.6, depending on the regularity of the continuous zone. The effective thermal conductivities of these materials fulfil the equation (2). The critical exponents for low conductivity inclusions were considered equal to 1.0 and the values of the exponents for the high conductivity components are in table 1. The critical volumes of the high conductivity components were considered to be negligibly small.

5. Conclusions

The effective thermal conductivity of dry fired clay bricks, mortars, plasters and insulation boards can be modelled by the serial configuration of the high conductivity inclusions and the low conductivity zone conductivities (weighed by the power functions of their volume fractions). Thermal conductivity of bricks, mortars and plasters is in the first approximation proportional inversely to the second power of their total porosity.

The effective thermal conductivity of materials with continuous high conductivity components with the low conductivity inclusions can be modelled by the parallel configuration of the high conductivity zone and the low conductivity inclusions conductivities (weighed by the power functions of their volume fractions).

The exponents include the fractal dimensions of particular components and correspond to a regularity of their continuity in the materials.

6. References

Bagel, L. (2002) Microstructural parameters of plasters. Internal report. Institut of Construction and Architecture, SAS, Bratislava. (in Slovak)

Berkowitz B., Balberg I. (1993) Percolation theory and its application to groundwater hydrology. *Water resources research*, Vol 29, p. 775-794.

Bunde A., Dietrich W. (2000) Percolation in composites. *Journal of electroceramics*, Vol 5, p. 81-92.

Hashin Z. (1983) Analysis of composite materials – a survey. *Journal of Applied Mechanics*, Vol 50, p. 481-505

Klarsfeld S. (1984) Guarded Hot Plate Method for Thermal Conductivity Measurenent, in *Compendium of Thermophysical Property Measurement Methods, Vol.1 Survey of Measurement Techniques*, (Maglic K.D, Cezairliyan A., Peletsky V.E., editors), Plenum Press, London p. 169-230.

Koronthalyova O., Matiasovsky P. (2003) Thermal conductivity of fibre reinforced calcium silicate hydrate-based materials. Journal of Thermal Envelope and Building Science, Vol 26, p. 71-89.

Matiasovsky P., Koronthalyova O. (2003) Determination of thermal parameters of the composite building materials solid phase. *Research in Building Physics. Proceedings of the 2nd International Conference on Building Physics* (Carmeliet J., Hens H., Vermeir G, editors) Balkema, Antwerpen, Belgium, p. 109-113.

Matiašovský P. – Koronthályová O. (2006) Critical moisture contents for water and air transport in case of imbibition and drying tests. *Research in Building Physics and Building Engineering. Proceedings of the*

3rd International Building Physics Conference (Fazio, P., editor), Taylor & Francis Group, London, p. 43 – 48.

Meng, B (1994) Calculation of moisture transport cofficients on the basis of relevant pore structure parameters, Materials and Structures, Vol 27, p. 125-134.

Sahimi M. (1996) Linear and nonlinear, scalar and vector transport processes in heterogeneous media: Fractals, percolation, and scaling laws. *The chemical engineering journal*, Vol 64, p. 21-44.

Wiener O. (1912) Die Theorie des Mischkorpers fur das Feld des stationaren Stromung. *Abh. Math. –Physischen Klasse Konigl. Sacsh. Gesel. Wissen*, Vol 32, p. 509-604.

Zmeškal O, et al. (2001) HarFA – Harmonic and fractal image analysis. http://www.fch.vutbr.cz/lectures/imagesci/harfa.htm 3-5.

Ion binding isotherms of building materials

Milena Pavlíková, Ing., Ph.D.
Department of Materials Engineering and Chemistry, Faculty of Civil Engineering,
Czech Technical University in Prague, Thákurova 7, 166 29 Prague 6, Czech Republic
milena.pavlikova@fsv.cvut.cz, http://tpm.fsv.cvut.cz/

Lukáš Fiala, Ing.
Department of Materials Engineering and Chemistry, Faculty of Civil Engineering,
Czech Technical University in Prague, Thákurova 7, 166 29 Prague 6, Czech Republic
fialal@fsv.cvut.cz, http://tpm.fsv.cvut.cz/

Robert Černý, Prof., Ing., DrSc.
Department of Materials Engineering and Chemistry, Faculty of Civil Engineering,
Czech Technical University in Prague, Thákurova 7, 166 29 Prague 6, Czech Republic
cernyr@fsv.cvut.cz, http://tpm.fsv.cvut.cz/

KEYWORDS: chloride binding isotherms, cement paste, ceramic brick, sandstone, mineral wool, calcium silicate

SUMMARY:
Determination of chloride binding isotherms is mostly confined to the concrete research because combination of chloride penetration and concrete carbonation accelerates the process of steel corrosion. However, the presence of chlorides can present a potential danger also for many other materials. For instance, very frequent source of chlorides in building materials are salts used for winter maintenance of pavements and footways. They can diffuse either into underground soil or directly into the masonry so that they can damage renders, insulation materials and the masonry itself. The corrosion effects of these salts are mostly related to their crystallization from the solution, recrystallization from the solid phase, sometimes also to chemical reactions with building materials themselves. Chloride binding isotherms are mostly determined by the method of Tang and Nilsson based on the adsorption from solution. The measuring procedure is developed originally for crushed samples of cement paste and it is assumed that the content of cement is the main criterion for a possible recalculation to real concrete or cement mortar. However, the chloride binding capacity can be affected by many other factors, such as the change in the porous structure and pore distribution due to the application of different aggregates, the presence of various admixtures etc. In this paper, the chloride binding isotherms are determined for several different types of building materials; among them cement paste, ceramic brick, sandstone, mineral wool, and calcium silicate. Several different techniques are used for the concentration measurement, and the comparison of applied methods is done. The measurements involve common analytical determination of chloride concentration, application of ion selective electrodes, measuring of electrical conductivity, and using ion chromatography. The experiments are performed basically on small but not crushed specimens so that the effect of the porous structure is respected.

1.　Introduction

The presence of salts in building structures and porous building materials represents potential risk from the point of view of their durability and service life. Negative effect of salts consists in their crystallization from the salt solution owing to water evaporation and their recrystallization from the solid phase. Characteristic for crystallization process is the rise of crystallization pressures on the porous space walls that are dependent not only on amount of crystallized salt but also on material's porous structure, in fact on its texture and morphology. High crystallization pressures can then evoke failures of material and in some cases its destruction. On this account the water soluble salts together with moisture are considered to be one of frequent causes of breakdowns of building structures. Typical source of salts in building structures is intrusion of salty water from the grounds of buildings or capillary action of ground moisture. The problem of salt transport, their crystallization and thereby caused degradation, is very tricky question especially in sea coast areas, where the salt transport is realized in the form of sea water or in the solid phase by wind and secondary by force of water movement.

Water movement is the most significant factor in the process of transporting ions from the surface into the porous matrix. However, the matrix is not inert to the ions and only a part of them penetrating into the porous system can be freely transported in the solution, another part of ions can be bound on the pore walls due to either physical or chemical mechanisms [Černý R. and Rovnaníková P. (2002)]. Therefore, two basic ion phases are generally presented in material, namely free ions that are dissolved in pore water and bound ions that are fixed on the pore walls. Among the mechanisms bonding the ions to the pore walls, the adsorption due to van der Waals forces seems to be a very important effect. In addition to the adsorption of ions on the pore walls, there is also another effect that could play a significant role in ion binding to the pore walls. This is a possible reaction of ions with active phases of material that may be considered as the most important potential chemical mechanism of ion binding in porous materials. However, it should be noted that these reactions are not yet explored in all detail at the moment and there are even not any conclusions concerning their products that would be generally accepted by the investigators' community.

It is very difficult to distinguish between the physical and chemical bonding mechanisms on the macroscopic level, so, for practical reasons both these effects are usually unified into one phenomenological ion storage parameter. This is the dependence of the amount of bound ions c_b in the material on the free ion concentration c_f in the pore solution in equilibrium conditions that is called the ion binding isotherm. From that definition is clear, for its determination it is necessary to measure both the content of free ions and the content of bound ions in the same specimen under equilibrium isothermal conditions. This is a very restricting condition; for that reason the number of techniques for determination of ion binding isotherms is rather limited. Basically, just two methods for measuring the ion binding isotherms are used in the current research practice. The first of them is based on the determination of the amount of free ions by the pore solution extraction from a sample using high pressure [Dhir, R.K., Jones, M.R. and Ahmed, H.E.H. (1990)]. The second method is based on the adsorption of ions in a sample due to a contact with external solution and was proposed by Tang and Nilsson [Tang L. and Nilsson L.O. (1993)].

However, despite the high frequency of application of both methods for determination of ion binding isotherms described above they should be taken with care. It has been found [Glass G.K., Wang Y. and Buenfeld N.R. (1996)] that the pore solution expression method under high pressure may lead to an overestimation of the level of free ions as high as 20% due to the release of some loosely bound ions. It has also been noted that the acid-soluble extraction may underestimate the total ion content by more than 10%, which has been proven again in later investigations.

In this paper, a slight modification of the adsorption method, taking into account the above considerations and problems associated with its original version and so using the specimens of more realistic dimensions is chosen for the nitrate binding isotherms determination. Several building materials with different composition and structure, among them cement paste, ceramic brick, sandstone, mineral wool, and calcium silicate, exposed to NaCl solution are analyzed with different methods, namely analytical determination of chloride concentration, application of ion selective electrodes, measuring of electrical conductivity, and using ion chromatography.

2.   Analytical methods using for ion concentration determination

The concentration of chlorides can be determined by Mohr's analytical analysis, which is based on coagulating titrimetry. The reaction of chlorides with silver ions results in the little soluble silver chloride. The titrimetry end-point is indicated by a chromium ion, which reacts with silver ions and forms reddish brown precipitate. The reaction is affected by the pH of the titrimetric solution. It was found that the best results are obtained for the pH value of the solution between 6.5 and 10. At first it is important to prepare standard 0.05 M NaCl solution with the exactly known substance concentration. Then the measuring solution 0.05 M $AgNO_3$ is prepared. The next step is to pinpoint the titre of the measuring solution by titration of NaCl with $AgNO_3$ on the K_2CrO_4 indicator. The concentration of chlorides in the tested solutions can be then calculated from the consumption of the measured solution during titration, the known tested solution volume, and titre of the measuring solution. This is very time consuming method, which is influenced by human factor.

The amount of chloride ions in liquid samples can be easily and rapidly determined using chloride selective electrodes. The measuring apparatus consists of pH/ION measuring device and electrochemical (ISE) cell, which is formed by combined electrode. Combined chloride ion selective electrode is equipped with silver chloride membrane and Ag/AgCl electrode. The main component of the electroactive membrane is a neutral compound which is able to convert the complex ions and to transfer them through the membrane. The most important step

is to calibrate ion selective electrode with NaCl standard solution. To create optimum conditions for measurement, conditioning solution is put into measured solution. It provides a constant ionic strength and similar diffusion potentials at combined electrode in standard and test samples. Then the ISE cell is immersed into measured solution and chloride concentration in mg/l solution is shown on the display of the pH/ION measuring device. This analytical method is easy to use but a lot of effects can influence precision, for example interfering ions can raise 10% measuring error. Also measuring conditions, high temperature, rapid temperature changes or frequent measuring with high ions concentrations negatively affect measuring precision.

EASY TEST, Poland, constructed the measured equipment LOM/RS/6/mps, which is based on the TDR technology with $\sin^2$-like needle pulse having rise-time of about 200 ps. This device makes possible to record time dependent values of moisture, water capillary pressure (water matrix potential), temperature, and water electrical conductivity in wet material [Pavlík Z. (2004)]. LP/ms probe (Fig. 1) is designed for monitoring changes in water and salt distribution in material. The sensor is made of two 53 mm long parallel stainless steel rods, having 0.8 mm in diameter and separated by 5 mm. The probe cable length from the sensor to the multiplexer is 1 m and cable feeder length from the multiplexer to LOM is 3m.
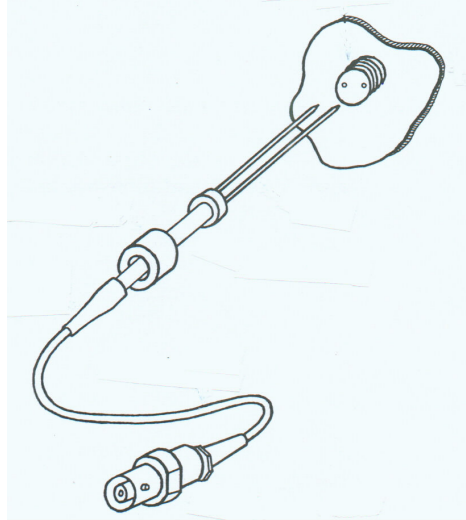
FIG.1: LP/ms minihygrometry probe.

The miniaturized probes can be used for measuring electrical conductivity in the range from 0.000 to 1.000 Sm^{-1} in solution or water and salt distribution in material. Firstly, electrical conductivity is calibrated from known solution concentrations, measured for example with pH/ION device. Then, probes are placed in prepared holes in dry samples. Fig. 2 shows the output of measurement. Using of miniaturized probes is comfortable in the case of soils and solutions with low salt concentrations; in the case of porous building materials it is difficult to install probes in the right way. Producer declares measurement relative error ± 5 %.
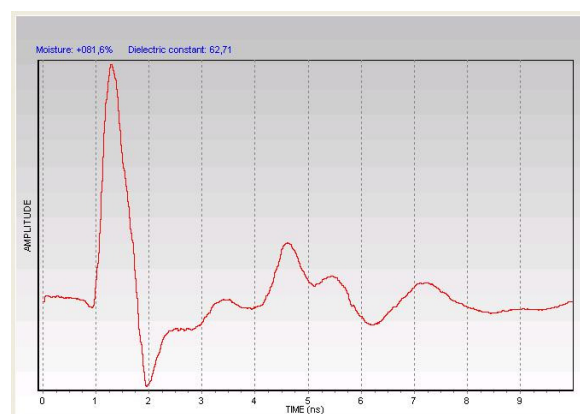
FIG. 2: Output of measurement with miniaturized probe.

The ion chromatography is used for analysis of aqueous samples in parts-per-million (ppm) quantities of common anions, such as fluoride, chloride, nitrite, nitrate, and sulphate, and common cations like lithium, sodium, ammonium, and potassium, using conductivity detectors. Liquid-solid adsorption chromatography (LSC) is one of the forms of liquid chromatography in which the stationary phase is a solid adsorbent [Navi L., Saari-Nordhaus R. and Anderson J. M. (1993)]. In our case glass column is filled with hydroxyethylmethacrylate sorbent which is stable for pH 2-12. For anion concentration measurement as a mobile phase 5mM KHP, 5% CAN is used. Firstly, measuring device should be calibrated with no less than two different concentrated solutions. Tested solution has to be filtered into the syringe to remove solid particles. Then filtered solution is diluted and with Hamilton syringe injects into Rheodyne Injection Kit. This simple manual device for accurate and reproducible sample injecting consists of Rheodyne 7725i injecting valve, 20 µl sample loop, and holder for mounting of the valve to a pump or to a detector. MIK 010 enables injection of 1 µl to 5 ml of a sample according to used sample. Conductivity detector is designed to continuously determine electrical conductivity of liquids that pass through its detector cell (capacity 2.5 µl) which is connected to an ion chromatograph. As the solution conductivity is highly affected by its temperature, temperature around the detector cell is kept at a constant level by temperature control system using a heater. The last part of measuring device is intelligent instrument interface box designed to collect analogue data, and input and output digital signals. Special scientific software enables to control measuring process, to calibrate device, and to collect and evaluate results. Fig. 3 represents output of ion concentration measurement.
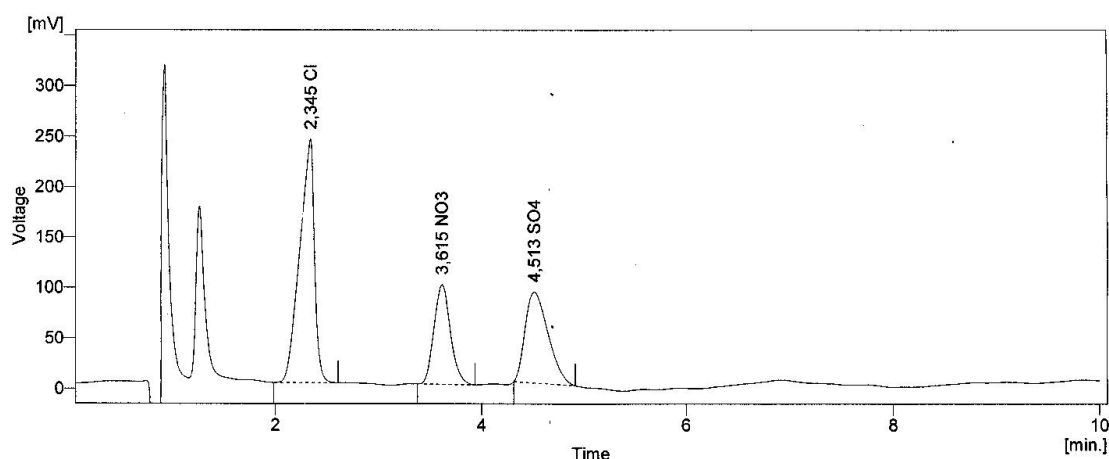
FIG. 3: Output of ion chromatography measurement.

The ion chromatography greatest utility is for analysis of anions for which there are no other rapid analytical methods, for example sulphates. It is also commonly used for cations and biochemical species such as amino acids and proteins. It is the most precise analytical method for very low ions concentrations determination. It should be noted, that liquid chromatography is high sensitive device and it is important to use ultra-pure water with conductivity below 0.1 µS/cm.

3. Materials and samples

Five different types of building materials, namely cement paste, ceramic brick, sandstone, mineral wool, and calcium silicate were chosen for measuring chloride binding isotherms.

The samples of cement paste were prepared from Portland cement CEM I 42.5R, and deionised water in the form of standard prisms (40x40x160 mm). The water/cement ratio was 0.4. After the hardening period of 28 days, the samples were stored at the laboratory temperature of 22±2°C to remove moisture.

Ceramic brick were made from brick-clay, clay and sand as it is usual in their production. In our experimental work we have chosen a standard ceramic brick produced in the Czech Republic.

Mšené sandstone is fine-grained, white-greyish, and mostly yellow in colour with yellowish to brownish stains. It is psamitic equigranular rock, about 95% of which is made up of suboval quartz clasts [Pavlík Z. (2007)].

Other mineral grains are present only as accessories (tourmaline, epidote, muscovite and zircone). Quartz grains reach up to 0.1 mm in diameter, but those of muscovite are larger, up to 0.3 mm. The matrix is formed by clay minerals, mainly kaolinite.

The mineral wool was of Czech origin and contained hydrophilic substances. For its manufacturing basaltoids extracted in the Bílčice quarry were used as a petrurgical raw material due to their fine-grained and homogeneous texture [Slivka V. and Vavro M., (1996)]. The final material consisted of bassinet, greystone, limestone and cokes.

The calcium silicate plate was a low-density board product mainly used as capillary active inside insulation because of its very high capillary absorption coefficient and capillary moisture content. The raw materials were calcium oxide and silica, which reacted with water to form calcium silicates. In our experiments we used a material with the bulk density of 310 kgm^{-3} which was produced in Germany. The material had the following basic composition: calcium silicate hydrate 75-90%, mineral loading 0-20% and cellulose 3-6%. The material was largely composed of synthetic mineral xonotlite, a complex calcium silicate hydrate [Hamilton M. and Hall C. (2003)], and of cellulose fibers, clearly visible on SEM-images of low magnification.

The samples for the measurements of chloride binding isotherms were cut from the standard prisms in the case of cement paste and from the commercially produced plates in the case of brick, sandstone, mineral wool and calcium silicate (size of 40x40x10 mm).

4.   Experimental results and discussion

In the experimental work, the adsorption procedure by Tang and Nilsson [Tang L. and Nilsson L.O. (1993)] was followed with some modifications. The dry samples were placed into the cups with 200 ml chloride solution. Then they were stored in laboratory at the temperature of 22±2°C to reach equilibrium. The inside solutions were analyzed after 4 months, the concentration of chlorides was determined by methods mentioned before. The lowest concentrations were measured with ion chromatography, intermediate and high concentrations with pH/ION device and by Mohr's analysis. Continuously salt contents in samples were monitored with equipment LOM/RS/6/mps until the steady state was reached. From the obtained data the bound chloride content was calculated and chloride binding isotherms were plotted.
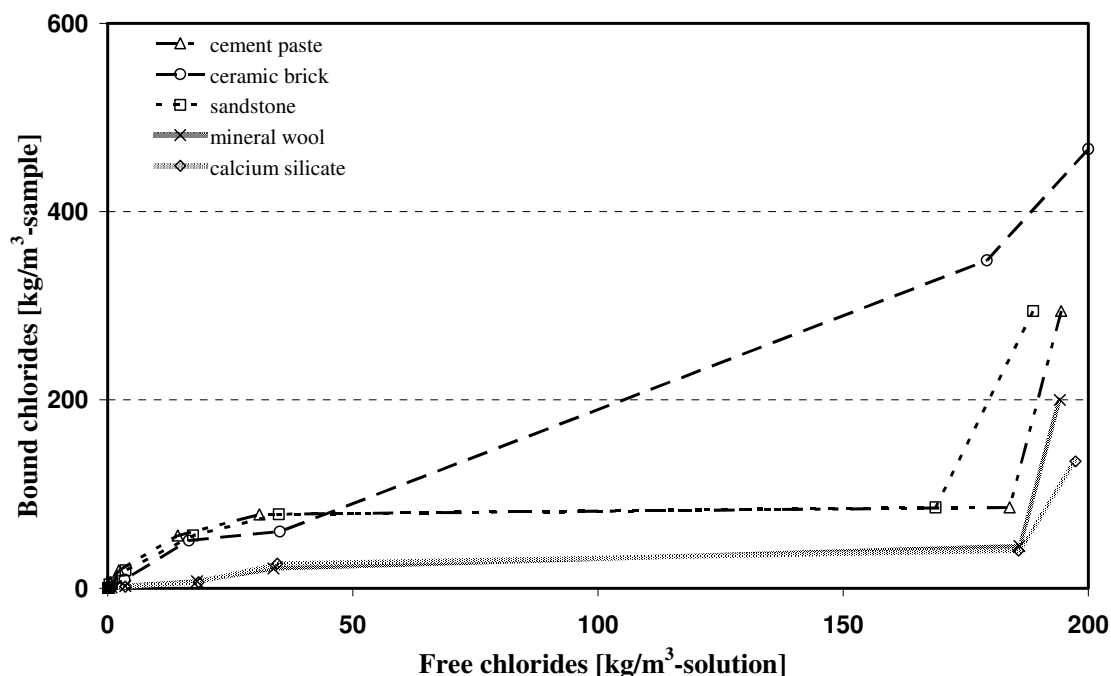
FIG. 4: Chloride binding isotherms.

The measured results are summarized in Fig. 4. We can see that the highest chloride binding capacity in lower chloride concentration range exhibited cement paste and sandstone and in higher chloride concentration range ceramic brick. This is primarily due to the bulk densities of tested materials because the amount of bound chlorides is expressed in kg/m^3-sample. The remarkable differences in the shape of chloride binding isotherms of ceramic brick and the other materials are clearly due to their different internal structure. Shapes of the chloride binding isotherm of measured materials evoked the shape of their sorption isotherms. This could mean that the fast increase of the amount of bound chlorides for higher concentration than 0.5 M was due to the chloride bonding on the pore walls of larger pores which have much higher capacity.

5.   Conclusions

The chloride binding isotherms of five different types of building materials were determined in the paper. These materials had various composition and structure, pore distribution and size, as well as bulk density and specific pore surface. The materials were tested in the form of small samples using different analytical methods.

The main conclusion following from the experiments performed in the paper is that the chloride binding capacity of porous building materials depends besides the material composition also on many other factors such as the volume and surface of pores, the pore distribution, the texture and morphology of the porous space. For future work it seems reasonable to assess the chloride binding capacity of a material as a relative quantity, i.e., to recalculate the amount of bound salts to the interior pore surface. In this way the role of material composition in chloride bonding would be expressed in a more appropriate way.

6.   References

Černý R. and Rovnaníková P. (2002). Transport Processes in Concrete. Spon Press, London.

Dhir R.K., Jones M.R. and Ahmed H.E.H. (1990). Determination of total and soluble chlorides in concrete. Cement and Concrete Research, Vol. 20, p. 579-590.

Glass G.K., Wang Y. and Buenfeld N.R. (1996). An investigation of experimental methods used to determine free and total chloride contents, Cement and Concrete Research, Vol. 26, p. 1443-1449.

Hamilton M. and Hall C. (2003). Water movement in porous building materials-VI. Evaporation and drying in brick and block materials. BLDG. Vol. 19, p.13-20.

Navi L., Saari-Nordhaus R. and Anderson J. M. (1993). Chromatographia, Journal of Chromatographia, Vol. 640, p. 41-48.

Pavlík Z. (2004). Development of a Semi-scale Technique for the Assessment of Hygro-thermal Performance of Multi-layered Systems of Building Materials, Praha: Czech Technical University in Prague, p. 88.

Pavlík Z. (2007). Basic approaches to the determination of hygrothermal performance of building structures In: Complex System of Methods for Directed Design and Assessment of Functional Properties of Building Materials. Praha: Czech Technical University in Prague, p. 67-72.

Slivka V. and Vavro M., (1996). The Significance of Textural and Structural Properties of North-Moravian basaltoids for the Manufacture of Mineral Fibres. Ceramics-Silikaty, Vol. 40.

Tang L. and Nilsson, L.O. (1993). Chloride binding capacity and binding isotherms of OPC pasted and mortars. Cement and Concrete Research, Vol. 23, p. 247-253.

Parametric Study of Salt Transport and Phase Transition Parameters in Simulations of Porous Materials Saturated with Salt Solutions under Drying Conditions

Andreas Nicolai, PhD
TU Dresden
andreas.nicolai@tu-dresden.de

John Grunewald, Prof. Dr.-Ing.
TU Dresden
john.grunewald@tu-dresden.de

KEYWORDS: *salt transport, phase transitions, HAM, simulation, parametric study, diffusion coefficient, tortuosity, drying experiment*

SUMMARY:
The influence and importance of the parameters of a comprehensive salt transport and phase transition model is investigated using simulations of drying experiments. First, the salt transport and phase transition model incorporated in the simulation program Delphin 5 is reviewed. Then, a discussion of simulations of drying experiments with brick materials saturated with salt solutions follows. The processes occurring in drying experiments with salt solutions are investigated and explained. A variation study on the influence of the diffusion coefficient and kinetic phase transition parameter is done. The influence of the parameters on the simulation results is shown.

1. Introduction

The durability of building materials and built-structures, and the costs related to material damage remain a central motivation for research aiming at improving construction designs and materials. The focus of this research paper is on salt-related damage to building materials. In addition to experimental research and field testing, the use of models and simulation tools can provide valuable insight into the phenomena resulting in or contributing to salt-related damage. Hereby, models are particularly useful for developing an in-depth understanding of the complex, interconnected processes occuring within building materials.

However, modeling salt transport in porous media requires many parameters in addition to a comprehensive hygrothermal material parametrization. Since moisture is the transport medium for salt, an accurate model for liquid transport in porous media is a necessity. The influence of salt on moisture transport has to be taken into account. Salt phase transitions, such as hydration and dehydration, also affect the moisture storage and transport in the porous media. These dependencies need to be incorporated in a hygrothermal transport model in form of parametric model extensions and additional balance equations.

Calibration and evaluation of salt transport models are typically done using laboratory experiments. Hereby, drying experiments are significantly more complex than other experiments, such as the solution absorption or diffusion-cell experiments. In drying experiments the moisture saturation of the material reduces from saturation to the hygroscopic range. The concentration of the solution varies between the initial concentration and saturation or super-saturation with respect to one or more salt phases. Salt phases may crystallize, dissolve, and form lower hydrate phases through dehydration. Salt convection and diffusion occurs simultaneously, wheras the corresponding salt mass fluxes vary over several orders of magnitude depending on location and time. Also, heat, moisture, and salt interactions are particularly strong in drying experiments. Therefore, simulations of drying experiments can be used to study the importance of various model parameters, as done below. First, however, an overview of the salt transport and phase transition model incorporated in the Delphin 5 model and simulation code will be given.

2. Overview of the Salt Transport and Phase Transition Model

The model described and used in this article has been recently published in Nicolai et al. (2007), and Nicolai (2008) and is based on the model of Grunewald (1997). It is a macroscopic continuum model that describes porous media as system of pores or voids within a solid material. The pores can be filled with gas phase, liquid phase, or crystalline salt phases. In the current model the material matrix phase is assumed to be inert. The liquid phase contains the components water and dissolved salt. In the model discussed here, salt solutions are by definition binary solutions. Thus, the dissolved salt can be described as single component of the liquid phase. Several solid salt phases can be present concurrently, which is necessary when several hydrate phases of a salt are thermodynamically stable in the considered temperature and humidity range. The set of conserved quantities can be summarized in the vector E

$$E = \left\{ U, m_{w+v}, m_s, m_{p,j} \right\}$$

where U = internal energy, m_{w+v} = moisture mass (liquid water and water vapor), m_s = dissolved salt mass and $m_{p,j}$ = precipitated salt phase j (depending on the salt, several hydrate phases of the salt may be thermodynamically stable). The material model, and in particular the moisture storage relation, allows calculation of intrinsic variables such as temperature, humidity, and pressures. The Pitzer-based salt mixture model provides thermodynamic properties of the salt solution, including the water activity and solution density. With the intensive quantities and a set of material functions (such as the liquid conductivity and vapor diffusivity) it is now possible to describe fluxes and source terms. These are used in balance equations, which are formulated for all densities $\rho^{<E>}$ of the conserved quantities E.

The details of the model can be found in Nicolai (2008). Here, only the relevant salt transport and phase transition terms will be presented. Also, the equations describing the salt-moisture interaction will be discussed below.

2.1 Salt Convection

Convection of dissolved salt is expressed in terms of the liquid mass flux density $\dot{j}_{conv,k}^{m_\ell}$. Equation (1) gives the mass flux density of the dissolved salt component with the mass concentration c_s defined as ratio of the masses of the dissolved salt and the salt solution $c_s = m_s / m_\ell$.

$$\dot{j}_{conv,k}^{m_s} = c_s \, \dot{j}_{conv,k}^{m_\ell} \tag{1}$$

The driving potential for liquid flux is the gradient of liquid pressure and the mass flux density is given in Equation (2).

$$\dot{j}_{conv,k}^{m_\ell} = -f_{K,\ell} K_\ell \frac{\partial p_\ell}{\partial x_k} \tag{2}$$

K_ℓ is the liquid conductivity determined for the salt-free material. The reduction factor $f_{K,\ell}$ expresses the overall effect of salt on liquid transport in the porous media. This includes the different viscosity of salt solutions compared to water, and the effect of salt on the driving potential (Nicolai et al., 2007). Assuming proportionality between the salt-related reduction of the liquid conductivity and the concentration of the solution, Equation (3) can be used to describe the dependence of the reduction factor on the concentration.

$$f_{K,\ell} = 1 - m_s f_{visc} \tag{3}$$

The propertionality factor f_{visc} can be obtained from solution absorption experiments using the relation given in Equation (4).

$$A_\ell^V \big/ A_{H_2O}^V = \sqrt{f_{K,\ell}} \tag{4}$$

2.2 Salt Diffusion

In addition to convective salt transport the diffusion of salt in the liquid phase needs to be considered. Salt diffusion is described using Fick's law (5). Here, the driving potential is the gradient of the molarity $c_{m,s}$.

$$j_{diff,k}^{\dot{m}_s} = -D_s \frac{\partial c_{m,s}}{\partial x_k} \tag{5}$$

The diffusion coefficient D_s must describe a number of effects and influencing factors, such as

- Deviation from ideal solution (the actual driving force for diffusion is the gradient of the chemical potential, which becomes after transformation the gradient of activity)

- Diffusion paths through the porous system

- Saturation degree, pore connectivity in unsaturated media, and availability of cross section for diffusion

- Temperature.

In this model the temperature influence is assumed to be negligible. However, the other factors are critical for describing salt diffusion correctly.

a) Effective diffusion path in saturated medium (tortuosity)

b) Longer diffusion paths in unsaturated material (effective tortuosity)

c) Reduced cross section available for diffusion in unsaturated material

d) Only isolated liquid filled pores, diffusion no longer possible
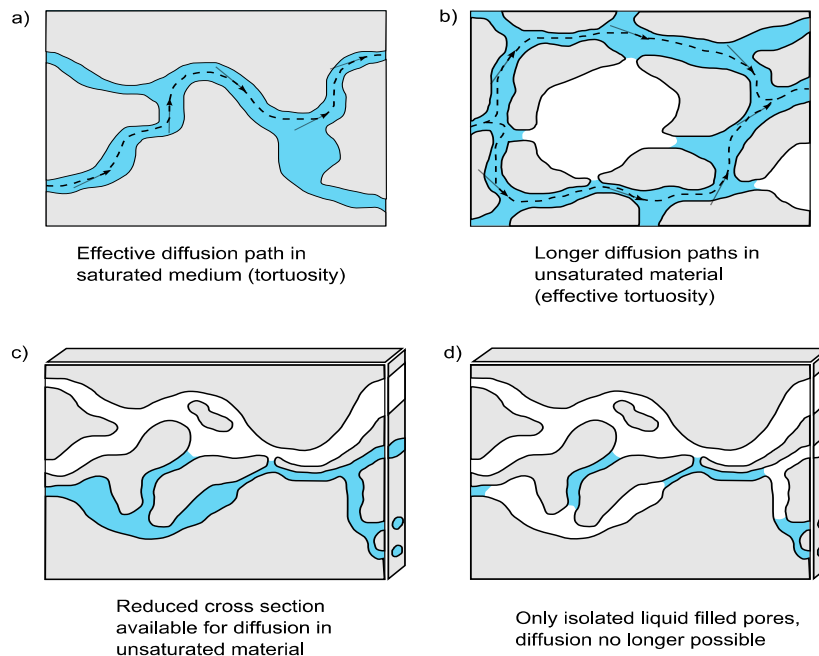
FIG. 1: Influence of Moisture Saturation on Salt Diffusion.

Following the approach of Buchwald (2000), the diffusion coefficient for salt diffusion inside the porous media is described as product of the diffusion coefficient for free solutions and various correction factors that account for the porous media (6).

$$D_s = D_{s,sol} \cdot \frac{1}{\tau} \left(\frac{\theta_\ell}{\theta_{\ell,sat}} \right)^n \tag{6}$$

The diffusion coefficient for free solutions $D_{s,sol}$ is concentration dependent, so that the gradient of molarity can be used as driving potential. The meaning of the other factors is illustrated in Figure 1. At lower moisture contents the diffusion of salt is slower then for fully saturated media. Figure 1a shows the extension of the diffusion path in the saturated material, expressed through the tortuosity τ. Two effects, illustrated in Figure 1b

and Figure 1c, result in reduction of the effective diffusivity in unsaturated materials. The saturation degree is expressed by the quotient $\theta_\ell / \theta_{\ell,sat}$ (equal to 1 for saturation, equal to 0 for the completely dry material). The moisture exponent n remains a fitting parameter to express the non-linearity of the moisture dependence of the salt diffusivity. Finally, Figure 1d shows that below a certain moisture content, salt diffusion may no longer be possible because the liquid phase becomes disconnected. Vogt introduced the limiting moisture content (Grunewald et al., 2005), which can be estimated using the liquid conductivity function in the low moisture content range. The moisture content, below which the liquid conductivity becomes very small and vapor diffusion becomes the dominating transport mode for moisture, can be interpreted as limiting moisture content for salt diffusion, also.

Of the parameters included in the diffusion coefficient model, only the tortuosity can be determined in diffusion experiments with saturated materials, provided that the diffusion coefficent for free solutions is known as concentration-dependent value. The moisture exponent can only be estimated from experiments with unsaturated materials.

2.3 Salt Phase Transitions

Salt phase transitions are described by kinetic source and sink terms for the different salt phases. Also the phase transitions between solid salt phases, hydration and dehydration, are described by kinetic parameters. The ability of the model to calculate super-saturations (only possible with a kinetic model) is critical for obtaining an important indicator for salt related damage Nicolai (2008). The kinetic model used here, first suggested by Espinosa (Espinosa et al., 2005), is based on the simple observation that the growth rate of crystals should be propertional to the super-saturation or sub-saturation of the solution. Hence, Equations (7) and (8) can be used to describe the formation and dissolution rates of a salt crystal, respectively.

$$\sigma_p = K_p \left(U - 1 \right)^{g_p} \qquad\qquad \sigma_{sol} = K_{sol} \left(1 - U \right)^{g_{sol}} \qquad\qquad (7), (8)$$

The saturation ratio U determines the direction of the process (the solution is exactly saturated when $U = 1$). The source or sink terms σ are described using the kinetic parameters K and g, whereas the latter describes the non-linearity of the $\sigma - U$ relation. The subscripts p and sol indicate crystallization/precipitation and dissolution, respectively. Hydration reactions can be described as combinations of dissolution of the anhydrate and crystallization of the hydrate phase (Nicolai, 2008). The kinetic constants are particularly important when the hygrothermal conditions change quickly due to variations in the ambient climate. Drying processes, but also quickly reduced temperatures may lead to significant super-saturations if the salt phase transition reactions are relatively slow.

2.4 Salt-Related Reduction of Vapor Pressure in Porous Media

The presence of salt within porous media results in reduction of vapor pressure and, thus, in change of the transport potential for vapor diffusion. Also, hydration and dehydration reactions depend on the actual vapor pressure inside the porous system. The effective relative humidity inside the pore system must be described as combination of capillary effects and reduction of equilibrium relative humidity of free salt solutions. The latter is expressed by the water activity, a thermodynamic property of salt solutions. The Kelvin Equation (9) describes the reduction of vapor pressure over a capillary meniscus and Equation (10) gives the effective relative humidity within the porous system partially saturated with salt solution.

$$\varphi_{Kelvin} = \exp\left(\frac{p_c}{\rho_w R_w T} \right) \qquad\qquad (9)$$

$$\varphi = \varphi_{Kelvin} \cdot \varphi_{Solution} = \exp\left(\frac{p_c}{\rho_w R_w T} \right) \cdot a_{H_2O} \qquad\qquad (10)$$

With increasing concentration the water activity and thus, also the relative humidity within the porous media decreases. This reduction of the relative humidity is the reason for the observed hygroscopicity of salt-containing

materials. Effectively, higher moisture contents are required in the material so that the relative humidity calculated with the Kelvin equation compensates the water activity.

The equations above have been implemented in the simulation tool Delphin 5 (Nicolai, 2008) which was used to simulate the drying experiment discussed below.

3. Drying of Porous Materials Saturated with Salt Solution

3.1 Principal Simulation Setup and Observed Processes

Drying experiments with salts have previously been done with emphasis on extension measurements (Poupeleer, 2007). Here, the transport processes and interactions between moisture and salt shall receive focus. Surface effects, such as efflorescence and related change of transfer coefficients are neglected in this study, as are clogging effects due to crystallization within the material matrix.

One-dimensional drying experiments are done with specimen saturated with pure water or salt solutions and sealed at all but one side. The specimen is then dried under controlled conditions (constant temperature, relative humidity, air velocity over evaporation side), and the weight loss and surface temperature are monitored. In drying experiments with pure water two distinct phases can be observed. While the drying rate in the first phase is nearly constant, the second phase is a long term process with decreasing drying rate. In the first phase the process is controlled only by surface conditions at the evaporation side. Moisture transport from the inside of the moist material to the evaporation side is fast and air movement over the evaporation surface, which is considered in the model through the heat and vapor exchange coefficients, is the limiting process. In the second phase the moisture transport to the evaporation side decreases and the drying rate is controlled by liquid and vapor transport properties of the material. Figure 2 (left) shows the simulated evaporation flux density and surface temperature.The latter descreases in stage I substancially as result of the evaporation cooling effect. Figure 2 (right) also shows the moisture mass integral within the material. The constant rate of drying in the first phase of the experiment is clearly visible in this chart. The simulations were done for a 5 cm brick material (one-dimensional simulations). The material properties and moisture transport and storage characteristics of the material were provided by Scheffler (Grunewald et al., 2005).
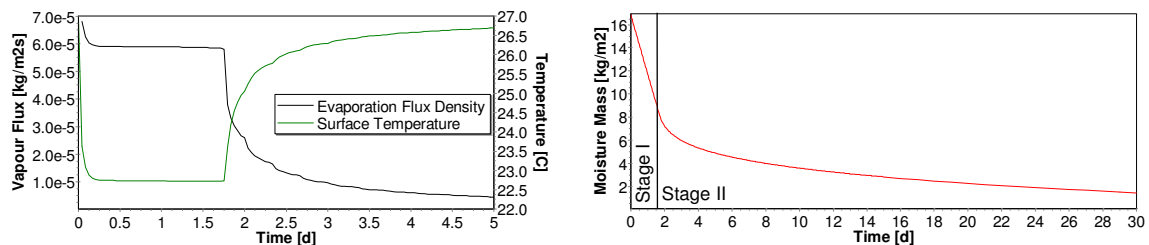
FIG. 2: Surface Temperature and Evaporation Flux Density (left) and Moisture Mass Integral (right) Obtained in a Simulation of a Drying Experiment with Water

3.2 Drying Experiments with Salt

In drying experiments with salt a number of different processes occur simultaneously. In the first phase the liquid transport to the evaporation side and associated salt convection leads to an increase in concentration at the evaporation side, a concentration gradient and consequently back-diffusion. However, salt convection remains the dominant transport mode throughout the first phase and the salt concentration at the evaporation side continues to increase. At some point the solution may become super-saturated and salt may crystallize. Depending on the kinetic parameters and drying conditions, significant super-saturations may be reached that allow crystallization even of thermodynamically unstable salts. The super-saturation reached at the evaporation side and also the crystallization depths depend on the kinetic phase transition coefficients and the salt diffusion coefficient.

The increasing concentration at the evaporation side also results in a lower water activity and relative humidity. Therfore, the drying rate in the first phase is no longer constant, once salt solutions are used. The effect is more

pronounced for solutions with higher concentrations. Also, the transition from the first to second drying phase is less visible for higher concentrated solutions. This is shown in Figure 3, where the vapor flux across the evaporation surface (left) and integral moisture masses (right) are shown for simulations with different initial concentrations of NaCl solutions.
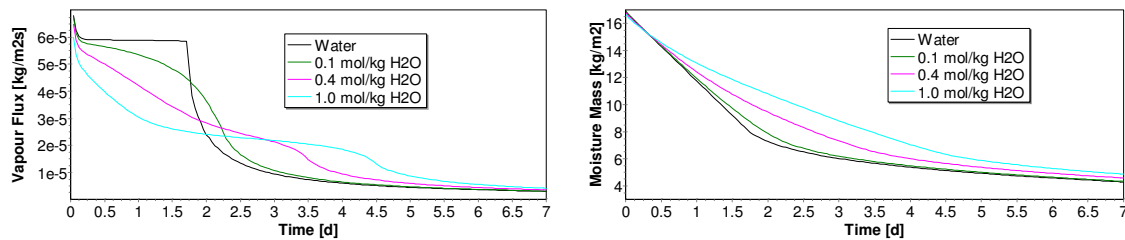
FIG. 3: Evaporation Flux Densities and Integral Moisture Masses for Various Initial Salt Concentrations of NaCl Solutions
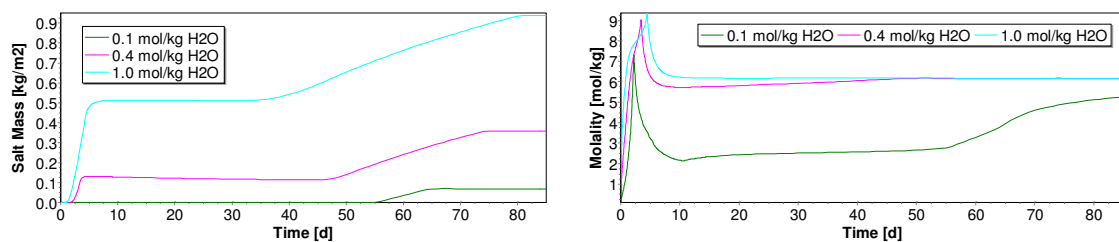
FIG. 4: Crystalline Salt Masses and Solution Concentrations at the Surface for Various Initial Salt Concentrations of NaCl Solutions

At the begin of the second stage the drying rate reduces, as does the convective salt transport. Consequently, the ratio between salt convection and salt diffusion changes and salt diffusion becomes temporarily the dominant mode of salt transport. This is illustrated in Figure 4 (right), where the concentrations of the salt solution at the evaporation surface are shown for the simulation cases with different initial NaCl concentrations. The characteristic peak, visible for each simulation case, marks the end of the first stage.

Also shown in Figure 4 (left) are the integral salt masses. In the simulations with higher concentrated NaCl solutions, crystallization occurs already in phase one. In stage two the transport rate of salt to the evaporation side is reduced and further crystallization at the surface results in a lower salt concentration of the solution. Because of back-diffusion, the solution can even become sub-saturated, as can be seen in Figure 4 (right).

Later in stage II the drying front moves further into the material. The drying front is hereby the zone with the transition from mostly liquid transport to mostly vapor transport. The continuing evaporation and increasing salt concentration within the material eventually leads to crystallization. A crystallization range, distinct from the surface crystallization zone is created, visible at the left side of Figure 5, which corresponds to the sealed part of the material. The right side is the evaporation side.

Aside from the moisture transport properties of the material, which defines the progressing of the drying zone, the limiting moisture content for salt diffusion is an important parameter that controls the distribution of the salt crystals within the porous media.

Important indicators for salt related damage is the maximum of the solution concentration (corresponding to super-saturations and crystallization rates), and the distribution of the salt. A variation study can help with identifying critical parameters that influnce these indicators.
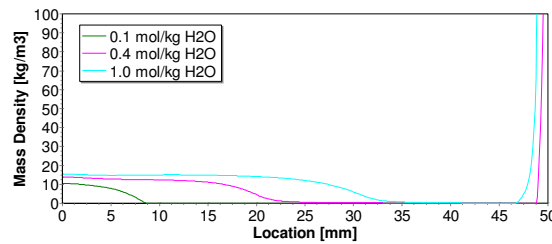
FIG. 5: Distribution of Precipitated Salt for Various Initial Concentrations of NaCl Solutions

3.3 Influence of the Diffusion Coefficient

In the present model, the diffusion coefficient is based on the diffusion coefficient for free solutions, and the material dependence is taken into account with the tortuosity and moisture exponent. A variation of the tortuosity over 2 orders of magnitude shows the relative importance of the diffusion coefficient in drying experiments.

A selection of simulation results is shown in Figure 6. The simulations were done as before on a 5 cm brick material. The diffusion coefficients varied between 0.1Ds and 10Ds (with respect to the original diffusion coefficient).
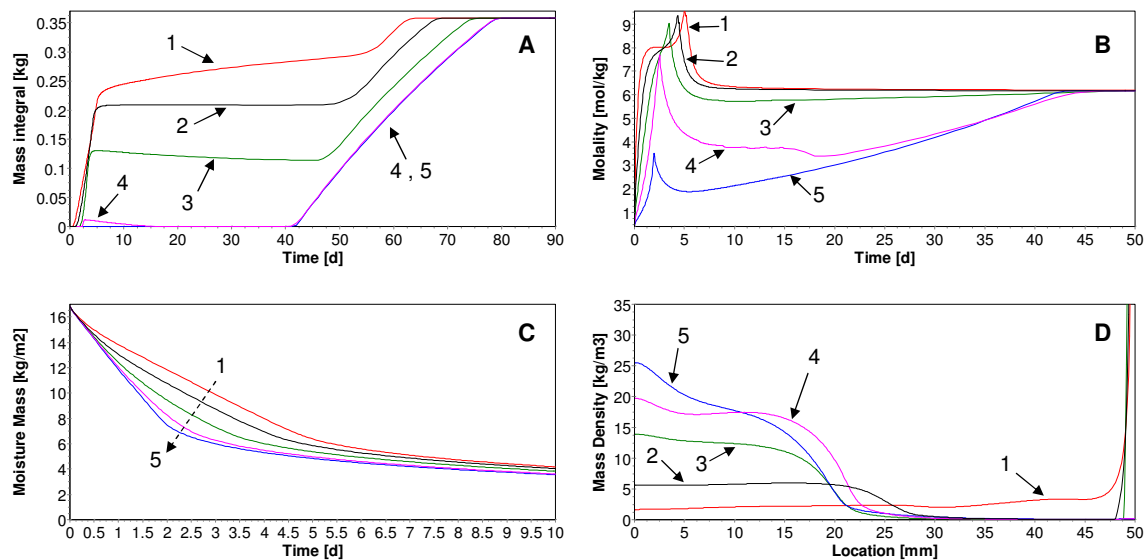
FIG. 6: Variation Study using NaCl Solution with Initial Concentration of 0.4 mol/kg H2O and Different Diffusion Coefficients: 1=0.1Ds, 2=0.3Ds, 3=1Ds, 4=3Ds, 5=10Ds

The diffusion coefficient most importantly affects the rate of back-diffusion. Figure 6b shows again the surface molalities and it is apparent that for large diffusion coefficients lower concentrations were calculated near the surface compared to the simulations with smaller diffusion coefficients. For case 4 the solution near the surface became temporarily super-saturated and salt crystallized (see Figure 6a). However, after begin of stage 2 the solution becomes sub-saturated because of back-diffusion and the salt dissolves again. The increased concentrations near the surface for the simulations with small diffusivities explain the slower drying rates (Figure 6c). Clearly, the vapor pressure reduction effect, expressed in Equation (10), must not be neglected. Finally the diffusion coefficient influences the shape of the second crystallization range. This is visible in the case of variant 1, where the diffusion coefficient is so small that even the strong gradients occurring near the end of the drying process will not result in a sufficient diffusion rate and the salt crystallizes at its current location.

While cases 1 and 5 are certainly extreme variations, the diffusion coefficients of the cases 2, 3, and 4 are in the same order of magnitude. Still, the results are quite different and it can be concluded that the diffusion coefficient is an important parameter and influences the results of drying experiments significantly.

A second parameter to be studied is the kinetic crystallization rate parameters K_p and K_{sol}.
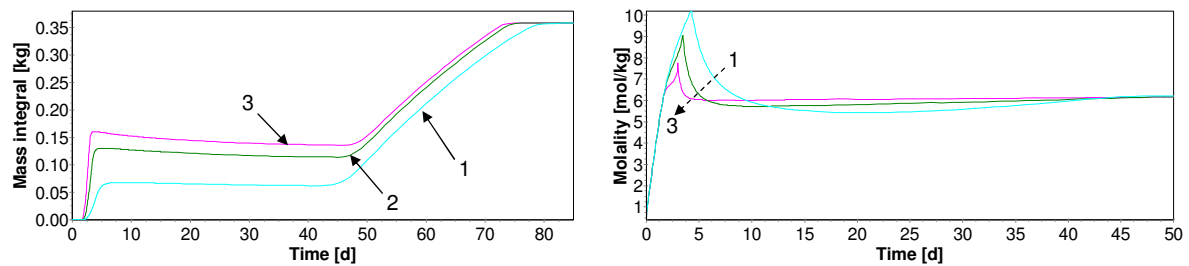
FIG. 7: Variation Study using NaCl Solution with Initial Concentration of 0.4 mol/kg H2O and Different Kinetic Reaction Coefficients: 1=1/10, 2=1, 3=10

The reaction rate parameters were varied over two orders of magnitude. The coefficients were reduced by a factor of 10 in case 1, and in case 3 the reaction rate coefficients were enlarged by one order of magnitude. As expected, the amount of crystallized salt increases with larger kinetic coefficients in the first stage as shown in Figure 7a. Figure 7b shows that the maximum of solution concentration also varies substantially. Lower reaction rates give rise to higher super-saturations and would allow precipitation of meta-stable phases.
Considering the calculated variations, the drying process does not seem to be as sensitive on the kinetic reaction coefficients as it is on the diffusion coefficient. It can be concluded that the order of magnitude of the kinetic reaction coefficients is important, but variations by a factor of two or similar will not give very different results.

4. Conclusions

For drying experiments with salt solutions the diffusion coefficient for salt and the kinetic phase transition parameters are critical parameters. The amount of crystallization in the first phase of the experiment depends on both parameters. Also the location of the crystallized salt at the end of the experiment depends on these parameters.
In the variation study it was found that the drying process is more sensitive to the diffusion coefficient compared to the kinetic reaction rate coefficients. Already variations of the diffusion coefficients within the same order of magnitude significantly altered.

5. References

Buchwald A. (2000) Ionentransportprozesse zur Verminderung von Schadsalzgehalten in porösen, feuchten Mauerwerksbaustoffen, Bauhaus-Universität Weimar. (english version not available)

Espinosa R., Franke L., Deckelmann G. (2007), Phase Changes of Salts in Porous Materials: Crystallization, Hydration and Deliquescence, Construction and Building Materials.

Grunewald J. (1997), Diffusiver und konvektiver Stoff- und Energietransport in kapillarporösen Baustoffen, Dissertation, University of Technology Dresden. (english version available in part as:

Grunewald J, et al. (2005) Modellierung, Software-Implementation and Verifikation des Feuchte- und Salztransportes, der Salzkristallisation und -schädigung in kapillar-porösen Mauerwerksbaustoffen DFG SPP 1122: Vorhersage des zeitlichen Verlaufs von physikalisch-chemischen Schädigungsprozessen an mineralischen Werkstoffen, Report Nr. 2. (english version not available)

Nicolai A., Grunewald J., Zhang, J.S. (2007), Salt Mixture Transport and Phase Transitions, Modeling and Numerical Solution in Delphin 5, Proceedings for the 12th Symposium for Building Physics, University of Technology Dresden.

Nicolai A. (2008), Modeling and Numerical Simulation of Salt Transport and Phase Transitions in Unsaturated Porous Building Materials, Dissertation, Syracuse University.

Poupeleer A. (2007), Transport and Crystallization of Dissolved Salts in Cracked Porous Building Materials, Dissertation, KU Leuven.

Simultaneous Heat, Moisture and Salt Transfer in Clothing

Masaru Abuku, PhD student,
Laboratory of Building Physics, Department of Civil Engineering, Katholieke Universiteit Leuven;
masaru.abuku@bwk.kuleuven.be

Shuichi Hokoi, Professor,
Department of Architecture and Architectural Engineering, Graduate School of Engineering, Kyoto University;
hokoi@archi.kyoto-u.ac.jp

Satoru Takada, Associate Professor,
Department of Architecture, Graduate School of Engineering, Kobe University;
satoruta@kobe-u.ac.jp

KEYWORDS: clothing, sweat, salt, heat and moisture transfer, sorption isotherm, vapour pressure depression, water uptake, modelling.

SUMMARY:
The simultaneous heat, moisture and salt transfer in a porous material is modelled in order to quantify the salt influences on the heat and moisture transfer in clothing. A model of the sorption isotherm of a cloth considering salt influences is proposed and then implemented in the system of the transport equations. Laboratory experiments of pure and salt water uptake are briefly presented. The experimental results are numerically analysed with the proposed model. The calculation results agreed fairly well with the measured ones.

1. Introduction

Sweat is of importance for the response of human body in a thermal environment. It is usually simplified as pure water when the influence of sweat on the human body temperature is analysed for the prediction of the thermal comfort (e.g. Farnworth, 1986; Takada, 2002). However in reality sweat is salt water with low concentration (e.g. the normal ranges of Na^+ and Cl^- concentrations of sweat at skin surfaces are 24 - 56 and 18 - 54 mmol/L respectively (Patterson et al., 2000)). The salt in the water has two influences on the water transport in porous materials: (1) it changes the vapour pressure of the water; (2) it also affects the permeability of water in clothing because of the blocking of water movement by salt. These influences of salt are also one of the great concerns in the field of building physics. The influence of salts on the permeability of building materials has been studied by e.g. Funk et al. (2006), Koniorczyk and Gawin (2006, 2007) and Poupeleer et al. (2006). On the other hand, although the sorption isotherm of a porous material containing salt water is dependent on the concentrations of salts in the water, this dependency seems to be often ignored. Amongst the past studies, Koniorczyk and Gawin (2007), however, modelled the dependency with use of reflection coefficient. This paper gives a mathematical basis to this model of the simultaneous heat, moisture and salt transfer in order to investigate the salt influences on the heat and moisture transfer in clothing. First, a model of the sorption isotherm of a cloth considering salt influences is proposed and then implemented in the system of the transport equations. The second part briefly reports on laboratory experiments of pure and salt water uptake, using sodium chloride that is the main impurity of sweat. Lastly the experimental results are numerically analysed with the proposed model.

2. Modelling of Heat, Moisture and Salt Transfer in a Cloth

2.1 Modelling of a sorption isotherm of a cloth containing salt water

The relative humidity x' [-] in a cloth which contains salt water can be given (Brocken et al., 1999) by:

$$x' = (1 - x_s) x \tag{1}$$

where x_s is the molar fraction [-] of salt in the salt water and x is the relative humidity [-] in a cloth which contains the same amount of pure water as the water in the salt water. Here x_s is expressed as:

$$x_s = i\phi \frac{C_s}{M_s} \bigg/ \left(\frac{1}{M_w} + i\phi \frac{C_s}{M_s} \right) \tag{2}$$

with i (=2 for sodium chloride) the Van't Hoff factor [-], ϕ ($\approx$1.5 for sodium chloride) the osmotic coefficient [-], C_s the salt concentration [kg(NaCl)/kg(H$_2$O)], and M_s and M_w the molar mass [kg/kmol] of salt and water respectively. Note that C_s is the ratio of the mass of salt to that of water in the cloth. The chemical potential μ [J/kg] of the water in the cloth is thus defined as:

$$\mu = R_v T \ln x' = R_v T \ln x + R_v T \ln(1 - x_s) = \mu_0 + \mu_c \tag{3}$$

with R_v the specific gas constant [J/kgK] of water vapour and T the temperature [K]. Here,

$$\mu_0 = R_v T \ln x \; ; \quad \mu_c = R_v T \ln(1 - x_s) \tag{4}$$

R_v is defined by:

$$R_v = R/M_w \tag{5}$$

where R is the universal gas constant [J/kmolK].

When the cloth only contains pure water, the component μ_0 can be given as a function of moisture content in mass fraction φ_w [kg/kg]. Based on the measurement data provided by Morton and Hearle (1962) for hygroscopic region and based on the one by Takada (2002) for saturation region, the following function is determined for 100 % cotton with a thickness of 0.25 mm:

$$\mu_0 = -10^4 \exp(-1000\varphi_w) - 4.8 \times 10^5 \exp(-25\varphi_w) - 1.95\exp(-0.5\varphi_w) + 1.005 \tag{6}$$

When the cloth contains salt water, μ_0 is considered to be dependent on the salt water content. Although μ_0 has to be determined based on measurements, no such measurement data is available. Assuming that the relative humidity in equilibrium with the cloth filled with the saturated salt water is 75 %, and taking into account the dependency of the density of the salt water on the salt concentration, the following function of μ_0 for the cloth containing the salt water is proposed:

$$\mu_0 = -10^4 \exp\left(-1000\frac{\rho_w}{\rho_{sw}}\varphi_{sw}\right) - 4.8 \times 10^5 \exp\left(-25\frac{\rho_w}{\rho_{sw}}\varphi_{sw}\right) - 1.95\exp\left(-0.5\frac{\rho_w}{\rho_{sw}}\varphi_{sw}\right) + 1.005 \tag{7}$$

with ρ_w and ρ_{sw} the density [kg/m^3] of pure water and salt water respectively, and φ_{sw} $(= (1 - C_s)\varphi_w)$ the salt water content in mass fraction [kg/kg].
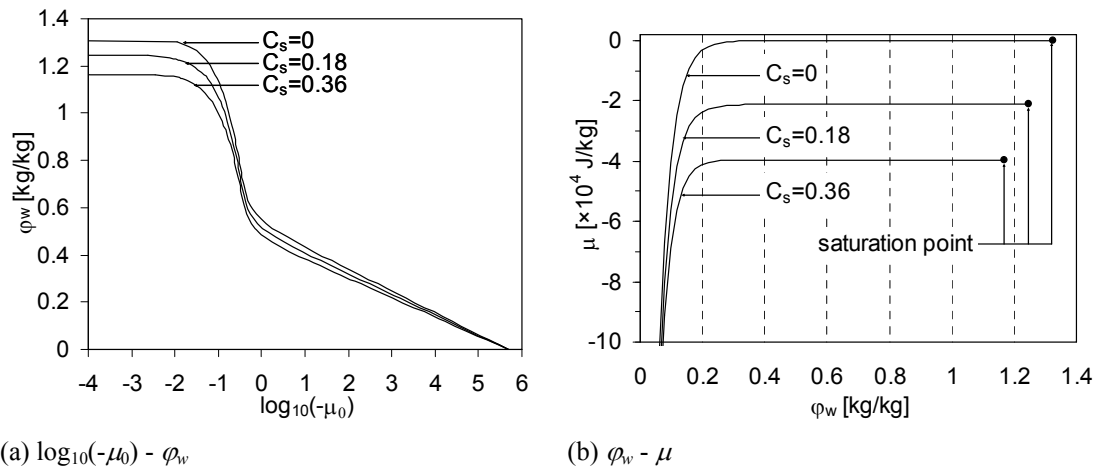
(a) $\log_{10}(-\mu_0)$ - φ_w (b) φ_w - μ

FIG. 1: (a) $\log_{10}(-\mu_0)$ and (b) μ of the cotton as a function of moisture content in mass fraction φ_w for pure water, salt water of C_s=0.18 and saturated salt water (C_s=0.36) in an absorption process at a temperature of 25 ºC.

Fig. 1 illustrates μ_0 and μ of the cotton as a function of moisture content in mass fraction φ_w for pure water, salt water of C_s=0.18 and saturated salt water (C_s=0.36) in an absorption process at a temperature of 25 ºC. The moisture content keeps an almost constant value when $\log_{10}(-\mu_0)$ is below -4. In Fig. 1 (b), the right end point of the lines is a saturation point where the cloth is saturated with pure or salt water. The more concentrated the salt water, the lower the moisture content at the saturation point is. However note that the crystallisation of salt in and at the surface of the cloth may require further consideration due to the change of the pore structure.

2.2 Influences of salt on liquid water transfer

This section provides a mathematical basis to implement the sorption isotherm proposed above in the equation of a liquid water flow based on the theory of Staverman (1951). A cloth which has absorbed sweat contains air, water vapour, liquid water and salt. But now only the liquid water and salt are taken into consideration in order to focus on the influence of the salt on the liquid water transfer. Note that no external force (e.g. gravity) is considered.

In an isothermal condition, the entropy production rate s per unit volume [J/Km^{3}s] due to the flow of the liquid water and salt in the cloth is defined by:

$$s = -\frac{J_l}{T}\nabla\mu_l - \frac{J_s}{T}\nabla\mu_s \tag{8}$$

with J_l and J_s the fluxes [kg/m^{2}s] of the liquid water and salt, and μ_l and μ_s the chemical potential [J/kg] of the liquid water and salt. Thus the linear phenomenological law to relate the fluxes and the conjugated forces is expressed as:

$$J_l = -\frac{L_{ll}}{T}\nabla\mu_l - \frac{L_{ls}}{T}\nabla\mu_s \tag{9}$$

$$J_s = -\frac{L_{sl}}{T}\nabla\mu_l - \frac{L_{ss}}{T}\nabla\mu_s \tag{10}$$

where L is the transfer coefficient, the first suffixes l and s refer to the flux of liquid water and salt, and the second suffixes l and s represent gradients in μ_l and μ_s.

On the other hand, the flux J_s can also be given by the following advection-diffusion equation:

$$J_s = (1-\sigma)C_s J_l - \rho_w\psi_w D_e\nabla C_s \tag{11}$$

where σ is Staverman's solute reflection coefficient [-] (Staverman, 1951), ρ_w is the density of water [kg/m^3], ψ_w is the volumetric moisture content [m^3/m^3] and D_e is the effective diffusion coefficient of salt in the water in the cloth [m^2/s]. Staverman's reflection coefficient σ is the mass ratio of salt reflected due to the pore structure to the advected salt. The value of σ in general depends on the sizes of pores and solute molecules or ions. The material reflects all salt when σ is one; while it does not reflect salt at all when σ is zero. Some measurements of σ are seen in building physics (Koniorczyk and Gawin, 2007), biological physics (Durbin, 1960), soil science (Bresler, 1981), etc.

When Eq. (9) is substituted into Eq. (11), the comparison of the obtained equation and Eq. (10) results in:

$$L_{sl} = (1-\sigma)C_s L_{ll} \tag{12}$$

This equation and Onsager's reciprocal theory yield:

$$L_{ls} = (1-\sigma)C_s L_{ll} \tag{13}$$

Substituting Eq. (13) into Eq. (9) gives:

$$J_l = -\frac{L_{ll}}{T}\{\nabla\mu_l + (1-\sigma)C_s\nabla\mu_s\} \tag{14}$$

Here, μ_l and μ_s are defined as:

$$\mu_l = p\upsilon_l + R_v T \ln x_l \quad ; \quad \mu_s = p\upsilon_s + R_s T \ln x_s$$
$$= \mu_{l0} + \mu_{lc} \qquad\qquad = \mu_{s0} + \mu_{sc}$$

(15)

with p the pressure of the salt water [Pa], v_l and v_s the partial volume [m³/kg] of the liquid water and salt in the salt water, x_l and x_s (=1-x_l) the molar fraction [-] of the liquid water and the salt in the salt water, R_s the specific gas constant [J/kgK] of the salt. μ_{l0} for the cotton equals μ_0 given by Eq. (7). Note that, in this paper, R_s is defined by:

$$R_s = i\phi R / M_w$$

(16)

Finally Eqs. (14) - (16) conclude the flux of the liquid water with the following equation:

$$J_l = -\frac{L_{ll}}{T}\left\{1 + (1-\sigma)C_s \frac{\upsilon_s}{\upsilon_l}\right\}\nabla\mu_{l0} - \frac{L_{ll}}{T}\sigma\nabla\mu_{lc}$$

(17)

The last term of this equation represents the flux due to osmotic pressure. This equation for salt water corresponds to the one for pure water when C_s is zero. L_{ll} for C_s=0 can be determined based on the water uptake experiment with use of the following relation, assuming the diffusivity of the vapour water is zero:

$$\frac{L_{ll}}{T} = \frac{D_{\psi_w l}}{\dfrac{\partial\mu_{l0}}{\partial\psi_w}}$$

(18)

where $D_{\psi_w l}$ is the diffusivity [kg/ms] of the liquid water due to ψ_w gradient.

When the cloth contains the salt water, $D_{\psi_w l}$ is considered to be dependent on both the water content and the salt content, not only because the density and viscosity of salt water depend on the salt concentration, but also because the pore structure can be changed by a partial crystallisation of salt on the surface of pores. Note the assumption that Eq. (18) still stands in such case.

2.3 Simultaneous heat, moisture and salt transfer equations

When the heat, gaseous water and gravity are taken into account based on Matsumoto (1984) in addition to the liquid water and salt, the simultaneous heat, moisture and salt transfer equations are expressed as:

$$\rho c \frac{\partial T}{\partial t} = \nabla(\lambda + r\lambda'_{Tg})\nabla T + \nabla r\lambda'_{\mu g}(\nabla\mu - F)$$

(19)

$$\rho_w \frac{\partial\psi_w}{\partial t} = \nabla\lambda'_{Tg}\nabla T + \nabla\lambda'_{\mu_0}(\nabla\mu_{l0} - F) + \nabla\lambda'_{\mu_c}\nabla\mu_{lc}$$

(20)

$$\rho_s \frac{\partial\psi_s}{\partial t} + \nabla(1-\sigma)C_s J_l = \nabla\rho_w\psi_w D_e\nabla C_s$$

(21)

where ρ and c are respectively the density [kg/m³] and specific heat [J/kgK] of the cloth containing the salt water, t is the time [s], λ is the heat conductivity [W/mK] of the cloth containing the salt water due to T gradient, r is the heat [J/kg] of vapourisation of water, λ'_{Tg} and $\lambda'_{\mu g}$ are the conductivity [kg/ms(J/kg)] of gaseous water due to T and μ gradients respectively, μ (= $\mu_l = \mu_{l0} + \mu_{lc}$) is the chemical potential [J/kg] of water, F is the external force [N/kg] (e.g. gravity), λ'_{μ_0} and λ'_{μ_c} are the conductivity [kg/ms(J/kg)] of both liquid and gaseous water due to μ_0 and μ_c gradients respectively, ρ_s is the density [kg/m³] of salt, and ψ_s is the volumetric salt content [m³/m³]. λ'_{μ_0} and λ'_{μ_c} in Eq. (20) are expressed by:

$$\lambda'_{\mu_0} = \lambda'_{\mu_{l0}l} + \lambda'_{\mu g} \;;\; \lambda'_{\mu_c} = \lambda'_{\mu_{lc}l} + \lambda'_{\mu g}$$

(22)

with $\lambda'_{\mu_{l0}l}$ and $\lambda'_{\mu_{lc}l}$ the conductivity [kg/ms(J/kg)] of the liquid water due to μ_{l0} and μ_{lc} gradients respectively, and $\lambda'_{\mu g}$ the conductivity [kg/ms(J/kg)] of the gaseous water due to μ gradient. $\lambda'_{\mu_{l0}l}$ and $\lambda'_{\mu_{lc}l}$ are defined by:

$$\lambda'_{\mu_{l0}l} = \frac{D_{\psi_w}l}{\frac{\partial \mu_{l0}}{\partial \psi_w}}\left\{1 + (1-\sigma)C_s \frac{\upsilon_s}{\upsilon_l}\right\}; \quad \lambda'_{\mu_{lc}l} = \frac{D_{\psi_w}l}{\frac{\partial \mu_{l0}}{\partial \psi_w}}\sigma \tag{23}$$

Furthermore, J_l in Eq. (21) is redefined by:

$$J_l = -\lambda'_{\mu_{l0}l}(\nabla \mu_{l0} - F) - \lambda'_{\mu_{lc}l}\nabla \mu_{lc} \tag{24}$$

Note finally that, when the salt concentration reaches the saturated concentration, the solid phase of salt has to be taken into account.

3. Analyses of Pure and Salt Water Uptake

3.1 Experiments

Experiments of pure (case 1) and salt (sodium chloride) (case 2) water uptake were conducted using a cloth in a laboratory with a constant air temperature of 25 ºC and a constant relative humidity of 50 %. Note that the same experiment of pure water uptake is seen in Takada (2002). The airflow in the room was rather stagnant (wind speed: 0.25~0.33 m/s). In these experiments, the water absorbed into the cloth evaporates at the surfaces of the cloth. The specimens of the cloth used in the experiments are made of cotton and has a surface area of 10 cm (x) $\times$ 3 cm (y) and a thickness of 0.25 mm (z). Note that the pure/salt water is absorbed into direction x. Each specimen was cut by scissors into 10 small pieces in 1 cm intervals from the bottom to the top at 100, 300, 600 and 1800 s. The 10 small pieces of 1 cm (x) $\times$ 3 cm (y) $\times$ 0.25 mm (z) are called P1, P2, P3… and P10 respectively. Each piece was immediately wrapped by a thin aluminium foil after it had been cut off and their weights were, then, measured by the decimal balance to quantify moisture and salt contents in the pieces. Results of the experiments will be provided together with simulation results.

3.2 Numerical analyses

The experimental results described in section 3.1 are numerically analysed with the model proposed in section 2.

3.2.1 Conditions of numerical analyses

Important conditions in these simulations are briefly described below. Material properties of the cloth (slightly modified from Takada (2002)) and initial and boundary conditions are given in Tables 1, 2 and 3 respectively.

TABLE. 1: Material properties of the cloth.

Diffusivity [kg/ms kg/kg]:	2.4×10^{-7};	Density [kg/m^3]:	1540
Thermal conductivity [W/mK]:	0.0556;	Porosity [-]:	0.671
Specific heat [J/kgK]:	1380;	Thickness [mm]:	0.25

TABLE. 2: Initial conditions of the cloth.

Moisture content [kg/m^3]:	0.0645;	Salt concentration [kg(NaCl)/kg(H$_2$O)]:	0;	Temperature [ºC]:	25

TABLE. 3: Boundary conditions.

Indoor air temperature [ºC]:		25;	Indoor RH [%]:	50
Salt concentration of solutions [kg(NaCl)/kg(H$_2$O)]:		0 (case 1), 0.18 (case 2)		
Temperature at the bottom of solutions [ºC]:		22.0 (case 1), 22.7 (case 2)		

3.2.2 Analysis of pure water uptake

Takada (2002) proved that given an appropriate value of $D_{\psi_w l}$ and appropriate heat and moisture transfer coefficients, pure water uptake by a cloth can be accurately analysed by a numerical analysis based on the theory of Matsumoto (1984). In this section an analysis of the pure water uptake is conducted to determine $D_{\psi_w l}$ and the transfer coefficients at the surface of the cloth used in the experiments of 3.2.1. The determined $D_{\psi_w l}$ is:

$$\frac{\psi_w}{\Phi_0} \le 0.95 : \quad D_{\psi_w l} = \rho_w \cdot 7.0 \cdot 10^{-10} \cdot \exp\left\{ 10.7 \cdot \left(\frac{\psi_w}{\Phi_0} \right) \right\} \tag{25}$$

$$\frac{\psi_w}{\Phi_0} > 0.95 : \quad D_{\psi_w l} = \rho_w \cdot 7.0 \cdot 10^{-10} \cdot \exp(10.7 \cdot 0.95) \tag{26}$$

Also the determined convective heat transfer coefficient, radiative heat transfer coefficient and moisture transfer coefficient are 2 [W/m^{2}K], 4 [W/m^{2}K] and 2×10^{-3} [kg/m^{2}s(kg/kg)] respectively. The results of this simulation will be shown in 3.2.4.

3.2.3 Analysis of salt water uptake

In this case two unknown parameters in Eqs. (23), diffusivity $D_{\psi_w l}$ of liquid water in the cloth containing salt water and Staverman's reflection coefficient σ, are optimised. Due to space limitation, only optimised values of them and the simulation results with the optimised values are presented in this paper. Note that the transfer coefficients used in this analysis are the same as those of the previous analysis because the measurements of pure and salt water uptake were performed in the same environmental conditions.

Although σ is typically regarded as a constant value [e.g. Bresler, 1981; Koniorczyk and Gawin, 2007], this coefficient for porous materials like the cloth under study is considered to depend on the size of pores which relate to liquid water transfer in the cloth. The size of such pores is generally dependent on the content of salt water. Thus the value of σ was optimised as the following function of the salt water content:

$$\sigma = 2 \times 10^{-4} \left(\frac{\Phi_0 - \psi_{sw}}{\Phi_0} \right)^{0.5} \tag{26}$$

$D_{\psi_w l}$ was optimised as a function of the salt water content and salt concentration for the three reasons: (1) the viscosity and density of the salt water depend on salt concentration; (2) the pore structure can be changed by the salt (Koniorczyk and Gawin, 2006); and (3) pores which relate to liquid water transfer in the cloth are not considred to be influenced by the salt when the moisture content is high. The optimised $D_{\psi_w l}$ is:

$$D_{\psi_w l} = D'_{\psi_w l} \cdot \left\{ 1 + 14 \cdot \left(\frac{C_s}{C_{sm}} \right) \cdot \left(\frac{\psi_{sw}}{\Phi_0} \right) \right\}^{-1} \tag{25}$$

with $D'_{\psi_w l}$ defined by:

$$\frac{\psi_w}{\Phi_0} \le 0.95 : \quad D'_{\psi_w l} = \rho_w \cdot 7.0 \cdot 10^{-10} \cdot \exp\left\{ 10.7 \cdot \left(\frac{\psi_{sw}}{\Phi_0} \right) \right\} \tag{25}$$

$$\frac{\psi_w}{\Phi_0} > 0.95 : \quad D'_{\psi_w l} = \rho_w \cdot 7.0 \cdot 10^{-10} \cdot \exp(10.7 \cdot 0.95) \tag{26}$$

The effective diffusion coefficient D_e of the salt in the water in the cloth was kept constant at 1.6×10^{-9} for sake of simplicity, because it was confirmed that the value of D_e does not influence results of the current study.

3.2.4 Results and discussion

Results of the experiments and numerical analyses for five pieces P1, P2, P3, P4 and P5 are given in Fig. 2.

Figs. 2 (a) and (b) show the time course of the average moisture content of each piece for cases 1 and 2 respectively, comparing the results of each experiment (indicated as "exp." in Fig. 2) and the corresponding numerical simulation (indicated as "sim." in Fig. 2). In general, the simulation results agree fairly well with the experimental ones. However some differences are seen. For both cases, the simulated moisture contents of 4 pieces P1, P2, P3 and P4 at 1800 s are rather different from the measured ones. The simulated moisture contents of piece P1 at 300, 600 and 1800 s for case 1 and at 1800 s for case 2 are even higher than the saturated moisture contents. This is attributable to the water adhered to the both surfaces of piece P1 due to surface tension.

For case 2, the simulated results of the total mass of salt are compared to the measured ones in Fig. 2 (c). The difference in total mass of salt between the simulation results and the measured ones somewhat resembles to that in average moisture content shown in Fig. 2 (b) but is larger. Specifically the difference at piece P3 is very large. Although there is no clear explanation for this difference, it can be improved if the moisture content is better predicted. In this respect material properties which are more appropriate for the specimens used in the current study are needed.

The simulated average temperatures of the two cases are compared in Fig. 2 (d). Significant differences of up to 4.4 °C (piece P4 at 930 s) are seen due to the influences of the salt. The influences of salt on heat and moisture transfer in clothing ultimately result in a higher temperature of clothing due to a reduced evaporation rate. In this respect, the salt influences can not be ignored when the salt concentration becomes high after several sweating and drying processes.
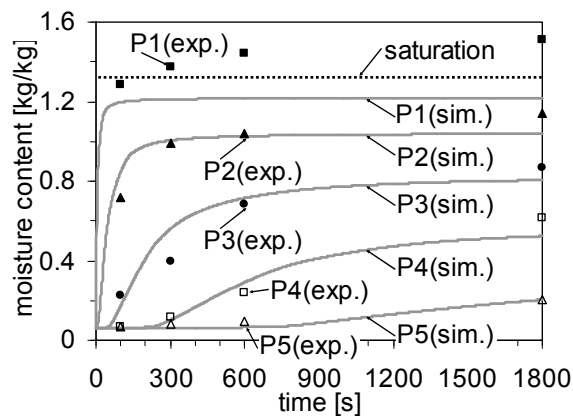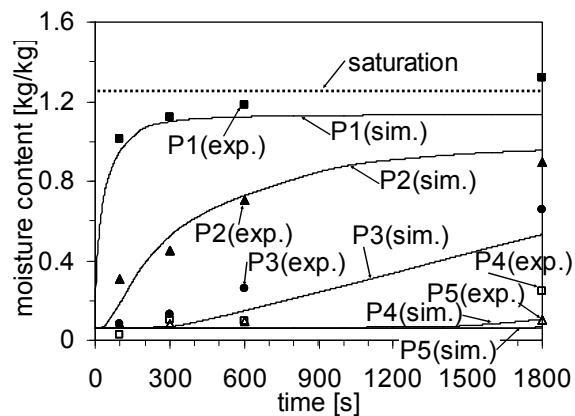
(a) Average moisture content of each piece (case 1)   *(b) Average moisture content of each piece (case 2)*
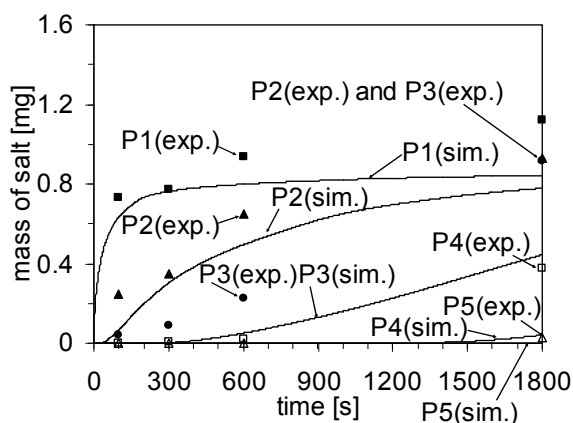
(c) Total mass of salt in each piece (case 2)   *(d) Average temperature of each piece (case 1 and 2)*
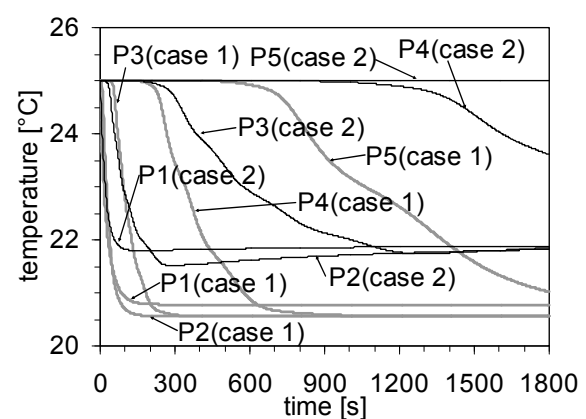
FIG. 2: Results of experiments (exp.) and numerical analyses (sim.) of pure (case 1) and salt (case 2) water uptake. The solid black lines show the simulation results of case 1 (pure water); the bold light grey lines those of case 2 (salt water); the five different symbols the experimental results of the five pieces P1, P2, P3, P4 and P5 respectively.

4. Conclusion

A model of the sorption isotherm of a cloth containing salt water was proposed. Based on this sorption isotherm, a numerical model of simultaneous heat, moisture and salt transfer was presented to quantify the influence of salt on the heat and moisture transfer in the cloth. With the model proposed the pure water and salt water uptake accompanying the evaporation of water was numerically analysed. It was shown that given appropriate liquid water diffusivity and Staverman's reflection coefficient, a fairly good agreement can be obtained between the simulation results and the experimental ones. Also the comparison of the simulation results of pure water and those of salt water suggested that when the salt accumulates in clothing, the influence of the salt results in a higher temperature of clothing due to a reduced evaporation rate and can, thus, be of importance for thermal comfort.

5. References

Bresler E. (1981). Transport of salts in soils and subsoils, Agricultural Water Management, Vol. 4, 35-62.

Brocken HJP, et al. (1999). Salinization Effects on The Water Sorption of Porous Building Material, Proceedings of CIB W40 Meeting.

Durbin RP. (1960). Osmotic flow of water across permeable cellulose membranes, The Journal of General Physiology, Vol. 44, 315-326.

Farnworth B. (1986). A numerical model of the combined diffusion of heat and water vapor through clothing, Textile Research Journal, Vol. 56, 653-665.

Funk M, Nicolai A, Grunewald J. (2006). Incorpolation of salt related effects into a hygrothermal transport model. In :Proceedings of the 3rd International Building Physics Conference - Research in Building Physics and Building Engineering, P. Fazio, H. Ge, J. Rao, G. Desmarais (eds.), Montreal, Canada, August 27-31, 2006, 161-169.

Koniorczyk M, Gawin D. (2006). The influence of salt on hygrothermal behaviour of building materials. In: Proceedings of the 3rd International Building Physics Conference - Research in Building Physics and Building Engineering, P. Fazio, H. Ge, J. Rao, G. Desmarais (eds.), Montreal, Canada, August 27-31, 2006, 139-146.

Koniorczyk M, Gawin D. (2007). Modelling of transportation processes in building materials with different pores structures considering osmosis. In: Proceedings of the 12th Symposium for Building Physics, Dresden, Germany, 29-31, March, 2007, 823-830.

Matsumoto M. (1984). New Series of Fundamentals of Architecture, Vol. 10, Shokokusya, Tokyo (in Japanese).

Morton WE and Hearle JWS. (1962). Physical properties of textile fibres, The Textile Institute, Manchester, 164.

Patterson MJ, Galloway SDR, Nimmo MA. (2000). Variation in regional sweat composition in normal human males, Experimental Physiology, Vol. 85, 869–875.

Pavlik Z, Jirickova M, Fiala L, Cerny R. (2006). Inverse modeling of salt diffusion and advection in building materials. In: Proceedings of the 3rd International Building Physics Conference - Research in Building Physics and Building Engineering, P. Fazio, H. Ge, J. Rao, G. Desmarais (eds.), Montreal, Canada, August 27-31, 2006, 155-160.

Poupeleer A-S, Carmeliet J, Roels S, Van Gemert D. (2006). Combining expansion/shrinkage monitoring and X-ray measurement for water and salt transport in calcium silicate beam. In: Proceedings of the 3rd International Building Physics Conference - Research in Building Physics and Building Engineering, P. Fazio, H. Ge, J. Rao, G. Desmarais (eds.), Montreal, Canada, August 27-31, 2006, 147-154.

Staverman AJ. (1951). The theory of measurement of osmotic pressure, Recueil des Travaux Chimiques des Pays-Bas, Vol. 70, 344-352.

Takada S. (2002). Transient Response of Human Body to the Thermal Environment, Considering the Moisture Movement and Accumulation in Clothes, PhD thesis, Kyoto University, Kyoto (in Japanese).

Coupled Water and Sulfate Transport Parameters of Materials Used in Historical Buildings

Zbyšek Pavlík, Ph.D.
Department of Materials Engineering and Chemistry, Faculty of Civil Engineering, Czech Technical University in Prague
pavlikz@fsv.cvut.cz, http://tpm.fsv.cvut.cz

Lukáš Fiala, Eng.
Department of Materials Engineering and Chemistry, Faculty of Civil Engineering, Czech Technical University in Prague
fialal@fsv.cvut.cz, http://tpm,fsv.cvut.cz

Milena Pavlíková, Ph.D.
Department of Materials Engineering and Chemistry, Faculty of Civil Engineering, Czech Technical University in Prague
milena.pavlikova@fsv.cvut.cz, http://tpm.fsv.cvut.cz

Robert Černý, Professor
Department of Materials Engineering and Chemistry, Faculty of Civil Engineering, Czech Technical University in Prague
cernyr@fsv.cvut.cz, http://tpm.fsv.cvut.cz

KEYWORDS: coupled moisture and sulphate transport, diffusion-advection model, sandstone.

SUMMARY:
Identification of transport parameters describing the coupled water and sulphate transport in sandstone frequently used in Central Europe as masonry and ornamental material for historical buildings is studied in the paper. In the experimental work, rod-shaped samples are used for the measurement of moisture and sulfate concentration profiles. In the determination of moisture and sulfate concentration profiles, the specimens are put in contact with distilled water or Na_2SO_4 solution. After chosen time interval, the samples are cut into several pieces. The moisture content is determined in each piece by gravimetric method, the sulfate concentration is measured by ion chromatography. Experimentally determined Na_2SO_4 concentration profiles and moisture profiles are used for identification of sulfate diffusion coefficient and moisture diffusivity on the basis of inverse analysis using the diffusion-advection model. The moisture diffusivity in dependence on moisture content is calculated in three different ways. First, the moisture diffusivity is calculated from moisture profiles measured for the penetration of distilled water into a specimen. Then, the moisture diffusivity vs. moisture content function is calculated from moisture profiles measured for the penetration of Na_2SO_4 solution. Finally, the third moisture diffusivity vs. moisture function is obtained by the inverse analysis of sulfate concentration profiles under assumption that no sulfate diffusion takes place in the liquid phase, i.e., D=0. The sulphate diffusion coefficient is detemirned applying the diffusion-advection model where the salt bonding on the pores walls is taken into account.

1. Introduction

The deterioration and functionality decrement of porous building materials is without doubt strongly related to the presence of moisture and water soluble salts. Most chemical degradation processes such as the transformation of calcite into expansive gypsum in limestone and the dissolution of calcium in concrete, require moisture [Roels S. (2000)].

From the point of view of mechanical properties, the presence of higher moisture content significantly decreases the compressive and bending strength of bearing-structures materials and whole structures. The seriousness of this effect clearly documents fact that the amount of contained moisture is taken into account in calculation of

mechanical properties according to Czech and international standards. Due to hindered hygric expansion of materials inbuilt in structures, the micro-cracks can originate as well.

Furthermore, in damp conditions, porous building materials are susceptible to frost damage, because of the volume changes accompanying the phase conversion from the liquid into the solid phase. The volume changes are typically about 9%. This volume rising can lead, in dependence on the shape and dimension of porous system, to the damage of the material and in some cases to its total destruction, whereas the decrease of frost resistance will be more remarkable for materials having lower strength and elastic modulus.

Moist or damp buildings have been in several studies related to the negative health effects. Most building materials contain excess water when are moisten during their service life and this water must be removed to prevent deterioration of the indoor quality due to the biological growth, ranging from bacteria, algae and fungi to moss [Fennema O. R. (1985), Nielsen K. F. (2002), Adan O. C. G. (1994)]. Micro-organisms cause damage by producing acidic secretions such as oxalic acid, whereas plants can create mechanical stresses by sending roots into crevices.

In the common service life conditions of buildings, not only pure water is transported into the materials. Usually the transported water contains certain amount of dissolved salts that can (depending on the environment conditions) accelerate and intensify the materials degradation and damage.

Salt weathering is a major decay mechanism in a wide range of materials and environments (e.g. Goudie A. S. and Viles H. 1997)). It can cause damage to buildings, roads, runways, dams and other structures (e.g. Sayward J. M. (1984), Doornkamp J. C. and Ibrahim H. A. M. (1990), Thorborg von Konow (2006), etc.).

In this work we have focused on sandstone used in historical masonry and sculpture. The salt weathering is just one of the primary agents in the loss of the built culture heritage, through surface degradation, structural destabilization or complete disintegration [Cooke R. U. and Gibbs G. B. (1995), Price C. (1996)]. It is therefore a common hazard with significant cultural and economic implications in the field of cultural heritage.

Although the salt damage and action have been intensively investigated for several decades, the mechanisms and factors that govern the behaviour of salt solutions, the formation of salt crystals and the development of damage by crystal growth are not yet fully understood.

In the salt damage and weathering research, many conservation and redevelopment treatments have been developed for the consolidation and protection of porous building materials affected by salt weathering. However, these methods commonly do not stop the further development of salt damage [Price C. (1996)]. Protection efforts may even enhance salt damage, by preventing the migration of saline solutions towards the material/air interface, thereby inducing subflorescence growth when salts are already present in the pores or when they are supplied by capillary rise. On the other hand, current desalination methods are mainly inefficient in some ways (e.g. poulticing, reverse osmosis). Hence, there is a need for the development of new conservation treatments, which can preferably be applied both for preventing salt damage development and for obtaining effective desalination.

Therefore, the better understanding to the coupled moisture and salt transport mechanism is needed especially for the optimisation of the conservation and reconstruction treatments, and for the damage assessment of buildings and their inbuilt materials. Moisture transport in saturated porous media has since long been adequately described. On the other studies of moisture transport in unsaturated media, which apply to most practical situations, have only much more recently been attempted. These studies are further complicated by the wide range in pore size in building materials, which can span several orders of magnitude. It is therefore difficult to develop a good model for coupled moisture and salt transport, especially with regard to transport in the vapour phase.

The main objective of the presented work is to contribute to the identification of salt solution transport mechanism and to the assessement of salt related properties of material used in historical buildings and sculptures.

2. Determination of parameters describing the coupled water and salt transport

Determination of material parameters describing the mechanism of coupled salt and moisture transport is based on the assumed mode of this transport. In this work, the moisture dependent moisture diffusivity is calculated in

three different ways on the basis of inverse analysis of experimentally obtained moisture and salt concentration profiles. First, the moisture diffusivity is calculated from moisture profiles measured for penetration of distilled water into the dry specimen. Then, the moisture diffusivity vs. moisture content function is calculated from moisture profiles measured for the penetration of 1M Na_2SO_4 solution. Finally, the third moisture diffusivity vs. moisture function is obtained by the inverse analysis of suphates concentration profiles under assumption that no sulphates diffusion takes place in the liquid phase.

The diffusion mechanism of moisture transport where the dependence of moisture diffusivity κ [m^{2}s^{-1}] on moisture concentration w [m^{3}m^{-3}] was taken into account was assumed in the first two cases. For the inverse analysis of experimentally determined moisture profiles $w(x,t)$ Matano method was employed. Its application leads to the following solution for moisture diffusivity vs. moisture concent function

$$\kappa(w_0) = \frac{1}{2t_0(\frac{dw}{dz})_{z=z_0}} \int_{z_0}^{\infty} z \frac{dw}{dz} dz \,,$$
(1)

where $t_0 = const.$ is a given time where the moisture field $w(z,t_0)$ is known and z is the space variable (for details see Drchalová J., Pavlík Z. and Černý R. (2002)).

For description of coupled salt and moisture transport, diffusion-advection model proposed by Bear and Bachmat [Bear J. and Bachmat Y. (1990), Pel L., Kopinga K. and Kaasschieter E. F. (2000)] was used. This model employs the system of parabolic equations describing salt and moisture transport.

The salt mass balance is expreseed by relation

$$\frac{\partial(wC_f)}{\partial t} = div(wD\ gradC_f) - div(C_f\vec{v}) - \frac{\partial C_b}{\partial t} \,,$$
(2)

where C_f is the concentration of free salts in water [kgm^{-3}], C_b the concentration of bonded salts in the whole porous body [kgm^{-3}], D the salt diffusion coefficient [m^{2}s^{-1}], $\vec{v}$ the Darcy's velocity [ms^{-1}], and w the volumetric moisture content [m^{3}m^{-3}].

The water mass balance is expressed in equation

$$\frac{\partial w}{\partial t} = div(\kappa\ gradw) \,.$$
(3)

Expressing Darcy's velocity in terms of moisture diffusivity,

$$\vec{v} = -\kappa\ gradw \,,$$
(4)

the salt solution transport can be described by a system of two parabolic partially coupled differential equations with two principal material parameters, D and κ, and three input variables, C_f, C_b, w that must be determined experimentally.

System of equations (2) – (4) can be subjected to an inverse analysis in a similar way as for one parabolic equation, provided the initial and boundary conditions are simple enough, and the material parameters D and κ can be identified as functions of water content and salt concentration. The simplest possibility of such an inverse analysis is again an extension of the Boltzmann-Matano treatment under the same assumptions of constant initial conditions and Dirichlet boundary conditions on both ends of the specimen for both moisture content and salt concentration where one of the Dirichlet boundary conditions is equal to the initial condition. After applying Boltzmann transformation and performing some straightforward algebraic operations, we arrive at the following formula for the determination of salt diffusion coefficient

$$D(z_0) = -\frac{C_f(z_0)\kappa(z_0)\left(\dfrac{dw}{dz}\right)_{z_0}}{w(z_0)\left(\dfrac{dC_f}{dz}\right)_{z_0}} + \frac{\displaystyle\int_{z_0}^{\infty} z\left(\dfrac{d(wC_f)}{dz} + \dfrac{dC_b}{dC_f}\dfrac{dC_f}{dz}\right)dz}{2t_0 \cdot w(z_0)\cdot\left(\dfrac{dC_f}{dz}\right)_{z_0}} ,$$

<div align="right">(5)</div>

where z is the space variable, t_0 the time corresponding to the chosen moisture and concentration profiles $w = w(z,t_0)$, $C_f = C_f(z,t_0)$, the chosen values of moisture and concentration are $w_0 = w(z_0, t_0)$, $C_{f0} = C_f(z_0, t_0)$, the corresponding moisture diffusivity and salt diffusion coefficient $\kappa(z_0) = \kappa(w_0, C_{f0})$, $D(z_0) = D(w_0, C_{f0})$ and $C_b = f(C_f)$ is the ion binding isotherm. For details on inverse analysis procedure, see Pavlík Z., Jiřičková M., Fiala L. and Černý R. (2006).

Using diffusion-advection model, the third moisture diffusivity function was also calculated neglecting the sulphate diffusion in the liquid phase *(D = 0)*. The relation for moisture diffusivity calculation using this procedure is given as

<div align="right">(6)</div>

$$\kappa(z_0) = \frac{\displaystyle\int_{z_0}^{\infty} z\left(\dfrac{d(wC_f)}{dz} + \dfrac{dC_b}{dC_f}\dfrac{dC_f}{dz}\right)dz}{2t_0 \cdot C_f(z_0)\cdot\left(\dfrac{dw}{dz}\right)_{z_0}} .$$

3. Experimental

Many historical buildings in the Czech Republic were built using similar kinds of sandstone. Siliceous raw-grained sandstone was usually used for historical architectural constructions (walls, portals, window frames) for its strength. Ornamental parts of the architecture (gothic flowers, romantic shells) and sculptures (from the Romanesque period up to now) were made of fine-grained calcite-argillaceous sandstone. Sandstone from Mšené-lázně quarry, the so-called Mšené sandstone, which was chosen to our research, belongs to the latter.

Mšené sandstone is fine-grained white-greyish material. It is psamitic equigranular rock, about 95% of which is made up of suboval quartz clasts. Other mineral grains are present only as accessories (tourmaline, epidote, muscovite and zircone). Quartz grains reach up to 0.1 mm in diameter, but those of muscovite are larger, up to 0.3 mm. The matrix is formed by clay minerals (mainly kaolinite).

For easier interpretation of obtained results, basic laboratory tests of sandstone properties were performed. Nominally, bulk density ρ_b, matrix density ρ_{mat}, total open porosity ψ, and saturation moisture content w_{sat}, were determined on vacuum water saturation principle (for details see Jiřičková M. (2004)). The measured results are presented in *TABLE. 1*.

TABLE. 1: Basic material properties of the studied sandstone.

Bulk Density ρ_b [kgm^{-3}]	Matrix Density ρ_{mat} [kgm^{-3}]	Saturation moisture content w_{sat} [kgm^{-3}]	Total Open Porosity [m^{3}m^{-3}]
1807	2627	310	0.31

The rod shaped samples with the dimensions of 20 x 40 x 160 mm were used for the determination of moisture and sulphate concentration profiles in simulated 1-D water and sulphate solution transport. The dry, on lateral sides vapour-proof insulated samples were exposed by their 40 x 20 mm face to the penetrating 1M Na$_2$SO$_4$ solution (concentration 142 g/l of solution). Duration of the experiment was 30, 60 and 90 minutes for three different groups of samples. After this time, the samples were cut into 8 pieces and in each piece water content and sulphate concentration were measured.

Moisture content was determined by the gravimetric method using weighing the moist and dried specimens. In the determination of suphate concentration, the particular samples were after drying first ground by a vibration mill so that grains smaller than 0.063 mm were obtained. Then the ground samples were overflowed by 80 °C

warm distilled water and leached. The sulphate contents in particular leaches were determined using ion chromatography device Chrom SDS 150, SHOdex.

For the determination of ion binding isotherm, Tang and Nilsson modified absorption method was chosen. This modification consisted in using the specimens of more realistic dimensions (40 x 40 x 10 mm) instead of crushed specimens [Jiřičková M. and Černý R. (2006)]. On the basis of the measured ion binding isotherm of Na_2SO_4, $C_b = f(C_f)$, the profiles of bound and free sulphates were determined.

4. Results and Disccusion

The measured moisture and sulphate concentration profiles are given in *FIGs. 1 – 3*. For the computational inverse analysis it was necessary to smooth the measured data to obtain continuous functions. The linear filtration method was used for that purpose. The smoothed data and smoothing parameters α are also presented in *FIGs. 1 – 3*.
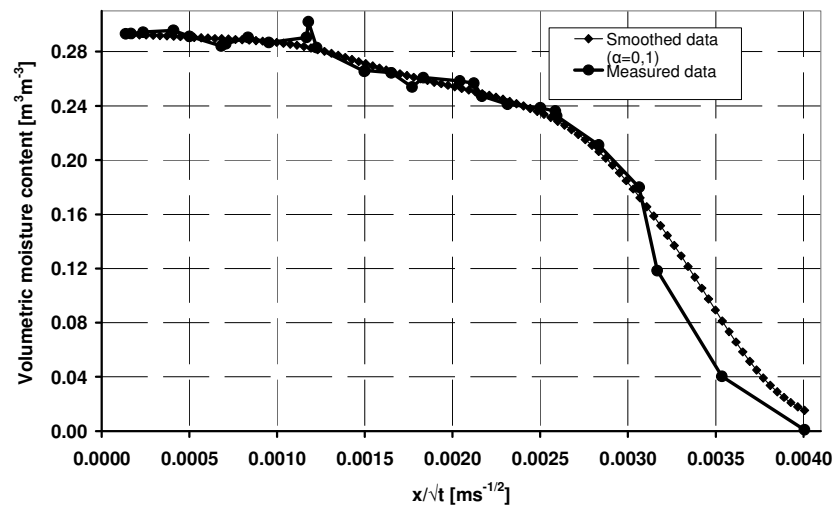
FIG. 1: Volumetric moisture content profile for distilled water penetration.
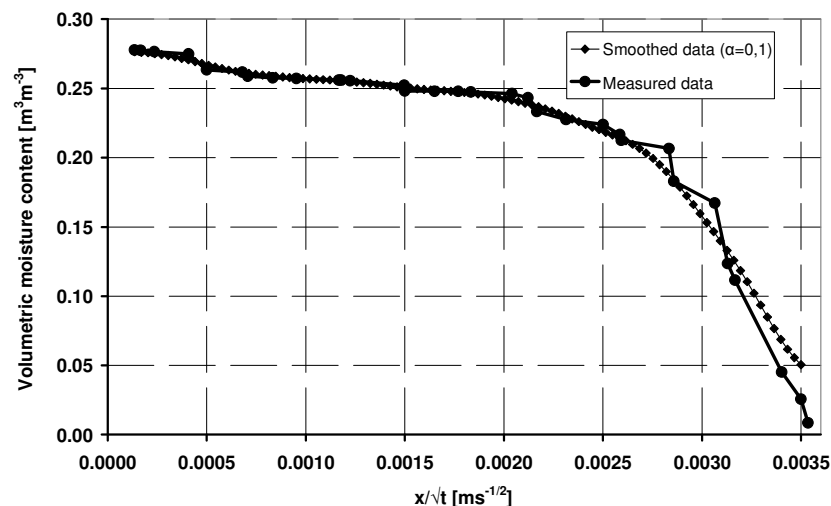
FIG. 2: Volumetric moisture content profile for penetration of 1M Na_2SO_4 solution.

The volumetric moisture content profiles demonstrate the velocity of distilled water and 1M Na_2SO_4 solution transport. We can see that in the immersed end of the sample, almost the saturation moisture content value was reached. From the comparison of obtained profiles, there is evident, the distilled water was transported slightly

faster than Na_2SO_4 solution. This feature can be assigned to the higher density and viscosity of sulphate solution as compared with pure water.
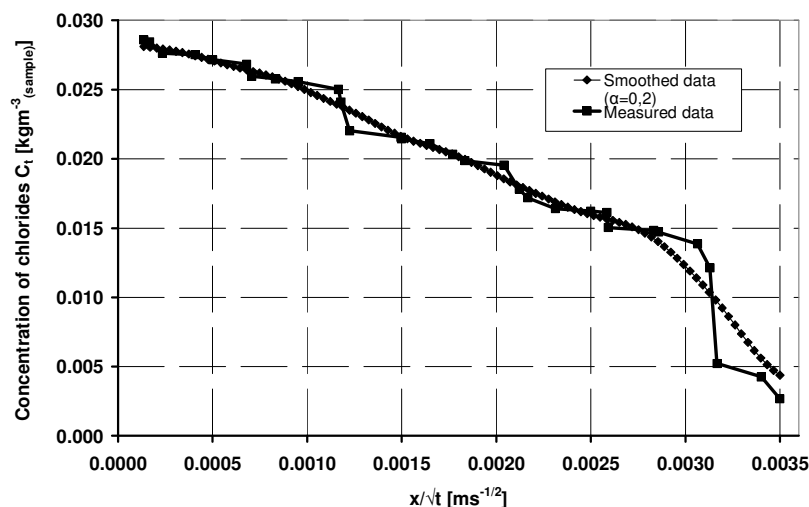
FIG. 3: Total sulphate concentration profile.

The sulphate binding isotherm measured by modified Jiřičková and Černý adsorption method is shown in FIG. 4. The obtained binding isotherm gives evidence about the rather low sulphate binding capacity of the studied material.
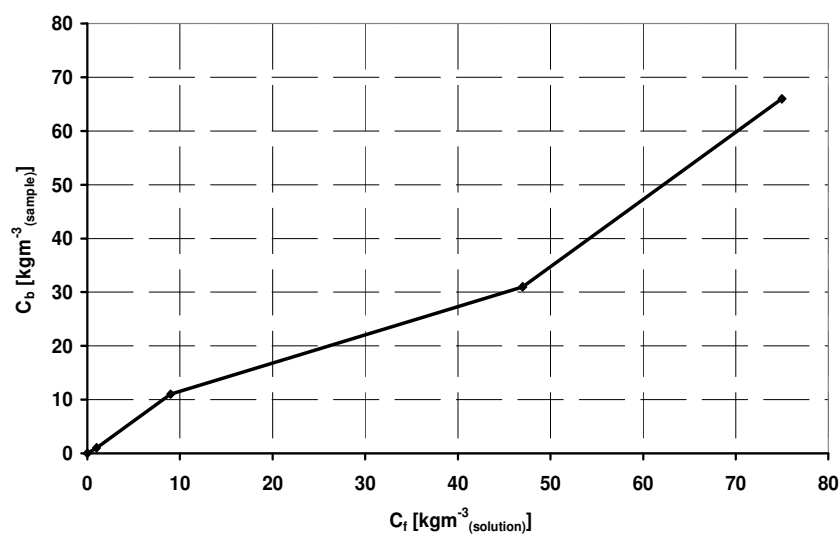
FIG. 4: Binding isotherm of Na_2SO_4 for Mšené sandstone.

In the previous works (see e.g. Fiala L., Pavlík Z., Jiřičková M. and Černý R. (2006), Pavlík Z., Fiala L., Pavlíková M. and Černý R. (2007)) we have already studied the transport and binding of nitrate and chloride ions in sandstone. The results presented in these papers clearly describe fact that the binding capacity of Mšené sandstone is completely different for particular salt solutions.

The results of moisture diffusivity calculations are presented in *FIG. 5*. The moisture diffusivity calculated for penetration of distilled water is systematically higher than the moisture diffusivity obtained for Na_2SO_4-in-water solution. This is probably the consequence of the higher viscosity of Na_2SO_4 solution compared to viscosity of distilled water. The results of inverse analysis also show that the possible neglect of sulphate diffusion in the liquid phase is apparently wrong, because the moisture diffusivity calculated from sulphate concentration

profiles under this assumption is two to three orders of magnitude higher than moisture diffusivity calculated from moisture profiles. The dependence of sulphate diffusion coefficient on concentration is shown in Fig. 6. From the quantitative point of view, the calculated sulphate diffusion coefficient is quite high, about three orders of magnitude higher than the diffusion coefficients of most ions in free water. Therefore, the common diffusion mechanism is probably not the only driving force for sulphate transport within the liquid phase and some other driving forces are taking place here. This acceleration of sulphate transport can be attributed most probably to surface diffusion on pore walls and/or to osmotic effects, and electrochemical forces.
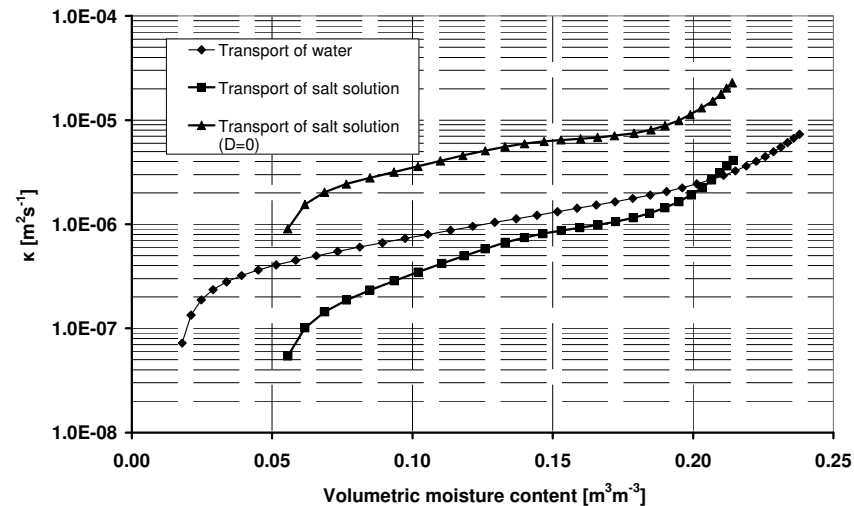
FIG. 5: *Moisture diffusivity of sandstone calculated in three different ways.*
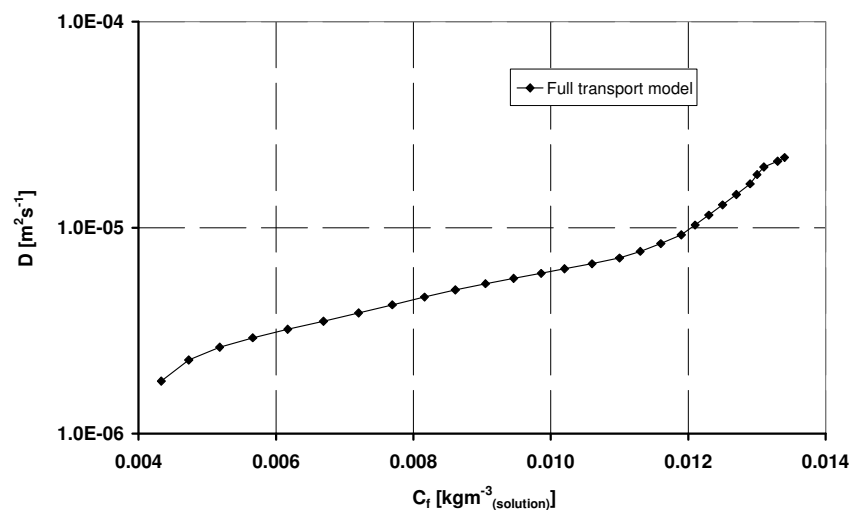
FIG. 6: *Sulphate diffusion coefficient of Mšené sandstone.*

5. Conclusions

The main practical outcome of the presented work represents determination of two main parameters describing the coupled water and sulphate transport in sandstone. The performed experiments and calculations have revealed important fact that different salt solutions are transported in the porous structure of materials with specific velocity. This finding is in agreement with differences in diffusion coefficients of chloride, sulphate and nitrate ions in water (CRC Handbook of Chemistry and Physics, 85th Edition, Ed. David R. Lide, 2004 – 2005, CRC Press). In our opinion, the crucial factor that affects the transport of salt ions is the shape and dimension of their molecules. Hence, the sulphate ions are transported very slowly and in the lower volume because of the complicated shape of $(SO_4)^{2-}$ molecules and their bigger dimension.

6. References

Adan O. C. G. (1994) On the fungal defacement of interior finishes, Ph.D. Thesis, Eindhoven University of Technology, Eindhoven.

Bear J. and Bachmat Y. (1990) Introduction to Modelling of Transport Phenomena in Porous Media, Vol. 4, Kluwer, Dordrecht.

Cooke R. U. and Gibbs G. B. (1995) Crumbling Heritage, Studies of Stone Weathering in Polluted Atmospheres, National Power plc and PowerGen plc, Swindon, 68 pp..

Doornkamp J. C. and Ibrahim H. A. M. (1990) Salt weathering,　Progress in Physical Geography 14, p. 335-348.

Drchalová J., Pavlík Z. and Černý R. (2002) A Comparison of Various Techniques for Determination of Moisture Diffusivity from Moisture Profiles, Proceedings of the 6th Symposium on Building Physics in the Nordic Countries, Trondheim, Norwegian University of Science and Technology, Vol. 1, p. 135-142.

Fiala L., Pavlík Z., Jiřičková M. and Černý R. (2006) Calculation of Moisture Diffusivity and Chloride Diffusion Coefficient of Sandstone Using Data from a Single Experiment, Symposium Trwalosc Materialów i Konstrukcji Budowlanych [CD-ROM], Opole: Politechnika Opolska, p. 103-106.

Fenema O. R. (1985) Water and Ice. Food Chemistry (Ed. Fenema O. R.), Marcel Dekker Inc., New York, p. 23-67.

Goudie A. S. and Viles H., (1997) Salt Weathering Hazards, John Wiley & Sons, Chichester, 241 pp..

Jiřičková M. (2004) Application of TDR Microprobes, Minitensiometry and Minihygrometry to the Determination of Moisture Transport and Moisture Storage Parameters of Building Materials, Prague: Czech Technical University, 2004. 102 pp.

Jiřičková M. and Černý R. (2006) Chloride Binding in Building Materials, Journal of Building Physics Vol. 29, p. 189-200.

Nielsen K. F. (2002) Mould growth on building materials, secondary matebolits, mycotoxines and biomarkers. The Mycology group, Biocentrum – DTU, Technical Univesity Denmark, Lyngby.

Pavlík Z., Jiřičková M., Fiala L. and Černý R. (2006) Inverse Modeling of Salt Diffusion and Advection in Building Materials, Research in Building Physics and Building Engineering, London: Taylor and Francis, p. 155-160.

Pavlík Z., Fiala L., Pavlíková M. and Černý R. (2007) Water and Salt Transport and Storage Parameters of Stone Masonry Materials, In: 12th Symposium for Building Physics. Dresden: Technical University, p. 331-338.

Pel L., Kopinga K. and Kaasschieter E. F. (2000) Saline absorption in calcium-silicate brick observed by NMR scanning, J. Phys. D: Appl. Phys, 33, p. 1380–1385.

Price C. (1996) Stone Conservation, An Overview of Current Research, The Getty Conservation Institute, Los Angeles, 73 pp..

Roels S. (2000) Modelling Unsaturated Moisture Transport in Heterogeneous Limestone, Katholiek Univesiteit Leuven, Belgium.

Sayward J. M. (1984) Salt action on concrete, US Army Corps of Engineers Special Report 84-25, 69 pp..

Thorborg von Konow (2006) Proceedings of the ARCCHIP Workshops, European Research on Cultural Heriatge, Vol. 5, p. 213-223.

Impact of furnishing on room airflows

L.H. Mortensen, Ph.D.,
ALECTIA A/S;
lomo@alectia.com

C. Rode, Associate Professor, Ph.D.,
Department of Civil Engineering, Technical Univeristy of Denmark;
car@byg.dtu.dk

R. Peuhkuri, Senior Research Scientist, Ph.D.,
Technical Research Centre of Finland;
ruut.peuhkuri@vtt.fi

KEYWORDS: *Boundary conditions, natural convection, PIV measurements, CFD simulation.*

SUMMARY:
 In building simulation it is common to use idealized empty rooms for simulation. However, furnishing elements may cause local microclimates. These microclimates can be critical for instance if furniture is placed close to poorly insulated external walls in Nordic countries, where the external temperatures in the winter season may lead to condensation or high relative humidity on the internal side of the building envelope. Therefore it was important to investigate the influence of furniture on the airflow patterns in rooms and on the local airflow behind the furniture. The current paper presents an investigation of the airflow patterns behind a piece of furniture placed near a cold external wall. The investigation is based on a combination of Particle Image Velocimetry experiments and Computational Fluid Dynamics. The main topic of the investigation is to highlight the effect of increasing the distance between the wall and the furniture as well as between the wall and the floor. As expected the results showed that increased gap widths give increased airflow rates. Comparison of measurements and simulations indicated a good predictability for the cases, where radiation played a minor role.

1. Introduction

1.1 Background

Moisture interactions between room air and surrounding constructions and furniture have a great influence on the indoor environment. High moisture production or cold areas can cause high relative humidity, which can lead to mould growth. This is unwanted in the indoor environment due to concern for the indoor air quality. A review study of humidity in dwellings has been performed by Bornehag et al. (2001) and their advice is to avoid moist buildings. Typically, the critical areas in dwellings occur in insufficient ventilated bedrooms in microclimates behind furniture placed next to exterior walls with poor insulation, The surface temperature of the exterior wall is typically 5-8 °C colder than the room temperature in dwellings with problems. It is assumed that the furniture limits the airflow near the wall and the lack of warm room air near the surface will decrease the surface temperature even more, which can cause problems. When this is combined with a high moisture production rate from sleeping persons during night, the lower temperature in the microclimate causes increased relative humidity and the outcome can be biological growth. However, to be able to quantify the effect of such a microclimate on the indoor environment, there is a lack of knowledge about the airflow velocities behind furniture in dwellings.

Conventional building energy simulations tools can calculate temperatures in walls whereas the room air is represented by just one node. For overall energy performance this simplification is reasonable but for microclimatic investigations more details are needed. The local airflow patterns will influence the microclimate due to changes in the surface heat transfer coefficient and temperature differences. Computational fluid dynamics (CFD) solves the Navier-Stokes equations, which provides both global and local airflow patterns. Many earlier investigations of airflows in rooms have been done with CFD (Nielsen 1998; Murakami & Kato1989; Gan 1995; Teodosiu et al. 2003; Kuznik et al. 2007). The CFD technique is widely used, but the reliability of obtained quantitative information obtained from CFD remains difficult to determine. Therefore experimental validation is usually required.

Several people have used CFD numerical simulation of airflow pattern in full scale rooms and compared them to measured PIV data (Zhao et al. 2001; Sun et al. 2004, Posner et al. 2003). However, Posner used a scaled model for the PIV measurements. Also, numerous studies of airflow patterns in indoor environments have been performed, but in most cases the rooms are idealized empty rooms. Therefore, in the current investigation the room contained a piece of furniture. An earlier investigation by computational fluid dynamics (CFD) showed that different placement of furniture near colder external walls may affect the relative humidities in the microclimate (Mortensen et al., 2007a). In this study the main focus is on the airflow behind the furniture.

1.2 Paper outline

The objective of the present study is to clarify the behaviour of natural convection in microclimates between an external wall and furniture with special focus on airflow patterns and velocities. The natural convection behind furniture in dwellings was investigated by different cases of distance between the furniture and the wall in combination with different leg heights of the furniture. The investigation was performed with a commercial CFD code (Fluent, 2003) and the simulation results were compared to PIV measurements of the same cases.

The PIV measurements of the different cases provide 2D images of the airflow in a few given positions. The numerical 3D model of the room provides a clearer view on the natural convection in the entire test room. The idea was that the numerical simulation could help understand the measurements better since this would reveal 3D effects.

2. CFD model

Obstacles in rooms are known to cause turbulence and most room airflows are turbulent. Therefore, a viscous turbulence model is used. The dilemma is to choose the most appropriate turbulence model because a wide selection is available. The simplest and most widely used is the standard k-ε model, or modifications of it like the Realizable or RNG k-ε models. The presented CFD simulations were performed with the Realizable k-ε viscous model for turbulence, which have been found to predict well the airflow velocities in a room (Teodosiu et al. 2003;Kuznik et al. 2007). However, a comparison of 6 turbulence models by Sun et al. (2004) found indications that the RNG k-ε model would generally be preferred for airflow in full-scale rooms, but also their investigation showed good results with the Realizable k-ε model, and therefore it was used in the current study. The advantage of the Realizable k-ε model proposed by Shih et al. (1995) is that the model satisfies some constraints on Reynolds stresses that are consistent with physics of turbulent flows, which is neither the case for the standard k-ε model nor the RNG k-ε model. The turbulence model was used in combination with enhanced wall treatment.

The enhanced wall treatment is a near-wall modelling method that combines a two-layer model with enhanced wall functions. When the near-wall mesh is fine enough (typically y+ ~1, y+ ≡ $\rho \cdot u_T \cdot y / \mu$, ρ is density, u_T is friction velocity, y is distance to wall and μ is fluid viscosity) the laminar sublayer will be resolved by the traditional two-layer zonal model. However, the enhanced wall treatment does not require all walls to have fine meshes because a blending function combines the viscosity affected region with the outer region (Fluent 2003). Kuznik et al. (2007) found that better flow predictions are obtained when the k-ε model is combined with a two-layer near-wall treatment.

The main focus of the present investigation concerns natural convection caused by buoyancy effects in the air gap near the chilled wall. Therefore the simulations were performed using the Boussinesq approximation, which is given in Equation 1.

$$\rho = \rho_0 \left(1 - \beta \cdot \Delta T\right) \tag{1}$$

where ρ is the actual density at a given position, ρ_0 is the operating density, β is the thermal expansion coefficient and ΔT is the temperature difference between the actual temperature and the operating temperature.

When the density changes are small, the approximation in Equation 1 is accurate enough.

3. PIV measurements

The Particle Image Velocimetry (PIV) measurements provided 2D velocity vector fields of the flow in the air gap behind the furniture.

3.1 Test Room

A test room was set-up for PIV-measurements on furniture near a colder external wall. An ordinary room with internal dimensions of 3.6 x 4.5 x 2.5 m³ was created inside a larger test facility. A chilled internal wall was built in the chamber, and a plexiglass box was positioned against that wall to imitate a cupboard placed next to an external wall in a real building. The plexiglass box was used because it provides the transparency that is needed in PIV measurements. An air gap behind the plexiglass furniture allows room air to pass over the chilled surface, and this imitates the microclimates found in ordinary dwellings, see Figure 1. The dimensions of the furniture were 1.5 x 0.46 x 2.0 m³ (width x depth x height).The set-up of the test room can be seen in Figure 2. Further details of the experimental set-up can be found in Mortensen et al. (2007b).

3.2 PIV Equipment

The two-dimensional flow field was measured by using a smoke of small oil droplets (glycol 0.1 – 1.0μm) as tracers and their motion was captured by a CCD camera (Dantec HiSense camera, 1024 x 1280 pixels). The tracer particles were illuminated by a light sheet of (about 3 mm in thickness) discharged from a water cooled double pulse Nd:YAG laser system (100 mJ/pulse).

An external processor unit triggers signals to the camera and the laser, and coordinates the transportation of data from the camera to the computer processor. Further description of the equipment and measurements can be found in Mortensen et al. (2007b).

4. Description of cases

The purpose of the investigation was to gain information about the airflow distribution patterns in small air gaps between cold exterior walls and furniture placed near it. Figure 1 shows a picture and a perspective projection of the experimental set-up, the same geometry was studied by numerical simulation.

The study involved 2 different distances between the furniture and the wall in combination with 4 different distances between the furniture and the floor. In one of these the furniture is placed directly on the floor. The surface temperature of the chilled wall behind the furniture was constantly 16°C. During the measurements the average room temperature was 22°C (giving a temperature difference of 6°C) but in the numerical simulation the air temperature was slightly smaller, 21.2°C. This lower temperature was caused by the chilled wall together with the temperatures of the other surfaces of the room that were set to 22°C. Table 1 gives the different cases and their distances between the furniture and floor or chilled wall. The absolute camera and laser positions are described in Table 2 and illustrated in Figure 2. Position F is used to compare simulations and measurements.

4.1 Simulations

The simulation model has the same geometry as the measurements.The discretization of the computational domain was accomplished with an unstructured mesh consisting of tetrahedral elements. The advantage of the unstructured mesh is that it can easily be refined in specified areas without addition of unnecessary cells in other parts. This advantage was used in the air gap between the furniture and the wall to obtain a better resolution of the obtained flow velocities. However, the unstructured mesh can cause problems near the walls and this is compensated for by use of the so-called enhanced wall treatment (Teodosiu et al., 2003).

The simulations were split in two parts; first simulations were performed with a rough grid (~400,000 cells) for the entire room to resolve the overall flow pattern, then adaptation of the grid was added in the air gap behind the furniture (>1,100,000 cells) and further iterations were performed to resolve the airflow velocities in the air gap. Even further adaptation was made in the area of the measuring positions to ensure y+~1.

The simulations focused only on the airflow in the room so energy and viscous airflow models were used. In the material database, the air properties were set as dry air at 22°C and a boussinesq density. The cold wall was set to 16°C and the other walls 22°C except the gypsum board wall that extends the chilled wall to reach the side wall (behind the camera in Figure 2). This wall was assumed adiabatic. The measuring positions A-G of the PIV equipment are given in Table 2. Here only results from position F will be compared for different furniture position cases (see Table 1).

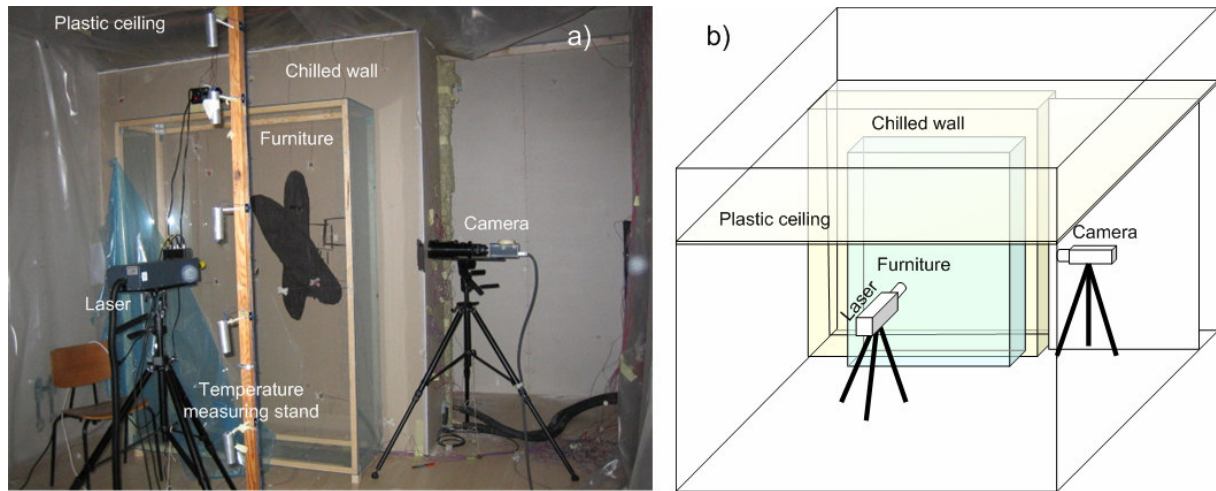*FIG. 1: The experimental set-up, where the camera points into the air gap between the chilled wall and the furniture and the laser sheet is pointed in through the plexiglass furniture. a) A picture of the experimental set-up. b) A diagram of the PIV set-up.*
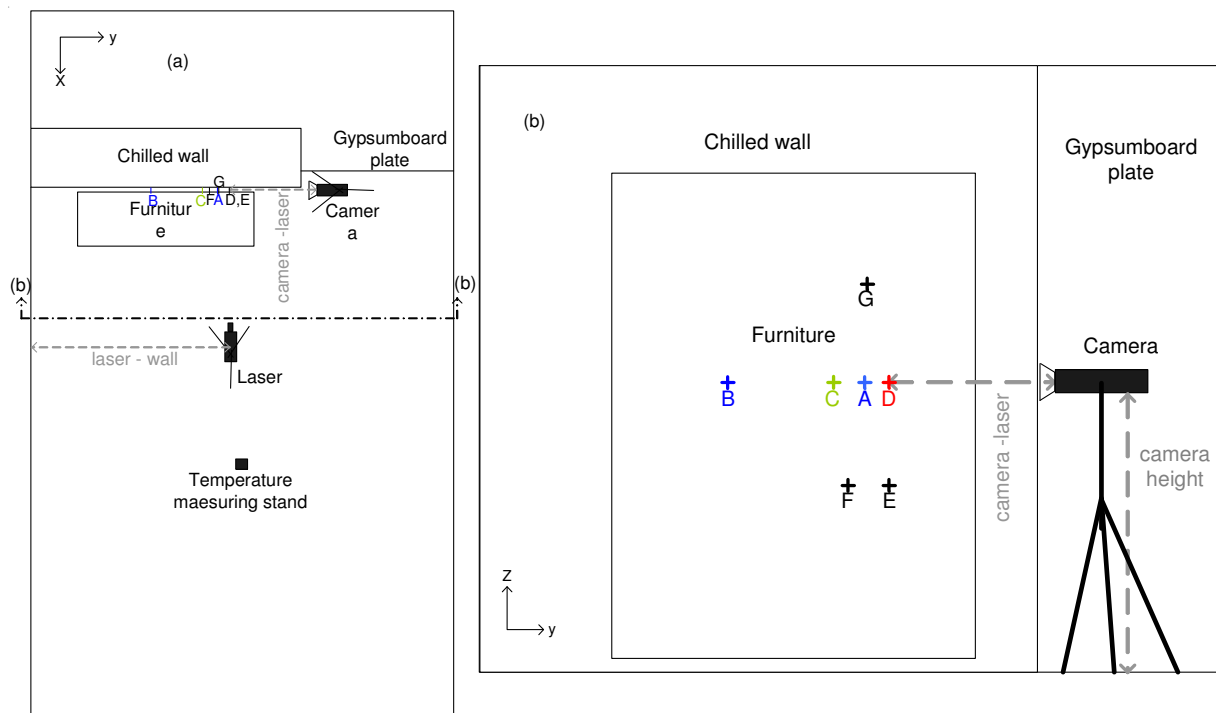

FIG. 2: Part (a) show a plane of the measured PIV set-up and (b) show a front view of the room. The letters A-F show the measuring positions given in table 2.

TABLE 1: The different tested positions of the furniture.

Furniture position	Gap (mm) furniture - floor	Gap (mm) furniture - chilled wall
1	0	25
2	0	50
3	50	25
4	50	50
5	100	25
6	100	50
7	200	25
8	200	50

TABLE 2: Description of PIV measuring positions. The physical image size changes with distance between camera and laser. Only image widths of maximum 50mm is used; the rest is masked out.

Position	Distance (mm) camera – laser	Image height (mm)	Camera height (mm)	Laser height (mm)	Distance (mm) laser – wall	Measured furniture position
A	1050	124	1183	1192	1570	1-8
B	1420	187	1183	1192	1000	3-4
C	1200	136	1183	1192	1440	3-6
D	920	106	1183	1192	1670	1-8
E	930	113	770	760	1670	3-4
F	1080	130	770	760	1500	1-8
G	970	119	1595	1570	1580	4

5. Results

Only the vertical velocities in the vertical air gap will be shown and discussed, since the horizontal velocities are very small. The horizontal velocities (x-direction in Fig. 2) are in the order of magnitude of 2 % of the vertical velocities in the air gap between the furniture and the chilled wall. The velocity field is set to be positive upwards (z-direction in Fig. 2). In the current paper, PIV measurements results will be presented in form of comparison to numerical simulations.

5.1 Simulation Results for the Entire Room

Figure 3 illustrate the airflow pattern of the room. The highest airflow velocities are seen in the air gap behind the furniture and the velocities behind the furniture increases all the way to the bottom of the air gap.

5.2 Comparison of measurements with CFD

In Figure 4 a comparison is shown between the PIV-measurements and the numerical simulation of the airflow in a gap between the chilled wall and the furniture. The average velocity is calculated and shown in the legend. The figure shows that the shape of the velocity profile is the same for the cases with different distance to the floor but at different velocity levels. However, the shape of the velocity profile changes when the gap is increased from 25 mm to 50 mm. The comparison of the simulation results and the measured data shows that the general shape of the velocity profiles is fairly well predicted by the simulation. The simulated velocities are about half of the measured values for the 25 mm air gap. Opposite to this, the velocity levels are predicted quite well for the cases with a 50 mm air gap, except for the case where the furniture is placed on the floor. The calculated average velocities confirm that the simulation underestimates the velocities. The model predicts the velocities for the 50 mm air gap very accurately but there are some minor differences. For instance, the maximum velocity is underestimated since the measurements found the maximum velocities near the chilled wall at x ~ 40 mm, whereas the simulation have maximum at x~35 mm.
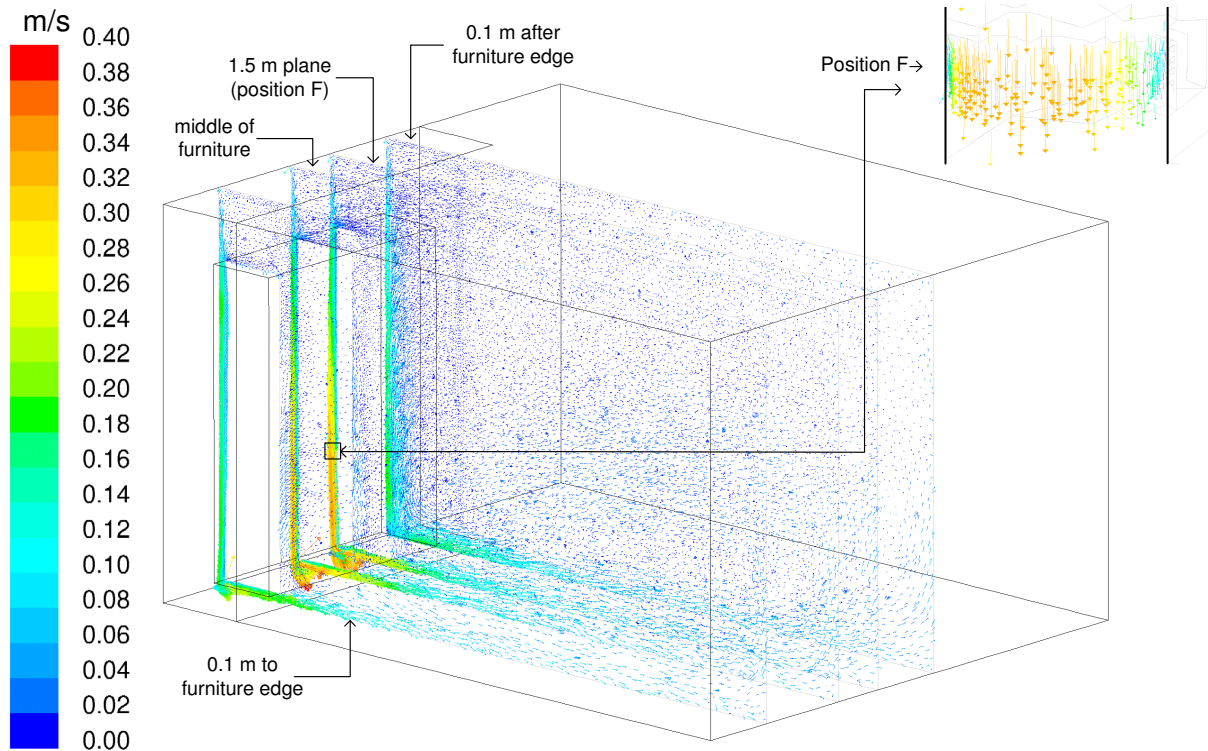
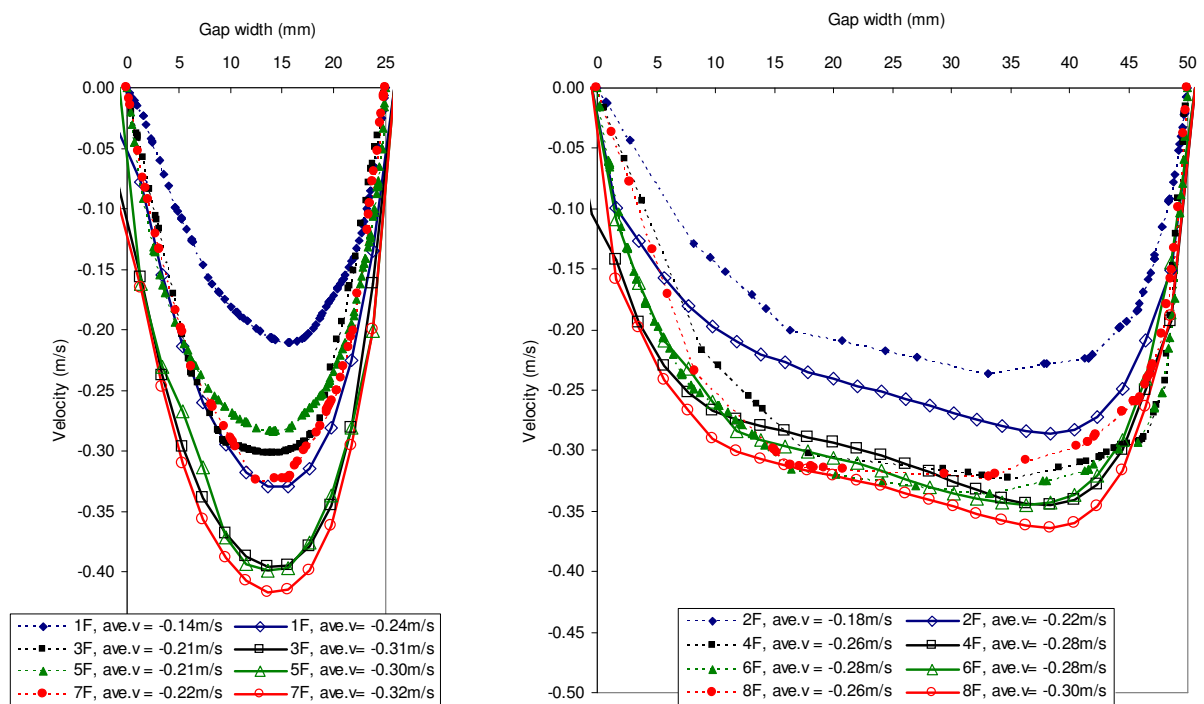*FIG. 3: Airflow patterns are presented as vectors in 3 planes.*

FIG. 4: Comparison of measured (solid) and simulated (dashed) results for position F for a gap width of 25mm and 50mm, furniture surface at x = 0 mm. In the legend the calculated average velocity is given.

6. Discussion

The objective of the current study was to investigate the natural convection between furniture and an exterior wall. The measured data have been compared to simulated data for a similar geometrical setup. The highest air-flow velocities in the room are found in the air gap behind the furniture as seen in Figure 3. Two gap widths of 25 and 50 mm have been investigated. The highest measured and simulated velocities were found closest to the chilled wall, see Figure 4. This confirms that density changes dominate the flow by air-cooling in the gap. Both simulations and measurements also confirm that elevation of the furniture will increase the flow behind the furniture. Whether the effect will be enough to avoid problems with condensation or humidity levels suitable for mould growth has not been investigated in this study.

In Figure 3 it is clearly seen that the velocities are highest at the bottom of the airgap, which is a 3D effect as air must have entered from the sides of the furniture. This effect was actually confirmed by the PIV measurements in the other measuring positions as shown in Mortensen et al. (2007b).

In Figure 4 it is seen that the predicted shape of the velocity profiles seem similar to the measured. Especially the simulation results for the 50 mm air gap match the measured data very well. This clearly indicates that CFD simulations can be used to predict airflow velocities in microclimates. However, the model underestimates the velocities in the narrower 25 mm air gap. The profile is predicted well but the velocity level is only about half the measured value. This may be explained by influence of radiation between the surfaces of the wall and furniture, which was not included in these simulations. The velocity of the airflow in the gap is very temperature dependent as the denser cold air will fall towards the floor. This can explain why the narrow gap is highly underestimated as radiation between the surfaces of the chilled wall and the furniture surface may be more pronounced for the 25 mm gap than for the wider 50 mm gap where the distance between the surfaces are twice as wide. For the 50 mm air gap a preliminary test with radiation showed that it had little influence on the results, and since the radiation model cannot be used in Fluent in combination with mesh adaptations, no radiation model was used in the simulations. This implies that for narrow air gaps, initial simulations must be performed in order to investigate what is the influence of radiation, and only if the influence is neglible, the unstructured mesh combined with adaptations can be used to zoom in on a small microclimate.

The good results of the comparison between the simulated and measured data suggest that CFD simulation can be used to accurately calculate the surface heat transfer coefficient which again can be used to predict the water vapour surface resistance. Therefore, this implies that the CFD simulation can be a useful tool for investigation of hygrothermal microclimates in dwellings. However, one should be cautious when radiation plays an import role in the heat transfer in the microclimate, because this might influence the simulated airflow velocities.

This investigation has shown that further analysis should be made where the CFD simulations include radiation in order to see what effect it will have on the prediceted airflow velocities in the air gap.

The starting point for this investigation was the moisture interactions in rooms and particularly the relative humidity in microclimates. However, it is not expected that the airflow velocities in the gap behind the furniture will be affected by moisture in the air as the moisture driven convection potential is much smaller than the buoyancy driven convection. Even though the airflow velocity is properly not influenced by moisture in the air there may still be RH variations behind the furniture compared to the general average in the room as shown in Mortensen et al. (2007a). The narrow air gap has higher airflow velocities but the total volume flow rate is smaller than for the wider 50 mm gap, so less moisture can be transported away from the air gap and a lower airtemperature generally gives higher RH, which may be critical.

7. Conclusion

An investigation was performed using PIV and CFD of the airflow pattern in a small air gap between a chilled wall imitating an exterior wall and a piece of furniture placed next to it. The two investigated gap widths of 25 and 50 mm showed different patterns of velocities but they both seem to be dominated by the boundary flow near the chilled wall, since the maximum velocity was found closest to this wall. The study also confirms that the airflow behind the furniture will increase if the furniture is elevated from the floor.

For a 50 mm air gap the simulated and measured results were rather uniform, which indicates that CFD models can be used to predict airflow velocities in local microclimates. However, the differences between the measurements and the simulations of the narrow 25 mm gap cannot be fully accounted for.

8. Acknowledgements

9. References

Bornehag C.-G., Blomquist G., Gynteberg F., Järvholm B., Malmberg P., Nordvall L., Nielsen A., Pershagen G., Sundell J. (2001). Dampness in buildings and health. Nordic Interdisciplinary Review of the Scientific Evidence on Associations between Exposure to "Dampness" in Buildings and Health Effects (NORDDAMP), *Indoor Air*, Vol. 11, No. 2, 72–86.

Fluent (2003). FLUENT® User's Guide, Lebanon, NH, USA: Fluent Inc.

Gan G. (1995). Evaluation of room air distribution systems using computational fluid dynamics, *Energy and Buildings,* Vol. 23, No. 2, 83-93.

Kuznik F., Rusaouën G., Brau J. (2007). Experimental and numerical study of a full scale ventilated enclosure: Comparison of four two equations closure turbulence models, *Building and Environment*, Vol. 42, No. 3, 1043–1053.

Mortensen L.H., Woloszyn M., Rode C., Peuhkuri P. (2007a). Investigation of microclimate by CFD modelling of moisture interactions between air and constructions, *J. of Building Physics*, Vol. 30, No. 4, 279-315.

Mortensen L.H., Rode C., Peuhkuri R.(2007b). Microclimate investigation of airflow patterns by Particle Image Velocimetry (PIV), Accepted for publication in *Building and Environment*, doi: 10.1016/j.buildenv.2007.11.012

Murakami S., Kato S. (1989). Numerical and experimental study on room airflow-3-D predictions using the k-ɛ turbulence model, *Building and Environment,* Vol. 24, No. 1, 85-97.

Nielsen P.V. (1998). The Selection of Turbulence Models for Prediction of Room Airflow, *Ashrae Transactions,* Vol. 104, No. 1B, 1119-1127.

Posner J.D., Buchanan C.R., Dunn-Rankin D. (2003). Measurement and prediction of indoor air flow in a model room, *Energy and Buildings,* Vol. 35, No. 5, 515-526.

Shih T.-H., Liou W.W., Shabbir A., Yang Z., Zhu J. (1995). A new k-ɛ eddy viscosity model for high Reynolds mumber turbulent flows. *Computers & Fluids*, Vol. 24, No. 3, 227-238.

Sun Y., Tan Z., Zhang Y., Zhao L. (2004). Comparison of six CFD models for room airflow study with PIV measurement data, *ASAE Annual International Meeting*, 5239-5259.

Teodosiu C., Hohota R., Rusaouën G., Woloszyn M. (2003). Numerical prediction of indoor air humidity and its effect on the indoor environment, *Building and Environment,* Vol. 38, No. 5, 655-664.

Zhao L., Zhang Y., Wang X., Riskowski G.L., Christianson L.L. (2001). Measurement of two-dimensional air velocities in a full-scale room using particle image velocimetry, *Ashrae Trans.,* Vol. 107, No. 2, 434-444.

Experimental Confirmation on the Theoretical Model for the Velocity Profile in a Rectangular Wind Tunnel

Goce Talev, PhD candidate
Department of Civil and Transport Engineering,
Norwegian University of Science and Technology (NTNU)
Goce.Talev@ntnu.no

Arild Gustavsen, Professor
Department of Architectural Design, History and Technology
Norwegian University of Science and Technology (NTNU)
Arild.Gustavsen@ntnu.no

Jan Vincent Thue, Professor
Department of Civil and Transport Engineering,
Norwegian University of Science and Technology (NTNU)
Jan.Thue@ntnu.no

KEYWORDS: CFD Simulation, Measurements, Wind Tunnel, Velocity profile

Summary:

A new open-loop, low-speed wind tunnel has been designed and constructed, at the Norwegian University of Science and Technology (NTNU) in Trondheim Norway, in order to determinate the convective mass transfer coefficient. It has a working section of 0.45 m wide, 0.3 m high and 1 m long with maximum wind speed of 5m/s under typical operating conditions. The design was specially constructed by a need to provide a uniform air flow without excessive turbulence and to verify its adequate influence of the simulated external boundary layer on the local convective mass transfer coefficient. This paper presents the results of longitudinal velocity measurements in an empty tunnel using a Pitot-static tube without honeycomb at the inlet, as well as flow characteristics. The measurements of the mean velocity were found to compare well with a computational fluid dynamic (CFD) tool, FLUENT.

1. Introduction

Large amounts of moisture accumulate in the building construction, e.g. due to condensation or leakage of liquid water from either the outside or inside, defects or other problems may arise. This may lead to damage to the construction such as decay of wood, corrosion of metals, degradation of binders and adhesives, swelling of materials, reduced frost resistance etc. Wet or even humid constructions may have a noticeably larger heat loss than they would have had if they were dry.

Humidity and temperature are important comfort factors. Many health-related problems in the indoor environment can be associated with high indoor humidity. High humidity can also contribute to the growth of biological agents such as fungi (O'Reilly et al. 1998). Further, low humidity contributes to dry mucous membranes, which in turn can make the nose and throat feel scratchy, lead to nosebleeds, make throat and nasal membranes more susceptible to chemical and other irritants, and continue to susceptibility to viral infection.

Ventilation with fresh air may be a way to improve the problems of high indoor humidity, but ventilation requires energy to condition the air and run the fans of the ventilation systems. So there is an interest in designing buildings for suitable balance between moisture supply and required ventilation.

To be able to accurately simulate and predict heat, air and moisture flows in buildings there is a need for detailed knowledge regarding the building envelope, building installations and usage, and the boundary conditions. In particular, transient calculation of moisture transfer requires knowledge of the convective moisture transfer coefficients and the moisture buffering properties of building materials, furniture and fixtures.

Boundary conditions are represented by defining a transfer of thermodynamic property (flux) between these walls and the air flow, or by defining a fixed state at the wall. In order to model the interaction between the wall

(state) and the fluid (state) a transfer coefficient is often used, know as a friction coefficient, heat transfer coefficient or mass transfer coefficient. This transfer coefficient is in fact a modelling assumption in itself.

Determination of the convective mass transfer coefficients as a function of the exterior condition as well as material properties in the specimen is a big scientific challenge. New better knowledge about the convective mass transfer coefficients and their application on the moisture buffering effects of building material is expected to be provided.

Thus, based on the above discussion, to be able to predict the indoor temperature and relative humidity by numerical simulations there is a need for more experimental research on the buffering effects of materials used in buildings, and the boundary conditions.

A new open-loop, low speed wind tunnel with a unique design has been constructed at the Norwegian University of Science and Technology (NTNU), intended to allow testing of different building materials under a wide range of flow conditions. The primary goal of the wind tunnel design was to provide the experimental information of the convective mass transfer coefficients as a function of the exterior condition and material properties of the specimen. In order to carry out desired measurements, the wind tunnel must meet the following requirements:

- The velocity profile through the test section should be as near as possible to a parallel steady flow with uniform speed, with minimal boundary layer thickness along the surface

- Turbulence intensity should be as close as possible to zero to allow easier comparison of the results, and to avoid velocity fluctuations within the wind tunnel. As a desired goal, the turbulence intensity should be as small as possible.

2. Wind Tunnel Design

The design requirements of the wind tunnel were base upon experience gained from the previous research work of Talev et al. (2006). Most of the detailed wind tunnel design work was been described by Barlow et al. (1984), Sætran (1984), and Bell and Metha (1988). The design was a result of the need for obtaining a flow in the test section that is as near as possible to a parallel steady flow with uniform speed through the test section without excessive turbulence. It was judged that constructing an open loop circuit wind tunnel would be the most economical solution to control the boundary condition of the air in order to provide a value of the convective moisture transfer coefficients. The wind tunnel is made of several distinct sections, the settling chamber, the contraction cone, the test/working section, the diffuser and the fan. Several considerations have to be made in order to achieve a wind tunnel with the wanted properties. Below is brief explanation of the various parts and considerations done as building the wind tunnel. The configuration of the wind tunnel is shown in Figure 1.

2.1 Settling Chamber

The settling chamber has the largest cross section of the wind tunnel. It contains an entrance section (bell-mouth inlet), a hexagonal cell-aluminium honeycomb and screens in order to achieve the low-turbulence characteristic as well as straightened of the desired airflow. It is worth to mention that the honeycomb and the screens were not installed in the settling chamber during the experimental measurements presented in this paper.

2.2 Contraction Cone

A large volume of air with low velocity from the settling chamber is moving toward the contraction cone where the cross section is reduced and the air velocity increased. The design of the contraction cone was based on a fifth order polynomial contraction cone developed by Bell and Metha (1988). The design was confirmed by CFD simulations (Fluent 2006); the results of these are not presented here. The primary function of the contraction cone is to make the path of the air entering the test section more symmetrical and to erase the "memory" of the return flow. The contraction ratio is 8:1.

2.3 Test Section

A one-meter long test section was designed to produce an external flow along the test section floor. The wind tunnel floor and roof are made of plywood and the side walls of the test section are made of Plexiglas. The low thermal conductivity and capacity of the plywood structure leads to good insulation between the external and internal part of the wind tunnel. In addition very stable temperatures on the bottom of the wind tunnel and in the

free air stream are found during the measurements. However, the development of thermal boundary layer is not a subject of this paper. The test section has a rectangular shape, with an area of 0.135 m² that results from a 0.3 m height and 0.45 m width. The side walls are parallel and have very smooth surface. The Plexiglas walls enable access and inspection of the model and measurement probes. At the top plate there are slots enabling horizontal and vertical traversing of measurement equipment, such as a Pitot tube. Access to this section is achieved through a wide door on the left side of the tunnel.

2.4 Diffuser

Diffuser is the longest section of the wind tunnel where the velocity of the airflow is reduced with as little energy loss as possible by flowing into an increasing cross-sectional area along the axial direction of the wind tunnel.

2.5 Fan

The Fan is an axial-ventilator type ASB, manufactured by Nordisk Ventilator Co., Denmark. The pitch angle of the fan blades can be continuously regulated manually. The housing is made of the steel and connection to the wind tunnel is made in order to avoid any vibrations.
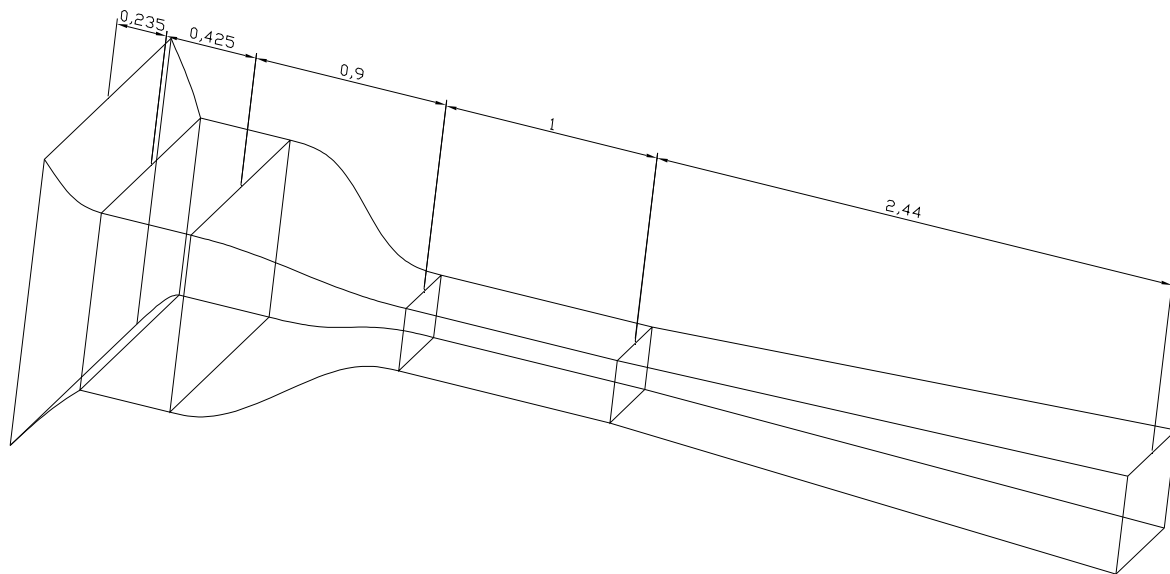
FIG. 1: Figure of the designed wind tunnel with dimensions.

3. Methods

The wind tunnel design was tested by performing wind profile measurements along a vertical line located in the middle of the wind tunnel 50 cm from the test section entrance. The wind profile was compared to the design simulations. The measurements were carried out for velocities of about 1, 2, 3, 4 and 5 m/s, see below. Average and integrated velocities have been used to determine the mass-flow-inlet value (used in the simulations). The arithmetic average velocity was provided as a ratio between the measured velocity and number of measurements, see Eq. 1. The integrated velocity has been provided from the integration method over the length of the profile, see Eq. 2. The mass-flow rate was found from Eq. 3.

$$U_{av} = \frac{u_1 + u_2 + \cdots + u_n}{n} = \sum_{i=1}^{n} \frac{u_i}{n} \tag{1}$$

$$U_I = \sum_{i=1}^{n} \frac{(x_i - x_{i-1})}{d} \cdot \frac{u_i + u_{i-1}}{2} \tag{2}$$

$$G = \rho \cdot A \cdot U \tag{3}$$

u_i represents the values of the sample velocities and n is the number of measurements. x_i is the local position. The mass-flow rate G (kg/s) is calculated as a product of the density ρ (kg/m³), air velocity (U_{av} or U_l) and cross section area A. An air temperature of 20°C and relative humidity of 30% was measured during the measurements. A density of 1.2 (kg/m³) was therefore used, according to Hagentoft (2001).

3.1 Experimental Studies

The experimental work was conducted for air velocities up to 5m/s. The air flow was controlled by frequency regulation of the axial fan. The wind tunnel was placed in a climatic room with a constant temperature of 20 ± 1 °C. Air enters into the wind tunnel from the surrounding side of the settling chamber (bell-mouth inlet), passes through settling chamber, arrives to the test section and continues to the diffuser which is connected to the fan. The uniformity of the free stream was investigated by measuring the mean velocity profile using a Pitot tube and a micro-manometer. The Pitot probe was traversed vertically across the test section at a position corresponding to the centre point of the test section, i.e. 50 cm downstream in the test section. At each measurement location, the velocity was measured for one minute. The output electrical signal of the manometer was transferred to a PC through the LABVIEW program (NI, 2007).

3.2 CFD Simulations

GAMBIT 2.3.16 has been used as a pre-processor to create the wind tunnel model and to construct the computational domain. A two and three-dimensional structure of the wind tunnel has been chosen. FLUENT 6.3.26 (Fluent, 2006) was used to compute the velocity field through the test section of the wind tunnel. A laminar viscous model with no-slip along the upper and lower walls of the wind tunnel section was selected. Air was selected as a fluid, and the properties calculated for an atmospheric pressure of 1 atm. At the exit of the diffuser the mass flow was set, with the flow direction normal to the boundary. The convergence criterion of the velocity in x- and y-direction, continuity and energy equations were selected on the absolute criteria of 10^{-5}. The solution was initialized and iterations of 200 ± 50 were required.

Figure 2 shows the mesh for the test section for one of the cases that that was analysed. The number of elements in the vertical direction is equal to 30. Cases were also simulated where the number of element in the vertical direction was 40 and 60. Both 2D and 3D analyses were performed. In the horizontal direction 50 nodes were used in all cases. In the third direction, in the 3D simulations, 50 nodes were used.

FLUENT solves the governing equation by a finite-volume formulation on a structured, non-orthogonal curvilinear coordinate grid system using a collocated variable arrangement. SIMPLE was used to solve the fluid flow which is described in a set of algebraic equations which are solved using a line-by-line traditional matrix algorithm, accelerated by an additive-correction type of multi-grid-method and block correction. Based on the analysis, a laminar flow solver is used to compute the air flow inside the test section of the wind tunnel.
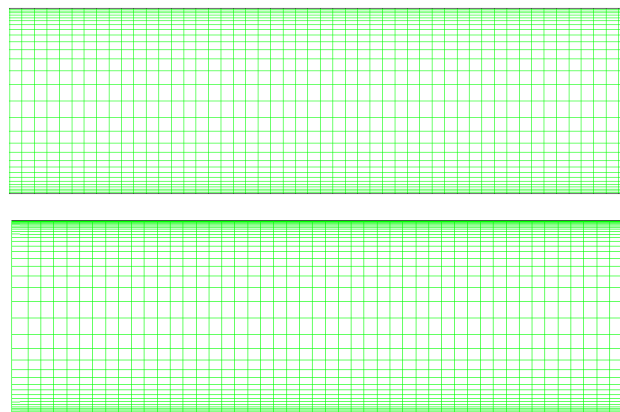

FIG. 2: Test section mesh (2D) for the cases with 30 and 60 nodes in the vertical direction.

4. Results and Discussion

Figures 3 to 7 show the various wind profiles for different wind velocities, for velocities between about 1 and 5 m/s, where the actual wind velocity can be seen from the figures. The abscissa shows the air velocity (in m/s) and the ordinate display the local position (in millimetres) in the wind tunnel test section. The floor of the test section is numerated 0.

The mesh elements are chosen to be closely spaced in regions of strong gradients i.e. near the wall regions where the velocity variation reaches its maximum. Mesh grading of 1.2 was used both for 2d and 3d models.

The simulations were an essential part of this research because they provided theoretical values to compare to the velocity measurements. The numerical simulations were also used, in the fist place, to design the wind tunnel with the desired properties.

In the simulations, the specific mass-flow rates used as boundary conditions were calculated from the measured velocity profile in the middle of the test section (the profiles presented in the figures below), according to Eq. 3. Because the wind velocity in the middle of the test section will be larger than the velocity close to the walls, the mass-flow rate based on this velocity will be somewhat larger than the actual mass-flow rate. This can be seen in the Figures, where the simulated results are slightly larger than the measured results.

The figures have in common that the 3D simulations show a more uniform profile that more closely resemble the measurements in the middle of the tunnel, than the 2D simulations. The difference between the 2D and 3D simulations is larger for the highest velocities. Close to the wall both 2D and 3D simulations seem to compare well with the measurements, except for small velocities (close to 1 m/s), however further investigations is needed here. Better agreement between measured and simulated results at lower air speed are expected after installing a hexagonal cell-aluminium honeycomb and screens in the settling chamber. All mesh resolutions seem to give comparable results.

FIG. 3: Comparison of velocity profile between calculated and measured data at 1.2 m/s.

FIG. 4: Comparison of velocity profile between calculated and measured data at 2 m/s.

FIG.5: Comparison of velocity profile between calculated and measured data at 3 m/s.

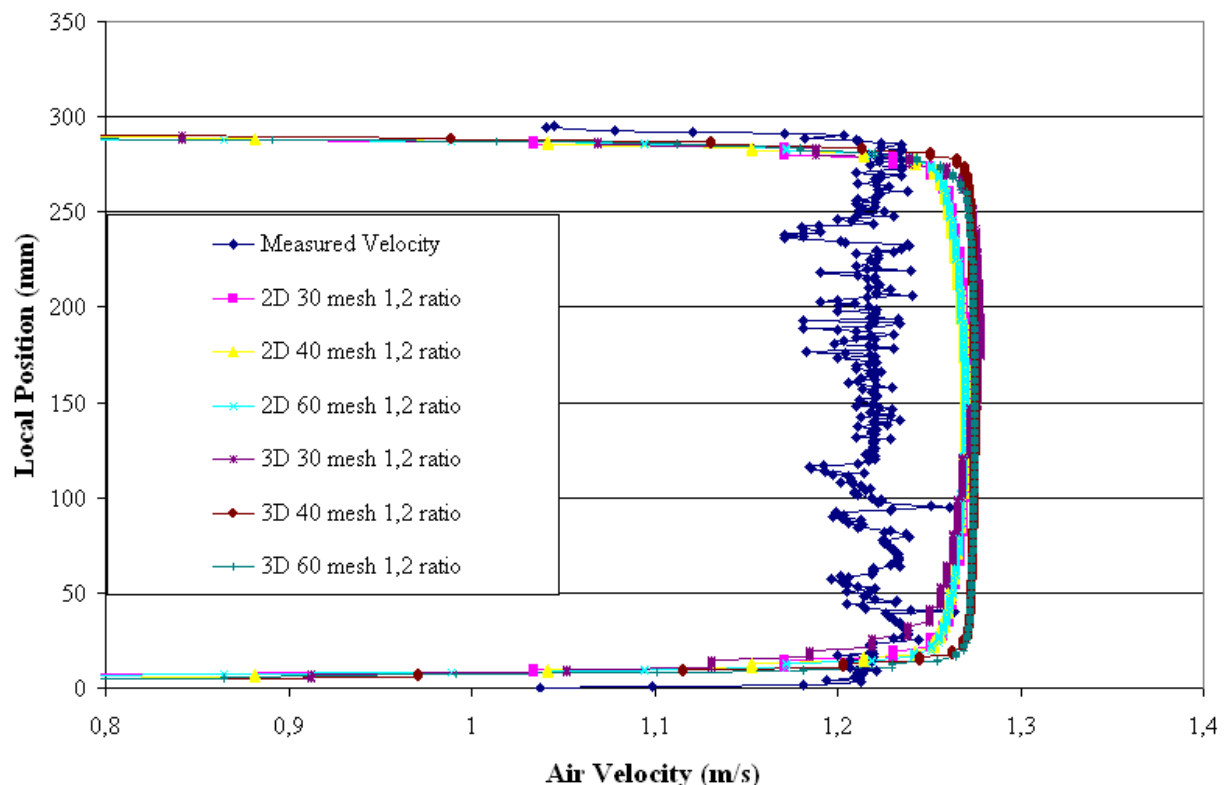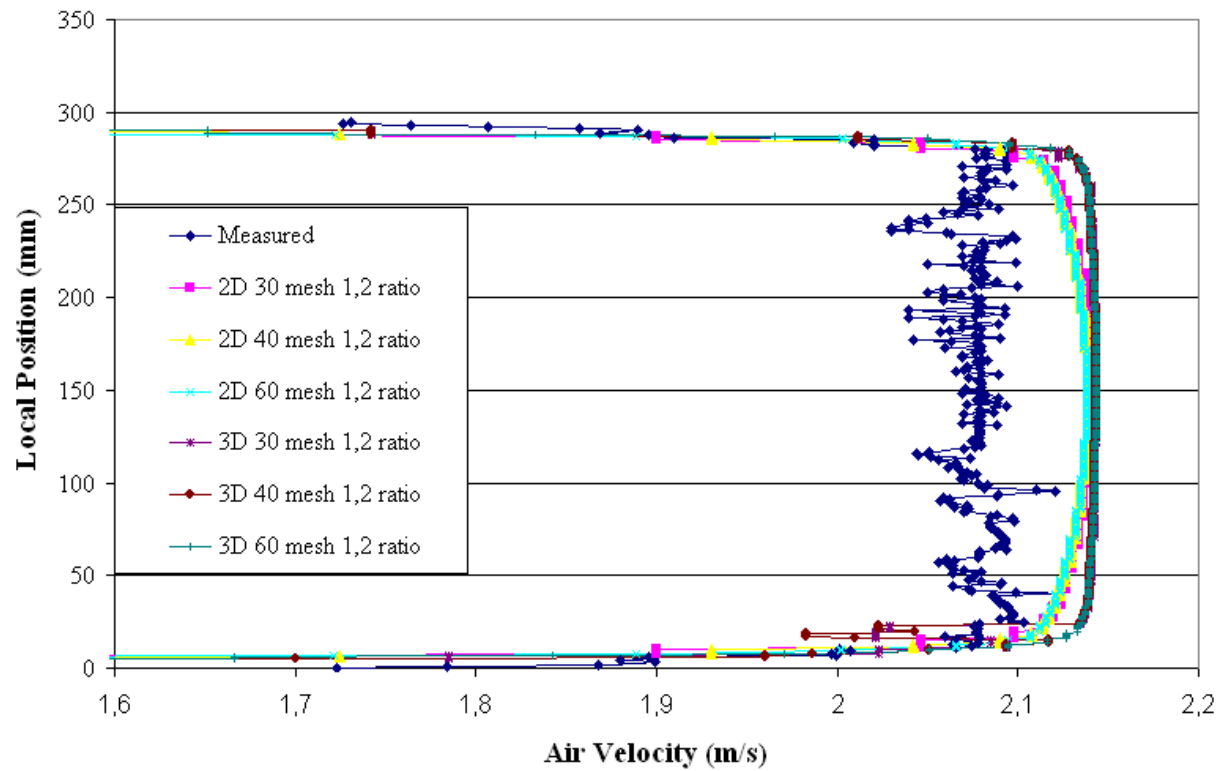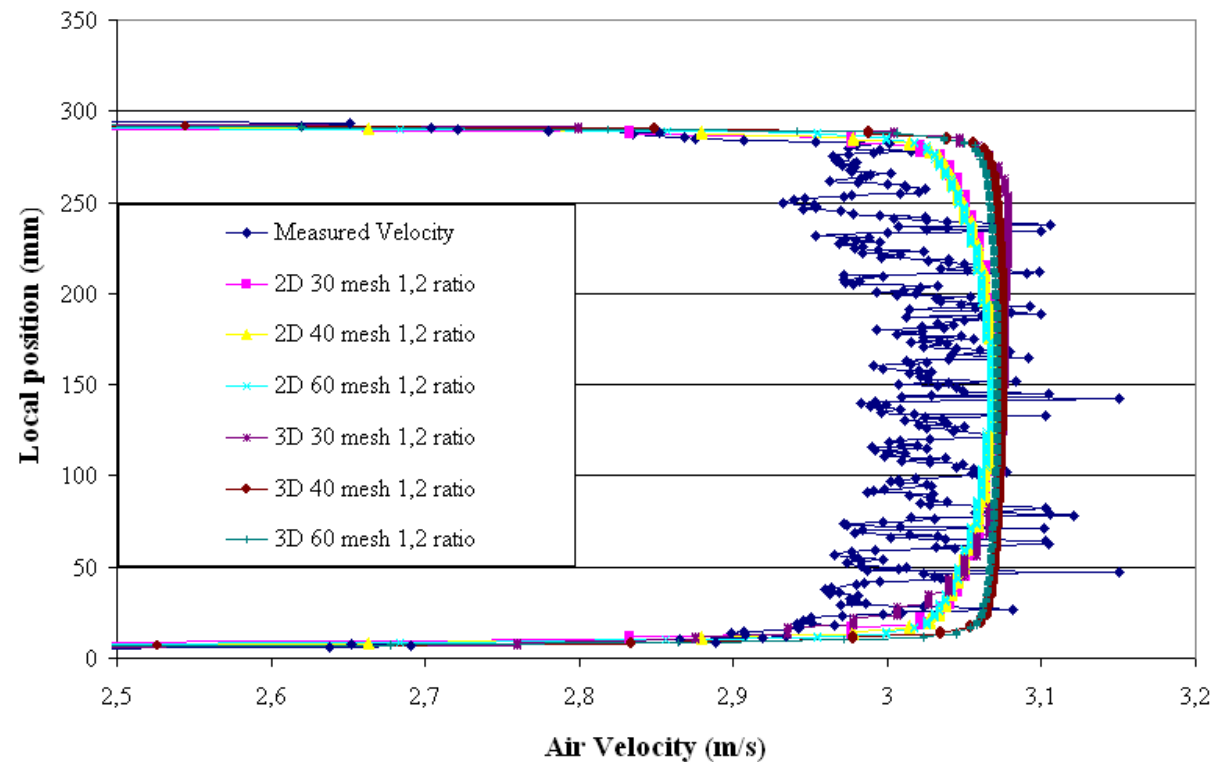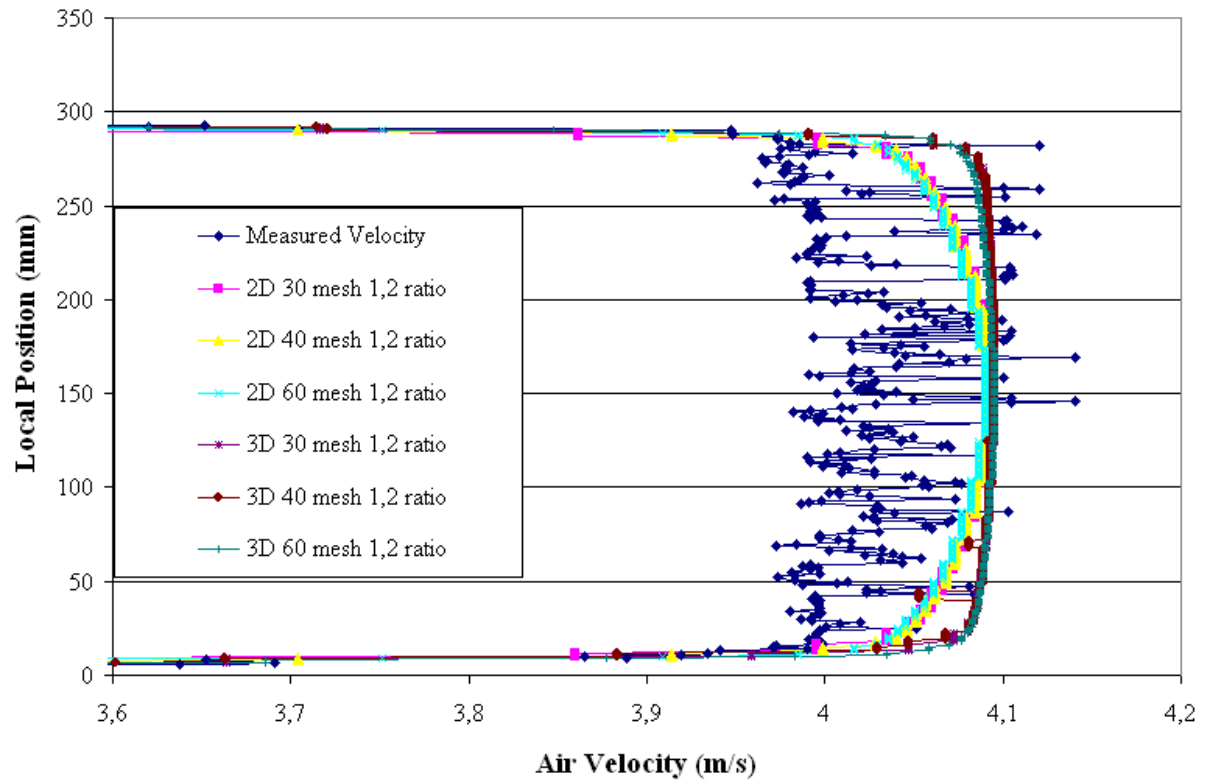*FIG.6: Comparison of velocity profile between calculated and measured data at 4 m/s.*
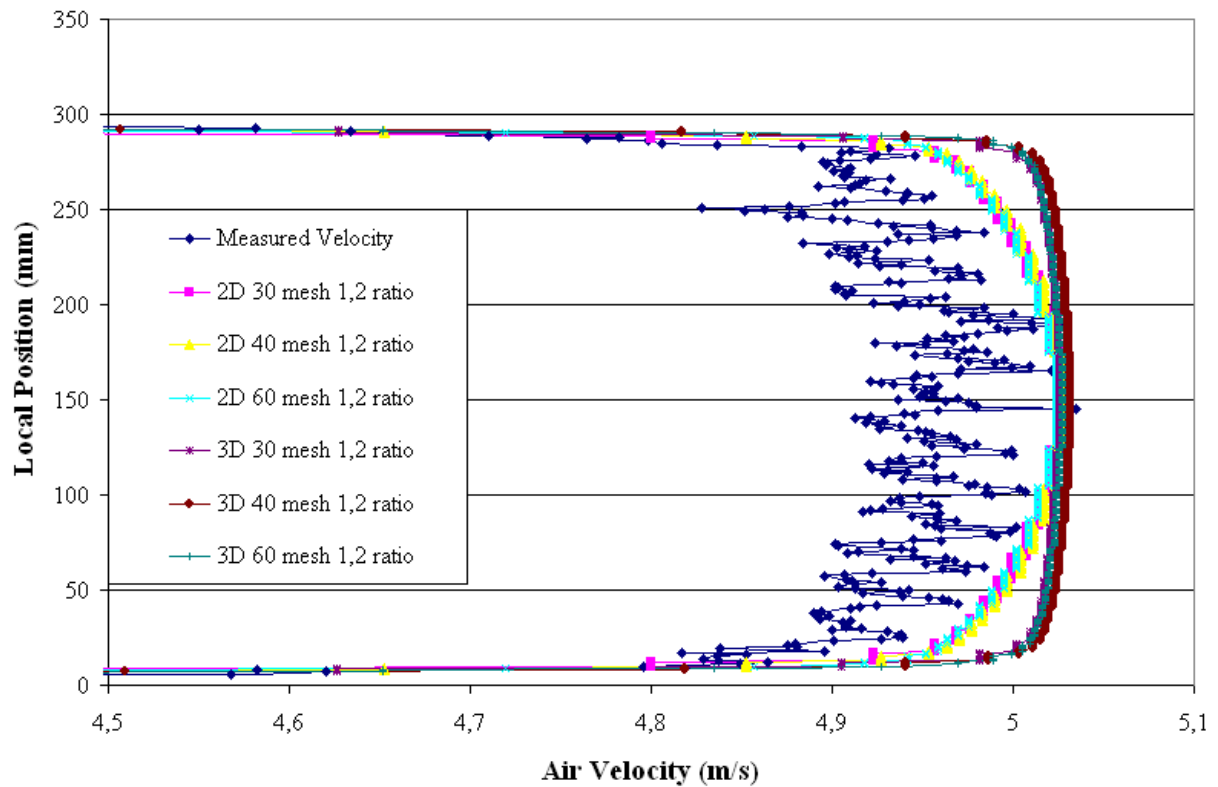

FIG.7: Comparison of velocity profile between calculated and measured data at 5 m/s.

5. Conclusion

The purpose of this research work was to evaluate the low-speed wind tunnel to verify its adequacy for structural analysis applications as well as to simulate the velocity profile at the centre of the test section, i.e. 50 cm downstream in the test section. Measurements of the velocity in the empty wind tunnel showed a uniform field. In order to have confidence in the results from such simulations, validation is required. The CFD simulations showed quite good agreement with the vertical velocity profiles which were measured by Pitot-static tube. 3D simulations compared better to the measured results than 2D simulations.

The new designed tunnel at NTNU is, therefore, a very good device to provide parallel steady flow with uniform speed through the test section without excessive turbulence.

Future work will consider the evaluation of the flow condition on the value of the convective moisture transfer coefficients and their application in the buffering moisture effects of the building materials. In addition, the turbulence intensity profile will be also subject of further work after installation of a hexagonal cell-aluminium honeycomb and screens in the settling chamber. Comparation between the wind tunnel results and boundary layer condition observed for real building will be carried out after installation of the honeycomb and screens in the settling chamber of the wind tunnel.

6. References

Barlow J.B., Rae W.H., and Pope A. (1984). *Low-Speed Wind Tunnel Testing,* 3rd edition, John Wiley ISBN 0-471-55774-9.

Bell J.H. and Mehta R.D. (1988). *Contraction design for small low-speed wind tunnels*, Department of aeronautic and acoustics, Stanford University.

Fluent 2006. FLUENT 6.3 User's Guide, Fluent Inc.

Hagentoft, C.E. (2001). *Introduction to Building Physics*, Studentlitteratur, Lund, Sweden ISBN91-44-01896-7.

NI (2007). LABVIEW 8.2. National Instruments.

O'Reilly J., Hagan P., and Gots, R. and Hedge, A. (1998). Keeping buildings healthy. How to monitor and prevent indoor environmental problems. John Wiley Sons, INC., New York, USA ISBN 0-471-29228-1

Sætran R. L. (1984). *Experimental Investigation and Mathematical Modelling of Momentum, Heat and mass Transport in Some Turbulent Flows,* Institute of Applied Mechanics, University of Trondheim, NTH, Norway ISBN 82-7152-070-9.

Talev G., Gustavsen A. and Næss E. (2006). *"The influence of air velocity and transport properties on the surface mass transfer coefficient in a rectangular tunnel –theory and experiments"* Presented in IEA, ECBCS, Annex 41in Lyon, France.

Measurements and simulations of airflow in a mechanically ventilated active facade

Evelien A. Pegge, MASc
Eindhoven University of Technology, The Netherlands
evelien.pegge@gmail.com

Bert Blocken, PhD, MASc
Eindhoven University of Technology, The Netherlands
b.j.e.blocken@tue.nl

Martin H. de Wit, Prof, PhD, MASc
Eindhoven University of Technology, The Netherlands

Jan Carmeliet, Prof, PhD, MASc
Chair of Building Physics, Swiss Federal Institute of Technology ETHZ, Zürich, Switzerland
Empa, Swiss Federal Laboratories for Materials Testing and Research, Laboratory for Building Technologies, Switzerland

Walter Bosschaerts, Prof, PhD, MASc
Royal Military Academy, Brussels, Belgium

KEYWORDS: *active facade; multiple-skin facade; Computational Fluid Dynamics; validation*

SUMMARY:
Simplified methods to predict the flow between vertical plates cannot be applied to predict the flow patterns in active facades. Due to the presence of blinds and asymmetric inlet or outlet openings and heat transfer through the glazed surfaces (e.g. sun radiation), the flow is much more complex. This research provides an onset for a model that is capable of predicting the airflow in the cavity of an active facade (without any heat transfer). Therefore measurements and simulations are performed. The airflow is measured with two-dimensional Particle Image Velocimetry (PIV) and one-dimensional hot-film anemometry (HFA) under isothermal conditions. The measurements show some distinct flow features and low-frequency large-scale instationary behaviour and illustrate that the boundary conditions (e.g. dimensions of the inlet) have a major influence on the flow pattern in the facade. The results of Computational Fluid Dynamics (CFD) simulations are compared with the experimental results. It is shown that the two-dimensional CFD model is capable of predicting the general tendencies of the flow. The measurements suggest that the airflow in the facade is three-dimensional, which could not be confirmed by the steady three-dimensional simulations performed in this study.

1. Introduction

An active facade is a system consisting of two (often glazed) panes placed in such a way that air flows in the intermediate cavity. The cavity often employs sun shading devices and is much wider than the standard double glass cavities. Due to the presence of these blinds and asymmetric inlet or outlet openings, simplified methods are often not able to predict the flow patterns in the cavity. A better understanding of the flow behaviour in active facades is necessary to be able to predict the performance; especially the pressure losses suffered in the facade and the boundary layer evolution. In the past, a number of simulations and measurements about the airflow in mechanically ventilated active envelopes have been performed (Ziller 1996, Oesterle et al. 2001, Saelens 2002, Manz et al. 2004, Safer et al. 2005]. However the knowledge about the flow in the facade is still limited. In the past, the measurements were often performed on real facades in buildings. In these cases, the measurements are influenced by a lot of parameters. More measurements in a controlled environment are needed to study the flow phenomena thoroughly, in order to evaluate the importance of all the parameters influencing the flow behaviour. This paper reports on the airflow in a mechanically ventilated active facade at the laboratory of the Royal Military Academy in Brussels, Belgium. A mechanically ventilated active facade is chosen because it is generally assumed to be more controllable than naturally ventilated variants. Two measurement techniques

are applied; PIV and HFA. Computational Fluid Dynamics (CFD) is used to study the feasibility and accuracy of this approach for calculating the airflow in the facade, because it has proved to resolve the airflow for similar problems properly (Saelens 2002, Manz et al. 2004, Safer et al. 2005).

2. Methods

2.1 Experimental set-up

Measurements are performed in a one-storey-high active facade placed in an indoor laboratory environment. The facade has an inlet at the bottom and an extraction fan at the top. Three walls of the facade are made of PMMA and one side is closed with plywood (Figure 1a). An artificial floor is placed at the inlet to minimize the amount of connections, with possible chinks, in the facade. An elevation of the floor was necessary for practical purposes and measurement convenience. The three-dimensional configuration of the facade is shown in Figure 1a.
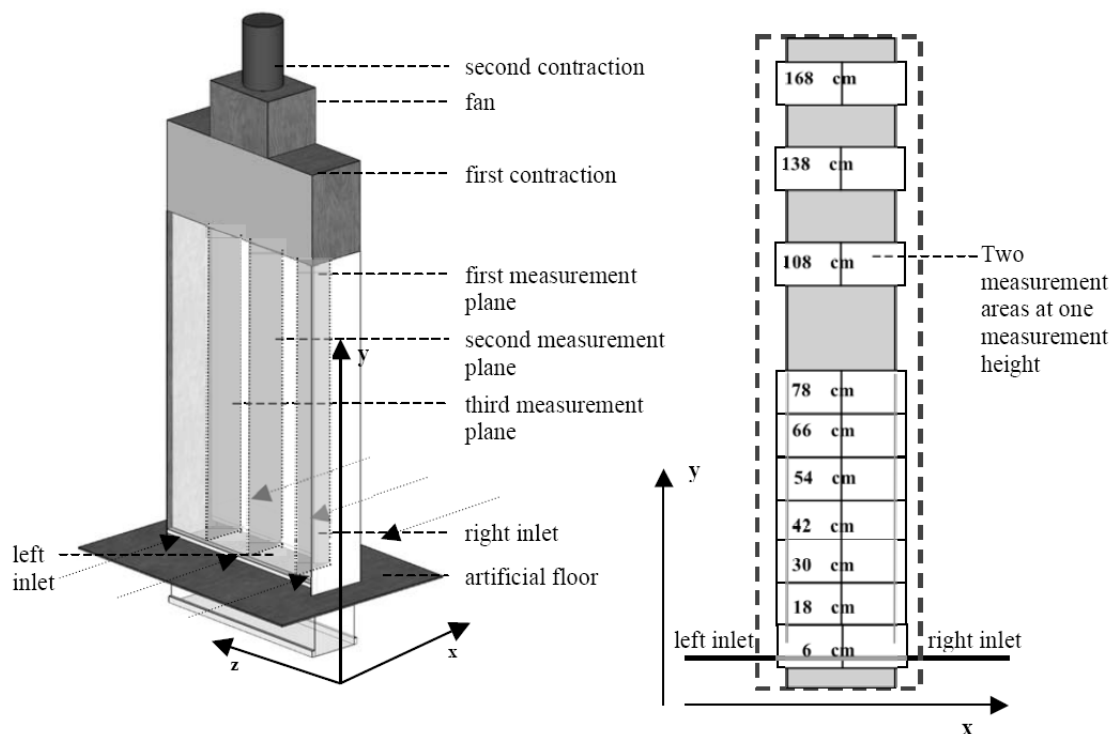
FIG. 1: Left: Three-dimensional physical model of the facade with coordinate system. Right: Measurement areas over the height of the facade at the measurement plane.

The facade is 300 mm wide (x-axis), 1300 mm long (z-axis) and 2540 mm high (y-axis) from the artificial floor up to the first contraction. Figure 1b shows the PIV measurement areas in the xy-plane. The measurement height is defined as the distance from the top of the artificial floor to the middle of the measurement area. The facade configuration is almost symmetrical, with a two-sided inlet. The height of the left inlet is slightly larger (±57 mm) than that of the right inlet (±49 mm). The airflow rate measured through the inlet is 168 m³/h, this is calculated from the average velocity profile at the inlet. The situation in the laboratory is expected to be isothermal. Infrared thermography showed that this assumption is justified. The case is tested several times. Measurements are performed in three planes in the facade (Figure 1a) and are repeated at given time intervals. These cases enable us to study whether the flow pattern can be considered two-dimensional or not and to study whether the measurements are repeatable or not.

2.2 PIV measurements

The major part of the experimental work in this research is carried out with a two-dimensional PIV technique. It is a whole-flow-field technique providing air velocities in a 2D test section. Measurements are done over the

width of the facade (x-direction in Figure 1a), because the most interesting air movements are likely to take place in this plane. This plane is perpendicular to the air inlets and the flow might be two-dimensional in this plane. The PIV measurement set-up is not capable of capturing the whole width of the facade in a single target area without significantly reducing the spatial resolution. Therefore two measurement positions are needed to cover the width of the facade. The measurements are carried out at ten different heights (see Figure 1b). At each height one measurement series is carried out. Each measurement series consists of 50 recordings. The laser generates two pulses per recording, at an interval of 150 µs. The time between the recordings is set at 266 ms. During the postprocessing of the measurement data the ten highest and ten lowest values are considered as outliers. This reduces the scatter at some positions significantly. These outliers are eliminated from further postprocessing. Small olive oil particles with a size of 1 µm are suspended in the flow (also called seeding). The two components of the air velocity in the 2D section are calculated by applying adaptive correlation. The initial size of the interrogation area is 64 x 64 pixels and the final interrogation area is 16 x 16 pixels. The overlap between the interrogation areas is set at 50%. The conditions of the PIV measurements in this setup made sure that an accuracy within 5% is obtained for all the measurements (Pegge 2007).

2.3 HFA measurements

Additional control measurements, with hot-film sensors, are performed to check the validity of the PIV measurement technique in this experimental set-up. The velocity is measured at four sampling heights in the cavity (18 cm, 42 cm, 78 cm and 168 cm). Additional sampling points are placed at the inlet. These sampling points are used to calculate the airflow rate at the inlet and to obtain the velocity profile over the height of the inlet. Sample duration and frequency are set at 10 seconds and 10.000 Hz. The accuracy of the hot-film sensor is generally within 5-10%, except for the four sampling heights in the cavity of the facade, because the turbulence intensity at these positions is higher than 30% (Bottema 1993).

2.4 CFD simulations

The commercial CFD code *Fluent 6.2.16* is employed to simulate the airflow pattern in the cavity of the facade. The CFD simulations should be able to reproduce the PIV and HFA measurement results. The turbulence model used in this study is the realizable k-ε model (Shih et al. 1995). The facade is represented in a two-dimensional and three-dimensional model. The geometrical model is discretised with a structured mesh, which is selected from a mesh sensitivity analysis. Mesh refinement is applied towards the wall surface, to be able to apply enhanced wall treatment ($y^+ < 4.5$). The mesh is built up with a total number of 80,848 cells. 170 cells are applied over the width of the facade, 83 cells are positioned over the height of the left inlet and 67 over the height of the right inlet.

The facade has been modelled using two principles that cause the air to flow (Figure 2); (1) the first principle uses applied inlet profiles, obtained from the hot-film measurements; (2) the second principle uses a pressure difference over the facade. At the position of the fan an underpressure is applied. The reference pressure of zero is applied near the inlet region.
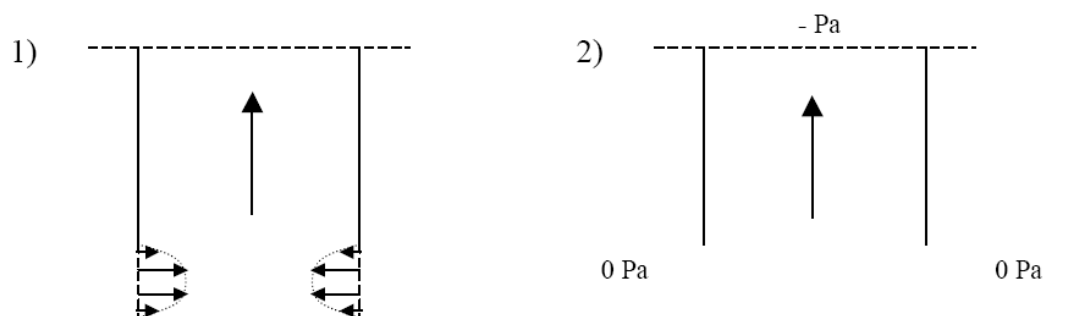

FIG. 2: The two principles used for flow generation in the simulations: (1) Inlet profiles applied; (2) Pressure difference applied over the facade.

3. Results

3.1 Measurements

The PIV and the HFA measurement results are compared. Average values of both measurements at two positions (78 cm and 18 cm) are displayed in Figure 3. Figure 3a shows that there are sometimes significant discontinuities between the velocities measured in the middle of the facade. As explained, the width of the facade can not be measured at once, without significant loss of the measurement accuracy. Therefore two measurements are taken to cover the width of the facade. These measurements could not be taken simultaneously. The results seem to indicate that the velocity fluctuates highly within a long period of time. The differences between PIV and the HFA measurements are caused by errors in both methods and the sensitivity of the hot-film sensor for airflow from other directions. The hot-film sensor will not only register the airflow perpendicular to the film, the film is also sensitive, although less, for flow from the other direction. This unintended measured airflow causes higher air velocities with the hot-film anemometer than with the PIV (Figure 3b). Both measurement techniques predict the same tendencies of the flow. However the spread on the PIV results is quite significant (Figure 4). Because of this high deviation and the low mean velocities, the turbulence intensity becomes relatively high. To investigate if there is any pattern in the fluctuations, the HFA results are studied. The HFA sensor has a good frequency response. The HFA results also showed considerable fluctuations, however no frequencies of the facade system are observed, only a harmonic frequency of 50 Hz, originating from the power network. This irregularity or randomness is one characteristic of turbulent flows. The Reynolds number for the airflow in the cavity of the facade, based on the inlet height and the maximum velocity at the inlet, lies between 1350 and 1750. This Reynolds number is about the lower limit of the transition zone between laminar and turbulent flow if a tube flow is considered. However if one assumes the flow over the glazed surface as a flat plate flow, the flow is laminar. It is clear that due to the high aspect ratio (width to depth ratio) the flow is in fact a mixture between flat plate and tube. On top of that the inlet forces the flow to separate and the flow direction is changed (90°). For this reason one can assume that the flow is turbulent and the model that will be chosen for the numerical calculations is correct. When the fluctuations are studied, it becomes clear that the airflow is quite turbulent. However the boundary layer thickness complies with a laminar boundary layer. Despite the considerable spread, the tendencies of the airflow can be observed.
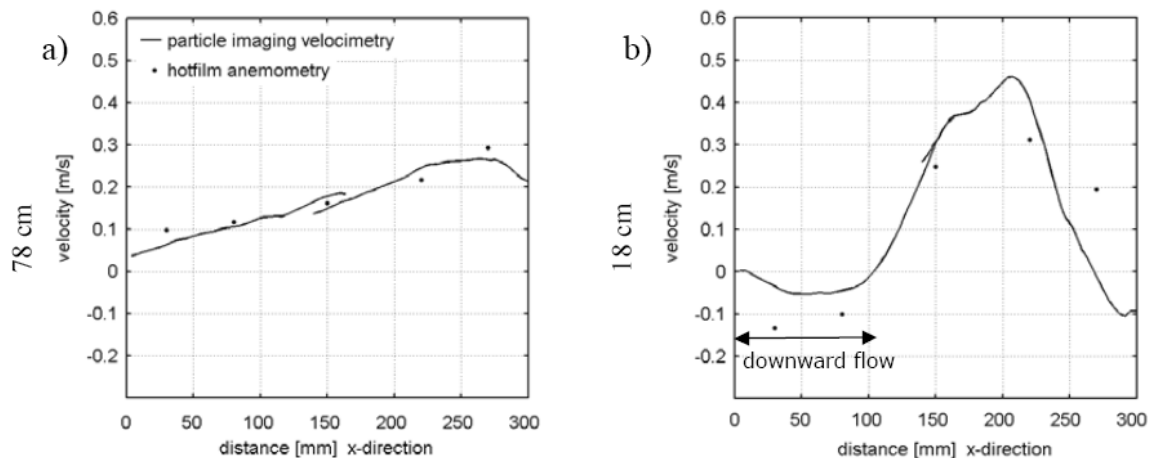
FIG. 3: PIV and HFA measurement results of case 1, the average vertical component of the velocity vector is shown across the facade, at a height of (a) 78 cm and (b) 18 cm.

To study the two-dimensionality of the airflow in the facade, the case is measured in three planes (shown in Figure 1a). The PIV results of these three planes for two measurement heights (78 cm and 18 cm) are shown in Figure 5. As shown in Figure 5, the airflow patterns show quite some differences in the three planes. Overall, the velocities are lower in the first measurement plane. At 18 cm the third plane has an almost symmetric pattern, while the peak velocity in the second plane is located at approximately 200 mm and in the first plane at 225 mm. The different peak positions are attributed to the fact that the inlet height is not constant over the length of the facade. At the first plane the difference between inlet heights is the largest. The left inlet is 9 mm higher than

the right inlet. It is likely that this causes the upward stream to flow on the right-hand side. However a more or less symmetric velocity profile does not mean that there is no difference in height. In the third plane, there is a difference between the inlet heights of 6 mm and inspite of that the profile is relatively symmetric. The figures show that the flow can not be considered two-dimensional, however the second plane seems to be a representative plane for the airflow. This assumption is strengthened by the average airflow rates found in these three planes. The airflow rates are obtained from the area underneath the average velocity profiles of the PIV measurements. The higher airflow rates are found in the third plane and the lowest in the first plane. Within one measurement plane the values differ significantly. In the second plane the airflow rate varies between 118 m³/h and 223 m³/h. The average airflow rate in this plane is 179 m³/h. The velocities and the airflow rates differ a lot between the measurement planes, but also within one plane.
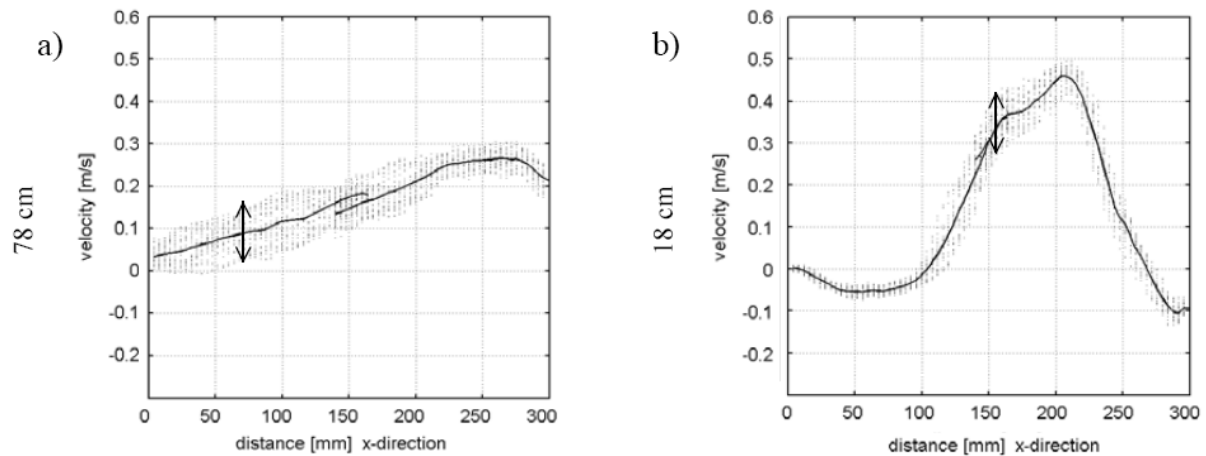

FIG. 4: Spread on the PIV results of the vertical component of the velocity vector for the 30 measurements in one measurement series of 13.3 seconds.
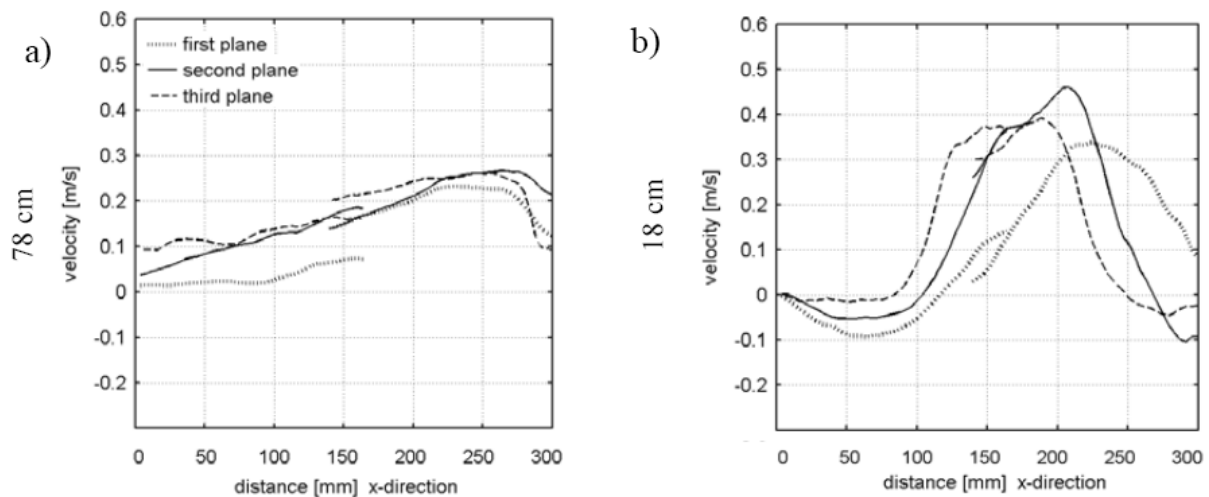

FIG. 5: Results of the measurements in the first, second and third measurement plane. Vertical component of the velocity vector.
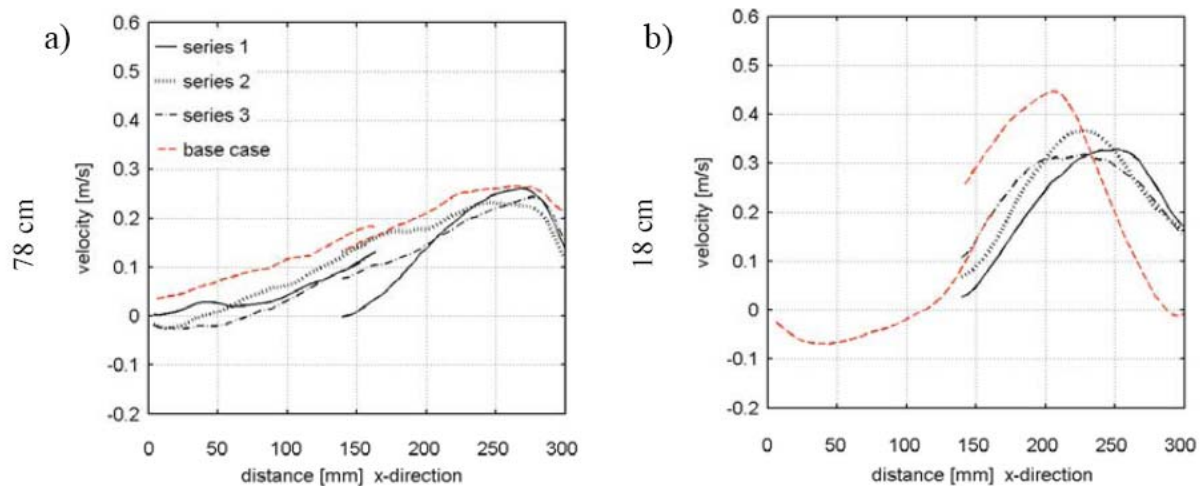
FIG. 6: Three measurement series at an interval of 65 seconds.

To study the repeatability of the measurements, the same measurement series are repeated at an interval of 65 seconds (Figure 6). The results of the first measurements (base case) are displayed as well (in Figure 6), but do not belong to the sequence. The graph shows that the airflow patterns are similar, although the absolute velocity differs. The maximum deviation is approximately 0.05 m/s at a mean velocity of 0.12 m/s. These values lie within the range of the previous results. The spread on the results within one measurement series is about 30% and the spread on the velocities in the different planes (Figure 6a) is even larger with almost 50% at this height. The high deviations measured in all the measurement series can be attributed to large scale instationary behaviour. The measurements are repeatable, although the fluctuation is still significant. Note that the absolute mean value can vary within a certain range. The large fluctuations in airflow rate might be attributed to flow perpendicular to the measurement plane. Two-dimensional measurements appear to be not able to accurately measure the three-dimensional airflow in an active facade. Even if the geometry of the facade implies that the flow will be two-dimensional, three-dimensional flow patterns can develop and three-dimensional measurements are required. It is likely that the third component of the velocity has a major influence on the total airflow pattern, qualitatively and quantitatively. Despite the considerable spread on the results, the tendencies of the airflow can be observed.

3.2 CFD simulations

The simulation results of the facade obtained from a two-dimensional model are shown in Figure 7. They are in relatively good agreement with the measurements. The asymmetric effect of the inlets is still present at the highest position (168 cm). This effect is visible over the whole height of the facade (Figure 7). In addition, the asymmetric effect causes a downward flow from 0 to (approximately) 100 mm at the width of the facade (Figure 7b). This downward flow is also slightly overestimated in the simulations. As explained before, two principles of the driving forces are used in the simulations. The annotation 'CFD simulations – inlet conditions' refers to the fact that the hot-film velocity profiles are applied at the inlet and that the outlet is defined as an 'outlet vent' with no gauge pressure. The annotation 'CFD simulations – outlet conditions' refers to the fact that the driving force of the airflow is a pressure difference over height the facade. The model seems to incorrectly predict the flow on the left side ($0 < x < 150$ mm) of the cavity. At a height of 18 cm, the simulation with the inlet conditions (dashed line) gives a slightly better prediction than the simulation with the outlet conditions (dotted line). The inlet conditions obtained from the HFA measurements are in closer agreement with the reality, than the inlet conditions obtained from applying the pressure difference. The inlet conditions are important for the flow patterns in the whole facade, but especially at the lower positions. The asymmetric velocity profiles are caused by the asymmetric inlet geometry. The left inlet is 7 mm higher than the right inlet. The simulations are performed with this asymmetry included. In addition, a completely symmetric geometry was also modelled. The contour plots of the velocity (Figure 8) show that the symmetrical geometry does not result in a symmetrical airflow pattern (Figure 8b). By modelling half of the facade and applying a symmetry-axis as a boundary condition, the contours of Figure 8c are obtained. The vertical dashed line in Figure 8c is the symmetry-axis. These results show that when the geometry and the boundary conditions are fully symmetric, the calculated flow field is not necessarily symmetric and shifts from the left wall to the right wall or the opposite. A completely symmetric case is unstable and the preferential flow seems to shift from side to side.
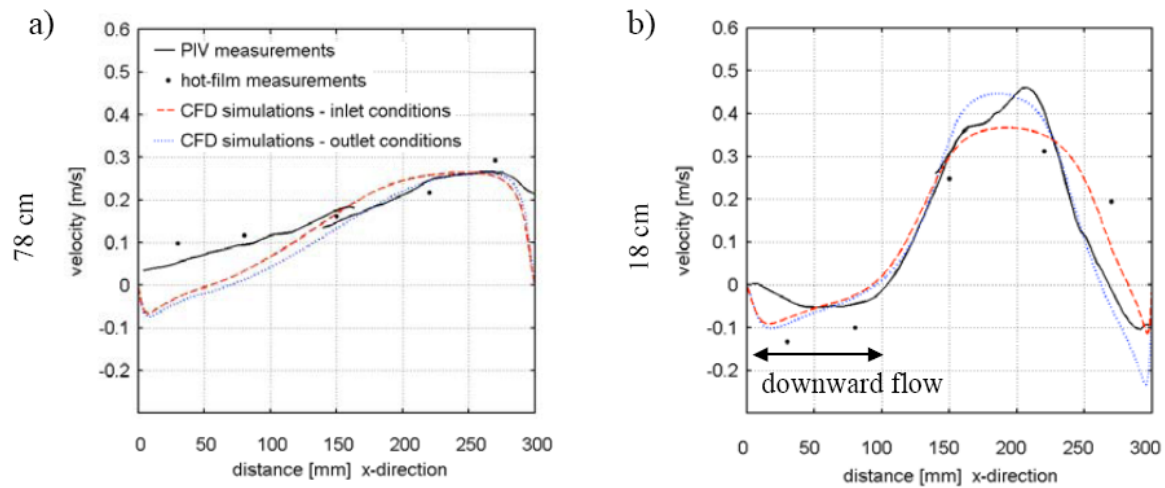
FIG. 7: Velocity profiles of the vertical component, simulated in 2D.
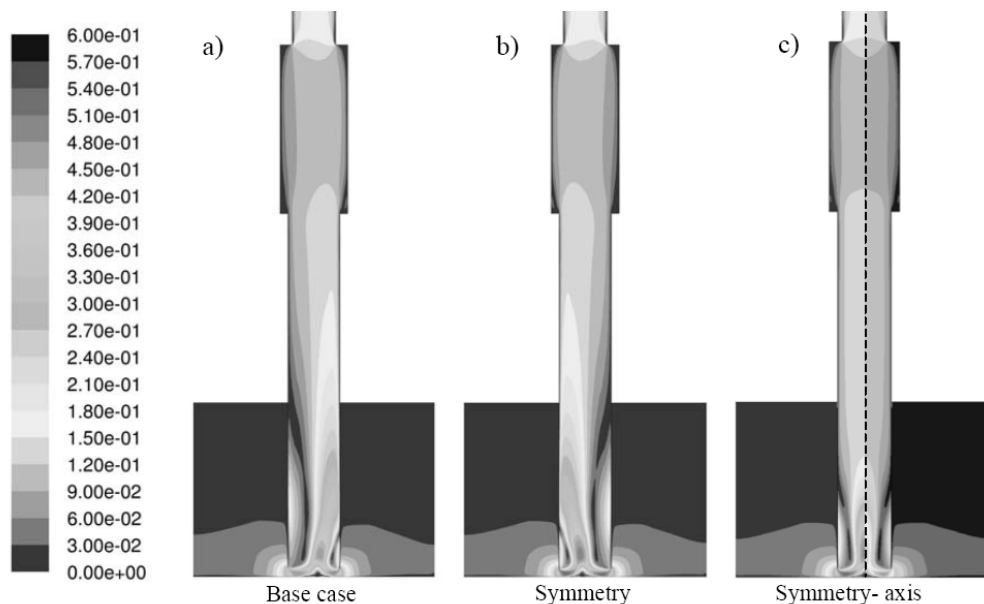
FIG. 8: Contour plots of the velocities (m/s) in (a) the base case with unequal inlet heights; (b) a case with equal inlet heights on both sides; and (c) a case where flow symmetry is imposed in the simulations.

Which shifted mode is obtained depends on the numerical details of the governing equations, grid asymmetries, the transient nature of the flow problem and in which direction the mesh is iterated. Small roundoff errors can also make the solver go into one direction. Using the same solver will often result in the same mode, unless perturbations are used or the flow is solved in the other solution direction. In the base case, the small difference in inlet height causes the airflow to shift to the right side, just like in the measurements. The completely symmetric case is in unstable balance, so in practice a minor disturbance will also cause the flow to go in one direction or it will alternate within the time (in transient simulations). The measurements indicate a pronounced three-dimensional flow behaviour, therefore three-dimensional modelling is also applied. The results of the three-dimensional steady-state simulations however do not show significant flow in the third direction (Figure 9). Figure 9 shows that the air flows upward in the whole yz-plane and the airflow pattern in this plane is symmetric. The attenuating effect of the walls is noticeable, but they do not change the direction of the airflow. One can conclude that the airflow in the yz-plane, suggested by the measurements, is not reproduced in the steady state 3D simulations. Therefore it might be rewarding to perform unsteady simulations in future research, maybe these simulations will then show the expected flow in the third direction. Because of unknown transient input parameters, a transient simulation is not performed in this study.

FIG. 9: Contour (a) and vector (b) plot in the yz-plane, simulated in 3D.

4. Discussion and conclusions

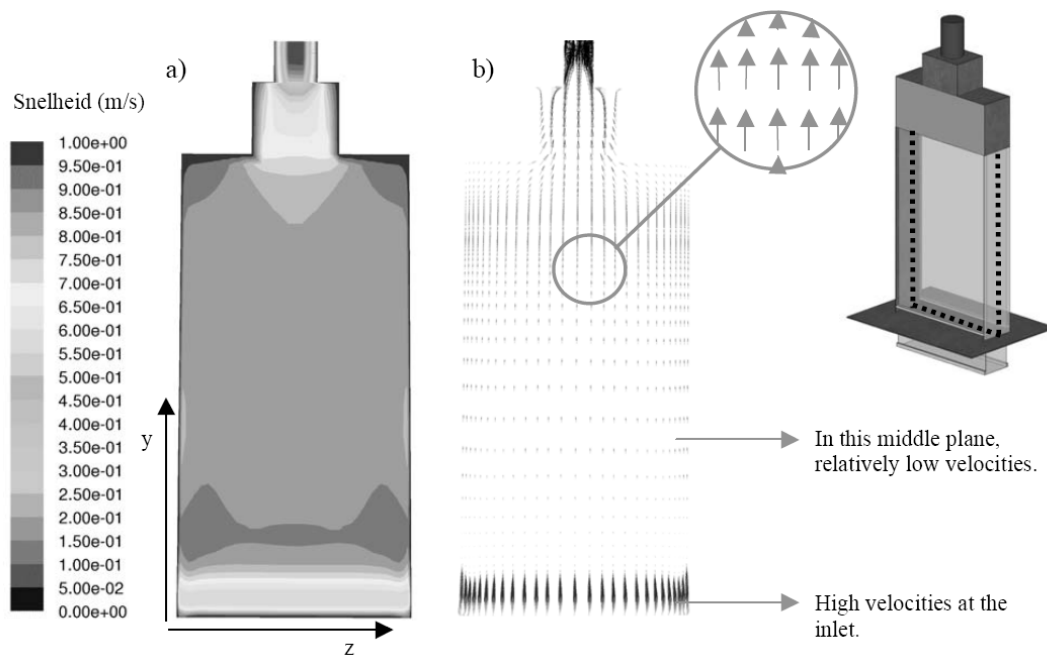Although the measurements showed some distinct flow features and low-frequency large-scale instationary behaviour, the two measurement techniques appeared to provide accurate measurements. However this applied for this specific configuration, in another experimental set-up the results could be different. The comparison between the measurements and the simulations showed that the CFD model is capable of predicting the measurements to some extent. The range of uncertainty is partly attributed to the measurements. As a consequence the two-dimensional simulation model was not sufficient for obtaining qualitative results. However the tendencies of the flow were well predicted.

The airflow in the facade seems to be three-dimensional. This observation is unfortunately not confirmed by the three-dimensional steady-state simulations performed in this study. Transient simulations can be performed to get to know more about flow in the third direction. In addition three-dimensional measurement techniques can be used to completely investigate the airflow in the facade. This would require measurements in the other plane stereo (three-dimensional) PIV. Another conclusion that can be drawn from this study is that detailed information about the boundary conditions is essential for a proper understanding and simulation of the behaviour of the facade. The measurements illustrated that the boundary conditions (e.g. dimensions of the inlet) have a major influence on the flow pattern in the facade.

5. References

Bottema M. 1993. Wind climate and urban geometry. Ph.D. thesis, Eindhoven, T.U. Eindhoven.

Manz H, Schaelin A, Simmler H. 2004. Airflow patterns and thermal behavior of mechanically ventilated glass double facades. *Building and Environment*. Vol. 39, pp. 1023-1033.

Oesterle E, Lieb R, Lutz M. 2001. Double-skin facades : integrated plannning : building physics, construction, aerophysics, air-conditioning, economic viability. Munich, Presel.

Pegge EA. 2007. A study on the airflow in a mechanically ventilated one-storey-high active facade. Master thesis, Eindhoven, T.U. Eindhoven.

Saelens D. 2002. Energy performance assessment of single storey multiple skin facades. Ph.D. thesis, Leuven, K.U. Leuven.

Safer N, Woloszyn M, Roux JJ. 2005. Three-dimensional simulation with a CFD tool of the airflow phenomena in single floor double-skin facade equipped with a venetian blind. *Solar Energy*. V. 79, pp.193-203.

Shih TH, Liou WW, Shabbir A, Yang Z, Zhu J. 1995. A New - Eddy-Viscosity Model for High Reynolds Number Turbulent Flows - Model Development and Validation, *Computers and Fluids*, Vol. 24, nr. 3, pp.227-238.

Ziller C. 1996. Natürliche Belüftung eines Hochhauses mit Doppelfassade (Natural ventilation of a high rise building with a twin-face-facade). KI 32, H. 8, pp. 343-346.

Thermal Transfer through Membrane Cushions Analyzed by Computational Fluid Dynamics

Florian Antretter, M.Eng. Dipl.-Ing.(FH),
Fraunhofer Institut für Bauphysik, Holzkirchen, Germany;
antretter@hoki.ibp.fhg.de

Wolfram Haupt, Dr.,
Technische Universität München;
haupt@tum.de

Andreas Holm, Dr.,
Fraunhofer Institut für Bauphysik, Holzkirchen, Germany;
andreas.holm@ibp.fraunhofer.de

KEYWORDS: *membrane cushions, natural convection, CFD, heat transfer.*

SUMMARY:
The use of membrane cushions in architecture is highly growing. These systems are used as exterior facades or roofs. They need to fulfil all the requirements that are applied to conventional building technologies. In terms of heat transfer a general method or standard to identify the heat loss through the membrane cushions is not available. Furthermore complex processes inside the membrane cushion are not well enough understood to improve the cushions and avoid building physical problems. A test set-up was built to assess the processes inside the cushions. To enlarge the results from these tests computational fluid dynamics (CFD) simulations were performed, where varying boundary conditions in terms of inclination and temperature difference were applied. The simulations showed compareable results for the experimentally measured temperature and heat fluxes. Three different flow conditions were determined by the parameter variation simulations. Surface to surface radiation was determined to be mainly independent from the flow conditions inside the panel. It can therefore be calculated separately. With knowledge of the installation situation and the temperature boundary conditions the flow pattern inside the panel can be predicted. This allows an approximate calculation of the heat transfer through the cushion. Possible improvements of the cushions in terms of thermal performance are shown.

1. Introduction

Building envelopes built of membrane cushions are sometimes called the new face of architecture. This new and innovative building technology stands out due to an increasing growth worldwide. Sometimes it is referred to as "the new building material".

Because of its newness some standards as for example for U-value or g-value, which are long time established for other types of constructions like massive walls or windows, are not available for membrane cushions. This new construction type differs significantly in terms of used material, shape dimension, or curvature compared to conventional building components. That is why existing standards can not be applied on membrane cushion systems in terms of characteristic building physical values. Standards for these values are nonetheless necessary to avoid expensive special testing of the components and to give ingenieurs and architects tools at hand to easily proof that their construction complies with the requirements.

All three heat transfer mechanisms, radiation, convection and conduction, play an important role for the assessment of the thermal performance of membrane cushions. Even so those mechanisms are well understood in general, a basic understanding of what is happening inside the closed spaces of membrane cushions and the interaction of these transport mechanisms is often missing. There is no deeper knowledge of the dependencies and of the magnitudes of the transport mechanisms under different boundary conditions. In practice this leads to a number of different building physical problems, which can neither be understood nor solved because of missing understanding of the system performance.

2. Approach

Because of the shown problems with the use of membrane cushion systems in practice, a deeper understanding of what happens around and inside the panels is necessary with respect to the development or adaption of codes and standards. A characterization of membrane cushions and their application in practice needs to be done. Furthermore the main transport mechanisms need to be detected and the most influencing boundary conditions need to be assessed.

Depending on the characterization of the membrane cushions and the found important boundary conditions, a test setup was buildt. This setup couldn't represent the whole operating range of membrane cushions. To enlarge possible findings, CFD (computational fluid dynamics) simulations were undertaken. This enabled a comparison of experimental findings with simulations. In a next step simulations with different boundary conditions helped to transfer the findings to changed conditions. This should contribute to a successful processing of the above mentioned problem definitions. The field of application of numerical fluid dynamic simulation for the calculation of the heat transfer through membrane cushions will be shown.

For this purpose only the closed, air-filled inner space of the ETFE (Ethylene Tetrafluoroethylene) membrane cushion is examined. The influence of thermal bridges around the edges of the cushion and of the clamping is not part of the simulations. Boundary conditions are directly applied on the cushion, i.e. possible interactions of the panel with its surroundings are not regarded.

For the simulation of fluid dynamics the definition of the geometry, in which the flow should be examined, is the first step. A grid on which the transport equations are solved needs to be produced to fill this geometry. For a proper CFD simulation more steps than just the comparison with experimental data were necessary. That's why the simulations were run with different physical models for e.g. turbulence and the results were compared to the experimental data. After finding the "best" modelling settings the parameter variations were performed.

This results in a general characterization of the flow conditions inside the panels. Results generalization leads to basic approaches for the simplified calculation of the heat transfer through membrane cushions. All the simulation results are confronted with the real measurements to show how good numerical simulation can reproduce reality.

3. ETFE cushion construction

Membrane cushions consist of two or more layers of ETFE membrane, which are in general welded and clamped around the edges. In the production process the membrane is cut in a way, that the completed cushion offers a camber. A detailed description of the complete system can be found in (Kaufmann, 2004).

In general a cushion can be defined to have a likewise diameter on every location with similar side length. Only in extreme cases like very narrow and stretched cushions a bigger difference is found. But basically also here the distance between the membrane layers is zero on the edges and proportionate to the camber in the middle. The easiest way for the characterization is a round cushion.

This characterizes only the cushion itself. Attached to the cushion is in general a pressure hose with a diameter of four to ten centimeter. The pressure hose provides the compressed air to keep the cushion under an over-pressure between 200 and 1000 Pa. This means that there are defined limitations for lowest and highest pressure and if the pressure in the panels falls below the defined minimum, air is supplied until the maximal pressure is reached. The time for these loading cycles is, compared to the time in which the pressure inside the cushion falls from maximum pressure to minimum pressure, very marginal. The pressure inside the panel drops only because of leaks. Therefore it is useful for the quasi-statical consideration to assume a constant inner pressure.

Furthermore the clamping plays only a minor role for the convection inside the panel. Temperature differences between membrane and frame can only be transmitted by conduction in the membrane. As the membrane is not a good conductor and does not store a lot of heat, this effect can also be neglected.

4. Experimental set-up

On the outdoor testing facility at the Fraunhofer Institut für Bauphysik in Holzkirchen, Germany, a test set-up for the experimental data gathering at a membrane-cushion-system was built. This test set-up allows the acquisition of hygrothermal and interior climate data on ETFE-cushions and its surrounding under realistic conditions.

The test set-up consists of a pentagonal tower with 7.45 m height and an inner diameter of 4.75 m. A horizontal cushion with a maximum distance between its two layers in the middle of the diameter from 1 m serves as roof, as shown in FIG. 1. These dimensions are real cushion dimensions and geometries. The building can be heated to keep the interior temperature at a constant level in winter.
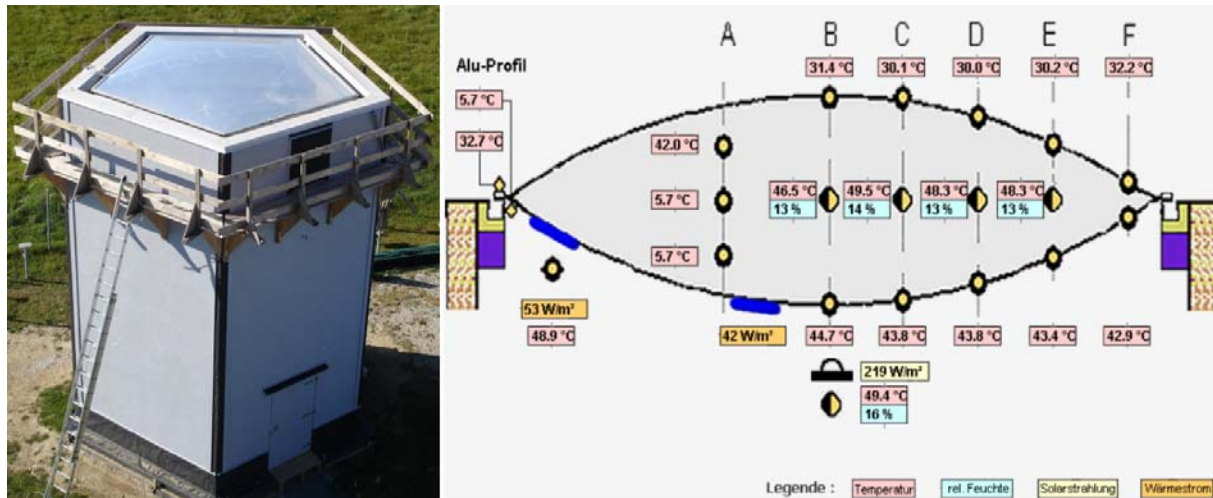

FIG. 1: Picture of the test set-up for membrane cushion tests and distribution of all sensors inside the cushions with visualization of the measured data

In five axes the temperature is measured on the interior and exterior surface as well as in half height of the cross section. The axis in the middle of the cushion is equipped with five temperature sensors across the cross section height. FIG. 1 shows a screenshot of the data visualization of all measured values within the cushion and gives a good overview about the arrangement of the sensors within the pillow. These sensors are ment to provide information about the temperature distributions within the cushion. Temperature sensors are PT100 sensors with an accuracy of +/- 0.1 °C.

In addition to the temperature sensors two heat flux transducers are mounted to the membrane, one in the middle of the inside membrane, one 30 cm from the edge of the cushion. The measurements of all sensors are logged every 30 seconds and saved in an internet based data base for later analysis.

Besides the sensors in and on the cushion also the temperature and relative humidity inside the room below the cushion are measured. These combined with the measurement values from the weather station at the Fraunhofer Institut für Bauphysik provide the boundary conditions for internal and external climate.

5. Model set-up

For the simulation cushions with similar diameter and maximum height as the pentagonal cushion in the test set-up were used. The cushion itself was not modelled as pentagonal but as round. That means that the cushions are defined by the diameter d of the footprint and the maximum height h in the middle of the cushion. For the standard model the height h was 1 meter and the diameter d was 4.75 m.

The boundary conditions were directly applied on the exterior surfaces of the cushions, which enclose the whole volume. This volume was meshed with unstructured tetrahedrons for the whole volume and a structured mesh on every surface. The distance between the two surfaces was set to 0.04 m to avoid meshing problems in the edges

The tetrahedrons maximum size within the volume was set to 0.1 m for the whole volume. Close to the edges the maximum element size was set to 0.02 m. The ratio for growth between two neighboring mesh volumes was set to 1.1. All around the surface a structured grid with 10 element layers was buildt to obtain a higher resolution for the simulation and to apply some of the physical models, which require a very fine mesh (Ansys, 2006). Finer and coarser meshes were also used to find the best mesh for the simulations. The selection process is described in (Antretter, 2007). A grid sensitivity analysis as recommended in e.g. (Ferziger, 2002) was not carried out, as an exact duplication or bisection is not possible for the mixed meshes.

Steady state and transient simulations were performed. In the transient case a total time of 25 seconds with timesteps of 0.1 seconds was simulated. This period seems adequate to simulate the transient behaviour of the flow under steady state boundary conditions if the simulation domain is initialized with the results of the steady state simulations.

Fluid models need to be choosen for heat transfer, turbulence and radiation. A study on natural convection inside closed spaces (Haupt, 2001) was used for model selection. A detailed description of the models and other parameters and reasons for their selection for this study can be found in (Antretter, 2006). Parameter simulations with different models in (Antretter, 2007) show the differences among the models. All boundary conditions for exterior and interior surface are set to no slip walls. This represents the real condition on the wall, where the particles closest to the surface do not move because of friction with the wall. It results in the development of a boundary layer. For standard simulations the temperatures on the inner surface were set to 20 °C and on the exterior surface to -10 °C. This does, because of missing heat transfer on the layers, not represent reality, but the simulations are more exact specified with this assumption and easier to compare. With all these settings the fluid domain is specified.

The parameter variations were performed with different temperature differences between the inside and the outside of the cushion. Realistic temperature ranges, where membrane cushions may be used, are between -30 °C and 60 °C. For this study it was assumed that the membrane cushions delimit a room where people stay. The interior temperature is therefore set to 20 °C. The exterior temperature was varied from -10 °C and +30 °C. To limit the effort for the simulations only exterior temperatures of 0 °C, 10 °C, 15 °C and 30 °C were performed additionally to the ones with -10 °C.

Membrane cushions are used as facades as well as for roofs. The main application is therefore 0 degree or 90 degree inclination. However all inclinations between can be found. Therefore simulations with 45 degree inclination were also performed. The different inclinations of the cushion showed the resulting variations of the flow patterns.

6. Results

Temperature differences are the driving force for natural convection. The gravity counteracts the buoyant force, resulting from the temperature differences. Therefore the main focus of this research is to understand the flow patterns inside the cushions on varying temperature differences and different directions of the gravity.

6.1 Temperature

Velocities averaged over the whole domain weighed by volume ratio decreased with a decreasing temperature difference. As the air velocities on the boundaries are mainly responsible for the heat flux through the corresponding boundaries, it is obvious that the convectional heat fluxes also decrease with decreasing temperature difference. TABLE 1 shows the results for simulations with different temperature differences in transient and steady state simulations. Because of transient nature of the flow that can be found inside the panel the steady state simulations are not converged. But a comparison between the results for transient and steady state conditions shows no differences for the values averaged over the whole domain or the surfaces respectively.

TABLE 1: Results for average values of selected variables with different temperature differences for transient and steady state simulations

Transient	-10°C/20°C	0°C/20°C	10°C/20°C	15°C/20°C	30°C/20°C
	Trans / Steady	Trans / Steady	Trans / Steady	Trans / Steady	Trans / Steady
Temperature [K]	278.4 / 278.4	283.1 / 283.1	288.2 / 288.2	290.7 / 290.7	298.1 / 298.1
Velocity [m/s]	0.10 / 0.10	0.08 / 0.08	0.06 / 0.06	0.04 / 0.04	0.01 /0.01
Heat Flux Density Total [W/m²K]	146.3 / 146.6	99.8 / 99.1	49.0 / 48.8	24.3 / 24.2	-44.4 / -44.5
HFD Conv. [W/m²K]	41.9 / 42.2	26.5 / 25.8	10.5 / 10.3	4.5 / 4.4	-1.8 / -1.9
HFD Radiation [W/m²K]	104.4 / 104.4	73.3 / 73.3	38.6 / 38.6	19.8 / 19.8	-42.6 / -42.6

TABLE 2: Convective and radiative ratio of heat flux density on inner surface

Temperatures	-10°C / 20°C	0°C / 20°C	10°C / 20 °C	15°C / 20°C	30°C / 20°C
Convection Ratio	0.29	0.27	0.21	0.19	0.04
Radiation Ratio	0.71	0.73	0.79	0.81	0.96

The total heat flux on the surface sums up from convective and radiative heat flux components. TABLE 2 shows the comparison between the fraction of convective and radiative heat flux on the different temperature differences on the inner surface. At a temperature difference of 30 K approximately 30 percent of the total heat flux is caused by convection and 70 percent is caused by radiation with the membrane properties and emissivity as described above.With higher temperature differences the convective heat flux increases. With negative temperature differences between the inside and the outside, which means a higher temperature on top of the horizontal cushion than on the bottom, a stable temperature layering results in almost no convective fraction and almost all the energy transferred by surface to surface radiation.

6.2 Inclination

FIG. 2 shows streamlines of the flow inside the cushion colored by temperature. In the horizontal case several different eddies are found. Already at 45 degree inclination one big roll on the surfaces with secondary flow to the upper and lower edges fills the whole volume. The same behaviour is found for the vertical cushion. A look at the temperatures shows, that the temperature inside the horizontal cushion is very uniform throughout the whole volume because of very effective mixing inside the panel. Only in the edges and very close to the surfaces higher temperature gradients are found, which cause most of the energy transport by convection. The temperature distribution in the inclined and vertical cushions is different. Some kind of a temperature layering with highest temperatures on top and lowest temperatures on bottom of the volume is found. Only on the surfaces, which are whether at constant 20 °C or constant -10 °C, the temperatures differ from the general temperature at the given height above zero, which is very constant from a distinct distance of the wall. The average velocity for the horizontal case is 9,6 cm/s but the maximum velocity is only 29,3 cm/s.
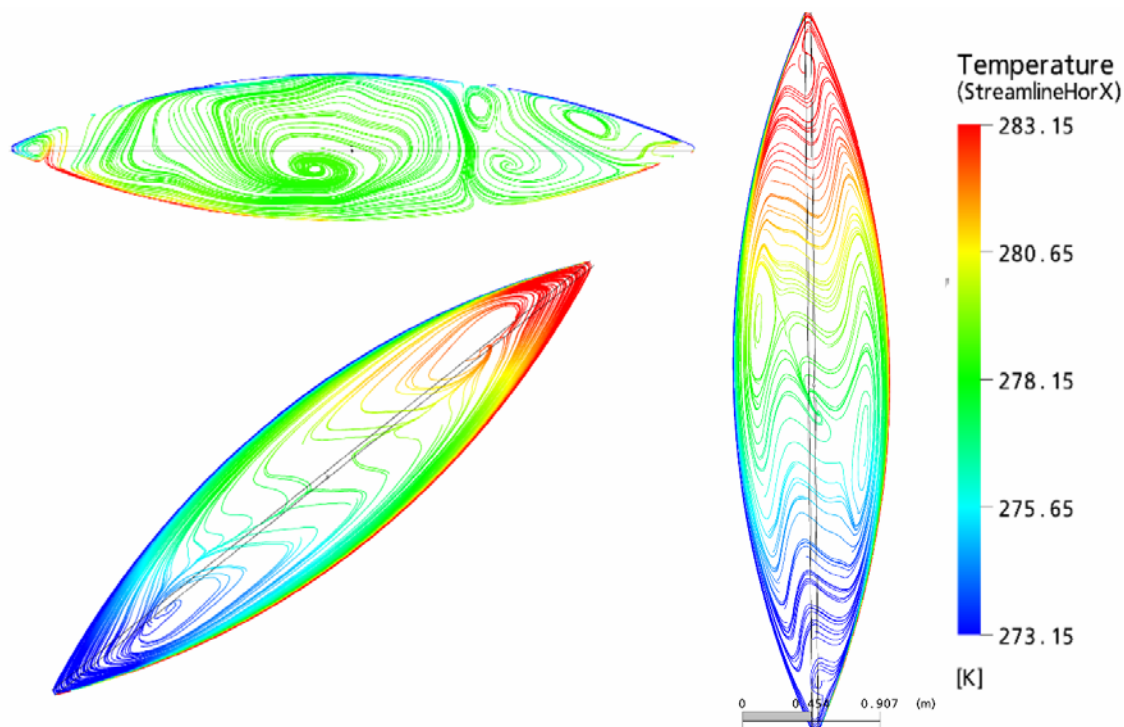

FIG. 2: Streamlines colored by temperature for different inclinations of the cushion

A comparison of the mean values shows as expected, that the surface to surface radiation causes a similar radiative heat flux and is therefore independent of the inclination. It depends only on the temperature difference.

The convective portion of the total heat flux rises with the inclination of the cushion. The increase of the convective heat flux from 0° to 45 ° inclination is double the increase from 45° to 90°. Also these simulations showed that for the mean values no significant difference was found between steady state and transient simulations.

A closer look at the velocities in the enclosed space shows that indeed the mean velocities decrease from horizontal to inclined to vertical cushions. The maximum values for each case show however that higher velocities are achieved in the inclined cushions. The found average and maximum velocities are summed up in TABLE 3.

TABLE 3: Comparison of average and maximum velocities on cushions with different inclinations

Velocities [m/s]	Average	Maximum
Horizontal	0.096	0.293
45 Degree	0.079	0.484
Vertical	0.064	0.420

7. Discussion

The found flow pattern can be divided into three different conditions. The following description of the temperature, velocity and turbulence fields refers to the characterization of these three conditions.

Flow in the first condition feature many small eddies. These flows develop if the membrane layers are horizontal and the temperature rises in direction of the gravity. On the in gravity direction warmer membrane layer energy is supplied to the fluid, which causes a reduction of the fluid density. The buoyant force of the less dense and therefore lighter fluid on the surface prevails the friction forces within the fluid and ascends against the gravity direction. A critical temperature difference between the surfaces must be exceeded, which is small because of the little viscosity of air. Friction acts against further rise. Additionally heat conduction between the fluid particles balances the driving temperature and density differences. Effective mixing and energy exchange occurs within the cushion. This thermal cellular convection or Rayleigh-Bénard convection produces in the ideal case between two infinite parallel plates equal rolls. On the lightly bent surfaces of the membrane cushions a similar behaviour of the flow can be found, but the rolls influence each other because of curvature and the edgewise boundarys. An unstructured, time dependend flow pattern with rising and falling plumes is the result.

This means an effective mixing for the temperature. The heat transfer occurs in a very thin boundary layer, evenly distributed over the surface. The temperature in the middle of the cushion is relatively uniform. Only in the edge zones with smaller distances between the surfaces warmer plumes rise completely from the inner to the outer surface. The velocity distribution in this condition can not be predicted without simulation. The mean velocity is not very high because of the interdependent impact of rising and falling plumes.

The second condition results from gravity not normal to the temperature difference causing walls. This is in the most extreme case a vertical cushion. With rising inclination the fluid particles move a longer way along the walls. They collect more energy on the warm wall and they can more efficiently deliver energy to the cold wall. The result is one big roll within the cushion with high energy exchange and high velocities close to the walls. The mixing over the whole cushion volume reduces compared to the first condition with a horizontal cushion. The temperature field in this case is a layering over the height of the cushion, which is not exactly horizontal because of the movement of the fluid inside the cushion in one big roll. Because of the current, warm air close to the warm surface is pushed upward; cold air is pushed downward on the cold surface. This results in high velocities close to the walls but low velocities in the inside of the volume.

The third condition that can be defined is a stable layering inside the cushion. This is again only possible in a horizontal cushion. The temperature decreases in direction of the gravity. In this case there is no driving potential because of density differences. The most dense – and therefore heaviest – particles are on the bottom, the lighter ones are on the top. This means a stable temperature layering inside the cushion with the biggest temperature gradient in the horizontal middle of the cushion. Air movement happens only on the areas where the surfaces are bent close to the edges. The three described conditions can be found in FIG. 3. It shows the streamlines for all three conditions colored by the temperature of the fluid at every location.
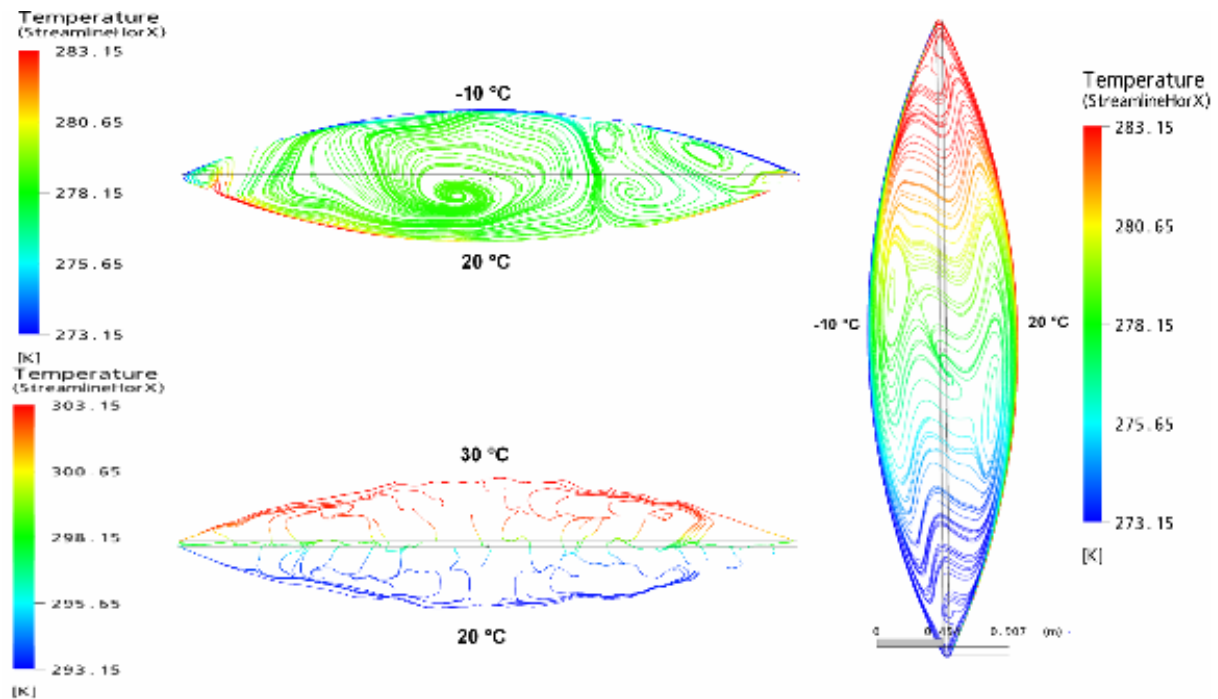
FIG. 3: Comparison of the temperatures on the streamlines for three different conditions

8. Comparison with measurements

The simulations were performed transient, but with steady state boundary conditions. Furthermore the development of the flow patterns is clearer with higher temperature differences. Therefore a short period of time was choosen from the whole measurement period of one and a half year, where the surface temperatures are as constant as possible at high temperature differences. As radiation on the cushion was not modelled, a period without radiation, which means at night, was to be found. Nightly irradiation was not a problem, because the real measured surface temperatures were used as boundary conditions for the simulation. In the choosen night of January 25th, 2007 average surface temperatures of 14.4 °C at the inside and -4.2°C on the outside were calculated. The distribution of the surface temperatures on the four sensors per surface showed only small differences between the measurements, which justifies the assumption of a constant temperature at the whole surface. These temperatures were used as boundary conditions for comparison simulations.

The distribution of the temperatures inside the cushion shows fluctuations of maximal 2 °C around the mean value for the measurements as well as for the simulations. The good mixing and the therefore even temperature distribution can be reproduced by simulation. The rising and falling plumes in the edges with obvious effects on the air temperature found with simulation can be shown with different measured surface temperatures in these areas. The additionally measured heat flux densities with 66.5 W/m² in the middle of the cushion and 85.2 W/m² close to one edge can be compared with an average simulated heat flux density of 84.9 W/m². A better comparison between measurements and simulation is currently not possible, as the experimental set-up was not designed as simulation validation case. However, the general temperature distribution and the order of the heat flux through the panel can be compared.

9. Conclusions

As a result of the parameter variations three different conditions of airflow inside the panel can be defined. The development of these three conditions can be physically explained. For every installation situation with every possible temperature difference between the exterior surfaces of the membrane cushion the resulting flow pattern can be estimated, also without simulation.

A comparison between simulation and measurement was difficult, as the measurement was not intended to provide a basis for simulation validation. However, the found conditions inside the panels are compareable to the conditions as result of the simulation. The measured order of the temperatures and heat flux can be imaged by numerical simulation. The results of the parameter variation can be considered as realistic.

With the shown results an estimation of the U-Value is, simplified, possible. The surface to surface radiation can be calculated with different approaches. The convection inside the panel depends on the temperature differences and the inclination of the cushion. But the heat transfer coefficients can be estimated with knowledge of the installation details of the cushion.

The simulations were carried out as closed systems with temperature boundary conditions. Further simulations should include the influence of the pressure hose as well as possible leakage. The temperature boundary conditions do not represent the real world. Further research is necessary to obtain reasonable heat transfer coefficients. Furthermore heat transport through frames and clamping was not regarded. Radiation from the outside like solar radiation or surface to surface radiation between membrane and internal walls and floor plays an important role in reality but was not part of this study.

Despite these limitations room for improvement for the membrane cushion systems can be detected. The whole heat transfer through the membranes can be reduced with surface coatings with a low emissivity. Especially in the edges the heat loss is high. This may result in condensate at the inner surfaces and lead to further building physical problems. Improvements can be made with thermal isolation of the edge areas and a forced distance between the two membrane surfaces at the edges.

In total it is to say that small changes in the boundary conditions or in the used models produce big changes in the results. Following points may help for good further simulations:

- 3-dimensional: All the flows are three dimensional, therefore two dimensional simulations are disadvised

- Steady state / transient: The mean values of the simulations do not show significant differences between the results, even with no convergence of the simulations because of the transient behaviour of the flow in reality

- Initialization: A good initialization is necessary to obtain quick converging results

- Convergence: The residuals alone are not enough to judge convergence. Imbalances and the observation of variables and global variables during the simulation allow an estimation of the correctness.

- Radiation: With given temperatures on the boundarys the simulation of the convection inside the cushion is possible without the simulation of surface to surface radiation.

- Boundary layer: A fine resolution and the use of complex boundary models are necessary to represent the real situation on the walls.

10. References

Ansys Inc. (2006). CFX solver release 10. Software Manual.

Antretter F. (2006). Analyse relevanter Randbedingungen zur Simulation von Strömungen in Membran-Kissen-Systemen. Project Work, University of Applied Sciences Rosenheim.

Antretter F. (2007). Anwendung eines Computational-Fluid-Dynamic-Systems zur numerischen Simulation der natürlichen Konvektion in leichten transparenten Bauteilen. Master Thesis, University of Applied Sciences Rosenheim.

Ferziger J.H. and Peric M. (2002). Computational methods for fluid dynamics. Springer Verlag.

Haupt W. (2001). Zur Simulation von auftriebsinduzierten Innenraumströmungen. Dissertation, University Kassel.

Kaufmann A. and Mitterer C. (2004). Membrane im Bau – bauphysikalische Optimierung und neue Einsatzbereiche. Fraunhofer Institut für Bauphysik, IBP report RKB-15/2004.

Numerical Studies of Heat and Air flow in
Ventilated Insulated Slanting Roofs

Arild Gustavsen, Professor,
Department of Architectural Design, History and Technology,
Norwegian University of Science and Technology;
Arild.Gustavsen@ntnu.no and www.ntnu.no

Sivert Uvsløkk, Senior Scientist,
SINTEF Building and Infrastructure;
Sivert.Uvslokk@sintef.no and www.sintef.no

KEYWORDS: *Ventilated roof, Numerical simulation, CFD, Natural convection, Air flow.*

SUMMARY:
A common roof design in the Scandinavian countries is the ventilated slanting roof. Ventilation of the roof has two purposes; to transport any moisture that has penetrated the roof construction out of the roof and to keep the outer roof surface cold enough to avoid snow melting. Snow melting on the roof outer surface can cause pools of water freezing near the eave construction, which again can cause mechanical degradation and leakage. There have been some discussions regarding how large the air gap in ventilated roofs should be in order to provide sufficient ventilation for ensuring low temperatures and for allowing transport of moisture out of the roof. Previous studies have mostly been based on simplified analyses where the driving pressure and pressure loss coefficients have been used to calculate the air flow through the roof. These pressure loss coefficients are however usually for simpler geometries than the air gap geometries found in roofs, and some questions can be raised regarding their usability for such analyses. In this paper we use a CFD tool to calculate the mass flow rates through some ventilated slanting roofs with various designs. Stream contours and temperature distribution in some roofs are also presented.

1. Introduction

Two typical roof designs are common in Norway; the compact flat unventilated roof, and the slanted ventilated roof. The compact roof is common for larger commercial buildings, and the ventilated roof is common for smaller buildings, and in particular for residential buildings. Some typical ventilated roof constructions are shown in Figure 1, with the cold attic and the roof with insulation in the roof deck being the most common designs. In this paper the focus is on the roof with insulation in the roof deck (the hygrothermal performance of the ventilated attic is studied in detail by Uvsløkk, 2005).

For the roof with insulation in the roof deck, a ventilation channel is located above the insulation layer and wind barrier (roofing underlay) but below the roofing layer, see Figure 2. Ventilation of the roof has two purposes; to transport any moisture that has penetrated the roof construction out of the roof and to keep the outer roof surface cold enough to avoid snow melting. Snow melting on the roof can cause pools of water freezing near the eave construction, which again can cause mechanical degradation and leakage. Formation of icicles may also occur which again may be of danger to passing pedestrians.

In Norway there have been some discussions regarding how large the air gap in ventilated roofs should be in order to provide sufficient ventilation for ensuring low temperatures and for allowing transport of moisture out of the roof. Previous studies have mostly been based on simplified analyses where the driving pressure and pressure loss coefficients have been used to calculate the air flow through the roof (Blom, 1990). In this paper a Computational Fluid Dynamic (CFD) tool is used to study the air flow rates, temperature distribution and flow pattern in the air cavity of some ventilated roofs.

2. Geometric Model

The different roofs simulated are named H1 to H8. Two-dimensional cases were simulated, see below. Details of the ridge and the eave constructions are shown in Figure 3, with dimensions shown in Table 1 and Table 2. Table
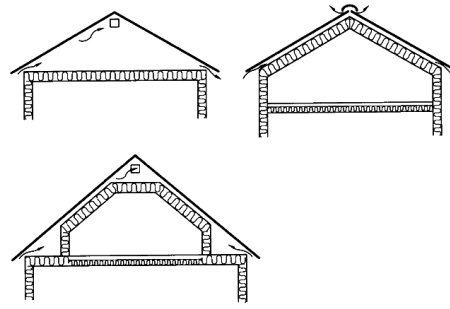
FIG. 1: Examples of typical ventilated roof designs. (Figure from SINTEF Building Research Design Sheets.)
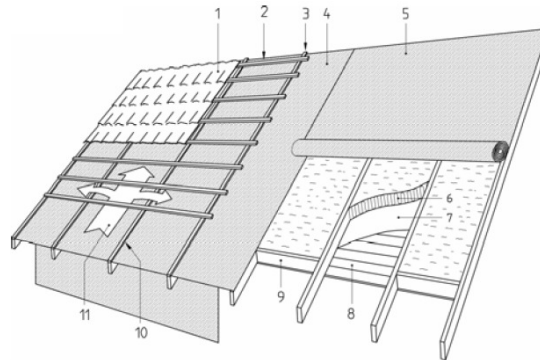

FIG. 2: Figure of a typical ventilated roof with ventilation directly above the roofing underlay (wind barrier). The numbers refer to: 1. roofing tiles or sheets, 2. roofing battens, 3. counterbattens, 4. roofing underlay, 5. example of a specific underlay system installation, 6. thermal insulation, 7. vapour barrier, 8. ceiling, 9. noggings, 10. cautiously clamped overlap joints, and 11. cross ventilation between underlay and roofing. (Figure from http://tjenester.byggforsk.no/prodok/ntg/dok/2375/2375ge.pdf.)

1 presents common dimensions for all roofs, while Table 2 presents dimensions that are different for the various configurations. All roofs were of the type where the wind barrier and roof underlay is combined into one single layer. This is different to the other common practice where the wind barrier is below a separate underlay layer.

Because the roof was simulated in two dimensions a two-dimensional representation of the rather complex three-dimensional ventilation channel had to be made. That is, highly three-dimensional objects like profiled roofing tiles were converted to a flat plane sheet, while the air gap openings between the battens and roofing tiles were retained by using an equivalent distance between "roofing tiles" and roofing battens. In real Norwegian roofs the rafters (and counterbattens mounted on the rafters) are spaced 600 mm apart. The height of the channel, which equals to the sum of the height of the battens and counterbattens, is usually smaller than 100 mm. The flow in the middle of each section may therefore be close to two dimensional. The ridge and the eave of the roofs are also simplified compared to a real three-dimensional roof configuration. The eave is simulated without an eave box, which is used quite a lot in Norway. The eave box limits the amount of snow that may penetrate into the ventilation channel (Thiis et al. 2007). The ridge is simulated without a ridge band that usually is installed to avoid rain penetration into the roof. Such a thin band would be difficult to model.

The main difference between the eight houses can be seen from Table 2. H1 to H5 may be thought of as "real" roof constructions, while the others are included to see the effect of the ridge and eve details by themselves. House H1 is the reference:

H1 is about 10 m wide, and has 18 battens in each side of the roof. The height of the counter-battens and battens are 36 mm and 30 mm, respectively. The angle of the roof is 30º.

The difference between roof H1 and the roofs H2 to H5 are:

H2 has a house width that is double the width of H1,

H3 has a roof angle that is 20º, compared to 30º for H1 (this results in a slightly shorter roof ventilation channel and a reduction in number of roofing battens from 18 to 17),

H4 has counterbattens that are 48 mm tall, compared to 36 mm for the other roofs.

H5 has battens that are 36 mm tall instead of the 30 mm that is common for the other roofs.

Roofs H6-H8 are variants of roof H1, where

H6 has a roofing channel without battens, but where the ridge and eave details are included

H7 has roofing battens but is without eave and ridge constructions,

H8 has no battens or eave and ridge constructions.

3. Numerical Simulations

To examine the air flow in the ventilation channel of the roof, numerical simulations with a CFD program (Fluent, 1998) was carried out. Only air flow by natural convection was considered, that is there was no external wind acting on the building. This is the case with the least air flowing through the roof.

3.1 Natural convection simulations

Only the ventilation channel of the roof was considered in these simulations. A pressure inlet boundary condition was used on the inlet (the eave) and a pressure outlet was used at the opening in the ridge. Because of symmetry, only half the roof was simulated. That is, a symmetry boundary condition was used at the center of the ridge.
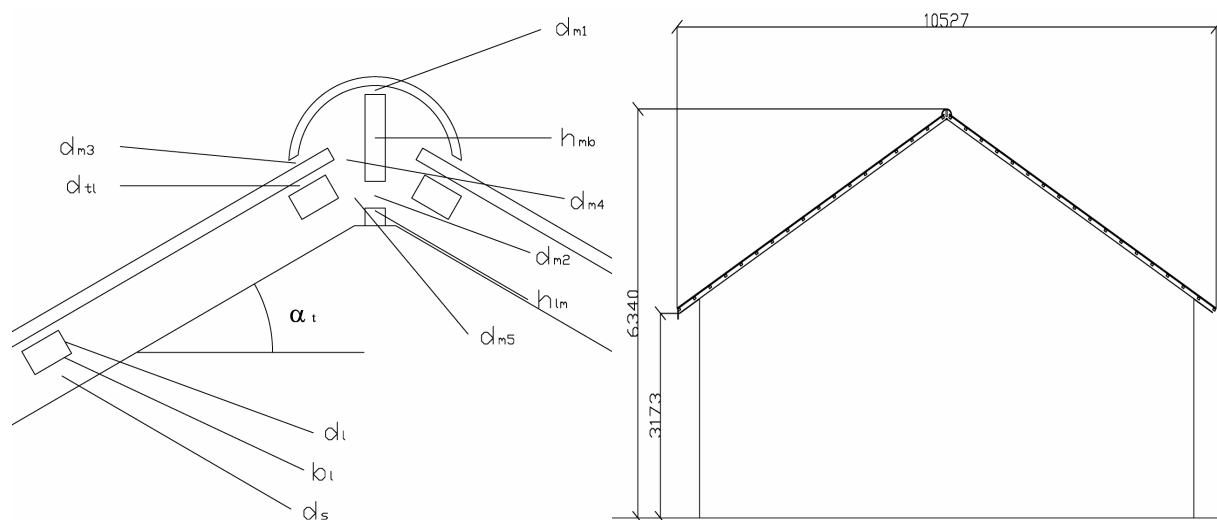

FIG. 3: Ridge for house H1 to the left and figure of the entire house to the right. Refer to Table 1 and Table 2 for dimensions (Hofseth 2003).

TABLE 1: Common dimensions for the various roofs.

Description	Symbol	Value	Dimension
Roofing thickness	t_t	20	mm
Equivalent distance between roofing and roofing battens	d_{tl}	10	mm
Width of roofing battens	b_l	48	mm
Size (horizontal) of eave	b_r	400	mm
Height of eave board	t_{fb}	148	mm
Size of opening between ridge tile and ridge board	d_{m1}	10	mm
Height of ridge board	h_{mb}	61	
Height of opening between ridge board and lath	d_{m2}	30	mm
Size of opening between ridge tile and roofing tile	d_{m3}	10	mm
Size of opening between ridge board and roofing tile	d_{m4}	30	mm
Size of opening between roofing battens and ridge board	d_{m5}	30	mm
Distance from underlay to eave board	d_{rl}	18	mm
Distance between roofing battens		350	mm

TABLE 2: Dimensions separating the various roofs.

Case	Height of counter-battens, d_s [mm]	Height of roofing battens, d_l [mm]	House width [m]	Channel length on each side of ridge[m]	Angle of roof [º]	Number of roofing battens
H1	36	30	10	5.998	30	18
H2	36	30	20	11.598	30	42
H3	36	30	10	5.321	20	17
H4	48	30	10	5.998	30	18
H5	36	36	10	5.998	30	18
H6	-	-	10	5.998	30	0
H7	36	30	10	5.998	30	18
H8	-	-	10	5.998	30	0

The exterior air temperature was set equal to 0 ºC. Thus, air entering the ventilation channel had this temperature. A heat resistance of 0.04 m²K/W was assumed on the outside surface of the roof (fluid flow was not simulated there). Inside the building a temperature of 20 ºC was assumed. Heat resistances of 4.5 and 6.7 m²K/W were assumed between inside of the building and the exterior wall surface and the roof underlay surface, respectively. These resistances are based the U-value requirements in the Norwegian Building Code from 1997 (NBC 1997).

Incompressible and steady laminar flow was assumed. Further, viscous dissipation was not addressed, and all thermophysical properties were assumed to be constant except for the buoyancy term of the y-momentum equation where the Boussinesq approximation was used. The Semi-Implicit Method for Pressure-linked Equations Consistent (SIMPLEC) was used to model the interaction between pressure and velocity. The energy and momentum variables at cell faces were found by using the First order upwind scheme. In addition, the CFD code used central differences to approximate diffusion terms and relied on the PREssure Staggering Option scheme (PRESTO) to find the pressure values at the cell faces. PRESTO is similar to the staggered grid approach described by Patankar (1980). Radiant heat transfer was included in the simulations through use of the discrete transfer radiation model (DTRM), which relies on a ray-tracing technique to calculate surface-to-surface radiation. The internal cavity walls were assumed to be diffuse gray and to have an emissivity of 0.9, and air did not interact with the radiative process. The double precision solver of the CFD code was used.

In the Boussinesq model, which is used for finding the buoyancy effects in y-momentum equation, the operating temperature is among the parameters. Correct determination of this temperature is important in order to find the right flow through the channel. Because the operating temperature is equal to the mean air temperature of the ventilation channel, an iterative process was used. Fist, an operating temperature was guessed, then after some iterations the operating temperature was adjusted to reflect the new temperature in the channel. This procedure was repeated until the temperature hardly changed any more.

The air properties used in the simulations were calculated at the mean temperature of air in the ventilation channel and at atmospheric pressure, P = 101325 Pa. A standard acceleration of gravity of -9.81 m/s² was used in all calculations. The conductivity of the wooden battens and the roofing material was set equal to 0.12 and 1.7 W/mK, respectively.

As the results section will show, only transient solutions of the specified problems were found. That is, first a stationary solution procedure was tried (with under-relaxation to avoid divergence), but the residuals did not decrease. Therefore a transient solution procedure was selected. A time step of 0.1 s was chosen (Fluent, 1998).

A small part of the wall was included in the numerical simulations. Thus, there were two inlet boundaries at the eave; the opening between the lower batten and the roofing layer and the horizontal opening between the bottom part of the eave board and the wall of the building. This was done to allow some air flow along the wall against the eave openings.

4. Results and Discussion

Transient solutions were found for all the various cases in Table 1. Below some snapshots of the velocity steam function and temperature plots are shown. Air flow rates are also reported and discussed.

4.1 Velocity results

Figures 4 and 5 show the stream contours for the ridge and the eave for roof configuration H1, respectively. Both figures show that air circulation occurs between the battens. Although there are some exceptions, the air flows upward on the right side (upper side) and downward on the left side (lower side), between each pair of battens. Figures 4 and 5 also show that more irregular patterns may develop between the battens. The reason for this air circulation is that the lower surface is warmer than the upper surface. As we will see below, similar flow also occurs in roof H6, where there are no battens.

Another feature that can be seen from the figures is that most of the air flows along the lower surface of the roof, between the battens and the roof underlay. Here the flow direction is upward, from the eave toward the ridge. Above the battens and beneath the roofing layer (the equivalent spacing that that takes into account the flow between profiled tiles and battens) the main air flow direction is downward. At the eave, where the air enters the roof, Figure 5 shows that most of the air enters through the opening between the batten and the roofing layer. Less air enters the ventilation channel between the batten and the roof underlay. The reason for the small amount of air entering the roof from the opening below the batten, may be that the air flow direction outside the opening is away from the opening. This movement is caused by the rising heated air along the wall.

Figures 6 and 7 display stream contours for roof configuration H6. This roof does not have any battens between the eave and the ridge, and was included in order to see the effect of the battens versus the eave and ridge details on the air flow through the roof. Both figures show that a complex flow pattern also develops inside this roof; even if there are no roof battens. Similar flow patterns have been reported by e.g. Corcione (2003), but then for rectangular horizontal closed cavities.

Two typical cell sizes are found inside the ventilation channel, large ones and small ones. The size of the different cells seems to be quite constant except for the larger cell close to the eave. The larger cells circulate clockwise and the small cells circulates counter clockwise. Studies of whether the cells move upward was not performed, but this is expected because there is some air flow through the roof, from the eave to the ridge.
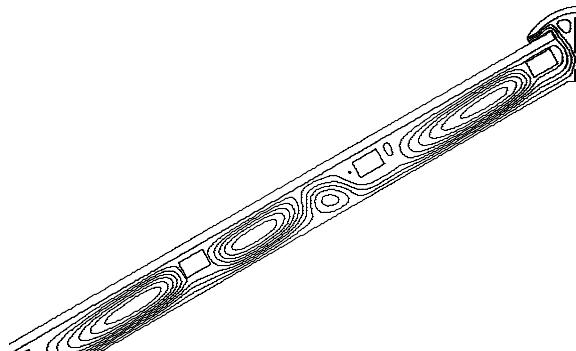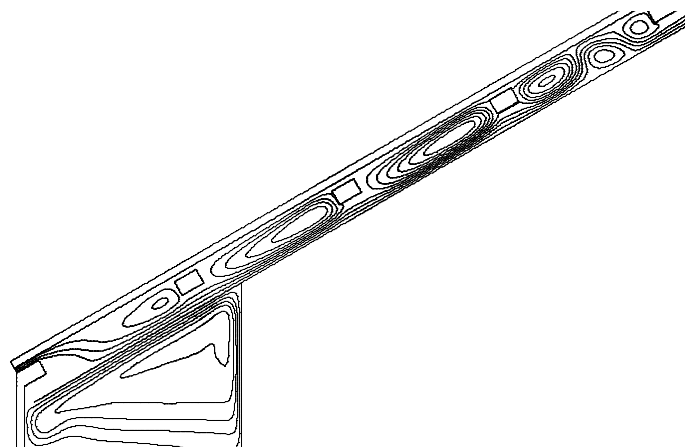

FIG. 4: Stream contours for the ridge of roof H1.

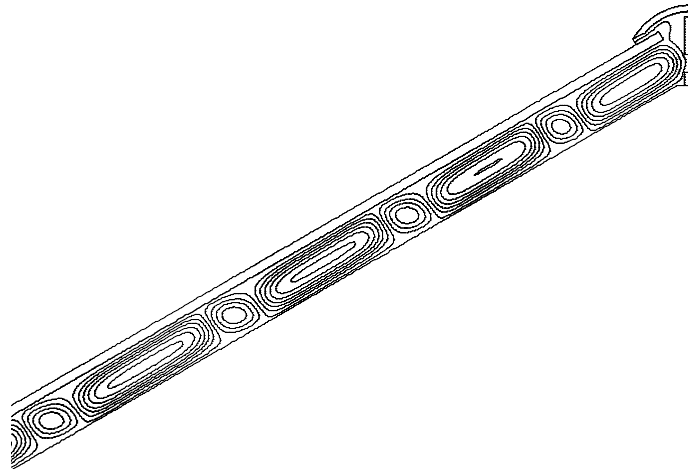*FIG. 5: Stream contours for the eave of roof H1.*
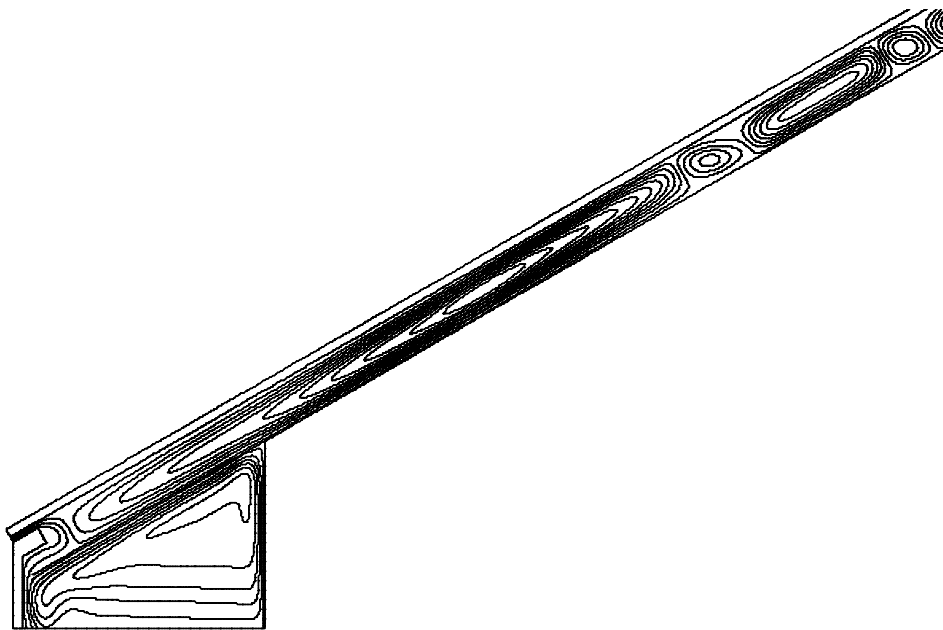
FIG. 6: Stream contours for the ridge of roof H6.

FIG. 7: Stream contours for the eave of roof H6.

4.2 Roof temperature

The temperature distribution in roof H1 (close to the ridge) is shown in Figure 8. As seen from the colour bar to the left, the temperature difference between the warmest and the coldest part of the roof is not large. The coldest temperature (about 273.15 K) can be found close to the eave while the warmest temperature (about 274.3 K) can be found in the ridge. The effect of the air circulation on the temperature distribution of the air in the ventilation channel can easily be seen. Where the air rises the temperature is high, and vice versa. A similar temperature pattern was observed for roof H6, even if there were no battens inside the roof.

Figure 9 displays the outside surface temperature of roof H1. The horizontal axis shows the distance from the eave in millimetres (mm), while the vertical axis shows the temperature in K. The figure shows that the temperature of the roofing material is close to the outside air temperature of 273.15 K close to the eave. Further, the figure shows that the temperature increases quite rapidly, from the eave, to about 273.25 K, where it oscillates for the remaining part of the roofing layer, except for a rather small area close to the ridge. In the middle part of the roof, where the oscillations take place, the lowest temperature is found close to the battens. This is because the battens act as thermal radiation shields. The average surface temperatures for all the various roofs were practically equal (to 273.25 K).
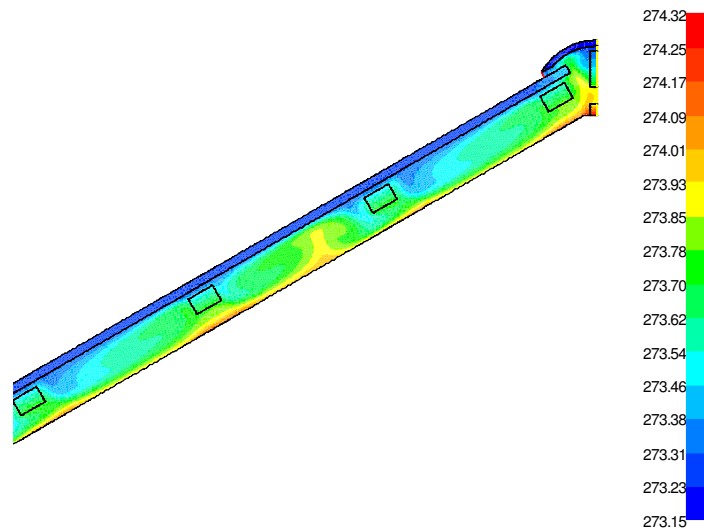
FIG. 8: Temperature contours for roof configuration H1. Temperatures are in Kelvin.
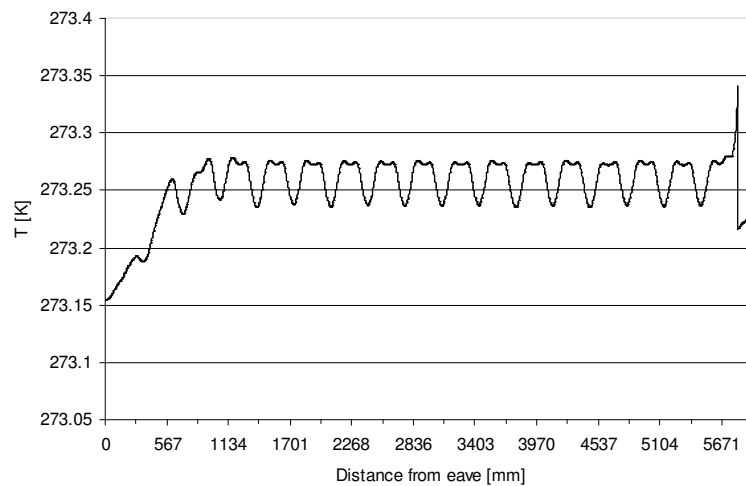

FIG. 9: Figure showing outside surface temperature for roof H1.

4.3 Mass flow rates

Table 3 shows the mass flow rate and the mean velocity in the ventilation channel. The results reported are time averaged data for the outlet of the ventilation channel. That is, the simulation ran for several cycles, and the average during these cycles was reported. If a repeating pattern was found in the mass flow rate through the exit opening, the average is reported for a complete cycle.

By looking at the table the following results can be observed: 1) Increasing the height of the counter-battens from 36 mm (H1) to 48 mm (H4) increases the flow rate from $2.61×10^{-4}$ kg/s to $3.71×10^{-4}$ kg/s. 2) Increasing the height of the battens from 30 mm (H1) to 36 mm (H5) also increases the flow rate (from $2.61×10^{-4}$ kg/s to $3.5×10^{-4}$ kg/s). The latter is because the height of the ventilation channel (height of battens and counter-battens) as a whole increases. Increasing the width of the building (going from configuration H1 to H2) also increases the flow rate (keeping the same roof angle of 30°). What is more surprising is that reducing the roof angle from 30° (H1) to 20° (H3) also increases the mass flow rate. This may partly be explained by the shortening of the ventilation channel (the channel has less battens), but also by a changing flow pattern that changes with roof angle and roof configuration. That the latter is the case, may be shown by looking at the results for cases H6 (no battens but with contractions in the eave and ridge), H7 (battens, but no contractions at the eave and ridge) and H8 (open channel – no battens and no contractions at the eave and ridge). From looking at the stream contours of roof H6 (see Figure 6), it can be seen that there hardly is any air movement through the roof, but that air circulates within the ventilation channel. This is the reason for the low mass flow rate through this roof.

TABLE 3: Mass flow rates for the various roofs.

Case	Mass flow rate [kg/s]	Average velocity at outlet [m/s]
H1	2.61×10^{-4}	0.020
H2	3.91×10^{-4}	0.030
H3	3.00×10^{-4}	0.023
H4	3.71×10^{-4}	0.029
H5	3.50×10^{-4}	0.027
H6	4.69×10^{-5}	0.0036
H7	4.75×10^{-4}	(two exit openings between battens)
H8	2.97×10^{-3}	0.0349

These results should be validated by experiments, which to some extent were tried, but controlling and measuring the flow rate through the roof at these small temperature differences was difficult. The CFD code has however been used to predict similar flow patterns in windows and frames which have been verified by experiments (Gustavsen et al. 2001).

5. Conclusions

The numerical simulations show that a complex flow pattern exists within the roof ventilation channel. Changing one parameter, i.e. the roof angle or removing the battens, may not always give the results that seems obvious in the fist place. The reason for this is that a circular flow pattern occurs, and that this pattern changes with changing geometry and roof angle. Still, there seem to be a relationship between the height of the ventilation channel (height of battens and counter-battens) and the mass flow rate through the channel.

The mass flow rates may for instance be used in moisture simulation software to analyze whether the various designs produce large enough air flow rates in the ventilated cavity of the roof for transporting moisture, which has penetrated the roof construction from the interior space of the building, out of the roof.

6. Acknowledgement

7. References

Blom, P. 1990. Ventilation of insulated slanting roofs. Ph.D. dissertation, Department of Building and Construction Engineering, Norwegian University of Science and Technology.

Corcione, M. 2003. Effects of the thermal boundary conditions at the sidewalls upon natural convection in rectangular enclosures heated from below and cooled from above, International Journal of Thermal Sciences, Vol. 42 (2), pp. 199-208.

Fluent (1998). FLUENT 5 User's Guide, Fluent Inc., UK.

Gustavsen A., Griffith B.T., and Arasteh, D. 2001. Three-Dimensional Conjugate Computational Fluid Dynamics Simulations of Internal Window Frame Cavities Validated Using Infrared Thermography, *ASHRAE Transactions*, Vol. 107(2), pp. 538-549

Hofseth, V. 2003. Air flow in ventilated insulated roofs (in Norwegian). Project report, Department of Civil and Transport Engineering, Norwegian University of Science and Technology.

NBC 1997. Norwegian building code 1997 (in Norwegian).

Patankar, S.V. 1980. Numerical Heat Transfer and Fluid Flow. Washington: Hemisphere.

Thiis, T.K., Barfoed, P., Delpech, P., Gustavsen, A., Hofseth, V., Uvsløkk, S., and de Virel, M.D. 2007. Penetration of snow into roof constructions—Wind tunnel testing of different eave cover designs, *Journal of Wind Engineering and Industrial Aerodynamics*, Vol. 95(9-11), pp. 1476-1485.

Uvsløkk, S. Roofs with a cold attic (in Norwegian), Project report 396, SINTEF Building and Infrastructure.

Estimation of air flow rates in large buildings based on measurements

Hannes Konder, Mr,
research assistent;
hannes.konder@tuwien.ac.at, www.bph.tuwien.ac.at

Thomas Bednar, Prof.,
assoc. Professor;
thomas.bednar@tuwien.ac.at, www.bph.tuwien.ac.at

KEYWORDS: air flow rate, large building, measurement, CO_2, tracer gas, atrium

SUMMARY:
The estimation of large wind and buoyancy driven air flow rates in large buildings is essential for the calculation of the annual energy use for cooling and heating. In this paper a new method is presented, how to measure these large air flow rates. The design of a stable CO_2 emitting source with large rates is shown. This source has been applied to measure the time-dependent air flow rate in a multi-storey office building, where the five storeys are connected one to another by an atrium. The air-flow rate at the inlet opening calculated from the measurement of the CO_2 concentration is compared with the air-flow rate calculated from the mean air velocity at the inlet opening. Both time-dependend rates show a good agreement. Furthermore the source is powerful enough so that the tracer gas can be detected in the upper floors even if the air flow rate rises due to increasing air velocity.

1. Introduction

The estimation of large wind and buoyancy driven air flow rates in large buildings is essential for the calculation of the annual energy use for cooling and heating. Researchers in the past have carried out measurements of buoyancy-driven air flows in the staircase of a residential building (see Peppes et.al. 2001 and Peppes et. al. 2002). In this paper the measurement of these transient air flow rates in a multi-storey office building is presented. The measured data in this case was used, to estimate the efficiency of natural cooling during the night in the summer. The measurements had to give the answer to the following questions: How large is the air flow rate into the office building and are offices located far away from the main air flow reached by the natural ventilation.

2. The building

The governmental office building in which the measurements took place, is part of a series of identic buildings located, one next to the other in a row, in Austria. For a description of the buildings see Dreyer et. al. 2006. The five storeys of the building are connected one to another by an atrium, which is situated next to the staircase. The offices are accessible by gangways on both sides of the atrium and of the staircase. In FIG. 1 a wire frame model of the building is illustrated, where only one office and one gangway on one side of the atrium is shwon. The natural ventilation during the night can be activated by three openings, connected in series, in the ground floor and one single opening on the roof at the top of the atrium (see FIG. 1).

3. Measurement-setup

3.1 The source

Tracer gases can be used to measure air flow rates within buildings. Since both, CO_2 as a tracer gas and CO_2 – sensors, like they are used by the building service departurements, are not very expensive, CO_2 has been used for these measurements. Another reason for using CO_2 as a tracer gas was that the measurements where carried out whilest the building was ordinary used by the owner and therefor a gas had to be used, which is detectable even far below the maximum allowable concentration (MAC). But as in this case large air flow rates where expected,

a conventional CO_2-source like a gas bottle with a rather low production rate could not be used. Earlier measurements in single offices in this building have shown that such a conventional source has a maximum production rate up to 0.5 g/s. This upper limit in the production rate is due to icing of the blow-off valve, caused by the decompression of the gas.
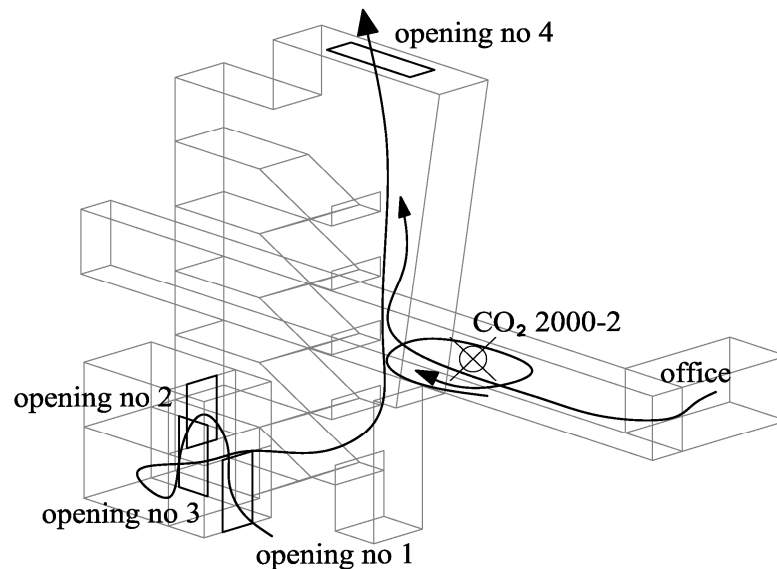

FIG. 1: wire frame model of the office building

The solution of the icing problem was found in a simple, new source that instead of compressed CO_2 uses dry ice (see FIG. 2). Within the isolating walls of the box-source made of extruded polystyrene, an electric heater is covered on all sides by dry ice. The power of the heater has to be equal to the energy demand of the dry ice to perform the production rate required. In this case an electric power of 2.4 kW was installed to run a production rate of approximate 3.2 g/s. (see FIG. 2). As due to local sublimation next to the bars of the heater, the heater sometimes was not completely covered by dry ice and the production rate varies therefor from 3.1 to 3.4 g/s. Some peaks in FIG. 2 are due to the crashing of a small dry ice dome above the electric heater. The gas produced is blown off the source from a hole with a diameter of 10 cm. As the gas coming out of the source was rather cold in comparison to the temperature of the air driven into the building by buoyancy, a small fan was placed next to the hole of the box to achive a well mixing of the gas with the air. The installed power inside the source had no influence on the natural buoyancy, since the whole power installed is consumed by the dry ice. The box used is 1.4 m high with a volume of approximate 0.5 m³. With that volume, the source can be run for about 5 hours without refilling. That way a rather stable source could be build for the further measurements.
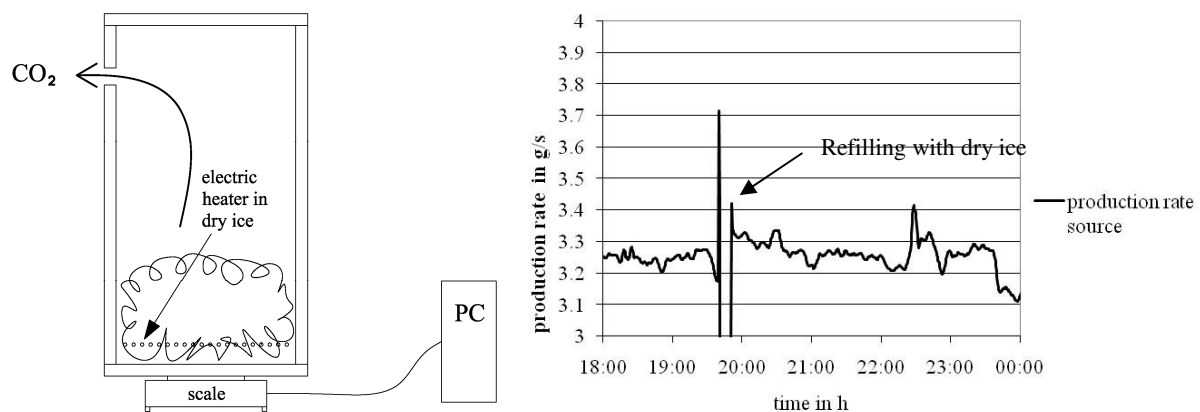

FIG. 2: section of the new CO_2 source with a production rate > 3 g/s

3.2 Location of the sensors and of the source

As determining the air flow rate with the tracer gas at the inlet opening of the building was one of the aims of the measurements, various CO_2 detectors have been set in the foyer of the office building.
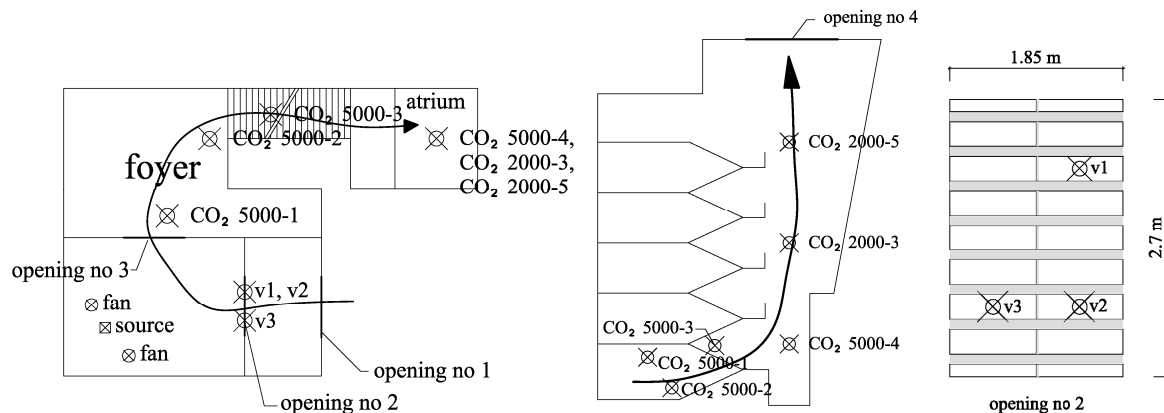

FIG. 3: ground floor of the foyer and section of the atrium and of the staircase of the building including the positions of the CO_2 sensors and of the hot-wire anemometers

In FIG. 3 the ground floor of the foyer is illustrated where most of the CO_2 sensors were installed. Next to the ground floor a section of the staircase and of the atrium with all the vertical positions of the sensors are shown. Since the reliability of the measured data is not known, for validation hot-wire anemometers were used in the measurement setup at the opening n° 2 (see FIG. 3).

The source was located in the corner of the room between opening n° 2 and opening n° 3. The room was provided with two fans to garantee a sufficient air mixing. This is one of the fundamental conditions to meet when measuring with tracer gases.

4. Results and discussion

The measurements took place in a late September night. Therefore, the buoyancy driven natural ventilation started rather late that day, because the temperatures within the building where not so high as they usually are during a hot period in the summer.

Nevertheless between 6:00 pm and midnight, when the indoor – outdoor temperature difference increased, also the measured mean air velocity at opening n° 2 continuosly increased and reached a final value around 0.6 m/s (FIG. 4). At the same time, with an increasing air velocity and therefore an increasing air flow rate, the measured concentrations of the tracer gas decreased in the foyer (sensors CO_2 5000-1, CO_2 5000-2, CO_2 5000-3) and increased in the upper part of the atrium (sensors
CO_2 2000-3 and CO_2 2000-5). Also the sensor located in the gangway on the 2nd floor, about 15 m far away from the atrium (sensor CO_2 2000-2), was reached by the tracer gas and a concentration comparable with that one in the atrium at the fifth floor was reached. The high concentration of CO_2 in the foyer, measured before 6:00 pm is due to the early start of the measurement. Since the CO_2 source has already been activated at 12:00 am, a high amount of the tracer was accumulated in the foyer due to the lack of a distributing air flow. These measurement results show that the production rate of the source was high enough to supply the whole building with a detectable concentration of the tracer. All graphs shown in FIG. 4 include the background content c_0 of $c_0 = 350$ ppm CO_2 in the air.

As measuring the air flow rate into the building by using the tracer was one of the main aims of that work, the air flow rate was deduced out of the measured production rate of the source divided by the measured concentration in the foyer. This was done with the following equation

$$\dot{V} = \frac{p}{c - c_0}$$

where $\dot{V}$ is the air flow rate into the building in m³/h, p is the measured production rate of the source in g/h, c is the mean measured concentration of the tracer in the foyer using the sonsors CO_2 5000-1, CO_2 5000-2 and CO_2 5000-3 in g/m³ and c_0 is the background content of the tracer in the outdoor air in g/m³. The time dependent air flow rate for this measurement is shown in FIG. 6, named as CO_2 measurement.

For validation of this calculated data, the result was compared with the air flow rate calculated from the air velocity measurement. This second air flow rate was obtained by multiplying the mean air velocity at opening n° 2 by its area. Since opening n° 2 due to security reasons was covered by a fence (see FIG. 3) not the whole area but only 71% of it could be taken into account.
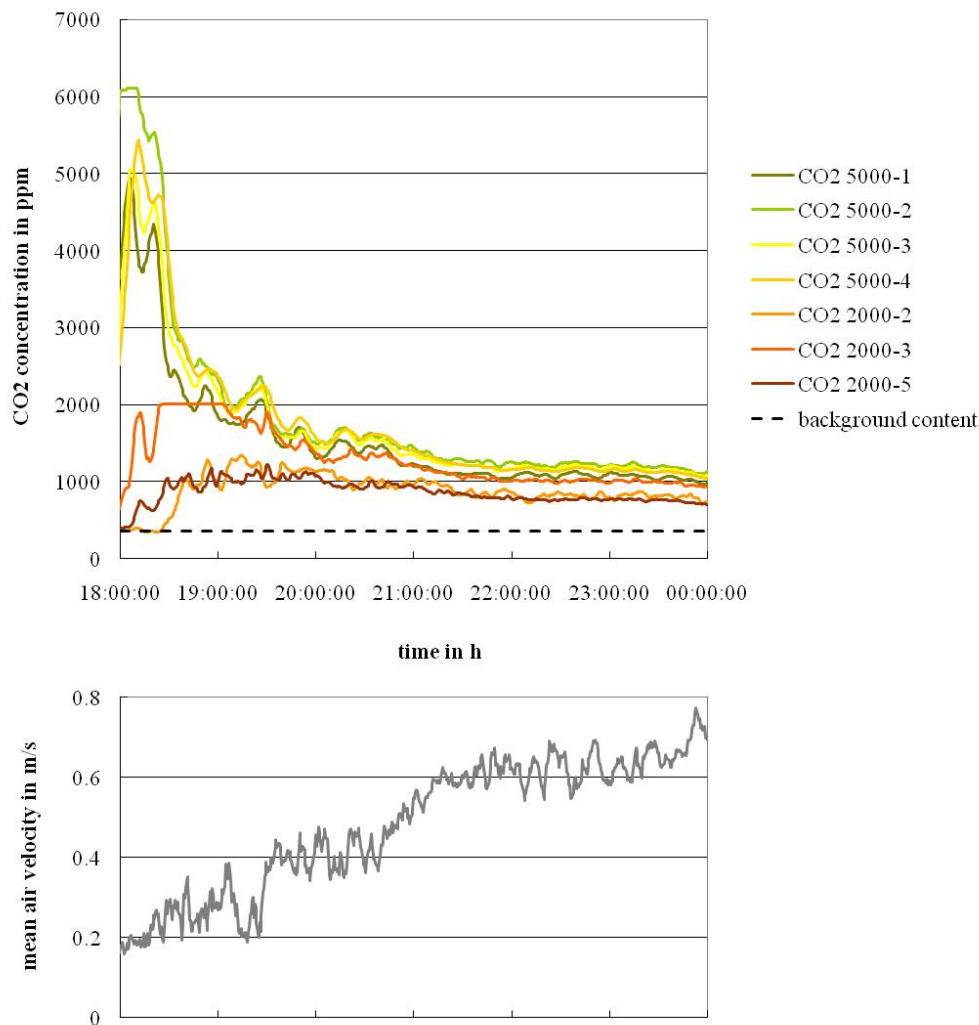

FIG. 4: measured data: air velocity at the inlet at opening n° 2 and concentrations of the tracer gas

FIG. 3 shows opening n° 2 with the position of the hot-wire anemometers used to measure the air velocities. As only 3 sensors where available, the air velocity v_4 in the fourth quadrant of the opening had to be calculated. To

do this, the ratios of the air velocities v1/v2 and v3/v2 were built (see FIG. 5). As theses ratios can asumed to be linear, the velocity v_4 in the fourth quadrant was calculated with the following assumption:

$$v_4 = \frac{v_1 \cdot v_3}{v_2}$$

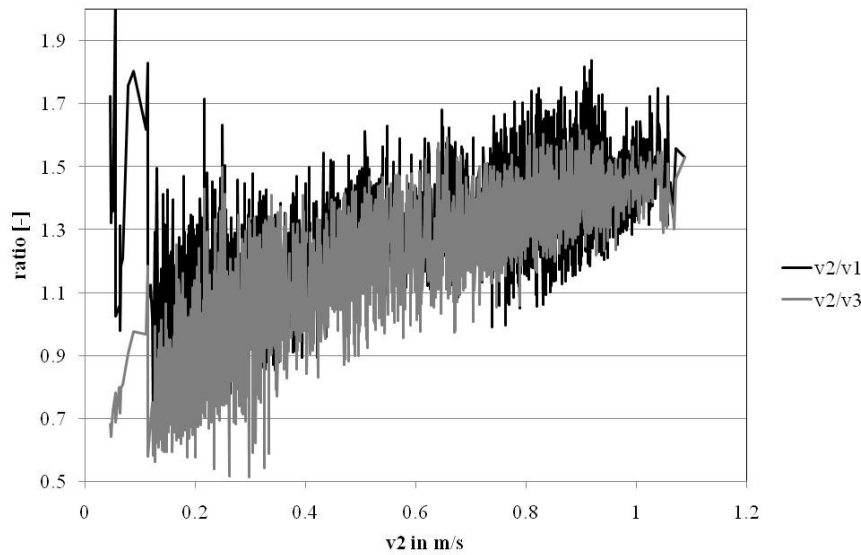With this assumption the mean air velocity (FIG. 4) was calculated.

FIG. 5: ratio v2/v1 and v2/v3 against v2 at opening n° 2
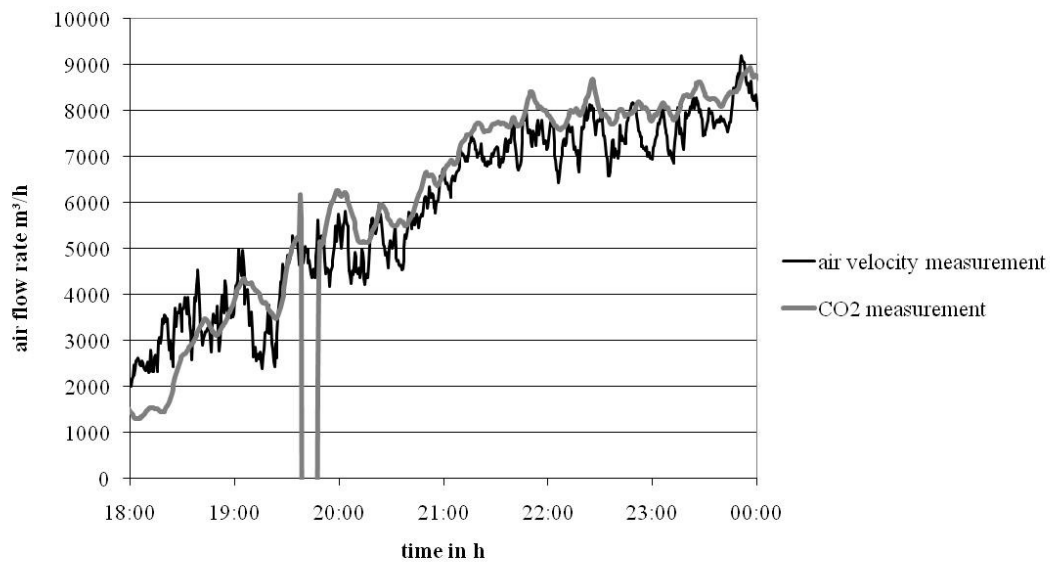

FIG. 6: comparison of the two calculated air flow rates at the inlet of the office building

As one can see, the two air flow rates are well comparable and only at rather small air flow rates the measuremet with the tracer gas underestimates the air flow rate measured by the air velocity.

5. Conclusions

Using a new, stable source of the tracer gas CO_2, air flow rates in large building can be measured. The measured data is validated with simultaneous measurements of the air velocity at the inlet opening of the large building. Furthermore the source is powerful enough to elevate the measured concentration of the tracer gas above the background content at sensors far away from the inlet even if the air flow rate at the inlet opening increases up to 8000 m³/h.

6. References

Peppes A.A., Santamouris M., Asimakopoulos D. N. (2001). Buoyancy-driven flow through a stairwell, Building and Environment, Vol. 36, p. 167-180

Peppes A.A., Santamouris M., Asimakopoulos D. N. (2002). Experimental and numercal study of buoyancy-driven stairwell flow in a three storey building, Building and Environment, Vol. 37, p. 497-506

Dreyer J., Bednar T., Konder H., Sofic M. (2006). Kurzbericht über die messtechnische Erfassung der Effektivität der Fenster-, Gebäude- und mechanischen Lüftung unter verschiedenen Betriebszuständen und Randbedingungen, Vienna University of Technology, Institut für Hochbau und Technologie, Fachbereich für Bauphysik und Bauakustik

Measurement of air temperature using infrared thermography in rooms equipped with UFAD systems in cold climate

Marianne Bérubé Dufour, B.Arch MaSc PhD student,
Concordia University;
mar_beru@alcor.concordia.ca

Dominique Derome, arch ing PhD,
Concordia University

Michel Tardif, ing,
Natural Ressources Canada

Radu Zmeureanu, ing PhD,
Concordia University

KEYWORDS: *whole-field methods, thermography, UFAD.*

SUMMARY:
UFAD systems for the cooling and the ventilation of rooms are increasingly used in new buildings. The advantages of these systems are energy savings and high level of air quality while possible drawbacks concern thermal comfort. To better understand the indoor environment produced by such systems, it is relevant to obtain instantaneous and detailed mappings of the air conditions. To do so infrared thermography in combination with a low mass screen has been used in laboratory for the visualization of whole temperature-field and measurement studies of clear zones, close to swirl diffusers. This paper presents infrared thermography measurements taken in situ. *Located in Montreal, the building investigated is equipped with an underfloor air distribution system operated in displacement mode. The method has been applied successfully to visualize and measure temperature of air between bookshelves at the center of the building. However, in the offices at the periphery the arrangement of the office furniture and diffusers, prensece of windows and heating systems make it more challenging to visualize air flow and take accurate measurements.*

1. Introduction

In the last 10 years, more and more buildings are designed with under floor air distribution (UFAD) systems for the distribution of air within the rooms. UFAD systems are actually known to lead to energy savings and excellent indoor air quality conditions compared to the conditions found in buildings with mixing ventilation systems. The main drawback of the UFAD systems is the possibility for high vertical temperature gradient and/or cold draft effects. To better understand the indoor environment produced by such systems, it is relevant to obtain instantaneous and detailed mappings of conditions, i.e. temperature, velocity and pollutant concentration. Unfortunately, traditional point measuring techniques give low resolution information and are time consuming.

For the visualization and measurement of whole temperature field in rooms, infrared thermography (IRT) in combination with a low mass screen can be used. An IRT camera directed at a surface detects the emitted and reflected thermal radiation, which wavelength range extends from 0.7 to 100 μm in the electromagnetic spectrum. Camera built-in calculation tools allow for taking into account the parameters involved in radionetric measurements such as emissivity of the surface, surroundings temperature and distance. The resulting thermogram is a thermal image of the surface. More commonly, infrared cameras are used in buildings to locate thermal insulation discontinuities and air leakages throughout the building envelope during building energy audits. As air has no solid surface, the concept of the measurement technique used in this paper is to install a screen as the target across the field of interest, thus, becoming the support for visualization of the air temperature. Hassini and Stetz (1994) introduced the technique and presented measurements of air temperature of an air jet from a nozzle with an initial velocity of more than 1 m/s and about 15°C below ambient. Also, using the same technique, Cehlin et al (2000 and 2002) published measurements for an air jet from a low velocity

diffuser used for displacement ventilation systems. However, the technique presents drawbacks and the following issues have to be controlled:

- the screen introduced can disturb the flow;

- the screen may not be at the same temperature as the air;

- the infrared camera may not measure the exact surface temperature.

The purpose of the work presented in this paper is to show how this technique can be used to visualize and measure air temperature in situ in stratification conditions. The paper addresses specifically the means to reduce the impact of the 3 items listed above. The paper presents the experimental method developed and the measurements obtained, and discusses the results.

Whole air temperature field measurements using IRT were carried out in January (average outside air temperature -10°C) in a large public library located in Montreal. The building includes the traditional bookshelves areas, consultation areas of different geometries and administration areas. The floors of the six-storey building are equipped with underfloor air distribution system (UFAD) operated in displacement mode. In general, displacement systems produce stratified indoor climates. To ensure adequate fresh air to the occupants, the UFAD systems use swirl floor-mounted diffusers to generate a zone of mixing conditions close to the floor. The clear zones close to the diffusers and the occupants are critical for thermal comfort such displacement ventilation conditions.

2. Description of the experiment method

The objective of this experiment is to visualize the temperature field resulting from airflow using IRT in rooms with mixing and stratified conditions and to assess the accuracy of these air temperature measurements.

A long wave sensitive IRT camera designed for research purposes, ThermaCAM S60 developed by FLIR Systems (FLIR Systems 2004), is used for the experiment. The camera has thermal resolution of 0.06°C and a spatial resolution of 1.3mRad. The accuracy specified by the manufacturer in the case of measurement without reference is 2°C for blackbody object in ambient condition. A proprietary software is used for the post processing and data analysis (FLIR Systems 2003). For the sake of the qualititative study presented here, the temperature scale of the thermograms is not added later. All the thermograms scales vary from 20 (dark purple) to 25°C (yellow).

A screen net, material normally used as mosquitos screen in windows, is selected as screen target for the experiment. Cehlin *et al* (2000) found out that the use of a screen does not affect the velocity or the temperature fields of airflow from low velocity diffusers in displacement. However, they recommended the use of a smooth solid high emissivity screen like normal paper in order to avoid the creation of local perturbations. In fact, Hassini and Stetz (1994) found that boundary layer thickness increase with the roughness of the paper screen. For the case studied in this article, a porous screen is preferred to paper because of the rotating nature of the flow produced by the swirl diffusers.

First, screens of various porosity and material emissivity have been tested. Table 1 shows the characteristics of three porous screens: glass fiber covered with rubber, aluminum and rubber. The bulk emissivity is calculated based on the emissivity of the mesh material, weighted by the porosity. Figure 1 shows thermograms of the three different screens subjected to a similar hot air blow of a hair dryer. The rubber net with a lower porosity and higher emissivity leads to the best detection of temperature, as verified by a thermocouple. This better result with rubber is due to its higher emissivity which results in a higher amount of the radiation detected by the camera that belongs to the object inspected. Thus, the accuracy of the temperature measured is higher with the rubber screen.

Table 1 Porous screens tested

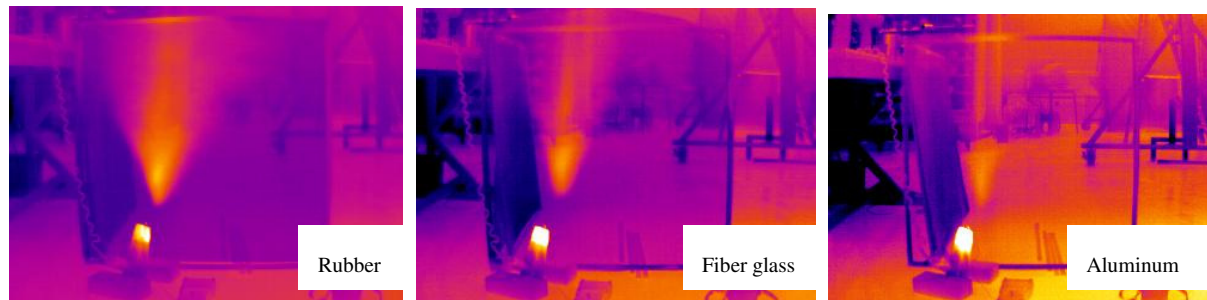| SCREEN	Porosity	Emissivity
Glass fiber	approx. 0.6	0.95 (rubber covered)
Aluminum	approx.0.6	0.2
Rubber	approx. 0.4	0.95

Figure 1 Thermograms of an air jet using screens made of different materials

Smoke visualization has been done also to assess the disturbance of the airflow by the rubber porous screen. Figure 2 shows the smoke driven by the supplied air with and without the rubber screen. The airflow crosses the screen. Some disturbance of the flow crossing the screen is observed as a thin film of smoke is stagnant at the surface of the screen. The quantification of this disturbance will be studied further in a later part of the project.
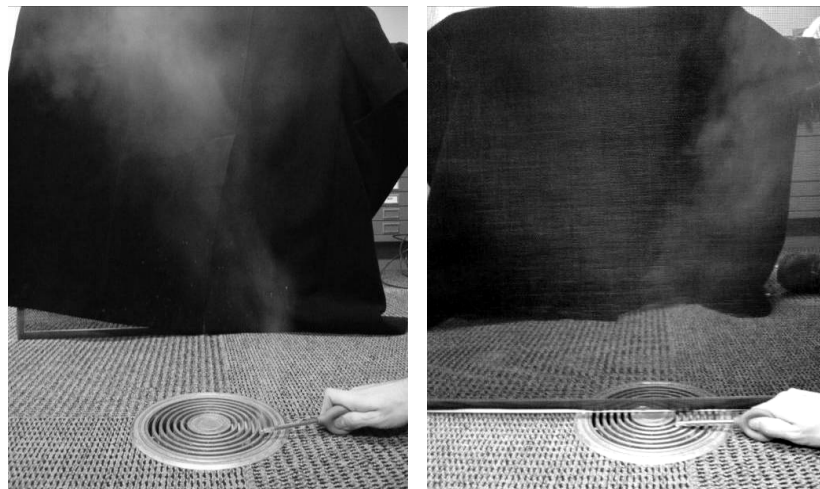

Figure 2 Smoke visualization of an air jet from a swirl diffuse: <u>Left</u> without any screen, <u>Right</u> with a rubber porous screen

In order to have an estimate of the accuracy of the air temperature using thermography, temperature measurements were taken along a vertical at the center of the diffuser axis at 0.1 and 0.6 1.1 and 1.7 m. Figure 3 shows surface temperature profile obtained by infrared thermography and the air temperature measured using RTD's at the corresponding locations. The temperature differences between are within 1°C. This difference is further discussed in section 4.
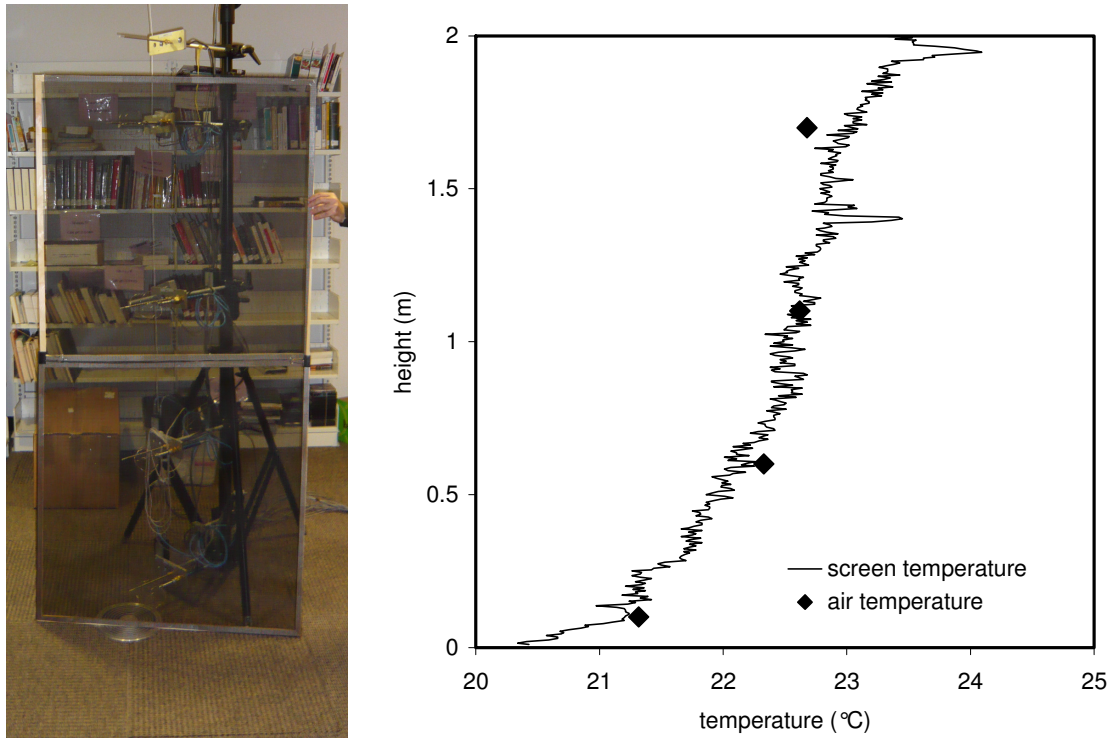
Figure 3 <u>Left</u> Measurement set up, <u>Right</u> Air temperature and screen surface temperature

Two locations are used to investigate the possibilities of visualization of air temperature field: one in between parallel sets of shelves in the center zone and one administration zone at the periphery. For each location, 1mx1m screens were installed to cover the height of the space and the cross section studied. A paper screen was also installed behind the target screen to insure the most uniform background possible. Figure 4 shows a schematic of the experimental set up. The ambient temperature and supply air temperature were measured using thermocouples. A directional anemometer was used to estimate the velocity at the diffuser. The airflow was measured using a balometer. The recorded thermograms are presented in the next section.
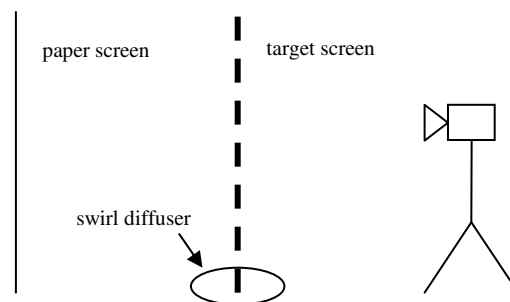

Figure 4 Experimental set up

3. RESULTS

3.1 Location 1: Bookshelves

Bookshelves, as found traditionally in libraries, cover the center of the building floor. Their height is 1,8 m and are 1,2 m apart. Floor diffusers are aligned in the center of the bookshelf corridor at a distance of 3m apart. The ambient air conditions are presented in Table 2, and the spliced thermogram is presented in Figure 5 <u>Left</u>. The temperature gradients along the height of the thermogram are found in the graph of Figure 5 <u>Right</u>. The expected

slow rate of change of the temperature across the height is clearly shown, as well as the more mixed conditions found in the bottom part of the air space.

Table 2 Room and diffuser conditions Location 1

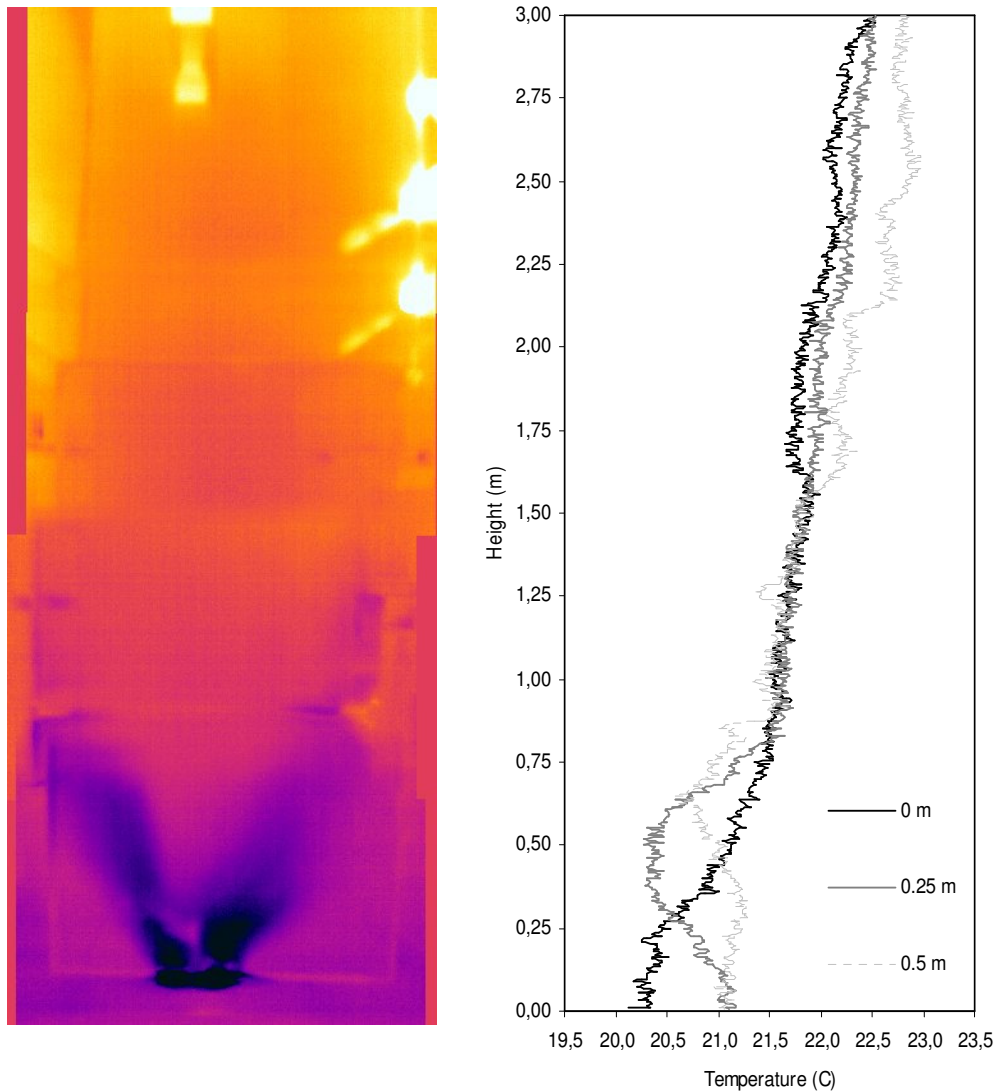|	
Ambiant air temperature	21.1 °C
Supplied air temperature	19.4 °C
Velocity at the diffuser	1.1 m/s
Airflow	30 cfm

Figure 5 <u>Left</u> Thermal image of air jet from one swirl diffuser <u>Right</u> Temperature gradient along vertical in between the book shelves lines at 0, 0.25 and 0.5m from the center of the diffuser

3.2 Location 2: Administration Office

The office space of the library is a classical open floor system using low partitions cubicles between the offices of the library employees. The geometries of the offices vary greatly as well as the furniture layout. For this study, an office space beside the exterior wall is chosen. The lower part of the wall is opaque and equipped with

an electric heating system and receives 0,8m from the floor a strip window of 1,2m high. Table 3 presents the air conditions of the location. First, Figure 6 presents the flow out of two adjacent floor diffusers. Figure 7 shows the thermal images of the air flow along the perimeter of the office, against the window.

Table 3 Room and diffuser conditions Location 2

Ambiant air temperature	24.3 °C
Supplied air temperature	45 °C
Velocity at the diffuser	1.65 m/s
Mean airflow	50 cfm
Temperature at heater	43 °C

Figure 6 Right. Thermal image of air jet from two adjacent swirl diffusers in the office space. <u>Left</u>, Photo of the set-up.
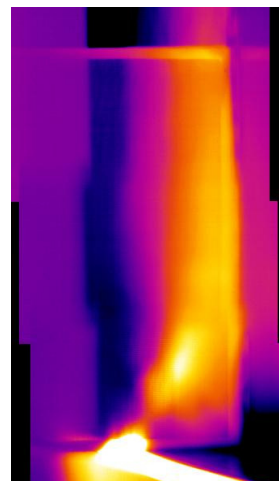

Figure 7 <u>Left</u>. Photo of set-up. <u>Right</u>, Thermal image of air airflow along a window above a wall heating unit.
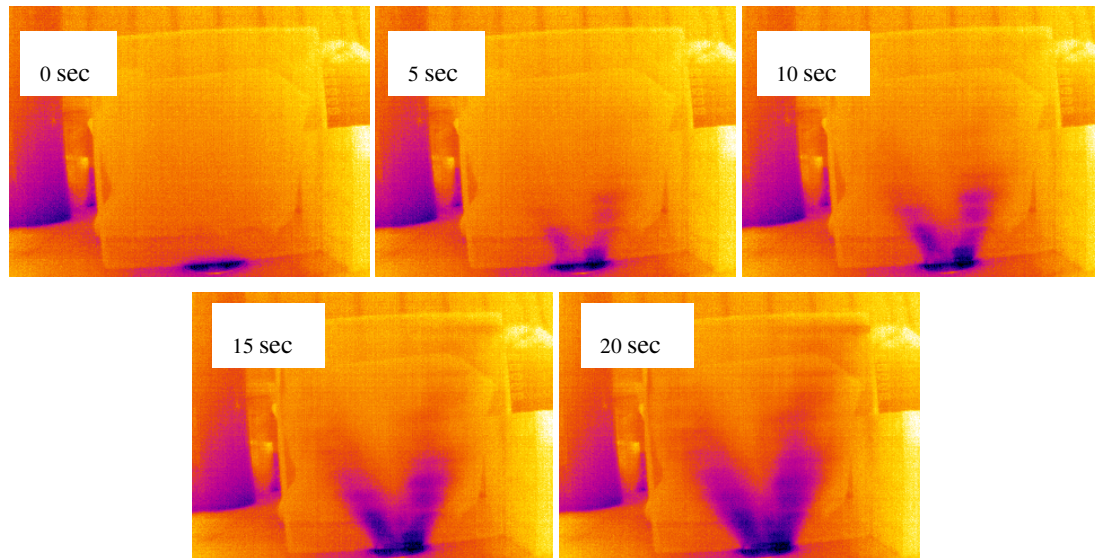
Figure 8 Sequence of thermal images recorded during the opening of a diffuser damper

Finally, Figure 8 shows the capacity of the method to capture change of air temperature versus time, with thermgrams taken at frequency of 1Hz during the opening of the damper of the floor diffuser.

4. Discussion on measurement uncertainty measuring air temperature using infrared camera

As mentioned above, the difference measured between the air and screen temperature was 1°C maximum, as presented in Figure 3. Another study looked at the range of temperature differences for different measurements conditions. In this study, Cehlin *et al* (2002) used an energy balance between the surroundings and the screen. They calculated the theoretical temperature differences between the screen and air temperature for airflow from displacement ventilation diffusers in different conditions to be between 0.2 and 2.4 °C. The smallest temperature differences and errors were calculated when using a low emissivity screen as the radiative exchange between the low emissity screen with the surroundings is minimized, compared to what would be with a high emissivity screen. Thus, our measurements are within the calculated range. However, good thermographic data analysis should always include the estimation of the error. The error in our study and in the study of Cehlin *et al* (2002) are compared next.

When using an IRT camera in the field, the magnitude of the error can increase significantly because of the error in estimating the parameters involved in the radiometric measurements and because a reference temperature is not usually included in the field of view. The accuracy of the camera is equal to the the sum of the partial errors of each parameter of the radiometry equation (Öhman 2001). The total accuracy on temperature measurement is calculated with:

$$\Delta T = \pm \sqrt{\left(\frac{\delta T_s}{\delta \varepsilon} \cdot \Delta \varepsilon\right)^2 + \left(\frac{\delta T_s}{\delta T_r} \cdot \Delta T_r\right)^2 + \left(\frac{\delta T_s}{\delta \tau} \cdot \Delta \tau\right)^2 + \left(\frac{\delta T_s}{\delta T_{amb}} \cdot \Delta T_{amb}\right)^2 + \left(\frac{\delta T_s}{\delta T_{tot}} \cdot \Delta T_{tot}\right)^2} \qquad (2)$$

where ε is the emissivity of the object; τ the transmissivity of the atmosphere; T_s, is the surface temperature [K]; T_r and T_{amb}, are the reflected temperature and ambient temperature [K]; and T_{tot}, the equivalent black body temperature of the total radiation that reaches the detector of the camera [K]. For the calculation of the actual error on temperature measurement, it was first assumed that there is no error in the calculation of transmittance of ambient air. The infrared camera automatically computes this transmittance by using the distance and the ambient temperature. This assumption was acceptable because the atmosphere transmittance was equal to unity for the distance and condition tested. An error of 0.2 was assumed for the emissivity. The error on ambient temperature was equal to the thermocouple error of 0.5°C. For the reflected temperature the error assumed was 5°C because of the non uniformity of the background. No reference emitter was used for the measurement.

Therefore using Equation 2, the accuracy for a non-blackbody in the conditions of this experiment has been estimated to be ±3.79°C. This error has to be taken into account when analyzing the results shown in Figure 3. Thus, the differences smaller to 1°C observed between air temperature measured using RTD and screen temperature measured using an IRT camera show a difference 1°C ±3.79°C.   This error is entirely the result of the use of the infrared camera.

In their calculation for the range of temperature difference to be expected between the screen and the air, Cehlin *et al* (2002) estimates the error of the calculation resulting from the expected errors of the measurements to be included in the energy balance calculation. The combined error estimated is ±1°C, for the theoretical difference between the screen and the air temperature calculated using an energy balance between the surroundings and the screen. This calculation includes an error of the surface temperature measurements of 0.3°C, which reflects infrared measurements done in controlled laboratory conditions. It seems that further investigation to more accurately reflects the error of in situ measurements is needed.

5. Conclusion

A method using an infrared camera and a target screen to measure air temperature has been adapted and tested for the study of temperature fields close to swirl diffusers in displacement ventilation conditions. Smoke tests have shown that the use of a porous screen allows for the airflow from a swirl diffuser to develop. However, certain disturbances have been qualitatively observed. The comparison with RTD and air temperature have shown that the air temperature is well estimated measuring the temperature of a porous screen: the differences smaller to 1°C between air temperature measured using thermocouples and screen temperature measured with an IRT camera. An energy balance would have to be used to precisely estimate the air temperature. The accuracy of the IRT camera measurement in field conditions would have to be taken into account in the estimation of the temperature and its accuracy.

The method has been applied successfully to visualize and take good measure temperature of air between bookshelves at the center of the building. However, in the offices at the periphery the arrangement of the office furniture and diffusers, prensece of windows and heating systems make it more challenging to visualize air flow at perimeter and take accurate measurements. Transient thermal events, such as the developpement of the air jet due to the opening of one diffuser damper, have been recorded successfully.

Further investigations on the effect of the porous screen on the airflow have to be carried out. CFD modeling validated with measurement in laboratory could be used. A parametric study on the effects of the conditions on the difference between the screen and air temperature has to be undertaken taking into account the error on the screen temperature measurement with the infrared camera. High resolution calculation of thermal comfort indicators, such as feet-to-head temperature difference, at different positions in the cross sections studied could be done for the different spaces studied based on the air temperature measurement obtained.

6. References

Hassani,Vahab A.; Stetz,Mark (1994) Application of infrared thermography to room air temperature measurements, *Proceedings of the ASHRAE Annual Meeting*, Vol 100 Issue 2., Orlando, FL, USA, p. 1238-1247.

Cehlin,M.; Moshfegh,B.; Sandberg, M. (2000) Visualization and measurment of air temperature using infrared thermography, *Proceedings of the ROOMVENT*, Vol.1, Oxford, p.339.347.

Cehlin,M.; Moshfegh,B.; Sandberg,M. (2002) Measurements of air temperatures close to a low-velocity diffuser in displacement ventilation using an infrared camera, *Energy and Buildings*, Vol 34. Issue 7, Amsterdam, p.687-698.

FLIR Systems. 2004. ThermaCAM S60 Operator's manual, Danderyd, 174 p.

FLIR Systems. 2003. ThermaCAM Researcher User's manual, Danderyd, 136 p.

Öhman, C. 2001. Measurement in Thermography, Danderyd, 119 p.

Distribution of carbon dioxide in a naturally ventilated room with high internal heat load

Simone Steiger, M. Eng.,
Dept. Indoor Environment and Climatic Impacts, Fraunhofer Institute for Building Physics, Germany;
simone.steiger@hoki.ibp.fraunhofer.de

Runa Tabea Hellwig, Dr. - Ing.,
Group Manager Indoor Environment, Dept. Indoor Environment and Climatic Impacts Fraunhofer Institute
for Building Physics, Germany;
runa.hellwig@hoki.ibp.fraunhofer.de

Elmar Junker, Professor,
Dept. for General Studies, University of Applied Sciences Rosenheim, Germany;
junker@fh-rosenheim.de

KEYWORDS: carbon dioxide, measurement points, natural ventilation, high occupant density, classroom.

SUMMARY:
The paper shows results of measuring the carbon dioxide distribution in a test room with natural ventilation and high occupant density. The test room represented one tier of a classroom with tiltable windows on one side. Dummies emitting heat and carbon dioxide simulated the pupils. The measurements of carbon dioxide were carried out at various places and heights to see the characteristics of carbon dioxide and indoor air flow and also to find possible measuring positions for carbon dioxide sensors to control indoor air quality.

The distribution of the carbon dioxide was influenced by several issues. First of all it depended on the disposal of carbon dioxide, second on the status of the window and at last on the heat emission of the dummies. With an open window and carbon dioxide emitted, the concentration of the gas varied in a wide range over the room. The highest concentrations were measured below the ceiling, the lowest above the floor, but there was not always a stable stratification. With the window closed and no carbon dioxide emitted, the concentration equaled over the room in a few minutes. When there was no thermal buoyancy at the dummies, more carbon dioxide emitted from the dummies dropped down to the floor because of its higher density.

Near the window as well as below the ceiling high fluctuations of the carbon dioxide concentration appeared. The measured values near the wall were also more stable than the values in the middle of the room but comparable to them. Therefore appropriate measuring points for classrooms could be at the wall at breathing height with an adequate distance from the windows. Higher measurement points at the wall, out of the students reach, could also be possible, but may show too high values. Measurement points near the floor and near the windows are inappropriate to estimate indoor air quality.

1. Introduction

In rooms with fluctuating or high occupancy over the day, like conference rooms or classrooms, there are often used demand controlled ventilation systems. In most cases there are used carbon dioxide sensors to estimate the air quality. Therefore it is necessary to know the characteristic of carbon dioxide and the indoor air flow of the chosen ventilation system to put the sensor at the right place. In our case natural ventilation was of interest.

Already in the 1850s Max von Pettenkofer had measured carbon dioxide to estimate air quality in naturally ventilated living rooms and hospitals and detected that the gas disperses equally over the room or accumulates rather at the ceiling than at the floor, although carbon dioxide is heavier than ambient air [von Pettenkofer M. (1858)]. This is obviously due to the fact that the carbon dioxide is mixed with the warm breathing air and turns upwards with it. Generally in most cases the density of a gas doesn't matter, if emission of gas is linked with emission of heat [Fitzner K. (2003)].

In the report of Annex 18 "Demand controlled ventilation systems" [Mansson L. (1993)] there are described two different tests about the dispersion pattern of carbon dioxide. Both tests were made in mechanically ventilated rooms with a low occupant density. The ventilation systems were mixing ventilation and displacement ventilation. With mixing ventilation distribution of carbon dioxide was nearly uniform over the room. Only above the dummies the concentration was higher. But when additionally the doors were opened, the differences of measured carbon dioxide grew up to 75%. The location of the highest concentration was depending on the temperature difference between room and corridor. With displacement ventilation the gas emitted near the dummies was directly carried to the upper mixed zone and was not mixed back in the lower zone. The concentration round the dummies was always lower than in the mixing zone, even when the interface was lower than the breathing zone. Therefore these tests showed that the dispersion pattern can be very different depending on the ventilation system or on large connections to surrounding spaces.

Similar results were found in another research [Mattsson M. (2003)], when carbon dioxide concentration was measured in real classrooms with usual occupant density. With mixing ventilation the differences in concentration over the height were negligible, although the values at 0.6 m were slightly lower than in 3.0 m. With displacement ventilation the concentration of carbon dioxide nearly doubled from 0.6 m to 2.1 m.

2. Methods

The test room (2.6 m x 5.6 m x 2.7 m) is situated on the south-east end of a single-storey building (FIG. 1). The room conforms to one tier of a typical classroom with 2.1 m² and 5.9 m³ for one pupil. For the tests only the left sash of the southward bottom hung window was opened and closed automatically. Below the tiltable window there is an electrical radiator, which is dimensioned like in a real classroom for a twofold air change rate. Because of the surrounding buildings very little direct sunlight shines through the window.
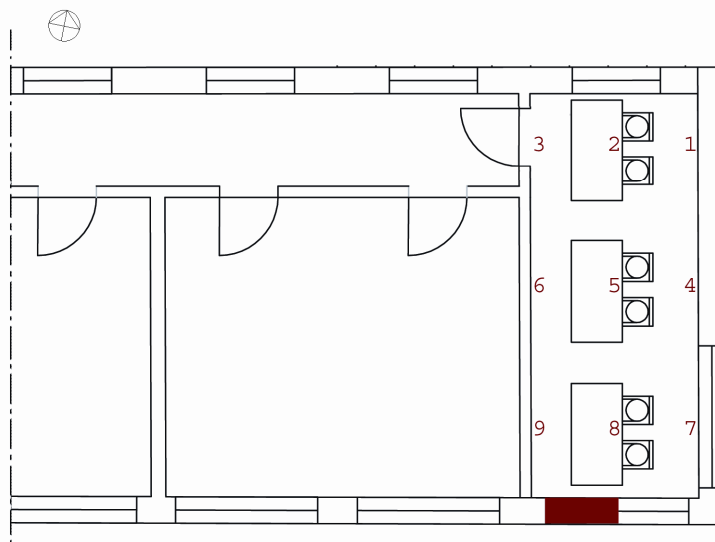

FIG. 1: Floor plan of the test room (without scale).

To simulate the heat loss from the persons there were used dummies. The heat emission of the dummies was accordant to a metabolic rate of 1.2 met. The dummies also emitted preheated carbon dioxide with a temperature from 28 to 30 °C. The amount of emitted carbon dioxide was set to 0.006 l/s per Dummy.

The concentration of carbon dioxide in the room was measured with a photo-acoustic multi-gas sensor. The instrument has six measuring channels to draw air from different points of the room with small tubes by turns. The sensor has a sampling rate of 250 s for each measuring point which results from the measuring procedure and the flushing times of the tubes. The concentration was measured in kg/m³ and then converted into ppm (parts per million). For the conversion it was used the molar volume of air at 20°C and the mathematical air pressure of 930 hPa (680 m height above sea level) for the measuring site. The difference to real air pressure was neglected.

Each measuring point is identified with a number, for its location in the room (FIG. 1), and with its height. Therefore the point 5_1.2 is at the location number 5 in a height of 1.2 m.

Most tests were carried out with the following test procedure or the iteration from parts of it (TABLE. 1).

TABLE. 1: Test procedure for measuring carbon dioxide.

phase	1	2	3	4	5
carbon dioxide	on	off	on	on	off
window	open	closed	closed	open	open
duration [h]	1.5	0.5	0.5	1.0	0.5

3. Results

The test procedure produced certain episodes of carbon dioxide concentration in the room as can be seen in FIG. 2 and FIG. 3. When the window is open in the phases 1, 4 und 5, the adjustments of carbon dioxide concentration to a balance concentration are clearly visible.
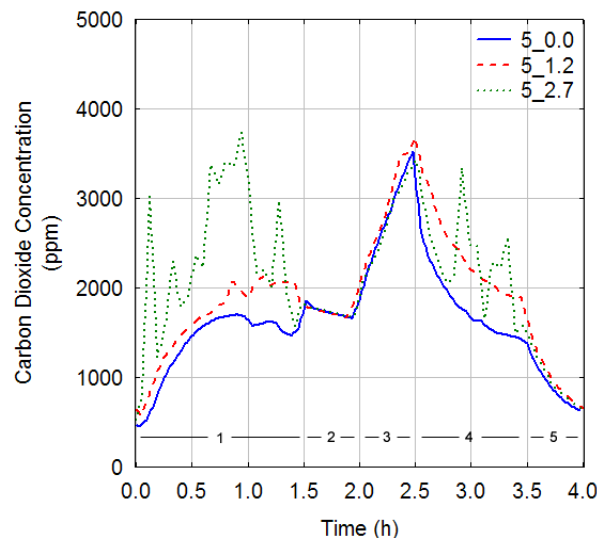

FIG. 2: Episodes of carbon dioxide concentration during the test procedure in a vertical axis (indentification of measuring points in chapter 2).
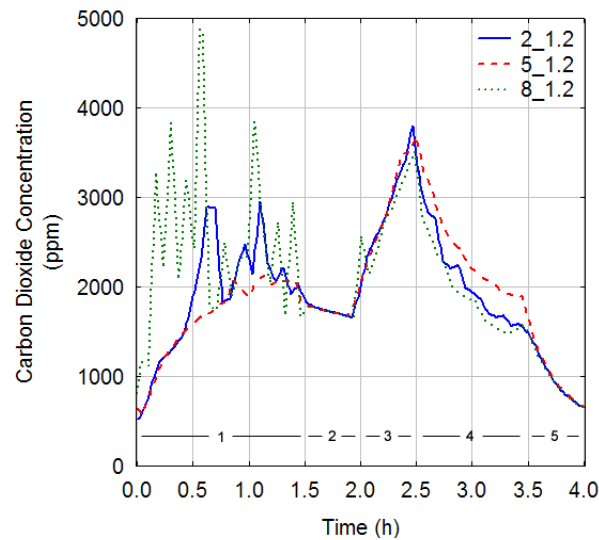
FIG. 3: Episodes of carbon dioxide concentration during the test procedure in a horizontal axis (indentification of measuring points in chapter 2).

But due to this sequence of actions it is not possible to compare different measurement points directly with the measured values, because the variations depending on the test procedure are bigger than the variations depending on location or time. Therefore the measured values are applied to a reference point to be evaluated (e.g. D6_2.7). As reference point was chosen the point 5_1.2 in the middle of the room. The shown values range from the 25. to the 75. percentile within the boxes, within the whiskers there are values without outliers and extreme values. Outliers are defined bigger than 1.5 times of the quartiles, extreme values bigger than 3 times of the quartiles.
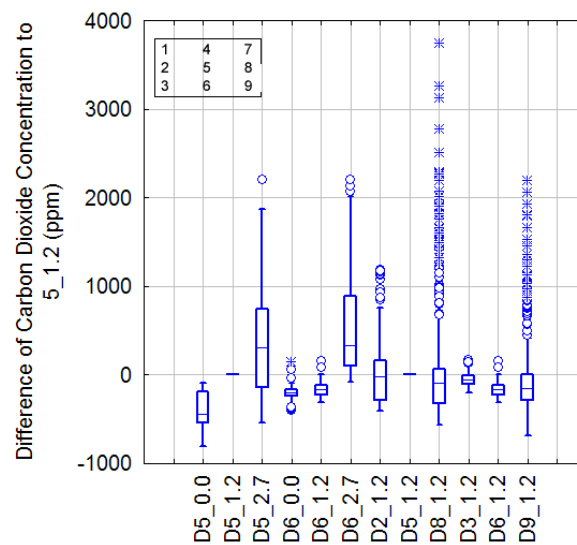

FIG. 4: Distribution of carbon dioxide concentration in the test phases 1 and 4.

The distribution of the carbon dioxide in the room was determined both from the status of the window (opened or closed) and the emission of carbon dioxide in the test procedure. With an open window and carbon dioxide emitted (FIG. 4 left), the concentration of the gas varied in a wide range over the room and it also varied over the time. Especially below the ceiling (D5_2.7 and D6_2.7) and near the opened window (D8_1.2 and D9_1.2) the variations of carbon dioxide distribution were rather high. The high fluctuation below the ceiling suggested the assumption that the low lintel of the window (about 0.4 m below the ceiling) inhibited a fully developed air flow in this zone. That's why further test runs were made with measuring positions at the height of the lintel. The tests showed much less fluctuations at this height than below the ceiling. Nevertheless in these phases the stratification from floor to ceiling was most apparent even when the stratification near the wall wasn't so much incisive.
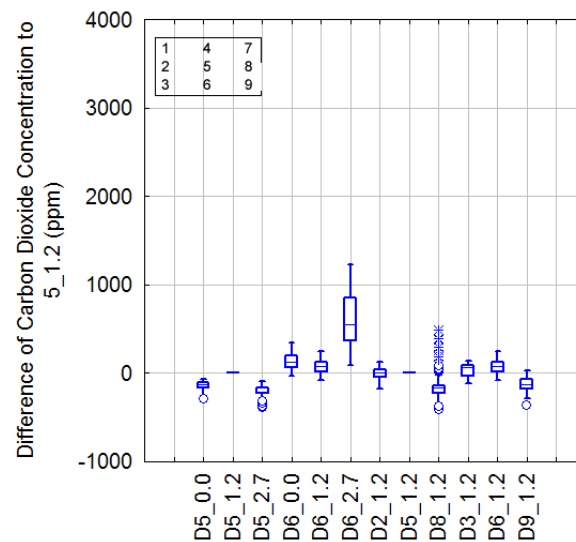

FIG. 5: Distribution of carbon dioxide concentration in the test phase 3.

With only carbon dioxide emitting and a closed window (FIG. 5) the variations over time decreased, but the variation over the room was still over 500 ppm (Median).
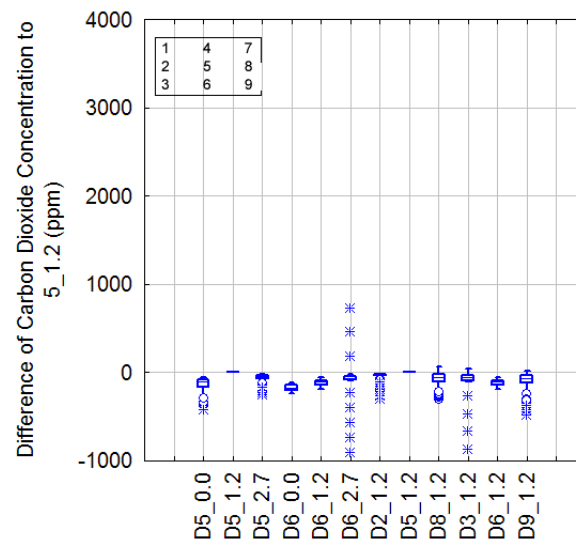

FIG. 6: Distribution of carbon dioxide concentration in the test phase 5.

In phase 5 (FIG. 6) the variations with time were negligible and the variation over the room was less than 100 ppm. The lowest values occurred on the floor. The effect occurs because of the airflow pattern of natural ventilation through a window during low temperatures outside, which is comparable to the airflow pattern of displacement ventilation, like it was also seen in [Mattsson M. (2003)].
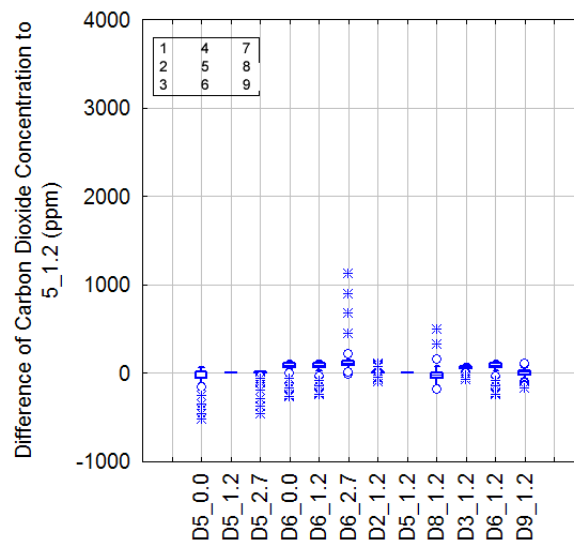

FIG. 7: Distribution of carbon dioxide concentration in the test phase 2.

When there is no gas emitted and no window open (FIG. 7), both variations with time and variations with height are less than in phase 5. Even when the phase before has great fluctuations, the concentrations at the different places equal in a minute or two.

All together in these test runs at the location 3_1.2 the measured values were most similar to the values in the middle of the room (5_1.2) and had the lowest fluctuations. Further tests were made at the points 1 and 4 (enough distance to the opened window) each at the heights 1.2 m and 2.3 m. These measurement points showed values very similar to the middle of the room with little fluctuations. Although the values in the height 2.3 m were located about 100 ppm higher than in 1.2 m.

Furthermore from these figures it can be seen that the carbon dioxide doesn't accumulate at the ground, although the density of the heated carbon dioxide (1.77 kg/m³) is still significant higher than the density of ambient air (1.20 kg/m³). It must be the buoyancy of warm ambient air at the heated dummies, which takes the emitted gas, which is used here only in small amounts, upwards. This effect is supported when the incoming cold air from the open window is powering the rotor of indoor air.
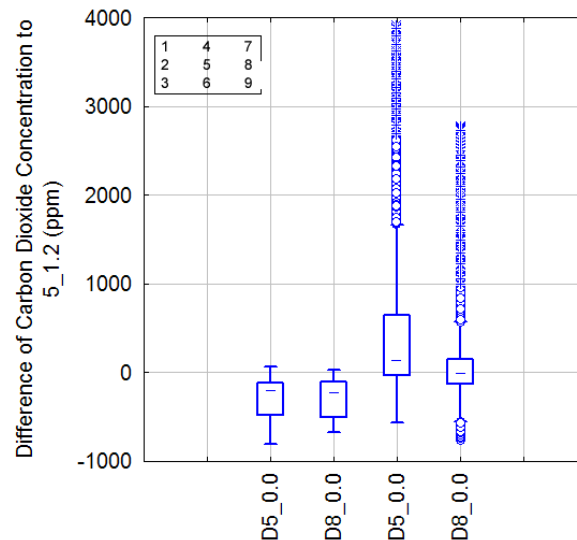
FIG. 8: Distribution of carbon dioxide concentration with and without heat emission from the dummies.

This assumption was affirmed by another test run without heat emission from the dummies. Then the measured values above the floor are visibly higher than with heat emission in phases 3 and 4 (FIG. 8). In addition there are extreme fluctuations of carbon dioxide concentration without heat emissions. These indicate an unstable flow of indoor air.

4. Discussion

The results found above can not be transferred one-to-one to real cases. There have to be considered a few limitations of the experimental setup:

- The carbon dioxide emitted from the dummies makes up only 4 % of the warm air naturally emitted from a real person and this is already mixed with the air when it comes out of the mouth. The exhalation air (1.18 kg/m³) is less dense than ambient air (1.20 kg/m³) and turns upwards without the buoyancy at the human body. This might enforce the stratification of carbon dioxide. The dummies are emitting carbon dioxide constantly, not like a real person, who is breathing in and out. And the emitting gas from dummies didn't have an impulse too, like a real exhalation. But these two points might be less important for the air flow;

- Another point, that has to be considered, is that dummies can't move. But real humans, especially pupils in classrooms might move in the room. This fact has certainly influence on the fluctuations of measured carbon dioxide in the middle of room, but probably less on carbon dioxide concentrations near the wall;

- The test room has nearly the same depth and the same height as a real classroom, but the width is only that of one tier (2.55 m). So the room is very narrow. Influences on the air flow, which always occur near walls, might here have affected the whole room. The detected similarity of values from the middle of the room and the wall could partly result from this fact. This will be improved in following tests, which will take place in two identical rooms with dimensions of a real classroom for 24 dummies per room.

5. Conclusions

The concentration of carbon dioxide is not uniformly distributed, at some times similar to displacement ventilation, like it was seen in a former research [Mattsson M. (2003)]. Therefore the positioning of the control sensor is essential. The distribution of carbon dioxide was influenced by disposal of carbon dioxide, the status of the window and heat emission of the dummies/persons. The greatest variations of measured values in the room appear with an open window and carbon dioxide emitted.

The measurements showed similar results than the measurements of mixing ventilation in the case of open doors in Annex 18 [Mansson L., (1993)]. The differences of gas concentration were very high over the room with open windows and there was not always a clear stratification. Although window ventilation is mostly compared with displacement ventilation in this case the contaminant gas was not carried up in the upper zone on the whole, it was also partly mixed back in the lower zone.

In Annex 18 there is suggested a sensor position in breathing height with distance to openings, air outlets, persons and the walls [Mansson L., (1993)].

According to this measurements appropriate sensor positions for rooms with natural ventilation could be at the wall at breathing height (or higher) with an adequate distance from windows or other openings. The results of the experiment gained in a narrow room situation will be verified in an experimental arrangement with classroom-like dimensions.

6. Acknowledgement

7. References

von Pettenkofer M. (1858). Über den Luftwechsel in Wohngebäuden, Munich Germany.

Fitzner K. (2003). Verteilung von Luftverunreinigungen und Temperaturen im Raum. *Lecture at the ‚Gesundheittechnische Gesellschaft e. V.'*, Hermann-Rietschel-Institut, TU Berlin Germany.

Mansson L., (1993). Demand controlled ventilation systems, *Annex 18* (Mansson L., editor), International Energy Agency, Stockholm Sweden, 17 – 39.

Mattsson M., Smedje G., Holmquist L., Vesterberg O., Walinder R. (2003). Mixing and displacement ventilation compared in classrooms; distribution of particles, cat allergen, and CO2. Proceedings of Healthy Buildings, Singapore.

Sensing and detoxification devices in public building spaces

Steen Traberg-Borup, senior researcher,
Department of Health and Comfort, Danish Building Research Institute, Aalborg University;
stb@sbi.dk

Lars B. Gunnarsen, senior researcher,
Department of Health and Comfort, Danish Building Research Institute, Aalborg University;
lbg@sbi.dk

Alireza Afshari, senior researcher,
Department of Health and Comfort, Danish Building Research Institute, Aalborg University;
ala@sbi.dk

KEYWORDS: Sensing and detoxification devices, toxic agent, public space, public security, ventilation.

SUMMARY:
This paper describes commonly used ventilation principles and where sensing and detoxification devices could be integrated in public buildings in an effort to warn and protect citizens against surprise attacks by toxic agents. The release of toxic agents may be outdoors, in a single indoor spot or their origin may be diffuse.

It is common to classify ventilation systems by their functions, distribution strategies, ventilation principles or a combination of them all. As this paper is meant as a guide to developers and manufacturers of sensing and detoxification devices, focus will be on ventilation principles and where to integrate these devices. Two principles will be discussed, namely the displacement principle and the mixed principle. These ventilation principles are widely used in public buildings. The differences in air distribution using the displacement or the mixed principle are discussed in three different scenarios.

The scenarios exemplified are: A very densely populated space (Theatres and Cinemas), A large airtight space with dominant air change by mechanical ventilation (Airport Terminal) and an Underground space (Subway or metro station).

For sensing and detoxification devices to be effective and preferably ahead of situation, this paper will point out strategic areas where to integrate these devices into the building space and in its immediate surroundings.

This work is part of WP3 in the NANOSECURE integrated project supported by the European Union's Sixth Framework Programme.

1. Introduction

For sensing and detoxification devices to be effective and preferably ahead of situation, this paper will point out typical ventilation principles used and strategic areas where to integrate sensing and detoxification devices into the building space and in its immediate surroundings. Examples of deployment of sensing devises may be in exhaust and inlet openings of ventilation systems, in openings as windows and doors and along conveyer belts. The paper will also list typical figures for ventilation rates, The following scenarios will be looked at: Very densely populated space (Cinemas and Theatres), Large airtight space with dominant air change by mechanical ventilation (Airport Terminal) and an Underground space (Subway or Metro station).

1.1 Classification of Ventilation systems

It is common to classify ventilation systems by their functions, distribution strategies, ventilation principles or by combinations of them all. This paper will not go into a discussion on functions or distribution strategies. Focus will be on ventilation principles. Within the mentioned distribution strategies two different principles are in use,

namely displacement airflow and mixed airflow. In both principles air can be distributed through the room as a constant air volume CAV or as a variable air volume VAV.

1.1.1 Displacement principle

With the displacement principle heat and pollution from people and equipment are transferred from the residence zone near the floor, up to the ceiling where it is evacuated through the outlet system. Make up air is supplied to the room within the residence zone at low speed. The displacement principle is illustrated in figure 1.

With displacement ventilation the outlet pollution concentration is higher than the pollution concentration in the residence zone. The ventilation efficiency can be higher than one.
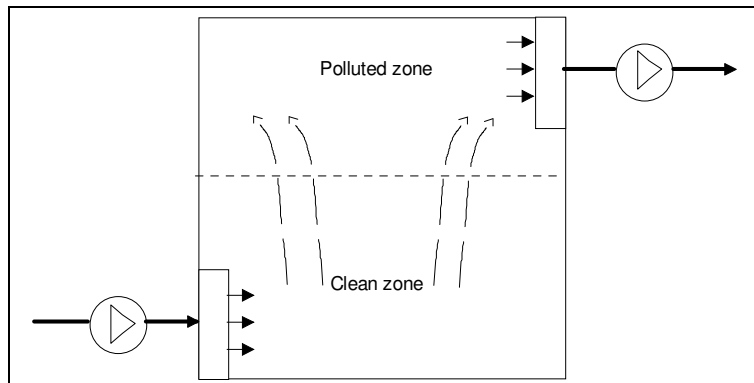

FIG. 1. Ventilation system using displacement principle.

1.1.2 Mixed principle

In a ventilation system utilising the mixed principle, make up air is supplied to the room above the residence zone at high speed. The mixed principle is illustrated in figure 2.

With mixed ventilation the outlet pollution concentration is close to the pollution concentration in the residential zone and the ventilation efficiency will approach to one.

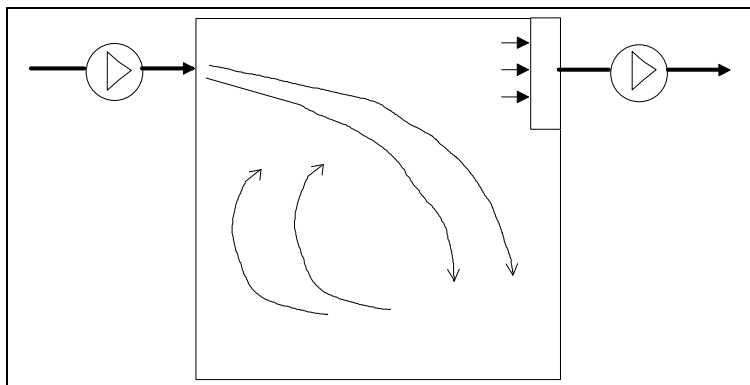*FIG. 2. Ventilation system using the mixed principle.*

1.1.3 Ventilation rates

When dimensioning a ventilation system the determining factor is the amount of air to be conditioned and distributed by the system. Fresh air is an important part of this air. The room air has to be exchanged several times per hour to clear the air from odours, dust and eventually toxic agents. The air exchange rate varies with a lot of

factors; the number of people present in the room, the desired comfort level, etc. Therefore it is not possible to state a specific air exchange rate. Various sources on designing HVAC systems will provide rules of thumb for air exchange rates. Commonly recommended air exchange rates (The Engineering ToolBox. 2005) are shown in table 1.

TABLE 1. Commonly recommended air exchange rates in some rooms and buildings.

Building/room	Air exchange rate n, [1/h]
Auditoriums, Cinemas, Theatres	8 - 15
Cocktail Lounges , Bars	20 - 30
Cafeterias	12 - 15
Department Stores, Malls, Supermarkets	4 - 10
Municipal Buildings	4 - 10
Restaurants	8 - 12

In many cases local regulations and building codes will govern the ventilation requirements.

Typically the fresh air supply to a room can be calculated as:

$Q = n\ V$ (1)

Where

Q = *fresh air supply [m³/h]*

n = *air exchange rate [1/h]*

V = *Volume of room [m³]*

As an example, the fresh air supply to a cinema/theatre with a volume of 2000 m³ and an air exchange rate of 10 can be calculated as:

$Q = 10[1/h]\ 2000\ [m^3]$

  $= 20000\ [m^3/h]$

2. Sensing and detoxification devices

In NANOSECURE, research laboratories and manufacturers are developing sensing and detoxification devices. The first prototypes are about to be tested in small scale.

In this project a sensing device is a device developed to be able to sense and recognise a specific toxic agent. This means, you have to use a different sensing device for every toxic agent you want to trace.

A detoxification device is a device able to decompose a specific toxic agent into non-toxic components. Again, this means you have to use a different detoxification device for every toxic agent you want to detoxify.

Right now it is not possible to have one device being able to sense or detoxify every known toxic agent. As mentioned, the first prototypes are about to be tested in the laboratory. Therefore it has not yet been possible to do a full-scale testing of the equipment. Nano-technology is used in the development of these devices, so the new sensing devices will be far more sensitive than similar known devices, if any. They will be able to react on quite small air samples, whereas detoxification devices have to be able to process really large air volumes to be effective in real life.

This could lead to a discussion on which device type to give the highest priority. Should it be the sensing or the detoxification device? For reasons of public safety, the sensing devices are most important. The newly developed sensing devices will be able to react very fast, which means that connected monitoring and alarm systems will be able to alert people immediately for evacuation. Detoxification devices on the other hand has to process thousands of cubic meters of air before a toxic contamination comes below a given threshold level.

How many different sensing devices to apply in a building is related both to how many different toxic agents you want to be able to detect and to how high the security level should be in the building.

In chapter 1 normally used ventilation principles were introduced. To be able to relate these principles to real life buildings, the following chapter will introduce three scenarios using different ventilation principles. Although describing typical ventilation systems and principles in scenarios without being specific on ventilation rates, air volumes processed etc., it could be important to developers and manufacturers to know, which systems and principles are used. Normally they don't deal with ventilation systems at all.

3. Scenarios

The following paragraphs show three target areas or scenarios, which could be of interest to terrorists, namely theatres and cinemas, airport terminals and subway stations. The gathering of many people is common to all of them and it is indoor spaces. In indoor spaces people are highly vulnerable to exposure from for example toxic agents as seen in the Tokyo Subway on March 20, 1995, where terrorists exposed innocent people to Sarin.

Focus will be on ventilation principles normally used in these places. A brief discussion on where to integrate sensing and detoxification devices into the building space and in its immediate surroundings will follow.

Not knowing the exact design of the buildings, their ventilation and security systems etc. makes it difficult to point out exact solutions on where to integrate sensing and detoxification devices and how many to use.

3.1 Theatres and Cinemas

Typically many people are gathered in theatres and cinemas for two or three hours during a performance. This makes it very important to be able to maintain a suitable indoor climate. Three ventilation principles will be shown.

3.1.1 Upwards ventilation principle

The upwards ventilation principle is shown in figure 3. This ventilation principle is widely used in large theatres and cinemas. Typically conditioned inlet air is coming from a plenum beneath the floor. The inlet air is then leaving the plenum through inlet openings in the floor or through integrated openings in the bottom of the chairs. Contaminated air is let out through openings in the ceiling.
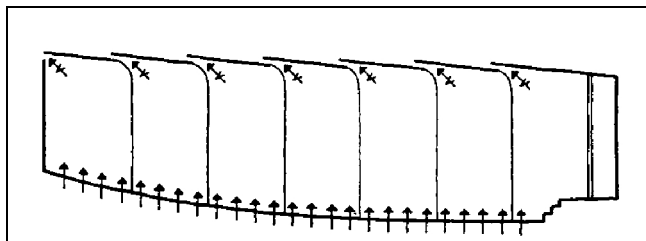
FIG. 3. Upwards ventilation principle used in theatres or cinemas.

3.1.2 Downwards ventilation principle

Different downwards ventilation principles are shown in figure 4. These ventilation principles are also widely used in large theatres and cinemas. Typically conditioned air is let into the room through openings or fans in the ceiling. Contaminated air is let out through openings in the floor or through openings integrated in the bottom of the chairs.
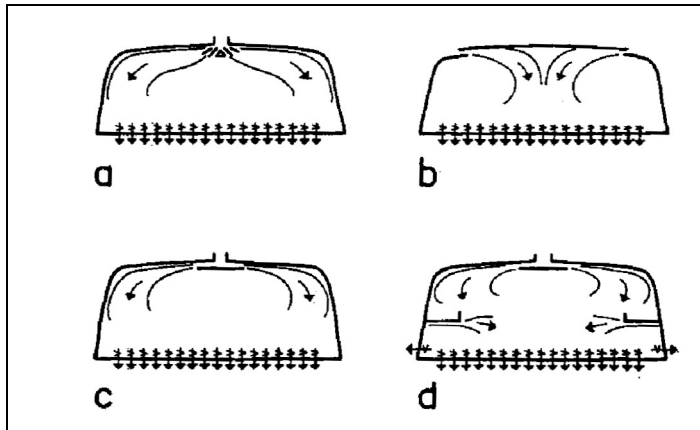
FIG. 4. Downwards ventilation principle used in theatres and cinemas.

3.1.3   Horizontal ventilation principle

The horizontal ventilation principle is shown in figure 5. Conditioned air is let into the room at high speed through jets. Hereby conditioned air is mixed with contaminated air. Mixed contaminated air is then let out through openings in for example a balcony or through openings in the back wall.
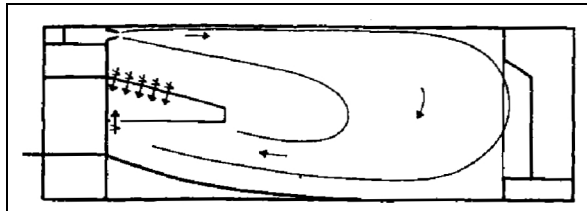

FIG. 5. Horizontal ventilation principle as used in theatres and cinemas.

3.2 Airport Terminal

Often people are queuing from the very moment they enter the terminal. In the first place they are queuing in front of the check-in counter and then at the security gate. Before boarding the flight, people may go to the shopping or waiting areas and finally they often have to wait at the gate before entering the flight. At peak hours all these areas, where people are gathered in long queues, are potential target areas, which could be of interest to terrorists (Edwards B. 2005).

Mostly airport terminals are very complex buildings often integrated with a subway station. This also makes ventilation systems very complex. Normally several sub-systems have to be used to maintain a suitable indoor climate for the staff at work and for the passengers. Airport terminal buildings can normally be characterised as long wide-spanned buildings with ceiling heights of maybe 20 – 25 m. To be able to maintain a suitable indoor climate in very large spaces, ventilation systems are to be considered global and local within the building site.

The global part of the ventilation system may consist of air diffusers that push conditioned air down toward floor level, as shown in figure 4a, b and c. Diffusers would normally be placed just beneath the ceiling. Contaminated air would then be returned through outlet openings placed in the floor, at columns or in the walls. A ventilation system with wall-mounted diffusers could also be used. Here diffusers would also push conditioned air down toward the floor. Contaminated air would be returned as before.

The local part of the ventilation system would typically be placed in a shopping area, behind ticketing desks, at service desks in cafeterias etc. Here conditioned low-velocity air would be supplied from outlet openings at floor level. Contaminated air would be returned through outlet openings in walls or ceilings.

As stated before, airport terminals normally are large open buildings. Therefore, to prevent toxic agents from spreading throughout the whole building, techniques used in fire fighting could be used. During a fire the building would normally be parted into airtight sections. Horizontal and vertical firewalls will isolate part of the

building until fire is under control (Cui E. and Chow W. K., 2001). Similar precautions could come into use if toxic agents were released in very large spaces.

3.3 Subway or Metro Station

Subway stations are typically crowded with people at rush hours. Besides the subway station the building also could have a shopping mall as seen in many places. Two, three or maybe four stories on top of each other often centered around an atria.

Without knowing the exact layout of the subway station, it is not possible to describe how a ventilation system should be designed and which ventilation principle to be used. Today, the complex design of a modern subway ventilation system would be carried out using computer simulation (Tabarra M., Abi-Zadeh D. and Saadokierski S., 2004). Figure 6 show the layout of a modern subway ventilation system. Abbreviations in figure 6 are; OTE duct *Over Train Exhaust duct*, UPE duct *Under Platform duct*.
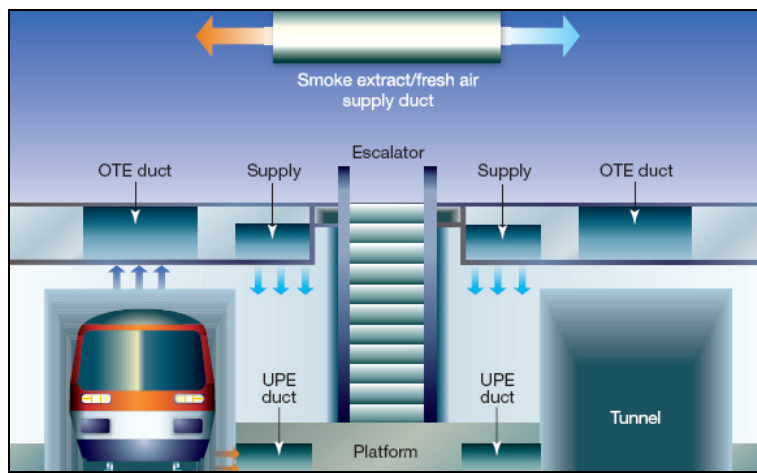

FIG. 6. Layout of modern subway ventilation system. Source: Arup (London).

4. Integrating sensing and detoxification devices

Until now the most common sensing devices integrated in ventilation systems are sensors for inlet and outlet air temperatures, humidity and CO_2. Temperature sensors are integrated in inlet and outlet openings. Humidity sensors could be integrated in the same openings or within the room itself. CO_2 sensors would be integrated in outlet openings. All these sensors are normally used for maintaining a suitable indoor climate.

How and where to integrate sensing and detoxification devices into building spaces as the ones described in the scenarios is not obvious. These sensors and devices are used strictly for preventive purposes, and the use of them is new.

Detoxification devices could be integrated as part of the central ventilation unit. This is where the very large air volumes are processed. In case of Subway and Metro stations and adjacent platforms and tunnels detoxification devices could be integrated locally.

To prevent people from carrying toxic agents into (public) buildings would of course be the best solution. But this is not always possible. Therefore sensing devices have to be integrated both into rooms and into ventilation systems. Most places will be common to all the scenarios, and some will be specific in relation to the purpose of the building. Obvious places to integrate sensing devices would be:

- In fresh air inlet openings

- In outlet openings

- Numerous places throughout entrance, lounge and check-in areas

- Numerous places throughout a theatre or cinema room near the floor

- Numerous places throughout platform areas near the floor in Subway and Metro stations

- Numerous places within security gate areas

- Throughout baggage handling systems, conveyer belts etc.

- In smoking areas, toilets and nursery rooms

- In front of ticket offices near the floor or at places nearby where people will put their bags or luggage

- Any other well-ventilated area within the building

- Inside-ventilated equipment such as vending machines for soft drinks, candies, popcorn etc

- Inside self-service check-in computers

- Inside self-service ticket machines

- In tunnel ducts adjacent to Subway and Metro stations

- In subway trains, specially around entrance areas

Some of the suggestions state that sensors have to be placed near the floor. The reason is, that some toxic agents, when in the gas phase, is heavier than air and therefore will sink to floor level when released. Then again some toxic agent will stick to for example clothing and other surfaces for a period. This means that, although sensors have detected a toxic agent and people are getting evacuated, the exposed surfaces (and peoples clothing) still are a source of contamination.

As mentioned before, until now none of these sensing and detoxification devices have been used in real life. Therefore the above mentioned places to integrate sensing devices have to be a "best guess".

5. Conclusion

For sensing and detoxification devices to be effective and preferably ahead of situation, this paper focuses on typical ventilation principles used and strategic areas where to integrate sensing and detoxification devices into the building space and in its immediate surroundings. Manufacturers of sensing and detoxification devices need to know where to integrate their devices into the ventilation systems and into the building space itself. This paper therefore outlines two commonly used ventilation principles, namely the displacement and the mixed principle. To maintain a certain comfort level in a room or space, it is necessary to know the air exchange rate and to know the amount of fresh air to supply. In table 1 a list of commonly recommended air exchange rates is shown. An example of calculating the amount of fresh air needed in a cinema/theatre is also shown.

The following scenarios are looked at:
- Very densely populated space (Cinemas and theatres)

- Large airtight space with dominant air change by mechanical ventilation (airport terminal)

- Under-ground space (Subway or Metro station)

Ventilation principles for the scenarios are looked at. Obvious places to integrate sensing and detoxification devices are also looked at. Due to the complexity of the buildings in the scenarios and the complexity of the ventilation systems, only the most obvious solutions are suggested.

Prevention of attacks with toxic gases is still a new discipline. An obvious way to find preventive solutions would be the use of computer simulations. In recent years these techniques have been widely used for simulating fire hazards. Simulating an attack with toxic gases is not the same as simulating a fire, producing heavy heat and smoke loads on the environment. Research on how and where contaminated air moves in a densely populated space and knowing how various toxic gases blends with air, water and surfaces are still to be carried out.

6. References

Cui E. and Chow W. K. (2001). Numerical studies on smoke filling process in an airport terminal, *Journal of Architectual Engineering*, September 2001

Edwards B. (2005). The Modern Airport Terminal, New approaches to airport architecture, *Taylor & Francis*

Facts about Sarin, (2005). Centers for Disease Control and Prevention, CDC, http://www.bt.cdc.gov/agent/sarin/basics/facts.asp (Accessed 2008-01-31)

Tabarra M., Abi-Zadeh D. and Saadokierski S. (2004). Design of a modern subway ventilation system, http://www.arup.com/_assets/_download/download265.pdf (Accessed 2008-31-01)

The Engineering ToolBox. (2005). Air Change Rates in some typical Rooms and Buildings, http://www.engineeringtoolbox.com/air-change-rate-room-d_867.html (Accessed 2008-01-31)

Experimental Setup and Initial Results of Moisture Transport through Horizontal Openings

Sergio Vera, Ph.D. Candidate,
Department of Building, Civil and Environmental Engineering,
Concordia University, Montreal, Canada
svera@ing.puc.cl

Paul Fazio, Professor,
Building Envelope Performance Laboratory, Centre for Building Studies,
Department of Building, Civil and Environmental Engineering,
Concordia University, Montreal, Canada
fazio@alcor.concordia.ca   http://www.bcee.concordia.ca/index.php/Dr._P._Fazio

Jiwu Rao, Senior Researcher,
Department of Building, Civil and Environmental Engineering,
Concordia University, Montreal, Canada
raojw@alcor.concordia.ca

KEYWORDS: *moisture transport, horizontal opening, full-scale test.*

SUMMARY:
Horizontal openings in dwellings, such as staircases, provide large paths for air and moisture transport between floors. They play an important role in the moisture transport from a moisture-source room to the rest of the house. The phenomenon, however, has been barely studied. The objective of this research is to study the moisture transport through a horizontal opening under different ventilation strategies, temperature differences between the upper and lower room, and locations of the moisture source. This paper presents the experimental setup and initial results.

The study was carried out in a full-scale test-hut composed of two rooms connected by a large horizontal opening measuring 1.19m × 0.91m and 0.22m thick. The inner dimensions of each room are 3.62m × 2.44m × 2.43m. Moisture was generated for 10 hours at known rates between 106 and 113 g/h followed by 14 hours without moisture generation. Two ventilation strategies were studied, downward net flow through the opening and independent ventilation in each room. Also, temperature difference between the two rooms ranged from -3.5ºK to 2.7ºK.

Comparison among the different cases is based on the averaged values for maximum, average and minimum humidity ratio in each room that reached steady-state values at the end of the moisture generation period. Humidity ratios are calculated based on the relative humidity and temperature measurements across the two rooms.

The main results show that moisture exchange between the two rooms starts when the moisture generation begins and two-way airflow exists through the opening. A colder upper room promotes moisture and air exchange between the two rooms. Ventilation strategy and temperature difference between the two rooms also influence the humidity level in each room.

1. Introduction

In most dwellings, indoor relative humidity (RH) is not directly controlled and it can fluctuate significantly outside the acceptable range of 30% to 70% according to ASHRAE (2005). For instance, in highly airtight dwellings with low ventilation rate and high occupancy, the RH can increase above 90%. In contrast, combined low outdoor humidity and overheating in winter season can decrease RH to as low as 20% or less in cold climates. Several studies have found that indoor RH can significantly influence the thermal comfort (Berglund and Cunningham, 1986; Toftum et al, 1998), indoor air quality and occupants' health (Bornehag et al, 2001,

2004; Davies et al, 2004), building durability (Merrill and TenWolde, 1989), and energy consumption (Simonson, 2000; Osanyintola and Simonson, 2006).

There are several factors that can significantly influence the indoor humidity level within a space: moisture produced by occupant's activities, moisture exchange with the exterior by ventilation and/or infiltration, moisture buffering of building materials and furnishing, heat and moisture transfer through the envelopes, and finally, moisture exchange between connected zones through large openings. The influence of most of these factors on indoor humidity level have been and are being studied extensively by means of experimental work and implemented into simulation tools such as WUFI+ (Holm et al, 2003), BSim (Rode and Grau, 2003) and PowerDomus (Mendes et al, 2003).

In contrast, the moisture exchange through large openings, such as doorways and staircases, has received little attention. In terms of inter-zonal moisture transport through vertical openings, El Diasty et al (1993) found that pressure differences between connected zones induced by air leakage and temperature differences help promoting the moisture transport through doorways; otherwise, diffusion plays a negligible role in this phenomenon. Oldengarm and de Gids (1991) and Woloszyn (1999) carried out field tests and found that moisture buffering restricts inter-zonal moisture transport. However, these two tests were performed for a very short moisture production period and with no significant pressure differences among zones.

On the other hand, comprehensive studies on the inter-zonal moisture transport through horizontal openings are yet to be carried out. Understanding the moisture transport through large horizontal openings, such as staircases, is essential to predict the humidity level in all zones of dwellings.

2. Mass transport through horizontal openings

Horizontal openings in buildings (i.e. staircases and ventilation shafts) provide large pathways between connected floors, and they play an important role in the transport of heat, pollutants, and moisture between floors and across the building. Experimental studies have been carried out to investigate buoyancy-driven flows (Kohal, 1995; Blomqvist and Sandberg, 2004), where opposite and equal airflows occurs, resulting in a zero net flow through the opening (Figure 1a). For example, Kohal (1995) studied the airflow through a large horizontal opening (1.3m x 1.3m x 0.3m) using the tracer gas technique, which was driven only by the temperature difference between the upper and lower rooms. This research determined the discharge coefficient of the opening and a simple relationship between the mass flow and temperature difference between the two rooms.

On the other hand, Klobut and Siréns (1994) carried out a unique study of mass flow through large horizontal openings due to temperature differences from -2ºK to 3ºK (temperature difference is positive when the upper room is warmer than the lower room) and net flow from 0.152 to 0.907 l/s. Two different opening sizes were studied, 0.455m × 0.455m x 0.05m and 0.64m x 0.64m x 0.05m. Based on the steady-state gas concentration in the upper and lower rooms, and the mass balance for the air and the gas in each compartment, the upward (Q_{21}) and downward (Q_{12}) volumetric flow rates were estimated.

Klobut and Siréns (1994) found that counter-current flow exists (Q_{21} in Figure 1b). They found that the mass exchange between both rooms is influenced by the temperature difference between the two rooms, the size of the
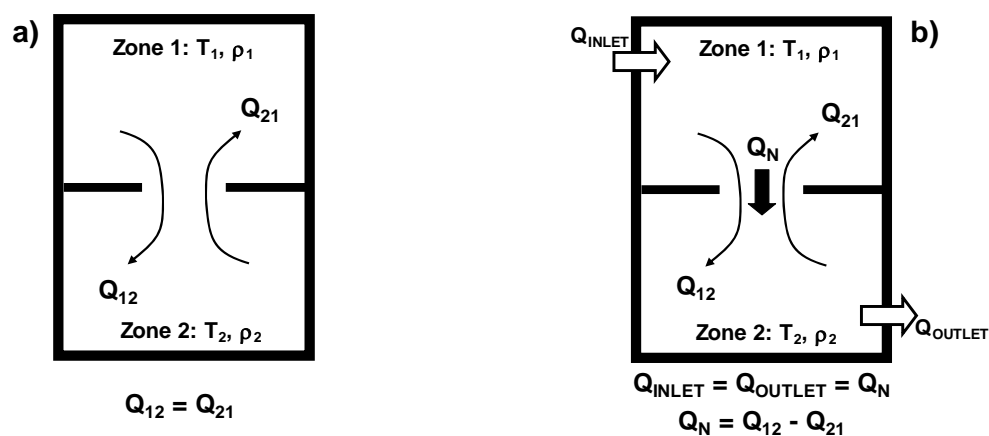

FIG. 1: a) Buoyancy-driven flow. b) Combined forced and buoyancy-driven flows.

opening and the direction and magnitude of the net flow. The main limitation of this study is the small scale of the experiment, which can influence significantly the airflow pattern, and hence the mass transport between the compartments.

In conclusion, there is no research about the inter-zonal moisture transport through horizontal openings. For that reason, the aim of this research is to study the influence of temperature differences between the upper and lower rooms, ventilation strategies, and moisture source locations on the moisture transport through a horizontal opening. In this paper the experimental setup and initial results are presented.

3. Experimental setup

3.1 Test conditions and tested cases

A full scale two-story test-hut was built inside the Environmental Chamber at Concordia University. Figure 2 shows a schematic drawing of the test-hut and the wall cross section, which represents the typical wood-framed construction of Canadian houses. The interior surfaces of the east and west walls were covered with polyethylene (0.15 mm thickness) and the rest of surfaces were covered with aluminum sheets (0.8 mm thickness) to avoid moisture buffering effects. A heater (1,000 W) was located at the bottom part of the door in each room and was controlled by a thermostat (with a proportional 0-100% capacity control) to provide the desired indoor temperature. This paper presents the main components of the experimental setup for two-room tests. More details of the experimental setup can be found in Fazio et al (2008).
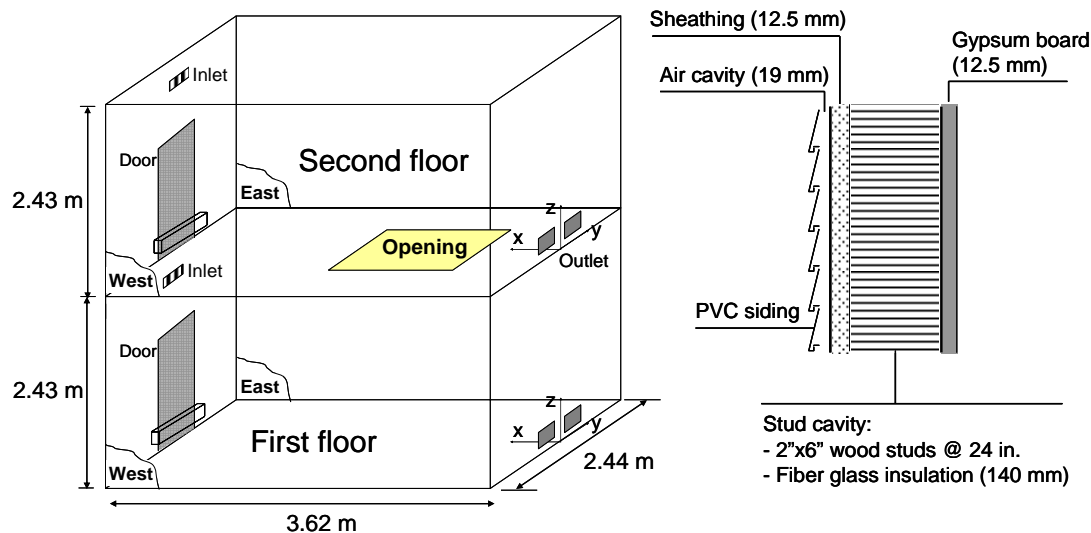

FIG. 2: Schematic drawings of two-story test-hut and wall cross section.

A horizontal opening of 1.19m x 0.91m and 0.22m thick, which tried to simulate the staircase openings, connected the two rooms, and allowed heat, air and moisture exchange between the upper and lower rooms. Figure 3 shows the location of the opening.

The main tested conditions are presented below. Table 1 summarizes the cases that are analyzed in this paper:

Outdoor conditions: -4.7±0.2ºC and 68±4%RH

Inlet condition: 18ºC and 38%RH

Air change rate: 0.5 and 0.75 h^{-1}

Moisture generation: Moisture was generated for 10 hours followed by 14 hours without moisture production.

Ventilation strategy and moisture source location: two different ventilation strategies were tested, forced downward net flow through the opening (II and III in Figure 4) and independent ventilation in both rooms (IV in Figure 4). The moisture source was placed in the first floor or second floor in the location shown in Figure 3.

The combinations of ventilation strategies and moisture-source locations presented in this paper are shown in Figure 4.

Temperature difference: it corresponds to the difference between the average temperature in the first and second floors during the moisture generation period. The temperature difference between the two rooms ranged from about 2.7ºK to -3.5ºK. The temperature difference is positive when the upper room is warmer than the lower room, whereas it is negative when the lower room is warmer than the upper room. The temperature difference was provided by changing the thermostat setpoint in each room. In some cases the heater in the upper floor was turned off to provide a much colder upper room.
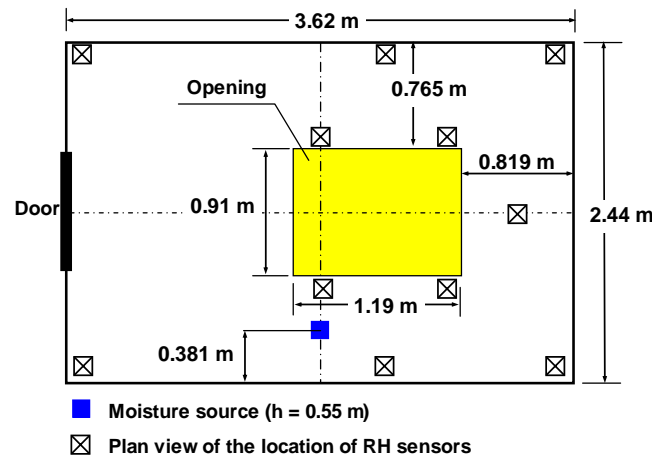

■ Moisture source (h = 0.55 m)

⊠ Plan view of the location of RH sensors

FIG. 3: Location and dimensions of the opening.

TABLE 1: Summary of cases analyzed in this paper.

Ventilation strategy and moisture source location	Air change rate (h^{-1})	Moisture generation (g/h)	Temperature difference[1] between the two rooms (ºK)
II	0.50	109.00	+0.7
		N.I.[2]	-0.2
			-1.6
			-2.7
			-3.5
	0.75	108.59	+1.3
		108.44	+0.4
		108.66	-2.5
III	0.50	112.88	+1.8
		112.00	-1.6
IV	0.50	106.53	+2.7
		106.29	+0.8
		109.63	-0.2
		109.35	-1.5
Notes:[1] Temperature differences shown are approximated values.[2] A problem with the load cell monitoring occurred. The moisture generation rates for the test before and the test after this problem were 109.00 and 109.35 g/h, respectively.			

3.2 Monitoring of indoor relative humidity and temperature

The indoor RH and temperature were monitored by means of thirty-two RH sensors (Vaisala Humitter 50Y and HMP50) placed across each room. Figure 3 shows the plane view with the schematic locations of RH sensors, which were installed at different heights, such as 0.1, 1.13, 1.8 and 2.24 m. RH probes were calibrated before the test to 2%RH accuracy. Calibration was performed using the RH calibration chamber with a 0.6% chilled mirror RH sensor and more than 20 data points for each probe.
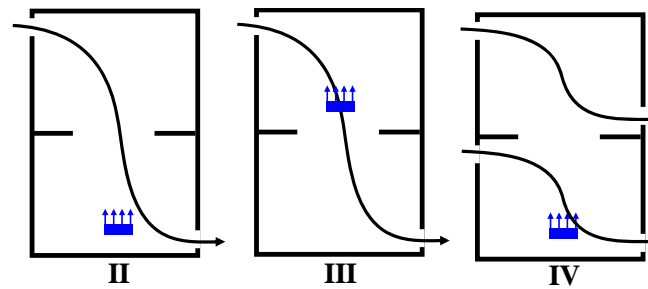
FIG. 4: Combination of ventilation strategies and moisture source locations.

4. Initial results and analyses

4.1 Methodology for comparing different cases

Humidity ratio (HR) was calculated for each RH probe across the room for 24 hours. Then, the maximum, average and minimum HR curves in each room were obtained from the 32 sensor locations as plotted in Figure 5 for ventilation strategy and moisture source location II at 0.5 ach and temperature difference of 0.7ºK. Comparison among different cases based on these curves is difficult; therefore, a simpler method is used. Since the HR (maximum, average and minimum) is steady-state at the end of the moisture generation period, average values for the maximum, average an minimum HR in each room are calculated and used to compare the influence of temperature differences, ventilation strategies and locations of the moisture source on the humidity level.
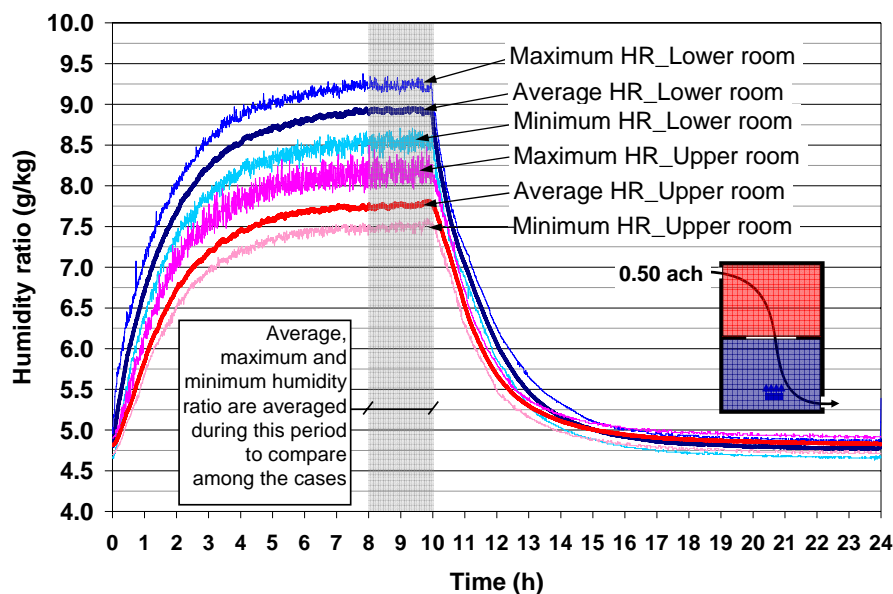

FIG. 5: Maximum, average and minimum humidity ratio curves for II, 0.5 ach and 0.7ºK.

4.2 General results

Figure 5 shows that the HR values in both rooms increase immediately after the moisture generation starts, which indicates that water vapor moves fast from the lower room to the upper room. The existence of upward water vapor flow through the opening confirms the existence of two-ways airflows through the opening. Similar results were found by Klobut and Siréns (1994).

Also, it can be seen that the HR variation across each room is about 0.6 g/kg, which indicates that non-uniform air and water vapor distribution exists across the rooms, thus air is not well mixed.

4.3 Influence of temperature difference

Figure 6 shows the influence of temperature differences between the two rooms on the average HR for each room at different ventilation rates, ventilation strategies and locations of the moisture source. The bar shows the range between the maximum and minimum HR found in each room. It can be observed that in all cases, higher HR differences between the two rooms occur when the upper room is warmer than the lower room, whereas closer HRs are found when the upper room is colder than the lower room. For instance, cases with downward net flow at 0.75 ach (Figure 6b) show that the average HR difference between the two rooms is 1.52 g/kg at 1.3ºK, while the difference is 0.46 g/kg at -2.5ºK.

These results show that colder upper room strongly promotes the warmer and moist air in the first floor to go up by buoyancy forces, and helps the air and moisture exchange between both rooms. As a consequence, in these cases, HR in the upper room is significantly influenced by the temperature difference between the two rooms; however, HR in the lower room stays more stable among temperature differences.

Water vapor transport and air movement through the opening are also found for cases with a warmer upper room for all the ventilation strategies. In these cases, the upward air movement is not attributed to the temperature difference between the two rooms. However, warm air currents in the rooms caused by the baseboard heaters and hotplate and cold air movement from the air supply at inlets and air leakage may be the cause for the observed air movement and vapor transport through the opening. Further analyses are required to study this phenomenon.
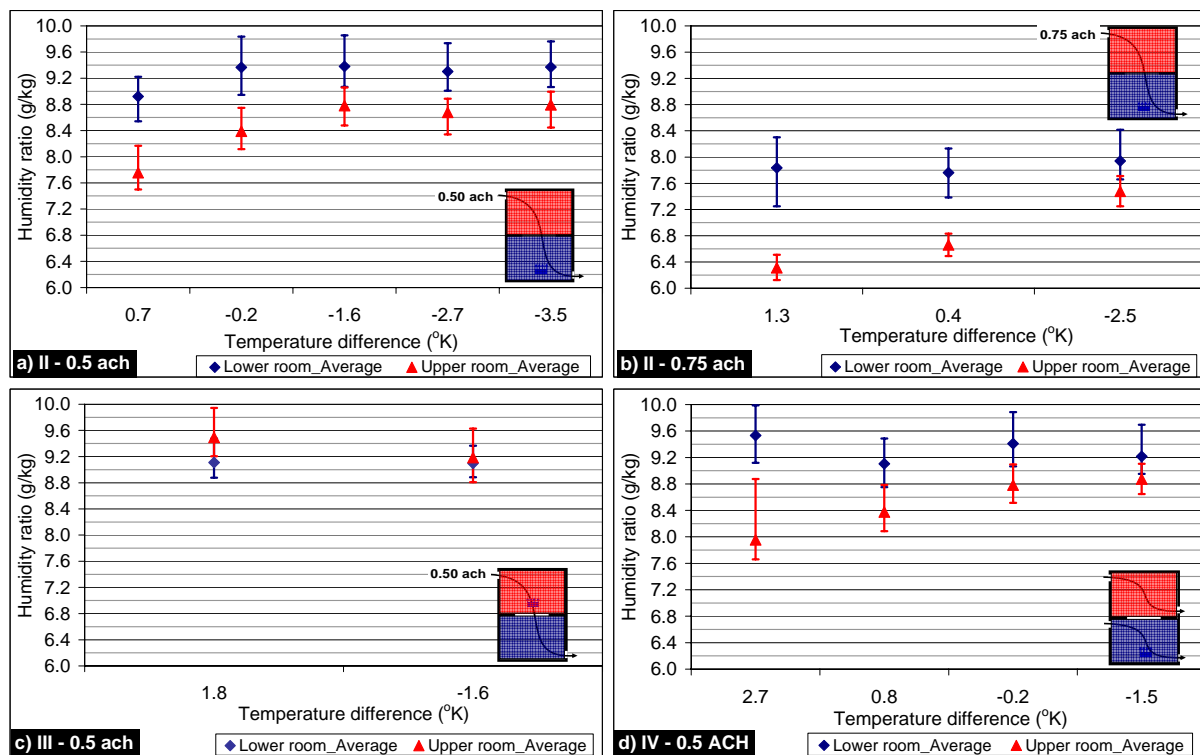

FIG. 6: HR range and average HR at different ventilation rates and strategies, location of moisture source and temperature differences.

4.4 Influence of ventilation strategy

The average HR in the lower and upper rooms at several temperature differences for II and IV at 0.5 ach are compared in Figure 7. HR differences between the lower and upper floors are smaller for independent ventilation in both rooms (IV) at any temperature difference. This means that this ventilation strategy helps mixing air and moisture between the two rooms because of the absence of downward net flow through the opening. Also, it can be seen that the influence of ventilation strategy in the average HR of each room is much less at negative temperature differences. For example, average HR of II and IV at -1.6ºK/-1.5ºK shows negligible difference between the lower and upper rooms (0.16 and 0.09 g/kg for II and IV, respectively).

4.5 Influence of moisture source location

Figures 6a and 6c show the results when the moisture source is placed in the lower and upper floors, respectively, for downward net flow. It can be seen that higher humidity occurs in the room where moisture source is placed, and much less HR difference exists between the two rooms when the moisture source is placed in the upper floor.
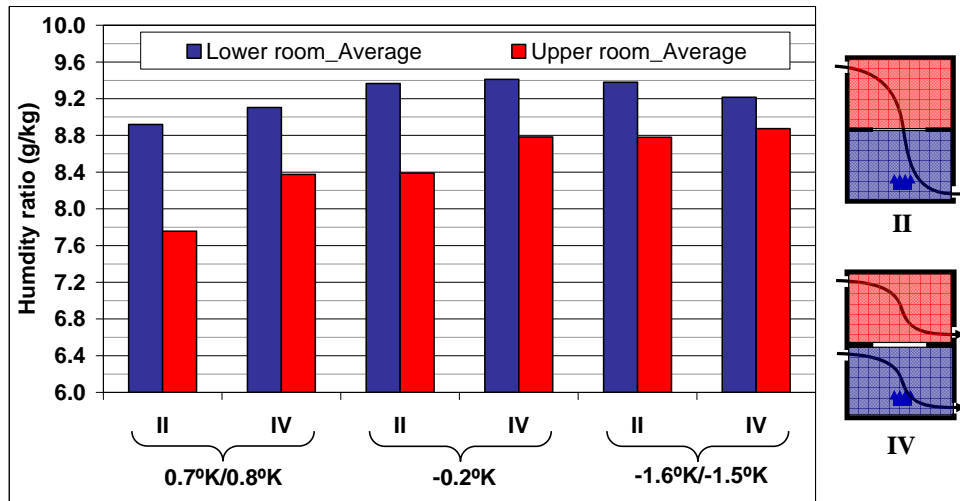

FIG. 7: Comparison of HR values in two rooms under different ventilation strategies and temperature differences.

5. Conclusions

The aim of this paper was to present initial results on an experimental study of the moisture transport through a horizontal opening under different ventilation strategies, temperature differences between the upper and lower rooms, and locations of the moisture source. The following conclusions can be drawn from the preliminary analyses of the experimental results:

- Moisture exchange between the two rooms is strongly linked to the temperature difference between the two rooms. Buoyancy-driven airflows transport moisture from the first floor to the second floor when the upper room is colder, while warm air currents from the heater and hotplate, and cold air currents from the air supply and air leakage may cause upward moisture flows when the upper room is warmer.

- Even with combined downward net flow and warmer upper room, two-way airflows still exist through the opening.

- Ventilation strategy and temperature difference between the two rooms have a strong impact on the humidity level in the upper room when the moisture source is located in the lower floor.

Further analyses are needed to quantitatively estimate the interzonal airflows and vapor transports through the horizontal openings. The Computational Fluid Dynamic (CFD) application can be employed to complement the experimental results.

6. Acknowledgement

7. References

ASHRAE (2005) Handbook fundamentals. American Society of Heating, Refrigerating and Air-Conditioning, Atlanta.

Berglund L.G. and Cunningham D.J. (1986) Parameters of human discomfort in warm environments. *ASHRAE Transactions*, Vol. 92, Part B, 732-746.

Blomqvist C. and Sandberg M. (2004) Air movements through horizontal openings in buildings – A model study. *International Journal of Ventilation*, Vol. 3, No. 1, 1-10.

Bornehag C.G., Blomquist G., Gyntelberg F., Järvholm B., Malmberg P., Nordvall L., Nielsen A., Pershagen G. and Sundell J. (2001) Dampness in building and health. *Indoor Air*, Vol. 11, No 2, 78-86.

Bornehag C.G., Sundell J., Bonini S., Custovic A., Malmberg P., Skerfving P., Sigsgaard T. and Verhoeff A. (2004) Dampness in building as a risk factor for health effect. *Indoor Air*, Vol. 14, No 4, 243-257.

Davies M., Ucci M., McCarthy M., Oreszczyn T., Ridley I., Mumovic D., Singh J. and Pretlove S. (2004) A Review of evidence linking ventilation rates in dwellings and respiratory health - A focus on house dust mites and mould. *International Journal of Ventilation*, Vol. 3, No 2, 155-168.

El Diasty R., Fazio P. and Budaiwi I. (1993) The dynamic modelling of air humidty behaviour in multi-zone space. *Building and Environment*, Vol. 28, No. 1, 33-51.

Fazio P., Vera S., Rao J., Yang X. and Ge H. (2008) Datasets of whole-building HAM and indoor conditions for single room and two-room experimental setups. Submitted to Annex 41 of the International Energy Agency. Building Envelope Performance Laboratory, Centre for Building Studies, Department of Building, Civil and Environmental Engineering, Concordia University, Montreal, Canada.

Holm A., Kuenzel H.M. and Sedlbauer K. (2003) The hygrothermal behaviour of rooms: combining thermal building simulation and hygrothermal envelope calculations. *Eight International IBPSA Conference*, Eindhoven, Netherlands, 499-505.

Kohal, J. S. (1995) Airflow through horizontal openings. Ph.D. Thesis. University of Nottingham. Institute of Building Technology.

Klobut, K. and Siréns K. (1994) Experimental investigation of air flows through large openings in a horizontal partition. Report B35. Helsinki University of Technology. Laboratory of Heating, Ventilating and Air-Conditioning.

Mendes N., Oliveira C.L.F. and dos Santos G.H. (2003) DOMUS 2.0: A whole-building hygrothermal simulation program. *Eight International IBPSA Conference, Eindhoven*, Netherlands, 863-870.

Merrill J.L. and TenWolde A. (1989) Overview of moisture-related damage in one group of Wisconsin manufactured homes. *ASHRAE Transactions*, Vol. 95, Part 1, 405-414.

Oldengarm J. and de Gids W. F. (1991) Field experiments on airborne moisture transport. *Air Infiltration Review*, Vol. 12, No 2, 8-11.

Osanyintola O.F. and Simonson C.J. (2006) Moisture buffering capacity of hygroscopic building materials: experimental facilities and energy impact. *Energy and Buildings*, No. 38, 1270-1282.

Rode C. and Grau K. (2003) Whole building hygrothermal simulation model. *ASHRAE Transactions*, Vol. 109, Part 1, 572-582.

Simonson C.J. (2000) Moisture, thermal and ventilation performance of Tapanila ecological house. *VTT Research Notes*, Technical Research Centre of Finland. ESPOO.

Toftum J., Jorgensen A.S. and Fanger P.O. (1998) Upper limits of air humidity for preventing warm respiratory discomfort. *Energy and Buildings*, Vol. 28, 15-23.

Woloszyn M. (1999) Modelisation hygro-thermo-aeraulique des batiments multizones: Porposition d'une strategie de resolution du systeme couple. *Ph.D. Thesis*, INSA-CETHIL, Lyon, France.

Stochastic versus deterministic approach to threshold criteria for building/environment system performance

Krystyna Pietrzyk, Ph.D.,
Affiliation; Built Environment and Sustainable Development, School of Architecture, Chalmers University of Technology, Gothenburg, Sweden;
krystyna.pietrzyk@chalmers.se http://www.chalmers.se/

KEYWORDS: *building performance, probabilistic, reliability, load-resistance model, air change rate.*

SUMMARY:

Stochastic versus deterministic approach to threshold values as performance criteria for building/environment system is discussed in the paper. Methodology for specification of threshold characteristics as random variables is discussed.

An example of calculation of the reliability of air exchange performance assuming first deterministic, and then stochastic performance criteria is carried out. The results obtained using these two approaches are analysed. The types of additional information that can be built in a model and its influence on performance evaluation are concluded.

1. Introduction

Building performance depends on the structure and the way that it is used, but also on the environmental conditions of the site and the microclimate in a vicinity of structure, which is influenced by the building itself. It supports the idea to use the concept of building/environment system performance.

Probabilistic model for evaluation of building/environment system performance based on load-resistance (demand-capacity) model (Kottegoda 1997) is referred to in this paper. It gives opportunity to take into account a random character of system load and also random character of system capacity expressed in the form of performance criteria stated for human health, human comfort, to meet economic standards or in order to prioritise the sustainable solutions.

In the field of building physics, mostly deterministic performance criteria have been included in the probabilistic reliability models (Pietrzyk et all 2004, Pietrzyk 2005, Pietrzyk & Hagentoft 2008 b). The needs of using the stochastic thresholds for the moisture conditions of materials against mould growth have been expressed in (Nevander & Elmarsson 1991).

Taking into account random character of the performance criterion one can come closer to the reality. It is obvious that the assumption that a failure is detected as soon as the threshold is crossed or that is not detected when the threshold is not crossed is not the proper one for most of the building physics applications. In this paper stochastic threshold in reliability applications is discussed. Stochastic performance criterion for air change rate has been implemented in the model of reliability analysis of air exchange in a building. The examples calculated with this model are presented and discussed. The type of additional information that can be built into a model and its influence on the performance evaluation are concluded.

2. Performance modelling

Building/environment system failure (unacceptable performance) can threaten its serviceability, safety, durability, and compatibility. It appears in the form of: damage of the materials, unhealthy conditions, discomfort, excessive energy use, and environmental damage. To prevent failure events prognostic evaluation of system performance at the design stage is needed.

There are many ways to evaluate building/environment system performance. Among the quantitative methods, those relying on probabilistic evaluation of system reliability are chosen. Climatic conditions of a site and human activities inside a building are random in nature and even the properties of a structure are comparatively uncertain. Probabilistic analysis appears as the appropriate approach to account for those uncertainties when

evaluating building performance in terms of fulfilling specified requirements. Evaluation of building/environment system performance in terms of reliability is proposed.

There are many types of uncertainty that can exist in building performance applications. Fundamentally, two common types of uncertainties may be present in any calculation: uncertainty resulting from the lack of information or uncertainty caused by the natural variability in a parameter. Uncertainties that arise from the lack of knowledge about parameters can be modelled with the help of expert judgement that can lead to assignment of probability distribution. Uncertainties that arise from variability can be modelled with the help of statistical analysis of experimental or simulation data.

The probabilistic model for reliability analysis in building physics design based on limit state approach and load-resistance called also demand-capacity model has been presented in (Pietrzyk & Hagentoft, 2008 a).
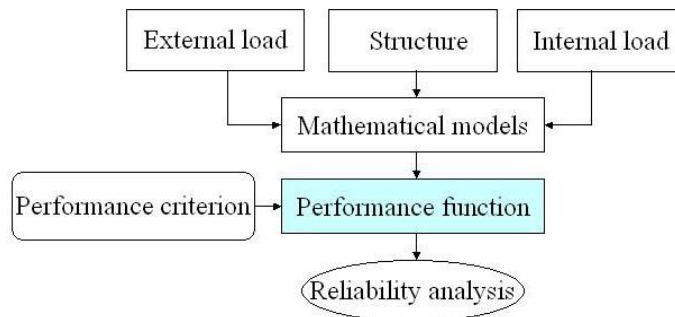

FIG. 1: Probabilistic Model for Reliability Analysis of Building/Environment System Performance.

In the probabilistic modelling the design variables and parameters are explicitly identified, and eventually load (demand) S and resistance (capacity) R probability distributions can be determined (see Figure 2). Probability density function of load S is approximated, taking into account variability and uncertainty of input parameters describing external and internal load and the structure (see Figure 1). Requirements for the system are specified in the form of performance criteria. Generally, variability of performance criterion (threshold) can be confronted in different ways: it can be ignored and a deterministic value can be assigned to that parameter, it can be disaggregated by considering all the relevant subgroups, it can be characterised by the range between minimum and maximum value and a measure of central tendency, and it can be described by a probabilistic description of its range. Hence, resistance (capacity) can be estimated in the form of deterministic or stochastic parameter as shown in Figure 2.
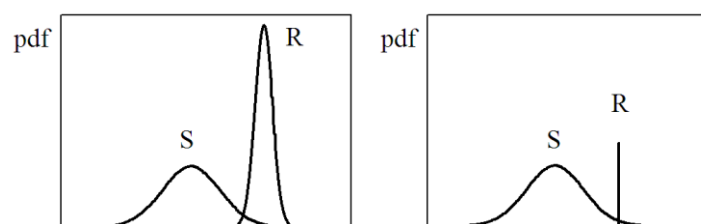
FIG. 2: Concept of load-resistance model left: probabilistic performance criterion, right: deterministic performance criterion (after Pietrzyk et al. 2004).

Reliability of the design is estimated by comparing if the system can carry effect of applied loads without jeopardizing well-being of people. It can be done with the help of performance function $Z = R – S$. The state $Z = R_2 – S = 0$ (for maximum type with threshold R_2) or $Z = S – R_1 = 0$ (for minimum type with threshold R_1) divides the response space into safe (positive Z) and unsafe (failure) (negative Z) regions characterized by reliability or probability of failure P_f.

3. Modelling resistance (capacity)

While evaluating a building performance the very important issue is to find criteria to differentiate between good and bad performance. A critical state dividing the space of the possible results into two subspaces the reliable one and the failure one does it. This state can be described by a single performance parameter. The critical state can be defined by a deterministic value, or by probability distribution function assigned to that parameter. The way of presenting performance criterion depends on the investigated problem and availability of data. Stochastic threshold criterion is built up because of the uncertainties regarding the resistance of materials or humans response.

While modelling resistance as a random variable the type of uncertainties concerning the resistance parameter has to be investigated. Variability in time, space, and among individuals can be included in the performance criterion. The chosen kind of variability depends on the performance aspect considered. When taking into account the response of people to a certain state described by a physical parameter, inter-individual variability in the form of the number of people being affected can be included in stochastic threshold. Variability among individuals in the response to specified interior conditions are caused by their different physical and behavioural conditions. Hence, a criterion for human's well being can be stated for the population, specified group of people or for the individuals depending on the client group in focus, in the form of esitmated for the group probability density function. Then, the general standards based design or client controlled (adapted) design responding to the needs of target group can be considered.

Variability of material resistance can be derived from the experiment. Experts, on the basis of experience and physical considerations, can also deliver it in case of lack of experimental data. In the case, when not one material, but a structural member is considered, it is often necessary to develop resistance models using the results of experiment and/or numerical simulations (Nowak & Collins 2000). It can take into account also the functional relationship with some other input parameters.

Evaluation of material resistance can be considered in the aspect of the consequences associated to specific values. Then, variability of consequences regarding the absolute values of the performance parameter can be incorporated in the stochastic model of performance criterion. The consequences of performance failure can concern changes of the material as well as their effect on human comfort or health. That is why even in this case variability of human response can be considered in modelling of random character of performance criterion. In such a case the dose-effect models developed in health science can give extra input to stochastic threshold modelling. They describe the relationship between a measurable agent and the response (reaction) of human to that agent during a given time. The same methodology can be applied to investigate humans' comfort and the statistical results about percentage of satisfied and dissatisfied people can contribute to stochastic modelling of humans' resistance.

Generally, performance criteria result from the analysis of economic and social costs and benefits. Some of them are defined in the Code of Practice or in the international standards elaborated by International Organization for Standardization (ISO) or European Committee for Standardization (CEN). Minimum air exchange rate, minimum or maximum internal temperature, maximum speed of airflow inside the building, maximum relative humidity, the maximum overall average U-value of a building envelope or the minimum air tightness are examples of type minimum and type maximum limits for building physics parameters. Although in design these quantities are considered deterministic, in reality there is some uncertainty associated to each quantity. It is why the resistance R should be treated as random variable. Experimental methods can be involved in the modelling the resistance. For example, analysis of the frequency of the development of the problems of mould growth on the samples of material with the same relative humidity leads to evaluation of the probability distribution of the critical relative humidity of the material.

The spectacular example of the capacity requirements - existing in engineering practice in Denmark (Brohus et al. 2006) - that could be represented by a stochastic threshold criterion, is guidance for judgment of the allowable excess of operative temperature in offices. It provides a maximum number of working hours where the operative temperature may exceed a certain limit for a typical year. It specifies the maximum number of hours when the operative temperature is allowed to exceed 26°C as equal to 100, and the maximum number of hours when the operative temperature is allowed to exceed 27°C as equal to 25. These requirements should be met simultaneously. They could be described by the probability density function (pdf) of the threshold criterion for operative temperature fulfilling following conditions:

$$P_{f1} = P(T > 26) = 1 - P(T \leq 26) = 1 - F_T(T = 26) = \frac{100}{N} \tag{1}$$

$$P_{f2} = P(T > 27) = 1 - P(T \leq 27) = 1 - F_T(T = 27) = \frac{25}{N} \tag{2}$$

where N is a number of working hours during a year, and F_T cumulative distribution function of the threshold variable T.

The shape (family) of probability distribution function assigned to the threshold should be stated using informations included in Equations *(1-2)* and all other information about the required interval of threshold random variable and their preferable value. If, for example, an exponential probability density function given by Equation 3 (Bury 1999) is chosen to represent stochastic threshold for operative temperature in office, the parameters of that function can be estimated from the two eqations describing two quantiles of order $q_1 = 1-(100/N)$ and $q_2 = 1-(25/N)$.

$$f(T;\mu,\sigma) = \frac{1}{\sigma} \exp\left\{-\frac{T-\mu}{\sigma}\right\}; \quad T > \mu, \quad \mu \geq 0, \quad \sigma > 0 \tag{3}$$

where: μ – location parameter, σ – scale parameter

The assumption of *N=2000* results in $q_1 = 0.95$ and $q_2 = 0.99$. Then, the parameters μ and σ, estimated with the help of Equations 4 and 5 become: $\mu = 24.14$ and $\sigma = 0.62$. The mean value of threshold is equal to 24.76 °C.

$$26 = \mu - \sigma \ln(-0.95) \tag{4}$$

$$27 = \mu - \sigma \ln(-0.99) \tag{5}$$

The exponential probability density function estimated for the performance criterion for the operative temperature in offices is shown in Figure 3.
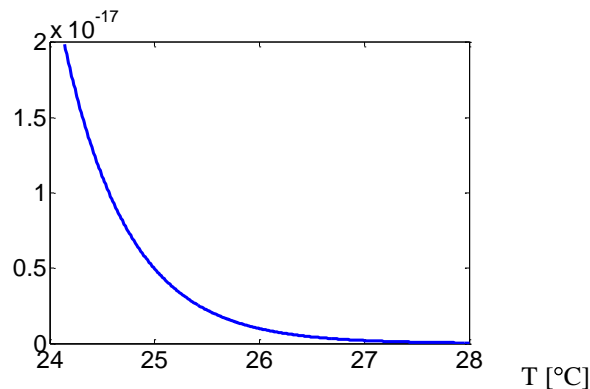

FIG. 3: Exponential probability density function of the performance criterion for the operative temperature in offices estimated on the basis of judgment of the allowable excess of operative temperature.

It is interesting to investigate how the stochastic resistance can influence the estimated reliability. There are only a few cases that a tractable form of analytical solutions can be presented. Then, the influence of variability of threshold criteria can be directly followed. One of such examples is the case when load, as well as resistance, are represented by the independent normal distribution functions. Then, the random variable Z (called safety margin) is normally distributed with mean value $\mu_Z = \mu_{R2} - \mu_S$ (maximum type) or $\mu_Z = \mu_S - \mu_{R1}$ (minimum type), and standard deviation $\sigma_Z = \sqrt{\sigma_R^2 + \sigma_S^2}$. Then reliability is given by Equation *(6)*:

$$Re\,liability = 1 - P_f = P(Z > 0) = \int_{y_0}^{\infty} \frac{1}{\sqrt{2\pi}} e^{-y^2/2} dy = 1 - \Phi(y_0) \tag{6}$$

where: Y is a reduced variable of Z, y_0 is a reduced value $z = 0$, and $\Phi(.)$ is the standard normal cumulative distribution function.

For a maximum type of threshold, y_0 is given by:

$$y_0 = -\frac{\mu_{R2} - \mu_S}{\sqrt{\sigma_{R2}^2 + \sigma_S^2}}$$

(7)

For a minimum type of threshold, y_0 is given by:

$$y_0 = -\frac{\mu_S - \mu_{R1}}{\sqrt{\sigma_{R1}^2 + \sigma_S^2}}$$

(8)

Calculations performed with the help of Equations *(6–8)* could show how reliability changes with the variability of performance criteria for the case of independent, normally distributed *R* and *S*.

4. Reliability analysis of air exchange – case study

The research example has been calculated for the problem of air exchange in a 2-storey building with volume of 486 m^3, and total area of the envelope of 336 m^2, described in (Pietrzyk 2005). Natural ventilation has been assumed. The reliability model (PROMO) has been applied for the calculations. It includes the limit state approach based on load-resistance model where FORM (First-Order Reliability Method) technique is implemented as a tool for probabilistic approximations and reliability analysis in building physics design (Pietrzyk & Hagentoft 2008 a). The results obtained by probabilistic approximation of joint distribution function of basic random variables (temperature difference, wind speed and direction) (Pietrzyk 2005) are given in the form of probability density function of air change rate. One example has been chosen. It concerns a house situated in Gothenburg exposed to western winds. A probability density function approximated by lognormal pdf describes the variability of load *S = ACH*.

The results obtained by reliability models using deterministic and stochastic threshold criteria are compared. Different probability distributions for performance limit are chosen. As it has been mentioned earlier there are not many cases that a tractable analytic form for reliability can be obtained. Therefore, the results obtained by probabilistic approximations are used for comparison. Load *S* and threshold *R* have been considered as independent random variables.

A minimum type of performance criterion is considered when calculating reliability of air change rate. It means that a minimum allowable value of air change rate in a building is modelled by R_1. The serviceability limit state $Z = S - R_1 = 0$ divides the response space into safe and unsafe (failure = insufficient air exchange) regions characterized by reliability $P(S \geq R_1) = 1 - P_{f1}$ and probability of failure $P_{f1} = P(S < R_1)$. Probability of failure can be computed as the area under pdf of variable Z and is equal to the shaded area in Figures 4-7.
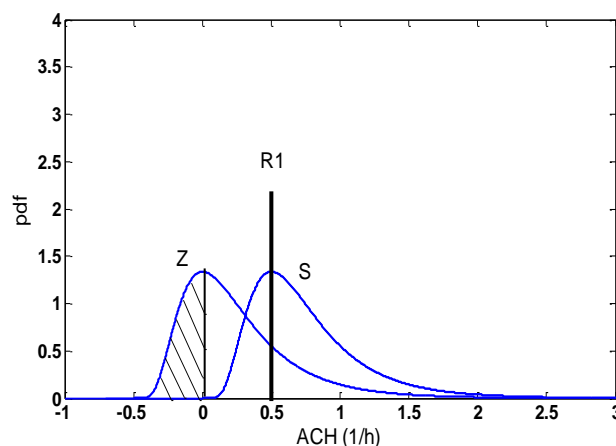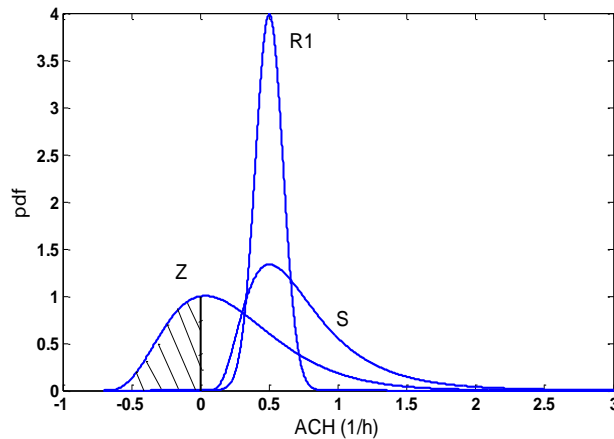

	Mean	Standard deviation	Distribution
S	0.75	0.42	Lognormal
R_1	0.5	-	-
Z	0.25	0.42	Lognormal
			$P_f = 0.33$

FIG. 4: Results of performance evaluation of air exchange based on the deterministic threshold criterion.

The deterministic limit R_1 against unhygienic conditions in the building is assumed to be equal to 0.5 changes per hour (based on Swedish Code of Practice). The results of simulations are shown in Figure 4. Probability density function of variable $Z = S - R_1$ is, as expected, of the same kind as pdf of *S = ACH*, but shifted to the left by R_1.

In the following example the stochastic limit against unhygienic conditions in the building R_1 is assumed being normally distributed with mean value 0.5/h and standard deviation 0.1/h. In that way certain variability of required air change rate is taken into accont. It can, for example, correspond to the variability in expert opinion about the consequences of a specific air exchange in a building. The value around $R_1 = 0.5$ is in this case indicated as a critical limit by majority of experts, but other values like 0.3, 0.4 or 0.6, 0.7 are also indicated at least by some of them. The results obtained by probabilistic approximation are shown in Figure 5.
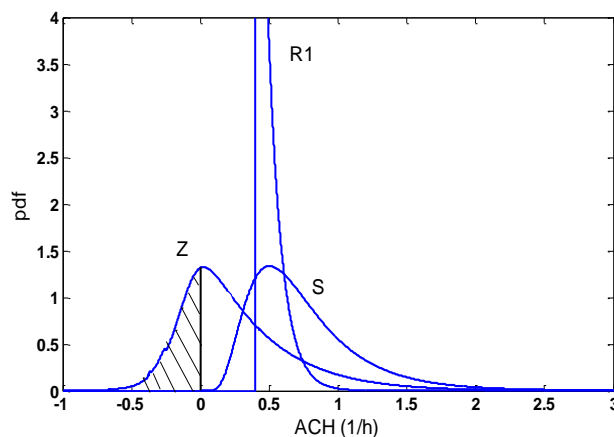

	Mean	Standard deviation	Distribution
S	0.75	0.42	Lognormal
R_1	0.5	0.10	Normal
Z	0.24	0.44	3-p. Gamma
			$P_f = 0.34$

FIG. 5: Results of performance evaluation of air exchange based on the threshold criterion modelled by the normal distribution (mean 0.5, st.dev. 0.1).

Probability of failure is similar to that obtained with deterministic threshold above, mainly due to the symmetric threshold probability density function concentrated around the mode of the pdf of the load.

Another example shows stochastic threshold modelled by an exponential probability density function with parameters referring to the same values of mean and standard deviation like in the previous example (see Figure 6). The difference is in the shape of the distribution, which has got influence on reliability measures (see different P_f for these examples). Exponential probability density function applied as the threshold variable could be estimated on the basis of the expert opinion, that the minimum ACH should not be lower, but rather close to 0.4/hour (indicated by majority of experts), while some of the experts wanted to have a minimum ACH even up to 1 change/hour.
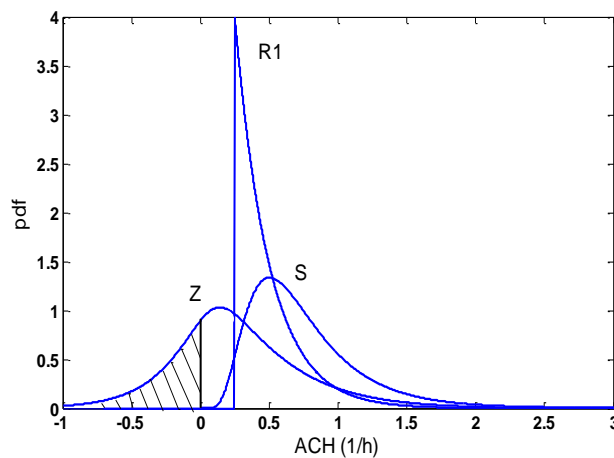

	Mean	Standard deviation	Distribution
S	0.75	0.42	Lognormal
R_1	0.50	0.10	Exponential
Z	0.27	0.44	3-p. Gamma
			$P_f = 0.29$

FIG. 6: Results of performance evaluation of air exchange based on the threshold criteria modelled by the exponential distribution (mean 0.5, st.dev. 0.1).

For stochastic threshold modelled by an exponential probability density function with parameters referring to the same value of mean 0.5/hour but with the standard deviation 0.25/hour, the results are shown in Figure 7. It represents higher variability in expert opinion. This threshold allows smaller values of min ACH (already from

0.25) against fewer much higher values (up to 1.5) comparing with the previous example. This is why the probability of failure has decreased.

	Mean	Standard deviation	Distribution
S	0.75	0.42	Lognormal
R_1	0.50	0.25	Exponential
Z	0.28	0.50	3-p. Gamma
			$P_f = 0.27$

FIG. 7: Results of performance evaluation of air exchange based on the threshold criteria modelled by the exponential distribution (mean 0.5, st.dev. 0.25).

The 3-parameter Gamma distribution serves well as a model of the variable Z characterising performance of ACH for the examples with stochastic threshold criteria.

5. Conclusions

Reliability/risk analysis of building performance benefits of improved information on variability of thresholds criteria, which brings it closer to reality. The additional information about the material resistance or human resistance describing their uncertainty and variability in time, in space or among the individuals, can be built into the reliability model. It influences the results of reliability analysis. The examples of the calculations of the probability of insufficient air exchange for different models of performance criteria show that the significance of their variability for evaluation of probability of failure depends on the shape of distributions and their mutual location.

Despite that in building physics the acceptable risk levels can be much higher than e.g. in structural mechanics, the mean values and even the mode of the performance distributions should be relatively far from the threshold criteria. With threshold criterion described by a skew distribution concentrated on a slope of the performance distribution, the stochastic threshold formulations can lead to results different than those obtained with deterministic thresholds. This field is relatively unexplored and requires further research.

6. Acknowledgment

7. References

Brohus H., Bendtsen A., Sorensen M. (2006). Comfort Indicators for the assessment of indoor environmental building performance. Conference Proceedings of *Healthy Buildings*. Lisboa, Portugal. Vol. III, pp 169-174.

Bury K. (1999). *Statistical distributions in engineering.* Cambridge University Press.

Kottegoda N.T. & Rosso R. (1997). *Probability, Statistics, and Reliability for Civil and Environmental Engineers*. The McGraw-Hill Companies, Inc.

Nevander L.E., Elmarsson B. (1991). *Fuktdimensionering av träkonstruktioner – riskanalys*, Statens råd för byggnadsforskning, 1991:38. (In Swedish).

Nowak A.S. & Collins K.R. (2000). *Reliability of structures*. McGraw-Hill.

Pietrzyk K., Kurkinen K., Hagentoft C.-E. (2004). An example of application of limit state approach for reliability analysis of moisture performance of a building component. *Journal of Thermal Envelope and Building Science (Journal of Building Physics)*. Vol. 28, No.1, pp 9-26.

Pietrzyk K. (2005). Probability-based design in ventilation. *The International Journal of Ventilation*. Vol. 4 Number 2, pp 143-156.

Pietrzyk K., Hagentoft C-E. (2008 a). Reliability analysis in building physics design. *Building and Environment*. Vol 43/4 pp 558-568.

Pietrzyk K., Hagentoft C-E. (2008 b). Probabilistic analysis of air infiltration in low-rise buildings. *Building and Environment*. Vol 43/4 pp 537-549.

Measuring and modeling transport of microbes from crawl space to indoors

Miimu Airaksinen, Dr.,
Technical Research Centre of Finland, VTT
miimu.airaksinen@vtt.fi, www.vtt.fi

Pertti Pasanen, Prof.,
University of Kuopio, Department of Environmental Sciences;
pertti.pasanen@uku.fi, www.uku.fi

SUMMARY:
A mechanical exhaust ventilation system is typical in apartment buildings in Finland. In most cases the base floor has leakages, and as the apartment building has lower pressure than crawl space, thus air and fungal spores may flow from the crawl space to the apartment. Usually the concentration of fungal spores is clearly higher in the crawl space than inside the building. In this study, in most cases for the same species, the size distributions of fungal spores were similar in shape in the crawl space and indoors. The size distribution of fungal spores varied depending on the fungal species. Correlation between the fungal spores in the crawl space and indoors depended on microbe species. Some species have sources inside the building, which makes the correlation study more complicated. However, some species like Acremonium do not normally have a source indoors, and the concentration of Acremonium in the indoor air correlated to the crawl space concentration. It seems that the penetration is highest in the viable particles whose aerodynamic diameter varies between 1.4-2.6 µm.

1. Introduction

Commonly in Finland, dwellings have mechanical exhaust ventilation, Figure 1.Mechanical exhaust ventilation creates under pressure into the apartment. Very often the base floor has some leaks, and pressure measurements show that air is flowing through the leaks in the base floor to the apartment. The increase or decrease in ventilation rates in the dwelling affects to the air change in the crawl space. The pressure difference between indoor and outdoor or between indoor and crawl space is often in a range of 5 –15 Pa.
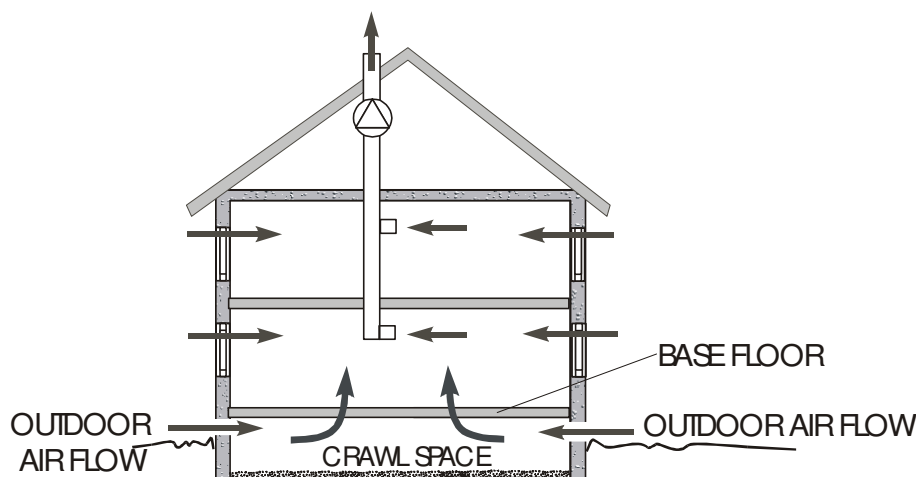

Figure 1. A principle of a mechanical exhaust ventilation in an apartment building with a crawl space.

The microbial contamination in the crawl space is typically much higher than inside the building. The level of fungal spores in the crawl space is about ten times higher than indoors. In the crawl spaces, the spore densities in

a range of 10^3-10^5 colony-forming units per gram (cfu/g) of material are common. The levels have usually been highest on wood-based boards and on timber (Kurnitski and Pasanen 2000). Under heavy fungal colonization, airborne spore concentrations up to 10^3-10^4 cfu/m^3 are detected (Kurnitski and Pasanen 2000). Microbes are transported inside the building through leakages and are potential health risk.

The object of this study was to find out whether there is a relation between indoor and crawl space concentration of fungal spores, and whether microbes are transported from crawl space to indoors. A data of eight buildings with a crawl space were used in development of method to model the possible relations.

2. Methods

2.1 Measurements

The concentrations of airborne fungal spores and bacteria were measured in eight buildings in Southern Finland (Helsinki region). The buildings were chosen to represent typical buildings with crawl space foundations. Some of the crawl spaces were suspected of causing indoor air quality problems. Three of the buildings were primary schools, two day care centres, and three dwellings. Half of the buildings had a wooden base floor. The dwellings had mechanical exhaust ventilation. Both of the day care centres had mechanical exhaust ventilation in the crawl space, but all the other crawl spaces had natural ventilation except for two crawl spaces without any ventilation.

Airborne fungal spores were sampled by using six-stage cascade Andersen impactors (Andersen 1958). Samples were taken from indoor, outdoor, and crawl space air. Sets of samples were taken in the winter and others in the late spring. The fungal spores were collected on 2% malt extract agar (MEA). To avoid contamination due to spore transportation on clothes, the indoor successive samples (2 samples) were taken first. Two successive samples were also taken from the crawl space, but if the crawl space had clearly different sections, such as different ground cover materials, two samples were taken from each section. According to previous studies, e.g. Reponen (1994), fungal spore concentrations are low during winter. During the winter sampling, the temperature was below 0°C, and, therefore, outdoor samples were not taken. In the summer, one sample from outdoor air was taken on each study site. The sampling time was 10 min indoors and outdoors and 5 min in the crawl space, and thus the computational limit of identification was 7 CFU/m^3 and 3.5 CFU/m^3. The incubation time of the samples was seven days (14 days for the actinomycetes) at 25°C.

2.2 Simulation model

The simulation model was used to estimate the penetration of the microbes from the crawl space and outdoor to the indoor air. The mathematical model based on that presented by Kulmala et. al. (1999), and it was modified suitable for the simulation environment.

$$V \frac{dC_{Indoor}}{dt} = s \cdot q_{v,Outdoor-Indoor} \cdot C_{Outdoor} - q_{v,Indoor-Outdoor} \cdot C_{Indoor} - a \cdot C_{Indoor} \cdot V + re \cdot B \cdot V + Q$$

where V is the volume of the room [m^3], C_{Indoor} the microbe concentration Indoors [CFUm^{-3}], t time [s], s penetration factor [-], $q_{v,Outdoor-Indoor}$ air flow from outdoor to indoor [m^{3}s^{-1}], $C_{Outdoor}$ the microbe concentration outdoors [CFUm^{-3}], $q_{v,Indoor-Outdoor}$ air flow from indoor to outdoor [m^{3}s^{-1}], a deposition rate [s^{-1}], re re-emission rate [m^{-1}s^{-1}], B particle surface accumulation on indoor surfaces [CFUm^{-2}], Q sink or source of microbes indoors [CFUs^{-1}].

The deposition rate was calculated from $a = v_{deposition} \cdot \dfrac{A}{V}$

where $v_{deposition}$ is the deposition velocity [ms^{-1}], and A the total indoor surface area including furniture etc. [m^2].

Measurements of deposition velocity was reported in (Fisk 2001). The used deposition velocity is adapted from reported results, and it is average values. The equation for deposition velocity is valid only for particle diameters between 0.3 - 10 µm.

$$v_{deposition} = 3 \cdot 10^{-5} \cdot \left(d_{particle} \cdot 10^6\right)^{1.58} - 1 \cdot 10^{-6}$$

where $d_{particle}$ is the aerodynamic diameter of the particle [µm].

Particle surface accumulation on indoor surfaces was calculated from

$$\frac{dB}{dt} = (a \cdot I - re \cdot B) \cdot \frac{V}{A}$$

Since the measurements were done when the inhabitants were absent, the re-emission was assumed to be very small ($2.7 \cdot 10^{-6}$ m^{-1}s^{-1}) (Kulmala et. al. 1999).

The simulation was carried out in an IDA simulation environment (Sahlin 1996 a). IDA is a modular simulation environment which consists of an NMF (Neutral Model Format) translator, solver and modeller. The solver and the modules are separate, which makes it possible to change the mathematical formula of any component without changing the model description file. Via the translator, the modules can be used in several modular simulation environments. The used computer language for the models is NMF which serves as a readable document of the code, as well (Sahlin 1996).

3. Results

3.1 Pressure difference between crawl space and indoors

There was a significant leakage between the crawl space and apartments that can be seen from the air change measurements. The mechanical exhaust ventilation of the building was performed with a two-speed fan. The use of full speed of the fan increased under-pressure in apartments and increased the pressure difference over the floor. The outdoor air flow to the crawl space increased as well. This change can be clearly seen from the outdoor air flow through ventilation pipes to crawl space, Figure 2.
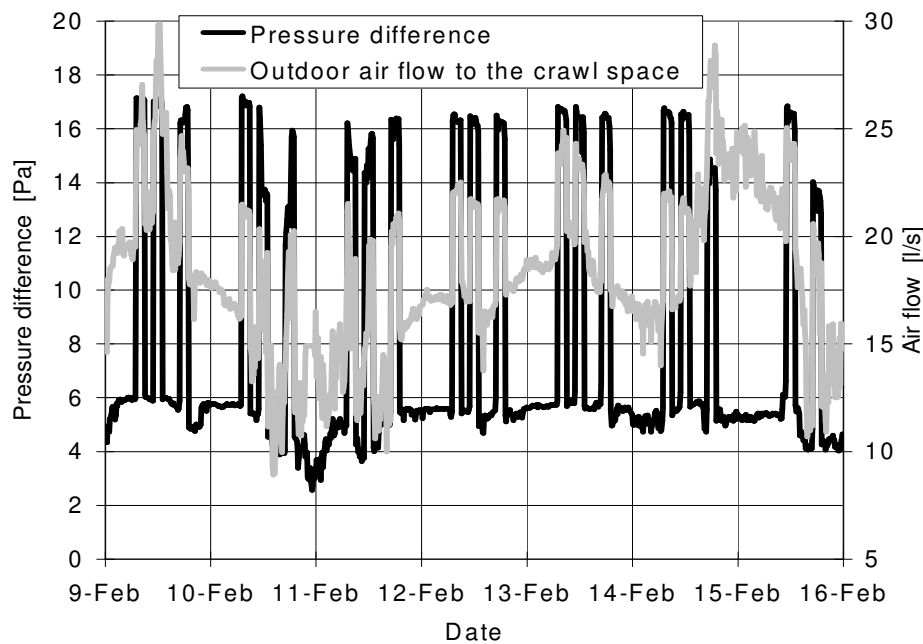
Figure 2. The pressure difference between crawl space and indoor, and outdoor air flow to the crawl space. Apartment has under-pressure and crawl space over-pressure. Outdoor air flow of 20 l/s corresponds to air change rate of 1 ach in the crawl space

3.2 Correlation between crawl space and indoor microbes

The correlation between indoor and crawl space concentration of microbes was tested with Pearson correlation coefficient. The concentrations of *Penicillium* indoors and in the crawl space did not correlate (Pearson coefficient 0.11). *Penicillium* is a very typical microbe indoors and outdoors, and there are several sources of *Penicillium* also indoors, which makes the correlation study complicated, Figure 3.
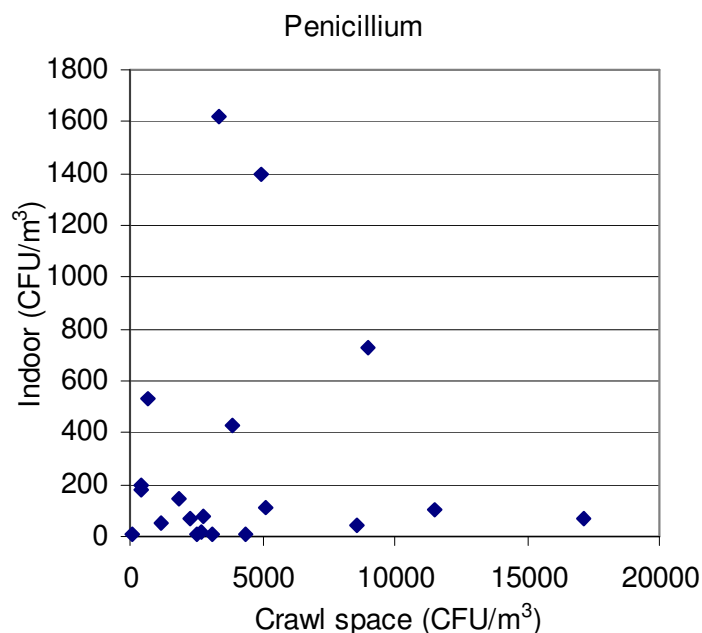

Figure 3. Scatter plot of Penicillium spores indoors and crawl space.

The concentration of *Acremonium* indoors and crawl space had a relationship (Pearson coefficient 0.89), indicating presence of high counts in crawl spaces to be high also in indoor air, Figure 4. As *Acremonium* is not a typical indoors and it does not have a source there, it most probably originates from crawl space via leakage through the base floor.
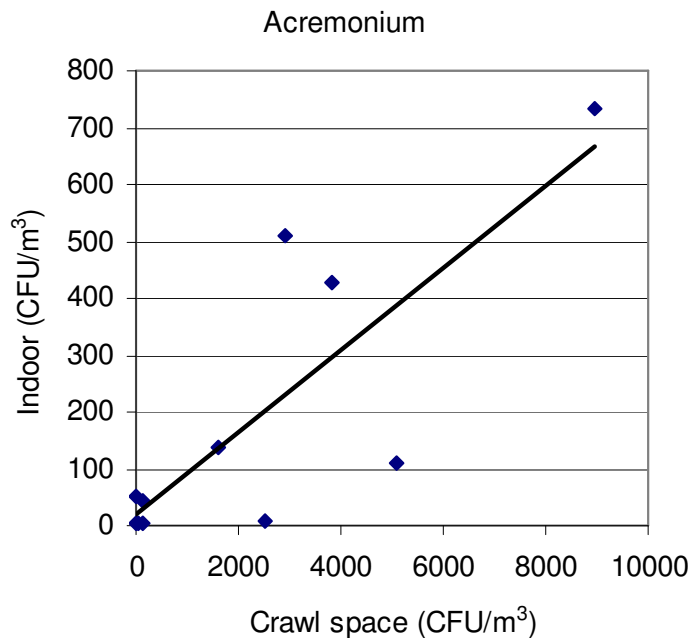

Figure 4. Correlation between indoor and crawl space Acremonium spores

3.3 The size distribution of fungal spores

The concentration of microbes was clearly highest in the crawl space. The size distribution varied depending on microbial species. The size distribution of *Penicillium* in the crawl space and indoor air were similar in shape, most microbes were impacted in a stage whose the mean average aerodynamic diameter was 1.4 μm. However, the concentration was clearly higher in the crawl space, Figure 5. Outdoors the highest counts were received in smaller sizes. (on epätäsmällisemmin sanottu, mutta lienee ymmärrettävä) The concentrations of *Cladosporium* were low, even in the crawl space the maximum was 31 CFU/m³. The size distributions of *Cladosporium* were equal in shape in indoors, in crawl space and in outdoor air. Most of fungal spores of *Cladosporium* were impacted in a stage whose average aerodynamic diameter was 2.6 μm. Compared to *Penicillium* the size distribution of *Cladosporium* is clearly skewed towards bigger particles. This is in agreement with reported larger diameter of Cladosporium spores. Previous studies have shown that the size of the spores increase when humidity increase (Pasanen A.-L. et. al. 1991).
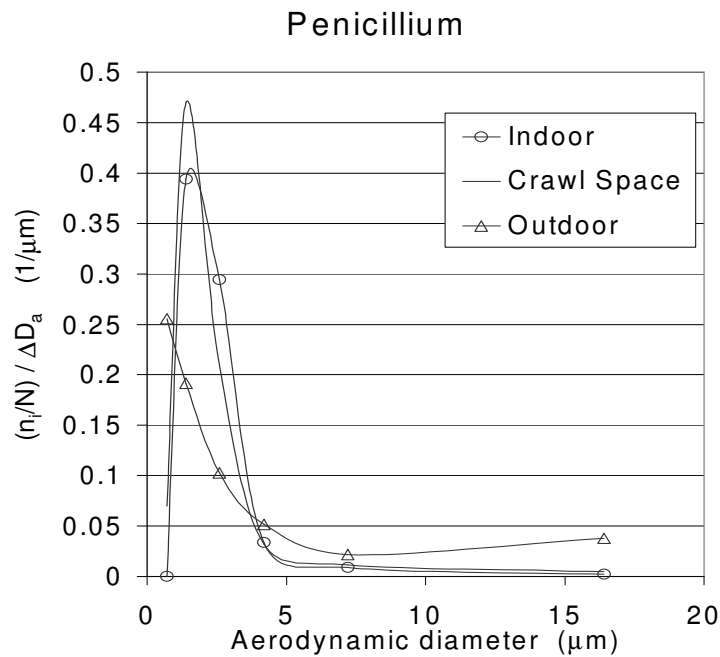
Penicillium

Figure 5. The count size distribution of fungal spores indoors, outdoors and in the crawl space of different microbes. The explanations of abbreviations in the figure: n_i number of spores in size interval i, N total number of spores, ΔD_a width of a size interval.

Size distributions of *Acremonium* were similar in all measured environments. The fungus is not a typical genus in indoors, which makes it a good indicate of leakages from the crawl space to indoors, Figure 6. Yeasts have equal size distributions in the crawl space and outdoors, the most of the yeasts impacted on the lowest stages. Yeast indoors were clearly bigger in size, most microbes were impacted in a stage whose the mean average aerodynamic diameter was 4.2 µm. There were only a few non-sporulating microbes and their size distributions differed in the different environments. This may indicate different species growing on the plates. The presented data are based on the counts and identification of the fungi growing on the malt extract agar.
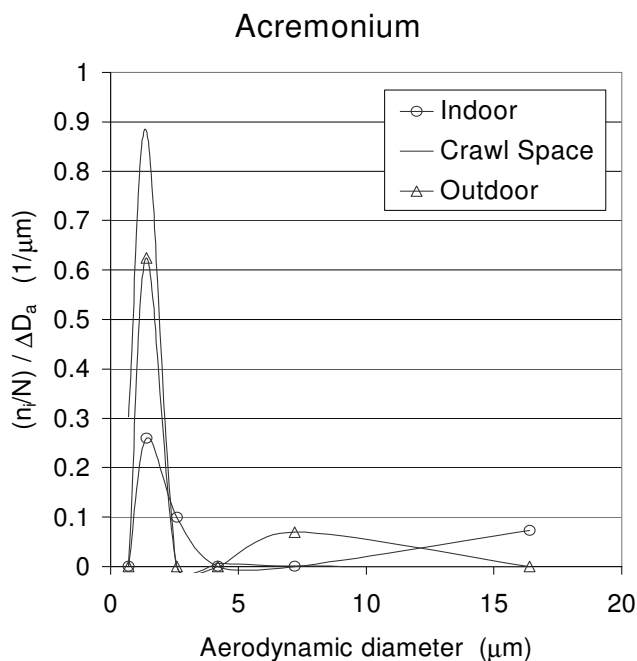
Acremonium

Figure 6. The count size distribution of Acremonium spores indoors, outdoors and in the crawl space of different microbes.

3.4 Penetration factor

The penetration factor (s) is calculated from the equation given in the section 2.2. Penetration factor from the crawl space to the indoor air was estimated by using simulations in the IDA simulation environment. The calculations were done for the apartment building with a mechanical exhaust ventilation. It seems that the penetration coefficient is highest at particle sizes whose aerodynamic diameter varies between 1.4-2.6 µm, Figure 7. However a further study of the transport of fungal spores is needed.
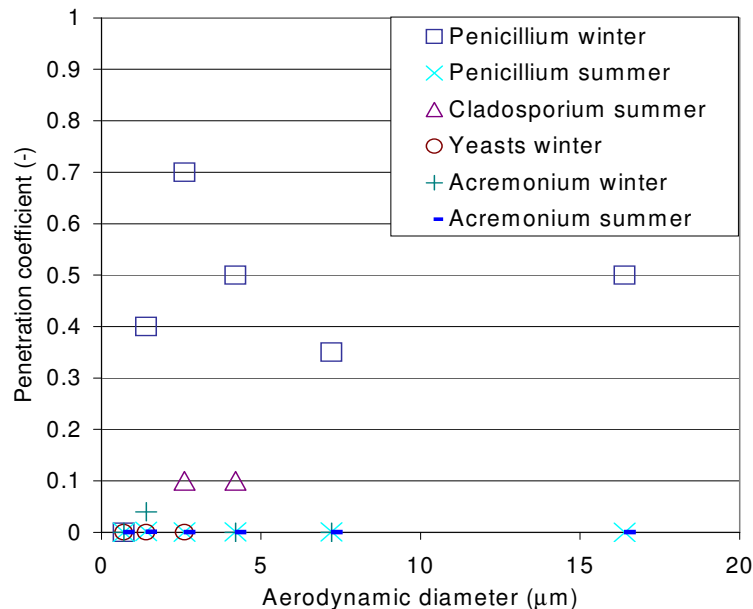

Figure 7. Penetration coefficient of some fungal spores. Penetration factor is defined as penetration coefficient.

4. Conclusion

In mechanical exhaust ventilation, if the base floor has some leaks, pressure measurements show that air is flowing through leaks in the base floor to the apartment. The change of ventilation rate in the dwelling reflects directly to that in the crawl space. In some case buildings all the extract air from the crawl space flows through the base floor to the apartment.

A comparison of the fungal spore concentrations in indoors, in crawl spaces and outdoors usually results the highest concentration in the crawl spaces. The size distributions of spores of fungal species were mainly similar in the shape in the crawl space and indoors in the studied buildings. The shape of the size distribution varied between fungal species.

Correlation between the fungal spores in the crawl space and indoors depended on the microbial species. Some common species, like *Penicillium*, have many type of sources inside the building, which makes the study of correlation more complicated. However, species like *Acremonium* is usually not reported to have sources indoors, and thus the concentration of *Acremonium* correlated to the indoor concentration indicating air leakage from crawl space to indoor air.

It seems that the penetration through the base floor is highest at the size range of 1.4-2.6 µm of viable particles.

5. References

Andersen A.A., 1958, New sampler for the collection, sizing, and enumeration of viable airborne particles. *Journal of Bacteriology*, **76**:471-484.

Fisk W. J., Faulkner D., Palonen J., Seppänen O., 2002 Performance and costs of Particle Air Filtration Technologies, , *Indoor Air,* Vol 12 (4): 223-234.

Kulmala M., Asmi A., & Pirjola L., 1999, Indoor air aerosol model: the effect of outdoor air, filtration and ventilation on indoor concentrations, Atmosperic Environment 33 (1999) 2133-2144

Kurnitski J, Pasanen P.2000. Crawl space moisture and microbes, *Proceedings of Healthy Bbuildings 2000*, Vol 3, 205-210, Espoo, Finland.

Pasanen A.-L., Pasanen P., Jantunen M. J., Kalliokoski P., 1991, Significance of air humidity and air velocity for fungal spore release into the air, Atmospheric Environment Vol 25A, No.2, pp.459-462

Reponen T., 1994. Viable Fungal Spores as Indoor Aerosols, Academic Dissertation, University of Kuopio, Finland.

Sahlin P., 1996, Modelling and Simulation Methods for Modular Continuous Systems in Buildings, Doctoral Dissertation, Department of Building Sciences, The Royal Institute of Technology, Stockholm

Air tightness performance of different sealing methods for windows in wood-frame buildings

Thor-Oskar Relander, Ph.D Student,
Department of Civil and Transport Engineering, Norwegian University of Science and Technology;
thor.oskar.relander@ntnu.no

Jan Vincent Thue, Professor,
Department of Civil and Transport Engineering, Norwegian University of Science and Technology;
jan.thue@ntnu.no

Arild Gustavsen, Professor,
Department of Architectural Design, History and Technology, Norwegian University of Science and Technology;
arild.gustavsen@ntnu.no

KEYWORDS: *air tightness, window joint, sealing techniques*

SUMMARY:
Energy use in buildings has come more into focus in recent years. Achieving an energy efficient building is very dependent on the building's air tightness. This can be quantified using the blower door pressurization technique. The air tightness requirements in the Norwegian building regulations, cause considerable concern for the building industry. This leads to a growing interest for air tight constructions and methods.

Air leakages in buildings have many origins, where joints around windows are one of them. This depends on the sealing materials being chosen, the sealing technique as well as the craftsmanship. This paper is a part of a PhD study, and discusses the effects on air leakages from window joints only, depending on the sealing technique chosen. Measurements of 7 different sealing techniques have been carried out on a window of 1.2m x 1.2m with a continuous joint of 15 mm. The pressure chamber testing rig at SINTEF Building and Infrastructure has been used. From the laboratory measurements it is shown that tape, wind barrier strips and backer rod contribute most to the air tightness of the window joint. A comparison has also been made between a 50 mm pulled-in and a regular mounting of vapour barrier. The measurements show that when the vapour barrier is squeezed against the jamb liner, the pulled-in variant should be sealed in the corners to reduce air leakages. Measurements of the air tightness of a self expanding sealing strip show that this product has the same air tightness as 50 mm mineral wool insulation.

1. Introduction

After the recent revision of the Norwegian building regulations, energy saving in buildings is becoming even more important (TEK 2007). To achieve energy efficient buildings, the air tightness is of vital importance. This leads to a growing interest of knowledge of the various contributions to the total air change rate of whole buildings.

For windows the air leakages are from the window itself as well as the joints around the window. The air tightness of the window *itself* is dependent on the window design and the manufacturer. On the other hand, the craftsmanship as well as sealing technique chosen, is decisive for the air leakages from the window joints *around* the window. The sealing of the window joints can be provided by various materials and techniques. This paper provides an insight in the air tightness of 7 different sealing techniques used in practice.

Similar work has been performed by Proskiw (1994). Proskiw repeated the measurements 5 times for each sealing technique to be measured, whereas in this paper only one measurement was done for each technique tested. However, Proskiw measured at internal overpressure only, whereas in this paper both over- and underpressure measurements are reported. Further Proskiw used a different arrangement of the joint to be measured. Interior casing and battens (Proskiw used the word exterior brick mould for battens) were used for all measurements, whereas in this paper the starting point was a completely empty joint. For the comparable sealing techniques also measured in this paper, i.e. backer rod and tape, Proskiw used mineral wool insulation in the

joint in addition. So to say, Proskiw focused on plural layer measurements, whereas in this paper only one-layer measurements are done. Consequently this gives a different basis for evaluation of the different layers' tightening performance and parametric variations for each layer tested. Proskiw also measured the air tightness of a sealing technique which somehow is comparable to the wind barrier strips measured here. However, this measurement was also with mineral wool in the joint making the measurements not directly comparable. Further Proskiw also measured the leakages in a small area around the wall, i.e. not exclusively through the joint, making these measurements strictly applicable to similar types of walls.

2. Method

To reduce the complexity as well as introducing the possibility of reliable parameter variations of the sealing techniques, only *one-layer* measurements were performed. The laboratory measurements were performed by the use of a dummy wall made of timber studs and gypsum boards as can be seen in figure 1 a) and b). To reduce unwanted leakages from the wall, the connections between the gypsum boards were sealed using tape.

A 1.2 m x 1.2 m window was mounted in the wall and the wall was inserted in a pressure chamber testing rig as can be seen in figure 1 a) and b). The window was drawn out 42 mm from the gypsum board allowing for the possibility of mounting wind barriers on the side of the window frame. The window had a continuous joint width of 15 mm. For the case of the pulled-in vapour barrier, the arrangement in figure 1 c) was used. For all other measurements, the arrangement in figure 1 d) was used. For further configuration of the vapour barrier see subsequent chapters.

To ensure no air flows from the connection between the window frame and the jamb liner, this was sealed using tape, as can be seen from figure 1 c) and d). The leakages from the wall, pressure chamber and the window itself were measured after each reinstallation. This made it possible to accurately measure the air flows *merely* passing through the joints around the window depending on sealing techniques chosen.
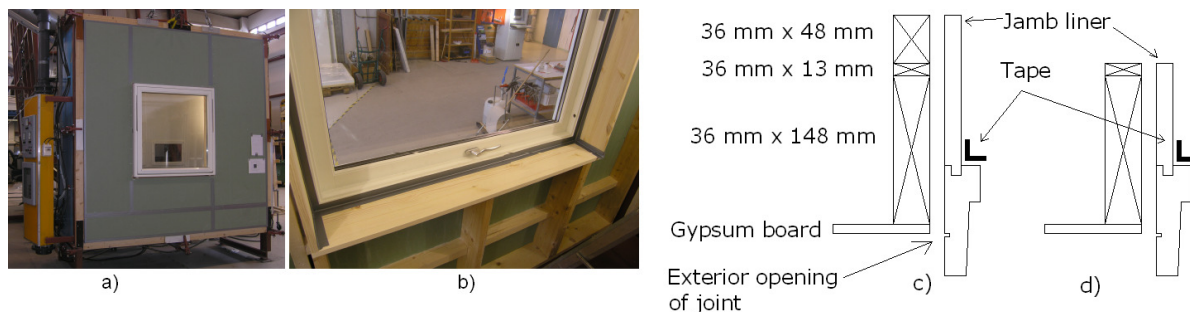

FIG. 1: Pressure chamber testing rig and dummy wall from outside, a) and inside, b) respectively. The arrangement of the joint for pulled-in vapour barrier is indicated in c), and the other measurements in d). c) represents both horisonal and vertical section. d) represents both horizontal and vertical section.

The pressure chamber testing rig was exposed to both over- and underpressure. Internal overpressure resulted in an air flow passing through the joint from *inside* to *outside*. Pressure differences were 10, 30, 50, 100 and 200 Pa. To ensure small temperature differences and thus negligible density differences, temperatures in 3 different heights of the pressure chamber were compared with the temperature in the laboratory. To ensure reliable measuring points, sufficient time was spent ensuring equilibrium of pressure and air flow to be reached. A rough estimate of the measurement uncertainty is 10 %. It will be a combination of the uncertainty of the manometer, the air flow meter and the operator effects (the uncertainty associated with an operator reading a meter scale). All measurements in this paper are curve fitted using the power law of the form (Etheridghe and Sandberg, 1996).

$$Q = \alpha \Delta P^{\beta} \tag{1}$$

Δ P is the pressure difference and α and β are constants obtained from curve fitting. The β-value can be used to interpret the type of air flow. For flows through building envelopes, a β-value of 0.5 indicates orifice flow, i.e. through holes, whereas a β-value of 1 indicates friction loss, for instance flow through porous media.

3. Sealing techniques measured

Knowledge of sealing techniques used in practice was gained by a survey in a Norwegian standard house contraction firm. In addition to sealing techniques recommended by SINTEF Building and Infrastructure, this gave a relevant basis for selection of sealing techniques to be measured. The measured cases are described below.

3.1 Mineral wool insulation and self expanding sealing strip

Mineral wool insulation, abbreviated *M*, will contribute to the air tightness of the joint. Special designed shreds of mineral wool insulation for joints were used. It was normally packed in the joint. The mineral wool was compressed by about 40 % in the width and by about 17 % in the depth. The air tightness performance of depths 50mm, 100 mm and 150 mm were measured.

For the self expanding sealing strip, abbreviated, SESS, three variations were investigated and suggested by the importer. A self expanding sealing strip of *correct* size, *SESSc*, being handpicked by the importer for the size of the joint was measured. Further the same self expanding sealing strip was opened in the 4 corners, *SESSc4*. This can be the case when mounting the self expanding sealing strip on the window frame before mounting the window in the wall, not taking into account the extra length required to fill the joint completely. This is usually not a problem when mounting the strip directly in the joint. The other variation was the effect of choosing a self expanding sealing strip of *wrong* size, *SESSw*, i.e. smaller than recommended. Since this also was a simulation of faulty workmanship, the corners were not perfectly tightened, and tiny openings were observed in the corners of the joints. The SESS was for all variants placed close to the exterior opening, as indicated in figure 2 c).

3.2 Backer rod and tape

From the manufacturer it is recommended that the backer rod is laid non-continuous, *BRn-c*, in each of the windows 4 joints. Alternatively, a continuous backer rod, *BRc*, can be chosen. Both these variants were measured. In order to measure the effect of these different techniques most accurately, sealing mastic was not used. The backer rod was handpicked for the size of the joint and placed at the same position as the SESS.

Tape for joint sealing is a relatively new product on the Norwegian market. For this sealing technique the effect of 1, 2 and 3 open corners, *T1, T2, T3*, were measured and compared with no open corners, *T*. This was suggested by the producer of sealing tape and simulated the effect of faulty workmanship. The tape was placed similarly as for the wind barrier strips, but without any battens. This can be seen in figure 2 c).

3.3 Vapour and wind barriers

Vapour barriers and wind barriers are of great importance to the air tightness of a whole wood-frame building. For vapour barrier a 0.15 mm PE-foil was used. A spunbonded polyethylene wind barrier of 60 g/m^2 was used as wind barrier. There are many ways of mounting both vapour barriers and wind barriers. The pulled-in vapour barrier, *VBp-i* and regular vapour barrier, *VB*, were mounted as indicated in figure 2 a) and b) respectively. For the vapour barrier three parametric variations were studied.

The effect of a pulled in variant compared to a regular vapour barrier was studied. The corners of the 13 mm x 48 mm casings could be glued in order to reduce leakages in the corners. For *VBp-i* the effect of this sealing, *VBp-is,* was measured. Finally for *VB,* the leakage as function of distance between the nails in the casing, abbreviated *cc,* was investigated. The same distance between the nails was used for both the casing against the jamb liner and for the casing against the wall. Nails of size 1.7 mm x 40 mm were used for both *VBp-i* and *VB*. Nail distances were 600 mm, 300 mm and 150 mm for *VB*, and 600 mm and 300 mm for *VBp-i*. The wind barrier strips, *WB*, were mounted as indicated in figure 2 c) with a nail distance of 600 mm in all battens and all thinner battens. For both the battens and the thinner battens against the wall, nails of 2.8 mm x 75 mm were used. For the battens against the window frame, 1.7 mm x 35 mm nails were used. No parametric studies were done for this case.
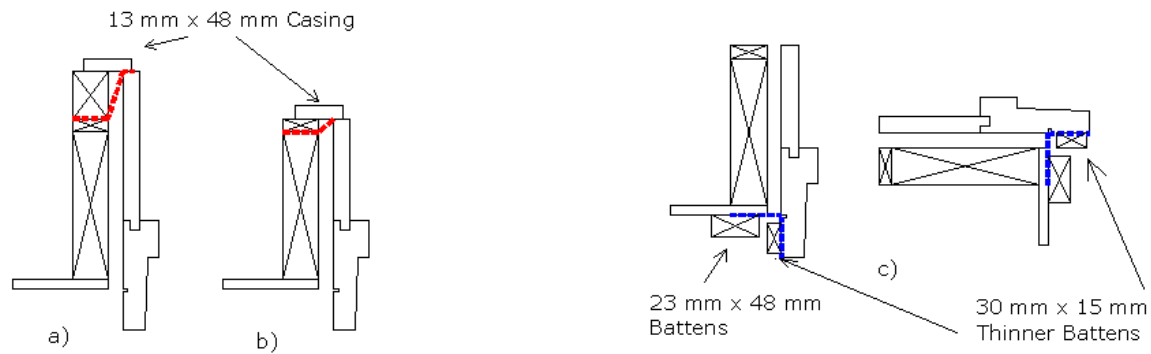
FIG. 2: Vapour barrier pulled-in a) and regular in b). Wind barrier in c) in horizontal and vertical section respectively. Vapour and wind barriers in thick lines.

4. Results and discussion

The measurement results are summarized below. Some sealing techniques are only covered briefly. Others are covered in more detail. *All* measurements are summarized in table 2 at 50 Pa mean pressure difference. In section 5 a comparison between the sealing techniques is given. Consequences of different sealing techniques on the total air leakage of whole wood-frame buildings are discussed in Relander (2008).

4.1 Mineral wool insulation and self expanding sealing strips

Measurements of the mineral wool insulation are not shown here in detail, only highlights are mentioned. For further information, see Relander (2007). The measurements clearly show that the air flow is practically independent of flow direction, and that the only parameters of interest are the pressure difference and the depth of the mineral wool insulation.

Measurements of the air flow of the self expanding sealing strips are shown in figure 3 for different cases as function of mean pressure difference. Similar to the mineral wool insulation, the flow direction was found to be practically insignificant.
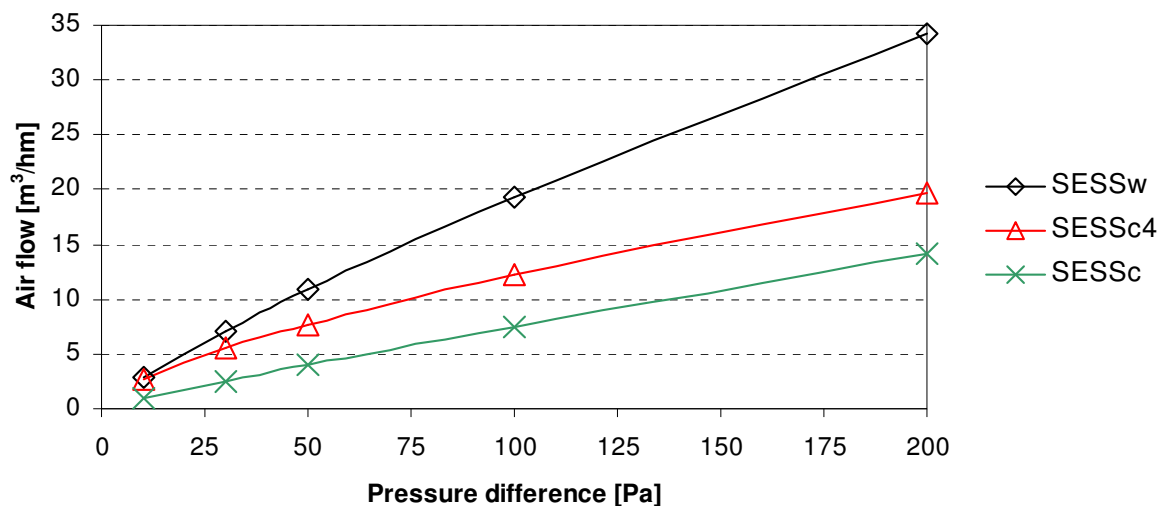

FIG. 3: Self expanding sealing strips, air flow [m³/hm] as function of pressure difference [Pa].

The air tightness of a joint sealed by a porous medium is very dependent on its density, as described for the case of mineral wool insulation by Birkeland and Wigen (1955). When a self expanding sealing strip of smaller size than recommended is used, this will affect the density. The consequences of this can be seen from figure 3 when comparing *SESSw* and *SESSc*. Wrongly chosen size of the strip, *SESSw*, results in a considerable increase in the air flow passing through the joint.

From curve fitting the ß-value for *SESSw* was found to be 0.83 indicating that the tiny wholes are of smaller importance to the total leakage thus implying the *material* leakage being an important contributor to the total leakage in this case. For *SESSc* a ß-value of 0.93 was found, and therefore indicates that the material leakage for this mounting is almost fully dominant. But when the 4 holes are introduced, *SESSc4*, the ß value reduces to 0.68 implying that the material leakages are not the only contributor to the total leakages. By introducing the holes it is evident from figure 3 that the air leakage increases as could be expected.

4.2 Backer rod, tape and wind barrier strips

For the backer rod, tape and wind barrier strips only highlights are listed here. For further discussion, reference is given to Relander (2007).

The ß values of the continuous backer rod, *BRc* and the piecewise *BRn-c* were found to be 0,54 and 0,48 respectively. The value of 0,48 must be interpreted as a result of the so-called *predictive uncertainty* in connection with the curve fitting, and therefore both values must be considered approximately 0,5 (Etheridge and Sandberg, 1996). This indicates that the air flow is through the corners for both mountings, and that the material itself can be considered air tight. At 50 Pa mean pressure difference it was found that *BRc* was about 30 percent less air tight than *BRn-c*. This is due to more open corners for *BRc*.

Tape, *T*, was found to be the unquestionable tightest material tested and *no* measurable leakage was found. Therefore the effect of holes in the corners, *T1, T2* and *T3,* dramatically increased the air flow. Since the holes were of the same size, it was possible to measure a linear relation between the air flow and number of holes.

For the wind barrier strips, *WB*, the air leakage increased as the pressure difference rose for both over- and underpressure. For practically all pressure differences the air flow was found to be larger for overpressure than for underpressure. This reflects the fact that the battens and the thinner battens opened for overpressure, whereas they were closing for underpressure. This is also in accordance with results found in Sagen (2003).

4.3 Vapour barriers
Table 1 shows measured air flow [m^3/hm] at 50 Pa pressure difference for both over- and underpressure and the mean values for cases *VB* and *VBp-i* at different nail distances.

TABLE 1: Cases VB and VBp-i. Air flow at 50 Pa pressure difference at over- and underpressure and mean. Indexes o, u and m refer to overpressure, underpressure and mean respectively. Nail distance in mm.

	Overpressure			Underpressure			Mean
	q_0	α_o	β_o	q_u	α_u	β_u	q_m
VB cc 600	2.25	0.208	0.61	3.05	0.11	0.85	2.65
VB cc 300	1.63	0.11	0.70	1.82	0.08	0.80	1.72
VB cc 150	1.27	0.08	0.70	1.29	0.06	0.79	1.28
VBp cc 600	6.46	1.08	0.46	7.46	0.83	0.56	6.96
VBps cc 600	6.12	1.09	0.44	7.15	0.77	0.57	6.64
VBps cc 300	2.24	0.10	0.80	2.29	0.09	0.82	2.27

From table 1 it is evident that the regular mounting is more air tight than the pulled-in variant for any flow direction. This can be explained with reference to figure 2 a) and b) showing that the jamb liner causes the angle of the vapour barrier to be steeper for *VBp-i* than for *VB*. In turn, this induces the holes in the corners to be bigger for *VBp-i* than for *VB*. Therefore the air flow is bigger for *VBp-i* than for *VB*. The difference between *VBp-is cc 600* and *VBp-i cc 600* also indicates that little air is escaping through the corners of the casings, but rather under the casings.

The nail distance is also a parameter influencing the air flow through the joint. For the regular variant, with measurements at nail distances 600 mm, 300 mm and 150 mm, this effect can be further investigated. Figure 4 shows the air flow for *VB* as function of distance between the nails for different pressure differences.

As expected, the air flow increases as the pressure difference rises for both over- and underpressure. The effect is more clear for the underpressure than for the overpressure. As the distance between the nails increases, the effect of opening and closing is further clarified. This ascribes from the fact that the casings open for the underpressure and closes for the overpressure. This is analogous to the conditions observed with the wind barrier strips.
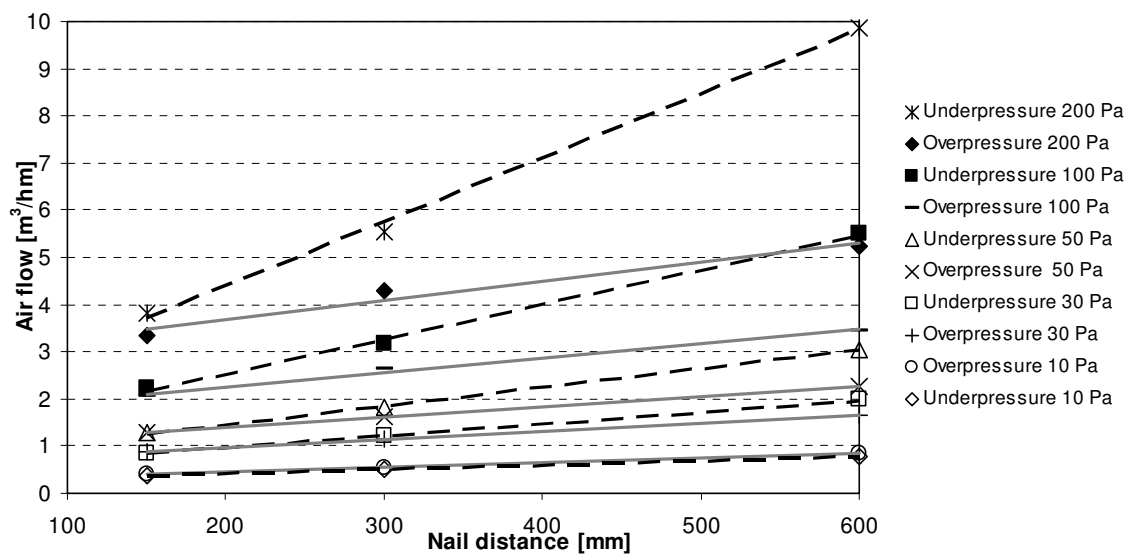

FIG. 4 Case regular variant. Air flow [m³/hm] for different pressure differences [Pa] as function of nail distance [mm]. Dotted and solid curves represent under- and overpressure, respectively.

Laboratory measurements of vapour barriers have also been conducted by Johansson (2004). Johansson did not measure the air flow *through* the joints of the window. This therefore complicates a direct comparison. However, Johansson found that the holes in the corners increase the air flow. This can also be seen here from the difference between *VBp-i* and *VB*.

5. Conclusions

Table 2 shows a ranking of all sealing methods in ascending order by air flow [m^3/hm].

TABLE 2 Ranking in ascending order of all 7 sealing techniques. Mean values of the air flow [m^3/hm] at 50 Pa mean pressure difference. For quicker comparison between the sealing techniques in general, abbreviations are indicated from the third column and used in columns indicating the leakages.

Ranking	Sealing technique	Abbreviation	Leakage at 50 Pa pressure difference [m^3/hm]						
			T	SESS	BR	WB	VB	VBp-i	M
1	Tape	*T*	0						
2	Wind barrier strips	*WB*				0.31			
3	Tape, one hole	*T1*	0.93						
4	Backer rod, non-continuous	*BRnc*			0.97				
5	Backer rod, continuous	*BRc*			1.24				
6	Vapour barrier, nail distance 150 mm	*VB cc 150*					1.28		
7	Mineral wool 150 mm	*M 150*							1.49
8	Vapour barrier, nail distance 300 mm	*VB cc 300*					1.72		
9	Tape, two holes	*T2*	1.74						
10	Mineral wool, 100 mm	*M 100*							2.09
11	Vapour barrier, pulled in, nail distance 300 mm, sealed corners	*VBp-is cc 300*						2.27	
12	Tape, 3 holes	*T3*	2.45						
13	Vapour barrier, nail distance 600 mm	*VB cc 600*					2.65		
14	Self expanding sealing strip correct size	*SESSc*		3.93					
15	Mineral wool 50 mm	*M 50*							4.03
16	Vapour barrier, pulled in, nail distance 600 mm, sealed corners	*VBp-is cc 600*						6.64	
17	Vapour barrier, pulled in, nail distance 600 mm	*VBp-i cc 600*						6.96	
18	Self expanding sealing strip correct size, 4 holes	*SESSc4*		7.72					
19	Self expanding sealing strip wrong size	*SESSw*		10.87					

From table 2 it is evident that tape was the tightest sealing technique measured. Tape therefore is vulnerable to faulty workmanship. Tape is a time-saving sealing technique. The benefit of tape with high adherence over time should therefore be obvious.

When sealing the joint with a backer rod, the measurements show that the non-continuous, piecewise mounting will be the tightest. However, improved air tightness performance will be expected when combining backer rod with sealing mastic. Taking a possible loss of adherence of the joint-filler with time into account, the comparison of the two mountings can be of interest.

For the case with vapour barriers, table 2 shows that the regular mounting is the tightest due to the smaller openings of the corners. When the pulled-in variant is used, the corners should be sealed using for instance vapour barrier tape.

For the self expanding sealing strip measured *here*, it was found that if correctly mounted it gave practically the same air tightness as 50 mm of mineral wool insulation. Nevertheless if the self expanding sealing strip is used, one should, according to the measurements, be careful selecting strips in accordance with the size of the joint.

There were substantial deviations in the air tightness of the sealing techniques tested. Tape was the most air tight and self expending sealing strip was the least air tight. These two differ by 10.87 m^3/hm. Large deviations among different sealing techniques were also found by Proskiw (1994).

6. Acknowledgements

7. References

Birkeland, Ø. and Wigen, R. (1955). Fuge mellom karm og vegg. Forsøk med lufttetthet av dyttefuger og fuger uten dytt, bind 1 (Joint between frame and wall. Laboratory measurements of the air tightness of joints filled with mineral wool and joints filled without mineral wool, volume 1, Norges Byggforskningsinstitutt, Oslo, Norway, in Norwegian

Etheridge, D.W. and Sandberg, M. (1996). Building Ventilation Theory and Measurement, John Wiley & Sons Ltd, West Sussex, England

Johansson, M. (2004). Air tightness in Buildings – a study of design and practical performance of construction details in the air tight layer in the building envelope, Master thesis, Department of Building Technology, Chalmers University of Technology, Gothenburg, Sweden (in Swedish)

Proskiw, G. (1994). Air leakage characteristics of various rough-opening sealing methods for windows and doors, Energy Technology Branch, CANMET – Energy Sector, Department of Natural Resources Canada, Ottawa, Ontario

Relander, T.O. (2007). Building design and air infiltration. The influence of window joints on air leakage, Master thesis, Department of Civil and Transport Engineering, Norwegian University of Science and Technology, Trondheim, Norway, (in Norwegian)

Relander, T.O. (2008). The influence of different sealing methods of window and door joints on the total air leakage of wood-frame buildings, submitted to Nordic Symposium on Building Physics 2008, Copenhagen

Sagen, V. (2003). The Air tightness of wind barriers depending on moisture and sealing technique of the battens – laboratory experiments, Department of Civil and Transport Engineering, Norwegian University of Science and Technology, Project report, Trondheim, Norway, (in Norwegian)

TEK (2007). Technical regulations under the planning and building act 2007, National Office of Building Technology and Administration Norway

Wind induced airflow through lightweight pitched roof constructions: Test roof element – measurements and model validation

Christoph Deseyve, Dipl.-Ing.,
Vienna University of Technology, Institute of Building Construction and Technology, Center of Building Physics and Building Acoustics;
email: christoph.deseyve@tuwien.ac.at, http://www.bph.tuwien.ac.at

Thomas Bednar, ao. Univ. Prof., Dr. techn., Dipl.-Ing.,
Vienna University of Technology, Institute of Building Construction and Technology, Center of Building Physics and Building Acoustics;
email: thomas.bednar@tuwien.ac.at, http://www.bph.tuwien.ac.at

KEYWORDS: compact pitched roof, wind tightness, windproof, airflow, glass fibre insulation, air tight, wind washing.

SUMMARY:
In the case of non ventilated compact roofs the wind tightness of the construction is usually warranted by a windproof underlay membrane and the flow resistance of the thermal insulation, as well as sealed eave and ridge details. Because of the current construction practice of wind tight layers in Austria there are numerous small leakages in the eaves, the ridge and the underlay area. Because of this and the low density and length of the thermal insulation in common Austrian constructions the wind induced pressure differences between the eaves and loft area cause an air flow which cancels the thermal insulating effect of the mineral wool partially or completely. During periods of high wind speed this leads however to uncomfortable low operative temperatures caused by an increased heat loss and lower surface temperatures. Based on different in-situ measurements (thermal performance and air propagation) a test roof element was constructed and implemented in a common slope of 45° in a climate chamber (hot box – cold box) to investigate different tightening measures and to validate a simulation model. In the paper the results from air flow and heat flow measurements of the test roof element variants are presented. Heat fluxes rise up to 900% of the stationary calculated values at the eaves with a ventilation duct at the warm side and wind speed of about 5 m/s (ΔP=33Pa) and up to 300% in fully insulated elements. The results lead to the validation of the 3 dimensional simulation tool HAM3D-VIE. HAM3D-VIE allows variation studies of the hydrothermal performance and comfort regarding to durability and construction practice auf lightweight constructions.

1. Introduction

As already shown in Deseyve & Bednar (2005 and 2006) pitched, light weight roofs with thermal insulation should be insulated air- and wind tight sandwich constructions. Otherwise the construction could cause inconvenient low surface and operative temperatures and uncommon high heat losses caused by wind washing. Wind washing means infiltration of the building envelope with cold outdoor air forced by temperature and pressure differences. Heat conduction seems to be just one of the factors causing heat transport, especially wind washing and wind and stack induced air flow through the building envelope insulated with mineral wool with low density are important factors. The most common building practice for light weight pitched roof constructions presently in Austria is the described compact system with no intended air flow in or above the thermal insulation. The air flow through and within the building envelope is a complex combination of different flows with some dominant factors. Riesner (2003) showed that there are some constrictive rotational flows in completely insulated roof constructions caused by the high air permeability of the thermal insulation. In Deseyve & Bednar (2006) is shown that standard Austrian light weight roof constructions have no significant effect of natural convection and that the dominant effect for the rising heat flux is the wind induced air flow. Following current construction practice different test roof elements were built to investigate the in-situ measured effects of the wind induced airflow and air patterns and to validate a simulation model to assess different building scenarios with different quality standards.

2. Test roof element

2.1 System description

The climate chamber is constructed out of 10 cm extruded polystyrene (XPS) 1.15 m wide, 3.95 m long and 3.80 m high as shown in figure 1. The temperature difference of up to 25 K is warranted by a refrigerator at the cold side and a heater mat at the warm side. The roof element is fixed on a wooden construction on the warm side with a slope of 45°. On the warm side as well as on the cold side ventilators ensure that there is no thermal layering. At the eaves and the ridge the airflow through the roof element is controlled by fans assembled in pipes. The air flow is recorded by hot wire anemometers. Pressure differences were measured between the airspace at the "eaves" and the airspace at the "ridge". The roof element was constructed following Austrian building practice for light weight roof constructions defined in table 1. The hot and the cold side are separated by the roof element and a vertical and a horizontal XPS element.
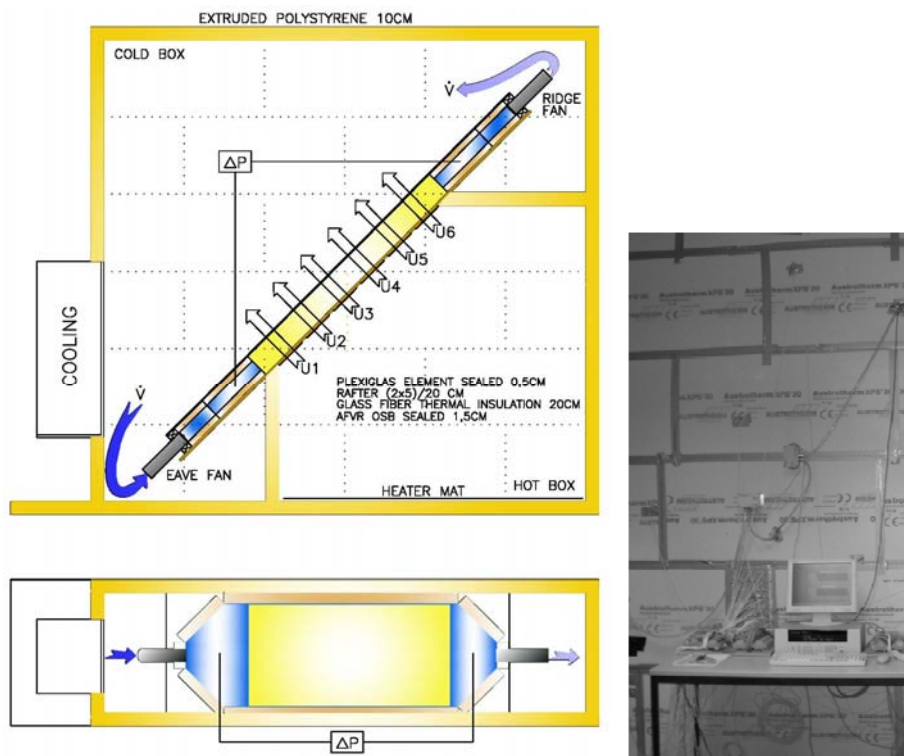

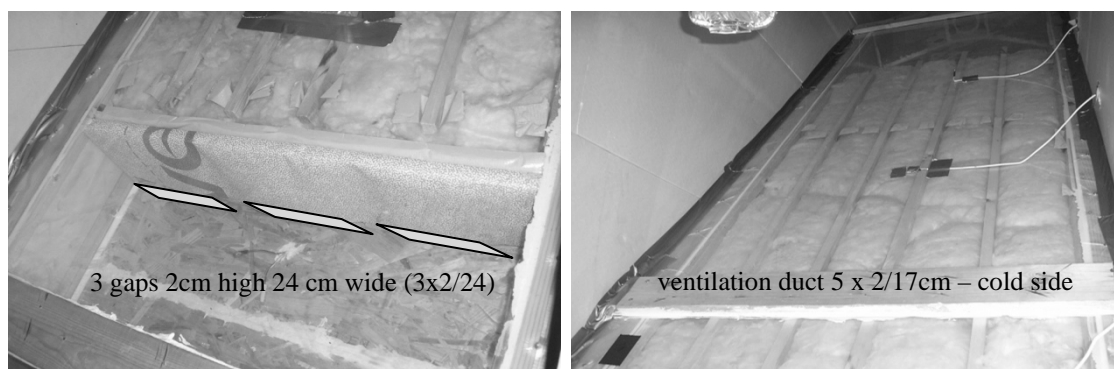*FIG.1: Cross section of the test roof element box & view of the test box - enclosure xps 10cm.*

FIG.2: Cold side of the test roof element – eave variation and air flow channel above the thermal insulation.

TABLE. 1: Construction definition.*

layer	d [m]	λ [$^W/_{mK}$]	ρ [$^{kg}/_{m^3}$]	c [$^J/_{kgK}$]	k_L [m²]
Acryl glass	0.010	0.190	1180	1440	0
Glass wool	0.200	0.038	14.5	1030	$9x10^{-9}$
OSB	0.015	0.130	600	1700	0

* U = 0,193 $^W/_{m^2K}$, k_L = air permeability in m²

The properties of air are assumed to η = dynamic viscosity in Pas = 17,1 x 10-6; ρ_L = air density in $^{kg}/_{m^3}$ according to the Boussinesq-Approximation, β = isobar volume expansion coefficient in $^{1/}_K$ = 3,7 x 10-3.

2.2 Measurement equipment

During the reference period air temperature (PT 1000, M-FK 222, Heraeus) and relative humidity (humichip, Vaisala) were measured at a few points in the air volume on both sides of the roof element. Surface temperature (PT1000) at different points, heat flows (heat flux measuring film, RdF, typ 20457) at the interior surfaces and pressure differences (halstrup & walcher, Delta_p) between the eaves and the ridge air space were monitored. The positions of the sensors are shown in Figures 1, 2, 3.

FIG.3: Hot side of the test roof element – heat flux measuring films and PT 1000.

2.3 Case specification

To be able to validate the simulation model according to different air flow patterns 7 different variations of a roof element were built. Thereby means "ventilation duct" a 20 mm wide air flow channel above or beneath the thermal insulation layer. The tightness variation of the eaves is secured by an underlay frame with 3 gaps 20 x 240 mm at the warm or the cold side as shown in figure 2.

TABLE. 2: Case specification.

Roof element	Thermal insulation		Ventilation duct		Eaves	Gap	Ridge/Attic
	material	size [cm]	situation	size [cm]	variation	size [cm]	
1	glasswool 14.5kg/m³	20	no duct	-	open	-	open
2	glasswool 14.5kg/m³	18	warm side	2	open	-	open
3	glasswool 14.5kg/m³	18	warm side	2	cold side	3 x 2/24	open
4	glasswool 14.5kg/m³	18	warm side	2	warm side	3 x 2/24	open
5	glasswool 14.5kg/m³	18	cold side	2	open	-	open
6	glasswool 14.5kg/m³	18	cold side	2	cold side	3 x 2/24	open
7	glasswool 14.5kg/m³	18	cold side	2	warm side	3 x 2/24	open

2.4 Test Results

Based on the insitu measured data (concerning the correlation between pressure distribution and wind speed) different pressure differences were applied to the roof element. At the stage of an almost steady state condition the heat fluxes were recalculated to U-values and compared with the insitu measured with different roof element variations. The dynamic heat loss coefficient U* in W/m²K was calculated according to Deseyve & Bednar (2005) to an hourly mean value [$U^*_{(t)} = q_{(t)}/(T_{i(t)} - T_{e(t)})$] (measurement error 5.4 %).
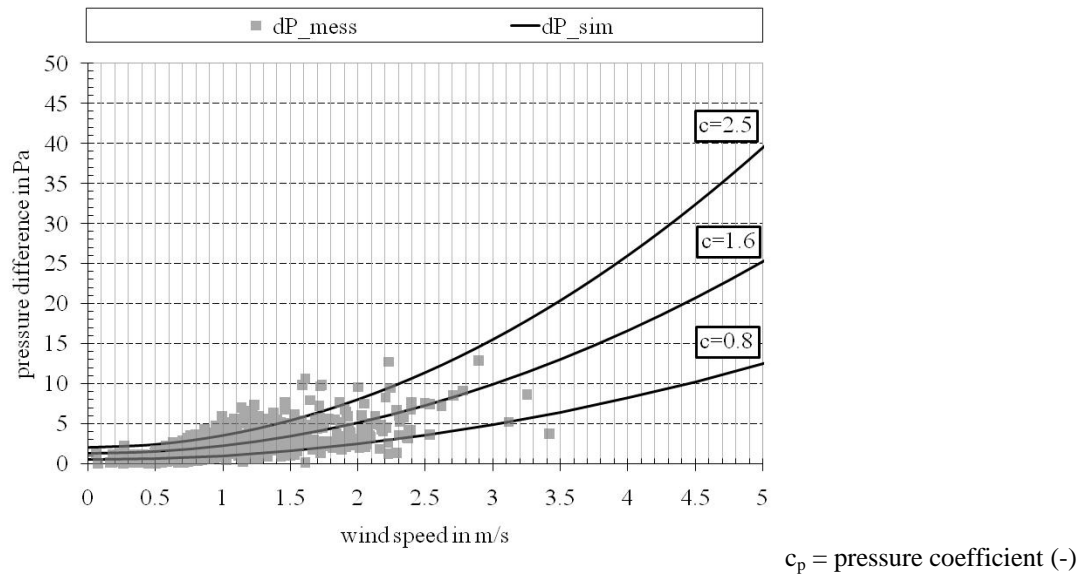
2.4.1 Basics

c_p = pressure coefficient (-)

FIG.4: Correlation between wind speed and pressure difference – Test roof and insitu – measurements Deseyve & Bednar (2006)

Figure 4 shows the correlation between the wind speed and the insitu measured pressure differences between the eaves and the attic (ridge) air space. For the further testing series regarding the pressure differences across the test roof element the values of the highest curve (c=2.5) where used to calculate the worst case.
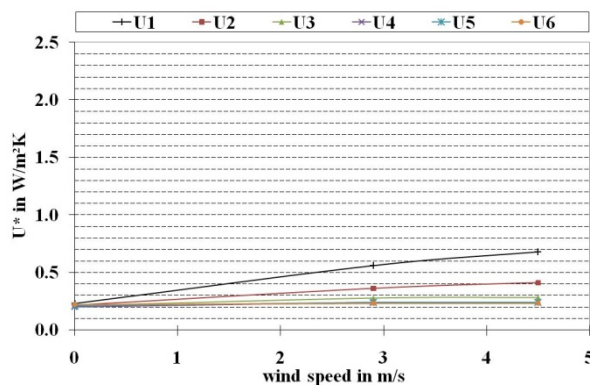
2.4.2 First Results

FIG.5: Test roof element 1- correlation between wind speed and current heat loss coefficient
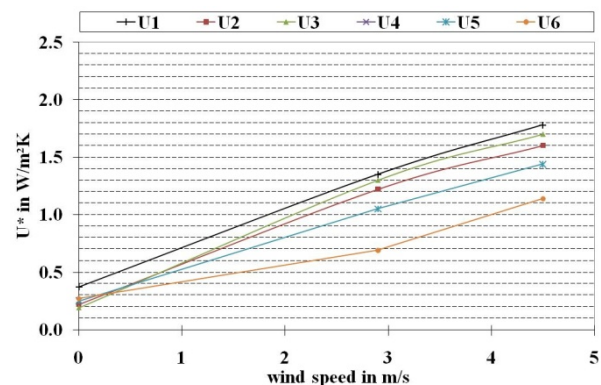
FIG.6: Test roof element 2- correlation between wind speed and current heat loss coefficient

Test roof element 1 (full filled thermal insulation) has an increase of the heat flux according to the wind speed as expected and shown in figure 5. The heat flux rose mostly at the eaves and the fewer the nearer to the ridge. The maximum U-value at a wind speed of 4.5 m/s (equals about 30 Pa pressure difference) was measured at the eaves up to 0.7 W/m²K.
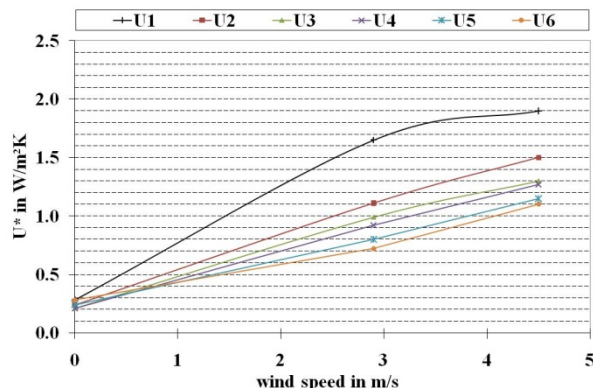
FIG.7: Test roof element 3- correlation between wind speed and current heat loss coefficient
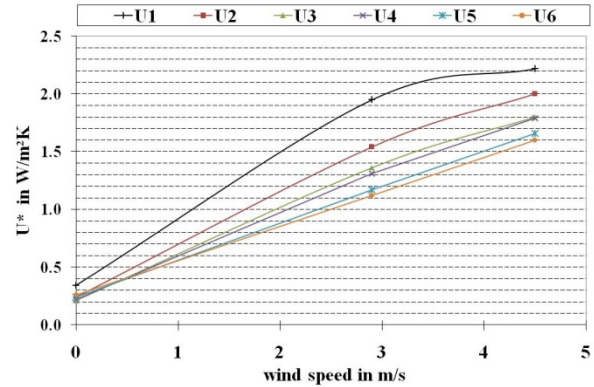

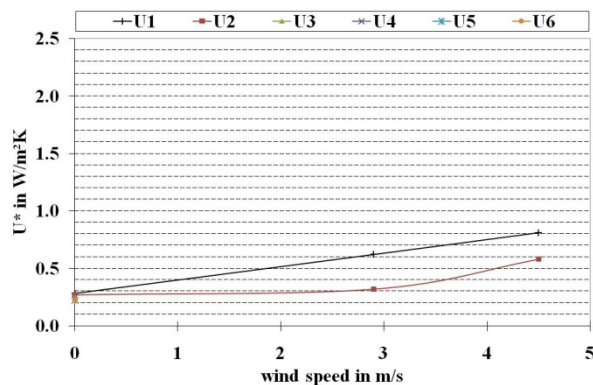FIG.8: Test roof element 4- correlation between wind speed and current heat loss coefficient

FIG.9: Test roof element 5- correlation between wind speed and current heat loss coefficient
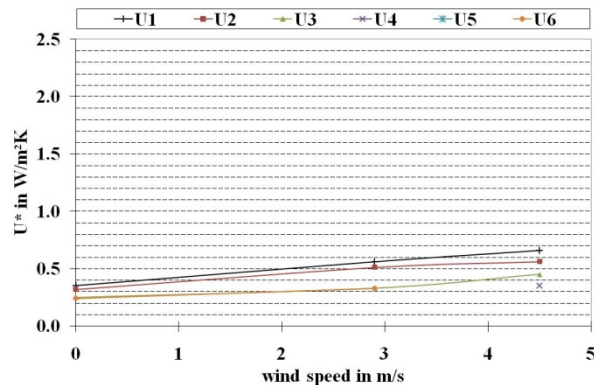

FIG.10: Test roof element 6- correlation between wind speed and current heat loss coefficient
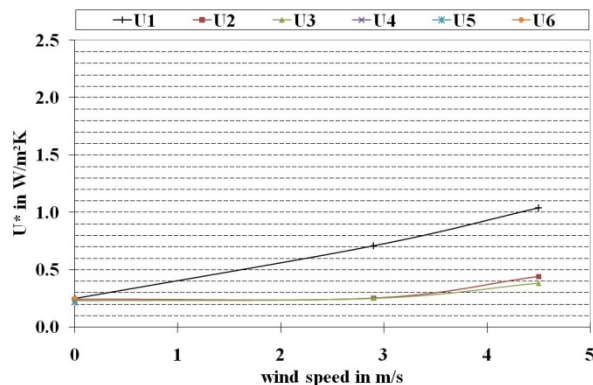

FIG.11: Test roof element 7- correlation between wind speed and current heat loss coefficient

As shown in figure 6 the duct at the warm side raised the heat flux and the U-value in correlation to the wind speed of 4.5 m/s up to 1.80 W/m²K. If we compare U1 of figure 6 to the run of U1 in figure 7 and 8 there is clearly shown that the routing of the air flow has an important impact too. Especially if the whole thermal insulation section is protected with the underlay and the air flow is directed in the duct as shown in figure 8. As we can see in figure 9 there is hardly any difference of the heat flux run whether there is no duct or the duct at the cold side. Figure 10, where the air is directed into the duct at the cold side, shows a better behaviour than the fully filled variant. Figure 11 shows the impact of the air flow routing in the same way as shown for elements 3 and 4 in figure 7 and 8. Most of the air is directly routed into the thermal insulation layer. This causes higher heat fluxes especially in the eaves area at higher wind speeds. The impact of the ventilation duct on the cold side is very small at the eaves and higher the longer the air is transported through the mineral wool (realation of resistance).

2.4.3   Relation to former insitu - measurements
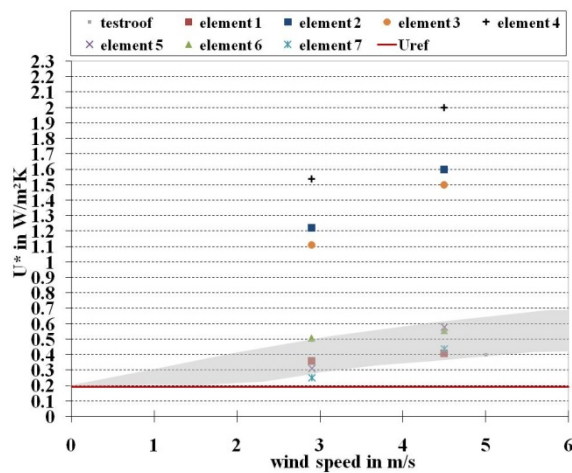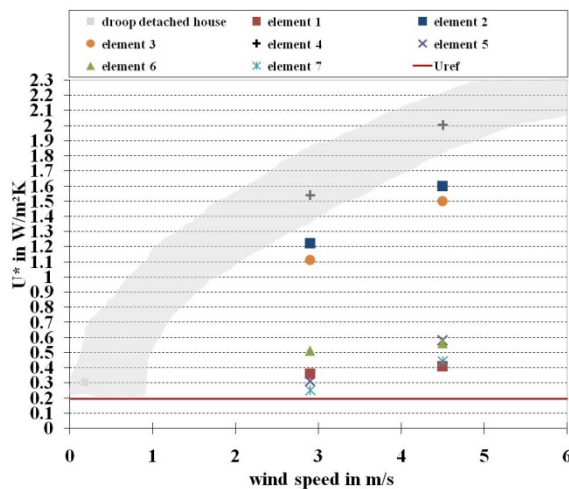
Correlation between wind speed and current heat loss coefficient – laboratory and insitu –measurements

FIG.12 according to Deseyve & Bednar (2005)   *FIG.13: according to Deseyve & Bednar (2006)*

Figure 12 shows the correlation between the rising U-value and the wind speed depending on different variations of duct and thightness level. The instu measured data of a light weight roof construction in different detached houses in Austria fit well to the laboratory measured U-values of the worst case test roof element. As we expected the values for element 4 fit very well to the insitu measured system There was a wind induced airflow under the thermal insulation form the eaves to the attic caused by the duct effect at higher pressure differences between the thermal insulation and the polyethylene foil (AFVR). The values are based on the situation of U2 as shown in figure 1.

Based on the reference data of the test roof figure 13 shows the wind dependent U-values of element 5, 6, 7 and 1 well fitting to the measured data according to Deseyve & Bendnar (2006).

All in all we can assume that the data obtain out of the test roof element are comparable to the insitu measured date and consequential we can use the measured data of the test roof element to validate HAM3d-VIE to calculate real buildings under real climate conditions.

3.   Simulation Model

3.1   Basics

The mathematical modelling for the three dimensional heat and moisture transport is based on the prEN 15026 (2004) and Bednar (2005) and considers moisture dependent heat conductivities, vapour diffusion and capillary forces but no air flow. The already existing program HMS (Bednar 2005) was adapted as described in 3.2 according to Deseyve & Bednar (2006) to simulate the combined heat, moisture and air transport (intrusion, infiltration or convection). For a first step only the pitched roof area was simulated with HAM3D-VIE to get data for the validation. During the simulation the measured values where used for the boundary conditions of the interior (hot box) and the ridge as well as the outdoor climate (cold box).

3.2   Air flow

For the calculation of air flow effects equation (1) according to Wang (2003) has been used. The air volume is simulated with an effective permeability of 3.5e-7 m² and a thermal conductivity of 0.025 W/mK.

$$q_a = \rho_a \frac{k}{\eta}\left[\nabla P_a + \rho_a g \beta \left(T - T_{ref}\right)\right] \qquad (1)$$

where q_a = mass flow rate in kg/(m²s), ρ_a = air density in kg/m³, k = air permeability in m², η = dynamic viscosity in Pas, ∇P_a = pressure gradient in Pa/m, g = gravity constant in m/s², ß = volume expansion coefficient in 1/K, T = temperature in K and T_{ref} = reference temperature in K. At the inlet and outlet the measured mass flow rate is used as a boundary condition.

3.3 Results

FIG.14: Test roof element 1- correlation between measured and simulated U-values – 0 Pa
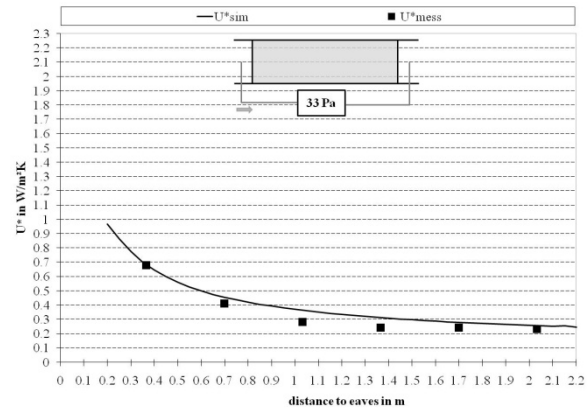
FIG.15: Test roof element 1- correlation between measured and simulated U-values – 33 Pa

As shown in figures 14 to 17 the simulated heat fluxes fit well to the measured values of the test roof element.
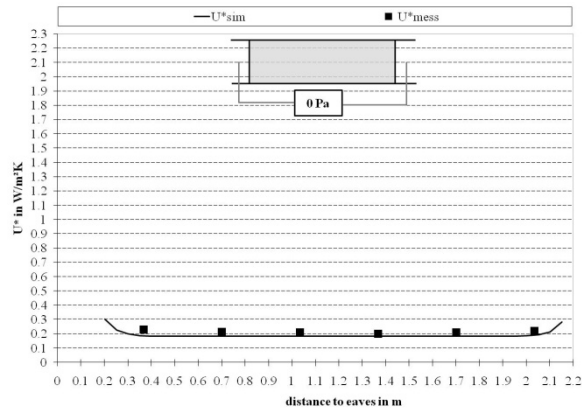

FIG.16: Test roof element 2- correlation between measured and simulated U-values – 0 Pa

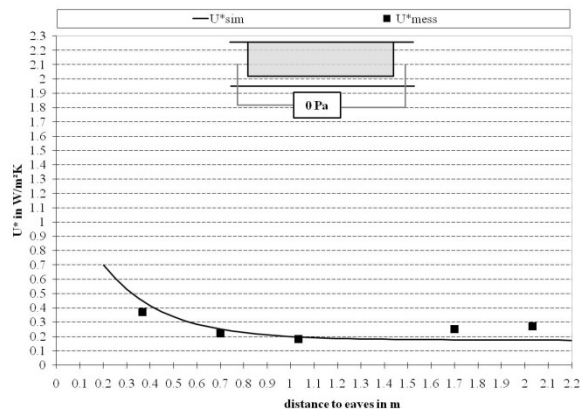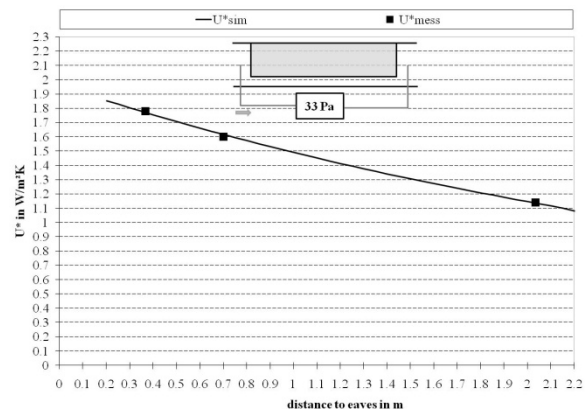

FIG.17: Test roof element 2- correlation between measured and simulated U-values – 33 Pa
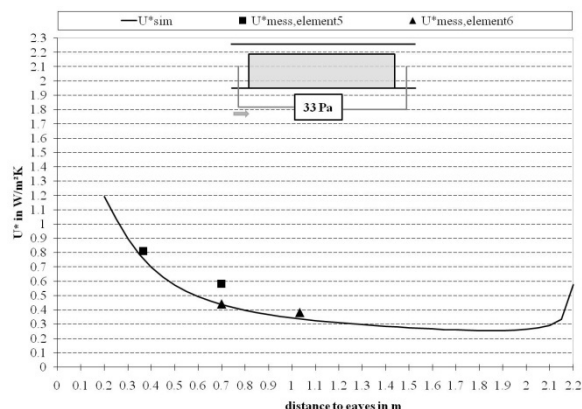

FIG.18: Test roof element 5,6 - correlation between measured and simulated U-values – 33 Pa

The simulation for the duct at the cold side (figure 18) correlate very well with the measured values for the eave variation of element 5 (open eave) near to the eave and ongoing to the ridge the simulated values fit to the measured data of element 6 (only a gap on the cold side – no airflow through the thermal insulation), so that we can assume that the flow resistance of the air duct is lower as we expected in relation to the flow resistance of the thermal insulation.

4. Conclusions

It is important to ensure that the thermal performance and the durability of light weight building envelopes. The heat fluxes of the fan forced air flow variants through the test roof element correlate with the insitu measurements of light weight roof constructions of detached houses. Heat fluxes rise up to 900% of the stationary calculated values at the eaves with a ventilation duct at the warm side and wind speed of about 5 m/s (ΔP=33Pa) and up to 300% in fully insulated elements. The measurements could be reproduced by the simulation tool HAM3D-VIE. HAM3D-VIE allows variation studies of the hydrothermal performance and comfort regarding to durability and construction practice auf lightweight constructions.In the next step the results of the case study with the validated simulation model should lead to construction recommendations to achieve a moisture tolerant roof construction without relevant wind induced heat losses as well as to coefficients for building codes concerning the additionally heat losses and the decrease of surface temperatures in relation to wind incidence.

5. Acknowledgements

6. References

Bednar, T. (2005). *Hygrothermische Gebäudesimulation. Modellentwicklung und Anwendung in der Neubau- und Sanierungsplanung.* Professorial dissertation. Vienna: Vienna University of Technology.

Deseyve, C. & Bednar, T. (2005). Increased Thermal Losses caused by Ventilation through compact Pitched Roof Constructions – In Situ Measurements. *Proceedings of the 7th Symposium on Building Physics in the Nordic Countries*. Vol. 2: 881-887. Reykjavik: The Icelandic Building Research Institute.

Deseyve, C. & Bednar, T. (2006). Wind induced thermal losses through compact pitched roof constructions – Test roof – measurements, simulation model und validation. *3rd International Building Physics Conference*. in Research in Building Physics and Building Engineering. 459 - 464. Taylor & Francis Group. Montreal: Concordia University.

prEN 15026 Draft. (2004). *Hygrothermal performance of building components and building elements – Assessment of moisture transfer by numerical simulation*. Brussels: European Committee for Standardization

Riesner, K. (2003). *Natürliche Konvektion in losen Außendämmungen – Untersuchungen zum gekoppelten Wärme-, Luft- und Feuchtetransport*. Dissertation, Rostock: Ingenieurwissenschaftliche Fakultät, Fachbereich Baukonstruktionen und Bauphysik, Universität Rostock.

Wang, J. (2003). *Heat and Mass Transfer in Built Structures – Numerical Analyses*. Dissertation, Göteburg: Department of Building Physics, Chalmers University of Technology.

Measurements and CFD simulations for the analysis of wind flow in a semi-enclosed stadium

Reinier Maas, MSc.
Eindhoven University of Technology, The Netherlands
r.p.w.maas@student.tue.nl

Jan Diepens, Ing.
Eindhoven University of Technology, The Netherlands
j.f.l.diepens@tue.nl

Bert Blocken, Dr. Ir.
Eindhoven University of Technology, The Netherlands
b.j.e.blocken@tue.nl

SUMMARY:
CFD simulations can be a powerful tool to investigate the relationship between stadium geometry and the wind flow pattern inside the stadium. The CFD model has to be validated to ensure reliable results. This paper presents a validation study by comparing the results of full-scale measurements and steady-state and transient CFD simulations of the wind flow pattern inside the Koning Boudewijn athletics stadium in Brussels. The comparison shows that transient CFD simulations are better able to predict the turbulent wind flow pattern inside the stadium compared to steady-state CFD simulations. Nevertheless, discrepancies remain, which are attributed to simplifications in model geometry and to the differences in inlet atmospheric turbulence between the measurements and the simulations.

1. Introduction

Stadium geometry determines to a large extent the type and strength of wind flow in semi-enclosed stadiums. Wind flow inside such a stadium can have a large effect on results of sports events. For example the wind resistance experienced by an athlete can have a large influence on the achievement during a track and field event (Hill; 1927, Pugh; 1970, Pugh; 1971, Davies; 1980, Linthorne; 1994, Mureika; 2001). It is therefore important to investigate the wind flow pattern inside a semi-enclosed sports stadium in the design stage. Guidelines, wind tunnel measurements and numerical simulations could be the onset for this investigation. However there are almost no guidelines available for designing the geometry of a semi-enclosed sports stadium with regard to stadium wind flow patterns. The few guidelines that are available are based on spectator comfort (John & Sheard; 2000). Wind tunnel measurements are labour-intensive and thus expensive (Kundu & Cohen; 2004, Blocken & Carmeliet; 2006). They also only provide a limited view of the wind flow pattern inside the wind tunnel model (Szucs; 2004, Bouyer et al; 2007). Numerical simulations with Computational Fluid Dynamics (CFD) on the other hand are only reliable when they have been made with a validated model (Blocken & Carmeliet; 2006). To the knowledge of the authors, no previous efforts on CFD simulations and validation of wind flow patterns inside sports stadiums have been reported.

The aim of this research is the validation of a numerical model for simulating the wind flow pattern inside a semi-enclosed sports stadium. The validated CFD model can be a powerful tool for optimizing stadium geometry with regard to the wind environment.

This paper presents a comparison between full-scale measurements and CFD simulations of the wind flow pattern inside the Koning Boudewijn stadium in Brussels, Belgium. In section 2, the full-scale measurement set-up and data processing procedures are briefly described. Section 3 presents the CFD simulations. Results are provided and discussed in Section 4. Section 5 (discussion and conclusions) concludes the paper.

2. Full-scale measurements

The first part of this research consists of full-scale measurements of the wind flow pattern inside the Koning Boudewijn stadium (Fig. 1). This stadium has been chosen because of its geometry, location and the willingness of the stadium authorities to co-operate in this research.

The outer dimensions of the stadium are approximately 300 m long, 200 m wide and 32 m high. The stadium consists of two rings with a total capacity of 50,000 seated spectators. The stands are divided in two parts which are separated by two large openings in the facade (Fig. 2). These openings are thought to have a large effect on the wind flow inside the stadium. This wind flow is known to change very suddenly during sports events.

Figure 1: Interior of the stadium. View from stand 1 (see Fig. 3).

Figure 2: Passage between stand 1 and 4 of the stadium (see Fig. 3).

2.1 Measurement set-up

The measurements have been carried out with ultrasonic anemometers. The measurement positions inside the stadium are placed at 1.75 m above ground level on the track and on the centre field (Fig. 3). A reference position is placed 10 m above the roof of stand 1 (Figs. 3 and 4). This position does not provide measurements of the undisturbed wind flow (KNMI; 2000, WMO; 2006), but only a measurement that can be used as a reference for the measurements inside the stadium.

The measurement at the reference position has been carried out with a 3D ultrasonic anemometer running continuously. The measurements inside the stadium have been carried out with two 3D and one 2D ultrasonic anemometer. These anemometers are placed on mobile posts in order to measure the wind flow pattern on different measurement positions during a measurement day (Fig. 5).

The measurements have been carried out during nine measurement days between January and March 2007. The amount of measurement days was limited due to the limited time available for this research and the scheduled events in the stadium. During the measurement days, the anemometers inside the stadium were placed for time intervals of approximately one hour at a certain measurement position after which they were placed on another position in order to obtain data at many positions.

2.2 Data processing and interpretation

The collected data were processed into 10-minute averages (KNMI; 2000, Blocken & Carmeliet; 2005, WMO; 2006). The averaged wind direction was derived out of the averaged components of the wind velocity vector. The averaged wind directions on the reference position were grouped in intervals of 10°.
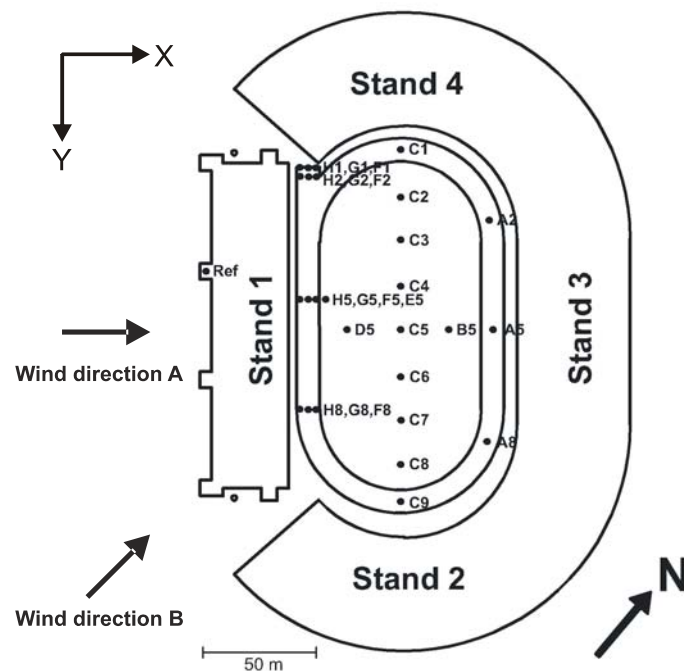
Figure 3: Measurement positions in the plan of the stadium. Wind directions A and B are used in both the steady-state and the transient CFD simulations.

Figure 4: Reference measurement with a 3D ultrasonic anemometer elevated 10 m above the roof of stand 1 of the stadium.
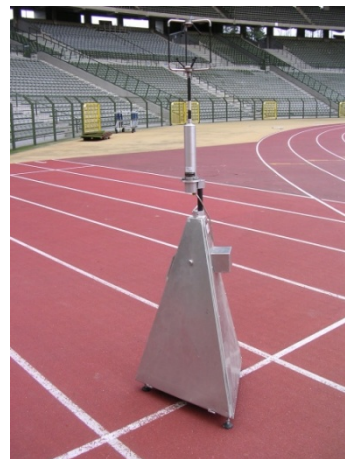
Figure 5: Measurement inside the stadium with a 3D ultrasonic anemometer placed on a mobile post.

The 10-minute averages did not provide a clear and unambiguous view of wind flow patterns inside the stadium. This is probably due to the large scale instationary flow features around and inside the stadium and the large time delay between the measured wind flow at the reference position and the resulting wind flow measured inside the stadium. The latter is caused by the time it takes for the wind to travel from the upstream reference position to the positions inside the stadium. To reduce the influence of the time delay, 60-minute averages (Van der Hoven; 1956) and 10-minute averages belonging to large wind speeds (> 6 m/s) at the reference position were calculated. These showed little improvement with regard to obtaining clear wind flow patterns inside the stadium. On the other hand, averaging the 10-minute averages per measurement position can produce clearer and useful wind flow patterns inside the stadium.

3. CFD simulations

The second part of this research consists of CFD simulations of the wind flow pattern inside the stadium. The numerical model formed the basis for steady-state and transient simulations.

3.1 Numerical model

A 3D model was constructed based on guidelines for simulating wind flow in the urban environment (Blocken & Carmeliet; 2004, Bartzis et al; 2004, Kundu & Cohen; 2004, Fluent; 2006, Blocken et al; 2007, Franke et al; 2007). The geometry of the urban environment surrounding the stadium was simplified in the model by the use of an aerodynamic roughness length y_0 (Wieringa; 1992). The grid was based on grid sensitivity analysis and resulted in a final grid of 2,049,463 cells (Fig. 6).
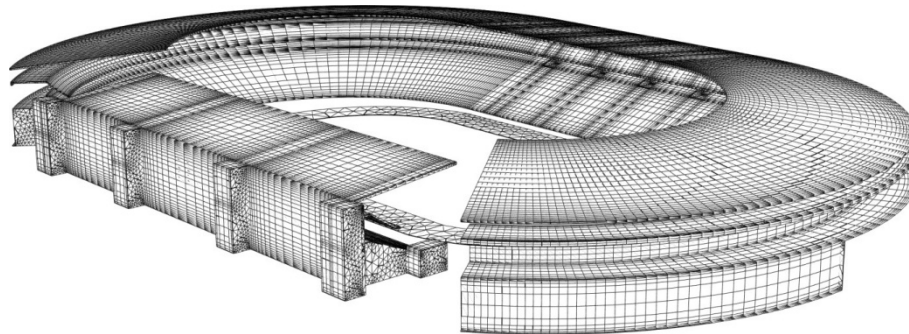

Figure 6: Grid of the stadium.

The boundary conditions used in the model are 'wall' for the geometry of the stadium, 'symmetry' for the upper and side boundaries of the domain, 'pressure outlet' for the outlet of the domain and 'velocity inlet' for the inlet of the domain. The inlet flow was a log-law with an aerodynamic roughness length $y_0 = 1$ m (Wieringa; 1992) and a reference wind speed at a height of 10 m $U_{10} = 10$ m/s. The roughness length was estimated based on the topographic map of the surroundings. Turbulence intensity ranged from 45% near ground level to 10% at gradient height. Calculations were made for two different wind directions. Wind direction A is perpendicular to Stand 1 and wind direction B has a 45° deviation from wind direction A (Fig. 3).

The simulations have been made with the commercial CFD code Fluent 6.3.26. The segregated solver was used with implicit linearization and second order discretization. Pressure-velocity coupling was calculated via the SIMPLE scheme for the steady-state simulations and via the PISO scheme for the transient simulations (Fluent; 2006).

3.2 Steady-state simulations

The steady-state simulations were performed with different turbulence models to compare their performance. The turbulence models under investigation were the Spalart-Allmaras model, Standard k-ε model, RNG k-ε model, Realizable k-ε model, Standard k-ω model, SST k-ω model and the Reynolds Stress model. It was impossible to obtain convergence with the Reynolds Stress model on this complicated grid. The standard k-ω model reached convergence with first order discretization only.

3.3 Transient simulations

The measurements indicate large-scale instationary behaviour of the turbulent wind flow pattern around and inside the stadium. Transient simulations could be able to predict this behaviour (Martinuzzi & Havel; 2004, Fluent; 2006). The frequency of vortex shedding is dependent on the characteristics of the stadium wind flow pattern and the geometry of the stadium (Kundu & Cohen; 2004). This can be expressed using the Strouhal number and the Reynolds number (Roushan & Wu; 2005, Ponta & Aref; 2004). The separation of vortices in flows around beams and rectangular objects is determined by the location of the edge of the object (Ozgoren; 2006). These geometries have a characteristic Strouhal number between 0.12 and 0.16 (Sarioglu & Yavuz; 1999). The time step and duration of simulation are based on the frequency of vortex shedding, which is based on the Strouhal number, the flow characteristics (based on the steady-state simulations) and the geometry of the

stadium. A time step of 0.15 s is used based on a minimum period of vortex shedding of 3 s. An initial duration of simulation of 150 s based on a maximum period of vortex shedding of 50 s is used in order to fill up the stadium with vortices, and to provide "initial conditions" for the part of the simulations that will be retained for analysis. A second duration of simulation of 100 s is used to collect data for comparison with the measurements. The transient simulations have been carried out using Detached Eddy Simulation (DES). This method combines transient RANS and LES (Fluent; 2006). The inlet flow is similar to the inlet flow used in the steady-state simulations. This means that a steady-state inlet flow is used with the transient simulations. Variations in the wind flow pattern inside the model can therefore only be caused by building generated turbulence (vortex shedding).

4. Results

4.1 Steady-state simulations versus measurements

The results from the simulations with the different turbulence models are compared to the results from the measurements (averages per measurement position of the 10-minute averages). This shows that the results from the simulations with the different turbulence models generally did not show large differences (Figs. 7 and 8). It also shows that the general qualitative and quantitative agreement between the measurements and the steady-state simulations is rather poor (Figs. 7 and 8). Model improvements to obtain a better resemblance between the model and reality (including horizontal homogeneous ABL over uniformly rough terrain (Blocken et al; 2007), detailed geometry, porous objects) did not provide significantly better results in this case.
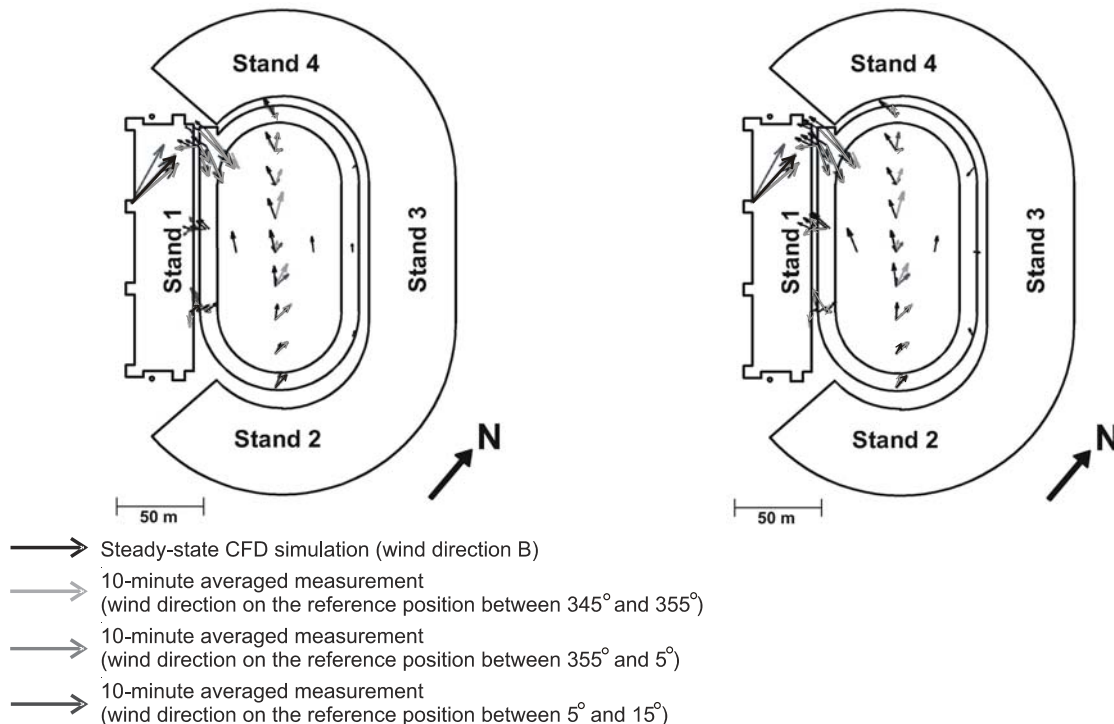
Figure 7: Measurements versus steady-state CFD results with the Spalart-Allmaras turbulence model.   *Figure 8: Measurements versus steady-state CFD results with the Realizable k-ε turbulence model.*

4.2 Transient simulations versus measurements

The transient simulations with DES showed large-scale instationary behaviour of the wind flow pattern inside the stadium (Fig. 9). A clear comparison with the measurements was hindered because it proved to be difficult to compare the two sets of transient data because of the superposition of various sources of instationary behaviour. Therefore the results from the measurements and the transient simulations are compared with regard to the general behaviour of the flow.
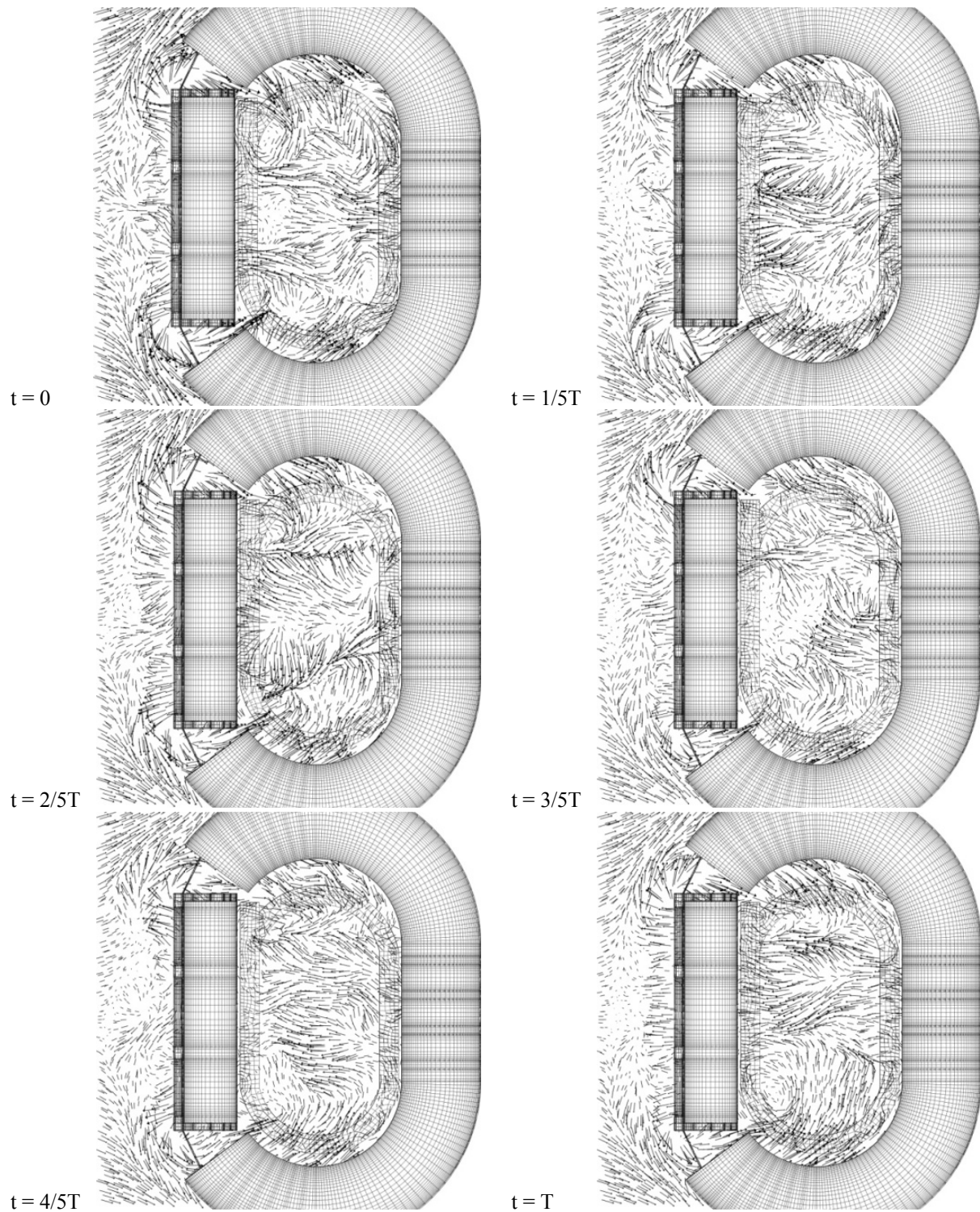
Figure 9: Wind velocity vectors illustrating the transient wind flow pattern at 1.75 m above ground level during one maximum period (T_{max} = 50 s). Transient CFD simulation with DES with wind direction A.

A representation of the instantaneous data at measurement position C5 (Fig. 3) is made by plotting the components of the wind velocity in the horizontal plane (u-component in x-direction and v-component in y-direction (see Fig. 3 for coordinate system)) (Figs. 10 and 11). Both the results from the transient simulation (wind direction B) and the measurements (wind direction at the reference position between 355° and 5° from north, equal to wind direction B) are plotted.

Figures 10 and 11 show that the results from the measurements fluctuate with a higher frequency than the results from the transient simulation. An explanation for this can be found in the steady-state inlet flow that is used in the transient simulations. The turbulent wind flow pattern upstream of the stadium is thought to be responsible for this higher frequency of fluctuation in the results of the measurements.

u-component of the wind velocity at measurement position C5   v-component of the wind velocity at measurement position C5

—— Transient simulation with DES
·········· Measurement

Figure 10: u-component of the wind velocity at C5. Comparison between the measurements (wind direction at the reference position between 355° and 5° from north, equal to wind direction B) and the transient CFD simulation (wind direction B).
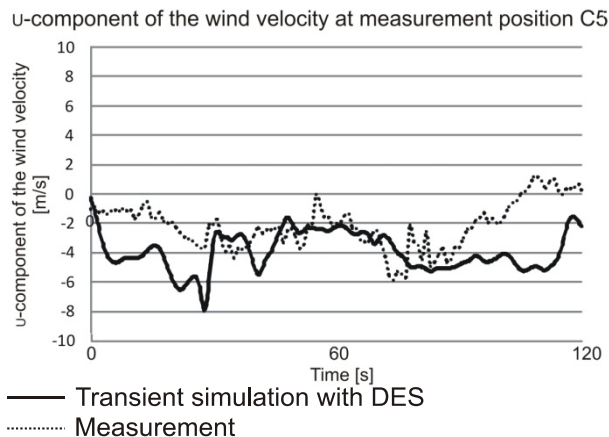
Figure 11: v-component of the wind velocity at C5. Comparison between the measurements (wind direction at the reference position between 355° and 5° from north, equal to wind direction B) and the transient CFD simulation (wind direction B).
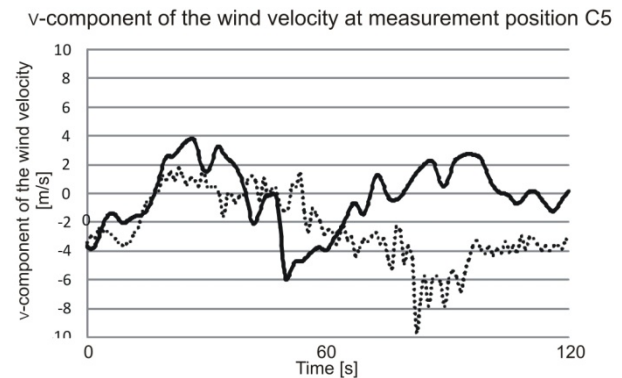
5. Discussion and conclusions

The goal of this research was to validate a numerical model for simulating the wind flow pattern inside a semi-enclosed sports stadium and in particular the Koning Boudewijn stadium. Therefore full-scale measurements were compared with steady-state and transient CFD simulations. The full-scale measurements showed large-scale instationary behaviour of the turbulent wind flow pattern inside the stadium. This behaviour can only be captured with transient CFD simulations.

The comparison between the measurements and the simulations showed large differences in the results. These can be caused by the simplifications made in constructing the CFD model. For example the simplified modelling of the urban environment surrounding the stadium with an aerodynamic roughness length y_0 and the use of a steady-state inlet flow and the fact that thermal effects were neglected.

For the validation of a CFD model for simulating the wind flow pattern inside a semi-enclosed sports stadium, further research is necessary. This includes full-scale measurements in several semi-enclosed sports stadiums. These measurements have to be executed for longer periods to include a wide range of circumstances. They also have to be done at various locations throughout these stadiums to obtain a clear overview of the wind flow patterns inside these stadiums.

Further CFD simulations include adding a transient inlet flow, explicitly modelling the urban environment and adding thermal effects. A validated CFD model for simulating the wind flow pattern inside a semi-enclosed sports stadium can be used as a powerful tool for optimizing the stadium geometry with respect to stadium wind flow patterns.

6. Acknowledgements

The technical assistance by Wout van Bommel and Geert-Jan Maas, members of the Laboratory of the unit Building Physics and Systems at Eindhoven University of Technology, is very much appreciated.

7. References

Bartzis J.G., Vlachogiannis D. and Sfetsos A. (2004). Thematic area 5: best practice advice for environmental flows, The QNET-CFD Network Newsletter, Vol. 2, 34 – 39.

Blocken B. and Carmeliet J. (2004). Pedestrian wind environment around buildings: Literature review and practical examples, Journal of Thermal Envelope and Building Science, Vol. 28, No. 2, 107 – 159.

Blocken B. and Carmeliet J. (2005). High-resolution wind-driven rain measurements on a low-rise building – experimental data for model development and model validation, Journal of Wind Engineering and Industrial Aerodynamics, Vol. 93, 905 – 928.

Blocken B. and Carmeliet J. (2006). An introduction to CFD in wind engineering, College sheets, Technische Universiteit Eindhoven, Katholieke Universiteit Leuven.

Blocken B., Stathopoulos T. and Carmeliet J. (2007). CFD simulation of the atmospheric boundary layer – wall function problems, Atmospheric Environment, Vol. 41, Issue 2, 238 – 252.

Bouyer J., Vinet J. and Carré S. (2007). Thermal comfort assessment in semi-outdoor environments: Application to comfort study in stadia, Journal of Wind Engineering and Industrial Aerodynamics, Vol. 95, 963 – 976.

Davies C.T.M. (1980). Effects of wind assistance and resistance on the forward motion of a runner, Journal of Applied Physiology, Vol. 48, 702 – 709.

Fluent Inc. (2006). FLUENT 6.3 user's guide, Fluent Inc., Lebanon.

Franke J., Hellsten A., Schlünzen H. and Carissimo B. (2007). Best practice guideline for the CFD simulation of flows in the urban environment, COST Action 732.

Hill A.V. (1927). The air resistance to a runner.

John G. and Sheard R. (2000). Stadia: a design and development guide, Architectural Press.

Kundu P.K. and Cohen I.M. (2004). Fluid mechanics, Elsevier Academic Press.

KNMI. (2000). Handboek waarnemingen, KNMI.

Linthorne N.P. (1994). The effect of wind on 100 m sprint times, Journal of Applied Biomechanics, Human kinetics publishers Inc., 110 – 131.

Mureika J.R. (2001). The legality of wind and altitude assisted performances in the sprints, arXIV, Physics.

Ozgoren M. (2006). Flow structure in the downstream of square and circular cylinders, Flow Measurement and Instrumentation, Vol. 17, 225 – 235.

Ponta L.P. and Aref H. (2004). Strouhal-Reynolds number relationship for vortex streets, Physical Review Letters, The American Physical Society, Vol. 93, No. 8.

Pugh L.G.C.E. (1970). Oxygen intake in track and treadmill running with observations on the effect of air resistance, Journal of Physiology, 823 – 835.

Pugh L.G.C.E. (1971). The influence of wind resistance in running and walking and the mechanical efficiency of work against horizontal or vertical forces, Journal of Physiology, 255 – 276.

Roushan P. and Wu X.L. (2005). Structure-Based Interpretation of the Strouhal-Reynolds Number Relationship, Physical Review Letters, Vol. 94.

Sarioglu M. and Yavuz T. (1999). Vortex Shedding From Circular and Rectangular Cylinders Placed Horizontally in a Turbulent Flow, Turkish Journal of Engineering & Environmental Sciences, Vol. 24, 217 – 228.

Szucs A. (2004). Stadia in the environment – environment in stadia, Proceedings of the 21st International Conference of Passive and Low energy Architecture (PLEA), Eindhoven, The Netherlands, 169 – 174.

Van der Hoven. (1956). Power spectrum of horizontal wind speed in the frequency range from 0.0007 to 900 cycles per hour, Journal of Meteorology, Vol. 14, 160 – 164.

Wieringa J. (1992). Updating the Davenport roughness classification, Journal of Wind Engineering and Industrial Aerodynamics, Vol. 41 & 44, 357 – 368.

WMO. (2006). Guide to metereological instruments and methods of observation, WMO, No. 8.

Results of measured and simulated hygrothermal loads acting on mineral fiber insulation suggest a revision of durability test

D. Zirkelbach, Dipl.-Ing.
Department of Hygrothermics, Fraunhofer-Institute of Building Physics;
daniel.zirkelbach@ibp.fraunhofer.de, www.bauphysik.de

H. M. Künzel, Dr.-Ing.,
Head of Department of Hygrothermics, Fraunhofer Institute of Building Physics;
hartwig.kuenzel@ibp.fraunhofer.de

Ch. Bludau, Dipl.-Ing.,
Department of Hygrothermics, Fraunhofer Institute of Building Physics;
christian.bludau@ibp.fraunhofer.de

SUMMARY:
Flat roofs with dark membranes experience higher thermal loads than most other building components. To increase also the moisture loads in the roof two litres of water per m² were inserted to a test roof on the field test site of the Fraunhofer IBP in Holzkirchen. The measured conditions in the roof serve to validate hygrothermal simulations which allow transfer the test to colder and warmer regions in Europe. As result the maximum temperature and moisture conditions and their coincidence occuring in an insulation layer of a building envelope in Europe can be determined. These results are compared to the climate conditions of current test procedures to determine the durability of mineral fibre insulation materials. The rather extreme temperatures and humidities (above 60 or 70 °C and 95 to 100 % RH) applied during these tests lead to a significant reduction of the tensile and compressive strength of glass fibre materials which cannot be observed in real life. Neither in the insulation layer of an ETICS - which was subject of earlier investigations - nor in the flat roof insulation layer such combinations of high temperature and RH were detected. A test procedure shall accelerate the normal degradation process but not make fail a solution which performs well in reality. Therefore a new test procedure is proposed which is closer to the real maximum conditions and should therefore lead to a more realistic performance assessment of the insulation material.

1. Introduction

Due to solar radiation and night time sky radiation flat roofs with dark roofing membranes experience higher thermal loads than other building components. Therefore this construction type was chosen to evaluate extreme hygrothermal conditions in mineral fibre insulations by the help of a field test and hygrothermal simulations. To increase the moisture content in the roof two litres of water per m² were inserted to the test roof on the field test site of the Fraunhofer IBP in Holzkirchen before closing the construction. The measured conditions in the roof serve to validate hygrothermal simulations and allow in a second step to "transfer" the test roof to other locations in Northern and Southern Europe. As result of this transfer the maximum temperature and moisture conditions and their coincidence occuring in an insulation layer of a building envelope in Europe can be determined.

These results are compared to the climate conditions of current test procedures to determine the durability of mineral fibre insulation materials. The rather extreme temperatures and humidities (above 60 or 70 °C and 95 to 100 % RH) applied during these tests lead to a significant reduction of the tensile and compressive strength of glass fibre materials which cannot be observed in real life. Aim of this study is therefore to determine test conditions that allow an acceleration of the natural aging process without damaging the insulation product in a way that will never occur in reality. The testing conditions have to be backed up by results from field tests and validated hygrothermal simulations to develop the basis for new test methods with more realistic temperature and humidity conditions.

2. Investigations

2.1 Field test

Subject of this study are the measured and simulated hygrothermal conditions in an insulated flat roof with the following composition from inside to outside:

- Load bearing wooden sheathing

- Vapour barrier (aluminium foil, sd > 1500 m)

- Insulation layer: 90 mm respectively 175 mm glass fibre boards

- Impermeable roofing membrane (elastomer bitumen)

A foto of the test roof in Holzkirchen and a schematic drawing of the roof construction with the measurement positions is displayed in Fig. 1. The placement of the sensors at the positions where peak loads are expected has been selected according to preliminary calculations. The temperature measurements are performed by using PT100 temperature sensors. The relative humidity is determined by capacitive sensors. Prior to the installation, all sensors are calibrated in the laboratory. The roof was set up at the field test site of the Fraunhofer Institute for Building Physics (IBP) in Holzkirchen (South Germany) in August 2006.
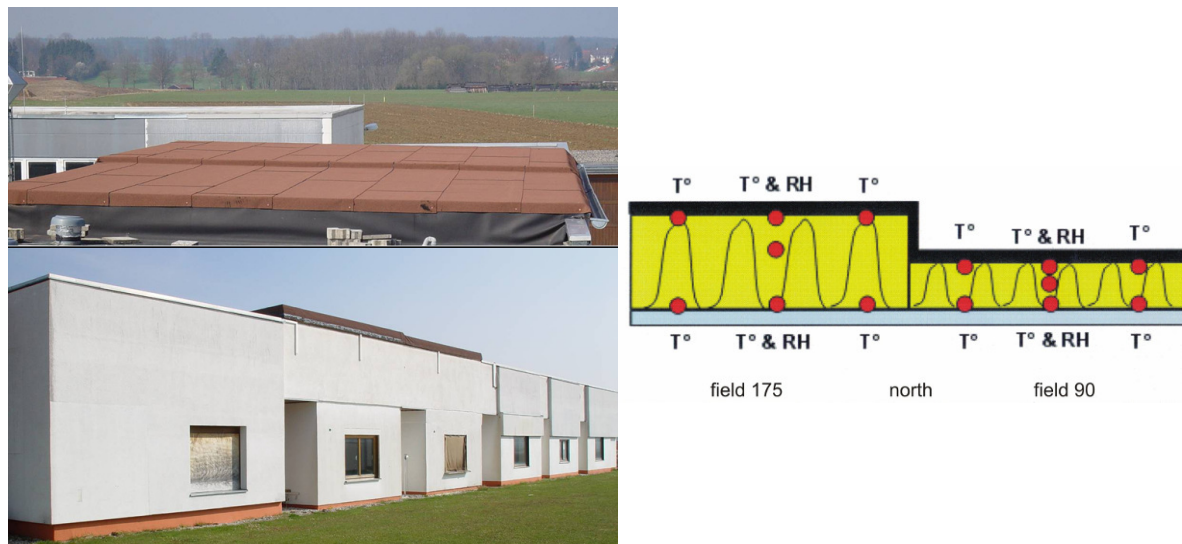

FIG. 1: Foto and sensor positions in the test roof (side and top view). The data recorded at the centre positions are used for validating the hygrothermal simulations.

In order to get an extreme scenario with a high initial moisture content about 2 kg/m² of water are added to the glass fibre insulation. It is expected that this moisture will be trapped in the construction between the vapour barrier and the vapour-tight roofing membrane. With the temperature variations during changing seasons or during a night and day cycle the moisture is expected to migrate between bottom and top of the insulation.

2.2 Hygrothermal simulations

The hygrothermal simulations are performed by applying WUFI® [Künzel 1995], which allows the transient calculation of the coupled heat and moisture transport in building components under real climate conditions. The model was developed at the Fraunhofer Institute for Building Physics and has been experimentally validated by comparison with numerous field tests. For the mineral wool a moisture retention curve based on the paper by Peuhkuri et al. [2005] and adapted to fit the measured results was used. The other material parameters are taken from the WUFI® database. As outdoor conditions the measured climate from August 2006 to January 2007 in Holzkirchen including solar radiation and long wave sky radiation from the atmosphere is used. As indoor

climate serve the recorded temperature and humidity conditions in the attic space beneath the flat roof. The time period for which experimental and calculation results are compared lasts from August 2006 to January 2007.

If a good agreement between measurement and calculation in Holzkirchen can be achieved, the investigation may be broadened by repeating the simulations with climate conditions at other locations. The selected locations are Copenhagen in Denmark representing a Northern European climate and Naples in Southern Italy representing the warm regions of Europe. The meteorological data sets for Copenhagen and Naples are taken from the ASHRAE [2001] climate data which were compiled for building energy calculations. While the climate of Copenhagen appears to be mild compared to Holzkirchen, Naples shows higher air temperatures but not much difference in peak radiation. The indoor climate is assumed to be the same at all locations. According to the WTA-Guideline 6-2 [2004] sinusoidal curves between 20 °C / 40% RH in winter and 22 °C / 60 % RH in summer represent the indoor conditions in residential buildings with normal moisture load. However, since the roof is water and vapour tight the humidity conditions are rather irrelevant.

3. Results

3.1 Field Test

The field test described above is still ongoing - for the current paper a time period of six months from August 2006 to January 2007 is analyzed. The temperatures during the winter 2006 / 07 were quite moderate with only little snow. There were only a few days with temperatures below -5 °C while in a normal cold winter the temperatures can drop to -20 °C at times. The measured temperature and relative humidity within the construction are shown and discussed in comparison with the calculated results in the Figs 3 to 5. In the result diagrams the three sensor positions located at the centre of the roof sections are labelled from outside to inside with "exterior", "middle" and "interior".
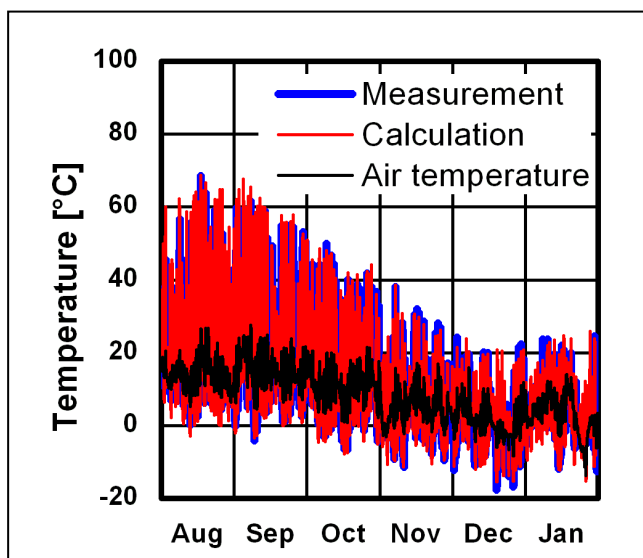
FIG. 2: Comparison of measured and calculated exterior surface temperature variations of the roof with 90 mm insulation and the outdoor air temperature at Holzkirchen.

3.2 Comparision of calculation and experiment

Figure 2 shows the measured (blue curve, sensor beneath the roofing membrane) and calculated (red curve) surface temperature of the roof with 90 mm insulation layer. The agreement between the two curves is very good - only sometimes the peak values show a small difference of two or three degree Celsius. The comparison with the outdoor air temperature (black curve) shows the strong influence of solar radiation (energy source during day-time) and sky radiation (energy sink during night-time) which is accurately captured by the new model for radiation and surface heat exchange in WUFI® version 4.1.
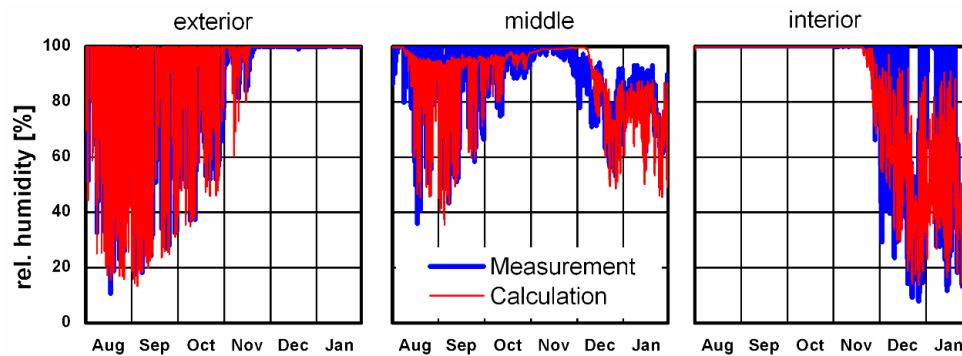
FIG. 3: Comparison of measured and calculated relative humidity variations at the three sensor position in the roof with 90 mm insulation under the indoor and outdoor climate conditions recorded during the test in Holzkirchen.

Figure 3 shows the relative humidity at the three positions within the insulation layer. The overall agreement between measured and calculated curves is quite acceptable. At the exterior position of the insulation the calculated and the measured curves coincide rather well. This is important, since the most extreme temperature and humidity conditions in the insulation layer are observed at the exterior sensor. In summer the RH at this position varies between 20 % at noon (when the sun shines and heats up the exterior surface) and 100 % during night. With lower temperatures and shorter days in autumn and winter the RH at noon increases and remains from midmonth of November permanently at 100 %. At the middle and the interior positions of the insulation layer the mean progression of the curves is very similar, but the spread of the measured values is slightly larger to both directions compared to the calculation. This difference may be due to a remaining uncertainty concerning the material properties (sorption isotherm, vapour diffusion resistance) of the glass fibre boards or the assumption of the initial water content in the roof.
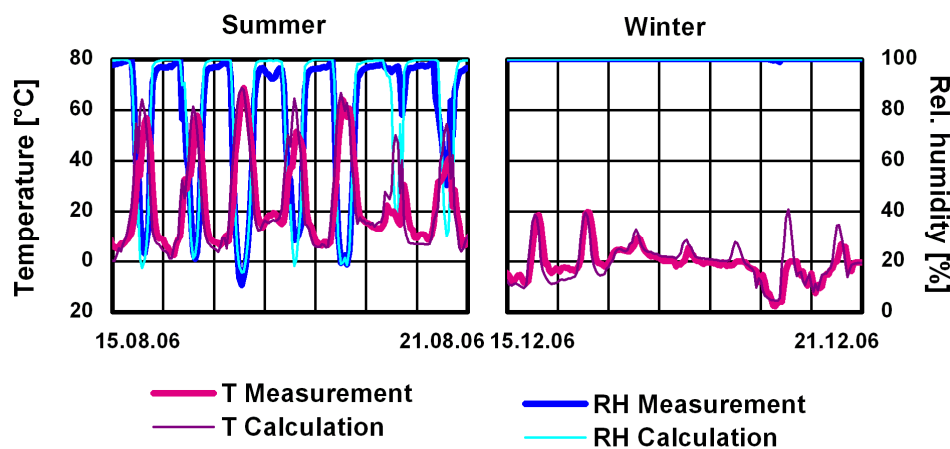
FIG. 4: Comparison of measured and calculated temperature and humidity variations at the exterior sensor position in the roof with 90 mm insulation for two se¬lected weeks in August and December.

A more detailed plot of the hygrothermal conditions for two single weeks in summer and winter (Fig. 4) at the exterior sensor position confirms the generally good agreement between simulation and experiment. The deviation in surface temperature on Dec. 20 is due to a thin snow cover of the roofing membrane which is disregarded in the simulation. An important observation concerning the durability assessment of the glass fibre insulation is the opposed variation of temperature and RH beneath the surface of the roofing membrane in Fig. 4. Every time, the temperature rises the relative humidity measured res. calculated for the same position drops in an inverse manner. That means high temperature and high RH never coincide at this point. The results of the roof with 175 mm insulation layer show less severe hygrothermal conditions with similar good agreement between measurement and calculation. Therefore these results are not plotted and discussed in this paper.

3.3 Evaluation of peak conditions

Laboratory tests have shown that the coincidence of high temperature and high humidity has a significant degradation effect on glass fibre insulation. Under dry conditions, a high temperature doesn't do any harm and a high relative humidity is not a great problem as long as the temperature remains low. Therefore, the measured and calculated hygrothermal conditions in the roof are displayed in a special graph where temperature and humidity are plotted against each other for time intervals of one hour.

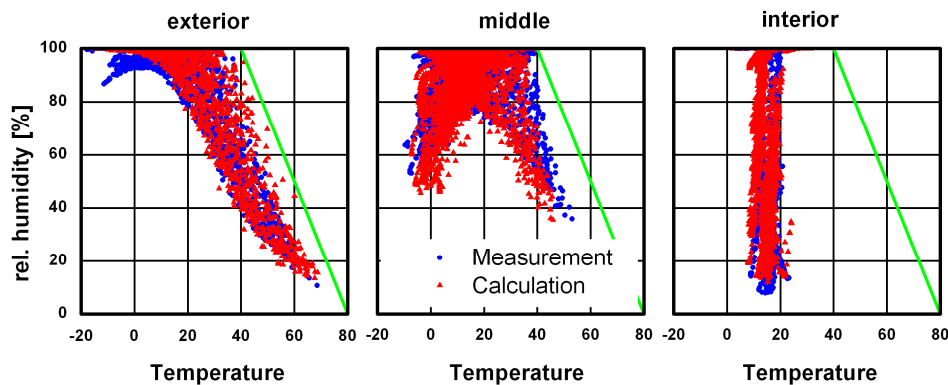*FIG. 5: Coinciding temperature and humidity conditions on an hourly basis measured and calculated at three sensor positions in the roof with 90 mm insulation. The green line represents the limiting curve for the hygrothermal conditions deter¬mined for the climate conditions in Holzkirchen.*

Such a graph is shown in Fig. 5 for the three sensor positions in the roof with 90 mm thick insulation. The highest temperatures with more than 60 °C (maximum 70 °C) occur at the exterior position beneath the roofing membrane. However, the coinciding RH values remain very low, between 10 % and 30 %. The maximum RH of 100 % is frequently reached at all sensor positions. While the coinciding temperatures stay around 20 °C at the bottom of the roof (interior position) they can reach a maximum of nearly 40 °C in the middle and upper parts of the roof. The limit curve that will not be exceeded at any position in the insulation layer of the investigated roof can be drawn as a straight green line from 40 °C / 100 % RH to 80 °C / 0 % RH.

FIG. 6: Coinciding temperature and humidity conditions on an hourly basis calculated at three monitor positions within the roof with 90 mm insulation located in Copenhagen. The green line represents the limiting curve defined in Fig. 5.

The selected locations for the further hygrothermal simulations are Copenhagen and Naples. The plot of the calculated hourly RH plotted over temperature at Copenhagen is displayed in Fig.6. The results are very similar to the data of the flat roof in Holzkirchen (Fig. 5). However, the Copenhagen results for the exterior position come a bit closer to the limit curve (green line) and go even slightly over the limit a couple of times. In order to obtain more detailed information the coincident temperatures and relative humidities are classified in steps of 10 % RH starting with 50 % and steps of 10 K between -10 and +80 °C to analyse the different peak levels. The

accumulated results are listed in Table 1. About 7700 hours a year a RH between 90 % and 100 % prevails, more than 3200 hours thereof at a temperature range between 0 and 10 °C and 1600 between -10 and 0 °C. In the higher temperature ranges the hours where RH exceeds 90 % become increasingly scarce. At Copenhagen the temperature within the construction never exceeds 70 °C. A temperature above 40 °C and a coincident relative humidity of above 80 % occurs during about 90 hours a year - this represents only 1.0 % of the service life of a roof.

TABLE. 1: Hourly classification of the simultaneous RH and temperature at the ex¬te¬rior position of the flat roof with 90 mm of glass fibre insulation for Copenhagen:

Temperature °C	Relative Humidity [%]					
	0 - 50	50 - 60	60 - 70	70 - 80	80 - 90	90 - 100
< -10						189
-10 - 0						1634
0 - 10						3262
10 - 20					1	1618
20 - 30			8	47	86	640
30 - 40	16	48	86	61	74	305
40 - 50	143	67	52	52	35	49
50 - 60	197	14	7	6	3	2
60 - 70	56					
70 - 80						
> 80						

The same hygrothermal analysis is repeated with the climate data for Naples. The relative humidity over temperature plot is displayed in Fig. 7. Compared to Copenhagen the values show a similar distribution - only the maximum temperature level in summer is 15 K higher but with a lower humidity of just about 10 % RH.
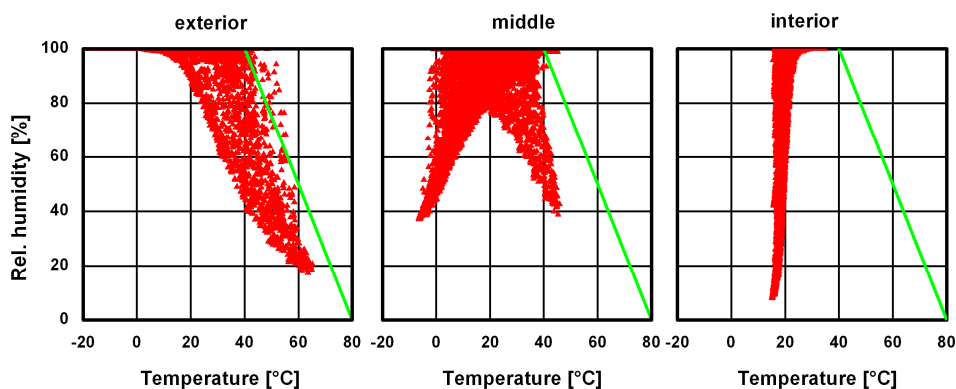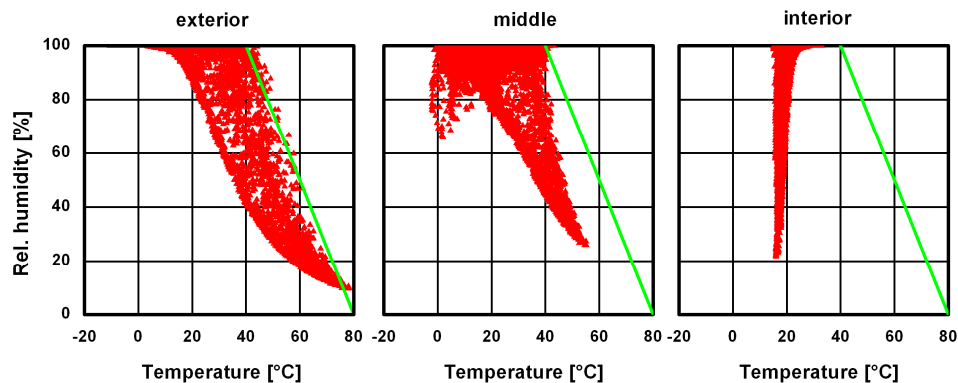

FIG. 7: Coinciding temperature and humidity conditions on an hourly basis calculated at three monitor positions within the roof with 90 mm insulation located in Naples. The green line represents the limiting curve defined in Fig. 5.

The hourly classification of temperature and humidity in Table 2 shows with about 6600 fewer hours between 90 and 100 % RH than the locations further north. Due to the higher surface temperature in summer the RH decreases faster during day. Most frequent in Naples are with about 2700 hours conditions from 90 to 100 % RH combined with a temperature between 10 and 20 °C followed by 2200 hours with the same RH at temperatures between 0 and 10 °C. Values above 80 % RH and 40 °C occur during less than 100 hours - so apart from the

higher temperatures of 80 °C the number of hours in a higher range of RH and temperature differs hardly from the situation in Copenhagen.

TABLE. 2: Hourly classification of the simultaneous RH and temperature at the exterior position of the flat roof with 90 mm of glass fibre insulation for Naples:

Temperature °C	Relative Humidity [%]					
< -10	0 - 50	50 - 60	60 - 70	70 - 80	80 - 90	90 - 100
< -10						11
-10 - 0						599
0 - 10						2177
10 - 20					26	2659
20 - 30			37	56	166	778
30 - 40	41	108	53	67	110	348
40 - 50	240	80	83	41	49	48
50 - 60	384	26	10	4		
60 - 70	409					
70 - 80	148					
> 80						

4. Conclusion

The investigations show, that neither in Holzkirchen nor in northern or southern Europe a combination of RH above 95 % and temperatures of more then 60 °C can occur in vapour permeable insulation materials like mineral fibre – even not if there is a high initial water content in the roof of about 2 kg/m² like in the current case. The simultaneous occurrence of humidity conditions above 80 % RH and maximum temperatures between 40 and 50 °C at the most critical position within the insulation layer of a flat roof (beneath the roofing membrane) does generally not exceed 100 hours a year under European climate conditions. It should be noted that these conditions do not prevail continuously for several subsequent hours and they do not affect the entire insulation layer. They represent only short peaks that happen under particular weather situations at the most exposed part of the insulation layer, the zone directly below the roofing membrane. Other parts of the glass fibre boards experience less severe conditions.

Therefore iIt is proposed to define new durability test conditions based on the study presented here. Both the experimental results and the simulations have shown that coinciding peaks of temperature and relative humidity ranging from 40 °C to maximum 50 °C res. from 80 % to 100 % (average 90 % RH) add up to less than 100 hours per year. Consequently, there is good reason to set the durability test conditions to 50 °C and 90 % RH. However, the question concerning the duration of such test remains. Field tests periodically checking the durability of mineral fibre insulation in external wall insulation systems have shown that the greatest loss in pull-off strength happens in the first few month of service life. After that period the mechanical properties remain stable [Zirkelbach et al. 2005]. Continuous exposure of mineral wool to constant test conditions in the laboratory may show a slightly different picture (e.g. [Franke & Deckelmann 1999]), but they do not reflect the permanently altering hygrothermal conditions in the real world. The field tests indicate that there are periods (probably those with dominantly dry conditions) where the insulation material seem to recover its strength. This cannot happen during prolonged laboratory tests with constant peak conditions lasting 1000 hours or more. Thus, a test period in excess of the summed-up intervals of peak conditions occurring during a year in a real flat roof do not make much sense. It is therefore proposed to limit the test period to one week which is still on the safe side compared to the 100 hours of peak conditions actually occurring. For this conclusion, the long-term performance of glass fibre boards in flat roof constructions is assumed to be comparable to that of mineral fibre boards in external thermal insulation composite systems (ETICS), where the temporal development of the pull-

off strength has been determined by field tests. In order to confirm this assumption field tests monitoring the compressive strength of glass fibre insulation in flat roofs should be carried out in future.

5. References

Künzel, H.M.: Simultaneous Heat and Moisture Transport in Building Components. One- and two-dimensional calculation using simple parameters. IRB-Verlag Stuttgart 1995.

Peuhkuri, R., Rode, C. and Hansen, K.K. (2005): Effect of method, step size and drying temperature on sorption isotherms. 7th Nordic Symposium on Building Physics, Reykjavík, pp. 31-38.

ASHRAE: International Weather for Energy Calculations (IWEC) CD-ROM, Atlanta 2001.

WTA-Guideline 6-2-01/ E: Simulation of heat and moisture transfer. Fraunhofer IRB Verlag, 2004, ISBN 978-3-8167-6827-2

Zirkelbach, D., Holm, A. & Künzel, H.M.: Influence of temperature and relative humidity on the durability of mineral wool in ETICS. Proceedings 10DBMC, Lyon April 2005, TT2-87.

Franke,L. & Deckelmann, G.: Vergleich der Auswirkungen hygrothermischer Beanspruchungen von Mineralfaserdämmstoffen im baupraktischen Einsatz und unter Laborbedingungen. Proceedings 10th International Symposium for Building Physics, Dresden 1999, pp 587-596.

Computational modelling of heat and moisture transport in a building envelope with hydrophilic mineral wool insulation

Miloš Jerman, Ph.D. Student,
Department of Materials Engineering and Chemistry, Faculty of Civil Engineering, Czech Technical
University in Prague;
milos.jerman@fsv.cvut.cz

Jiří Maděra, Assistant Professor,
Department of Materials Engineering and Chemistry, Faculty of Civil Engineering, Czech Technical
University in Prague;
madera@fsv.cvut.cz

Robert Černý, Professor,
Department of Materials Engineering and Chemistry, Faculty of Civil Engineering, Czech Technical
University in Prague;
cernyr@fsv.cvut.cz

KEYWORDS: interior thermal insulation systems, coupled heat and moisture transport, hydrophilic mineral wool.

SUMMARY:
Computational modelling of coupled heat and moisture transport in a brick wall provided with interior thermal insulation system based on advanced type of hydrophilic mineral wool in the conditions of difference climate is presented in the paper. Heat and moisture transport is modeled using the computer code TRANSMAT 6.2. Temperature, relative humidity and overhygroscopic moisture fields are calculated for the time period of fivel years. The results of computational simulations reveal that in the studied system the best hygrothermal performance is achieved with a water vapor retarder having similar water vapor diffusion properties as the load bearing structure.

1. Introduction

The problem of water condensation inside the building envelope with thermal insulation involved plays a significant role in the building-physics solution. During the winter period, when the water condenses in much easier way, there is an increased risk of water vapor condensation in the insulation layer and on the interface between this layer and the load-bearing structure (particularly when the air gaps are present). Liquid water inside these gaps is very difficult to evaporate and in the long run, it may cause serious damage to the structure. One among the solutions of this problem consists in placing vapor barrier right under the internal plaster, i.e. between the plaster and internal thermal insulation. However, this solution is not so appropriate as it may seem, because of a few reasons. A sole nail or hook driven into the wall during its life-time period damages the barrier with no doubts. Even in the case that barrier would perform without mechanical damage, undesirable increase of relative humidity in the interior may appear in winter periods. The reason of this increase is limited air ventilation during this period and the impossibility to remove the water vapor from the interior through the envelope (because of the installed barrier).

The interior thermal insulation system using water vapor retarder instead of water vapor barrier and hydrophilic mineral wool insulation which can be considered as a viable alternative to the traditionally used systems was studied extensively during the past ten years by both computational (Maděra and Černý, 2002) and experimental (Pavlík et al., 2005, Pavlík et al., 2008) techniques. This system was dependent – as for the material of water vapor retarder – on the material of load bearing structure. In this paper, we present a new material solution of the interior thermal insulation system which is characterized by improved liquid water transport properties of the hydrophilic mineral wool. Consequently, the application of the system should not depend on the material of the retarder. Also, contrary to the old computational analyses, which were done using Delphin computer code (Grunewald, 2000), a newer computer simulation tool (TRANSMAT, 2005), which was developed in the

Department of Materials Engineering and Chemistry, Faculty of Civil Engineering, Czech Technical University in Prague and is based on different type of mathematical model, is used in the calculations.

2. Materials and building envelopes

The interior thermal insulation system analyzed in this paper consisted of internal plaster, insulation material and water vapor retarder. On the interior side there was lime-metakaolin plaster with the thickness of 10 mm. As the thermal insulation material, hydrophilic insulation boards on the mineral wool basis Acoustic with the thickness of 100 mm which were developed by Rockwool, SA, were used. The thickness of water vapor retarder was 10 mm. No air gap between the water vapor retarder and the load-bearing structure was assumed. The water vapor retarder was applied directly on the old structure which was a brick wall with the thickness of 450 mm. On the external side there was the same plaster as inside, with the thickness of 10 mm. The basic parameters of materials of the described building envelope are shown in Table 1 (notation common in building physics is used).
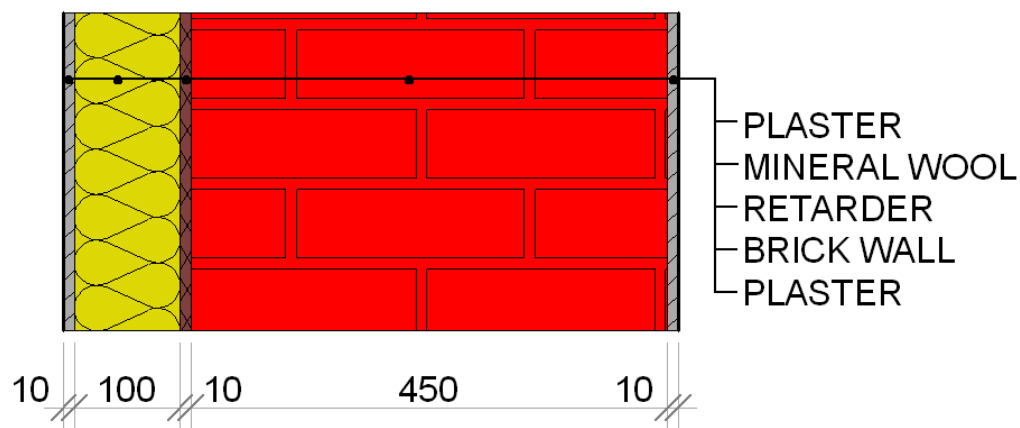

Figure 1: Composition of building envelope used to computational simulations

Table 1: Basic material properties of materials of building envelopes

	ρ	θ_{hyg}	θ_{sat}	λ_{dry}	κ	c	μ
	[kg/m^3]	[m^3/m^3]	[m^3/m^3]	[W/mK]	[m^2/s]	[J/kgK]	[-]
Plaster	1490	0.095	0.42	0.87	8.0e-9	1004	18
Brick	1746	0.0015	0.33	0.69	3.0e-6	895	8.5
Acoustic	71	0.000046	0.97	0.043	8.40e-6	810	4.3

The main aim of the computational simulations performed was to analyze the hygrothermal performance of the designed insulation system with three different types of water vapor retarder. All retarders were produced by Mamut-Therm s.r.o. The first of them was fine lime plaster (denoted as M1 in what follows). The second retarder, denoted M3, was flexible cement adhesive. The third retarder, denoted M5, was hydraulic-setting insulation plaster. The basic material parameters of the retarder are shown in Table 2.

Table 2: Basic material properties of retarder

	ρ	θ_{hyg}	θ_{sat}	λ_{dry}	κ	c	μ
	[kg/m^3]	[m^3/m^3]	[m^3/m^3]	[W/mK]	[m^2/s]	[J/kgK]	[-]
M1	1493	0.01	0.41	0.61	7.3e-7	1100	6.4
M3	1385	0.01	0.44	0.61	2.5e-10	1050	12.2
M5	1445	0.0021	0.12	0.73	4.4e-13	1100	150

For the calculations we employed the computer simulation tool TRANSMAT 6.2 (2005) which was developed in the Department of Materials Engineering and Chemistry, Faculty of Civil Engineering, Czech Technical University in Prague. The construction of the code is based on the application of the general finite element computer simulation tool SIFEL (SImple Finite ELements). The moisture and heat balance equations were formulated in the simplified form suggested by Künzel (1995). The proper initial and boundary conditions of the model are a crucial factor affecting the reliability of the calculations. Therefore, the calculations should be done for exactly the same situation as in the practical reconstruction on building site. First, the boundary conditions for the external side should be as accurate as possible. This can be achieved by using the meteorological data for the locality as close as possible to the real object. From the point of view of long term reliability, the application of so called "reference year" data should be preferred. Second, the initial conditions should be realistic. To this point, the calculations should be done first for the construction without the interior insulation system in order to find the long-term conditions in the wall before the reconstruction. In this paper, the 1st of July was chosen as the starting point for the calculations. The systems with interior thermal insulation were exposed from inside to constant conditions (temperature equal to 21 °C and relative humidity equal to 55 %) and from outside to climatic conditions corresponding to the reference year for Prague (Fig. 2). The comparison of calculated data for two subsequent years in a longer time period was chosen as the main evaluation factor.
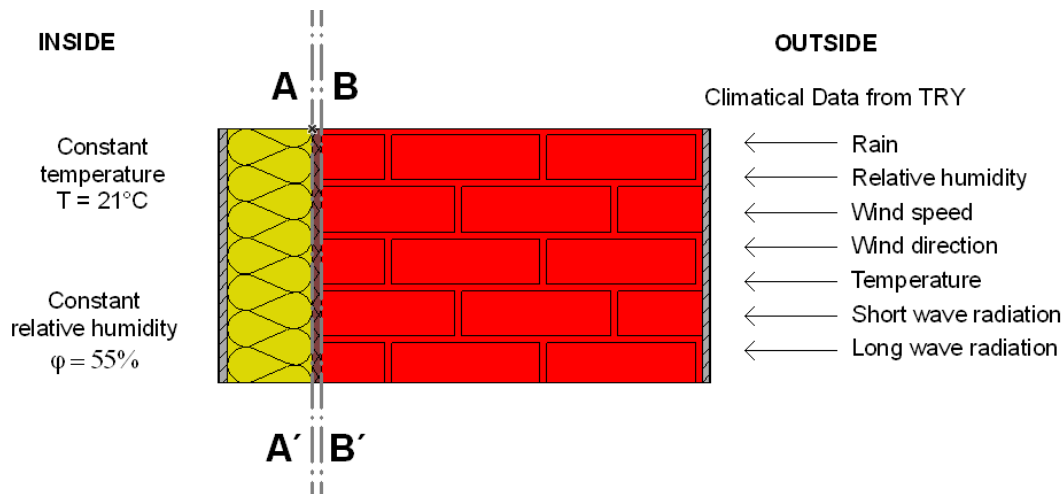

Figure 2: Boundary conditions for the studied envelopes

3. Computational results

The long-term performance of the system should be characterized not only by calculated temperature and relative humidity. Also overhygroscopic moisture fields have to be determined, which decide about the real hygrothermal performance of the system. The critical places, where long-term water accumulation can appear, should be detected. We have chosen three critical profiles in the evaluation of the hygrothermal performance of

the envelope, A-A´, B-B´, C-C´, where the profile A-A´ was between water vapor retarder and insulation material, B-B´ between the load-bearing structure and water vapor retarder and C-C´ was the cross section of the wall from the interior to the exterior. In these profiles we calculated the dependence of the relative humidity, overhygroscopic moisture and temperature on time. The results are organized according to the particular alternatives.

3.1 Retarder M1

Fig. 3 shows a survey of the relative humidity fields in the system during the last calculation year. Fig. 4 presents the details of calculation of relative humidity as function of time in the profiles A-A´and B-B´. The computed data for both profiles coincided completely. The maximum value of relative humidity was equal to 87% which was safely below the condensation limit. Therefore, the overhygroscopic moisture content was equal to zero in the whole structure over the whole analyzed time period of five years.
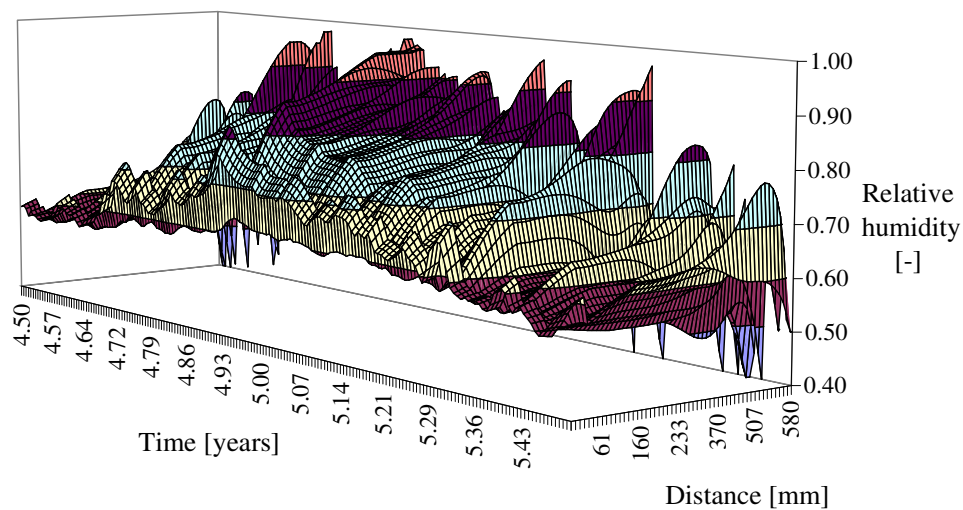

Figure 3: Relative humidity in the brick wall – water vapor retarder M1

Figure 4: Relative humidity in the two critical profiles – water vapor retarder M1

3.2 Retarder M3

Fig. 5 shows the relative humidity fields in the system during the last calculation year. Fig. 6 presents the details of calculation of relative humidity as function of time in the profiles A-A´and B-B´. The maximum value of relative humidity in the A-A´ profile was equal to 72 %, which is quite safe from the point of view of condensation but in the B-B´ profile it was 93%, which is relatively close to the condensation limit. The calculated overhygroscopic moisture content was equal to zero in the whole structure over the whole analyzed time period of five years.

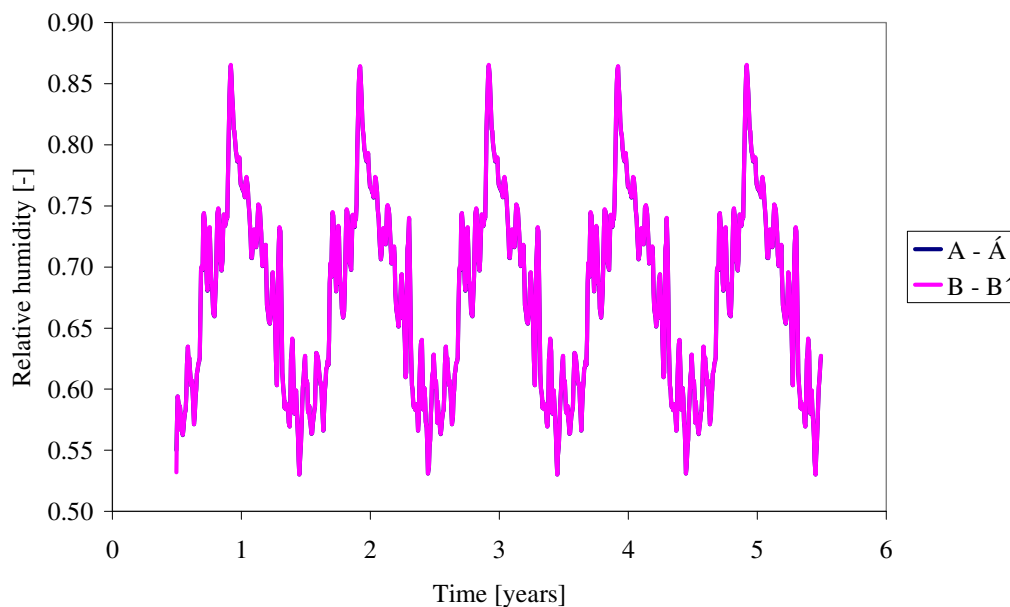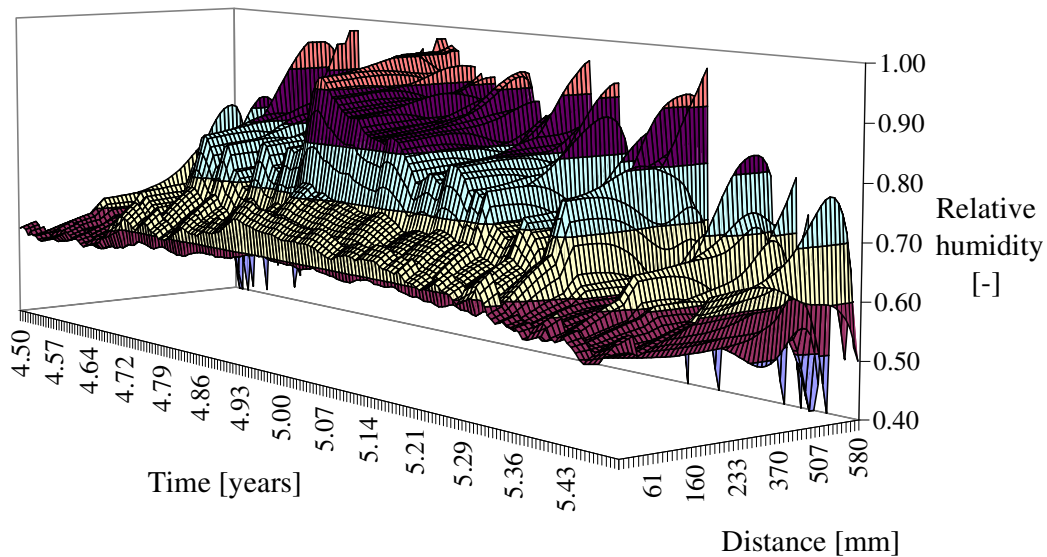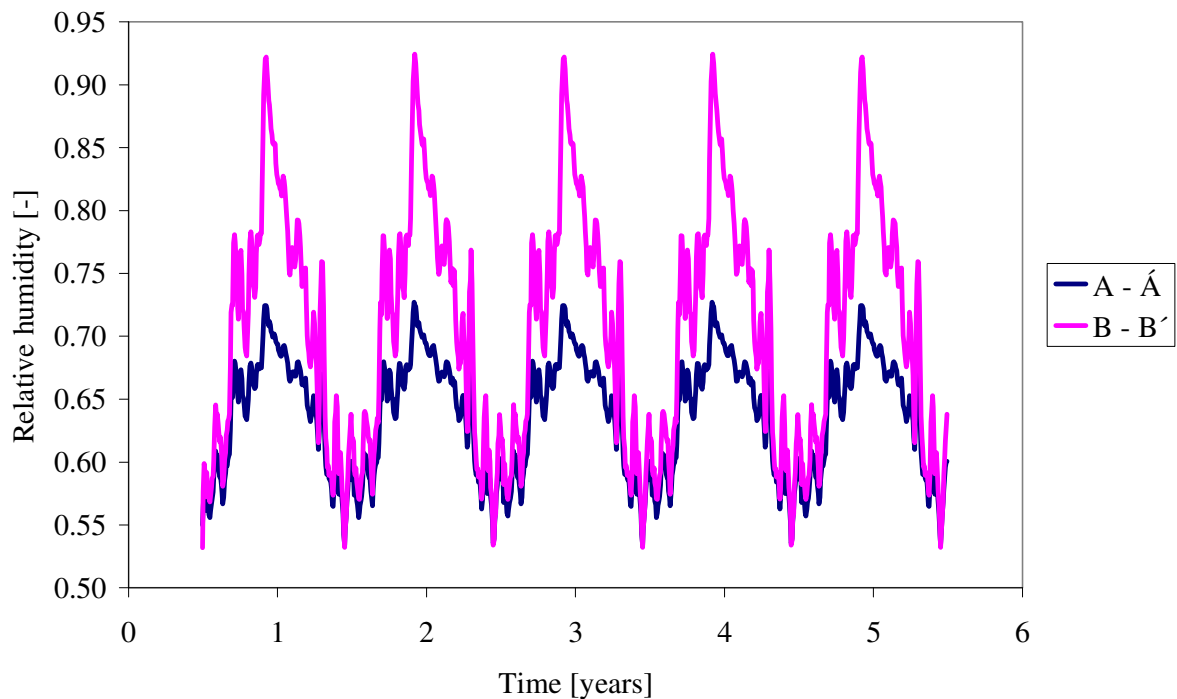*Figure 5: Relative humidity in the brick wall – water vapor retarder M3*

Figure 6: Relative humidity in the two critical profiles – water vapor retarder M3

3.3 Retarder M5

Fig. 7 presents the overview of the relative humidity fields in the system during the last calculation year. Fig. 8 demonstrates the details of calculation of relative humidity as function of time in the profiles A-A´and B-B´.The maximum value of relative humidity in the A-A´ profile was equal to 65 %, which was far from any condensation danger. However, in the B-B´ profile it was 95%, thus very close to the condensation limit.
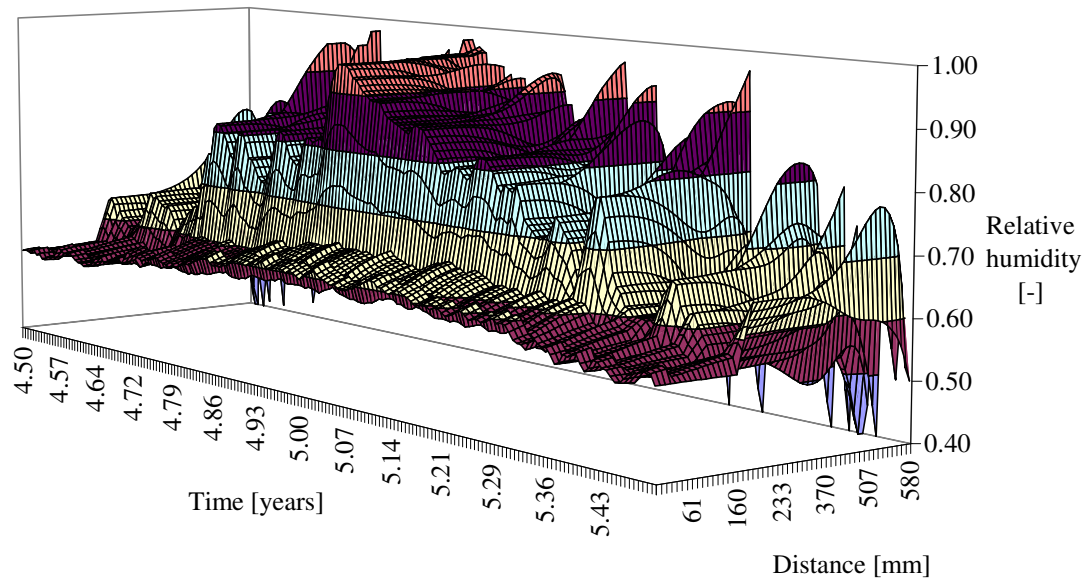
Figure 7: Relative humidity in the brick wall – water vapor retarder M5
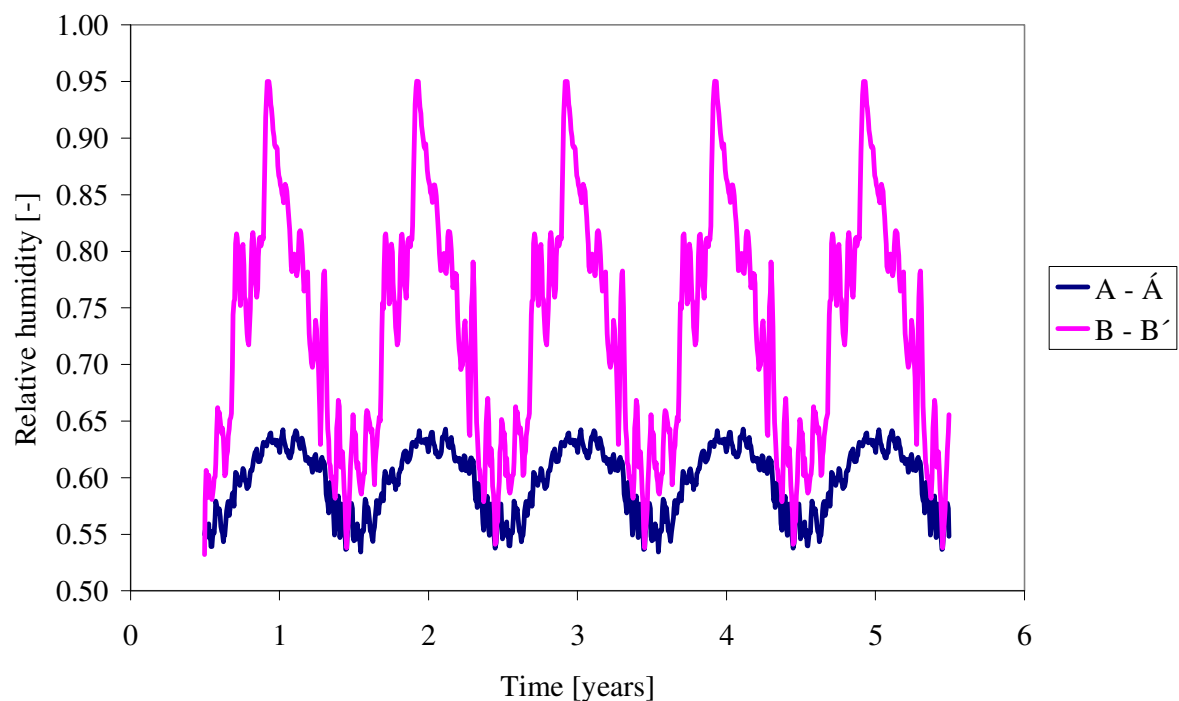
Figure 8: Relative humidity in the two critical profiles – water vapor retarder M5

4. Discussion

Figs. 9, 10 show a comparison of the relative humidity and temperature profiles in the brick wall for January 4 which can be considered as characteristic for the winter period.

Figure 9: Relative humidity in the profile C-C´, January 4.

Figure 10: Temperature in the profile C-C´, January 4.

While the temperature profiles almost coincided for all three retarders, the relative humidity profiles differed in a very significant way. The relative humidity in the load bearing structure increased with the increasing water vapor diffusion resistance factor of the retarder but in the thermal insul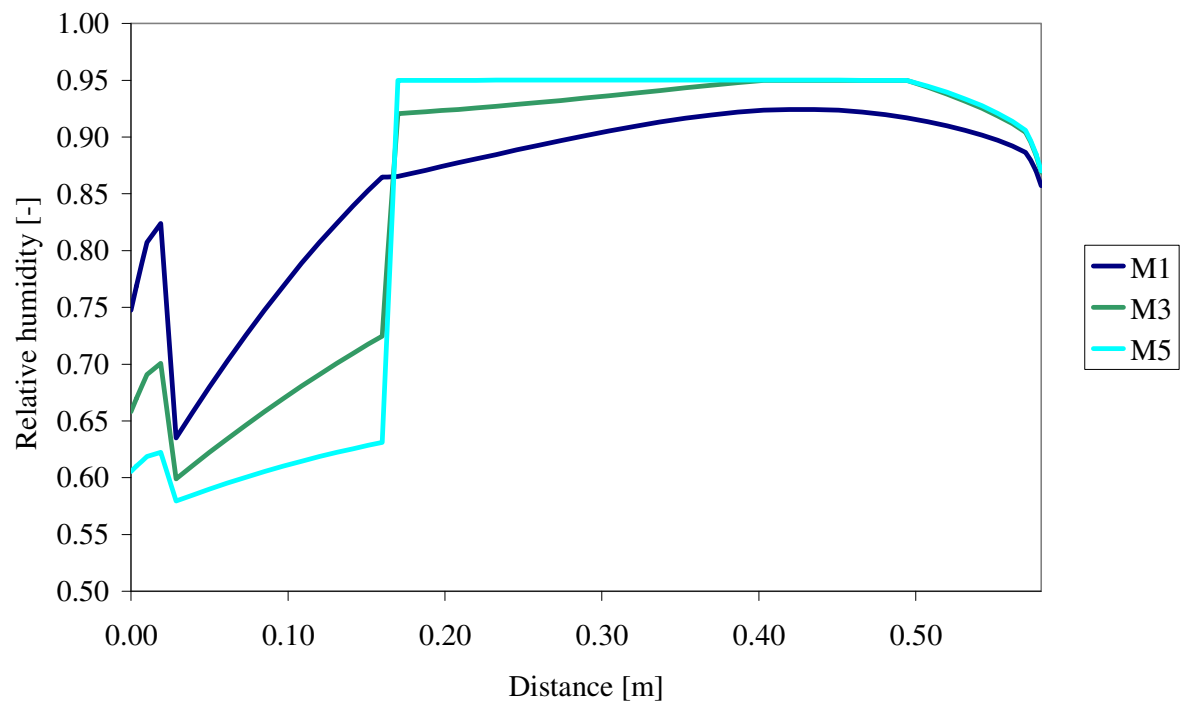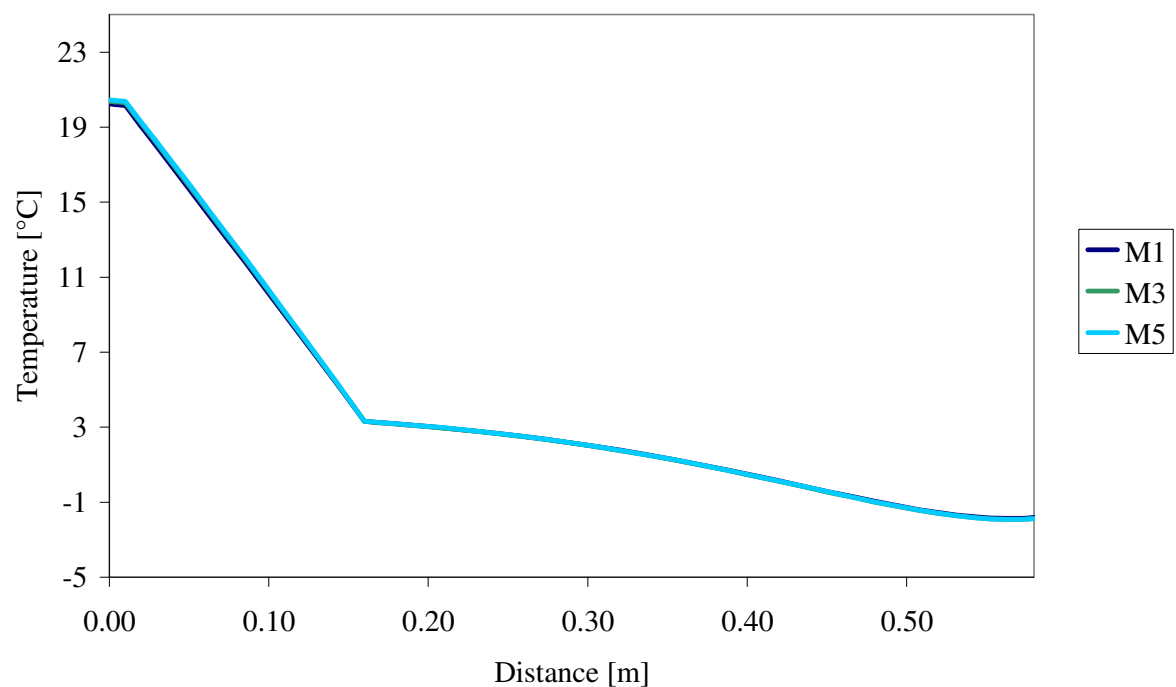ation layer a quite opposite trend was observed. This means that the majority of the moisture in the wall was not originating from the water vapor diffusion from the interior to the exterior as it is often characteristic for the winter period. The appearance of high relative humidity in the load bearing structure was for the systems including water vapor retarders with high water vapor diffusion resistance factor rather a consequence of the temperature decrease in the winter period combined with the limited possibility of water vapor removal to either exterior or interior. On the other hand, the hygric performance of the hydrophilic interior thermal insulation could be considered as quite superior because it was able to handle the water vapor diffusion flux from the interior in the winter period very effectively and return its surplus back very quickly. As a matter of fact, the hydrophilic thermal insulation layer was due to its excellent hygric properties capable of replacing the supposed function of water vapor retarder in the system.

5. Conclusions

The results of computational simulations presented in this paper showed that in the studied thermal insulation system on hydrophilic mineral wool basis the best hygrothermal performance was achieved with a water vapor retarder having similar water vapor diffusion properties as the load bearing structure. However, also the use of retarder with very high value of water vapor diffusion resistance factor did not lead to the condensation in the investigated wall. The apparent reason for this good performance was the very high values of both moisture diffusivity and water vapor diffusion coefficient of the hydrophilic thermal insulation layer. The thermal insulation material in this case in fact replaced the water vapor retarder, which acted as glue only in the system.

6. Acknowledgement

7. References

Grunewald J. (2000). DELPHIN 4.1 - Documentation, Theoretical Fundamentals, Dresden: TU Dresden

Kunzel H.M (1995). Simultaneous Heat and Moisture Transport in Building Components, PhD Thesis. IRB Verlag, Stuttgart.

Maděra J., Černý R. (2002). Computational Simulation of Hygrothermal Performance of Interior Thermal Insulation Systems on the Mineral Wool Basis. Proceedings of the 6th Symposium on Building Physics in the Nordic Countries, A. Gustavsen, J. V. Thue (eds.), Skipnes AS, Trondheim, p. 1-8.

Maděra J., Černý R. (2005). TRANSMAT – a Computer Simulation Tool for Modeling Coupled Heat and Moisture Transport in Building Materials, Proceedings of Workshop 2005 - Part A,B, Prague: CTU p. 470-471.

Pavlík Z, Jiřičková M, Pavlík J, Černý R. (2005). Interior Thermal Insulation System Based on Hydrophilic Mineral Wool. Journal of Building Physics 2005; 29: 21-35.

Pavlík Z, Černý R. (2008). Experimental Assessment of Hygrothermal Performance of an Interior Thermal Insulation System Using a Laboratory Technique Simulating On-Site Conditions. Energy and Buildings 2008; 40: 673-678.

Experimental Testing of the Wick-Concept Insulation

Vit Koverdynsky, Ing., Ph.D.
Brno University of Technology, Department of Building Services;
vit.kov@email.cz

KEYWORDS: Wick-Concept Insulation, Self-Drying Insulation, Cold Piping, Moisture Accumulation.

SUMMARY:
The wick-concept insulation of cold piping is based on capillary suction of a fibre fabric to remove excess water from the pipe surface by transporting it to the outer surface of the insulation. From the surface of the insulation jacket the water will evaporate to the ambient air. This will prevent long term accumulation of moisture in the insulation material. The wick keeps the hydrophobic insulation dry, allowing it to maintain its thermal performance. The only liquid moisture is kept in the wick fabric. The article presents principle of operation and some experiments that have been carried out to investigate the conditions for exploiting the drying capabilities of the system. The results show that the wick-concept insulation works for pipes with temperature above 0 °C and for ambient conditions within common ranges for industrial applications.

1. Introduction

Cold piping means piping where the surface temperature of the cold pipes in periods is below the dew point of the ambient air. In these periods there will be a movement of water vapour from the ambient air towards the cold pipes, where the vapour will condense and cause dripping. This is a situation which can cause considerable costs – not only for repairing damage, but perhaps also in the form of resulting costs such as water-damage to ceilings, spoilt goods or disruptions to the production process.

Therefore the cold pipe must be insulated. The wall thickness of the insulation must be sufficient for increasing the outer surface temperature of the insulation above the dew point of the ambient air. But still there will be a water vapour drive towards the cold pipe. When water vapour enters a material layer where the dew point temperature is met, it condenses to water or even if the temperature is below freezing point, ice is formed. This affects seriously the insulation efficiency, because insulation must be dry and stay dry.

2. Wick-concept insulation

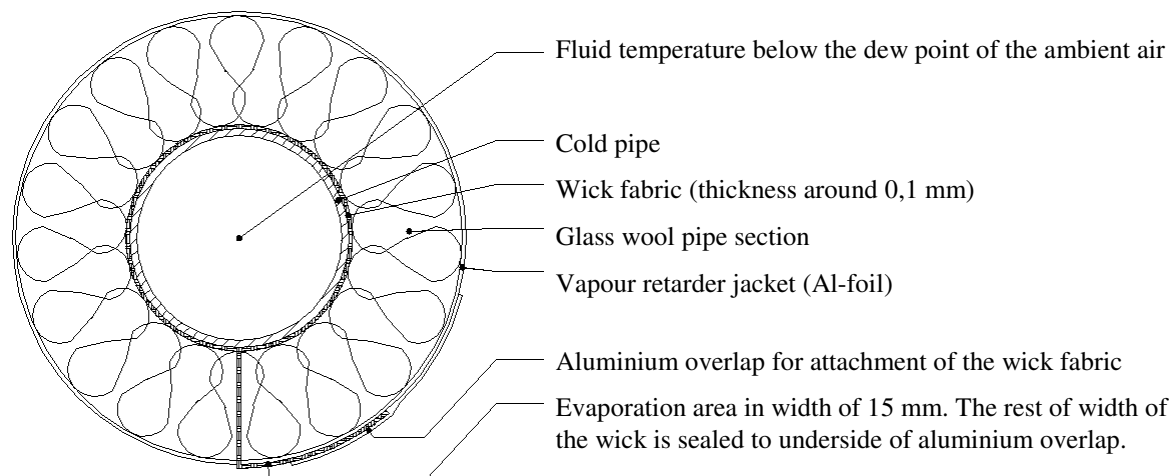*FIG. 1: Cross section of the self-drying insulation.*

The idea behind self-drying insulation (or the wick-concept) is the fact that in practice it is not possible to make a perfectly tight insulation job, which will prevent moisture accumulation in the insulation. Even if this is possible, flaws will arise over time. Prevention of moisture accumulation in cold pipe insulation is possible by

means of a concept utilizing the wicking action of a hydrophilic fabric to remove condensed moisture from the pipe surface (a place with a higher moisture content) through a slot in the insulation to the outer surface of the insulation (a place with a lower moisture content). From there it can evaporate into the ambient air, as long as the temperature is above the freezing point. The system to remove condensed water from a below-ambient pipe insulation system was conceived and patented by Professor Vagn Korsgaard from the Technical University of Denmark.

The tubular insulation shown in Figure 1 has an internal lining of the fabric with good capillary suction properties, which extends into the slot and protrudes to the outer insulation surface. For horizontal pipes the longitudinal slot should preferably be placed downward to allow gravitation to help removing the condensed water. Moisture is constantly removed by capillary suction of the wick fabric from the pipe surface to the protruding part of the wick, from where it will evaporate to the ambient air as long as the dew point of the ambient air is below the surface temperature of the jacket.

3. Experimental testing

Experimental methods were used to test self-drying insulation. Trials with different configuration should indicate how the insulation works under various boundary conditions. Experiments were carried out in a laboratory of the Technical University of Denmark in Copenhagen, with four horizontal environmental chambers and a vertical chamber (for configuration see Figure 2). In all chambers there were single ended cold pipes – two in each horizontal chamber, one in the vertical chamber. In order to have flow inside the single ended pipes each one consisted of two concentric pipes, where the inner pipe functions as the return pipe. This test configuration will be called a "cold finger" and allows for periodic removal and weighing of the pipe sections to determine the weight change due to water vapour ingress.

FIG. 2: Configuration of the horizontal and the vertical environmental chamber.

For the first experiment 1" black pipes with a length of 0.6 m were used. Other trials were done with 1" stainless steel pipes with a length of 0.5 m. Pipes were covered with insulation pipe sections with the outer diameter of 92 mm. Thickness of the insulation was 30 mm. Butt ends of samples were covered by PVC-end caps and were sealed by caulking around. These samples were weighed initially and then placed on cold fingers. Temperatures of cold fingers were maintained at the desired temperature.

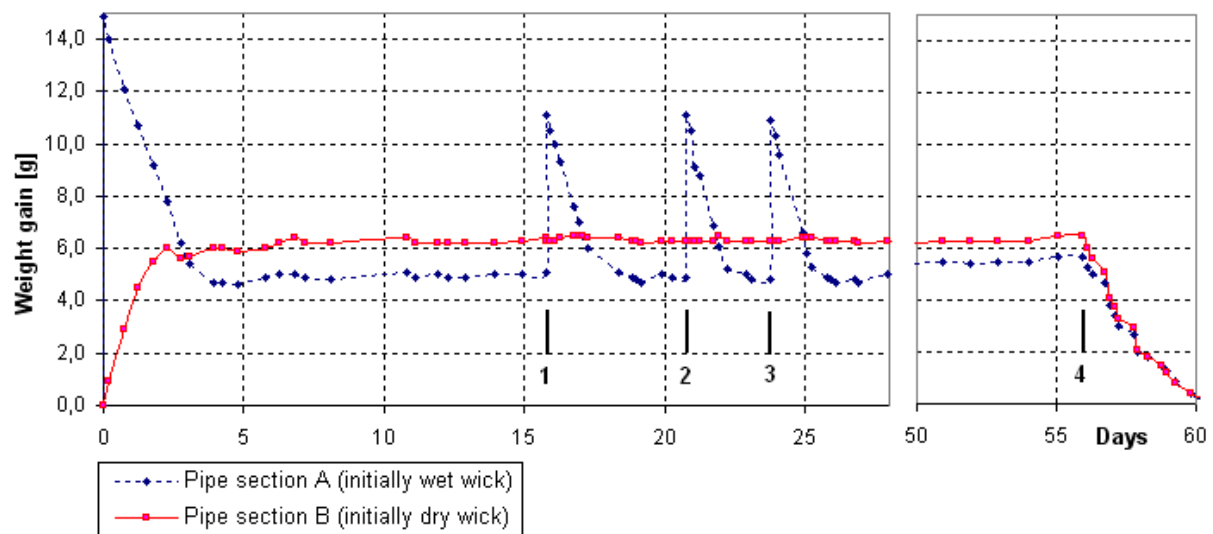## 3.1 Samples under the most common boundary conditions

FIG. 3: Weight gain over time for insulation under the most common boundary conditions.

In the experiment two insulation pipe sections were installed on a cold finger. In order to have wicking action in one of the sample from the beginning, the sample was installed with a fabric which was wetted by 15 ml of water. This amount of water fully saturated the wick fabric. The other sample was installed dry. As illustrated in Figure 3, the initially dry pipe section B had a rapid weight gain within the first two days of testing. Afterwards, the weight of the sample remained constant. This is consistent with the assumption that an initial period of water accumulation must occur prior to saturation of the wick. During this initial transient period, there is no liquid water at the slot, and the water vapour can diffuse into the system. The longitudinal "flaw" (joint) in the retarder jacket is narrow but runs along the length of the pipe.

In comparison, pipe section A, which had a wet wick fabric installed, began to remove condensed water through the slot to the evaporation area immediately. After three days, the flow of water vapour diffusion into the system equalled the flow rate of liquid water out of the system and the state of equilibrium was reached.

After 16 days (time mark 1), the wick fabric was wetted by adding 6 ml of water, and within three days the moisture content of the wick fabric was at the same level as before it was made wet. At time mark 2 (day 21) and 3 (day 24), the wick fabric was wetted again with 6 ml of water but now the pipe insulation and the wick was turned in the "slot-up" configuration. As can be seen, the wick works also without gravitational help. At time mark 4 (day 56) the cooling plant was switched off, pipe temperature increased to the ambient air temperature very quickly. All moisture trapped in the wick fabric evaporated to the ambient air within four days.

These data show that the weight gain during the initial transient period is roughly 5 to 6 grams per pipe section. This corresponds to approximately 10 g/m. The volume of the wick is approximately 12 ml. If the wick fabric had been fully saturated the weight gain should have been 12 grams per pipe section (20 g/m). From this the conclusion can be drawn that: (1) the weight gain measured is confined to the wick fabric (it means that the insulation is dry), (2) the wick material is less than 50 % saturated. Recommended position of a pipe section is the "slot-down" configuration. However, the experiment indicated that the insulation works also in the "slot-up" configuration. The wick works without gravitational help, capillary suction is strong enough.

TABLE. 1: Boundary conditions during the experiment under conditions occurring mostly in industry.

Type of boundary condition (from day 0 to 56)	Average value
Temperature in the environmental chamber	20.2 °C
Relative humidity in the environmental chamber	71 %
Pipe temperature	6.0 °C

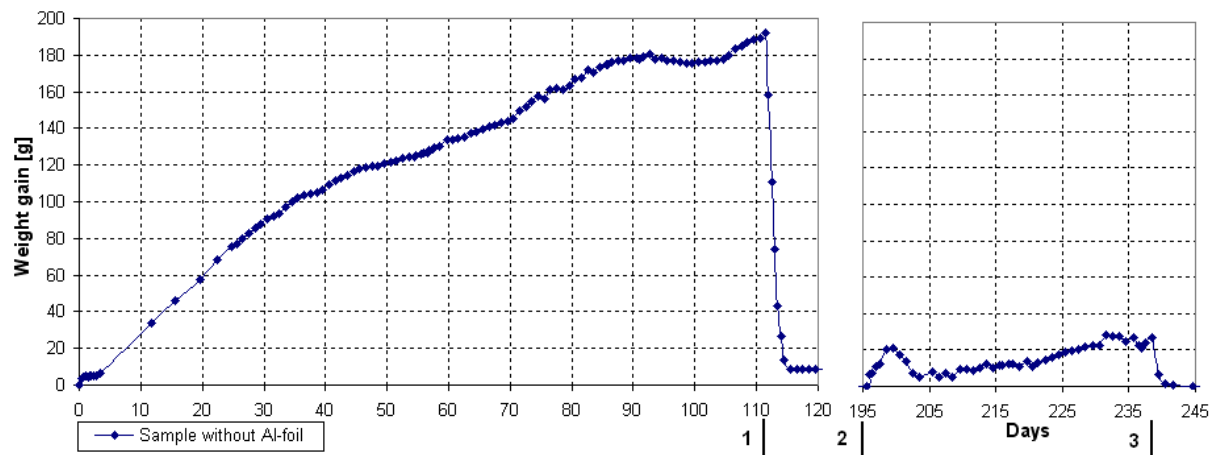## 3.2 Sample without a vapour retarder jacket

FIG. 4: Weight gain over time for insulation without a vapour retarder jacket.

The goal of the experiment was to find out if self-drying insulation without a vapour retarder jacket can work on cold piping and under which boundary conditions. In such case water vapour can freely diffuse through the insulation towards the cold pipe, where it condenses and if the capillary suction of the wick fabric would not be strong enough it would also cause accumulation of condensed water in the insulation.

As illustrated in Figure 4, there was a gradual weight gain – 190 g of water accumulated in the insulation during 112 days. From this the conclusion can be drawn that a vapour retarder jacket is needed if RH is more than 70 %; the insulation under such conditions is wet.

After 112 days the sample was removed from the cold finger (time mark 1) and was placed in room conditions (table 2). The most of the accumulated moisture evaporated to the ambient air in one day. The trial continued after 75 days, other experiments were made in the meantime. The sample was placed on the cold finger again on day 196 (time mark 2) into the open environment chamber. From day 196 to 245 the average weight gain was 14.3 g (32 g/m). The weight gain of the sample remained almost constant, after start-up period (first four days of testing – days 195 to 199). The amount of accumulated moisture was dependent on RH of the ambient air – there was higher accumulation with increasing RH. On day 238 (time mark 3) the sample was removed from the cold finger and placed in the laboratory. The moisture dried out very quickly.

Trial showed that self-drying insulation can work successfully even without a vapour retarder jacket if RH is less than 50 %. For higher RH there was gradual moisture accumulation in the insulations, however the insulation is normally installed with the vapour retarder jacket needed to slow down diffusion towards the cold pipe. Therefore moisture accumulation in the insulation is prevented. This trial proved that self-drying insulation can compensate for poor workmanship and flaws under any boundary conditions.

TABLE. 2: Boundary conditions during the experiment with sample without a vapour retarder jacket.

Type of boundary condition	Average value in time period		
Testing period (from day to day)	0 to 112	112 to 120	196 to 240
Temperature in the environmental chamber	19.3 °C	23.4 °C	25.0 °C
Relative humidity in the environmental chamber	71 %	57 %	57 %
Pipe temperature	6.6 °C	-	6.3 °C

3.3 Sample with the wick fabric only in the longitudinal slot

The experiment should find out if self-drying insulation can work also when the wick fabric is not wrapped around the pipe, but when it only touches the pipe through the longitudinal slot (see Figure 5).
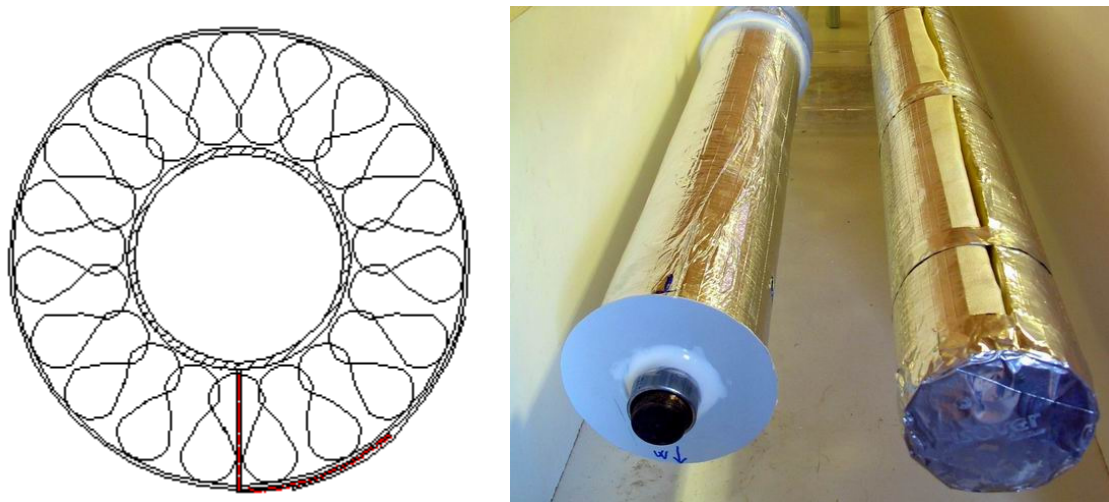
FIG. 5: Sample with the wick only in the longitudinal joint (sample on the left hand side).
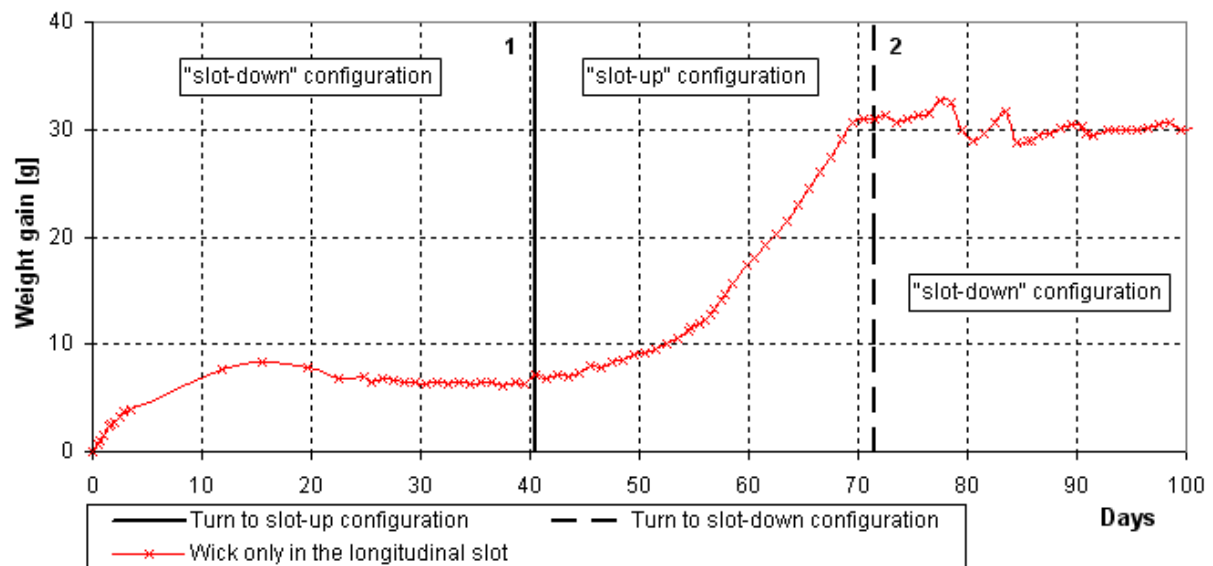

FIG. 6: Weight gain over time for insulation with the wick only in the longitudinal joint.

The first 40 days, in Figure 6, showed that the pipe section worked well in "slot-down" configuration. Condensed water vapour ran by gravitation pull to the lowest part of the pipe and it was sucked by the wick, which touched the cold pipe, and was removed to the ambient air. Problem occurred when the pipe section was turned to "slot-up" configuration on day 40 (time mark 1). Condensed water moved along the pipe to the lowest part by gravitation force. It could not be sucked up by the wick fabric and that was why water accumulated in the insulation material. On day 72 (time mark 2) the sample was turned back to "slot-down" configuration. Accumulated moisture from insulation material could not be sucked up, because wet insulation was not in contact with the hygrophilic wick fabric. However, additional moisture uptake was prevented.

TABLE. 3: Boundary conditions during the experiment with sample where the wick was only in the longit. slot.

Type of boundary condition	Average value
Temperature in the environmental chamber	22.1 °C
Relative humidity in the environmental chamber	74 %
Pipe temperature	6.6 °C

3.4 Samples under freezing temperatures

The goal of the experiment was to find out if the wick-concept insulation could be used for subzero pipe temperatures. Since the insulation is diffusive open, at least in the longitudinal slot, there will be a weight gain in the start-up period. Problem is when condensed water vapour freezes in the wick where subzero temperature is met. The idea was that if there was an anti-freezing liquid (glycerine, glycol) in the wick then a continuous removal of condensed water from the pipe surface to the ambient air would be kept.

First of all it was necessary to determine different concentrations of glycerine/water mixture content for different pipe temperatures to prevent ice formation. In Table 4 there are glycerine concentrations needed to decrease the freezing-point.

TABLE. 4: Freezing temperatures for glycerine/water mixture.

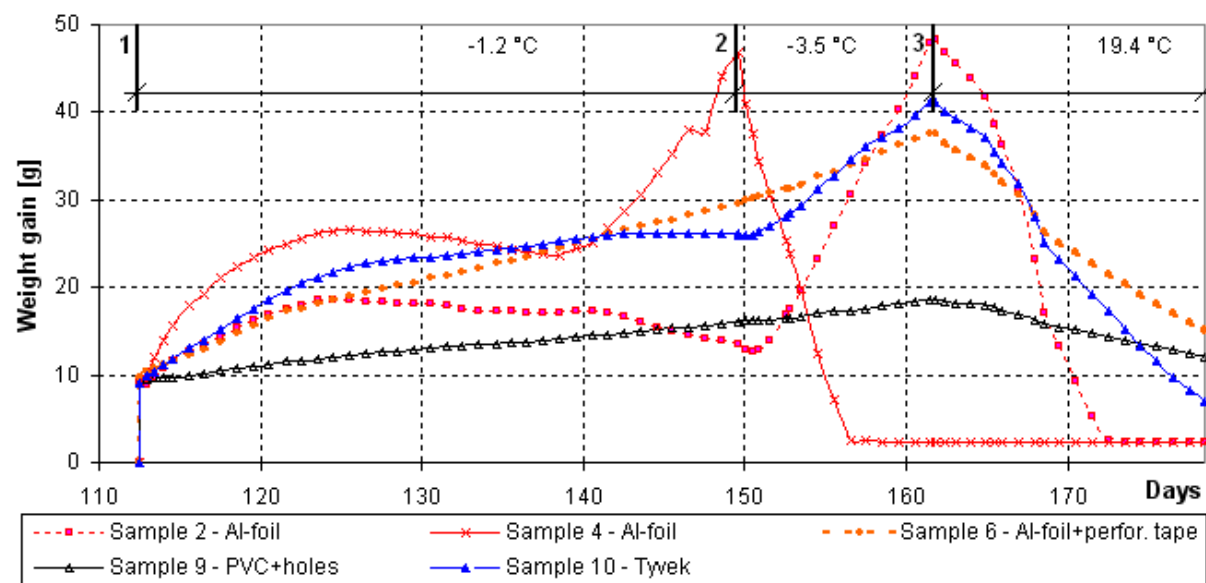| Glycerine [% of weight]	10	20	30	40	50	60	70	80	90	100
Freezing temperature [°C]	-1.6	-4.8	-9.5	-15.4	-23.0	-34.0	-38.9	-20.3	-1.6	17.0

FIG. 7: Weight gain over time for different samples under freezing temperatures.

As illustrated in Figure 7, on day 112 (time mark 1) 9 g of 20 % glycerine was injected to samples. It corresponded to almost saturated wick (12 g/sample). If there is not upward weight gain more than 12 g that would mean that injection of anti-freezing liquid could prevent ice-formation in the wick. However, there was weight gain in all samples. Only sample with the second jacket (9 – PVC jacket with taped longitudinal joint and with holes above the evaporation area) had little weight gain, which means it may work. On day 149 (time mark 2) sample 2 was removed from the cold finger and placed in the laboratory. On day 162 (time mark 3) the cooling plant was switched off, pipe temperature increaded to ambient air temperature. As illustrated in Figure 7 (for samples 2 and 4), glycerine did not evaporate from samples, only moisture did. That meets the requirement that glycerine must not evaporate from the wick to prevent ice formation over a long time period.

TABLE. 5: Boundary conditions during the experiment with freezing temperatures.

Type of boundary condition	Average value in time period		
Testing period (from day to day)	112 to 149	149 to 162	162 to 179
Temperature in the environmental chamber	20.3 °C	21.4 °C	21.5 °C
Relative humidity in the environmental chamber	71 %	71 %	75 %
Pipe temperature	-1.2 °C	-3.5 °C	19.4 °C

Conclusion is that the wick-concept insulation cannot be used for cold piping where permanent minus temperatures are, unless other deeper investigations into this subject are made. The insulation however may work on freezing temperatures. The wick must content an anti-freezing liquid (suitable is glycerine or glycol). Then there is a continuous removal of condensed water from the pipe surface to the ambient air. But it is a slow process. Experiments showed that it was not sufficient to prevent a weight gain. This was because more water vapour got into the system not only through the slot, but moisture by-passed the wick. It is therefore necessary to ensure proper closing of the longitudinal joint and install the second vapour retarder to slow down diffusion into the system. The system should be as closed to water vapour diffusion as possible. Recommendation is to seal the evaporation area with perforated tape and then use the second jacket, for example a PVC jacket (with open longitudinal joint or with holes in the jacket above the evaporation area).

Contrary the trial also showed that the insulation is suitable for piping where subzero temperatures are not permanent. Frozen moisture will melt in periods when the pipe surface has temperature above zero, will be sucked up by the wick and moved to the ambient air. It is confirmed by Figure 7 – from time mark 2 for sample 4 and from time mark 3 for all other samples).

Application of self-drying insulation for permanent minus pipe temperatures is now possible only by applying of two insulation layers (see Figure 8). First one increases the surface temperature above zero. Such insulation must be vapour tight. Closed-cell insulation (e.g synthetic rubber) or mineral wool with aluminium facing can be used. Then self-drying insulation is applied in such thickness to either avoid dripping from outer surface or to reduce heat losses (to be maximally economical). The wick fabric is wrapped around the aluminium jacked of the first insulation layer or touches directly the synthetic rubber. The temperature of the wick is higher than 0 °C, which means that the system will work permanently. In the start-up period there will be a water vapour drive from the ambient air towards a layer with the wick. After the start-up period the wick fabric will get moist and the vapour pressure in the gap opening near the ambient will increase to almost saturation at room temperature. This means that there will be a drying potential from the protruding wick towards the room air, and therefore water vapour from the room air cannot diffuse into the slot in the jacket. Water vapour can only diffuse into the insulation through the vapour retarder jacket and flaws. This amount of water vapour will condense at the vapour retarder jacket under the wick, will be absorbed by the wick and safely sucked up to the ambient air. Inner vapour retarder jacket is protected against mechanical abuse by the second insulation layer. Therefore, there is almost no danger of failure of the first insulation layer which would lead to the failure of the whole insulation system.

1 – Fluid temperature below freezing point

2 – Cold pipe

3 – First insulation layer (e.g. mineral wool pipe section)

4 – Vapour retarder jacket (Al-foil)

5 – Wick fabric

6 – Second insulation layer (self-drying insulation)

7 – Vapour retarder jacket (Al-foil)

8 – Aluminium overlap for attachment of the wick fabric

9 – Evaporation area in width 15 mm. The rest of width of the wick is sealed to underside of aluminium overlap.
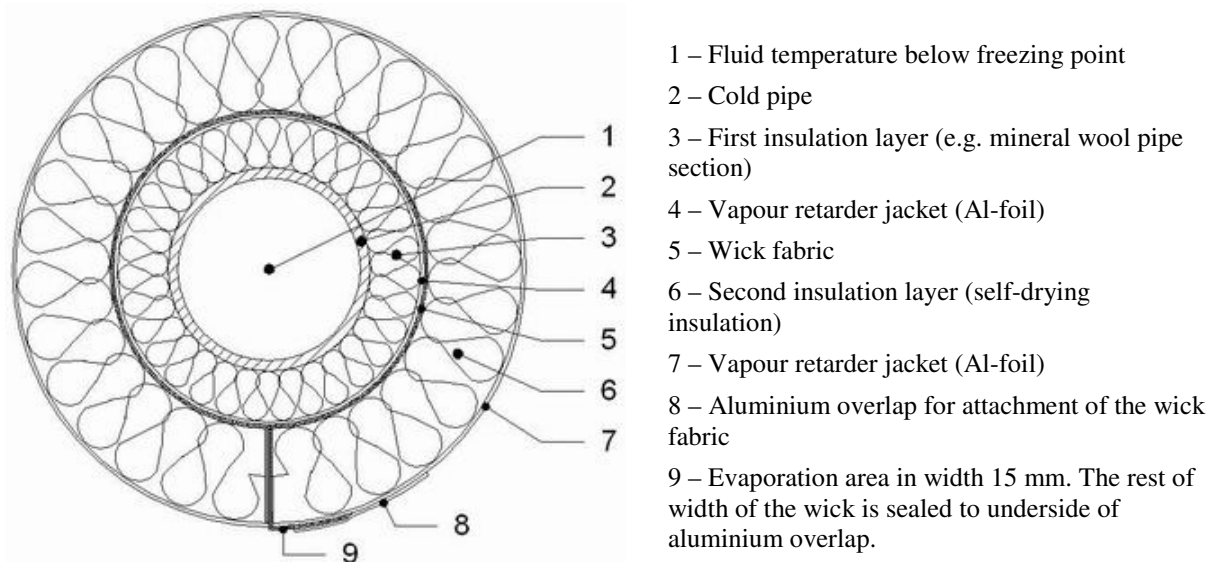
FIG. 8: Double layering for minus pipe temperatures.

4. Conclusions

The wick-concept insulation can avoid moisture accumulation in the insulation and allow to use advantages of mineral wool insulations also for cold piping. However, there are some disadvantages. The insulation therefore cannot be used for all applications.

Advantages of the wick-concept insulation:

The active element (the wick fabric) keeps the insulation dry, allowing it to maintain its thermal conductivity at the same value during the whole lifetime of the system. The only condensed water is trapped in the wick. The energy requirement to keep the right low temperature is thus also less when the insulation is dry which saves costs for cooling and released CO_2 with positive environmental implications.

No glue is needed. The insulation do not need to have an absolutely tight vapour retarded jacket, because water vapour that diffused through the jacket or possible flaws towards the cold pipe is sucked up by the wick into the ambient air.

The insulation may readily be installed on operating systems even if the pipes are wet. The system do not have to be shut down during the product's installation.

Disadvantages of the wick-concept insulation:

The insulation cannot be used for applications where boundary conditions do not allow evaporation from protruding part of the wick, e.g. direct burial for underground piping.

Slightly wet wick may lead to corrosion under insulation if a steel pipe is not properly protected by two layer anticorrosive painting. Here in Europe, essentially all piping is coated for corrosion protection, it is considered to be as part of good design practice. However, corrosion inhibitor can be injected into the wick fabric which can protect steel cold pipe. Then there would be even lower anticorrosive demands than for closed cell insulations. The necessity of further investigation is needed.

5. References

Ashrae Handbook (2005). Fundamentals, Chapter 26 – Insulation for Mechanical Systems, Atlanta, USA, Chapter 26, p.26.10, ISBN 1-931862-71-0.

Choudhary M.K., Karki K.C., Patankar S.V. (2004). Mathematical modelling of heat transfer, condensation, and capillary flow in porous insulation on a cold pipe, International Journal of Heat and Mass Transfer 47, p.5629-5638.

Crall C. (2004). Chill out! Insulation Outlook, August 2004, p.14-22.

Korsgaard V. (1993). Innovative Concept to Prevent Moisture Formation and Icing of Cold Pipe Insulation, ASHRAE Transactions, Vol 99, Part 1.

Korsgaard V. (1994). Novel Concept for Self-Drying of the Insulation of Cold Piping, Journal of Thermal Insulation and Building Envelopes, Vol 17, April 1994.

Korsgaard V. (1997). Innovative Self-drying Concept for Thermal Insulation of Cold Piping, Insulation Materials: Testing and Applications: Third Vol, ASTM STP 1320, R.S. Graves and R.R. Zarr, Eds., American Society for Testing and Materials, p.416-425.

Korsgaard V., Guldbrandsen T. (1999). Analytical and Numerical Calculations of Moisture Accumulation from Flaws in Insulated Cold Piping, Proceedings of the 5th Symposium on Building Physics in the Nordic Countries, Chalmers University of Technology, Göteborg, Sweden, ISBN 91-7197-795-3.

Koverdynsky V., Korsgaard V., Rode C. (2006). The Wick-Concept for Thermal Insulation of Cold Piping, Journal of Building Physics, Vol 29, No. 4/April 2006, London: SAGE Publications, Great Britain, p.313-327, ISSN 1744-2591.

Koverdynsky V. (2007). Self-Drying Insulation for Cold Piping, Ph.D. Thesis, Brno: BUT, Czech Republic, 147p.

"Condensation and drainage of condesate in train enclosure systems exposed to high moisture loads"

Folke Björk, Docent
Div of Building Technology, Kungl Tekniska Högskolan; SE-10044, Stockholm, Sweden.
folke.bjork@byv.kth.se

Tomas Enochsson Civ Ing.
Ramböll Sverige AB, Box 1932 , SE-791 19 Falun, Sweden.
tomas.enochsson@ramboll.se

KEYWORDS: *Thermal insulation, condensation, drainage, Basotect, Moniflex, Isover, railway carriages.*

SUMMARY:
In this experimental study properties of condesate formation and drainage were studied for three different thermal insulation materials, glass wool (from Isover), melamine foam (Basotect) and corrugated sheets of cellulose plastics (Moniflex). The materials are quite different with respect to condesate formation and maximal moisture accumulation at similar environmental conditions. Depths of materals refers to railway applications but the processes studied are relevant to all wall construction.

1. Introduction

In this experimental study properties of condesate formation and drainage were studied for three different thermal insulation materials. This kind of processes may occur in any kind of building construction although the starting point this time was the needs for understanding of processes occurring in walls in railway carriages. So the process of condesate formation and drainage was studied for three different thermal insulation materials that are common in railway carriages.

When condesate formation occur in building constructions the moisture will impair the thermal resistance of the construction. The moisture could also make harm to the thermal insulation material. In case the moisture will drain to other parts of the construction it may increase the moisture content in construction materials and cause different types of damage.

In railway carriages, that also is some kind of a building construction that need thermal insulation, the outdoor environment could change very quickly because of the train moving in and out of tunnels or between different climate zones. Condensate formation could occur in this kind of constructions. So this is worth studying.

The effect of moisture on heat transfer in thermal insulation materials is formalised in the ISO-standard 10051 (1). There are a number of researchers who have given contributions to the understanding in this field.

Peuhkuri (2) has studied combined moisture and heat for a number of thermal insulation materials with the aim to investigate how a number of different porous insulation materials (mineral wool,cellulose fibre etc.) performed hygrothermally under conditions similar to those in a typical building envelope.

The liquid distribution, total moisture gain, heat flux and temperature distributions for moisture absorption in fibrous insulation materials were studied by Wijesundera et. al. 1992 (3). Moisture transport mechanisms along the fibre direction and perpendicular to the fibre direction were not the same. Capillary rise occur along the fibres but not perpendicular to them. Wijeysundera et al , 1996 (4) mention four stages of transport processes: 1: A relatively short initial transient stage in which the temperature and vapour concentration fields are developing within the insulation slab. 2:Heat and vapour transfer reach a quasi-steady state, and the temperature and vapour density fields are invariable with time. Liquid is accumlated in the wet region, but is still at a low level and does not have significant effect on the transport properties. 3: When liquid accumulation exceeds a critical value the liquid starts to move due to the generated liquid pressure and will flow towards the wet-dry interface. 4: In the last step the liquid front will eventually reach the exposed surface, and liquid accumulation in the slab continues.

Simonson et al (5) have studied simultaneous heat and mass transfer through a medium-density fibreglass insulation bay. During the study the insulation was open to ambient air at a specific humidity on the warm side. The cold side boundary was an impermeable cold plate at specific temperatures. Thermal hysteresis was noted at high levels of relative humidity, i.e. when condensation occurred in the fibrous insulation material. This study exemplifies how condensation occurs in insulation materials.

2. Aim of this work

Aim of this work was to study condesate formation and drainage of condence in wall constructions that are used in railway carriages and with such materials that occur there. However, these processes are to be anticipated in any wall construction.

3. Materials in the study

Three materials were studied and their properties are compiled in TABLE 1;

Glass wool; Isover AB in Sweden had produced the material for this study. It was the common quality used for railway applications.

Melamine foam; Trade mark of this material, produced by BASF, is Basotect. It is stated to be flame resistant to 200ºC and flame retarding, as well as an acoustically absorbent and thermally insulating material because of the open structure. This cellular plastic material is commonly used in railway carriages. (Press release 22 and 23 June 2004 From BASF).

Corrugated sheets of cellulose plastics (CSCP); This insulation material is produced out of corrugated sheets of cellulose plastics. The sheets are at about 0,09 mm thick. After folding they are glued to boards, as shown in FIGURE 1 below. Every pair of two layers in the board adds at about 10 mm to its thickness. The folded structure gives CSCP quite special properties regarding diffusion resistance and possibility for any condence water to run off. Since the 1930ies this material has been used as thermal insulation especially in railway cars, where good properties regarding vibrations and moisture and low weight are of importance. Because it is translucent the material has also found applications in facades and roofs made of glass. The material will be called "CSCP" in this report. Trade mark for this material is "Moniflex".
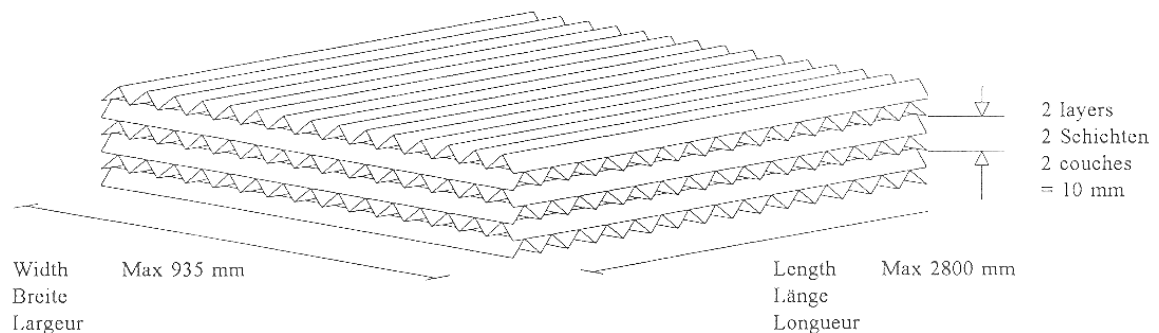

FIGURE 1, Corrugated sheets of cellulose plastics (CSCP).

TABLE 1 Material properties

Material		CSCP	Glass wool (Isover)	Melamine foam (BASF)
Density	ρ [kg/m^3]	13	20	10
Thermal conductivity	λ_{10} [W/(m*°C)]	0,056	0,038	0,035
Diffusion resistance factor	μ [1/1]	280	1-2	1-2
Coefficient of permeability	δ_v [m^2/s]	$0,09 \cdot 10^{-6}$	$20 \cdot 10^{-6}$	$20 \cdot 10^{-6}$

4. Experimental

In this work condesate formation in walls with the insulation materials more or less open to conditioned indoor air is studied. Testing was done in a climate simulator, FIGURE 2, with a cold and a warm compartment separated by a wall. The compartments are 2,8 m high and 2,8 m. Six openings were made in the wall for the cassettes for test of different options for thermal insulation of railway carriages shown in Figures 3 and 4.

The warm side of the climate simulator was adjusted to a temperature of 20°C +/- 1 and 55 % RH +/- 3. The cold side was adjusted to keep the wall cassettes in the study facing this side at 0ºC. The relative humidity on the cold side was not regulated, which however did not influence the results because the test walls were well sealed towards this side. These conditions might seem extreme but could actually be the case from time to time. As aim of the work was study of condensate formation conditions need to be aligned to that.
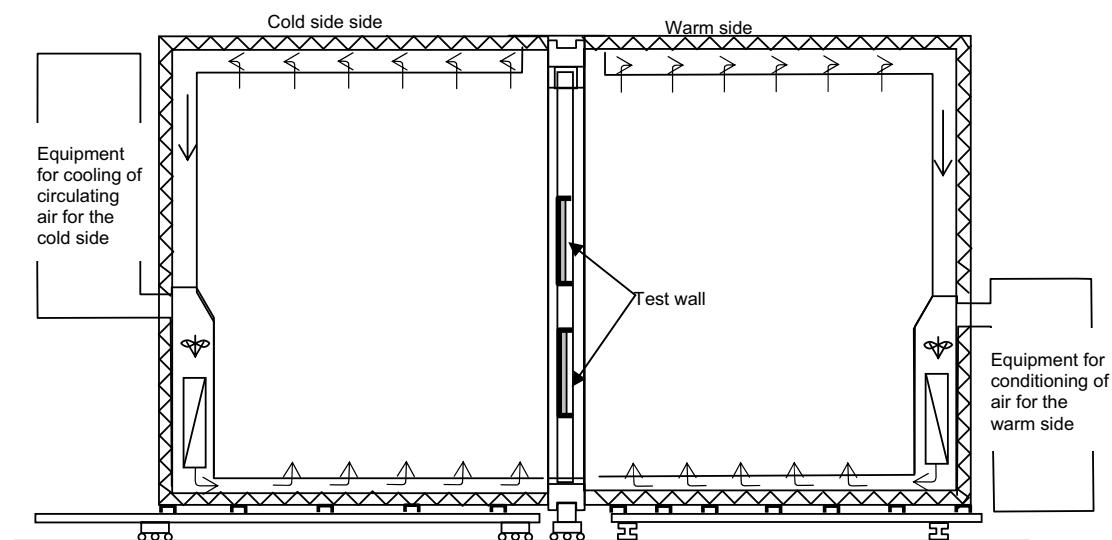

FIGURE 2. Climate simulator

The test wall cassettes were made of 1 mm thick galvanized steel, FIGURES 5 and 6. They were 400 mm wide, 600 mm high and 80 mm deep. In these wall cassettes thermal insulation could be built up to a thickness of 80 millimetres. Besides samples of a single material also some combinations of two materials were tested. The cassettes were in some of the tests capped with sheet metal. Water that was leaving the material by gravity was collected and measured, all to find out how the materials drain in these conditions.

In the bottom of each cassette a 10 millimetre hole was drilled for drainage of any condensed water. This water was captured by use of a funnel placed under the hole. The water was led through a plastic hose to a glass bottle. The amount of captured water was weighed. A fillet, 30 mm high, was mounted at the bottom of each cassette to avoid suction of condensation up into the other materials in the cassettes. A pipette was used for collecting water remaining at the bottom of the cassettes before being weighed.

Thermometers were placed on the side of the cassette facing the cold part of the simulator in order to record surface temperatures (see FIGURE 3). The cassettes were weighed regularly, to see the uptake of condensed water in the construction. Weighing was done with a resolution of 0,1 grams in an electronic balance.

FIGURE 3. *The cold side of the climate chamber, with thermometers on the wall cassettes.*

FIGURE 4. *The wall cassettes shown from the warm side of the climate chamber.*

Tests were done with open and capped walls. In the test with open walls the thermal insulation material was without any capping and exposed to the climate chambers atmosphere (20 ºC, RH 55%) on the warm side. Tests were done with pure insulation materials and also with a number of combinations between two materials, which is described in the results section. The tests were carried out during 120 hours.

To simulate the effect of an inner panelling that is not completely tight measurements were done with the cassettes capped with sheet metal also on the warm side. The joints between cassette and steel sheet were sealed with caulking compound of silicone type. Different levels of tightness were achieved by drilling of one or five holes, 14 mm diameter, in the steel sheets. Tests were performed over a period of 168 hours. With one hole the share of the capping that was open was 0,64‰ and with five holes 3,2 ‰ was open. The amount of holes was selected in order to mimic circumstances in practice.

Tests on the capped walls were done with 60 millimetres of thermal insulation in the wall casettes. The walls were insulated with only Glass wool, CSCP and Melamine foam respectively. Tests were also done on a wall with a combination of 20 mm Melamine foam and 40 mm CSCP, with the CSCP on the warm side.

Figure 8. Wall casette with 5 holes, 3,2 ‰ of total surface.

Figure 9. Wall casette with 1 hole, 0,64 ‰ of total surface.

5. Results and discussion

In open walls the total amounts of condensed moisture and the amount remaining in the material after 120 h are given as grams per square meter of the panel is shown in Table 3. Also the share drained out is indicated.

TABLE 3. Results for walls open to the ambient air, 0ºC on the cold side, 20ºC and 55% RH on the warm side. Moisture after 120 h of exposure

Wall construction		Thermal transmittance	Condesate after 120 h	Remaining moisture in thermal insulation	Drained
Cold side	Warm side				
		$(W/m^2\,°C)$	g/m^2	g/m^2	(%)
Glas wool 60 mm		0,572	457,1	114,3	75
Glas wool 80 mm		0,440	391,7	156,7	60
Melamine 60 mm		0,531	300,0	258,0	14
CSCP 60 mm		0,806	166,7	33,3	80
CSCP 20 mm	Glas wool 40 mm	0,633	275,0	68,8	75
CSCP 20 mm	Melamine 40 mm	0,599	243,8	56,1	77
CSCP 40 mm	Glas wool 20 mm	0,709	358,3	96,8	73
CSCP 40 mm	Melamin 20 mm	0,687	337,5	158,6	53
CSCP 40 mm	Glas wool 40 mm	0,516	279,2	83,8	70
Glass wool 40 mm	CSCP 20 mm	0,633	227,1	74,9	67
Melamine 40 mm	CSCP 20 mm	0,599	243,8	126,8	48

It was noted that:

- In all constructions the steel sheet on the cold side was wet on the side facing the warm room, except for 60 millimetres CSCP, where it was completely dry.
- A lower thermal transmittance of a certain material results in a somewhat lower amount of condesate.
- Walls with only glass wool produced twice as much condence as a construction with only CSCP
- In walls with glass wool 60 – 75 % of condesate was drained away. The remaining water was to a high extent stored in the lowest two centimetres of the wall.
- The wall with Melamine foam had somewhat lower condesate formation than mineral wool, but only 14 % of the condesate was drained away. The remaining water was to a high extent stored in the lowest five centimetres of the material.
- In CSCP 80% of condesate was drained away. The remaining water was collected as small droplets around the outer borders of the insulation plates.
- Combinations with 20 – 40 millimetres of CSCP to the cold side results in 244 – 337 g/m^2 of condesate, of which 53 to 77% was drained away.
- Combinations with 20 millimetres of CSCP to the warm side gives 227– 244 g/m^2 of condesate, of which 48 – 67% was drained away.

Water was easily drained from the CSCP material which also had the lowest level of condensation formation. The high diffusion resistance factor (μ) of the material, or the low coefficient of permeability (δ_v), could also explain this. Glass wool and Melamine foam both had much higher condesate formation. In glas wool 60 – 75% of the condesate was drained off, but in Melamine foam most of condesate remained in the material.

TABLE 4. Results for capped walls, 0ºC on the cold side, 20ºC and 55% RH on the warm side. One hole = 0,64 ‰ of total surface. Moisture after 168 hours of exposure.

Wall construction		Condesate	Remaining moisture in thermal insulation	Drained
Cold side	Warm side	(total)		
		g/m^2	g/m^2	(%)
Glas wool 60 mm		48	48	0
Melamine 60 mm		66	66	0
CSCP 60 mm		12	12	0
Melamine 40 mm	CSCP 20 mm			
Melamine part		20	20	0
	CSCP part	8	8	0

TABLE 5. Results for capped walls, 0ºC on the cold side, 20ºC and 55% RH on the warm side. Five holes = 3,2 ‰ of total surface. Moisture after 168 hours of exposure.

Wall construction		Condensate (total)	Remaining moisture in thermal insulation	Drained
Cold side	Warm side			
		g/m²	g/m²	(%)
Glass wool 60 mm		234	72	69
Melamin 60 mm		138	138	0
CSCP 60 mm		30	18	40
Melamine 20 mm	CSCP 40 mm			
Melamine part		32	32	0
	CSCP part	12	12	0

The results from studies of capped walls are presented in TABLES 4 and 5. It was noted that:
- The highest amount of condensed water was formed in the wall with Glass wool.
- The amount of remaining condesate water, not drained out, was higher in Melamine foam than in Glass wool.
- CSCP has a considerably lower amount of condesate; reason for this is probably its diffusion resistance.
- Although a leakage may look small, it can result in a considerable condensation. When for example the wall with glass wool had a leak corresponding to 0,64‰ of the area to the warm side 48 g/m² of condesate was produced in one week. In this wall however no drainage occurred during the test.
- A layer of 40 mm CSCP on the warm side combined with 20 mm Melamine foam will result in 50% lower moisture build up when compared to a wall with only 60 mm Melamine foam in the wall with 0,64‰ of the area open. In the wall with 6,2‰ of the area open difference was even greater.

6. Conclusions

In this experimental study properties of condesate formation and drainage were studied for three different thermal insulation materials which are quite different with respect to condesate formation and maximal moisture accumulation at similar environmental conditions; glass wool (from Isover), melamine foam (Basotect) and corrugated sheets of cellulose plastics (Moniflex). The materials are often used in railway carriages.

CSCP had very little condesate formation and a big share of the moisture ran off immediately.

Glass wool had the biggest condesate formation of the three materials studied, but also here a big share of the moisture ran off. Much of the remaining moisture was stored in the lowest two cm of the materials sample in tests where the materials were open to warm humid air.

Melamine foam had less condesate formation than glass wool, but also much less drainage, and a considerable amount of moisture remained in the material. Moisture that was not drained away was to a high extent stored in the lower five centimetres of the material.

Combinations of two materials, with CSCP on either the warm side or the cold side in the test set up were methods to decrease condesate formation or to increase drainage.

By choosing thermal insulation material with low vapour conductivity and god run off effects for the condensed water (for example CSCP alone or combined with glass wool), many negative factors that moisture has on a wall construction are being avoided. Because the amount of condesate formed is considerable it is of great importance being able to take care of any run off to avoid damage.

7. References

1   ISO standard 10051 "Thermal insulation – moisture effects on heat transfer – determination of thermal transmissivity of a moist material".

2   Ruut Peuhkuri, Moisture dynamics in building envelopes, Ph.D. Thesis, Report R-071, Department of Civil Engineering, Technical University of Denmark 2003.

3   N.E. Wijeysundera and M.N.A. Howlander, Effects of condensation and liquid transport on the thermal performance on fibrous insulations, Int. J. Heat Mass Transfer 35 (1992) pp. 2605 – 2616.

4   N.E. Wijeysundera, B.F.Cheng and E.G. Hauptmann, Numerical simulation of the transient moisture transfer through porous insulation, Int J. Heat Mass Transfer 39 (1996) pp 995 – 1004.

5   C.J. Simonson, Y.X.Tao an R.W. Besant, Thermal performance and hysteresis in fibrous insulation exposed to moisture and step changes in boundary condition, Energy and buildings 21 (1994) 251 – 257

Frost Formation and Condensation in Stone-wool Insulations

T. Vrána, Ph.D-student,
Department of Civil and Architectural Engineering, Division of Building Materials, Royal Institute of
Technology in Stockholm;
tomas.vrana@byv.kth.se, www.byv.kth.se

F. Björk, Docent
Department of Civil and Architectural Engineering, Division of Building Technology, Royal Institute of
Technology in Stockholm;
folke.bjork@byv.kth.se, www.byv.kth.se

KEYWORDS: *Stone wool, material properties, frost formation, condensation, moisture transport.*

SUMMARY:
Practical experience from building sites show evidence of negative effects of moisture condensation on insulating materials with fibrous structure. Condensed moisture, as well as moisture trapped in thermal insulation during construction, can results in serious reduction of thermal properties and, in consequence, systemic upset of living qualities in dwellings. It can also result in increased dust contamination, algae or mould growth and structural damages due to a frost formation of condensate happening in winter periods.

This contribution reports on a laboratory experiment aimed at growth of frost formation and moisture condensation in stone wool opened to air for specific temperature fields (+20; -20ºC), (+20; -15ºC), (+20; -10ºC) over stone-wool specimens with varying density during a testing period that lasted 100 hours. Air on the warm side was saturated with moisture. In the part facing the warm humid air condensate formation occurred, while frost accumulated with time in the part of the specimen facing the cold air. Transition between frost and liquid condensate was clearer in the stone-wool specimens of higher density and for tests with broader temperature fields. Moisture resistance factor µ, a basic moisture characteristic of an insulating material, also had an upward trend for broader temperature intervals.

Deeper knowledge about the phenomenon of frost formation in stone wool can help to insight into actual problems in the building sector resulting from usage of thermal insulations with high thicknesses.

1. Introduction

This paper is a first step in research project intent on finding damages of mineral insulation based on stone wool caused by frosting condensate and inbuilt moisture in time. The usage of thicker insulation, according to higher requirements on low thermal transmittance of building constructions (U-value), opens new questions about life-quality of dwellings under offense of moisture contained in building envelopes. To provide a detailed study of a building material and its use, it is important to know the real material qualities, which might be slightly distinct from tabulated values. Connected important issues are how fibrous insulation materials respond to circumstances when condensation or frost formation annually repeats and how this kind of processes affects material properties and durability of the material itself.

Moisture resistance factor µ, according to ISO/FDIS 9346, is the ratio between moisture resistance of a space filled with a thermal insulation material and the moisture resistance of the same space when only containing stagnant air. This is a basic moisture characteristic for thermal insulating materials. When surface temperatures of a stone-wool specimen differ in tens of degrees Celsius, we can observe a formation of frost in the material and, in consequence, aforementioned discrepancies in moisture properties. Findings on water transport and travel of condensate, as well as, formation of frost from inbuilt moisture in stone-wool insulations can contribute

to sort out what kind of damage mineral wool may undergo and how moisture may impact durability of fibrous materials.

Heat and moisture transport processes have been a matter of study in some previous researches. Moisture dynamics in building envelopes was presented by Peuhkuri (2003). The role of absorbent building materials in moderating changes of relative humidity was described by Padfield (1999). Impact of moisture on thermal conductivity is formalized in the standard ISO 10051.
A contribution about coupled heat and moisture transfer through fibrous insulation, which (for the first time) takes into account evaporation and mobile condensates, was elaborated by Jintu Fan and Xinghuo Wen in 2001. The same authors (et al.) came two years later with an improved model of heat and moisture transfer and its comparison with experimental results.

2. Moisture Transfer in Porous Materials

Moisture transport in porous materials is represented by vapour diffusion, surface diffusion and capillary conduction. The executed laboratory measurements were based on a fundamental moisture transport theory by diffusion represented by Fick´s law and its variations. A computational model concerns about the moisture resistance factor μ as the key moisture characteristics of building materials.
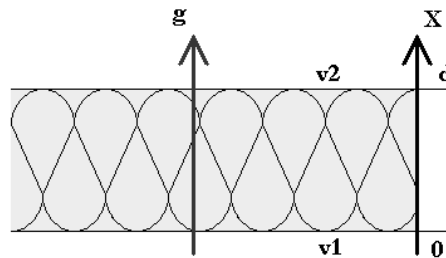

FIG. 1: Diffusion of water vapour flux through a layer of a porous material (e.g. stone wool). Vapour permeability of a material is termed δ_v (see Equation 1). Humidity by volume v is kept at v1 at one side of the layer and at v2 on the other side. The steady-state diffusive flux is defined as g.

According to Fick´s empirical law the steady-state diffusive flux g is:

$$g = \delta_v * \frac{v_1 - v_2}{d} \quad [kg/(m^2 s)] \qquad (1)$$

Diffusive flux multiplied by cross-section surface of a sample gives us moisture flow rate G:

$$G = A*g \ [kg/s] \qquad (2)$$

Since moisture flow rate G in our case was obtained by laboratory measurement (see Chapter 5), we can rearrange equation 1 and use it for calculation of g:

$$g = \frac{G}{A} \quad [kg/(m^2 s)] \qquad (3)$$

Courses of outdoor temperatures (T_e) and outdoor relative humidity (Rh_e), as well as, indoor conditions (T_i, Rh_i) were registered by sensors during all measurements and used in particular calculation –for instance in the Ideal gas law, which gives the relation between the vapour content and the partial pressure:

$$p_v=461,4*(T+273,15)*v \ [Pa] \qquad (4)$$

The water vapour content of air, or humidity by volume, is denoted by v (see equation 4). At the same time, relative humidity Φ (Rh_i, Rh_e were registered during each laboratory measurement) is defined as proportion between humidity by volume and water vapour content in air at saturation v_s:

$$\Phi = \frac{v}{v_s} \; [-] \quad \rightarrow \quad v = \frac{\Phi}{v_s} \; [kg/m^3] \qquad (5)$$

Whereas v_s is:

$$v_s = \frac{a*(b+\dfrac{T}{100})^n}{461,4*(T+273,15)} \; [kg/m^3] \qquad (6)$$

And can be calculated with the appropriate coefficients a, b, n for both outdoor and indoor temperatures (T_e, T_i)
$0 \leq T \leq 30°C$ $a = 288,68\,Pa$ $b = 1,098$ $n = 8,02$ $-20 \leq T \leq 0°C$ $a = 4,689\,Pa$ $b = 1,486$ $n = 12,3$

Finally, moisture resistance factor μ is defined as:

$$\mu = \frac{D}{\delta_v} \; [-] \qquad (7)$$

Where vapour permeability δ_v is known from equation 1 and coefficient of diffusion water vapour in air D is generally expressed:

$$D = (22.2+0.14*\theta)*10^{-6} \; [m^2/s] \qquad (8)$$

θ is temperature in °C.

The moisture resistance factor μ is defined for an isothermal case. In this study it is a thermal field over the stone-wool specimens. The μ value is here calculated using the value for the coefficient of diffusion D that is valid at the mean temperature of the tested sample.

3. Materials

Tested material specimens were fibrous insulations based on stone-wool with different densities and specific sphere of use. All used samples are commercial products taken from a product portfolio of a major producer. Samples with dimensions 300mm (length) x 300mm (width) x 100mm (thickness) were dried and weighed prior to measurements and their dry densities ρ_d were calculated.

The heaviest material sample – SPECIMEN A is primarily used for flat-roof constructions. It is a stiff heavy board of stone wool with integrated double-layer characteristics and water-resistance throughout whole volume. Fibres are bonded by organic resin.
The second fibrous material – SPECIMEN B is a rigid stone-wool board, fully water-resistant, used mainly for flat roofs.
The lightest insulation in the laboratory measurement – SPECIMEN C is a semisoft bat, fully water-resistant. It is used for pitched-roof insulation, ventilated facades and sandwich walls.

Specimen	Declared thermal conductivity λ_D [$Wm^{-1}K^{-1}$]	Dry density ρ_d [kgm^{-3}]
A	0,040	145
B	0,039	112
C	0,035	44

TABLE 1: Declared basic technical parameters of the tested material specimens with stone-wool structure

4. Experimental

4.1 Test Equipment

At the Department of Civil and Architectural Engineering of the Royal Institute of Technology in Stockholm we designed and built up a special testing device simulating a room with high moisture load to observe condensation and frost formation in fibrous insulations.

The testing set-up consists of a plastic box with open roof, which was settled by thermal insulation specimens based on stone wool. All samples were 100mm thick and with surface 300*300mm. Walls and the bottom of the box were insulated with 40mm thick XPS boards on the outside and coated by an aluminous foil to prevent any weight-gain in surrounding walls caused by moisture uptake from ambient air.
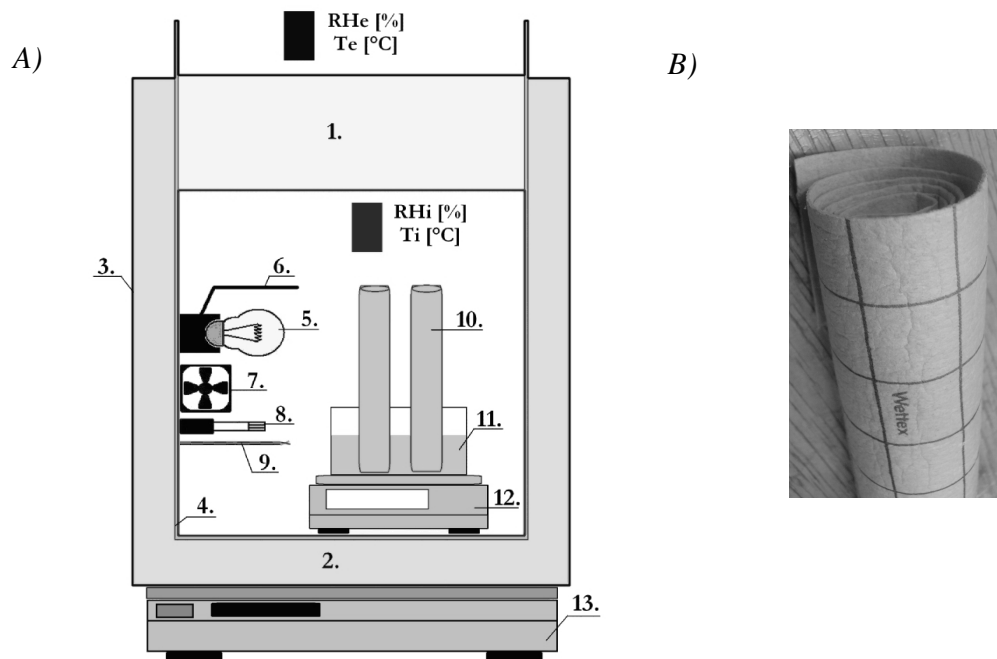
FIG. 2: A) Composition of testing set-up including numbered list of components; B) Wettex – a piece of non-woven material based on cellulose with high water retention and water sorption.

1.material sample (SPECIMEN A, B, C; d= 100mm), 2.XPS insulation of the box-walls (th. 40mm), 3.aluminium-foil coating, 4.plastic wall of the box, 5.light bulb providing heating of the box, 6.cover of the light bulb to avoid radiation, 7.ventilation fan providing circulation of air in the testing box, 8.calibrated humidity sensor (Mitec HMP50U-1), 9.temperature sensor, 10.Wettex textile installed to increase evaporation of moisture in the box, 11.water reservoir with circa 400 ml of water, 12.precision laboratory balance (Kern EW 1500-2M) registering evaporation of water from the reservoir, 13.precision laboratory balance (Mettler PM-11N) registering a change of weight of the entire system.

In the box was placed a vessel with water. Volume of water was 400ml. For faster spread of moisture in the box, the water reservoir was equipped with two tubes of Wettex textile – a piece of non-woven material based on cellulose with high water retention and water sorption. Evaporating water from the inner reservoir was registered by a precision laboratory balance under the vessel. The box was also equipped with calibrated moisture and temperature sensors collecting data about inner conditions (T_i, Rh_i). Stable indoor temperature in

the box was provided by a light bulb connected to a voltage transformer. Light bulb shielding protected specimens from heat radiation. To keep circulation of warm air in the inner space, we used a tiny ventilation fan. Any weight change of the entire system was registered by the second precision balance placed under the testing box. Thanks to both inner and outer balances, it was possible to observe the amount of moisture evaporating in the system and the amount that truly left the system.

To control temperature gradient and relative humidity in material specimens, extra three moisture and temperature sensors were installed into outer sides and centre of each material sample, see Figure 3. That gave us a complex view of moisture processes in different altitudes. Moisture leakages in joint around the material sample were denied by sealing with non-absorbent polypropylene tube and silicon bonding agent.
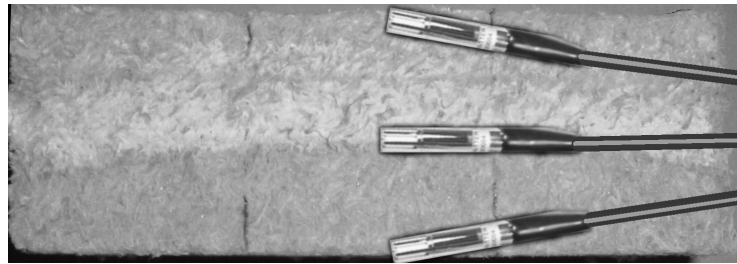
FIG. 3: Compound humidity and temperature sensors Mitec HMP50U-2 and their installation in the material specimen (Specimen B, T_e= -20 °C, T_i=+20 °C).

The entire testing set-up was placed in a climate chamber with regulated temperature T_e. Conditions of the climate chamber were recorded by another couple of temperature and humidity sensors. The testing cycle lasted for 100 hours. Conditions remained stable during the measurements and were disturbed just by short freezing intervals of the climate chamber providing demanded thermal conditions (T_e). Thanks to two pieces of Wettex (mentioned above) the inner volume of the plastic box (30 litres) became saturated by water flux within a few minutes. After reaching the saturated state, relative humidity in the box (RHi) remained stable for the rest of the testing interval.

The collected data were analyzed and charted into figures. Thanks to the methodology of the practical measurement, moisture flow rate G (kg/s), diffusive flux g (kg/m^{2}s) and, consequently, moisture resistance factor μ (-) could be calculated.

5. Results and Discussion

5.1 Proceedings
Specimens were tested for three different outdoor temperatures (T_e=-20°C, T_e=-15°C, T_e=-10°C), while the indoor temperature was the same for all measurements, T_i=+20°C. All the sensors stored information about internal (T_i, Rh_i) and external (T_e, Rh_e) conditions in two minutes intervals. Each measurement lasted 100 hours. Within a few minutes after ending the testing period, material samples were sawn into pieces at two altitudinal levels and each piece was weighed before drying. Also a detailed analysis of moisture balance in the entire system was carried out and we observed how much water evaporated from the inner vessel, amount of condensate in the testing box, frost and condensate in stone-wool specimens, as well as, weight change of the entire system.

Water in the upper part of specimens was in form of frost (see Figure 4), which accumulated in time. The frost was quite equally spread over the depth of tested materials. Growth of frost formation in specimens was clearly visible in cross-sections of material samples A and B (materials with higher densities). There was no visible zone of frost formation and condensation in the specimen C (material with the lowest density) even it occurred.

The collected data were analyzed and charted into figures. Moisture characteristics like moisture flow rate G (kg/s), diffusive flux g (kg/m^2 s) and, consequently, moisture resistance factor μ (-) were calculated in accordance with the theory for diffusive moisture transport theory in porous materials described in section 2.
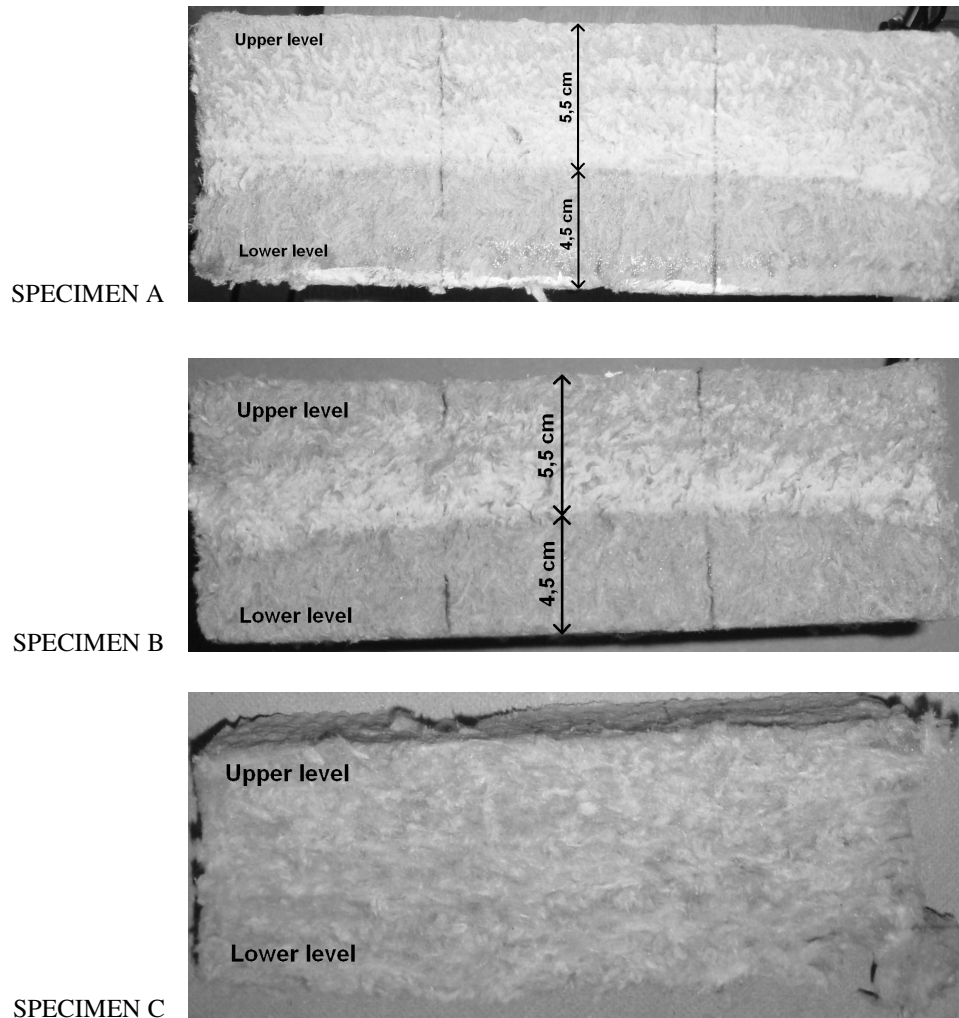

SPECIMEN A

SPECIMEN B

SPECIMEN C

FIG. 4: Frost formation (upper level) and the region of condensation (lower level) in specimens A,B,C for the temperature field T_i=+ 20°C, T_e=− 20ºC. The bottom surface of the lower level seems to be saturated by condensate, which could drain out of the material.

Measured and calculated data are summarized in Table 2 below. Moisture resistance factors μ for all tested materials were highest for outdoor temperature Te=– 20ºC and also the frost formation was most widespread in this case. The frost was stationary and also in practical cases it does not melt and evaporate until outdoor conditions turn.

Mu factors were compared with those given in standards. They were found to be 2,5 times or 3 times higher than standard values, that are equal to 1 for both dry or wet mineral wool with density between 10-200 kg/m^3, for the highest temperature gradient through the material (Te=-20°C; Ti=+20°C). Consequently, EN 13162 says:" In the absence of measurements, the moisture resistance factor, μ, of mineral wool products, either unfaced or faced with a fabric with an open structure, may be assumed to be equal to 1." Remaining μ values for the

temperature gradients (Te=-15°C; Ti=+20°C), (Te=-10°C; Ti=+20°C) had a downward trend (see Table 2) towards the tabulated values.

Previous laboratory measurements worked with the same testing set-up, the same type of the stone-wool specimen (Specimen A), as well as dimensions of material samples and with the climate chamber at the temperatures: T_e=+20°C, +15°C, +10°C and +05°C. The detected μ values were in the interval 1,1-1,3. This coincides with tabulated values introduced in EN standards mentioned above.

SPECIMEN A				
External conditions		Internal conditions		μ [-]
T_e=-20°C Rh_e=63%		T_i=+20°C Rh_i=72%		3,05
T_e=-15°C Rh_e=66%		T_i=+20°C Rh_i=75%		2,03
T_e=-10°C Rh_e=72%		T_i=+20°C Rh_i=78%		1,94

SPECIMEN B				
External conditions		Internal conditions		μ [-]
T_e=-20°C Rh_e=66%		T_i=+20°C Rh_i=72%		2,44
T_e=-15°C Rh_e=67%		T_i=+20°C Rh_i=75%		1,82
T_e=-10°C Rh_e=73%		T_i=+20°C Rh_i=77%		1,81

SPECIMEN C				
External conditions		Internal conditions		μ [-]
T_e=-20°C Rh_e=63%		T_i=+20°C Rh_i=72%		2,85
T_e=-15°C Rh_e=68%		T_i=+20°C Rh_i=75%		1,92
T_e=-10°C Rh_e=72%		T_i=+20°C Rh_i=76%		1,65

TAB. 2: Experimentally measured moisture resistance factors µ of stone-wool specimens with varying density for the temperature field over the specimen + 20 and – 20ºC, + 20 and – 15ºC, + 20 and – 10ºC and the time interval 100 hours.

Taking into account results from others´ research, water vapour transport properties of stone wool are also influenced by fibre orientation and bulk densities of used specimens.

5.2 Future work
To get wider perspective about formation of frost in stone wool insulations, we plan to complete our laboratory measurement with thermal fields (+20°C; -5°C) and (+20°C; 0°C). Further studies are worth to explain why the moisture resistance factor is comparatively high under these circumstances.

6. Conclusions

The constructed testing set-up as well as the chosen research method was found effective in the studies of moisture processes in stone-wool based insulating materials. It also proved that the phenomenon of frost formation in the stone wool can exist for specific temperature gradient and moisture load.

Frost formation in samples of stone wool open to air was noted in all cases when the temperature field over the specimen was between + 20 and – 20ºC, + 20 and –15ºC, + 20 and – 10ºC and the air on the warm side was saturated with moisture. In the part of the specimen facing the warm humid air condensate formation occurred.

The studied specimens had varying densities (Specimen A - ρ_d=145kg/m^3, specimen B - ρ_d=112kg/m^3, specimen C - ρ_d=44kg/m^3). Samples with higher densities (A, B) were visibly divided into the zone of frost formation and the zone of condensation. Also in the lightest sample (C) frost formation and condensation occurred, but no sharp borderline was observed.

Moisture resistance factors μ, that were calculated from collected data, for all three types of material samples for the temperature field over the specimens $T_i=+20°C$, $T_e=-20°C$ are 2,5 times up to 3 times higher than the tabulated value (EN 12524), which is $\mu = 1$ for mineral wool with density between 10-200 kg/m^3.
Measured μ values for all three types of material samples for the temperature field over the specimens $T_i=+20°C$, $T_e=-15°C$ and $T_i=+20°C$, $T_e=-10°C$ have a downward trend and get closer to the tabulated value.

Further studies are relevant in finding why moisture resistance factor (μ) in stone wool is comparatively high under circumstances of frost formation and if this can deteriorate in time. Last but not least, consequential degradation of the material structure together with loss of insulating qualities is paramount from the view of new trends in building industry, energy costs and sustainable development.

7. References

ISO/FDIS 9346 (2007). Hygrothermal performance of buildings and building materials – Physical quantities for mass tranfer - Vocabulary, ISO Geneva, p. 1-10.

Peuhkuri R. (2003). Moisture dynamics in building envelopes, *Ph.D. Thesis,* DTU Lyngby.

Padfield T. (1999). The role of absorbent building materials in moderating changes of relative humidity, *Ph.D. Thesis*, DTU Lyngby.

Jintu Fan, Xinghuo Wen (2002). Modeling heat and moisture transfer through fibrous insulation with phase change and mobile condensates, *International Journal of Heat and Mass Transfer 45*, p 4045-4055.

Jintu Fan, Xiaoyin Cheng, Xinhuo Wen, Weiwei Sun (2004). An improved model of heat and moisture transfer with phase change and mobile condensates in fibrous insulation and comparison with experimental results, *International Journal of Heat and Mass Transfer 47*, p. 2343-2352.

Hagentoft, C.E. (2001). Introduction to Building Physics, Lund: Studentlitteratur, p. 87-149.

Jóhannesson, G. (2004). Lectures on Building Physics, Stockholm, p. 117-147.

EN 13162 (2001). Thermal insulation products for buildings – Factory made mineral wool (MW) products – Specification, Brussels: European Committee for Standardization, p. 8-23.

EN 12524 (2000). Building materials and products – Hygrothermal properties – Tabulated design values, Brussels: European Committee for Standardization, p. 1-9.

Vrána T., Björk F. (2007). A laboratory equipment for the study of moisture processes in thermal insulation materials when placed in a temperature field. *E-Journal Construction and building materials*, Ms. Ref. No.CONBUILDMAT-D-07-00180.

Michálek P., Jiřičková M., Pavlík Z., Černý R. (2006). Hydrophilic mineral wool materials: The effect of fiber orientation, *Proceedings of 3rd International Building Physics Conference*, Montreal, p. 91-95.

Jiřičková M., Černý R. (2006). Effect of hydrophilic admixtures on moisture and heat transport and storage parameters of mineral wool. *E-Journal Construction and Building Materials 20 (2006)*, p. 425–434.

Hygrothermal Properties and Performance of Sea Grass Insulation

Marlene Stenberg Hagen Eriksen, M.Sc. Student,
Technical University of Denmark;
m_hagen@ofir.dk

Theresa Back Laursen, M.Sc. Student,
Technical University of Denmark;
theresa_back@ofir.dk

Carsten Rode, Associate Professor,
Department of Civil Engineering, Technical University of Denmark;
car@byg.dtu.dk

Kurt Kielsgaard Hansen, Associate Professor,
Department of Civil Engineering, Technical University of Denmark;
kkh@byg.dtu.dk

Summary: In the attempt to obtain knowledge of the hygrothermal properties of sea grass as thermal insulation, experiments have been carried out in the laboratory to determine the thermal conductivity, sorption properties and the water vapour permeability of the material.
In order to investigate the hygrothermal performance in the field, four test walls have been built. The relative humidity and temperature in the constructions have been measured during a winter period and are presented in this paper.

1. Introduction

Historically, sea grass has been known and used for years as thermal insulation. However, it is not recognized as a contemporary building material, and thus information regarding its hygrothermal properties and performance in modern constructions is scarce.

As an organic building material it is of interest, however, to investigate the hygrothermal properties and performance of sea grass as thermal insulation. This is done by performing experiments in the laboratory as well as measurements in the field. The laboratory experiments consist of determination of thermal conductivity, determination of hygroscopic sorption properties and determination of water vapour transmission properties. Similar experiments have previously been performed on other alternative insulation materials such as paper wool, sheep's wool and straw, however, results concerning sea grass have been difficult to identify. The measurement in the field consists of measurement of temperature and relative humidity throughout the constructions.

2. Description of sea grass insulation

Sea grass is an excess product from the sea. The width of one straw is typically 3-6 mm, while the length varies from a few centimetres to pieces as long as 50 cm. The material investigated is a loose fill material having a density of 53 kg/m^3.

In this paper investigations are performed with both regular and washed sea grass. The regular sea grass is going through an initial process, where it is washed and dried naturally outside and then baled. Since the material is not further processed, it might contain salt, when used in buildings as thermal insulation.

3. Determination of thermal conductivity

To determine the thermal conductivity of regular sea grass, a hot plate apparatus was used. A sketch of the equipment as well as a photo can be seen in Figure 1.
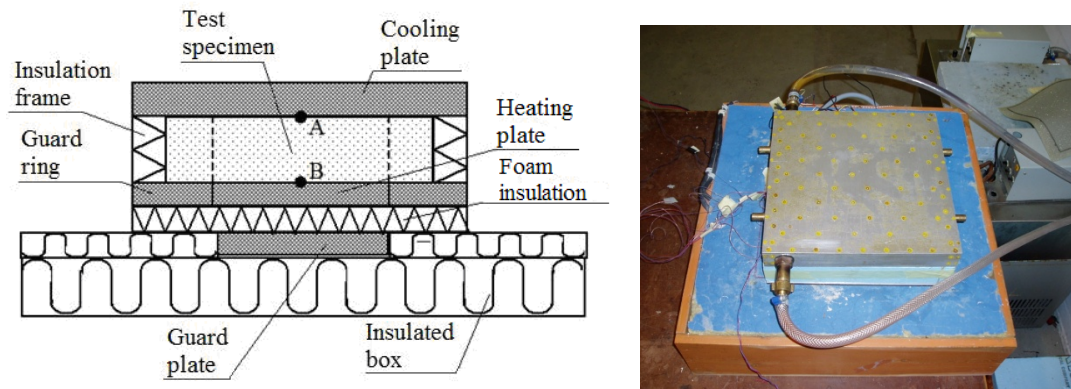

FIG. 1 Equipment used for determination of thermal conductivity of regular sea grass.

To investigate the correlation between density and thermal conductivity a number of measurements have been carried out on regular sea grass with different densities. The results of these experiments are shown in Figure 2.
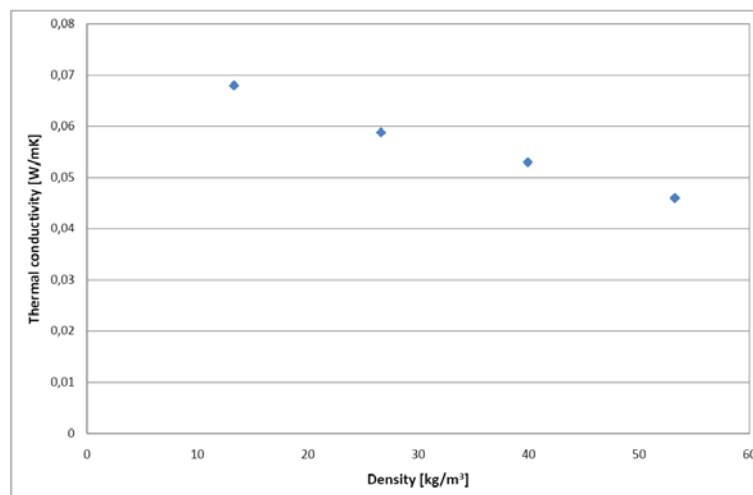
FIG. 2: Thermal conductivity of regular sea grass insulation as a function of density.

As can be seen from the results, the thermal conductivity is decreasing with an increasing density, and an approximately linear correlation between density and thermal conductivity can be seen. The lowest thermal conductivity of 0.046 W/mK is obtained at a density of 53 kg/m^3.

4. Determination of hygroscopic sorption properties

As previously mentioned regular sea grass contains salt, which is known to have a great influence on the hygroscopic sorption properties. Therefore, the hygroscopic sorption properties of both regular and washed sea grass have been determined.

The determination of the sorption properties is performed in a climatic chamber according to ISO 12571 (2000) where the temperature in the chamber is sought maintained at 23 °C while the relative humidity is altered. The specimens are arranged in fine-meshed bags of polyester, which are tacked in order to prevent the specimens from falling to the bottom of the bags. After finalizing the measurements, the specimens are dried at 105 °C until constant mass is reached. A sketch and a photo of the arrangement of the bags inside the climatic chamber with automatic weighing equipment can be seen in Figure 3.
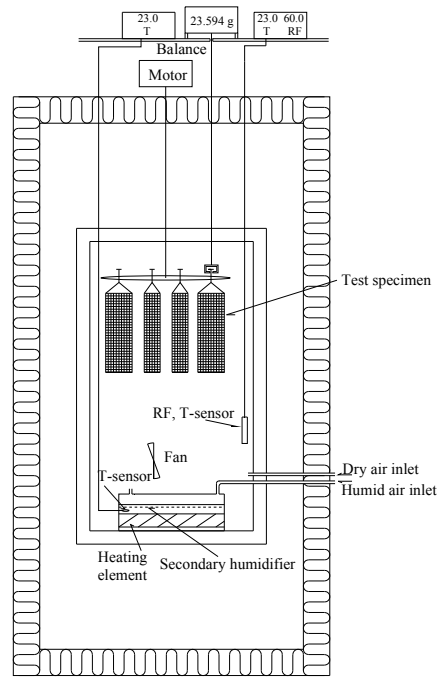
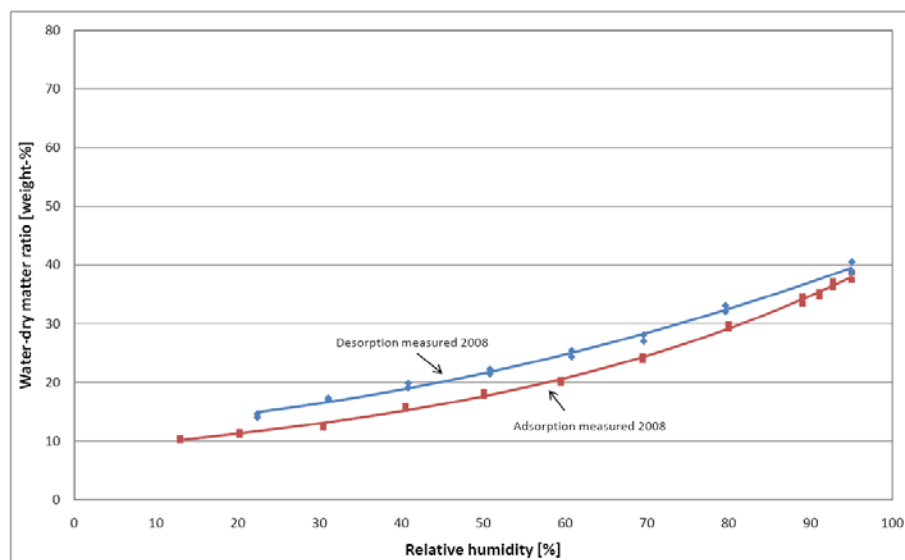*FIG. 3: Arrangement of bags with specimens in climatic chamber.*

FIG. 4: Sorption properties of washed sea grass dried at 105 °C.
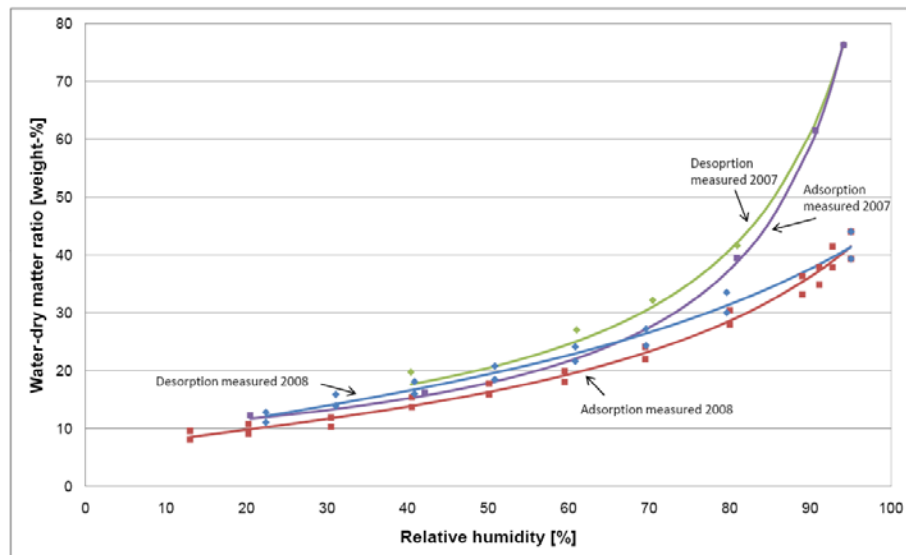
FIG. 5: Sorption properties of regular sea grass dried at 105 °C.

The results show that sea grass can be characterized as a hygroscopic material. It is seen from Figure 4 and 5 that the regular sea grass absorbs more water than the washed sea grass at a relative humidity above 70 %.

In Figure 5 the results of two separate experiments are shown, and as can be seen the difference in the results are significant. Yet, the specimens investigated are from the same batch of sea grass.

This difference between the measurements might also be caused by the lack of systematic processing of the sea grass, such as if it had been an industrial product, and therefore it may indeed be a rather inhomogeneous material with diverse hygroscopic properties.

5. Determination of water vapour transmission properties

Determination of the water vapour transmission of regular sea grass is performed using the wet cup method according to Hansen & Hansen (1999). However, since the sea grass is a loose fill material, the design of the cup used in this experiment is changed. Instead of the cup, a double bucket is used. In the bottom of the top bucket a fine mesh is placed to keep the specimen in place. The lower bucket is a cut off from the bottom of another bucket, and is used to contain a saturated salt solution. These two parts are fastened to each other using waterproof tape to seal the double bucket. At the top of the specimen inside the top bucket, a metal net is placed in order to keep compression on the specimen to achieve the desired density at 53 kg/m^3. The principle of the bucket and the arrangement can be seen in Figure 6.
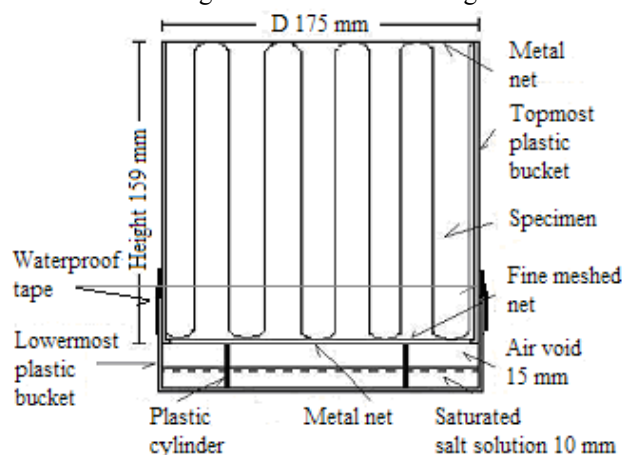

FIG. 6: Section of bucket used for determination of water vapour resistance (left) and photo of buckets in climatic chamber (right).

The results of the experiment can be seen in Table 1.

TABLE. 1: Water vapour resistance and permeability of regular sea grass.

Specimen	Specimen no. 1	Specimen no. 2	Specimen no. 3
Water vapour resistance Z_p [m²sGPa/kg]	1.4	1.3	1.4
Water vapour permeability δ_p 10^{-12} [kg/(m·s·Pa)]	113	124	116

6. Measurements in the field

In order to be able to investigate the actual temperature and relative humidity distribution in an exterior wall containing regular sea grass insulation at a density of 53 kg/m³, four test elements were built in a test shed where it was possible to control the indoor climate. The shed was located in an outdoor area at the Technical University of Denmark. Each element has the dimensions given in Figure 7 below. Five sensors of the type Sensirion SHT75 are placed in each element in order to measure temperature and relative humidity through the construction. The placement of the sensors can be seen as the dots also marked with A, B, C, D, and E in the cross sections of the elements.
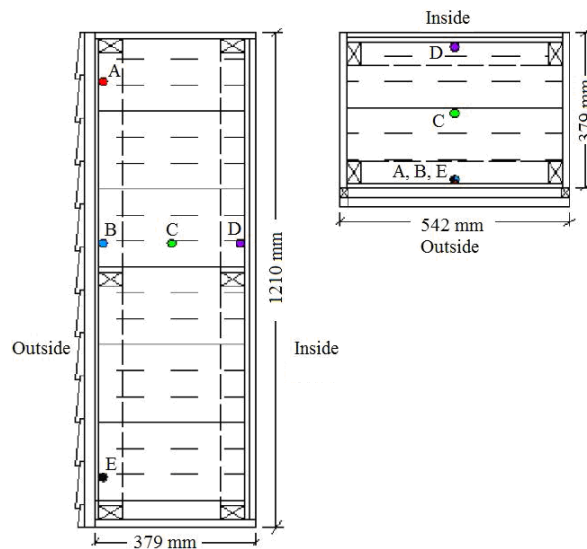

FIG. 7: Vertical and horizontal cross sections of test elements used for measurements in the field.

The different layers inside each of the four test elements are listed in Table 2. Element no. 1 is the reference element and only one parameter is changed for each element compared to this element.

TABLE 2: Description of test elements.

	Element no.1	Element no. 2	Element no. 3	Element no. 4
	Inside			
26 mm	Gypsum	Gypsum	Gypsum	Gypsum
	0.17 mm PE Vapour barrier	-	0.34 mm Eco-vapour retarder	0.17 mm PE Vapour barrier
343 mm	Regular sea grass	Regular sea grass	Regular sea grass	Glass wool
9.5 mm	Wind-proof gypsum	Wind-proof gypsum	Wind-proof gypsum	Wind-proof gypsum
25 mm	Ventilated void	Ventilated void	Ventilated void	Ventilated void
10.5 mm	Wood facing	Wood facing	Wood facing	Wood facing
	Outside			

The eco-vapour retarder used in element no. 3 consists of two layers of kraft paper unified with a mesh of fibreglass and polyethylene glue. The water vapour permeability is found to be $9.8 \cdot 10^{-5}$ µg/(m·s·Pa) using the cup method referred to in Section 5.

Investigations of relative humidity inside the constructions are interesting, since too high relative humidity will cause high moisture content for a shorter or longer period which can damage the surrounding construction as well as increase heat transmission through the construction. The measurements will show where high relative humidity occurs and for how long a period.

Temperature and relative humidity were measured in a winter period from 18th of December 2007 till 17th of January 2008. During this period the relative humidity indoors was kept at approximately 60 % and 20 °C to obtain a significant difference in vapour pressure between inside and outside and thereby increasing the moisture flow. Before the measurements began, the elements had been situated in the shed from February 2007. During this period the relative humidity and temperature were only held constant at 60 % and 20 °C respectively until May 2007.
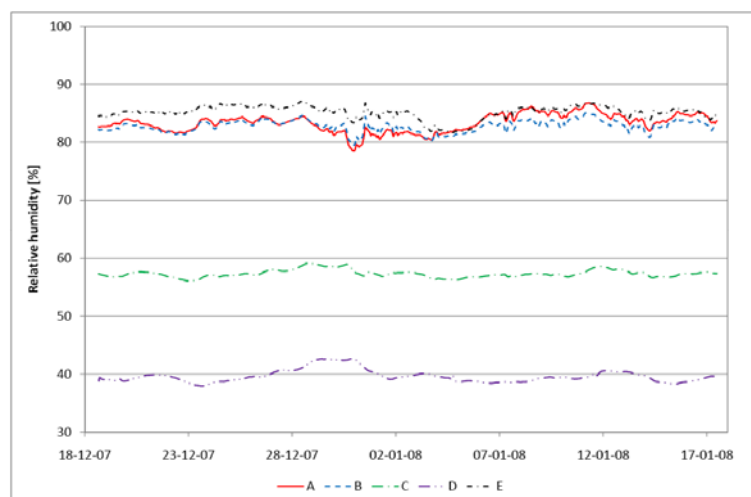

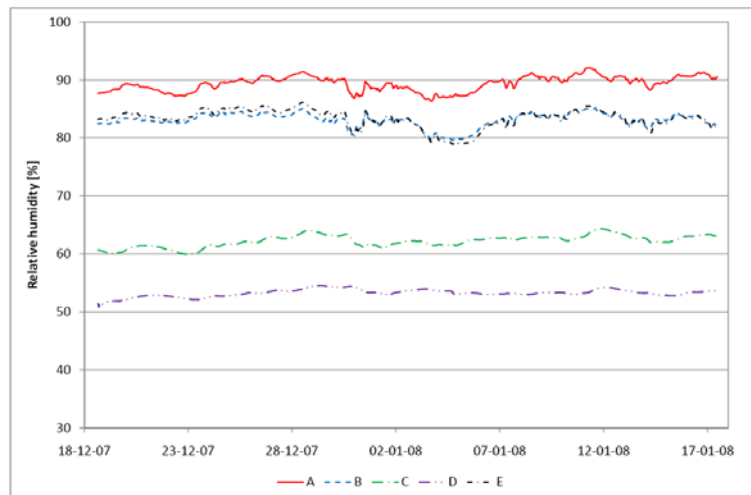*FIG. 8: Measured relative humidity in Element no. 1*

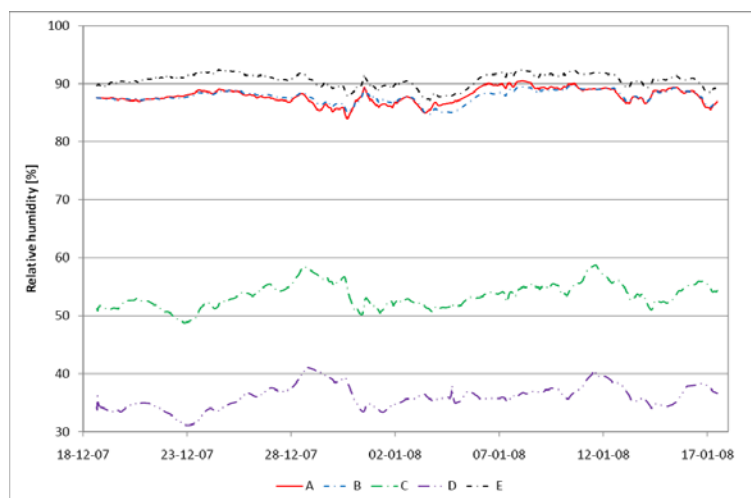FIG. 9: Measured relative humidity in Element no. 2.
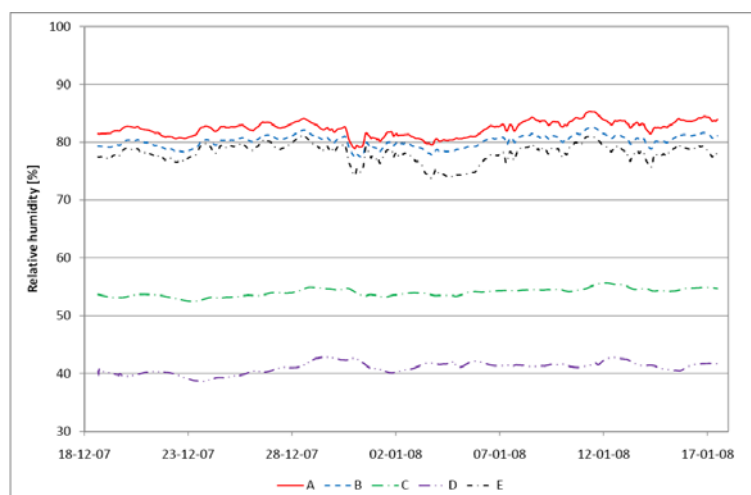

FIG. 10: Measured relative humidity in Element no. 3.

FIG. 11: Measurement of relative humidity in Element no. 4.

FIG. 12: Measured temperature and relative humidity in point A in all four elements.

As the period of measurement was not long, it is difficult to conclude if the high relative humidity which can be seen in the outer part of the construction will result in damage of the construction. When comparing the measurements, the results for Element no. 1 and no. 4 are similar compared to Element no. 2 and no. 3. However, the relative humidity in the element containing regular sea grass is slightly higher than seen in Element no. 4 containing glass wool. This tendency is also verified in Figure 12, where the relative humidity in point A for all elements is unified in one figure.

Also, it can be seen from Figure 12 that the relative humidity in the outer part of the construction is quite high. As the temperature is quite low, a sudden drop in temperature of only a few degrees could result in condensation and thereby possible damage to both the regular sea grass and wooden parts in the construction.

7. Conclusion

Through the experiments it is found that regular sea grass is a material with some parameters appropriate for thermal insulation. However, the high hygroscopicity for the regular sea grass, especially at high relative humidity, is of some concern due to the risk of rot in both the material as well as the wood in the construction. This might indicate that the regular sea grass should be further processed before it is used in constructions to avoid corrosion, due to the high salt content or other severe damage on the constructions. It is found, though, that the relative humidity in the outer part of element no. 1 is approximately at the same level as the relative humidity in element no. 4 containing glass wool, which is a commonly used insulation product. The thermal conductivity of regular sea grass is not quite as low as that of conventional insulation materials, but approaches desired values for an insulation product if the density is high.

8. References

Hansen E. J. de Place and Hansen K. K. (1999). Sorption isotherms – part of heat and moisture investigations of alternative insulation materials (in Danish) ISBN 87-7740-263-4.

ISO 12571 (2000). Hygrothermal performance of building materials and products – Determination of hygroscopic sorption properties.

ISO 12572 (2001). Hygrothermal performance of building materials and products – Determination of water vapour transmission properties.